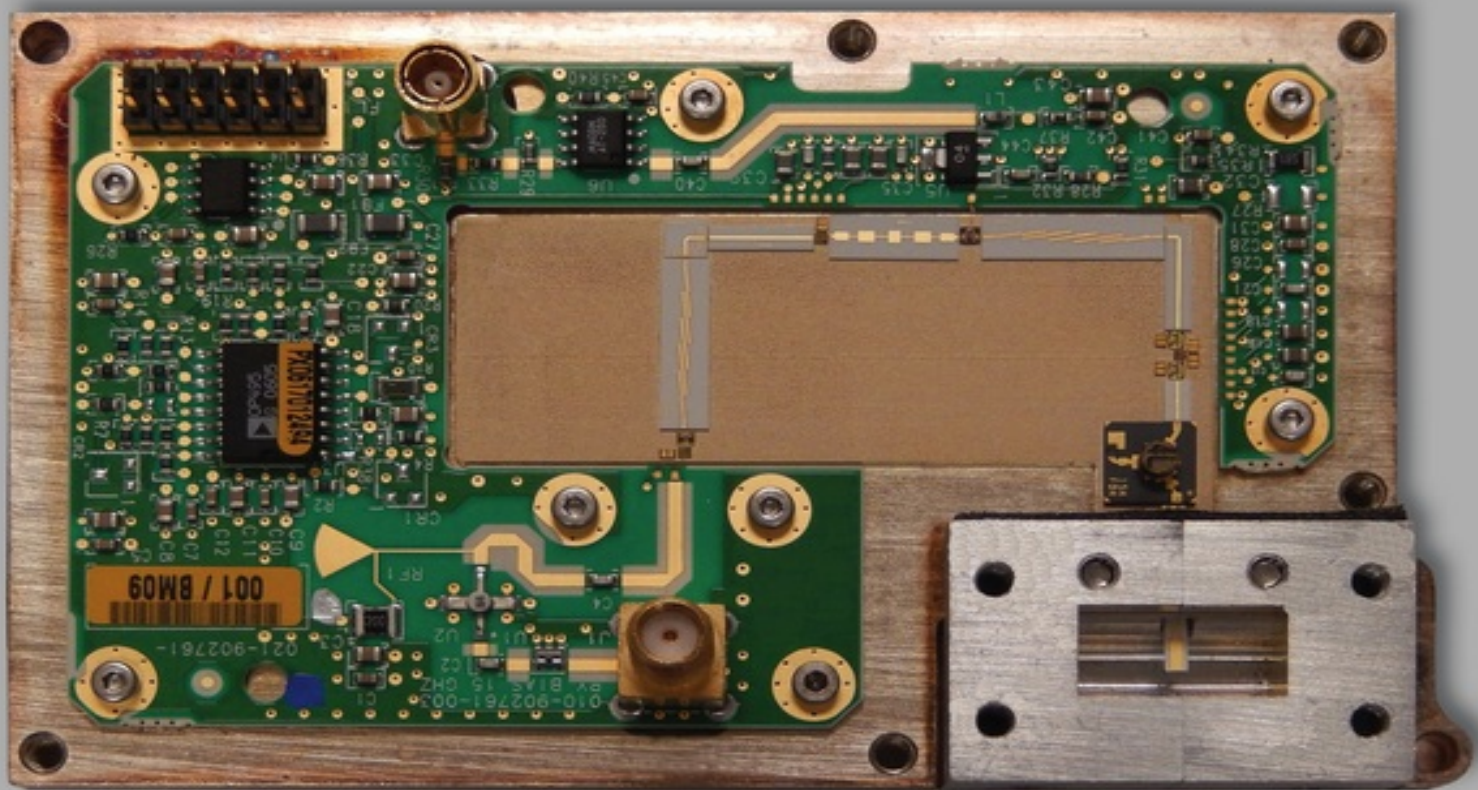


# FOUNDATIONS FOR MICROSTRIP CIRCUIT DESIGN

FOURTH EDITION

TERRY EDWARDS

MICHAEL STEER



# Table of Contents

[Cover](#)

[Title Page](#)

[Copyright](#)

[List of Trademarks](#)

[Dedication](#)

[Preface](#)

[Acknowledgements](#)

[Chapter 1: Introduction to Design Using Microstrip and Planar Lines](#)

[1.1 Introduction](#)

[1.2 Origins of Microstrip](#)

[1.3 RF and Microwave Modules](#)

[1.4 Interconnections on RF and Microwave Integrated Circuits](#)

[1.5 High-speed Digital Interconnections](#)

[1.6 Summary](#)

[References](#)

[Chapter 2: Fundamentals of Signal Transmission on Interconnects](#)

[2.1 Introduction](#)

[2.2 Transmission Lines and Interconnects](#)

[2.3 Interconnects as Part of a Packaging Hierarchy](#)

[2.4 The Physical Basis of Interconnects](#)

[2.5 The Physics, a Guided Wave](#)

[2.6 When an Interconnect Should be Treated as a Transmission Line](#)

[2.7 The Concept of RF Transmission Lines](#)

[2.8 Primary Transmission Line Constants](#)

[2.9 Secondary Constants for Transmission Lines](#)

[2.10 Transmission Line Impedances](#)

[2.11 Reflection](#)

[2.12 Multiple Conductors](#)

[2.13 Return Currents](#)

[2.14 Modeling of Interconnects](#)

[2.15 Summary](#)

## References

### Chapter 3: Microwave Network Analysis

3.1 Introduction

3.2 Two-port Networks

3.3 Scattering Parameter Theory

3.4 Signal-flow Graph Techniques and  $S$  Parameters

3.5 Summary

References

### Chapter 4: Transmission Line Theory

4.1 Introduction

4.2 Transmission Line Theory

4.3 Chain ( $ABCD$ ) Parameters for a Uniform Length of Loss-free Transmission Line

4.4 Change in Reference Plane

4.5 Working With a Complex Characteristic Impedance

4.6 Summary

References

### Chapter 5: Planar Interconnect Technologies

5.1 Introductory Remarks

5.2 Microwave Frequencies and Applications

5.3 Transmission Line Structures

5.4 Substrates for Planar Transmission Lines

5.5 Thin-film Modules

5.6 Thick-film Modules

5.7 Monolithic Technology

5.8 Printed Circuit Boards

5.9 Multichip Modules

5.10 Summary

References

### Chapter 6: Microstrip Design at Low Frequencies

6.1 The Microstrip Design Problem

6.2 The Quasi-TEM Mode of Propagation

6.3 Static-TEM Parameters

6.4 Effective Permittivity and Characteristic Impedance of Microstrip

6.5 Filling Factor

- [6.6 Approximate Graphically Based Synthesis](#)
- [6.7 Formulas for Accurate Static-TEM Design Calculations](#)
- [6.8 Electromagnetic Analysis-based Techniques](#)
- [6.9 A Worked Example of Static-TEM Synthesis](#)
- [6.10 Microstrip on a Dielectrically Anisotropic Substrate](#)
- [6.11 Microstrip and Magnetic Materials](#)
- [6.12 Effects of Finite Strip Thickness, Metallic Enclosure, and Manufacturing Tolerances](#)
- [6.13 Pulse Propagation along Microstrip Lines](#)
- [6.14 Recommendations Relating to the Static-TEM Approaches](#)
- [6.15 Summary](#)
- [References](#)

## [Chapter 7: Microstrip at High Frequencies](#)

- [7.1 Introduction](#)
- [7.2 Frequency-dependent Effects](#)
- [7.3 Approximate Calculations Accounting for Dispersion](#)
- [7.4 Accurate Design Formulas](#)
- [7.5 Effects due to Ferrite and to Dielectrically Anisotropic Substrates](#)
- [7.6 Field Solutions](#)
- [7.7 Frequency Dependence of Microstrip Characteristic Impedance](#)
- [7.8 Multimoding and Limitations on Operating Frequency](#)
- [7.9 Design Recommendations](#)
- [7.10 Summary](#)
- [References](#)

## [Chapter 8: Loss and Power-dependent Effects in Microstrip](#)

- [8.1 Introduction](#)
- [8.2  \$Q\$  Factor as a Measure of Loss](#)
- [8.3 Power Losses and Parasitic Effects](#)
- [8.4 Superconducting Microstrip Lines](#)
- [8.5 Power-handling Capabilities](#)
- [8.6 Passive Intermodulation Distortion](#)
- [8.7 Summary](#)
- [References](#)

## [Chapter 9: Discontinuities in Microstrip](#)

- [9.1 Introduction](#)
- [9.2 The Main Discontinuities](#)
- [9.3 Bends in Microstrip](#)
- [9.4 Step Changes in Width \(Impedance Step\)](#)
- [9.5 The Narrow Transverse Slit](#)
- [9.6 Microstrip Junctions](#)
- [9.7 Recommendations for the Calculation of Discontinuities](#)
- [9.8 Summary](#)
- [References](#)

## [Chapter 10: Parallel-coupled Microstrip Lines](#)

- [10.1 Introduction](#)
- [10.2 Coupled Transmission Line Theory](#)
- [10.3 Formulas for Characteristic Impedance of Coupled Lines](#)
- [10.4 Semi-empirical Analysis Formulas as a Design Aid](#)
- [10.5 An Approximate Synthesis Technique](#)
- [10.6 Summary](#)
- [References](#)

## [Chapter 11: Applications of Parallel-coupled Microstrip Lines](#)

- [11.1 Introduction](#)
- [11.2 Directional Couplers](#)
- [11.3 Design Example: Design of a 10 dB Microstrip Coupler](#)
- [11.4 Frequency- and Length-Dependent Characteristics of Directional Couplers](#)
- [11.5 Special Coupler Designs with Improved Performance](#)
- [11.6 Thickness Effects, Power Losses, and Fabrication Tolerances](#)
- [11.7 Choice of Structure and Design Recommendations](#)
- [11.8 Summary](#)
- [References](#)

## [Chapter 12: Microstrip Passive Elements](#)

- [12.1 Introduction](#)
- [12.2 Lumped Elements](#)
- [12.3 Terminations and Attenuators](#)
- [12.4 Microstrip Stubs](#)
- [12.5 Hybrids and Couplers](#)
- [12.6 Power Combiners and Dividers](#)

[12.7 Baluns](#)

[12.8 Integrated Components](#)

[12.9 Summary](#)

[References](#)

## [Chapter 13: Stripline Design](#)

[13.1 Introduction](#)

[13.2 Symmetrical Stripline](#)

[13.3 Asymmetrical Stripline](#)

[13.4 Suspended Stripline](#)

[13.5 Coupled Stripline](#)

[13.6 Double-sided Stripline](#)

[13.7 Discontinuities](#)

[13.8 Design Recommendations](#)

[13.9 Summary](#)

[References](#)

## [Chapter 14: CPW Design Fundamentals](#)

[14.1 Introduction to Properties of Coplanar Waveguide](#)

[14.2 Modeling CPWs](#)

[14.3 Formulas for Accurate Calculations](#)

[14.4 Loss Mechanisms](#)

[14.5 Dispersion](#)

[14.6 Discontinuities](#)

[14.7 Circuit Elements](#)

[14.8 Variants on the Basic CPW Structure](#)

[14.9 Summary](#)

[References](#)

## [Chapter 15: Slotline](#)

[15.1 Introduction](#)

[15.2 Basic Concept and Structure](#)

[15.3 Operating Principles and Modes](#)

[15.4 Propagation and Dispersion Characteristics](#)

[15.5 Evaluation of Guide Wavelength and Characteristic Impedance](#)

[15.6 Losses](#)

[15.7 End-effects: Open Circuits and Short Circuits](#)

[15.8 Summary](#)

[References](#)

## [Chapter 16: Slotline Applications](#)

[16.1 Introduction](#)

[16.2 Comparators and Couplers](#)

[16.3 Filter Applications](#)

[16.4 Magic T](#)

[16.5 The Marchand Balun](#)

[16.6 Phase Shifters](#)

[16.7 Isolators and Circulators](#)

[16.8 A Double-sided, Balanced Microwave Circuit](#)

[16.9 Summary](#)

[References](#)

## [Chapter 17: Transitions](#)

[17.1 Introduction](#)

[17.2 Coaxial-to-microstrip Transitions](#)

[17.3 Waveguide-to-microstrip Transitions](#)

[17.4 Transitions between CPW and other Mediums](#)

[17.5 Slotline Transitions](#)

[17.6 Other Microstrip Transitions](#)

[17.7 Summary](#)

[References](#)

## [Chapter 18: Measurements of Planar Transmission Line Structures](#)

[18.1 Introduction](#)

[18.2 Instrumentation Systems for Microstrip Measurements](#)

[18.3 Measurement of Scattering Parameters](#)

[18.4 Measurement of Substrate Properties](#)

[18.5 Microstrip Resonator Methods](#)

[18.6 Q Factor Measurements](#)

[18.7 Measurements of Parallel-coupled Microstrips](#)

[18.8 Time-domain Reflectometry Techniques](#)

[18.9 Summary](#)

[References](#)

## [Chapter 19: Filters Using Planar Transmission Lines](#)

[19.1 Introduction](#)  
[19.2 Filter Prototypes](#)  
[19.3 Microstrip Filters](#)  
[19.4 Microstrip Bandpass Filters](#)  
[19.5 Parallel-coupled Line Bandpass Filters](#)  
[19.6 Filter Design Accounting for Losses](#)  
[19.7 Dielectric Resonators and Filters Using Them](#)  
[19.8 Spurline Bandstop Filters](#)  
[19.9 Summary](#)  
[References](#)

## [Chapter 20: Magnetic Materials and Planar Transmission Lines](#)

[20.1 Introduction](#)  
[20.2 Microwave Magnetic Materials](#)  
[20.3 Effective Permeability of Magnetic Materials](#)  
[20.4 Microstrip on a Ferrite Substrate](#)  
[20.5 Isolators and Circulators](#)  
[20.6 Transmission Lines Using Metaconductors](#)  
[20.7 Frequency Selective Limiter](#)  
[20.8 Summary](#)  
[References](#)

## [Chapter 21: Interconnects for Digital Systems](#)

[21.1 Introduction](#)  
[21.2 Overview of On-chip Interconnects](#)  
[21.3 RC Modeling of On-chip Interconnects](#)  
[21.4 Modeling Inductance](#)  
[21.5 Clock Distribution](#)  
[21.6 Resonant Clock Distribution](#)  
[21.7 Summary](#)  
[References](#)

## [Appendix A: Physical and Mathematical Properties](#)

[A.1 SI Units](#)  
[A.2 SI Prefixes](#)  
[A.3 Physical and Mathematical Constants](#)  
[A.4 Basis of Electromagnetic SI Units](#)

[A.5 Relationship of SI Units to CGS Units](#)

[Appendix B: Material Properties](#)

[References](#)

[Appendix C: RF and Microwave Substrates](#)

[C.1 Hard substrates](#)

[C.2 Soft Substrates](#)

[Index](#)

[End User License Agreement](#)

## List of Illustrations

Chapter 1: Introduction to Design Using Microstrip and Planar Lines

[Figure 1.1 Microstrip transmission line.](#)

[Figure 1.2 Evolution of the stripline transmission line: \(a\) coaxial line with a round center conductor; \(b\) square coaxial line with a square center conductor; \(c\) rectangular coaxial line with a flat center conductor; and \(d\) stripline.](#)

[Figure 1.3 A 14.4–15.35 GHz receiver module itself consisting of cascaded modules interconnected by microstrip transmission lines. Surrounding the microwave circuit are DC conditioning and control circuitry. RF in is 14.4–15.35 GHz, LO in is 1600.625–1741.875 MHz. The frequency of the IF is 70–1595 MHz. © M. Steer, used with permission.](#)

[Figure 1.4 Microstrip bends: \(a\) detail of bend from the reference LO section of Figure 1.3; \(b\) layout representation of a microstrip transmission line; \(c\) microstrip rectangular bend; \(d\) partially mitered bend; and \(e\) mitered microstrip bend.](#)

[Figure 1.5 Frequency conversion section of the 15 GHz receiver of Figure 1.3: \(a\) annotated photograph; and \(b\) block diagram. The frequencies identified in \(a\) are the center frequency of the LO range \(1.67 GHz\) and the center frequency of the RF signal \(14.9 GHz\). The center frequency of the resulting IF signal is at 1.43 GHz. © M. Steer, used with permission.](#)

[Figure 1.6 Detail of the transition from softboard to the frequency conversion section. © M. Steer, used with permission.](#)

[Figure 1.7 Component sub-modules of the frequency conversion section of the 15 GHz receiver of Figure 1.5: \(a\) edge-coupled parallel-coupled microstrip line bandpass filter; \(b\) microstrip lowpass filter; and \(c\) microstrip mitered bend. © M. Steer, used with permission.](#)

[Figure 1.8 Bond structures: \(a\) wire bonds; and \(b\) ribbon bond. © M. Steer, used with permission.](#)

[Figure 1.9 IF section of the 15 GHz receiver of Figure 1.3: \(a\) annotated image; and \(b\) block diagram. © M. Steer, used with permission.](#)

[Figure 1.10 Channel arrangement of the 15 GHz fixed wireless service based on a 28 MHz channel spacing.](#)

[Figure 1.11 GaAs X-band MMIC 8–12 GHz amplifier showing the RF input,  \$RF^{IN}\$ , and output  \$RF^{OUT}\$ . S indicates a stub, SO indicates the output stub with a spiral inductor, and F indicates a feedback RF path with a spiral inductor.](#)

[Figure 1.12 A CPW with a strip carrying the signal current and the signal return on the ground strips on either side of the signal carrying strip: \(a\) CPW on the surface of a substrate; \(b\) a coaxial-to-CPW adaptor, a GSG probe, formed by extending and shaping the center conductor of a coaxial line, and welding needles to the outer conductor of the coaxial line shown here probing an integrated circuit.](#)

[Figure 1.13 Scanning electron micrograph of a silicon integrated circuit showing a multilevel interconnect structure of a digital chip. The first \(bottom\) level is tungsten, as are the vias. The other metal levels are copper. The perspective was obtained after removal by etching of the oxide dielectric. From IBM web page. © IBM, used with permission.](#)

## Chapter 2: Fundamentals of Signal Transmission on Interconnects

[Figure 2.1 Coaxial transmission line with a voltage source applying a pulse: \(a\) three-dimensional view; \(b\) its longitudinal cross-section; \(c\) the output of the pulse generator in time; and \(d\) the fields at the beginning of the line at time  \$t\_2\$ .](#)

[Figure 2.2 Coaxial transmission line with pulsed voltage source showing voltage at different times. The plus and minus signs indicate net charge.](#)

[Figure 2.3 Cross-sections of some common TEM-mode transmission lines: \(a\) parallel two-wire transmission line; \(b\) coaxial line; \(c\) stripline; and \(d\) perspective of a stripline.](#)

[Figure 2.4 Cross-sectional view of a microstrip interconnect: \(a\) the electric and magnetic field lines, and positive and negative charges; and \(b\) current flow. The electric and magnetic fields are in two mediums, the dielectric and air.](#)

[Figure 2.5 Cross-sectional view of the charge distribution on an interconnect at different frequencies: \(a\) DC; \(b\) 100 MHz; and \(c\) 1 GHz. The dots and crosses indicate charge concentrations of different polarity.](#)

[Figure 2.6 Dispersion of a pulse along an interconnect.](#)

[Figure 2.7 The uniform transmission line: \(a\) transmission line of length  \$l\$ ; and \(b\) primary constants assigned to a lumped-element model of a transmission line.](#)

[Figure 2.8 Notation applicable to a general, uniform line.](#)

[Figure 2.9 Line terminations: \(a\) short-circuit termination with  \$Z\_{SC}\$  being the](#)

impedance looking into the short-circuited line; and (b) open-circuit with  $Z_{oc}$  being the impedance looking into the open-circuited line.

Figure 2.10 Reflection of a pulse at a load that is lower in resistance than the characteristic impedance of the line.

Figure 2.11 Reflection of a pulse at a load that is higher in resistance than the characteristic impedance of the line.

Figure 2.12 Reflection of a pulse on an interconnect showing forward and backward traveling pulses.

Figure 2.13 A digital signal in an interconnect: (a) resulting from multiple reflections; and (b) sources of reflection.

Figure 2.14 Two parallel-coupled transmission lines.

Figure 2.15 Parallel-coupled coaxial lines: (a) fields; (b) even mode; and (c) odd mode. (For simplicity only the electric field is indicated in (b) and (c)).

Figure 2.16 Coupled microstrip lines in perspective.

Figure 2.17 Coupled microstrip lines showing the signal induced on the quiet (or victim) line due to a pulse on the driven line.

Figure 2.18 Signal paths going from an integrated circuit (IC) through a package to a printed circuit board.

Figure 2.19 Shared current return path forming a common impedance connection (a) and the voltage waveforms resulting (b).

Figure 2.20 A mixed signal system with (a) poor and (b) better isolation of analog and digital signal return paths.

Figure 2.21 RLC model (a) of an interconnect and (b) incorporating a driver and a receiver.

Figure 2.22 Cross-section of a microstrip interconnect with a passivation covering layer modeled as a simplified structure with an idealized zero thickness microstrip line and an improved structure with multiple zero thickness metal lines.

## Chapter 3: Microwave Network Analysis

Figure 3.1 A two-port network: (a) port voltages; and (b) with transmission lines at the ports.

Figure 3.2 Circuit equivalence of the  $z$  and  $y$  parameters for a reciprocal network: (a)  $z$  parameters; and (b)  $y$  parameters (in (b) the elements are admittances).

Figure 3.3 Cascade of two-port networks.

Figure 3.4 Two-port network with cascadable voltage and current definitions.

Figure 3.5 A two-port network.

[Figure 3.6 A two-port network with input and output reference transmission lines.](#)

[Figure 3.7 A two-port network showing forward- and backward-traveling waves on the reference transmission lines.](#)

[Figure 3.8 Two-port network with root power variables.](#)

[Figure 3.9 A shunt susceptance element with admittance  \$y = jB\$ .](#)

[Figure 3.10 An  \$N\$ -port network.](#)

[Figure 3.11 Two cascaded two-ports.](#)

[Figure 3.12 Two-port with parameters suitable for defining  \$S\$  and  \$ABCD\$  parameters.](#)

[Figure 3.13 Terminated two-port used to define return loss.](#)

[Figure 3.14 Two-port insertion and definition of variables for defining insertion loss: \(a\) source and load before insertion; and \(b\) insertion of two-port network with source level unchanged.](#)

[Figure 3.15 SFG showing distribution of input reflection and output transfer to the response leaving port 1 of a two-port network.](#)

[Figure 3.16 Complete SFG of a two-port network.](#)

[Figure 3.17 SFG representation of addition.](#)

[Figure 3.18 Cascade reduction of SFG: \(a\) three cascaded blocks; and \(b\) reduced form.](#)

[Figure 3.19 SFG simplification eliminating a variable.](#)

[Figure 3.20 SFGs having a self-loop: \(a\) original SFG; and \(b\) after eliminating  \$a\_2\$ .](#)

[Figure 3.21 SFG of \(a\) a self-loop; and \(b\) with the loop eliminated.](#)

## Chapter 4: Transmission Line Theory

[Figure 4.1 A two-port network with connecting transmission lines showing forward- and backward-traveling waves on the lines.](#)

[Figure 4.2 Standing wave pattern produced by a half-wave resonator.](#)

[Figure 4.3 Transmission line system with a single shunt stub.](#)

[Figure 4.4 Quarter-wave impedance transformer.](#)

[Figure 4.5 Equivalent two-port networks of a section of transmission line: \(a\) T network; and \(b\)  \$\pi\$  network.](#)

[Figure 4.6 Simple equivalent network of a transmission line segment with  \$\Delta L = L\ell\$  and  \$\Delta C = C\ell\$ .](#)

[Figure 4.7 A two-port transmission line network used to define  \$ABCD\$  parameters.](#)

[Figure 4.8 Two-port measurement setup: \(a\) a two-port comprising an embedded two-](#)

[port network and transmission line sections between reference planes 1 and 2; and \(b\) representation as cascaded two-port networks.](#)

## Chapter 5: Planar Interconnect Technologies

[Figure 5.1 Common transmission line structures suited to planar fabrication.](#)

[Figure 5.2 Cross-sections: \(a\) conventional CPW; and \(b\) “inverted-V” CPW showing vias connecting conductor layers.](#)

[Figure 5.3 Cross-section view of an interconnect on a PCB.](#)

[Figure 5.4 An MCM-D interconnect: \(a\) cross-section of the second layer; and \(b\) longitudinal view showing vias. Adapted from Lipa \*et al.\* \(1996\) \[48\], Figure 1, p. 123. Reprinted with permission of IEEE.](#)

[Figure 5.5 Measured characteristic impedance of the microstrip interconnects shown in Figure 5.4 for three different line widths: \(a\) with the lines on layer 1; and \(b\) with the lines on layer 2.](#)

[Figure 5.6 Conductive and dielectric attenuation constants,  \$\alpha\_C\$  and  \$\alpha\_D\$  respectively, of an interconnect on a two-layer MCM-D: \(a\) first-layer metallization \(layer 1\); and \(b\) second-layer metallization \(layer 2\). Adapted from Lipa \*et al.\* \(1996\) \[48\], Figure 4 and 5, p. 124. Reprinted with permission of IEEE.](#)

## Chapter 6: Microstrip Design at Low Frequencies

[Figure 6.1 Input network arrangement \(a\) and microstrip circuit \(b\) for a microwave transistor amplifier. The guide wavelength,  \$\lambda\_g\$ , is the wavelength of the signal on the microstrip line.](#)

[Figure 6.2 The general geometry of a microstrip line, including choice of coordinates.](#)

[Figure 6.3 Transverse cross-section of microstrip, showing the electric field.](#)

[Figure 6.4 Three-dimensional views of the magnetic \(a\) and electric \(b\) fields surrounding a shielded microstrip line. The magnetic field lines in \(a\) alternate between dashed and solid to aid in clarity. For simplicity, only the electric field in the air and on the left-hand side of the strip is shown in \(b\).](#)

[Figure 6.5 A typical transverse cross-section of a shielded microstrip line showing representative magnetic \( \$H\$ \) and electric \( \$E\$ \) fields.](#)

[Figure 6.6 Microstrip lines: \(a\) extremely wide \( \$w \gg h\$ \); and \(b\) extremely narrow \( \$w \ll h\$ \) lines.](#)

[Figure 6.7 Characteristic impedance of a microstrip line versus aspect ratios,  \$w/h\$ , for various substrate relative permittivities,  \$\epsilon\_r\$  \(From EM simulation\).](#)

[Figure 6.8 Effective permittivity of a microstrip line versus aspect ratios,  \$w/h\$ , for various substrate relative permittivities,  \$\epsilon\_r\$  \(From EM simulation\).](#)

[Figure 6.9 Normalized characteristic impedance and normalized effective permittivity](#)

of a microstrip line as a function of  $u = w/h$ .

Figure 6.10 Filling factor for a microstrip line versus aspect ratios,  $w/h$ , for various substrate relative permittivities,  $\epsilon_r$ . Results calculated using electromagnetic simulation except for the curve identified as ‘Formula’, which was calculated using Equation (6.32).

Figure 6.11 Curves for the graphical analysis or synthesis of microstrip:  $Z_{01}$  is the free-space characteristic impedance and  $q$  is the filling factor as a function of aspect ratio  $w/h$ . (Developed using Sonnet with a frequency of 100 MHz and the  $q$  curves evaluated with  $\epsilon_r = 10$ ).

Figure 6.12 Electric field distributions, in the transverse plane, applicable to microstrip on an anisotropic substrate (sapphire) for three shape ( $w/h$ ) ratios: (a) small, (b) moderate and (c) large. The  $z$  direction is out of the page.

Figure 6.13 Illustrating the concept of equivalent isotropic substrate relative permittivity ( $\epsilon_r$ ): (a) sapphire substrate; and (b) equivalent isotropic substrate.

Figure 6.14 Design curves for microstrip lines on a sapphire substrate (C axis perpendicular to the ground plane). Curve I uses  $\epsilon_{r,y}$  as “ $\epsilon_r$ ”. Curve II uses  $\epsilon_{r,eq}$  from Equation (6.55): (a) equivalent relative permittivity; (b) effective relative permittivity; and (c) characteristic impedance. Adapted from Owens *et al.* (1976) [20], Figure 6.3–6.5, pp. 502–503. Reproduced with permission of IEEE.

Figure 6.15 A model for microstrip on an anisotropic substrate with C axis perpendicular to the ground plane.

Figure 6.16 Changes in the distribution of electric field (transverse cross-section) as the thickness of microstrip is altered.

Figure 6.17 Cross-section of shielded microstrip:  $h' = a - h$ .

Figure 6.18 A microstrip circuit structure yielding substantial delay: (a) microstrip layout; and (b) equivalent circuit.

## Chapter 7: Microstrip at High Frequencies

Figure 7.1 The dispersive effect in any general structure or system, non-linearity when frequency  $f$  is plotted against wave number or phase coefficient  $\beta$ .

Figure 7.2 Transverse cross-section of shielded microstrip, showing the nomenclature. The strip is the conductor of width  $w$  and the ground plane is the bottom, grounded conductor.

Figure 7.3 Normalized current and charge magnitudes on an alumina microstrip line at 1 GHz: (a) normalized scale; (b) longitudinal current,  $i_z$ , on the strip and (c) on the ground plane; and (d) the charge on the strip and (e) on the ground plane.

Figure 7.4 Normalized current and charge magnitudes on an alumina microstrip line at 10 GHz: (a) normalized scale; (b) longitudinal current,  $i_z$ , on the strip and (c) on the

ground plane; and (d) the charge on the strip and (e) on the ground plane.

Figure 7.5 Normalized current and charge magnitudes in an alumina microstrip line at 30 GHz: (a) normalized scale; (b) longitudinal current,  $i_z$ , on the strip and (c) on the ground plane; and (d) the charge on the strip and (e) on the ground plane.

Figure 7.6 Normalized instantaneous current distribution on the microstrip line: (a) normalized scale; (b) magnitude of the longitudinal current,  $i_z$ , on the microstrip and (c) on the ground plane; and (d) magnitude of the transverse current,  $i_x$ , on the microstrip and (e) on the ground plane. In all cases an alumina substrate applies and the frequency is 30 GHz.

Figure 7.7 Normalized instantaneous charge distribution,  $q$ , on the microstrip line at 30 GHz: (a) scale; (b) strip; and (c) ground plane.

Figure 7.8 Dispersion of microstrip interpreted as an effective relative permittivity  $\epsilon_{\text{eff}}$  plotted to a base of frequency.

Figure 7.9 Steady-state description of the skin effect: (a) an electromagnetic wave from the left incident at the interface of air and a conductor; and (b) profiles of the electric field magnitude (top) and current magnitude (bottom) as the wave travels into the conductor.

Figure 7.10 Representation of a microstrip line as groups of current filaments.

Figure 7.11 Current density on the strip and finite-thickness ground plane shown in cross-section. Dark shading indicates the area of high current density and different scales are used for the current density on the strip and on the ground plane. Current density in the ground plane is much lower than in the strip.

Figure 7.12 Skin effect on the transverse current density in a strip of a microstrip transmission line for various thicknesses of strip,  $t$ , relative to a skin depth  $\delta_s$ : (a) is at DC; (b), (c), and (d) are for thicknesses near the skin depth; and (d) and (e) have the same thickness but the strips have different widths.

Figure 7.13 Getsinger's model for dispersion analysis: (a) actual microstrip; and (b) microstrip model. Adapted from Getsinger (1973) [37], Figure 2, p. 35. Reproduced with permission of IEEE.

Figure 7.14 A comparison of the results derived from five different dispersion calculation techniques for a microstrip line on a  $650 \mu\text{m}$  thick substrate with  $\epsilon_r = 9.9$ . Simulated results were obtained using SONNET.

Figure 7.15 Dispersion curves applicable to three microstrip lines on an alumina substrate ( $\epsilon_r = 9.9$ ).

Figure 7.16 Dispersion of microstrip with gold metallization on a  $127 \mu\text{m}$ -thick GaAs substrate with  $\epsilon_r = 13$  and a strip width of  $254 \mu\text{m}$ . Simulation results were obtained using SONNET. RMS error relative to EM simulation: Getsinger 1.4%, Kobayashi 0.8%, and Kirschning and Jansen 0.2%.

Figure 7.17 Frequency dependence of the real and imaginary parts of  $Z_0$  of a gold microstrip line and alumina substrate with  $\epsilon_r(\text{DC}) = 9.9$  and  $w = h = 635 \mu\text{m}$ .

Figure 7.18 Frequency dependence of the real and imaginary parts of  $\epsilon_{\text{eff}}$  of a gold microstrip line and alumina substrate with  $\epsilon_r(\text{DC}) = 9.9$  and  $w = h = 635 \mu\text{m}$ .

Figure 7.19 Comparative dispersion curves for microstrip on a GaAs substrate ( $\epsilon_r = 13$ ,  $w = 0.254 \text{ mm}$ ,  $h = 0.127 \text{ mm}$ ). Simulated results were calculated using SONNET.

Figure 7.20 Microstrip propagation coefficient as a function of frequency. Adapted from Hsia *et al.* (1990) [45], Figure 2(a), p. 667. Reproduced with the permission of IEEE.

Figure 7.21 Effective permittivity for shielded microstrip. Adapted from Dumbell *et al.* (1989) [60], Figure 5, p. 764. Reproduced with the permission of the European Microwave Association.

Figure 7.22 Effective permittivity for shielded microstrip with dielectric overlay. Adapted from Dumbell *et al.* (1989) [60], Figure 7, p. 765. Reproduced with the permission of the European Microwave Association.

Figure 7.23 Simulation results for the propagation of a 35 ps single-sided exponential pulse along  $50 \Omega$  microstrip lines on a GaAs substrate. Adapted from Qian and Yamashita (1990) [61], Figure 3, p. 954. Reproduced with permission of IEEE.

Figure 7.24 Planar waveguide model for microstrip.

Figure 7.25 Transverse resonance: standing wave ( $|E_y|$ ) and equivalent transmission line of “length” ( $w + 2d$ ).

Figure 7.26 An (isotropic) substrate viewed as a dielectric slab, showing the nomenclature.

Figure 7.27 Eigenvalue solutions for TM waves for various normalized substrate thickness,  $h/\lambda_0$ .

Figure 7.28 TM threshold excitation frequency  $f_{\text{TEM},1}$  as a function of substrate thickness  $h$  and relative permittivity  $\epsilon_r$ .

## Chapter 8: Loss and Power-dependent Effects in Microstrip

Figure 8.1 Parallel (a) and series (b) resonant circuits.

Figure 8.2 Transfer characteristic of resonant circuit.

Figure 8.3 Gap coupled quarter-wave section.

Figure 8.4 Open-circuited microstrip resonator.

Figure 8.5 Reflection diagram.

Figure 8.6 Parameters governing the choice of substrate for any microstrip application: acceptable  $Q$  factor, operating frequency, substrate thickness, and relative permittivity

$\epsilon_r$ . Adapted from Vendelin (1970) [1], Figure 2, p. 65. Reprinted with permission of Horizon House.

Figure 8.7 Power losses versus frequency for open-end discontinuity ( $\epsilon_r = 10.2$ ,  $w = 0.610 \text{ mm}$ ,  $h = 0.635 \text{ mm}$ ). Adapted from Horng *et al.* (1990) [9], Figure 5, p. 1804. Reprinted with permission of IEEE.

Figure 8.8 Losses in microstrip on a GaAs substrate (350  $\mu\text{m}$  width on 100  $\mu\text{m}$  GaAs). The lines are simulated data. Adapted from Goldfarb and Platzker (1990) [10], Figure 5, p. 1959. Reprinted with permission of IEEE.

Figure 8.9 Attenuation coefficients at 77 K for superconducting and aluminum microstrip lines. Adapted from Lee *et al.* (1989) [22], Figure 2, p. 759. Reprinted with permission of the European Microwave Association.

Figure 8.10 Phase velocities at 77 K for superconducting and aluminum microstrip lines. Adapted from Lee *et al.* (1989) [22], Figure 3, p. 759. Reprinted with permission of the European Microwave Association.

Figure 8.11 Spectrum at the output of a transmission line generating PIM distortion tones. The input of the line consists of two discrete tones.

Figure 8.12 Microstrip transmission line showing the skin effect region in which heat is generated. Adapted from Wilkerson *et al.* (2011) [27], Figure 1, p. 1191. Reproduced with permission of IEEE.

Figure 8.13 Comparison of measured and modeled PIM on a microstrip transmission line. Adapted from Wilkerson *et al.* (2011) [27], Figure 8, p. 1198. Reproduced with permission of IEEE.

## Chapter 9: Discontinuities in Microstrip

Figure 9.1 Layout of a simple hybrid microwave amplifier using a GaAs MESFET, showing several discontinuities in the microstrip lines (DC bias filters are not shown).

Figure 9.2 Microstrip open circuit and gap: (a) layout with electric fields; and (b) equivalent lumped capacitive network.

Figure 9.3 Development of the equivalent end-effect length concept: (a) physical transmission line; (b) transmission line with equivalent end fringing capacitance  $C_f$ ; and (c) transmission line with equivalent extra transmission line of length  $\ell_{eo}$ .

Figure 9.4 Normalized end-effect length ( $\ell_{eo}/h$ ) as a function of shape ratio  $w/h$  for  $\epsilon_r = 11.0$ .

Figure 9.5 The series gap and its equivalent lumped circuit: (a) physical arrangement; and (b) lumped capacitive equivalent circuit.

Figure 9.6 A shunt metallized hole which may form a short circuit in a microstrip line.

Figure 9.7 Right-angled microstrip bend: (a) structure and nomenclature; and (b)

[equivalent circuit](#).

[Figure 9.8 Lumped equivalent circuit for the microstrip bend calculated in the text.](#)

[Figure 9.9 Mitered, right-angled bend together with its equivalent circuit and parameter variations \(as a function of the amount of miter\): \(a\) structure and nomenclature; \(b\) equivalent circuit; and \(c\) parameter trends as a function of chamfer fraction \( \$1 - b/\sqrt{2w}\$ \). \(c\) adapted from Easter \*et al.\* \(1978\) \[17\], Figure 11, p. 80. Reprinted with permission of IEEE.](#)

[Figure 9.10 Magnitude of the current densities on \(a\) a right-angled bend and \(b\) an optimally mitered bend \(in both cases on alumina substrate at 10 GHz\). The dark region corresponds to low current density.](#)

[Figure 9.11 Magnitude of the \(a\) horizontal and \(b\) vertical current densities on an optimally mitered right-angled bend under the same conditions as those shown in Figure 9.10.](#)

[Figure 9.12 Magnitude of the \(a\) horizontal and \(b\) vertical current densities on a right-angled bend under the same conditions as those shown in Figure 9.10.](#)

[Figure 9.13 Structure and equivalent circuit of the symmetrical microstrip step \(change in width\): \(a\) structure and nomenclature; and \(b\) equivalent circuit.](#)

[Figure 9.14 The symmetrical step, parameter variations: \(a\) capacitance; and \(b\) inductance for  \$w\_1/h = 1.0\$  and  \$Z\_{01} = 50 \Omega\$ . \(a\) adapted from Benedek and Silvester \(1972\) \[9\], Figure 8, p. 733. Reprinted with permission from IEEE. \(b\) adapted from Thomson \*et al.\* \(1976\) \[18\], Figure 4, p. 653. Reprinted with permission of IEEE.](#)

[Figure 9.15 Magnitude of the current densities for symmetrical step in width: \(a\) normalized scale \(b\) longitudinal current; and \(c\) transverse current. The signal is 10 GHz and the microstrip line is on alumina.](#)

[Figure 9.16 Structure and equivalent circuit of the asymmetrical microstrip step.](#)

[Figure 9.17 The narrow transverse slit: \(a\) actual slit; and \(b\) equivalent circuit.](#)

[Figure 9.18 The T junction in microstrip: \(a\) structure and nomenclature; and \(b\) equivalent circuit.](#)

[Figure 9.19 Parameter trends for the T junction: \(a\)  \$\epsilon\_r = 9.9\$ ; and \(b\)  \$\epsilon\_r = 9.8\$  \(a\) Adapted from Silvester and Benedek \(1973\) \[12\], Figure 8, p. 345. Reprinted with permission of IEEE. \(b\) Adapted from Easter \*et al.\* \(1978\) \[17\], Figure 17, p. 82. Reprinted with permission of the Institution of Engineering and Technology.](#)

[Figure 9.20 T junction: \(a\) reference planes,  \$T\_1\$  and  \$T\_2\$ , effective width  \$w\_{\text{eff1}}\$ , and dimensions; \(b\) model of T junction; and \(c\) model connected to transmission lines.](#)

[Figure 9.21 A compensated form of T junction.](#)

[Figure 9.22 The asymmetric cross-over junction: \(a\) structure; and \(b\) equivalent](#)

circuit.

Figure 9.23 Magnitude of the current densities on the strips of a symmetrical cross-over junction: (a) normalized scale; (b) current on the top metal; and (c) current on the lower metal layer (between the top metal and the ground plane).

Figure 9.24 Instantaneous current and charges on the strips of a symmetrical cross-over junction: (a) normalized current scale; (b) normalized charge scale; (c) current on the top metal; (d) charge on the top metal; (e) current on the lower metal; and (f) charge on the lower metal.

Figure 9.25 Open-circuit normalized equivalent end-effect length ( $\ell_{eo}/h$ ) as a function of frequency. The data refer to a  $t = 0.65$  mm thick alumina substrate with  $\epsilon_r = 10$ , except for one case where the values were  $t = 0.5$  mm and  $\epsilon_r = 11$ , as indicated. Adapted from James and Henderson (1979) [25], Figure 10, p. 214. Reprinted with permission of IET.

Figure 9.26 Radiation conductance  $G_{oc}$  and normalized capacitance  $C_{oc}/w$  of an open-circuited microstrip line as functions of frequency ( $\epsilon_r = 9.6$ ,  $w/h = 1$ ,  $h = 0.6$  mm). Adapted from Katehi and Alexopoulos (1985) [27], Figure 4, p. 1032. Reprinted with permission of IEEE.

Figure 9.27 Gap-discontinuity radiation conductances  $G_g$  and  $G_p$ , and normalized capacitances  $C_g/w$  and  $C_p/w$  as functions of frequency ( $\epsilon_r = 9.6$ ,  $w/h = 1$ ,  $h = 0.6$  mm,  $s/h = 0.3762$ ). Adapted from Katehi and Alexopoulos (1985) [27], figure 7, p. 1032. Reprinted with permission of IEEE.

Figure 9.28 Open-circuit normalized excess length and normalized capacitances as functions of frequency ( $\epsilon_r = 9.6$ ,  $w/h = 1$ ,  $h = 0.6$  mm). Adapted from Katehi and Alexopoulos (1985) [28], figure 8, p. 1033. Reprinted with permission of IEEE.

Figure 9.29 Gap-discontinuity normalized capacitances  $C_p/w$  and  $C_g/w$  as functions of frequency ( $\epsilon_r = 9.6$ ,  $w/h = 1$ ,  $h = 0.6$  mm,  $s/h = 0.3762$ ). Adapted from Katehi and Alexopoulos (1985) [27], Figure 9, p. 1033. Reprinted with permission of IEEE.

Figure 9.30 Right-angled single bend: (a) direct (i.e., unmitered); (b) mitered; and (c) double-mitered. The phase reference point is chosen at the center of the straight bend.

Figure 9.31 Magnitude of  $S$  parameters of a right-angle crossing junction ( $\epsilon_r = 10.2$ ,  $h = 0.635$  mm,  $w = 0.61$  mm). Adapted from Wu *et al.* (1990) [36], Figure 8, p. 1841. Reprinted with permission of IEEE.

Figure 9.32 Variations in  $|S_{11}|$  of a right-angle bend for cut ratio (degree of miter)  $R = 0, 0.5, 0.8, 1.2$ .  $W_{1,\text{eff}} = W_{2,\text{eff}} = 1.882$  mm,  $d = 0.65$  mm,  $\epsilon_r = 2.53$ . Adapted from Chang *et al.* (1989) [37], Figure 3, p. 977. Reprinted with permission of the European Microwave Association.

Figure 9.33 Lumped equivalent model for cross-junction discontinuity.

Figure 9.34 The radial microstrip bend: (a) physical; (b) equivalent lumped model; and

### (c) waveguide model.

Figure 9.35 Return loss for  $50 \Omega$ ,  $90^\circ$  bends with  $R = 2w$  on MIC (0.635 mm thick alumina) and MMIC (0.1 mm thick GaAs) substrates. Adapted from Weisshaar *et al.* (1990) [39], Figure 2, p. 1054. Reprinted with permission of IEEE.

Figure 9.36 Normalized radiation loss for  $50 \Omega$  bends with  $R = 2w$  on MIC (0.635 mm thick alumina) and MMIC (0.1 mm thick GaAs) substrates. Adapted from Weisshaar *et al.* (1990) [39], Figure 4, p. 1054. Reprinted with permission of IEEE.

Figure 9.37 Rounding and tapering techniques that may be applied to reduce the discontinuity effects associated with: (a) bends; (b) T junctions; and (c) step in width.

## Chapter 10: Parallel-coupled Microstrip Lines

Figure 10.1 A pair of parallel, edge-coupled microstrip lines.

Figure 10.2 Coupled microstrip lines in perspective.

Figure 10.3 Two parallel-coupled transmission lines.

Figure 10.4 Parallel-coupled coaxial lines: (a) showing fields; (b) even mode; and (c) odd mode. For simplicity only the electric field is indicated in (b) and (c).

Figure 10.5 Terminated coupled-line configuration.

Figure 10.6 Even and odd mode coupled-line representations: (a) even mode; and (b) odd mode.

Figure 10.7 Cross-section of three-line structure with four conductors.

Figure 10.8 Combinations of conductors leading to various capacitance measurements.

Figure 10.9 Field distributions resulting from (a) even-mode and (b) odd-mode excitation of parallel-coupled microstrip lines.

Figure 10.10 Cross-sectional dimensions: nomenclature.

Figure 10.11 Numerical results for the even- and odd-mode characteristic impedances of parallel-coupled microstrip lines: (a)  $\epsilon_r = 1$ ; and (b)  $\epsilon_r = 9$ . Adapted from Bryant and Weiss (1968) [3], Figure 6.7, p. 1025. Reprinted with permission of IEEE.

Figure 10.12 Normalized even-mode and odd-mode characteristic impedances of a pair of coupled microstrip lines.

Figure 10.13 Normalized characteristic impedance and normalized effective permittivity of a microstrip line as a function of  $u = w/h$ . The effective permittivity of an individual microstrip line with the same width  $u$  is  $\epsilon_{eff}$ .

Figure 10.14 Normalized even-mode and odd-mode effective permittivity of a pair of coupled microstrip lines. These results are for all  $\epsilon_r$ .

Figure 10.15 Normalized even-mode and odd-mode effective permittivity of a pair of coupled microstrip lines for extremes of  $u$ . Each family of three curves (almost on top

of each other) is for  $\epsilon_r = 4, 10$ , and  $20$ .  $Z_0$  is the characteristic impedance of an individual microstrip line with the same normalized width  $u$ .

Figure 10.16 Normalized even-mode and odd-mode effective permittivity of a pair of coupled microstrip lines with normalized width  $u = 0.5$  as a function of normalized gap spacing  $g$ .

Figure 10.17 Separation of capacitances for use in the analysis: (a) even-mode capacitances; and (b) odd-mode capacitances.

Figure 10.18 “General” curves for use in the synthesis technique.  $w/h|_{\text{single}}$  is the aspect ratio ( $w/h$ ) from a single microstrip line design procedure. Adapted from Akhtarzad *et al.* (1975) [15], Figure 3, p. 487. Reprinted with permission of IEEE.

## Chapter 11: Applications of Parallel-coupled Microstrip Lines

Figure 11.1 Directional couplers: (a) schematic; and (b) backward-coupled microstrip.

Figure 11.2 Illustration of the defining parameters for coupled transmission lines:  $C$ , coupling factor;  $T$ , transmission factor; and  $D$ , directivity factor.

Figure 11.3 Graphical design procedure yielding the shape ratios for a 10 dB microstrip directional coupler.

Figure 11.4 Parallel-coupled microstrips with the substrate (a) present and (b) absent (only the odd mode is indicated).

Figure 11.5 Final numerical dimensional values for the -10 dB coupler design shown in the text.

Figure 11.6 The characteristic shape of the frequency response for a loosely coupled ideal matched coupler.

Figure 11.7 A four-finger Lange coupler: (a) microstrip layout; and (b) circuit symbol.

Figure 11.8 The “unfolded” Lange coupler.

Figure 11.9 Parallel-coupled microstrips with a grounded shielding top plate.

Figure 11.10 Parallel-coupled microstrips with overlaid dielectric compensation. The substrate and overlay have the same permittivity.

Figure 11.11 Schematic illustration of parallel-coupled lines with lumped capacitors bridging the ends to provide compensation: (a) coupled lines; and (b) coupled lines with capacitors.

Figure 11.12 Schematic diagram of a quadruplexer using four 3 dB hybrids.

Figure 11.13 A plan schematic view of a single section semi-re-entrant coupler.

Figure 11.14 A cross-sectional view of a semi-re-entrant coupled section.

Figure 11.15 The plan-schematic view of a five-section directional coupler.

[Figure 11.16 Microstrip re-entrant mode coupler cross-section.](#)

[Figure 11.17 Geometry of a microstrip patch coupler.](#)

[Figure 11.18 The general layout of a planar combline directional coupler.](#)

## Chapter 12: Microstrip Passive Elements

[Figure 12.1 Segment of a 15 GHz microstrip circuit showing passive elements including stubs, bends, surface-mount resistors, transistor, capacitors, and inductor.](#)

[Figure 12.2 Lumped capacitors for microstrip circuits: \(a\) gap capacitor; \(b\) extended gap capacitor; \(c\) interdigitated capacitor; \(d\) another interdigitated capacitor; and \(e\) surface-mount chip capacitor.](#)

[Figure 12.3 A spiral inductor: \(a\) plan view; and \(b\) side view.](#)

[Figure 12.4 A microstrip toroidal inductor fabricated on a silicon circuit board: \(a\) layout view; and \(b\) response. From Liu \*et al.\* \(2004\) \[8\], Figure 6, 8, p. 649, 652. Used with permission of IEEE.](#)

[Figure 12.5 A microstrip solenoidal inductor fabricated on a silicon circuit board: \(a\) layout of a three-turn inductor; and \(b\) measured response of a three-turn inductor \(the thin lines are the simulated responses\). Adapted from Feng \*et al.\* \(2007\) \[9\], Figure 6, p. 1907. Reprinted with permission of IEEE.](#)

[Figure 12.6 A microstrip solenoidal transformer fabricated on a silicon circuit board: \(a\) layout of a three-turn inductor; \(b\) transformer circuit element showing the orientation of the winding connections; and \(c\) measured response of a four-turn transformer.](#)

[Figure 12.7 Network and microstrip circuit layout for a  \$\pi\$ -type attenuator: \(a\) circuit topology; and \(b\) microstrip circuit with open-circuited stubs.](#)

[Figure 12.8 Various representations of an open-circuit microstrip stub: \(a\) longitudinal section; \(b\) layout view; transmission line model; \(d\) compact transmission line model; \(e\) alternative compact transmission line; and \(f\) shunt stub.](#)

[Figure 12.9 Various representations of a short-circuit microstrip stub: \(a\) longitudinal section; \(b\) layout view; transmission line model; \(d\) compact transmission line model; and \(e\) shunt stub.](#)

[Figure 12.10 Microstrip radial stubs: \(a\) series connected; \(b\) shunt connected; and \(c\) butterfly structure.](#)

[Figure 12.11  \$S\$  parameters of the radial stub. Alumina substrate,  \$\epsilon\_r = 9.768\$  \(measured\), height  \$h = 0.635\$  mm, width  \$w = 0.61\$  mm, gap = 0.61 mm, radius = 3.253 mm: \(a\)  \$|S\_{21}|\$  and \(b\)  \$\angle S\_{21}\$ . Adapted from Rittweger and Wolff \(1990\) \[21\], Figure 1, p. 1149. Reprinted with permission of IEEE.](#)

[Figure 12.12 Ring form of microstrip 3 dB branch-line directional coupler.](#)

[Figure 12.13](#) Balanced mixer circuit based on the structure of Figure 12.12: (a) schematic layout; and (b) microstrip circuit with surface-mount diodes.

[Figure 12.14](#) Two-branch coupler with two-fold symmetry ( $\theta_{1,2}$  = line lengths,  $Z_{1,2}$  = characteristic impedances). Adapted from Mayer and Knochel (1990) [22], Figure 1, p. 393. Reprinted with permission of IEEE.

[Figure 12.15](#) Extended two-branch coupler with open stubs at the symmetry planes. Adapted from Mayer and Knochel (1990) [22], Figure 2, p. 393. Reprinted with permission of IEEE.

[Figure 12.16](#) Broadbanded  $0^\circ/180^\circ$  coupler. Adapted from Knochel and Mayer (1990) [23], Figure 6, p. 473. Reprinted with permission of IEEE.

[Figure 12.17](#) Conventional and port-interchanged rat-race hybrids: (a) circuit diagram of a conventional rat-race hybrid; (b) circuit diagram of a port-interchanged rat-race hybrid. Adapted from Nakamoto *et al.* (1989) [27], Figure 1, p. 314. Reprinted with permission of the European Microwave Association.

[Figure 12.18](#) Rat-race or hybrid-ring coupler.

[Figure 12.19](#) Wilkinson combiner: (a) circuit schematic; and (b) microstrip implementation.

[Figure 12.20](#) Chireix combiner.

[Figure 12.21](#) Branch-line directional coupler in MIC form: (a) microstrip layout; (b) odd-mode equivalent circuit; and (c) even-mode equivalent circuit.

[Figure 12.22](#) Circuit construction and cross-sectional views of baluns: (a) circuit construction of monolithic or hybrid balun; and (b) typical balun structure cross-section. Adapted from Pavio and Kikel (1990) [40], Figure 2 and 3, p. 484. Reprinted with permission of IEEE.

[Figure 12.23](#) Planar baluns: circuit cell and cross-sections: (a) planar balun circuit cell; and (b) cross-section of a circuit cell. Adapted from Barber (1990) [41], Figure 1 and 2, p. 496. Reprinted with permission of IEEE.

## Chapter 13: stripline design

[Figure 13.1](#) Stripline circuit: (a) symmetrical stripline; and (b) asymmetrical stripline; (c) stripline cross-over.

[Figure 13.2](#) Symmetrical stripline circuit (3D view).

[Figure 13.3](#) Fringe capacitance at the corners of the strip in stripline transmission lines.

[Figure 13.4](#) High-Q suspended stripline, the strip is supported by a membrane.

[Figure 13.5](#) Cross-section of an asymmetrical stripline.

[Figure 13.6](#) Edge-coupled striplines: (a) cross section; and (b) nomenclature.

[Figure 13.7 Broadside-coupled striplines: \(a\) thick strips; and \(b\) nomenclature.](#)

[Figure 13.8 Doubled-sided parallel stripline: \(a\) aligned; and \(b\) offset.](#)

[Figure 13.9 Cross-section of an asymmetrical stripline.](#)

[Figure 13.10 Right-angled stripline bend: \(a\) structure and nomenclature; and \(b\) equivalent circuit.](#)

[Figure 13.11 Striplines with ground-plane vias.](#)

## Chapter 14: CPW Design Fundamentals

[Figure 14.1 Structure of \(a\) slotline; and \(b\) differential line or CPS.](#)

[Figure 14.2 Structure of a CPW: \(a\) conventional; and \(b\) FGCPW.](#)

[Figure 14.3 Instantaneous normalized current magnitude and charge distribution along a CPW line along with respective normalized scales: \(a\) longitudinal current; \(b\) transverse current; and \(c\) charge. The current and charge are normalized and use the scale shown on the left-hand side. The maximum of the transverse current is 500 times smaller than that of the longitudinal current. \(The line is 1 mm long, the frequency is 100 GHz,  \$s = 10 \mu\text{m}\$ , and  \$w = 20 \mu\text{m}\$ \).](#)

[Figure 14.4 Expanded view, current magnitude, and charge distribution along a CPW line: \(a\) longitudinal current; \(b\) transverse current; and \(c\) charge.](#)

[Figure 14.5 Asymmetric CPW.](#)

[Figure 14.6 CPW with an intervening  \$\text{SiO}\_2\$  layer. HR, high resistivity.](#)

[Figure 14.7 Dispersion in a  \$39 \Omega\$  CPW on alumina \( \$\epsilon\_r = 9.5\$ ,  \$h = 0.635 \text{ mm}\$ \).](#)

[Figure 14.9 Dispersion in a  \$70 \Omega\$  CPW on alumina \( \$\epsilon\_r = 9.5\$ ,  \$h = 0.635 \text{ mm}\$ \).](#)

[Figure 14.10 Dispersion of CPW on GaAs with no backing: \(a\) effective permittivity; and \(b\) characteristic impedance.](#)

[Figure 14.11 Dispersion of CPW on GaAs ignoring dielectric and metallic losses.](#)

[Figure 14.12 CPW on GaAs with lossy gold metallization and ignoring dielectric losses, showing real  \$\epsilon\_{\text{eff}}\$  and  \$Z\_0\$ .](#)

[Figure 14.13 CPW on lossy GaAs with  \$3 \mu\text{m}\$  of covering polyimide.](#)

[Figure 14.14 CPW on GaAs: variation of parameters with  \$h\$ .](#)

[Figure 14.15 CPW on GaAs: variation of parameters with coplanar ground plane width  \$w\_1\$ .](#)

[Figure 14.16 CPW on standard silicon with loss included.](#)

[Figure 14.17  \$50 \Omega\$  CPW on alumina: frequency-dependent behavior.](#)

[Figure 14.18  \$50 \Omega\$  CPW on alumina: parameter variations with separation \(at 30 GHz,](#)

small  $s$  ).

Figure 14.19  $50 \Omega$  CPW on alumina: parameter variations with separation (at 30 GHz, large  $s$  ).

Figure 14.20 Patterned backside metallization suppressing unwanted surface or parallel-plate modes. Adapted from Hesselbarth and Vahldieck (1999) [20], Figure 4, p. 873. Reprinted with permission of IEEE.

Figure 14.21 Step changes in (a) ground plane separation; (b) center conductor width; and (c) equivalent circuit.

Figure 14.22 Normalized current distribution on the conductors of a CPW impedance step realized using a step of the width of the internal conductor: (a) normalized scale; (b) magnitude of the longitudinal current; and (c) magnitude of the transverse current (frequency is 30 GHz).

Figure 14.23 Normalized current distribution on the conductors of a CPW impedance step realized using a step of the conductor separation: (a) normalized scale; (b) magnitude of the longitudinal current; and (c) magnitude of the transverse current (frequency is 30 GHz).

Figure 14.24 Estimates of the capacitance associated with step changes in width.

Figure 14.25 Step capacitance versus width/gap ratio for two substrates.

Figure 14.26 Quasi-open circuit (a) and alternative equivalent circuits (b).

Figure 14.27 Symmetric series gap layout and capacitive  $\pi$  equivalent circuit indicating reference planes 1 and 2.

Figure 14.28 Pseudo short circuit: (a) layout; and (b) cross-section.

Figure 14.29 Pseudo short circuit: (a) layout and (b) alternative equivalent circuits.

Figure 14.30 Normalized magnitude of the current distribution on the conductors of a CPW pseudo short circuit: (a) scale; (b) short at 100 GHz showing standing wave pattern of longitudinal current; (c) magnitude of the longitudinal current at 30 GHz in greater detail; and (d) magnitude of the transverse current at 30 GHz.

Figure 14.31 Right-angle bend: (a) layout; and (b) equivalent circuit.

Figure 14.32 Right-angle bend inductance as a function of parameter  $k$ .

Figure 14.33 T junction: (a) layout; and (b) lumped equivalent circuit.

Figure 14.34 T-junction transformer ratio  $N$  as a function of frequency.

Figure 14.35 The T junction (a) structure analyzed by Mirshekar-Syahkal [37] together with its equivalent circuit (b). Dimensions are  $a = 200 \mu\text{m}$ , substrate height  $h = 200 \mu\text{m}$ ,  $s = 20 \mu\text{m}$ ,  $w = 40 \mu\text{m}$ , air bridge height =  $2 \mu\text{m}$ , and  $w = 40 \mu\text{m}$ . Adapted from Mirshekar-Syahkal (1996) [37], Figure 4, p. 982. Reprinted with permission of IEEE.

Figure 14.36 Effects of the coupled slotline mode on air bridges. Adapted from Sewell and Rozzi (1994) [38], Figure 14, p. 2086. Reprinted with permission of IEEE.

Figure 14.37 SEM micrographs of CPW cross-over junctions: (a) conventional CPW; and (b) FGCPW. The lines have the same dimensions. Adapted from Ponchak and Tentzeris (2000) [41], Figure 1 and 2, p. 1892. Reprinted with permission of IEEE.

Figure 14.38 (a) Interdigital or stub structure; and (b) its equivalent circuit. The reference planes are denoted by T and T'.

Figure 14.39 Through-connected interdigital stub: (a) structure; and (b) its equivalent circuit. The reference planes are denoted by T and T'.

Figure 14.40 Layout of a 30% bandwidth bandpass filter on an alumina substrate.

Figure 14.41 Transmission response ( $S_{21}$ ) of the bandpass filter.

Figure 14.42 Return loss ( $S_{11}$ ) of the bandpass filter.

Figure 14.43 Basic structure of an MMIC-implemented bandpass filter. Adapted from Mernyei *et al.* (1994) [45], Figure 2, p. 1862. Reprinted with permission of IEEE.

Figure 14.44 Two-section in-phase CPW power divider. Adapted from Fan and Chang (1996) [51], Figure 8, p. 2415. Reprinted with permission of IEEE.

Figure 14.45 Energy leakage due to the various modes occurring in flip-chip structures: (a) modes; and (b) detail. Adapted from Lee and Lee (1998) [52], Figure 1, p. 366. Reprinted with permission of IEEE.

Figure 14.46 CPW with top and bottom metal shields.

Figure 14.47 Cross-sections: (a) conventional CPW; and (b) “inverted-V” CPW.

Figure 14.48 A 3D multilayer stack of FGCPW structures. Adapted from Herrick *et al.* (1999) [60], Figure 1, p. 61. Reprinted with permission of IEEE.

Figure 14.49 Trenched CPW on an HRS substrate: (a) plan view; and (b) cross-section.

Figure 14.50 CPS or differential line structures on (a) the surface of a dielectric or (b) embedded.

Figure 14.51 Instantaneous normalized current magnitude and charge distribution along a differential line: (a) longitudinal current; (b) transverse current; and (c) charge. The current and charge are normalized and use the scales shown on the left-hand side. The peak transverse current is 1500 times smaller than the peak of the longitudinal current. The frequency is 10 GHz,  $s = 2.5 \mu\text{m}$ , and  $w = 10 \mu\text{m}$ .

Figure 14.52 Characteristic impedance and effective relative permittivity of open differential line fabricated on HRS ( $\epsilon_r = 11.9$ ) for various  $s/w$  ratios. Frequency = 10 GHz, height above ground plane,  $h = 650 \mu\text{m}$ .

Figure 14.53 Frequency dependence of characteristic impedance and effective relative

permittivity of open differential line fabricated on HRS ( $\epsilon = 11.9$ ). Height above ground plane,  $h = 650 \mu\text{m}$ .

Figure 14.54 Characteristic impedance and effective relative dielectric constant of an embedded differential line fabricated in LTCC with  $\epsilon = 7.3$  for various  $s/w$  ratios. Frequency = 10 GHz, height from the line to each ground plane,  $h = 340 \mu\text{m}$ . Results derived using SONNET simulations.

Figure 14.55 Characteristic impedance of an embedded differential line fabricated in LTCC with  $\epsilon = 7.3$  for various  $h/s$  ratios. Frequency = 2.45 GHz, separation,  $s = 100 \mu\text{m}$ , and width,  $w = 70 \mu\text{m}$ . Results derived using SONNET simulations.

## Chapter 15: Slotline

Figure 15.1 Slotline. Adapted from Cohn (1969) [1], Figure 1, p. 1149. Reprinted with permission of IEEE.

Figure 15.2 Slotline field distribution: (a) slotline transverse  $E$  and  $H$  fields; (b) longitudinal cross-section showing the  $H$ -field pattern; and (c) top elevation view showing the current,  $I$ , and the  $H$ -field pattern. Adapted from Cohn (1969) [1], Figure 2, p. 769. Reprinted with permission of IEEE.

Figure 15.3 3D representation of slotline. Adapted from Robinson and Allen (1969) [13], Figure 1, p. 1097. Reprinted with permission of IEEE.

Figure 15.4 Electric and magnetic field distributions for higher-order modes in slotline: (a) dominant slotline mode, the  $e_{01}$  mode; (b) the  $e_{11}$  mode; (c) the  $e_{01}$  mode; (d) the  $o_{11}$  mode; and (e) the  $o_{02}$  mode. The  $e$  indicates an even mode while an  $o$  indicates an odd mode. Adapted from Citerne *et al.* (1975) [14], Figure 1, p. 1097. Reprinted with permission of the European Microwave Association.

Figure 15.5 Measured phase coefficient ( $\beta$ ) versus frequency for slotline and microstrip. Adapted from Robinson and Allen (1969) [13], Figure 3, p. 1098. Reprinted with permission of IEEE.

Figure 15.6 Slotline dispersion characteristics. (Here  $\lambda = \lambda_0$  is the free space wavelength). Adapted from Knorr and Kuchler (1975) [15], Figure 2, p. 543. Reprinted with permission of IEEE.

Figure 15.7 Dispersion characteristics of slotlines computed using Svacina's analysis [16] and Cohn's analysis [1]. Substrate permittivity  $\epsilon_r = 9.7$ . Adapted from Svacina (1999) [16], Figure 3, p. 1828. Reprinted with permission of IEEE.

Figure 15.8 Normalized phase coefficient for the dominant and first higher-order mode in slotline:  $\epsilon_r = 9.6$ ,  $d = 1 \text{ mm}$ ,  $w = 1 \text{ mm}$ ,  $t = 0$ . Adapted from Kitazawa *et al.* (1980) [17], Figure 3, p. 391. Reprinted with permission of IEEE.

Figure 15.9 Normalized phase coefficient for slotlines having thickness-width ratios ranging from zero (0.00) to 0.1. Adapted from Kitazawa *et al.* (1980) [17], Figure 4, p.

391. Reprinted with permission of IEEE.

[Figure 15.10 Characteristic impedance of a slotline. Adapted from Knorr and Kuchler \(1975\) \[15\], Figure 3, p. 544. Reprinted with permission of IEEE.](#)

[Figure 15.11 Characteristic impedance for slotlines having thickness-width ratios ranging from zero \(0.00\) to 0.1. Adapted from Kitazawa \*et al.\* \(1980\) \[17\], Figure 5, p. 391. Reprinted with permission of IEEE.](#)

[Figure 15.12 Losses in microstrip and slotline \( \$50\Omega\$ \) compared. The points are measured loss of slotline. Adapted from Robinson and Allen \*et al.\* \(1969\) \[13\], Figure 5, p. 1098. Reprinted with permission of IEEE.](#)

[Figure 15.13 Slotline: threshold for the onset of dielectric leakage. Substrate thickness  \$d\$  versus frequency with  \$\epsilon\_r = 9.8\$ . Adapted from Rozzi \*et al.\* \(1990\) \[19\], Figure 5, p. 1071. Reprinted with permission of IEEE.](#)

[Figure 15.14 Conductor and dielectric losses in slotline as functions of the double-width  \$2w\$  for 2, 7, 12, 18, 24, and 30 GHz; losses increase with frequency. Adapted from Rozzi \*et al.\* \(1990\) \[19\], Figure 9, p. 1075. Reprinted with permission of IEEE.](#)

[Figure 15.15 Dielectric and ground plane losses in slotline as a function of dielectric loss tangent \(curves \(b\) and \(d\)\) and as a function of ground plane conductivity normalized to that of copper \(curves \(c\) and \(e\)\). Curves \(b\)–\(e\) use the analysis of Das and Pozar. Curves \(a\) and \(f\) use a perturbation analysis with low loss substrate and ground plane. The frequency is 3 GHz, the substrate has a thickness of 1.6 mm and permittivity of 2.2, and the line width is 5 mm. Adapted from Das and Pozar \(1991\) \[20\], Figure 8, p. 60. Reprinted with permission of IEEE.](#)

[Figure 15.16 Slotline losses as a function of slot width. Each curve was calculated using a different method with \(b\) considered to be more accurate. Adapted from Das and Pozar \(1991\) \[20\], Figure 10, p. 61. Reprinted with permission of IEEE.](#)

[Figure 15.17 An assortment of planar transmission line structures. Adapted from Jansen \*et al.\* \(1981\) \[21\], Figure 1, p. 77. Reprinted with permission of the Institution of Engineering and Technology.](#)

[Figure 15.18 Shorted slot end-effect data in comparison with the measured results of Knorr and Saenz.  \$h\_2 = 3.07\$  mm,  \$\epsilon\_2 = \epsilon\_r \epsilon\_0\$ ,  \$\epsilon\_r = 12\$ ,  \$h\_1/h\_2 = 5\$ ,  \$h\_3/h\_2 = 5\$ ,  \$a/h\_2 = w/h\_2 + 15\$ ,  \$\ell\_b/h\_2 = 3\$ . Adapted from Jansen \*et al.\* \(1981\) \[21\], Figure 7, p. 83. Reprinted with permission of the Institution of Engineering and Technology.](#)

[Figure 15.19 Equivalent end-effect length applying to a single short-circuited slotline on an alumina substrate.  \$h\_2 = 0.635\$  mm,  \$\epsilon\_1 = \epsilon\_3 = \epsilon\_r \epsilon\_0\$ ,  \$\epsilon\_r = 9.7\$ ,  \$h\_1/h\_2 = 10\$ ,  \$h\_3/h\_2 = 10\$ ,  \$a/h\_2 = w/h\_2 + 20\$ . Adapted from Jansen \*et al.\* \(1981\) \[21\], Figure 8, p. 84. Reprinted with permission of the Institution of Engineering and Technology.](#)

[Figure 15.20 A family of short circuit reactance curves derived for  \$\epsilon\_r = 12\$ ,  \$h\_2 = d\$ ,  \$h\_1 = 0\$ ,  \$\epsilon\_2 = \epsilon\_r \epsilon\_0\$ . Adapted from Knorr and Salenz \(1973\) \[22\], Figure 4, p. 580.](#)

[Reprinted with permission of IEEE.](#)

[Figure 15.21 End effect of a shorted pair of coupled slotlines in odd mode.  \$h\_2 = 0.635\$  mm,  \$\epsilon\_r = 9.7\$ ,  \$h\_1/h\_2 = 10\$ ,  \$h\_3/h\_2 = 10\$ ,  \$a/h\_2 = w/h\_2 + 20\$ ,  \$s/h\_2 = 1.0\$ . Adapted from Jansen et al. \(1981\) \[21\], Figure 8, p. 84. Reprinted with permission of the Institution of Engineering and Technology.](#)

[Figure 15.22 End effect of a shorted pair of coupled slotlines in even mode. Parameters not specified are as in Figure 15.21. Adapted from Jansen et al. \(1981\) \[21\], Figure 8, p. 84. Reprinted with permission of the Institution of Engineering and Technology.](#)

[Figure 15.23 Experimental setup: \(a\)–\(d\) slotline test patterns; and \(e\) apparatus. Adapted from Chramiec \(1989\) \[23\], Figure 1 and 2, p. 1639. Reprinted with permission of IEEE.](#)

[Figure 15.24 Measured reactances of slotline short end on an alumina substrate. Adapted from Chramiec \(1989\) \[23\], Figure 3, p. 1639. Reprinted with permission of IEEE.](#)

[Figure 15.25 Measured reactance of the slotline nonuniform resonator of Figure 15.23\(d\). Adapted from Chramiec \(1989\) \[23\], Figure 6, p. 1640. Reprinted with permission of IEEE.](#)

## Chapter 16: Slotline Applications

[Figure 16.1 Schematic diagram of a symmetrical eight-port circuit. The solid lines represent microstrip lines on the top of the circuit. The dashed lines represent slotlines in the ground plane on the bottom of the circuit board. Adapted from Riblet \(1990\) \[1\], Figure 1, p. 1421. Used with permission of IEEE.](#)

[Figure 16.2 Version 1 of the planar microstrip-slotline symmetrical comparator. The circumference is three wavelengths at midband. Adapted from Riblet \(1990\) \[1\], Figure 2, p. 1423. Reprinted with permission of IEEE.](#)

[Figure 16.3 Schematic diagram of a two-port circuit which may be used to determine the theoretical performance of the eight-port circuit in Figure 16.2. Optimum performance is obtained if  \$Y = 1\$ . Adapted from Riblet \(1990\) \[1\], Figure 3, p. 1423. Reprinted with permission of IEEE.](#)

[Figure 16.4 Optimum return loss versus normalized frequency for Version I \(Figure 16.2\) and Version II \(Figure 16.5\). Adapted from Riblet \(1990\) \[1\], Figure 4, p. 1423. Reprinted with permission of IEEE.](#)

[Figure 16.5 Version II of the planar microstrip-slotline symmetrical comparator. The circumference is only a wavelength at midband. Adapted from Riblet \(1990\) \[1\], Figure 5, p. 1423. Reprinted with permission of IEEE.](#)

[Figure 16.6 Even- and odd-mode characteristic impedance of coupled slotlines with  \$W/D = 0.25\$  and  \$\epsilon\_r = 11\$ . Adapted from Knorr and Kuchler \(1975\) \[2\], Figure 6, p. 544. Reprinted with permission of IEEE.](#)

[Figure 16.7 Even- and odd-mode dispersion characteristics of coupled slotlines with  \$W/D = 0.25\$  and  \$\epsilon\_r = 11\$ . Adapted from Knorr and Kuchler \(1975\)\[2\], Figure 6, p. 544. Reprinted with permission of IEEE.](#)

[Figure 16.8 Layout of a wideband coupler, including microstrip ports. Adapted from Abbosh and Bialkowski \(2007\) \[3\], Figure 1, p. 190. Reprinted with permission of IEEE.](#)

[Figure 16.9 Equivalent configuration used to determine the initial dimensions. Adapted from Abbosh and Bialkowski \(2007\) \[3\], Figure 1, p. 190. Reprinted with permission of IEEE.](#)

[Figure 16.10 Resonator configurations for slotline bandpass filters: \(a\) quarter-wave-coupled resonant slots; and \(b\) end-coupled resonant slots. Adapted from Mariani and Agrios \(1970\) \[4\], Figure 1, p. 1090. Reprinted with permission of IEEE.](#)

[Figure 16.11 Filter applications: \(a\) bandstop filter using cascaded resonant slots; and \(b\) parallel-coupled slotline bandpass filter. Adapted from Cohn \(1969\) \[5\], Figure 6, p. 770. Reprinted with permission of IEEE.](#)

[Figure 16.12 Basic design concept of a magic T. Adapted from Aikawa and Ogawa \(1989\) \[6\], Figure 4, p. 408. Reprinted with permission of IEEE.](#)

[Figure 16.13 Planar magic Ts. Adapted from Aikawa and Ogawa \(1980\) \[7\], Figure 4, p. 408. Reprinted with permission of IEEE.](#)

[Figure 16.14 Schematic behaviors for in-phase and out-of-phase couplings: \(a\) in-phase coupling \(odd mode in the coupled slotlines\); and \(b\) out-of-phase coupling \(even-mode in the coupled slotlines\). Adapted from Aikawa and Ogawa \(1980\) \[7\], Figure 2, p. 524. Reprinted with permission of IEEE.](#)

[Figure 16.15 Schematic and equivalent circuit of microstrip type magic T. Adapted from Aikawa and Ogawa \(1980\) \[7\], Figure 3, p. 525. Reprinted with permission of IEEE.](#)

[Figure 16.16 Obtainable isolation and return loss at the average center frequency, where  \$\(\theta\_{EVEN} + \theta\_{ODD}\)/2\$  is  \$\pi/2\$ . Note that  \$\(\theta\_{ODD} - \theta\_{EVEN}\)/\(\theta\_{ODD} + \theta\_{EVEN}\)\$  is the normalized length deviation.  \$Z\_H/Z\_0 = 2.0\$ ,  \$Z\_E/Z\_0 = 0.8\$ ,  \$Z\_{EVEN}/Z\_0 = 1/\sqrt{2}\$ , and  \$Z\_{ODD}/Z\_0 = \sqrt{2}\$ . Adapted from Aikawa and Ogawa \(1980\) \[7\], Figure 7, p. 527. Reprinted with permission of IEEE.](#)

[Figure 16.17 Circuit configuration of the conventional Marchand balun.](#)

[Figure 16.18 Slotline Marchand balun: \(a\) Marchand balun using slot-coupled microstrip lines, and its \(b\) A-A' and \(c\) B-B' cross-sectional views; and \(d\) the equivalent structure of the diamond-shape slot-coupled microstrip line. Adapted from Tseng and Hsiao \(2010\) \[8\], Figure 2, p. 157. Reprinted with permission of IEEE.](#)

[Figure 16.19 Even-mode and odd-mode impedances versus the slot and strip widths. Adapted from Tseng and Hsiao \(2010\) \[8\], Figure 3, p. 158. Reprinted with permission](#)

of IEEE.

[Figure 16.20 Circuit photographs of \(a\) top and \(b\) bottom views of the slotline Marchand balun. Adapted from Tseng and Hsiao \(2010\) \[8\], Figure 4, p. 158. Reprinted with permission of IEEE.](#)

[Figure 16.21 S parameters for the slotline Marchand balun. Adapted from Tseng and Hsiao \(2010\) \[8\], Figure 5, p. 159. Reprinted with permission of IEEE.](#)

[Figure 16.22 Geometry of a multilayer microstrip-slotline. Adapted from El-Sharawy and Jackson \(1990\) \[9\], Figure 5, p. 280. Reprinted with permission of IEEE.](#)

[Figure 16.23 Effect of microstrip-slot dimensions on differential phase shift in the multilayer structure of Figure 16.22. Adapted from El-Sharawy and Jackson \(1990\) \[9\], Figure 6, p. 280. Reprinted with permission of IEEE.](#)

[Figure 16.24 Geometry of structure \(derived from that of Figure 16.22\) with an additional top layer of low-dielectric material. Adapted from El-Sharawy and Jackson \(1990\) \[9\], Figure 9, p. 281. Reprinted with permission of IEEE.](#)

[Figure 16.25 Physical configurations of slot-guide Y circulators: \(a\) common top view; \(b\) stack without metal cap; \(c\) stack with metallic foil as a cap; and \(d\) ferrite substrate on its own. Adapted from Ogasawara and Kaji \(1971\) \[10\], Figure 2, p. 220. Reprinted with permission of the Institution of Engineering and Technology.](#)

[Figure 16.26 Insertion loss and isolation versus DC magnetic field as measured on the experimental coplanar-guide Y circulator illustrated in Figure 16.25\(d\). Adapted from Ogasawara and Kaji \(1971\) \[10\], Figure 3, p. 221. Reprinted with permission of the Institution of Engineering and Technology.](#)

[Figure 16.27 Enclosed slotline circulator: \(a\) structure of the device; and \(b\) distribution of energy in the ferrite slab. Adapted from Courtois and de Vecchis \(1975\) \[11\], Figure 1, p. 512. Reprinted with permission of IEEE.](#)

[Figure 16.28 Double-sided balanced microwave circuit with a PSK modulator, phase detector, and mixer. Adapted from Aikawa and Ogawa \(1989\) \[6\], Figure 15, p. 411. Reprinted with permission of IEEE.](#)

## Chapter 17: Transitions

[Figure 17.1 Compensated coaxial-microstrip transition \(all dimensions in millimeters\): \(a\) plan view; and \(b\) longitudinal section. The width of the microstrip strip is  \$w\$  and the thickness of the substrate  \$h = 0.5\$  mm. Adapted from England \(1976\) \[2\], Figure 1, p. 47. Reprinted with permission of IEEE.](#)

[Figure 17.2 Rectangular waveguide-to-microstrip transition using a ridgeline transformer for the 27.5–31.3 GHz band: \(a\) complete mechanical structure; and \(b\) ridgeline transformer dimensions \(all in millimeters\). Adapted from Schneider \*et al.\* \(1969\) \[3\], Figure 5, p. 1717. Reprinted with permission of the American Telephone and Telegraph Company.](#)

[Figure 17.3 Microstrip transitions: \(a\) photograph of a 15 GHz microstrip-to-waveguide transition; \(b\) cross-section of structure in \(a\); and \(c\) alternative microstrip to waveguide transition using a ridge. Figure \(c\) adapted from Menzel and Klaassen \(1989\) \(1989\) \[6\], Figure 1, p. 1265. Reproduced with the permission of the European Microwave Association.](#)

[Figure 17.4 Waveguide-to-microstrip transition using tapers and a balun: \(a\) waveguide-end view; and \(b\) longitudinal view. Adapted from van Heuven \(1976\) \[7\], Figure 1 and 2, p. 145. Reproduced with permission of IEEE.](#)

[Figure 17.5 Waveguide-to-microstrip power splitter: \(a\) structure of the waveguide to microstrip power divider: \(i\) the side view illustrates that the microwave signal is coupled to two T antennas on an alumina substrate; \(ii\) the front view of the power divider consists of two T-shaped coupling antennas; and \(b\) simplified model using the symmetry of the waveguide-to-microstrip power divider: \(i\) side view; and \(ii\) front view. The plane of symmetry in \(a\) is an electric wall where a metal plate can be inserted without changing the field distribution. Thus, the power divider design problem is changed to one of waveguide-to-microstrip transition design. Adapted from Wu \*et al.\* \(1990\) \[8\], Figure 1 and 2, p. 477. Reprinted with permission of IEEE.](#)

[Figure 17.6 CPW transitions: \(a\) CPW-to-finline; \(b\) CPW-to-microstrip; and \(c\) cross-section of the CPW line for both structures. \(Dimensions are in millimeters unless otherwise indicated.\) Adapted from Jin and Vahldieck \(1993\) \*et al.\* \[10\], Figure 2 and 3, p. 1540. Reprinted with permission of IEEE.](#)

[Figure 17.7 CPW-to-slotline transition. Adapted from Ma \*et al.\* \(1999\) \[13\], Figure 1, p. 427. Reprinted with permission of IEEE.](#)

[Figure 17.8 A 30–40 GHz bandstop filter within a mixer and a ring-slot antenna. Adapted from Vaupel and Hansen \(1999\) \[20\], Figure 8, p. 1798. Reprinted with permission of IEEE.](#)

[Figure 17.9 Geometry of a general microstrip-slotline transition. Adapted from Antar \*et al.\* \(1992\) \[21\], Figure 1, p. 516. Reprinted with permission of IEEE.](#)

[Figure 17.10 Common model of a slotline-microstrip transition.](#)

[Figure 17.11 Variations of  \$n\$  and  \$X\$ , with frequency for a microstrip-slotline transition on alumina substrate \( \$h = w = 0.5\$  mm,  \$\epsilon\_r = 9.7\$ ,  \$t = 0.5\$  mm,  \$\theta\_s = 0\$ \). Adapted from Antar \*et al.\* \(1992\) \[21\], Figure 6, p. 519. Reprinted with permission of IEEE.](#)

[Figure 17.12 Alternative model of a slotline-microstrip transition.](#)

[Figure 17.13 Slotline-microstrip transition: \(a\) two-stub transition; \(b\) parameters of slotline; and \(c\) equivalent circuit of transition. Adapted from Podcameni and Coimbra \(1980\) \[26\], Figure 1, p. 80. Reprinted with permission of IEEE.](#)

[Figure 17.14 Theoretical \(solid line\) and experimental \(dashed line\) VSWR for slotline-microstrip double transition on an anisotropic substrate.  \$\epsilon\_{r,xy} = 13\$ ,  \$\epsilon\_{r,z} = 10.2\$ .](#)

$H = 0.635 \text{ mm}$ . Adapted from Podcameni and Coimbra (1981) [26], Figure 4, p. 82. Reprinted with permission of IEEE.

Figure 17.15 Microstrip-slot transmission line: (a) structure; and (b) dispersion characteristics of microstrip-slot lines.  $L = 6.35 \text{ mm}$ ,  $d = 11.43 \text{ mm}$ ,  $t = 1.27 \text{ mm}$ ,  $h = 24.13 \text{ mm}$ ,  $w_s = 0.635 \text{ mm}$ ,  $w_m = 0.635 \text{ mm}$ ,  $\epsilon_r = 8.875$ . Adapted from Itoh (1980) [27], Figure 4 and 6, pp. 735 and 736. Reprinted with permission of IEEE.

Figure 17.16 The microstrip-slotline transition investigated by Yang and Alexopoulos. Adapted from Yang and Alexopoulos (1988) [28], Figure 1, p. 286. Reprinted with permission of IEEE.

Figure 17.17 Microstrip-slotline transition. Transmission Line Matrix (TLM) data results use the transmission line method due to Knorr [23].  $w_s = 2.057 \text{ mm}$ ,  $w_m = 1.575 \text{ mm}$ ,  $L_s = 6.88 \text{ mm}$ ,  $L_m = 6.88 \text{ mm}$ ,  $\epsilon_r = 20$ , substrate thickness  $d = 3.175 \text{ mm}$ . Adapted from Yang and Alexopoulos (1988) [28], Figure 7, p. 552. Reprinted with permission of IEEE.

Figure 17.18 Various microstrip-to-slotline transitions (solid lines indicate microstrip circuitry and dashed lines indicate slotline circuitry): (a) microstrip short and uniform  $\lambda/4$  slotline; (b) virtual short with uniform  $\lambda/4$  open microstrip and uniform  $\lambda/4$  slotline; (c) soldered microstrip short and slotline open circuit; and (d) virtual microstrip short circuit and slotline open circuit. Adapted from Shuppert (1988) [29], Figure 1, p. 1272. Reprinted with permission of IEEE.

Figure 17.19 Microstrip-slotline transition with uniform stubs. Adapted from Shuppert (1988) [29], Figure 6, p. 1275. Reprinted with permission of IEEE.

Figure 17.20 Transmission coefficient of a cascade of two microstrip/slotline transitions, separated by a slotline of length  $L_s = 15 \text{ mm}$ : (a)  $Z_{mo} = 50 \Omega$ ; and (b)  $Z_{mo} = 19 \Omega$ . Adapted from Shuppert (1988) [29], Figure 10, p. 1276. Reprinted with permission of IEEE.

Figure 17.21 Single and multiplane discontinuities: (a) open coupled microstrip lines; (b) shorted CPW line over ground; (c) shorted CPW line; (d) microstrip cross-over; (e) microstrip coupled to CPS line; (f) microstrip line with coupled resonator; (g) coupled microstrip on different layers; and (h) slotline coupled microstrip lines. Adapted from Schwab and Menzel (1992) [30], Figure 1, p. 67. Reprinted with permission of IEEE.

Figure 17.22 Microstrip-slotline-microstrip transition: (a) structure; and (b) measured and calculated transmission coefficient of a microstrip-slotline-microstrip transition.  $\epsilon_r = 11.1$ ,  $h = 1.27 \text{ mm}$ ,  $s = 0.53 \text{ mm}$ ,  $w = 1.0 \text{ mm}$ ,  $\ell = 20.4 \text{ mm}$ ,  $d_s = 6.65 \text{ mm}$ . Adapted from Schwab and Menzel (1992) [30], Figure 5, p. 70. Reprinted with permission of IEEE.

Figure 17.23 Microstrip-slot transition with open- and short-circuited lines. Adapted from Schiek and Kohler (1976) [31], Figure 3, p. 232. Reprinted with permission of IEEE.

[IEEE.](#)

[Figure 17.24 Dimensions of the circuit layout of two transitions in series. Adapted from Schiek and Kohler \(1976\) \[31\], Figure 4, p. 232. Reprinted with permission of IEEE.](#)

[Figure 17.25 Measured characteristics of two transitions in series shown in Figure 17.24: \(a\) insertion loss; and \(b\) return loss. Adapted from Schiek and Kohler \(1976\) \[31\], Figure 5, p. 232. Reprinted with permission of IEEE.](#)

[Figure 17.26 Coax-slotline transition. Adapted from Knorr \(1974\) \[23\], Figure 1, p. 548. Reprinted with permission of IEEE.](#)

[Figure 17.27 Coaxial line to slotline transition: \(a\) simplified model of coaxial-slot transition; and \(b\) equivalent circuit of the coaxial-slot transition. Adapted from Knorr \(1974\) \[23\], Figure 2, p. 549. Reprinted with permission of IEEE.](#)

[Figure 17.28 Configuration of slotline-stripline series T junction and equivalent circuit: 1, input of the stripline; 2, one end of the slotline; 3, the other end of the slotline. Adapted from Aikawa and Ogawa \(1989\) \[32\], Figure 3, p. 407. Reprinted with permission of IEEE.](#)

## Chapter 18: Measurements of Planar Transmission Line Structures

[Figure 18.1  \$S\$  parameter measurement system: overall setup. A high frequency \(HF\) or intermediate frequency signal \(e.g., 100 MHz\) passes between the network analyzer and the  \$S\$  parameter test set. The DUT is the device under test.](#)

[Figure 18.2 The use of ground-signal-ground \(GSG\) coplanar probes: \(a\) configuration showing the use of GSG with the coaxial lines coming from the network analyzer; and \(b\) used in measurement of an on-chip interconnect.](#)

[Figure 18.3 Contact pads for coplanar probes with a  \$100 \mu m\$  pitch: \(a\) GSG configuration; and \(b\)  \$GS\_1GS\_2G\$  configuration for differential probing.](#)

[Figure 18.4 Power flow breakdown using normalized scattering parameters.](#)

[Figure 18.5 Measurement connections: \(a\) through connection; and \(b\) line connection.](#)

[Figure 18.6 Metallized substrates forming rectangular microwave resonators: \(a\) parallel-plate resonator; and \(b\) dielectric-filled, almost wholly metallized resonator.](#)

[Figure 18.7 Coaxial line coupling to a parallel-plate resonator. Adapted from Ladbrooke \*et al.\* \(1973\) \[15\], Figure 1 and 3, p. 561. Reprinted with permission of IEEE.](#)

[Figure 18.8 Coupling via an aperture to an almost wholly metallized resonator: \(a\) overall view; and \(b\)  \$H\$  fields. In \(b\) only the  \$H\$  field is shown and the mica washer omitted for clarity. Adapted from Ladbrooke \*et al.\* \(1973\) \[15\], Figure 1 and 3, p. 561. Reprinted with permission of IEEE.](#)

[Figure 18.9 Ring resonator.](#)

[Figure 18.10 Side-coupled open-ended straight resonator.](#)

[Figure 18.11 Illustrating the effective length of an open-ended straight resonator.](#)

[Figure 18.12 Practical microstrip series-gap-coupled arrangements: \(a\) unequal widths at gap; \(b\) equal widths at gap; \(c\) unequal widths at gap; and \(d\) equal widths at gap.](#)

[Figure 18.13 Open-circuited pairs of straight resonators: \(a\) practical arrangement; and \(b\) effective lengths of the resonators.](#)

[Figure 18.14 The two-stage resonator technique originally devised by Richings and Easter: \(a\) stage 1; and \(b\) stage 2 with the section of length  \$\ell\_2\$  removed.](#)

[Figure 18.15 Symmetrically loaded resonator technique: \(a\) stage 1; and \(b\) stage 2 with the load and load-section removed.](#)

[Figure 18.16 T-junction measurement arrangements: \(a\)  \$L\_1\$  measurement; \(b\)  \$L\_2\$  measurement; \(c\) measurement of  \$C\$ ; and \(d\) measurement of  \$n\$ . Adapted from Easter \(1975\) \[23\], Figure 5, p. 658. Reprinted with permission of IEEE.](#)

[Figure 18.17 Equivalent equal loads  \$\(G + jB\)\$  at both ends of a straight, symmetrical, open-ended resonator.](#)

[Figure 18.18 Resonant method for determining the phase velocities in two parallel-coupled microstrips.](#)

[Figure 18.19 Resonant method for determining the coupling factor between two parallel-coupled microstrips,  \$\ell = \lambda\_{gm}/4\$ .](#)

## Chapter 19: Filters Using Planar Transmission Lines

[Figure 19.1 Ladder prototype filters: \(a\) type 1  \$n\$  th-order lumped-element prototype for  \$n\$  odd; \(b\) type 1  \$n\$  th-order lumped-element prototype for  \$n\$  even; \(c\) type 2  \$n\$  th-order lumped-element prototype for  \$n\$  odd; and \(d\) type 2  \$n\$  th-order lumped-element prototype for  \$n\$  even.](#)

[Figure 19.2 Butterworth lowpass filter response for various orders  \$n\$ .](#)

[Figure 19.3 Chebyshev lowpass filter response for a seventh-order filter with a ripple of 0.7 dB. The passband is below 1 radian/s and the stopband is above 1 radian/s.](#)

[Figure 19.4 Transmission of the Chebyshev lowpass prototype filters for a passband ripple of 0.01 dB.](#)

[Figure 19.5 Impedance and admittance inverters as two-ports: \(a\) impedance inverter; \(b\) admittance inverter; \(c\)  \$50\Omega\$  impedance inverter; and \(d\) 0.02 S admittance inverter.](#)

[Figure 19.6 Alternative representation of two-port impedance and admittance inverters with an impedance element for comparison: \(a\) impedance inverter; \(b\) admittance inverter; \(c\)  \$50\Omega\$  impedance inverter; \(d\) 0.02 S admittance inverter; and \(e\)](#)

impedance.

Figure 19.7 (a) Impedance inverter with load  $Z_{in} = K^2/Z_L$ ; and (b) admittance inverter with load  $Y_{in} = J^2/Y_L$ .

Figure 19.8 Inverter equivalence: (a) two-port impedance inverter (of impedance  $K$ ); (b) a quarter-wave transmission line of characteristic impedance  $Z_0 = K$ ; and (c) a terminated one-quarter wavelength long line.

Figure 19.9 Transformation of a series inductor in (a) to an equivalent network with a shunt capacitor with inverters and transformer in (b) with  $C = L/K^2$ .

Figure 19.10 Transformation of a series capacitor in (a) to an equivalent network with a shunt inductor with inverters and transformer in (b) with  $C = L/K^2$ .

Figure 19.11 Ladder prototype filters using inverters: (a)  $n$  th-order lumped-element prototype for  $n$  odd; (b)  $n$  th-order lumped-element prototype for  $n$  even; (c) first stage in transformation of series elements to shunt elements using inverters; (d) final inverter-based prototype for  $n$  even; and (e) final inverter-based prototype for  $n$  odd.

Figure 19.12 Impedance inverter: (a) schematic of an impedance inverter with impedance  $K$ ; and (b) its lumped-element equivalent model.

Figure 19.13 Admittance inverter: (a) schematic of admittance inverter with admittance; (b) lumped-element equivalent model with admittance elements; and (c) lumped-element equivalent model with impedance elements.

Figure 19.14 Narrowband inverter equivalents at frequency  $f_0$ : (a) impedance inverter with characteristic impedance  $K$ ; (b) lumped-element equivalent network; and (c) inverter realized by short- and open-circuited stubs.

Figure 19.15 Exact (broadband) equivalent model of a lossless transmission line of characteristic impedance  $Z_0$  and electrical length  $\theta$ : (a) lossless line; (b) unit element (UE); and (c) model,  $K = Z_0 / \sin(\theta)$ . The stubs in (c) have electrical length  $\theta$ .

Figure 19.16 Equivalent  $\pi$  network of impedances representing a transmission line with an electrical length of  $\theta = \beta\ell$  where  $\ell$  is the physical length and  $\beta$  is the phase constant.

Figure 19.17 Inductive length of line with adjacent capacitive lines: (a) lumped circuit; (b) lumped-distributed equivalent; and (c) microstrip form.

Figure 19.18 Capacitive length of line with adjacent inductive lines: (a) microstrip; and (b) lumped equivalent.

Figure 19.19 Inductive length of microstrip line with adjacent capacitive lines: (a) microstrip line; and (b) lumped equivalent circuit including discontinuity (step) capacitances and inductances.

Figure 19.20 Transformed, lumped-element, bandpass filter network.

[Figure 19.21 Bandpass prototype filters with admittance inverters: \(a\) bandpass prototype filter with shunt resonators; and \(b\) bandpass prototype filter with series resonators.](#)

[Figure 19.22 General microstrip layout for an end-coupled bandpass filter \(series coupling gaps between cascaded straight resonator elements\).](#)

[Figure 19.23 Performance of quasi-planar broadside end-coupled bandpass filter. Adapted from Tzuang \*et al.\* \(1990\) \[7\], Figure 6, p. 410. Reprinted with permission of IEEE.](#)

[Figure 19.24 Interdigital bandpass filter with  \$\ell \approx \lambda\_g/4\$ : \(a\) single cell; and \(b\) multicell.](#)

[Figure 19.25 Edge-coupled bandpass PCL filter with  \$\ell \approx \lambda\_g/4\$ : \(a\) single cell; and \(b\) multicell. The dotted lines are not part of the layout but serve to illustrate that a long microstrip line combines to sections each of length  \$\ell\$ .](#)

[Figure 19.26 A seven-section, parallel-coupled microstrip bandpass filter.](#)

[Figure 19.27 Broadband equivalent model of coupled transmission lines in open interdigital configuration: \(a\) coupled line; and \(b\)  \$Z\_0 = \frac{1}{2}\(Z\_{0e} - Z\_{0o}\)\$ .](#)

[Figure 19.28 Broadband equivalent model of coupled transmission lines in open interdigital configuration: \(a\) coupled line; and \(b\) unit element,  \$Z\_0 = \frac{1}{2}\(Z\_{0e} - Z\_{0o}\)\$ .  
 \$Z\_{0,STUB} = \frac{1}{2}\(Z\_{0e} + Z\_{0o}\)\$ .](#)

[Figure 19.29 Frequency definitions for the example: \(a\) lowpass filter; and \(b\) bandpass filter.](#)

[Figure 19.30 Comline filter with  \$\ell \approx \lambda\_g/4\$ : \(a\) single cell; and \(b\) multicell.](#)

[Figure 19.31 Hairpin filter with  \$\ell \approx \lambda\_g/4\$ : \(a\) single cell; \(b\) multicell; and \(c\) physical layout.](#)

[Figure 19.32 Comline filter with the multicell form having extended stopband with  \$\ell\_2 \approx \ell/2 \approx \lambda\_g/8\$  typically: \(a\) single cell; and \(b\) multicell.](#)

[Figure 19.33 Insertion-loss characteristic for the bandpass filter of the example.](#)

[Figure 19.34 Transmission of Chebyshev lowpass prototype filters for various orders  \$n\$  and for a passband ripple of 0.01 dB.](#)

[Figure 19.35 Final design dimensions in millimeters of the bandpass filter calculated in the worked example.](#)

[Figure 19.36 Measured compared with specified insertion-loss characteristics for the 10–11 GHz parallel-coupled bandpass filter.](#)

[Figure 19.37 A microstrip-connected dielectric resonator bandpass filter configuration.](#)

[Figure 19.38 A series stub in a microstrip transmission line.](#)

Figure 20.1 Magnetic ordering of elementary magnetic moments in materials: (a) diamagnetic; (b) ferromagnetic; (c) antiferromagnetic; and (d) ferrimagnetic.

Figure 20.2 BH curves of a ferromagnet or ferrimagnet: (a) magnetization,  $M$ ; and (b) magnetic induction (CGS) or flux density (SI),  $B$ .  $H_c$  is the coercive field and  $B_r$  is the remanence or remanent magnetic flux density corresponding to the remanent magnetization  $M_r$  after a large external magnetic field has been removed. Magnetic hysteresis is shown in these curves as the trajectory depends on the history of applied magnetic fields.

Figure 20.3  $B = H$  curves of an unmagnetized ferromagnet or ferrimagnet showing hysteresis even at small levels of magnetic field.

Figure 20.4 Interaction of a magnetic moment,  $\bar{m}$  with the DC magnetization  $M_0$ : (a) without an RF field; and (b) with an RF field. In (a)  $\bar{m}$  aligns with the net DC magnetization  $\bar{M}_0$ . In (b) it has a component perpendicular to  $\bar{M}_0$ .

Figure 20.5 Frequency variation of the relative permeability  $\mu_r$  of a saturated magnetized magnetic material. Note that  $\mu_r$  is an element of the Polder tensor.

Figure 20.6 Frequency variation of the relative permeability in the plane perpendicular to the direction of magnetization for propagation in the direction of magnetization.

Figure 20.7 Effective relative permeability  $\mu_{r,\text{eff}}$  to be used for magnetized substrates and thin films: (a) magnetized normal to substrate,  $\mu_{r,\text{eff}} = \mu_\perp$ ; (b) magnetized in plane of substrate,  $\mu_{r,\text{eff}} = \mu_\perp$ ; (c) magnetized normal to thin film,  $\mu_{r,\text{eff}} = \mu_\perp$ ; and (d) magnetized in plane of thin film,  $\mu_{r,\text{eff}} = \mu_r$ .

Figure 20.8 Effective microstrip permeability  $\mu_{\text{eff}}$  as a function of  $w/h$ . The effective relative permeability of the substrate material  $\mu_\perp$  is the parameter. Adapted from Pucel and Masse (1972) [13], Figure 2, p. 306. Reprinted with permission of IEEE.

Figure 20.9 Microstrip junction circulator: (a) microstrip line passing over an unmagnetized ferrite showing propagation paths of equal strength; (b) microstrip line passing over a magnetized ferrite showing propagation paths of unequal strength; and (c) a three-port microstrip junction circulator.

Figure 20.10 Photograph of a 15 GHz microstrip isolator based on a junction circulator. The microstrip network is fabricated on a ferrite substrate and above the coupling region is a cylindrical permanent magnet.

Figure 20.11 An edge-guide mode microstrip isolator with transverse slot discontinuity: (a) perspective view; and (b) top view. Adapted from Kane and Wong (1990) [15], Figure 1, p. 1007. Reprinted with permission of IEEE.

Figure 20.12 CPW transmission with semi-infinite ground planes. The metal thickness  $t = 8.24 \mu\text{m}$ , strip width  $w = 30 \mu\text{m}$ , gap  $g = 25 \mu\text{m}$ , and overall width  $d = 1 \text{ mm} \gg w$ . The borosilicate glass substrate has a thickness of  $500 \mu\text{m}$ , loss tangent of 0.0009, and relative permittivity of 6.1.

[Figure 20.13 Current density in cross-section at 10 GHz inside the copper CPW transmission line of Figure 20.12: \(a\) CPW line showing center strip and parts of the side ground planes; \(b\) scale; and \(c\) the strip enlarged and modeled using a finer grid than in \(a\). The darkest regions inside the conductor have a current density that is 1/10th of the peak current density. The horizontal lines in \(c\) are at integer multiples of  \$0.69 \mu\text{m}\$ , which is slightly more than the skin depth of  \$0.65 \mu\text{m}\$ . The total thickness of the strip and ground planes is  \$8.24 \mu\text{m}\$ . Calculated using Ansys HFSS.](#)

[Figure 20.14 The strip of a CPW line realized as a metaconductor \(or superlattice\) with alternating metal, here copper, layers and magnetic material layers. Shown here is the cross-section of a metaconductor with 12 copper layers and 11 magnetic layers with  \$t\_{\text{Cu}} = 0.65 \mu\text{m}\$ ,  \$t\_{\text{M}} = 0.04 \mu\text{m}\$ , and  \$t = 8.24 \mu\text{m}\$ . Other dimensions are shown in Figure 20.12. Propagation is  \$z\$ -directed and is out of the page.](#)

[Figure 20.15 Attenuation of CPW lines, one with a copper conductor and one with a metaconductor. The metaconductor has lower loss than the unmodified line over a better than 18 GHz bandwidth from 1.5 GHz to 19.75 GHz. Adapted from Iramnaaz et al. \(2012\) \[11\], Figure 4, p. 4141. Reprinted with permission of IEEE.](#)

[Figure 20.16 Magnitudes of the current and field profiles at  \$x = 0\$  and 10 GHz of the strip of CPW line with a solid copper strip with the dimensions shown in Figure 20.12. The directions of  \$H\_x\$  and  \$E\_y\$  reverse at the center of the strip \(i.e., at  \$y = 4.12 \mu\text{m}\$ \) while the directions of  \$E\_z\$  and  \$J\_z\$  are unchanged.](#)

[Figure 20.17 Magnitudes of the current and field profiles at  \$x = 0\$  and 10 GHz of the strip of a CPW line with a metaconductor CPW strip of layered copper and magnetized high-resistivity ferrite with the dimensions shown in Figure 20.12 and 20.14. The directions of  \$H\_x\$  and  \$E\_y\$  reverse at the center of the strip \(i.e., at  \$y = 4.12 \mu\text{m}\$ \) while the directions of  \$E\_z\$  and  \$J\_z\$  are unchanged.](#)

[Figure 20.18 Magnitudes of the current and field profiles at  \$x = 0\$  and 10 GHz of the strip of a CPW line with a metaconductor CPW strip of layered copper and magnetized permalloy with the dimensions shown in Figure 20.12 and 20.14. The directions of  \$H\_x\$  and  \$E\_y\$  reverse at the center of the strip \(i.e., at  \$y = 4.12 \mu\text{m}\$ \) while the directions of  \$E\_z\$  and  \$J\_z\$  are unchanged.](#)

[Figure 20.19 Current profile for three CPW strip compositions. The Cu–Py metaconductor results are for the layered metaconductor with permalloy layers sandwiched between copper layers, the alternative metaconductor results are for a CPW line with the strip comprising layers of copper and low-conductivity ferrite, and the Cu conductor results are for a solid copper strip. The semi-infinite grounds in all cases are solid copper.](#)

[Figure 20.20 Current density in cross-section at 10 GHz inside the strip of the CPW transmission line of Figure 20.12: \(a\) with a solid copper conductor having a total thickness of  \$8.24 \mu\text{m}\$ ; and \(b\) with a metaconductor consisting of 12 copper layers, each  \$0.65 \mu\text{m}\$  thick, and 11 permalloy layers, each  \$0.04 \mu\text{m}\$  thick for a total strip](#)

thickness of  $8.24 \mu\text{m}$ . Calculated using Ansys HFSS.

Figure 20.21 A microstrip frequency selective limiter: (a) with the strip on a magnetized magnetic film; and (b) spectrum of the input RF signal showing the limiting threshold; and (c) spectrum of the output RF signal.

## Chapter 21: Interconnects for Digital Systems

Figure 21.1 The layout of a CMOS inverter.

Figure 21.2 Neighboring nets and the region of influence used in capacitance extraction.

Figure 21.3 The interconnects of the CMOS inverter of Figure 21.1: (a) top view; (b) bottom view; and (c) a top view with a different perspective and the lines treated as though they had zero thickness.

Figure 21.4 The conventional H tree clock distribution architecture.

Figure 21.5 The conventional H tree clock distribution with digital buffer amplifiers.

Figure 21.6 A differential H tree clock distribution: (a) architecture; and (b) a CPS line or differential line often used with this architecture.

Figure 21.7 A rotary clock: (a) layout of a 2.5 GHz oscillator with 25 interconnected rings of differential lines; (b) details of one ring showing anti-parallel inverter pairs and an inset showing CPS line (or differential line) with strip width of  $30 \mu\text{m}$  and strip separation of  $60 \mu\text{m}$ . Adapted from Wood *et al.* (2001) [27], Figure 25.5.1, p. 401. Reprinted with permission of IEEE.

# List of Tables

## Chapter 2: Fundamentals of Signal Transmission on Interconnects

Table 2.1 Modeling criteria for sinusoidal and digital signals

Table 2.2 Comparison of critical length criteria for different digital technologies The critical length criterion is  $t_r = 2.5t_f$  (for Si  $\epsilon_r = 11.9$ ,  $\text{SiO}_2 \epsilon_r = 3.8$ , GaAs  $\epsilon_r = 12.85$ , FR-4  $\epsilon_r = 4.4$ , alumina  $\epsilon_r = 9.8$ , and Teflon<sup>TM</sup>  $\epsilon_r = 2.08$ ).

## Chapter 3: Microwave Network Analysis

Table 3.1 ABCD parameters of a transmission line and of several stubs configured as two-ports. The transmission lines are lossless with a propagation constant of  $\beta$  ( $\beta\ell$  and  $\theta$  are electrical lengths of transmission lines in radians)

Table 3.2 Two-port S parameter conversion chart. The Z and Y parameters are normalized to  $Z_0$ .  $Z'$  and  $Y'$  are the actual parameters

Table 3.3 Mathematical relations expressed as SFGs

## Chapter 4: Transmission Line Theory

Table 4.1 Transmission line waves used in scattering parameter analysis

Table 4.2 Properties of traveling waves and pseudo waves at the junction of two transmission lines with the same characteristic impedance

Table 4.3 Power flow,  $p$ , across a reference plane on a transmission line with traveling waves and pseudo waves

Table 4.4 Power flow,  $p$ , across a reference plane on a transmission line with pseudo waves and power waves

## Chapter 5: Planar Interconnect Technologies

Table 5.1 Characteristic impedance ( $Z_0$ ) ranges for the various structures with a substrate relative permittivity of 10

Table 5.2 Comparison of typical unloaded  $Q$  factors ( $Q_u$ ) at a frequency of 30 GHz for the structures shown in Figure 5.1. The substrate permittivity is 10 for all structures except finline, where it is 3.3

Table 5.3 Properties of some typical substrate materials. GaN is typically used as an epitaxial layer on Si or SiC and so the dielectric properties of Si or SiC are used. Most hard substrates (including semiconductors) have thermal conductivities in the range of 1 to 40 W/(m · K). Important exceptions include GaN (150 W/(m · K)), quartz (500 W/(m · K)) and silicon (138 W/(m · K)). Dielectric strengths range from 300 V/cm to 4 kV/cm. Many types of soft substrates are available. Soft substrates mostly have permittivities in the range  $2.0 \leq \epsilon_r \leq 6.1$  (lower than for hard substrates), dielectric loss tangents in the range  $0.0012 \leq \tan \delta \leq 0.005$  (higher than for hard substrates), dielectric strengths in the range of 140 to 240 kV/cm (much higher than for hard substrates) and thermal conductivities in the range 0.26 to 0.76 W/(m · K) (slightly lower than for hard substrates). Extensive substrate data is given in Appendix C.

Table 5.4 Some specific observations regarding alumina substrates

Table 5.5 Specific properties of LTCC materials

Table 5.6 A selection of semiconductor substrates (mainly from Ponchak *et al.* [46]).

Table 5.7 MIC/MMIC technology: manufacturing costs and operational capability comparisons

Table 5.8 Permittivity  $\epsilon_r$  and dielectric loss tangent  $\tan \delta$  of the major organic PCB materials at 10 GHz.

Table 5.9 Comparison of typical parameters of interconnects on the various MCM substrates.

Table 5.10 Parameters of the MCM-D interconnects

## Chapter 6: Microstrip Design at Low Frequencies

Table 6.1 Microstrip line normalized width  $u$  and effective relative permittivity  $\epsilon_{\text{eff}}$  for

specified characteristic impedance  $Z_0$ . Data derived from analysis in Section 6.4.1

Table 6.3 Microstrip line normalized width  $u$  and effective permittivity  $\epsilon_{\text{eff}}$  for specified characteristic impedance  $Z_0$

Table 6.4 Comparison of two fitted equations for the effective permittivity and characteristic impedance of a microstrip line. Equation (6.21) has an accuracy of better than 0.2% and Equation (6.28) has an accuracy of better than 1%

Table 6.5 Adjustments required in  $w$  for a 1% increase in  $Z_0$

## Chapter 7: Microstrip at High Frequencies

Table 7.1 Peak charge and longitudinal,  $i_z$ , and transverse,  $i_x$ , current levels for the microstrip line. The currents and charges are normalized to the peak strip levels at 30 GHz

Table 7.2 Skin depth of various conductors at 20°C

## Chapter 9: Discontinuities in Microstrip

Table 9.1 Coefficients  $K_i(\epsilon_r)$  in Equation (9.1) for various substrate permittivities. Adapted from Silvester and Benedek 1972 [4], Table 1, p. 515. Reprinted with permission of IEEE

## Chapter 10: Parallel-coupled Microstrip Lines

Table 10.1 Design parameters for coupled lines for  $\epsilon_r = 4$  corresponding to design on an  $\text{SiO}_2$  or FR-4 (printed circuit board) substrate. The normalized gap,  $g$ , is chosen to obtain the desired coupled-line mode impedance ratio  $Z_{0e}/Z_{0o}$ . Data derived from the analysis in Section 10.3.  $Z_0$  is the characteristic impedance of an individual microstrip line with a normalized width  $u$  on the same substrate

Table 10.3 Design parameters for a microstrip coupler on a substrate with a relative permittivity  $\epsilon_r$  of 11.9 corresponding to a Si substrate. Data derived from the analysis in Section 10.3.  $Z_0$  is the characteristic impedance of an individual microstrip line with a normalized width  $u$  on the same substrate

Table 10.4 Design parameters for a microstrip coupler on a substrate with a relative permittivity  $\epsilon_r$  of 12.85 corresponding to a GaAs substrate. Data derived from the analysis in Section 10.3.  $Z_0$  is the characteristic impedance of an individual microstrip line with a normalized width  $u$  on the same substrate

## Chapter 11: Applications of Parallel-coupled Microstrip Lines

Table 11.1 Parameters for compensated and uncompensated coupled sections. The data in this Table are due to Dydyk [17]

Table 11.2 Ideal and typical parameters of a directional coupler

## Chapter 12: Microstrip Passive Elements

Table 12.1 On-chip resistor properties. Material from Lee [42] and other sources.

[Table 12.2 On-chip capacitor properties. Material from Lee \[42\] and other sources \[43–47\]](#)

[Table 12.3 Inductance and  \$Q\$  of planar inductors:  \$d\$  is the side-dimension shown in Figure 12.3\(a\),  \$n\$  is the number of turns,  \$L\$  and  \$Q\_{\max}\$  are at  \$f\_0\$ ,  \$f\_0\$  is the operating frequency, and  \$f\_{SR}\$  is the self-resonant frequency.  \$M\_n\$  indicates the metal layer used. Adapted in part from Burghartz \[79\].](#)

## Chapter 19: Filters Using Planar Transmission Lines

[Table 19.1 Coefficients of the Butterworth lowpass prototype filter with a radian corner frequency of 1 radian/s and a  \$1 \Omega\$  system impedance \( \$g\_0 = 1 = g\_{n+1}\$ \)](#)

[Table 19.2 Coefficients of normalized third-order Chebyshev lowpass filter prototypes](#)

[Table 19.3 Coefficients of normalized fifth-order Chebyshev lowpass filter prototypes](#)

[Table 19.4 Coefficients of normalized seventh-order Chebyshev lowpass filter prototypes](#)

[Table 19.5 Coefficients of normalized ninth-order Chebyshev lowpass filter prototypes](#)

[Table 19.6 Lowpass prototype to highpass filter transformation. The corner frequency of the lowpass prototype is 1 radian/s](#)

[Table 19.7 Lowpass prototype to bandpass filter transformation. The corner frequency of the lowpass prototype is 1 radian/s. Here  \$\omega\_c = 1/\sqrt{L\_1 C\_1} = \sqrt{\omega\_1 \omega\_2}\$ ,  \$\omega\_1\$  and  \$\omega\_2\$  are the band-edge frequencies, and  \$\alpha\$  is the transformation constant,  \$\alpha = \omega\_c/\(\omega\_2 - \omega\_1\)\$](#)

[Table 19.8 Lowpass prototype to bandstop filter transformation. The corner frequency of the lowpass prototype is 1 radian/s. Here  \$\frac{\omega\_c}{1/\sqrt{L\_1 C\_1}} = \sqrt{\omega\_1 \omega\_2}\$ ,  \$\omega\_1\$  and  \$\omega\_2\$  are the band-edge frequencies, and  \$\alpha\$  is the transformation constant,  \$\alpha = \omega\_c/\(\omega\_2 - \omega\_1\)\$](#)

[Table 19.9 Summary chart for inductive and capacitive elements formed using microstrip lines](#)

[Table 19.10 Coefficients for a sixth-order Chebyshev filter](#)

[Table 19.11 Step 3 results](#)

[Table 19.12 Summary of the main bandpass filter parameters](#)

## Chapter 20: Magnetic Materials and Planar Transmission Lines

[Table 20.1 Magnetic properties of ferrites and garnets, both ferrimagnetic materials, used in microwave applications. The saturation magnetization is  \$4\pi M\_s, \text{CGS}\$  in the CGS unit system \(corresponding to Equation \(20.1\)\) and  \$M\_s\$  in the SI unit system. Saturation magnetization at room temperature is given in CGS \(Gaussian\) units, as provided by manufacturers, and SI units, as used in microwave design. The ranges given are for different material preparations \(except for frequency ranges\). For a particular preparation the values are fixed](#)

[Table 20.2 Electrical properties of important ferrimagnetic materials used in microwave applications. The frequency given is the typical range of application. Properties are measured at 9.4 GHz or 10 GHz except for resistivity, which is at DC. The dielectric loss tangent is  \$\tan \delta\$ . The ranges given are for different material preparations](#)

[Table 20.3 Critical frequencies of magnetic materials at room temperature and in saturation.  \$AFMR\_{MIN}\$  is the minimum antiferromagnetic resonance frequency determined by the saturation magnetization, that is,  \$AFMR\_{MIN} = \min\(f\_{AFMR}\)\$](#)

[Table 20.4 Material properties used in the CPW-based metaconductor study. Properties are at 9.4 GHz. The substrate is a borosilicate glass. The ferrite here is a low conductivity and low resistivity material whereas most ferrites have high resistivity](#)

[Table 20.5 Thermal properties of selected materials](#)

## Appendix A: Physical and Mathematical Properties

[Table A.1 Main SI units used in RF and microwave engineering](#)

[Table A.2 Main SI units used in RF and microwave engineering](#)

[Table A.3 SI prefixes](#)

[Table A.4 Physical and mathematical constants in SI units](#)

[Table A.5 Standard temperatures.](#)

[Table A.6 Conversions of electromagnetic CGS \(Gaussian\) units to SI units.](#)

## Appendix C: RF and Microwave Substrates

[Table C.1 Properties of typical hard substrate materials](#)

[Table C.2 Properties of typical soft substrate materials. Typical surface roughness is 4–6  \$\mu\text{m}\$ . Typical dielectric strength is > 50 kV/cm](#)

# **FOUNDATIONS FOR MICROSTRIP CIRCUIT DESIGN**

**FOURTH EDITION**

**Terry C. Edwards**

*Consultant*

**Michael B. Steer**

*North Carolina State University*



**WILEY**

This edition first published 2016

© 2016 John Wiley & Sons, Ltd

*Registered office*

John Wiley & Sons Ltd, The Atrium, Southern Gate, Chichester, West Sussex, PO19 8SQ, United Kingdom

For details of our global editorial offices, for customer services and for information about how to apply for permission to reuse the copyright material in this book please see our website at [www.wiley.com](http://www.wiley.com).

The right of the author to be identified as the author of this work has been asserted in accordance with the Copyright, Designs and Patents Act 1988.

All rights reserved. No part of this publication may be reproduced, stored in a retrieval system, or transmitted, in any form or by any means, electronic, mechanical, photocopying, recording or otherwise, except as permitted by the UK Copyright, Designs and Patents Act 1988, without the prior permission of the publisher.

Wiley also publishes its books in a variety of electronic formats. Some content that appears in print may not be available in electronic books.

Designations used by companies to distinguish their products are often claimed as trademarks. All brand names and product names used in this book are trade names, service marks, trademarks or registered trademarks of their respective owners. The publisher is not associated with any product or vendor mentioned in this book.

**Limit of Liability/Disclaimer of Warranty:** While the publisher and author have used their best efforts in preparing this book, they make no representations or warranties with respect to the accuracy or completeness of the contents of this book and specifically disclaim any implied warranties of merchantability or fitness for a particular purpose. It is sold on the understanding that the publisher is not engaged in rendering professional services and neither the publisher nor the author shall be liable for damages arising herefrom. If professional advice or other expert assistance is required, the services of a competent professional should be sought.

*Library of Congress Cataloging-in-Publication Data*

ISBN: 9781118936191

A catalogue record for this book is available from the British Library.

Cover Image: © Michael Steer, Steven Lipa and Alan Victor

## **List of Trademarks**

Ansys® is a registered trademark of SAS IP, Inc.

AT&T® is a registered trademark of AT&T Intellectual Property II, L.P.

Cuflon®, Polyflon® and Norclad® are registered trademarks of Crane Co.

DuPont® and Teflon® are registered trademarks of E. I. du Pont de Nemours and Company.

RT/Duroid® is a registered trademark of World Properties, Inc.

SONNET® is a trademark of Sonnet Software Inc.

Ultem® is a trademark of SABIC Global Technologies B.V.

LTE® is a registered trademark of the European Telecommunications Standards Institute.

WiMAX® is a registered trademark of the WiMAX Forum

All other trademarks are the properties of their respective owners.

*Terry dedicates this book to his wife Patricia*

*Michael dedicates this book to his son Killian*

# Preface

Interconnects have achieved a prominent position in determining the performance of high-speed digital, RF, and microwave circuits. In digital circuits, interconnect delay exceeds that of individual gates and is the primary determinant of clock speed. In RF and microwave circuits, interconnects and passive elements defined using them are critical circuit components.

This design text is both a sequel and an update to the original well-received first, second, and third editions. The expanded text provides foundations for the accurate design of microstrip components and of circuits applicable to microwave, millimeter-wave, and high-speed digital sub-systems.

The text is primarily intended for design engineers and research and development specialists who are active in these areas. It has been our attempt to show the commonalities in the design of interconnects in high-speed digital, RF, and microwave applications. This is done by showing the common principles of signal transmission. It is also likely to prove useful to instructors and students in advanced undergraduate and graduate electronics and computer engineering courses. The text is also intended to be used in short courses and in graduate level courses.

The direction is strongly focused toward explaining the fundamentals of operation, and toward useful design formulas and approaches—a repeat coverage of well-documented analyses of microstrip structures has been considered unnecessary and out of place here, but is fully cited.

The work is partly based on research and teaching extending over four decades. Microwave and interconnect courses were presented at La Trobe University (Melbourne, Australia), the University of Bradford (Great Britain), North Carolina State University (Raleigh, North Carolina, USA), and the University of Leeds (UK). The work is also based on short courses on the signal integrity of and interconnect design for high-speed digital circuits. The majority of the research forming the basis of important sections of this book was undertaken at North Carolina State University and at the Royal Military College of Science (Shrivenham, England).

The text is organized into 21 chapters, leading from the physical principles of signal transmission on interconnects, through the fundamental aspects of interconnect and microstrip design, on to circuit applications in RF, microwave, millimeter-wave, and high-speed digital circuits.

The design of high-speed interconnects for digital circuits and of RF and microwave transmission lines has significant common elements, but also significant differences. There are common underlying physical principles, and throughout the text this is stressed. The successful design of the highest performance digital interconnects, for example a clock distribution net, requires considerable transmission line knowledge. Generally, in treatments in papers and chapters of relevant books “just enough” transmission line theory and technology is presented. Not all of the options are covered. Our approach has been to provide the digital interconnect

designer with a comprehensive treatment. [Chapter 2](#) covers signal transmission on interconnects in detail, including answering such questions as “When are inductive effects important?” However, the interconnect treatment provides the digital designer with the tools for interconnect design now and in the future. The final chapter considers a number of clock distribution designs and, drawing from the material presented throughout the book, illustrates the importance of transmission line knowledge in the design of the highest performance interconnect. In contrast to how this material is often presented to digital designers, we contend that providing just enough knowledge is not enough to develop advanced and competitive interconnect designs.

This book provides a solid basis for RF, microwave, and millimeter-wave design. The material enables the designer to make technology choices and provides insight that supports the early stages of design. The many examples in the book show how these technology choices are made.

[Chapter 1](#) introduces design using microstrip and planar transmission lines. A basic review of interconnects and of TEM-mode transmission line theory is presented in [Chapter 2](#). This is intended to provide the fundamentals for concepts and expressions used in many later chapters. [Chapter 3](#) covers microwave network analysis ( $ABCD$  parameters,  $S$  parameters, etc.). This chapter may be used as a source of initial interconnect technology decisions.

[Chapters 4](#) through [20](#) consider specific transmission line structures and interconnect discontinuities. Considerable insight is provided by using current and charge profiles of the various structures.

[Chapter 8](#) considers loss effects, and power and current handling capability. Transitions between different transmission line structures are considered in [Chapter 17](#), and measurement techniques are considered in [Chapter 18](#).

Filter design is covered in depth in [Chapter 19](#). The fundamentals of microwave magnetic materials are considered in [Chapter 20](#). Included is a discussion of developments in using magnetic materials to suppress the skin effect that otherwise leads to increased losses at higher frequencies, an effect that is critically significant at microwave frequencies.

[Chapter 21](#) addresses the unique aspects of interconnects in high-speed digital systems, for example transmission line principles are used in the development of a digital clock architecture capable of supporting clocking at 10 GHz or more.

Through these chapters the book presents a unifying foundation for the design of interconnects and microstrips. It then shows application of these lines in a variety of passive and active digital, analog, RF, and microwave circuits.

Terry C. Edwards and Michael B. Steer  
*Yorkshire, England, UK, and Raleigh, North Carolina, USA*

# Acknowledgements

During the preparation of all editions of this text there were a number of people who made significant contributions and thanks to whom the quality of the material was decidedly enhanced. Most of these were at La Trobe University (Melbourne, Australia), the University of Bradford (England), North Carolina State University (NC State, Raleigh, North Carolina, USA), the Royal Military College of Science (RMCS, Shrivenham, England) and the University of Leeds (UK). The authors wish to particularly thank Dr. Ashwain Rayit, whose dissertation on coplanar waveguides was used as the basis for some of the material in [Chapter 14](#). La Trobe, Bradford, Leeds, and NC State universities were indeed fortunate with their quality of undergraduate, graduate, and postgraduate students who were responsible for guiding the development of the text, and both learnt from and contributed to the eventual form of the text.

Terry wishes to thank several of his former colleagues at RMCS, particularly at what was known as the School of Electrical Engineering and Science: past (Honorary) Professors Michael Potok, Chris Harris, and the late Jim James for their advice and stimulation during the preparation of the original manuscript. Dr. Ann Henderson also read parts of the original text, and her suggestions proved extremely helpful. At La Trobe University, thanks are extended to the late Professor Daryl Hooper, who exhibited infectious drive and enthusiasm. Also to Dr. Laurie Cahill for many deep and helpful ideas. Dr. Roger Owens was of great assistance with his critical reading of the original manuscript, and made many useful suggestions for the second edition.

Michael wishes to express gratitude to several of his former graduate students whose research led to many of the results presented here, as well as to design insight. In particular, he wishes to thank Dr. Mark Basel, Mr. Jeffrey Kasten, Mr. Steven Golberg, Dr. Steven Lipa, Dr. Alan Glasser, Mr. Bari Biswas, Dr. Meta Ozkar, and Dr. Carlos Christoffersen. These individuals are now involved in leading-edge design of high-speed digital circuits, microwave circuits, RFICs, MMICs, and in the computer-aided engineering industry. Michael also wishes to express gratitude to his colleague and friend Professor Paul Franzon, who undertook many joint interconnect research projects, and with whom he presents well-attended interconnect short courses. The feedback received from the working engineers who took part in these short courses helped refine the way in which this material is presented to people with both rudimentary knowledge in electromagnetics as well as those on the leading edge of high-speed interconnect design. The third edition of this book was written when Michael was at the University of Leeds, UK, during 1999 and 2000, and he wishes to thank his colleagues there for the conducive academic environment.

The attention of the reader is drawn to those at John Wiley & Sons for their strong support, backing, and patience that led to the production of this text.

Finally, we want to express our gratitude to the forbearance and support of our families during

the preparation of this text. Terry thanks his wife Patricia, and Michael thanks his wife Mary and his children Cormac, Fiona, and Killian.

Terry C. Edwards and Michael B. Steer

# Chapter 1

## Introduction to Design Using Microstrip and Planar Lines

### 1.1 Introduction

The microstrip line is the most widely used interconnect at radio frequency (RF) and microwave frequencies. The microstrip line, shown in [Figure 1.1](#), is the main member of a broad class of transmission lines that are built using printed circuit board technology. Here the microstrip line is typically created starting with a low loss dielectric slab or substrate that has a metal sheet bonded to both sides. The strip of the line is formed by patterning the top conductor and etching away the unwanted metal. Sometimes the metal pattern forming the strips is patterned by silk screening or by growing metal in the appropriate place. At RF, microwave and high-speed digital frequencies it is necessary to provide a return current path as well as the signal current path defined by the strip. At low frequencies, below a few tens of megahertz, it is also necessary to provide a signal return path but then it is less critical that the cross-sectional geometries be precisely established. The cross-sectional geometry, the width,  $w$ , of the strip and the thickness,  $h$ , of the substrate define the ratio of the voltage and current signals traveling along the microstrip line. This ratio is called the characteristic impedance of the line and it is critical for reliable signal transmission, that is, good signal integrity, that the cross-sectional geometry be the same along the line as then the characteristic impedance of the line is constant.

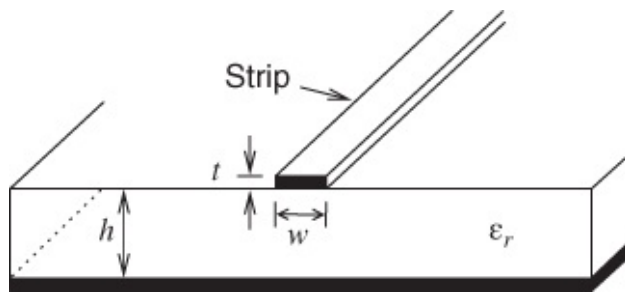


[Figure 1.1](#) Microstrip transmission line.

When microwave engineers refer to microstrip design they are referring to the design of RF and microwave circuits using the major types of planar transmission line technologies. While simple in concept, it is a technology that needed to be invented. As well as conceptualizing a transmission line that can be realized by etching a planar metallic conductor on the printed circuit board, it is essential to provide the analytic tools that enable the propagation characteristics of the line to be calculated and enable structures such as couplers and filters to be synthesized using planar transmission lines.

## 1.2 Origins of Microstrip

The origins of microstrip trace back to the development, by Rumsey and Jamieson during the early 1940s, of a coaxial line with a flat center conductor forming a rectangular coaxial line [[1]]. At this time there were also concepts developed for a conductor between two metal slabs, most notably Hewlett Packard Company's slabline tuner. At the same time printed circuit boards were employed for low-frequency circuits. These came together in an understanding in 1949 by Barrett that the thick center conductor of the rectangular coaxial transmission line could be very thin with little effect on the properties of the line. This then meant that low-frequency printed circuit board techniques could be employed in microwave circuits and the transmission line system became known as stripline [[1, 2]]. The conceptual evolution of stripline is shown in [Figure 1.2](#). The stripline configuration is developed by sandwiching a metallic strip between two metal-clad dielectric sheets. As initially envisioned, the strip could be stamped out or silk-screened using silver ink. Today it is most common to begin with a continuous metallic sheet bonded to one or both sides of a dielectric sheet. A pattern of an etch resistant material is then photolithographically defined on the sheet and the strip pattern appears after etching.

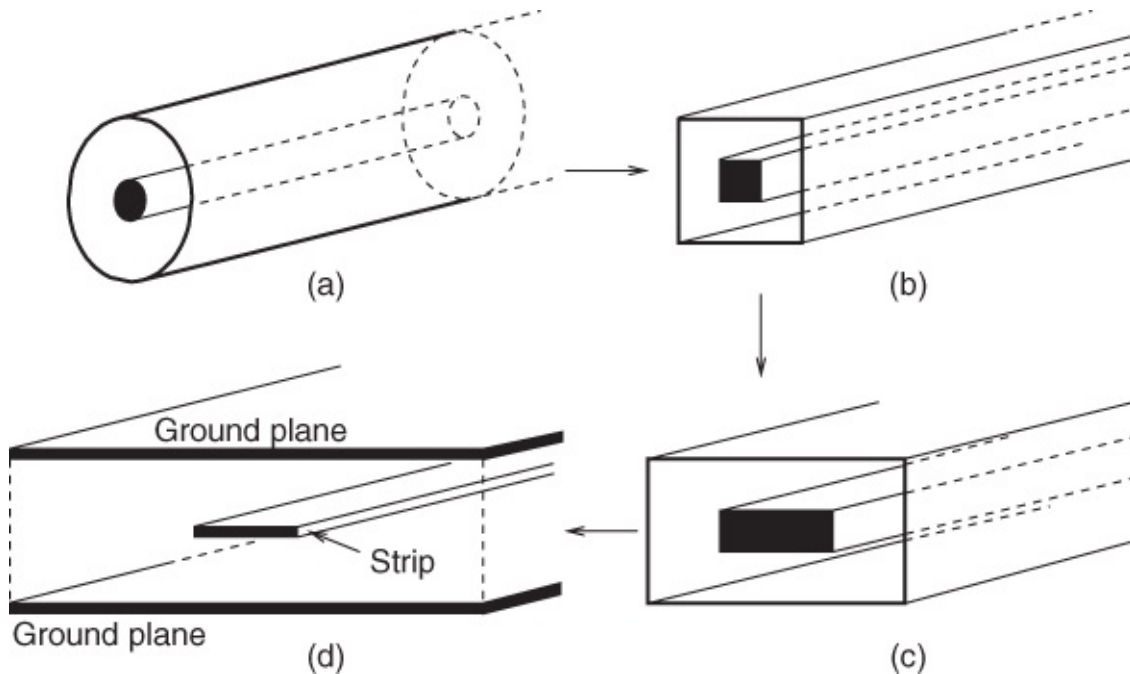


[Figure 1.2](#) Evolution of the stripline transmission line: (a) coaxial line with a round center conductor; (b) square coaxial line with a square center conductor; (c) rectangular coaxial line with a flat center conductor; and (d) stripline.

While stripline has tremendous manufacturing advantages compared to the coaxial line, it is difficult to attach lumped components to it (it is after all buried) and to make circuit adjustments such as mechanically adjusting the patterned circuit. The next advance came with the development of microstrip by Grieg and Engelmann in 1952 as they removed one of stripline's ground planes [[3]]. This microstrip line has become the most important microwave transmission line and the basis for all printed microwave circuits, microwave monolithically

integrated circuits (MMICs), and radio frequency integrated circuits (RFICs). Stripline, which can be extended to having multiple levels of strip, is mostly used where the interconnect density must be high, such as with integrated circuit packages and with high speed digital circuits.

Fundamentally the most important aspect of microwave circuits is the provision of a signal current path and a signal return current path on the ground planes in the case of stripline and microstrip. However at tens of megahertz and above the proper electrical design requires a precise ratio of the voltage and current waves on the lines. To design for this characteristic it is necessary to have analytic design formulas. Thus conceptualization of the planar transmission line structures is not sufficient, it is necessary to develop analytic formulas and design curves for the electrical properties of stripline and microstrip. It is not sufficient to rely on electromagnetic (EM) simulation as there is little physical insight provided. Many of the effects that are important and derive from such parameters as strip thickness and roughness cannot be modeled. Indeed many of the effects that impact the performance of microwave planar circuits, for example multimoding, cannot be predicted by EM simulation alone as the undesired effects usually will not show up when perfectly symmetrical geometries and uniform materials are considered. The essential electrical properties of a transmission line are its characteristic impedance, the ratio of the traveling voltage and current waves on the line, and its propagation coefficient which relates to the speed of propagation of the voltage and current waves on the lines. Knowing these is essential in using the lines in RF and microwave circuits. Among the first useful formulas for the electrical characteristics of stripline were those developed by Cohn in 1954 [[4]], and by Pease and Mingins in 1955 [[5]]. Grieg and Engelmann were the first to develop the formulas for the characteristic impedance of microstrip [[3]]. This situation is typical of all microwave and RF design developments: it is not enough to conceptualize a structure, it is necessary to develop the design formulas that enable the structure to be used in design.

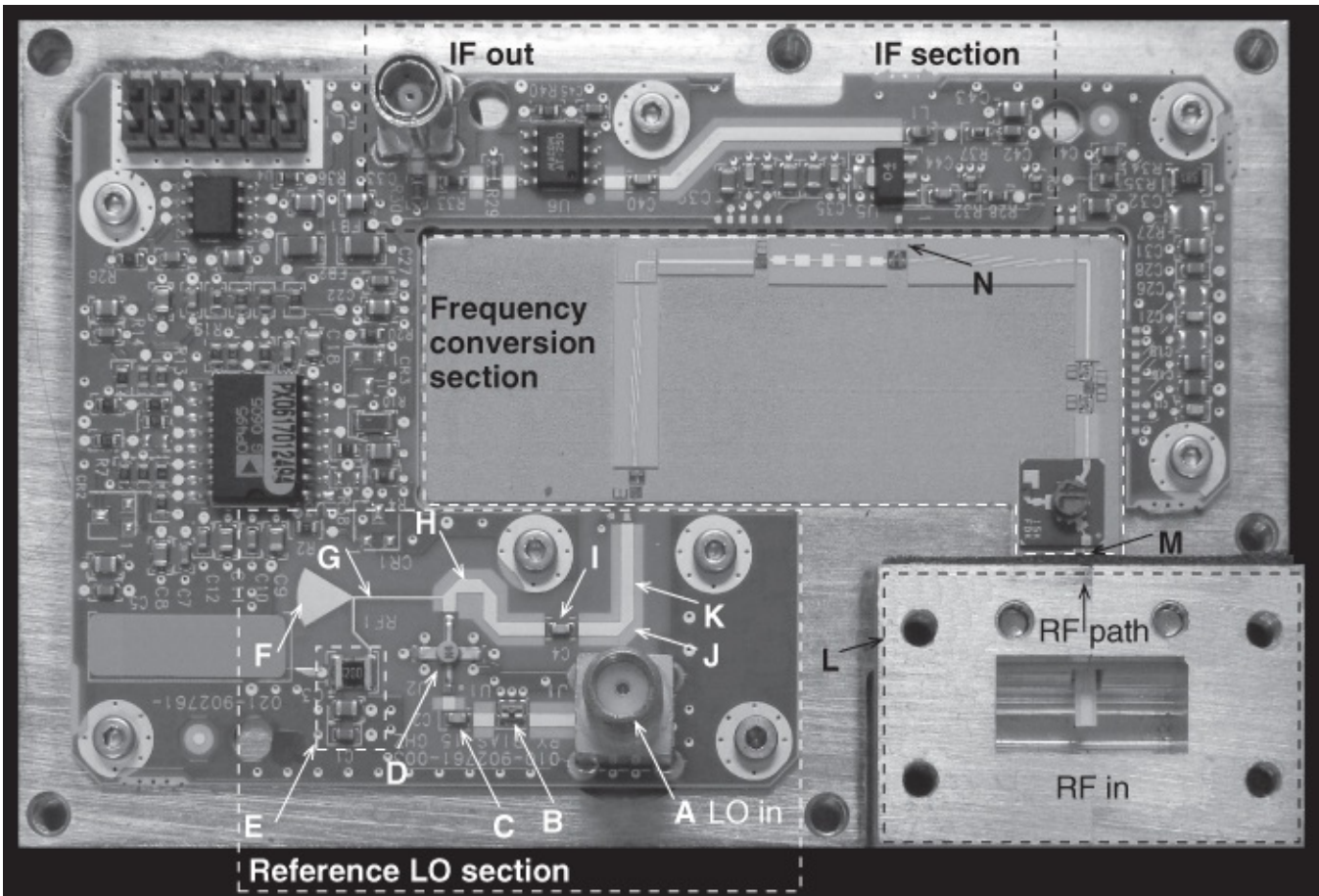
Planar transmission line technology has developed considerably over the decades with considerable functionality, such as filtering, derived using patterned planar lines. Overwhelmingly the preference is to realize these functions and interconnections using planar technology and, if space and extremes of frequency operation are not of concern, preferably with microstrip that can be easily adjusted by the user. Once a microstrip design has been optimized, it can be faithfully and cheaply reproduced using photographically defined geometries.

The value of printed microwave circuits was immediately recognized when stripline and microstrip were introduced. This resulted in significant investments in the development of ever more accurate design formulas as well as the development of circuit structures that enabled such functions as filtering and coupling to be realized in printed circuit technology. This book collects the most important developments and the ones that have emerged as providing the best design insight. Many other types of planar lines have been developed that have properties superior to those of microstrip and stripline in particular applications. All of the planar technologies that are currently used are considered in this book.

## 1.3 RF and Microwave Modules

The great majority of RF and microwave design engineers are employed in realizing microwave systems using RF and microwave modules. This includes the design of modules using smaller modules such as monolithically integrated circuits (ICs). Economics necessitate that RF integrated circuits be developed for multiple applications, and in RF and microwave module design ICs as well as discrete semiconductor devices are interconnected using planar transmission lines in printed microwave circuit technology. In this section a microwave module implementing a 15 GHz microwave receiver is considered with the aim of illustrating RF and microwave module design. This book considers the technology required to realize such printed microwave circuits.

Most RF and microwave systems convert information at one frequency to information at another frequency that can either be more conveniently processed, in the case of a receiver, or more conveniently radiated, in the case of a transmitter [[6, 7]]. [Figure 1.3](#) is a 15 GHz receiver module which itself consists of interconnected modules. This unit is used in a point-to-point microwave link (a microwave fixed service) employed mostly in cellular systems to communicate between base stations. The subsystem modules such as the amplifiers, frequency multipliers, mixers, circulator, and waveguide adaptor are available as off-the-shelf components from companies that specialize in developing such modules and selling them to a large user base. Using modules enables high-performance systems to be realized cost effectively.



- |                                    |   |
|------------------------------------|---|
| A SMA connector, Reference LO in   | H 50 Ω transmission line                    |
| B Attenuator                       | I DC blocking capacitor                     |
| C DC blocking capacitor            | J Mitered bend                              |
| D Reference LO amplifier           | K 50 Ω transmission line                    |
| E Bias line                        | L Waveguide-to-microstrip adaptor, RF in    |
| F Radial stub                      | M Interface to frequency conversion section |
| G High-impedance transmission line | N Interface to IF section                   |

**Figure 1.3** A 14.4–15.35 GHz receiver module itself consisting of cascaded modules interconnected by microstrip transmission lines. Surrounding the microwave circuit are DC conditioning and control circuitry. RF in is 14.4–15.35 GHz, LO in is 1600.625–1741.875 MHz. The frequency of the IF is 70–1595 MHz. © M. Steer, used with permission.

The receiver shown in [Figure 1.3](#) has a local oscillator (LO) section with components A–K, an RF input section comprising a waveguide-to-microstrip adaptor L, a frequency conversion section, and an intermediate frequency (IF) section. The other parts of the printed circuit surrounding the microwave sections provide the supply voltage and control logic.

The RF signal is presented to the waveguide-to-microstrip transition L from an antenna feed that is also a rectangular waveguide. The waveguide-to-microstrip transition is also called a waveguide-to-microstrip adaptor or a waveguide-to-microstrip launcher. It converts the RF signal in the rectangular waveguide to a microstrip line and the signal follows the RF path and is presented to the frequency conversion section at M. This signal is eventually mixed with the

LO signal to produce the desired low intermediate frequency at N.

### 1.3.1 Reference LO Section

A reference LO signal is provided by a coaxial cable to the SMA connector A. The sinusoidal reference LO has a frequency that can be varied from 1600.625 MHz to 1741.875 MHz but it is not at the desired mixing frequency to convert the modulation on the approximately 15 GHz RF signal to the IF signal below 1595 MHz. Thus the LO frequency must be multiplied, which is done in the frequency conversion section. The main function of the complete LO path, from the connector A to the mixer immediately prior to N, is to amplify the reference LO signal and then to multiply its frequency.

The SMA connector, A, is a board-mounted connector that transitions the RF signal from the coaxial input to a microstrip line. This carefully designed component maintains a constant characteristic impedance from the coaxial transmission line through to the microstrip line. The characteristic impedance of the coaxial line is determined by the geometry of the inner and outer coaxial conductors and the dielectric between the conductors. The characteristic impedance of the microstrip line is also geometrically defined, now by the width of the strip and the distance from the strip to the ground plane, which is just the thickness of the dielectric of the circuit board. The first surface-mounted reference LO component on the circuit board is an attenuator B. This reduces the level of the applied reference LO signal and its main function is to ensure that the reference LO applied to the coaxial adaptor sees a matched load so that there are negligible reflections from the LO port of the receiver board. This is very typical in RF and microwave module design. As long as a signal is sufficiently large, one of the design objectives is to ensure reflectionless connections from one major module to another; in this case the module that produces the reference LO signal and the receiver module. The easiest way to do this over a broad bandwidth is to use an attenuator. While this dissipates microwave power, it considerably simplifies design, enabling major modules to be designed independently of each other. This, of course, is a problematic strategy with battery-powered devices. As a result the RF portion of mobile devices is tightly specified and module design is highly orchestrated.

The next component in the LO path is a DC blocking capacitor, C, and then a packaged integrated circuit amplifier, D. The amplifier requires the application of DC bias through bias circuitry E, F, and G. The input and output of the reference LO amplifier is matched to  $50 \Omega$ , which is typical of sub-modules available off-the-shelf. The design strategy for the bias network is for the bias circuit to present an RF open circuit to the output of the amplifier. F is an open-circuited radial stub which together with the transmission line section, G, presents the required open circuit to the output of the transistor. The surface-mount components in E present the required bias voltage to the reference LO amplifier. The transmission line path provided by line sections H and K presents the reference LO signal to the frequency conversion section.

Along the reference LO path defined by H and K are several mitered bends, one of which is identified by K. Detail of the bend in this path is shown in [Figure 1.4\(a\)](#), which shows two short sections of microstrip transmission line on either side of a bend. Typically in a schematic

view the layout of a planar transmission line is as shown in [Figure 1.4\(b\)](#). This is the two-dimensional representation of the microstrip line shown in [Figure 1.1](#). This is what is seen by an observer looking at a microstrip line from above. Microstrip is so commonly used that the layout view of microstrip components is often used in RF and microwave circuit schematics. One would normally think that an acceptable bend would be the rectangular bend shown in [Figure 1.4\(c\)](#). With more metal this bend would have lower resistance but its microwave properties are not as good as that of the mitered bends shown in [Figures 1.4\(d\) and \(e\)](#). [Figure 1.4\(d\)](#) shows a partially mitered bend and [Figure 1.4\(e\)](#) shows a fully mitered bend corresponding to the bend in [Figure 1.4\(a\)](#). The fully mitered bend, [Figure 1.4\(e\)](#), has better microwave properties which can only be understood by appreciating that first the microstrip line, or more specifically the metallic conductors forming the microstrip line, guide an electromagnetic wave confined mostly between the strip and the ground plane. Then the miter of the bend can be viewed as forming an open-circuited mirror (a magnetic mirror rather than an electric mirror) of the wave which has fringing fields that extend beyond the edges of the strip. The rectangular bend of [Figure 1.4\(c\)](#) reflects part of the incident signal back, the partially mitered bend of [Figure 1.4\(d\)](#) has lower reflection, and the fully mitered bend of [Figure 1.4\(e\)](#) is an almost perfect bend with negligible reflection. Understanding this behavior is one of the aims of this book. Microstrip design is distinguished from many other branches of electrical engineering by heavily relying on the intuition of the behavior of electromagnetic fields.

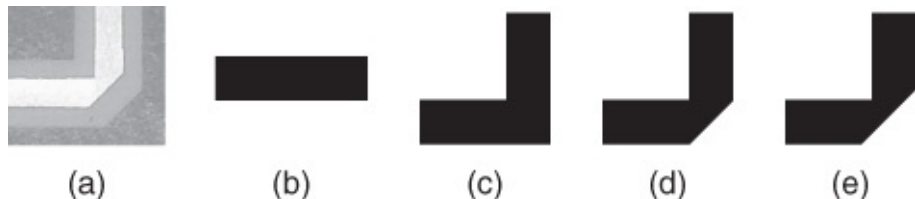


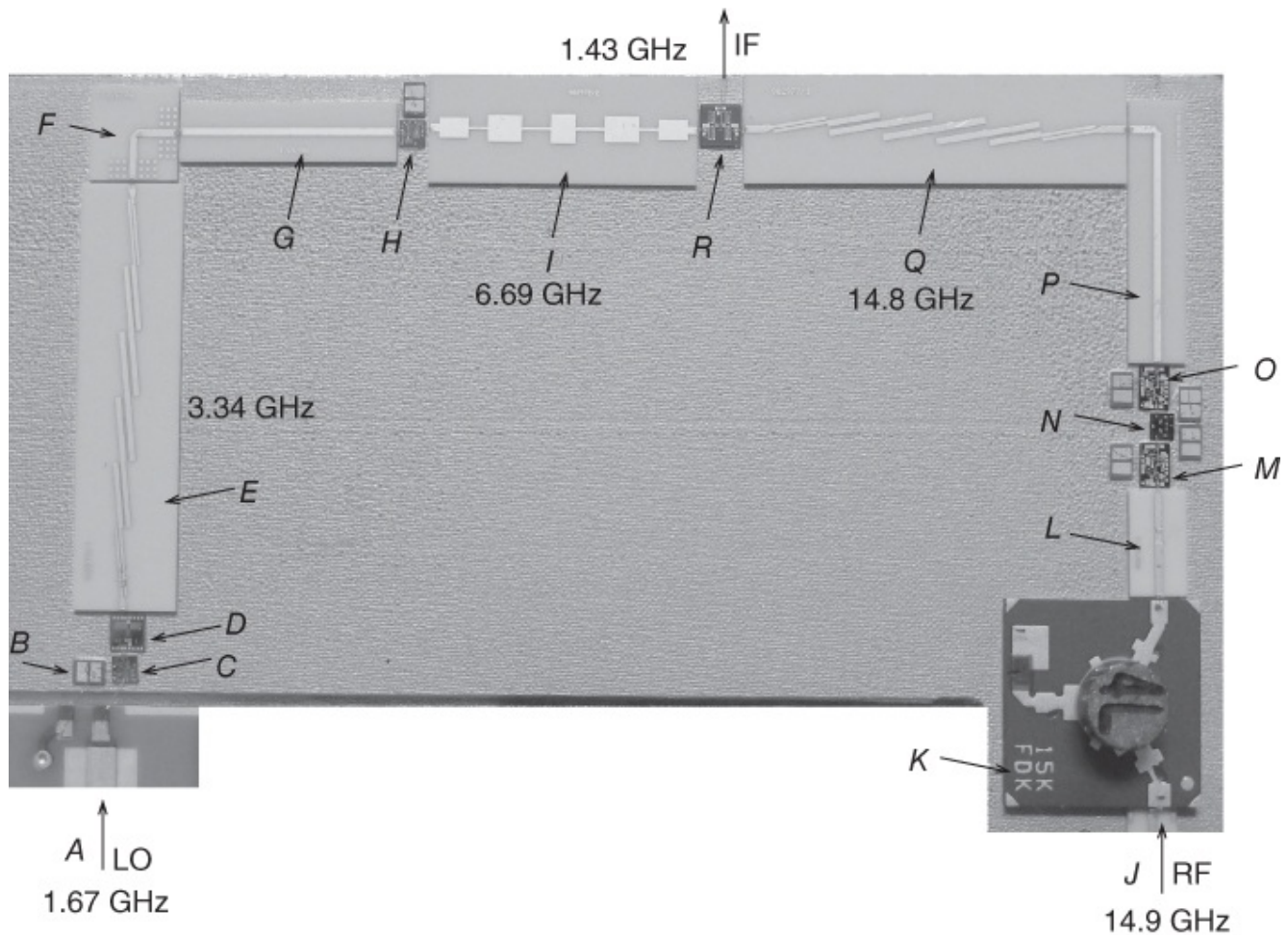
**Figure 1.4** Microstrip bends: (a) detail of bend from the reference LO section of [Figure 1.3](#); (b) layout representation of a microstrip transmission line; (c) microstrip rectangular bend; (d) partially mitered bend; and (e) mitered microstrip bend.

The detail of the microstrip bend in [Figure 1.4\(a\)](#) has a number of other typical characteristics. The metal is copper plated by a very thin layer typically of tin or gold to prevent the growth of oxide, which would contribute additional loss. The plated metal is so thin that the underlying copper is visible. Since an oxide cannot form on the plated line, the passivation layer, visible as the darker region on the softboard, is not needed over the microstrip line. This reduces the line capacitance and the variability of this capacitance that results because the thickness of the solder resist layer is not well controlled. In addition, by exposing the strip metal, rework and tuning are possible.

### 1.3.2 Frequency Conversion Section

The frequency conversion section mixes the frequency-scaled reference LO with an amplified RF signal to produce an intermediate frequency, IF, signal processed in the IF section. Detail of the frequency conversion section is shown in [Figure 1.5\(a\)](#). The printed circuit board forming

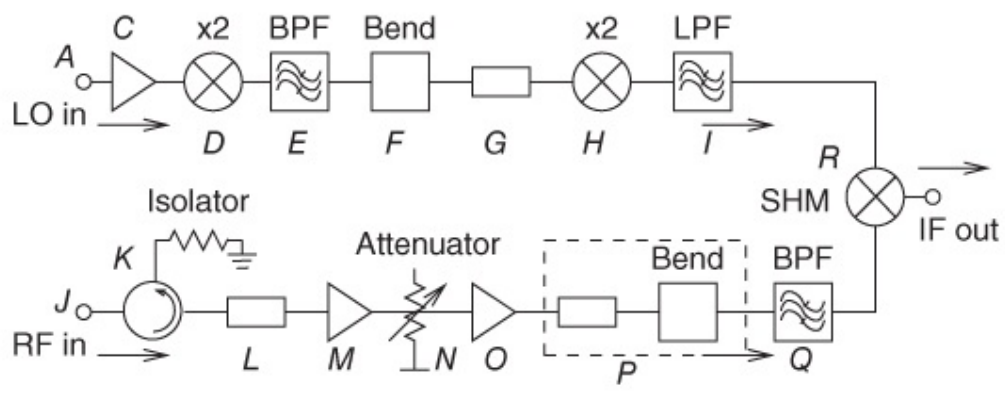
the bulk of the receiver is mounted on a brass housing and a portion of the printed circuit board has been cut out to enable mounting of the components of the frequency conversion section. The components consist of integrated circuits and microstrip structures on ceramic substrates that cannot be mounted directly on the brass housing. Instead a conductive mounting mat is silk-screened onto the brass housing. The mat provides a compliant surface, providing good conductivity and allowing for differences in the thermal expansion of the microstrip and die components relative to the brass housing.



- A** LO in from softboard
- B** Power supply decoupling capacitor
- C** Driver amplifier
- D**  $\times 2$  frequency multiplier
- E** Bandpass filter
- F** Bend
- G** Transmission line section
- H**  $\times 2$  frequency multiplier
- I** Lowpass filter

- J** RF in from waveguide adaptor
- K** Isolator
- L** Transmission line section
- M** Amplifier
- N** Voltage variable attenuator
- O** Amplifier
- P** Transmission line section and bend
- Q** Bandpass filter
- R** Subharmonic mixer

(a)



(b)

**Figure 1.5** Frequency conversion section of the 15 GHz receiver of [Figure 1.3](#): (a) annotated photograph; and (b) block diagram. The frequencies identified in (a) are the center frequency of the LO range (1.67 GHz) and the center frequency of the RF signal (14.9 GHz). The center frequency of the resulting IF signal is at 1.43 GHz. © M. Steer, used with permission.

Description of the operation of the receiver, and in particular the frequency conversion section, is made with reference to the module block diagram shown in [Figure 1.5](#)(b), with the italic sans serif identifying letters also used in [Figure 1.5](#)(a).

The LO path in the frequency conversion section begins with injection of the amplified reference LO signal at *A*. The signal from the printed circuit board (also referred to as the softboard) is wirebonded directly to a driver amplifier *C*. Detail of the transition from the softboard is shown in [Figure 1.6](#). The softboard is at the bottom of the image and the RF transition from the softboard uses two double bond wires, *Z*, to the amplifier integrated circuit *C*. The amplifier is epoxied to the conductive mat that is silk-screened directly onto the brass housing and provides good thermal, mechanical, and electrical bonding of integrated circuits and ceramic sections. The back of the amplifier is a metal ground plane that is electrically connected to the brass housing through the conducting epoxy. *B* comprises two parallel plate capacitors, the right one of which is used here. The two capacitors share a common plate on the back of the structure that is epoxied to the brass housing. The capacitor *B* is known as a DC decoupling capacitor and is the last line of defense, removing power supply ripples before the DC voltage supply is presented to the amplifier. DC power is supplied via the single bond wire *Y* with the capacitor eliminating ripples on the DC supply before it is provided to the amplifier *C*. The amplifier is internally matched, which means that the input and the output of the amplifier both look like  $50\Omega$ . The manufacturer of the amplifier has designed the amplifier this way so that it can be easily incorporated in microstrip designs. The output of the amplifier drives a passive  $\times 2$  (“times two”) frequency multiplier chip, *D*, which increases the frequency of the LO signal by a factor of 2.

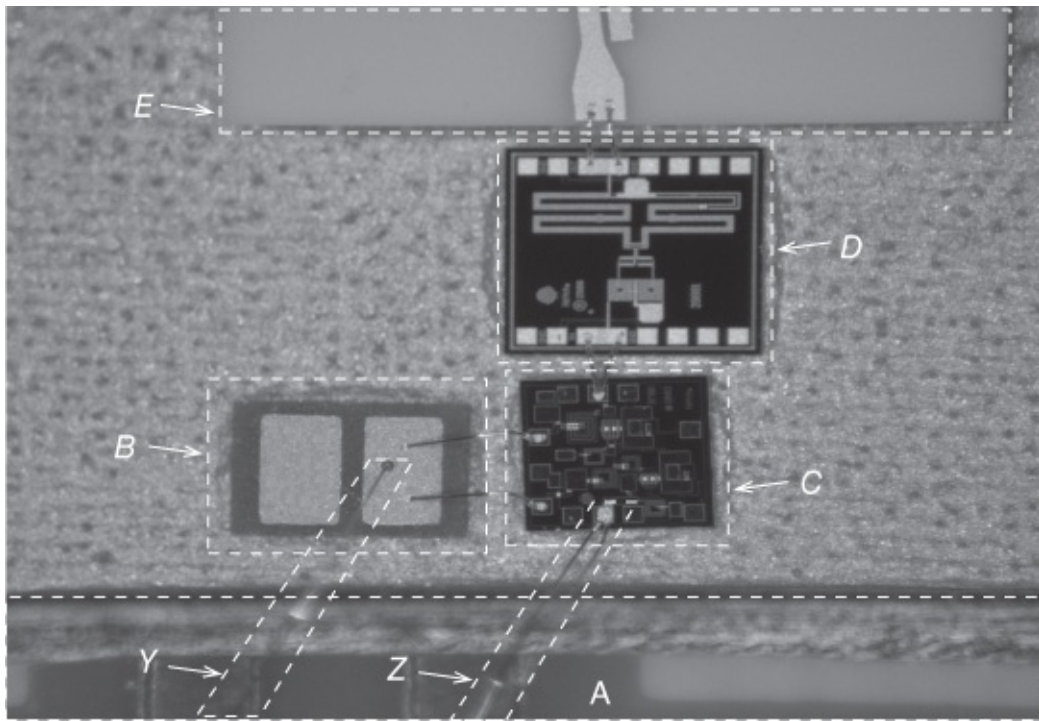


**Figure 1.6** Detail of the transition from softboard to the frequency conversion section. © M. Steer, used with permission.

There are many ways to implement a frequency multiplier function but typically a number of harmonics of the original signal are generated. It is necessary to follow the frequency multiplier by a bandpass filter  $E$ , which passes only the second harmonic of the reference LO signal. Thus the intermediate LO at the output of  $E$  is a sinusoid that can be varied from 3200.25 MHz to 3483.75 MHz.  $E$  is an edge-coupled bandpass filter and is a particular type of filter constructed using parallel-coupled microstrip lines. Detail of the edge-coupled bandpass filter is shown in [Figure 1.7\(a\)](#). There is a precise methodical approach to designing such filters. The filter is fabricated on an alumina substrate rather than softboard. This is because the dimensional tolerance of the alumina substrate, a hard ceramic, is much better than that of soft board. This enables the filter to be simulated accurately in an electromagnetic simulator. If adjustment is required, such as changing the separation of lines, this can be made during the design and test cycles, and then once the design is fixed it can be faithfully reproduced generally without the need for subsequent tuning.

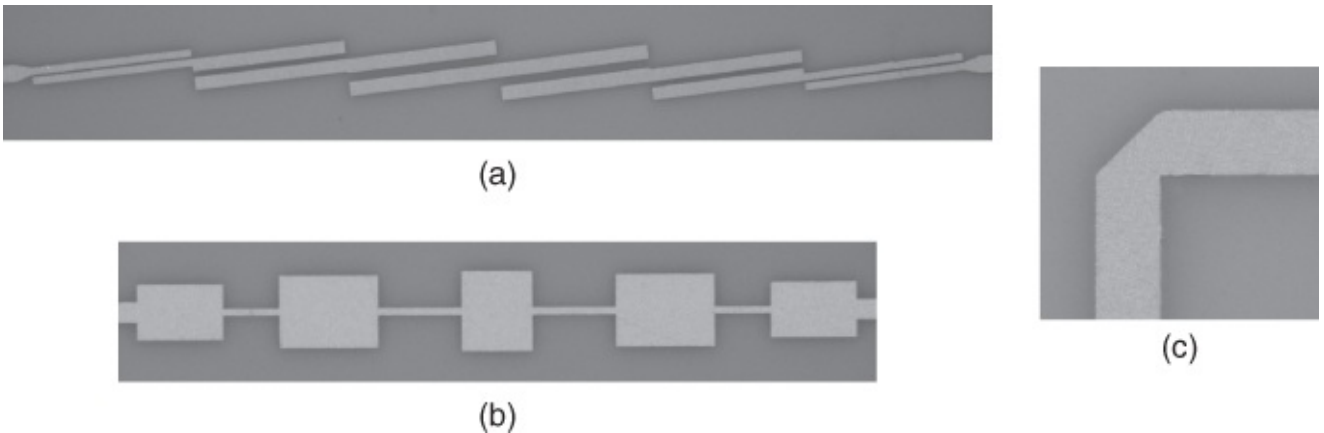


**Figure 1.7** Component sub-modules of the frequency conversion section of the 15 GHz receiver of [Figure 1.5](#): (a) edge-coupled parallel-coupled microstrip line bandpass filter; (b) microstrip lowpass filter; and (c) microstrip mitered bend. © M. Steer, used with permission.

The bandpass filter is followed by a bend,  $F$  (see also [Figure 1.7\(c\)](#)), another transmission line section,  $G$ , and a second  $\times 2$  frequency multiplier, the output being an LO signal that can be varied from 6.40125 GHz to 6.9675 GHz as the frequency of the reference LO signal has been increased in total by a factor of 4. The harmonics at the output of the second frequency multiplier are removed by a low pass filter,  $I$ , see also [Figure 1.7\(b\)](#). Finally, the frequency-scaled LO signal is presented to the mixer  $R$ .

The RF signal is applied to the frequency conversion section at  $J$  (the same as  $M$  in [Figure 1.3](#)). The RF signal presented to the frequency conversion section ranges from 14.4 to 15.35 GHz, but the receiver unit was designed to support a slightly wider RF signal. The desired signal is in a number of spectrum slices narrower than this bandwidth and the range of reference LO signals enables different sub-bands to be selected. Immediately following the waveguide-to-microstrip adaptor (also called a waveguide-to-microstrip launcher) is an isolator, part of the frequency conversion section, identified by  $K$ . This isolator is derived from a three-port circulator with one of the ports terminated in a  $50 \Omega$  resistor. This is quite a remarkable element and makes use of a quantum-mechanical effect that can be exploited at microwave frequencies to preferentially route microwave signals. A transmission line section,  $L$ , with a characteristic impedance of  $50 \Omega$  follows, presenting the RF signal to a low noise amplifier,  $M$ . The low noise amplifier is an integrated circuit and is designed to have  $50 \Omega$  input and output impedances. This amplifier is followed by a voltage-variable attenuator chip,  $N$ , and a second amplifier,  $O$ . Surrounding  $M$ ,  $N$ , and  $O$  are power supply decoupling capacitor chips, each identical to the decoupling capacitor identified in [Figure 1.6](#) and [Figure 1.5\(a\)](#). The DC voltage is supplied from the surrounding circuit board, with the voltage supply wire-bonded to one plate of a capacitor while the other side is electrically connected to the conductive mounting mat and then to the brass housing.

The RF path continues with a transmission line section incorporating a bend,  $P$ . This is followed by a bandpass filter  $Q$  finally presenting the RF signal to the mixer  $R$ . The bandpass filter prevents harmonics of the RF signal generated by the amplifiers  $P$  and  $O$  from being presented to the mixer,  $R$ . It also prevents unwanted signals coming from the mixer from being

presented to the output of the amplifier O and producing distortion.

The mixer, R, is a subharmonic mixer, the most common type of microwave mixer. In the simple form of a mixer the center frequency of the IF signal is the difference between the frequency of the LO and the center frequency of the RF signal. In the most common type of subharmonic mixer the center frequency of the IF signal is the difference between the second harmonic of the LO and the center frequency of the RF signal. However, some subharmonic mixers are designed to use higher harmonics. The advantage of a subharmonic mixer is that the design of the LO drive section is simplified and there is very high isolation of the LO and RF terminals of the mixer.

The frequency conversion section comprises a large number of die and microstrip sections (filters, bends, and transmission lines) that are interconnected by wire bonds. One of the connections is shown in [Figure 1.8\(a\)](#). Low-frequency bonds are often made using just one bond wire but here three are used. The use of more than one bond wire reduces the inductance of the connection. With the three bond wires the inductances of the individual bond wires are in parallel and so the total inductance is one third of the inductance of an individual bond wire. An alternative view is that the multiple bond wires approximately continue the strip of the microstrip line. A better approximation to the continued line is made by the ribbon bond shown in [Figure 1.8\(b\)](#). This more faithfully reproduces the strip of the microstrip line and introduces a smaller discontinuity than the bond wire connection. Ribbon bonding is more difficult than wire bonding and is used in critical microwave and millimeter wave situations.

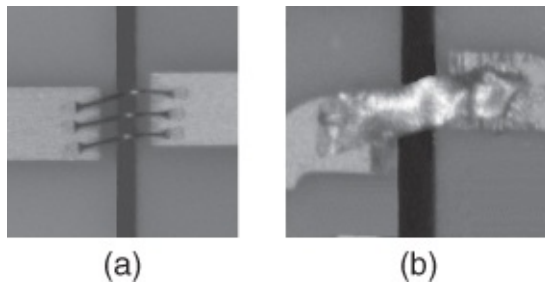
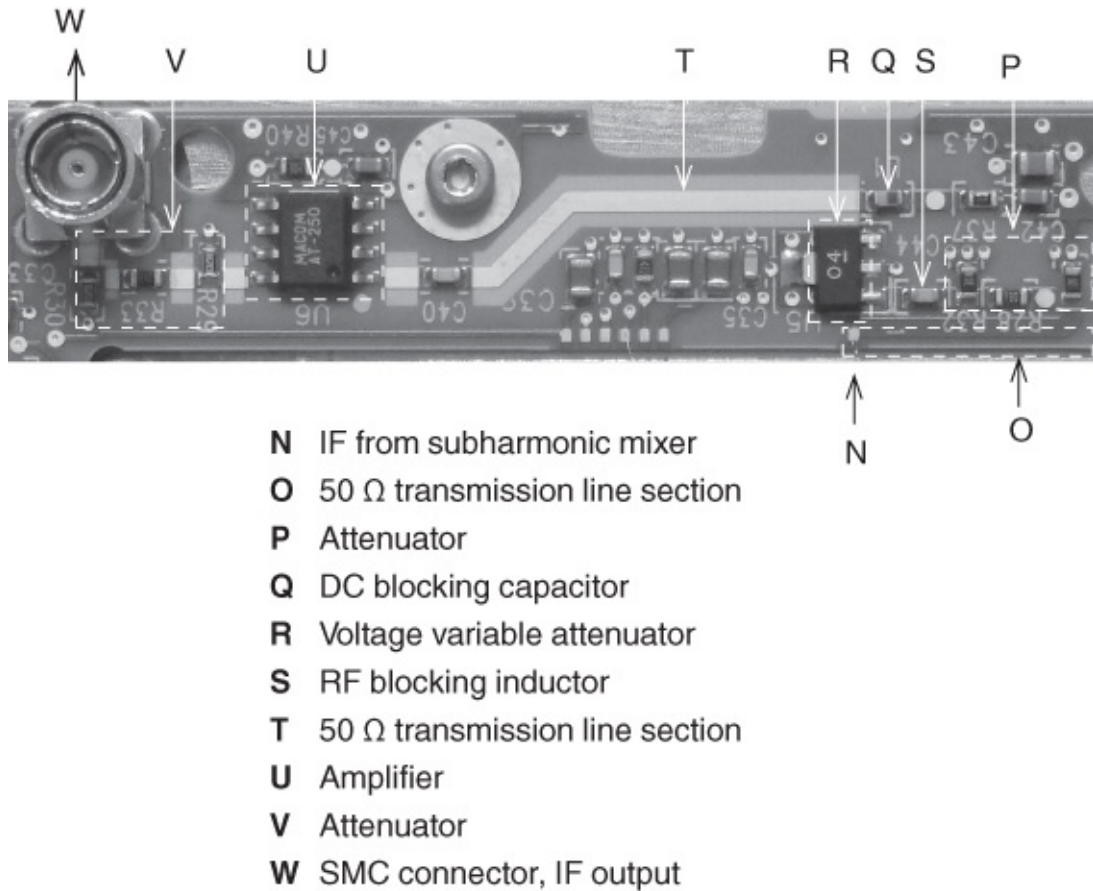


[Figure 1.8](#) Bond structures: (a) wire bonds; and (b) ribbon bond. © M. Steer, used with permission.

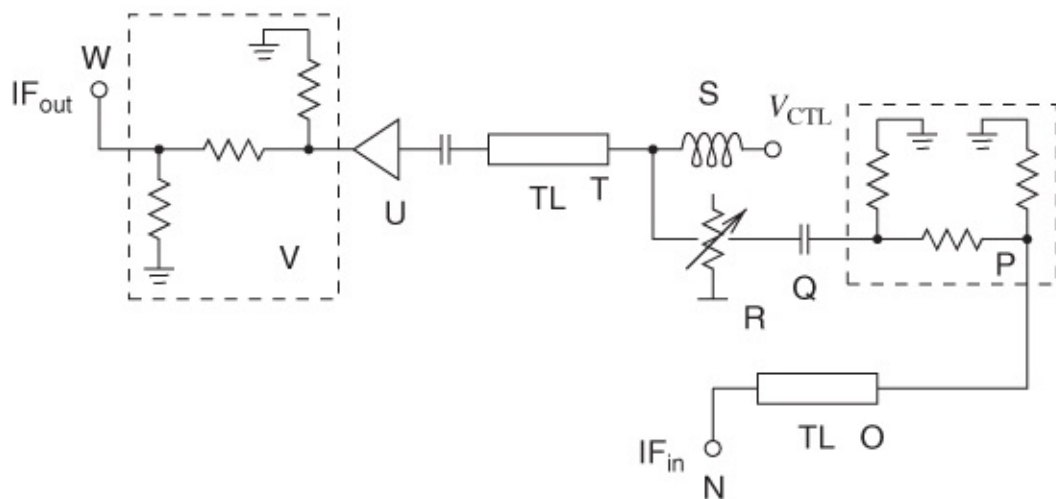
### 1.3.3 Intermediate Frequency Section

The intermediate frequency section, at the top in [Figure 1.3](#), receives the signal from the mixer at connection N in [Figure 1.3](#). The frequency of the IF is 70–1595 MHz. A circuit that operates over such a wide bandwidth requires broadband functional units. Detail of the IF section and its block diagram are shown in [Figure 1.9](#). The IF is output from the subharmonic mixer and inserted into the IF section at N. The signal then passes along the transmission line O to a fixed resistive attenuator P comprising a Pi network of resistors. The IF is then attenuated by a voltage-controlled variable attenuator R (with a bandwidth of DC to 2 GHz) after first passing through a DC blocking capacitor Q. The control voltage,  $V_{CTL}$ , sets the level of attenuation and the control circuitry is isolated from the IF path by the blocking inductor S. The IF signal then travels along the transmission line T and through a DC blocking capacitor to an amplifier U.

The amplified signal is then attenuated by the Pi resistive attenuator V, finally reaching the SMC output connector at W. The output attenuator isolates the nonlinear output of the amplifier from the external circuitry so that the external circuitry has little effect on the performance of the IF circuitry.



(a)



(b)

**Figure 1.9** IF section of the 15 GHz receiver of [Figure 1.3](#): (a) annotated image; and (b) block diagram. © M. Steer, used with permission.

### 1.3.4 Frequency Planning

Frequency planning is a critical part of module design. The receiver has three different signals, the RF signal, the LO signal, and the IF signal. The fixed mobile service at 15 GHz uses the band from 14.4 to 15.35 GHz, with channels having various widths as follows: 2.4, 3.5, 7, 14, 28, and 56 MHz. [Figure 1.10](#) shows the channel arrangement of the 15 GHz fixed wireless service based on a 28 MHz channel spacing. Operators can use different channel arrangements based on the various channel spacings and can use one or more contiguous channels. Provision of full demodulation capability to process all of the channels simultaneously can be expensive and so a subset is processed simultaneously, but frequency planning of the receiver must enable groups of channels to be selected and presented in a narrower intermediate frequency range than the full 950 MHz. In addition, frequency planning must allow for future frequency expansion of the fixed wireless service. This flexibility is enabled by having a variable LO.

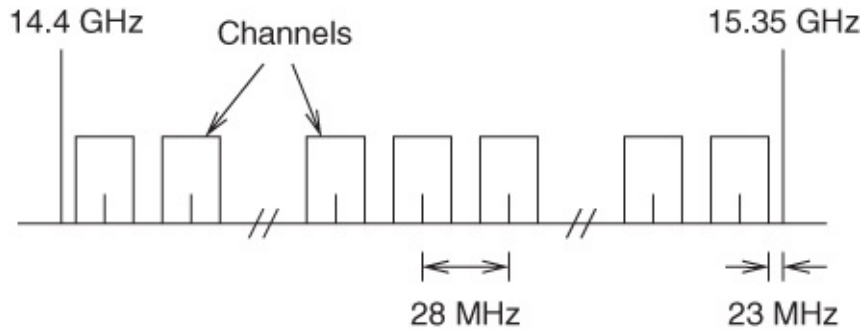


[Figure 1.10](#) Channel arrangement of the 15 GHz fixed wireless service based on a 28 MHz channel spacing.

The ultimate performance of the receiver is described by its minimum detectable RF signal level. Prior to insertion of the RF signal to the receiver module there is a waveguide filter (not shown) that only passes signals between 14.4 and 15.35 GHz. It is critical that signals originating in the receiver module are not re-radiated as that would have severe system implications. These spurious signals could be signals that arise from nonlinear mixing at the input of the first amplification stage in the RF path of the receiver. The most effective component that eliminates such signals is an isolator ( $K$  in [Figure 1.5](#)). This, however, introduces loss and noise, and raises the level of the minimum detectable RF signal. This is a tradeoff that is very commonly made. Following the isolator the RF signal is amplified by a low noise amplifier ( $M$  in [Figure 1.5](#)) and then noise introduced by the circuit is of much less concern. The following voltage-variable attenuator ( $N$  in [Figure 1.5](#)) is necessary to reduce the signal to avoid distortion in the following stages if the RF signal is too large.

The LO in a direct implementation would be slightly above or slightly below the RF band. However, generating an LO at, say, 14 GHz directly is problematic. Also this LO would be used by the transmitter module and it is then necessary to route the LO signal. Instead what is normally done is to generate a lower microwave reference LO signal that can be more easily generated and routed in the system. In this receiver system the reference LO can be varied from 1600.625 MHz to 1741.875 MHz. To increase the frequency one of two technologies are commonly used. One of these is frequency multiplication and another is to use a subharmonic

mixer ( $R$  in [Figure 1.5](#)). Most mixers exploit a switching conductance that switches at a frequency close to the RF frequency to be converted. However, to achieve a conductance that switches at the appropriate rate it is only necessary to drive the mixer with an LO at half the required switching frequency [[8, 9]]. Thus the RF path is designed to increase the frequency of the input reference LO by a factor of four. Thus the frequency of the LO presented to the mixer varies from 6401.5 to 6967.5 MHz. The frequency of the IF produced is the difference between the RF signal and twice the frequency of this final LO.

The operating frequencies of the LO, RF and IF are designed so that the signals in each path have different frequencies. The lowest reference LO frequency of 1600.625 MHz sets the upper bound on the IF frequency, which here is 1595 MHz. No frequency in the LO path is more than half of the RF frequencies, ensuring isolation of the LO and RF signals. Frequency planning ensuring maximum isolation of signals, limiting the complexity of the IF demodulation frequency, and providing maximum flexibility while also allowing minimum IF demodulation complexity is an elaborate and iterative process.

### 1.3.5 Summary

This completes the description of the receiver module. Many of the elements of this module are common to a very large number of RF and microwave systems. The most important feature that enables the design of high-performance modules and systems is the availability of high-performance sub-modules from vendors who can allocate significant resources to their design as they will be inserted in many different systems. Invariably vendors design the sub-modules to be internally matched to  $50\Omega$  so that the module designer is not overly concerned with impedance matching. The module designer must architect the whole system and usually design filters and attenuators to ensure that the input and output connections have little effect on the performance of the module. The challenge for the sub-module vendor is to design sub-modules that have sufficient flexibility that they can be used in many different systems. It is the intent of this book to present the fundamentals of microstrip design, and of related planar transmission lines, that enable the design of high-performance RF and microwave modules and systems.

## 1.4 Interconnections on RF and Microwave Integrated Circuits

RF and microwave integrated circuits nearly always use microstrip lines for connecting active devices as well as implementing microwave functionality. There are two types of RF and microwave integrated circuits: compound semiconductor-based integrated circuits called microwave monolithic integrated circuits (MMIC) and circuits based on silicon called radio frequency integrated circuits (RFIC). The active device design is different as generally many more transistors are used in silicon technology than in compound semiconductor technology. However, from a passive circuit perspective the design is similar. An MMIC providing wideband amplification from 8 to 10 GHz is shown in [Figure 1.11](#). The circuit has two stages of amplification fundamentally provided by transistors TR<sub>1</sub> and TR<sub>2</sub>. On the left-hand side of

the MMIC is the RF input with three pads arranged as ground (G), signal ( $\text{RF}_{\text{IN}}$ ), and ground (G). This is called a GSG (for ground-signal-ground) connection and is in the format of the coplanar waveguide (CPW) transmission line shown in [Figure 1.12\(a\)](#). CPW is used when a ground plane cannot be easily provided. Although the chip has a backing metal ground plane, testing generally requires a CPW connection. A CPW connection can be implemented by attaching extensions to the end of a coaxial line, as shown in [Figure 1.12\(b\)](#). The circuit under test showing the probe connecting with the GSG pads of a chip is shown in [Figure 1.12\(b\)](#). Thus microwave measurements of planar circuits invariably use a CPW probe. The CPW connections must be provided on the chip with the ground connections connected to the backing metal conductor of the IC by vias. Following measurements the signal connection is wire bonded to external circuitry. Sometimes the ground pads are wire-bonded to external grounds but more commonly the metal on the back of the IC provides the ground connection, as was seen with the integrated circuit components in the receiver section previously considered (e.g., see the connections in [Figure 1.6](#)).

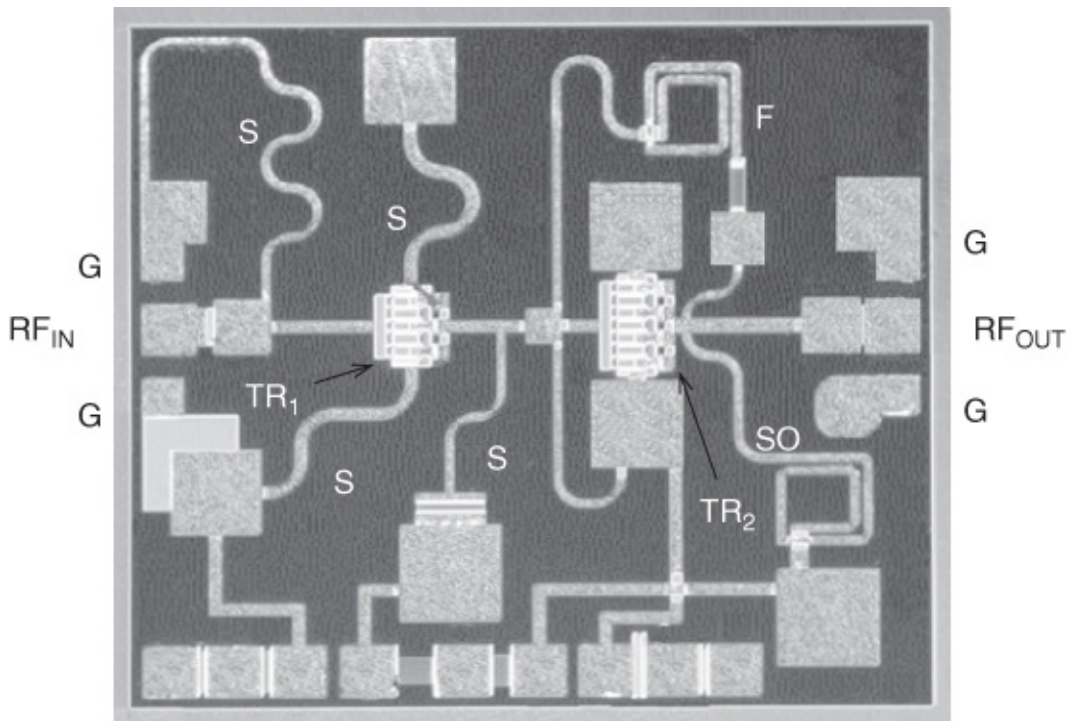


**Figure 1.11** GaAs X-band MMIC 8–12 GHz amplifier showing the RF input,  $\text{RF}_{\text{IN}}$ , and output  $\text{RF}_{\text{OUT}}$ . S indicates a stub, SO indicates the output stub with a spiral inductor, and F indicates a feedback RF path with a spiral inductor.

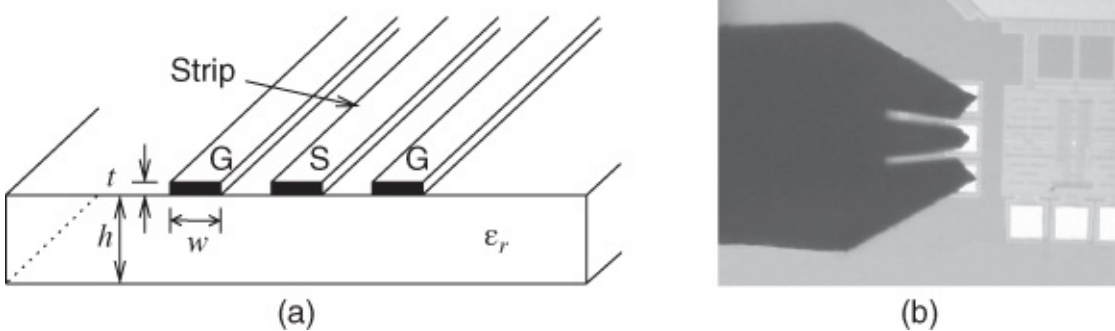


**Figure 1.12** A CPW with a strip carrying the signal current and the signal return on the ground strips on either side of the signal carrying strip: (a) CPW on the surface of a substrate; (b) a coaxial-to-CPW adaptor, a GSG probe, formed by extending and shaping the center conductor of a coaxial line, and welding needles to the outer conductor of the coaxial line shown here probing an integrated circuit.

The stub S in the MMIC amplifier before transistor TR<sub>1</sub> (see [Figure 1.11](#)) presents an appropriate impedance to match the input of the amplifier to  $50\Omega$ . The stubs (S again) above and below TR<sub>1</sub> are connected to the source of TR<sub>1</sub> and again provide appropriate impedances. The stub S between the transistors provides interstage matching and also allows bias to be applied to the transistors. The output stub also has a dual function, providing impedance matching as well as appropriate bias to TR<sub>2</sub>. The feedback network identified by F levels the gain of the transistors, yielding a flat gain over the 8–10 GHz bandwidth of the amplifier. With most integrated amplifiers, as is the case here, the module designer must provide appropriate DC blocking capacitors. These microstrip design principles are followed in the design of RF and microwave integrated circuits.

## 1.5 High-speed Digital Interconnections

Interconnect issues related to delay, path loss, signal integrity, and coupling between interconnects dominate the performance of high-speed digital circuits. These effects can largely be eliminated in high-speed digital circuits by using well-defined and well-spaced microwave transmission lines. However, this is not practical because it would significantly reduce the density of digital circuits. Thus proper transmission line design can only be tolerated for the most critical of interconnections but even for other digital interconnects some of the basic principles of transmission line design should be followed if there is negligible impact on circuit density.

On long-haul interconnects, either on-chip or off-chip, first incidence switching is required, rather than a resistor-capacitor (RC)-charging-like voltage rise, which occurs with multiple reflections and a low-current, high-impedance driver typical of the output of digital logic. Typical examples of such connections are clock distribution nets, data buses extending across a chip, and chip-to-chip interconnections. Here loss and signal integrity (e.g., coupling and reflections) are especially important. These connections have larger cross-sectional dimensions and are designed as transmission lines using the principles presented throughout this book. For short-haul nets the use of the narrow interconnections means that loss is high and

there are only a few reflections. The short length means that it takes a relatively short time for voltage levels to reach switching levels.

With transmission lines the most important principle is the provision of a signal return path that is in close proximity to the signal path. For connections that are not designed as transmission lines, being mindful of signal return minimizes inductive effects. Another transmission line principle is avoiding structures that interrupt the electric and magnetic fields as such disruptions will delay signal transmission by requiring additional time to store excess electric and magnetic energy. These principles are inherently followed when long-haul interconnects are designed as transmission lines and should be followed for short- and medium-haul interconnections.

The requirement of high circuit density means that many of the connections are not microstrip lines. Common transmission line technologies include stripline with a signal strip between two metal layers and coplanar lines both having well-defined signal return paths. The stripline uses considerably more metal than other coplanar technologies to provide a signal return path, although the process of design is considerably simplified. The most common coplanar lines are CPW and differential line, a two-conductor version of CPW. These technologies and principles are migrating to intermediate metal layers as signal speeds increase.

With high-speed digital integrated circuits passivated copper (Cu) conductors (having lower resistivity than aluminum (Al)) are used to keep losses as low as possible in many instances. Low permittivity materials (replacing  $\text{SiO}_2$ ) have been introduced to reduce capacitance and interconnect delay. (These developments are described in [Sections 5.7.3](#) and [5.7.4](#).) Other factors include:

- extremely small geometry
- a thin  $\text{SiO}_2$  dielectric layer
- metal that is thin, in fact comparable with a skin depth of the highest frequency component, which complicates the loss mechanisms
- the fact that the  $\text{SiO}_2$  (the type most commonly used) dielectric layer is itself lossy although this loss can be reduced dramatically by what is known as ‘patterning,’ a process also increasingly applied to the conductor-backing metallization in many planar structures
- since the  $\text{SiO}_2$  dielectric layer is also thin and the conductor backing is present, fields are drawn down to this grounded backing metal so that field lines extend into the silicon, which has finite conductivity, and loss increases because of this effect.

Digital integrated circuits have very high transistor density and to support this there must be many levels of conductors, which must be narrow and thin. A portion of a high-speed digital integrated circuit showing short-haul interconnects is shown in [Figure 1.13](#). Clearly there is very little that can be defined as uniform transmission line structures. The widths and thicknesses of most interconnects are much less than  $1\mu\text{m}$ . As a result, the resistance of most interconnects in digital circuits is very high and the  $\text{RC}$  delay of most short- and medium-haul high-speed digital interconnects is much greater than the transmission line delay. Still design

proceeds by explicitly providing a signal return path rather than just hoping that signal currents will find their way back. In addition, attention is given to providing reflectionless terminations, especially for long interconnect lengths. Circuit modeling of the interconnect structures for a high-speed integrated circuit is very challenging and the best modeling approach for all but the most critical networks is to develop a large three-dimensional network of resistors, capacitors, inductors, and coupled inductors (so-called RLCK circuits).

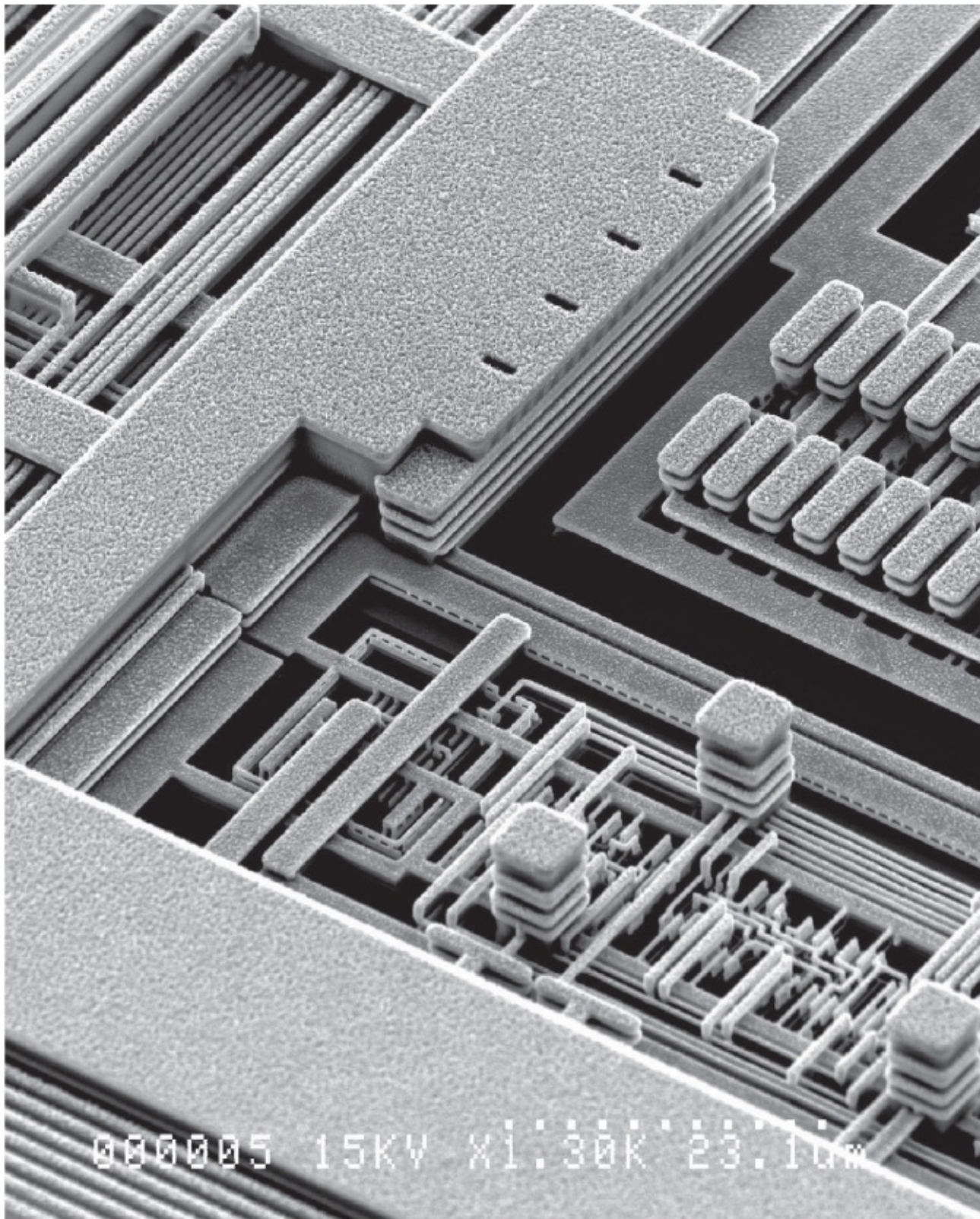


**Figure 1.13** Scanning electron micrograph of a silicon integrated circuit showing a multilevel interconnect structure of a digital chip. The first (bottom) level is tungsten, as are the vias. The other metal levels are copper. The perspective was obtained after removal by etching of the oxide dielectric. From IBM web page. © IBM, used with permission.

The most critical signal to be distributed on a digital integrated circuit is the clock signal and

for this defined transmission line structures are used.

Open coplanar stripline (CPS) has losses of around 3 dB/mm but, because of the above effects, the losses in this case, where the CPS has the specific complementary metal-oxide-semiconducor (CMOS)-silicon structure indicated, may well increase to approximately 4 or 5 dB/mm. In practice this means that for a 6 mm length this leads to a total worst case loss of around 13.5 dB. This implies a power reduction factor exceeding 22 or, more relevantly, a voltage reduction factor of 4.73. This means that a pulse traveling along the 3 mm line will suffer a reduction in level to approximately one-fifth of the sending value. These data apply to a line width of 5  $\mu\text{m}$ . By increasing the width to 30  $\mu\text{m}$  the voltage reduction can be reduced to a factor of three rather than five. It is necessary in both cases to use buffering to maintain voltage levels.

## 1.6 Summary

Microstrip evolved from the stripline, which itself evolved from a coaxial line with a flat center conductor. This has led to a large number of planar transmission line structures that can be fabricated using printed circuit technologies, principally etching dielectric sheets with metal bonded to one or more surfaces. Combining these concepts with substrates with tightly controlled thickness and uniform characteristics has resulted in printed microwave circuit (PMC) technology. For RF and microwave circuits microstrip is the dominant member of the planar transmission line family, but all of the members of the family will be considered in this book. It is critical that the description of each member of the family be combined with analytic treatments yielding the transmission line properties and forming the basis of a systematic approach to planar circuit components. This is a characteristic of all microwave and RF design developments, not just for printed microwave circuits. It is not enough to conceptualize a structure, it is necessary to develop the design formulas to enable the structure to be used in design. While the stripline and microstrip line are simple structures, it is not possible to simulate their performance precisely in electromagnetic simulation tools. The effects of strip thickness, for example, cannot be so easily handled. A very large number of design formulas have been developed in the decades since the development of planar transmission lines around 1950. This book gathers these developments as well as design insights and design guidelines for the entire class of planar transmission lines.

## References

- [1] R. Barrett, “Microwave printed circuits—a historical survey,” *IRE Trans. on Microwave Theory and Techniques*, vol. 3, no. 2, pp. 1–9, Mar. 1955.
- [2] R. M. Barrett, “Microwave printed circuits—the early years,” *IEEE Trans. on Microwave Theory and Techniques*, vol. 32, no. 9, pp. 983–990, Sep. 1984.
- [3] D. Grieg and H. Engelmann, “Microstrip—a new transmission technique for the kilomegacycle range,” *Proc. IRE*, vol. 40, no. 12, pp. 1644–1650, Dec. 1952.

- [4] S. B. Cohn, “Characteristic impedance of the shielded-strip transmission line,” *IRE Trans. on Microwave Theory and Techniques*, vol. 2, no. 2, pp. 52–57, Feb. 1954.
- [5] C. Mingins and R. Pease, “A universal approximate formula for characteristic impedance of strip transmission lines with rectangular inner conductors,” *IRE Trans. on Microwave Theory and Techniques*, vol. 3, no. 2, pp. 144–148, Feb. 1955.
- [6] M. Steer and W. Palmer, Multifunctional Adaptive Microwave Circuits and Systems. Scitech Pub Inc, 2008.
- [7] M. Steer, *Microwave and RF Design: a Systems Approach*, 2nd ed. SciTech Pub., 2013.
- [8] S. A. Maas, *Microwave Mixers*. Artech House, 1986.
- [9] B. Henderson and E. Camargo, *Microwave Mixer Technology and Applications*. Artech House, 2013.

# **Chapter 2**

## **Fundamentals of Signal Transmission on Interconnects**

### **2.1 Introduction**

This chapter presents the major concepts required to understand the movement of signals on transmission lines. The important concept of traveling waves is introduced and the origin of reflections on transmission lines identified. The guiding of an EM wave by an interconnect is achieved through the movement of charges, that is, currents on conductors. These charges terminate electric fields and prevent the EM fields from freely propagating away from the interconnect and the circuit. At low frequencies these charges penetrate deep inside conductors but at high frequencies the charges bunch due to the finite speed of movement of the EM signals through the dielectric separating conductors. Thus at RF these charges tend to be concentrated in the vicinity of both conductors in a two-conductor interconnect if one of the conductors is smaller than the other. In addition, the very slow movement of EM information within a conductor results in a skin effect as the density of alternating charges in a conductor decreases rapidly away from the surface of a conductor. The skin of charges is thinner the higher the frequency of the signal. Current bunching and skin effect result in the propagation characteristics of an interconnect varying with frequency.

### **2.2 Transmission Lines and Interconnects**

The speed at which electrical signals can be moved around in a circuit is limited by the speed of an EM wave, with the ultimate speed of information transmission being limited by  $c$ , the speed of light in a vacuum.

Energy is stored in the electric and magnetic fields of the propagating EM wave with the ability to store energy in electrical form being captured by capacitance and the ability to store energy in magnetic form being captured by inductance. In circuits the electromagnetic signals are guided by conductors, which form the interconnects or transmission lines.

Strategies have been developed so that interconnections over a small physical region can be ignored, perhaps by slowing the clock speed of a digital circuit, or the interconnects can be modeled by a large network of inductors ( $L$  s), capacitors ( $C$  s), resistors ( $R$  s), and magnetic transformers ( $K$  s), with the  $K$  s describing the magnetic field coupling of nearby conductors. Also in digital circuits there is usually not a universal ground but rather a densegrid or mesh of conductors providing ground and power supply connections. With RF circuits interconnects significantly affect (often overwhelmingly) performance but the density of interconnects is much less than with digital circuits. Since the RF interconnects have significant impact on RF circuit performance it is nearly always essential to include transmission effects in design and to include accurate models in circuit simulations of RF circuits. To facilitate both the

conceptual impact of RF interconnects and rapid RF circuit modeling it is nearly always essential that RF interconnects have regular cross-sections. RF interconnects with regular cross-sections are called transmission lines. The propagation of signals on transmission lines with sufficiently small cross-sections can be understood almost entirely by considering the fields in cross-section.

## 2.3 Interconnects as Part of a Packaging Hierarchy

Electrical connections are part of a hierarchy that connects lower levels of design to higher levels of design. Design proceeds by using a partitioning process whereby individual modules that have been designed separately are then combined to realize the complete system functionality. At the lowest level in an RF circuit interconnects connect individual active devices and passive circuit elements to form modules. These modules are connected to other modules with well-defined interfaces. High-speed digital design proceeds similarly, with modular components such as portions of chips and chips themselves interconnected with well-defined interfaces, substrate technologies, and packaging units [1–3]. A complete system nearly always combines RF, digital and low-frequency analog signals. While digital systems may not have RF modules, an RF system always contains digital circuitry for the control and processing of signals.

One way of defining the interconnect hierarchy is as follows:

- Level 1 Interconnect: Chips and passive functional components (e.g., filters)
- Level 2 Interconnect: Multichip modules (MCM, Package)
- Level 3 Interconnect: Printed circuit board (PCB) or printed wiring board (PWB)
- Level 4 Interconnect: Backplane (Package)
- Level 5 Interconnect: Rack, connect systems (Package)

The size of interconnects varies with interconnect level, with both the smallest interconnects, both in cross-section and in length, being at the chip level. The way they are designed and modeled also depends on the physical size of the connections, whether digital or analog circuitry is being interconnected, and on the clock or operating frequency.

A generalization of the interconnect hierarchy is that the higher levels of interconnect ‘breakout’ the lower levels, that is, smaller and higher loss interconnects at the chip level to larger interconnects (with lower loss and more controlled characteristics) at the next higher level for longer haul connections. This breakout process is repeated as long as necessary. Every aspect of the interconnect path must be modeled and designed. The complete path can involve nearly every interconnect technology, but there is considerable physics that is common. Today's high-performance digital systems have many interconnect issues in common with microwave (generally 1–30 GHz) and millimeter wave (above 30 GHz) systems and it is appropriate to consider the interconnect issues as a continuum. For example, it will be seen in [Chapter 21](#) that the long-haul interconnects on a chip (comparable in length to the edge dimensions of the chip) are conceived of and designed with the same criteria used to realize millimeter-wave circuits.

## 2.4 The Physical Basis of Interconnects

Electrical interconnections are generally made using metallic conductors, although conductive

paths can be made using doped semiconductors and superconductors. In this book we restrict ourselves to metallic interconnects. Metallic conductors, such as copper and aluminum the most common types used, are crystals with positively charged ions locked into position in a regular lattice. The ion here is made up of the nucleus of an atom which is positively charged and a complement of electrons local to each atom which almost, but not quite, balance the positive charge. In a metallic crystal there are some ‘free’ electrons shared by several ions with the overall affect being that the positive and negative charges are balanced and the free electrons can wander around the lattice. The wandering electrons travel in random directions at a speed that is a substantial fraction of  $c$ , the ultimate speed of light. This speed can typically be  $c/3$  at room temperature in copper. These electrons are moving randomly with no overall average movement, therefore they do not transmit information.

When an electric force field,  $E$ , is applied to a conductor, the electrons begin to accelerate in the opposite direction to  $E$ . This gives rise to an average movement of electrons in one direction and this movement of charge carriers, crossing a fixed position per unit of time, constitutes current  $I$ . At absolute zero temperature the lattice is motionless and the electrons can, essentially, move through the lattice unimpeded. With an applied  $E$  field (the voltage  $V$  divided by the distance over which  $E$  is applied) the electrons would eventually reach a speed only limited by speed-of-light considerations. As temperature increases the lattice begins to vibrate and the electrons start colliding with it. These collisions impede the movement of the electrons and this constitutes electrical resistance  $R$ . Therefore, the ultimate average speed of the electrons is limited, and thus so is the current. The higher the temperature the higher the electrical resistance and the lower the average speed or current. This is the underlying physical basis of Ohm's law ( $V = IR$ ). The movement of charge, and the electric and magnetic fields that this establishes, is also the basis for information transfer in interconnects. The electrons accelerated by an electric field in a conductor reradiate an EM wave in all directions, not just the propagating direction of the electric field that initially accelerated the electrons. Consequently the average speed of an EM wave in a conductor is much slower than in air, about  $c/1000$  at microwave frequencies. Note, however, that EM signals outside the conductors can move much faster than the electrons themselves and the EM fields inside a conductor.

The movement of charge results in a magnetic field, and hence magnetic energy storage. The ability of a structure to store magnetic energy is described by its inductance  $L$ . Similarly, the rearrangement of charge to produce localized net positive or negative charge results in electric field, and thus electric energy storage, with the capacitance  $C$  indicating the amount of electrical energy that can be stored. The ratio of the energy stored in the magnetic and electric fields ( $\propto \sqrt{L/C}$ ) and the rate at which the energy can be moved ( $\propto 1/\sqrt{LC}$ ) determine the characteristics of a transmission line.

Our first important point is that to transfer information energy must be transferred. Indeed in the quest to develop integrated circuits (ICs) that consume very little power it is common to talk about the amount of energy required to transfer a bit of information or the amount of energy required to switch a transistor. To come to grips with the fundamentals of transmission lines we must become comfortable with the notion of energy transfer, how it is transferred and how

the transfer of energy is disrupted (i.e., signal integrity degraded) by interrupting the quantities (e.g., the electric and magnetic field or the current path) transferring energy from one point to another.

### **2.4.1 What an Interconnect is and How Information is Transmitted**

An interconnect can take various forms, either delivering power to part of an electronic circuit or being the means by which information is transmitted from one point to one or more other points in a circuit. We are concerned with the design of interconnects to ensure reliable undistorted transmission of information. In low-frequency analog and digital circuits interconnects can be viewed simply as wires and, provided that the wire has sufficiently low resistance and good current carrying capability, the interconnect can be largely ignored. However, if the transmission must be over a considerable distance then the interconnect must be considered as part of a circuit.

The earliest fundamental understanding of signal transmission on interconnects was for the transmission of digital signals—telegraph signals. Initially signal integrity was poor and telegraphy could only be used over short distances. It was not until Oliver Heaviside in 1887 [4] developed the first understanding of signal transmission on interconnects that telegraphy could be used over more than short distances. The key ingredient that Heaviside brought to the fundamental understanding of interconnects was to consider the behavior of the signal in the frequency domain. This is still the best way of developing a fundamental understanding of interconnects, even if they are used for purely digital signals.

The key determinant of whether an interconnect can be considered as an invisible connection is whether the signal anywhere along the interconnect has the same value at a particular instant. If the value of the signal (say voltage) varies along the line (at an instant), then it may be necessary to consider transmission line effects. Jumping ahead a little, a typical criterion used is that if the length of the interconnect is less than 1/20th of the wavelength of the highest frequency component of a signal, then transmission line effects can be safely ignored and the circuit can be modeled as a simple *RLC* circuit. The actual threshold used, 1/20th, 1/10th or 1/5th, is based on experience. For example, an interconnect on a silicon chip clocking at 3 GHz has an appreciable frequency component at 15 GHz. An interconnect reaches the 1/10th threshold when it is 0.6 mm long. This is less than the dimensions of most chips, which can be up to 2 cm on a side. Thus it takes a finite time for the variation of a voltage at one end of an interconnect to impact the voltage at the other end. The ultimate limit is determined by the speed of light, but this is reduced by the relative permittivity of the material in which the fields exist. The best term describing this physical phenomenon is retardation. In addition to retardation other properties of the interconnect must be considered, including its resistance, current-carrying capability, interaction of a signal with those on other interconnects, and other effects to be discussed in this book.

At high clocking speeds, and at RF and microwave frequencies, retardation can be significant and an interconnect cannot be considered to be an instantaneous connection. As a result, it can be used as a circuit element in microwave and millimeter-wave circuits and even in quite

sophisticated circuits, for example filters can be constructed by configuring interconnects in a prescribed manner.

## 2.5 The Physics, a Guided Wave

A good deal of electrical and electronic engineering is based on manipulating the energy stored in an EM field, which we generally consider as separate electric and magnetic fields. While it is hard to appreciate, since they are introduced at very early stages in electro-technology education, current and voltage concepts are abstractions—albeit very convenient ones.

(Current is less abstract than voltage except at microwave frequencies, which will be seen when we look at current flow on interconnects.) The fundamental understanding of what an interconnect is, and how information is transmitted, requires that we consider EM fields. The insight required to manage signal integrity is greatly enhanced by understanding these. To be rigorous, information (energy) is transferred by the movement of the EM field and not by current, voltage, or charge.

### 2.5.1 Transmission of a Pulse

When a voltage pulse is applied to an interconnect an electric field in the interconnect is produced. We will use the coaxial line configuration shown in [Figure 2.1\(a\)](#), without a dielectric, to illustrate this discussion. The positive voltage side of the pulse is applied to the centre conductor of the coaxial line and results in an electric field that is essentially directed from the center conductor to the outer conductor, see [Figure 2.1\(b\)](#). However, the electric field will also be slightly directed along the line. The direction of the electric field is the direction in which positive charges would move if released into the field. The component of the field that is directed along the shortest path from the center conductor to the outer conductor (in what is called the transverse plane) will be denoted  $E_T$ , and the component directed along the line denoted  $E_L$ . (The subscripts  $T$  and  $L$  denote transverse and longitudinal components respectively.) Thus while  $E_L \ll E_T$ , it is necessary to accelerate electrons on the conductors and so give rise to current flow to support EM fields. Introducing  $E_L$  presents some difficulties as there is no analytic way of solving for its value, and only EM field simulation programs are capable of modeling it. However, it is small and so usually we restrict ourselves to talking about the transverse voltage and EM field, but restricting ourselves to this alone misses out on essential physics. The transverse voltage,  $V_T$ , is given by  $E_T$  multiplied by the distance between the inner and outer conductors:  $V_T = E_T(a - b)$ . This is a good measure provided that the transverse dimensions are sufficiently small compared to a wavelength.

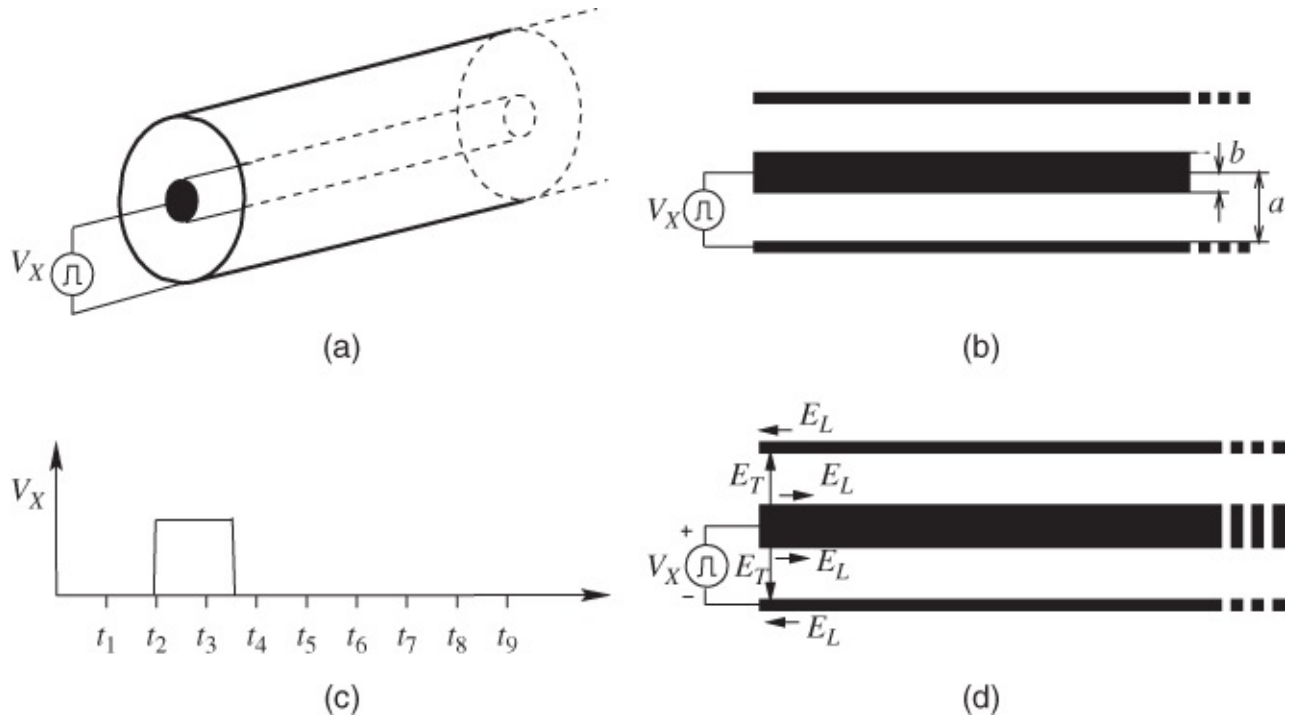


**Figure 2.1** Coaxial transmission line with a voltage source applying a pulse: (a) three-dimensional view; (b) its longitudinal cross-section; (c) the output of the pulse generator in time; and (d) the fields at the beginning of the line at time  $t_2$ .

Now let's get back to talking about  $E_L$ .  $E_L$  is small but is essential in producing a signal that moves along the line. The movement of a signal on the line is shown in [Figure 2.2](#) at various times that are referred to those shown in [Figure 2.1\(c\)](#). At time  $t_1$  the signal has not yet been initiated and at time  $t_2$  the voltage pulse has just been applied to the line. The small longitudinal field  $E_L$  (exaggerated here) is directed as shown in [Figure 2.1\(d\)](#) and again in [Figure 2.2](#). We know that it is in this direction as the voltage at the very beginning of the line is positive and the voltage along the line away from the start of the line is zero. There is only a longitudinal field very close to the beginning of the line initially as the influence of the electric field cannot travel faster than  $c$ , the speed of light in a vacuum.  $E_L$  causes electrons in the conductors to start moving in a direction opposite to that of the electric field. The electrons of course constitute current, which is in the opposite direction to electron flow. The influence of the electric field moves along the line comparable to the speed of light and over time initiates current flow further down the line, as shown in [Figure 2.2\(b\)](#). At time  $t_4$  the voltage of the source drops to zero, as in [Figure 2.2\(c\)](#), and the influence of this also moves along the line at a speed near  $c$ . The electric field moving down the line under this influence is zero and so current drops to zero, see [Figure 2.2\(d\)](#) at time  $t_5$ . At all times displacement of the electrons 'unmasks' the positively charged ions of the lattice and so an electric field directed away from the ions towards the electrons is produced with the effect that  $E_L$  is opposed and the net longitudinal electric field is very small.

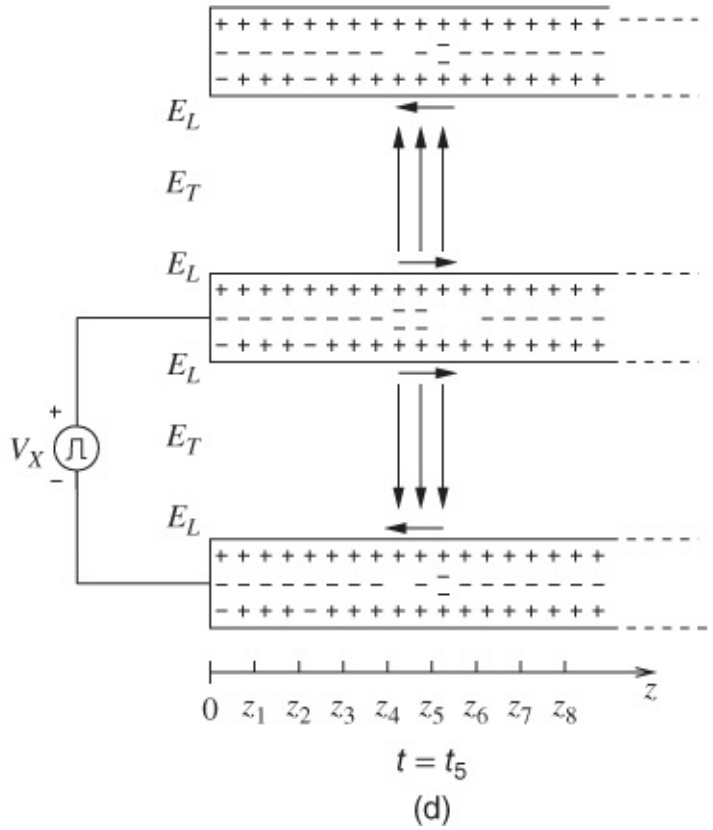
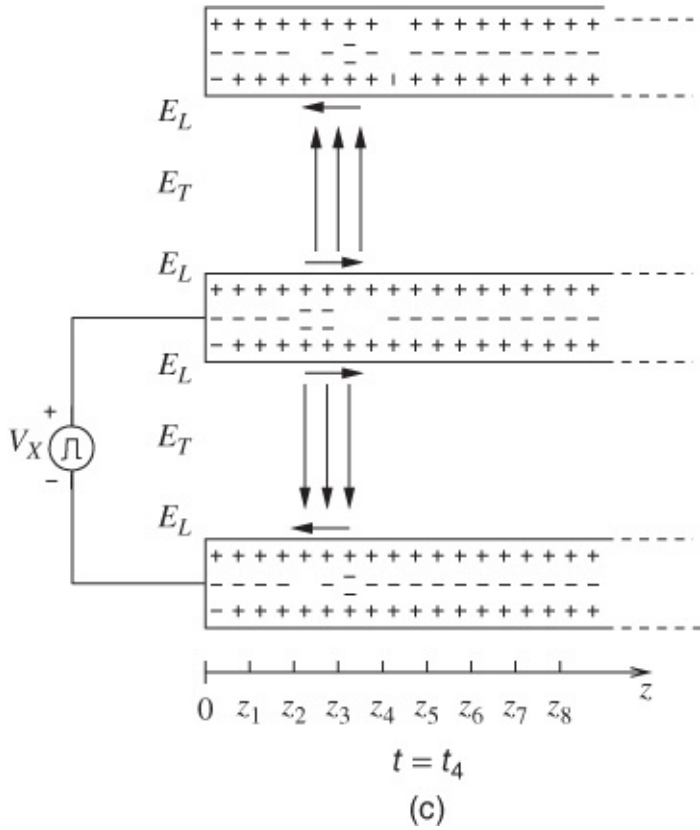
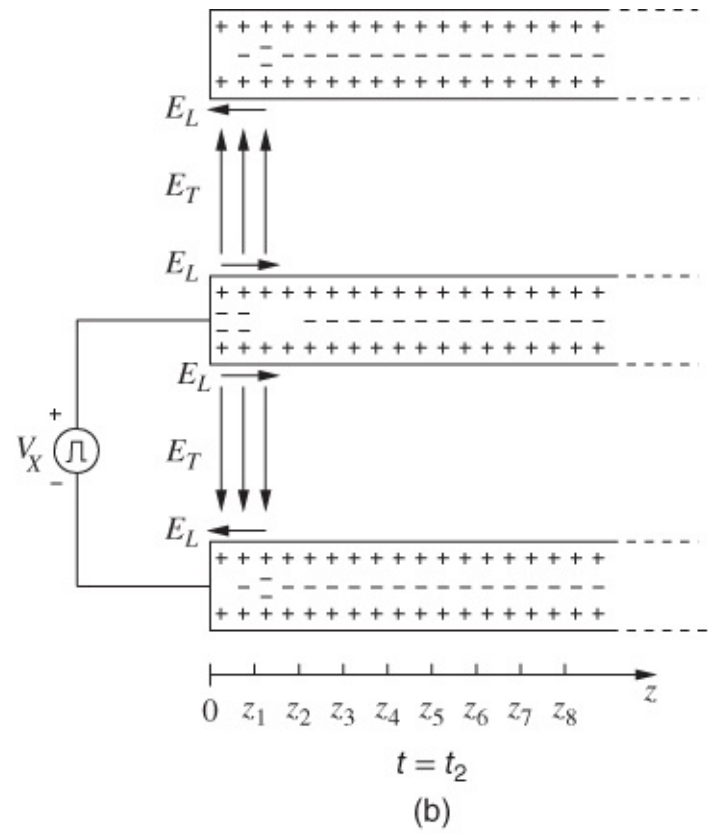
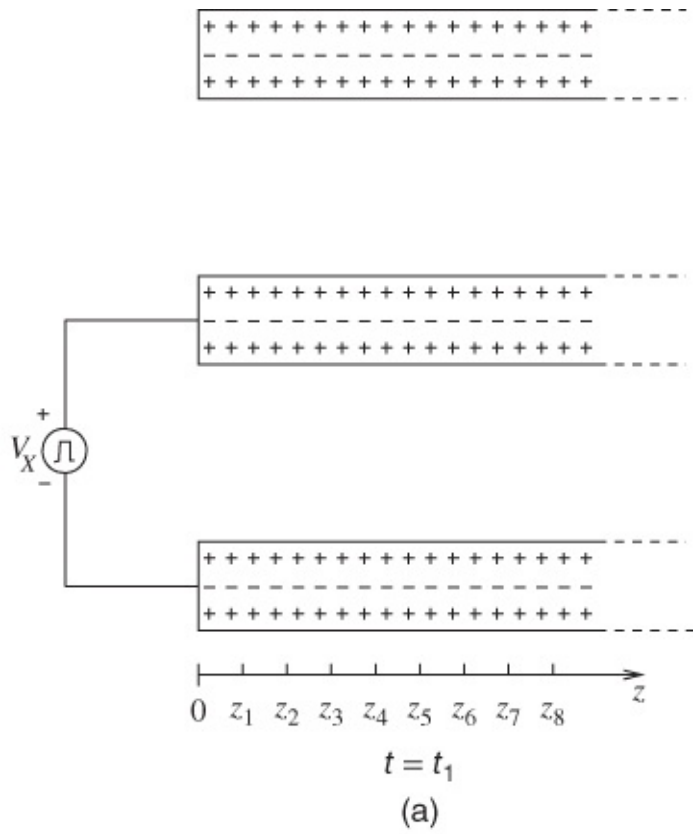


**Figure 2.2** Coaxial transmission line with pulsed voltage source showing voltage at different times. The plus and minus signs indicate net charge.

The signal that travels down the line is a packet of energy. We can see energy in the pulse as moving along in two equivalent ways. The first, and physically correct, interpretation is to

consider that the current gives rise to a magnetic field  $\mathbf{H}$ . This field too is composed of a transverse component  $H_T$  and a very small longitudinal component  $H_L$ . The energy contained in the pulse is the integral over volume of the product of  $\mathbf{E}$  and  $\mathbf{H}$  (actually  $\int_V \mathbf{E}_T \times \mathbf{H}_T \cdot dV$ ). The other way of calculating the energy in the pulse is to integrate the product of the current and voltage over the duration of the pulse, but this is only valid at low microwave frequencies (and below) when voltage and current can be easily determined.

The wave moves down the line at what is called the propagation velocity  $v_p$ , which is determined by the physical properties of the region between the conductors. The permittivity  $\epsilon$  describes the energy storage capability associated with  $\mathbf{E}$ , and the energy storage associated with  $\mathbf{H}$  is described by the permeability  $\mu$ . (Both  $\epsilon$  and  $\mu$  are properties of the medium—the material.) It has been determined that<sup>1</sup>

$$v_p = 1/\sqrt{\mu\epsilon} \quad 2.1$$

In a vacuum  $\epsilon = \epsilon_0$ , the ‘free space’ permittivity, and  $\mu = \mu_0$ , the ‘free space’ permeability. These are physical constants and have the values:

$$\begin{aligned} \text{permittivity of free space } \epsilon_0 &= 8.854 \times 10^{-12} \text{ F/m} \\ \text{permeability of free space } \mu_0 &= 4\pi \times 10^{-7} \text{ H/m} \end{aligned}$$

### 2.5.2 Transverse Electromagnetic Lines

In coaxial lines virtually all of the fields are in the plane transverse to the direction of propagation along the line, that is,  $E_T \gg E_L$  and  $H_T \gg H_L$ . Such lines are called transverse electromagnetic lines or TEM lines.

Cross-sections of some common TEM-mode lines that have been fully analyzed and are well understood are shown in [Figure 2.3](#). The parallel line structure of [Figure 2.3\(a\)](#) is rarely used for carrying RF signals because, being unshielded, it radiates energy and is easily disturbed electrically by any nearby objects. Notice that both the parallel line and the coaxial line, shown in [Figure 2.3\(b\)](#), need only have dielectric supports at intervals along their lengths to maintain correct separation of the conductors. Furthermore, these supports may be filamentary, so that the ‘dielectric filling’ can consist almost entirely of air and the dielectric losses are low. However, the stripline, [Figure 2.3\(c\)](#), inherently requires a solid, low-loss, dielectric filling. The stripline is known as a planar interconnect as it can be built up using slabs of material either grown, in the case of a semiconductor, or sandwiched in the case of a PCB. The metallic connection is usually fabricated by etching (removing) material from a continuous sheet of metal.

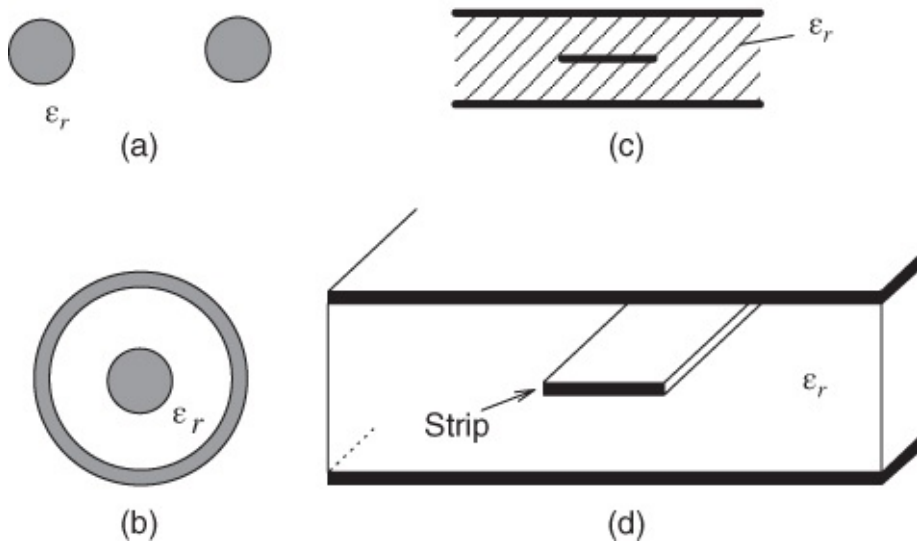


**Figure 2.3** Cross-sections of some common TEM-mode transmission lines: (a) parallel two-wire transmission line; (b) coaxial line; (c) stripline; and (d) perspective of a stripline.

Another common planar interconnect is the microstrip line shown in cross-section in [Figure 2.4](#). This cross-section is typical of what would be found with a semiconductor or multichip module. In the deposited multichip module (MCM-D) the metal layer is deposited primarily by sputtering or electroplating on a layer of dielectric applied in the liquid state by spinning. This is built up on a supporting substrate of ceramic or silicon. The interconnect is defined using a photolithographic process and etching. The line is finally covered by another layer of deposited dielectric to produce the conformal shape. Current flows in both the top and bottom conductor, but in the opposite direction. Electric field lines start on one of the conductors and finish on the other, and are located almost entirely in the transverse plane. The magnetic field is also mostly confined to the transverse plane. This line is more commonly called a quasi-TEM line, as the longitudinal fields are not as negligible as with the coaxial line that we considered above. The relative level of the longitudinal fields increases with frequency, but the transverse dimensions are kept sufficiently small that the fields on the line are still essentially TEM. [Figure 2.4](#) illustrates an important point: current flows in the strip and a return current flows in what is normally regarded as the grounded conductor. More about this in [Section 2.13](#).

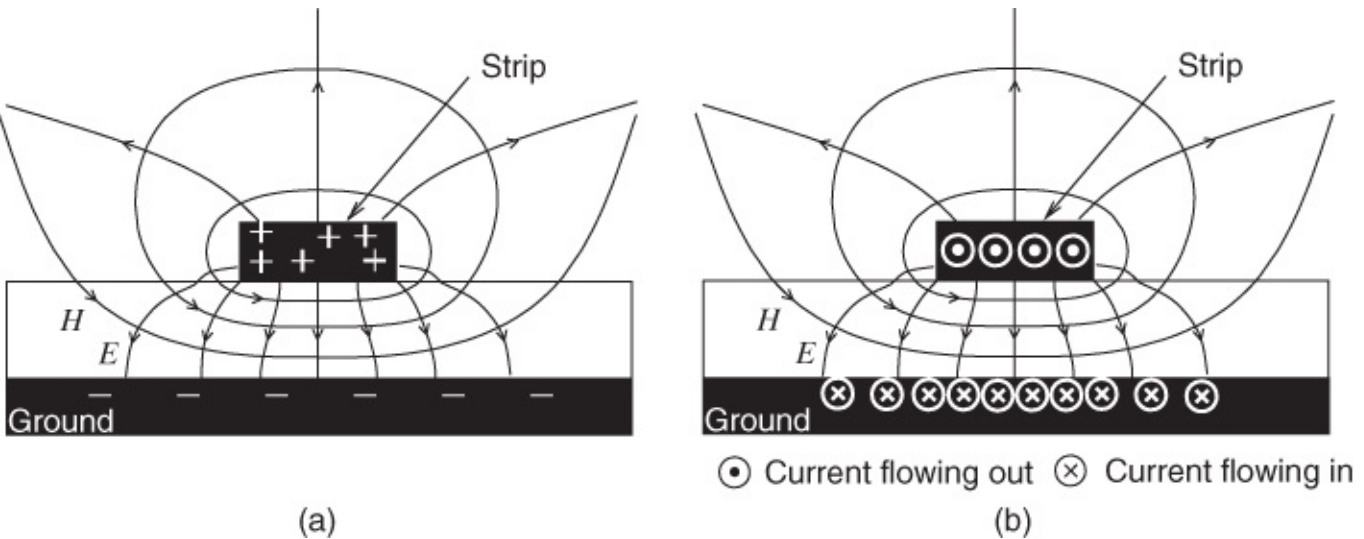


**Figure 2.4** Cross-sectional view of a microstrip interconnect: (a) the electric and magnetic field lines, and positive and negative charges; and (b) current flow. The electric and magnetic fields are in two media, the dielectric and air.

In [Figure 2.4\(a\)](#) the electric field is directed from the positive charges to the negative charges. The relationship of the magnetic field direction and current flow comes directly from Maxwell's equations. This is most clearly seen by applying the right-hand rule to the current flow in the strip. With the thumb of the right hand in the direction of current flow, the magnetic field lines follow the direction of the fingers when the hand is clenched with the thumb pointing out.

### 2.5.3 Multimoding

The TEM mode is one possible solution of Maxwell's equations that describe EM fields with conductors. However, there are other solutions that can exist at high frequencies (when the conductors are  $\lambda/2$  or more apart, or when there are more than two conductors). These situations result in two or more different field configurations being supported, each configuration being called a mode. This is usually an undesirable situation as the modes travel at different speeds. Thus the transverse dimensions of an interconnect must be kept small enough, and separations of adjacent interconnects sufficiently large, to ensure only one mode per interconnect. One of the rare exceptions is when coupling is desired, as in some microwave and millimeter-wave circuits.

### 2.5.4 The Effect of Dielectric

The presence of a material between the conductors alters the electrical characteristics of the interconnect. With a dielectric, the application of an electric field moves the centers of positive and negative charge at the atomic and molecular level. Moving the charge centers changes the amount of energy stored in the electric field, a process akin to storing energy in a stretched spring. The extra energy storage property is described by the relative permittivity  $\epsilon_r$ , which is the ratio of the permittivity of the material to that of free space:

$$\epsilon = \epsilon_r \epsilon_0.$$

2.2

The relative permittivities of materials commonly used with interconnects range from 2.08 for Teflon™, used in high performance PCBs, 11.9 for silicon (Si), 3.8–4.2 for silicon dioxide ( $\text{SiO}_2$ ), to 12.85–13.1 for gallium arsenide (GaAs) chips. (Values for other materials are given in Appendix B.)

When the fields are in more than one medium (a nonhomogeneous transmission line), as for the microstrip line shown in [Figure 2.4](#), the effective relative permittivity  $\epsilon_{\text{eff}}$  is used. The characteristics of the nonhomogenous line are then, more or less, the same as for the same structure with a uniform dielectric of relative permittivity  $\epsilon_{\text{eff}}$ . The  $\epsilon_{\text{eff}}$  changes with frequency as the proportion of energy stored in the different regions changes. This effect is called dispersion and it causes a pulse to spread out as the different frequency components of the pulse travel at different speeds. Dispersion is elaborated on more in [Section 2.5.8](#).

A similar effect on energy storage in the magnetic field occurs for a few materials. The magnetic properties of materials are due to the magnetic dipole moments resulting from alignment of electron spins, an intrinsic property of electrons. In most materials the electron spins occur in pairs with opposite signs, with the result that there is no net magnetic moment. However, in magnetic materials some of the electron spins are not canceled by matching pairs and there is a net magnetic moment. This net magnetic moment aligns itself with an applied  $H$  field and so provides a mechanism for additional storage of magnetic energy. The relative permeability  $\mu_r$  describes this effect and

$$\mu = \mu_r \mu_0.$$

2.3

Nearly all materials used with interconnects have  $\mu_r = 1$ . One notable exception is nickel, which has a high permeability, is a very convenient processing material, and often appears in packages.

## 2.5.5 Dielectric Loss Tangent, $\tan \delta$

Loss in a dielectric is due to (i) dielectric damping and (ii) conduction losses in the dielectric. Dielectric damping originates from the movement of charge centers that results in the movement of the dielectric lattice. This vibrational energy is lost from the electric field. This loss increases linearly with frequency and is zero at DC. It is described by incorporating an imaginary term in the permittivity with the effective permittivity becoming

$$\epsilon_e = \epsilon_{\text{eff}} \epsilon_0 = \epsilon' - j\epsilon'' = \epsilon_0 (\epsilon'_r - j\epsilon''_r). \quad 2.4$$

Another type of dielectric loss is due to the movement of charge carriers in the dielectric. This is described by the conductivity,  $\sigma$ . Dielectric loss due to conduction in the dielectric is relatively independent of frequency at microwave and millimeter-wave frequencies. However, dielectric damping is almost linearly proportional to frequency for microwave substrates. Combining the two sources of dielectric loss, the energy lost in a microwave substrate is proportional to  $\omega \epsilon'' + \sigma$ . Since the energy stored in the electric field is proportional to  $\omega \epsilon'$ , a loss tangent is introduced to describe loss in a dielectric:

$$\tan \delta = \frac{\omega \epsilon'' + \sigma}{\omega \epsilon'}.$$

2.5

This leads to the effective relative permittivity

$$\epsilon_{\text{eff}} = \epsilon_{r,e} = \epsilon'_{r,e} - J\epsilon''_{r,e} = \epsilon'_r - J \left( \epsilon''_r + \frac{\sigma}{\omega \epsilon_0} \right) \quad 2.6$$

$$= \epsilon'_r - J(\epsilon''_r + \sigma/\omega) \approx \epsilon'_r(1 - J \tan \delta). \quad 2.7$$

Now  $|\epsilon''_{r,e}| \ll |\epsilon'_{r,e}|$  for practical dielectrics used in microwave transmission lines and so

$$|\epsilon| \approx \epsilon', \quad 2.8$$

and this is what is quoted as the permittivity of a material.

## 2.5.6 Magnetic Material Effect

Enhanced magnetic energy storage occurs for a few materials known as magnetic materials with the increased magnetic energy storage property due to alignment of magnetic dipole moments. In most materials the electron spins that produce the magnetic moments occur in pairs with opposite signs, with the result that there is no net magnetic moment. However, in magnetic materials, some of the electron spins are not balanced and there is a net magnetic moment. With an unmagnetised material the magnetic moment aligns itself with an applied  $H$  field and so provides a mechanism for additional storage of magnetic energy. This property is described by the relative permeability,  $\mu_r$ , and the magnetic permeability of the material is

$$\mu = \mu_r \mu_0. \quad 2.9$$

Most materials have  $\mu_r = 1$ .

As with dielectrics, the effect of loss in a magnetic material can be described by its complex permeability:

$$\mu = \mu' - J\mu''. \quad 2.10$$

Loss in magnetic materials is due to the movement of magnetic dipoles creating vibrations in a material.

## 2.5.7 Frequency-dependent Charge Distribution

Interconnects on chips, PCBs and backplanes are essentially planar, like the stripline shown in [Figure 2.3\(c\)](#) and the microstrip line shown in [Figure 2.4](#). Such lines have what at first seems to be an unusual frequency-dependent behavior. Consider the charge distribution for the microstrip line shown in [Figure 2.5\(a\)](#). The charge distribution shown here applies when there is a positive DC voltage on the strip (the top conductor). In this case there will be positive charges on the top conductor generally arranged in a fairly uniform distribution. The individual net positive charges tend to repel each other, but this has little effect on the charge distribution

for practical conductors with finite conductivity. In the bottom conductor, known as the ground plane, there are balancing negative charges so that the electric field lines begin on the positive charges and terminate on the negative charges. At DC the negative charges on the ground plane are uniformly distributed over the whole of the ground plane. An important point is that where there are unbalanced, or net, charges there can be current flow. So the charge distribution at DC, shown in [Figure 2.5\(a\)](#), indicates that for the top conductor there will be current flow uniformly distributed throughout the top conductor, and the return current in the ground plane will be distributed over the whole of the ground plane.

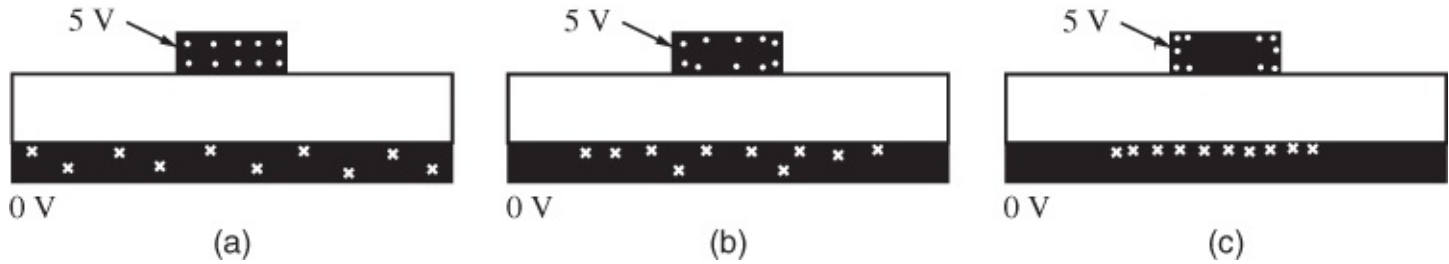


[Figure 2.5](#) Cross-sectional view of the charge distribution on an interconnect at different frequencies: (a) DC; (b) 100 MHz; and (c) 1 GHz. The dots and crosses indicate charge concentrations of different polarity.

As the frequency of the signal increases, that is, a sinusoidally varying voltage is applied between the top and bottom conductor, the charges do not have sufficient time to rearrange and the charges do not spread out uniformly. Also, the EM fields, now being time-varying, are not able to penetrate the conductors as much when the frequency increases, this effect is known as the skin effect. This is shown in [Figure 2.5\(b\)](#) at 100 MHz. The situation is more extreme as the frequency continues to increase, for example to 1 GHz, as in [Figure 2.5\(c\)](#). There are several important consequences of this. On the top conductor the negative charges are not uniformly distributed with respect to the depth of penetration into the conductor. Consequently, current flow is mostly concentrated near the surface of the conductor and the effective cross-sectional area of the conductor, as far as the current is concerned, is less. Thus, the resistance of the top conductor increases. A more dramatic situation exists for the charge distribution in the ground plane. Now the charge is not uniformly distributed over the whole of the ground plane, but instead becomes more concentrated under the strip. Thus the resistance of the ground plane increases as again the effective cross-sectional area has reduced from something that could have been quite large. The electric field lines shift as a result of the different distributions of charge, with more of the electric energy being in the dielectric.

At high frequencies the fundamental result of the field rearrangement is that the capacitance of the line increases, but this change can be quite small, typically less than 10% over the range of DC to 100 GHz. (This effect is described by the frequency dependence of the effective permittivity of the transmission line.) The redistribution of the current results in a change in the inductance with frequency. This is principally because magnetic energy is stored inside as well as outside the conductors at low frequencies. As frequency increases the magnetic field becomes confined to the region outside the conductors and the inductance remains approximately constant. At intermediate frequencies the inductance reduces with frequency.

Only above 1 GHz or so can the inductance be treated as approximately constant for the interconnect dimensions we are concerned with. The most significant frequency-dependent effect is the resistance of the line, which increases indefinitely approximately as the square root of frequency.

## 2.5.8 Dispersion

Dispersion is principally the result of the velocity of the different frequency components of a signal being different. To a lesser extent, dispersion is also the result of other parameters changing with frequency, such as an interconnect's resistance. The effect of dispersion can be seen in [Figure 2.6](#) for a pulse traveling along an interconnect. The pulse spreads out as the different frequency components travel at different speeds along the line. It becomes harder to recognize the pulse, and in a digital system the level of the pulse could become less than that required to trigger a receive circuit. You can imagine a long telegraph line with this problem: successive pulses would start merging and the signal would become unintelligible.

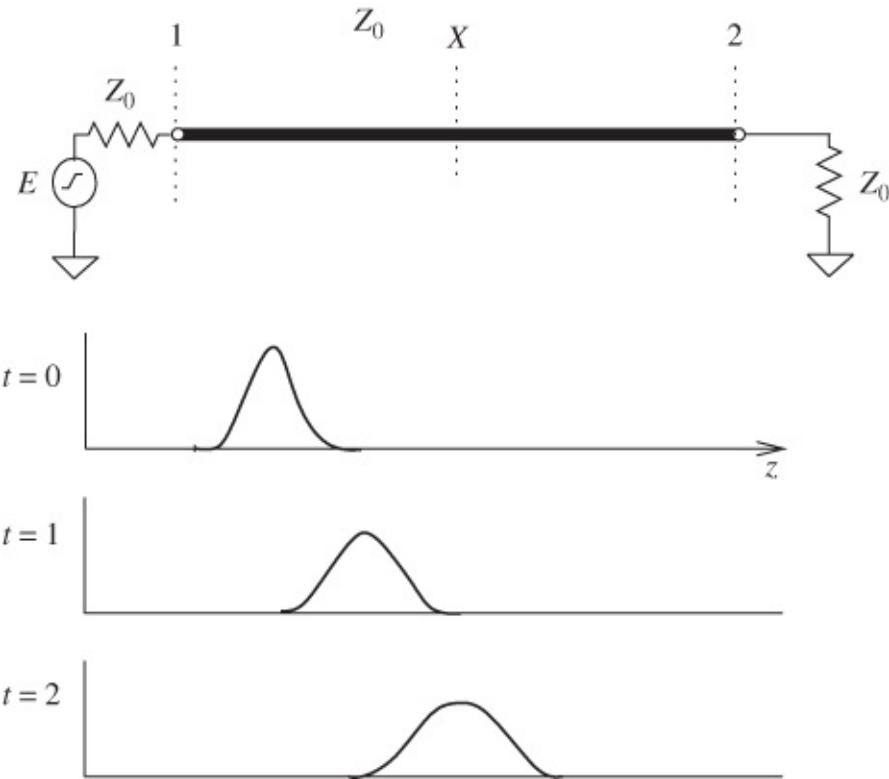


**Figure 2.6** Dispersion of a pulse along an interconnect.

Different interconnect technologies have different dispersion characteristics. For example, with the microstrip line of [Figure 2.4](#) the effective permittivity changes with frequency as the proportion of the EM energy in the air region to that in the dielectric region changes. Dispersion is reduced if the fields are localized and cannot change orientation with frequency. This is the case with the stripline of [Figure 2.3\(c\)](#), which has low dispersion as the fields are confined in one medium and the effective permittivity is just the permittivity of the medium. Thus there are interconnect choices that can be made that effect the integrity of a signal being transmitted.

## 2.6 When an Interconnect Should be Treated as a Transmission Line

If the level of a signal is reasonably constant along the entire length of an interconnect, then it can safely be treated as a lumped element and need not be treated as a transmission line. If the signal is a sinusoid then it is generally agreed that the signal does not change much in time over an interval equal to 1/20th of the period,  $T$ , of the signal. Consider a sinusoidally varying signal  $x(t) = A \sin(\omega t)$ , where  $\omega = 2\pi f$  is the radian frequency of the signal and  $f = 1/T$  is its frequency so that  $x(t) = A \sin(2\pi t/T)$ . The maximum change occurs when the signal goes from a time  $t = -\alpha T/2$  to  $t = +\alpha T/2$ , where  $\alpha$  is the fraction of the period. So in 1/20th of the period ( $\alpha = 0.05$ ) the signal can change by 16% of its maximum possible change in value. When the interconnect line length is less than 1/20th of the wavelength,  $\lambda$ , of the signal, it is regarded as safe to use a circuit model of a resistor, capacitor, and inductor (an  $RLC$  model) for an interconnect. Specifying a length in terms of a fraction of a wavelength is the same as using the signal duration in time as a fraction of the period. (In 1/10th of the period it can change by 31% and in 1/5th of the period it can change by 59%.) With digital signals the time of flight delay  $t_f$  is compared to the rise time  $t_r$  of the signal in determining whether or not a transmission line model is necessary. The rise time  $t_r$  is defined as the time required for the signal to change from 10% to 90% of its final value. The time of flight delay is

$$t_f = \ell/v \quad 2.11$$

where  $\ell$  is the interconnect length and  $v$  is the propagation speed. The general guideline is that for a digital circuit transmission line modeling is necessary when

$$t_r < 2.5t_f \quad 2.12$$

as then the signal has changed by more than 40% of its value. It is generally regarded that the line can be modeled by capacitors and resistors when

$$t_r > 5t_f \quad 2.13$$

The criteria are summarized in [Table 2.1](#).

**Table 2.1** Modeling criteria for sinusoidal and digital signals

Signal type	Model required	
	Transmission line or $RLC$	Lumped $R, C$
Sinusoid	$\ell > \lambda/10$	$\ell < \lambda/20$
Digital pulse	$t_r < 2.5t_f$	$t_r > 5t_f$

When a transmission line model is necessary, either a Spice-compatible distributed  $RLC$  model is used or else a full transmission line model is needed. Which is chosen depends on the accuracy needed and the capability of an available circuit simulation program. Note that the

*RLC* model cannot fully capture the retardation phenomenon as with a lumped element circuit there is always a finite response almost instantaneously and not just after a time-of-flight delay. For both sinusoidal and pulsed signals there is a grey area in which it is not clear which type of modeling should be used. Only experience and the accuracy needed for a particular application are a guide as to which type of modeling should be used. It is definitely preferable to use a lumped-element model if possible.

The criterion for digital systems, that is, Equation (2.13), comes from considering the harmonic content of the rising edge of a pulse in a digital system. The relative levels of the harmonics to the total signal swing depend on the technology of the circuit used to produce the pulse (e.g., the characteristics of a CMOS driver). Typically about five harmonics are significant in a rising pulse and the level of the  $n$ th harmonic is  $\beta$  times that of the total signal swing. This leads to the very approximate relationship

$$t_r \approx \alpha \beta n T / n \quad 2.14$$

where  $n$  is the index of the maximum significant harmonic,  $\beta$  is its level relative to the total pulse swing,  $T$  is the period of the fundamental component (so that  $T/n$  is the period of the  $n$ th harmonic), and  $1/\alpha$  (about a quarter) is the fraction of the pulse that is rising. The criterion for modeling an interconnect as lumped *RC* elements for a sinusoid,  $\ell < \lambda/20$ , becomes, after using  $\lambda = v/f = vT$ ,

$$\ell < vT/20. \quad 2.15$$

Using Equation (2.11) the criterion can be expressed as

$$t_f < T/20. \quad 2.16$$

Now using Equation (2.14) the criterion is

$$t_f < \frac{1}{20} \frac{n}{\alpha \beta} t_r. \quad 2.17$$

With  $n = 5$ ,  $\alpha = 15/4$ , and  $\beta = 1/3$ , the criterion from sinusoidal considerations becomes

$$t_r > 5t_f, \quad 2.18$$

that is, when the rise time is five times the time of flight, a simple *RC* lumped-element model of an interconnect can be used.

The above discussion of interconnects is pertinent to off-chip interconnects and to on-chip interconnects of sufficient size (cross-section) that the resistance of the interconnect is not very large. Consequently RF and microwave chips have relatively large interconnects of reasonably low resistance but the high density of digital circuitry means that nearly all on-chip interconnects for digital ICs have high loss. This is because when the interconnect is very narrow (e.g., around a few microns in width or less) the resistance of the line dominates and the signal dissipates before transmission line lengths are significant (see Table 2.2). (In

practice buffer circuits are used to boost the signal level along a long line.) Most narrow on-chip interconnects can therefore be modeled by lumped-element circuits. In addition, with digital circuits the close packing of the interconnects on-chip, and thus coupling of the interconnects to each other, requires that computer-based model extraction be used to develop a large *RLC*-like circuit describing the interconnect network. A program that does this is called a *parasitic extractor*.

**Table 2.2** Comparison of critical length criteria for different digital technologies. The critical length criterion is  $t_r = 2.5t_f$  (for Si  $\epsilon_r = 11.9$ ,  $\text{SiO}_2 \epsilon_r = 3.8$ , GaAs  $\epsilon_r = 12.85$ , FR-4  $\epsilon_r = 4.4$ , alumina  $\epsilon_r = 9.8$ , and Teflon<sup>TM</sup>  $\epsilon_r = 2.08$ ).

Technology(interconnect medium)	On-chip		Off-chip		
	Rise time (ps)	Critical length (cm)	Rise time (ps)	Substrate	Critical length (cm)
CMOS ( $\text{SiO}_2$ )	50–700	0.3–4.3	1000–4000	Alumina	3.8–15
Bipolar Si ( $\text{SiO}_2$ )	25–100	0.15–0.6	100–400	Alumina	0.1–1.5
MESFET, PHEMT, HBT (GaAs)	5–100	0.02–0.33	50–200	Alumina	0.2–0.8
				FR-4	0.25–1.0
				Teflon	0.4–1.7

<sup>a</sup> MESFET, metal-epitaxy-semiconductor field effect transistor; PHEMT, pseudomorphic high-electron mobility transistor; HBT, heterojunction bipolar transistor.

## 2.7 The Concept of RF Transmission Lines

A review of important TEM-mode RF transmission line theory is essential here because interconnects with uniform cross-sections along their length can be treated, at least to a first approximation, by assuming the static-TEM situation. We shall see that many significant interconnect design calculations require TEM-mode results from transmission line theory.

When transmission line structures have dimensions that are substantially smaller than the wavelengths of the signals being transmitted, then the structures may be satisfactorily analyzed on the basis of line voltages and currents. As the frequency goes higher, and therefore the wavelength becomes smaller, it becomes necessary to set up a complete EM field solution in order to analyze the line structures. Here we can often assume that small transverse line dimensions prevail, and therefore a number of useful results are obtained on a voltage and current basis. The theory thus developed is called distributed circuit theory.

## 2.8 Primary Transmission Line Constants

In this section we are concerned only with uniform transmission lines. Regardless of the actual structure, such lines are shown schematically in [Figure 2.7\(a\)](#). Primary constants are indicated in [Figure 2.7\(b\)](#) and can be defined as follows:

resistance along the line	$= R$	
inductance along the line	$= L$	all specified
conductance shunting the line	$= G$	per unit length.
capacitance shunting the line	$= C$	

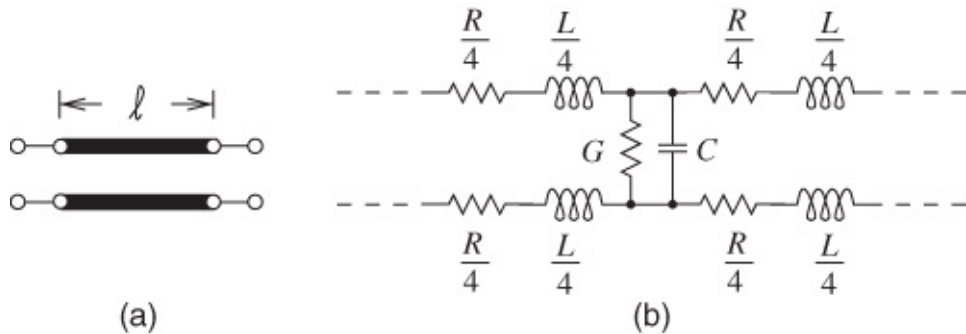


[Figure 2.7](#) The uniform transmission line: (a) transmission line of length  $l$ ; and (b) primary constants assigned to a lumped-element model of a transmission line.

$R$ ,  $L$ ,  $G$  and  $C$  are also referred to as resistance, inductance, conductance, and capacitance per unit length.

The ‘per unit length’ specification means that each quantity is determined on a ‘go and return’ basis. For example, to find the total value of  $R$  per loop meter for a coaxial line we must add the resistance of 1 m of the inner conductor to that of the outer conductor. The return signal path is just as important as the ‘go’ signal path in determining the parameters of an interconnect. In most RF transmission lines the effects due to  $L$  and  $C$  tend to dominate because of the relatively high inductive reactance and capacitive susceptance, respectively. In such cases we refer to ‘loss-free’ or lossless lines, although in practice some information about  $R$  or  $G$  is necessary to determine power losses. The lossless concept is just a useful and good approximation. Note that the lossless approximation is not valid for narrow on-chip (digital) interconnections, as then resistance is very large. The propagation of a wave along the line is characterized by the (complex) propagation coefficient  $\gamma$ :

$$\gamma = \sqrt{(R + j\omega L)(G + j\omega C)} \quad 2.19$$

or

$$\gamma = \alpha + j\beta \quad 2.20$$

where  $\alpha$  is the attenuation coefficient, in Nepers per meter, and  $\beta$  is the phase-change coefficient, in degrees, or radians, per meter.

Neglecting losses, Equations (2.19) and (2.20) yield the important result:

$$\beta = \omega \sqrt{LC}. \quad 2.21$$

## 2.9 Secondary Constants for Transmission Lines

In one complete wavelength along the line (called the guide wavelength  $\lambda_g$ ) the traveling wave must experience  $2\pi$  radians of phase shift. Thus

$$\beta \lambda_g = 2\pi \quad 2.22$$

or

$$\beta = 2\pi/\lambda_g. \quad 2.23$$

(Hence,  $\beta$  is also called the wave number.) From the relationship for the velocity  $v_p = f\lambda_g$  we can also write the velocity of propagation as

$$v_p = \omega/\beta. \quad 2.24$$

Now  $v_p$  is called the phase velocity and it is the apparent speed of a point of constant phase on a traveling sinewave. By using Equation (2.21) we also obtain

$$v_p = 1/(\sqrt{LC}). \quad 2.25$$

The velocity of propagation is also given in terms of the absolute permeability  $\mu$  and permittivity  $\epsilon$  of the medium through which the wave passes:

$$v_p = \frac{1}{\sqrt{\mu\epsilon}} = \frac{c}{\sqrt{\mu_r\epsilon_r}} \quad 2.26$$

where  $c = 2.99793 \times 10^8$  m/s, the velocity of light in free space—often approximated to  $c = 3 \times 10^8$  m/s.

Most lines do not possess any magnetic materials and thus have  $\mu_r = 1$ . For the stripline, Figure 2.3(c), the filling consists of a uniform dielectric, and Equation (2.26) then gives the phase velocity as

$$v_p = c/\sqrt{\epsilon_r}. \quad 2.27$$

We note that the wave is slowed by the dielectric medium.

By noting that  $c = f\lambda_0$ , where  $\lambda_0$  is the wavelength of the signal in free space, and  $v_p = f\lambda_g$ , we can use Equation (2.27) to show that

$$\lambda_g = \lambda_0/\sqrt{\epsilon_r}. \quad 2.28$$

(The subscript ‘g’ means ‘guide’; we can look upon the transmission line as a ‘guiding’ structure as the EM fields are guided along the interconnect.) This expression, Equation (2.28), is particularly significant. It explicitly states that the wavelength is reduced according to the square root of the relative permittivity of the material in which the line is embedded. For example, with a stripline with alumina ( $\epsilon_r \approx 10$ ) as the dielectric and excited at 10 GHz, the free-space wavelength would be 3 cm, but the wavelength in the stripline is only  $3/\sqrt{10} = 0.95$  cm. Thus, distributed components become shorter and occupy less space if high-permittivity materials can be used. This has important implications for microstrip and all line structures.

The final secondary constant to be discussed is the characteristic impedance  $Z_0$ . This is generally given by

$$Z_0 = \sqrt{\frac{R + j\omega L}{G + j\omega C}} \quad 2.29$$

At high radio frequencies this simplifies to

$$Z_0 = \sqrt{\frac{L}{C}} \quad 2.30$$

which is a purely resistive result. For coaxial lines the most common value is  $Z_0 = 50 \Omega$ , which results in the lowest loss if the coaxial line is filled with Teflon, the most common situation. A coaxial cable with  $Z_0 = 75 \Omega$  is sometimes used as this corresponds to an air-filled coaxial line with the lowest loss. On-chip it is sometimes preferable to have a higher characteristic impedance as this reduces the current drive requirements and  $I^2R$  (resistive) losses.

Changing  $Z_0$  requires a change in the dimensions of the line. Specifically, in the case of coaxial lines, it requires changing the ratio of the radii of the inner and outer conductors. Dimensional alterations are much more easily carried out with stripline or its derivatives, and therefore such structures can be fabricated for a wide range of characteristic impedances (typically 20–150  $\Omega$  for stripline). Equation (2.30) can be re-expressed, with the aid of Equation (2.25), in the following alternative forms:

$$Z_0 = v_p L \quad 2.31$$

or

$$Z_0 = 1/(v_p C). \quad 2.32$$

Equation (2.32) is particularly useful in establishing some fundamental microstrip parameters.

## 2.10 Transmission Line Impedances

The input impedance of a terminated transmission line varies with the length of the line,

therefore a suitable distance notation is required, which is shown in [Figure 2.8](#). Many standard textbooks derive the expressions given as Equations [\(2.33\)](#) to [\(2.39\)](#) here.

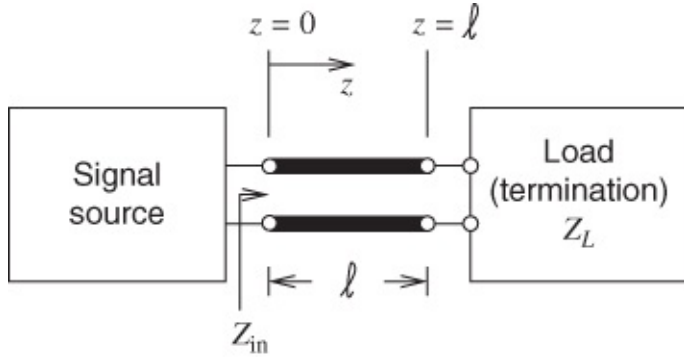


[Figure 2.8](#) Notation applicable to a general, uniform line.

By setting down the distance limits into expressions for the voltage and current at any point along the line we obtain, for the load impedance  $Z_L$ , the following expression for the input impedance at  $z = 0$ :

$$Z_{in} = Z_0 \left( \frac{Z_L \cosh \gamma \ell + Z_0 \sinh \gamma \ell}{Z_0 \cosh \gamma \ell + Z_L \sinh \gamma \ell} \right). \quad 2.33$$

This expression is completely general. For lossless lines the result simplifies to

$$Z_{in} = Z_0 \left( \frac{Z_L + jZ_0 \tan \beta \ell}{Z_0 + jZ_L \tan \beta \ell} \right). \quad 2.34$$

The input impedances of lines having short-circuit or open-circuit terminations (see [Figure 2.9](#)) follow from Equation [\(2.34\)](#), and these impedances can now be easily written down.

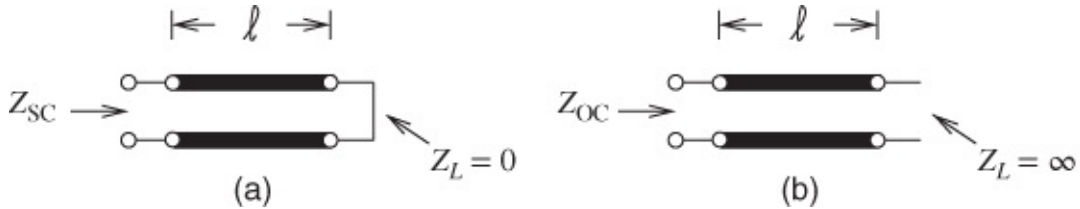


[Figure 2.9](#) Line terminations: (a) short-circuit termination with  $Z_{SC}$  being the impedance looking into the short-circuited line; and (b) open-circuit with  $Z_{OC}$  being the impedance looking into the open-circuited line.

For the short-circuit case  $Z_L = 0$  and Equation [\(2.34\)](#) gives

$$Z_{SC} = jZ_0 \tan \beta \ell. \quad 2.35$$

For the open-circuit case  $Z_L = \infty$  and Equation [\(2.34\)](#) gives

$$Z_{OC} = -jZ_0 \cot \beta \ell. \quad 2.36$$

Short-circuit or open-circuit terminated lines are very useful structures in a wide variety of circuits.

By choosing the correct lengths ( $\ell$ ) inductive or capacitive circuit elements are automatically realized in transmission line form, as can be seen from Equations (2.35) and (2.36). There are many applications in resonators, filters, and matching and coupling networks. When the line is terminated in a load impedance exactly equal to the characteristic impedance ( $Z_0$ ) of the line itself, it is perfectly broadband matched. The denominator is equal to the numerator in the right-hand parentheses of Equation (2.33) and hence

$$Z_{in} = Z_0. \quad 2.37$$

This completely matched condition is often used in test and measurement procedures.

## 2.11 Reflection

### 2.11.1 Reflection and Voltage Standing-wave Ratio

In all cases, except the completely matched condition, the load termination reflects some of the energy originally sent down the line. Interference between the incident and reflected waves, traveling at the same velocity but in opposite directions, causes a ‘standing-wave’ field pattern to be set up.

The voltage reflection coefficient  $\Gamma$  (the ratio of reflected to incident voltage at the load) is given by

$$\Gamma = \frac{Z_L - Z_0}{Z_L + Z_0}. \quad 2.38$$

The ratio of maximum to minimum amplitude of the standing wave is called the voltage standing-wave ratio (VSWR), given by

$$\text{VSWR} = \frac{1 + |\Gamma|}{1 - |\Gamma|}. \quad 2.39$$

Notice that, in general,  $\Gamma$  may be complex but VSWR is necessarily always real. For the matched condition,  $\Gamma = 0$  and  $\text{VSWR} = 1$ . The load reflection coefficients for short-circuit and open-circuit terminated conditions are  $-1$  and  $+1$ , respectively, and in both cases the VSWR is infinite.

### 2.11.2 Forward- and Backward-traveling Pulses

Forward- and backward-traveling pulses are shown in [Figure 2.10](#), when the resistance at the end of the line is lower than the characteristic impedance of the line ( $Z_L < Z_0$ ). The voltage source is a step voltage, which is zero for times  $t < 0$ . At time  $t = 0$  the step is applied to the line, and it begins traveling down the line as shown at time  $t = 1$ . At time  $t = 2$  the leading edge of the step reaches the load, and as the load has lower resistance than the characteristic impedance of the line, the reflection coefficient  $\Gamma$  is negative and the total voltage on the line, which is all we can directly observe, drops. A reflected, smaller and opposite step signal

travels in the backward direction and adds to the forward-traveling step to produce the waveform shown at  $t = 3$ . The impedance of the source is matched to the transmission line impedance so that the reflection at the source is zero. The signal on the line at time  $t = 4$ , the round trip propagation time of the line, therefore remains at the lower value. The easiest way to remember the polarity of the reflected pulse is to consider the situation with a short-circuit at the load. Then the total voltage on the line at the load end must be zero. The only way this can occur when a signal is incident is if the reflected signal is equal in magnitude but *opposite* in sign, in this case  $\Gamma = -1$ . So whenever  $|Z_L| < |Z_0|$ , the reflected pulse will tend to subtract from the incident pulse.

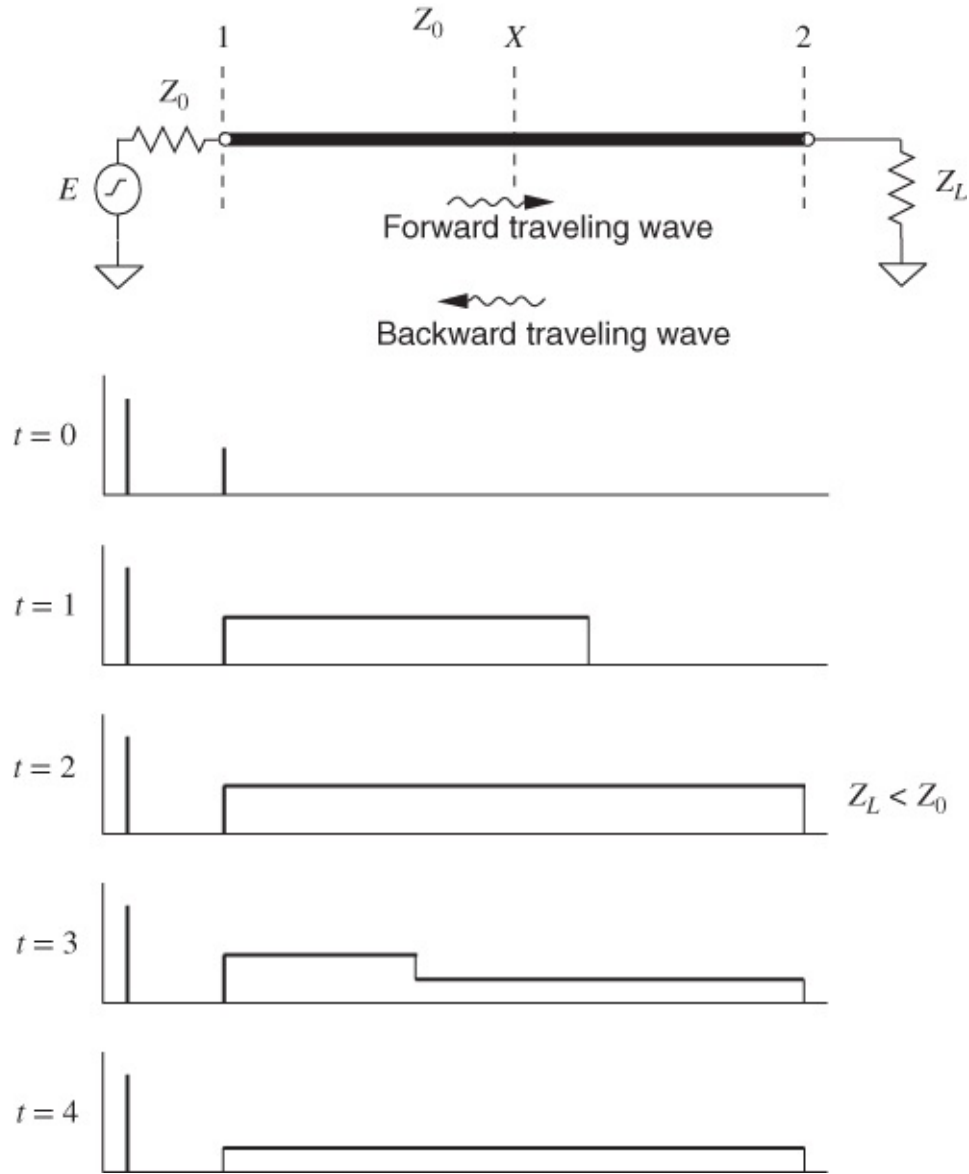


**Figure 2.10** Reflection of a pulse at a load that is lower in resistance than the characteristic impedance of the line.

The opposite situation occurs when the resistance at the load end is higher than the characteristic impedance of the line ([Figure 2.11](#)). Then the reflected pulse has the same polarity as the incident signal. Again, to remember this, think of the open-circuited case. The voltage across the load does not need to be zero and indeed doubles as the reflected pulse has

the same sign as well as magnitude as that of the incident signal, in this case  $\Gamma = +1$ .

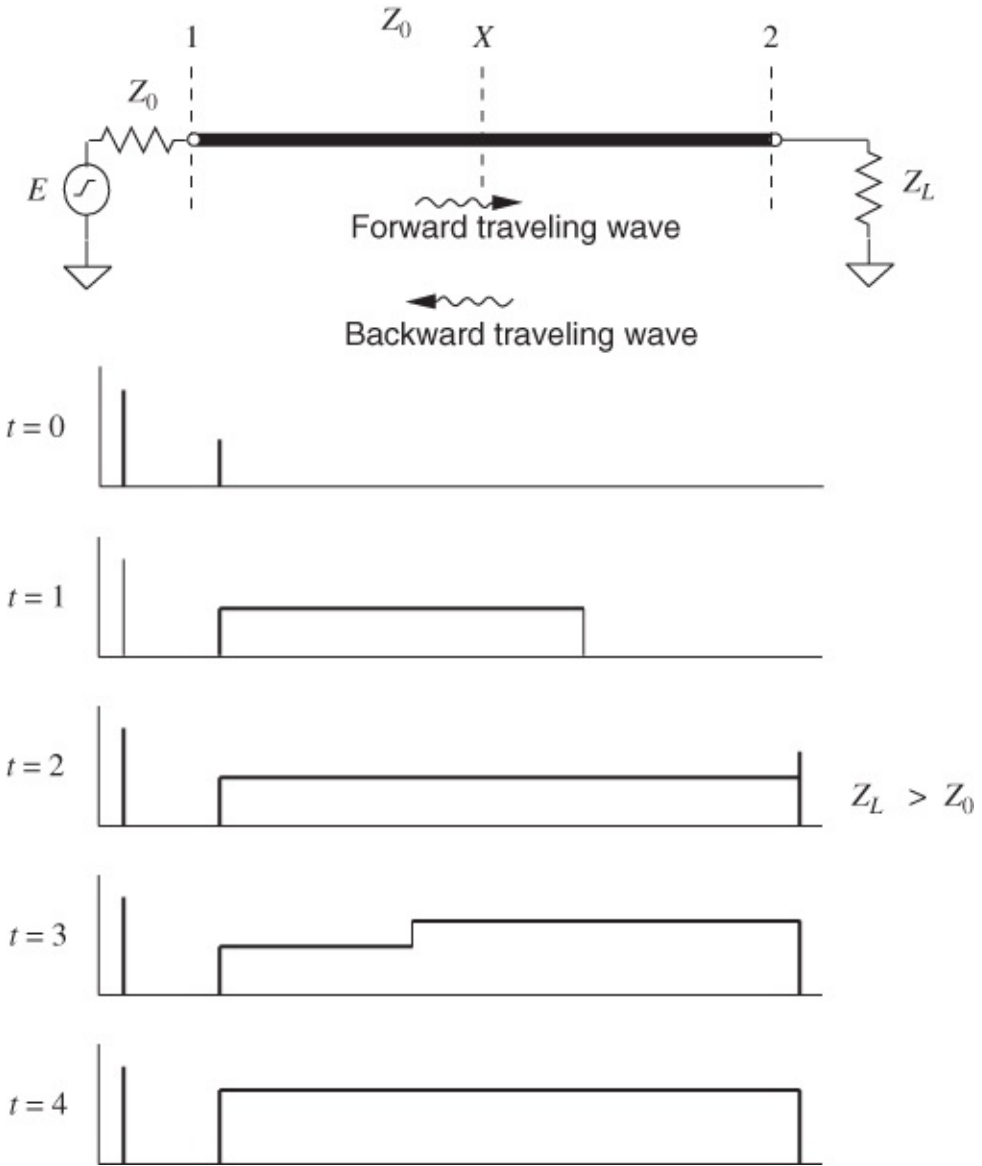


**Figure 2.11** Reflection of a pulse at a load that is higher in resistance than the characteristic impedance of the line.

A more illustrative situation is shown in [Figure 2.12](#), where a signal like that of a pulse is incident on a load that has a resistance higher than that of the characteristic impedance of the line. The peaking of the voltage that results at the load is typically a design objective in many long digital interconnects, as less overall signal energy needs to be transmitted down the line, or equivalently a lower current drive capability of the source is required to achieve first incidence switching. This is at the price of having reflected signals on the interconnects, but these can be dissipated through a combination of interconnect loss and absorption of the reflected signal at the driver.

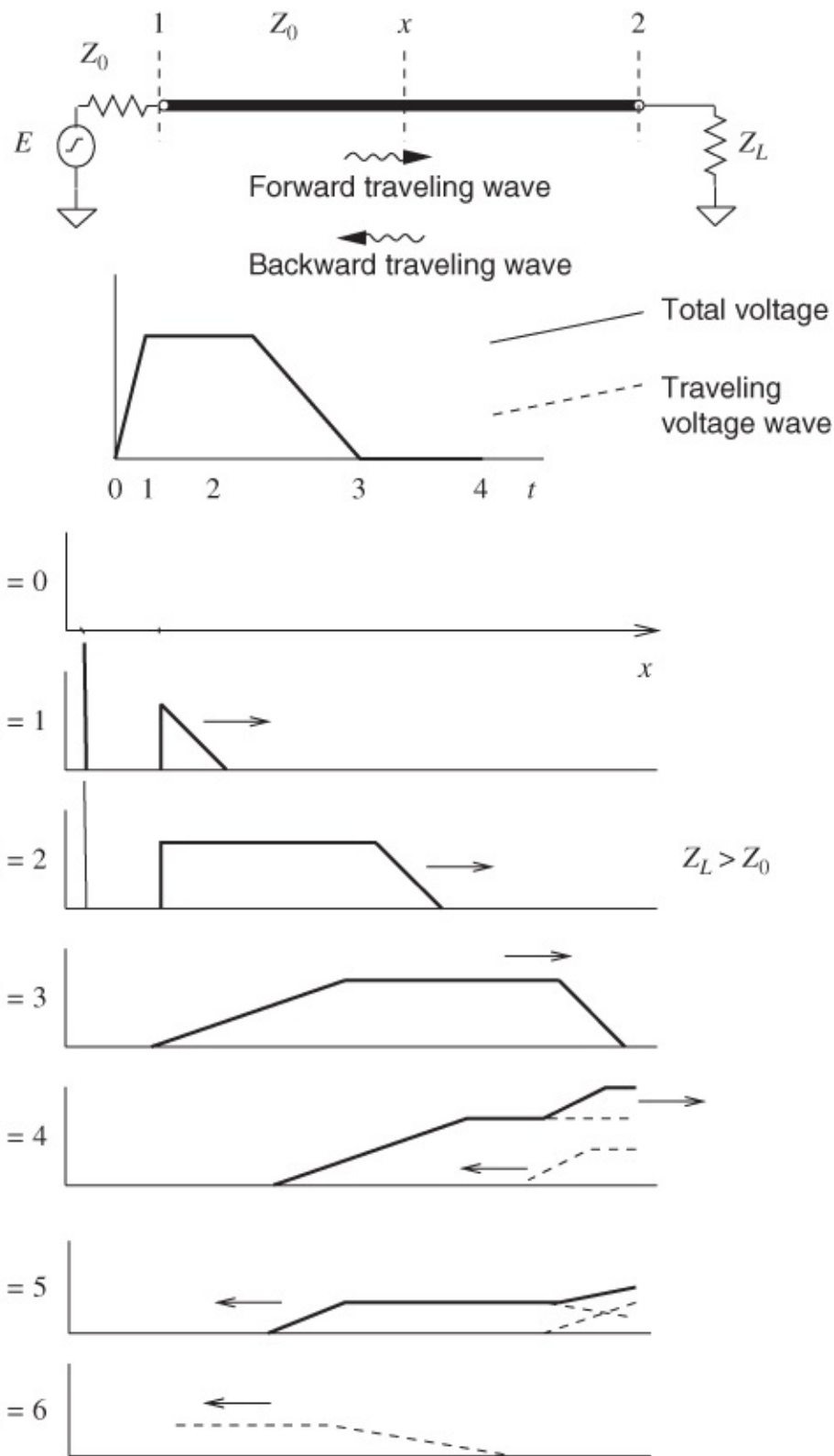


**Figure 2.12** Reflection of a pulse on an interconnect showing forward and backward traveling pulses.

### 2.11.3 Effect on Signal Integrity

Multiple reflections can effect the integrity of the signal in a digital system. A typical waveform resulting from multiple reflections is shown in [Figure 2.13\(a\)](#). One of the classic

results of poorly defined matching of an interconnect, a driver and a receiver is the production of a metastate, as shown. The metastate often results from reflection at first incidence of a signal that has an initial level that is below that required for switching (the minimum logic 1 switching level is  $V_{IH}$ ) This situation occurs when the current drive capability of the digital driver is lower than that required to establish the full output high voltage level  $V_{OH}$  on the line. This is a necessary compromise with most digital circuits in order to keep the transistors small. A disastrous situation can occur when the metastate crosses the switching threshold more than once for each edge. If the circuitry is switched asynchronously (i.e., is not clocked) false switching may occur. Similar situations occur at the falling edge.

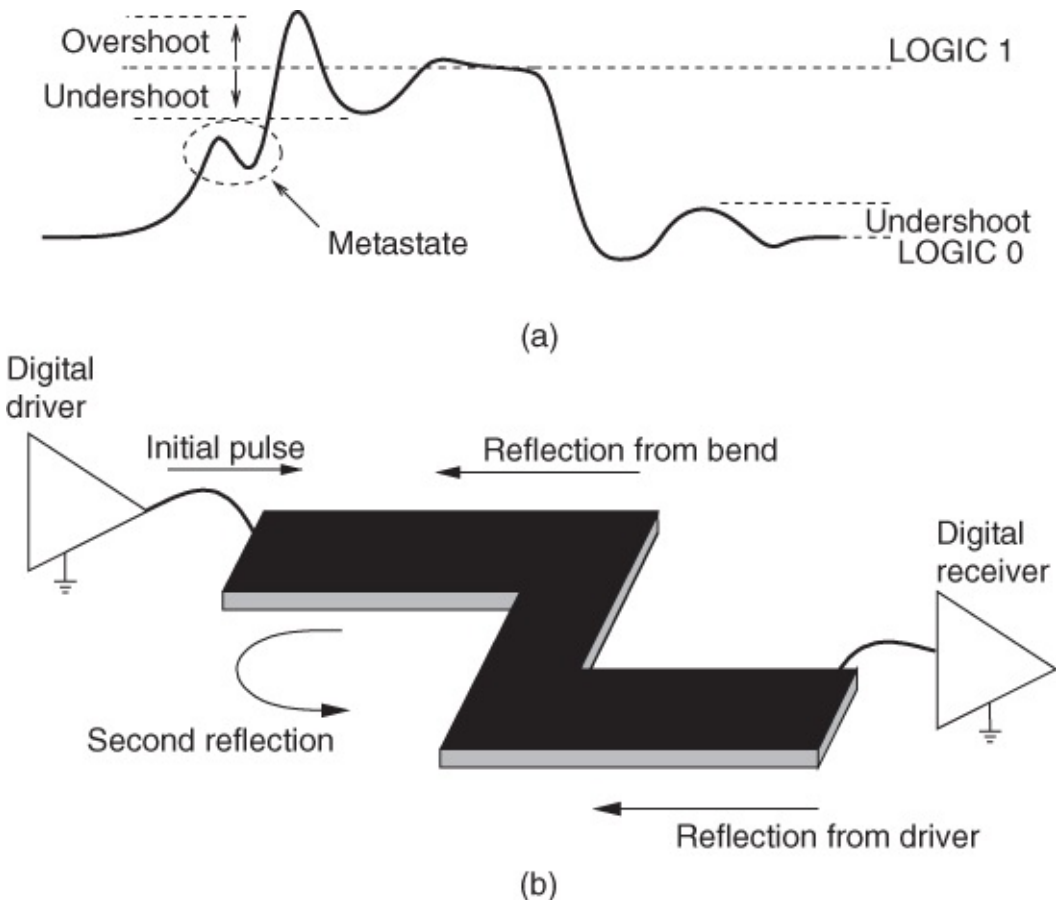


**Figure 2.13** A digital signal in an interconnect: (a) resulting from multiple reflections; and (b) sources of reflection.

## 2.12 Multiple Conductors

Any parallel-coupled pair of transmission lines, regardless of their practical realization, may be described by the four-port configuration indicated schematically in [Figure 2.14](#). The dashed lines indicate mutual coupling; input and output connections and terminations have been omitted for simplicity.

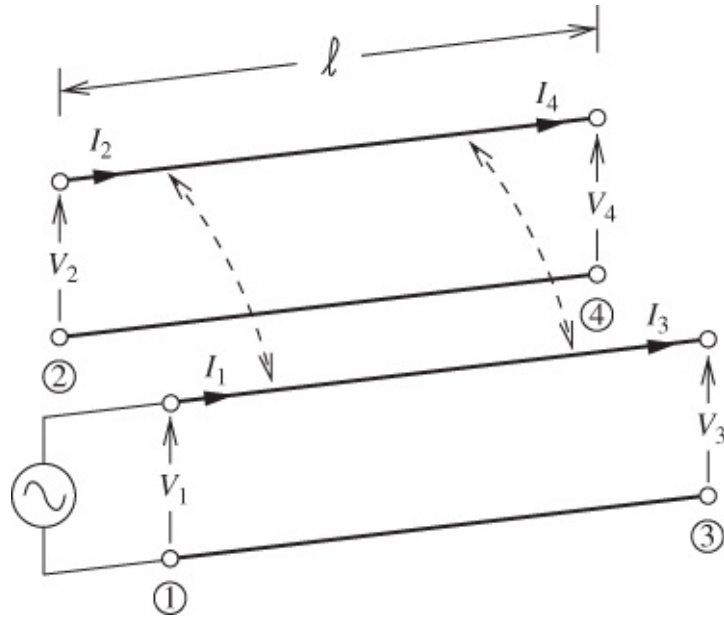


**Figure 2.14** Two parallel-coupled transmission lines.

In terms of  $y$  parameters the characteristics of the coupled interconnects are described by

$$\begin{bmatrix} I_1 \\ I_2 \\ I_3 \\ I_4 \end{bmatrix} = \begin{bmatrix} y_{11} & y_{12} & y_{13} & y_{14} \\ y_{21} & y_{22} & y_{23} & y_{24} \\ y_{31} & y_{32} & y_{33} & y_{34} \\ y_{41} & y_{42} & y_{43} & y_{44} \end{bmatrix} \begin{bmatrix} V_1 \\ V_2 \\ V_3 \\ V_4 \end{bmatrix} \quad 2.40$$

Coupling is described by the terms  $y_{12}$  ( $= y_{21}$ ),  $y_{14}$  ( $= y_{41}$ ),  $y_{23}$  ( $= y_{32}$ ), and  $y_{34}$  ( $= y_{43}$ ). Coupling, however, is understood by considering the effect of the overlapping EM fields produced by each of the coupled interconnects.

To examine the coupling modes that are established, we now concentrate on a pure TEM-mode type of structure. The simplest structure to consider is the dual, coaxial, coupled-line system, in which electric and magnetic fields couple through a narrow slot cut into the adjacent outer conductor along a certain length. Such a structure is shown in [Figure 2.15\(a\)](#). Notice that the consistent field patterns correspond to waves traveling in opposite directions along the respective lines, and it may be stated that any parallel-coupled pair of transmission lines yield contra-directional traveling waves. This coupling is called backward-wave coupling.

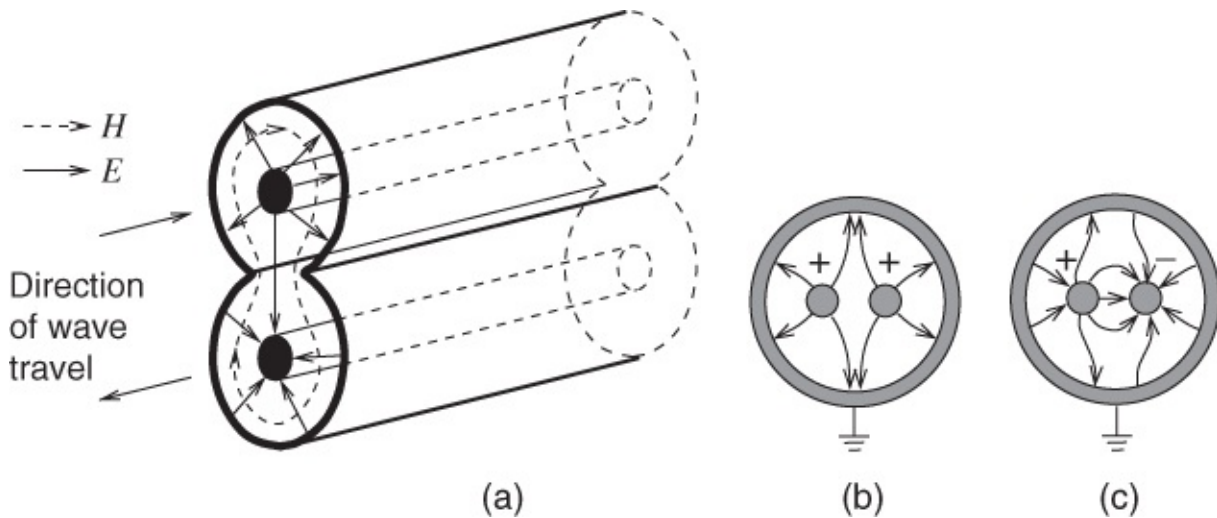


**Figure 2.15** Parallel-coupled coaxial lines: (a) fields; (b) even mode; and (c) odd mode. (For simplicity only the electric field is indicated in (b) and (c)).

The coupled coaxial arrangement constitutes a pure TEM-mode system, assuming either a uniform dielectric filling or an air-filled structure. At any instant the relative polarities of the voltages, taken at any specific plane along the structure, will either be alike or opposite. We refer to different field configurations set up by such polarities as the even-mode and the odd-mode respectively. [Figures 2.15\(b\)](#) and [\(c\)](#) illustrates these effects. The complete behavior of the coupled structure can be obtained by superposition of the effects due to these two modes.

Because of the assumed uniform dielectric filling, any signal traveling in such a pure TEM-mode system will always travel at the same velocity,  $v = c/\sqrt{\epsilon_r}$ . Thus the velocity associated with the even mode is identical to that associated with the odd mode here.

The equivalent primary constants for the coupled lines having even- or odd-modes, taken separately, must differ because of the different field distributions. As a result of this, two distinct characteristic impedances may be defined, one for each mode, expressed in terms of the different primary constants by equations of the form of [Equation \(2.30\)](#). We term these impedances the even-mode and odd-mode characteristic impedances, denoted by  $Z_{0e}$  and  $Z_{0o}$  respectively. This applies to any TEM-mode or quasi-TEM mode parallel-coupled line structure, and the characteristic impedances are major parameters in design procedures. Many microwave circuits, such as bandpass filters and directional couplers, exploit this phenomenon.

In many planar interconnects the fields extend indefinitely and this is the case with the two parallel microstrip interconnects shown in [Figure 2.16](#), where only the left line is driven. Part of the magnetic field on the driven line encompasses the quiet line on the right, inducing current flow as shown. The electric field also extends from the driven interconnect and induces a voltage on the quiet (or victim) line. The result is that a reverse-traveling wave is induced on the quiet line. The signal induced is called crosstalk noise, and the crosstalk resulting from many neighbouring nets can constitute a signal voltage that could result in false switching in a digital system. The type of crosstalk signal induced by a pulse traveling down a microstrip line is illustrated in [Figure 2.17](#).

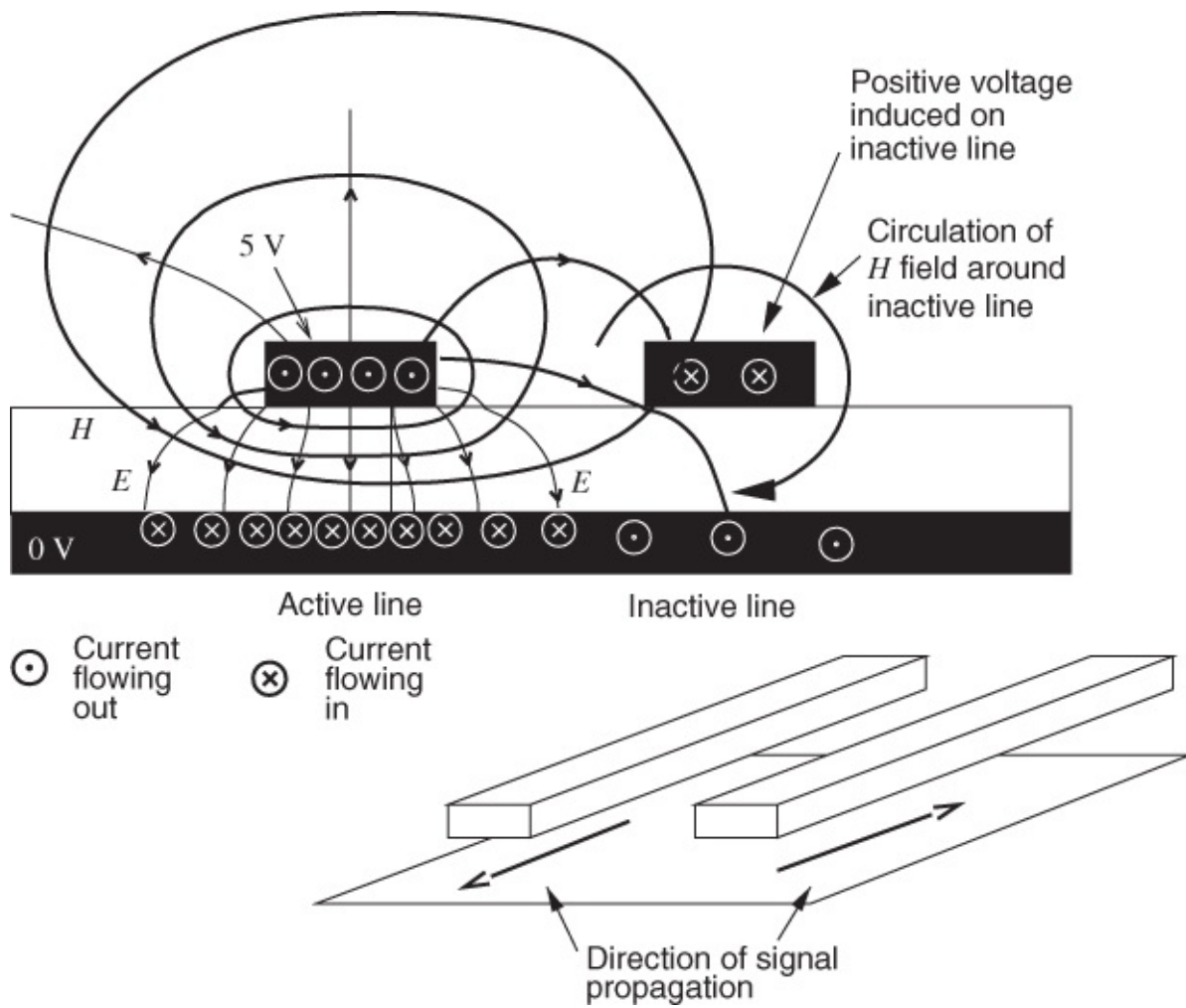


**Figure 2.16** Coupled microstrip lines in perspective.

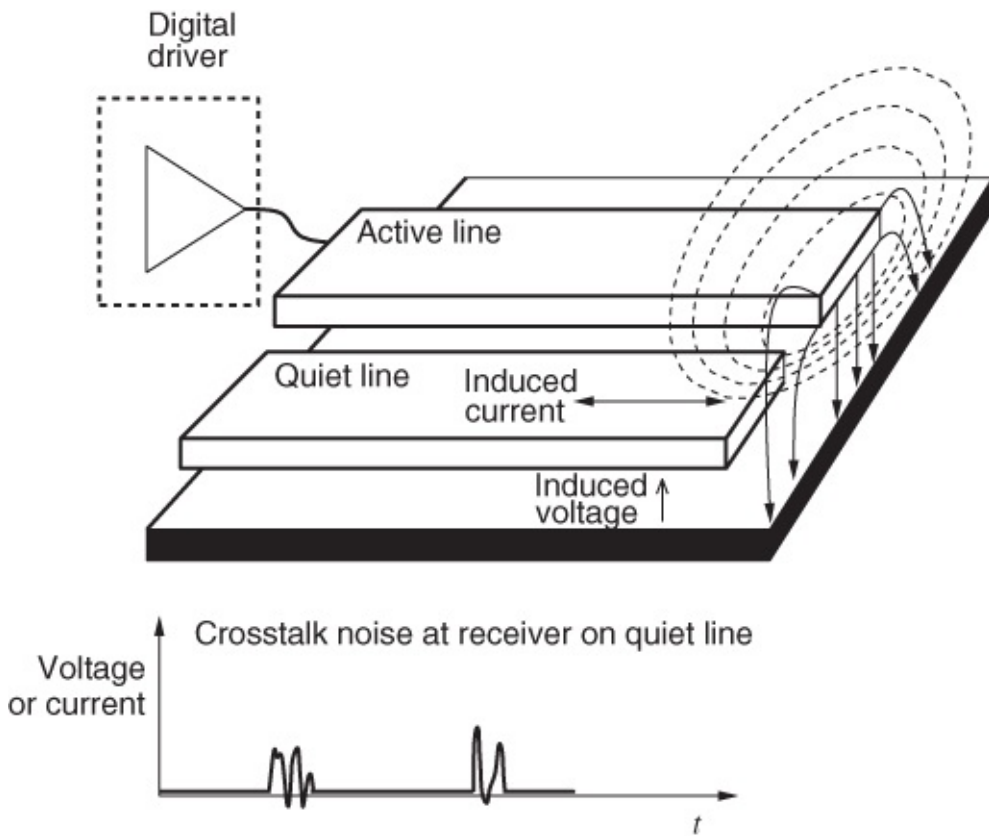


**Figure 2.17** Coupled microstrip lines showing the signal induced on the quiet (or victim) line due to a pulse on the driven line.

## 2.13 Return Currents

We have already introduced the concept of return currents when we considered the current flowing on a microstrip line ([Figure 2.4](#)). The physics is such that if there is a signal current there must be a return signal current which will tend to be as close to the signal current as possible to minimize stored energy. The provision of a signal return path is important in maintaining the integrity (i.e., predictable signal waveform) of an interconnect. In most interconnects each interconnect is confined to its own conductor, but the return signal path is used by signals on many other conductors.

The return signal path for a packaged system is shown in [Figure 2.18](#). The most common signal integrity problem that is introduced at the design stage is not making provision for the signal return path. An example is the provision of a return (say, ground) pin remote from the signal pin at a chip-to-PCB interface. As well as slowing the signal down considerably this situation also increases the level of crosstalk. Of course it is not feasible to provide an individual signal return path for every net on a digital chip. However, the practice of providing return paths dedicated to two or just a few signal pins is common. Provision of individual return current paths is appearing for long haul nets on large digital chips, for example clock and data buses, which can be close to the chip-edge dimension in length. Commonly this is done using ground planes or using differential lines such as CPS.

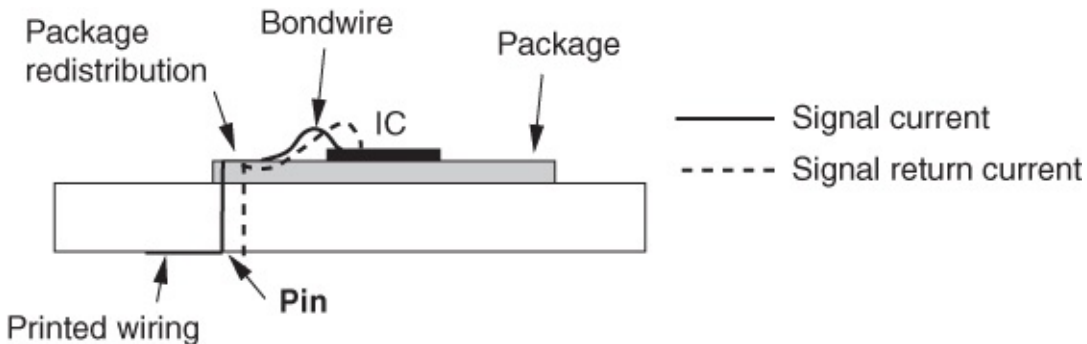
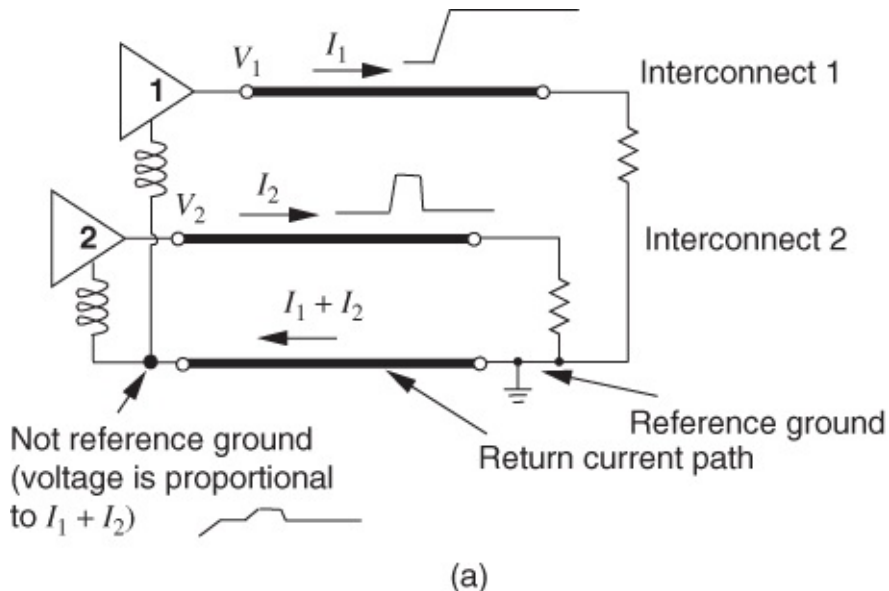


**Figure 2.18** Signal paths going from an integrated circuit (IC) through a package to a printed circuit board.

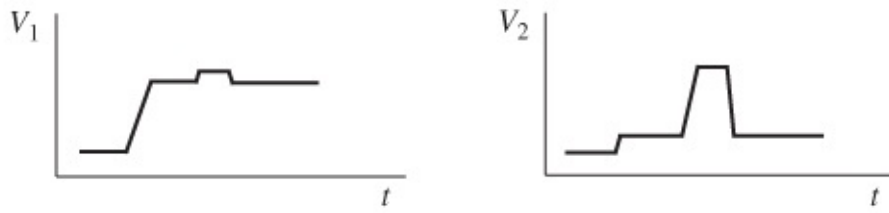
Silicon-based RFIC chips generally use differential signaling to overcome the limitations of metal-oxide-semiconductor (MOS) devices. The currents on each of the differential signal paths balance each other and so each provides the signal return path for the other. This design practice effectively eliminates RF currents that would occur on ground conductors. The off-chip RF interconnects interfacing the chip to the outside world also require differential signaling but now, because of the larger electrical dimensions, differential transmission lines are required.

### 2.13.1 Common Impedance Coupling

Sharing of a return path results in coupling of signals and crosstalk on a pair of transmission lines. Coupling resulting from the sharing of a signal return path is shown in [Figure 2.19](#). This type of coupling is often called common impedance coupling as there is a circuit element common to two or more interconnects. The simplest situation is a shared impedance, rather than a shared transmission line return, so that the return current attributed to one interconnect induces a voltage across the common impedance element. This signal then appears as though it was on the victim line. This is the situation with ground bounce, a common problem that occurs when connecting a packaged chip to the next higher level in the packaging hierarchy. The problem can be illustrated by considering a ground pin, forming part of the current return path, that is utilized by several off-chip drivers. The ground pin has an effective impedance resulting from bond wire inductances which connect the die to the package and from the package pin itself. Return current spikes effectively boost the voltage of the on-chip ground above that of the off-chip ground so that the drive signal of one chip appears at the output of other drivers. This phenomenon is known as ‘ground bounce.’ While the false signal resulting from one driver is small, the switching of many drivers can result in an appreciable signal. Since the common impedance element is inductive, the voltage induced is proportional to the switching speed of the drivers. The only solutions are to use many ground connections so that few nets share the same current return path, now a common practice with high-performance parts, and to slow down the transitions of off-chip signals, a necessary requirement in any case with current technology. Also to reduce the current levels, it is becoming necessary to use higher impedance drivers off-chip so that current levels are lower. However, given the reduced voltage levels being used in digital systems the energy contained in these off-chip connections is low and so more susceptible to EM interference.



(a)



(b)

**Figure 2.19** Shared current return path forming a common impedance connection (a) and the voltage waveforms resulting (b).

In a mixed signal system with analog and digital circuitry, digital signals have large amplitudes with high frequency content. It is important that the digital and analog signal return paths be isolated to minimize common impedance coupling, as shown in [Figure 2.20](#).

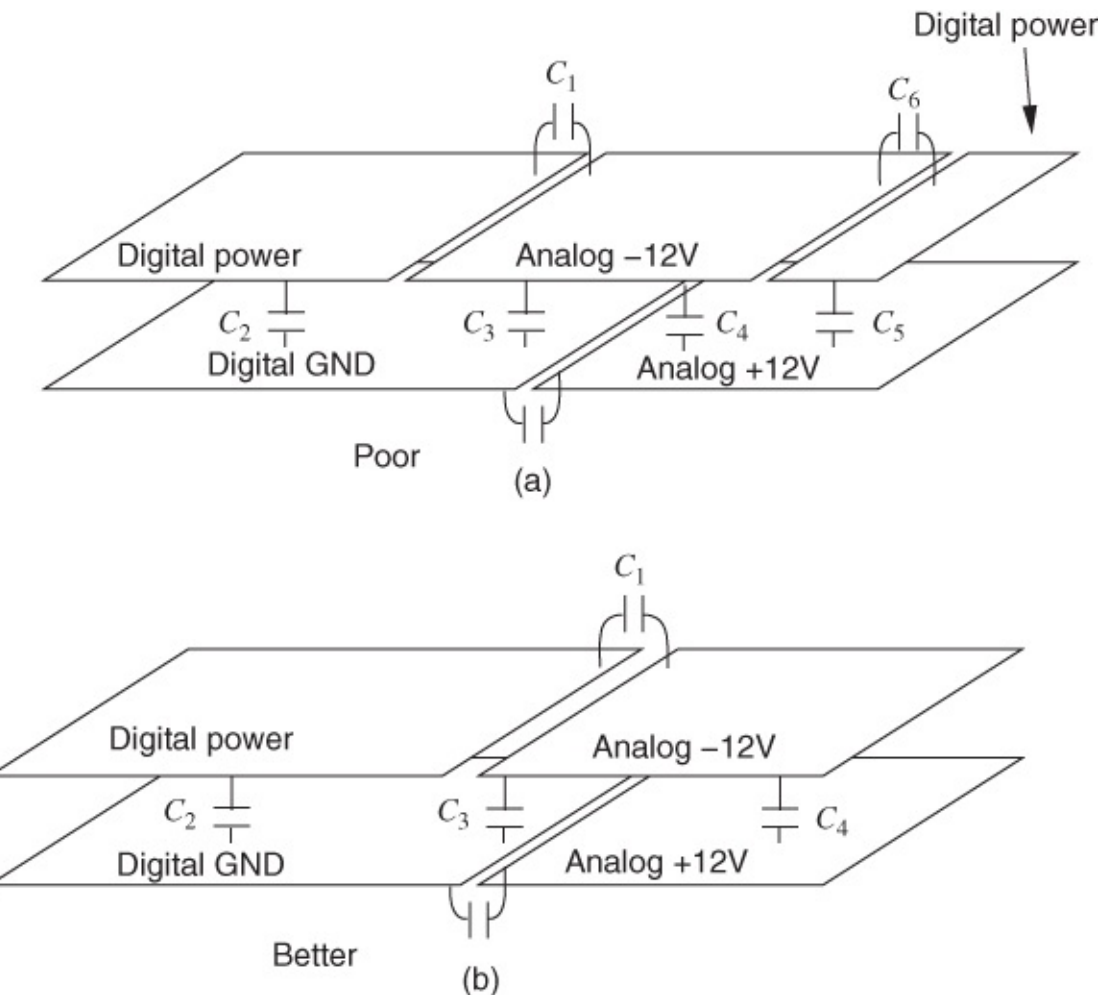


**Figure 2.20** A mixed signal system with (a) poor and (b) better isolation of analog and digital signal return paths.

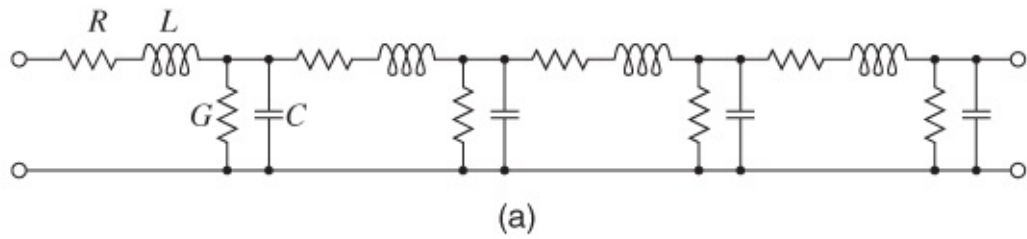
## 2.14 Modeling of Interconnects

A range of models are used for interconnects depending on:

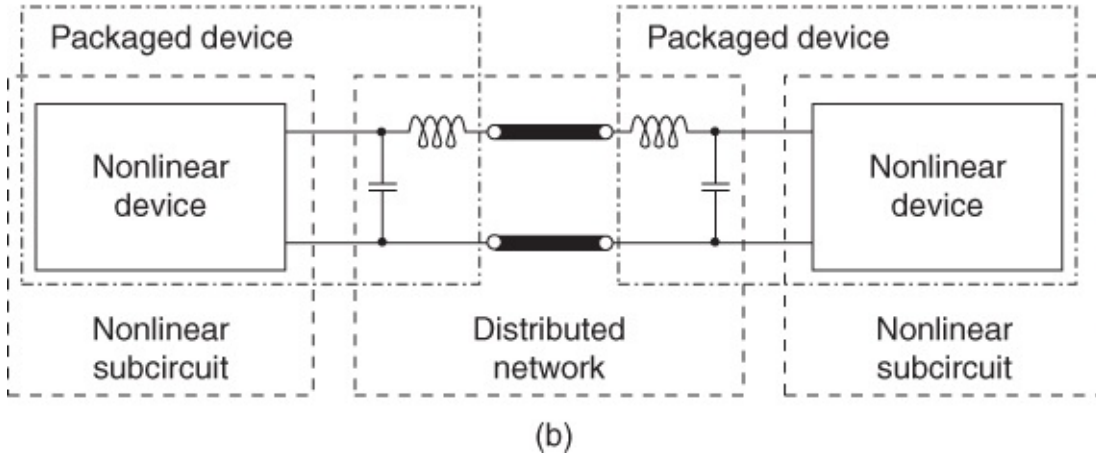
- the accuracy required—nets carrying analog signals need to be modeled more accurately than those carrying digital signals
- the amenability of the net to modeling
- the frequency of operation.

Short on-chip interconnects are commonly modeled as *RLC* networks where the inductor and capacitor networks are arrived at separately using static calculations of the effect of very small segments of interconnect on other small segments.

Uniform interconnects (with regular cross-section) can be modeled by determining the characteristics of the transmission line, for example  $Z_0$  and  $\gamma$  versus frequency, or arriving at a distributed lumped-element circuit, as shown in [Figure 2.21\(a\)](#). This model can be combined with driver and receiver models to realize a circuit model for a complete system.



(a)



(b)

**Figure 2.21** *RLC* model (a) of an interconnect and (b) incorporating a driver and a receiver.

Entire microwave and millimeter-wave structures can be modeled using EM modeling software. This software yields the network parameters of the structure that can readily be used in microwave circuit simulation programs. The most useful EM modeling software models planar interconnects as having zero thickness, as shown in [Figure 2.22](#). Such software is called a  $2\frac{1}{2}$ D EM simulator and only considers current flow in the horizontal plane of the interconnect or in the vertical direction. Arbitrary current flow in any direction is not considered. This is reasonable for microwave interconnects as the thickness of a planar strip is usually much less than the width of the interconnect. Arbitrary EM simulators, 3D EM simulators, can analyze structures with arbitrarily directed current flow. They are about 1000 times slower than  $2\frac{1}{2}$ D EM simulators and can only consider relatively small structures due to the large matrix sizes that would otherwise result. Many analytic formulas have also been derived for the characteristics of uniform interconnects. These formulas are important in arriving at synthesis formulas that can be used in design, that is, arriving at the physical dimensions of an interconnect structure from its required electrical specifications. Microwave circuit simulators use other tricks to handle transmission lines. One approach is to use algebraic formulas for the important transmission line parameters (i.e., the characteristic parameters and propagation coefficient). Another approach that works with complex transmission line structures calculates the capacitance and inductance matrices, as well as the resistance and conductance matrices, of multiconductor transmission lines. Using a 2D EM simulation of the transmission line cross-section can be 1000 times faster than  $2\frac{1}{2}$ D EM simulators but is less general.

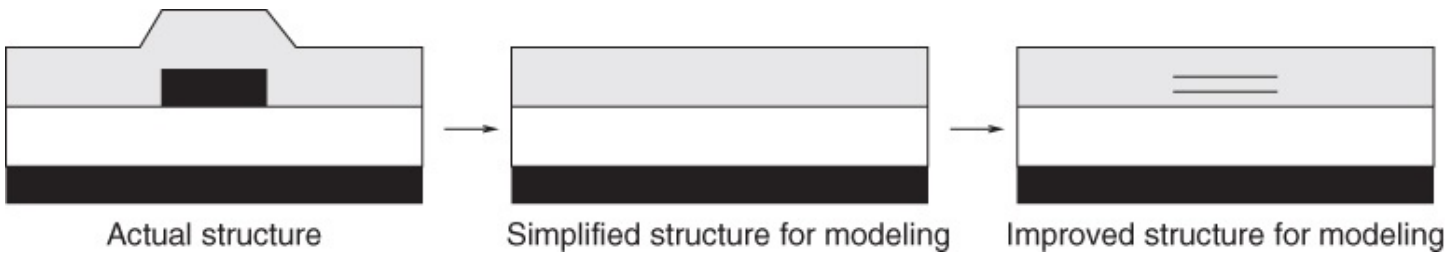


**Figure 2.22** Cross-section of a microstrip interconnect with a passivation covering layer modeled as a simplified structure with an idealized zero thickness microstrip line and an improved structure with multiple zero thickness metal lines.

## 2.15 Summary

This chapter introduced the basics of signal transmission on interconnects. Interconnects determine the limits on the performance of digital systems and the characteristics of analog circuits. Indeed at RF and microwave frequencies, interconnects are part of the circuit and must be designed accordingly. The essential aspect of signal transmission on transmission lines (having uniform cross-sections) and interconnects (not necessarily having uniform cross-sections) is that forward- and backward-traveling waves are supported. This is a consequence of the finite speed of an EM signal. With transmission lines and interconnects, conductors are used to guide an EM wave, with the conductors supporting both charges and current flow. In this book we are concerned with interconnects having two or more conductors to guide the EM signal. In a two-conductor system one of the conductors passes the signal current and the other passes the matching signal return current. Signal integrity requires that a good signal return path be provided and that the generation of backward-traveling signals from reflections be knowingly controlled.

While powerful EM tools are available to model interconnects and optimize interconnect networks for specific properties, it is always preferable to synthesize a design and to intuitively understand signal propagation. The remaining chapters in this book describe the characteristics of different types of planar interconnects and present design equations and strategies that enable the physical parameters to be derived from the electrical specifications. These are backed up with results from EM simulations that demonstrate the applicability of the design formulas.

## References

- [1] H. B. Bakoglu, Circuits, *Interconnections and Packaging for VLSI*. Addison-Wesley Publishing Co., 1990.
- [2] D. A. Doane and P. D. Franzon, *Multichip Module Technologies and Alternatives: The Basics*. Van Nostrand Reinhold, 1993.
- [3] C. A. Harper, *Electronic Packaging & Interconnection Handbook*. McGraw-Hill Inc., 1997.

[4] O. Heaviside, Electromagnetic induction and its propagation, *Electrician*, Jun. 1887.

<sup>1</sup> This is derived from a set of physical principles called Maxwell's equations; there is no underlying theory for these, but they have been verified by numerous experiments.

# Chapter 3

## Microwave Network Analysis

### 3.1 Introduction

At microwave frequencies voltage reflection and transmission coefficients can be quite readily measured and are related to power flow. In addition, in RF and microwave circuit design the power of signals and noise is always of interest. Thus there is a predisposition to focus on measurement parameters that are related to the reflection and transmission of power.

Scattering parameters,  $S$  parameters, embody the effects of reflection and transmission. As will be seen, it is easy to convert these to more familiar network parameters such as admittance and impedance parameters. In this chapter  $S$  parameters will be defined and related to impedance and admittance parameters, then it will be demonstrated that the use of  $S$  parameters helps in the design and interpretation of RF circuits.  $S$  parameters have become the most important parameters for RF and microwave engineers, and many design methodologies have been developed around them.

### 3.2 Two-port Networks

With transmission lines (and circuit elements that utilize distributed effects) for each signal current there is a signal return current. Thus at microwave frequencies ports are used, as shown in [Figure 3.1\(a\)](#), which define the port voltages and port currents for a two-port network, or just two-port. The network in [Figure 3.1\(a\)](#) has four terminals and two ports. A port voltage is defined as the voltage difference between a pair of terminals with one of the terminals in the pair becoming the local reference terminal. The current entering the network at the top terminal of Port 1 is  $I_1$  and there is an equal current leaving the reference terminal. This arrangement clearly makes sense when transmission lines are attached to Ports 1 and 2, as in [Figure 3.1\(b\)](#). With transmission lines at Ports 1 and 2 there will be traveling-wave voltages, and at the ports the traveling-wave components add to give the total port voltage. In dealing with nondistributed circuits it is preferable to use the total port voltages and currents,  $V_1$ ,  $I_1$ ,  $V_2$ , and  $I_2$ , shown in [Figure 3.1\(a\)](#). However, with distributed elements it is preferable to deal with traveling voltages and currents,  $V_1^+$ ,  $V_1^-$ ,  $V_2^+$ , and  $V_2^-$ , shown in [Figure 3.1\(b\)](#), with  $V_1 = V_1^+ + V_1^-$  and  $V_2 = V_2^+ + V_2^-$ . RF and microwave design necessarily requires switching between the two forms.

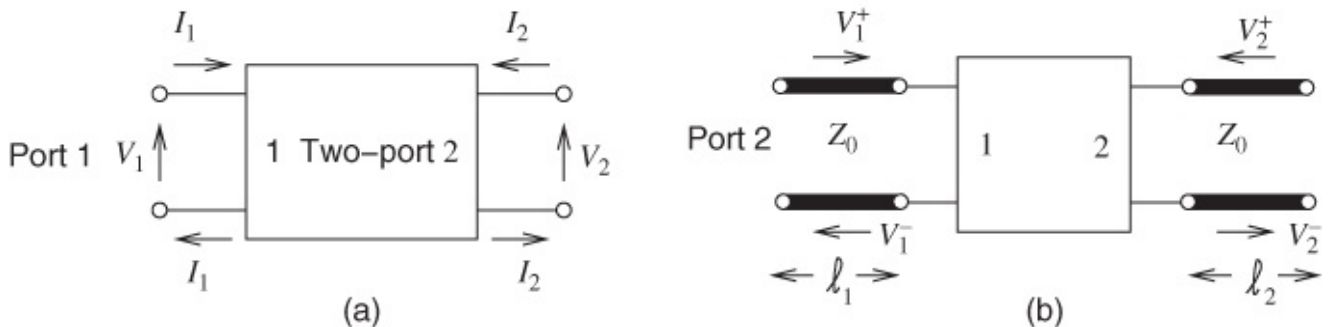


**Figure 3.1** A two-port network: (a) port voltages; and (b) with transmission lines at the ports.

### 3.2.1 Reciprocity, Symmetry, Passivity, and Linearity

A network is linear if the response (voltages and currents) is linearly dependent on the drive level and superposition also applies. So if the two-port shown in [Figure 3.1\(a\)](#) is linear, the currents  $I_1$  and  $I_2$  are linear functions of  $V_1$  and  $V_2$ . An example of a linear network would be one with resistors and capacitors. A network with a diode would be an example of a nonlinear network. A passive network has no internal sources of power and so a network with an embedded battery is not a passive network. A symmetrical two-port has the same characteristics at each of the ports. An example of a symmetrical network is a transmission line with a uniform cross-section.

Finally, a reciprocal two-port has a response at Port 2 from an excitation at Port 1 that is the same as the response at Port 1 to the same excitation at Port 2. As an example, consider the two-port in [Figure 3.1\(a\)](#). If the network is reciprocal, then the ratio  $I_2/V_1$  with  $V_2 = 0$  will be the same as the ratio  $I_1/V_2$  with  $V_1 = 0$ . Networks with resistors, capacitors, and transmission lines, for example, are reciprocal. A transistor amplifier is not reciprocal, as gain, analogous to the ratio  $V_2/V_1$ , is just in one direction (or unidirectional).

### 3.2.2 Two-ports and Voltage and Current

First, port-based impedance parameters will be considered based on total port voltages and currents as defined for the two-port in [Figure 3.1](#). These parameters are also referred to as port impedance parameters or just impedance parameters when the context is understood to be ports. Impedance parameters, or  $z$  parameters, are defined as

$$V_1 = z_{11}I_1 + z_{12}I_2 \quad 3.1$$

$$V_2 = z_{21}I_1 + z_{22}I_2, \quad 3.2$$

or in matrix form as

$$\mathbf{V} = \mathbf{Z}\mathbf{I}. \quad 3.3$$

The double subscript on a parameter is ordered so that the first refers to the output and the second refers to the input, so  $z_{ij}$  relates the voltage output at Port  $i$  to the current input at Port  $j$ . If the network is reciprocal, then  $z_{12} = z_{21}$ , but this simple type of relationship does not apply

to all network parameters. The reciprocal circuit equivalence of the  $z$  parameters is shown in [Figure 3.2\(a\)](#). It will be seen that the  $z$  parameters are convenient parameters to use when an element is in series with one of the ports, as then the operation required in developing the  $z$  parameters of the larger network is just addition.

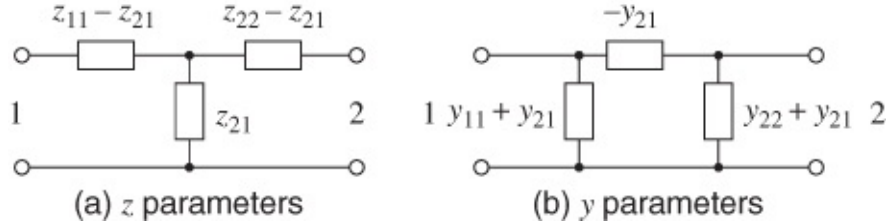


[Figure 3.2](#) Circuit equivalence of the  $z$  and  $y$  parameters for a reciprocal network: (a)  $z$  parameters; and (b)  $y$  parameters (in (b) the elements are admittances).

When an element is in shunt with a two-port, admittance parameters, or  $y$  parameters, are the most convenient to use. These are defined as

$$I_1 = y_{11}V_1 + y_{12}V_2 \quad 3.4$$

$$I_2 = y_{21}V_1 + y_{22}V_2, \quad 3.5$$

or in matrix form as

$$\mathbf{I} = \mathbf{Y}\mathbf{V}. \quad 3.6$$

Now, for reciprocity,  $y_{12} = y_{21}$  and the circuit equivalence of the  $y$  parameters is shown in [Figure 3.2\(b\)](#).

The choice of which network parameters to use depends on convenience, but as will be seen throughout this text, some parameters naturally describe a particular characteristic desired in a design. In this book the situation of most interest is the cascade connection of two-ports. To combine these and obtain the overall two-port parameters of a cascade it is most convenient to use  $ABCD$  parameters.

### 3.2.3 $ABCD$ Matrix Description of Two-port Networks

$ABCD$  parameters are used when cascading two-ports, working with transmission line systems, as in [Figure 3.3](#), and when total voltage and current relationships are required. The most significant use of  $ABCD$  parameters in microwave design is in equating circuits with lumped elements to circuits with transmission lines.

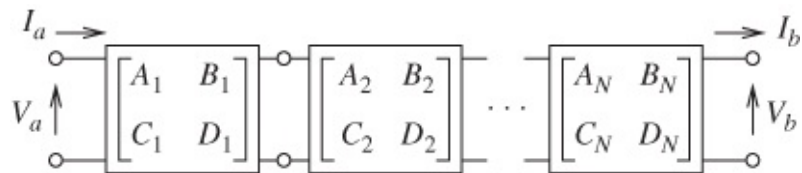


[Figure 3.3](#) Cascade of two-port networks.

First, consider [Figure 3.4](#), which puts the voltages and currents in cascadable form so that

$$\begin{bmatrix} V_a \\ I_a \end{bmatrix} = \begin{bmatrix} A & B \\ C & D \end{bmatrix} \begin{bmatrix} V_b \\ I_b \end{bmatrix}. \quad 3.7$$

The reciprocity relationship of the  $ABCD$  parameters is not as simple as for the  $z$  and  $y$  parameters. To see this, first express the  $ABCD$  parameters in terms of  $z$  parameters. Now, referring to [Figure 3.1\(a\)](#),

$$\begin{aligned} V_a &= V_1 & I_a &= I_1 \\ V_b &= V_2 & I_b &= -I_2 \end{aligned} \quad 3.8$$

$$V_a = z_{11}I_a - z_{12}I_b \quad 3.9$$

$$V_b = z_{21}I_a - z_{22}I_b. \quad 3.10$$

From Equation (3.10),

$$I_a = \frac{z_{22}}{z_{21}}I_b + \frac{1}{z_{21}}V_b, \quad 3.11$$

and after substituting this into Equation (3.9)

$$V_a = \frac{z_{11}}{z_{21}}V_b + \left( z_{11}\frac{z_{22}}{z_{21}} - z_{12} \right) I_b. \quad 3.12$$

Comparing Equations (3.7), (3.11), and (3.12) leads to

$$\begin{aligned} A &= z_{11}/z_{21} & B &= \Delta_z/z_{21} \\ C &= 1/z_{21} & D &= z_{22}/z_{21}, \end{aligned} \quad 3.13$$

where

$$\Delta_z = z_{11}z_{22} - z_{12}z_{21}. \quad 3.14$$

Rearranging,

$$\begin{aligned} z_{11} &= A/C & z_{12} &= (AD - BC)/C \\ z_{21} &= 1/C & z_{22} &= D/C. \end{aligned} \quad 3.15$$

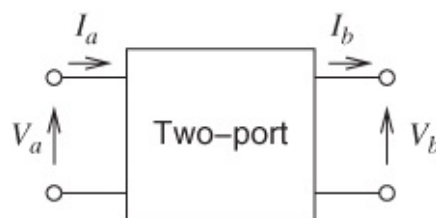


[Figure 3.4](#) Two-port network with cascadable voltage and current definitions.

For  $z$  parameters,  $z_{12} = z_{21}$  for reciprocity, that is, from Equation (3.15), for a reciprocal

network,

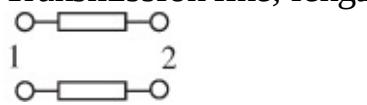
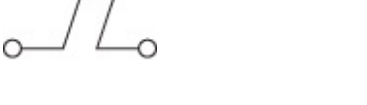
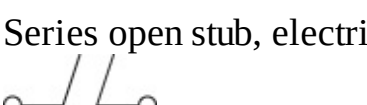
$$\frac{AD - BC}{C} = \frac{1}{C}. \quad 3.16$$

Thus for a two-port network to be reciprocal,  $AD - BC = 1$ . The  $ABCD$  matrix of the cascade connection of  $N$  two-ports in [Figure 3.3](#) is equal to the product of the  $ABCD$  matrices of the individual two-ports:

$$\begin{bmatrix} A & B \\ C & D \end{bmatrix} = \begin{bmatrix} A_1 & B_1 \\ C_1 & D_1 \end{bmatrix} \begin{bmatrix} A_2 & B_2 \\ C_2 & D_2 \end{bmatrix} \dots \begin{bmatrix} A_N & B_N \\ C_N & D_N \end{bmatrix}. \quad 3.17$$

[Table 3.1](#) gives the  $ABCD$  parameters of several two-port networks.

**Table 3.1**  $ABCD$  parameters of a transmission line and of several stubs configured as two-ports. The transmission lines are lossless with a propagation constant of  $\beta$  ( $\beta\ell$  and  $\theta$  are electrical lengths of transmission lines in radians)

 Transmission line, length $\ell$ , $Z_0 = 1/Y_0$	$A = \cos(\beta\ell) \quad B = jZ_0 \sin(\beta\ell)$ $C = jY_0 \sin(\beta\ell) \quad D = \cos(\beta\ell)$
 Series shorted stub, electrical length $\theta$	$A = 1 \quad B = jZ_0 \tan \theta$ $C = 0 \quad D = 1$
 Series open stub, electrical length $\theta$	$A = 1 \quad B = -jZ_0 / (\tan \theta)$ $C = 0 \quad D = 1$
 Shunt shorted stub, electrical length $\theta$	$A = 1 \quad B = 0$ $C = -j / (Z_0 \tan \theta) \quad D = 1$
 Shunt open stub, electrical length $\theta$	$A = 1 \quad B = 0$ $C = j \tan \theta / Z_0 \quad D = 1$

## 3.3 Scattering Parameter Theory

### 3.3.1 Introduction

Characterization and design at frequencies ranging from audio to some hundreds of megahertz proceeds on the basis of admittances, impedances and dimensionless factors. Above a few hundred megahertz it is neither practical nor meaningful to measure voltage, current or impedance, at least not in any direct manner. It is important to appreciate that the circuits are distributed, and so are the voltages and currents. On the other hand, useful quantities such as *voltage reflection coefficient* and *microwave power* can be quite readily measured. A significant set of parameters known as scattering parameters, or more briefly *S* parameters, embody the effects of reflection or through transmission of power for any network. It matters not whether the network is passive or active, nor whether it comprises one port or one hundred ports; scattering parameters remain very convenient to use but, as will be seen, it is easy to convert these to more familiar network parameters.

In order to see why a new parameter set is highly desirable, we first review the more ‘conventional’ sets of parameters.

### 3.3.2 Network Parameters

It is well known that several parameter sets are available for the characterization of a two-port network (i.e., a four-terminal network), as illustrated in [Figure 3.5](#). In an *N*-port network there are  $2N$  terminals as each port has two terminals, with one of the terminals used as a reference. Although each parameter, in any set, should strictly be written as a function of complex frequency *s* (or at least as a function of the operator  $j\omega$ ), this fact is generally left understood. For example, in admittance parameters,  $y_{11}$  really means  $y_{11}(s)$  or  $y_{11}(j\omega)$ .

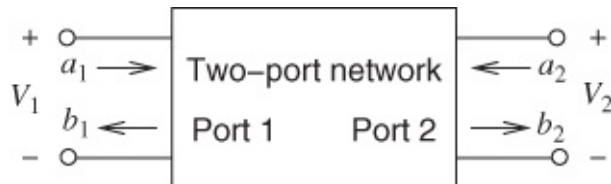


[Figure 3.5](#) A two-port network.

Recall the various network parameters that have already been introduced and the way they describe the terminal characteristics of a two-port network.

Impedance parameters or *z* parameters:

$$\begin{aligned} V_1 &= z_{11}I_1 + z_{12}I_2 \\ V_2 &= z_{21}I_1 + z_{22}I_2 \end{aligned} \quad 3.18$$

Admittance parameters or *y* parameters:

$$\begin{aligned} I_1 &= y_{11}V_1 + y_{12}V_2 \\ I_2 &= y_{21}V_1 + y_{22}V_2 \end{aligned} \quad 3.19$$

Chain parameters or *ABCD* parameters:

$$\left. \begin{aligned} V_1 &= AV_2 - BI_2 \\ I_1 &= CV_2 - DI_2 \end{aligned} \right\}. \quad 3.20$$

All the parameters are interrelated (any set of  $N$ -port parameters can be exactly related to any other set), and the relationships are given in matrix notation in [Table 3.2](#).

**Table 3.2** Two-port  $S$  parameter conversion chart. The  $Z$  and  $Y$  parameters are normalized to  $Z_0$ .  $Z'$  and  $Y'$  are the actual parameters

$S$	In terms of $S$		
$z$	$Z'_{11} = z_{11}Z_0$	$Z'_{12} = z_{12}Z_0$	$Z'_{21} = z_{21}Z_0$
			$Z'_{22} = z_{22}Z_0$
$\delta_z = (1 + z_{11})(1 + z_{22}) - z_{12}z_{21}$		$\delta_S = (1 - S_{11})(1 - S_{22}) - S_{12}S_{21}$	
$S_{11} = [(z_{11} - 1)(z_{22} + 1) - z_{12}z_{21}] / \delta_z$		$z_{11} = [(1 + S_{11})(1 - S_{22}) + S_{12}S_{21}] / \delta_S$	
$S_{12} = 2z_{12} / \delta_z$		$z_{12} = 2S_{12} / \delta_S$	
$S_{21} = 2z_{21} / \delta_z$		$z_{21} = 2S_{21} / \delta_S$	
$S_{22} = [(z_{11} + 1)(z_{22} - 1) - z_{12}z_{21}] / \delta_z$		$z_{22} = [(1 - S_{11})(1 + S_{22}) + S_{12}S_{21}] / \delta_S$	
$y$	$Y'_{11} = y_{11}/Z_0$	$Y'_{12} = y_{12}/Z_0$	$Y'_{21} = y_{21}/Z_0$
			$Y'_{22} = y_{22}/Z_0$
$\delta_y = (1 + y_{11})(1 + y_{22}) - y_{12}y_{21}$		$\delta_S = (1 + S_{11})(1 + S_{22}) - S_{12}S_{21}$	
$S_{11} = [(1 - y_{11})(1 + y_{22}) + y_{12}y_{21}] / \delta_y$		$y_{11} = [(1 - S_{11})(1 + S_{22}) + S_{12}S_{21}] / \delta_S$	
$S_{12} = -2y_{12} / \delta_y$		$y_{12} = -2S_{12} / \delta_S$	
$S_{21} = -2y_{21} / \delta_y$		$y_{21} = -2S_{21} / \delta_S$	
$S_{22} = [(1 + y_{11})(1 - y_{22}) + y_{12}y_{21}] / \delta_y$		$y_{22} = [(1 + S_{11})(1 - S_{22}) + S_{12}S_{21}] / \delta_S$	

Each parameter, in every set of parameters, is sensitive to change in frequency, bias conditions, or temperature (especially for active devices), and this important fact must always be remembered. For design at higher frequencies, especially beyond a few hundred megahertz,  $y$  parameters become less useful and a new concept is required. There are two principal reasons for this:

1. The difficulty in realizing accurate, well-defined, broadband short circuits as required for  $y$  parameters.
2. The considerable chance that the device or amplifier may become unstable and oscillate under short-circuit test.

As has been discussed, the direct measurement of  $S$  parameters is the preferred approach above a few hundred megahertz but one that can be used even down to a few hundred kilohertz. The only hurdle inhibiting most people adopting them for every situation is that they are defined in terms of traveling wave voltages and not total (conventional) voltages and currents, as are the other parameters considered above. As will be seen,  $S$  parameters are particularly convenient to use in characterizing interconnects as they naturally relate to signals entering a line at one end and appearing at the other.

### 3.3.3 Normalized Scattering Parameters

It will already be well known that the reflection coefficient of a one-port network can quite easily be measured. This quantity ( $\Gamma$ ) is simply related to the load impedance ( $Z_L$ ) of such a one-port:

$$\Gamma = \frac{Z_L - Z_0}{Z_L + Z_0} \quad 3.21$$

where  $Z_0$  is the characteristic impedance of the connecting transmission line. When a network is more complicated, that is, one consisting of two or more ports, then quantities beyond reflection coefficients are required to fully characterize its behaviour. We will be able to make considerable use of two-port networks and these may well include active (i.e., amplifying) elements. One basic way of identifying four parameters is suggested in [Figure 3.6](#). Here  $\Gamma_{in}$  and  $\Gamma_{out}$  are, respectively, the input and output port reflection coefficients,  $\mu_F$  is a forward transmission parameter and  $\mu_R$  is a reverse transmission parameter. These four ‘parameters’ have only been mentioned in passing at this stage. They have not been properly defined and are not in the notation used for  $S$  parameters.

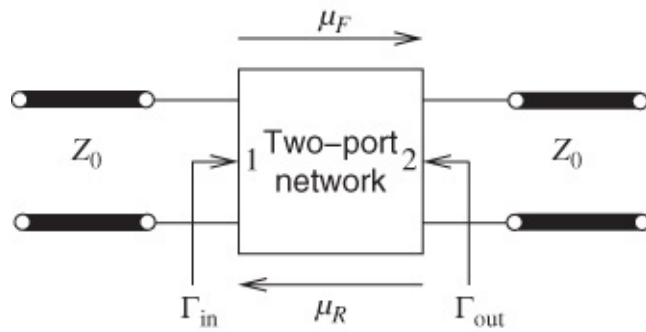


[Figure 3.6](#) A two-port network with input and output reference transmission lines.

It was previously mentioned that power is another quantity that can be directly measured at microwave frequencies. The  $S$  parameters will lead explicitly to power relationships (such as interconnect power transmission loss) and, conceptually, these  $S$  parameters are based on the incident and reflected proportions of power around the network. More precisely, quantities having the dimensions ‘square-root’ of ‘power’ are considered and are generally referred to as waves. A transmission parameter (or transfer parameter) through a circuit or a junction is a relative measure of the amplitude and phase of the transmitted wave as compared with the amplitude and phase of the incident wave. In other words, the directly measurable quantities are the amplitudes and phase angles of the waves reflected, or scattered, from a junction or port relative to the incident wave amplitudes and phase angles. In view of the linearity of the field equations for interconnects and a variety of important microwave devices, the scattered-wave amplitudes are linearly related to the incident wave amplitudes. The matrix describing this linear relationship is called the scattering matrix.

Scattering matrices are therefore particularly significant and useful in a high-speed transmission environment. Impedance as such cannot, however, be discarded, since the characteristic impedance  $Z_0$  of the transmission lines will be vitally and inextricably involved with the elements of these scattering matrices.

A basic treatment, applicable to circuits where the characteristic impedance is real and positive, is given here. Furthermore, if the reference characteristic impedance is real and the same at each port, the scattering parameters are called normalized scattering parameters. When the reference impedances at each port are different or the reference impedance is complex, the scattering parameters are called generalized scattering parameters. Generalized scattering parameters should only be used when there is a particular utility as the range of analysis tools that can be used is much less than if the normalized scattering parameters are used.

### 3.3.4 Scattering Parameters for a Two-port Network

Linear RF and microwave networks can be readily characterized in terms of their scattering or  $S$  parameters.  $S$  parameters are therefore very important and worthy of detailed examination. [Figure 3.7](#) shows a two-port network connected to a load  $Z_L$  by means of a length of transmission line and fed from a source with impedance  $Z_S$ .  $Z_S$  is also connected by means of a length of transmission line. The transmission line serves to separate forward- and backward-traveling waves. They can also be vanishingly short without affecting the following discussion.

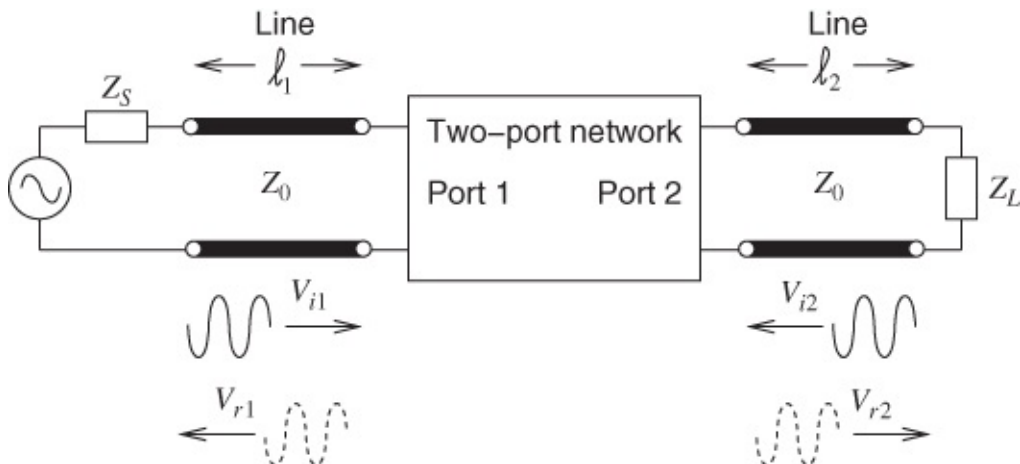


[Figure 3.7](#) A two-port network showing forward- and backward-traveling waves on the reference transmission lines.

The reference transmission lines will here be assumed to have identical characteristic impedances  $Z_0$ . ( $S$  parameters are still defined if the reference impedances are different.) The equivalent voltages  $V_{in}$  are incident voltage waves traveling along the transmission line towards port  $n$ , and the equivalent voltages  $V_m$  are reflected voltage waves traveling along the transmission line away from port  $n$  ( $n = 1, 2$ ).

Since each reflected wave must be a linear combination of both a port 1 incident term and a port 2 incident term we have:

$$V_{r1} = x_{11}V_{i1} + x_{12}V_{i2} \quad 3.22$$

$$V_{r2} = x_{21}V_{i1} + x_{22}V_{i2} \quad 3.23$$

provided  $Z_0$  is real. Where  $x_{nm}$  depends on the precise characteristics of the network. We do not need to dwell upon the precise nature of these  $x_{nm}$  coefficients.

Now the incident power wave traveling along the transmission line towards port 1 has a value given by

$$P_{il} = \frac{1}{2} \frac{|V_{il}|^2}{Z_0} \quad 3.24$$

The square root of this power, conventionally given the symbol  $a$ , is simply related to the incident voltage  $V_{il}$  by

$$|a_1| = \sqrt{2P_{il}} \quad \text{as} \quad a_1 = V_{il}/\sqrt{Z_0}. \quad 3.25$$

Similar arguments apply to the waves reflected from port 1, and incident on and reflected from port 2 to yield:

$$b_1 = V_{r1}/\sqrt{Z_0} \quad a_2 = V_{i2}/\sqrt{Z_0} \quad b_2 = V_{r2}/\sqrt{Z_0}.$$

When both sides of both Equations (3.22) and (3.23) are divided through by  $\sqrt{Z_0}$  the variables automatically become  $a_n$  and  $b_n$ , and the coefficients are then called the scattering parameters.

The expressions can then be written:

$$b_1 = S_{11}a_1 + S_{12}a_2 \quad 3.26$$

$$b_2 = S_{21}a_1 + S_{22}a_2. \quad 3.27$$

In matrix form:

$$\mathbf{b} = \mathbf{S}\mathbf{a}. \quad 3.28$$

As a reminder, it has to be appreciated that:

$$|a| = \sqrt{2(\text{incident power})} \quad \text{and} \quad |b| = \sqrt{2(\text{reflected power})}.$$

Note that  $a$  and  $b$  also have phase. The network diagram may now be redrawn, with these root power variables and scattering parameters included, and the result is [Figure 3.8](#). Using this diagram, and Equations (3.26) and (3.27), the following definitions can be established.

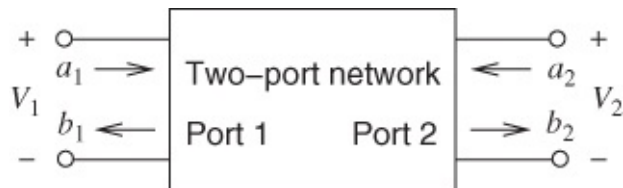


[Figure 3.8](#) Two-port network with root power variables.

### 3.3.5 Definitions of Two-port $S$ Parameters

$S_{11}$ : If the output line is matched,  $Z_L = Z_0$ , the load cannot reflect power,  $a_2 = 0$ , and

Equation (3.26) then yields 3.29  $S_{11} = \frac{b_1}{a_1} \Big|_{a_2=0}$ .

By alternately matching the input and output the remaining three parameters are defined as follows:

$$S_{22}: 3.30 \quad S_{22} = \frac{b_2}{a_2} \Big|_{a_1=0}$$

$$S_{21}: 3.31 \quad S_{21} = \frac{b_2}{a_1} \Big|_{a_2=0}$$

$$S_{12}: 3.32 \quad S_{12} = \frac{b_1}{a_2} \Big|_{a_1=0}.$$

Under these definitions, specific physical meanings can be ascribed to the  $S$  parameters as follows:

$S_{11}$  is the input reflection coefficient (i.e.,  $\Gamma_1$ ) when the output is matched.

$S_{22}$  is the output reflection coefficient (i.e.,  $\Gamma_2$ ) when the input is matched.

$S_{21}$  is the forward transfer (or ‘transmission’) coefficient with the output matched. ( $S_{21}$  directly describes the characteristics of a filter, indicates the loss of an interconnect, and indicates the gain of an amplifier.)

$S_{12}$  is the reverse transfer (or transmission) coefficient with the input matched. ( $S_{12}$  becomes particularly important in amplifier stability considerations.) For an interconnect  $S_{12} = S_{21}$ , indicating that the interconnect is reciprocal.

One of the more important things to note is that to measure the  $S$  parameters it is necessary to use terminations that absorb all of the power delivered to them so that  $a_1 = 0$  and  $a_2 = 0$ . At RF and microwave frequencies this is much easier to achieve than either short or open-circuits.

Whereas  $S_{21}$  and  $S_{12}$  may be complicated functions of network characteristics, the reflection coefficient parameters  $S_{11}$  and  $S_{22}$  are readily expressed in terms of driving-point impedances. It is already known that the reflection coefficient  $\Gamma$  for an impedance  $Z$  loading a transmission line is

$$\Gamma = \frac{Z - Z_0}{Z + Z_0}. \quad 3.33$$

Therefore

$$S_{11} = \frac{Z_{11} - Z_0}{Z_{11} + Z_0} \quad 3.34$$

and

$$S_{22} = \frac{Z_{22} - Z_0}{Z_{22} + Z_0} \quad 3.35$$

where  $Z_{11}$  and  $Z_{22}$  are, respectively, the input and output driving-point impedances for the two-port network when the appropriate opposite port is matched.

The scattering parameters are small-signal quantities and therefore to remain consistent with the other small-signal parameters a lower-case  $s$  should strictly be used. However, we have retained the conventional upper-case  $S$  here.

Also, it is understood that each parameter is (like any small-signal parameter) a function of frequency, bias conditions and temperature. The strict frequency function  $S(j\omega)$  is left understood and just  $S$  is used.

### 3.3.6 Evaluation of Scattering Parameters

A simple example of a shunt susceptive element is used to illustrate this (see [Figure 3.9](#)). To find  $S_{11}$  assume that the output side is matched so that  $a_2 = 0$ . The reflection coefficient on the input side is then:

$$S_{11} = \frac{Y_0 - Y_{in}}{Y_0 + Y_{in}}. \quad 3.36$$

However, in this case  $Y_{in} = Y_0 + jB$  because the (matched) output line shunts the susceptance  $jB$ , therefore:

$$S_{11} = \frac{Y_0 - Y_0 - jB}{2Y_0 + jB} = \frac{-jB}{2Y_0 + jB} \quad 3.37$$

From symmetry considerations it is clear that:

$$S_{22} = S_{11}. \quad 3.38$$

Next,  $S_{12}$  can be evaluated by finding the transmitted ‘voltage’  $b_2$  (i.e.,  $\sqrt{\text{power}}$ ) with the output line matched. This is the  $a_2 = 0$  condition. For a pure shunt one-port element we must have  $b_2 = S_{21}a_1$  (see also [Equation \(3.31\)](#) here). We can combine expressions to obtain

$$\begin{aligned} b_2 &= a_1 + b_1 \\ &= a_1(1 + S_{11}). \end{aligned} \quad 3.39$$

Since with this matched load situation  $a_2 = 0$ , we also have

$$S_{21} = 1 + S_{11} = S_{12} \quad 3.40$$

and we have already found  $S_{11}$  as [Equation \(3.37\)](#). Therefore, after substituting and clearing we obtain:

$$S_{12} = \frac{2Y_0}{2Y_0 + jB}. \quad 3.41$$

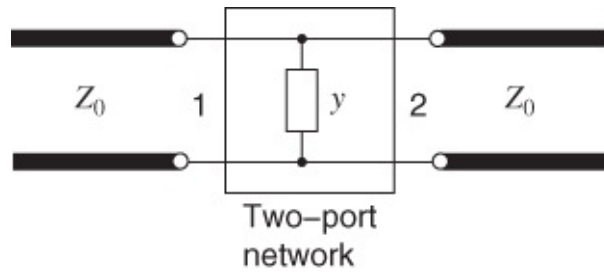


**Figure 3.9** A shunt susceptance element with admittance  $y = jB$ .

### 3.3.7 Multiport $S$ Parameters

The simple two-port scattering matrix extends naturally to cover multiport situations. An  $N$ -port network is shown in [Figure 3.10](#). The scattering matrix for this becomes:

$$\begin{bmatrix} b_1 \\ b_2 \\ \vdots \\ b_N \end{bmatrix} = \begin{bmatrix} S_{11} & S_{12} & S_{13} & \dots & S_{1N} \\ S_{21} & S_{22} & S_{23} & \dots & S_{2N} \\ \vdots & \vdots & \vdots & \ddots & \vdots \\ S_{N1} & S_{N2} & S_{N3} & \dots & S_{NN} \end{bmatrix} \begin{bmatrix} a_1 \\ a_2 \\ \vdots \\ a_N \end{bmatrix} \quad 3.42$$

$$[b] = [S][a] \quad 3.43$$

or, more briefly and concisely,

$$\mathbf{b} = \mathbf{Sa}. \quad 3.44$$

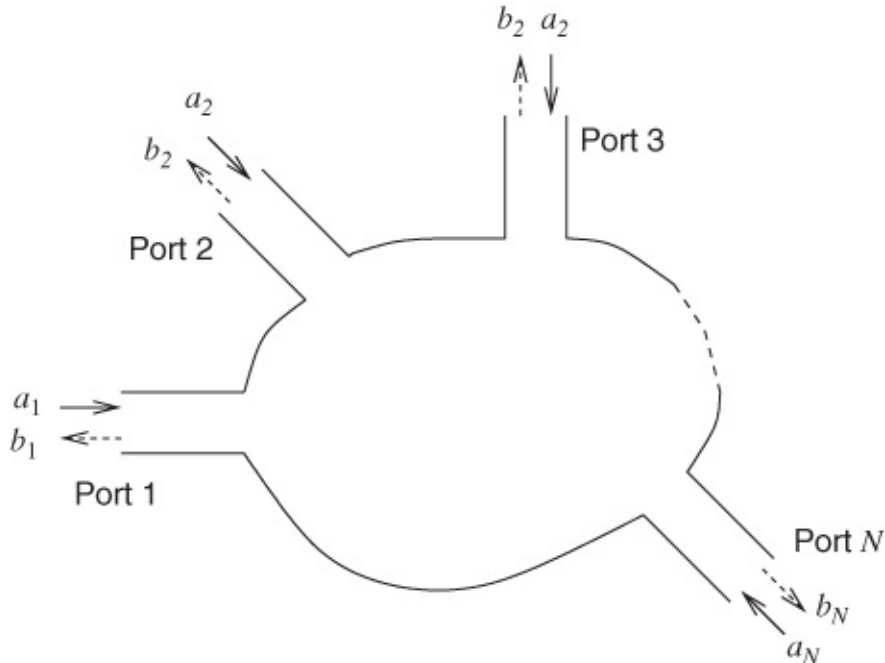


**Figure 3.10** An  $N$ -port network.

In [Section 18.3.1](#) the unitary conditions, Equations (18.6)–(18.9), will be developed for a lossless two-port network. A similar development for a lossless multiport yields the unitary condition for a multiport [1]:

$$\mathbf{S}\mathbf{S}^* = \mathbf{I}$$

3.45

where  $\mathbf{S}^*$  is the complex conjugate transpose of  $\mathbf{S}$ .

### 3.3.8 Three-port $S$ Parameters

Usually when networks are designed an attempt is made to match the ports of the network so that there is no reflection. That is, it is desirable to design so that  $S_{ii} = 0$  where  $i$  is the port index. In this section it is shown that this is not possible for a lossless reciprocal three-port network. (Procedures for extracting the three-port parameters from two-port  $S$ -parameter measurements are described in [2, 3].)

The development first begins by assuming that the three ports of the three-port network are matched. It is then seen that this violates the unitary condition for a lossless network. We start by noting the complete three-port scattering matrix:

$$\mathbf{S} = \begin{bmatrix} S_{11} & S_{12} & S_{13} \\ S_{21} & S_{22} & S_{23} \\ S_{31} & S_{32} & S_{33} \end{bmatrix}. \quad 3.46$$

If the junction can be matched then we have

$$S_{11} = S_{22} = S_{33} = 0. \quad 3.47$$

Also, for reciprocity,

$$S_{21} = S_{12}, \quad S_{31} = S_{13}, \quad \text{and} \quad S_{32} = S_{23}. \quad 3.48$$

Substituting the conditions described by Equations (3.47) and (3.48) into Equations (3.44) and (3.46) we obtain:

$$\mathbf{S} = \begin{bmatrix} 0 & S_{12} & S_{13} \\ S_{12} & 0 & S_{23} \\ S_{13} & S_{23} & 0 \end{bmatrix}. \quad 3.49$$

The conditions described in [Section 3.3.8](#) are also demanded for this lossless three-port junction. They may be expressed as

$$\sum_{n=1}^3 |S_{mn}|^2 = 1 \quad 3.50$$

for  $m = 1, 2, 3$ , and

$$\sum_{n=1}^3 S_{ln} S_{mn}^* = 0 \quad 3.51$$

for  $l, m = 1, 2, 3$ . Equations (3.50) and (3.51) can be conveniently combined into the unitary scattering matrix equation:

$$\mathbf{S}\mathbf{S}^* = \begin{bmatrix} S_{11} & S_{12} & S_{13} \\ S_{21} & S_{22} & S_{23} \\ S_{31} & S_{32} & S_{33} \end{bmatrix} \begin{bmatrix} S_{11}^* & S_{21}^* & S_{31}^* \\ S_{12}^* & S_{22}^* & S_{32}^* \\ S_{13}^* & S_{23}^* & S_{33}^* \end{bmatrix} = \begin{bmatrix} 1 & 0 & 0 \\ 0 & 1 & 0 \\ 0 & 0 & 1 \end{bmatrix}. \quad 3.52$$

For a reciprocal matched lossless three-port network the unitary condition becomes

$$\mathbf{S}\mathbf{S}^* = \begin{bmatrix} 0 & S_{12} & S_{13} \\ S_{12} & 0 & S_{23} \\ S_{13} & S_{23} & 0 \end{bmatrix} \begin{bmatrix} 0 & S_{12}^* & S_{13}^* \\ S_{12}^* & 0 & S_{23}^* \\ S_{13}^* & S_{23}^* & 0 \end{bmatrix} = \begin{bmatrix} 1 & 0 & 0 \\ 0 & 1 & 0 \\ 0 & 0 & 1 \end{bmatrix}. \quad 3.53$$

Note that only six terms are involved here, and expanding the unitary matrix yields

$$S_{12}S_{12}^* + S_{13}S_{13}^* = 1 \quad 3.54$$

$$S_{12}S_{12}^* + S_{23}S_{23}^* = 1 \quad 3.55$$

$$S_{13}S_{13}^* + S_{23}S_{23}^* = 1. \quad 3.56$$

We also have

$$S_{13}S_{23}^* = 0 \quad 3.57$$

$$S_{12}S_{13}^* = 0 \quad 3.58$$

$$S_{12}S_{23}^* = 0. \quad 3.59$$

To satisfy Equations (3.57)–(3.59) we must have:

$$S_{13} = 0 \quad \text{or} \quad S_{23} = 0 \quad \text{or} \quad S_{12} = 0. \quad 3.60$$

If we initially suppose that  $S_{12} = 0$ , then Equation (3.54) gives:

$$S_{13}S_{13}^* = 1$$

and Equation (3.55) gives

$$S_{23}S_{23}^* = 1$$

hence

$$S_{13}S_{13}^* + S_{23}S_{23}^* = 2.$$

This directly contradicts the necessary result expressed as Equation (3.56), being double the required quantity, and thus an intolerable inconsistency exists. We therefore conclude that a lossless, reciprocal three-port junction cannot be simultaneously matched at all three ports.

Such a result indicates a fundamental limit of what can be achieved and realistically indicates what can be achieved. An example is the design of a transmission line T where one

transmission line drives two other transmission lines. Ideally the inputs of each of the three transmission lines would be reflection-less but this cannot be achieved.

### 3.3.9 Cascaded Two-port Networks

Two two-port networks in cascade are shown in [Figure 3.11](#). Here  $(A)$  and  $(B)$  are used as superscripts to distinguish the parameters of each two-port network, but the subscripts  $A$  and  $B$  are used for matrix quantities. Since (for a real reference impedance)

$$a_2^{(A)} = b_1^{(B)} \quad \text{and} \quad b_2^{(A)} = a_1^{(B)}, \quad 3.61$$

it is convenient to put the  $a$  and  $b$  parameters in cascadable form, leading to the following two-port representation:

$$\begin{bmatrix} a_1 \\ b_1 \end{bmatrix} = \begin{bmatrix} T_{11} & T_{12} \\ T_{21} & T_{22} \end{bmatrix} \begin{bmatrix} b_2 \\ a_2 \end{bmatrix}, \quad 3.62$$

where the  $T$  matrix or chain scattering matrix is

$$\mathbf{T} = \begin{bmatrix} T_{11} & T_{12} \\ T_{21} & T_{22} \end{bmatrix}. \quad 3.63$$

This is related to the  $S$  parameters of the two-port by

$$\mathbf{T} = \begin{bmatrix} S_{21}^{-1} & -S_{21}^{-1}S_{22} \\ S_{21}^{-1}S_{11} & S_{12} - S_{11}S_{21}^{-1}S_{22} \end{bmatrix} \quad 3.64$$

and

$$\mathbf{S} = \begin{bmatrix} T_{21}T_{11}^{-1} & T_{22} - T_{21}T_{11}^{-1}T_{12} \\ T_{11}^{-1} & -T_{11}^{-1}T_{12} \end{bmatrix}. \quad 3.65$$

For a two-port network, using Equations [\(3.61\)](#) and [\(3.62\)](#),

$$\begin{bmatrix} a_1^{(A)} \\ b_1^{(A)} \end{bmatrix} = \mathbf{T}_A \begin{bmatrix} b_2^{(A)} \\ a_2^{(A)} \end{bmatrix} \quad \text{and} \quad \begin{bmatrix} a_2^{(B)} \\ b_2^{(B)} \end{bmatrix} = \mathbf{T}_B \begin{bmatrix} b_2^{(B)} \\ a_2^{(B)} \end{bmatrix}, \quad 3.66$$

thus

$$\begin{bmatrix} a_1^{(A)} \\ b_1^{(A)} \end{bmatrix} = \mathbf{T}_A \mathbf{T}_B \begin{bmatrix} b_2^{(B)} \\ a_2^{(B)} \end{bmatrix}. \quad 3.67$$

For  $n$  cascaded two-port networks, Equation [\(3.67\)](#) generalizes to

$$\begin{bmatrix} a_1^{(1)} \\ b_1^{(1)} \end{bmatrix} = \mathbf{T}_1 \mathbf{T}_2 \dots \mathbf{T}_n \begin{bmatrix} b_2^{(n)} \\ a_2^{(n)} \end{bmatrix}, \quad 3.68$$

and so the  $\mathbf{T}$  matrix of the cascaded network is the matrix product of the  $\mathbf{T}$  matrices of the individual two-ports. Two aspects are important here:

- a.** The matrices must be multiplied in the proper order (matrix multiplication is not commutative).
- b.** The proper order to use is that in which the networks are actually connected.

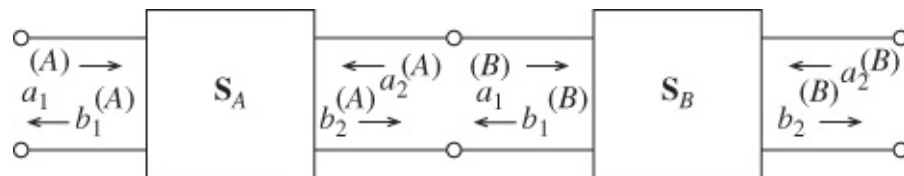


**Figure 3.11** Two cascaded two-ports.

An alternative definition of a scattering matrix that can be used in cascading is called the scattering cascade matrix,  $\mathbf{R}$ , in which the order of the waves is exchanged:

$$\begin{bmatrix} b_1 \\ a_1 \end{bmatrix} = \begin{bmatrix} R_{11} & R_{12} \\ R_{21} & R_{22} \end{bmatrix} \begin{bmatrix} a_2 \\ b_2 \end{bmatrix}, \quad 3.69$$

where the  $\mathbf{R}$  matrix or cascading matrix is

$$\mathbf{R} = \begin{bmatrix} R_{11} & R_{12} \\ R_{21} & R_{22} \end{bmatrix}. \quad 3.70$$

This is related to the  $S$  parameters of the two-port by

$$\mathbf{R} = \begin{bmatrix} S_{12} - S_{11}S_{21}^{-1}S_{22} & S_{21}^{-1}S_{11} \\ -S_{21}^{-1}S_{22} & S_{21}^{-1} \end{bmatrix} \quad 3.71$$

and

$$\mathbf{S} = \begin{bmatrix} R_{12}R_{22}^{-1} & R_{11} - R_{12}R_{21}R_{22}^{-1} \\ R_{22}^{-1} & -R_{21}R_{22}^{-1} \end{bmatrix}. \quad 3.72$$

For a two-port network, using Equations (3.61) and (3.69),

$$\begin{bmatrix} b_1^{(A)} \\ a_1^{(A)} \end{bmatrix} = \mathbf{R}_A \begin{bmatrix} a_2^{(A)} \\ b_2^{(A)} \end{bmatrix} \quad \text{and} \quad \begin{bmatrix} b_1^{(B)} \\ a_1^{(B)} \end{bmatrix} = \mathbf{R}_B \begin{bmatrix} a_2^{(B)} \\ b_2^{(B)} \end{bmatrix}, \quad 3.73$$

thus

$$\begin{bmatrix} b_1^{(A)} \\ a_1^{(A)} \end{bmatrix} = \mathbf{R}_A \mathbf{R}_B \begin{bmatrix} a_2^{(B)} \\ b_2^{(B)} \end{bmatrix}. \quad 3.74$$

For  $n$  cascaded two-port networks, Equation (3.74) generalizes to

$$\begin{bmatrix} b_1^{(1)} \\ a_1^{(1)} \end{bmatrix} = \mathbf{R}_1 \mathbf{R}_2 \dots \mathbf{R}_n \begin{bmatrix} a_2^{(n)} \\ b_2^{(n)} \end{bmatrix}, \quad 3.75$$

and so the cascade matrix of the cascaded network is the matrix product of the  $\mathbf{R}$  matrices of the individual two-ports.

### 3.3.10 Conversion between $S$ Parameters and $ABCD$ Parameters

[Figure 3.12](#) can be used to relate the appropriate parameters for the two views of the network. If both ports have the same reference impedance  $Z_0$ , then

$$\begin{bmatrix} V_1 \\ I_1 \end{bmatrix} = \begin{bmatrix} A & B \\ C & D \end{bmatrix} \begin{bmatrix} V_2 \\ I_2 \end{bmatrix} \quad 3.76$$

$$\begin{bmatrix} b_1 \\ b_2 \end{bmatrix} = \begin{bmatrix} S_{11} & S_{12} \\ S_{21} & S_{22} \end{bmatrix} \begin{bmatrix} a_1 \\ a_2 \end{bmatrix}. \quad 3.77$$

The  $S$  parameters are then expressed as

$$\begin{aligned} S_{11} &= \frac{A + B/Z_0 - CZ_0 - D}{\Delta} & S_{12} &= \frac{2(AD - BC)}{\Delta} \\ S_{21} &= \frac{2}{\Delta} & S_{22} &= \frac{-A + B/Z_0 - CZ_0 + D}{\Delta}, \end{aligned} \quad 3.78$$

where

$$\Delta = A + B/Z_0 + CZ_0 + D. \quad 3.79$$

The  $ABCD$  parameters can be expressed in terms of the  $S$  parameters as

$$A = \frac{(1 + S_{11})(1 - S_{22}) + S_{12}S_{21}}{2S_{21}} \quad 3.80$$

$$B = Z_0 \frac{(1 + S_{11})(1 + S_{22}) - S_{12}S_{21}}{2S_{21}} \quad 3.81$$

$$C = \frac{1}{Z_0} \frac{(1 - S_{11})(1 - S_{22}) - S_{12}S_{21}}{2S_{21}} \quad 3.82$$

$$D = \frac{(1 - S_{11})(1 + S_{22}) + S_{12}S_{21}}{2S_{21}}. \quad 3.83$$

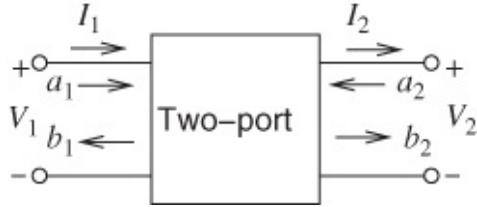


**Figure 3.12** Two-port with parameters suitable for defining  $S$  and  $ABCD$  parameters.

### 3.3.11 Return Loss

Return loss, also known as reflection loss, is a measure of the fraction of power that is not delivered by a source to a load. If the power incident on a load is  $P_i$  and the power reflected by the load is  $P_r$ , then the return loss in decibels is [4, 5]

$$RL_{dB} = 10 \log \frac{P_i}{P_r}. \quad 3.84$$

The better the load is matched to the source, the lower the reflected power and hence the higher the return loss. RL is a positive quantity if the reflected power is less than the incident power. If the load has a complex reflection coefficient  $\rho$ , then

$$RL_{dB} = 10 \log \left| \frac{1}{\rho^2} \right| = -20 \log |\rho|. \quad 3.85$$

That is, the return loss is the negative of the reflection coefficient expressed in decibels [6].

When generalized to terminated two-ports, the return loss is defined with respect to the input reflection coefficient of a terminated two-port [7]. The two-port in [Figure 3.13](#) has the input reflection coefficient

$$\Gamma_{in} = S_{11} + \frac{\Gamma_L S_{12} S_{21}}{(1 - \Gamma_L S_{22})}, \quad 3.86$$

where  $\Gamma_L$  is the reflection coefficient of the load. Thus the return loss of a terminated two-port is

$$RL_{dB} = -20 \log |\Gamma_{in}| = -20 \log \left| S_{11} + \frac{\Gamma_L S_{12} S_{21}}{(1 - \Gamma_L S_{22})} \right|. \quad 3.87$$

If the load is matched, that is, when  $Z_L = Z_0^*$  (but of course  $Z_0$  is real most of the time so this is the same as saying that  $Z_L = Z_0$ ). Now  $Z_0 = Z_{ref}$ , the reference impedance, so that  $Z_{ref} = Z_0$ . Then

$$RL_{dB} = -20 \log |S_{11}|. \quad 3.88$$

This return loss is also called the input return loss since the reflection coefficient is calculated at port 1. The output return loss is calculated looking into port 2 of the two-port, where now the termination at port 1 is just the source impedance.

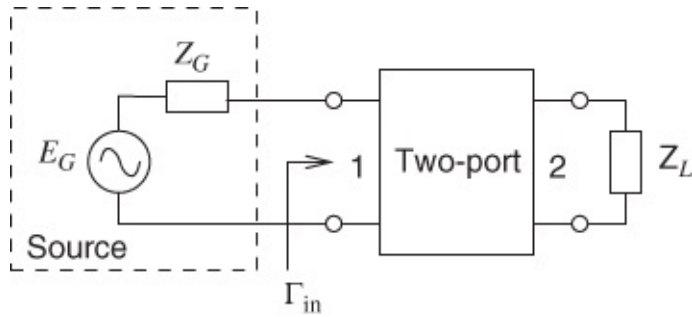


**Figure 3.13** Terminated two-port used to define return loss.

### 3.3.12 Insertion Loss

Insertion loss of a two-port network is defined as the ratio, in decibels, of voltages immediately beyond the point of insertion, before insertion and after insertion [4, 8]. Referring to [Figure 3.14\(a\)](#) and [\(b\)](#), insertion loss is expressed in decibels as

$$IL_{dB} = 20 \log \left| \frac{E_2}{E'_2} \right|, \quad 3.89$$

where  $E_2$  is the voltage across the load ( $Z_L$ ) before insertion of the two-port and  $E'_2$  is the voltage across the load ( $Z_L$ ) after insertion of the two-port. The power delivered to the load is proportional to the square of the magnitude of the voltage across the load, so an equivalent definition of the insertion loss, again in decibels, is

$$IL_{dB} = 10 \log \frac{P_L}{P_T}, \quad 3.90$$

where  $P_L$  is the power delivered to the load before the insertion of the two-port and  $P_T$  is the power delivered to the load following insertion. In terms of  $S$  parameters (referenced to  $Z_0$ ) [9, 10],

$$IL_{dB} = 10 \log \left| \frac{(1 - S_{11}\Gamma_G)(1 - S_{22}\Gamma_L) - S_{12}S_{21}\Gamma_G\Gamma_L}{S_{21}(1 - \Gamma_G\Gamma_L)} \right|^2. \quad 3.91$$

(The formula for IL is extended to complex reference impedances in [10].) In Equation (3.91)  $\Gamma_G$  is the source reflection coefficient using a reference impedance of  $Z_0$ , and  $\Gamma_L$  is the load reflection coefficient using a reference impedance of  $Z_0$ . The important point here is that in general the insertion loss is not simply determined by the transmission scattering parameter  $S_{21}$ .

.

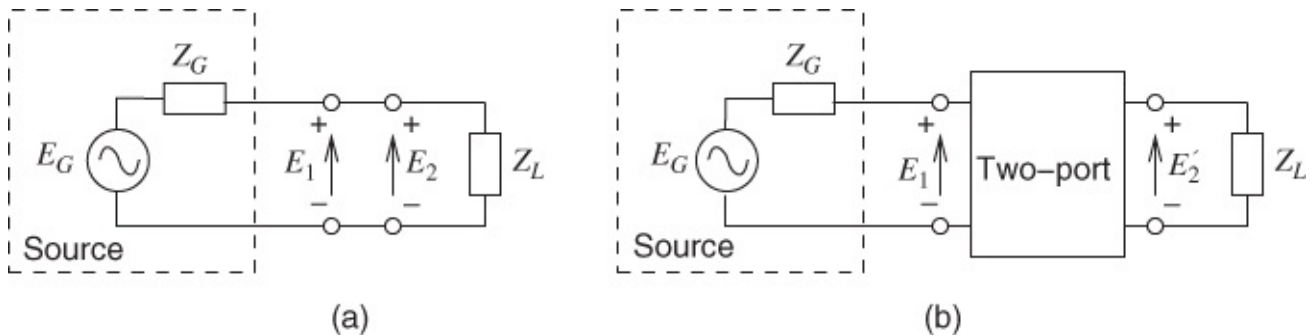


**Figure 3.14** Two-port insertion and definition of variables for defining insertion loss: (a) source and load before insertion; and (b) insertion of two-port network with source level unchanged.

A typical situation is when there is only a single reference impedance,  $Z_0$ , and the source is matched, that is,  $\Gamma_G = 0$ , then

$$IL_{dB} = 10 \log \left| \frac{(1 - S_{22}\Gamma_L)}{S_{21}} \right|^2. \quad 3.92$$

Here the  $S$ s and  $\Gamma_L$  are normalized with respect to  $Z_0$ . One of the consequences of a mismatched load is that the inserted two-port can increase the power delivered to the load (consider a negative  $S_{22}\Gamma_L$ ) and so the insertion loss, in decibels, can be negative, indicating gain due to the inserted two-port. In this case the two-port network provides matching that increases power transfer.

In the special case where the load and source impedances are equal to the real system reference impedance, that is,  $Z_G = Z_0 = Z_{01} = Z_{02} = Z_L$ , then

$$IL_{dB} = 10 \log \frac{1}{|S_{21}|^2}. \quad 3.93$$

This is also called the attenuation ( $A_{dB}$ ) of the two-port [10].

It is clear that if the source and load are mismatched, the insertion loss is due to both reflection and the resistive loss in the two-port.

## 3.4 Signal-flow Graph Techniques and $S$ Parameters

So-called signal-flow graphs (SFGs) form a logical and convenient means for analysing microwave circuits of virtually any form and complexity, provided only that they can be treated as linear and  $S$  parameters are applicable. Typical problems requiring this kind of analysis include measurement error assessment and amplifier gain calculations.

To set up equivalent  $S$  parameter SFGs, each port of the network is given two ‘nodes,’ one for the incident wave ( $a_k$ ) and the other for the reflected wave ( $b_k$ ). Branches, represented as lines between these nodes, carry the appropriate scattering parameters for each particular section of the network. Thus, the input reflection and reverse transfer sections appear as shown in [Figure](#)

[3.15](#). When the forward transfer and output reflection parameters are included, the full flow-graph for the two-port network appears as shown in [Figure 3.16](#). This SFG diagram represents the equations

$$b_1 = S_{11}a_1 + S_{12}a_2 \quad 3.94$$

$$b_2 = S_{21}a_1 + S_{22}a_2. \quad 3.95$$

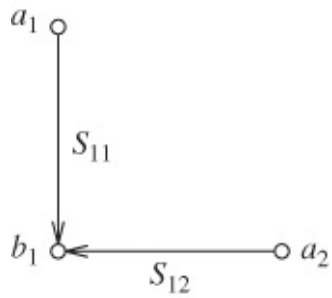


[Figure 3.15](#) SFG showing distribution of input reflection and output transfer to the response leaving port 1 of a two-port network.

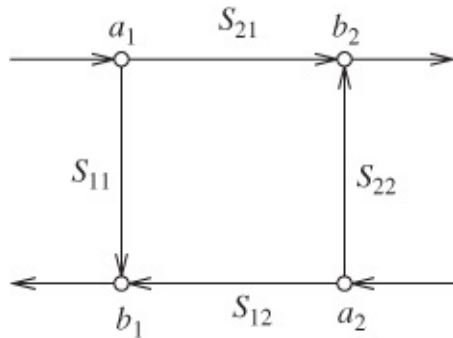


[Figure 3.16](#) Complete SFG of a two-port network.

### 3.4.1 Signal-flow Graphs

SFGs are convenient ways to graphically represent systems of simultaneous linear equations [11, 12]. SFGs can be used in many disciplines, but they are particularly useful with RF and microwave circuits. Several linear equations represented in SFG form are shown in [Table 3.3](#).

**Table 3.3** Mathematical relations expressed as SFGs

(a)		$y = a_1x_1 + a_2x_2$
(b)		$y_1 = ax_1$ $y_2 = ax_1$
(c)		$y_1 = a_3(a_1x_1 + a_2x_2)$ $y_2 = a_4(a_1x_1 + a_2x_2)$

In this section the basic rules for manipulating SFGs are presented. Think back to when you first started working with circuits. The great abstraction came about when the physical world was represented graphically as connections of circuit elements. Provided that a few simple rules were followed, the graphical representation resulted in recognition of circuit topologies and the selection of appropriate solution strategies (e.g., applying the voltage divider rule). When it comes to working with  $S$  parameters and interconnections of multiport networks, SFGs serve much the same purpose. In addition, SFG analysis enables the development of symbolic expressions. Only a portion of SFG theory is considered here—the aspects relevant to manipulating scattering parameter descriptions. Balabanian [13], Abrahams and Coverly [14], and Di Stefano *et al.* [15] provide a more detailed and general treatment.

### 3.4.2 Simplification and Reduction of SFGs

The power of SFG analysis is that an SFG can be formulated by building up the set of equations describing a network by connecting together the SFGs of sections. Pattern recognition can be used to identify patterns that can be reduced and simplified.

#### 3.4.2.1 Addition

[Figure 3.17](#) depicts SFG addition. [Figure 3.17\(a\)](#) and (b) denotes

$$x_2 = f_1x_1 + f_2x_1. \quad 3.96$$

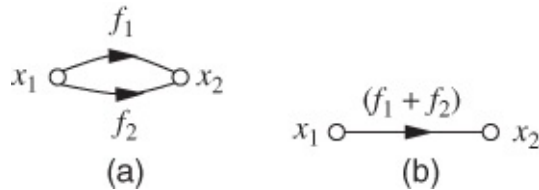


[Figure 3.17](#) SFG representation of addition.

#### 3.4.2.2 Multiplication

Consider the two cascaded blocks represented by the SFG of Figure 3.18(a). Here the output of the first block,  $x_2$ , is described by  $x_2 = f_1 x_1$ . The total response is the product of the individual responses (see Figure 3.18(b)):

$$x_4 = f_1 f_2 x_1. \quad 3.97$$

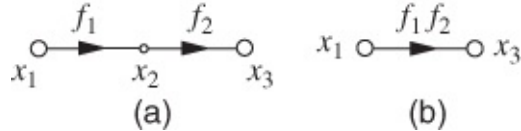


**Figure 3.18** Cascade reduction of SFG: (a) three cascaded blocks; and (b) reduced form.

### 3.4.2.3 Commutation

Consider the removal of the mixed node,  $b_3$ , in Figure 3.19(a). Here

$$b_3 = f_1 a_1 + f_2 a_2 \quad \text{and} \quad b_4 = f_3 b_3. \quad 3.98$$

Node  $b_3$  is called a mixed node, as it is both an input and an output node. Now  $b_3$  can be eliminated and so

$$b_4 = f_1 f_3 a_1 + f_2 f_3 a_2, \quad 3.99$$

which has the SFG of [Figure 3.19\(b\)](#). In [Figure 3.19\(b\)](#) the node representing the variable  $b_3$  has been eliminated. Thus elimination of a node from an SFG corresponds to the elimination of a variable. It is sufficient to recognize the SFG pattern shown in [Figure 3.19\(a\)](#) and replace it with the SFG of [Figure 3.19\(b\)](#) to achieve SFG reduction, and there is no need to write down the equation specifically to eliminate the variable.

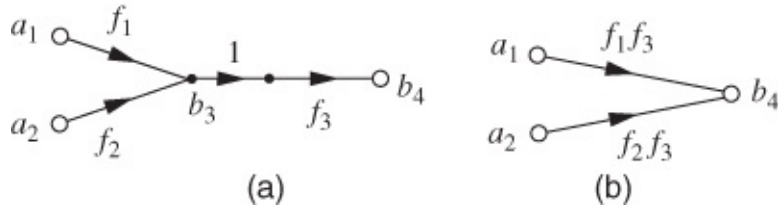


**Figure 3.19** SFG simplification eliminating a variable.

### 3.4.2.4 Self-loop

Recognizing a self-loop and applying the SFG technique for eliminating it is the best example yet of identifying patterns and applying SFG reduction strategies. Consider the SFG of [Figure 3.20\(a\)](#), which has a self-loop. The equations for this graph are

$$b_3 = f_2 a_2, a_2 = b_2, b_2 = f_1 a_1 + f_3 a_3, a_3 = b_3. \quad 3.100$$

Thus

$$b_3 = f_2 f_1 a_1 + f_2 f_3 b_3 \quad \text{and} \quad (1 - f_2 f_3) b_3 = f_2 f_1 a_1, \quad 3.101$$

where the variable  $b_2$  has been eliminated. The graph of Equation (3.101) is shown in [Figure 3.21\(a\)](#). The loop attached to node  $b_3$  is called a self-loop. Such loops are not particularly convenient and can be removed by writing Equation (3.101) in the form

$$b_3 = \frac{f_1 f_2}{1 - f_2 f_3} a_1. \quad 3.102$$

The SFG for this equation is shown in [Figure 3.21\(b\)](#). The rule for removing self-loops follows from the manner in which [Figure 3.21\(a\)](#) was transformed into [Figure 3.21\(b\)](#).

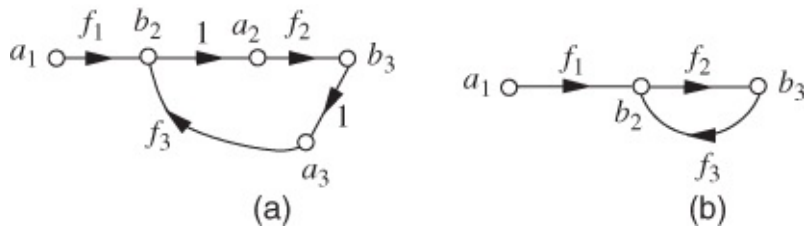


[Figure 3.20](#) SFGs having a self-loop: (a) original SFG; and (b) after eliminating  $a_2$ .

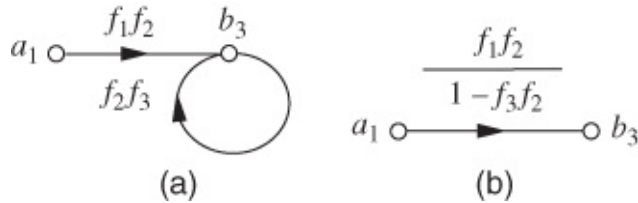


[Figure 3.21](#) SFG of (a) a self-loop; and (b) with the loop eliminated.

## 3.5 Summary

This chapter presented the essentials of microwave network theory required for the understanding and description of signal flow on transmission lines. Single transmission lines are two-port networks having four terminals, with one port at each end of the line comprising a signal terminal and a reference terminal. The two reference terminals are required as it is not possible to define a global ground that is common to the two ends of a transmission line. Doing so would require that charges in the ground redistribute themselves instantaneously. However, provided that there is no feedback path, that is, transmission lines and other two-port networks are arranged in cascade, then the distinction between the two reference terminals can be ignored.

The two sets of network parameters of greatest importance in describing transmission line networks are  $ABCD$  parameters and  $S$  parameters (i.e., scattering parameters).  $ABCD$  parameters find their greatest utility in relating two networks such as a transmission line network and an equivalent lumped-element network. The equivalence, however, is usually only approximate over a limited bandwidth.  $S$  parameters relate naturally to traveling voltage and current waves. Considering traveling voltage and current, in particular forward- and backward-traveling voltage and current, is a primary distinction in the way transmission lines must be viewed and analyzed compared to the total voltage and current used with lumped-

element networks. A more complete treatment of microwave network theory, not just limited for transmission lines, is presented in [16].

## References

- [1] K. Kurokawa, “Power waves and the scattering matrix”, *IEEE Trans. on Microwave Theory and Techniques*, vol. **13**, no. 2, pp. 194–202, Feb. 1965.
- [2] S. Goldberg, M. Steer, and P. Franzon, “Accurate experimental characterization of three-ports”, in *1991 IEEE MTT-S Int. Microwave Symp. Dig.*, 1991, pp. 241–244.
- [3] S. Goldberg, M. Steer, P. Franzon, and J. Kasten, “Experimental electrical characterization of high speed interconnects”, in *Proc. 41st Electronic Components and Technology Conf.*, 1991, pp. 85–88.
- [4] “Telecommunications: Glossary of Telecommunication Terms”, Federal Standard 1037C, U.S. General Services Administration Information Technology Service, Aug. 7, 1996.
- [5] T. S. Bird, “Definition and misuse of return loss [report of the trans. editor-in-chief],” *IEEE Antennas and Propagation Magazine*, vol. **51**, no. 2, pp. 166–167, Apr. 2009.
- [6] IEEE, *IEEE Standard Dictionary of Electrical and Electronic Engineering Terms*, 4th ed. IEEE Press, 1988.
- [7] T. Otoshi, “Maximum and minimum return losses from a passive two-port network terminated with a mismatched load”, *IEEE Trans. on Microwave Theory and Techniques*, vol. **42**, no. 5, pp. 787–792, May 1994.
- [8] “MIL-STD-220C: Test method standard, method of insertion loss measurement.” U.S. Department of Defence, MIL-STD-188-220C, [http://www-cnrwg.itsi.disa.mil/docs/MS188\\_220C\\_R13\\_Final\\_2.pdf](http://www-cnrwg.itsi.disa.mil/docs/MS188_220C_R13_Final_2.pdf), 2009.
- [9] R. Beatty, “Mismatch errors in the measurement of ultrahigh-frequency and microwave variable attenuators”, *J. Research National Bureau of Standards*, vol. **52**, pp. 7–9, 1954.
- [10] R. Beatty, “Insertion loss concepts”, *Proc. of the IEEE*, vol. **52**, no. 6, pp. 663–671, Jun. 1964.
- [11] S. Mason, “Feedback theory-some properties of signal flow graphs”, *Proc. of the IRE*, vol. **41**, no. 9, pp. 1144–1156, Sep. 1953.
- [12] A. Tustin, *Direct Current Machines for Control Systems*. The Macmillan Company, 1956.
- [13] N. Balabanian, *Fundamentals of Circuit Theory*. Allyn and Bacon, 1961.
- [14] J. Abrahams and G. Coverley, *Signal Flow Analysis*. Pergamon Press, 1965.

- [15] J. Distefano, A. Stubberud, and I. Williams, *Theory and Problems of Feedback Control Systems*. McGraw-Hill, 1990.
- [16] M. Steer, *Microwave and RF Design: a Systems Approach*, 2nd ed. SciTech Pub., 2013.

# Chapter 4

## Transmission Line Theory

### 4.1 Introduction

This chapter presents aspects of transmission line theory that are beyond the techniques used to describe general two-port networks using scattering parameters, as was considered in [Chapter 3](#). [Chapter 3](#) introduced  $ABCD$  and  $S$  parameters, which can be used to describe two-port networks. The extension of  $S$  parameters to multiport networks is straightforward and the extension of  $ABCD$  parameters to multiport networks is limited practically to coupled transmission line networks.

A two-port transmission line network often appears in cascade with other transmission line two-ports and/or with general two-port networks. Such a situation is shown in [Figure 4.1](#), where there is a cascade of a generator with Thevenin impedance  $Z_s$ , a transmission line network with the line having a characteristic impedance  $Z_{01}$ , a two-port network, and a second transmission line having characteristic impedance  $Z_{02}$ . The cascade is terminated in a load  $Z_L$ . This cascade, for example, could be what is encountered when performing measurements. This chapter presents the transmission line theory required to change the reference plane of  $S$  parameters along the transmission line, and how to work with cascades when the characteristic impedance of the lines is complex.

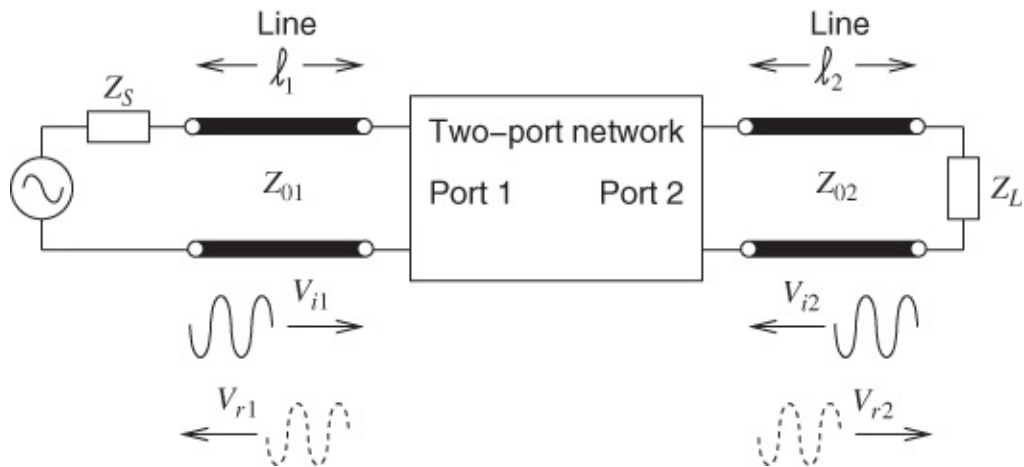


[Figure 4.1](#) A two-port network with connecting transmission lines showing forward- and backward-traveling waves on the lines.

### 4.2 Transmission Line Theory

This section presents an outline of microwave transmission line theory, including impedance matching using transmission lines. A more complete treatment of transmission line theory is available in [1]. The background for the developments here is the TEM-mode transmission line

theory presented in [Section 2.8](#). Recall that a TEM-mode transmission line has its electric and magnetic field lines in the plane transverse to the direction of the line (direction of propagation). Thus TEM-mode stands for transverse electro-magnetic mode. The coaxial line is the most common such line. Other lines, such as microstrip, have field distributions that are only approximately transverse, and these are called quasi-TEM. Nevertheless, their characterization is referenced to a TEM-mode line.

### 4.2.1 Half-, Quarter- and Eighth-wavelength Lines

Transmission lines that are half of a wavelength long at some desired frequency of operation are often encountered in RF and microwave circuits. Various combinations of short-circuit or open-circuit terminations may be used. When there is either an open circuit at both ends or a short circuit at both ends, such lines then form ‘half-wave resonators.’ When both ends are short-circuit terminated, as in [Figure 4.2](#), coupling to the line would have to be provided by some separate probe. The actual length of such a resonator may be extended to  $n\lambda_g/2$ , where  $n$  is an integer. It is again left as an exercise to examine the behavior of open-circuit terminated resonators. Lines which are a quarter of a wavelength long can provide useful properties. Clearly, for a short-circuit terminated quarter-wave line we obtain half, longitudinally, of the standing wave pattern shown in [Figure 4.2](#). At the input plane location P, the standing wave has a voltage maximum that corresponds to an open-circuit condition. Thus we effectively transform from the short circuit to an open circuit. This is consistent with an input impedance calculation using Equation [\(2.35\)](#), and substituting  $\beta = 2\pi/\lambda_g$  yields

$$Z_{sc}|_{\lambda_g/4} = jZ_0 \tan(\pi/2) = \infty \quad 4.1$$

which is certainly the impedance of an open circuit. This feature can be used in many circuit designs to deliberately ensure that an open circuit appears in a desired location, at one frequency.

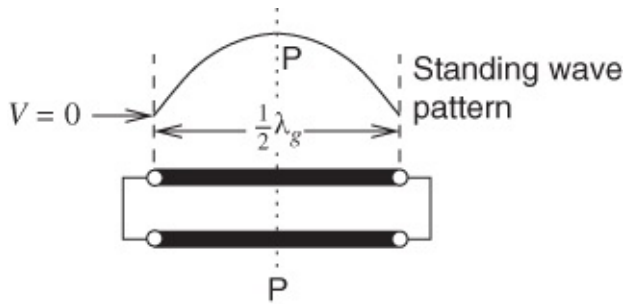


[Figure 4.2](#) Standing wave pattern produced by a half-wave resonator.

### 4.2.2 Simple (Narrowband) Matching

At RF and microwave frequencies the transfer of maximum power from one part of a circuit to another is critical. The aim is to achieve maximum power transfer, thus the load impedance is the complex conjugate of the effective input impedance. Matching is achieved by inserting a network called a matching network. When matching is implemented on chip at a few gigahertz

or less or on a circuit board at slightly lower frequencies, it is usual to implement lumped elements in the matching network. Lumped element matching network design is beyond the scope of this book. The reader is referred to [1] for a comprehensive treatment, including broadband matching. Above a few gigahertz, and possibly because of the lower losses that can be achieved even at megahertz and low gigahertz frequencies, connections of transmission lines are used. Transmission line-based matching networks also have higher power-handling capability than their lumped-element equivalents.

In most practical situations a transmission line ultimately feeds some load that has an impedance possibly differing considerably from the characteristic impedance of the line, that is, it is mismatched, possibly quite severely. Examples include feeds to solid-state amplifying devices such as transistors and antenna feeders. By connecting a suitably designed network between the feed line and the load we can adjust impedances in order to obtain a good overall match. If this match is required to hold over a specified range of frequencies, the network design may become quite complicated.

This section briefly reviews two simple methods for narrowband matching: the single-shunt stub and the quarter-wave transformer. Broadband matching, not considered here, also matches derivatives.

A schematic representation of the single-shunt stub technique is shown in [Figure 4.3](#). Although a short-circuit termination is indicated here, an open-circuit termination could be used, provided that the termination quality is sufficiently good. In this arrangement all lines are shown with identical characteristic impedances. This may not always be so, and some extra flexibility is offered if the stub and main line impedances are of different values. The best method for ‘hand calculating’ the required lengths  $\ell_1$  and  $\ell_2$  to obtain the matched condition  $Z_{in} = Z_0$  is to use a Smith chart. This is fully described in a number of standard texts and will not be outlined here.

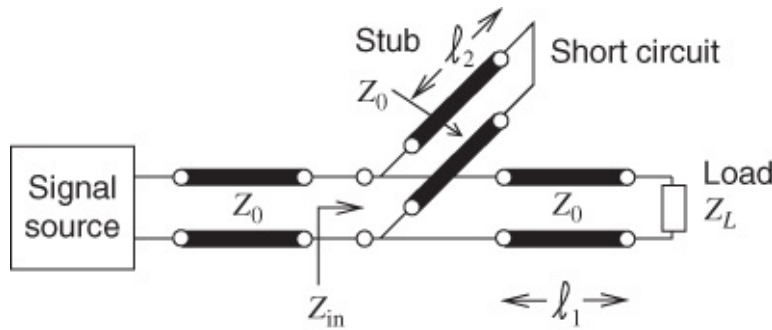


[Figure 4.3](#) Transmission line system with a single shunt stub.

For computer-aided design (CAD) suitable expressions are required, which are now stated for  $\ell_1$  and  $\ell_2$ . The results are (for a resistive load):

$$\ell_1 = \frac{\lambda_g}{2\pi} \tan^{-1} \sqrt{\frac{Z_L}{Z_0}} \quad 4.2$$

and

$$\ell_2 = \frac{\lambda_g}{2\pi} \tan^{-1} \left( \frac{\sqrt{Z_L Z_0}}{Z_L - Z_0} \right).$$

It is important to note that these results are satisfactory only when  $Z_L$  is real (resistive). If  $Z_L$  is complex the basic expressions must be re-examined in order to proceed with the analysis, which becomes quite lengthy. With the use of two, three, or sometimes more stubs the distance  $\ell_1$  can be kept fixed and then broader-band matching is achievable. Naturally, full analyses yielding lengths and separations become very unwieldy.

There is a simpler technique available for matching resistive loads: the quarter-wave transformer. In the single-section quarter-wavelength basic method this represents, again, a narrowband approach. The basic arrangement is shown in [Figure 4.4](#).

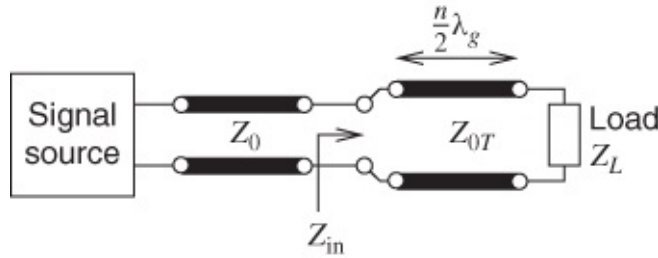


[Figure 4.4](#) Quarter-wave impedance transformer.

We set  $Z_L = R_L$  (resistive) and  $\ell = n\lambda_g/4$  in Equation (2.34) to obtain

$$Z_{in} = \frac{Z_{0T}^2}{R_L} \quad 4.4$$

whence the required characteristic impedance of the quarter-wave line is

$$Z_{0T}^2 = Z_0 R_L. \quad 4.5$$

For example, to match a  $50 \Omega$  line into a  $10 \Omega$  resistive load the impedance required is

$$Z_{0T}^2 = 500 \Omega^2 \quad 4.6$$

or

$$Z_{0T} = 22.4 \Omega. \quad 4.7$$

In stripline or microstrip circuits this would be relatively easy to implement.

A broader-band match is obtained if several quarter-wave sections are connected in cascade. The drawbacks are that space may be wasted in the layout, the match may remain poor at the band edges, and only resistive loads are accommodated.

### 4.2.3 Equivalent Two-port Networks

There are applications where it is useful to employ a lumped-parameter, equivalent, two-port

network for a particular length of line. One example is in the realization of filters consisting of cascaded lengths of transmission lines. Any equivalent network must be constrained to have the same terminal characteristics as those of the length of transmission line it represents, and this will only hold at one single frequency. Having said this, the behavior may well be satisfactorily represented over at least a narrow band of frequencies. The propagation constant  $\gamma$  will usually be the most frequency sensitive parameter. The general equivalent T network is given in [Figure 4.5\(a\)](#) and the equivalent  $\pi$  network is given in [Figure 4.5\(b\)](#).

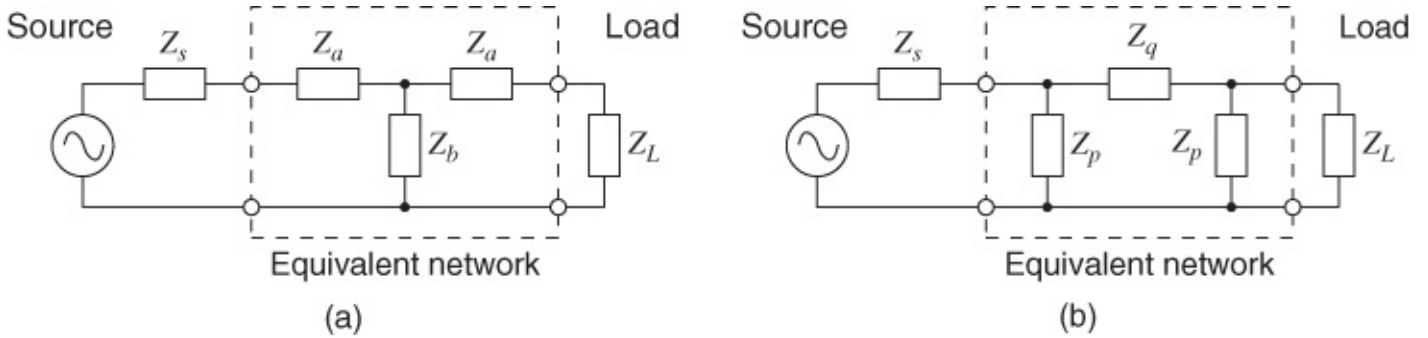


**Figure 4.5** Equivalent two-port networks of a section of transmission line: (a) T network; and (b)  $\pi$  network.

Expressions for the various impedances, given next, are readily obtained by equating transmission line terminal voltages and currents with network terminal voltages and currents:

$$Z_a = Z_0 \tanh \frac{\gamma \ell}{2} \quad \text{4.8}$$

$$Z_b = \frac{Z_0}{\sinh \gamma \ell} \quad \text{4.9}$$

and

$$Z_q = Z_0 \sinh \gamma \ell \quad \text{4.10}$$

$$Z_p = Z_0 \coth \frac{\gamma \ell}{2}. \quad \text{4.11}$$

For loss-free lines (so that  $\gamma = j\beta$ ) these expressions become reactance terms as follows:

$$Z_a = jZ_0 \tan \frac{\beta \ell}{2} \quad \text{4.12}$$

$$Z_b = \frac{-jZ_0}{\sin \beta \ell} \quad \text{4.13}$$

and

$$Z_q = jZ_0 \sin \beta \ell \quad \text{4.14}$$

$$Z_p = -jZ_0 \cot \frac{\beta\ell}{2}.$$

This set of formulas is useful, for example, in some microstrip filter designs.

For very short lengths of loss-free transmission line, such that  $\ell \ll \lambda_g/4$ , a very simple approximate equivalent network, shown in [Figure 4.6](#), is adequate.

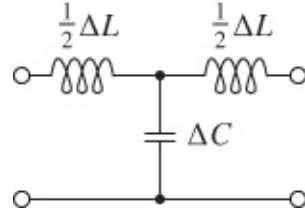


[Figure 4.6](#) Simple equivalent network of a transmission line segment with  $\Delta L = L\ell$  and  $\Delta C = C\ell$ .

## 4.3 Chain (*ABCD*) Parameters for a Uniform Length of Loss-free Transmission Line

*ABCD* parameters were introduced in [Chapter 3](#) and here the *ABCD* parameters of a transmission line are developed.

The notation for the equivalent two-port network, to be characterized in terms of *ABCD* parameters, is shown in [Figure 4.7](#). With this choice of quantities, including directions, the independent variables are now assumed to be the output variables ( $V_2$  and  $I_2$ ). The *ABCD* parameters then directly provide the related input (dependent) variables, assuming the network is linear:

$$V_1 = AV_2 + BI_2 \quad \text{4.16}$$

$$I_1 = CV_2 + DI_2 \quad \text{4.17}$$

where  $A$ ,  $B$ ,  $C$  and  $D$  are constants that characterize the network.

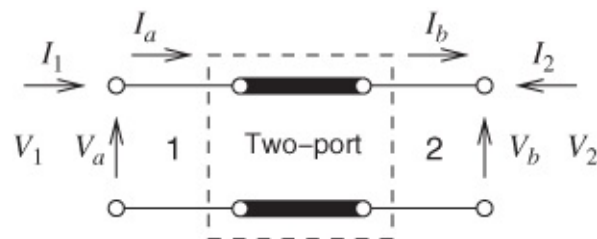


[Figure 4.7](#) A two-port transmission line network used to define *ABCD* parameters.

In matrix form Equations (4.16) and (4.17) become

$$\begin{bmatrix} V_1 \\ I_1 \end{bmatrix} = \begin{bmatrix} A & B \\ C & D \end{bmatrix} \begin{bmatrix} V_2 \\ I_2 \end{bmatrix}. \quad \text{4.18}$$

This  $ABCD$  matrix is often called the chain matrix because it is so useful in analyzing cascaded (or chained) networks.

For a length  $\ell$  of uniform loss-free transmission line the voltages and currents are interrelated by

$$V_1 = V_2 \cos \beta\ell + jI_2 Z_0 \sin \beta\ell \quad 4.19$$

and

$$I_1 = j\frac{V_2}{Z_0} \sin \beta\ell + I_2 \cos \beta\ell. \quad 4.20$$

These expressions can be written in the following matrix form:

$$\begin{bmatrix} V_1 \\ I_1 \end{bmatrix} = \begin{bmatrix} \cos \beta\ell & jZ_0 \sin \beta\ell \\ jY_0 \sin \beta\ell & \cos \beta\ell \end{bmatrix} \begin{bmatrix} V_2 \\ I_2 \end{bmatrix}. \quad 4.21$$

Comparing Equation (4.18) with Equation (4.21) gives the final result for the transmission line chain matrix:

$$\begin{bmatrix} A & B \\ C & D \end{bmatrix} = \begin{bmatrix} \cos \beta\ell & jZ_0 \sin \beta\ell \\ jY_0 \sin \beta\ell & \cos \beta\ell \end{bmatrix}. \quad 4.22$$

This result is useful in analysing many single and multiple transmission line structures. One area where it will be required in this work is in coupler considerations, leading to coupler design, as described in detail in [Chapter 10](#).

## 4.4 Change in Reference Plane

It is often necessary to translate the  $S$  parameters of a two-port by adding or subtracting lengths of transmission line. This is a good example of how transmission lines alter the  $S$  parameters of a two-port network. Consider the situation shown in [Figure 4.8\(a\)](#). Beginning with the  $S$  parameters of the cascaded network, the  $T$  matrix at planes 1 and 2 can be obtained. These parameters can then be referenced to planes  $1'$  and  $2'$  to obtain the parameters, for example  $T_X$ , of the embedded two-port. Now,

$$T = T_{\theta_1} T_X T_{\theta_2}, \quad 4.23$$

and so

$$T_X = T_{\theta_1}^{-1} T T_{\theta_2}^{-1}. \quad 4.24$$

A section of line with electrical length  $\theta$  and port impedances equal to its characteristic impedance has

$$\mathbf{S} = \begin{bmatrix} 0 & e^{-j\theta} \\ e^{-j\theta} & 0 \end{bmatrix}$$

and

$$\mathbf{T}_\theta = \begin{bmatrix} e^{j\theta} & 0 \\ 0 & e^{-j\theta} \end{bmatrix}. \quad 4.26$$

Therefore Equation (4.24) becomes

$$\mathbf{T}_X = \begin{bmatrix} T_{11}e^{-j(\theta_1+\theta_2)} & T_{12}e^{-j(\theta_1-\theta_2)} \\ T_{21}e^{j(\theta_1-\theta_2)} & T_{22}e^{j(\theta_1+\theta_2)} \end{bmatrix}, \quad 4.27$$

and then the desired  $\mathbf{S}$  parameters of the embedded two-port are obtained as

$$\mathbf{S}_X = \begin{bmatrix} S_{11}e^{j2\theta_1} & S_{12}e^{j(\theta_1+\theta_2)} \\ S_{21}e^{j(\theta_1+\theta_2)} & S_{22}e^{j2\theta_2} \end{bmatrix}. \quad 4.28$$

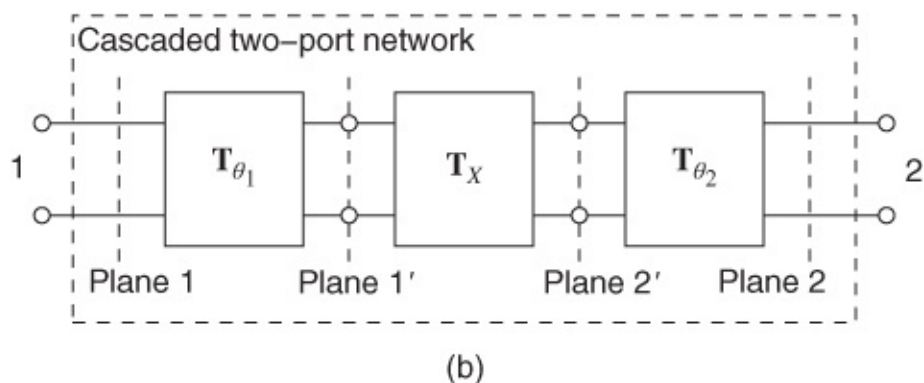
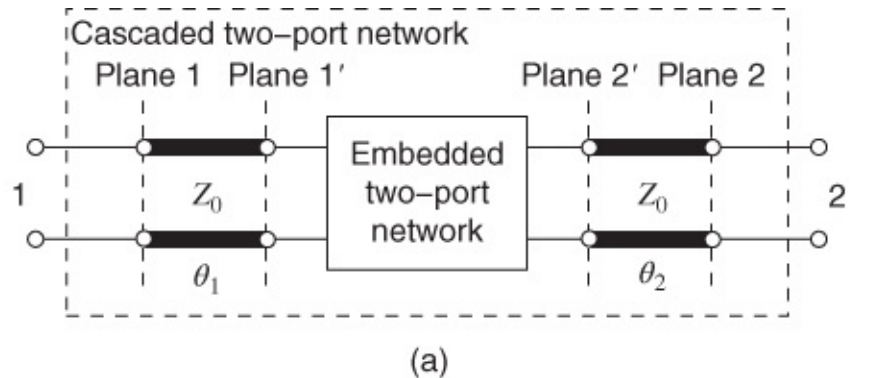


**Figure 4.8** Two-port measurement setup: (a) a two-port comprising an embedded two-port network and transmission line sections between reference planes 1 and 2; and (b) representation as cascaded two-port networks.

## 4.5 Working With a Complex Characteristic Impedance

This section considers traveling waves on a transmission line with a possibly complex characteristic impedance. Concepts are presented that enable problems to be solved using

scattering parameters with complex characteristic impedances. Such situations occur in measurements where realistic lines can be lossy, especially microstrip lines at high frequencies, and measurements most conveniently yield scattering parameters. Matching problems directed at maximum power transfer most conveniently use a type of scattering parameter referenced to complex impedances. We therefore cannot simply avoid the complex reference impedance problem by using impedance parameters, for example.

What is described in this section is subtle and the ramifications of the complex impedance of a low-loss line can often be safely ignored. However, erroneous results are encountered when attempting to experimentally characterize a low-loss component or if the transmission line environment of a measurement system is not low loss, as encountered at millimeter-wave frequencies.

Until now scattering parameters have been used with a real reference impedance. When a transmission lines is lossless, the characteristic impedance is real and the reference impedance is conveniently taken as the characteristic impedance of the transmission line. Most of the time using a real reference impedance is adequate even for low-loss lines such as coaxial lines. Planar lines such as microstrip can have appreciable loss and so the real characteristic impedance approximation may not be adequate in characterizing lines and particularly in interpreting measurements. The approximation is also not adequate in some calculations of transmission line systems [2]. When it is necessary to work with a complex reference impedance there are three types of waves: traveling waves, pseudo waves, and power waves. [Table 4.1](#) compares the three types of waves.

**Table 4.1** Transmission line waves used in scattering parameter analysis

Wave	Symbols	Physical	Property
Traveling waves	$V^+, V^-$	Physical	For a lossless line and $Z_{\text{ref}} = Z_0$ the waves are
$Z_0, Z_{\text{ref}}$ real	$I^+, I^-$ $a, b$		directly related to voltage (electric field) and current (magnetic field) waves on the transmission line.
Pseudo waves	$a, b$	Not physical	Lossy line and so $Z_0$ is complex.
$Z_{\text{ref}}$ real			Conventional $S$ parameter analysis (e.g., $S$ parameter matrix calculation, SFG, and Smith chart) can be used. Identical to traveling waves if the line is lossless and $Z_{\text{ref}} = Z_0$ .
Pseudo waves	$a, b$	Not physical	Lossy line so $Z_0$ is complex and $Z_{\text{ref}} = Z_0$ .
$Z_{\text{ref}}$ complex			Cannot use most conventional $S$ parameter analyses. $a$ and $b$ are linear combinations of the actual traveling waves.
Power waves	$\hat{a}, \hat{b}$	Not physical	Conveniently describe power flow at transmission line junctions. Used in matching. $\hat{a}$ and $\hat{b}$ are linear combinations of the actual traveling waves.
$Z_{\text{ref}}$ complex			

### 4.5.1 Traveling Waves

Traveling waves are the waves most engineers think of when working with microwave circuits. They are real and can be linked directly to Maxwell's equations. Our intuitive understanding of scattering parameter theory and of signal propagation on a transmission line works well as long as the line is lossless as then the characteristic impedance of the transmission line,  $Z_0$ , is real. When  $Z_0$  is real then we define  $a$  and  $b$ , commonly called root power waves, at the  $n$ th port of a network as (the voltages and currents here are peak and not rms quantities)

$$a_n = \frac{|v_0|}{v_0} \frac{V_n^+}{\sqrt{Z_{0n}}} \quad \text{and} \quad b_n = \frac{|v_0|}{v_0} \frac{V_n^-}{\sqrt{Z_0}} \quad 4.29$$

where the term  $|v_0|/v_0$  is a normalization term that provides the correct units and  $v_0$  is the line integral of the transverse electric field and is typically ignored so that

$$a_n = \frac{V_n^+}{\sqrt{Z_{0n}}} \quad \text{and} \quad b_n = \frac{V_n^-}{\sqrt{Z_{0n}}}. \quad 4.30$$

The  $a$  and  $b$  values have the units of root power, ( $\text{V}^{\frac{1}{2}} \cdot \text{A}^{\frac{1}{2}}$ ) and are power-normalized versions of the traveling waves. (Note that the voltages and currents here are peak quantities.)

If different real impedances are used at each port of the transmission line then the more general expressions are

$$a_n = \frac{V_n + I_n Z_{\text{ref},n}}{2\sqrt{Z_{\text{ref},n}}} \quad \text{and} \quad b_n = \frac{V_n - I_n Z_{\text{ref},n}}{2\sqrt{Z_{\text{ref},n}}} \quad 4.31$$

where  $V_n$  and  $I_n$  are the total voltage and current, respectively, at the  $n$ th port. The  $a_n$  and  $b_n$  are now linear combinations of the traveling voltage waves  $V_n^+$  and  $V_n^-$  at the  $n$ th port. Thus  $a_n$  (and  $b_n$ ) on its own does not correspond to an actual traveling wave on the transmission line.

## 4.5.2 Pseudo Waves

Pseudo waves are used with a lossy line, which then has a complex  $Z_0$ . While taking  $Z_{\text{ref}}$  as real does not yield an accurate representation of the traveling waves, it does enable convenient calculations using conventional  $S$  parameter analysis [3]. Sometimes it is necessary to use  $Z_{\text{ref}} = Z_0$ , which is complex. This is the situation in analyzing some transmission line problems and particularly in interpreting measurements of lossy transmission lines.

When  $Z_{\text{ref},n}$  is the complex reference impedance at the  $n$ th port then  $a$  and  $b$  are the pseudo waves, and at the  $n$ th port of a network are defined as (after dropping a normalization factor)

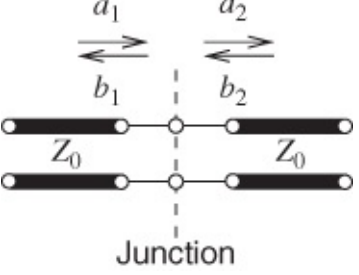
$$a_n = \frac{\sqrt{\Re\{Z_{\text{ref},n}\}}}{2|Z_{\text{ref},n}|}(V + IZ_{\text{ref},n}) \quad \text{and} \quad b_n = \frac{\sqrt{\Re\{Z_{\text{ref},n}\}}}{2|Z_{\text{ref},n}|}(V - IZ_{\text{ref},n}) \quad 4.32$$

The pseudo waves defined by Equation (4.32) reduce to those in Equation (4.30) when the line is lossless and  $Z_{\text{ref},n} = Z_0$ .

Even when a transmission line has a complex  $Z_0$ , using a real reference impedance (that may not even be close to  $Z_0$  but typically is taken as  $|Z_0|$ ) enables the intuition used with traveling waves to be used. Furthermore, using a real  $Z_{\text{ref}}$  enables the use of conventional  $S$  parameter analysis. Thus a real reference impedance enables the implementation of matrix operations, SFG analysis, and Smith chart analysis. A summary is given in [Table 4.2](#). The reader will note that the approximate relationship is indicated when the  $a$  and  $b$  pseudo waves are used. This is because there is a very slight deviation from equality due to a subtle difference between microwave equivalent circuit theory and the Lorentz reciprocity condition (see [3],[4], Appendix D). The reason for this apparent discrepancy is that the underlying voltage and current waves have difference phases. The approximation can nearly always be ignored and so

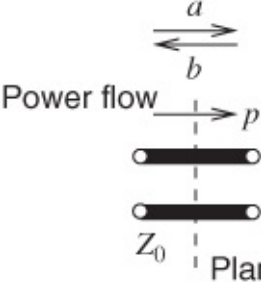
we can use the equalities  $a_2 = a_1$  and  $b_1 = b_2$  with negligible error.

**Table 4.2** Properties of traveling waves and pseudo waves at the junction of two transmission lines with the same characteristic impedance

Transmission line junction	Traveling waves	Pseudo waves	Pseudo waves
	$Z_0$ real	$Z_0$ complex	$Z_0$ complex
			
	$Z_{\text{ref}} = Z_0$	$Z_{\text{ref}}$ real	$Z_{\text{ref}} = Z_0$
	$a_2 = a_1$	$a_2 \approx a_1$	$a_2 \approx a_1$
	$b_1 = b_2$	$b_1 \approx b_2$	$b_1 \approx b_2$
	$a, b$ correspond to power flow.	$a, b$ correspond to power flow.	$a, b$ do not directly correspond to power flow.
	Defines conventional $S$ parameter	Conventional $S$ parameter	Limited $S$ parameter
	$S$ parameter analysis	analysis applies	analysis possible

When  $Z_{\text{ref}}$  is complex, conventional  $S$  parameter analysis cannot always be used. This is because with complex  $Z_{\text{ref}}$  the  $a$  and  $b$  values do not directly relate to power flow. This is illustrated in [Table 4.3](#), where the formula for power crossing a reference plane on a transmission line is compared for traveling waves and pseudo waves.

**Table 4.3** Power flow,  $p$ , across a reference plane on a transmission line with traveling waves and pseudo waves

Transmission line	Traveling waves	Pseudo waves	Pseudo waves
	$Z_0$ real	$Z_0$ complex	$Z_0$ complex
			
$Z_{\text{ref}} = Z_0$ real	$Z_{\text{ref}}$ real	$Z_{\text{ref}}$ real	$Z_{\text{ref}}$ complex
	$p = \frac{1}{2}( a ^2 -  b ^2)$	$p = \frac{1}{2}( a ^2 -  b ^2)$	$p = \frac{1}{2}( a ^2 -  b ^2) + 2\Im\{ab^*\} \frac{\Im\{Z_{\text{ref}}\}}{\Re\{Z_{\text{ref}}\}}$

The pseudo scattering parameter matrix  ${}^P\mathbf{S}$  defined by

$$\mathbf{b}={}^P\mathbf{S}\mathbf{a}, \quad 4.33$$

relates the pseudo waves with a complex reference impedance. If  $Z_{\text{ref}}$  is real then no special distinction of the  $\mathbf{S}$  parameters defined with traveling waves needs to be made. However, if  $Z_{\text{ref}}$  is complex only a limited number of  $\mathbf{S}$  parameter operations are allowed using  ${}^P\mathbf{S}$ . One of the allowable operations is the use of the scattering transfer matrix (or cascading matrix) described in [Section 3.3.9](#) and this is possible because of the approximate equality indicated in [Table 4.2](#). For example, cascading matrices are used in extracting desired measurements from raw measurements.

### 4.5.3 Power Waves

Power waves [5],  $\hat{a}$  and  $\hat{b}$ , were originally developed to enable a simple expression for power flow at a junction, as shown in [Table 4.4](#). [Table 4.4](#) compares the power flow passing a reference point such as a reference plane on a transmission line for pseudo waves and power waves.

**Table 4.4** Power flow,  $p$ , across a reference plane on a transmission line with pseudo waves and power waves

Transmission line	Pseudo waves, $a$ , $b$	Power waves, $\hat{a}$ , $\hat{b}$
	$Z_{\text{ref}}$ complex	$\hat{Z}$ complex
	$p = \frac{1}{2}( a ^2 -  b ^2 + 2\Im\{ab^*\} \frac{\Re\{Z_{\text{ref}}\}}{\Im\{Z_{\text{ref}}\}})$	$p = \frac{1}{2}( \hat{a} ^2 -  \hat{b} ^2)$

Power waves are defined so that the power flow relation  $p = |\hat{a}|^2 - |\hat{b}|^2$  can be used even if the reference impedance is complex 5–9. With power waves it is common to refer to the “reference impedance” as a “complex port number”  $\hat{Z}$  as it is generally set to the complex impedance of a load or a generator, enabling power waves to be used in matching problems. The power waves at the  $n$ th port with reference impedance (complex port number)  $\hat{Z}_n$  are defined as

$$\hat{a}_n = \frac{V + I\hat{Z}}{2\sqrt{\Re\{\hat{Z}\}}} \quad \text{and} \quad \hat{b} = \frac{V - I\hat{Z}_n^*}{2\sqrt{\Re\{\hat{Z}_n\}}}. \quad 4.34$$

The relationship of the power waves is given by the generalized scattering parameter matrix  $\mathbf{G_S}$ :

$$\mathbf{b} = {}^G \mathbf{S} \mathbf{a}. \quad 4.35$$

The relationship of  $\mathbf{G_S}$  to the conventional normalized  $S$  parameter matrix is given in [1].

Power waves are useful in matching problems [10] where the complex reference impedances at the ports are taken as the source and load impedances. However, the standard  $S$  parameter manipulations (SFG, Smith chart, matrix operations) used with traveling waves and pseudo waves with a real reference impedance cannot be used with power waves or generalized  $S$  parameters.

The reader is referred to [3, 10] if a complex reference impedance (and hence power waves) must be used.

#### 4.5.4 Summary

With pseudo waves, provided that a real reference impedance is used, the standard scattering parameter calculations used with lossless transmission lines can be used. These operations

include matrix operations, SFG analysis, and Smith chart analysis. However, when a complex reference impedance must be used, and this is common in matching problems and in algorithms for extracting transmission line parameters from measurements or in conjugate matching with complex transmission lines, care must be used in manipulating scattering parameters. It is always best to use a real reference impedance in calculations and only deal with complex reference impedances when the situation and need are clearly understood.

## 4.6 Summary

This chapter presented some powerful illustrations of why  $S$  parameters are the preferred network parameters to use with transmission lines. For example, it is a simple matter to change the  $S$  parameters of a network with leading and trailing lossless transmission lines by simply rotating the phase of the  $S$ -parameters of the transmission lines. The  $ABCD$  parameters of transmission lines were developed and these can be used with the  $ABCD$  parameters of lumped-element networks to equate lumped-element and transmission line networks. In particular it will be seen in several parts of this book that circuit synthesis, for example as used in filter design, often yields lumped-element networks. These can be translated to transmission line networks by equating  $ABCD$  parameters.

## References

- [1] M. Steer, *Microwave and RF Design: a Systems Approach*, 2nd ed. SciTech Pub., 2013.
- [2] D. Williams, “Traveling waves and power waves: building a solid foundation for microwave circuit theory,” *IEEE Microwave Magazine*, vol. **14**, no. 7, pp. 38–45, Jul. 2013.
- [3] D. Williams and R. B. Marks, “Reciprocity relations in waveguide junctions,” *IEEE Trans. on Microwave Theory and Techniques*, vol. **41**, no. 6, pp. 1105–1110, Jun. 1993.
- [4] R. B. Marks and D. F. Williams, “A general waveguide circuit theory,” *Journal of Research-National Institute of Standards and Technology*, vol. **97**, pp. 533–533, Sep.–Oct. 1992.
- [5] K. Kurokawa, “Power waves and the scattering matrix,” *IEEE Trans. on Microwave Theory and Techniques*, vol. **13**, no. 2, pp. 194–202, Feb. 1965.
- [6] D. Williams and B. Alpert, “Characteristic impedance, power, and causality [waveguide circuit theory],” *IEEE Microwave and Guided Wave Letters*, vol. **9**, no. 5, pp. 181–182, May. 1999.
- [7] D. Williams, B. Alpert, U. Arz, D. Walker, and H. Grabinski, “Causal characteristic impedance of planar transmission lines,” *IEEE Trans. on Advanced Packaging*, vol. **26**, no. 2, pp. 165–171, Feb. 2003.
- [8] D. Williams and B. Alpert, “Causality and waveguide circuit theory,” *IEEE Trans. on*

*Microwave Theory and Techniques*, vol. **49**, no. 4, pp. 615–623, Apr. 2001.

[9] D. Woods, “Concepts of voltage waves, current waves and power waves in s parameter definitions and measurements,” *Proc. of the Institution of Electrical Engineers*, vol. **119**, no. 12, pp. 1764–1765, Dec. 1972.

[10] J. Rahola, “Power waves and conjugate matching,” *IEEE Trans. on Circuits and Systems II: Express Briefs*, vol. **55**, no. 1, pp. 92–96, Jan. 2008.

# **Chapter 5**

## **Planar Interconnect Technologies**

### **5.1 Introductory Remarks**

Microstrip and similar planar interconnects, and circuits using them, form the principal subjects of this book. First it is important to establish the general setting with which we are concerned and also to briefly examine several alternative transmission line structures that sometimes exhibit special advantages over others.

### **5.2 Microwave Frequencies and Applications**

The use of the term ‘microwave’ is actually rather ambiguous, particularly at the lower end of the range. Sometimes signals at frequencies of only a few hundred megahertz are referred to as “microwaves.” For the present purposes we shall assume that appropriate frequencies extend from around 1 GHz to several hundred gigahertz. Corresponding wavelengths in free space are 30 cm at 1 GHz, 3 cm at 10 GHz, and 3 mm at 100 GHz. For digital systems, where the fifth (or higher) harmonic is contained in the digital pulses, our discussions relate to circuits clocking above 200 MHz.

The bulk of microwave technology occupies the spectrum including ultra high frequency (UHF) through to super high frequency (SHF), that is, from roughly 300 MHz to 30 GHz. At lower frequencies more conventional radio techniques take over. In the extra high frequency (EHF) bands (above 30 GHz) the wavelengths are extremely short, being less than 10 mm, and hence signals at such wavelengths are called millimeter waves.

A strong and significant core of applications exists for analog and digital signals at microwave frequencies, among them:

- radars (a very large family with a wide variety of demands and techniques)
- point-to-point and point-to-multipoint multichannel radio links (microwave radio)
- satellite communications systems
- tropospheric scatter (troposcatter) systems
- cellular (mobile) communications systems, mobiles and infrastructure
- cable television (CATV) and associated cable telecommunications
- subspace communications systems (e.g., high-flying aircraft)
- microwave transceivers for optical fibre transmission
- wireless local area networks (WiFi, WLANs)

- mobile internet networks (3G and 4G, LTE, WiMAX)
- microwave instrumentation.

At least as significant as any of the applications listed above, high-speed interconnects on semiconductor chips (integrated circuits, ICs), stacked ICs (3DICs), and multichip modules (MCMs) (and also on card) are now extending into gigabit rates, which means that transmission line design issues apply. MCMs are used to provide small, high-precision interconnects that can be cost-effectively produced with larger areas than for an IC, have lateral dimensions that are comparable or perhaps larger than on-chip, and have higher performance than interconnects on printed circuit boards (PCBs). Generally the distinguishing feature is that bare (unpackaged) die can be used with PCBs, but this is usually not acceptable with PCB assembly. MCM substrates and technologies are discussed throughout this chapter and reviewed in [Section 5.9](#). PCBs are also referred to as printed wiring boards (PWBs), but we will use the term PCB here. The PWB term is more common in North America, but PCB is preferred elsewhere. PCBs are briefly considered at the end of this chapter ([Section 5.8](#)) as many of the features of these are covered in the topics considered throughout the chapter.

The appropriate type of technology and its impact on systems costing will vary greatly depending on the application. At one extreme we can consider a relatively simple vehicle proximity radar, based on a milliwatt-level Doppler or clutter-reference system, attracting a unit price of only a few dollars. On the other hand, an earth station for a satellite communications system represents a considerable capital investment costing up to hundreds of thousands of dollars.

Circuits using microstrip can be economically implemented in many low-to-medium power radars, associated electronic countermeasures, some segments of point-to-point microwave radio links, and several modules within satellite communications systems. Microstrip transmission lines are widely used in microwave (hybrid) integrated circuits (MICs), MCMs, single-chip packages, monolithic integrated circuits such as radio frequency integrated circuits (RFICs) and microwave monolithic integrated circuits (MMICs), and heterogeneous integrated packages including 3DICs.

Microstrip transmission lines require a dedicated reference ground plane for the return signal and in high-performance digital integrated circuits the need for this ground plane results in a significant cost penalty because of the required addition of a metal layer. Other structures considered here provide more economical controlled-impedance lines, but with different performance.

Before proceeding further let us pause momentarily to consider the position of coaxial and rectangular waveguide<sup>a</sup> design. The evolution of MIC technologies does not mean that coaxial line and rectangular waveguide-based design are to be abandoned; on the contrary, such propagating structures assume continuing and significant roles. However, these structures are clearly inappropriate for integration although some novel use of micromachining techniques presents some interesting possibilities.

Carefully constructed coaxial lines and rectangular waveguides are used in precision

instrumentation equipment, the network analyzer, for example, and this situation is not likely to change radically in the foreseeable future. Waveguides also remain useful in at least three areas:

- a. high-power transmission (e.g., kilowatt-to-megawatt transmitters)
- b. circuits where a very high- $Q$  component is deemed necessary (e.g., very low loss filters)
- c. some millimetric-wavelength systems (e.g., some millimeter-wave automotive radar use these as they conveniently form an antenna)
- d. very low loss transmission systems.

Developments in planar technology are already tending to overcome problems in areas (b) and (c), but not (a) or (d).

The dramatic evolution of transistor switching speeds and microwave semiconductor devices has added extra impetus to the development of hybrid microelectronics (i.e., MCMs for digital applications and MICs for microwave applications) and, more recently, RFICs and MMICs. MCMs are considered in [Section 5.9](#) and this discussion draws heavily on the topics in the sections up to then.

For many years both bipolar junction transistors (BJTs) and field-effect transistors (FETs) have been readily available for operation as microwave transistors. More recently heterostructure bipolar transistors (HBTs) and high-electron mobility transistors (HEMTs and pHEMTs) have become of great interest yielding high efficiency amplifiers. Devices based on silicon (BJTs and MOSFETs), are useful up to and above 110 GHz. Compound semiconductor, GaAs, GaN, and InP, devices are also capable of providing useful power, gain and/or low-noise performance up to terahertz frequencies. Diode devices, such as Schottky, Gunn and IMPATT, are available to cost-effectively detect or generate power at millimeter-wave and terahertz frequencies. Furthermore, it has become apparent that hybrid microcircuit technology can readily be adapted to provide MICs. This combination of thick- and thin-film hybrid microcircuit technology and ‘chip’ components such as microwave transistors has formed a powerful design vehicle for modern integrated systems. The hybrid MIC approach extends to microwave and high-speed digital MCMs.

## 5.3 Transmission Line Structures

Many planar transmission line structures have been conceived and variants are still frequently being developed; [Figure 5.1](#) depicts a collection of such structures. Each one comprises a combination of metal, shown as dense black, and dielectric, indicated by its permittivity  $\epsilon$ . The region with permittivity  $\epsilon_0$  is free-space or air. In most cases the dielectric principally supports the metal pattern, acting as a substrate, and clearly influences the wave propagation, but the image guide is an exception in that propagation is actually via the dielectric slab. The actual choice of structure depends on several factors, including the type of circuit or subsystem and its operating frequency. For example, the image line is only suitable for consideration in

millimetric wavelength applications, whereas microstrip is capable of propagating DC, or AC at frequencies up to some tens of gigahertz at least. Each type of line structure has potential advantages for various applications, and therefore each is briefly discussed here. First we expand on the term transverse electromagnetic (TEM) mode.

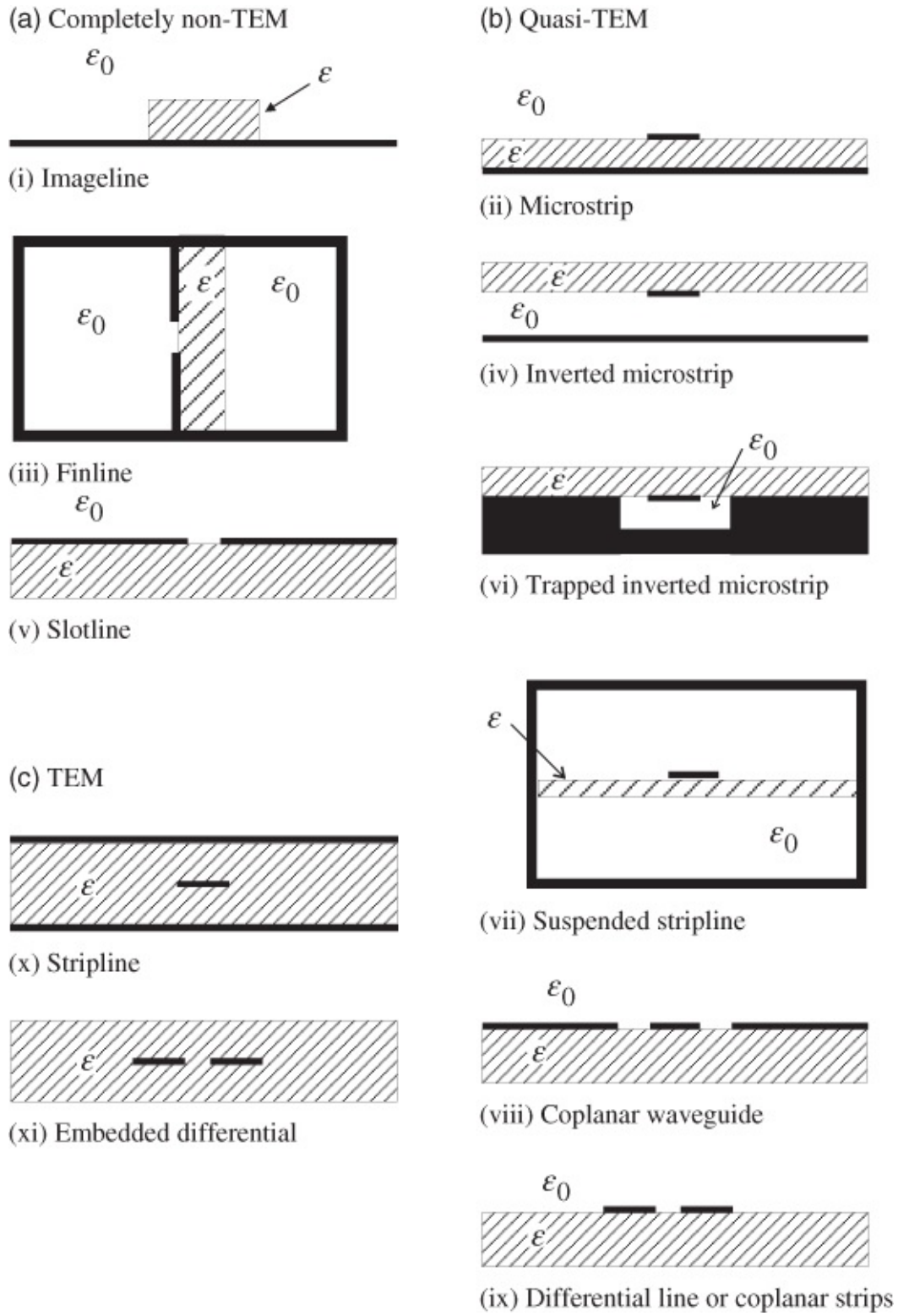


**Figure 5.1** Common transmission line structures suited to planar fabrication.

As discussed in [Chapter 2](#), the information in a signal is contained in the electromagnetic wave

and when the electric and magnetic fields are in the plane perpendicular to the direction of travel the fields are said to be TEM. If they are nearly confined to the transverse plane then they are called quasi-TEM modes. With non-TEM transmission lines the electric and magnetic fields, together, are not even approximately TEM.

### **5.3.1 Imageline ([Figure 5.1\(i\)](#))**

At very high microwave frequencies, into hundreds of gigahertz, the wavelengths become comparable with practically realistic dielectric ‘slab’ cross-sectional dimensions. If such a dielectric ‘slab’, in the form of a continuous strip of dielectric, is placed on a backing sheet of conductor it forms what is known as an imageline.

This structure then behaves like a dielectric waveguide which propagates a range of transverse electric (TE) and transverse magnetic (TM) modes<sup>b</sup> trapped within it, due principally to the dielectric-air interface. A substantial amount of work on this and related structures has been reported in the literature [1–3]. Imageline is formed by adhering a dielectric slab (or thick strip) onto a metal ground plane, and typical dielectrics which may be used include boron nitride, alumina and high-resistivity silicon (HRS). The dielectric slab is usually machined to a regular, approximately rectangular, shape.

Although unloaded  $Q$  factors of several thousand are common and operation above 100 GHz is best, many problems remain. There is poor compatibility with active devices, mutual coupling, radiation from discontinuities and bends. It is also apparent that the dielectric/metal adhesives are very lossy and this reduces the practical, loaded,  $Q$  factor. It is therefore clear that much more work is necessary before imageline, or some derivative thereof, becomes a really attractive practical proposition.

Because of these difficulties, some further low-cost contenders have been considered for operation at frequencies around and exceeding 100 GHz. One interesting possibility is afforded by dielectric-filled waveguides of approximately semicircular cross-section [4]. Although measurements have been made available at somewhat lower frequencies (28–40 GHz), unloaded  $Q$  factors of about 10<sup>3</sup> are obtained. The following advantages are also evident:

- no radiation losses, especially at bends
- line-packing density is potentially high due to the inherent shielding
- tolerance requirements in the manufacturing process will be somewhat less restrictive than for imagelines, since the flowing process involved in the manufacture of these waveguides equalizes irregularities in the longitudinal direction.

Many features, especially parameters determining predictable manufacture, need to be examined before this structure becomes useful in engineering terms.

### **5.3.2 Microstrip ([Figure 5.1\(ii\)](#))**

Although microstrip has a very simple geometric structure the electromagnetic fields involved

are actually complex. Accurate and thorough analysis requires quite elaborate mathematical treatment. However, simple approaches to the quasi-TEM mode calculations combined with frequency-dependent expressions yield quite acceptable design accuracy for many applications. Accuracies within 1% are generally achievable.

Micromachining enables microstrip lines to be fabricated on a membrane with effectively no dielectric [5–17]. This reduces loss considerable especially at millimeter-wave frequencies. Micromachining also enables the microstrip line to be partially or totally shielded and so eliminating surface waves, which can be a significant cause of loss, again at high frequencies. The line is then called a microshield line.

MICs using microstrip can be designed for frequencies ranging from a few gigahertz, or even lower, up to at least many tens of gigahertz.

At higher frequencies, particularly into the millimeter wavelength ranges, losses (including radiation) increase greatly, higher-order modes become a considerable problem, and fabrication tolerances become exceedingly difficult to meet using hybrid MICs. It is probable that the frequency limit for the extensive use of microstrip is in the region of 80 GHz. With ICs fabrication tolerances are much finer than with hybrid MICs and the options available for both microstrip and other transmission structures are extended considerably.

### **5.3.3 Finline (E-plane Circuits) ([Figure 5.1\(iii\)](#))**

With finline, a totally shielding rectangular conducting box (like a rectangular waveguide but avoiding waveguide modes) has a dielectric substrate fixed, usually centrally, across two of its faces [1, 2, 4, 18–22]. A metal circuit is deposited on one side of the substrate and a slot pattern in this metal forms the finline circuit.

It is essential to maintain an excellent continuous microwave short circuit to the upper and lower waveguide walls, but this is fairly straightforward to achieve in practice. Since the structure is connected in the E-plane (the plane of the electric field), circuits made using it are called E-plane integrated circuits. As a result, the transmission mode is also far removed from TEM. Some considerable advantages over other structures are obtained, mainly:

- a.** low losses (typically a factor about three better than microstrip)
- b.** simpler fabrication.

The second advantage, simpler fabrication, is very significant because many applications have been studied for finline at frequencies up to 220 GHz, and thus finline has to compete with structures such as inverted and trapped-inverted microstrip.

Despite some biasing problems, compatibility with solid-state devices is fairly good, especially in the case of beam-lead devices. Satisfactory bandpass filters, with approximately 10% bandwidth, have been built; quadrature hybrids, transitions to waveguide, and balanced mixer circuits have also been designed and manufactured. Discontinuities in finline have been analyzed on a modal basis, and the results have been presented in a form appropriate to the design of impedance-transforming and filter networks.

### **5.3.4 Inverted Microstrip ([Figure 5.1\(iv\)](#))**

With this arrangement the strip conductor pattern is manufactured in the same manner as for the microstrip. The main difference is the absence of any conductor on the opposite side of the substrate, a ground plane is air-space separated instead. Thus the substrate mainly supports the microstrip lines and most of the field lies within the air between the strip and the ground plane. This ensures that the wavelength is long relative to that in conventional microstrip operated at similar frequencies. It also infers that inverted microstrip can be operated satisfactorily at substantially higher frequencies and this has been achieved [23]. Compared with conventional microstrip, a wider line is obtained for a prescribed characteristic impedance, and this both reduces conductor dissipation and relaxes fabrication tolerances. The inverted microstrip interconnect leads to higher  $Q$  components than achievable using microstrip. Thus, for example, lower loss filters can be fabricated using inverted microstrip.

### **5.3.5 Slotline ([Figure 5.1\(v\)](#))**

This transmission line structure consists of a dielectric substrate metallized on one side only. The metallization has a narrow slot etched into it to form the slotline. The structure was first proposed by Cohn in 1968 and an extensive treatment is given in [Chapters 15](#) and [16](#).

Some clever circuit applications have been devised, but the following disadvantages should be noted for slotline:

- a. Characteristic impedances below about  $60 \Omega$  are difficult to realize.
- b. Circuit structures often involve difficult registration problems (especially with metallization on the opposite side to the slot).
- c. The  $Q$  factor is significantly lower than the other structures considered here.

There is another important derivative of slotline. When the conductors are made finite, that is, restricted such that we have two adjacent strips differentially driven and on one side of the substrate only, this structure is termed CPS, described in [Section 5.3.8](#).

### **5.3.6 Trapped Inverted Microstrip ([Figure 5.1\(vi\)](#))**

Trapped inverted microstrip (TIM) is similar to the inverted microstrip, except that now the ground plane is made into a slot- or ‘channel’-shaped section, effectively grounding and shielding three planes away from the strip conductor. This provides for inherent suppression of some higher-order modes which could otherwise propagate.

Both inverted microstrip and TIM structures are potential candidates for applications at frequencies extending up to and through 95 GHz, that is, for millimetric wave applications. Manufacturing difficulties are, however, considerable due to the tight fabrication tolerances that must be imposed on conductor/ground-plane spacing and channel dimensions. This is particularly significant with hybrid MICs, but may be less so when fabrication is on-chip (RFIC, MMIC, or 3DIC). Advances in micromachining of interconnects is allowing this structure to be revisited.

### **5.3.7 Coplanar Waveguide ([Figure 5.1\(viii\)](#))**

Although CPW supports a quasi-TEM mode of propagation, the actual shape of the structure is distinctly different from any of those considered so far because the “active” metallization and the ground planes are formed on one side of the substrate alone. Each ‘side-plane’ conductor is grounded and the center strip carries the signal; thus much less field enters the substrate when compared with microstrip. In conventional CPW the ground planes extend indefinitely but in finite ground CPW (FGCPW) the extent of the grounds is limited and this results in reduced coupling of adjacent and crossing CPW lines. Considerable design information is available and the structure has been used in many applications ranging upwards in complexity to complete amplifiers and subsystems. Semiconductor diodes or complete MMIC chips may be strapped across or ball-grid bonded on to the intermetallic gaps, meaning that there is often no need to drill the substrate or to etch vias into semiconductor substrates. An important modification is afforded by the conductor-backed CPW in which the opposite side of the substrate (the backside) is also metallized and often segmented to decrease losses.

[Chapter 14](#) deals with CPW in considerable detail, and also provides extensive references.

### **5.3.8 CPS and Differential Line ([Figures 5.1\(ix\) and \(xi\)](#))**

This simple transmission structure is formed by having just two conductors deposited on the same substrate, with no other conducting layer. This is shown in two forms: as a surface line in [Figure 5.1\(ix\)](#) and as an embedded line in [Figure 5.1\(xi\)](#). In both structures the possible existence of ground planes (as in microstrip or stripline) is incidental and ideally these should not influence the field pattern. Essentially, the substrate merely acts as a mechanical supporting element and a quasi-TEM mode forms the main propagating field distribution. In one realization, one of the conductors is grounded, and this form is called a coplanar stripline or coplanar strips (CPS) [24–34]. In this configuration CPS is used as an area-efficient variation of CPW. When neither of the conductors is grounded and the line is driven differentially, the interconnect is called differential line. Differential line is used extensively with RFICs and in critical nets in high-speed digital ICs. The two forms essentially have identical electrical characteristics with differences resulting from interaction with other metallic structures such as ground planes.

For a hybrid MIC this simple approach does not work well because of radiation losses and over-moding. However, the expansion of monolithic technology has rekindled interest in the differential line and work is developing intensively on the design and realization of this technology. This line is also popular for use in long bus lines and clock distribution nets on chip as the signal return path is well defined and the cross-sectional geometry is uniform along the interconnect's length (and hence the interconnect has a controlled impedance) and is on the same metallization layer as the signal path. This interpretation of the current paths, a signal path and a current return path, is not quite correct as neither metallization can be identified as the ‘ground’ reference for the other. Differential line and CPS are discussed in detail in [Section 14.8.4](#).

### **5.3.9 Stripline ([Figure 5.1\(x\)](#))**

This basic structure predates microstrip and any of the other planar transmission options described in this book. It comprises a completely filled microstrip, that is, a symmetrical structure somewhat like a coaxial line completely flattened out and rectangularized so that the center conductor is a rectangular metal strip and the outer grounded metal is simply a rectangular box. This is similar to microstrip in a box, the entire structure is filled with dielectric, and therefore the transmission is entirely TEM and dependent on the relative permittivity  $\epsilon_r$  explicitly. The wavelength is therefore simply the free-space value divided by the root of  $\epsilon_r$ . Further design criteria associated with stripline are developed in appropriate sections throughout this book.

If the ground “plane” is made to totally enclose the structure, with air gaps at top and bottom, we have suspended stripline ([Figure 5.1\(vii\)](#)). Although the losses are all relatively low, resulting in a fairly high  $Q$  factor, waveguide modes can easily be excited at higher frequencies. This could possibly be prevented by bringing the top and bottom walls very close together and/or by introducing various structures to act as mode suppressors. In the first place the separations become so small that there is insufficient space for the incorporation of semiconductor devices, etc., and the introduction of mode suppressors represents a new design problem. In any case, the basic structure is not compatible with shunt-mounted semiconductor devices.

### **5.3.10 Summary of Interconnect Properties**

For circuit applications the characteristic impedances and  $Q$  factors achievable with these various structures need to be known. [Table 5.1](#) lists the ranges of characteristic impedance that may be expected. These values are the practically realizable values determined by what can be fabricated given manufacturing tolerances and avoiding multimoding.  $Z_0$  varies as the inverse of  $\sqrt{\epsilon_r}$ , although this is modified slightly by the cross-sectional geometry of the line for non-homogeneous media such as open structures.

**Table 5.1** Characteristic impedance ( $Z_0$ ) ranges for the various structures with a substrate relative permittivity of 10

Structure	$Z_0$ ( $\Omega$ )
Microstrip	10–110
Inverted microstrip	11–130
Trapped inverted microstrip (TIM)	14–140
Suspended stripline	40–150
Coplanar waveguide (CPW)	40–110
Differential line, coplanar strips (CPS)	40–110
Slotline	35–250
Finline	10–400
Imageline	$\approx 26$

Each of the quasi-TEM structures is capable of being designed at lower characteristic impedances than those indicated in [Table 5.1](#). The general technique is simply to increase the width of the strip conductor, but this results in a risk of transverse resonance modes (dealt with in detail for microstrip in [Section 7.8](#)). At low-to-moderate frequencies microstrip impedances down to just below  $10 \Omega$  are thus achievable.

In most cases, the upper limit to characteristic impedance is set by manufacturing tolerances and the unreliability associated with a very narrow strip. For the quasi-TEM lines, especially microstrip, this is an embarrassment, since some circuit applications (e.g., RFICs) can demand  $Z_0 > 150 \Omega$ . Unless slotline or finline can then be used, alternative clever circuit/system design is necessary.

The characteristic impedance range of finline is remarkably large,  $10–400 \Omega$ , which is more than adequate for nearly all conceivable filter or matching network applications. On the other hand, the characteristic impedance of imageline is restricted to around one value ( $\approx 26 \Omega$ ), which is a further drawback with this structure. However, several useful circuits have been developed employing various directional couplers, ring resonators, etc. which do not depend on changes in characteristic impedance for their design and operation [4]. Unloaded  $Q$  factors are of great importance in resonant circuit applications (e.g. matching networks and filters) and these are indicated in [Table 5.2](#).

**Table 5.2** Comparison of typical unloaded  $Q$  factors ( $Q_u$ ) at a frequency of 30 GHz for the structures shown in [Figure 5.1](#). The substrate permittivity is 10 for all structures except finline, where it is 3.3

Structure	Unloaded $Q$ , $Q_u$
Microstrip	250
Inverted microstrip	400
Trapped inverted microstrip	450
Suspended stripline	600
Coplanar waveguide	200
Differential line, coplanar strips	200
Slotline	200
Finline	550
Imageline	2500

Most of the results are typical practical values, but imageline suffers dramatic reductions in unloaded  $Q$  factors when any bending or other shape discontinuity is introduced. The integration of multifunction circuits, especially for millimetric wave applications, is likely to require the use of more than one type of transmission structure to achieve the desired level of performance. Transitions would also be required to efficiently couple energy from one structure into another, for example waveguide to imageline, imageline to finline, TIM to finline, etc.

## 5.4 Substrates for Planar Transmission Lines

### 5.4.1 Substrate Choices

Many facets, mechanical and thermal as well as electronic and economic, influence the decision process leading to the correct choice of a particular substrate for a specific type of hybrid circuit and application. The kinds of questions that should be asked must include:

- Can the cost of the substrate under consideration be justified in the light of the application and attendant circuit/system costs?
- Is the technology to be thin- or thick-film?
- What frequency range or ranges are involved? (This will influence thickness and permittivity.)
- Will the surface finish be sufficiently good to keep conductor losses tolerably low, yet maintain metal-film adhesion?
- Are the mechanical strength and thermal conductivity sufficient for the application in mind?

- Are the substrates readily available with sufficient surface area, considering the circuit complexity and the operating frequencies?

This is not an exhaustive list and other considerations may well arise in certain situations. Before comparing materials it is useful to list a variety of possible substrate materials; these are shown in [Table 5.3](#). We now consider the three major hybrid microcircuit substrates and also a fundamental benchmark substrate, namely sapphire. We will return and consider two of these in much more detail later (PCBs and ceramic substrates in [Sections 5.8](#) and [5.9](#)).

**Table 5.3** Properties of some typical substrate materials. GaN is typically used as an epitaxial layer on Si or SiC and so the dielectric properties of Si or SiC are used. Most hard substrates (including semiconductors) have thermal conductivities in the range of 1 to 40 W/(m · K). Important exceptions include GaN (150 W/(m · K)), quartz (500 W/(m · K)) and silicon (138 W/(m · K)). Dielectric strengths range from 300 V/cm to 4 kV/cm. Many types of soft substrates are available. Soft substrates mostly have permittivities in the range  $2.0 \leq \epsilon_r \leq 6.1$  (lower than for hard substrates), dielectric loss tangents in the range  $0.0012 \leq \tan \delta \leq 0.005$  (higher than for hard substrates), dielectric strengths in the range of 140 to 240 kV/cm (much higher than for hard substrates) and thermal conductivities in the range 0.26 to 0.76 W/(m · K) (slightly lower than for hard substrates). Extensive substrate data is given in Appendix C.

Soft substrates	$\epsilon_r$ at 1 GHz	$\tan \delta$ at 1 GHz
Polyimide	3.2	0.005
FR4 circuit board	4.3–4.5	0.001
Teflon®	2.1	0.0003
Hard non-semiconductor substrates	$\epsilon_r$ at 1 GHz	$\tan \delta$ at 1 GHz
Alumina		
99.5%	10.1	0.0001–0.0002
96%	9.6	0.0006
85%	8.5	0.0015
Aluminum nitride	8.9	0.001
Sapphire (single crystal)		
$\perp$ plane	9.4	0.00004–0.00007
$\parallel$ plane	11.6	0.00004–0.00007
Glass (borosilicate)	6.1	0.0009
Quartz, fused	3.8	0.00075
Hard semiconductor substrates		
GaAs	12.85	0.0006
GaN (Wurtzite crystal)		
$\perp$ plane	9.5	—
$\parallel$ plane	10.4	—
InP	12.4	0.0004–0.0007
Silicon, high-resistivity ( $> 30 \Omega \cdot \text{cm}$ )	11.9	0.001–0.01
SiC	10.8	0.001

## 5.4.2 FR4 (PCB)

This substrate material is basically designed for conventional low-frequency printed circuit (or printed wiring) boards. It can be used at much higher frequencies, into the cellular bands, but losses increase rapidly and design is imponderable because of the great variability in basic substrate properties. For RF transmission, or very-high-speed pulse transmission, it is essential that the permittivity and thickness of any substrate are both known accurately and can be held repeatedly. FR4 is therefore unsuitable for many microwave applications.

## 5.4.3 Ceramic Substrates

Alumina, a typical ceramic used, is well suited for production circuits functioning at frequencies up to about 40 GHz. The grade to be used depends on a number of factors, including the choice of basic fabrication technique: thick-film or thin-film. Comparatively high conductor and dielectric losses and poor reproducibility usually exclude the choice of 85% purity (or worse) material. Since alumina substrates have become very popular for manufacturing circuits to operate at any frequency up to about 40 GHz (although higher is possible), a further table is now presented ([Table 5.4](#)) which summarizes some important features regarding alumina substrates.

**Table 5.4** Some specific observations regarding alumina substrates

Permittivity: average values	Within the approx. range $8.2 \leq \epsilon_r \leq 10.2$ Depends on purity and other factors
Permittivity: batch-to-batch variation	Considerable, therefore has to be taken into account in design (worsens with deteriorating purity)
Permittivity: material dispersion	Significant variation of $\epsilon_r$ with frequency through microwave frequencies (e.g., 8–12 GHz for some aluminas) Some dipolar behaviour, amount depends on impurities
Dielectric loss ( $\tan \delta$ )	Generally $< 1 \times 10^{-3}$ ( $1 \times 10^{-4}$ for > 99.5% purity material)
Anisotropy	Present to varying extents Depends on method of manufacture (caused by preferential orientation of crystallites)
Surface roughness	Around 5 $\mu\text{m}$ for 99.5% and 50 $\mu\text{m}$ for 85%
Surface flatness	Bowing can often occur to a significant extent with cheaper substrates (not necessarily just low-purity substrates)

A wide variety of commercially available substrates exists. Extensive microstrip measurements indicate that the maximum permittivity of high-purity substrates must be slightly less than 10.13 (the weighted value for sapphire, see [Section 5.4.4](#)).

Ceramic substrates such as high-temperature co-fired ceramics (HTCCs) are also used as the

basic medium for MCMs.

Low-temperature co-fired ceramics (LTCCs) have become very popular for ceramic substrate applications including MCMs and single-chip packages. They have tightly controlled tolerances, as shown in [Table 5.5](#), and can be stacked in 80 layers or more. As with all fired ceramics, metal patterns are printed on soft un-fired material using a thick film process. (The thick film process is discussed extensively in [Section 5.6](#).) Holes for vias are puched in the un-fired layers and are filled in the metallization process. The layers are then stacked, compressed, and fired when they soften, flow and shrink. The key to the process is the tight control of shrinkage.

**Table 5.5** Specific properties of LTCC materials

Parameter	Value	Tolerance
Permittivity ( $\epsilon_r$ )	7.8	$\pm 0.1$
Conductor thickness ( $\mu\text{m}$ )	9	$\pm 2$
$x-y$ shrinkage (%)	12.7	$\pm 0.3$
$z$ shrinkage (%)	15	$\pm 0.5$
Tape thickness tolerance (%)	—	$\pm 7$
Line width tolerance ( $\mu\text{m}$ )	—	$\pm 13$

#### 5.4.4 Sapphire—the ‘Benchmark’ Substrate Material

The weighted average permittivity of sapphire is within the range 10.1 to 10.3. This average can be calculated quite accurately by noting crystal orientations:

$$\epsilon_r \text{ (sapphire → average)} \approx \frac{1}{3}(2\epsilon_{\perp} + \epsilon_{\parallel}). \quad 5.1$$

Substituting  $\epsilon_{\perp} = 9.4$  and  $\epsilon_{\parallel} = 11.6$ , we obtain:

$$\epsilon_r \text{ (sapphire → average)} \approx \frac{1}{3}(18.8 + 11.6) = 10.13. \quad 5.2$$

The very highest grade of polycrystalline alumina has this bulk permittivity.

Although sapphire is usually the most expensive substrate likely to be entertained for hybrid MICs, it does offer some unique advantages:

- It is optically transparent, hence chip devices can be accurately registered for attachment since the underside may be viewed.
- It has a fairly high permittivity (around 10). This is almost compatible with high-resistivity silicon. It also means that microstrip components are fairly small due to the reduced wavelength.
- Sapphire substrates are highly reproducible; all pieces are essentially identical in

dielectric properties and they are not subject to bowing.

- Surface finish is optical grade, which results in low power loss from surface roughness.
- Thermal conductivity is quite high, being about 30% higher than the best alumina.

Against these advantages, and apart from the relatively high cost, we must bear in mind that sapphire substrate areas are limited (usually little more than 25 mm square) and the dielectric anisotropy poses some additional circuit design problems.

## 5.5 Thin-film Modules

Microwave-grade hybrid circuits place stringent demands on the accuracy and repeatability of the circuit technology. These demands can be met by carefully controlled thin-film manufacturing processes, which are therefore used for the great majority of MICs.

Various metals form the bulk material with gold, silver, copper and aluminum being in common use. Owing to its superior conductivity and also its lower price, copper is preferred, but a final gold film must be evaporated over the copper to provide an environmental protective layer. The necessary thickness of the metal film may be determined by considering the skin depth in the metal at the lowest frequency of interest. Taking this lowest frequency to be about 4 GHz, the skin depth in copper is then approximately 1  $\mu\text{m}$ . At least four skin depths are recommended, and therefore the required thickness should be 4–5  $\mu\text{m}$ . The processes actually used for making the circuit may be visualized, rather crudely, as precision (small-scale) printed circuit processes. Practical techniques involve three main steps:

- a. Evaporation or sputtering a thin ‘seed’ layer of a suitable metal on to the surface of the substrate.
- b. Evaporating or sputtering a thin layer of conductor metal on to this ‘seed’ layer.
- c. Electroplating the bulk conductor metal on to layer (b).

Steps (a) and (b) provide, respectively, mechanical and electrical foundation layers on which to electroplate good-quality bulk conductor metal. The techniques differ chiefly in the choice of evaporation or sputtering, and in the manner in which (using photolithographic methods) the circuits are defined. In one well-proven technique [35], step (a) comprises approximately 200  $\text{\AA}$  of chromium, step (b) comprises a layer of copper of similar thickness, and approximately 5  $\mu\text{m}$  of copper is plated in step (c). The thin layers are produced by magnetron sputtering [36] where the combined electric and magnetic fields produce efficient ionization of the metal (copper). The ions are attracted towards the substrate target, which behaves as an anode.

Circuit definition may be accomplished either by a plate-through technique or by an etch-back technique, and each of these techniques is now described.

### 5.5.1 Plate-through Technique

Substrates that are cleaned to a high specification have their surfaces sputter coated as

explained above. Next, a photoresist layer, of similar thickness to the final metal film required, is ‘spun’ on to the surfaces. Exposure with ultraviolet light through a precision contact photomask (with the required circuit pattern) is followed by subsequent processing to yield a pattern of slots in the photoresist layer. The copper is plated through these slots to form the circuit pattern and then the photoresist layer is washed away and the excess sputter coating is etched off. There are further details in reference [35].

### **5.5.2 Etch-back Technique**

Again, the process starts by coating the substrates with thin films of metal by sputtering, exactly as explained before, and a photoresist layer is also spun on to the surfaces. In this case, however, the photomask exposure step is arranged so that those larger areas of the surface where metal is not required are left unprotected by the photoresist layer. Thus, at this stage the circuit pattern is effectively defined by a fine pattern of the photoresist layer across the very thin sputtered layers. Etching-back then removes the unwanted areas of metal which were originally sputtered on. Electroplating yields the desired final thickness. This technique has the following advantages:

- a.** A thinner photoresist layer may be used, typically  $0.5 \mu\text{m}$ .
- b.** Plating is more uniform.
- c.** Microstrip edges are relatively square.

However, for the thinner photoresist layer to work satisfactorily, the substrate surface must be extremely smooth and free from dust or grit (otherwise the layer becomes perforated). Sapphire substrates, with their optical surface finish, are very good in this respect.

### **5.5.3 Equipment Required**

For precise and repeatable circuit production the following items of equipment are recommended:

- Class 10000 clean room, achieving class 500 in the main working area.
- Sputtering system operating in high vacuum, typically of the order of  $10^{-6}$  Torr.
- Vacuum spinner, having adjustable speed in the range 1000–7000 revs/min, and timer.
- High-intensity collimated ultraviolet light source, for exposing photoresist layers.
- Ultrapure water (UPW) system, delivering water of about  $18 \text{ M}\Omega$  resistivity.

Many other details should be considered by anyone contemplating the establishment of a thin-film circuit manufacturing facility, and the paper by Ladbrooke *et al.* [35] treats the topic very well, as do Jensen[37] and Sergent [38].

### **5.5.4 Thin Resistive Films**

Resistive films are required for many types of MICs, including circuit elements such as

terminations, bias networks and attenuators. These resistive films must have a low temperature coefficient of resistivity and be of good stability. Commonly used resistive materials include nichrome and tantalum. Resistance values within the range 50–5000  $\Omega$  typify MIC requirements and such values can readily be realized by the deposition of films using these materials. With abrasive trimming or, alternatively, laser trimming it is possible to achieve resistance tolerances to an accuracy exceeding 1%. The creation of these resistive films demands additional processes of deposition and etching beyond those of the thin-film metallization described above, and this complexity may be obviated by bonding chip resistors directly onto the conducting pattern (i.e., using surface mount or flip-chip components).

## 5.6 Thick-film Modules

Thick-film technology has become well established in the low-cost manufacture of hybrid microcircuits at lower-than-microwave frequencies and for densely packaged digital subsystems [39]. Large advantages in cost reductions are obtainable compared with thin-film technology, and even more so with monolithic integrated circuit technology, especially where small batch production runs are involved.

Thick-film materials and techniques have been developed for MICs operating at frequencies up to at least 40 GHz [36]. The losses associated with thick-film conductors have been shown to be (typically) about 20% worse than those associated with comparable thin-film conductors and this limitation, combined with tolerancing difficulties, tends to restrict production circuits to a maximum frequency of around 10 GHz. Circuits such as parallel-coupled and open-circuit stub filters, compensated couplers, attenuators and power levellers have all been satisfactorily realized.

Two methods are commonly encountered for the manufacture of thick-film cheap MICs:

- a. Thick-film patterns are printed and fired on to the ceramic substrate—usually alumina or an LTCC substrate, but occasionally quartz [36, 39–41].
- b. A printed circuit technique is used to etch the desired pattern in the copper cladding of what is usually a plastic substrate (see [Table 5.3](#)).

Either method is substantially simpler and less demanding on both equipment and environment than thin-film technology. Method (b) is very well known and need not be described here. Method (a) is used for LTCC, MIC, and single-chip package manufacture to an increasing extent and therefore it will be briefly described.

### 5.6.1 Pastes, Printing, and Processing for Thick-film Modules

The metal that will ultimately form the microcircuit conductors, often gold or silver but increasingly a copper-based material, is initially available to the circuit manufacturer as a paste or ‘ink’ contained in a jar. A few milliliters of this paste are placed on a fine-mesh “screen,” with areas open for the circuit pattern, and some of the paste is squeezed through these open areas and on to the surface of a substrate held rigidly just beneath the screen.

Settling, drying, and firing sequences complete the thick deposit, a very high proportion of which is pure metal. Although the process has earned the generic name ‘thick film’ the actual film thicknesses are only usually about twice that of thin films, that is, 10  $\mu\text{m}$  or so. The best way to explain the process is to briefly describe each step, and so we start with the pastes.

- a. The conductor pastes are special “fritless” materials. For substantial shelf life pastes should be kept in a refrigerator.
- b. The artwork is prepared using similar procedures to those described for thin-film technology and photographic processing is then used to obtain a positive transparency.
- c. Suitable screens are available, often with dimensions about 15  $\times$  20 cm and made of at least 305 mesh stainless steel or polyester. These are stretched to drum tightness over a rigid frame which will fit into the screen printer. They are also coated with a suitable photoresist layer.
- d. The positive transparency obtained in step (b) is held in intimate contact (image side) with the coated surface of a screen, and then standard ultraviolet exposure and wash-and-bake processes leave a screen with apertures for the required circuit. All other areas of the screen are then opaque with a durable photoresist layer.
- e. This screen is placed in a printing jig (preferably a machine with well-defined adjustments and controls). The substrate which is to receive the circuit is placed beneath the aperture region of the screen, with accurate registration. This substrate is held firm by vacuum suction and is usually about one substrate thickness clear of the base of the screen.
- f. A few milliliters of conductor paste are placed on the screen between the squeegee and the aperture region.
- g. When the parameters have all been optimized, the aperture region of the screen is wet and the action smooth, a satisfactory wet deposit of paste will be transferred on to the substrate.
- h. This wet-circuit deposit must be left to settle by placing it horizontally in a clean area for about 15 minutes. Following this it is dried at approximately 1000°C for about 15–20 minutes under an infrared drying unit.
- i. The firing process returns the material of the deposit to a predominantly metallic substance of high electrical conductivity. For gold-suspension pastes this generally entails about 10 minutes at a temperature set somewhere in the range 900–1000°C, depending on the specification of the paste.
- j. Immediately after firing the circuit is, in principle at least, ready for use.

In many instances, however, the precise definition required cannot be achieved with the as-fired circuit, and either laser trimming or an etch-back process is necessary. This is especially a problem in proximity-coupled microstrips, which are often required in MICs [21, 36].

As noted above, there exists a requirement for resistive films and these can also be provided in thick-film form. The deposition and processing mainly follows the steps given above for

conductive films except that the firing profile is more critical since, in conjunction with the resistive paste formulation, it controls the final resistivity of the film.

## 5.7 Monolithic Technology

### 5.7.1 Introduction

Conceptually, electronic integrated circuits (ICs) comprise the simultaneous, or near simultaneous, processing of all electronic functions within a semiconductor chip. At lower frequencies, and in by far the greater number of electronic applications, the basic semiconductor material used is silicon. At microwave frequencies silicon-based analog ICs are known as RFICs and extensively use differential circuits. ICs based on compound semiconductors are called MMICs and achieve much functionality using transmission line-based circuits. Silicon ICs that use transmission line-based functional units are sometimes called Si microwave millimeter-wave integrated circuits (SIMMWICs) [42].

Semiconductor substrates of suitable form for MMICs must have high resistivities, in the order of 2000  $\Omega \cdot \text{cm}$  or more, in order to maintain the transmission losses at sufficiently low levels, and also to provide enough isolation between components on the chip. HRS, semi-insulating gallium arsenide (GaAs), and other compound semiconductors such as GaN meet this requirement. In fact, semi-insulating GaAs provides significantly higher resistivity than does HRS (by a factor of well over 100). Indium phosphide (InP) represents another useful semiconductor, particularly for millimeter-wave applications and mixed microwave/optoelectronic. A comparison of the most important semiconductor substrates is given in [Table 5.6](#).

**Table 5.6** A selection of semiconductor substrates (mainly from Ponchak *et al.* [46]).

Substrate	Relative permittivity, $\epsilon_r$	Loss tangent, $\tan \delta$	Typical thickness, $h$ (mm)
Si <sup>1</sup>	11.9	$4 \times 10^{-3}$ at 30 GHz	0.36
Si <sup>2</sup>	11.9	$1 \times 10^{-4}$ at 30 GHz	0.36
GaAs	12.85	$5 \times 10^{-4}$	0.5
GaN	8.9	—	0.5 $\mu\text{m}$ thick GaN on SiC substrate 0.5–10 $\mu\text{m}$ thick GaN on sapphire substrate
InP	12.4	$5 \times 10^{-5}$	0.6

<sup>1</sup> Standard silicon with conductivity approximately 1000  $\Omega \cdot \text{cm}$ .

<sup>2</sup> HRS with conductivity approximately 4000  $\Omega \cdot \text{cm}$ .

Other suitable semiconductors include silicon-germanium (SiGe), which is being promoted by several companies, and silicon carbide (SiC) for very-high-stress and high-temperature applications.

Various lithographic processes are used to delineate device geometries and circuit patterns in ICs. For example, with photolithography, diffraction effects limit the resolution of microstrip and other lines to dimensions in the order of a wavelength of light. For substantially higher resolution electron beam lithography is used, particularly for the realization of deep submicron gates for devices, to operate at the higher microwave and into millimeter-wave frequencies. Combined processing techniques, using the best features of photolithography and electron beam lithography, are often used in the fabrication of commercial MMICs. Since passive circuit patterns use precisely the same lithographic techniques that are employed to define submicron transistor gates it follows that dimensional tolerances in the circuit patterns using this technology are controlled far more closely than they are in hybrid microelectronic technology.

In this text we are principally concerned with the design of hybrid and monolithic circuits, with a specific emphasis on the circuit design itself, that is, not active devices. Therefore in our brief discussion of monolithic technology here, we shall exclude any details regarding the processes required for the realization of active devices.

### 5.7.2 Multilayer Interconnect

The transmission medium options available to the RFIC or MMIC designer include a selection of those described earlier in this chapter: microstrip, slotline, differential line, CPW, CPS, and (possibly) inverted microstrip.

As described above, all forms of integrated circuits (whether microwave or otherwise) require technologies for interconnecting between several layers. Transistor drains and gates, and power requirements and connections between other devices such as lumped passive elements ( $C$ ,  $R$ ,  $L$ ) all demand conductive interconnections across layers.

Whilst the layers themselves must be formed, for microwave chips, using one or more of these transmission medium options, vias are necessary [43]. The general arrangement is shown in [Figure 5.2](#). In [Figure 5.2](#) several vias are shown, connecting between CPW and microstrip lines located in various regions of the chip. The structure can be continued longitudinally to reduce the resistance of the interconnect and skin effect.

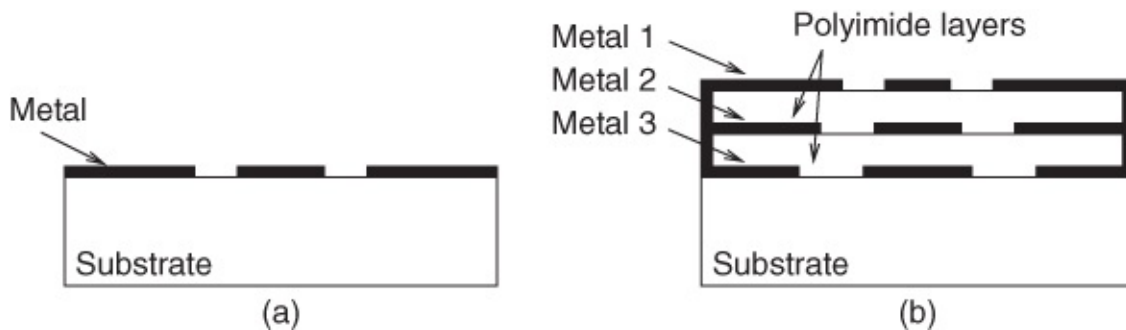


[Figure 5.2](#) Cross-sections: (a) conventional CPW; and (b) “inverted-V” CPW showing vias connecting conductor layers.

These entire structures, the active and passive devices plus the transmission lines and the vias, must all be modeled using CAE software that is proven fundamentally capable and reliable

over the frequency range or time intervals demanded by the circuit function. The demands on such software intensify as frequency increases (or time intervals decrease) towards the high tens of GHz ranges.

In general, never believe just what the software models are predicting alone, always seek additional support from measurements if possible. At the very least, ensure that predicted (computed) data makes sense in terms of engineering fundamentals. When two sets of predictions, derived from two completely independent CAE packages, agree reasonably closely then more confidence may be placed in either package regarding predicted results.

### **5.7.3 Metallization**

A variety of metals have been used to form the metal layers in MMICs, notably gold, copper and aluminum. Gold represents a relatively expensive solution, but its conductivity is not particularly high and in any event the process is less environmentally acceptable than other approaches. The major advantage with gold is the self-passivation effect—the metal resists corrosion and will not form alloys with other materials. In monolithic integration its use is restricted to MMICs.

Aluminum has traditionally been used for Si-based ICs. It is inert with Si and  $\text{SiO}_2$  but its conductivity is markedly worse than copper. Copper is an excellent electrical conductor but has some disadvantages in that it readily forms intermetallic compounds with several semiconductors, including silicon, and it has electromigration problems.

Aluminum-copper mixtures are also used because this approach provides the best compromise to exploit the advantages of each metal whilst avoiding the main problems associated with either metal on its own. Copper with buffer layers of other metals is also used.

For ICs having feature sizes below  $0.18 \mu\text{m}$  the use of copper, copper alloys, or copper with buffer layers is essential. As the feature size is reduced the resistance of the conductors, now with smaller cross-sections, increases and, as has been noted, the delay of a resistive line depends strongly on the resistance — the higher the resistance the longer the delay.

### **5.7.4 Low- $k$ Dielectrics**

Conventionally silicon-based integrated circuits have used aluminum conductors and silicon dioxide ( $\text{SiO}_2$ ) insulators between the conductors. For higher speeds it is necessary to use insulator materials with permittivities below that of  $\text{SiO}_2$  (4.0–4.2) to reduce the self-capacitance of lines and also to reduce the mutual capacitance of neighbouring interconnects.

Zarkesh-Ha *et al.* developed a simple formula for the speed improvement in a digital IC that can be achieved by replacing the conventional Al metallization and  $\text{SiO}_2$  dielectric [44]. For long interconnects, so that the interconnect delay dominates timing, the fractional reduction of the critical path delay with the modified material system relative to the Al/ $\text{SiO}_2$  system is [44]

$$\frac{\Delta T_{\text{CRITICAL}}}{T_{\text{CRITICAL}}} = \frac{\Delta \rho}{\rho_{\text{Al}}} + \frac{\Delta \epsilon}{\epsilon_{\text{SiO}_2}} - \left( \frac{\Delta \rho}{\rho_{\text{Al}}} \frac{\Delta \epsilon}{\epsilon_{\text{SiO}_2}} \right)$$

where  $\rho$  is the resistivity. Now the ratio of the copper resistivity to that of aluminum,  $\Delta\rho/\rho_{\text{Al}}$ , is 39% and, using a relative permittivity of 2.5 for the low- $k$  dielectric, the ratio of the low- $k$  permittivity to that of  $\text{SiO}_2$ ,  $\Delta\epsilon/\epsilon_{\text{SiO}_2}$ , is 36%. Then the ultimate speed improvement is 39% if Cu alone is used, 36% if the low- $k$  material alone is used, but when combined the improvement is 61% less than would be expected by considering the technologies individually. The actual improvement obtained would be somewhat less than this as critical timing is also determined by gate delay.

Considerable efforts are being directed at developing ultra-low dielectric constant materials for IC interconnects. The aim is to develop materials with adjustable relative permittivity to 1.5. Materials being investigated include inorganic materials derived from organosilicate polymers and organic thermosetting polymers. The technical challenges include developing a material which does not produce pores, has sufficient mechanical strength that capping layers are not needed, and can be deposited using low-cost manufacturing techniques.

### 5.7.5 Hybrid and Monolithic Approaches Compared

An outline comparison of hybrid MIC and monolithic MMIC technologies, focusing on their respective features and attributes, is provided in [Table 5.7](#). An excellent detailed coverage of economics, costs and other comparative aspects of MIC versus MMIC technology is provided by Sweet [45].

**Table 5.7** MIC/MMIC technology: manufacturing costs and operational capability comparisons

Technology	Approximate capital cost for fabrication facility <sup>1</sup> (US\$)	MM-wave capabilities?	Volume applications?
Thin-film hybrid MICs	$10^4$ – $10^6$	Yes, to well over 100 GHz	Not usually <sup>2</sup>
Thick-film hybrid MICs	$10^3$ – $10^5$	No, maximum perhaps to around 20 GHz	Not usually <sup>2</sup>
MMICs	$10^6$ – $10^8$	Yes, to 1000 GHz	Yes, well suited
			to high volume <sup>3</sup>

<sup>1</sup> Order-of-magnitude indications of the start-up capital requirements for an MIC or MMIC fabrication facility.

<sup>2</sup> Hybrid MICs are best restricted to low-to-moderate volume applications on economic grounds.

<sup>3</sup> There are many considerations apart from volume that may influence the decision to realize a circuit in MIC or MMIC form. Monolithic realization has certain specific technical advantages over hybrid approaches.

# 5.8 Printed Circuit Boards

PCBs are of two main types:

- a. Organic PCBs use organic resins generally reinforced with fibres but also with ceramic particles to form a rigid structure.
- b. Ceramic PCBs use ceramics as the dielectric layers. The conductor patterns are formed using a variety of processes. Ceramic PCBs include thin-film and thick-film modules, discussed previously.

In the next two subsections we review the essential properties of PCBs. The reader is referred to Brzozowski [47] for an extensive treatment of PCBs.

## 5.8.1 Organic PCBs

Organic PCBs are composed of dielectric layers that are conductor clad, generally with copper. The dielectric layers are formed from organic resins that are reinforced by fibres to form a rigid structure. The reinforcing material is referred to as a fabric and is generally woven. Typically the copper is patterned, that is, selectively coated by photoresist applied using silk-screening or photo imaging. Then the copper is etched. Vias are formed by drilling or punching through one dielectric layer at a time. The final stage of the fabrication process involves compression bonding the individual metallized dielectric layers. The vias are plated to form through holes either as a finished assembly or as individual layers.

The cross-section of an interconnect fabricated this way is shown in [Figure 5.3](#), where the solid black areas are conductors. This is a simple microstrip realization showing dielectric layers (shaded) with a surface conductor. This is coated by a solder resist layer.

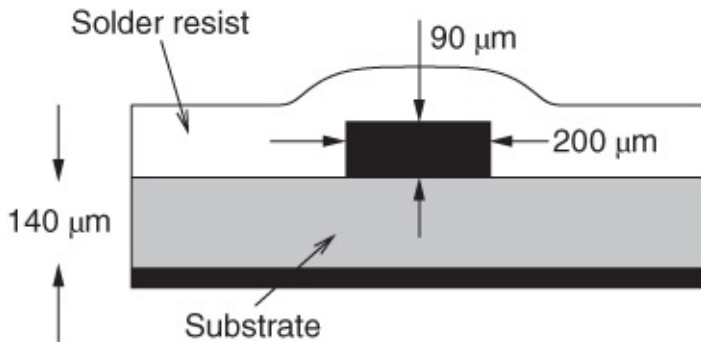


[Figure 5.3](#) Cross-section view of an interconnect on a PCB.

The permittivities of a sample of PCB board are given in [Table 5.8](#). Organic PCBs therefore comprise two materials of different permittivities. E-glass, the most common fabric, has a permittivity of 6.3 and the most commonly used epoxy resin (#5010) has a permittivity of 3.8. The permittivity of the composite material is somewhere between these values depending on the volume ratio of the component materials. The most common PCB material, FR-4, uses the E-glass/epoxy combination. More specifics on PCB materials and properties are provided by Brzozowski [47]. Since the fabric has a decidedly planar orientation the permittivity in the

board plane differs from that in the direction perpendicular to the plane of the board. Thus there is appreciable anisotropy of  $\epsilon_r$  due to preferred orientation of the glass fabric. This problem is addressed using non-woven glass fabrics. In non-woven glass fabrics random microfibres of glass support the epoxy, which is usually PTFE. RT/Duroid® 5870 (with  $\epsilon_r = 2.33$ ) and RT/Duroid® 5880 (with  $\epsilon_r = 2.2$ ) are the oldest of these products, developed as an alternative to woven glass products. These products are best suited to microwave and broadband applications where it is critical to achieve low loss and low dispersion. The main disadvantage is that the PTFE/microfibre glass boards are soft, leading to less precise dimensional control than is achievable using epoxy-based boards.

**Table 5.8** Permittivity  $\epsilon_r$  and dielectric loss tangent  $\tan \delta$  of the major organic PCB materials at 10 GHz.

Fabric/resin	$\epsilon_r$	$\tan \delta$
E-glass/epoxy (FR4)	4.3–4.5	0.010–0.020
E-glass/polyimide	3.7–4.8	0.015–0.025
E-glass/cyanate ester	2.8–3.9	0.003
Kevlar/polyimide	3.6	0.008
Ceramic/PTFE	2.9	0.0012
Non-woven epoxy-glass/PTFE	2.17–2.33	0.0009–0.0013
Woven epoxy-glass/PTFE	2.17–3.20	0.0013–0.009

The permittivity of PCBs can be reduced using an alternative glass such as S-glass, which has a permittivity of 5.3, and an alternative filler material such as PTFE, which has a permittivity of 2.2.

### 5.8.2 Ceramic PCBs

The use of a ceramic as the dielectric layer ensures that the PCB is rigid with precisely controlled tolerances, including surface flatness. This is particularly attractive for microwave circuits where the dimensions define the properties of transmission lines and when lengths of lines are used as circuit elements. In a typical ceramic PCB, PTFE and ceramic are mixed. Depending on the ratio of PTFE and ceramic, and the type of ceramic, these boards can have permittivities ranging from about 2.94 to 9.8, since the most common ceramics are alumina, which has a permittivity of 9.8, and LTCC substrates with various permittivities but values around 8 are usually chosen. The ceramic mix ensures that there is little or no directional dependence, and so these boards have negligible dielectric anisotropy.

## 5.9 Multichip Modules

MCMs are used to provide small, high-precision interconnects that can be cost-effectively produced with larger areas than for an IC, have lateral dimensions that are slightly larger than

on-chip but smaller than on a PCB. They have higher performance than interconnects on PCBs. In the interconnect performance hierarchy they are between on-chip interconnects and those on PCBs. MCMs include metallization structures that are fabricated using IC fabrication equipment, at the high end, and PCB-like structures at the lower performance end. One of the features that distinguish MCMs from PCBs is that bare (unpackaged) die (i.e., ICs) are generally used and there are usually no active devices on the MCM substrate, although there are instances of this. The intention is to connect two or more chips together using low-loss interconnects that can support higher speed digital or analog signals than is possible with PCBs. MCMs also have higher interconnect density than PCBs and have more regular metallization geometries than do ICs. MCMs are nearly always designed to provide well-defined signal return paths, interconnects have controlled impedance, and can be properly modeled as transmission line structures. They have multilevel metallization generally with solid or mesh power and ground planes. Low-cost versions could have just two metallization layers in addition to a ground plane. There are four dominant types of MCM technology:

- a.** MCM-L having a *laminated* PCB-like structure
- b.** MCM-C based on co-fired *ceramic* structures similar to thick-film modules
- c.** MCM-D using *deposited* metals and dielectrics in a process very similar to that used in semiconductor processing
- d.** MCM-C/D having *deposited* layers on an MCM-C base.

In the following sections we will consider the first three MCM types. A comparison of the typical dimensions that can be achieved with the different substrates is shown in [Table 5.9](#).

**Table 5.9** Comparison of typical parameters of interconnects on the various MCM substrates.

Parameter	MCM-L ( $\mu\text{m}$ )	MCM-C ( $\mu\text{m}$ )	MCM-D ( $\mu\text{m}$ )
Minimum metal spacing	75	20	15
Minimum trace width	75	15	10
Metal thickness	17–68	10	5
Minimum via diameter	150	20	15

### 5.9.1 MCM-L Substrates

Multichip module – laminate (MCM-L) substrates and processing are very similar to those for PCBs. The essential difference is that MCMs, as compared to PCBs, are the choice when performance is a premium and so it is cost-effective to use more exotic epoxies such as PTFE (teflon) and polyimide. These have relative permittivities of around 2.2 when laminated with a glass fabric compared to the permittivity of the most common type of PCB (FR4) of 4.2. More importantly, the mechanical aspects such as surface roughness and layer thickness—critical for defining the electrical characteristics of interconnects—are much better controlled than with PCBs, such as FR4 with woven fabrics. Many other materials can be used as the fabric and as the epoxy with varying characteristics. The mechanical characteristics of these materials are

very important and the choice of MCM-L substrate involves many trade-offs. Brzozowski [47] provides a comprehensive treatment of the issues involved.

### 5.9.2 MCM-C Substrates

Multichip module – ceramics (MCM-Cs), are rigid interconnect substrates which are very similar to the thick-film modules discussed in [Section 5.6](#), the functional difference being that MCM-Cs are multilayer. The base substrate is generally alumina, and layers are alumina, other ceramic, or ceramic/glass blend. The layers are fabricated individually. The base substrate and the ceramic layers are formed from a mix of ceramic powder and organic binders. The material at this stage is soft and flexible and is known as *green tape*. Conductor patterns are formed on the individual layers by silk-screening pastes, as discussed in [Section 5.6.1](#). Vias, formed by punching holes in the green-tape layers, are filled in the silk-screening process. The silk-screen mesh limits the minimum dimensions of lines, with the finest meshes yielding a minimum line width of 10  $\mu\text{m}$  and a minimum via diameter of 20  $\mu\text{m}$ . These minimum dimensions limit the use of MCM-C structures in digital systems. The MCM-D structure described below is more suitable for these applications because of the higher wiring densities that can be obtained using smaller dimensions.

As with the thick-film structures considered previously, the green-tape layers are stacked to form a multilayer structure and fired to drive off the organic compounds and form a rigid ceramic structure. The conductors also merge to form good metallic contact between layers at vias. If the firing is done at high temperatures the structure is known as high-temperature co-fired ceramic (HTCC) and considerable shrinkage of the structure in the range of 20–40% occurs. More recently, formulations have been developed that allow low firing temperatures and these structures are known as low-temperature co-fired ceramic (LTCC). LTCCs have little shrinkage and thus require less precise process control and are increasingly popular, especially for RF and microwave applications. When used for RF and microwave circuits, multilayer inductors can be efficiently formed with better characteristics than can be obtained when they are fabricated on-chip with the associated dielectric losses.

### 5.9.3 MCM-D Substrates

Multichip module – deposited (MCM-D) substrates, are most like semiconductor integrated circuits but without active devices in general. (Often previous generations of semiconductor processing equipment can be used, so it is possible to use some active devices.) The most common base substrate is a silicon wafer on which alternate layers of metal and dielectric are deposited. The dielectric layers can be grown in the case of  $\text{SiO}_2$  or spun-on in the case of polyimide. Metal layers are deposited typically by sputtering, possibly assisted by electro-plating for more rapid build up of conductor. After each layer is added, photolithography and etching are used to define conductor patterns or to open vias in the dielectric. The ultimate geometric limits are those used in semiconductor processing. However, the low-loss connections over long distances needed to connect multiple chips require relatively substantial interconnect cross-sectional dimensions. As with semiconductor processing, the metallic structures are often composed of two or more element types. Approximate modeling of these

structures can be performed using electromagnetic tools to develop the capacitance, resistance and inductance matrices of coupled line structures or by developing distributed transmission line modules. However, the dielectric density varies around the conductors and the multiple-metal structures cannot be modeled properly.

### 5.9.4 Characterization of Interconnects on a Multichip Module: A Case Study

Lipa *et al.* [48] undertook an experimental investigation of an MCM-D structure. The MCM had two metallization layers in addition to the ground. The interconnect structure was of microstrip construction and is shown in [Figure 5.4](#). Three different widths on two layers were considered as indicated in [Table 5.10](#).

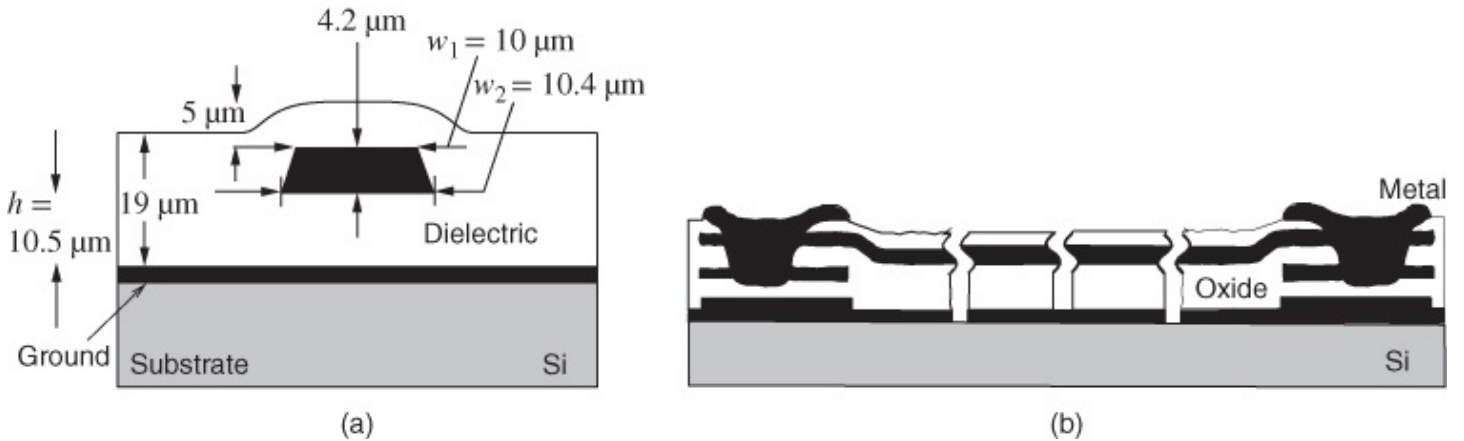


**Figure 5.4** An MCM-D interconnect: (a) cross-section of the second layer; and (b) longitudinal view showing vias. Adapted from Lipa *et al.* (1996) [48], figure 1, p. 123. Reprinted with permission of IEEE.

**Table 5.10** Parameters of the MCM-D interconnects

Interconnect	Layer	Height, $h$ (μm)	Width, $w_1$ (μm)	Width, $w_2$ (μm)	Capacitance (fF/mm)
1A	1	5	10	10.4	138
1B	1	5	16	16.4	171
1C	1	5	32	32.4	257
2A	2	10.5	10	10.4	82.4
2B	2	10.5	16	16.4	102
2C	2	10.5	32	32.4	156

One of the important things to note is that the cross-section of the interconnect has a low width-to-thickness ratio. This is typical of MCM-D interconnects (and also of on-chip interconnects) where special attention is given to supporting a process that leads to relatively thick interconnect so as to minimize resistance. Thus for the same resistance per unit length, the

interconnect widths can be less, resulting in a higher wiring density. This is especially important with the advent of wide buses to increase system performance.

The low aspect ratio of the interconnects means that many fast electromagnetic analyses that assume thin metallization cannot be used. Analytic formulas for interconnect parameters such as characteristic impedance and propagation constant are also derived assuming this thin metallization assumption. The inductance and capacitance matrix extractions considered in the previous chapter for modeling on-chip interconnects are not strictly appropriate as path lengths in MCM-Ds can be substantial compared to the wavelength of the highest significant frequency component of a signal.

The parameters of most interest for MCM interconnects are the loss constant, the delay, and whether or not it is reasonable to use constant per unit length lumped element parameters to describe the properties of MCM interconnects. One of the essential transmission line parameters is the characteristic impedance, which is shown in [Figure 5.5](#). As expected, the characteristic impedances of the lines reduces as the width increases. Thus, for the same power transmission level currents are lower for narrower lines.

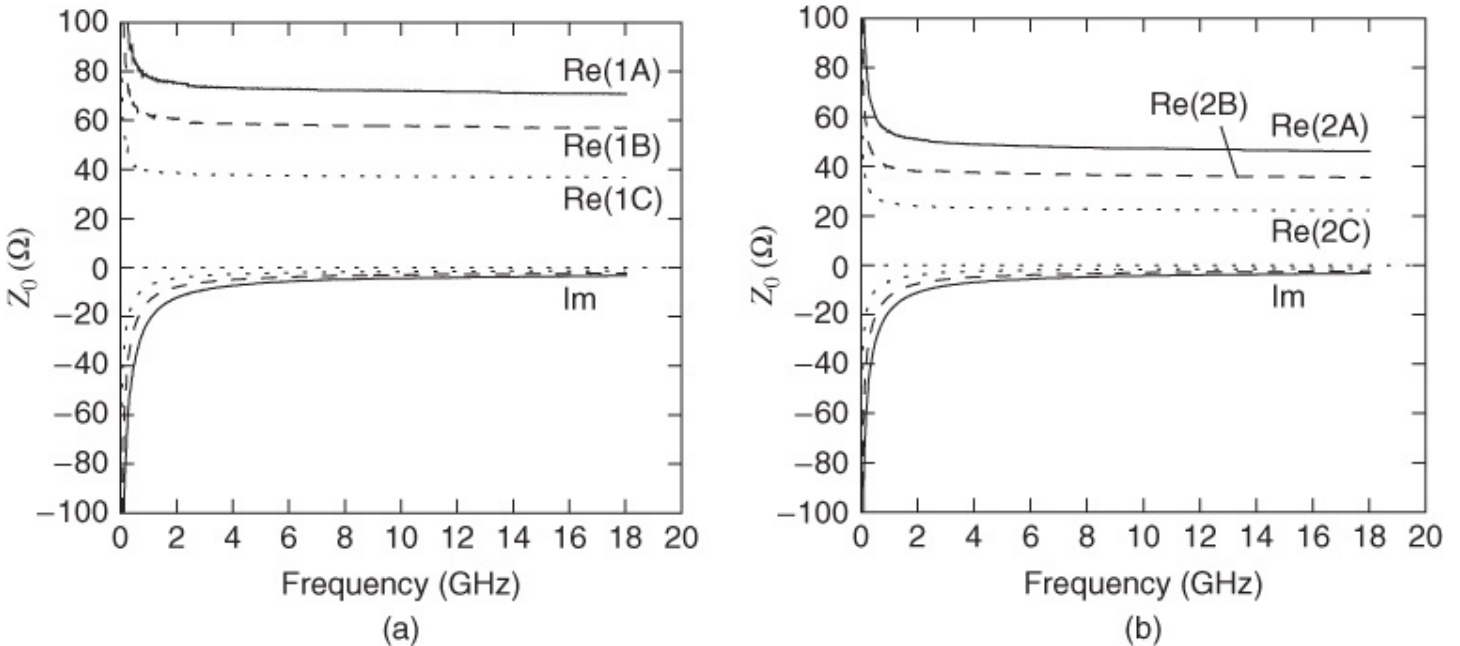


[Figure 5.5](#) Measured characteristic impedance of the microstrip interconnects shown in [Figure 5.4](#) for three different line widths: (a) with the lines on layer 1; and (b) with the lines on layer 2.

The interconnect loss is captured by the attenuation constant  $\alpha$ , which is composed of conductive  $\alpha_C$  and dielectric  $\alpha_D$  attenuation:

$$\alpha = \alpha_C + \alpha_D. \quad 5.4$$

In the work reported by Lipa *et al.*, accurate electromagnetic modeling was used to model the interconnect, taking full account of the skin effect and the actual shape of the interconnect [49]. The conductive and dielectric attenuation constants are shown in [Figure 5.6](#); [Figure 5.6\(a\)](#) when the interconnect is on the first layer and [Figure 5.6\(b\)](#) when the interconnect is on the

second layer. The layer associated with the measurements is indicated by the primary subscripts 1 and 2. Three different widths were considered, denoted by the secondary subscripts *A*, *B*, and *C*, respectively. As would be expected the conductive attenuation is higher the narrower the line:

$$\alpha_{C,1A} > \alpha_{C,1B} > \alpha_{C,1C}$$

$$\alpha_{C,2A} > \alpha_{C,2B} > \alpha_{C,2C}.$$

Also, the attenuation of the lines on layer 2, with a height above the ground greater than that of the corresponding width lines on layer 1, has lower attenuation:

$$\alpha_{C,1A} > \alpha_{C,2A}$$

$$\alpha_{C,1B} > \alpha_{C,2B}$$

$$\alpha_{C,1C} > \alpha_{C,2C}.$$

This is because the lines closer to the surface have some of the field lines in the air, have a lower permittivity, and hence travel faster. Since the signals travel faster, there is less loss, as this is largely proportional to the amount of time the signal is exposed to the loss mechanism.

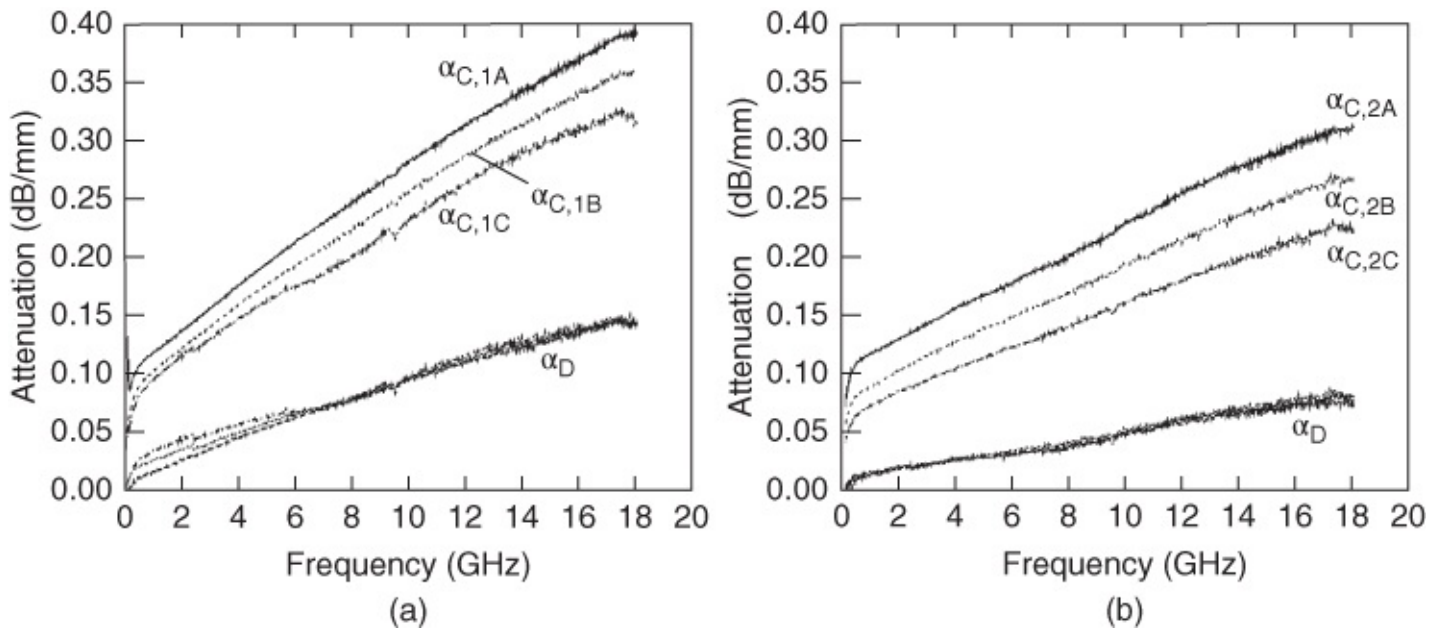


**Figure 5.6** Conductive and dielectric attenuation constants,  $\alpha_C$  and  $\alpha_D$  respectively, of an interconnect on a two-layer MCM-D: (a) first-layer metallization (layer 1); and (b) second-layer metallization (layer 2). Adapted from Lipa *et al.* (1996) [48], figures 4 and 5, p. 124. Reprinted with permission of IEEE.

The interesting point to note about the results presented in Figure 5.6 is that for lines on the same layer the dielectric loss, indicated by  $\alpha_D$ , depends on the layer number and not the width of the lines. For the same propagation velocity discussion as before,  $\alpha_D$  on layer 1 is greater than that on layer 2.

The dielectric loss makes up about one-third of the total loss. This loss is far in excess of the

loss due to relaxation in the dielectric, and is attributed to the excitation of slab waves and surface waves that travel in the dielectric or at the dielectric/air interface away from the microstrip line. This phenomenon has only recently been identified [50–53].

The attenuation constant can be related to the per unit length lumped-element parameters describing the line by considering the propagation constant:

$$\gamma = j\omega \sqrt{LC} \left(1 - j\frac{R}{\omega L}\right)^{\frac{1}{2}} \left(1 - j\frac{G}{\omega C}\right)^{\frac{1}{2}}. \quad 5.5$$

Approximating the terms in the parentheses by the first two terms in their power series expansion since  $R \ll \omega L$  and  $G \ll \omega C$  (except at very low frequencies), the conductive attenuation constant is interpreted as

$$\alpha_C = \frac{1}{2} R \sqrt{C/L} \quad 5.6$$

and the dielectric attenuation constant as

$$\alpha_D = \frac{1}{2} G \sqrt{L/C}. \quad 5.7$$

The total attenuation coefficient, of course, is  $\alpha = \alpha_C + \alpha_D$ , with the term  $\alpha_C$  describing the loss due to the interconnect resistance and  $\alpha_D$  representing the loss in the dielectric. Both  $\alpha_C$  and  $\alpha_D$  also include the effects of radiation loss.

### 5.9.5 MCM Summary

In summary, the principal advantages of an MCM over a PCB are:

- a. higher interconnect density
- b. finer interconnect geometries so that chips can be placed closer together, resulting in shorter interconnect lengths
- c. finer geometries that enable direct chip connect without needing intermediate chip packaging (e.g., using flip-chip or solder bump connections).

In addition to the three principal types of MCMs (MCM-L, MCM-C and MCM-D) MCM-C/D is sometimes used. This substrate begins as an MCM-C with interconnects of relatively large dimensions having low loss and especially suited to distributing power and ground. Additional layers of metallization and dielectric are deposited using the same process as for MCM-Ds. The MCM-D part of the structure provides the higher wiring density required to distribute digital signals where being able to accommodate wide buses boosts performance.

The reader is referred to books by Doane and Franzon [54] and Harper [55] for extensive treatments of MCMs.

## 5.10 Summary

Interconnect technologies continue to evolve as operating frequencies increase and compactness results in increased coupling of signals on adjacent interconnects. There is a need to maintain signal integrity by ensuring controlled dimensions of lines and so maintaining uniform field distributions and characteristic impedances. At the same time there is a need for more compact circuits, which has lead to the evolution of three-dimensional interconnect structures, for example see [56–58]. The more compact structures are difficult to modify during the design, fabricate, and test cycle, and so this trend increases the cost of design. It mandates an intuitive understanding of how signals travel on transmission lines and how discontinuities affect the integrity of signals.

## References

- [1] M. K. Barnoski, Ed., *Introduction to Fibre Optics*. Plenum Publishing Corporation, 1974.
- [2] R. Knox, “Dielectric waveguide microwave integrated circuits—an overview,” *IEEE Trans. on Microwave Theory and Techniques*, vol. **24**, no. 11, pp. 806–814, Nov. 1976.
- [3] M. Caulton and H. Sobol, “Microwave integrated-circuit technology-a survey,” *IEEE Journal of Solid-State Circuits*, vol. **5**, no. 6, pp. 292–303, Dec. 1970.
- [4] J. Hinken, “Waveguides for microwave integrated circuits,” in *9th European Microwave Conf.*, Sep. 1979, pp. 656–660.
- [5] C.-Y. Chi and G. Rebeiz, “Design of Lange-couplers and single-sideband mixers using micromachining techniques,” *IEEE Trans. on Microwave Theory and Techniques*, vol. **45**, no. 2, pp. 291–294, Feb. 1997.
- [6] T. Weller, L. Katehi, and G. Rebeiz, “High performance microshield line components,” *IEEE Trans. on Microwave Theory and Techniques*, vol. **43**, no. 3, pp. 534–543, Mar. 1995.
- [7] C.-Y. Chi and G. Rebeiz, “Planar microwave and millimeter-wave lumped elements and coupled-line filters using micro-machining techniques,” *IEEE Trans. on Microwave Theory and Techniques*, vol. **43**, no. 4, pp. 730–738, Apr. 1995.
- [8] M. Stotz, G. Gottwald, H. Haspeklo, and J. Wenger, “Planar millimeter-wave antennas using  $\sin_x$ -membranes on GaAs,” *IEEE Trans. on Microwave Theory and Techniques*, vol. **44**, no. 9, pp. 1593–1595, Sep. 1996.
- [9] J.-F. Kiang, “Characteristic impedance of microshield lines with arbitrary shield cross section,” *IEEE Trans. on Microwave Theory and Techniques*, vol. **46**, no. 9, pp. 1328–1331, Sep. 1998.
- [10] S. Iordanescu, G. Bartolucci, S. Simion, and M. Dragoman, “Coplanar waveguide stub/filters on thin membranes and standard substrates,” in *Proc. 1997 Int. Semiconductor Conf.*, Oct. 1997, pp. 357–360.

- [11] P. Blondy, A. Brown, D. Crost, and G. Rebeiz, “Low loss micromachined filters for millimeter-wave telecommunication systems,” in *1998 IEEE MTT-S Int. Microwave Symp. Digest*, Jun. 1998, pp. 1181–1184.
- [12] G. Sajin, E. Matei, and M. Dragoman, “Microwave straight edge resonator (SER) on silicon membrane,” in *1999 Int. Semiconductor Conf., CAS '99 Proceedings*, 1999, pp. 283–286.
- [13] L. Katehi and G. Rebeiz, “Novel micromachined approaches to MMICs using low-parasitic, high-performance transmission media and environments,” in *1998 IEEE MTT-S Int. Microwave Symp. Digest*, Jun. 1996, pp. 1145–1148.
- [14] K. Herrick, J. Yook, and L. Katehi, “Microtechnology in the development of three-dimensional circuits,” *IEEE Trans. on Microwave Theory and Techniques*, vol. **46**, no. 11, pp. 1832–1844, Nov. 1998.
- [15] K. Herrick, T. Schwarz, and L. Katehi, “Si-micromachined coplanar waveguides for use in high-frequency circuits,” *IEEE Trans. on Microwave Theory and Techniques*, vol. **46**, no. 6, pp. 762–768, Jun. 1998.
- [16] R. Drayton, R. Henderson, and L. Katehi, “Monolithic packaging concepts for high isolation in circuits and antennas,” *IEEE Trans. on Microwave Theory and Techniques*, vol. **46**, no. 7, pp. 900–906, Jul. 1998.
- [17] R. Henderson and L. Katehi, “Silicon-based micromachined packages for high-frequency applications,” *IEEE Trans. on Microwave Theory and Techniques*, vol. **47**, no. 8, pp. 1563–1569, Aug. 1999.
- [18] P. Meier, “Integrated fin-line millimeter components,” *IEEE Trans. on Microwave Theory and Techniques*, vol. **22**, no. 12, pp. 1209–1216, Dec. 1974.
- [19] P. Meier, “Millimeter integrated circuits suspended in the E-plane of rectangular waveguide,” *IEEE Trans. on Microwave Theory and Techniques*, vol. **26**, no. 10, pp. 726–733, Oct. 1978.
- [20] L. D. Cohen and P. J. Meier, “E-plane mm-wave circuits,” *Microwave Journal*, pp. 63–66, Aug. 1978.
- [21] R. Bates and M. Coleman, “Millimetre wave finline balanced mixers,” in *9th European Microwave Conf.*, Sep. 1979, pp. 721–725.
- [22] H. El Hennawy and K. Schunemann, “Analysis of fin-line discontinuities,” in *9th European Microwave Conf.*, Sep. 1979, pp. 448–452.
- [23] M. V. Schneider, “Microstrip lines for microwave integrated circuits,” *The Bell System Technical Journal*, pp. 1421–1444, May–Jun. 1969.
- [24] R. Simons, N. Dib, and L. Katehi, “Modeling of coplanar stripline discontinuities,” *IEEE*

*Trans. on Microwave Theory and Techniques*, vol. **44**, no. 5, pp. 711–716, May 1996.

- [25] D. Prieto, J. Cayrou, J. Cazaux, T. Parra, and J. Graffeuil, “Cps structure potentialities for mmics: a cps/cpw transition and a bias network,” in *1998 IEEE MTT-S Int. Microwave Symp. Dig.*, Jun. 1998, pp. 111–114.
- [26] K. Goverdhanam, R. Simons, and L. Katehi, “Micro-coplanar striplines-new transmission media for microwave applications,” in *1998 IEEE MTT-S Int. Microwave Symp. Dig.*, Jun. 1998, pp. 1035–1038.
- [27] K. Goverdhanam, R. Simons, and L. Katehi, “Coplanar stripline components for high-frequency applications,” *IEEE Trans. on Microwave Theory and Techniques*, vol. **45**, no. 10, pp. 1725–1729, Oct. 1997.
- [28] J. Knorr and K. Kuchler, “Analysis of coupled slots and coplanar strips on dielectric substrate,” *IEEE Trans. on Microwave Theory and Techniques*, vol. **23**, no. 7, pp. 541–548, Jul. 1975.
- [29] S. Pintzos, “Full-wave spectral-domain analysis of coplanar strips,” *IEEE Trans. on Microwave Theory and Techniques*, vol. **39**, no. 2, pp. 239–246, Feb. 1991.
- [30] M. Gunston, *Microwave Transmission-line Impedance Data*. Van Nostrand Reinhold Company, 1973.
- [31] P. Holder, “X-band microwave integrated circuits using slotline and coplanar waveguide,” *The Radio and Electronic Engineer*, vol. **48**, no. 1/2, pp. 38–43, Jan./Feb. 1978.
- [32] K. Gupta, R. Garg, and I. Bahl, *Microstrip Lines and Slotlines*, 2nd ed. Artech House, 1996.
- [33] B. Spielman, “Computer-aided analysis of dissipation losses in isolated and coupled transmission lines for microwave and millimetre-wave applications,” *NRL Formal Report*, no. 8009, 1976.
- [34] A. Ganguly and B. Spielman, “Dispersion characteristics for arbitrarily configured transmission media,” *IEEE Trans. on Microwave Theory and Techniques*, vol. **25**, no. 12, pp. 1138–1141, Dec. 1977.
- [35] P. Ladbrooke, E. England, and M. Potok, “A specific thin-film technology for microwave integrated circuits,” *IEEE Trans. Manufacturing Technology*, vol. **2**, no. 2, pp. 53–59, Dec. 1973.
- [36] D. Rickard, “Thick film MIC components in the range 10–20 GHz,” in *6th European Microwave Conf.*, Sep. 1976, pp. 687–691.
- [37] R. J. Jensen, “Thin film multilayer interconnection technologies for multichip modules,” in *Multichip Module Technologies and Alternatives: The Basics*, D. A. Doane and P. D. Franzon, Eds., 1993, pp. 255–309.

- [38] J. E. Sergent, “The hybrid microelectronics and mcm technology,” in *Electronic Packaging and Interconnection Handbook*, 2nd ed., C. A. Harper, Ed., 1997.
- [39] C. A. Harper, Ed., *Handbook of Thick Film Hybrid Microelectronics*. McGraw-Hill, 1974.
- [40] J.-P. Ramy, M.-T. Cotte, J. Bolloch, R. Schnitzler, J.-J. Guena, and C. Thebault, “Optimization of the thick-and thin-film technologies for microwave circuits on alumina and fused silica substrates,” *IEEE Trans. on Microwave Theory and Techniques*, vol. **26**, no. 10, pp. 814–820, Oct. 1978.
- [41] M. Goloubkoff and C. Thebault, “M.I.C. technology on fused silica substrate: Ku band transponder application,” in *9th European Microwave Conf.*, Sep. 1979, pp. 651–655.
- [42] R. Rasshofer, E. Biebl, K. Strohm, and J. Luy, “Long-term stability of passive millimeterwave circuits on high-resistivity silicon substrates,” in *1999 IEEE MTT-S Int. Microwave Symp. Digest*, Jun. 1999, pp. 585–588.
- [43] K. Strohm, P. Nuechter, C. Rheinfelder, and R. Guehl, “Via hole technology for microstrip transmission lines and passive elements on high resistivity silicon,” in *1999 IEEE MTT-S Int. Microwave Symp. Digest*, 1999, pp. 581–584.
- [44] P. Zarkesh-Ha, P. Bendix, W. Loh, J. Lee, and J. Meindl, “The impact of Cu/low  $\kappa$  on chip performance,” in *Twelfth Annual IEEE Int. ASIC/SOC Conf.*, 1999, pp. 257–261.
- [45] A. Sweet, *MIC and MMIC Amplifier and Oscillator Circuit Design*. Artech House, 1990, ch. 9.
- [46] G. Ponchak, M. Matloubian, and L. Katehi, “A measurement-based design equation for the attenuation of MMIC-compatible coplanar waveguides,” *IEEE Trans. on Microwave Theory and Techniques*, vol. **47**, no. 2, pp. 241–243, Feb. 1999.
- [47] V. J. Brzozowski, “Rigid and flexible printed wiring boards,” in *Electronic Packaging & Interconnection Handbook*. McGraw-Hill, 1997.
- [48] S. Lipa, M. Steer, A. Cangellaris, and P. Franzon, “Experimental characterization of transmission lines in thin-film multichip modules,” *IEEE Trans. on Components, Packaging, and Manufacturing Technology, Part A*, vol. **19**, no. 1, pp. 122–126, 1996.
- [49] T. Van Deventer, P. Katehi, and A. Cangellaris, “An integral equation method for the evaluation of conductor and dielectric losses in high-frequency interconnects,” *IEEE Trans. on Microwave Theory and Techniques*, vol. **37**, no. 12, pp. 1964–1972, Dec. 1989.
- [50] A. Oliner, “Leakage from higher order modes on microstrip line with application to antennas,” *Radio Science*, vol. **22**, no. 6, pp. 907–912, 1987.
- [51] J. Harokopus, W.P. and P. Katehi, “Radiation properties of open microstrip

discontinuities,” in *1989 AP-S Antennas and Propagation Society Int. Symp.*, Jun. 1989, pp. 1703–1706.

[52] T.-S. Horng, S.-C. Wu, H.-Y. Yang, and N. Alexopoulos, “A generalized method for distinguishing between radiation and surface-wave losses in microstrip discontinuities,” *IEEE Trans. on Microwave Theory and Techniques*, vol. **38**, no. 12, pp. 1800–1807, Dec. 1990.

[53] J. Harokopus, W.P., L. Katehi, W. Ali-Ahmad, and G. Rebeiz, “Surface wave excitation from open microstrip discontinuities,” *IEEE Trans. on Microwave Theory and Techniques*, vol. **39**, no. 7, pp. 1098–1107, Jul. 1991.

[54] D. A. Doane and P. D. Franzon, *Multichip Module Technologies and Alternatives: The Basics*. Van Nostrand Reinhold, 1993.

[55] C. A. Harper, *Electronic Packaging & Interconnection Handbook*. McGraw-Hill Inc., 1997.

[56] L. Katehi, W. Chappell, S. Mohammadi, A. Margomenos, and M. Steer, “Heterogeneous wafer-scale circuit architectures,” *IEEE Microwave Magazine*, vol. **8**, no. 1, pp. 52–69, Jan. 2007.

[57] J. Carlson, M. Lueck, C. Bower, D. Temple, Z. Feng, M. Steer, A. Moll, and W. Knowlton, “A stackable silicon interposer with integrated through-wafer inductors,” in *Proc. 57th Electronic Components and Technology Conf.*, 2007, pp. 1235–1238.

[58] W. Davis, J. Wilson, S. Mick, J. Xu, H. Hua, C. Mineo, A. Sule, M. Steer, and P. Franzon, “Demystifying 3D ICs: the pros and cons of going vertical,” *IEEE Design & Test of Computers*, vol. **22**, no. 6, pp. 498–510, 2005.

<sup>1</sup> Rectangular waveguide is a transmission structure which consists of a tube of rectangular cross-section that ‘guides’ an electromagnetic wave. It is quite different from the interconnect structures considered in this book that consist of two or more conductors.

<sup>2</sup> TE and TM modes are a departure, but not total departure, from TEM modes. With TE modes the electric fields are confined to the transverse plane, and with TM modes the magnetic fields are confined to the transverse plane.

# Chapter 6

## Microstrip Design at Low Frequencies

### 6.1 The Microstrip Design Problem

Microstrip is a particularly useful transmission line medium for implementation in distributed circuit designs at frequencies from below 1 GHz and up to 110 GHz. In this chapter we are concerned with some fundamental aspects of the microstrip structure and with the realization of dimensional design parameters for establishing desired electrical characteristics. This is chiefly for applications through the lower microwave frequencies up to tens of gigahertz. When the length of the interconnect is an appreciable fraction of a wavelength (say 1/20 th or more), then it must be regarded as a circuit element. Then the electrical requirement is often to realize a structure that provides maximum signal, or power, transfer.

#### 6.1.1 A Transistor Amplifier Input Network

One of the many areas where a microstrip design approach is attractive is that of microwave transistor amplifiers. The design techniques described here are quite accurate for this purpose. The general input arrangement for this type of amplifier is shown in [Figure 6.1\(a\)](#), where the low-noise optimizing network is sometimes referred to as a “noise-matching” network. This is typical of a microwave receiver “front-end.” In other cases power matching may be required and a different network would therefore be developed.

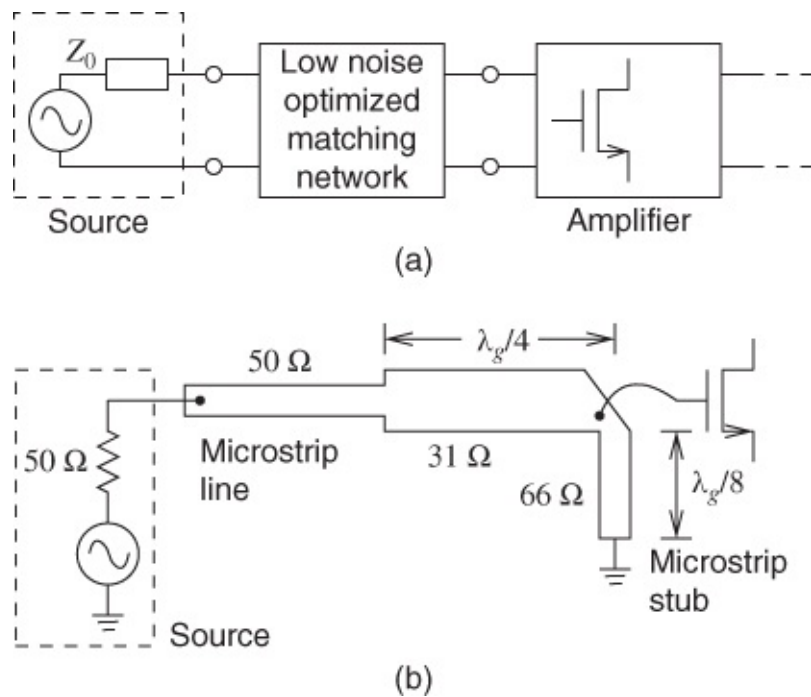


[Figure 6.1](#) Input network arrangement (a) and microstrip circuit (b) for a microwave transistor amplifier. The guide wavelength,  $\lambda_g$ , is the wavelength of the signal on the microstrip line.

A fairly simple microstrip realization of the input network is illustrated schematically in [Figure 6.1\(b\)](#). The signal source is assumed to be connected without any discontinuity through the  $50\ \Omega$  microstrip to the L-shaped microstrip network. This consists of two lines having characteristic impedances and electrical lengths determined by the network design. The main design problem is then to evaluate the physical widths and lengths of the microstrip lines (this applies to all microstrip designs). Many techniques have been developed for design networks such as those shown in [Figure 6.1](#) with the required broadband characteristics ensuring stability, minimizing noise, and maximizing power transfer [1]. In this chapter the focus instead is on realizing individual microstrip lines and components.

We shall see that the width of a microstrip line is principally a function of its characteristic impedance and the thickness of the substrate. The physical length depends on the wavelength, which is a function of the width, the substrate permittivity, and, of course, the signal frequency. Explicit techniques and formulas will be given here for the calculation of width and length to accuracies within about 1%.

From [Figure 6.1\(b\)](#) it should be clear that various discontinuities are inherent in the structures as follows: where the  $50\ \Omega$  and  $31\ \Omega$  lines join, at the right-angled junction of the  $31\ \Omega$  and  $66\ \Omega$  lines, and (less obviously) at the short-circuit to ground on the end of the  $66\ \Omega$  line. These and other discontinuities are described in more detail in [Chapter 9](#), where the details of the mitre to reduce the discontinuity effect of the right-angled bend are also considered.

### 6.1.2 The Geometry of Microstrip

The general geometry of microstrip is shown in [Figure 6.2](#). The materials and techniques for its manufacture were discussed in [Chapter 5](#), where the basic advantages were also described in comparison with other types of transmission lines. The most important dimensional parameters are the microstrip width,  $w$ , and the height,  $h$  (equal to the thickness of the substrate). Also of great importance is the relative permittivity of the substrate,  $\epsilon_r$ . In RF and microwave applications the thickness  $t$  of the metallic, top-conducting strip is generally of much lesser importance. However, microstrip lines on-chip are relatively thick as a result of the need to keep resistance down while still achieving high wiring density by keeping the width down. The effects of this thickness are dealt with in [Section 6.12](#). We shall consistently refer to the  $xyz$  coordinate description, as shown in [Figure 6.2](#).

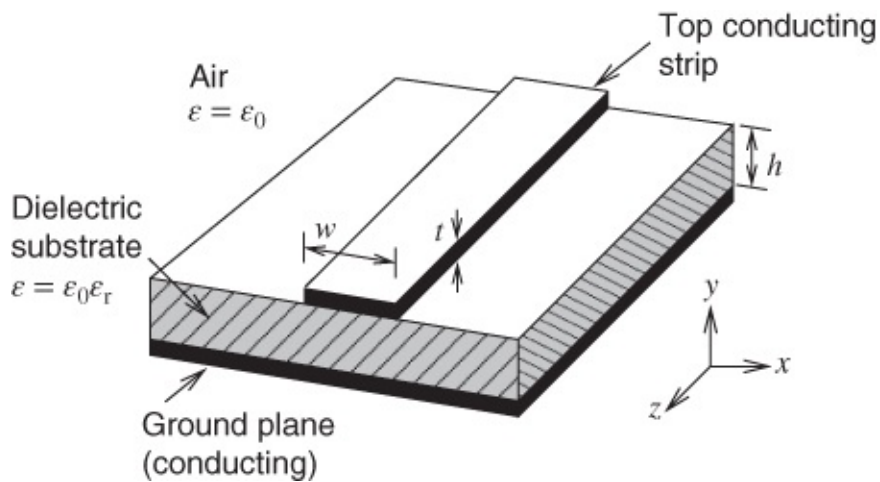


**Figure 6.2** The general geometry of a microstrip line, including choice of coordinates.

Some of the particularly useful characteristics of microstrip include the following:

- a. DC as well as AC signals may be transmitted.
- b. Active devices, diodes and transistors may readily be incorporated (shunt connections are also quite easily made).
- c. In-circuit characterization of devices is straightforward to implement.
- d. Line wavelength is reduced considerably (typically one-third) from its free-space value because of the substrate fields. Hence, distributed component dimensions are relatively small.
- e. The structure is quite rugged and can withstand moderately high voltages and power levels.

In [Sections 6.2–6.8](#) of this chapter we are concerned with basic considerations and microstrip synthesis where the substrate is a homogeneous, isotropic dielectric. Materials such as alumina, which is widely used, approximate to this description. We shall then consider synthesis using a dielectrically anisotropic substrate. Synthesis using a ferrite substrate is somewhat more complicated and [Chapter 20](#) is devoted to this topic. The chapter concludes with discussions on the effects of finite thickness and manufacturing tolerances, and a description of pulse propagation. Finally, recommendations for microstrip design are presented.

## 6.2 The Quasi-TEM Mode of Propagation

It is clear from [Figure 6.2](#) that microstrip involves an abrupt dielectric interface between the substrate and the air above it. Any transmission line that is filled with a uniform dielectric can support a single, well-defined mode of propagation, that is, orientation of the electric and magnetic fields, at least over a specified range of frequencies. Transmission lines that do not have such a uniform dielectric filling cannot support a single mode of propagation; microstrip is within this category. Although this is true, the bulk of the energy is transmitted along

microstrip with a field distribution that is quite close to being transverse but not quite and is referred to as being quasi transverse electromagnetic or quasi-TEM. Thus microstrip is referred to as a quasi-TEM transmission line. The detailed field distribution is quite complicated, but the main transverse electric field can be visualized as shown in [Figure 6.3](#).

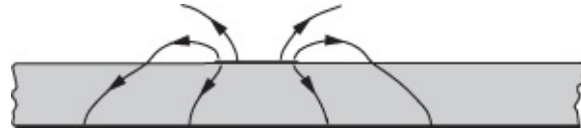


[Figure 6.3](#) Transverse cross-section of microstrip, showing the electric field.

Gupta *et al.* [2] used Maxwell's equations to convincingly demonstrate the necessity for longitudinal components of the electric and magnetic fields. This is clearly inconsistent with a pure TEM propagating mode.

Representative views of the magnetic and electric field distributions are given in [Figure 6.4](#). (These are not precisely determined field contours, and they must only be regarded as diagrammatic illustrations of the situation.) The longitudinal components can clearly be seen and these become increasingly significant as the frequency is raised.

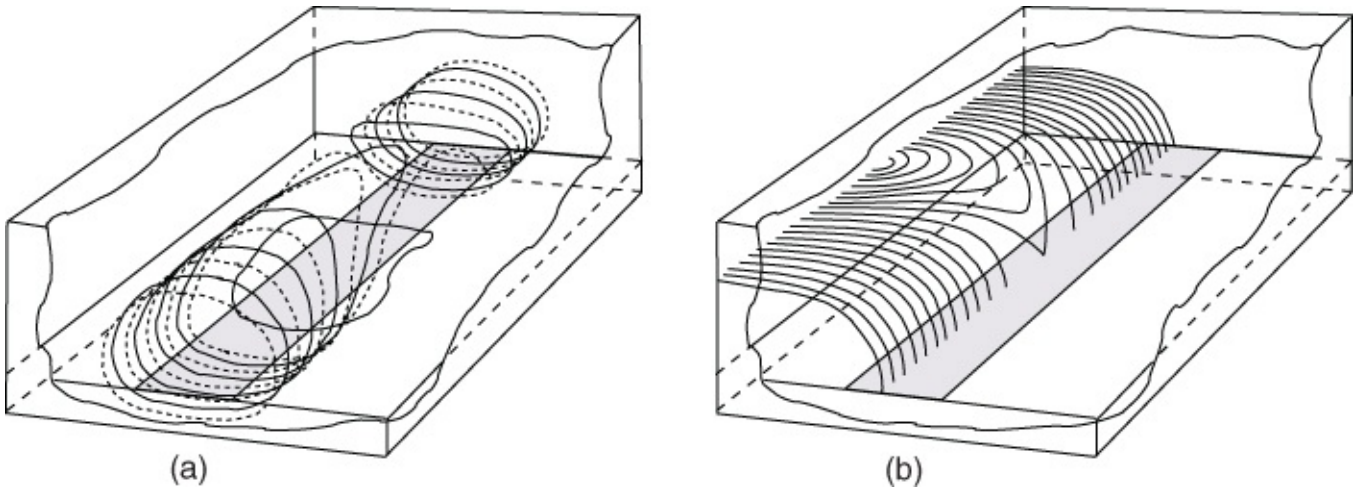


[Figure 6.4](#) Three-dimensional views of the magnetic (a) and electric (b) fields surrounding a shielded microstrip line. The magnetic field lines in (a) alternate between dashed and solid to aid in clarity. For simplicity, only the electric field in the air and on the left-hand side of the strip is shown in (b).

At most transverse cross-sectional planes, taken across the shielded microstrip, the electric ( $E$ ) and magnetic ( $H$ ) fields follow the distributions indicated in [Figure 6.5](#). Note the abrupt change in direction of the electric field line as it passes through the air–substrate interface. These fields have been analyzed by a number of researchers. We shall not study any of these techniques in detail here, but the results are powerful and significant for the circuit designer wishing to use microstrip. There are two reasons for this:

- a. For the majority of microstrip lines the statically derived results are quite accurate where the frequency is below a few gigahertz.
- b. At higher frequencies, up to the limits for the useful operation of microstrip, these

“static” results can still be used in conjunction with frequency-dependent functions in closed formulas. These are developed in detail in [Chapter 7](#).

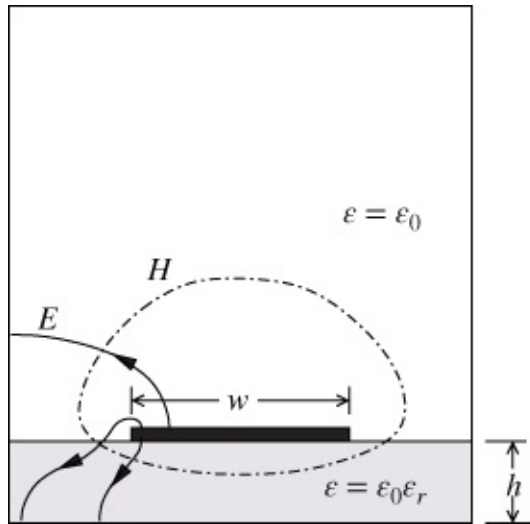


**Figure 6.5** A typical transverse cross-section of a shielded microstrip line showing representative magnetic ( $H$ ) and electric ( $E$ ) fields.

The earliest work concerning microstrip is generally accepted as that reported by Grieg and Engelmann [3]. Many other workers investigated basic characteristics of microstrip [4–6]. However, the major fundamental work on important and closely related parallel-strip transmission lines was due to Wheeler [7]. This led to analysis and synthesis on the static-TEM basis.

## 6.3 Static-TEM Parameters

The microstrip synthesis problem consists of finding the values of width  $w$  and length  $\ell$  corresponding to the characteristic impedance  $Z_0$  and electrical length  $\theta$  (in degrees or radians) defined at the circuit design stage.

Initially a suitable substrate of thickness  $h$  and relative permittivity  $\epsilon_r$  will need to be chosen. A basis for this choice is given in [Section 5.3](#) and the choice also depends on certain frequency limitations, which are discussed in [Chapter 7](#). The synthesis actually yields the normalized width-to-height ratio  $w/h$  initially, as well as a quantity called the effective microstrip (relative) permittivity  $\epsilon_{\text{eff}}$ . This quantity is unique to mixed-dielectric transmission line systems and it provides a useful link between various wavelengths, impedances, and propagating velocities. We shall shortly define the static-TEM effective microstrip permittivity ( $\epsilon_{\text{eff}}$ ) precisely.

### 6.3.1 The Characteristic Impedance $Z_0$

For any TEM-type transmission line the characteristic impedance at high frequencies may be expressed in any one of three alternate forms (see [Section 2.9](#)):

[6.1](#)

$$Z_0 = \sqrt{L/C}$$

or

$$Z_0 = v_p L$$

[6.2](#)

or

$$Z_0 = 1/(v_p C).$$

[6.3](#)

Both Equations [\(6.2\)](#) and [\(6.3\)](#) involve the phase velocity  $v_p$  of the wave traveling along the line. It is also recalled that this phase velocity is given by

$$v_p = 1/\sqrt{LC}.$$

[6.4](#)

When the substrate of the microstrip line is (effectively) removed we have an air-filled line along which the wave will travel at  $c$ , the velocity of light in free space ( $c = 2.99793 \times 10^8$  m/s). The characteristic impedance of this air-filled microstrip is

$$Z_{01} = \sqrt{L/C_1}$$

[6.5](#)

where  $L$  remains unaltered by the change in dielectric constant and  $C_1$  is the capacitance per unit length for this structure. Alternatively:

$$Z_{01} = cL$$

[6.6](#)

or

$$Z_{01} = 1/(cC_1).$$

[6.7](#)

Combining Equations [\(6.1\)](#), [\(6.6\)](#), and [\(6.7\)](#) yields the very significant result for the characteristic impedance of the original microstrip line with the dielectric substrate:

$$Z_0 = 1/\left(c\sqrt{CC_1}\right).$$

[6.8](#)

This means that the required characteristic impedance can be determined if we can evaluate the capacitances per unit length of the structure, with and without the presence of the dielectric substrate. One way in which this has been achieved will be outlined shortly (in [Section 6.8](#)).

### 6.3.2 The Effective Microstrip Permittivity $\epsilon_{\text{eff}}$

For the air-spaced microstrip line the propagation velocity is given by

$$c = 1/\sqrt{LC_1}$$

[6.9](#)

and, by dividing Equation [\(6.9\)](#) by Equation [\(6.4\)](#) and squaring, we obtain

$$\frac{C}{C_1} = \left( \frac{c}{v_p} \right)^2.$$

The capacitance ratio  $C/C_1$  is termed the effective microstrip permittivity  $\epsilon_{\text{eff}}$ , an important microstrip parameter. More completely  $\epsilon_{\text{eff}}$  could be referred to as the effective relative microstrip permittivity but the shorter expression is more commonly used. From Equation (6.10),  $\epsilon_{\text{eff}}$  is given by

$$\epsilon_{\text{eff}} = \left( \frac{c}{v_p} \right)^2. \quad 6.11$$

Although this result has been derived on a static basis here, it is fundamentally important for microstrip at all frequencies and will be used again where  $v_p$  is taken to be frequency dependent.

A useful relationship between  $Z_0$ ,  $Z_{01}$ , and  $\epsilon_{\text{eff}}$  can be obtained by combining Equations (6.3), (6.7), (6.10), and (6.11). The result is

$$Z_0 = Z_{01} / \sqrt{\epsilon_{\text{eff}}} \quad 6.12$$

that is

$$Z_{01} = Z_0 \sqrt{\epsilon_{\text{eff}}}. \quad 6.13$$

This will be useful in several respects, including the operation of a graphical design technique that is to be described shortly. It is also useful in developing intuitive understanding of all transmission lines with inhomogeneous dielectric.

Upper and lower bounds can readily be found for  $\epsilon_{\text{eff}}$ , in the static low-frequency limit, by considering the effects of very wide and very narrow lines, as indicated in Figure 6.6. For the very wide lines nearly all of the electric field is confined to the substrate dielectric, the structure resembles a parallel-plate capacitor, and therefore at this extreme

$$\epsilon_{\text{eff}} \rightarrow \epsilon_r.$$

In the case of very narrow lines, the electric field is almost equally shared by the air ( $\epsilon_r = 1$ ) and the substrate so that at this extreme

$$\epsilon_{\text{eff}} \approx \frac{1}{2}(\epsilon_r + 1).$$

The range of  $\epsilon_{\text{eff}}$  is therefore:

$$\frac{1}{2}(\epsilon_r + 1) \leq \epsilon_{\text{eff}} \leq \epsilon_r. \quad 6.14$$

It can be convenient to express the effective microstrip permittivity as

$$\epsilon_{\text{eff}} = 1 + q(\epsilon_r - 1)$$

**6.15**

where the new quantity, the filling factor  $q$ , has the bounds

$$\frac{1}{2} \leq q \leq 1. \quad \text{6.16}$$

Wheeler [7, 8] evaluated this filling factor and we shall employ it in an approximate graphical design technique.

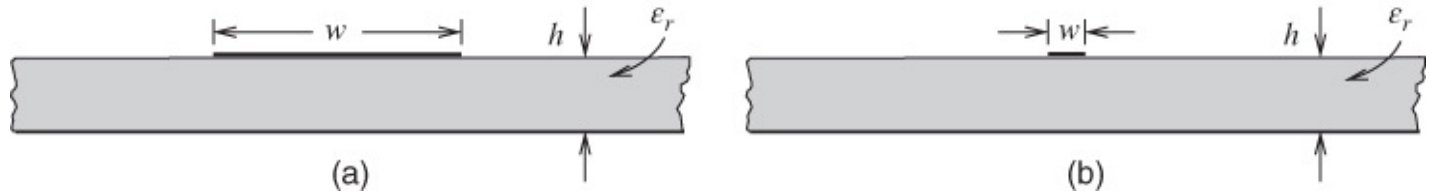


**Figure 6.6** Microstrip lines: (a) extremely wide ( $w \gg h$ ); and (b) extremely narrow ( $w \ll h$ ) lines.

### 6.3.3 Synthesis: The Width-to-height Ratio $w/h$

The width-to-height ratio ( $w/h$ ) is a strong function of  $Z_0$ , and of the substrate permittivity  $\epsilon_r$ . Wheeler's results [8] are particularly useful in this respect, although it has been found that some modifications are necessary for high accuracy (within 1%) to be achieved [9]. Closed formulas for  $w/h$  will be given in [Section 6.7](#).

### 6.3.4 Wavelength $\lambda$ , and Physical Length $\ell$

For any propagating wave the velocity is given by the appropriate frequency-wavelength product. In free space we have  $c = f\lambda_0$  and in microstrip the velocity is  $v_p = f\lambda_g$ , where  $\lambda_g$  is called the guide wavelength. Substituting these products into (6.11) we obtain

$$\epsilon_{\text{eff}} = (\lambda_0/\lambda_g)^2$$

or

$$\lambda_g = \lambda_0 / \sqrt{\epsilon_{\text{eff}}} \quad \text{6.17}$$

where  $\lambda_0$  is the free-space wavelength.

More conveniently, where the frequency is given in gigahertz and denoted by  $F$ , the wavelength can be expressed directly in millimeters as follows:

$$\lambda_g = 300 / (F \sqrt{\epsilon_{\text{eff}}}) \text{ mm.} \quad \text{6.18}$$

The physical length  $\ell$  of a microstrip line yielding a specified electrical length  $\theta$  (in degrees) is easily determined. In [Section 2.8](#) we derived the phase coefficient  $\beta$ , and  $\beta\ell$  is equal to this electrical length in radians, that is,

$$\beta\ell = \theta$$

6.19

and hence

$$2\pi\ell/\lambda_g = \theta.$$

With  $\theta$  in degrees this gives

$$\ell = \theta\lambda_g/360. \quad 6.20$$

Thus, with  $\lambda_g$  evaluated using Equation (6.18), we can simply find  $\ell$ .

## 6.4 Effective Permittivity and Characteristic Impedance of Microstrip

Before presenting formulas for effective permittivity and characteristic impedance we present the results of electromagnetic simulations.

It is found that the low-frequency characteristic impedance of a microstrip line only depends on the aspect ratio  $w/h$  and the permittivity of the substrate. The results of  $Z_0$  calculated using electromagnetic simulation are shown in [Figure 6.7](#). Wide lines, and so large  $w/h$ , therefore have a low  $Z_0$  and narrow lines have high  $Z_0$ . Also, if the substrate has a higher permittivity then the impedance of the line is lower for the same aspect ratio. This is consistent with the expression of characteristic impedance as  $Z_0 = \sqrt{L/C}$  as a wide line would concentrate the fields in the substrate and so increase the parallel-plate capacitance, and a microstrip line with a higher characteristic impedance would have a lower capacitance. The effect of the substrate on inductance is negligible. However, the effect of the aspect ratio on line inductance is not negligible. One of the reasons we study the formulas for characteristic impedance is to develop and reinforce this intuition.

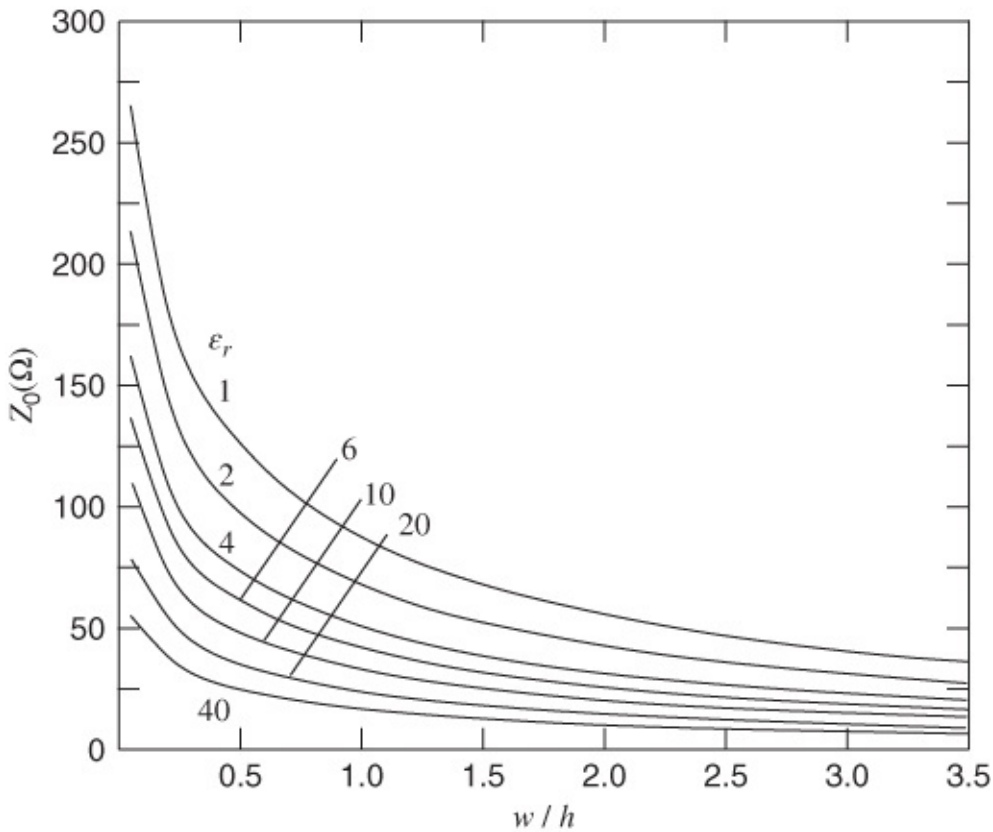


**Figure 6.7** Characteristic impedance of a microstrip line versus aspect ratios,  $w/h$ , for various substrate relative permittivities,  $\epsilon_r$  (From EM simulation).

[Figure 6.8](#) presents the results of a numerical electromagnetic simulation of the effective permittivity of a microstrip line. This has much less variation than was seen in the characteristic impedance plot. This variation with respect to both the aspect ratio ( $w/h$ ) and the substrate permittivity ( $\epsilon_r$ ) is much lower than was seen with the  $Z_0$  dependence in [Figure 6.7](#). The difference can be attributed to the effect that the aspect ratio has on both the magnetic and electric fields (which impact  $Z_0$ ) while the substrate on its own only affects the electric field distribution (and thus has a lower impact on  $\epsilon_{\text{eff}}$ ).

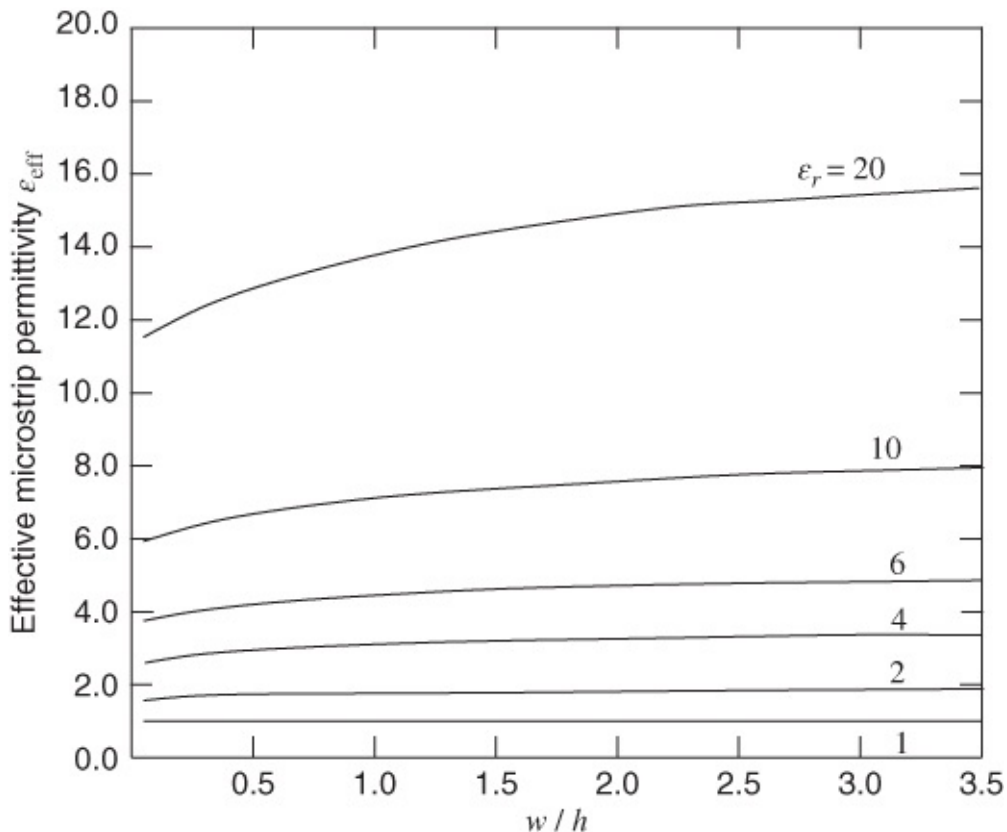


**Figure 6.8** Effective permittivity of a microstrip line versus aspect ratios,  $w/h$ , for various substrate relative permittivities,  $\epsilon_r$  (From EM simulation).

#### 6.4.1 Formulas For Effective Permittivity and Characteristic Impedance

We will now present formulas for the effective permittivity and characteristic impedance of microstrip. These formulas are fits to the results of detailed electromagnetic simulations and the form of the equations is based on good physical understanding. First assume that the thickness  $t = 0$ . This is not a bad approximation as in practice  $t < w, h$  for most microwave circuits.

Hammerstad and Jensen provided well-accepted formulas for calculating the effective permittivity and characteristic impedance of microstrip lines [10–12]. Given  $\epsilon_r$  and  $u = (w/h)$  the effective relative permittivity is

$$\epsilon_{\text{eff}} = \frac{\epsilon_r + 1}{2} + \frac{\epsilon_r - 1}{2} \left(1 + \frac{10h}{w}\right)^{-a \cdot b} \quad 6.21$$

where

$$a(u)|_{u=w/h} = 1 + \frac{1}{49} \ln \left[ \frac{u^4 + \{u/52\}^2}{u^4 + 0.432} \right] + \frac{1}{18.7} \ln \left[ 1 + \left( \frac{u}{18.1} \right)^3 \right] \quad 6.22$$

and

$$b(\epsilon_r) = 0.564 \left[ \frac{\epsilon_r - 0.9}{\epsilon_r + 3} \right]^{0.053} \quad . \quad 6.23$$

Take some time to interpret the formula above for effective relative permittivity, Equation (6.21). Let us assume for simplicity that the dimensions of the line are such that  $a \cdot b = 1$ . If  $\epsilon_r = 1$  then  $\epsilon_{\text{eff}} = (1+1)/2 + 0 = 1$  as expected. If  $\epsilon_r$  is not that of air then  $\epsilon_{\text{eff}}$  will be between 1 and  $\epsilon_r$  dependent on the geometry of the line or, more specifically, the ratio  $w/h$ . For a very wide line,  $w/h \gg 1$ ,  $\epsilon_{\text{eff}} = (\epsilon_r + 1)/2 + (\epsilon_r - 1)/2 = \epsilon_r$  corresponding to most of the electromagnetic energy being confined to the dielectric. For a thin line,  $w/h < 1$  and then  $\epsilon_{\text{eff}} = (\epsilon_r + 1)/2$ . This is just as expected from the discussion in [Section 6.3.2](#).

The characteristic impedance as a function of the aspect ratio  $u = w/h$  is given by

$$Z_0(u) = \frac{Z_{01}(u)}{\sqrt{\epsilon_{\text{eff}}}} \quad 6.24$$

where the characteristic impedance in free space

$$Z_{01}(u) = Z_0(u)|_{(\epsilon_r=1)} = 60 \ln \left[ F_1/u + \sqrt{1 + (2/u)^2} \right] \quad 6.25$$

where

$$F_1 = 6 + (2\pi - 6) \exp \left\{ -(30.666/u)^{0.7528} \right\}. \quad 6.26$$

The accuracy of Equation (6.21) is better than 0.2% for  $0.01 \leq w/h \leq 100$  and  $1 \leq \epsilon_r \leq 128$ . The accuracy of Equation (6.25) is also better than 0.1% for  $w/h < 1000$ .  $Z_0(\epsilon_r = 1)$  has a maximum value when  $w$  is vanishingly small. This is not seen in Equation (6.25) as this is only valid over a specific range of  $w$ .

[Figure 6.9](#) and [Tables 6.1–6.3](#) present the results of calculations using the formulas above for representative substrates.

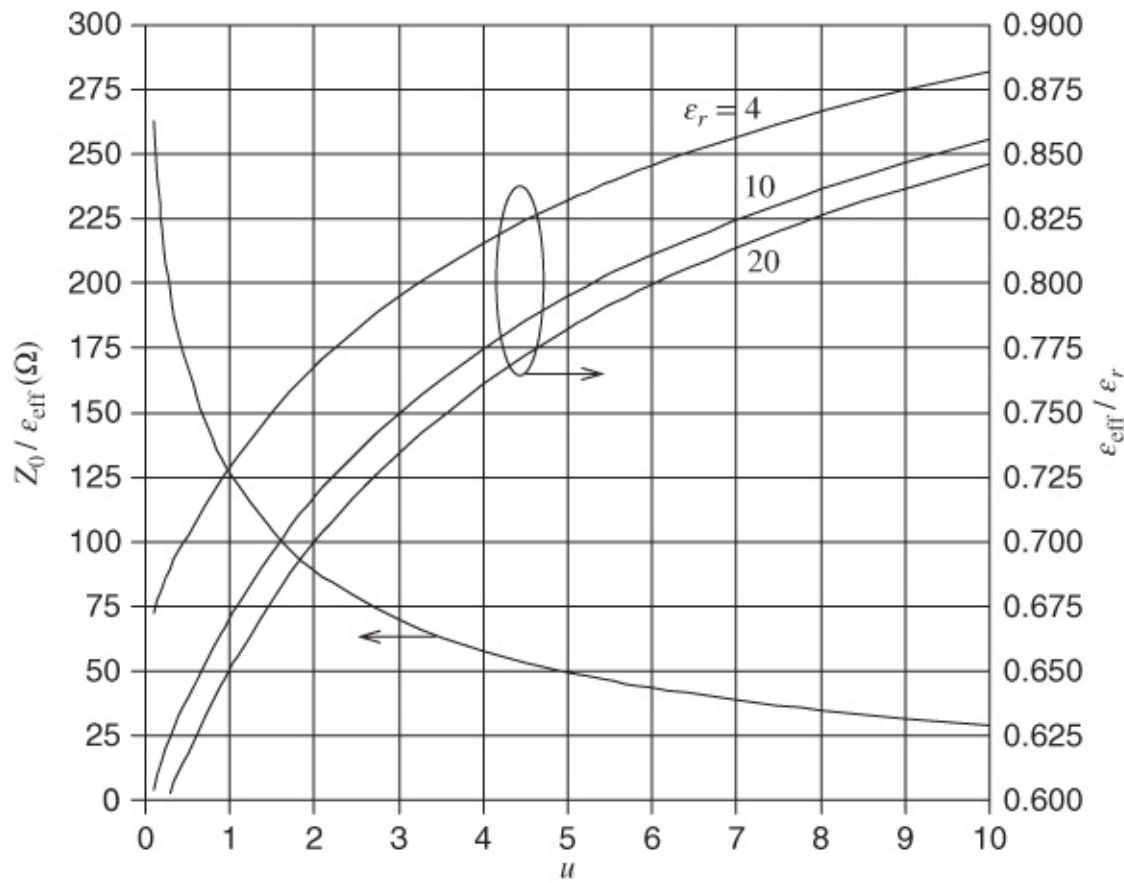


**Figure 6.9** Normalized characteristic impedance and normalized effective permittivity of a microstrip line as a function of  $u = w/h$ .

**Table 6.1** Microstrip line normalized width  $u$  and effective relative permittivity  $\epsilon_{\text{eff}}$  for specified characteristic impedance  $Z_0$ . Data derived from analysis in [Section 6.4.1](#)

$Z_0$ ( $\Omega$ )	$\epsilon_r = 4$ (SiO <sub>2</sub> , FR-4)	$\epsilon_r = 10$ (alumina)	$\epsilon_r = 11.9$ (Si)	$\epsilon_r = 12.85$ (GaAs)				
	$u$	$\epsilon_{\text{eff}}$	$u$	$\epsilon_{\text{eff}}$	$u$	$\epsilon_{\text{eff}}$	$u$	$\epsilon_{\text{eff}}$
140	0.171	2.718	0.028	5.914	0.017	6.907	0.014	7.401
139	0.176	2.720	0.029	5.917	0.018	6.910	0.015	7.404
138	0.181	2.722	0.030	5.919	0.019	6.914	0.015	7.407
137	0.185	2.723	0.031	5.922	0.020	6.919	0.016	7.413
136	0.190	2.725	0.032	5.924	0.021	6.923	0.017	7.416
135	0.195	2.727	0.033	5.927	0.022	6.925	0.017	7.418
134	0.201	2.729	0.035	5.931	0.022	6.927	0.018	7.424
133	0.206	2.731	0.036	5.933	0.023	6.930	0.019	7.429
132	0.212	2.733	0.037	5.936	0.024	6.934	0.020	7.433
131	0.217	2.734	0.038	5.939	0.025	6.937	0.021	7.438
130	0.223	2.736	0.040	5.942	0.026	6.941	0.022	7.442
129	0.229	2.738	0.043	5.949	0.028	6.948	0.023	7.446

128	0.235	2.740	0.044	5.951	0.029	6.951	0.024	7.450
127	0.241	2.742	0.046	5.955	0.030	6.954	0.025	7.454
126	0.248	2.744	0.048	5.958	0.031	6.957	0.026	7.458
125	0.254	2.746	0.050	5.962	0.033	6.963	0.027	7.461
124	0.261	2.748	0.052	5.966	0.034	6.966	0.028	7.465
123	0.268	2.750	0.054	5.970	0.035	6.969	0.030	7.472
122	0.275	2.752	0.056	5.973	0.038	6.977	0.031	7.475
121	0.283	2.755	0.058	5.977	0.039	6.980	0.032	7.478
120	0.290	2.757	0.061	5.982	0.041	6.985	0.033	7.481
119	0.298	2.759	0.063	5.985	0.043	6.990	0.035	7.486
118	0.306	2.761	0.066	5.990	0.045	6.995	0.036	7.491
117	0.314	2.763	0.068	5.993	0.047	6.999	0.039	7.499
116	0.323	2.766	0.071	5.998	0.049	7.004	0.041	7.505
115	0.331	2.768	0.074	6.003	0.051	7.008	0.042	7.508
114	0.340	2.771	0.077	6.007	0.053	7.013	0.044	7.513
113	0.349	2.773	0.080	6.012	0.055	7.017	0.046	7.518
112	0.359	2.776	0.083	6.016	0.057	7.022	0.048	7.523
111	0.368	2.778	0.086	6.021	0.060	7.028	0.050	7.528
110	0.378	2.781	0.089	6.025	0.062	7.032	0.053	7.535
109	0.389	2.783	0.093	6.031	0.065	7.038	0.055	7.540
108	0.399	2.786	0.097	6.036	0.068	7.044	0.058	7.547
107	0.410	2.789	0.100	6.040	0.071	7.050	0.060	7.552
106	0.421	2.791	0.104	6.046	0.074	7.055	0.063	7.558
105	0.432	2.794	0.109	6.052	0.077	7.061	0.066	7.565
104	0.444	2.797	0.113	6.057	0.080	7.066	0.068	7.569
103	0.456	2.800	0.117	6.062	0.084	7.073	0.071	7.575
102	0.468	2.803	0.122	6.069	0.087	7.079	0.075	7.583
101	0.481	2.806	0.127	6.075	0.091	7.085	0.078	7.589
100	0.494	2.809	0.132	6.081	0.095	7.092	0.081	7.595
99	0.507	2.812	0.137	6.087	0.099	7.099	0.085	7.603
98	0.521	2.815	0.143	6.094	0.103	7.105	0.089	7.610
97	0.535	2.819	0.148	6.100	0.108	7.113	0.093	7.618
96	0.550	2.822	0.154	6.106	0.112	7.120	0.097	7.625

95	0.565	2.825	0.160	6.113	0.117	7.127	0.101	7.632
94	0.580	2.829	0.167	6.121	0.122	7.135	0.106	7.641
93	0.596	2.832	0.173	6.127	0.128	7.144	0.111	7.649
92	0.612	2.836	0.180	6.134	0.133	7.151	0.115	7.656
91	0.629	2.839	0.187	6.142	0.139	7.159	0.121	7.666
90	0.646	2.843	0.195	6.150	0.145	7.168	0.126	7.674
89	0.664	2.847	0.202	6.157	0.151	7.176	0.132	7.684
88	0.682	2.851	0.210	6.165	0.158	7.185	0.138	7.693
87	0.701	2.855	0.219	6.173	0.164	7.193	0.144	7.702
86	0.721	2.859	0.228	6.182	0.171	7.203	0.150	7.711
85	0.740	2.863	0.237	6.190	0.179	7.213	0.157	7.721
84	0.761	2.867	0.246	6.198	0.187	7.223	0.164	7.731
83	0.782	2.872	0.256	6.208	0.195	7.233	0.171	7.741
82	0.804	2.876	0.266	6.216	0.203	7.242	0.179	7.752
81	0.826	2.881	0.277	6.226	0.212	7.253	0.187	7.763
80	0.849	2.885	0.288	6.235	0.221	7.263	0.195	7.774

**Table 6.2** Microstrip line normalized width  $u$  and effective permittivity  $\epsilon_{\text{eff}}$  for specified characteristic impedance  $Z_0$

$Z_0$ ( $\Omega$ )	$\epsilon_r = 4$		$\epsilon_r = 10$		$\epsilon_r = 11.9$		$\epsilon_r = 12.85$	
	$u$	$\epsilon_{\text{eff}}$	$u$	$\epsilon_{\text{eff}}$	$u$	$\epsilon_{\text{eff}}$	$u$	$\epsilon_{\text{eff}}$
79	0.873	2.890	0.299	6.245	0.230	7.274	0.204	7.786
78	0.898	2.895	0.311	6.255	0.240	7.285	0.213	7.797
77	0.923	2.900	0.324	6.265	0.251	7.297	0.222	7.809
76	0.949	2.905	0.337	6.276	0.262	7.309	0.232	7.821
75	0.976	2.910	0.350	6.286	0.273	7.321	0.243	7.834
74	1.003	2.915	0.364	6.297	0.285	7.333	0.254	7.847
73	1.032	2.921	0.379	6.309	0.297	7.345	0.265	7.860
72	1.062	2.926	0.394	6.320	0.310	7.359	0.277	7.874
71	1.092	2.932	0.410	6.332	0.323	7.371	0.289	7.888
70	1.123	2.937	0.426	6.344	0.338	7.386	0.303	7.903
69	1.156	2.943	0.444	6.357	0.352	7.399	0.316	7.917
68	1.190	2.949	0.462	6.369	0.368	7.414	0.330	7.932
67	1.224	2.955	0.480	6.382	0.384	7.429	0.345	7.948

66	1.260	2.961	0.500	6.396	0.400	7.444	0.361	7.964
65	1.298	2.968	0.520	6.410	0.418	7.460	0.377	7.980
64	1.336	2.974	0.541	6.424	0.436	7.476	0.394	7.997
63	1.376	2.980	0.563	6.439	0.455	7.492	0.412	8.015
62	1.417	2.987	0.586	6.454	0.475	7.509	0.431	8.033
61	1.460	2.994	0.610	6.470	0.496	7.527	0.450	8.051
60	1.504	3.001	0.635	6.486	0.518	7.545	0.471	8.071
59	1.551	3.008	0.661	6.502	0.541	7.564	0.492	8.090
58	1.598	3.015	0.688	6.519	0.564	7.583	0.515	8.111
57	1.648	3.022	0.717	6.538	0.589	7.603	0.538	8.131
56	1.700	3.030	0.746	6.556	0.616	7.624	0.563	8.153
55	1.753	3.037	0.777	6.575	0.643	7.645	0.589	8.176
54	1.809	3.045	0.809	6.594	0.672	7.667	0.616	8.199
53	1.867	3.053	0.843	6.614	0.702	7.690	0.644	8.223
52	1.927	3.061	0.878	6.635	0.733	7.713	0.674	8.248
51	1.991	3.069	0.915	6.657	0.766	7.738	0.705	8.273
50	2.056	3.077	0.954	6.679	0.800	7.763	0.738	8.300
49	2.125	3.086	0.995	6.702	0.837	7.790	0.772	8.328
48	2.197	3.094	1.037	6.726	0.875	7.817	0.808	8.357
47	2.272	3.103	1.081	6.750	0.914	7.845	0.846	8.386
46	2.350	3.112	1.128	6.775	0.956	7.874	0.886	8.418
45	2.432	3.121	1.177	6.801	1.000	7.904	0.928	8.450
44	2.518	3.131	1.229	6.828	1.047	7.936	0.972	8.483
43	2.609	3.140	1.283	6.856	1.096	7.968	1.019	8.518
42	2.703	3.150	1.340	6.884	1.147	8.002	1.068	8.553
41	2.803	3.160	1.400	6.913	1.201	8.036	1.120	8.590
40	2.908	3.171	1.464	6.944	1.259	8.072	1.174	8.628
39	3.019	3.181	1.531	6.974	1.319	8.108	1.232	8.668
38	3.136	3.192	1.602	7.006	1.384	8.147	1.294	8.709
37	3.259	3.203	1.677	7.039	1.452	8.186	1.359	8.751
36	3.390	3.214	1.757	7.073	1.524	8.226	1.428	8.795
35	3.528	3.226	1.841	7.108	1.600	8.268	1.501	8.840
34	3.675	3.237	1.931	7.143	1.682	8.311	1.579	8.886

33	3.831	3.250	2.027	7.180	1.769	8.355	1.662	8.934
32	3.997	3.262	2.129	7.218	1.862	8.402	1.751	8.984
31	4.174	3.275	2.238	7.258	1.961	8.449	1.846	9.036
30	4.364	3.288	2.355	7.298	2.067	8.498	1.948	9.089
29	4.567	3.301	2.480	7.340	2.181	8.549	2.057	9.144
28	4.785	3.315	2.615	7.384	2.304	8.601	2.175	9.201
27	5.020	3.329	2.760	7.428	2.436	8.655	2.301	9.260
26	5.273	3.344	2.917	7.475	2.579	8.712	2.438	9.321
25	5.547	3.359	3.087	7.523	2.734	8.770	2.587	9.385
24	5.845	3.374	3.272	7.573	2.902	8.831	2.749	9.451
23	6.169	3.390	3.474	7.625	3.086	8.894	2.925	9.520
22	6.523	3.407	3.694	7.679	3.287	8.960	3.118	9.591
21	6.912	3.424	3.936	7.734	3.508	9.028	3.330	9.666
20	7.341	3.441	4.203	7.793	3.752	9.100	3.565	9.744

**Table 6.3** Microstrip line normalized width  $u$  and effective permittivity  $\epsilon_{\text{eff}}$  for specified characteristic impedance  $Z_0$

$Z_0$ ( $\Omega$ )	$\epsilon_r = 4$		$\epsilon_r = 10$		$\epsilon_r = 11.9$		$\epsilon_r = 12.85$	
	$u$	$\epsilon_{\text{eff}}$	$u$	$\epsilon_{\text{eff}}$	$u$	$\epsilon_{\text{eff}}$	$u$	$\epsilon_{\text{eff}}$
19	7.815	3.459	4.499	7.854	4.022	9.174	3.824	9.825
18	8.344	3.478	4.829	7.917	4.323	9.252	4.114	9.911
17	8.936	3.497	5.199	7.983	4.661	9.334	4.438	10.000
16	9.603	3.517	5.616	8.053	5.043	9.419	4.805	10.094
15	10.361	3.538	6.090	8.126	5.476	9.509	5.221	10.192
14	11.229	3.559	6.633	8.202	5.972	9.604	5.698	10.296
13	12.233	3.581	7.262	8.282	6.547	9.704	6.251	10.406
12	13.407	3.604	7.997	8.367	7.219	9.809	6.897	10.521
11	14.798	3.628	8.868	8.456	8.016	9.920	7.663	10.644
10	16.471	3.652	9.916	8.550	8.975	10.038	8.584	10.774

#### 6.4.2 A Convenient Approximation of Effective Permittivity

Let us consider the special case where  $w$  is very small. Then  $Z_{01}$  is that of free space, that is,  $Z_{01} = \sqrt{\mu_0 \epsilon_0} = 377 \Omega$ . In addition,  $\epsilon_{\text{eff}}$  has its minimum value when  $w$  is vanishingly small. Then

$$\epsilon_{\text{eff}} = \frac{\epsilon_r + 1}{2}.$$

6.27

This leads to an approximate (and more convenient) form of Equation (6.21):

$$\epsilon_{\text{eff}} = \frac{\epsilon_r + 1}{2} + \frac{\epsilon_r - 1}{2} \frac{1}{\sqrt{1 + 12h/w}}. \quad 6.28$$

This approximation has its greatest error for low and high  $\epsilon_r$  and narrow lines,  $w/h < 1$ , where the maximum error is 1%. Again Equation (6.24) would be used to calculate the characteristic impedance. A comparison of the line characteristics using the more precise formula for  $\epsilon_{\text{eff}}$ , Equation (6.21), and the somewhat less accurate fit, Equation (6.28), is given in [Table 6.4](#).

**Table 6.4** Comparison of two fitted equations for the effective permittivity and characteristic impedance of a microstrip line. Equation (6.21) has an accuracy of better than 0.2% and Equation (6.28) has an accuracy of better than 1%

$\epsilon_r$	$w/h$	$\epsilon_{\text{eff}}$	$Z_0$	$\epsilon_{\text{eff}}$	$Z_0$
		Eq. (6.21), 0.2%		Eq. (6.28), 1%	
2	0.01	1.525	515.6	1.514	517.4
2	0.1	1.565	294.1	1.545	296.0
2	1	1.645	112.2	1.639	112.4
2	10	1.848	21.91	1.837	21.97
2	100	1.969	2.583	1.972	2.581
10	0.01	5.683	267.1	5.630	268.3
10	0.1	6.016	150.0	5.909	151.4
10	1	6.705	55.56	6.748	55.38
10	10	8.556	10.18	8.534	10.20
10	100	9.707	1.163	9.752	1.161
20	0.01	10.88	193.1	10.77	194.0
20	0.1	11.57	108.2	11.36	109.2
20	1	13.01	39.88	13.13	39.70
20	10	16.93	7.238	16.91	7.243
20	100	19.38	8.823	19.48	8.821
128	0.01	66.90	77.8	66.30	77.2
128	0.1	71.51	43.52	70.27	43.90
128	1	81.12	15.97	82.11	15.88
128	10	71.51	43.5	70.27	43.9
128	100	123.8	0.326	124.5	0.325

## 6.5 Filling Factor

The less accurate formula for effective permittivity, Equation (6.28), is in a form which enables a simple expression for the filling factor,  $q$ , to be derived. Equating Equations (6.15) and (6.28),

$$\epsilon_{\text{eff}} = \frac{\epsilon_r + 1}{2} + \frac{\epsilon_r - 1}{2} \left( \frac{1}{\sqrt{1 + 12h/w}} \right) \quad 6.29$$

$$= 1 + q(\epsilon_r - 1) \quad 6.30$$

that is,

$$q(\epsilon_r - 1) = \frac{\epsilon_r - 1}{2} + \frac{\epsilon_r - 1}{2} \left( \frac{1}{\sqrt{1 + 12h/w}} \right), \quad 6.31$$

and so the filling factor in terms of the geometry parameters is

$$q = \frac{1}{2} \left( 1 + \frac{1}{\sqrt{1 + 12h/w}} \right). \quad 6.32$$

$q$  is also approximately independent of frequency. From Equation (6.32)  $q$  has a maximum value of 1 when  $w \gg h$  and a minimum value of 0.5 when  $w < h$ . The filling factor calculated using the formula is compared to that extracted from electromagnetic simulation in [Figure 6.10](#). The maximum error is 6%.

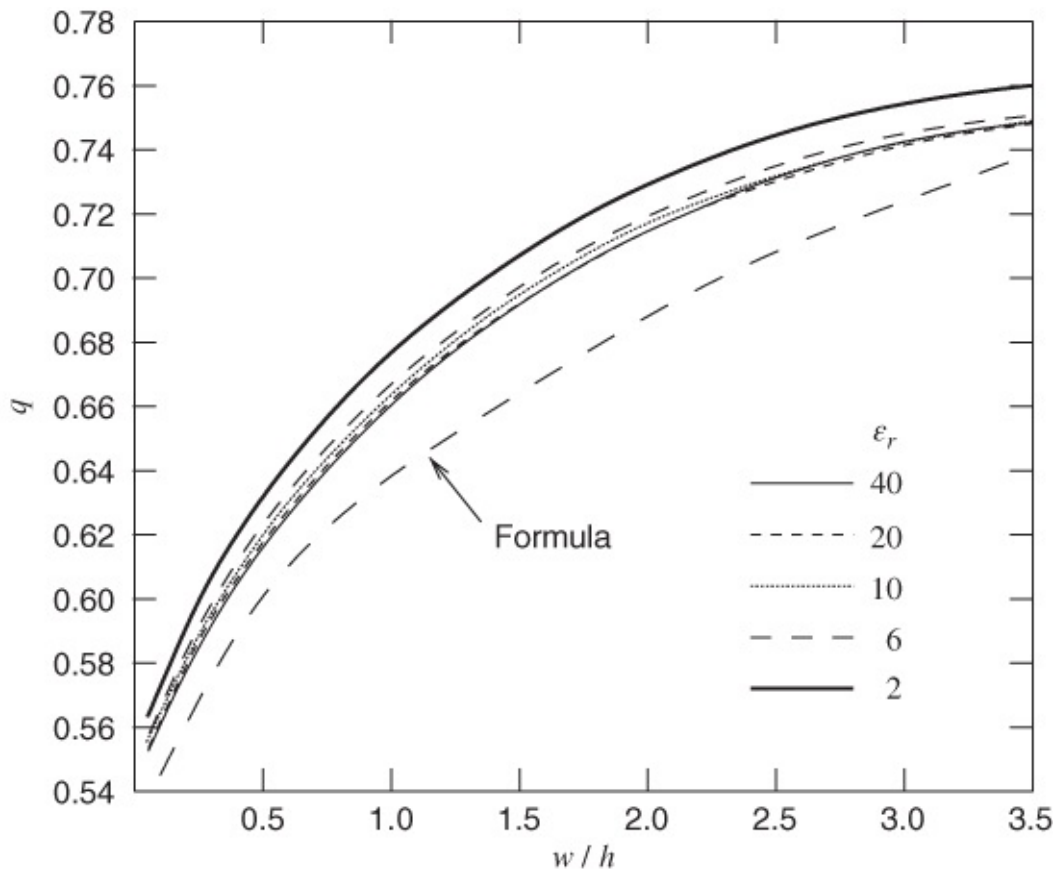


**Figure 6.10** Filling factor for a microstrip line versus aspect ratios,  $w/h$ , for various substrate relative permittivities,  $\epsilon_r$ . Results calculated using electromagnetic simulation except for the curve identified as ‘Formula’, which was calculated using Equation (6.32).

## 6.6 Approximate Graphically Based Synthesis

Presser [13] devised a graphical technique for the analysis and synthesis of microstrip lines. This concept is extended here, leading to the design curves presented in [Figure 6.11](#) where the free space characteristic impedance  $Z_{01}$  and filling factor  $q$  are plotted as functions of the aspect ratio  $w/h$ . The design curves were developed using EM simulation at a low frequency of 100 MHz corresponding to a static-TEM mode.

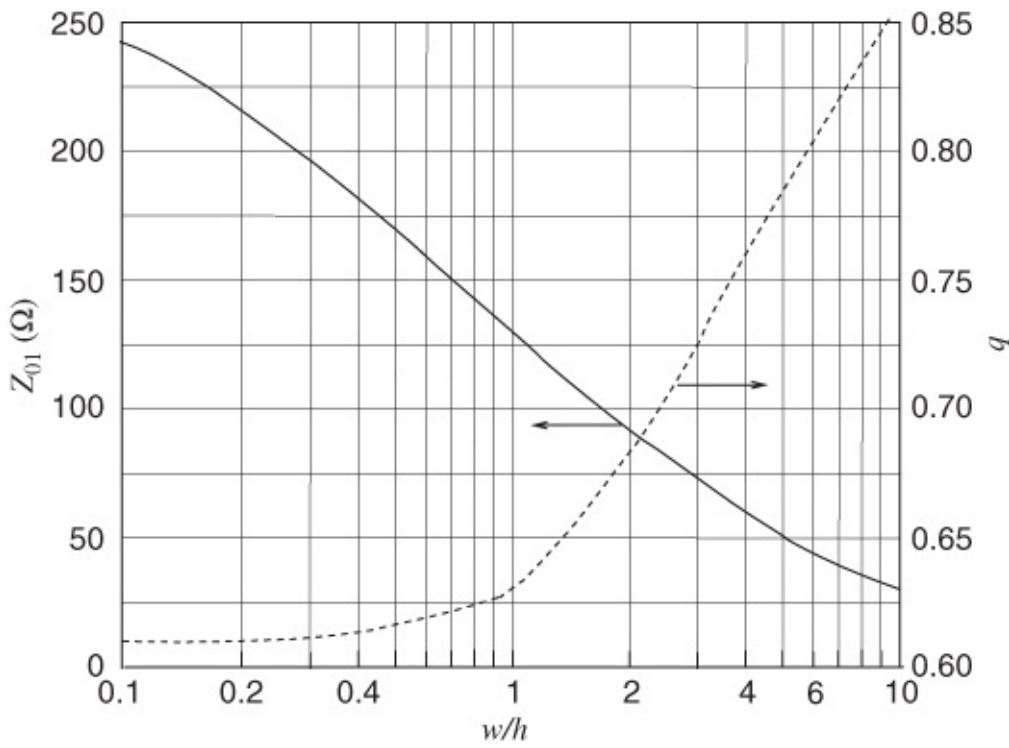


**Figure 6.11** Curves for the graphical analysis or synthesis of microstrip:  $Z_{01}$  is the free-space characteristic impedance and  $q$  is the filling factor as a function of aspect ratio  $w/h$ . (Developed using Sonnet with a frequency of 100 MHz and the  $q$  curves evaluated with  $\epsilon_r = 10$ ).

Graphical synthesis proceeds as follows:

- Make the initial, very rough, assumption  $\epsilon_{\text{eff}} \approx \epsilon_r$  to obtain starting values.
- Calculate the air-spaced characteristic impedance approximately, from Equation (6.13), with  $\epsilon_{\text{eff}} \approx \epsilon_r$ , that is, using  $Z_{01} \approx \sqrt{\epsilon_r} Z_0$ .
- Use the general two-curve graph (Figure 6.11) to find  $w/h$  applicable to this  $Z_{01}$  and also note the corresponding value of the microstrip filling factor  $q$ .
- Hence calculate the updated value of  $\epsilon_{\text{eff}}$  using Equation (6.15):

$$\epsilon_{\text{eff}} = 1 + q(\epsilon_r - 1).$$

This now ends one iteration. Steps (b) to (d) must be repeated using the progressively improved values of  $\epsilon_{\text{eff}}$  (instead of  $\epsilon_r$  in steps (a) and (b)). Fast convergence is generally obtained here, and only two or three iterations are usually necessary before  $\epsilon_{\text{eff}}$  is finally within about 1% of its previous value, that is, convergence has occurred.

The final value of  $w/h$ , and hence the width  $w$ , is of course the value appropriate to the final  $Z_{01}$ . Lastly, the wavelength must be calculated using Equation (6.18). The static-TEM part of the microstrip design procedure is then complete using this graphical technique.

However, any graphical approach will inevitably involve errors of several per cent and also clearly cannot form part of a computer-aided design (CAD) algorithm. This form of graphical

technique is mainly suitable for approximate guidance purposes. Most microstrip design work necessarily proceeds using CAD and demands relatively high accuracy (typically better than 1%). Therefore, closed formulas are very useful for synthesis; in the next section suitable formulas are presented. These closed formulas also provide an insight into trends and sensitivities that cannot be obtained using CAD programs alone. It should be noted that material characteristics, such as permittivity, are not known to better than 1% and so tuning of a fabricated microstrip circuit is sometimes required.

## 6.7 Formulas for Accurate Static-TEM Design Calculations

Closed formulas are highly desirable for use in microstrip calculations for the following reasons:

- a. a fairly high accuracy is achievable
- b. fast CAD algorithms can be implemented
- c. incorporation of static-TEM formulas in frequency-dependent calculations for higher-frequency design ([Chapter 7](#)).

Various researchers have reported formulas for microstrip calculations [7, 8, 11, 14]. Owens [9] carefully investigated the ranges of applicability of many of the expressions given by Wheeler [8], comparing calculated results with numerical computations. The formulas are most accurate for substrates with  $8 < \epsilon_r < 12$ .

### 6.7.1 Synthesis Formulas ( $Z_0$ and $\epsilon_r$ Given)

#### 6.7.1.1 Narrow Strip, High Impedance

For narrow strips (i.e., when  $Z_0 > (44 - 2\epsilon_r) \Omega$ ):

$$\frac{w}{h} = \left( \frac{\exp H'}{8} - \frac{1}{4 \exp H'} \right)^{-1} \quad 6.33$$

where

$$H' = \frac{Z_0 \sqrt{2(\epsilon_r + 1)}}{119.9} + \frac{1}{2} \left( \frac{\epsilon_r - 1}{\epsilon_r + 1} \right) \left( \ln \frac{\pi}{2} + \frac{1}{\epsilon_r} \ln \frac{4}{\pi} \right). \quad 6.34$$

We may determine the effective relative permittivity as

$$\epsilon_{\text{eff}} = \frac{\epsilon_r + 1}{2} \left[ 1 - \frac{1}{2H'} \left( \frac{\epsilon_r - 1}{\epsilon_r + 1} \right) \left( \ln \frac{\pi}{2} + \frac{1}{\epsilon_r} \ln \frac{4}{\pi} \right) \right]^{-2} \quad 6.35$$

where  $H'$  is given by Equation (6.34) (as a function of  $Z_0$ ) or, alternatively, as a function of  $w/h$ , from Equation (6.33):

$$H' = \ln \left[ 4 \frac{h}{w} + \sqrt{16 \left( \frac{h}{w} \right)^2 + 2} \right]. \quad 6.36$$

Another, somewhat simpler, expression for  $\epsilon_{\text{eff}}(Z_0)$  is furnished by Equation (15) of Owens [9], which is

$$\epsilon_{\text{eff}} = \frac{\epsilon_r + 1}{2} \left[ 1 + \frac{29.98}{Z_0} \left( \frac{2}{\epsilon_r + 1} \right)^{1/2} \left( \frac{\epsilon_r - 1}{\epsilon_r + 1} \right) \left( \ln \frac{\pi}{2} + \frac{1}{\epsilon_r} \ln \frac{4}{\pi} \right) \right]^{-2}. \quad 6.37$$

This formula for  $\epsilon_{\text{eff}}$  is known to be accurate to better than 1% for  $Z_0 > (63 - 2\epsilon_r) \Omega$  (i.e., when  $w/h < 1.3$ ) and  $8 < \epsilon_r < 12$  [9].

### 6.7.1.2 Wide Strip, Low Impedance

We now consider the ranges and formulas for “wide” strips. For wide strips (i.e., when  $Z_0 < (44 - 2\epsilon_r) \Omega$ ):

$$\frac{w}{h} = \frac{2}{\pi} [(d_{\epsilon r} - 1) - \ln(2d_{\epsilon l} - 1)] + \frac{(\epsilon_r - 1)}{\pi \epsilon_r} \left[ \ln(d_{\epsilon r} - 1) + 0.293 - \frac{0.517}{\epsilon_r} \right] \quad 6.38$$

where

$$d_{\epsilon r} = \frac{59.95\pi^2}{Z_0 \sqrt{\epsilon_r}} \quad d_{\epsilon l} = \frac{59.95\pi^2}{Z_0} . \quad 6.39$$

Alternatively, if  $Z_0$  is already known

$$\epsilon_{\text{eff}} = \frac{\epsilon_r}{0.96 + \epsilon_r(0.109 - 0.004\epsilon_r)[\log(10 + Z_0) - 1]} . \quad 6.40$$

For microstrip lines on alumina ( $\epsilon_r = 10$ ) this expression appears to be accurate to  $\pm 0.2\%$  over the impedance range

$$8 \leq Z_0 \leq 45 \Omega.$$

### 6.7.2 Analysis Formulas ( $w/h$ and $\epsilon_r$ Given)

For ‘narrow’ strips ( $w/h < 3.3$ ):

$$Z_0 = \frac{119.9}{\sqrt{2(\epsilon_r + 1)}} \ln \left[ 4 \frac{h}{w} + \sqrt{16 \left( \frac{h}{w} \right)^2 + 2} \right]. \quad 6.41$$

For ‘wide’ strips ( $w/h > 3.3$ ):

$$Z_0 = \frac{119.9\pi}{2\sqrt{\epsilon_r}} \left\{ \frac{w}{2h} + \frac{\ln 4}{\pi} + \frac{\ln(e\pi^2/16)}{2\pi} \left( \frac{\epsilon_r - 1}{\epsilon_r^2} \right) + \frac{\epsilon_r + 1}{2\pi\epsilon_r} \left[ \ln \frac{\pi e}{2} + \ln \left( \frac{w}{2h} + 0.94 \right) \right] \right\}^{-1} \quad 6.42$$

where  $e$  is the exponential base:  $e = 2.7182818 \dots$ .

The effective permittivity  $\epsilon_{\text{eff}}$  can be evaluated with considerable accuracy using Equation (6.35) (or Equation (6.37)). When  $w/h > 1.3$  and  $Z_0 > (63 - 2\epsilon_r) \Omega$ ,  $\epsilon_{\text{eff}}$  can be obtained using Equation (6.29) but with less accuracy.

### 6.7.3 Overall Accuracies to be Expected From the Previous Expressions

In all cases, the shape ratio  $w/h$  will be accurate to  $\pm 1\%$ . For narrow lines ( $w/h < 1.3$ ),  $\epsilon_{\text{eff}}$  has the error range  $\pm 0.5\%$ . When calculated using Equation (6.29),  $\epsilon_{\text{eff}}$  is accurate to  $\pm 0.25\%$ . The expressions for  $Z_0$  result in accuracies to  $\pm 1\%$ .

## 6.8 Electromagnetic Analysis-based Techniques

CAD can be used to synthesize microstrip circuits by including an analysis engine in an optimization loop with prescribed goals. From several viewpoints, for example initial concept development, understanding of sensitivities, and manufacturability, it is preferable to use the types of formulas presented here. However, as pointed out early in Section 6.7 the formulas only apply to a restricted range of substrates, and for design work using different substrates (e.g., quartz, plastics, etc.) a fundamental computation is necessary. In a typical approach a family of closed formulas or graphs is derived from the results of a design space exploration using computer-aided analysis. These computationally derived results are normally verified with experimental characterization of selected structures. It is worth noting that since semiconductor substrates such as HRS ( $\epsilon_r = 11.7$ ) or semi-insulating GaAs ( $\epsilon_r = 12.8$ ) have permittivities just 20–30% higher than high-grade alumina ( $\epsilon_r = 10$ ), the above formulas should work well. The applicability is even better for GaN ( $\epsilon_r = 9.5$  or 10.4 depending on crystal orientation). It is useful to be able to express the characteristic impedance entirely in capacitive terms [15]. This is already available in the form of Equation (6.8), which is repeated here for convenience:

$$Z_0 = 1/(c\sqrt{CC_1}). \quad 6.43$$

Thus, in order to compute  $Z_0$ , only the capacitances per unit length,  $C_1$  and  $C$ , are required.

Now a capacitance  $C_x$  may, in general, be expressed in terms of net charge  $Q$  and voltage  $V_T$  as

$$C_x = Q/V_T. \quad 6.44$$

The charge is obtainable by applying Gauss' theorem:

$$Q = \oint D \cdot ds \quad 6.45$$

in which  $D$  is the electric flux density and  $s$  is a surface enclosing the strip conductor. The procedure is therefore to determine the electric field,  $E$ , either numerically or analytically, and from that determine  $D$  at regular points on the closed surface  $s$  using

$$D = \epsilon E. \quad 6.46$$

Now the  $D$  values can be substituted in Equation (6.45).

In practice a shielded microstrip is generally considered (the shield can be progressively moved away from the strip to approach the unshielded case, if desired).

Of course, two complete calculations of capacitance, using Equation (6.44), are required: one with the substrate present, yielding  $C$ , and a second with the substrate removed, yielding  $C_1$ . Then Equation (6.43) gives the characteristic impedance. The effective microstrip permittivity  $\epsilon_{\text{eff}}$  is also known, via Equations (6.10) and (6.11):

$$\epsilon_{\text{eff}} = C/C_1. \quad 6.47$$

Great precision is readily achievable.

## 6.9 A Worked Example of Static-TEM Synthesis

Let us consider the  $30 \Omega$  transmission line of the microstrip matching circuit shown for the transistor amplifier in [Figure 6.1](#). We are required to calculate the width and approximate length of this element, and for the moment we shall neglect the effects of the discontinuities present at each end, that is, the step to  $50 \Omega$  microstrip and the bend. These and other discontinuities are dealt with in [Chapter 9](#). The initial specification is, from [Figure 6.1](#):

$$Z_0 = 30 \Omega \quad \ell = \lambda_g/4 \quad f = 2 \text{ GHz}$$

(We could alternatively have specified  $\theta = 90^\circ$ , which is identical to  $\ell = \lambda_g/4$ .) Also assume that a substrate is chosen having the following specification:

$$\text{relative permittivity } \epsilon_r = 9.8 \quad \text{thickness } h = 0.6 \text{ mm.}$$

Since the frequency is only 2 GHz the static-TEM methods described here will definitely be of ‘sufficient’ accuracy (i.e., within  $\pm 1\%$  when the accurate expressions are used). At first we carry out a rapid, approximate determination using Presser’s graphical technique.

### 6.9.1 Graphical Determination

Referring to step (a) given in [Section 6.6](#) we have an initial estimate of the equivalent characteristic impedance without a dielectric:

$$Z'_{01} = \sqrt{9.8} \times 30 \approx 94 \Omega.$$

From the graph of [Figure 6.11](#) we obtain, for this value of  $Z'_{01}$ , an initial estimate of the filling factor:

$$q' \approx 0.68.$$

From step (d) in [Section 6.6](#),

$$\epsilon'_{\text{eff}} \approx 7.0$$

and hence the improved value of  $Z'_{01}$  is

$$Z_{01} \approx \sqrt{7.0} \times 30 \approx 79 \Omega.$$

Using the graph again, with this new value of  $Z_{01}$  we obtain:

$$\frac{w}{h} = 2.7, \quad q = 0.71, \quad \text{and then } \epsilon_{\text{eff}} = 7.25. \quad \text{6.48}$$

This is the result of the graphically based synthesis. As a check, EM simulation using  $w/h = 2.7$  results in  $Z_0 = 29.1 \Omega$  and  $\epsilon_{\text{eff}} = 7.21$ , errors of less than 3%.

### **6.9.2 Accurately Calculated Results**

Iterative synthesis using EM simulation of a  $30-\Omega$  microstrip line with a substrate having a permittivity of 9.8 yields:

$$w/h = 2.59 \quad \text{and} \quad \epsilon_{\text{eff}} = 7.20.$$

Notice that the approximate graphical technique considered in the previous section gives fairly accurate results. The steps used in the graphical approach closely conform to the intuition microwave engineers utilize (or need to develop).

### **6.9.3 Final Dimensions of the Microstrip Element**

The accurately calculated results are employed here. Since the substrate thickness  $h = 0.6 \text{ mm}$ , with  $w/h = 2.59$ , we find the microstrip width:

$$w = 1.554 \text{ mm.}$$

The length is now required. An expression for the microstrip wavelength, Equation (6.18), was given earlier:

$$\lambda_g = 300/(F \sqrt{\epsilon_{\text{eff}}}) \text{ mm}$$

where  $F$  is in gigahertz.

Since the physical length  $\ell$  is required to be  $\lambda_g/4$  we obtain

$$\ell = \frac{\lambda_g}{4} = \frac{75}{2\sqrt{7.20}}$$

so that

$$\ell = 13.98 \text{ mm.}$$

Because of the reactive effects of the discontinuities ([Chapter 9](#)) the actual length of the line will be slightly less than the calculated value of 13.98 mm.

Physical length determinations at different frequencies and/or on different substrates follow precisely the same procedure as above. The physical length calculated above is substantial, too large for implementation in a mobile handset. On a ceramic substrate with  $\epsilon_r = 100$ , all physical lengths are decreased by the approximate factor  $\sqrt{\epsilon_{r1}/\epsilon_{r2}} = \sqrt{100/9.8} = 3.19$ . This means that a quarter-wave linear resonator on the  $\epsilon_r = 100$  material would have a physical length of 4.38 mm.

## 6.10 Microstrip on a Dielectrically Anisotropic Substrate

Many substrates, usually crystals, have very low loss and accurately controlled dimensions. Particularly useful substrates are HRS, sometimes referred to as silicon circuit board [16–19], and silicon. Many of these crystal-based substrates possess a degree of dielectric anisotropy. One particularly useful substrate material is sapphire, which possesses well-defined dielectric anisotropy and has been quite intensively investigated [20]. We will only consider sapphire here and before proceeding further it is worth listing the advantages of sapphire, as follows:

- a.** The material is extremely pure and the permittivity values are now accurately known (and very stable).
- b.** There is negligible batch-to-batch variation. That is to say, one piece of sapphire, taken from anywhere, will be almost exactly like any other piece of sapphire.
- c.** An optical surface finish is readily achievable, resulting in very uniform and precisely defined thin metal films for microstrip conductors.
- d.** The material is completely optically transparent. This means that the process of mounting chip devices can be accurately registered because the operator can see the underside.
- e.** Since the thermal conductivity of sapphire is about 30% higher than that of alumina it may be preferred to the latter for mounting power devices.
- f.** It has very low loss.

Some other advantages were discussed in [Chapter 5](#). It is also worth pointing out that silicon as a circuit board substrate has another unique advantage: it is perfectly thermally matched to the thermal coefficient of expansion of silicon-integrated circuits.

In this section we show that microstrip circuit design on sapphire may proceed in the manner

so far described for isotropic substrates, provided a preferred orientation is chosen and a suitable function for an equivalent permittivity is used.

With the axes as shown in [Figure 6.12](#), the relative permittivity tensor  $\check{\epsilon}_r$  may be written

$$\check{\epsilon}_r = \begin{bmatrix} \epsilon_{r,xx} & \epsilon_{r,xy} & \epsilon_{r,xz} \\ \epsilon_{r,yx} & \epsilon_{r,yy} & \epsilon_{r,yz} \\ \epsilon_{r,zx} & \epsilon_{r,zy} & \epsilon_{r,zz} \end{bmatrix} = \begin{bmatrix} \epsilon_{r,xx} & 0 & 0 \\ 0 & \epsilon_{r,yy} & 0 \\ 0 & 0 & \epsilon_{r,zz} \end{bmatrix} = \begin{bmatrix} \epsilon_{r,x} & 0 & 0 \\ 0 & \epsilon_{r,y} & 0 \\ 0 & 0 & \epsilon_{r,z} \end{bmatrix} \quad 6.49$$

and this interrelates the electric displacement and electric field vectors:

$$\bar{D} = \check{\epsilon}\epsilon_0\bar{\mathcal{E}}. \quad 6.50$$

Thus the effective permittivity of a sapphire substrate, if it is to be expressed as one number, depends on the direction of the field. Note that in Equation (6.49) the permittivity tensor is diagonal so it is common to replace  $\epsilon_{r,xx}$ ,  $\epsilon_{r,yy}$ , and  $\epsilon_{r,zz}$  by  $\epsilon_{r,x}$ ,  $\epsilon_{r,y}$ , and  $\epsilon_{r,z}$ , respectively. (There are many accents used to identify a tensor and most commonly none is used as it is represented as a matrix, i.e., in boldface. To minimize confusion a caron ( $\check{\cdot}$ ) will be used here to identify a tensor.) In all practical cases the principal axis of the sapphire is aligned to be very nearly perpendicular to the substrate–air interface, that is, along the  $y$  direction in [Figure 6.12](#). Therefore, Equation (6.49) may be written

$$\check{\epsilon}_r = \begin{bmatrix} \epsilon_{r,\perp} & 0 & 0 \\ 0 & \epsilon_{r,\parallel} & 0 \\ 0 & 0 & \epsilon_{r,\perp} \end{bmatrix}. \quad 6.51$$

Furthermore, the values are known accurately for sapphire, yielding

$$\check{\epsilon}_{r, \text{sapphire}} = \begin{bmatrix} 9.40 & 0 & 0 \\ 0 & 11.60 & 0 \\ 0 & 0 & 9.40 \end{bmatrix}. \quad 6.52$$

Thus, with this particular orientation, and the sapphire substrate forming the dielectric between two completely parallel plates with no fringing, only the 11.60 relative permittivity value affects the TEM propagation which would then apply. Since microstrip is certainly not a symmetrical (infinite) parallel plate and does involve considerable fringing fields, the effects of this anisotropy are significant. The problem was studied fundamentally by Owens *et al.* [20], who numerically solved for the potentials around the structure.

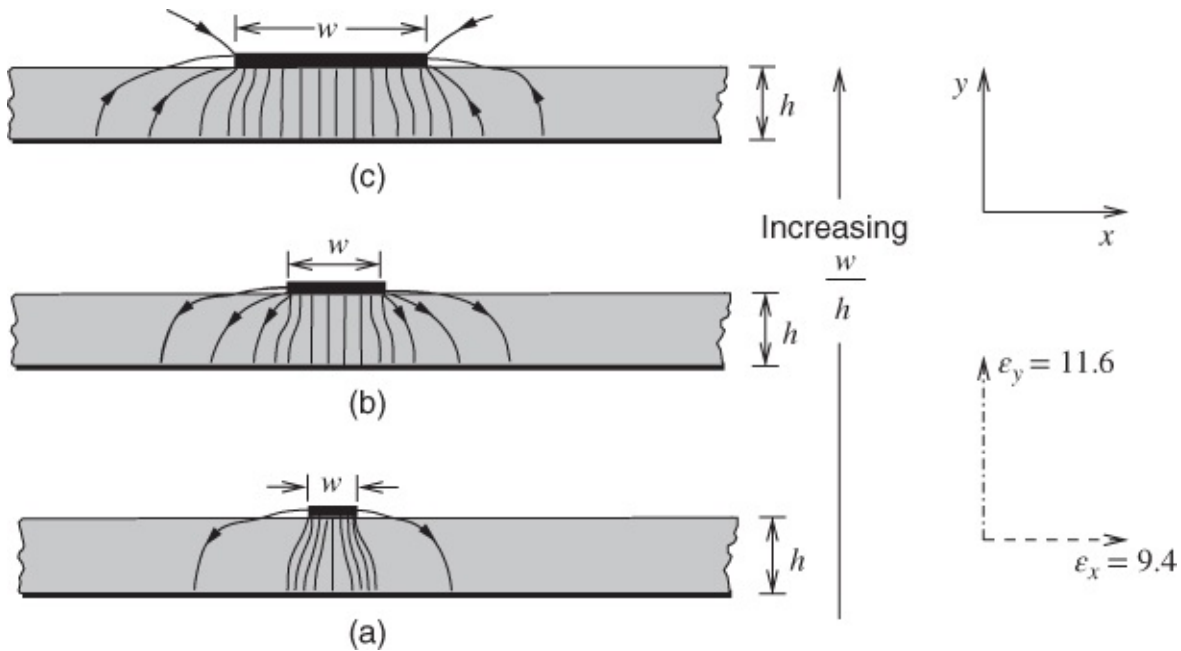


**Figure 6.12** Electric field distributions, in the transverse plane, applicable to microstrip on an anisotropic substrate (sapphire) for three shape ( $w/h$ ) ratios: (a) small, (b) moderate and (c) large. The  $z$  direction is out of the page.

The effective microstrip permittivity  $\epsilon_{\text{eff}}$  is finally found as a ratio of capacitances. However, because of the anisotropy,  $\epsilon_{\text{eff}}$  depends on  $w/h$  in a different manner to the isotropic dependence. To appreciate this more completely, the electric field distribution is shown in [Figure 6.12](#) for three different  $w/h$  values. In case (iii) the fields are almost entirely affected by  $\epsilon_{r,y}$  ( $= 11.60$ ). In the other extreme shown, case (i) for relatively small  $w/h$ ,  $\epsilon_{r,x}$  ( $= 9.40$ ) significantly affects the field because there is a considerable fraction of electric field in the  $x$  direction.

To simplify the synthesis of microstrip on a sapphire substrate, a new permittivity concept has been suggested to account for the gross anisotropic effects. This is termed the equivalent isotropic substrate relative permittivity,  $\epsilon_{r,\text{eq}}$ , and it is, of course, dependent on the width-to-height ratio  $w/h$ . A strict definition of  $\epsilon_{r,\text{eq}}$  is as follows:

The equivalent isotropic substrate relative permittivity  $\epsilon_{r,\text{eq}}$  is the permittivity of some fictitious uniform and isotropic substrate, supporting a microstrip transmission line, which would yield microstrip static-TEM design parameters having values identical to those for the same line geometry ( $w/h$ ) on sapphire.

The situation is illustrated in [Figure 6.13](#).

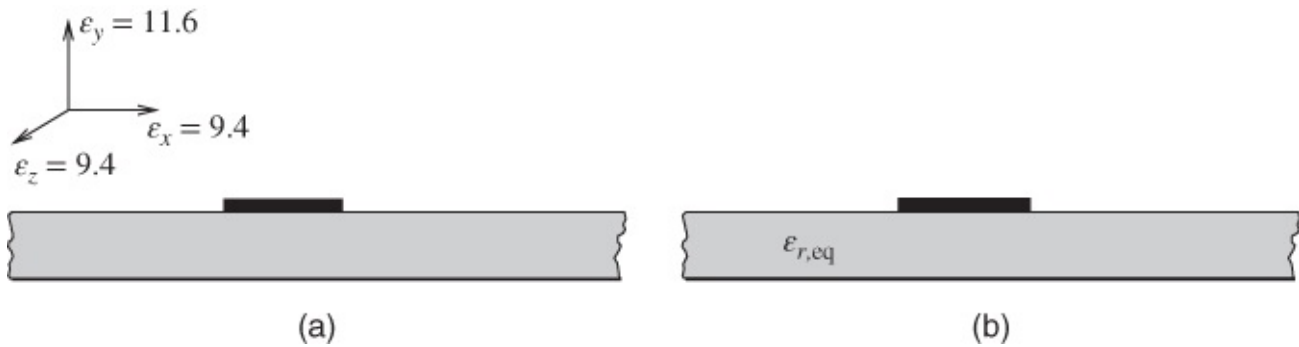


**Figure 6.13** Illustrating the concept of equivalent isotropic substrate relative permittivity ( $\epsilon_r$ ): (a) sapphire substrate; and (b) equivalent isotropic substrate.

For a known line geometry,  $w/h$ , an appropriate value of  $\epsilon_{r,\text{eq}}$  may be calculated and then used as  $\epsilon_r$  in microstrip design formulas. Three design curves for microstrip on sapphire, originally published in Owens *et al.* [20], are reproduced here as Figure 6.14.

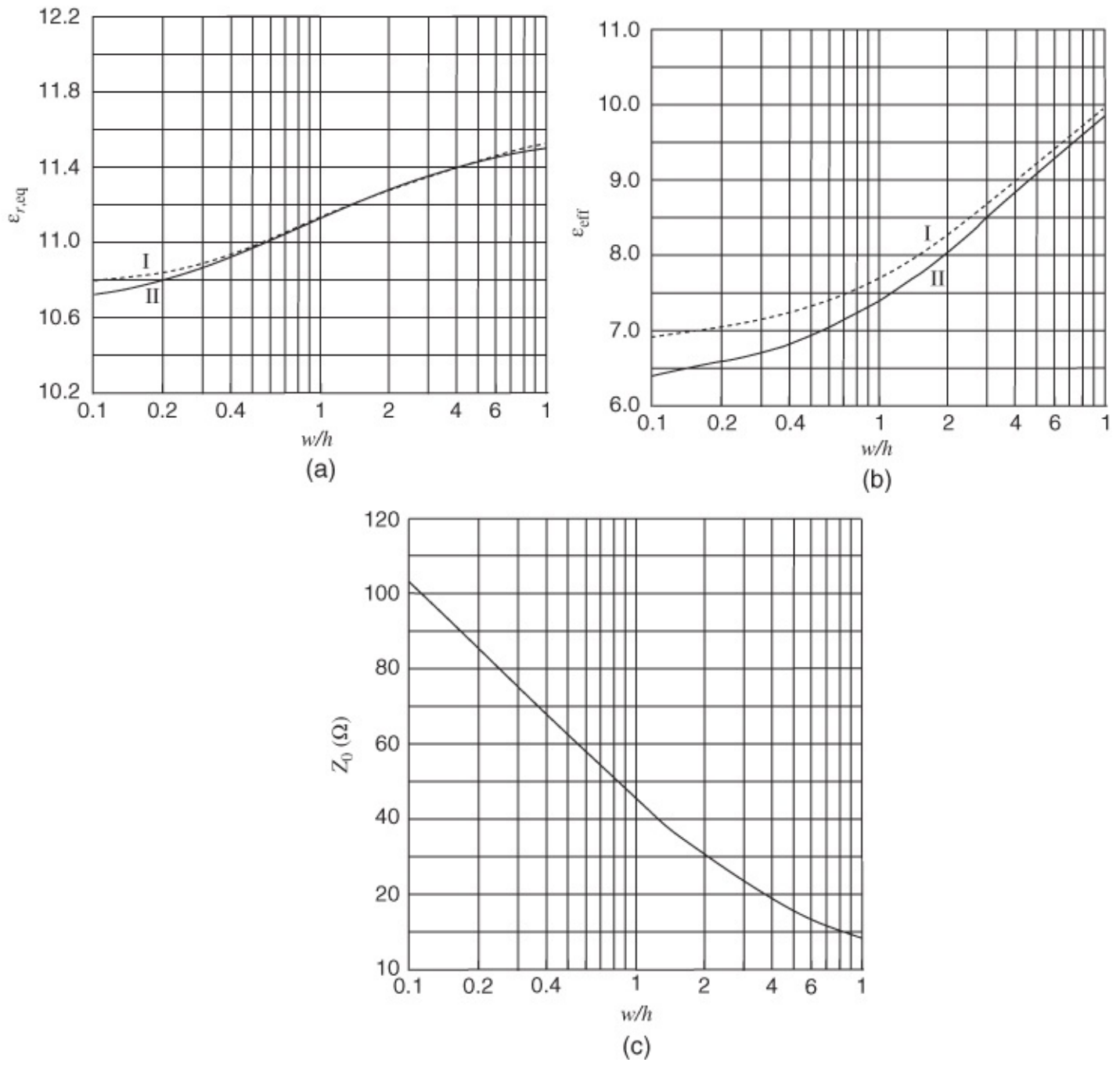


**Figure 6.14** Design curves for microstrip lines on a sapphire substrate (C axis perpendicular to the ground plane). Curve I uses  $\epsilon_{r,y}$  as “ $\epsilon_r$ ”. Curve II uses  $\epsilon_{r,\text{eq}}$  from Equation (6.55): (a) equivalent relative permittivity; (b) effective relative permittivity; and (c) characteristic impedance. Adapted from Owens *et al.* (1976) [20], figures 6.3–6.5, pp. 502–503. Reproduced with permission of IEEE.

Quite accurate values of  $\epsilon_{r,\text{eq}}$  may be obtained through a combination of simple considerations and conventional (isotropic substrate) calculation. A cross-sectional model for microstrip on an anisotropic substrate assists this calculation of  $\epsilon_{r,\text{eq}}$  and is shown in [Figure 6.15](#).

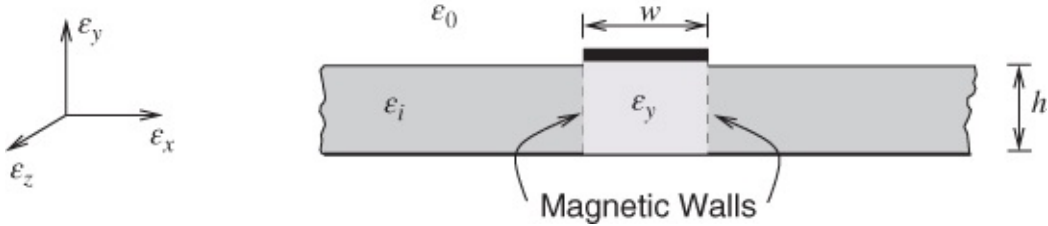


**Figure 6.15** A model for microstrip on an anisotropic substrate with C axis perpendicular to the ground plane.

The electric field immediately beneath the strip and down to the ground plane is almost entirely affected by  $\epsilon_{r,y}$  alone. Elsewhere in the substrate, and in the surrounding air, the direction and density of the electric flux is such that  $\epsilon_{r,x}$  and  $\epsilon_{r,y}$  have approximately equal influences on the remaining capacitance associated with the microstrip. Thus, in [Figure 6.15](#), we can treat the regions bounded by the magnetic walls separately. The total capacitance  $C$  per unit length of the microstrip line can thus be decomposed into separate quantities:

- a. the simple parallel-plate capacitance directly beneath the strip given by

$$C_y = \epsilon_{r,y} \epsilon_0 (w/h). \quad 6.53$$

- b. a fringing capacitance  $C_f$  accounting for the remaining flux regions.

As shown in [Figure 6.15](#), there is a hypothetical permittivity quantity  $\epsilon_{r,i}$  ascribed to the remaining substrate regions. If we calculate the total capacitance  $C_i$  per unit length for the microstrip, but on some uniform isotropic substrate of permittivity  $\epsilon_{r,i}$ , the fringing capacitance is then approximately the difference:

$$C_f \approx C_i - \epsilon_{r,i} \epsilon_0 (w/h) \quad 6.54$$

where  $C_i$  may be evaluated using any appropriate conventional technique as described earlier, the method outlined in [Section 6.8](#), for example. At present  $\epsilon_{r,i}$  is unknown, but it is quite a straightforward task to find a value for this quantity, as indicated shortly.

Finally, the equivalent relative permittivity  $\epsilon_{r,eq}$  is given by a combination of  $\epsilon_{r,x}$  and  $\epsilon_{r,y}$ , weighted by the respective capacitance ratios  $C_f/C$  and  $C_y/C$ :

$$\epsilon_{r,eq} = \epsilon_{r,i} \left( \frac{C_f}{C} \right) + \epsilon_{r,y} \left( \frac{C_y}{C} \right).$$

However, the total capacitance  $C = C_y + C_f$ , therefore

$$\epsilon_{r,eq} = \frac{\epsilon_{r,i} C_f + \epsilon_{r,y} C_y}{C_f + C_y}. \quad 6.55$$

An optimized value  $\epsilon_{r,i} = 10.60$  was obtained by curve fitting to the numerical values making up the discrete points shown alongside curve I of [Figure 6.14\(a\)](#), where curve II is the actual plot of Equation (6.55) using this value of  $\epsilon_{r,i}$ .

This value can be used as a constant in determining  $\epsilon_{r,\text{eq}}$  for particular microstrip-on-sapphire designs. According to [Figure 6.14\(a\)](#) the worst discrepancy, amounting to 0.65%, occurs at the  $w/h = 0.1$  extreme.

As a purely empirical alternative, the following expression gives  $\epsilon_{r,\text{eq}}$  and the only independent variable involved is  $w/h$ :

$$\epsilon_{r,\text{eq}} = 12.0 - \frac{1.21}{1 + 0.39[\log(10w/h)]^2}. \quad 6.56$$

The accuracy of Equation (6.56) when tested against other theoretical calculations and measurements, with results extrapolated to zero frequency, appears to be  $\pm 0.5\%$  throughout the range

$$0.1 \leq w/h \leq 10$$

which, on the sapphire substrate, approximates to the characteristic impedance range

$$10 \leq Z_0 \leq 100 \Omega$$

and this is quite sufficient for a wide variety of circuit design purposes.

When static-TEM analysis is applied to microstrip-on-sapphire designs the effective relative permittivity evaluated,  $\epsilon_{\text{eff}}$ , will depend on the shape ratio  $w/h$ . This is clearly shown by the curves of [Figure 6.14\(b\)](#), where curve I has been generated using  $\epsilon_{r,y}$  as  $\epsilon_r$  in the calculations, but curve II is generated using Equation (6.55) for  $\epsilon_{r,\text{eq}}$ . For [Figure 6.14\(c\)](#),  $\epsilon_{r,\text{eq}}$  was used in determining the continuous curve. Thus, curve II of [Figure 6.14\(b\)](#) and the curve of [Figure 6.14\(c\)](#) represent design curves for microstrip on sapphire.

There are several other dielectrically anisotropic substrate materials, notably single-crystal quartz and some semiconductor substrates, in particular GaAs. In any design using these materials, the principles outlined above may be developed in the same manner to provide a design basis.

## 6.11 Microstrip and Magnetic Materials

Magnetic materials have quite extraordinary properties and one section cannot describe their properties. It is possible to do microstrip design using an effective permeability of a substrate. However, if a magnetic material is used it is nearly always because a special characteristic of the magnetic material is being exploited. It could be that the magnetic material is being used to miniaturize a circuit, especially on-chip inductors and transformers. Even then the material must be treated in a special way. As a result a full chapter is devoted to magnetic materials, see [Chapter 20](#).

## 6.12 Effects of Finite Strip Thickness, Metallic Enclosure, and Manufacturing Tolerances

### 6.12.1 Effects of Finite Strip Thickness

Referring back to [Figure 6.2](#) we see that microstrip, in general, will have a finite thickness  $t$  which influences the field distribution. For most single microstrip lines the effect of this thickness on the design parameters is very small and may often be neglected. Even in the case of microstrip circuits manufactured using thick-film technology or created by etching, there is usually no need to allow for thickness when calculating impedance or effective microstrip permittivity because such strips invariably taper towards the strip edges. Notable exceptions are digital interconnects on chips, where the interconnects are kept as narrow as possible to ensure high wiring density.

The effect of thickness on the field distribution is shown in [Figure 6.16](#), with several investigations conducted. Some straightforward and accurate expressions have been reported [22], which are now stated here, starting with characteristic impedances:

**a.** For  $w/h \leq 1$ :

$$\text{6.57 } Z_0 = \frac{60}{\sqrt{\epsilon_{\text{eff}}}} \ln \left( 8 \frac{h}{w_{\text{eff}}} + 0.25 \frac{w_{\text{eff}}}{h} \right).$$

**b.** For  $w/h \geq 1$ :

$$Z_0 = \frac{120\pi}{\sqrt{\epsilon_{\text{eff}}}} \ln \left[ \frac{w_{\text{eff}}}{h} + 1.393 + 0.667 \left( \frac{w_{\text{eff}}}{h} + 1.444 \right) \right]^{-1} \quad \text{6.58}$$

where, in both cases for  $w/h \leq 1/2\pi$

$$\frac{w_{\text{eff}}}{h} = \frac{w}{h} \frac{1.25t}{\pi h} \left[ 1 + \ln \left( \frac{4\pi w}{t} \right) \right] \quad \text{6.59}$$

and for  $w/h \geq 1/2\pi$

$$\frac{w_{\text{eff}}}{h} = \frac{w}{h} + \frac{1.25t}{\pi h} \left[ 1 + \ln \left( \frac{2h}{t} \right) \right]. \quad \text{6.60}$$

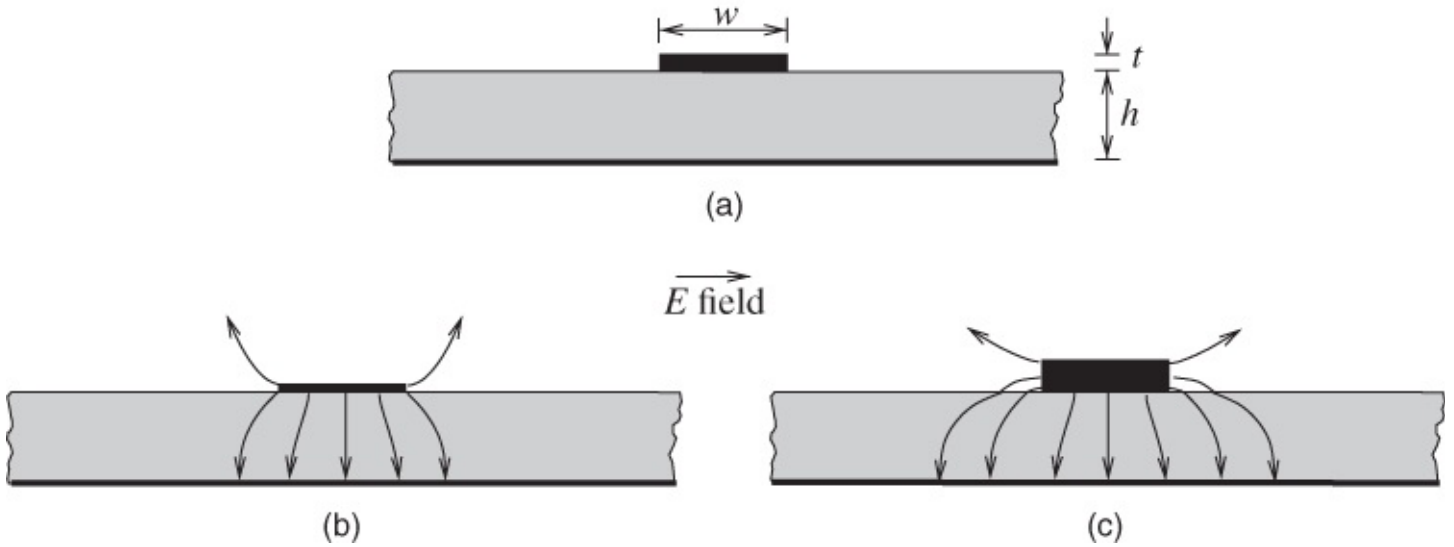


**Figure 6.16** Changes in the distribution of electric field (transverse cross-section) as the thickness of microstrip is altered.

Finally, the effective microstrip permittivity  $\epsilon_{\text{eff}}$  should be evaluated using expressions given previously ([Section 6.7](#)) and the following term subtracted [21]:

$$\Delta\epsilon_{\text{eff}}(t) = \frac{(\epsilon_r - 1)t/h}{4.6\sqrt{w/h}} \quad 6.61$$

so that the final value is given by

$$\epsilon_{\text{eff}}(t) = \epsilon_{\text{eff}} - \Delta\epsilon_{\text{eff}}(t). \quad 6.62$$

For microstrip having  $t/h \leq 0.005$ ,  $2 \leq \epsilon_r \leq 10$  and  $w/h \geq 0.1$ , the effects of this thickness on characteristic impedance and effective permittivity are negligible (within approximately 1% on  $Z_0$  or  $\epsilon_{\text{eff}}$ ). At smaller values of  $w/h$  or greater values of  $t/h$ , the significance of the thickness increases. These trends are clearly shown in curves published by Schwan [23], although he gave no details of their derivation. It is interesting to compare the trends exhibited in Schwan's results with those predicted by the expressions given here, Equations ([6.57](#)) to ([6.61](#)). An alumina substrate is chosen, with relative permittivity 10 and thickness 0.5 mm, and we also assume a strip conductor thickness of 0.032 mm, that is  $t/h = 0.064$ .

With a shape ratio  $w/h = 0.1$ , Schwan indicates a 20–30% reduction in  $Z_0$  and approximately a 14% reduction in  $\epsilon_{\text{eff}}$ , both compared with the  $t/h = 0$  values. Careful checks with the formulas given here confirm these trends, but show much smaller changes, approximately 7% for both the permittivity and the impedance. Measurements and other indications tend to support these smaller changes.

## 6.12.2 Alternative Treatment of the Effect of Strip Thickness

An alternative treatment of the effect of strip thickness was presented by Hammerstad and Jensen [10]. Their analysis separated the effect of strip thickness from the effect of the nonhomogeneity of the electrical environment, that is, the different permittivities of the substrate

and that of air. Hammerstad and Jensen (building on the results of Wheeler [24]) provide a correction accounting for finite strip thickness by calculating an increase in the effective width of the strip. The correction is comprised of two parts, one which corrects for the change in strip thickness alone and a second part that accounts for the effective permittivity of the dielectric.

The correction due to the thickness  $t$  of the strip is

$$\Delta w_1 = \frac{th}{\pi} \ln \left( 1 + \frac{4e}{t \coth^2(\sqrt{6.517w/h})} \right) \quad 6.63$$

where  $e = 2.7182818$ . Combined with the effective width of the homogenous structure the combined change in the effective width is

$$\Delta w_r = \frac{1}{2} \left( 1 + \frac{1}{\cosh \sqrt{\epsilon_r - 1}} \right) \Delta w_1 \quad 6.64$$

so that the effective width is

$$w_{\text{eff}} = w + \Delta w_r. \quad 6.65$$

With this new effective width the effective permittivity and characteristic impedance need to be recalculated using Equations (6.21)–(6.26) to account for the finite strip thickness.

### 6.12.3 Effects of a Metallic Enclosure

In many practical applications microstrip circuits are contained in a metallic enclosure. The enclosure serves the purposes of hermetic sealing, mechanical strength, electromagnetic shielding, connector mounting, and ease of handling of the module. The presence of conducting top and side walls lowers both the characteristic impedance and the effective microstrip permittivity, which is due to the increased proportion of electric flux in air. The effects of a top cover alone, as well as those due to a complete enclosure, have been reported by several researchers. Closed formulas [25] are given here which predict the effects of a conducting top cover, and show how both the characteristic impedance and effective microstrip permittivity are modified in comparison with the unshielded static-TEM expressions given in [Section 6.7](#). The nomenclature of [Figure 6.17](#) is used throughout.

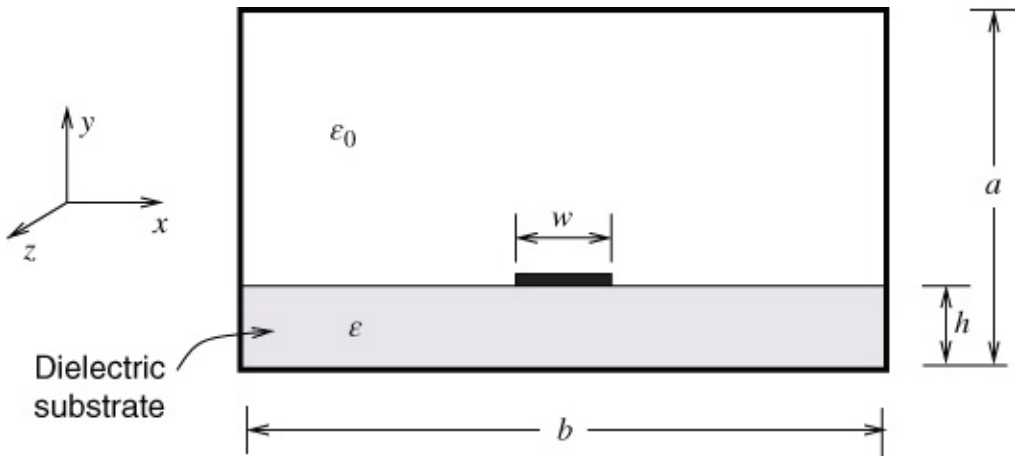


**Figure 6.17** Cross-section of shielded microstrip:  $h' = a - h$ .

The characteristic impedance is considered first: when  $w/h \leq 1.3$ :

$$Z_0(\text{shielded}) = Z_0(\text{unshielded}) - \Delta Z_{0s1} \quad 6.66$$

and when  $w/h \geq 1.3$ :

$$Z_0(\text{shielded}) = Z_0(\text{unshielded}) - \Delta Z_{0s2} \quad 6.67$$

in which

$$\Delta Z_{0s1} = 270 \left[ 1 - \tanh \left( 0.28 + 1.2 \sqrt{h'/h} \right) \right] \quad 6.68$$

and

$$\Delta Z_{0s2} = Z_{0s1} \left( 1 - \tanh \left\{ 1 + \frac{0.48[(w_{\text{eff}}/h) - 1]^{0.5}}{[1 + (h'/h)]^2} \right\} \right). \quad 6.69$$

The effective microstrip permittivity of a shielded (top cover only) microstrip line is given by

$$\epsilon_{\text{eff}} = \frac{\epsilon_r + 1}{2} + \left( \frac{\epsilon_r - 1}{2} R \right) \tanh \left[ 0.18 + 0.237(h'/h) - \frac{0.415}{(h'/h)^2} \right] \quad 6.70$$

in which

$$R = \begin{cases} [1 + 12(h/w)]^{-0.5} + 0.04[1 - (w/h)]^2 & \text{for } w/h \leq 1 \\ [1 + 12(h/w)]^{-0.5} & \text{for } w/h \geq 1 \end{cases}. \quad 6.71$$

The expressions quoted in [Section 6.7](#) might alternatively be used, but the nature of the shielding-modifying term is then uncertain.

In all these equations, Equations (6.66) to (6.70),  $w_{\text{eff}}$  has already been defined by Equations (6.59) and (6.60),  $Z_0(\text{unshielded})$  can be determined using expressions given previously in [Section 6.7](#).

Comparison with the theoretical results due to Kowalski and Pregla [25] shows discrepancies

within 1%. The effect of the enclosure is of course captured in the electromagnetic field simulation of shielded microstrip lines.

### 6.12.4 Effects Due to Manufacturing Tolerances

The effect on the various parameters due to tolerances in the physical dimensions has been quite intensively investigated and reported in detail by Gupta *et al.* [2]. Although often difficult, it is important to control the variations in thickness  $h$  and relative permittivity  $\epsilon_r$ . Some batch-to-batch variations are, however, inevitable, and the effects of these on electrical quantities such as impedance and VSWR must be determined [27]. In addition to the effects of thickness and permittivity variations, the surface finish of the substrate affects the precision with which the strip width can be manufactured.

With the maximum deviations of  $w$ ,  $h$ , and  $\epsilon_r$  represented by  $\Delta w$ ,  $\Delta h$ , and  $\Delta \epsilon_r$  respectively, the normalized maximum excursion in the characteristic impedance is given by

$$\frac{|\Delta Z_0|_{\max}}{Z_0} = \left| \frac{|\Delta w|}{w} S_{Z_0(w)} \right| + \left| \frac{|\Delta h|}{h} S_{Z_0(h)} \right| + \left| \frac{|\Delta \epsilon_r|}{\epsilon_r} S_{Z_0(\epsilon_r)} \right| \quad 6.72$$

and the normalized maximum excursion in the effective microstrip permittivity is given by

$$\frac{|\Delta \epsilon_{\text{eff}}|_{\max}}{\epsilon_{\text{eff}}} = \left| \frac{\Delta w}{w} S_{\epsilon_{\text{eff}}(w)} \right| + \left| \frac{\Delta h}{h} S_{\epsilon_{\text{eff}}(h)} \right| + \left| \frac{\Delta \epsilon_r}{\epsilon_r} S_{\epsilon_{\text{eff}}(\epsilon_r)} \right| \quad 6.73$$

where the sensitivity is, in general, defined by

$$S_{Q(p)} = \frac{p}{Q} \frac{\partial Q}{\partial p} \quad 6.74$$

in which  $Q$  is a quantity whose sensitivity is to be determined, here  $Z_0$ ,  $\epsilon_{\text{eff}}$ , and  $p$  is a controlling parameter, here  $w, h, \epsilon_r$ .

It is particularly important that the accuracy demanded in the manufacture of strip width be evaluated. This is the minimum selected from the two values of  $\Delta w$  obtained by rearranging Equations (6.72) and (6.73) for

$$\frac{\Delta w}{w} S_{Z_0(w)} \quad \text{and} \quad \frac{\Delta w}{w} S_{\epsilon_{\text{eff}}(w)}$$

respectively. Any of the required sensitivities may be obtained by appropriately differentiating expressions given in [Section 6.7](#).

Gupta *et al.* [2] show that the mismatch (described by the voltage standing wave ratio (VSWR)) due to tolerances in the various quantities ( $w, h, \epsilon_r$ ) may be directly related to the resultant characteristic impedance change. The following expression is given for the VSWR as a function of the relative change  $r$ , that is,  $\text{VSWR}(r)$ , where

$$r = \left( 1 - \frac{|\Delta Z_0|_{\max}}{Z_0} \right)^{-1}. \quad 6.75$$

Here  $|\Delta Z_0|_{\max}/Z_0$  is determined from Equation (6.72). Detailed graphs of parameter variations are given for an alumina substrate in the cited reference. In broad terms it is found that the VSWR can be held below 1.05 provided the tolerances are less than approximately 5%.

The maximum change in effective microstrip permittivity, from Equation (6.73), is approximately 4.3% on alumina, when the relative permittivity tolerance is also approximately 4.5%, or the substrate thickness tolerance about 4%, or the microstrip width tolerance is about 8%.

## 6.13 Pulse Propagation along Microstrip Lines

There are many instances in high-speed systems in which microstrip lines are used to carry signal pulses rather than analog microwave signals. This is of increasing importance. Examples of such applications include:

- very high speed computer logic (through GHz clock rates)
- high bit-rate digital communications (e.g., direct pulsing of a laser or LED for optical communications through tens of Gbit/s)
- high-speed samplers for oscilloscopes or time-domain reflectometers (below 20 ps rise times)
- pico-second resolution counters
- radars.

One of the most significant properties of microstrip in these applications is that of *propagation delay*. The delay time per meter,  $\tau_d$ , for a microstrip line is given simply by

$$\tau_d = \frac{1}{v_p} \text{ s/m} \quad 6.76$$

or, using Equation (6.11),

$$\tau_d = \frac{\sqrt{\epsilon_{\text{eff}}}}{c} \text{ s/m} \quad 6.77$$

where  $\epsilon_{\text{eff}}$  is the effective relative permittivity and  $c$  is the speed of light in a vacuum.

The static-TEM effective microstrip permittivity  $\epsilon_{\text{eff}}$  is determined using any appropriate method, as described earlier. As an example, let us consider a 50  $\Omega$  microstrip line on high-purity alumina which has  $\epsilon_{\text{eff}} \approx 6.7$ . We obtain, using Equation (6.77), a propagation delay

$$\tau_d = \sqrt{6.7}/(3 \times 10^8) \text{ s/m}$$

$$\approx 8.6 \text{ ns/m.}$$

In practice this means that the delay is 8.6 ps/mm and a length of 10 mm produces 86 ps of delay for a pulse. In some situations it is necessary to extend the delay. One possible way in which to increase the effective propagation delay is to build a slow wave transmission line, for example by introducing capacitive loading at intervals along the microstrip. The delay then becomes influenced by these capacitances ( $v_p = 1/\sqrt{LC}$ ) and  $v_p$  is reduced, that is, the pulse is slowed, if  $C$  is increased. Further, the effective inductance per unit length  $L$  may also be increased, and the microstrip takes on the general appearance shown in [Figure 6.18](#).

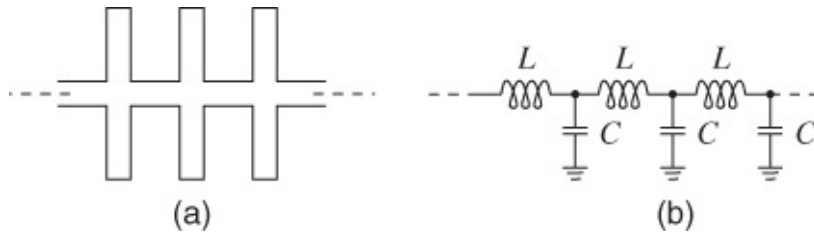


**Figure 6.18** A microstrip circuit structure yielding substantial delay: (a) microstrip layout; and (b) equivalent circuit.

## 6.14 Recommendations Relating to the Static-TEM Approaches

This section provides a summary of the principal design methods and formulas which were presented in this chapter. Although the static-TEM approaches, when used directly, exhibit significant errors at frequencies beyond a few gigahertz, they form a basis for powerful design expressions which are used at higher frequencies. This is discussed in [Chapter 7](#).

### 6.14.1 The Principal Static-TEM Synthesis Formulas

These were given in [Section 6.7](#). They are of proven accuracy to within 1% for  $w/h$  and 0.5% for  $\epsilon_{\text{eff}}$ ; some are repeated here for convenience.

a. For narrow strips (i.e., when  $Z_0 > (44 - 2\epsilon_r) \Omega$ ):

$$\frac{w}{h} = \left( \frac{\exp H'}{8} - \frac{1}{4 \exp H'} \right)^{-1}$$

under the slightly different condition,  $w/h < 1.3$ :

$$\epsilon_{\text{eff}} = \frac{\epsilon_r + 1}{2} \left[ 1 - \frac{1}{2H'} \left( \frac{\epsilon_r - 1}{\epsilon_r + 1} \right) \left( \ln \frac{\pi}{2} + \frac{1}{\epsilon_r} \ln \frac{4}{\pi} \right) \right]^{-2}$$

where, for both expressions,

$$H' = \frac{Z_0 \sqrt{2(\epsilon_r + 1)}}{119.9} + \frac{1}{2} \left( \frac{\epsilon_r - 1}{\epsilon_r + 1} \right) \left( \ln \frac{\pi}{2} + \frac{1}{\epsilon_r} \ln \frac{4}{\pi} \right).$$

**b.** For wide strips (i.e., when  $Z_0 < (44 - 2\epsilon_r) \Omega$ ):

$$\frac{w}{h} = \frac{2}{\pi} [(d_\epsilon - 1) - \ln(2d_\epsilon - 1)] + \frac{\epsilon_r - 1}{\pi \epsilon_r} \left[ \ln(d_\epsilon - 1) + 0.293 - \frac{0.517}{\epsilon_r} \right] \quad 6.78$$

where

$$d_\epsilon = \frac{59.9 \pi^2}{Z_0 \sqrt{\epsilon_r}} \quad 6.79$$

and, again with the slightly different condition,  $w/h > 1.3$ :

$$\epsilon_{\text{eff}} = \frac{\epsilon_r + 1}{2} + \frac{\epsilon_r - 1}{2} \left( 1 + 10 \frac{h}{w} \right)^{-0.555}. \quad 6.80$$

For the effects of shielding (top cover), finite thickness of strip, and manufacturing tolerances, [Section 6.12](#) should be consulted.

The approximate graphical method described in [Section 6.6](#) is useful at least for a first run analysis or synthesis, and is applicable to any substrate. Apart from lack of accuracy, its main drawback is the restricted range encompassed.

### 6.14.2 Microstrip on a Sapphire (Anisotropic) Substrate

This problem was discussed in detail in [Section 6.10](#). The main design expression is the empirical formula for the equivalent relative permittivity of the substrate:

$$\epsilon_{r,\text{eq}} = 12.0 - \frac{1.21}{1 + 0.39[\log(10w/h)^2]}.$$

Once more, this expression is only known to be accurate within  $\pm 0.5\%$  over the range

$$0.1 \leq w/h \leq 10.$$

On the sapphire substrate this approximates the characteristic impedance range

$$10 \leq Z_0 \leq 100 \Omega.$$

The value of  $\epsilon_{r,\text{eq}}$  obtained using the above expression is directly substituted for  $\epsilon_r$  in the static-TEM formulas which apply to the more useful isotropic substrate situation. However,  $w/h$  is initially not accurately known in design and some iterative CAD routine is therefore required. The designer might start with a rough initial value  $\epsilon_{r,\text{eq}} \approx 11$  for sapphire, compute  $w/h$  from a static-TEM expression, evaluate an updated  $\epsilon_{r,\text{eq}}$ , etc. Since  $\epsilon_{r,\text{eq}}(w/h)$  is a fairly slowly varying function, this would be a good, fast-converging approach.

### 6.14.3 Design Strategies Accommodating Manufacturing Tolerances

Once an MIC has been manufactured there is often little that one can do to trim the structure and hence improve upon the performance of the complete circuit. Where the passive (i.e., microstrip) circuitry can be tested in the absence of any active devices, the deviations in actual measured performance may be observed and used to calculate the required artwork/processing adjustments for an improved second attempt. Usually the spread of characteristics and the rejection costs preclude this approach when active devices have been incorporated. Sometimes it may also be possible to etch or laser-trim microstrip elements. Whatever the method, the following guidelines are applicable to microstrip on an alumina-type substrate:

- a. Always start with a slightly lower impedance than actually desired, i.e., larger  $w/h$ , if trimming is contemplated. [Table 6.5](#) indicates the approximate magnitude of adjustments for a 1% increase in  $Z_0$ .
- b. The physical lengths of sections should also initially be made slightly longer than finally required if trimming is contemplated. This is because the operating frequency for these lengths will then be slightly lower than required and the physical length (proportional to wavelength) must be reduced by etching or laser-trimming to increase the operating frequency back to the correct value. The adjustment may be made on a pro rata basis, that is, with a 1% reduction in length we can expect approximately a 1% increase in frequency.
- c. As a final suggestion the length of a top-cover shield might be adjusted to trim the performance of MICs. See [Section 6.12.3](#) for suitable expressions which would yield the values of adjustments required.

[Table 6.5](#) Adjustments required in  $w$  for a 1% increase in  $Z_0$

$\approx w/h$	$\approx Z_0 (\Omega)$	Reduction in $w$ (%)
0.1	110	3
1.0	50	2.5
8.0	12	1

## 6.15 Summary

Microstrip is the most versatile and economic type of microwave transmission line. It is conveniently realized using PCB technology and it is almost surprising that it needed to be invented [28]. It is not enough to conceive of a transmission line medium, it is necessary to have analytic formulas for transmission line parameters and modeling concepts. The most important concept used with microstrip transmission lines is the concept of effective permittivity. This enables intuitive understanding of the behaviour of a microstrip line which is, after all, inhomogenous with some of the field in air above the strip and the rest of the field in the substrate below the strip. The effective permittivity concept enables design to proceed using an effective planar transmission line embedded in uniform dielectric. Analysis of a line without dielectric yields the free-space characteristic impedance and the effective permittivity

enables the characteristic impedance of the actual microstrip line with dielectric substrate to be found.

This chapter described the frequency-independent characteristics of microstrip and presented analytic formulas applicable to conventional microstrip but also microstrip on anisotropic substrates and with finite thickness. [Chapter 7](#) considers the frequency-dependent behavior of microstrip.

## References

- [1] M. Steer, *Microwave and RF Design: a Systems Approach*, 2nd ed. SciTech Pub., 2013.
- [2] K. C. Gupta, R. Garg, I. J. Bahl, and P. Bhartia, *Microstrip Lines and Slotlines*, 2nd ed. Artech House, 1996.
- [3] D. Grieg and H. Engelmann, “Microstrip—a new transmission technique for the kilomegacycle range,” *Proc. IRE*, vol. **40**, no. 12, pp. 1644–1650, Dec. 1952.
- [4] W. E. Fromm and E. G. Fubini, “Characteristics and some applications of stripline components,” in *Proc. National Electronics Conf.*, Oct. 1954, pp. 58–59.
- [5] J. Dukes, “The application of printed-circuit techniques to the design of microwave components,” *Proc. IEE, Part B: Radio and Electronic Engineering*, vol. **105**, no. 20, pp. 155–172, Mar. 1958.
- [6] E. Yamashita and K. Atsuki, “Design of transmission-line dimensions for a given characteristic impedance,” *IEEE Trans. on Microwave Theory and Techniques*, vol. **17**, no. 8, pp. 638–639, Aug. 1969.
- [7] H. Wheeler, “Transmission-line properties of parallel wide strips by a conformal-mapping approximation,” *IEEE Trans. on Microwave Theory and Techniques*, vol. **12**, no. 3, pp. 280–289, May 1964.
- [8] H. Wheeler, “Transmission-line properties of parallel strips separated by a dielectric sheet,” *IEEE Trans. on Microwave Theory and Techniques*, vol. **13**, no. 2, pp. 172–185, Feb. 1965.
- [9] R. Owens, “Accurate analytical determination of quasi-static microstrip line parameters,” *Radio and Electronic Engineer*, vol. **46**, no. 7, pp. 360–364, Jul. 1976.
- [10] E. Hammerstad and O. Jensen, “Accurate models for microstrip computer-aided design,” in *1980 IEEE MTT-S Int. Microwave Symp. Digest*, May 1980, pp. 407–409.
- [11] E. Hammerstad and F. Bekkadal, “A microstrip handbook, ELAB Report STF44 A74169,” University of Trondheim, Norway, Tech. Rep., Feb. 1975.
- [12] E. O. Hammerstad, “Equations for microstrip circuit design,” in *5th European*

*Microwave Conf.*, Sep. 1975, pp. 268–272.

- [13] A. Presser, “RF properties of microstrip lines,” *MicroWaves*, vol. **7**, pp. 53–55, Mar. 1968.
- [14] L. W. Cahill, “Approximate formulae for microstrip transmission lines,” *Proc. Institute of Radio and Electrical Engineers*, vol. **35**, pp. 317–321, Oct. 1974.
- [15] T. Bryant and J. Weiss, “Parameters of microstrip transmission lines and of coupled pairs of microstrip lines,” *IEEE Trans. on Microwave Theory and Techniques*, vol. **16**, no. 12, pp. 1021–1027, Dec. 1968.
- [16] E. Vick, S. Goodwin, G. Cunningham, and D. S. Temple, “Vias-last process technology for thick 2.5 D Si interposers,” in *2011 IEEE Int. 3D Systems Integration Conf. (3DIC)*, 2012, pp. 1–4.
- [17] Z. Feng, M. R. Lueck, D. S. Temple, and M. B. Steer, “High-performance solenoidal RF transformers on high-resistivity silicon substrates for 3d integrated circuits,” *IEEE Trans. on Microwave Theory and Techniques*, vol. **60**, no. 7, pp. 2066–2072, 2012.
- [18] L. Katehi, W. Chappell, S. Mohammadi, A. Margomenos, and M. Steer, “Heterogeneous wafer-scale circuit architectures,” *IEEE Microwave Magazine*, vol. **8**, no. 1, pp. 52–69, Jan. 2007.
- [19] W. Y. Liu, J. Suryanarayanan, J. Nath, S. Mohammadi, L. P. Katehi, and M. B. Steer, “Toroidal inductors for radio-frequency integrated circuits,” *IEEE Trans. Microwave Theory and Techniques*, vol. **52**, no. 2, pp. 646–654, 2004.
- [20] R. Owens, J. Aitken, and T. Edwards, “Quasi-static characteristics of microstrip on an anisotropic sapphire substrate,” *IEEE Trans. on Microwave Theory and Techniques*, vol. **24**, no. 8, pp. 499–505, Aug. 1976.
- [21] Y. Hayashi and T. Kitazawa, “Analysis of microstrip transmission lines on a sapphire substrate,” *Trans. Inst. Electron & Common. Eng. Japan*, vol. **62**, no. 6, Jun. 1979.
- [22] I. Bahl and R. Garg, “Simple and accurate formulas for a microstrip with finite strip thickness,” *Proc. IEEE*, vol. **65**, no. 11, pp. 1611–1612, Nov. 1977.
- [23] K. P. Schwan, “Take the guesswork out of thick microstrip K,” *MicroWaves*, pp. 184–185, Dec. 1977.
- [24] H. Wheeler, “Transmission-line properties of a strip on a dielectric sheet on a plane,” *IEEE Trans. on Microwave Theory and Techniques*, vol. **25**, no. 8, pp. 631–647, Aug. 1977.
- [25] I. J. Bahl, “Use exact methods for microstrip design,” *MicroWaves*, pp. 61–62, Dec. 1978.
- [26] G. Kowalski and R. Pregla, “Dispersion characteristics of shielded microstrips with

finite thickness,” *Arch. Elek. Übertragung.*, vol. 25, no. 4, pp. 193–196, 1971.

[27] M. Kay, R. Pomerleau, and M. Steer, “Empirical statistical analysis of planar transmission lines on PCBs accounting for manufacturing variations,” in *IEEE Southeastcon'89 Proc.*, 1989, pp. 112–116.

[28] R. Barrett, “Microwave printed circuits—a historical survey,” *IRE Trans. on Microwave Theory and Techniques*, vol. 3, no. 2, pp. 1–9, Mar. 1955.

# Chapter 7

## Microstrip at High Frequencies

### 7.1 Introduction

In this chapter we study the behavior of microstrip above a few gigahertz where it can no longer be considered as a static structure. In [Chapters 5](#) and [6](#) it was explained that microstrip cannot support a pure TEM wave, or any other simple electromagnetic field mode, and the necessary longitudinal field components which exist lead to the propagation of hybrid modes. It was further indicated in [Chapter 6](#) that the quasi-TEM nature of the propagating fields can be approximately calculated by the use of some statically derived expressions. Such expressions have accuracies to within 1% where they are applicable, generally at frequencies below 1 or 2 GHz. They also form an important basis for calculations at higher frequencies.

The analysis in this chapter leads to fairly straightforward design calculations for frequencies above a few gigahertz. The following lists the principal topics discussed:

- dispersion in microstrip
- a model leading to design calculations which allow for dispersion
- improved accuracy calculations
- an example (a specific design calculation)
- a frequency-dependent electromagnetic field solution (using a numerical method and requiring a substantial computer program)
- characteristic impedance as functions of frequency
- operating frequency limitations.

### 7.2 Frequency-dependent Effects

When the frequency of a signal exciting a microstrip line is (say) doubled, the phase constant or wave number  $\beta$  ( $= 2\pi/\lambda_g$ ) is not exactly doubled. Several transmission line structures exhibit this type of behavior, indicated in [Figure 7.1](#), it is called dispersion. All planar lines, including microstrip lines, are dispersive and it follows that the ‘exact’ relationship between wavelength and frequency is complicated. Detailed time- and space-variant electromagnetic field analyses have led to the development of useful and accurate (typically within 1%) closed formulas. These formulas enable design calculations and also provide intuitive understanding of behavior as required in design.

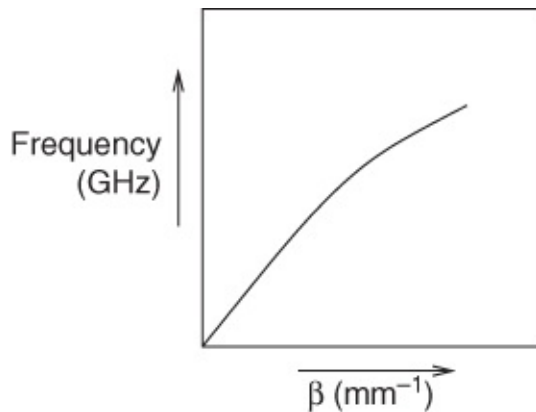


**Figure 7.1** The dispersive effect in any general structure or system, non-linearity when frequency  $f$  is plotted against wave number or phase coefficient  $\beta$ .

### 7.2.1 Frequency-dependent Charge Distribution

Frequency-dependent charge distribution results in part because of the finite time it takes for charges to move, but more importantly it results from the finite time it takes to send information conveyed by electromagnetic fields to cause charges to redistribute. Two partially separable effects occur. One of these is charge bunching, sometimes called the proximity effect, and the other is the skin effect. When a signal propagates down a planar transmission line the electromagnetic energy is confined principally between the strip of one conductor and the ground conductors. The electric field terminates on charges on the conductors and causes charges to move around. It takes a finite time for the charges to redistribute on and inside the conductors.

### 7.2.2 Dielectric Dispersion and Current Bunching

The hybrid mode (i.e., the quasi-TEM mode) of propagation along microstrip leads to the dispersive mechanism and an examination of the types of fields occurring in a shielded microstrip line helps to explain this dynamic situation (see [Figure 7.2](#)). Another important and revealing aspect concerns the changing current and charge distributions in both the strip and ground plane as frequency increases.

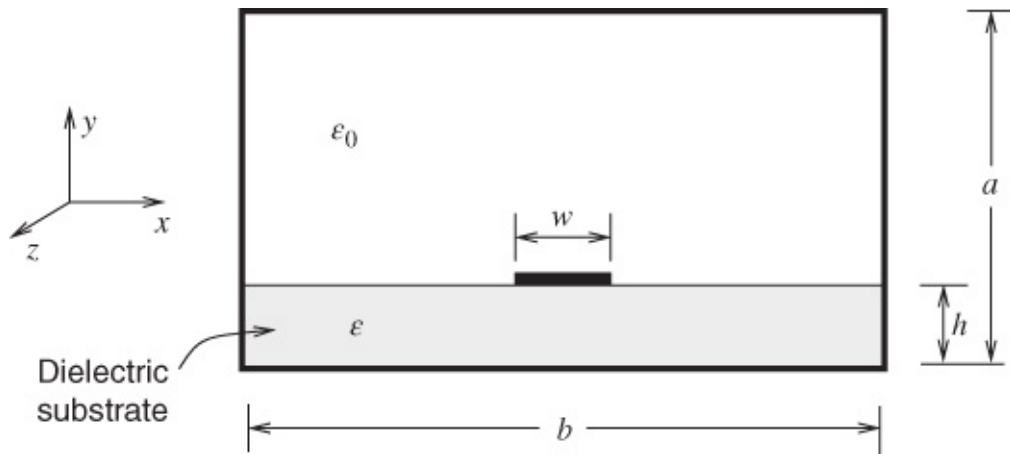


**Figure 7.2** Transverse cross-section of shielded microstrip, showing the nomenclature. The strip is the conductor of width  $w$  and the ground plane is the bottom, grounded conductor.

We have performed a series of SONNET® simulations of a  $50 \Omega$  alumina-substrate line at three frequencies: 1 GHz, 10 GHz and 30 GHz. The actual structure modeled is shown in [Figure 7.2](#) with a very distant top wall (i.e.,  $a \gg h$ ) and substrate thickness of 0.635 mm. The results are given for each frequency in [Figures 7.3](#), [7.4](#), and [7.5](#) where the longitudinal current and charge distributions on the strip and the ground plane are shown (in the  $xz$  plane). The longitudinal current, shown in [Figures 7.3\(b\)](#), [7.4\(b\)](#), and [7.5\(b\)](#), is the current that is the largest current component and is the only one considered in a first approximation. The transverse currents are much smaller and their relative levels are indicated in [Table 7.1](#).

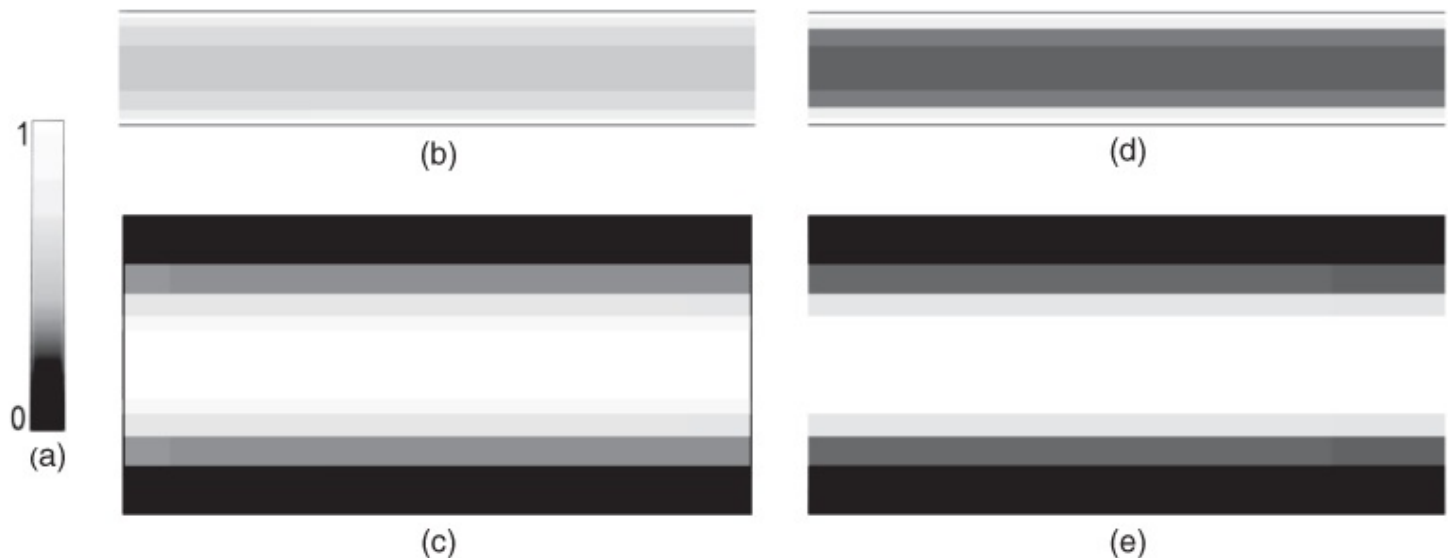


**Figure 7.3** Normalized current and charge magnitudes on an alumina microstrip line at 1 GHz: (a) normalized scale; (b) longitudinal current,  $i_z$ , on the strip and (c) on the ground plane; and (d) the charge on the strip and (e) on the ground plane.

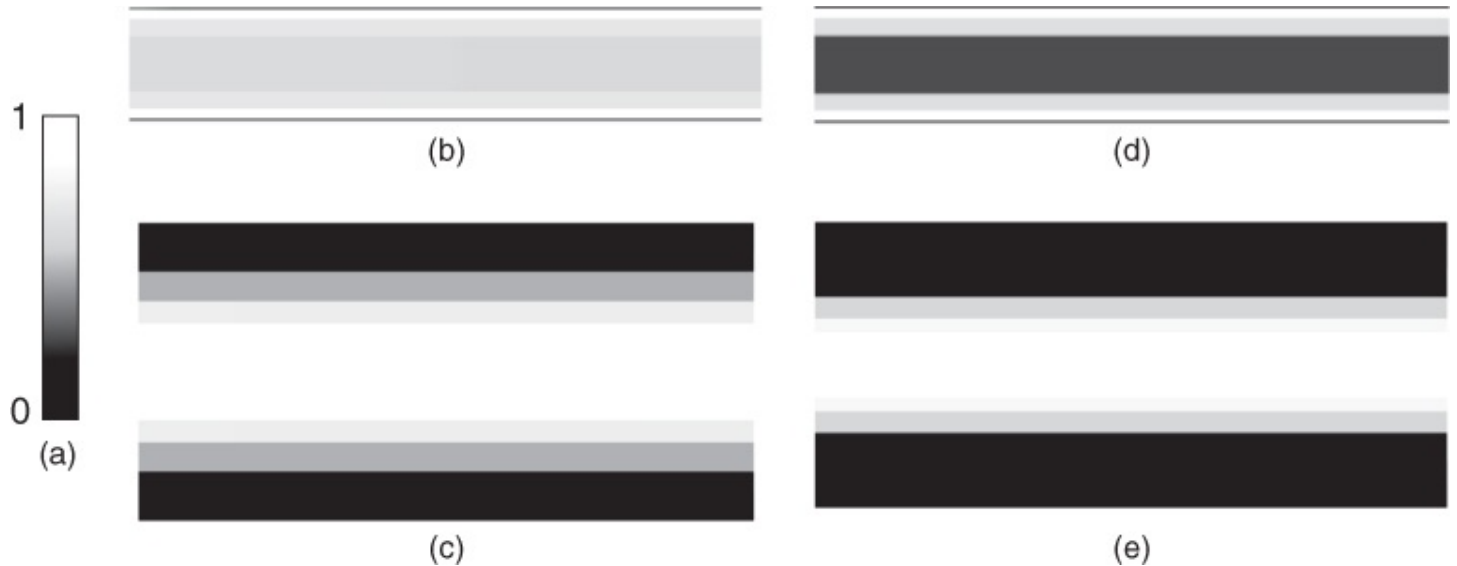


**Figure 7.4** Normalized current and charge magnitudes on an alumina microstrip line at 10 GHz: (a) normalized scale; (b) longitudinal current,  $i_z$ , on the strip and (c) on the ground plane; and (d) the charge on the strip and (e) on the ground plane.

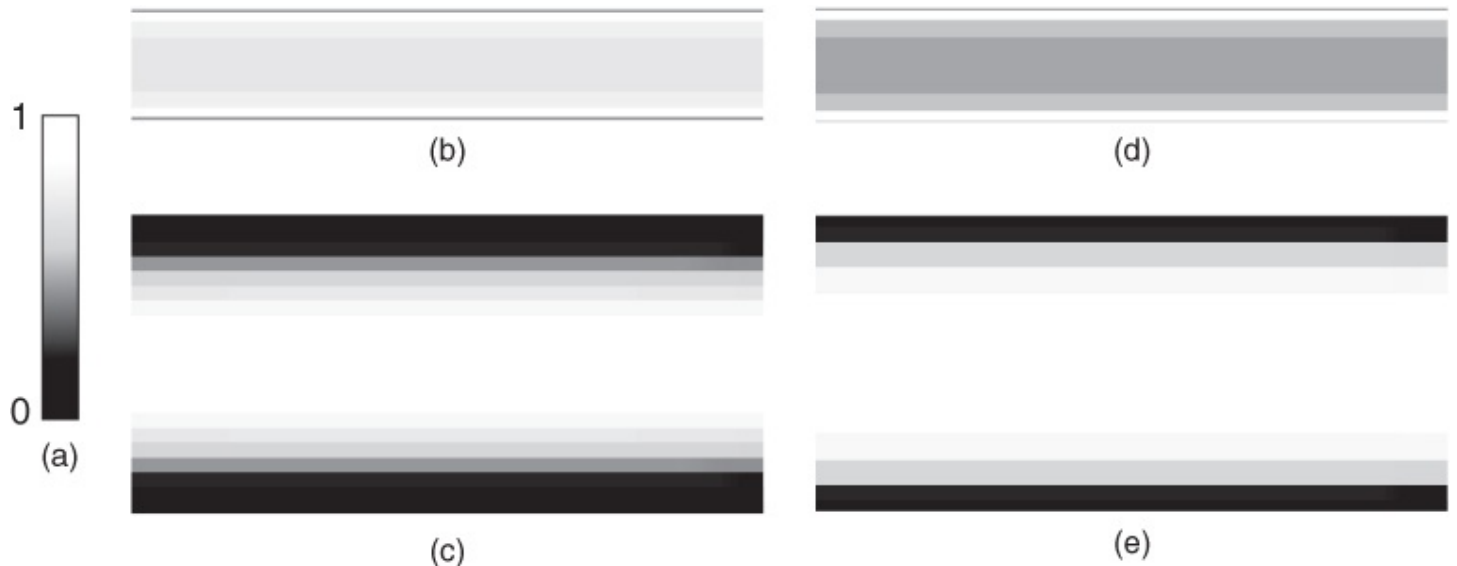


**Figure 7.5** Normalized current and charge magnitudes in an alumina microstrip line at 30 GHz: (a) normalized scale; (b) longitudinal current,  $i_z$  on the strip and (c) on the ground plane; and (d) the charge on the strip and (e) on the ground plane.

**Table 7.1** Peak charge and longitudinal,  $i_z$ , and transverse,  $i_x$ , current levels for the microstrip line. The currents and charges are normalized to the peak strip levels at 30 GHz

Freq. (GHz)	Strip current	Strip current	Ground current	Ground current	Strip charge	Ground charge
	$i_z$	$i_x$	$i_z$	$i_x$		
1	0.84	0.00052	0.10	0.0013	0.52	0.057
10	0.90	0.00081	0.11	0.012	0.61	0.058
30	1.00	0.0052	0.22	0.058	1.00	0.115

The ground plane was modeled realistically using the properties of the ground metallization, but it was necessary to terminate the ground plane in an ideal ground at the left and right extremes. The strip is modeled as infinitely thin and the surface resistance is calculated using an analytic formula which describes the skin effect. The effect of current bunching is accurately modeled. This type of simulator is very efficient and is in the general class of what is called  $2\frac{1}{2}$  D (two and a half dimensional) simulators. These simulators place restrictions on the directions of current flow that can be modeled. Current flow must be either in the plane of the strip or in the vertical direction. Modeling current flow in the vertical direction is important when modeling vias.

In all three instances the charge and current on the strip clearly intensify greatly near the edges, and this is a well-known phenomenon.

At 1 GHz ([Figure 7.3](#)) both the longitudinal and transverse currents are highly regular and in particular the longitudinal current flows directly down the microstrip. This can be seen by examining the relative levels of the various current components given in [Table 7.1](#). It is seen that at 1 GHz the transverse current is negligible compared to the longitudinal current so the current on the strip is almost entirely along the strip. The longitudinal current in the ground plane is at its highest level under the microstrip, but is 15% of the peak strip current. The transverse current in the strip is around 0.06% of the longitudinal current and for the ground current the relative level is around 1%. The transverse current in the strip and in the ground is zero along the centre line. This indicates that the current in the strip and the ground has a small circulatory component superimposed on the longitudinal current.

At one decade higher in frequency ([Figure 7.4](#)) clear changes in current distributions are evident. In the ground plane the maximum transverse current is now around 11% of the peak longitudinal ground current. However, for the microstrip the relative level is around 1%. When the frequency is increased still further, to 30 GHz, the effects noted here are more dramatic. In [Figure 7.5](#) the current distribution changes dramatically, with a bunching effect now pronounced in both the strip and the ground plane. At this frequency the peak transverse current on the ground is in the region of one quarter of the maximum longitudinal current. One other significant change is that the ground current is now much more localized under the strip at the higher frequency. The trend is obvious: as frequency increases the ground current tends to localize under the strip, transverse currents increase in both the strip and the ground, and the

strip longitudinal current becomes more concentrated on the edges of the strip. When the ground is lossy it is the increased localization of the current in the ground plane (or nearby interconnects) that is primarily responsible for the line's resistance increase.

The behavior of current and charges can be examined further by considering the current and charges on the microstrip line at one instant of time. [Figure 7.6](#) shows the longitudinal and transverse currents for a 30 GHz sinusoidal signal at one instant. The peak levels are the same as for the frequency domain variations shown in [Figure 7.5](#). The strong circulatory motion of the currents in the ground plane is most significant. The current in the ground (as well as on the strip) can be considered as being composed of longitudinal and circulatory components instead of longitudinal and transverse components. Here the circulatory current in the ground is one-third of the longitudinal component. The confinement of the current to the region under the strip is more evident than in the frequency domain case. The charge distributions corresponding to the currents of [Figure 7.6](#) are shown in [Figure 7.7](#).

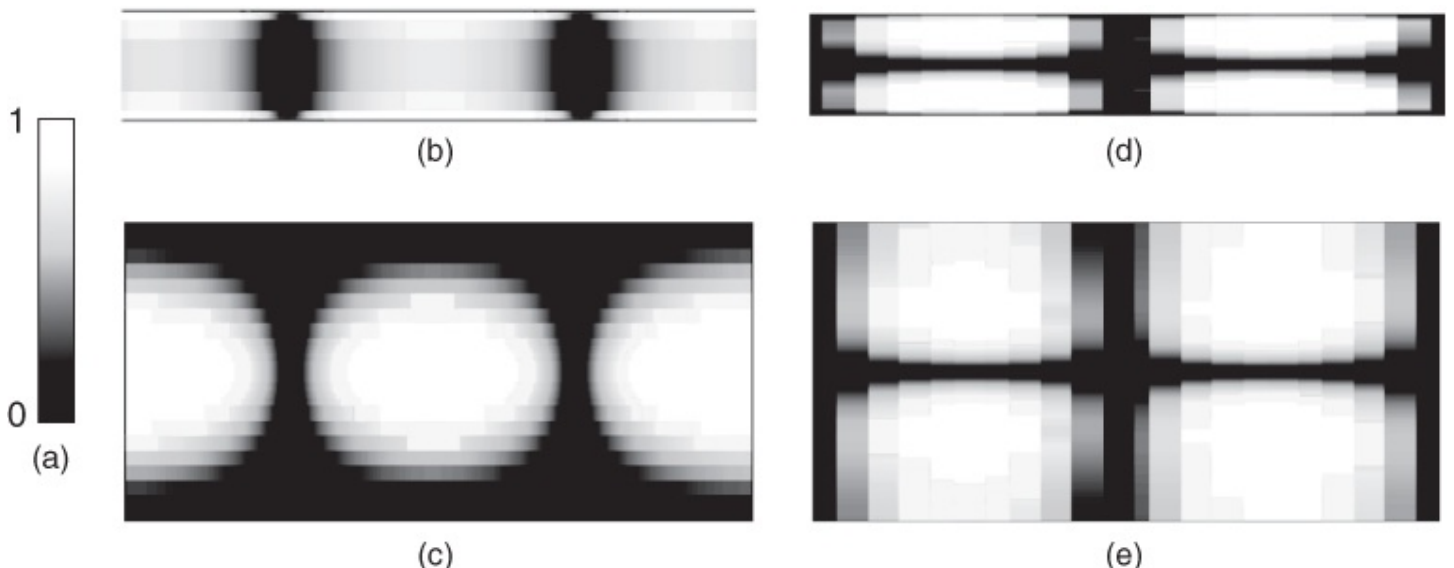


**Figure 7.6** Normalized instantaneous current distribution on the microstrip line: (a) normalized scale; (b) magnitude of the longitudinal current,  $i_z$ , on the microstrip and (c) on the ground plane; and (d) magnitude of the transverse current,  $i_x$ , on the microstrip and (e) on the ground plane. In all cases an alumina substrate applies and the frequency is 30 GHz.

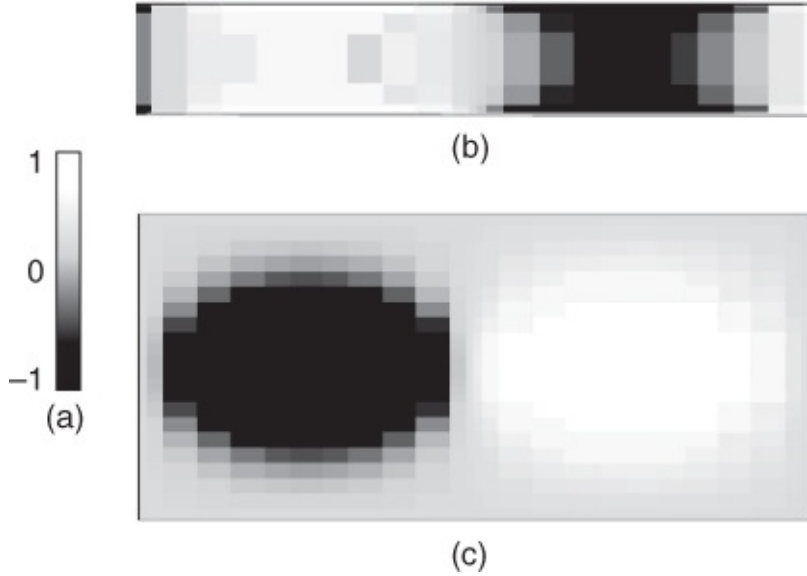


**Figure 7.7** Normalized instantaneous charge distribution,  $q$ , on the microstrip line at 30 GHz: (a) scale; (b) strip; and (c) ground plane.

This all amounts to clear evidence of significant dispersion in microstrip.

If the center strip is removed from the shielding enclosure (Figure 7.2) it reduces to a rectangular waveguide with partial dielectric filling that can support longitudinal section electric (LSE) or longitudinal section magnetic (LSM) modes. Pure TE or TM modes cannot, however, be supported, unlike the conventional unfilled waveguide. When the centre strip is inserted it causes currents to flow in both  $x$  (transverse) and  $z$  (longitudinal) directions on this strip; these currents serve to couple the LSE and LSM modes so that the final mode configuration is hybrid, what is called the quasi-TEM mode. As the frequency is increased, the mode-coupling efficiency increases and the fields become more concentrated in the region beneath the strip, where the substrate permittivity has already resulted in a relatively large electric field displacement. Since the fields are forced into the dielectric substrate to an increasing extent as the frequency rises, we can define a frequency-dependent effective microstrip permittivity  $\epsilon_{\text{eff}}(f)$ . This quantity clearly increases with frequency and the wave is progressively slowed down. We may continue to use the more general definition of effective microstrip permittivity given by Equation (6.10), except that  $\epsilon_{\text{eff}}$  must now be replaced by  $\epsilon_{\text{eff}}(f)$  and  $v_p$  by  $v_p(f)$  giving:

$$\epsilon_{\text{eff}}(f) = \{c/[v_p(f)]\}^2. \quad 7.1$$

Fundamentally, the dispersion problem then consists of solving the microstrip fields for the velocity  $v_p(f)$ . The limits of  $\epsilon_{\text{eff}}(f)$  are readily established: at the low-frequency extreme it reduces to the static-TEM value  $\epsilon_{\text{eff}}$ , while as frequency is increased indefinitely  $\epsilon_{\text{eff}}(f)$  approaches the substrate permittivity itself  $\epsilon_r$ . This is summarized as follows:

$$\epsilon_{\text{eff}}(f) \rightarrow \begin{cases} \epsilon_{\text{eff}} & \text{as } f \rightarrow 0 \\ \epsilon_r & \text{as } f \rightarrow \infty \end{cases}. \quad 7.2$$

Between these limits  $\epsilon_{\text{eff}}(f)$  changes continuously, as shown by the general curve of [Figure 7.8](#).

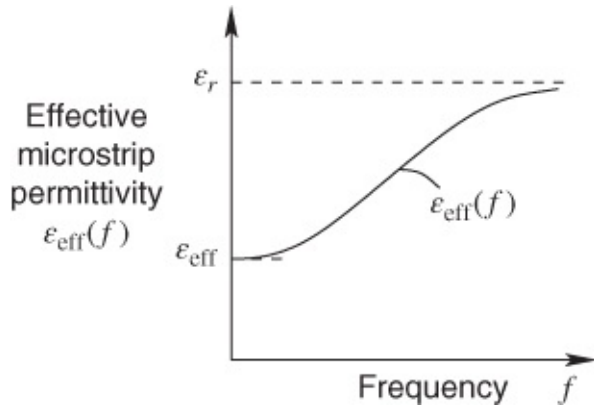


**Figure 7.8** Dispersion of microstrip interpreted as an effective relative permittivity  $\epsilon_{\text{eff}}$  plotted to a base of frequency.

There have been several approaches to the detailed hybrid-mode analysis of microstrip [1–13], and one example is described later in this chapter. A number of closed formulas based on various models of microstrip have also been developed, and some of these are briefly discussed and compared in [Section 7.3](#).

### 7.2.3 Skin Effect

The skin effect refers to the concentration of charge and current near the surface of a conductor due to the very low effective speed of an EM signal in a conductor. When an EM wave is incident on a conductor most of it is reflected but some of it penetrates and travels into the conductor. This is shown in [Figure 7.9\(a\)](#), where an incident EM field travels to the right and is partially reflected and some travels into the conductor. An RF electric field in the conductor results in an alternating current flow which then generates an opposing field and the magnitudes of both the time-varying electric field and the current reduce exponentially as the wave travels into the conductor, see [Figure 7.9\(b\)](#). Thus the current appears to be confined to the skin of the conductor. The depth at which the magnitude of the current falls to  $1/e$  of its value on the surface of the conductor is called the skin depth,  $\delta_s$ . The skin depth,  $\delta_s$ , depends on the frequency,  $f$ , permeability,  $\mu$ , and conductivity,  $\sigma_2$ , of the conductor:

$$\delta_s = 1/\sqrt{\pi f \mu \sigma_2}. \quad 7.3$$

The current will become increasingly concentrated near the surface of a conductor as frequency increases. (Note that for most conductors  $\mu = \mu_0$ .) The skin depths of various materials at different frequencies are shown in [Table 7.2](#).

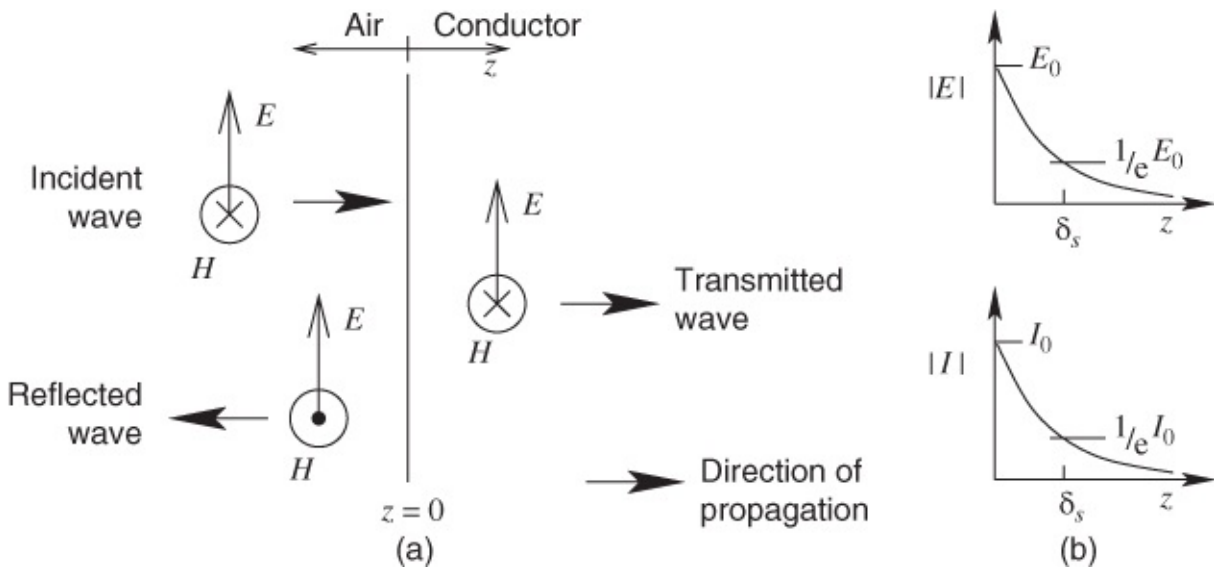


**Figure 7.9** Steady-state description of the skin effect: (a) an electromagnetic wave from the left incident at the interface of air and a conductor; and (b) profiles of the electric field magnitude (top) and current magnitude (bottom) as the wave travels into the conductor.

**Table 7.2** Skin depth of various conductors at 20°C

Metal	Resistivity ( $\text{n}\Omega \cdot \text{m}$ )	Conductivity ( $\text{MS/m}$ )	Skin depth, $\delta_s$ ( $\mu\text{m}$ )			
			100 MHz	1 GHz	10 GHz	100 GHz
Copper (Cu)	16.78	59.60	6.52	2.06	0.652	0.206
Silver (Ag)	15.87	63.01	6.34	2.01	0.634	0.201
Aluminum (Al)	26.50	37.74	8.19	2.59	0.819	0.259
Gold (Ag)	22.14	45.17	7.49	2.37	0.749	0.237
Platinum (Pt)	105	9.524	16.3	5.16	1.63	0.516
Tin (Sn)	115	8.696	17.1	5.40	1.71	0.540
Titanium (Ti)	4200	0.2381	103	32.6	10.3	3.26

At DC the skin depth is infinite and current is distributed uniformly throughout a conductor. However, the situation is different for an AC signal. At low frequencies the current is still essentially uniformly distributed throughout a conductor but at higher frequencies, especially at microwave frequencies and above, the situation changes because of the low speed at which an EM signal can be sent through a conductor. This speed of a microwave-frequency EM signal through a conductor is not known precisely and cannot be measured but it is believed to be about one-thousandth that of the speed in a vacuum.

At microwave frequencies the current density away from the surface of a conductor reduces quickly. With all transmission lines this concentration of current in the skin of conductors changes the line resistance (the  $R$  in the **RLGC** model of a transmission line). The skin effect is in addition to the current bunching effect described in the previous section, which relates to the finite speed of propagation of an EM signal in the dielectric. Modeling the skin effect in an EM

field simulator is not simple. One approach is to discretize the current flow in the strip and ground plane of a microstrip line into current filaments [14–16], akin to a number of thin wires, as shown in [Figure 7.10](#). The fields produced by these current filaments is calculated and the magnitude of the current phasor of each filament determined. Another approach is to use volume gridding as done in commercial EM simulators which can tolerate the tremendously dense gridding required to model the fields in a conductor. These EM simulator techniques were compared by Curran *et al.* [14] and shown to give very similar results. The typical result of such simulations is the cross-sectional current density shown in [Figure 7.11](#), where the current density on the strip and ground plane are shown. Here the thickness of the ground plane and the strip are both three skin depths. The current concentration on the strip is almost entirely due to the skin effect and little current bunching is seen. With the ground plane both effects are evident. In the ground plane in [Figure 7.11](#) the lateral concentration of current is due to current bunching while the vertical variation in current density is due to the skin effect. The peak current density on the ground plane is much lower than for the strip and as a result the line resistance due to the ground is lower than that due to the strip.

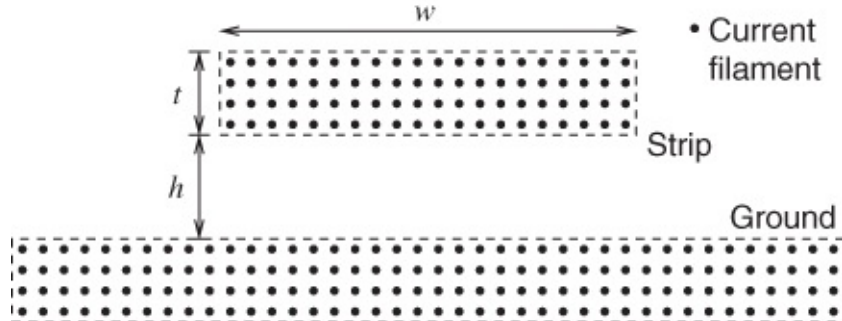


[Figure 7.10](#) Representation of a microstrip line as groups of current filaments.



[Figure 7.11](#) Current density on the strip and finite-thickness ground plane shown in cross-section. Dark shading indicates the area of high current density and different scales are used for the current density on the strip and on the ground plane. Current density in the ground plane is much lower than in the strip.

[Figure 7.12](#) shows the impact of the skin effect on current density using the thickness,  $t$ , of the strip relative to a skin depth,  $\delta_s$ , as the variable. This insight is based on the analyses of Curran *et al.* [14], Faraji *et al.* [17], and 3D EM simulations using Ansys HFSS®. At DC, see [Figure 7.12\(a\)](#), the current density on the strip is uniform and even when  $t = \delta_s$  the impact of the skin effect is negligible, see [Figure 7.12\(b\)](#). Increasing current localization is seen first with  $t = 3\delta_s$ , ([Figure 7.12\(c\)](#)), then with  $t = 5\delta_s$ , ([Figure 7.12\(d\)](#)). For a wide strip and when  $t > \delta_s$ , that is, the strips in [Figures 7.12\(c\) and \(d\)](#), the current flow is concentrated in the bottom of the strip

(the ground plane side) and up the sides of the strip. However, for a narrow strip, see [Figure 7.12\(e\)](#), there is significant current flow on both the top and bottom regions of the strip. These behaviors are why it has been difficult to arrive at a compact formula for the line resistance as a function of the microstrip dimensions, conductor properties, and frequency.

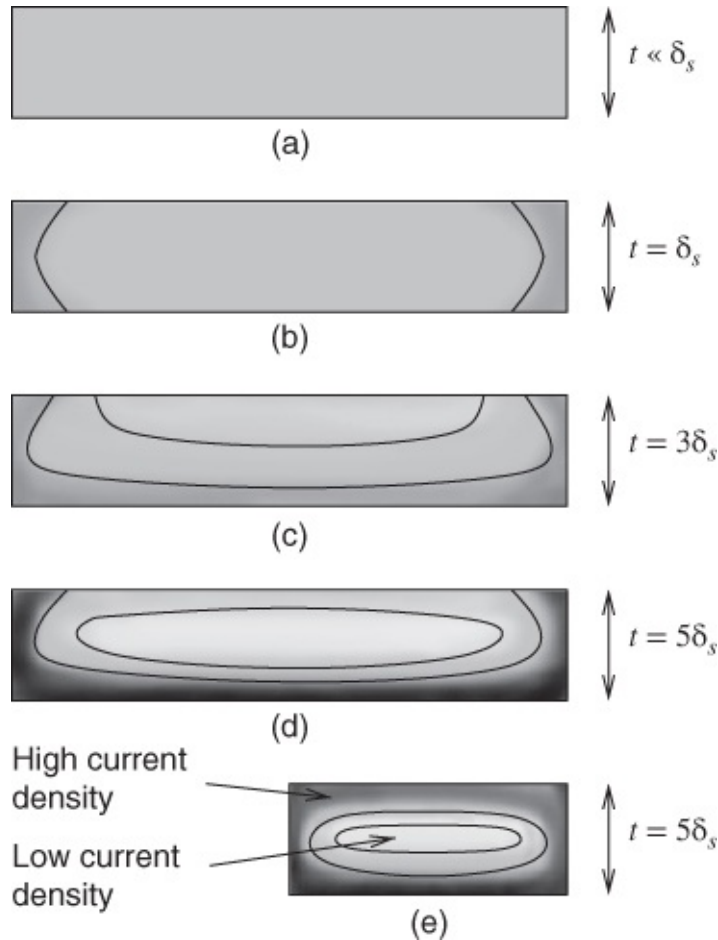


**Figure 7.12** Skin effect on the transverse current density in a strip of a microstrip transmission line for various thicknesses of strip,  $t$ , relative to a skin depth  $\delta_s$ : (a) is at DC; (b), (c), and (d) are for thicknesses near the skin depth; and (d) and (e) have the same thickness but the strips have different widths.

The existence of current within the conductors indicates that there is magnetic energy storage inside the conductors and hence internal line inductance. This magnetic energy storage reduces as the current becomes increasingly concentrated near the surface of the conductors. It turns out that it is easier to formulate the internal inductance than the conductor resistance so that the techniques developed for determining line resistance when the skin effect is not negligible are based on internal inductance considerations. This approach was first developed by Wheeler [18] and refined by several researchers [19–21]. The schemes separately determine the DC line resistance  $R_{DC}$  and the AC line resistance  $R_{AC}$ , which need to be combined. Hall *et al.* [22] and Curran *et al.* [14] showed that the best way to combine them is to use the following formula to obtain the line resistance  $R$  (the resistance per unit length):

$$R = \sqrt{R_{DC}^2 + R_{AC}^2}.$$

where  $R_{DC}$  is calculated in the usual way as the sum of the DC resistance of the strip and of the ground plane, that is,

$$R_{DC} = R_{strip,DC} + R_{ground,DC}, \quad 7.5$$

respectively. Similarly for the AC line resistance:

$$R_{AC} = R_{strip,AC} + R_{ground,AC}. \quad 7.6$$

The DC line resistance of the strip is

$$R_{strip,DC} = R_{s,DC}/w \quad R_{s,DC} = \rho_s/t, \quad 7.7$$

where  $R_{s,DC}$  is the DC sheet resistance of the strip,  $\rho_s$  is the resistivity of the strip's conductor,  $w$  is the strip width, and  $t$  is the thickness of the strip. The DC line resistance of the ground is

$$R_{ground,DC} = R_{sg,DC}/w \quad R_{sg,DC} = \rho_{sg}/t_g \quad 7.8$$

where  $R_{sg,DC}$  is the DC sheet resistance of the ground,  $\rho_{sg}$  is the resistivity of the ground conductor, and  $t_g$  is the thickness of the ground. With  $h$  being the distance between the strip and the ground plane, the AC line resistances of the strip,  $R_{strip,AC}$ , and of the ground,  $R_{ground,AC}$ , are (derived from [19]):

for  $\frac{w}{h} \leq \frac{1}{2\pi}$  (e.g.,  $Z_0 > 95 \Omega$  if  $\epsilon_r = 10$ )

$$R_{strip,AC} = \frac{R_{s,\delta}}{2\pi h} \left[ 1 - \left( \frac{w'}{4h} \right)^2 \right] \left\{ 1 + \frac{2h}{w'} \left[ 1 + \frac{t}{\pi w} + \frac{1}{\pi} \ln \left( \frac{4\pi w}{t} \right) \right] \right\} \quad 7.9$$

$$R_{ground,AC} = \frac{R_{sg,\delta}}{2\pi h} \left[ 1 - \left( \frac{w'}{4h} \right)^2 \right] \quad 7.10$$

for  $\frac{1}{2\pi} < \frac{w}{h} \leq 2$  (e.g.,  $33 \Omega < Z_0 < 95 \Omega$  if  $\epsilon_r = 10$ )

$$R_{strip,AC} = \frac{R_{s,\delta}}{2\pi h} \left[ 1 - \left( \frac{w'}{4h} \right)^2 \right] \left\{ 1 - \frac{t}{\pi w'} + \frac{2h}{w'} \left[ 1 + \frac{1}{\pi} \ln \left( \frac{4h}{t} \right) \right] \right\} \quad 7.11$$

$$R_{ground,AC} = \frac{R_{sg,\delta}}{2\pi h} \left[ 1 - \left( \frac{w'}{4h} \right)^2 \right] \left( 1 - \frac{t}{\pi w'} \right) \quad 7.12$$

for  $\frac{w}{h} \geq 2$  (e.g.,  $Z_0 < 33 \Omega$  if  $\epsilon_r = 10$ )

$$R_{\text{strip,AC}} = \frac{R_{s,\delta}}{h} \left\{ \frac{w'}{h} + \frac{2}{\pi} \ln \left[ 2\pi \left( \frac{w'}{2h} + 0.94e \right) \right] \right\}^{-2} \left[ \frac{w'}{h} + \frac{w' / (\pi h)}{w' / (2h) + 0.94} \right] \\ \times \left[ 1 - \frac{t}{\pi w'} + \frac{2h}{w'} + \frac{2h}{\pi w' \ln (2h/t)} \right] \quad 7.13$$

$$R_{\text{ground,AC}} = \frac{R_{s,\delta}}{\pi h} \left\{ \frac{w'}{h} + \frac{2}{\pi} \ln \left[ 2\pi \left( \frac{w'}{2h} + 0.94e \right) \right] \right\}^{-2} \left[ \frac{w'}{h} + \frac{(w' / (\pi h))}{w' / (2h) + 0.94} \right] \\ \times \left[ 1 - \frac{t}{\pi w'} \right] \quad 7.14$$

where the surface resistance of the strip is  $R_{s,\delta} = \sqrt{\pi f \mu_{\text{strip}} \rho_{\text{strip}}} = \rho_{\text{strip}} / \delta_{s,\text{strip}}$ , the surface resistivity of the ground is  $R_{s,\delta} = \sqrt{\pi f \mu_{\text{ground}} \rho_{\text{ground}}} = \rho_{\text{ground}} / \delta_{s,\text{ground}}$ , and the adjusted width accounting for the strip thickness is  $w' = w + (t/\pi) \ln (1 + 2h/t)$ . For the conductors  $\mu_{\text{strip}}$  and  $\mu_{\text{ground}}$ , and  $\rho_{\text{strip}}$  and  $\rho_{\text{ground}}$  are the permeability and resistivity of the strip and ground, respectively.

The formulas above for the AC resistance were derived considering that the skin depth is much less than the thickness of the strip but they have been found to be within 10% of the numerically calculated AC resistance for  $w/h \geq 2$  and less accurate (i.e., for  $w/h < 2$ ) below that [14]. Still, these analytic formulas are the best available.

## 7.2.4 Surface and Edge Effects

Planar transmission lines do not have the exact rectangular and smooth surfaces that are used in modeling. Principally because of random etching effects, the edges of a strip of a microstrip line meander and at fine scales have seemingly random variation, that is, the width of a strip varies randomly. In addition, the assumed rectangular shape of the strip is likely to more closely approximate a trapezoid. The surface of metal is rough and particularly with soft substrate technologies, such as FR-4, deliberate chemical processing of the metal surface that makes contact with the soft substrate results in small hook-like projections that ensure adhesion when the conductor is pressed into the substrate. These effects can be expected to be significant when the variations are comparable to a skin depth in dimension.

Surface roughness has been studied [18, 20, 21, 23–26], leading to a formula for attenuation based on dimensional and material properties. Hammerstad and Bekkadal [26] used curve fitting to arrive at the following formula for the additional attenuation due to the roughness of the strip of a microstrip line:

$$\alpha'_c = \alpha_c \left\{ 1 + \frac{2}{\pi} \tan^{-1} \left[ 1.4 \left( \frac{\Delta}{\delta_s} \right)^2 \right] \right\}. \quad 7.15$$

Here  $\alpha_c$  is the attenuation of the strip without roughness,  $\Delta$  is the r.m.s. surface roughness (in SI units of m) and  $\delta_s$  is the skin depth of the strip. For a low-loss line, Equation (7.15) leads to the line resistance due solely to roughness:

$$R_{\text{rough, AC}} = \frac{4Z_0}{\pi} \tan^{-1} \left[ 1.4 \left( \frac{\Delta}{\delta_s} \right)^2 \right]. \quad 7.16$$

This was developed using the usual approximation for the conductor attenuation of a low-loss line, that is  $\alpha \approx R/(2Z_0)$ .

In order to appreciate the typical magnitudes involved consider a copper microstrip, where the skin depth at 4 GHz is 1  $\mu\text{m}$ . Also assume that the r.m.s. surface roughness is of similar magnitude, that is, 1  $\mu\text{m}$  (typical of 99% alumina, see [Table 5.3](#)). Equation (7.15) then shows that the attenuation coefficient becomes

$$\alpha'_c \approx 1.6\alpha_c. \quad 7.17$$

that is to say, the loss is increased by approximately 60% when surface roughness is taken into account. The increase will be still greater for other grades of alumina and other substrates where roughness can exceed 10  $\mu\text{m}$ .

More recent studies [14, 27–29] have confirmed that the effect of surface roughness on attenuation is multiplicative, that is, the attenuation with surface roughness is

$$\alpha'_c = K'\alpha_c \quad 7.18$$

Theoretical studies of surface roughness and of edge variations are necessarily limited to regular dimensional variations. However, these combined with experimental observations support the contention that the attenuation effect of surface roughness, edge variations, and non-rectangular cross-sections can be modeled as being multiplicative of the attenuation of a microstrip line due to ohmic resistance alone [14–16, 30, 31]. Also for a low-loss line, each source of loss contributing to line resistance can be considered as having its own line resistance contribution, which can be summed to obtain the overall line resistance.

An alternative empirical approach can be used to characterize an established process (e.g., fixed  $h$ ,  $\epsilon_r$ , and processing technology). In this approach the attenuation per unit length,  $\alpha$ , of a line with a low-loss substrate can be measured under a range of conditions, usually as a function of characteristic impedance and frequency, and the resistance estimated as

$$R_{\text{AC}}(Z_0, f) = 2Z_0\alpha - R_{\text{DC}}(Z_0). \quad 7.19$$

Experimentally it is observed that  $R_{\text{AC}}(Z_0, f) \approx K(Z_0)\sqrt{f}$  where  $K(Z_0)$  is a weak function of  $Z_0$  and frequency.

Some general recommendations are that the effect of roughness and dimensional irregularities can be safely ignored if the skin depth is at least five times the dimensional variation. The effects of roughness and other dimensional irregularities becomes increasingly important as frequency increases and hence the use of polished substrates, including crystalline substrates and thin film processing techniques, is recommended for planar transmissions lines used at high microwave and millimeter-wave frequencies.

## 7.3 Approximate Calculations Accounting for Dispersion

As explained in [Chapter 5](#), the circuit designer needs to know the wavelength  $\lambda_g$  of the dominant mode in the microstrip whose characteristic impedance  $Z_0$  and aspect ratio  $w/h$  are already known (from electrical measurements). This implies that the relative effective permittivity  $\epsilon_{\text{eff}}(f)$  is required, since

$$\lambda_g = \frac{c}{f\sqrt{\epsilon_{\text{eff}}(f)}}. \quad 7.20$$

It is generally better to find expressions for  $\epsilon_{\text{eff}}(f)$  first because gross errors in calculating  $\epsilon_{\text{eff}}(f)$  can readily be detected (e.g., it must lie within the limits shown in [Figure 7.8](#)).

Fundamentally, this effective microstrip permittivity must be a function of frequency, substrate height, and substrate relative permittivity:

$$\epsilon_{\text{eff}}(f, h, \epsilon_r) \quad 7.21$$

where it should be noted that the substrate height  $h$  enters into the expressions because it influences the surface waves and thus also the complete hybrid electromagnetic field pattern. This can be seen by imagining the effect of increasing the proportion of dielectric substrate relative to air in [Figure 7.2](#).

Most of the “closed-formula” expressions for calculating dispersion also require the static-TEM value of  $\epsilon_{\text{eff}}$ , and sometimes  $Z_0$  also.<sup>1</sup> These are obtained by the methods given in [Chapter 6](#). Thus, the frequency-dependent effective microstrip permittivity may also be written as a function involving  $\epsilon_{\text{eff}}$  and  $Z_0$  as follows:

$$\epsilon_{\text{eff}}(f, h, \epsilon_r, \epsilon_{\text{eff}}, Z_0). \quad 7.22$$

One of the first attempts at developing a closed-formula for dispersion calculations is due to Jain, Makios, and Chudobiak [32–34]. Their first formula was derived empirically and showed only a first-order relationship with frequency [32].

This is known to be very inaccurate (clearly it is, at least, incapable of approaching the limit conditions already discussed here and shown in [Figure 7.8](#)) and their more comprehensive method must therefore be examined. Their approach consisted basically of analyzing the coupling between the TEM mode and a surface-wave mode  $\text{TM}_0$ .<sup>2</sup> Rather elaborate algebraic expressions are obtained for a special effective permittivity. The main expression used takes  $\epsilon_{\text{eff}}(f) > \epsilon_r$  at high frequencies, which is physically impossible as we have already seen. In fact the full dispersion curves given by Jain, Makios, and Chudobiak clearly show  $\epsilon_{\text{eff}}(f)$  progressing beyond the limit set by the substrate permittivity. Otherwise the theory shows quite close agreement with experimental results, except that these were obtained using ring resonators, which give somewhat unreliable results and are discussed later in [Chapter 18](#). The actual values of  $\epsilon_{\text{eff}}$  which were used in the work of Jain, Makios, and Chudobiak are all too

high due to substantial errors in the static-TEM expressions that were used at that time.

A fundamentally different approach was adopted by Schneider [35], who took four basic features regarding microstrip dispersion and identified a rational function that satisfied all these features.

The four basic features are as follows:

a.  $\epsilon_{\text{eff}}(f)$  always increases with frequency

b.  $\epsilon_{\text{eff}}(f) (f \rightarrow 0) \Rightarrow \epsilon_{\text{eff}}$  (see [Figure 7.8](#))

c.

$\epsilon_{\text{eff}}(f) (f \rightarrow \infty) \Rightarrow \epsilon_r$

It is also noted that  $\epsilon_{\text{eff}}(f)$  is asymptotic at both limits. The fourth feature concerns phase velocity  $v_p(f)$ . This suffers an inflection at some frequency close to the cut-off frequency  $f_c$  of the  $\text{TE}_1$  surface wave, therefore this fourth feature is:

a.  $\partial^2 v_p / \partial f^2 = 0$  when  $f = f_c$ .

The formulas which Schneider finally obtained were well suited to simple rapid calculations at the time, but Schneider pointed out that this theory can only be expected to yield an engineering approximation and quoted errors of somewhat less than 3% in phase velocity (i.e., about 6% in effective permittivity) calculated by this method compared with other data (for lines having characteristic impedances in the region of 50  $\Omega$ ). The method relied heavily on satisfying all the discrete conditions, especially (d), and this could be a main reason for the errors that arise. It should be observed that a 3% error in phase velocity, or wavelength, would be unacceptable for the design of many circuits, including filters or matching networks.

Carlin [36] reported a novel and interesting approach that involved setting up and analysing a circuit model of microstrip. His circuit model involved coupled lines where one of the lines propagates only a TEM wave while the other line propagates only a TE wave. The details will not be pursued here, but the final expressions involve frequency  $f$ , height  $h$ , permittivity  $\epsilon_r$ , static-TEM effective permittivity  $\epsilon_{\text{eff}}$ , and characteristic impedance  $Z_0$ , as well as some constants.

A comparison of calculations based on Carlin's expressions against several other approaches is given shortly in graphical form. Although more accurate methods are known (which are no more complicated than that due to Carlin) it may well be that fairly minor modifications to the expressions could yield improved accuracy.

In any event, the advances due to researchers including Getsinger, Edwards and Owens, Yamashita *et al.*, Kirschning and Jansen, and also Kobayashi provide more accurate and wide-ranging sets of expressions for predicting the effects of dispersion. As his approach effectively underlies most of these advances, we start with Getsinger's formulation here.

An apparently more accurate formula, applicable at least to microstrip on alumina-type substrates, was developed by Getsinger [37, 38]. The full derivation is too lengthy to be given

here, but a brief summary of the method is presented. Getsinger's approach begins with proposing an alternative "model" for microstrip which is arranged for more straightforward analysis than the microstrip itself. Essentially, the model aims to largely overcome the difficulties set up by the "horizontal" air-dielectric interface in real microstrip and the approach is illustrated in [Figure 7.13](#). It is important to note that the model is not physically realizable. It consists of three side-joined transmission lines as follows: (i) central parallel-plate line width  $w$  and height  $h$  filled with the substrate material of permittivity  $\epsilon_r$  and two additional parallel-plate lines, (ii) and (iii), attached to the sides of this central line (i). These two additional parallel-plate lines are identical in structure and electrically joined to the central line. Each has width  $a$ , height  $h$ , and is filled with air having permittivity  $\epsilon_0$ .

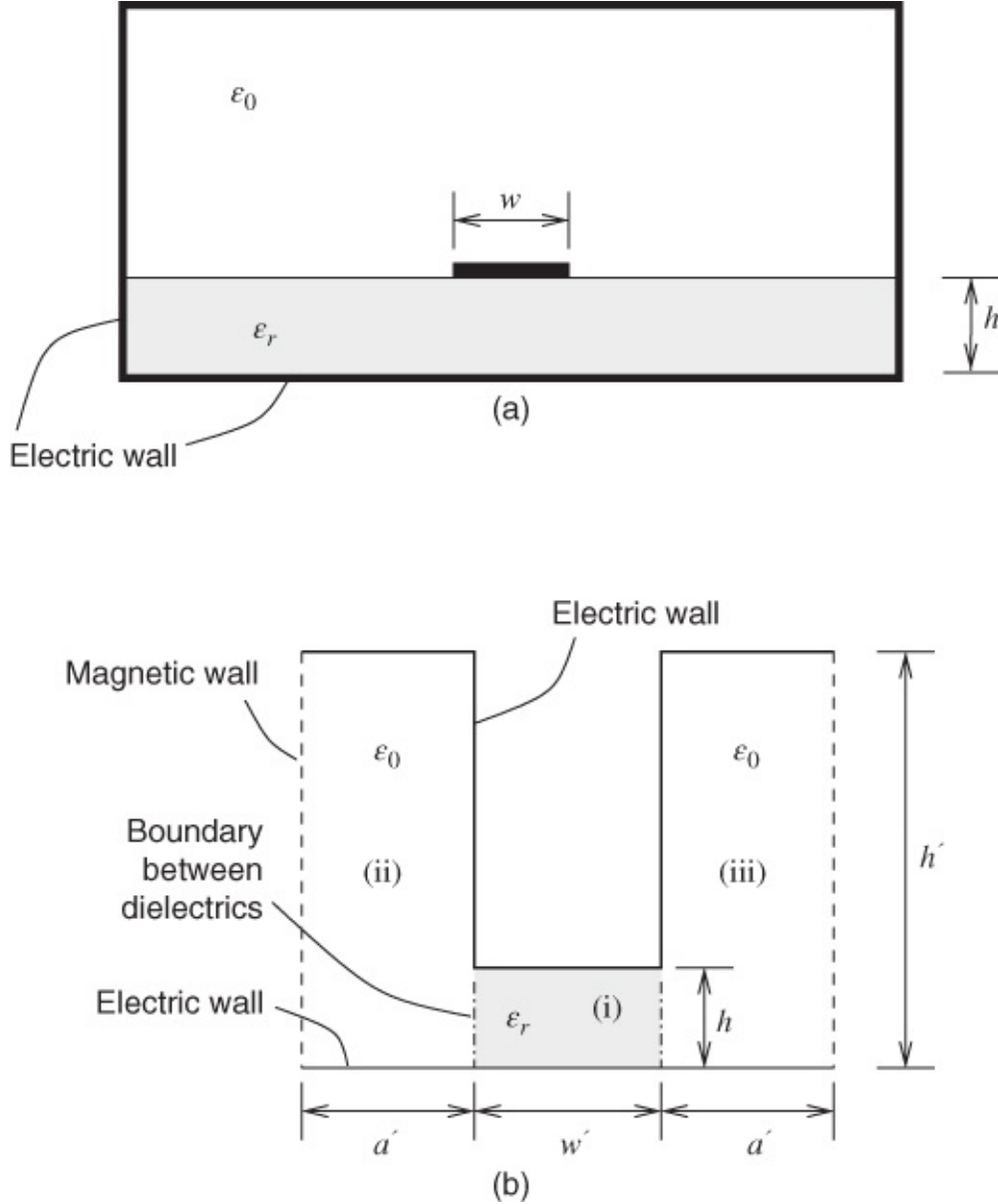


[Figure 7.13](#) Getsinger's model for dispersion analysis: (a) actual microstrip; and (b) microstrip model. Adapted from Getsinger (1973) [37], figure 2, p. 35. Reproduced with permission of IEEE.

Line (i) accounts for the substrate fields in the real microstrip. It is much easier to analyze

because it is simply a parallel-plate line. Lines (ii) and (iii) allow for the fields which exist in air with the real microstrip. The assumption is made that because the two regions, air filled and dielectric filled, of the model and the microstrip are grossly similar, the two structures will have the same dispersive behavior for the same mode of propagation. This hypothetical “microstrip model” involves corners with abrupt dielectric discontinuities, and Getsinger makes it clear quite early in his paper that junction capacitance should strictly be included to allow for the corner errors. However, this would clearly make the analysis overcomplicated, and almost certainly prevent a closed-form expression from being obtained, therefore no attempt is made to improve the accuracy by including these junction capacitances.

The first step in the analysis consists of mathematically forcing the model to have the same electrical characteristics, at the low-frequency limit, as the microstrip. Thus the static-TEM parameters of each structure are made equal [38]. A transverse resonance analysis of the model ([Figure 7.13](#)) is performed with the ultimate aim of obtaining an explicit formula for  $\epsilon_{\text{eff}}(f)$  as a function of known parameters. This transverse resonance technique demands that the sum of admittances looking to the left and right from either air–dielectric interface shown in [Figure 7.13](#) must be zero. Getsinger shows that this sum may be written

$$\frac{\gamma_a}{h'} \tanh(\gamma_a a') + \frac{\gamma_r}{h} \tanh\left(\frac{\gamma_r w'}{2}\right) = 0 \quad 7.23$$

where the subscripts  $a$  and  $r$  refer to air and substrate dielectric, respectively.

The propagation coefficients are related by

$$\gamma^2 + \gamma_i^2 = -\omega^2 \mu_0 \epsilon_0 \epsilon_r \quad 7.24$$

where  $i = a$  or  $r$  as appropriate. These expressions are combined, together with appropriate static-TEM relations, and solved to yield an expression for  $\epsilon_{\text{eff}}(f)$  as a function of  $\epsilon_{\text{eff}}$ ,  $\epsilon_r$ ,  $Z_0$ ,  $f$ , and  $h'/h$ . The reader is referred to the details in Getsinger's publications [37, 38] and only the result is given here:

$$\begin{aligned} \epsilon_{\text{eff}}(f) &= \epsilon_r - (\epsilon_r - \epsilon_{\text{eff}}) \left( 1 + f^2 \left( \frac{2\mu_0 h}{Z_0} \right) \right. \\ &\quad \times \left. \left\{ \frac{\pi^2}{12} \left[ \frac{(\epsilon_{\text{eff}} - 1) + (h'/h)^2 (\epsilon_r - \epsilon_{\text{eff}})}{\epsilon_r - 1} \right] \left[ \frac{(\epsilon_{\text{eff}} - 1)(\epsilon_r - \epsilon_{\text{eff}})}{\epsilon_{\text{eff}}(\epsilon_r - 1)} \right] \right\} \right)^{-1}. \end{aligned} \quad 7.25$$

There is one unknown parameter in this expression and that is  $h'/h$ . It turns out that, rather fortuitously, this parameter varies little as a function of  $Z_0$  over quite a wide range. For  $Z_0 \geq 35 \Omega$ ,  $h'/h \approx 3.0$ , and as  $Z_0$  falls below  $35 \Omega$  the parameter slowly increases, reaching approximately 6.2 at  $Z_0 = 15 \Omega$ , therefore  $h'/h$  can be introduced quite readily into Equation ([7.25](#)), although this procedure lacks some precision and is uncertain for characteristic impedances of less than  $15 \Omega$  or substantially greater than  $90 \Omega$ . The formula also remains rather complicated.

A somewhat simpler formula, based on the same foundations, may be written in the form [37]:

$$\epsilon_{\text{eff}}(f) = \epsilon_r - \frac{\epsilon_r - \epsilon_{\text{eff}}}{1 + G(f/f_p)^2} \quad 7.26$$

where

$$f_p = \frac{Z_0}{2\mu_0 h}. \quad 7.27$$

The parameter  $G$  is purely empirical, thereby giving some flexibility to the formula.  $G$  is dependent mainly on  $Z_0$ , but also to a lesser extent on  $h$ , and Getsinger deduced from measurements of microstrip ring resonators on alumina that

$$G = 0.6 + 0.009Z_0 \quad 7.28$$

when  $h = 0.635$  mm. Fortunately, Equation (7.26) is not particularly sensitive to  $G$ , and  $G = 1.0$  for the most common characteristic impedance of microstrip lines, that is, 50  $\Omega$ . For a wide range of lines on alumina-type substrates  $G$  has been found to vary over the range

$$0.3 \leq G \leq 1.7.$$

Substrates where this also applies include monocrystalline sapphire and GaN.

It has been found that Equations (7.26)–(7.28) give rise to discrepancies which increase as  $Z_0$  decreases and can exceed 3% as  $Z_0$  is reduced below 20  $\Omega$  [39]. The work of Getsinger, as outlined above, provides an excellent basis for the development of expressions having improved accuracy and which may be used in design. These are described in the next section.

## 7.4 Accurate Design Formulas

### 7.4.1 Edwards and Owens' Expressions

When careful measurements are made on microstrip lines over a wide range of frequencies and characteristic impedances, it is found that Getsinger's approach, while more accurate than any of the other methods, requires at least optimization of the  $G$  factor for any given 'family' of microstrip lines on a particular substrate. Edwards and Owens [39], for example, carried out extensive measurements on microstrip lines on monocrystalline sapphire substrates and established (by curve fitting) the following expression for  $G$ :

$$G = \left( \frac{Z_0 - 5}{60} \right)^{1/2} + 0.004Z_0. \quad 7.29$$

This works well in conjunction with Equations (7.26) and (7.27) for lines having characteristic impedances in the range

$$10 \leq Z_0 \leq 100 \ \Omega$$

and over the frequency range

7.30

$$2 \leq f \leq 18 \text{ GHz.} \quad 7.31$$

It should be noted that the sapphire substrates were nominally 0.5 mm thick and the equivalent isotropic relative permittivities (see [Section 6.14.2](#)) were 10.7 to 11.6. This should mean that the formula will also work well for semiconductor substrates such as HRS, GaAs, GaN, InP, etc.

Some careful measurements have also been carried out on microstrips on an alumina substrate [39]. In this case, a suitable expression for the  $G$  factor is

$$G = \left( \frac{Z_0 - 3}{60} \right)^{1/2} + 0.001Z_0 \quad 7.32$$

which works very well for lines on a 0.65 mm thick alumina substrate with the characteristic impedance range

$$30 \leq Z_0 \leq 70 \text{ } \Omega \quad 7.33$$

over the frequency range

$$2 \leq f \leq 18 \text{ GHz.} \quad 7.34$$

Equation (7.32) may give slightly high results where the characteristic impedance falls significantly below 30  $\Omega$ .

Alternatively, and applicable accurately at least to both alumina and sapphire, Edwards and Owens [39] suggest the following expression (combining their Equations 9 and 11) for dispersion:

$$\epsilon_{\text{eff}}(f) = \epsilon_r - \frac{\epsilon_r - \epsilon_{\text{eff}}}{1 + (h/Z_0)^{1.33} (0.43f^2 - 0.009f^3)} \quad 7.35$$

where  $h$  is in millimeters and  $f$  is in gigahertz.

Based on extensive measurements carried out with microstrip lines on alumina and sapphire over the impedance and frequency ranges indicated above, and also comparisons with computed results using the analysis due to Itoh and Mittra (to be described shortly), the estimated accuracy of Equation (7.35) is better than  $\pm 0.8\%$ .

Even this accuracy is still insufficient for many filters and some matching networks. Tolerances and substrate repeatability uncertainties reduce the prediction capability further still and post-production trimming is then mandatory. The use of monocrystalline substrates with controlled thickness removes some repeatability difficulties and tends to place the onus back on to the accuracy of a suitable dispersion formula again.

Since only alumina-type substrates have been tested, Equation (7.35) is only guaranteed to predict with the quoted accuracy, provided the substrate permittivity is within the approximate

limits:

$$10 \leq \epsilon_r \leq 12.$$

Measurements reported by York and Compton [40], however, suggest that Equation (7.35) may work well for plastic substrates at frequencies up to 18 GHz (their results indicate discrepancies consistently below 0.9%).

For consistently accurate calculations in cases where the substrates differ markedly from alumina, such as plastics, quartz, many ferrites, etc., it is recommended that new experiments should be carried out. Hence a new curve-fitted formula for  $G$  is determined for each case, allowing the use of Equations (7.26) and (7.27) to calculate  $\epsilon_{\text{eff}}(f)$ .

[Figure 7.14](#) shows a comparison of the five dispersion calculation methods just described. Two characteristic impedances are quite sufficient to indicate the trends: 25  $\Omega$  was chosen because, at lower impedances, dispersion is greater and 50  $\Omega$  was chosen because it is a commonly used value. Considerable overall discrepancies are evident although on these scales the Getsinger (i.e., Equation (7.25)), Edwards and Owens (i.e., Equation (7.35)), and Carlin [36] curves are fairly close to each other and to the simulated results.

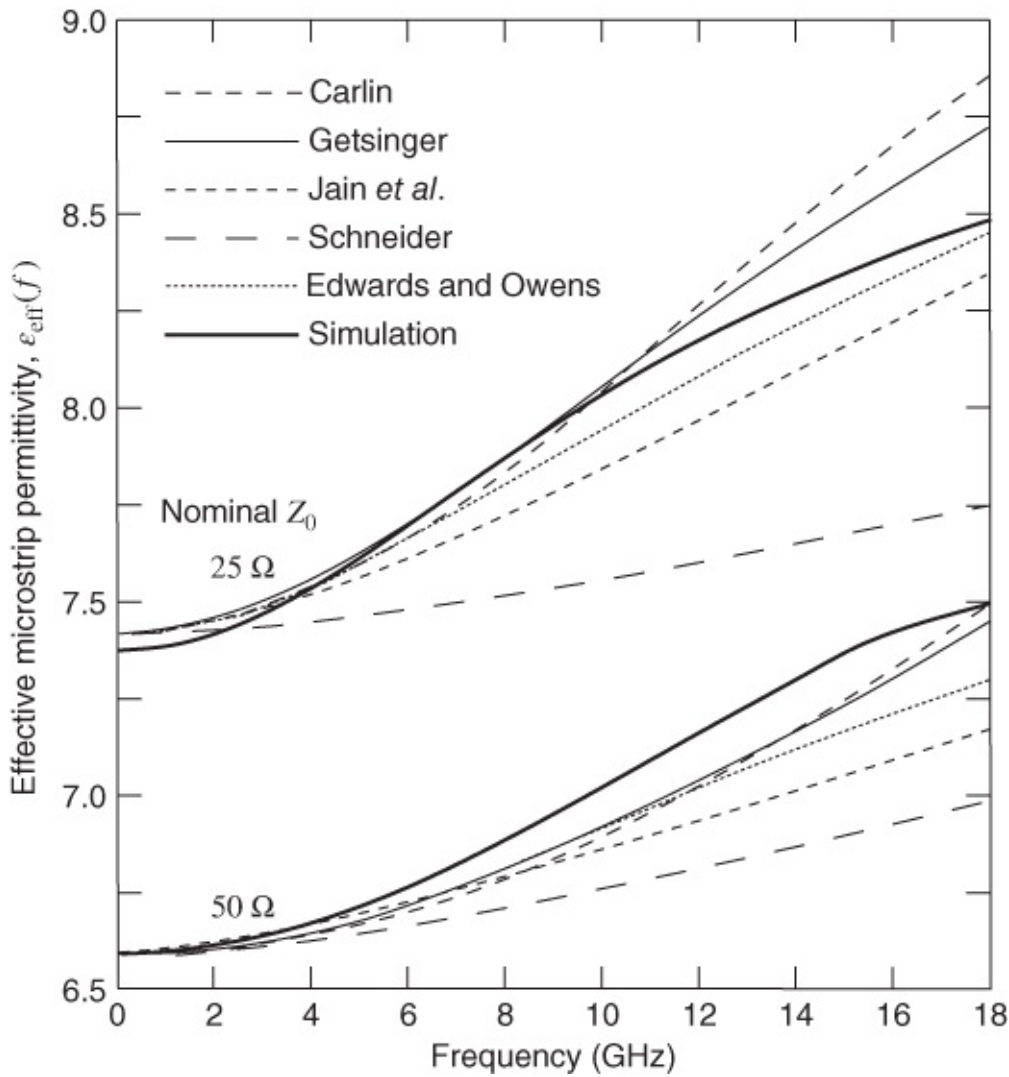


**Figure 7.14** A comparison of the results derived from five different dispersion calculation techniques for a microstrip line on a  $650 \mu\text{m}$  thick substrate with  $\epsilon_r = 9.9$ . Simulated results were obtained using SONNET.

A combination of comprehensive measurements, preferably backed by an independent set of theoretical calculations, is needed to decide on the validity and accuracy of particular formulas. Note that simulation cannot account for variability of substrate permittivity, such as local variability due to density variation near metallization, roughness, and etching effects. Simulation therefore cannot be used as the ultimate arbiter of characteristics and neither can measurements because of measurement uncertainty. A good microwave engineer balances intuition, analytic results, simulation results, and measurements.

A summary of results obtained by various methods is indicated by the curves of [Figure 7.15](#). The “polynomial fit” refers to Equation (7.35), Itoh and Mittra’s approach will shortly be outlined, and the experimental results were obtained using a technique which is explained in [Section 9.3.2](#). It is clear that consistent results are achieved over this wide frequency range and over the moderately wide range of characteristic impedances (31–71  $\Omega$ ).

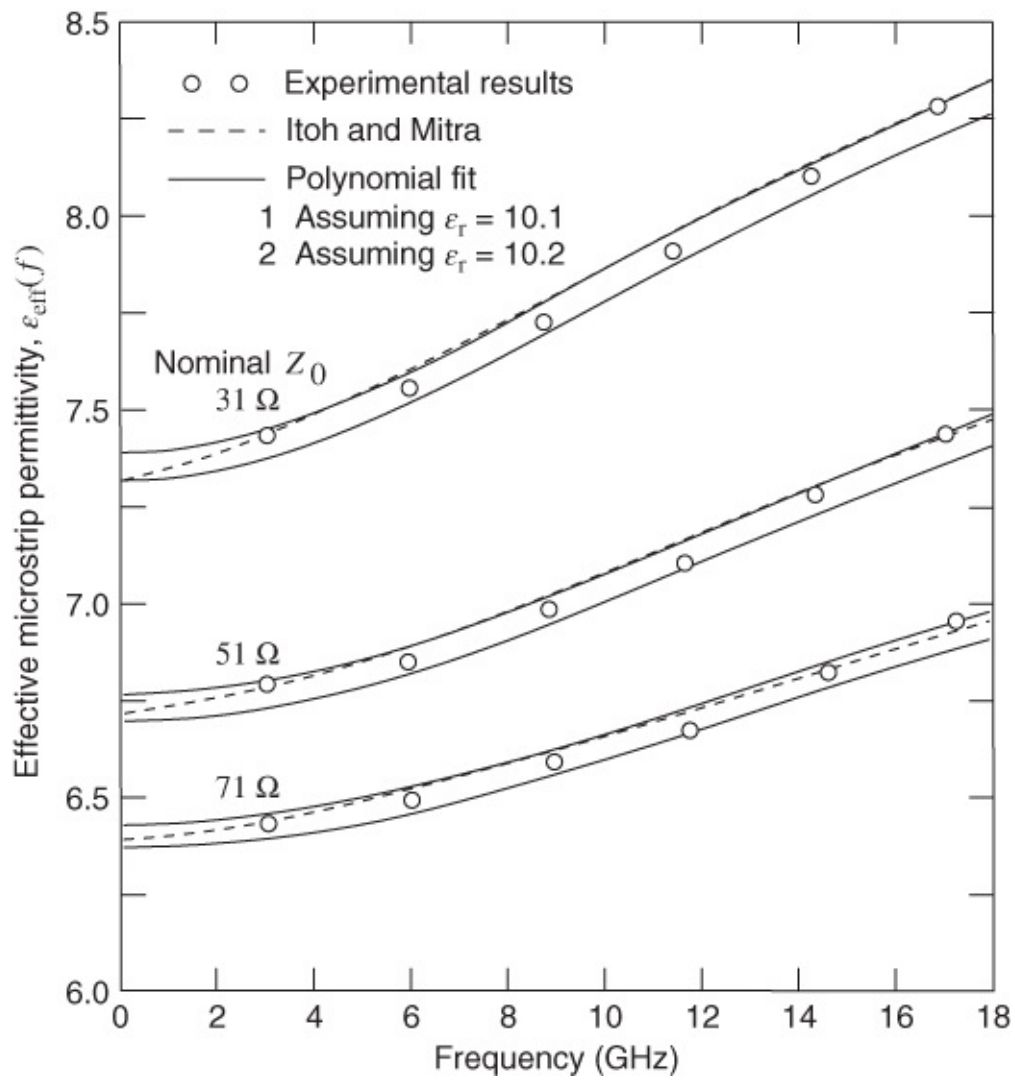


**Figure 7.15** Dispersion curves applicable to three microstrip lines on an alumina substrate ( $\epsilon_r = 9.9$ ).

### 7.4.2 Expressions Suitable for Millimeter-wave Design

The design expressions presented so far in this chapter have been well tested and checked against experimental measurements for frequencies up to approximately 18 GHz. This frequency is, however, far below the limits at which microstrip can be used, up to the vicinity of 100 GHz at least. It has therefore long been recognized that a requirement exists for closed formulas that would enable calculations to be conducted, including dispersion in microstrip at these high frequencies.

#### 7.4.2.1 Yamashita's Expressions

In 1979 Yamashita *et al.*[41] published an approximate dispersion formula covering the frequency range 1–100 GHz. Their expression can be written

$$\epsilon_{\text{eff}}(f) = \left( \frac{\sqrt{\epsilon_r} - \sqrt{\epsilon_{\text{eff}}}}{1 + 4F^{-1.5}} + \sqrt{\epsilon_{\text{eff}}} \right)^2 \quad 7.36$$

where

$$F = \frac{4hf\sqrt{\epsilon_r - 1}}{c} \left[ 0.5 + \left\{ 1 + 2 \log \left( 1 + \frac{w}{h} \right) \right\}^2 \right]. \quad 7.37$$

However, this expression is not particularly accurate, especially in the lower frequency range up to 18 GHz, where the expression due to Edwards and Owens is recommended.

Comparison of Yamashita's design formulas with analytical results determined using electromagnetic solutions shows considerable discrepancies over the full 1–100 GHz range.

#### 7.4.2.2 Kirschning and Jansen's Expressions

An improved design formula was developed by Kirschning and Jansen [42]. Their approach begins with a function that bears a close resemblance to Getsinger's, but they have a new and reportedly more accurate frequency-dependent denominator term. Also, their formula covers a much wider range of permittivities, aspect ratios, and frequencies than those considered by Getsinger or Edwards and Owens.

Kirschning and Jansen's basic expression is (with frequency  $F$  [=  $f/(1 \text{ GHz})$ ] in GHz and thickness  $H$  [=  $h/(1 \text{ cm})$ ] in cm):

$$\epsilon_{\text{eff}}(f) = \epsilon_r - \frac{\epsilon_r - \epsilon_{\text{eff}}}{1 + P(F)} \quad 7.38$$

and the form of the denominator frequency function is

$$P(F) = P_1 P_2 \left\{ (0.1844 + P_3 P_4) 10FH \right\}^{1.5763} \quad 7.39$$

where

$$\left. \begin{aligned} P_1 &= 0.27488 + \left[ 0.6315 + 0.525/(1 + 0.157FH)^{20} \right] (w/h) \\ &\quad - 0.065683 \exp(-8.7513w/h) \\ P_2 &= 0.33622 \left[ 1 - \exp(-0.03442\epsilon_r) \right] \\ P_3 &= 0.0363 \exp(-4.6w/h) \left\{ 1 - \exp[-(FH/3.87)^{4.97}] \right\} \\ P_4 &= 1 + 2.751 \left\{ 1 - \exp \left[ -(\epsilon_r/15.916)^8 \right] \right\} \end{aligned} \right\} \quad 7.40$$

These researchers used computer-based matching in conjunction with the available hybrid mode results (derived from full electromagnetic numerical computations) to force the correct asymptotic behavior of the function  $P(F)$ . An accuracy of better than 0.6% is claimed for all frequencies up to 60 GHz (although a full check only appears to have been conducted up to 30 GHz). The validity ranges are very wide, namely:

$$\begin{aligned}1 &\leq \epsilon_r \leq 20 \\0.1 &\leq w/h \leq 100 \\0 &\leq h/\lambda_0 \leq 0.13.\end{aligned}$$

There are further formulations enabling the effects of dispersion in microstrip to be calculated at frequencies through millimeter-wave. The position has been reached where reported accuracies are within 1% of measurements and independent theoretical results over a wide range. Having said this, it must be recognized that care is always required in selecting an appropriate accurate dispersion expression.

### 7.4.2.3 Expressions with the Widest Applicability

The final formulation presented here for dispersion calculation is that due to Kobayashi [43]. This work is based on the concept of a significant 50% dispersion point at which the effective microstrip permittivity is the arithmetic mean of the substrate relative permittivity and the low-frequency limit value. Kobayashi calculates the frequency for this condition and develops the following dispersion expressions:

$$\epsilon_{\text{eff}}(f) = \epsilon_r - \frac{\epsilon_r - \epsilon_{\text{eff}}}{1 + (f/f_a)^m}, \quad 7.41$$

where

$$f_a = \frac{f_b}{0.75 + (0.75 - 0.332 \epsilon_r^{-1.73})(w/h)} \quad 7.42$$

$$f_b = \frac{47.746 \times 10^6}{h \sqrt{\epsilon_r - \epsilon_{\text{eff}}}} \tan^{-1} \left\{ \epsilon_r \sqrt{\frac{\epsilon_{\text{eff}} - 1}{\epsilon_r - \epsilon_{\text{eff}}}} \right\} \quad 7.43$$

$$m = \begin{cases} m_0 m_c & m_0 m_c \leq 2.32 \\ 2.32 & m_0 m_c > 2.32 \end{cases} \quad 7.44$$

$$m_0 = 1 + \frac{1}{1 + \sqrt{w/h}} + 0.32 \left( 1 + \sqrt{w/h} \right)^{-3} \quad 7.45$$

$$m_c = \begin{cases} 1 + \frac{1.4}{1 + w/h} \{ 0.15 - 0.235 \exp(-0.45f/f_a) \}, & \text{for } w/h \leq 0.7 \\ 1, & \text{for } w/h > 0.7. \end{cases} \quad 7.46$$

SI units are used in these equations and recall that  $\epsilon_{\text{eff}} = \epsilon_{\text{eff}}(0)$ , that is, its DC value. The accuracy of the equations is better than 0.6% for  $0.1 \leq w/h \leq 10$ ,  $1 \leq \epsilon_r \leq 128$ , and for any value of  $h/\lambda$  provided that  $h < \lambda/10$ .

### 7.4.2.4 Which Expressions to Use

York and Compton [40] report measurements on microstrips ranging in impedance from 35 to 70  $\Omega$ , fabricated on both alumina and plastic substrates having thicknesses in the range 0.635 to 1.605 mm. Although York and Compton's results are limited to frequencies up to 18 GHz it is clear that, out of a total of nine models tested, only those due to Edwards and Owens, Kirschning and Jansen, and Kobayashi show deviations well within 1% of measurements and simulations. The comparisons of simulated results in [Figures 7.14](#) and [7.16](#) support these conclusions.

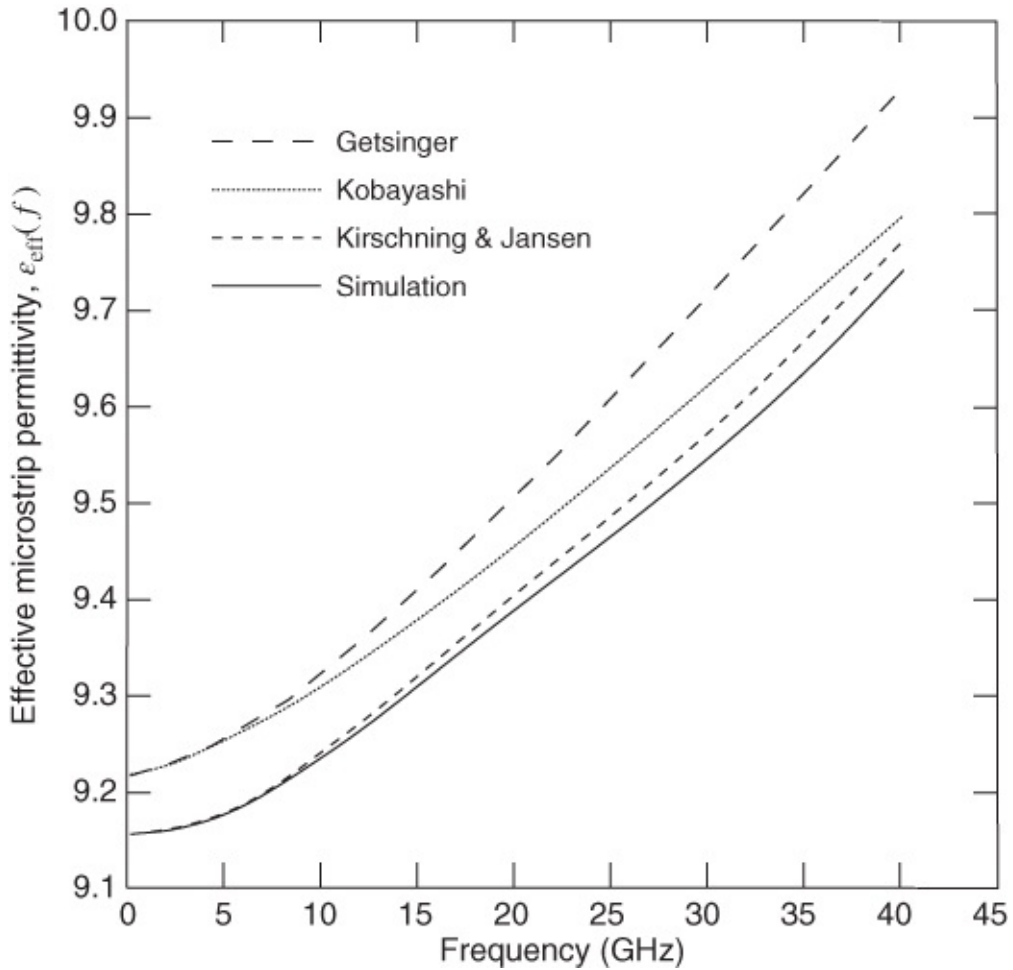


**Figure 7.16** Dispersion of microstrip with gold metallization on a 127  $\mu\text{m}$ -thick GaAs substrate with  $\epsilon_r = 13$  and a strip width of 254  $\mu\text{m}$ . Simulation results were obtained using SONNET. RMS error relative to EM simulation: Getsinger 1.4%, Kobayashi 0.8%, and Kirschning and Jansen 0.2%.

### 7.4.3 Dispersion Curves Derived from Simulations

All the above results apply generally to lossless microstrip lines. It is known, however, that in practice losses play a significant part in determining the dispersion and a set of SONNET® simulations have been run in order to generate dispersion curves for microstrip on various substrates, taking losses into account. In all cases the 1–40 GHz range is covered.

Simulated dispersion characteristics of a nominally 50  $\Omega$  lossy line on a 0.635 mm thick alumina substrate are shown in [Figures 7.17](#) and [7.18](#). When loss is incorporated  $\epsilon_{\text{eff}}$  and  $Z_0$

become complex and the relatively smaller imaginary components indicate loss. It is clear that, as expected, the real part of the effective permittivity steadily increases with frequency and, overall, this is also true of the characteristic impedance, with a more pronounced increase above 18 GHz.

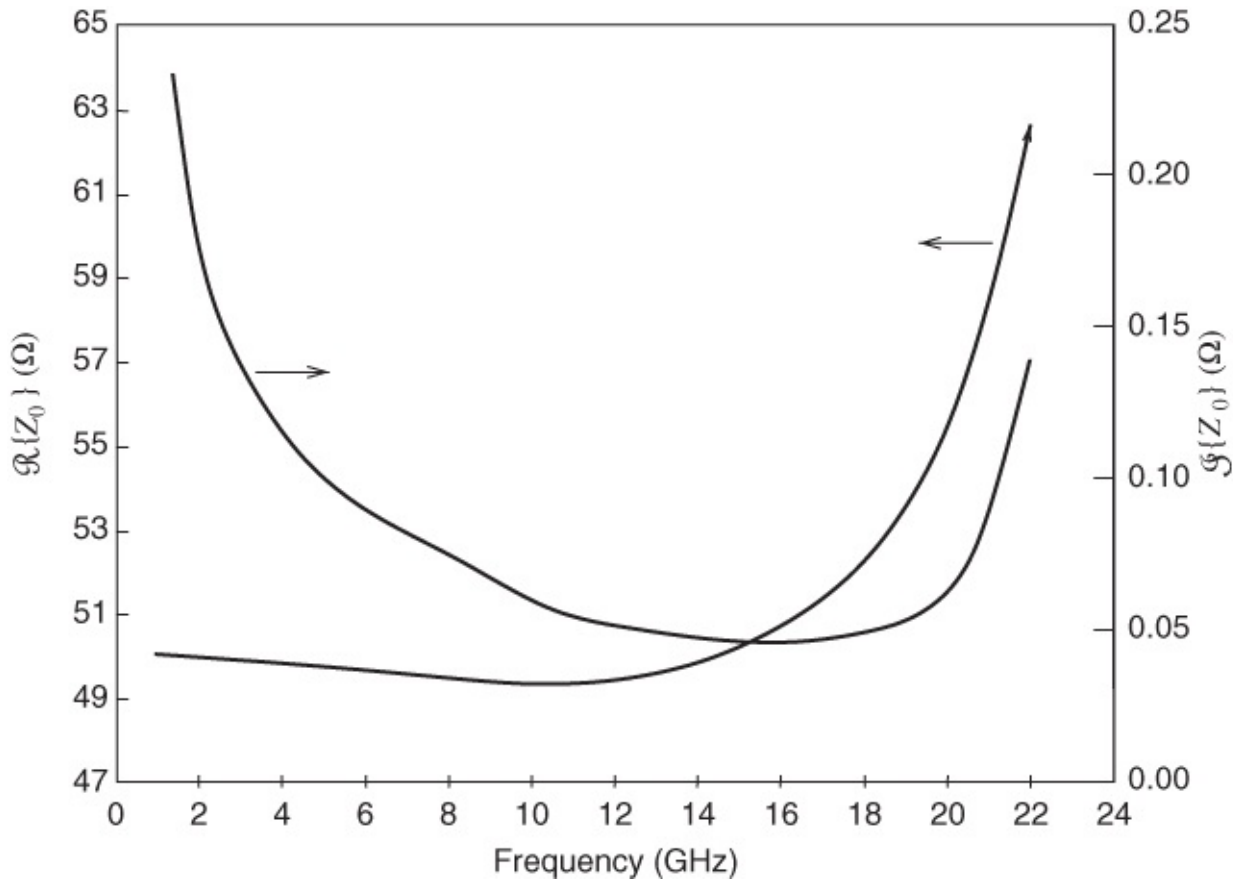


**Figure 7.17** Frequency dependence of the real and imaginary parts of  $Z_0$  of a gold microstrip line and alumina substrate with  $\epsilon_r(\text{DC}) = 9.9$  and  $w = h = 635 \mu\text{m}$ .

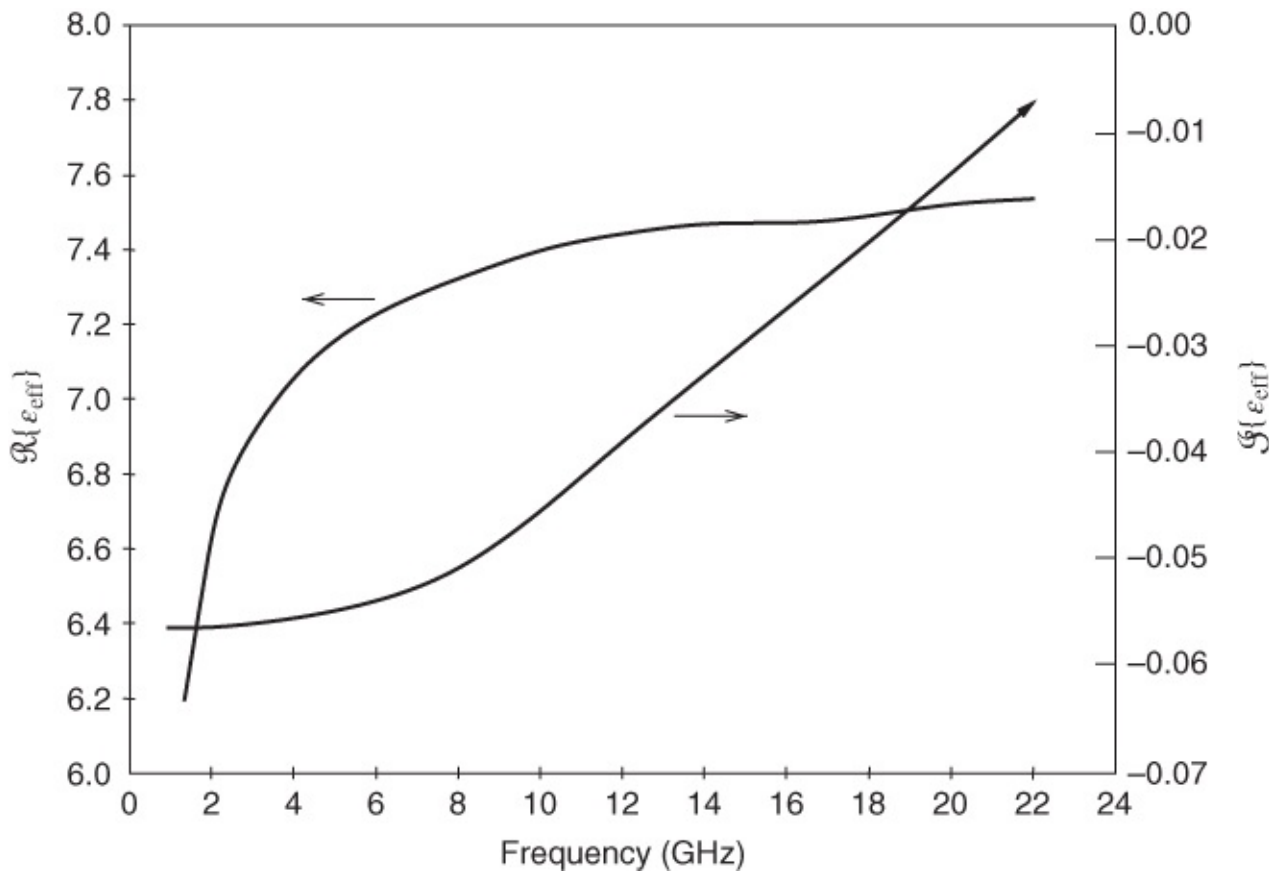


**Figure 7.18** Frequency dependence of the real and imaginary parts of  $\epsilon_{\text{eff}}$  of a gold microstrip line and alumina substrate with  $\epsilon_r(\text{DC}) = 9.9$  and  $w = h = 635 \mu\text{m}$ .

The effective permittivity,  $\epsilon_{\text{eff}}$ , increases with frequency as the fields become confined more to the substrate. Also, the real part of the characteristic impedance is plotted with respect to frequency. Up to 10 GHz a drop-off in  $Z_0$  is observed as frequency increases. This is due to both reduction of internal strip and ground inductances as charges move to the skin of the conductor and also to greater confinement of the EM fields in the dielectric as frequency increases. It is not long before the characteristic impedance increases. This effect is not due to the skin effect and current bunching that were previously described. Rather it is due to other EM effects that are only captured in EM simulation. It is a result of spatial variations being developed in the fields related to the fact that not all parts of the fields are in instantaneous contact.

#### 7.4.4 Designs Requiring Dispersion Calculations, Worked Example

For the first example we will recall the problem of calculating one element of a transistor matching network, which was calculated for 2 GHz in [Section 6.9](#). However, we now design the same element for a frequency of 12 GHz, where dispersion is significant.

The initial data, as previously, are

$$Z_0 = 30 \Omega \quad \epsilon_r = 9.8 \quad h = 0.6 \text{ mm}$$

but in this case the frequency  $f$  is 12 GHz. We shall also require the effective microstrip

permittivity from the static-TEM design completed in [Section 6.9](#). This is

$$\epsilon_{\text{eff}} = 7.39.$$

For a frequency of 12 GHz, Equation [\(7.35\)](#) is used to calculate  $\epsilon_{\text{eff}}(f)$ :

$$\epsilon_{\text{eff}}(f) = \epsilon_r - \frac{\epsilon_r - \epsilon_{\text{eff}}}{1 + (H/Z_0)^{1.33} (0.43F^2 - 0.009F^3)}. \quad 7.47$$

The thickness  $H = 0.6$  is directly substituted in millimeters (i.e.,  $h = 6$  mm) and the frequency  $F = 12$  in gigahertz, giving

$$\epsilon_{\text{eff}}(f) = 7.880 \quad 7.48$$

and the wavelength

$$\lambda_g = \frac{300}{f\sqrt{\epsilon_{\text{eff}}(F)}} = 8.906 \text{ mm.} \quad 7.49$$

From the wavelength we can readily derive the length of the microstrip element, required to be  $\lambda_g/4$ , that is,

$$\ell \approx 8.906/4 \approx 2.227 \text{ mm.} \quad 7.50$$

Again, this value neglects the effect of discontinuities that will slightly reduce the final length. These effects are dealt with in [Chapter 9](#).

Notice that our new length result, for 12 GHz, is significantly different from the value that would have been obtained had the previous (2 GHz) result been simply linearly scaled for frequency. This would have yielded the erroneous result of 2.313 mm, nearly 4% in error. This error also increases as the frequency is increased. Provided we assume here that we will neglect any change in  $Z_0$  with frequency (dealt with in [Section 7.7](#)), the microstrip width will remain at the value previously determined:  $w = 1.41$  mm.

At higher frequencies the results calculated including dispersion differ more markedly from those calculated using the static-TEM formulas. For example, let us consider a microstrip line to be designed for use in an MMIC, in this case fabricated on a semi-insulating GaAs substrate. The thickness is 0.127 mm and the relative permittivity is 13.0. Let us assume that the operating frequency is 40 GHz and that the line to be designed has an aspect ratio ( $w/h$ ) of 2.0.

Calculations using the static-TEM expressions yield the low-frequency limit permittivity as 9.136, whereas calculations using the formulas due to Kobayashi yield a value of 9.74 at 40 GHz. The discrepancy is around 4%, significant in many designs such as filters and multiplexers.

Similar approximate magnitudes of discrepancy occur where plastic, quartz or many other substrates are considered.

A comparison of calculated results for this 0.127 mm thick GaAs case, using the methods of

Yamashita, Kirschning and Jansen, and Kobayashi, is provided by the curves shown in [Figure 7.19](#). Discrepancies between the first two methods continually increase, reaching 1.07% at 40 GHz, whereas the differences between Kirschning and Jansen, and Kobayashi remain less than 0.25% over the entire frequency range.

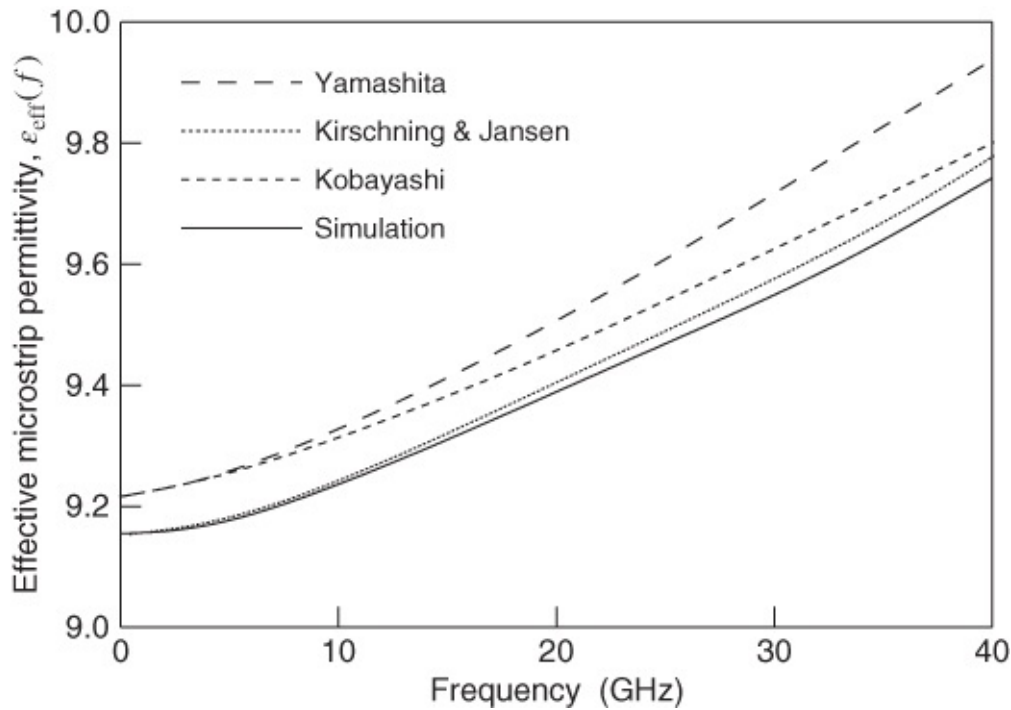


[Figure 7.19](#) Comparative dispersion curves for microstrip on a GaAs substrate ( $\epsilon_r = 13$ ,  $w = 0.254$  mm,  $h = 0.127$  mm). Simulated results were calculated using SONNET.

## 7.5 Effects due to Ferrite and to Dielectrically Anisotropic Substrates

### 7.5.1 Effects of Ferrite Substrates

The frequency dependence of the effective microstrip permeability of a ferrite substrate depends on whether it is magnetized or not. If it is unmagnetized the frequency dependence is very small, but however the magnetic loss is appreciable above 1 GHz or so. However, if the ferrite is magnetized the frequency dependence of the effective permeability can be very large and it can even be negative over a range of frequencies. Ferrite also behaves as a dielectric whose the frequency-dependent effective microstrip permittivity is important.

Kurushin *et al.* [44] have shown that as the frequency increases in the case of microstrip on a magnetized ferrite substrate at a high enough frequency, the conventional dispersion results approach those applicable to the case of a non-ferrite dielectric substrate. Therefore, all the design expressions previously given in this chapter continue to apply at high frequencies.

Since many ferrite devices are often placed on non-ferrite substrates (e.g., alumina, semiconductor) and microstrip is then fabricated on the ferrite device surface itself, it is important to gain some design appreciation of the behavior of this type of structure. The basic

properties of such a structure have been evaluated by Hsia *et al.* [45], who used a spectral domain exponential matrix method. These workers generalized their analysis to accommodate isotropic/anisotropic structures in terms of both permeability and permittivity. Most of the results presented by Hsia *et al.* refer to a ferrite with permittivity of 12.6 providing the top layer whilst GaAs having a permittivity of 12.9 formed the lower substrate. The magnetic bias field was conventionally disposed normally to the plane of this assembly. Hsia *et al.* give curves showing normalized wave number (corresponding to effective permittivity) and characteristic impedance as functions of frequency over the 5–30 GHz range. Their curves for normalized wave number are reproduced as [Figure 7.20](#), in which  $z = b$  refers to the case of microstrip deposited on the lower, non-ferrite, substrate whereas  $z = d$  refers to the case where the microstrip is deposited on the upper ferrite superstrate.

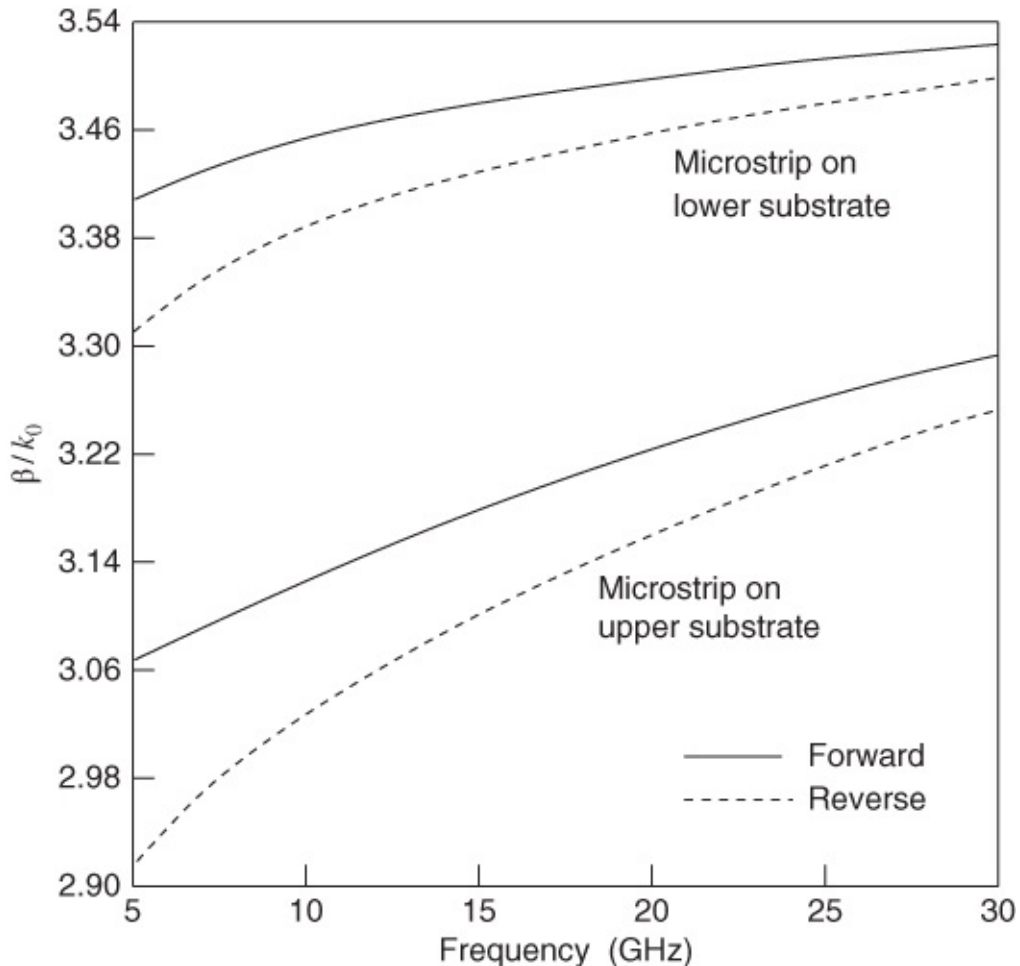


[Figure 7.20](#) Microstrip propagation coefficient as a function of frequency. Adapted from Hsia *et al.* (1990) [45], figure 2(a), p. 667. Reproduced with the permission of IEEE.

Many magnetic materials have significant variation of their permeabilities at microwave frequencies. This leads to realization of devices with exceptional characteristics. These are discussed in [Chapter 20](#).

### 7.5.2 Effects of a Dielectrically Anisotropic Substrate

Static-TEM calculations associated with microstrip on a dielectrically anisotropic substrate

were dealt with in [Section 6.14.2](#). In the case of sapphire, the most common anisotropic substrate, the measurements of Edwards and Owens [39] seem to indicate that the influence of the sapphire anisotropy on the detail of the dispersion characteristics is negligibly small in practice (up to 18 GHz).

As indicated in his Table II, and also his reported dispersion results, the data derived by Kobayashi [46] confirm excellent agreement with the predictions due to Edwards and Owens. The use of slightly modified versions of Yamashita's dispersion expression also provides very good agreement and it would be useful to study the effects of suitably adjusting Kirschning and Jansen's formulas in an effort to predict dispersion at high frequencies on dielectrically anisotropic substrates.

A more extensive study of the behavior of microstrip on a dielectrically anisotropic substrate has been performed by Mariki and Yeh [47]. These researchers used a three-dimensional transmission line matrix (TLM) analysis to determine the dispersive effects with this type of substrate. In particular the analysis derives the frequency-dependent effective microstrip permittivity and characteristic impedance. Considering a sapphire substrate Mariki and Yeh's results for microstrip permittivity at frequencies up to 21 GHz are very close to those predicted by Getsinger's original model. Characteristic impedance is also shown to increase with frequency, for example from 37.5 to 54  $\Omega$  when the aspect ratio ( $w/h$ ) is 1.5.

## 7.6 Field Solutions

### 7.6.1 One Example of a 'Classic' Frequency-dependent Computer-based Field Solution

In the methods for calculating effective microstrip permittivity outlined so far the emphasis has been on approximate approaches using closed formulas. These approximate approaches have a number of drawbacks, for example:

- i. They often suit only a specified microstrip 'family', for example those based on alumina substrates.
- ii. They require accurate static-TEM data to start with, that is,  $\epsilon_{\text{eff}}$  and  $Z_0$ .
- iii. Such methods are not fundamentally elegant (some empirical element usually has to be introduced).

Three-dimensional frequency-dependent field solutions requiring 'number crunching' have been published by a number of researchers [48–52] and are available with several commercial EM simulators. While these are comparatively expensive to run they provide the positive benefits of answering drawbacks (i), (ii), and (iii) above. They generally take up too much computer time and storage to be considered as candidates for inclusion in a larger microwave integrated circuit computer-aided optimization routine. Specific problems are accounting for skin effect, roughness, and permittivity variations. However, such solutions provide an excellent theoretical comparison with measured data and can therefore enable the accuracy of

the approximate design formulas to be checked. They can also be readily extended to handle more complex problems such as coupled lines.

When satisfactory agreement is reached regarding measurements and fundamental theoretical results then curve-fitted closed formulas can be deduced for  $\epsilon_{\text{eff}}(f)$ . It should be appreciated that these frequency-dependent field solutions require only the physical input data:

- a. microstrip geometry ( $w$ ,  $h$ , and box dimensions, if applicable)
- b. the permittivity of the substrate material ( $\epsilon_r$ ).

Such an approach can accommodate manufacturing variations and the inability to model real-world effects such as roughness and local permittivity variations [53–59].

### 7.6.2 Asymmetry Effects

The effects of asymmetrically disposed shielded microstrip are important in practice and Dumbell *et al.* [60] have reported an analyses of this situation. They analyzed asymmetric shielded microstrip both in single-layer and overlaid dielectric forms. They showed that the variation in propagation coefficient as a function of degree of asymmetry can be controlled by the introduction of a dielectric overlay to the extent that microstrip strips may be located close to conducting box walls and such variations then practically neglected.

Results obtained by Dumbell *et al.* [60] are shown in [Figure 7.21](#) for the case of a substrate having a relative permittivity of 10.5. This family of curves refers to microstrip with an aspect ratio of 0.866 enclosed in a conducting box 11.43 mm high by 12.7 mm wide. ‘Strip offset’ is the amount by which the strip is offset from the center line of the system.

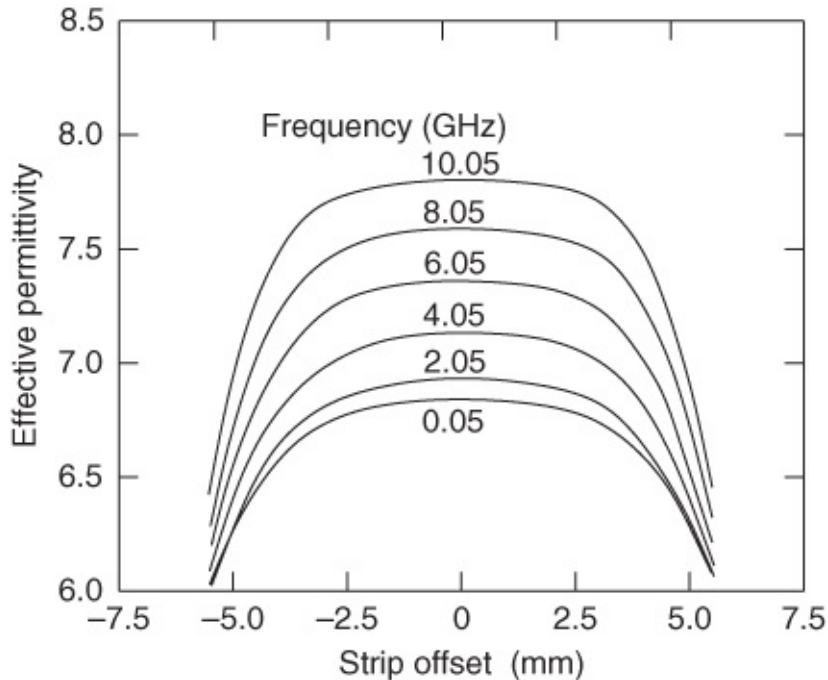


[Figure 7.21](#) Effective permittivity for shielded microstrip. Adapted from Dumbell *et al.* (1989) [60], figure 5, p. 764. Reproduced with the permission of the European Microwave Association.

A comparative family of curves, applicable to the same geometry but with a dielectric overlay having permittivity 7.0 and 1.27 mm thickness, is shown in [Figure 7.22](#). Clearly, at the lower frequencies particularly, the variations with strip offset are substantially reduced. Families of curves for the characteristic impedances are also determined by Dumbell *et al.*, and these indicate that variations caused by offset are less effectively compensated by the introduction of an overlay.

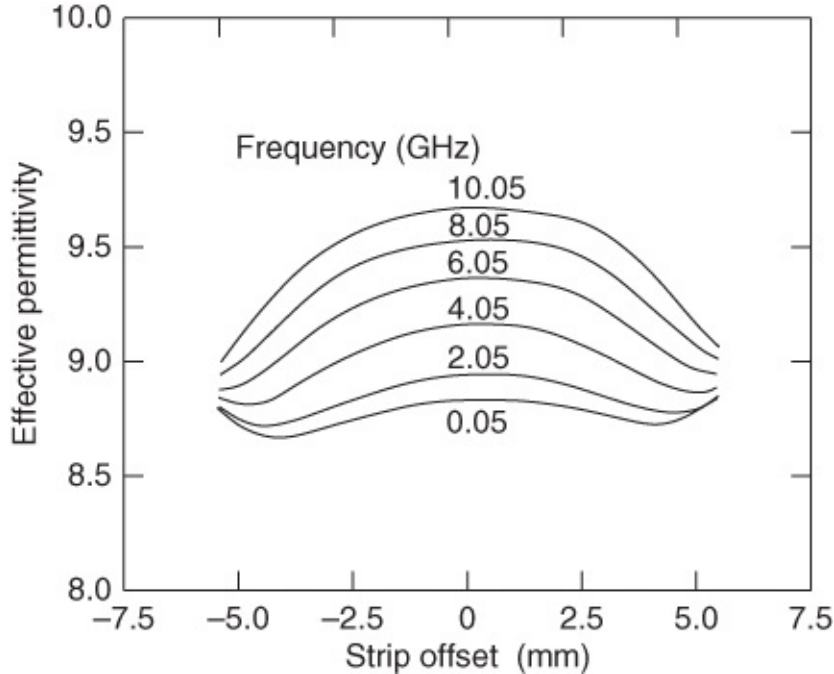


[Figure 7.22](#) Effective permittivity for shielded microstrip with dielectric overlay. Adapted from Dumbell *et al.* (1989) [60], figure 7, p. 765. Reproduced with the permission of the European Microwave Association.

### 7.6.3 Time-domain Approaches

A length of dispersive transmission line can be used as a phase equalizer to compensate for the phase distortion otherwise resulting in the transmission of asymmetric pulses. This equalization results in the effective reshaping and compression of ultrashort pulses which originate, typically, from high-speed photoconductive switches.

Qian and Yamashita [61] have shown that an optimum length of microstrip or coplanar waveguide can be used to correct the phase distortion. They begin with a Fourier spectrum of a single-sided exponential pulse that suitably quantifies this distortion and they adapt a microstrip dispersion expression (see [Section 7.4.2](#)). The phase function associated with the single-sided exponential pulse is expanded as a polynomial in which the frequency component at which the amplitude of the spectrum is 10% of its peak value is defined.

The microstrip dispersion expression is expanded using Taylor's series and used to formulate an expression for the phase delay. A comparison is finally made between the polynomial derived from the exponential pulse and this dispersion expression series expansion. Qian and Yamashita show that, if the second- and third-order terms in each series are made equal, then

the total phase of the signal after a specific distance has been traversed is close to a linear function of frequency. They report a straightforward formula for the length of line required. As an example, Qian and Yamashita provide details of a simulation for a 35 ps single-sided exponential pulse propagating along a 50  $\Omega$  microstrip line on a GaAs substrate and the resulting waveforms are repeated here in [Figure 7.23](#).

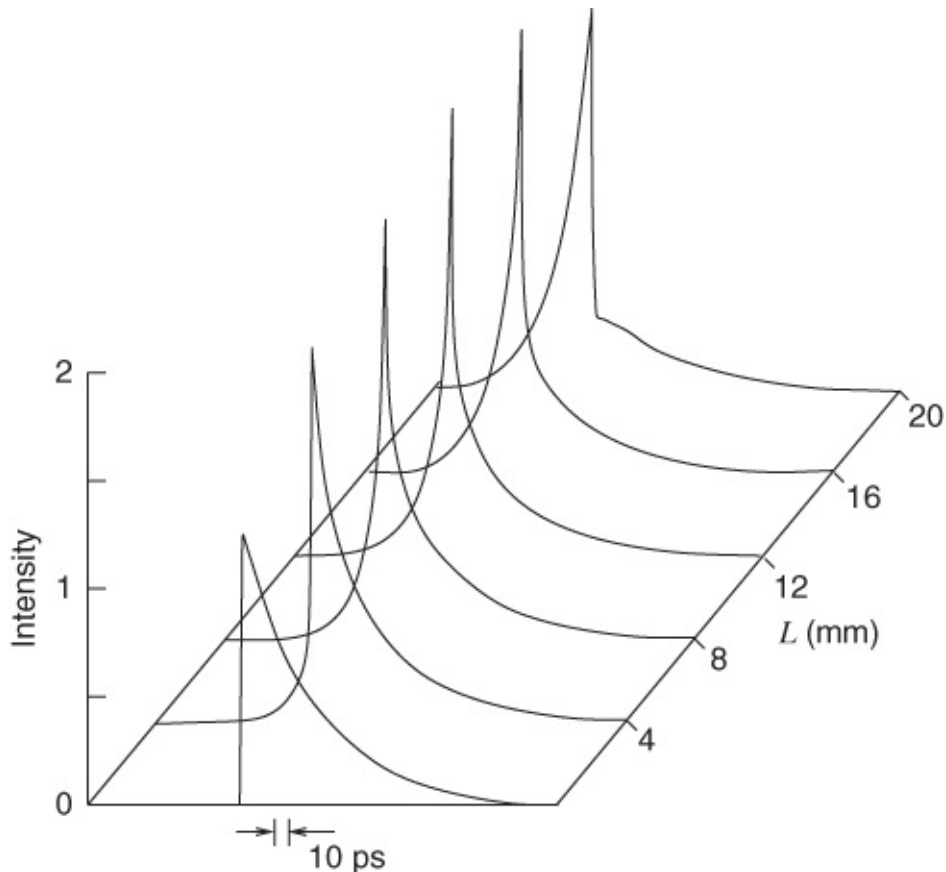


[Figure 7.23](#) Simulation results for the propagation of a 35 ps single-sided exponential pulse along 50  $\Omega$  microstrip lines on a GaAs substrate. Adapted from Qian and Yamashita (1990) [61], figure 3, p. 954. Reproduced with permission of IEEE.

## 7.7 Frequency Dependence of Microstrip Characteristic Impedance

There have been many different approaches to the dynamic problem of microstrip characteristic impedance and quite different functions of frequency have been predicted, even extending to opposing trends. With no definitive function available, microstrip designers have continued to use the static-TEM calculation for  $Z_0$ , but using the frequency-dependent permittivity. It is understood that the discrepancy is small.

The problem of characteristic impedance being a function of frequency is not simple but some background theory and tentative recommendations are presented here in an effort to provide some insight and assistance for the design engineer.

### 7.7.1 Different Definitions and Trends with Increasing Frequency

Fundamentally, characteristic impedance may be defined in the following different ways:

$$Z_{0,a}(f) = \frac{V}{I} \quad 7.51$$

$$Z_{0,b}(f) = \frac{P}{II^*} \quad 7.52$$

$$Z_{0,c}(f) = \frac{\mathbf{V}\mathbf{V}^*}{P}. \quad 7.53$$

where  $\mathbf{V}$  and  $\mathbf{I}$  are the mean voltage and current phasors, respectively, and  $P$  is the power traveling on the line. Different functions of frequency are obtained, depending on which of these definitions is selected. This is due mainly to different assumptions which have to be made regarding mode coupling as the frequency is increased. This mode coupling, it is recalled, is the fundamental dispersive mechanism for microstrip.

Bianco *et al.* [62] further define characteristic impedances in terms of mean voltage  $\mathbf{V}$  and centre voltage  $\mathbf{V}_c$  to yield a total of five definitions as follows:

$$Z_{0,1}(f) = \frac{V}{I} \quad 7.54$$

$$Z_{0,2}(f) = \frac{V_c}{I} \quad 7.55$$

$$Z_{0,3}(f) = \frac{P}{II^*} \quad 7.56$$

$$Z_{0,4}(f) = \frac{\mathbf{V}_c\mathbf{V}_c^*}{P} \quad 7.57$$

$$Z_{0,5}(f) = \frac{\mathbf{V}\mathbf{V}^*}{P}. \quad 7.58$$

The general theoretical conclusion is that both  $Z_{0,2}(f)$  and  $Z_{0,4}(f)$  always rise with increasing frequency whereas the remaining impedances all fall as the frequency rises. ( $Z_{0,3}(f)$  always exhibits the smallest variation.)

In all calculations based on Equations (7.47)–(7.54) the power  $P$  flowing in the microstrip is evaluated using Poynting's theorem.

Getsinger [63], using the model previously described in this chapter, developed an expression which (like that of Denlinger [13]) has microstrip characteristic impedance varying inversely with the square root of  $\epsilon_{\text{eff}}(f)$ . The development is based on Schelkunoff's definition of wave impedance and Getsinger is careful about the interpretation of the model for the analysis pursued. This derivation seems plausible, but it must be considered in the light of alternative

definitions and trends that will now be examined.

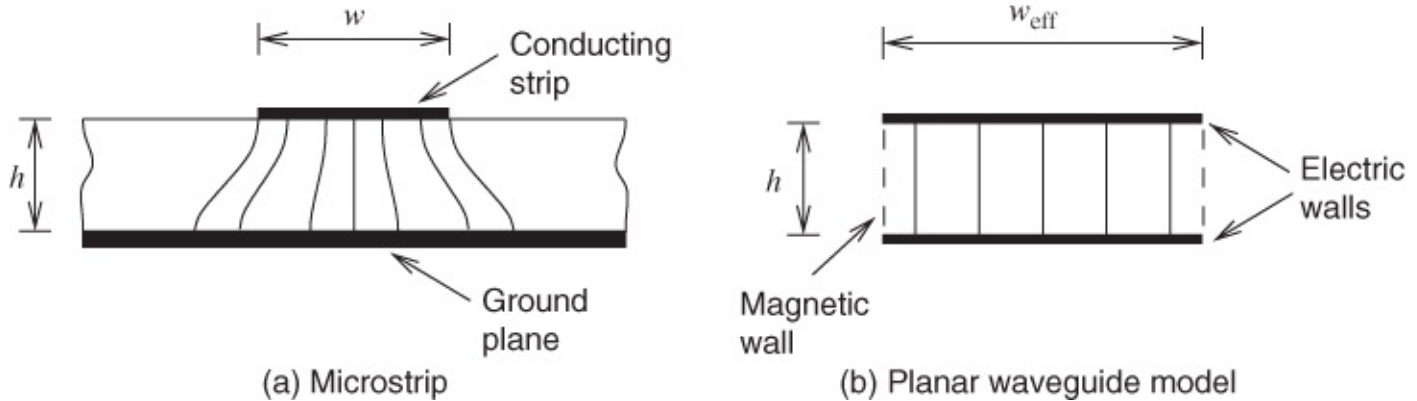


**Figure 7.24** Planar waveguide model for microstrip.

### 7.7.2 Use of the Planar Waveguide Model ([Figure 7.24](#))

Owens [64, 65] developed a radically different approach to the analysis of microstrip with the effective microstrip width concept [66] as a principal feature. Owens obtained the following approximate expression for characteristic impedance:

$$Z_0(f) = \frac{h\eta}{w_{\text{eff}}(f) \sqrt{\epsilon_{\text{eff}}(f)}} \quad 7.59$$

where, following the dispersion expressions given earlier (such as Equations [\(7.26\)](#) and [\(7.27\)](#)), the effective microstrip width  $w_{\text{eff}}(f)$  may be written as

$$w_{\text{eff}}(f) = w + \frac{w_{\text{eff}} - w}{1 + (f/f_p)^2}. \quad 7.60$$

(Note that the overall form of Equation [\(7.56\)](#) is very similar to the earlier equations provided by Getsinger.) In Equation [\(7.56\)](#)  $w_{\text{eff}}$  is the DC value of  $w_{\text{eff}}$ .

In Equation [\(7.56\)](#)

$$f_p = \frac{c}{2w_{\text{eff}}\sqrt{\epsilon_{\text{eff}}}} \quad 7.61$$

and  $\eta$  is the characteristic impedance of free space:

$$\eta = \sqrt{\mu_0/\epsilon_0} = 376.7 \Omega. \quad 7.62$$

From Equation [\(7.56\)](#) it is observed that  $w_{\text{eff}}(f)$ , which appears in the denominator of Equation [\(7.55\)](#), varies as a direct function of  $[1 + (f/f_p)^2]^{-1}$ , whereas  $\sqrt{\epsilon_{\text{eff}}(f)}$  is also involved in Equation [\(7.55\)](#). Hence the frequency-dependent effect of  $w_{\text{eff}}(f)$  dominates and this quantity decreases as the frequency increases.

Thus  $Z_0(f)$  increases with increasing frequency. For a 50  $\Omega$  line the increase is about 10%

over the 0–16 GHz range.

### 7.7.3 A First-order Expression for $Z_0(f)$

A first-order expression is based on modifying the static  $Z_0$  by its frequency-dependent effective permittivity. Thus

$$Z_0(f) = \frac{Z_{01}}{\sqrt{\epsilon_{\text{eff}}}} \quad 7.63$$

where  $Z_{01}$  is the characteristic impedance calculated for an air-filled line. Since  $\epsilon_{\text{eff}}$  monotonically increases with frequency, Equation (7.59) predicts a monotonically reducing characteristic impedance with respect to frequency. This is clearly not observed, see [Figure 7.17](#). However this does capture some of the essential frequency dependence at lower frequencies.

### 7.7.4 A Second-order Expression for $Z_0(f)$

A second-order expression is based on modifying the static  $Z_0$  of microstrip by its frequency-dependent effective permittivity as well as the change in the effective width of the line. Thus

$$Z_0(f) = \frac{Z_{01}}{\sqrt{\epsilon_{\text{eff}}}} \left( \frac{w}{w_{\text{eff}}} \right) \quad 7.64$$

where  $Z_{01}$  is the characteristic impedance calculated for an air-filled line and  $w_{\text{eff}}$  is the effective width of the line calculated in Equation (7.56).

### 7.7.5 A Further Alternative Expression

Another expression has been given by Bianco *et al.* [67], who also utilize the form of the main Getsinger dispersion formula, Equation (7.26), to develop the following result:

$$Z_0(f) = Z_{0T} - \frac{Z_{0T} - Z_0}{1 + G(f/f_P)^2}. \quad 7.65$$

In this formula  $Z_{0T}$  is twice the characteristic impedance calculated for a stripline transmission line having the same width  $w$  as the microstrip line, but twice the substrate height (i.e., the total stripline dielectric thickness is  $2h$ ).  $Z_{0T}$  is readily determined from standard design curves [68] or from some good approximate expressions (see [Section 13.2](#) for a formula for stripline characteristic impedance).

Again we consider a 50  $\Omega$  line on an alumina substrate and find that this expression, Equation (7.61), yields an increase of only about 5% over the 0–16 GHz frequency range. Now this order of magnitude (5%) is in fair agreement with a more fundamental calculation by Bianco *et al.* [62] based on Equation (7.41), the theoretical results due to Krage and Haddad [49] (also Kowalski and Pregla [48]) and the theoretical calculations by Knorr and Tufekcioglu [69]. It

may be significant that the latter researchers employed the spectral-domain techniques which have been demonstrably successful in the accurate prediction of  $\epsilon_{\text{eff}}(f)$  (see [Section 7.6](#)). Mirshekar-Syahkal and Davies [70] also obtain similar results.

For these reasons the use of Equation (7.61) is, rather tentatively, recommended here. Further work is needed to test against the theoretical predictions and to develop validating measurements. Both recommendations are needed to cover a wide range of nominal characteristic impedance values and, preferably, a range of useful substrates. This testing and validating should be performed in the light of any recent theoretical work.

### 7.7.6 A Design Algorithm for Microstrip Width

It is very useful to have the facility for evaluating microstrip width with the aid of static-TEM expressions, such as those given in [Chapter 6](#). The concept, and a routine for achieving this when the frequency-dependent characteristic impedance is known, was first suggested by Getsinger [38]. A modified form of this design algorithm is presented here. The design specification includes  $\epsilon_r$ ,  $h$ ,  $f$ , and  $Z_0(f)$ , and we require the microstrip width  $w$ .

Proceed as follows:

- a. As an initial approximation let  $Z_0(f) \approx Z_0$ .
- b. Find the approximate microstrip width  $w$  using this value of  $Z_0(f)$ , with  $\epsilon_r$  and  $h$ .
- c. Determine the frequency-dependent denominator  $1 + G(f/f_p)^2$ , as described in [Section 7.3](#), using this approximate value of  $Z_0(f)$ . (It may eventually be found that the denominator function in Equation (7.35) gives improved results, but this requires further investigation.)
- d. Evaluate  $Z_{0T}$  for stripline having the same strip width  $w$  as the microstrip, but twice the dielectric thickness ( $2h$ ). Design curves, or good approximations, may be used.
- e. Rearrange Equation (7.61) for  $Z_0$ , letting

$$A = 1 + G(f/f_p)^2. \quad 7.66$$

The result of this is

$$Z_0 = A [Z_0(f) - Z_{0T}] + Z_{0T}. \quad 7.67$$

- f. With this approximate value of  $Z_0$ , calculate  $w/h$  using the static-TEM expressions as given in [Chapter 6](#) and hence calculate  $w$  (knowing  $h$ ).
- g. Repeat steps (b) to (f) until negligible difference is observed in the values of  $w$  obtained (e.g., it may be desired that the result should be accurate to within 1%).

Further information is available regarding the characteristic impedance as a function of frequency. Brews [71] provided a theoretical study of microstrip characteristic impedance. His paper is entirely theoretical but he points out that the “very natural” requirement for complex power  $P$  is given by

$$P = \frac{1}{2} \mathbf{I}^* \mathbf{V}$$

7.68

This leads to a preferred choice of impedance-defining expressions following Equations (7.52) to (7.54) given above, and it is based on these definitions that calculations and measurements of  $Z_0(f)$  should be made and used.

## 7.8 Multimoding and Limitations on Operating Frequency

As the signal frequency applied to a microwave circuit is steadily increased some characteristic frequency may be reached at which undesirable effects occur. Two possible spurious effects restrict the desirable operating frequencies. These are

- a. the lowest-order transverse microstrip resonance
- b. the lowest-order TM mode.

In practice, one of these modes will be experienced at some frequency lower than the other and will thus set the frequency limitation.

### 7.8.1 The Lowest-order Transverse Microstrip Resonance

For a sufficiently wide microstrip line a transverse-resonant mode can exist which can also couple strongly to the quasi-TEM microstrip mode. At the cut-off frequency for this transverse-resonant mode the equivalent circuit is a resonant transmission line of “length” ( $w + 2d$ ), where  $d$  accounts for the microstrip side-fringing capacitance:  $d = 0.2h$ . The situation is illustrated in [Figure 7.25](#). A half-wavelength must be supported by the “length” ( $w + 2d$ ), therefore the cut-off half-wavelength is

$$\frac{\lambda_{CT}}{2} = w + 2d = w + 0.4h \quad 7.69$$

or

$$\frac{c}{2f_{CT}\sqrt{\epsilon_r}} = w + 0.4h. \quad 7.70$$

Hence

$$f_{CT} = \frac{c}{\sqrt{\epsilon_r}(2w + 0.8h)}. \quad 7.71$$

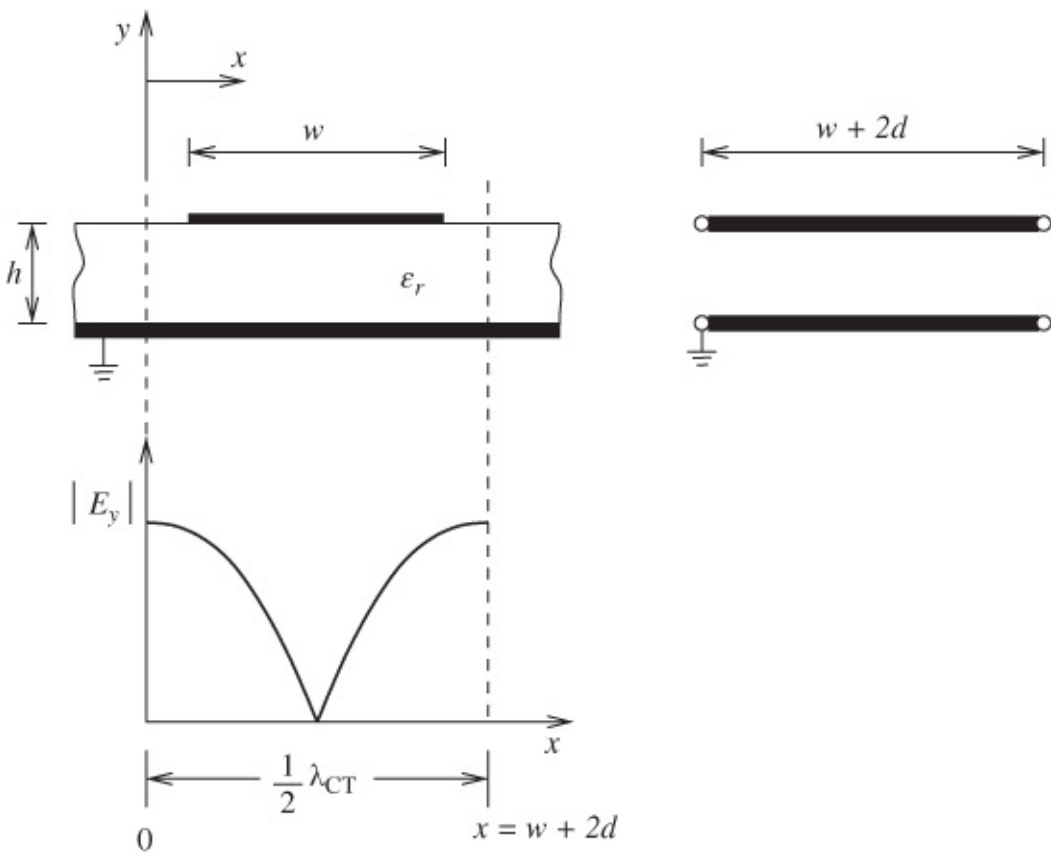


**Figure 7.25** Transverse resonance: standing wave ( $|E_y|$ ) and equivalent transmission line of “length” ( $w + 2d$ ).

Vendelin [72] indicated that slots, introduced into the metal strip, can suppress the transverse-resonant mode. However, this may not always be practicable (e.g., when short stubs are involved) and it should be checked, by calculating from Equation (7.67), whether the transverse resonance might be excited. Sometimes a change in the circuit configuration will enable the offending wide lines to be avoided altogether.

As an example, consider a  $50\text{-}\Omega$  microstrip line on an alumina substrate of permittivity 9.6 and thickness 0.65 mm. In this case  $w = 1\text{ mm}$  and  $f_{CT} = 39.02\text{ GHz}$ . We can safely operate at frequencies considerably above 10 GHz and with a “good”  $Q$  factor of several hundred.

### 7.8.2 The TM Mode Limitation

Vendelin [72] indicated that, aside from the transverse resonance effect, the most significant modal limitations in microstrip are associated with strong coupling between the quasi-TEM mode and the lowest-order TM mode. In the cited paper Vendelin gives the main relationships quoted here (although the original analysis is due to Collin [73]).

We start with the substrate viewed as a dielectric slab, having the coordinate notation shown in [Figure 7.26](#). This slab is a fair approximation for the situation with narrow microstrip lines.

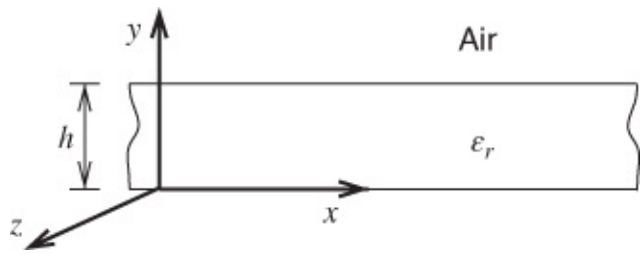


**Figure 7.26** An (isotropic) substrate viewed as a dielectric slab, showing the nomenclature.

Under these conditions, the eigenvalue expressions are

$$0.5ph = 0.5qh \tan(0.5qh) \quad 7.72$$

and

$$(0.5ph)^2 + (0.5qh)^2 = (\epsilon_r - 1)(0.5\beta_0 h)^2 \quad 7.73$$

where  $\beta_0$  is the free-space phase coefficient given in terms of the free-space wavelength  $\lambda_0$  by

$$\beta_0 = 2\pi/\lambda_0. \quad 7.74$$

Here  $p$  is the eigenvalue for the field in the air and  $q$  is the eigenvalue for the field in the substrate ( $\epsilon_r$ ). It is convenient to solve Equations (7.68) and (7.69) graphically for  $p$  and  $q$ , as shown in [Figure 7.27](#).

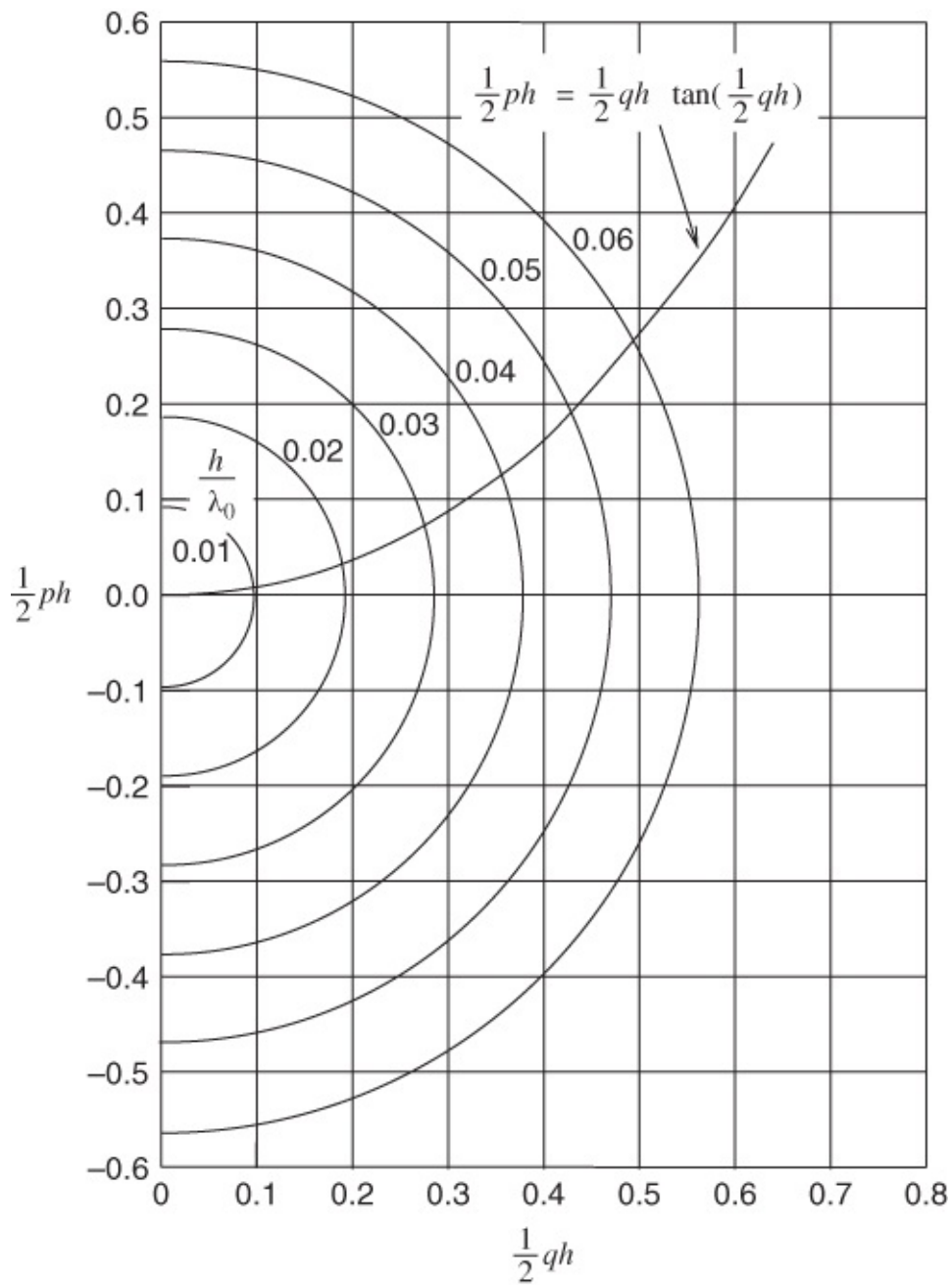


**Figure 7.27** Eigenvalue solutions for TM waves for various normalized substrate thickness,  $h/\lambda_0$ .

The following wave equation is then used to find the net phase coefficient for the TM wave:

$$\beta^2 = \beta_0^2 + p^2. \quad 7.75$$

A frequency for strong coupling between the quasi-TEM mode and the TM mode is identified when two associated phase velocities are close. The result is given by

$$f_{\text{TEM},1} = \frac{c \tan^{-1} (\epsilon_r)}{\sqrt{2\pi h} \sqrt{\epsilon_r - 1}}. \quad 7.76$$

This is an important relationship. Under the assumption that transverse resonances are

suppressed or avoided in some way, [Figure 7.28](#) shows the cut-off frequency limitation imposed by Equation (7.72) as a function of substrate thickness  $h$  for a variety of substrate materials.

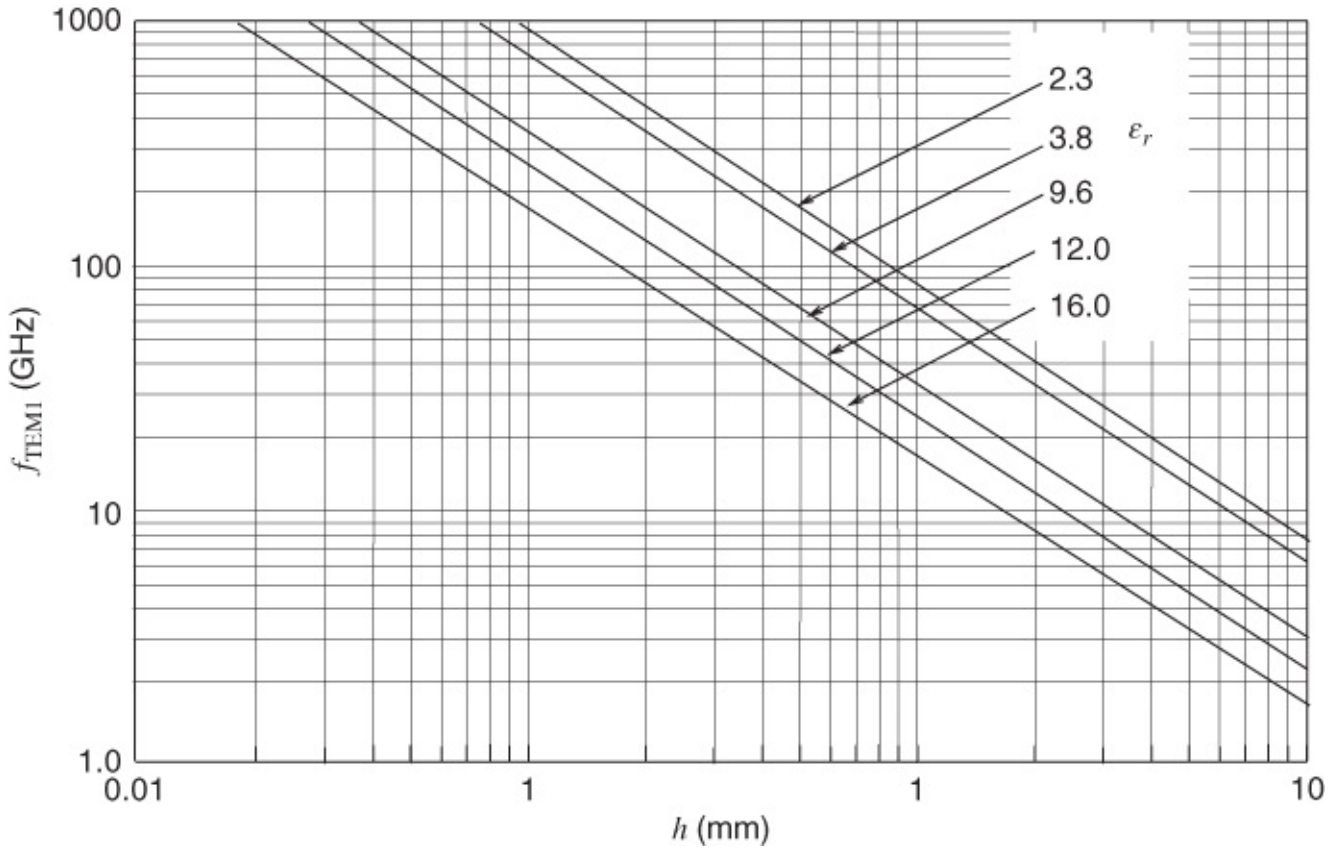


**Figure 7.28** TM threshold excitation frequency  $f_{\text{TEM},1}$  as a function of substrate thickness  $h$  and relative permittivity  $\epsilon_r$ .

Vendelin points out that the lowest-order TE wave has a cut-off frequency given by

$$f_e = c / \left( 4h\sqrt{\epsilon_r - 1} \right). \quad 7.77$$

This frequency merely happens to coincide with the  $f_{\text{TEM},1}$  result for wide microstrip lines, although the phenomena involved are different. In fact the frequency for the lowest-order TM wave to couple strongly to a wide microstrip line is given by

$$F'_{\text{TEM},1} = 75 / \left( H\sqrt{\epsilon_r - 1} \right) \quad 7.78$$

where  $F'_{\text{TEM},1}$  ( $= f'_{\text{TEM},1} / (1 \text{ GHz})$ ) is in gigahertz and  $H (= h / 1 \text{ mm})$  is in millimeters.

Returning to the more important case of narrow microstrip lines, where the permittivity  $\epsilon_r$  is high (say  $\epsilon_r > 10$ ), Equation (7.72) tends towards

$$f_{\text{TEM},1} = \frac{c}{2\sqrt{2}h\sqrt{\epsilon_r - 1}} \quad 7.79$$

or

$$F_{\text{TEM},1} = \frac{106}{H\sqrt{\epsilon_r - 1}} \quad 7.80$$

where  $F_{\text{TEM},1}$  ( $= f_{\text{TEM},1}' / (1 \text{ GHz})$ ) is in gigahertz and again  $H$  is in millimeters. The maximum restriction on usable substrate thicknesses is then easily obtained as

$$h = 0.354\lambda_0/\sqrt{\epsilon_r - 1}. \quad 7.81$$

Care should be exercised in the use of these expressions, Equation (7.71) being the more general and applicable to lower-permittivity substrates. It is recommended that substrates should be as thin as possible, Equation (7.77), and that operating frequencies be kept below  $f_{\text{TEM},1}$ , Equation (7.72).

## 7.9 Design Recommendations

In the light of the techniques presented in this chapter and also [Chapter 6](#), we can now summarize the main microstrip design recommendations.

Initially, system and network design procedures yield a specific value of characteristic impedance  $Z_0$  and of electrical length  $\theta$  for each microstrip line. We must determine the correct physical dimensions for the microstrip, that is,  $w$  and  $\ell$ . It is recommended that the following sequence be used.

### Recommendation 1

Select the substrate such that the TM mode effect is avoided, that is, the maximum intended operating frequency should be less than

$$f_{\text{TEM},1} = c \tan^{-1}(\epsilon_r) / \sqrt{2\pi h \sqrt{\epsilon_r - 1}}$$

as given by Equation (7.72).

Also ensure that parasitic coupling is sufficiently low, Equation (7.77).

### Recommendation 2

Carry out a “first-cut” design on the static-TEM basis explained in [Chapter 6](#). This yields  $w$  and  $\epsilon_{\text{eff}}$ .

### Recommendation 3

Check that the first-order transverse resonance cannot be excited at the highest frequencies using Equation (7.67):

$$f_{CT} = \frac{c}{\sqrt{\epsilon_r}(2w + 0.8h)}. \quad 7.82$$

In the event that such a resonance might occur, either redesign (using narrower microstrip lines) or, if possible, incorporate slots in the metal strips.

## **Recommendation 4**

Calculate the total losses and the total  $Q$  factor, and check that this meets the circuit requirements ([Section 8.3](#) gives the methods for this). If the  $Q$  factor is too low a major reappraisal of the design philosophy may be necessary or superconductivity might be used.

However, as a general indication, many satisfactory microstrip circuits may be designed with  $Q$  factors no greater than about 100.

## **Recommendation 5**

Evaluate the frequency-dependent effective microstrip permittivity  $\epsilon_{\text{eff}}(f)$  and hence the wavelength  $\lambda_g (= c/f\sqrt{\epsilon_{\text{eff}}(f)})$ .

For alumina-type substrates, where  $10 \leq Z_0 \leq 100 \Omega$  and  $2 \leq f \leq 18$  GHz, the recommended expression is the relatively simple Equation ([7.35](#)):

$$\epsilon_{\text{eff}}(f) = \epsilon_r - \frac{\epsilon_r - \epsilon_{\text{eff}}}{1 + (H/Z_0)^{1.33} (0.43F^2 - 0.009F^3)} \quad 7.83$$

where  $H$  is in millimeters and  $F$  is in gigahertz. The estimated accuracy is  $\pm 0.8\%$ . (Note that this includes errors in the static-TEM expressions for  $\epsilon_{\text{eff}}$  and  $Z_0$ , i.e., the  $\pm 0.8\%$  is overall.)

Where higher frequencies and/or substrates having permittivities differing substantially from 10 are involved, the more elaborate set of expressions due to Kirschning and Jansen or Kobayashi is recommended. These were provided earlier in this chapter and will not be repeated here (see [Section 7.4](#)). Since the electrical length  $\theta$  (degrees) is given in the circuit or antenna specification, the physical length  $\ell$  of the microstrip is

$$\ell = \theta \lambda_g / 360 \text{ (neglecting discontinuities).} \quad 7.84$$

## **Characteristic Impedance as a Function of Frequency**

This problem was discussed in [Section 7.7](#). The practical effects are fairly small, mainly amounting to a small degradation of VSWR in most cases. If initial calculations indicate that  $Z_0(f)$  is likely to be significant in a particular design problem the algorithm given in [Section 7.7.6](#) is recommended.

## **7.10 Summary**

This chapter considered the high-frequency properties of microstrip transmission lines. Nearly

all of the concepts that were introduced are applicable to other planar transmission lines. A dominant effect is due to the finite time, relative to the period of a signal, it takes to redistribute charges on the surface of and inside conductors. This results in frequency-dependent proximity and skin effects which increase resistive losses as frequency increases. For most microwave substrates other than semiconductors loss due to the conductivity of the substrate is negligible but this is not always the case for dielectric relaxation loss. This loss is due to the rotation of electric polarization resulting in transfer of electrical energy into crystal and molecular motion as the lattice is vibrated. At microwave frequencies this dielectric relaxation loss increases linearly with frequency as the rate of rotation of the electrical polarization is directly proportional to frequency. While these are serious effects, a more serious concern, sometimes, is the excitation of higher-order modes. These higher-order modes will occur with all planar transmission lines if the frequency is high enough. The modes will occur at lower frequencies than that predicted by the ideal perfectly symmetrical lines that are analyzed in electromagnetic analysis. Small irregularities can excite modes at lower frequencies than otherwise expected. It is usual to provide a design margin limiting the maximum signal frequency to 10–30% below the frequency at which higher-order modes are calculated to be possible. This measure allows for the additional mode-generation properties of discontinuities such as bends and junctions.

## References

- [1] P. Daly, “Hybrid-mode analysis of microstrip by finite-element methods,” *IEEE Trans. on Microwave Theory and Techniques*, vol. **19**, no. 1, pp. 19–25, Jan. 1971.
- [2] D. Gelder, “Numerical determination of microstrip properties using the transverse field components,” *Proc. Institution of Electrical Engineers*, vol. **117**, no. 4, pp. 699–703, Apr. 1970.
- [3] D. Corr and J. Davies, “Computer analysis of the fundamental and higher order modes in single and coupled microstrip,” *IEEE Trans. on Microwave Theory and Techniques*, vol. **20**, no. 10, pp. 669–678, Oct. 1972.
- [4] D. G. Corr, “*Finite difference analysis of hybrid modes in microstrip structures*,” Ph.D. dissertation, Univ. of London, Aug. 1970.
- [5] G. Grunberger, V. Keine, and H. Meinke, “Longitudinal field components and frequency-dependent phase velocity in the microstrip transmission line,” *Electronics Letters*, vol. **6**, no. 21, pp. 683–685, 1970.
- [6] G. K. Grunberger and H. H. Meinke, “A theory of the microstrip line including longitudinal components,” in *2nd European Microwave Conf.*, Aug. 1971, pp. 1–4.
- [7] A. Laloux and A. V. Vorst, “The dispersive character of microstrip lines,” in *2nd European Microwave Conf.*, Aug. 1971, pp. 1–3.

- [8] A. R. Van de Capelle and P. J. Luypaert, “An investigation of the higher order modes in open microstrip lines,” in *Proc. 5th Colloquium on Microwave Communication*, 1974, pp. 31–32.
- [9] J. H. Schmitt and K. H. Sarges, “Wave propagation in microstrip,” *Nachrichtentech Z.*, vol. **25**, pp. 260–264, May 1972.
- [10] J. Hornsby and A. Gopinath, “Numerical solutions of inhomogeneously filled guides with symmetrical microstrip line,” in *1st European Microwave Conf.*, Sep. 1969, pp. 114–117.
- [11] J. Hornsby, “Fourier analysis of a dielectric-loaded waveguide with a microstrip line,” *Electronics Letters*, vol. **5**, no. 12, pp. 265–267, Dec. 1969.
- [12] J. Hornsby and A. Gopinath, “Numerical analysis of a dielectric-loaded waveguide with a microstrip line-finite-difference methods,” *IEEE Trans. on Microwave Theory and Techniques*, vol. **17**, no. 9, pp. 684–690, Sep. 1969.
- [13] E. Denlinger, “A frequency dependent solution for microstrip transmission lines,” *IEEE Trans. on Microwave Theory and Techniques*, vol. **19**, no. 1, pp. 30–39, Jan. 1971.
- [14] B. Curran, I. Ndip, S. Guttowski, and H. Reichl, “On the quantification of the state-of-the-art models for skin-effect in conductors, including those with non-rectangular cross-sections,” in *2009 IEEE Int. Symp. on Electromagnetic Compatibility, EMC 2009*, 2009, pp. 141–146.
- [15] T. V. Dinh, B. Cabon, and J. Chilo, “New skin-effect equivalent circuit,” *Electronics Letters*, vol. **26**, no. 19, pp. 1582–1584, 1990.
- [16] T. V. Dinh, B. Cabon, and J. Chilo, “Time domain analysis of skin effect on lossy interconnections,” *Electronics Letters*, vol. **26**, no. 25, pp. 2057–2058, 1990.
- [17] R. Faraji-Dana and Y. Chow, “The current distribution and ac resistance of a microstrip structure,” *IEEE Trans. on Microwave Theory and Techniques*, vol. **38**, no. 9, pp. 1268–1277, Sep. 1990.
- [18] H. Wheeler, “Formulas for the skin effect,” *Proc. IRE*, vol. **30**, no. 9, pp. 412–424, Sep. 1942.
- [19] T. Leung and C. A. Balanis, “Attenuation distortion of transient signals in microstrip,” *IEEE Trans. on Microwave Theory and Techniques*, vol. **36**, pp. 765–769, 1988.
- [20] R. Pucel, D. Masse, and C. Hartwig, “Losses in microstrip,” *IEEE Trans. on Microwave Theory and Techniques*, vol. **16**, no. 6, pp. 342–350, Jun. 1968.
- [21] R. Pucel, D. Masse, and C. Hartwig “Correction to losses in microstrip”, *IEEE Trans. on Microwave Theory and Techniques*, vol. **16**, no. 12, p. 1064, Dec. 1968.
- [22] S. H. Hall, G. W. Hall, and J. A. McCall, *High-Speed Digital System Design: a Handbook of Interconnect Theory and Design Practices*. Wiley-IEEE Press, 2000.

- [23] M. V. Schneider, “Microstrip lines for microwave integrated circuits,” *The Bell System Technical Journal*, pp. 1421–1444, May–Jun. 1969.
- [24] J. D. Welch and H. J. Pratt, “Losses in microstrip transmission systems for integrated microwave circuits,” in *IEEE Northeast Electronics and Engineering Meeting Record (NEREM Record)*, vol. **8**, 1966, pp. 100–101.
- [25] R. Horton, B. Easter, and A. Gopinath, “Variation of microstrip losses with thickness of strip,” *Electronics Letters*, vol. **7**, no. 17, pp. 490–491, 1971.
- [26] E. Hammerstad and F. Bekkadal, “A microstrip handbook, ELAB report STFF A74169,” University of Trondheim, Norway, Tech. Rep., Feb. 1975.
- [27] S. Hall, S. G. Pytel, P. G. Huray, D. Hua, A. Moonshiram, G. A. Brist, and E. Sijercic, “Multigigahertz causal transmission line modeling methodology using a 3-d hemispherical surface roughness approach,” *IEEE Trans. Microwave Theory and Techniques*, vol. **55**, no. 12, pp. 2614–2624, Dec. 2007.
- [28] M. V. Lukic and D. S. Filipovic, “Modeling of 3-d surface roughness effects with application to  $\mu$ -coaxial lines,” *IEEE Trans. Microwave Theory and Techniques*, vol. **55**, no. 3, pp. 518–525, Mar. 2007.
- [29] X. Chen, “EM modeling of microstrip conductor losses including surface roughness effect,” *IEEE Microwave and Wireless Components Letters*, vol. **17**, no. 2, pp. 94–96, Feb. 2007.
- [30] S. Mei and Y. I. Ismail, “Modeling skin and proximity effects with reduced realizable RL circuits,” *IEEE Trans. Very Large Scale Integration (VLSI) Systems*, vol. **12**, no. 4, pp. 437–447, Apr. 2004.
- [31] T. Liang, S. Hall, H. Heck, and G. Brist, “A practical method for modeling PCB transmission lines with conductor surface roughness and wideband dielectric properties,” in *2006 IEEE MTT-S Int. Microwave Symp. Digest*, 2006, pp. 1780–1783.
- [32] W. Chudobiak, O. Jain, and V. Makios, “Dispersion in microstrip,” *IEEE Trans. on Microwave Theory and Techniques*, vol. **19**, no. 9, pp. 783–784, Sep. 1971.
- [33] O. Jain, V. Makios, and W. Chudobiak, “The dispersive behaviour of microstrip transmission lines,” in *2nd European Microwave Conf.*, Aug. 1971, pp. 14.
- [34] O. Jain, V. Makios, and W. Chudobiak, “Coupled-mode model of dispersion in microstrip,” *Electronics Letters*, vol. **7**, no. 14, pp. 405–407, 1971.
- [35] M. Schneider, “Microstrip dispersion,” *Proc. IEEE*, vol. **60**, no. 1, pp. 144–146, Jan. 1972.
- [36] H. Carlin, “A simplified circuit model for microstrip,” *IEEE Trans. on Microwave Theory and Techniques*, vol. **21**, no. 9, pp. 589–591, Sep. 1973.

- [37] W. Getsinger, “Microstrip dispersion model,” *IEEE Trans. on Microwave Theory and Techniques*, vol. **21**, no. 1, pp. 34–39, Jan. 1973.
- [38] W. J. Getsinger, “Microstrip dispersion model,” COMSAT Laboratories, Tech. Rep., Mar. 1972, Technical Memorandum CL-9-72.
- [39] T. Edwards and R. Owens, “2–18 GHz dispersion measurements on 10a 100- $\omega$  microstrip lines on sapphire,” *IEEE Trans. on Microwave Theory and Techniques*, vol. **24**, no. 8, pp. 506–513, Aug. 1976.
- [40] R. York and R. Compton, “Experimental evaluation of existing CAD models for microstrip dispersion,” *IEEE Trans. on Microwave Theory and Techniques*, vol. **38**, no. 3, pp. 327–328, Mar. 1990.
- [41] E. Yamashita, K. Atsuki, and T. Ueda, “An approximate dispersion formula of microstrip lines for computer-aided design of microwave integrated circuits,” *IEEE Trans. on Microwave Theory and Techniques*, vol. **27**, no. 12, pp. 1036–1038, Dec. 1979.
- [42] M. Kirschning and R. Jansen, “Accurate model for effective dielectric constant of microstrip with validity up to millimeter-wave frequencies,” *Electronics Letters*, vol. **18**, no. 6, pp. 272–273, 1982.
- [43] M. Kobayashi, “A dispersion formula satisfying recent requirements in microstrip CAD,” *IEEE Trans. on Microwave Theory and Techniques*, vol. **36**, no. 8, pp. 1246–1250, Aug. 1988.
- [44] E. P. Kurushin, V. A. Neganov, and E. I. Nefgdov, “Dispersion in microstripline on a ferrite substrate,” *Radio Physics and Quantum Electronics*, pp. 251–254, Mar. 1982.
- [45] I. Hsia, H.-Y. Yang, and N. Alexopoulos, “Basic properties of microstrip circuit elements on nonreciprocal substrate-superstrate structures,” in *1990 IEEE MTT-S Int. Microwave Symp. Digest*, May 1990, pp. 665–668.
- [46] M. Kobayashi, “Frequency dependent characteristics of microstrips on anisotropic substrates,” *IEEE Trans. on Microwave Theory and Techniques*, vol. **30**, no. 11, pp. 2054–2057, Nov. 1982.
- [47] G. Mariki and C. Yeh, “Dynamic three-dimensional TLM analysis of microstriplines on anisotropic substrate,” *IEEE Trans. on Microwave Theory and Techniques*, vol. **33**, no. 9, pp. 789–799, Sep. 1985.
- [48] G. Kowalski and R. Pregla, “Dispersion characteristics of single and coupled microstrips,” *Arch. Elek. Übertragung.*, vol. **26**, pp. 276–280, 1972.
- [49] M. Krage and G. Haddad, “Frequency-dependent characteristics of microstrip transmission lines,” *IEEE Trans. on Microwave Theory and Techniques*, vol. **20**, no. 10, pp. 678–688, Oct. 1972.

- [50] T. Itoh and R. Mittra, “Spectral-domain approach for calculating the dispersion characteristics of microstrip lines,” *IEEE Trans. on Microwave Theory and Techniques*, vol. **21**, no. 7, pp. 496–499, Jul. 1973.
- [51] T. Itoh and R. Mittra, “A technique for computing dispersion characteristics of shielded microstrip lines,” *IEEE Trans. on Microwave Theory and Techniques*, vol. **22**, no. 10, pp. 896–898, Oct. 1974.
- [52] R. Jansen, “High-speed computation of single and coupled microstrip parameters including dispersion, high-order modes, loss and finite strip thickness,” *IEEE Trans. on Microwave Theory and Techniques*, vol. **26**, no. 2, pp. 75–82, Feb. 1978.
- [53] B. Biswas, A. Glasser, S. Lipa, M. Steer, P. Franzon, D. Griffis, and P. Russell, “Experimental electrical characterization of on-chip interconnects,” in *IEEE 6th Topical Meeting on Electrical Performance of Electronic Packaging*, 1997, pp. 57–59.
- [54] S. Lipa, M. Steer, A. Morris, and P. Franzon, “Comparison of methods for determining the capacitance of planar transmission lines with application to multichip module characterization,” *IEEE Trans. on Components, Hybrids, and Manufacturing Technology*, vol. **16**, no. 3, pp. 247–252, Mar. 1993.
- [55] S. Goldberg, M. Steer, P. Franzon, and J. Kasten, “Experimental electrical characterization of high speed interconnects,” in *Proc. 41st Electronic Components and Technology Conf.*, 1991, pp. 85–88.
- [56] M. Steer, S. Lipa, P. Franzon, and A. Cangellaris, “Experimental characterization of interconnects and discontinuities in thin-film multichip module substrates,” *Topical Meeting on Electrical Performance of Electronic Packaging*, pp. 145–147, 1993.
- [57] C. Riedell, M. Kay, R. Pomerleau, M. Steer, J. Kasten, and M. Basel, “Dielectric characterization of printed circuit substrates,” in *Proc. IEEE Southeastcon'89*, 1989, pp. 102–106.
- [58] A. Glaser, M. Steer, G. Shedd, P. Russell, and P. Franzon, “A method for on-chip interconnect characterization,” in *1995 Electrical Performance of Electronic Packaging*, 1995, pp. 108–110.
- [59] M. Kay, R. Pomerleau, and M. Steer, “Empirical statistical analysis of planar transmission lines on pcbs accounting for manufacturing variations,” in *IEEE Southeastcon'89 Proc.*, 1989, pp. 112–116.
- [60] K. D. Dumbell, S. R. Pennock, and T. E. Rozzi, “Effects of asymmetry in shielded microstrip transmission lines,” in *19th European Microwave Conf.*, Sep. 1989, pp. 761–766.
- [61] Y. Qian and E. Yamashita, “Compression and reshaping of picosecond electrical pulses using dispersive microwave transmission lines,” in *1990 IEEE MTT-S Int. Microwave Symp. Digest*, May 1990, pp. 951–954.

- [62] B. Bianco, L. Panini, M. Parodi, and S. Ridella, “Some considerations about the frequency dependence of the characteristic impedance of uniform microstrips,” *IEEE Trans. on Microwave Theory and Techniques*, vol. **26**, no. 3, pp. 182–185, Mar. 1978.
- [63] W. Getsinger, “Microstrip characteristic impedance,” *IEEE Trans. on Microwave Theory and Techniques*, vol. **27**, no. 4, p. 293, Apr. 1979.
- [64] R. Owens, “Predicted frequency dependence of microstrip characteristic impedance using the planar-waveguide model,” *Electronics Letters*, vol. **12**, no. 11, pp. 269–270, 1976.
- [65] R. P. Owens, “The electrical characteristics of transferred-electron device package and mounts and their effects on oscillator performance,” Ph.D. dissertation, University of London, 1977.
- [66] G. Kompa and R. Mehran, “Planar waveguide model for calculating microstrip components,” *Electronics Letters*, vol. **11**, no. 19, pp. 459–460, 1975.
- [67] B. Bianco, M. Granara, A. Chiabrera, and S. Ridella, “Frequency dependence of microstrip parameters,” *Alta Frequenza*, vol. **43**, pp. 413–416, 1974.
- [68] H. Howe, *Stripline Circuit Design*. Artech House, 1974.
- [69] J. Knorr and A. Tufekcioglu, “Spectral-domain calculation of microstrip characteristic impedance,” *IEEE Trans. on Microwave Theory and Techniques*, vol. **23**, no. 9, pp. 725–728, Sep. 1975.
- [70] D. Mirshekar-Syahkal and J. Davies, “Accurate solution of microstrip and coplanar structures for dispersion and for dielectric and conductor losses,” *IEEE Trans. on Microwave Theory and Techniques*, vol. **27**, no. 7, pp. 694–699, Jul. 1979.
- [71] J. Brews, “Characteristic impedance of microstrip lines,” *IEEE Trans. on Microwave Theory and Techniques*, vol. **35**, no. 1, pp. 30–34, Jan. 1987.
- [72] G. Vendelin, “Limitations on stripline Q,” *Microwave Journal*, pp. 63–69, 1970.
- [73] R. E. Collin, *Foundations for Microwave Engineering*. John Wiley & Sons, 2007.

<sup>1</sup> We shall use  $\epsilon_{\text{eff}}$  to indicate the static-TEM value of the effective permittivity and  $\epsilon_{\text{eff}}(f)$  for the frequency-dependent values (thus  $\epsilon_{\text{eff}} = \epsilon_{\text{eff}}(0)$ ).

<sup>2</sup> Note that the hybrid field configuration can be conveniently decomposed into at least two combinations of compound modes, the LSE and LSM mode pair, and the TEM and  $\text{TM}_0$  mode pair, for example. At higher frequencies larger combinations of modes in each set must be considered.

# Chapter 8

## Loss and Power-dependent Effects in Microstrip

### 8.1 Introduction

This chapter describes the sources of loss with microstrip lines. The chapter begins by defining the quality factor, the  $Q$ , used to characterize energy storage relative to loss. This important metric enables different components to be compared and in particular different sources of loss and the performance of different transmission line systems. Loss affects power handling capability and also results in a form of distortion called passive intermodulation distortion (PIM). PIM is not fully understood but at least an important component is due to losses resulting in the line resistance changing as the level of the signal changes. With a signal having a finite bandwidth, PIM results in additional frequency components being generated.

### 8.2 $Q$ Factor as a Measure of Loss

#### 8.2.1 Definition

The  $Q$ , or quality, factor of a component or circuit is defined as the ratio of  $2\pi$  times the maximum energy stored to the energy lost per cycle. For a parallel resonant circuit with elements  $L$ ,  $C$ , and  $G$  (see [Figure 8.1\(a\)](#)) the  $Q$  is

$$Q = \omega_r C/G = 1/(\omega_r L G) \quad 8.1$$

where  $f_r = \omega_r/(2\pi)$  is the resonant frequency, which is the frequency at which the maximum amount of energy is stored. The conductance  $G$  describes the energy lost in a cycle. A series resonant circuit with  $L$ ,  $C$ , and  $R$  elements (see [Figure 8.1\(b\)](#)) has a similar expression for  $Q$ :

$$Q = \omega_r L/R = 1/(\omega_r C R). \quad 8.2$$

These resonant circuits have a bandpass transfer characteristic and the  $Q$  is a measure of how sharp the resonance is. The  $Q$  is then the inverse of the fractional bandwidth of the resonator. The bandwidth  $\Delta f$  is measured at the half power points, as shown in [Figure 8.2](#). ( $\Delta f$  is also referred to as the two-sided  $-3$  dB bandwidth.) Then

$$Q = \frac{f_r}{\Delta f}. \quad 8.3$$

Thus the  $Q$  is a measure of the sharpness of the bandpass filter frequency response.

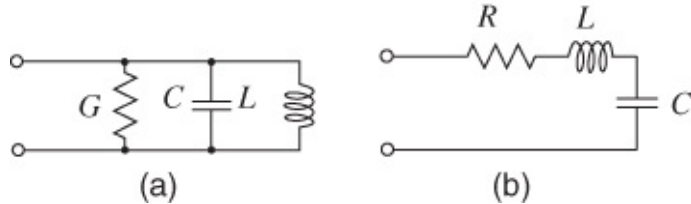


**Figure 8.1** Parallel (a) and series (b) resonant circuits.

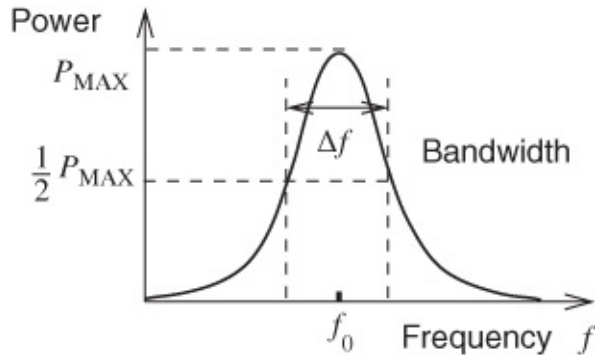


**Figure 8.2** Transfer characteristic of resonant circuit.

This relationship between the  $Q$  and the fractional bandwidth,  $\Delta f/f_r$ , is only fixed for a second-order system such as the series and parallel  $RLC$  circuits. A more general definition of  $Q$  relates to stored and dissipated energy, and this definition will be discussed soon. Nevertheless the inverse of  $\Delta f/f_r$  is a reasonable indication of the  $Q$  of a circuit if no other measure is available.

The determination of  $Q$  using the measurement of bandwidth together with Equation (8.3) is not very sensitive, so another definition that uses the much more sensitive phase change at resonance is preferred. This can usually be determined more easily from measurements which always have some uncertainty. With  $\phi$  being the phase (in radians) of the transfer characteristic, the definition of  $Q$  is now

$$Q = \frac{\omega_r}{2} \left| \frac{d\phi}{d\omega} \right|. \quad 8.4$$

This is another equivalent definition of  $Q$  for parallel  $RLC$  or series  $RLC$  resonant circuits.

$Q$  is used for more complicated circuits and then its meaning is always a ratio of the energy stored to the energy dissipated. Thus, it is meaningful to talk about the  $Q$  of circuits other than three-element  $RLC$  circuits, for example interconnects. The  $Q$  of these structures can no longer be determined by bandwidth or by rate of phase change considerations.

### 8.2.2 Loaded $Q$ Factor

The  $Q$  of a component as defined in the previous section is called the unloaded  $Q$ ,  $Q_u$ . However, if a component is to be measured or used in any way it is necessary to couple energy into and out of it. This leads to the use of the loaded  $Q$ ,  $Q_l$ . So a parallel  $LCG$  circuit with elements  $L_r$ ,  $C_r$ , and  $G_r$  (at resonance) loaded by a shunt conductance  $G_l$  has

$$Q_u = \omega_r C_r / G_r = 1 / (\omega_r L_r G_r)$$

8.5

and

$$Q_l = \omega_r C_r / (G_r + G_l).$$

8.6

So

$$\frac{1}{Q_l} = \frac{1}{Q_u} + \frac{1}{Q_x} \quad 8.7$$

or

$$Q_x = \left( \frac{1}{Q_l} - \frac{1}{Q_u} \right). \quad 8.8$$

$Q_x$  is called the external  $Q$  and it describes the effect of loading.  $Q_l$  is the  $Q$  that is actually measured.  $Q_u$  normally needs to be determined, but if the loading is kept very small  $Q_l \approx Q_u$ .

An example of a  $Q$  measurement setup is the gap-coupled quarter-wave section shown in [Figure 8.3](#). Here the gap (think of it as a capacitance) is the mechanism that couples energy from the left to the  $\lambda/4$  resonator.

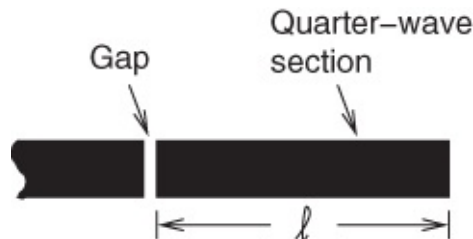


[Figure 8.3](#) Gap coupled quarter-wave section.

### 8.2.3 External $Q$ Factor of an Open-circuited Microstrip Resonator

In this section we consider a section of line which is terminated at both ends, see [Figure 8.4](#). We explore and characterize the conditions under which this line is resonant. Referring to the gap-coupled line in [Figure 8.3](#), the gap can be modeled as a capacitor and the quarter-wavelength-long section approximates a microstrip resonator that is open-circuited at both ends.

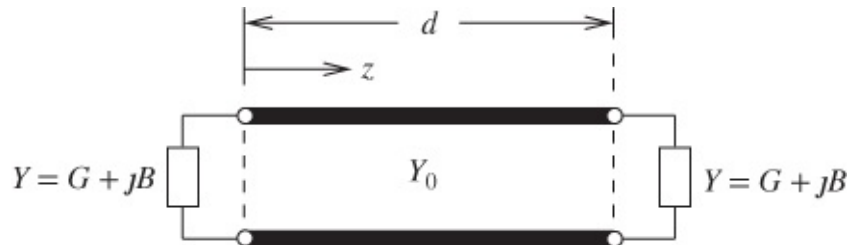


[Figure 8.4](#) Open-circuited microstrip resonator.

## Characterization of a Terminated Resonator

The reflection coefficients of the line terminations are equal and given by

$$\Gamma = \frac{Y_0 - Y}{Y_0 + Y} = \frac{(Y_0 - G) - jB}{(Y_0 + G) + jB}. \quad 8.9$$

Rationalizing we obtain

$$\Gamma = \frac{(Y_0 - G)(Y_0 + G) - B^2 - j2BY_0}{(Y_0 + G)^2 + B^2} \quad 8.10$$

or

$$\Gamma = |\Gamma| \exp(-j\theta) = \rho \exp(-j\theta) \quad 8.11$$

where  $\rho$  and  $\theta$  are the magnitude and phase angle of the reflection coefficient, respectively, given by

$$\rho = \frac{[(Y_0^2 - G^2 - B^2)^2 + 4B^2 Y_0^2]^{1/2}}{(Y_0 + G)^2 + B^2} \quad 8.12$$

and

$$\theta = \tan^{-1} \left( \frac{2BY_0}{Y_0^2 - G^2 - B^2} \right). \quad 8.13$$

These expressions will be required shortly, but first we must find the conditions for the maximum voltage on the line or equivalently the maximum electric field,  $E_{\max}$ , since this corresponds to the resonance condition. We now proceed to obtain the conditions for  $E_{\max}$  in terms of the reflection coefficient  $\Gamma$ , the phase coefficient  $\beta$ , and the resonator length. It is initially necessary to consider the multiple reflections occurring on the line (see [Figure 8.5](#)). The field amplitude  $E_0$  is merely a reference field, so that the other relative field strengths may be developed. The phase coefficient  $\beta = \omega_0 \sqrt{\epsilon_{\text{eff}}(f)} / c$ . From the fields shown on the diagram ([Figure 8.5](#)), we may add all the components at distance  $z$  to obtain the total field at that location:

$$E_x(z) = E_0 \exp(-j\beta z) + \Gamma E_0 \exp\{-j\beta(2d - z)\} + \dots + \Gamma^2 E_0 \exp\{-j\beta(2d + z)\} + \dots \quad 8.14$$

or

$$E_x = E_0 \exp(-j\beta z) \sum_{n=0}^{\infty} \Gamma^{2n} \exp(-j2\beta nd) + \dots + \Gamma E_0 \exp\{-j\beta(2d - z)\} \times \sum_{n=0}^{\infty} \Gamma^{2n} \exp(-j2\beta nd). \quad 8.15$$

Hence

$$E_x = \frac{E_0 \{ \exp(-j\beta z) + \Gamma \exp[-j\beta(2d-z)] \}}{1 - \Gamma^2 \exp(-j2\beta d)}. \quad 8.16$$

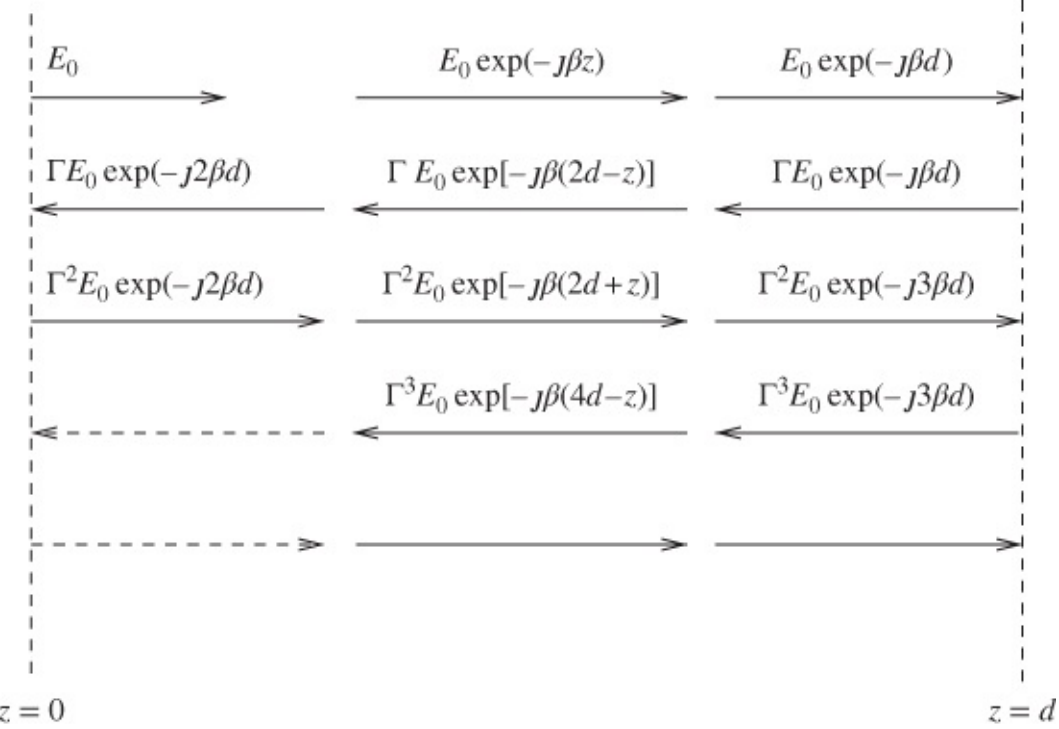


**Figure 8.5** Reflection diagram.

The resonance of the microstrip resonator, which corresponds to a maximum of this electric field  $E_x$ , occurs when the denominator ( $D$ , say) of Equation (8.16) is a minimum. Thus we require a minimum for

$$|D| = |1 - \Gamma^2 \exp[-j2(\beta d)]| \quad 8.17$$

or, inserting the polar form of  $\Gamma$  given earlier,

$$|D| = |1 - \rho^2 \exp \{ -j2(\beta_d + \theta) \}| \quad 8.18$$

and this is a minimum when

$$2(\beta d + \theta) = 2\pi l \quad 8.19$$

where  $l = 1, 2, 3, \dots$ , that is, an integer. In the “ideal” case where  $Y$  is either a true open circuit ( $G = 0, B = 0$ ) or a perfect short circuit ( $G = \infty, B = 0$ , or  $B \neq 0$ ), we obtain  $\theta = 0$  and the almost trivial solution to Equation (8.19), that is  $\beta d = \pi l$ , hence  $d = l\lambda_g/2$ . In our more practical case with finite  $Y$ , the full resonance condition of Equation (8.19) is required.

From Equations (8.17) and (8.18), the minimum value of  $|D|$  is clearly

$$|D|_{\min} = 1 - \rho^2. \quad 8.20$$

Now, as  $D$  increases,  $E_x$  will exhibit the usual resonant response curve as shown in [Figure 8.2](#).

Approximately the  $Q$  factor is then given by

$$Q_e = \omega_r / (2\Delta\omega) \quad 8.21$$

where  $E_{\max}$ , at  $\omega_r$ , is reduced to  $E_{\max}/\sqrt{2}$  at  $(\omega \pm \Delta\omega)$ . Equation (8.21) can also be written in terms of the phase coefficient

$$Q_e = \beta / (2\Delta\beta) \quad 8.22$$

where  $\beta$  is the phase coefficient at frequency  $\omega_r$ . We therefore now require an expression for  $\Delta\beta$  in order to finally obtain a formula for  $Q_e$  as a function of  $\rho$ . The field  $E_{\max}/\sqrt{2}$  occurs when  $|D|$  is increased to the value  $\sqrt{2}(1 - \rho^2)$  and the corresponding  $(\beta \pm \Delta\beta)$  and  $(\theta \pm \Delta\theta)$ , respectively. Therefore, we can write

$$\Delta(\beta d + \theta) = \Delta\beta d + \Delta\theta = \Delta\beta \left( d + \frac{\Delta\theta}{\Delta\beta} \right). \quad 8.23$$

To find the required quantity  $\Delta\beta$ , we replace  $(\beta + \theta)$  by

$$(\beta d + \theta) + \Delta(\beta d + \theta) \quad 8.24$$

in the expression for  $|D|^2$  and equate the result to

$$[\sqrt{2}(1 - \rho^2)]^2 = 2(1 - \rho^2)^2. \quad 8.25$$

First, expand the expression in  $\beta$ ,  $d$ , and  $\theta$  using Equations (8.19) and (8.23):

$$(\beta d + \theta) + \Delta(\beta d + \theta) = \pi l + \Delta\beta(d + \Delta\theta/\Delta\beta). \quad 8.26$$

Hence,

$$\begin{aligned} |D| &= |1 - \rho^2 \exp \{ -2J\pi l + \Delta\beta(d + \Delta\theta/\Delta\beta) \}| \\ &= |1 - \rho^2 \exp \{ -J2\Delta\beta(d + \Delta\theta/\Delta\beta) \}| \\ &= |1 - \rho^2 \cos 2\Delta\beta(d + \Delta\theta/\Delta\beta) + \rho^2 J \sin 2\Delta\beta(d + \Delta\theta/\Delta\beta)|. \end{aligned} \quad 8.27$$

We may also expand  $|D|^2$  as a complex product:  $|D|^2 = DD^*$  or

$$\begin{aligned} |D|^2 &= [1 - \rho^2 \cos 2\Delta\beta(d + \Delta\theta/\Delta\beta)]^2 + \rho^4 J \sin^2 2\Delta\beta(d + \Delta\theta/\Delta\beta) \\ &= (1 - \rho^2)^2 + 2\rho^2[1 - \cos 2\Delta\beta(d + \Delta\theta/\Delta\beta)]. \end{aligned} \quad 8.28$$

This is now equated to  $2(1 - \rho^2)^2$  to give

$$(1 - \rho^2)^2 = 2\rho^2 \{ 1 - \cos 2\Delta\beta(d + \Delta\theta/\Delta\beta) \}. \quad 8.29$$

Since, for moderate or high  $Q$ -factor resonators,  $\Delta\beta$  must be small and we may use the small-

angle ( $\delta y$ ) approximation:

$$1 - \cos \delta y \approx \frac{1}{2}(\delta y)^2$$

giving

$$(1 - \rho^2)^2 = 4\rho^2 \Delta\beta^2 (d + \Delta\theta/\Delta\beta)^2 \quad 8.30$$

whence

$$\Delta\beta = \frac{1 - \rho^2}{2\rho(d + \Delta\theta/\Delta\beta)}. \quad 8.31$$

Substituting this into Equation (8.22) gives

$$Q_e = \frac{\beta\rho(d + \Delta\theta/\Delta\beta)}{1 - \rho^2}. \quad 8.32$$

The quantity  $\Delta\theta/\Delta\beta$  is still required, and we obtain this by differentiating Equation (8.13):

$$\frac{\Delta\theta}{\Delta\beta} = \frac{\Delta}{\Delta\beta} \left\{ \tan^{-1} \left[ \frac{2BY_0}{(Y_0^2 - G^2 - B^2)} \right] \right\}. \quad 8.33$$

The result of this can be written down if we first note that

$$\frac{d}{dx} \left( \tan^{-1} \frac{x}{a} \right) = \frac{a}{x^2 + a^2} \frac{d}{dx} \left( \frac{x}{a} \right). \quad 8.34$$

Then

$$\frac{\Delta\theta}{\Delta\beta} = \frac{Y_0^2 - G^2 - B^2}{(Y_0^2 - G^2 - B^2)^2 + 4B^2 Y_0^2} \frac{1}{\Delta\beta} \left[ \Delta \left( \frac{2BY_0}{Y_0^2 - G^2 - B^2} \right) \right]. \quad 8.35$$

In order to evaluate this we really need to know the functional dependence of  $B$  and  $G$  on  $\beta$ .

## Open-circuit Terminations

Now we specifically treat the resonator as being terminated in open circuits. We make use of the additional information that the conductance of the open circuit will be less than its susceptance (i.e.,  $G \ll B$ ) and the susceptance of the open will be less than the characteristic admittance of the line (i.e.,  $B \ll Y_0$ ). This also implies that the reflection coefficient of the open will be very close to +1 so that  $\theta$  will be small. Consequently we can write

$$\begin{aligned}
\Gamma &= \frac{1 - Y/Y_0}{1 + Y/Y_0} \approx \frac{1 - jB/Y_0}{1 + jB/Y_0} \\
&\approx (1 - jB/Y_0)[1 - (jB/Y_0) + (jB/Y_0)^2 - \dots] \\
&\approx 1 - 2jB/Y_0.
\end{aligned} \tag{8.36}$$

In magnitude angle form

$$\begin{aligned}
\Gamma &= \rho \exp(-j\theta) = \rho(\cos \theta - j \sin \theta) \\
&\approx 1 - j\theta.
\end{aligned} \tag{8.37}$$

Equating Equations (8.36) and (8.37) results in

$$\theta = 2B/Y_0. \tag{8.38}$$

Since the open is essentially capacitive due to capacitive fringing at the end of the line with most of the electrical energy confined to the dielectric,  $B \propto \omega \sqrt{\epsilon_{\text{eff}}}$ . For the transmission line we already know that  $\beta \propto \omega \sqrt{\epsilon_{\text{eff}}} / c$ . Taking these two proportionalities together means that  $B \propto \beta$ . Now using the result in Equation (8.38) that means that  $\theta \propto \beta$ , that is, they are linearly dependent. So we have the important result

$$\beta \frac{\Delta \theta}{\Delta \beta} = \beta \frac{\theta}{\beta} = \theta. \tag{8.39}$$

Taking the result in Equation (8.39) and substituting, first in Equation (8.35) and finally in Equation (8.32), we obtain

$$Q_e = \frac{\rho(\beta d + \theta)}{1 - \rho^2}. \tag{8.40}$$

Also at resonance ( $\beta d + \theta$ ) will be integer multiples of  $\pi$  radians (i.e.,  $(\beta d + \theta) = l\pi$ ). Thus

$$Q_e = \frac{\pi l \rho}{1 - \rho^2}. \tag{8.41}$$

This is the classic result for the external  $Q$  factor when a resonator is terminated in (non-ideal) open circuits at both ends, and it is easily evaluated. Note that the derivation is based on the approximation that  $Q$  is equal to the inverse of the fractional bandwidth. The other approximations are that the radiation loss from the open is small, that is,  $G \ll B$ , and admittance of the open is mostly that of a fringing capacitor whose susceptance is much less than the characteristic admittance of the line, that is,  $B \ll Y_0$ .

## Determination of Loading from $Q$

If  $Q_e$  can be measured then the non-ideal terminations (the opens) can be characterized. The calculation of  $B$  and  $G$  follows from  $\rho$  and  $\theta$  as expressed by Equations (8.12) and (8.13).  $G$  is quite easily determined by combining Equations (8.12) and (8.13):

$$\rho = \frac{2BY_0\sqrt{1 + \cot^2\theta}}{(Y_0 + G)^2 + B^2}$$

or

$$G = \left( \frac{2BY_0\sqrt{1 + \cot^2\theta}}{\rho} - B^2 \right)^{1/2}. \quad 8.43$$

To obtain  $B$  we assume that  $G \ll Y_0$  and determine the appropriate  $\tan\theta$  expression from Equation (8.13), yielding

$$\tan\theta \approx \frac{2BY_0}{Y_0^2 - B^2} \quad 8.44$$

or

$$B = \frac{Y_0(-1 \pm \sqrt{1 + \tan^2\theta})}{\tan\theta}. \quad 8.45$$

We have to choose the correct sign on the root in this equation, and to decide this we study the effects of the extreme condition  $B \ll Y_0$ . This gives, from Equation (8.44),

$$\tan\theta \approx \frac{2B}{Y_0} \approx \theta$$

whence

$$B \approx \frac{Y_0}{2} \tan\theta \approx \frac{Y_0}{2}. \quad 8.46$$

If we set the condition  $\theta \ll 1$ , then  $\tan\theta \approx \theta$  and Equation (8.45) becomes

$$B \approx \frac{Y_0(-1 \pm \sqrt{1 + \theta^2})}{\theta} \approx \frac{Y_0\{-1 \pm (1 + \theta^2/2)\}}{\theta}.$$

This can only equal  $Y_0\theta/2$ , as in Equation (8.46), if the positive root is taken, hence the approximate expression for  $B$  is

$$B = \frac{Y_0(-1 + \sqrt{1 + \tan^2\theta})}{\tan\theta}. \quad 8.47$$

In a situation where the initial assumption,  $G \ll Y_0$ , is not valid, an iterative procedure must be carried out in order to find a corrected expression for  $\tan\theta$ . At each stage updated values of  $B$  and  $G$  are obtained, and the procedure is only halted when a satisfactory convergence to limiting values has been obtained.

In the above expressions  $Y_0$ , the characteristic admittance of the resonator, is equal to  $1/Z_0$  ( $Y_0 = 0.02$  S when  $Z_0 = 50$   $\Omega$ ,  $Y_0 = 0.1$  S when  $Z_0 = 10$   $\Omega$ , etc.).

The phase angle  $\theta$  of the reflection coefficient can be readily obtained from Equation (8.19):

$$\beta d + \theta = \pi l \quad 8.48$$

where  $\beta$  is  $c/(f\sqrt{\epsilon_{\text{eff}}(f)})$ ,  $d$  is the known length (physically measured), and  $l$  is the (integer) order of resonance.

## 8.3 Power Losses and Parasitic Effects

Four separate mechanisms can be identified for power losses and parasitic effects associated with microstrip lines and also applicable to all planar lines:

- a.** conductor losses
- b.** dissipation in the dielectric of the substrate
- c.** radiation losses
- d.** surface-wave propagation.

The first two items are dissipative effects whereas radiation loss and surface-wave propagation are essentially parasitic phenomena. Thus, both conductor and dielectric losses can be lumped together for the purposes of calculation and embodied as the attenuation coefficient ( $\alpha$ ) for a microstrip line.

Considering a fictitious microstrip resonator, which does not radiate or propagate surface waves, the dissipative losses may also be interpreted in terms of a  $Q$  factor (precisely) defined by the following expression:

$$Q = \omega_r U/W \quad 8.49$$

where  $U$  is the maximum stored energy and  $W$  is the average power lost per cycle.

Microstrip, compared with mediums such as rectangular waveguide or coaxial lines, has a rather low unloaded  $Q$  factor. The details of power losses, leading to  $Q$ , are discussed shortly. Arbitrarily assuming that a  $Q$  factor of at least 100 is often desirable, the hatched region of [Figure 8.6](#) then provides a “useful operating region” knowing the substrate material and the intended operating frequencies. Note that thinner substrates, while allowing higher frequencies to be used before the onset of restrictions due to TM modes, cause serious degradation of the  $Q$  factor, especially at the lower operating frequencies.

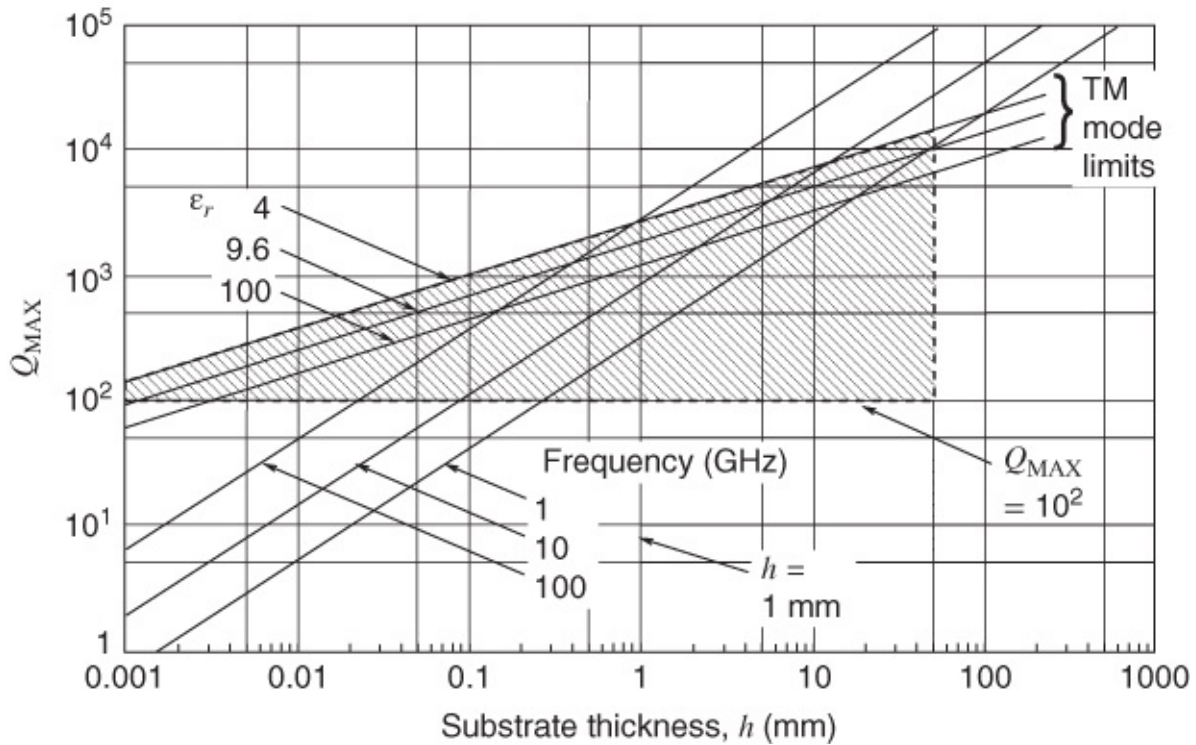


**Figure 8.6** Parameters governing the choice of substrate for any microstrip application: acceptable  $Q$  factor, operating frequency, substrate thickness, and relative permittivity  $\epsilon_r$ . Adapted from Vendelin (1970) [1], figure 2, p. 65. Reprinted with permission of Horizon House.

### 8.3.1 Conductor Loss

The effect of loss on signal transmission is captured by the attenuation coefficient,  $\alpha$ . There are two primary sources of loss: that resulting from the dielectric, captured by the dielectric attenuation coefficient,  $\alpha_d$ , and that from the conductor, captured by the conductor attenuation coefficient,  $\alpha_c$ . Thus

$$\alpha = \alpha_d + \alpha_c. \quad 8.50$$

Frequency-dependent conductor loss, described by the conductor attenuation  $\alpha_c$ , results from the concentration of current as frequency increases. For a low loss line [2]

$$\alpha_c(f) = \frac{R(f)}{2 Z_0}, \quad 8.51$$

where  $R(f)$  is the frequency-dependent line resistance described in [Section 7.2.3](#).

For example, a 50- $\Omega$  microstrip line with a 4- $\mu\text{m}$  thick copper strip of width 600  $\mu\text{m}$  has a low loss resistance of  $R = 7 \Omega/\text{m}$ . Then  $\alpha_c = 0.07 \text{ Np/m} = 0.61 \text{ dB/m}$ . The loss will increase with frequency due to the skin and proximity effects. (Note that 1 Np = 8.686 dB.)

### 8.3.2 Dielectric Loss

Dielectric loss has been analyzed by several researchers, including Gupta *et al.* [3] and Hammerstad and Bekkadal [4]. The first group [3] derive the following expression for dielectric attenuation coefficient,  $\alpha_d$ , per unit length:

$$\alpha_d = 27.3 \frac{\epsilon_r(\epsilon_{\text{eff}} - 1) \tan \delta}{\sqrt{\epsilon_{\text{eff}}}(\epsilon_r - 1)\lambda_0} \quad \text{dB/unit length} \quad 8.52$$

where  $\tan \delta$  is the loss tangent for the substrate material and the microstrip wavelength  $\lambda_g$  is given by

$$\lambda_g = \frac{\lambda_0}{\sqrt{\epsilon_{\text{eff}}}}. \quad 8.53$$

Equation (8.52) provides a good estimate for the attenuation when  $\epsilon_{\text{eff}}$  is replaced by the frequency-dependent effective relative permittivity,  $\epsilon_{\text{eff}}(f)$ . In the absence of the relatively small frequency dependence of  $\epsilon_{\text{eff}}(f)$ ,  $\alpha_d$  is linearly proportional to frequency.

Equation (8.52) can also be written

$$\alpha_d = 27.3 \frac{\epsilon_r(\epsilon_{\text{eff}} - 1) \tan \delta}{\epsilon_{\text{eff}}(\epsilon_r - 1)} \quad \text{dB/microstrip wavelength,} \quad 8.54$$

which is the expression given by Hammerstad and Bakkadal [4].

For a low loss line the attenuation due to dielectric loss is related to the line conductance, the  $G$  in the *RLGC* model of a transmission line [2]:

$$\alpha_d(f) = \frac{G(f)Z_0}{2}. \quad 8.55$$

For microstrip lines on alumina,  $\epsilon_{\text{eff}} \rightarrow \epsilon_r$  at least very approximately, and so the attenuation coefficient is, roughly,  $\alpha_d = 27 \tan \delta$ . For example, for a typical microwave substrate with  $\tan \delta = 10^{-4}$  and substrate conductivity negligible,  $\alpha_d = 0.0027$  dB/microstrip wavelength or 0.018 dB/m at 1 GHz with  $\epsilon_{\text{eff}} = 4$ . This is at least a factor of ten smaller than the conductor loss, which was calculated at the end of the last subsection. This relationship changes significantly if the substrate is lossier, the substrate has finite conductivity, and at higher frequencies.

Conductor losses greatly exceed dielectric losses for most microstrip lines on alumina or sapphire substrates and similar low-loss substrates. However, where plastic substrates are used this will by no means always be the case, and (especially) silicon or gallium arsenide substrates result in much larger dielectric losses (about 0.04 dB/mm, that is 0.4 dB/microstrip wavelength at 10 GHz for silicon).

### 8.3.3 Radiation

Microstrip is an asymmetric transmission line structure and it is often used in unshielded or poorly shielded circuits where any radiation is either free to propagate away or to induce

currents in the shielding. Further power loss is the net result.

In particular, discontinuities such as abruptly open-circuit microstrip (i.e., “open” ends), steps, and bends will all radiate to a certain extent. Such discontinuities form essential features of a microwave circuit and radiation cannot therefore be avoided altogether. Efforts must be made to reduce such radiation and its undesirable effects. In circuits such as filters, amplifiers, etc., this radiation is an acknowledged nuisance.

Both radiation and surface-wave propagation may be represented as a shunt admittance at the end of an open-circuit microstrip stub or at the plane location associated with some other abrupt discontinuity. This equivalent admittance is

$$Y = G_r + G_s + jB. \quad 8.56$$

James and Henderson [5] show that, at frequencies where the surface wave is highly trapped in the substrate and with  $h/\lambda_0$ ,  $w_{\text{eff}}/\lambda_0 \ll 1$ , the radiation conductance  $G_r$  is approximated by

$$G_r Z_0 \approx \frac{4\pi h w_{\text{eff}}}{3\lambda_0^2 \sqrt{\epsilon_{\text{eff}}}} \quad 8.57$$

in which  $w_{\text{eff}}$  is the effective microstrip width defined earlier in Equation (7.59).

The remaining terms in Equation (8.56),  $G_s$  and  $B$ , represent conductance due to surface-wave propagation and susceptance arising from the many field influences around the discontinuity.

For a 50- $\Omega$  microstrip line on 0.65 mm-thick alumina the equivalent radiation conductance due to an open-circuit, at 10 GHz, is approximately 30  $\mu\text{S}$ . Under similar conditions a 10- $\Omega$  line yields a conductance of about 120  $\mu\text{S}$ .

Radiation loss is also described by an attenuation factor,  $\alpha_r$ . At the frequencies at which a transmission line is generally used, it is usually smaller than dielectric and conductor losses. So, in full,

$$\alpha(f) = \alpha_d(f) + \alpha_c(f) + \alpha_r(f). \quad 8.58$$

### 8.3.4 $Q$ Factor and Attenuation Coefficient

With  $V_p$  and  $I_p$  being the peak voltage and current at some plane along the line, we may use Equation (8.49) to write, for a unit length,

$$Q = \omega_r \frac{(LI_p^2/2 + CV_p^2/2)/2}{(RI_p^2 + GV_p^2)/2} \quad 8.59$$

on substituting average energy stored.

If  $I_p = V_p/Z_0$  is now introduced, we get

$$Q = \omega_o \frac{CV_p^2}{RV_p^2/Z_0^2 + GV_p^2},$$

but  $Z_0 = \sqrt{L/C}$ , yielding

$$Q = \frac{\omega_o \sqrt{LC}}{R/Z_0 + GZ_0}. \quad 8.61$$

Now,  $\beta = \omega \sqrt{LC}$  and  $\alpha = R\sqrt{C/L} = R/Z_0 = GZ_0$  so that

$$Q = \frac{\beta}{\alpha \lambda_g}. \quad 8.62$$

The phase coefficient  $\beta$  is identical to  $2\pi/\lambda_g$  and hence Equation (8.62) finally becomes

$$Q = \frac{\pi}{\alpha \lambda_g}. \quad 8.63$$

In this important result it must be noted that  $\alpha$  is in units of Nepers per meter ( $1 \text{ Np} = 8.686 \text{ dB}$ ), therefore, since  $\alpha$  is usually given in decibels per meter, the expression must be divided by 8.686.

To clarify the meaning and use of this expression consider the following example. A  $Q$  factor of 200 is obtained for a microstrip resonator which is  $2\lambda_g$  in length and involves negligible parasitic effects. We require the total loss in decibels for this resonator. From Equation (8.63):

$$\alpha = \frac{\pi}{Q\lambda_g} \quad 8.64$$

with SI units of  $\text{Np/m}$ , and hence, for length  $\ell$ ,

$$\alpha(\ell) = \frac{8.686\pi\ell}{Q\lambda_g} \quad 8.65$$

in dB.

Substituting  $Q = 200$  and  $\ell = 2\lambda_g$ ,  $\alpha(\ell) = 0.27 \text{ dB}$  for the  $2\lambda_g$  length of line. If  $\lambda_g = 10 \text{ mm}$ , the attenuation coefficient is then  $\alpha = 0.27/20 \approx 0.013 \text{ dB/mm}$ .

Measurements of this  $Q$  factor are best made using ring resonators, where the parasitic effects can be kept very small.

### 8.3.5 Surface-wave Propagation

Surface waves, trapped just beneath the surface of the substrate dielectric, will propagate away from microstrip discontinuities in the form of a range of TE and radial TM modes. James and Henderson [5] have analyzed the problem thoroughly and developed an elaborate expression for  $G_s$ , the component of  $G$  due to the surface wave. The important conclusion is

that, for microstrip lines on alumina substrates up to frequencies around 10 GHz,  $G_s \ll G_r$  and  $G_r$  dominates. ( $G_r$  is the component of  $G$  due to radiation.) However, at higher frequencies  $G_s$  also becomes a very significant component. The curves in James and Henderson's paper (their Figures 4 and 6, particularly) are very illuminating in this respect and they should be studied for further information.

When we are concerned with a rectangular microstrip "patch" resonator, loosely coupled to some source of microwave excitation, there will be two equivalent end admittances, each given by Equation (8.56). In [Section 8.2.2](#) it was shown that the "external"  $Q$  factor due to such end loads may be written as

$$Q_e = \frac{l\pi\rho}{1 - \rho^2} \quad 8.66$$

where  $l$  is an integer and  $\rho$  is given by

$$\rho = \left| \frac{YZ_0 - 1}{YZ_0 + 1} \right|. \quad 8.67$$

With the aid of the expressions given in all the preceding sections James and Henderson calculate a total  $Q$  factor of 300 falling to 180, and 60 falling to 20 and lower, for rectangular microstrip patch resonators on alumina and plastic (polyolefin) substrates, respectively. The frequency ranges were 6 to 10 GHz for plastic. Agreement with  $Q$ -factor measurements was fairly good, although a  $Q$  of only 130 was measured for the resonator on alumina at 18 GHz. (Details of the resonators are given in the cited paper.)

Various techniques may be adopted to reduce radiation:

- a.** Metallic shielding or "screening."
- b.** The introduction of a small specimen of lossy (i.e., absorbent) material near any radiative discontinuity [6].
- c.** The utilization of compact, planar inherently enclosed circuits.
- d.** Reduction of the current densities flowing in the outer edges of any metal sections and concentrate currents towards the centre and in the middle of the microstrip.
- e.** Possibly shaping the discontinuity in some way to reduce the radiative efficiency.

Surface-wave propagation may be reduced by (b) above or by cutting slots into the substrate surface just in front of an open circuit [7].

### 8.3.6 Parasitic Coupling

It has been pointed out [5] that while screening the circuit removes the radiation it reinforces the surface-wave fields. Thus, we are often left with the option, (b) in the foregoing discussions, of introducing a lossy element to absorb the waves. This may not always be practicable due to space limitations and in any case it further reduces the  $Q$  factor.

In the absence of any such material or other technique the total power in the parasitic waves, ( $P_{\text{rad}} + P_{\text{sur}}$ ), is related to the incident power in the microstrip  $P$  by the ratio

$$\xi = \frac{P}{P_{\text{rad}} + P_{\text{sur}}} = \frac{1}{1 - \rho^2}. \quad 8.68$$

For a high degree of isolation the circuit must be operated at a relatively low frequency so that  $P_{\text{sur}} \ll P_{\text{rad}}$  and then, substituting Equations (8.57) and (8.67) into Equation (8.68),

$$\xi = \frac{1}{4G_r Z_0} = \frac{Z_0 \epsilon_{\text{eff}}}{640} \left( \frac{\lambda_0}{\pi h} \right)^2. \quad 8.69$$

Where possible, the following observations then apply for high isolation (i.e., minimizing loss due to radiation):

- a. Use relatively high permittivity substrates. Then  $\epsilon_{\text{eff}}$  is relatively large (e.g., alumina is better than plastic, which should be anticipated on physical grounds).
- b. Use fairly thin substrates ( $\lambda_0/h$  as large as possible).
- c. Employ high impedance ( $Z_0$ ) stubs, etc. wherever this is feasible.

### **8.3.7 Radiation and Surface-wave Losses from Various Discontinuities**

Although microstrip discontinuities are the principal subject of [Chapter 9](#), the losses originating from them should logically receive some consideration here. Horng *et al.* [8, 9] have reported a generalized method for calculating and clearly distinguishing between radiation and surface-wave losses. They base their method on a rigorous Poynting vector analysis in which the current distribution around the entire discontinuity is a result of a complete electromagnetic solution by the method of moments. These researchers provide self-consistency checks of their results, based upon power conservation calculations.

The losses calculated by Horng *et al.*, due to radiation and surface-wave propagation from the important open-end discontinuity, are shown as a function of frequency in [Figure 8.7](#). It must be appreciated that such losses are often highly significant from the circuit design standpoint and usually they need to be minimized.

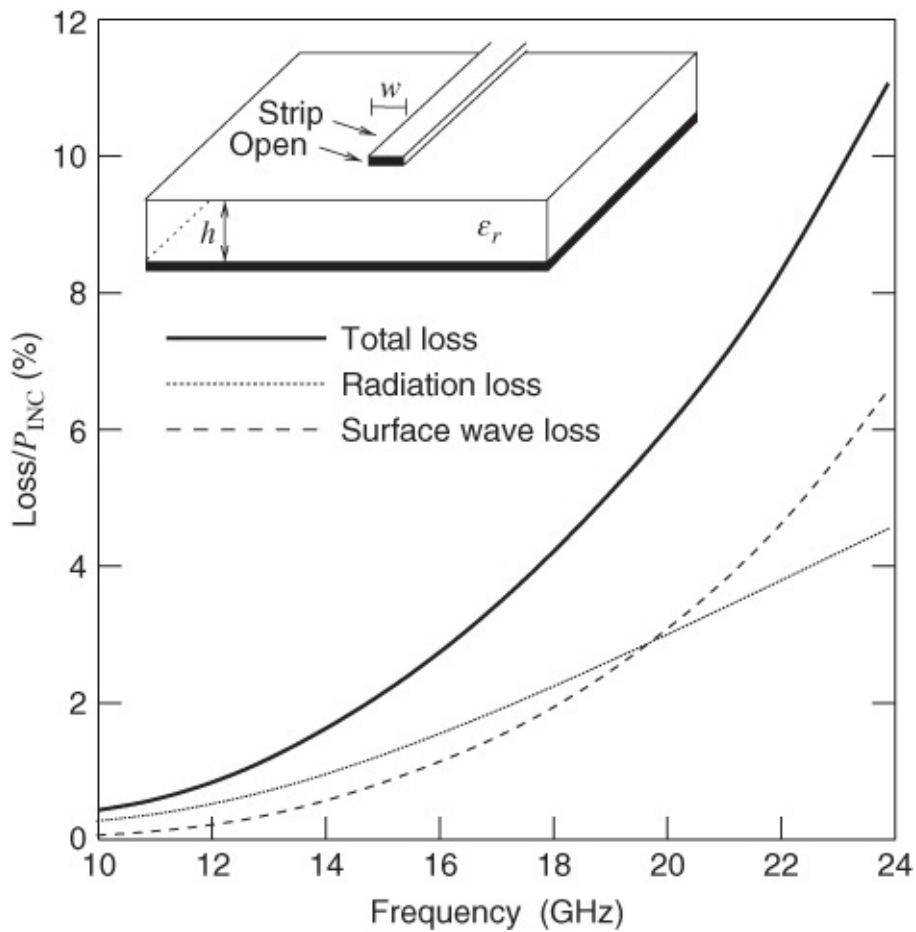


**Figure 8.7** Power losses versus frequency for open-end discontinuity ( $\epsilon_r = 10.2$ ,  $w = 0.610$  mm,  $h = 0.635$  mm). Adapted from Horng *et al.* (1990) [9], figure 5, p. 1804. Reprinted with permission of IEEE.

### 8.3.8 Losses in Microstrip on Semi-insulating GaAs

This specific and important subject has been addressed by several workers, for example Goldfarb and Platzker [10], who compare data measured over the frequency range 0–40 GHz with predictions made using three commercial CAD packages. For the measurements, microstrip resonators were formed on 0.1 mm thick GaAs substrates.

Goldfarb and Platzker's results for a 20  $\Omega$  line having such a structure are shown in Figure 8.8. Even with this relatively wide line operated at 27 GHz the radiation loss is negligible as a consequence of the high permittivity (12.9) and the small thickness of the substrate, so these results are dominated by conductor and dielectric losses. It is clear that all three CAD packages yield predictions of loss well within the range of the measurements, except for the losses as frequency approaches zero.

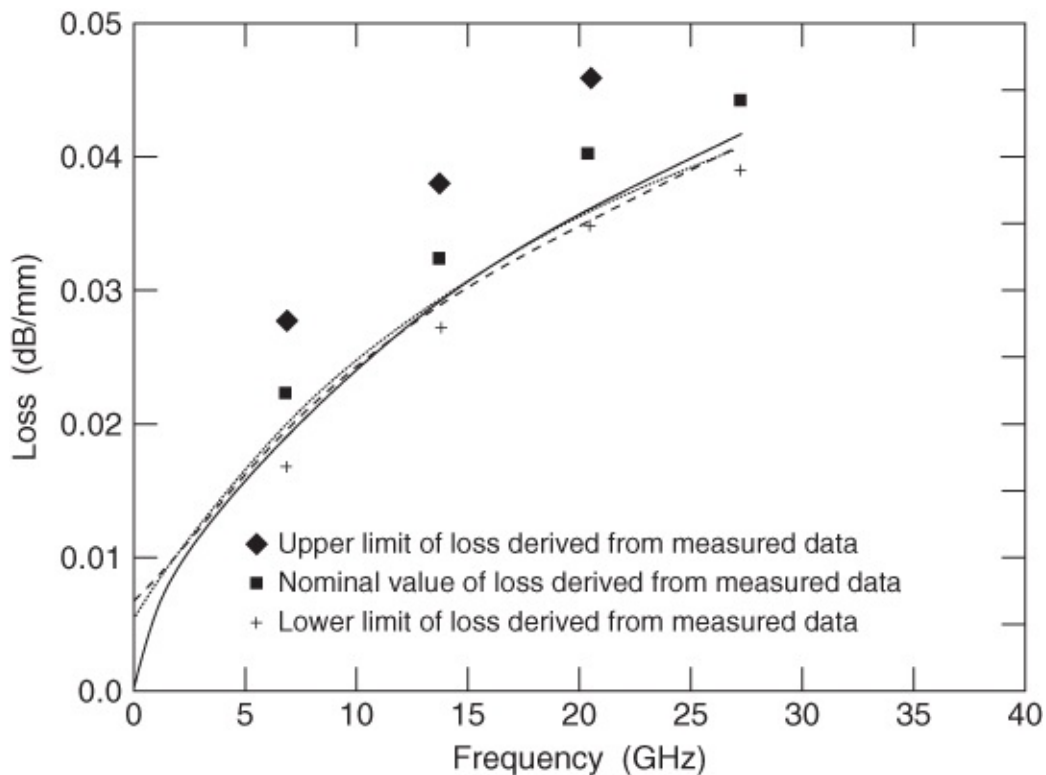


**Figure 8.8** Losses in microstrip on a GaAs substrate ( $350 \mu\text{m}$  width on  $100 \mu\text{m}$  GaAs). The lines are simulated data. Adapted from Goldfarb and Platzker (1990) [10], figure 5, p. 1959. Reprinted with permission of IEEE.

Many of the effects that contribute to loss are difficult to capture in electromagnetic simulation. This includes the skin effect, the effect of roughness, and radiation. Electromagnetic simulation needs to use idealized geometries such as strips having rectangular cross-sections and assume uniform material properties. Radiation loss as well as transfer of energy into other modes is greatly influenced by small irregularities. Thus it is essential to have an experimental campaign to characterize a process and calibrate the results of analytic formulations and electromagnetic simulations [11–21].

## 8.4 Superconducting Microstrip Lines

A major disadvantage of most planar transmission lines is the dissipative loss (when compared with mediums such as all-metallic waveguide or coaxial cable). This is an advantage for antenna applications, but represents a distinct difficulty in the realization of several types of circuits, notably filters.

Since the principal mechanism responsible for the power dissipation in microstrips is conductor loss it is clear that if this could be reduced then overall loss would also be significantly decreased. One direct method of achieving this is to “supercool” the structure, typically down to a specific temperature within the range 20–77 K.

Lee *et al.* [22] reported conductor loss calculations for superconducting microstrips. They describe the complex conductivity of the superconductor approximately, using the “two-fluid”

model. The resulting modeled conductivity is used to determine the conductor loss by means of the phenomenological loss equivalent method (PEM). A problem with this type of analysis is that for complete penetration of the current into the conductor the current distribution is uniform inside the conductor.

Contrastingly, where the current penetration is relatively moderate the current distribution becomes distinctly non-uniform inside the conductor. In order to obtain an equivalent strip for calculations Lee *et al.* consider two different superconducting materials to which are separately ascribed the shallow and deep penetrations.

The curves of [Figure 8.9](#) are repeated from the data presented by Lee *et al.* and they show results for both conventional (room temperature) microstrip having aluminum metallization and, alternatively, the superconducting line held at a temperature of 77 K (the critical temperature is 92.5 K).

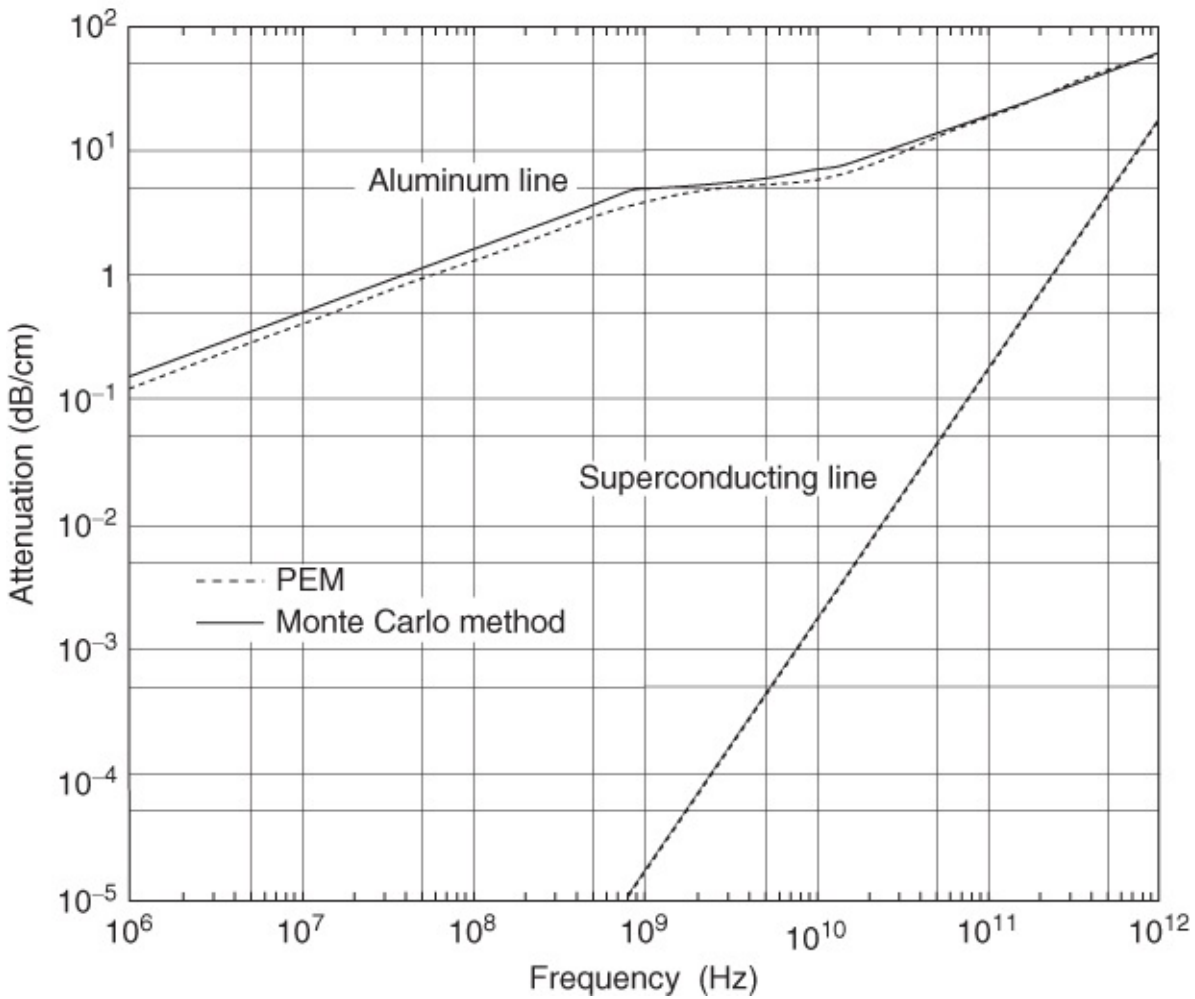


**Figure 8.9** Attenuation coefficients at 77 K for superconducting and aluminum microstrip lines. Adapted from Lee *et al.* (1989) [22], figure 2, p. 759. Reprinted with permission of the European Microwave Association.

A conventional microstrip line was fabricated on a quartz substrate with a permittivity (Lee *et al.* data) of 3.9. In both cases, results using the PEM are compared with results using an independent Monte Carlo method. Clearly, at all frequencies considered here the

superconducting line offers a much lower loss regime than conventional (room temperature) metallic microstrip. Even at 100 GHz the superconducting line attenuation is only 0.1 dB/cm in contrast to the conventional line for which a loss of 10 dB/cm is applicable at this frequency.

Phase velocity is also shown as a function of frequency in [Figure 8.10](#). The behavior associated with the aluminum line exhibits the usual variation of phase velocity, including the marked dispersion which, for this example, is pronounced above about 1 GHz. In the case of the superconducting line, however, the phase velocity is clearly approximately constant with frequency over the entire band considered (DC to 1000 GHz). Any dispersive effects at the higher frequencies are masked by the scale of this graph.

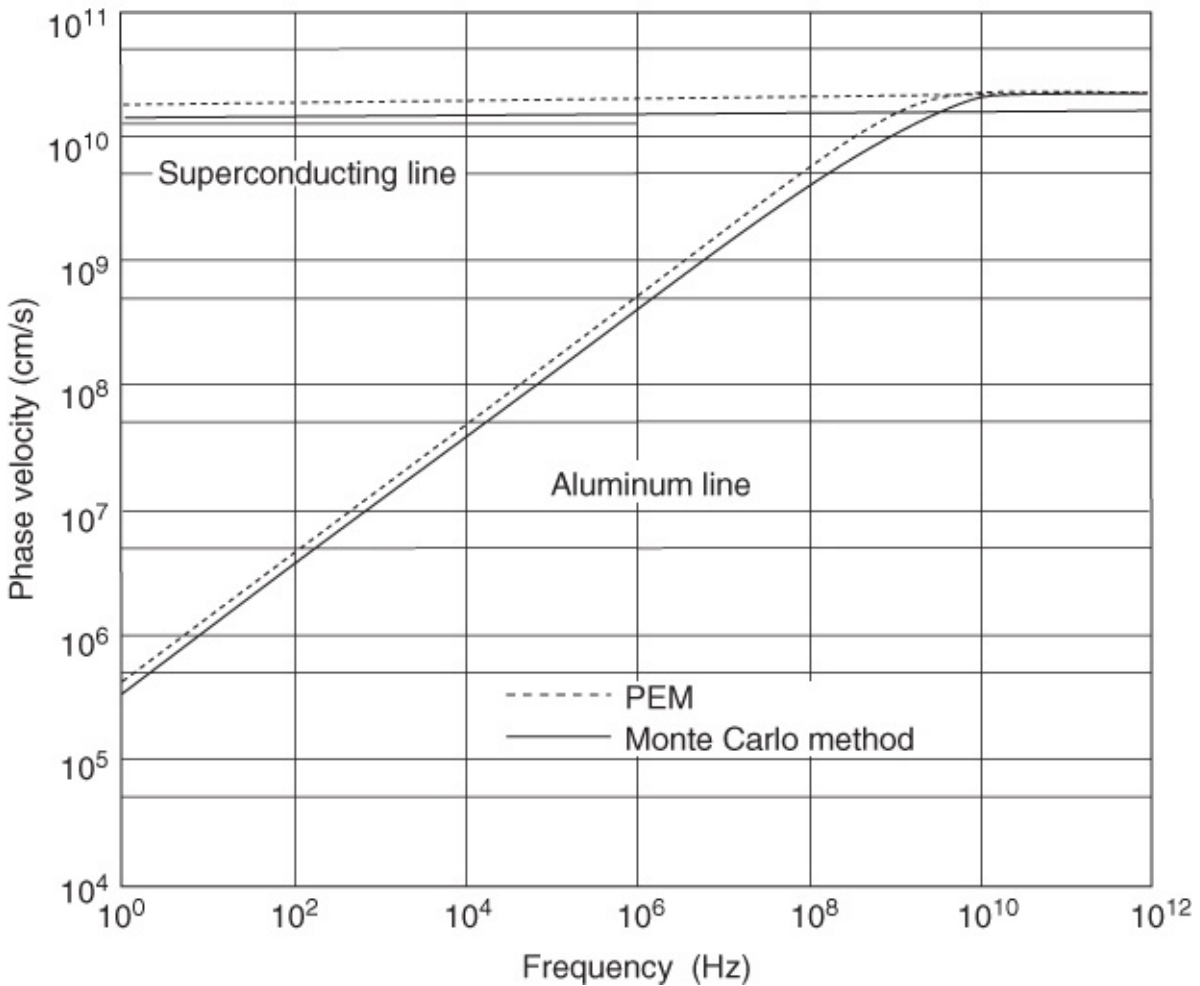


**Figure 8.10** Phase velocities at 77 K for superconducting and aluminum microstrip lines. Adapted from Lee *et al.* (1989) [22], figure 3, p. 759. Reprinted with permission of the European Microwave Association.

Bhasin *et al.* [23] also reported on the performance and modeling of superconducting ring resonators operating at 35 GHz ([Chapter 9](#) provides information on ring resonators). They showed that, at temperatures below 60 K, the superconducting strip exhibited a performance superior to that of a conventional gold-metallized microstrip. In the superconducting case the unloaded  $Q$  was higher by a factor of approximately 1.5. These researchers also show results for resonant frequency as a function of temperature.

Clearly there is a substantial amount of work required to refine both the models and/or the quality of the metallizations used for the microstrips. The difference between data obtained by theory and measurement approached a factor of two at the lower temperatures and remained about 25% at the higher temperatures for the superconductive case.

Closely related work has also been performed by van Deventer *et al.* [24]. This group used an integral equation approach to calculate the propagation characteristics of shielded superconducting microstrip lines. Phase and attenuation coefficients, as well as characteristic impedance, are presented as functions of frequency (DC to 10 GHz). It is shown that the attenuation coefficient remains below 0.5 dB/m in all cases, up to 10 GHz, except for the relatively extreme case where the substrate height is reduced to 25  $\mu$ m, when the attenuation increases to 0.83 dB/m at 10 GHz. However, unlike all other situations reported, in this case the phase coefficient stays constant over the entire band, that is, at these lower microwave frequencies design is relatively straightforward and there is negligible dispersion.

Characteristic impedance is also invariant with frequency over this range. Hammond *et al.* [25] reported the performance of superconducting microstrip resonators. Their measurements indicate that the loaded  $Q$  factor of superconducting, open-ended S-shaped microstrip resonators is always much greater than that of conventional copper or even silver microstrip resonators. The  $Q$  factors are, however, dependent on the level of input power and significant reductions occur as this input power approaches 1 W. As the power level is increased from -65 dBm to around 0 dBm, the  $Q$  factor falls slowly from around 5500 at the lower power to approximately 4000 at 0 dBm. Even so, across the entire range of power levels the  $Q$  factors are about one order of magnitude higher than is achievable with conventional resonators held at room temperature.

In summary, the performance achievable with superconducting microstrip renders the approach attractive, at least in situations where the other circuit components also benefit from operating at lower temperatures.

## 8.5 Power-handling Capabilities

There are two main aspects to any consideration of power-handling in microstrip: continuously working (CW) and pulse operation. Under CW conditions the major problems and limitations are thermal, whereas under pulse conditions the principal limitation is dielectric breakdown.

### 8.5.1 Maximum Average Power $P_{ma}$ Under CW Conditions

This is determined by heat flow and the associated temperature rise due to conductor and dielectric losses (principally conductor losses in most cases). The problem is very well treated in detail by Gupta *et al.* [26], and the salient features will be presented here. Gupta calculates the power absorbed by a unit length of microstrip line, due to conductor losses. The density of heat flow, resulting from both conductor and dielectric losses, is then determined and the consequent temperature rise is found. The final expression for the temperature rise above ambient is

$$\Delta T = \frac{0.2303h}{K} \left[ \frac{\alpha_c}{w_{\text{eff}}} + \frac{\alpha_d}{2w_{\text{eff}}(f)} \right] ^\circ C/W \quad 8.70$$

where  $\alpha_c$  and  $\alpha_d$  are the conductor and dielectric losses, respectively, in decibels per meter (length),  $w_{\text{eff}}$  and  $w_{\text{eff}}(f)$  are effective microstrip widths (note that  $w_{\text{eff}}(f)$  rises slowly with increasing frequency, see [Section 7.7.2](#)), and  $K$  is the thermal conductivity of the substrate. Thus, as expected, the substrate dominates the temperature rise due to continuous power transmitted along the line. Apart from beryllium oxide (BeO), alumina and sapphire give the best (lowest) temperature rise characteristics when compared with other common substrates. For a wide range of microwave frequencies, 4–20 GHz, 50  $\Omega$  lines on alumina and sapphire substrates yield a figure of approximately 0.02  $^\circ C/W$ . Progressively worse materials are, for the same conditions:

silicon	0.04 $^\circ C/W$
gallium arsenide (GaAs)	0.06 $^\circ C/W$
quartz	0.2 $^\circ C/W$
polystyrene	1.0 $^\circ C/W$ .

If we consider a temperature rise ( $\theta$ ) of 95  $^\circ C$  above ambient, a 50  $\Omega$  microstrip line on an alumina substrate could then carry a maximum average power of

$$P_{ma} = \frac{\theta}{\Delta T} = \frac{75}{0.02} = 3750 \text{ W.} \quad 8.71$$

In practice, this is somewhat (but not greatly) frequency dependent, but such microstrip lines can be expected to reliably carry a few kilowatts of average power. In contrast, lines on polystyrene or other plastic substrates are restricted to only around 100 W. Beryllium oxide provides a thermally excellent substrate, with  $\Delta T \approx 1 \times 10^{-3} \text{ }^\circ C/W$ , and an average power of about 95 kW can be handled by a 50  $\Omega$  line on beryllium oxide at 10 GHz. However, beryllium oxide is rarely used as a substrate because its dust is toxic.

In most cases, therefore, alumina or sapphire substrates are likely to be encountered. Some improvement can be obtained when wider microstrip lines are used, that is, lines of lower characteristic impedances. Since both the effective widths  $w_{\text{eff}}$  and  $w_{\text{eff}}(f)$  in Equation (8.70) are strongly dependent on the physical width  $w$ , then  $\Delta T$  will decrease as the width increases. If the previously calculated 50  $\Omega$  line on alumina is, instead, 20  $\Omega$ , then the power capacity will be increased by a factor of approximately four and up to about 15 kW may be transmitted. Unfortunately, most practical circuits will require narrow lines, of relatively high impedance, and the power capacity will therefore be decreased. Referring to the same example as before, a 100  $\Omega$  line will be restricted to approximately 490 W maximum CW power.

### 8.5.2 Peak (Pulse) Power-handling Capability

In a microwave system employing planar microwave circuits, coaxial connectors rather than the microstrip are likely to set the ultimate limit to the peak power. To maintain a low VSWR,

that is, to achieve a good transition, the final portion of the coaxial connector, which actually contacts the microstrip, is almost invariably of a 1 to 3 mm subminiature form. This is usually the case even where N-type or SMA coaxial lines are used in the main system external to the microwave circuit. The final portion of the coaxial connector sets a limit because of air breakdown. With any transmission line having a characteristic impedance  $Z_0$  and maximum (breakdown) voltage  $V_{mb}$ , the peak power allowable is given by

$$P_{ma} = \frac{V_{mb}^2}{2Z_0}. \quad 8.72$$

Now the breakdown electric field strength of dry air is 3 MV/m, and the internal difference in radii of the 50  $\Omega$  connector is approximately 1 mm, as can be seen from [Figure 17.1](#) (in a future section). Thus the breakdown voltage is

$$3 \times 10^6 \times 1 \times 10^{-3} = 3 \text{ kV} \quad 8.73$$

and the peak power is, from Equation (8.72):

$$P_{ma} \approx 133 \text{ kW.} \quad 8.74$$

In practice it would probably be unwise to operate microstrip circuits at these power levels.

Gupta *et al.* [26] mention two useful improvements which can be made to the microstrip itself in order to improve peak power handling:

- a.** Since sharp edges intensify the electric field and thus reduce the allowable breakdown voltage, thick, rounded conductors are preferred.
- b.** To avoid air breakdown near the edges, the strip conductor can be painted with a dielectric paint having a permittivity identical to that of the substrate. More commonly a mask, perhaps silk-screened on, is used.

A careful technique of preferential etching should enable (a) to be achieved and (b) is relatively straightforward to implement. However, the introduction of such a dielectric mask along the edges of the microstrip conductor will significantly alter the line parameters ( $\epsilon_{eff}$  and  $Z_0$ ) and it is not clear how one might calculate appropriate design adjustments. An empirical cut-and-try approach thus seems inevitable here, including tests for the final microstrip-limited peak power when this, and not the transitions, forms the limit.

## 8.6 Passive Intermodulation Distortion

One of the unexpected power-dependent effects that can occur with microstrip transmission lines is passive intermodulation distortion (PIM) [27–29]. The classic test of intermodulation distortion is to apply two large tones, close in frequency, to a passive device such as a transmission line [30]. If the transmission line has a nonlinear response it will produce third-order difference frequencies that are close in frequency to the applied tones, see [Figure 8.11](#). The spurious content that falls in the receive or transmit bands of a communications system

detrimentally affects dynamic range. The dominant mechanism of passive intermodulation distortion is apparently electro-thermal distortion, where the time-varying envelope of the large signal creates a time-varying heat dissipation and thus temperature variation. This results in time-varying resistance which mixes with the applied tones to produce intermodulation distortion. It is likely that there are other mechanisms but what these are is not understood.

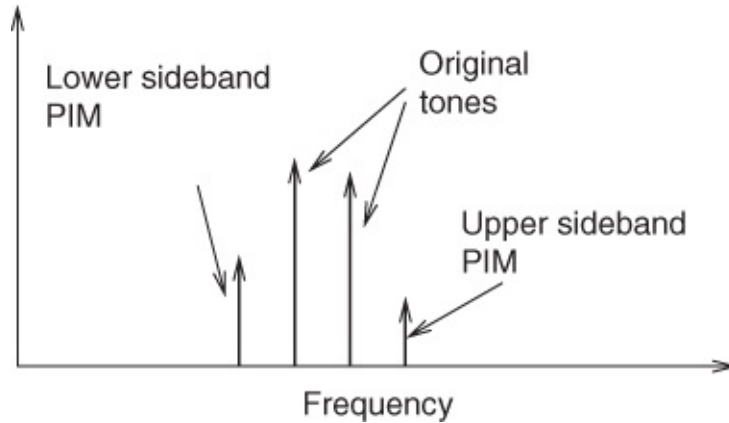


**Figure 8.11** Spectrum at the output of a transmission line generating PIM distortion tones. The input of the line consists of two discrete tones.

### 8.6.1 Origins of PIM

Many physical sources have been suggested, including ferromagnetism [31–35], constriction resistances [32], and nonlinear conductivity [36]. Recent studies addressed electro-thermally induced PIM by passive microwave components and microstrip transmission lines [27–29, 37]. The distributed nature of PIM on transmission lines was suggested in [38]. Near-field probing has shown growth of forward-wave PIM on microstrip lines [39, 40]. These observations indicate that the intrinsic generation of PIM on transmission lines is distributed along the line. Point sources of PIM, such as solder droplets, scratches, and debris, producing PIM on transmission lines have also been identified [39].

Ferromagnetic materials, conductor surface roughness, tunneling, and nonlinear conductivity could exist anywhere on a transmission line. Recent literature has shown that PIM generation is a current-related nonlinearity [32, 36, 41]. Maximums in distortion were found at current peaks while minimums were found at voltage peaks. Tunneling is a voltage-induced nonlinearity [42], greatly decreasing its likelihood as a dominant contributor to PIM on transmission lines. The dependency on current density seems to exist with and without ferromagnetic materials [32]. The authors in [29] established that the temperature dependence of conductivity produces appreciable electrical distortion in lossy lumped microwave elements, and this is solely dependent on material parameters and the amplitudes of the RF signals.

### 8.6.2 PIM on Microstrip Transmission Lines

In [27] it was established that thermally induced modulation of conductivity is a dominant physical mechanism for PIM on transmission lines. Consider the microstrip line shown in [Figure 8.12](#). Current flowing on the strip is concentrated in the skin effect region and the

dissipative losses result in the generation of heat  $q(t)$  which, in general, is time varying because microwave signals usually have a time-varying envelope. In a low VSWR environment heat flows from the skin effect region at the top of the strip into the bulk of the conductor. This joins the heat produced in the bottom skin effect region before both heat fluxes flow into the substrate. If the VSWR on the line is other than 1, then there will be heat flow along the conductor. Ignoring this heat flow along the strip, the heat flow into the substrate encounters a finite thermal resistance and thus the temperature of the strip varies. The temperature increase of the strip varies with the time-varying signal envelope. Since conductors have a finite thermal coefficient of resistance, the temperature variation results in a time-varying resistance. This time-varying resistance interacts with the microwave signal to produce additional spectral content which is distortion of the original signal.

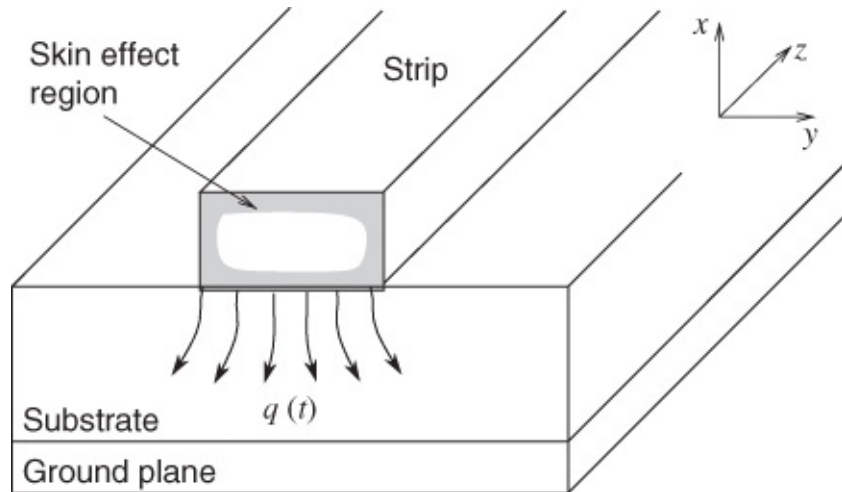


**Figure 8.12** Microstrip transmission line showing the skin effect region in which heat is generated. Adapted from Wilkerson *et al.* (2011) [27], figure 1, p. 1191. Reproduced with permission of IEEE.

The classic test for envelope-dependent nonlinear effects is a two-tone test in which a microwave signal consists of two sinusoids that are close in frequency but separated by  $\Delta f$ . The results of such a test of a microstrip line with a thin strip are shown in [Figure 8.13](#) where measurements of PIM are compared to the PIM predicted by a theoretical model. The horizontal axis here is  $\Delta f$ .

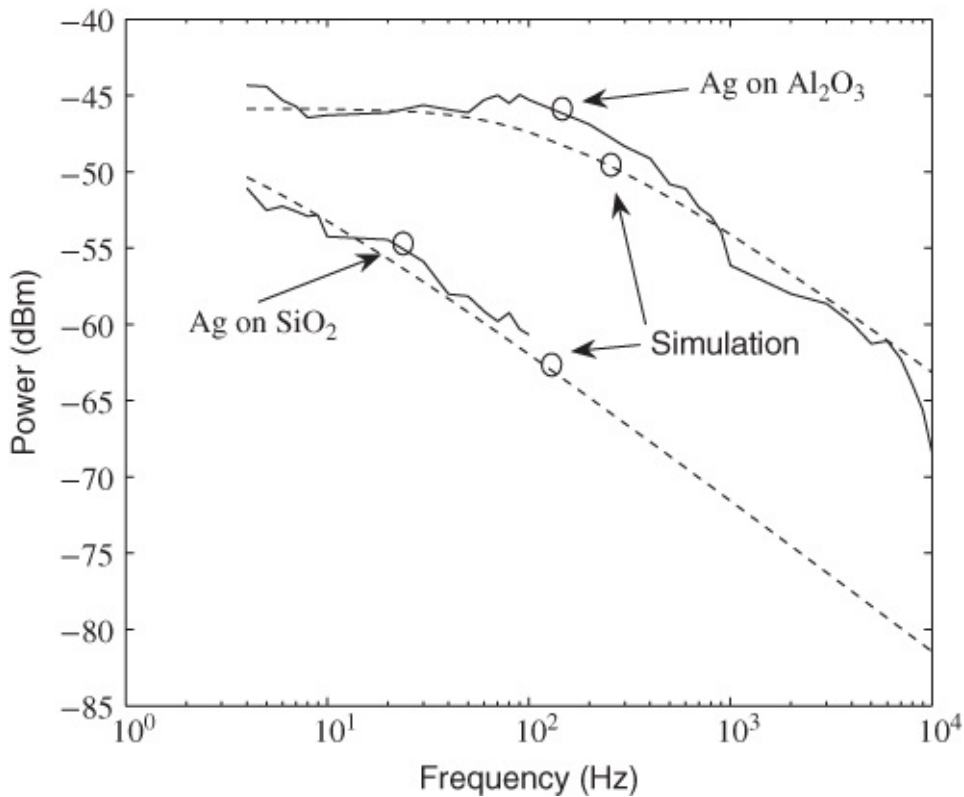


**Figure 8.13** Comparison of measured and modeled PIM on a microstrip transmission line. Adapted from Wilkerson *et al.* (2011) [27], figure 8, p. 1198. Reproduced with permission of IEEE.

Further details of the test are that the microstrip consists of single metal (either silver or gold) sputtered on polished single crystal sapphire and fused-quartz substrates. This fabrication eliminated any possible PIM distortion due to ferromagnetic materials, surface roughness, or tunneling as possible sources of PIM. The transmission lines were tested using a 480 MHz two-tone test signal with frequency separation of the tones ranging from 4 to 10 kHz. Measurements were made using a high dynamic range feed-forward measurement system [43]. The use of a two-tone test signal with varying tone separation result in a 10 dB/decade roll-off in distortion response. This was identified as the classic signature of distortion due to electro-thermal effects.

### 8.6.3 Design Guidelines

There are several steps that can be taken to reduce the level of the electro-thermal PIM induced on transmission lines for RF signals with nonconstant envelopes. One of these options is providing a heat-sinking mechanism with a very small time constant immediately adjacent to the heat-generating loss region. With low-loss substrates, the major source of heat generation is conductive loss within the skin depth of the conductors. Using thick metallization does little to change the level of resistive heat generation (because of the skin effect), but it does serve to provide rapid heat spreading, that is, a local heatsink with a very low time constant. A similar approach is to use a dielectric layer with a very high thermal conductivity immediately adjacent to the conductors. It is, of course, advantageous to use a bulk substrate with higher

thermal conductivity. In the case of microstrip, the key conductor is the strip as the current density in the ground plane is much lower than for the strip. Using a thicker substrate will enable the conductor cross-section dimensions (the width of the strip in the case of microstrip) to increase, and this reduces the current density and heat generated. This in turn reduces electro-thermally induced distortion. Finally, a lower system characteristic impedance can reduce the level of electro-thermal PIM. However, there is a cross-over point for long line lengths, see [27]. Both forward- and backward-traveling PIM are generated and the level of PIM measured at the ends of a transmission line is length dependent as a result of the coherent combining of PIM.

## 8.7 Summary

This chapter was concerned with characterizing and identifying effects due to loss on microstrip lines. Most of the work is directly applicable to other transmission lines. An expression for the  $Q$  of a lossy transmission line was developed and this is directly applicable to planar transmission lines. Many microwave circuits, matching networks and filters in particular, require a minimum  $Q$  for correct operation. This places an additional constraint on the thickness of the strip of a microstrip line. The design space is further constrained by the need to avoid exciting higher-order modes. Loss is due to many sources, including conductor, dielectric, surface wave leakage, and radiation. All of these effects limit  $Q$ . Of particular concern at high power levels is passive intermodulation distortion (PIM). Design guidelines for minimizing PIM on planar transmission lines are provided.

## References

- [1] G. Vendelin, “Limitations on stripline Q,” *Microwave Journal*, pp. 63–69, 1970.
- [2] M. Steer, *Microwave and RF Design: a Systems Approach*, 2nd ed. SciTech Pub., 2013.
- [3] K. C. Gupta, R. Garg, I. J. Bahl, and P. Bhartia, *Microstrip Lines and Slotlines*, 2nd ed. Artech House, 1996.
- [4] E. Hammerstad and F. Bekkadal, “A microstrip handbook, ELAB Report STF44 A74169,” University of Trondheim, Norway, Tech. Rep., Feb. 1975.
- [5] J. James and A. Henderson, “High-frequency behaviour of microstrip open-circuit terminations,” *Proc. IEE, Microwaves, Optics and Acoustics*, vol. 3, no. 5, pp. 205–218, Sep. 1979.
- [6] A. Armstrong and P. Cooper, “Techniques for investigating spurious propagation in enclosed microstrip,” *Radio and Electronic Engineer*, vol. 48, no. 1.2, pp. 64–72, Jan.–Feb. 1978.
- [7] J. James and P. Ladbrooke, “Surface-wave phenomena associated with open-circuited stripline terminations,” *Electronics Letters*, vol. 9, no. 24, pp. 570–571, 1973.

- [8] T. Horng, H. Yang, and N. Alexopoulos, “A full-wave analysis of shielded microstrip line-to-line transitions,” in *1990 IEEE MTT-S Int. Microwave Symp. Digest*, May 1990, pp. 251–254.
- [9] T.-S. Horng, S.-C. Wu, H.-Y. Yang, and N. Alexopoulos, “A generalized method for distinguishing between radiation and surface-wave losses in microstrip discontinuities,” *IEEE Trans. on Microwave Theory and Techniques*, vol. **38**, no. 12, pp. 1800–1807, Dec. 1990.
- [10] M. Goldfarb and A. Platzker, “Losses in GaAs microstrip,” *IEEE Trans. on Microwave Theory and Techniques*, vol. **38**, no. 12, pp. 1957–1963, Dec. 1990.
- [11] G. Stewart, M. Kay, C. Riedell, R. Pomerleau, and M. Steer, “Microstrip discontinuity modeling,” in *IEEE Proc. Southeastcon'89*, 1989, pp. 107–111.
- [12] S. Goldberg, M. Steer, and P. Franzon, “Accurate experimental characterization of three-ports,” in *1991 IEEE MTT-S Int. Microwave Symp. Dig.*, 1991, pp. 241–244.
- [13] B. Biswas, A. Glasser, S. Lipa, M. Steer, P. Franzon, D. Griffis, and P. Russell, “Experimental electrical characterization of on-chip interconnects,” in *IEEE 6th Topical Meeting on Electrical Performance of Electronic Packaging*, 1997, pp. 57–59.
- [14] S. Lipa, M. Steer, A. Morris, and P. Franzon, “Comparison of methods for determining the capacitance of planar transmission lines with application to multichip module characterization,” *IEEE Trans. on Components, Hybrids, and Manufacturing Technology*, vol. **16**, no. 3, pp. 242–252, Mar. 1993.
- [15] S. Goldberg, M. Steer, P. Franzon, and J. Kasten, “Experimental electrical characterization of high speed interconnects,” in *Proc. 41st Electronic Components and Technology Conf.*, 1991, pp. 85–88.
- [16] S. Goldberg, M. Steer, P. Franzon, and J. Kasten, “Experimental electrical characterization of interconnects and discontinuities in high-speed digital systems,” *IEEE Trans. on Components, Hybrids, and Manufacturing Technology*, vol. **14**, no. 4, pp. 761–765, Dec. 1991.
- [17] C. Riedell, M. Steer, M. Kay, J. Kasten, M. Basel, and R. Pomerleau, “Dielectric characterization of printed circuit board substrates,” *IEEE Trans. on Instrumentation and Measurement*, vol. **39**, no. 2, pp. 437–440, Feb. 1990.
- [18] M. Steer, S. Lipa, P. Franzon, and A. Cangellaris, “Experimental characterization of interconnects and discontinuities in thin-film multichip module substrates,” *Topical Meeting on Electrical Performance of Electronic Packaging*, pp. 145–147, 1993.
- [19] C. Riedell, M. Kay, R. Pomerleau, M. Steer, J. Kasten, and M. Basel, “Dielectric characterization of printed circuit substrates,” in *Proc. IEEE Southeastcon'89*, 1989, pp. 102–106.

- [20] A. Glaser, M. Steer, G. Shedd, P. Russell, and P. Franzon, “A method for on-chip interconnect characterization,” in *1995 Electrical Performance of Electronic Packaging*, 1995, pp. 108–110.
- [21] M. Kay, R. Pomerleau, and M. Steer, “Empirical statistical analysis of planar transmission lines on pcbs accounting for manufacturing variations,” in *IEEE Southeastcon'89 Proc.*, 1989, pp. 112–116.
- [22] H.-Y. Lee, K.-S. Kong, and T. Itoh, “Conductor loss calculation of superconducting microstrip line using a phenomenological loss equivalence method,” in *19th European Microwave Conf.*, Sep. 1989, pp. 757–760.
- [23] K. Bhasin, C. Chorey, J. Warner, R. Romanofsky, V. Heinen, K. Kong, H. Lee, and T. Itoh, “Performance and modeling of superconducting ring resonators at millimeter-wave frequencies,” in *1990 IEEE MTT-S Int. Microwave Symp. Digest*, May 1990, pp. 269–272.
- [24] T. van Deventer, P. Katehi, J. Josefowicz, and D. Rensch, “High frequency characterization of high-temperature superconducting thin film lines,” in *1990 IEEE MTT-S Int. Microwave Symp. Digest*, May 1990, pp. 285–288.
- [25] R. Hammond, G. Negrete, M. Schmidt, M. Moskowitz, M. Eddy, D. Strother, and D. Skoglund, “Superconducting Tl-Ca-Ba-Cu-O thin film microstrip resonator and its power handling performance at 77 K,” in *1990 IEEE MTT-S Int. Microwave Symp. Digest*, May 1990, pp. 867–870.
- [26] K. C. Gupta, R. Garg, I. J. Bahl, and P. Bhartia, *Microstrip Lines and Slotlines*, 2nd ed. Artech House, 1996.
- [27] J. Wilkerson, P. Lam, K. Gard, and M. Steer, “Distributed passive intermodulation distortion on transmission lines,” *IEEE Trans. on Microwave Theory and Techniques*, vol. **59**, no. 5, pp. 1190–1205, May 2011.
- [28] J. Wilkerson, K. Gard, and M. Steer, “Electro-thermal passive intermodulation distortion in microwave attenuators,” *36th European Microwave Conf.*, Sep. 2006, pp. 157–160.
- [29] J. Wilkerson, K. Gard, A. Schuchinsky, and M. Steer, “Electro-thermal theory of intermodulation distortion in lossy microwave components,” *IEEE Trans. on Microwave Theory and Techniques*, vol. **56**, no. 12, pp. 2717–2725, Dec. 2008.
- [30] J. Wilkerson, K. Gard, and M. Steer, “Wideband high dynamic range distortion measurement,” *2008 IEEE Radio and Wireless Symp.*, 2008, pp. 415–418.
- [31] G. C. Bailey and A. C. Ehrlich, “A study of RF nonlinearities in nickel,” *Appl. Phys.*, vol. **50**, no. 1, pp. 453–461, Jan. 1979.
- [32] Y. Yamamoto and N. Kuga, “Short-circuit transmission line method for PIM evaluation of metallic materials,” *IEEE Trans. on Electromagnetic Compatibility*, vol. **49**, no. 3, pp. 682–

- [33] J. Russer, A. Ramachandran, A. Cangellaris, and P. Russer, "Phenomenological modeling of passive intermodulation (pim) due to electron tunneling at metallic contacts," *2006 IEEE MTT-S Int. Microwave Symp. Digest*, Jun. 2006, pp. 1129–1132.
- [34] C. D. Bond, C. S. Guenzer, and C. A. Carosella, "Intermodulation generation by electron tunneling through aluminum oxide films," *Proc. IEEE*, vol. **67**, no. 12, pp. 1643–1652, Dec. 1979.
- [35] C. Vicente and H. L. Hartnagel, "Passive-intermodulation analysis between rough rectangular waveguide flanges," *IEEE Trans. on Microwave Theory and Techniques*, vol. **53**, no. 8, pp. 2515–2525, Aug. 2005.
- [36] D. E. Zelenchuk, A. P. Shitov, A. G. Schuchinsky, and V. F. Fusco, "Passive intermodulation in finite length of printed microstrip lines," *IEEE Trans. on Microwave Theory and Techniques*, vol. **56**, no. 11, pp. 2426–2434, Nov. 2008.
- [37] E. Rocas, C. Collado, N. Orloff, and J. C. Booth, "Third-order inter- modulation distortion due to self-heating in gold coplanar waveguides," in *2010 IEEE MTT-S Int. Microwave Symp. Dig.*, Anaheim, California, May 2010, pp. 425–428.
- [38] J. Wilcox and P. Molmud, "Thermal heating contribution to intermodulation fields in coaxial waveguides," *IEEE Trans. Commun.*, vol. **24**, no. 2, pp. 238–243, Feb. 1976.
- [39] A. P. Shitov, D. E. Zelenchuk, A. G. Schuchinsky, and V. F. Fusco, "Passive intermodulation generation on printed lines: Near-field probing and observations," *IEEE Trans. on Microwave Theory and Techniques*, vol. **56**, no. 12, pp. 3121–3128, Dec. 2008.
- [40] A. P. Shitov, D. E. Zelenchuk, A. G. Schuchinsky, and V. F. Fusco, "Passive intermodulation in printed lines: effects of trace dimensions and substrate," *Proc. IET Microwave Antennas and Propagation*, vol. **3**, no. 2, pp. 260–268, Feb. 2009.
- [41] A. Christianson and W. J. Chappell, "Measurement of ultra low passive intermodulation with ability to separate current/voltage induced nonlinearities," in *2009 IEEE MTT-S Int. Microw. Symp. Dig.*, Jun. 2009, pp. 1301–1304.
- [42] J. G. Simmons, "Generalized formula for the electric tunnel effect between similar electrodes separated by a thin insulating film," *Applied Physics*, vol. **34**, no. 6, pp. 1793–1803, Jun. 1963.
- [43] J. R. Wilkerson, K. G. Gard, and M. B. Steer, "Wideband high dynamic range distortion measurement," in *2008 IEEE Radio and Wireless Symp.*, Jan. 2008, pp. 415–418.

# Chapter 9

## Discontinuities in Microstrip

### 9.1 Introduction

In this chapter we consider discontinuity modeling based mostly on equivalent capacitor and inductor networks. Some discontinuities, however, especially an open-circuited line, can also incorporate a short length of line. All practical distributed circuits must inherently contain discontinuities. A straight uninterrupted length of any transmission structure (strictly speaking, with a perfectly invariant cross-section) would be genuinely continuous, that is, it would not contain any discontinuities. In fact such straight lines, taken alone, are of little engineering use, and in any case junctions are essential. In the region of bends, abruptly stopped open circuits, width changes, and transitions, discontinuities occur in the transmission line. Although such discontinuities give rise to only very small capacitances and inductances (often less than 0.1 pF and 0.1 nH) the reactances of these become particularly significant at high microwave and into millimeter-wave frequencies. The performance of amplifiers, for example, has been shown to be considerably affected by microstrip discontinuities [1]. As with dispersion, we can very often neglect these discontinuities when the frequencies involved do not exceed a few gigahertz. Above approximately 10 GHz they are definitely very significant.

It is beyond the scope of this treatment, being oriented towards circuit design, to consider in any detail the techniques that have been used to evaluate discontinuity capacitances and inductances.

At frequencies much beyond 10 or 12 GHz, the lumped  $C$  and  $L$  description of most discontinuities becomes less and less meaningful. Discontinuities at these higher frequencies are probably best described by means of scattering matrices, although in many cases considerable success has been enjoyed by using the lumped  $LC$  approach at frequencies up to around 18 GHz.

Radiation from various discontinuities gives rise to equivalent resistive elements. These will not be discussed in any detail here since they enter mainly into the province of those interested in antennas rather than circuits, except where the reduction in  $Q$  factor is significant.

In some cases techniques have been developed which compensate, at least over a particular range of frequencies, the existing discontinuity effects. Where this is the case less detailed attention is given here to the properties of the uncompensated discontinuity. Although “quasi-static,” the effectiveness of results obtained from these various previously mentioned approaches has been adequately vindicated by incorporating the methods in several full circuit designs and checking with careful measurements. The calculation of the reactive effects due to most discontinuities will now be shown, as far as is practicable.

## 9.2 The Main Discontinuities

Several forms of discontinuity emerge from circuit requirements:

1. foreshortened open circuits
2. series coupling gaps
3. short circuits through to the ground plane
4. right-angled corners or “bends” (unmitered and mitered)
5. step width changes
6. transverse slit
7. T junction
8. cross junctions.

An example of a microwave transistor amplifier layout [2] is shown in [Figure 9.1](#), and at least three of the discontinuities can be readily identified. Some of them are numbered on the diagram, in accordance with the quoted list. Many other circuits, such as filters, mixers, and oscillators, involve several discontinuities. All microwave circuit technologies inherently involve transmission discontinuities.

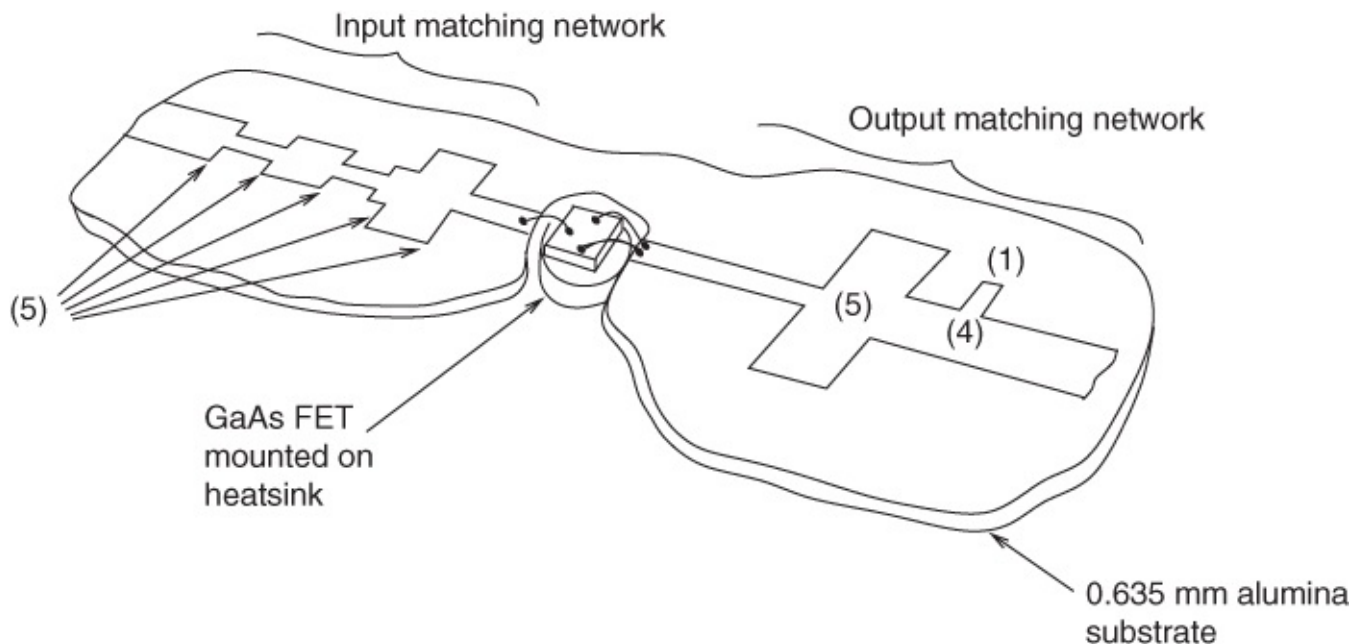


[Figure 9.1](#) Layout of a simple hybrid microwave amplifier using a GaAs MESFET, showing several discontinuities in the microstrip lines (DC bias filters are not shown).

### 9.2.1 The Open Circuit

There are essentially three phenomena associated with the open circuit:

- a. There will be fringing fields extending beyond the abrupt physical end of the metallic strip.

b. Surface waves will be launched from the end of the strip.

c. Energy will be radiated from the open end.

Item (a) may be accounted for by assuming some equivalent capacitance to be connected at the open end, and this feature nearly always dominates the “end-effect.” Items (b) and (c) require equivalent shunt conductance at the open end of the line. In most cases it will not be necessary to quantify these last two phenomena, but their minimization may be carried out on a practical basis in circuits involving microstrip. This has already been discussed in [Chapter 7](#), and James and Ladbrooke [3] indicated how substrate slots may be used to minimize surface-wave interactions.

The physical appearance of both a foreshortened open circuit and a series gap are shown in [Figure 9.2](#), where equivalent lumped capacitor networks are also given.

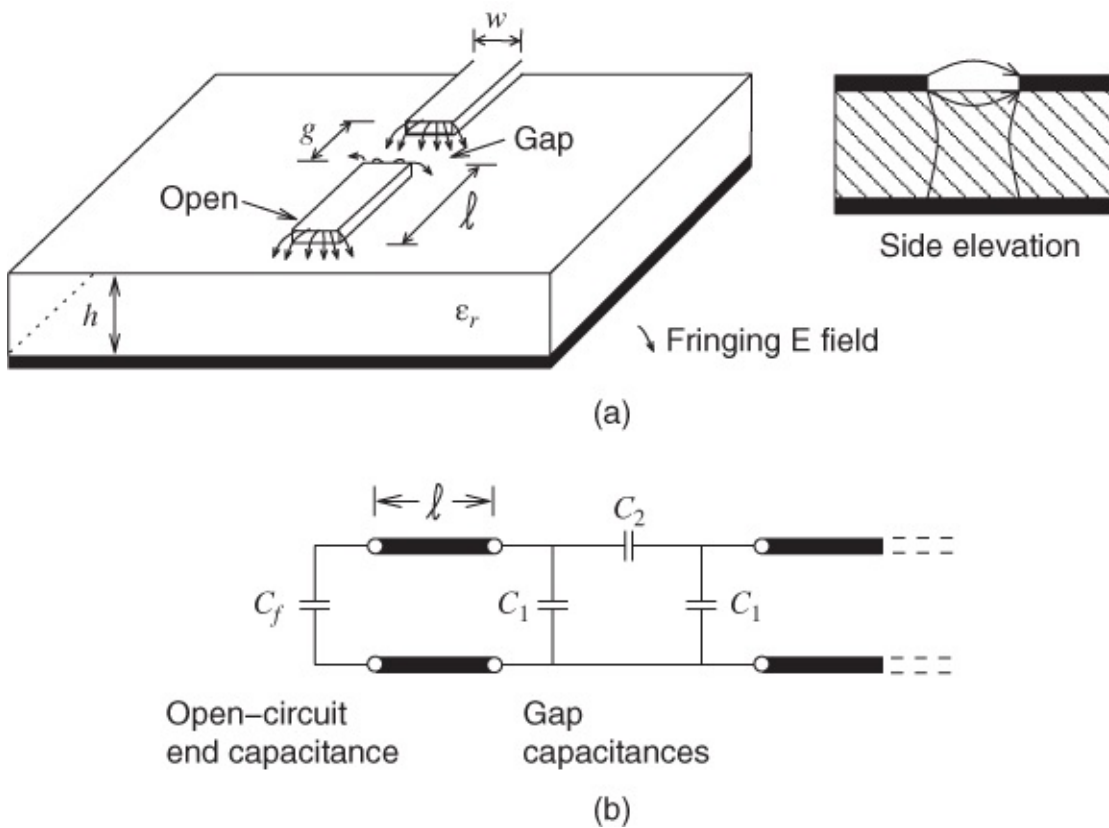


**Figure 9.2** Microstrip open circuit and gap: (a) layout with electric fields; and (b) equivalent lumped capacitive network.

Several quasi-static field calculations of capacitance  $C_f$  have been documented. The most reliable, judged by comparison with many independent measurements, seems to be the work of Silvester and Benedek [4]. While being thorough, the resulting curves of results need further interpretation and a curve-fitting formula can be deduced for microwave circuit design. In their paper, Silvester and Benedek give a formula which amounts to a series expansion fit to their theoretical data. The expression is

$$\frac{C_f}{w} = \exp \left[ 2.2036 \sum_{i=1}^5 K_i(\epsilon_r) \left( \log \frac{w}{h} \right)^{i-1} \right] \text{ pF/m}$$

where the coefficients  $K_i(\epsilon_r)$  are given in [Table 9.1](#).

**Table 9.1** Coefficients  $K_i(\epsilon_r)$  in Equation (9.1) for various substrate permittivities. Adapted from Silvester and Benedek 1972 [4], table 1, p. 515. Reprinted with permission of IEEE

	$\epsilon_r$					
$i$	1.0	2.5	4.2	9.6	16.0	51.0
1	1.110	1.295	1.443	1.738	1.938	2.403
2	-0.2892	-0.2817	-0.2535	-0.2538	-0.2233	-0.2220
3	0.1815	0.1367	0.1062	0.1308	0.1317	0.2170
4	-0.0033	-0.0133	-0.0260	-0.0087	-0.0267	-0.0240
5	-0.0540	-0.0267	-0.0073	-0.0113	-0.0147	-0.0840

These results may readily be plotted out as a set of curves, giving  $K_i(\epsilon_r)$  as a function of  $\epsilon_r$  and with  $i$  as parameter. Thus, coefficients  $K_i(\epsilon_r)$  for other materials may be found, within a fairly narrow range of permittivities but including all the important semiconductors with their permittivities lying between 9.6 and 16.0. A set of first-order linear approximation equations can be simply obtained from these curves by curve-fitting.

An empirical formula that yields, quite simply, the equivalent end-effect length is given shortly, but first we must properly define this quantity.

## Equivalent End-effect Length

In many aspects of circuit design it is very useful to approximate the microstrip line as being longer than it actually is, to account for the end effect. Then we can deal with fully distributed (microstrip) structures throughout, and do not need to work separately in terms of lumped capacitance. The concept is illustrated in [Figure 9.3](#). We can now define the equivalent end-effect length,  $\ell_{eo}$ :

$\ell_{eo}$  is the equivalent extra length of microstrip line, having all the propagation parameters applicable to the main line, continuing from the physical-end plane to the final electrically open-end plane.

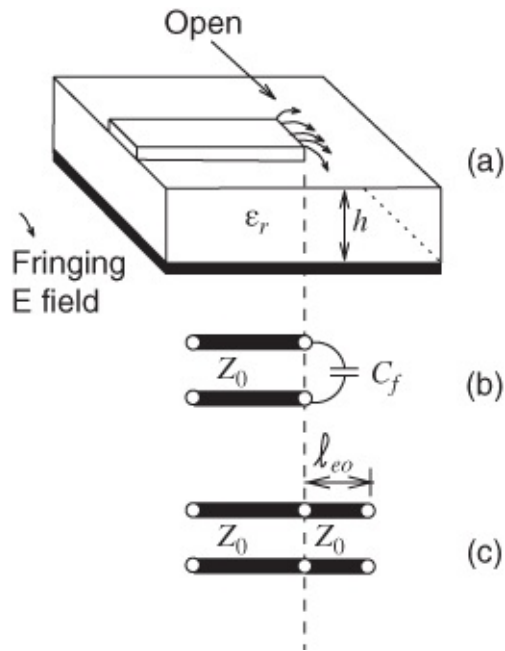


**Figure 9.3** Development of the equivalent end-effect length concept: (a) physical transmission line; (b) transmission line with equivalent end fringing capacitance  $C_f$ ; and (c) transmission line with equivalent extra transmission line of length  $\ell_{eo}$ .

Notice that the “line” of length  $\ell_{eo}$  must be an exact continuation of the main transmission line, same  $Z_0$ , and hence the same  $w/h$  and identical  $\epsilon_{eff}$ .

It is a simple matter to obtain the end-effect length as a function of  $C_f$ ,  $Z_0$ , and  $\epsilon_{eff}$ . The input reactance to the extra length of line is given by the standard open-circuit terminated line result:

$$X_{eo} = -jZ_0 \cot \beta \ell_{eo}. \quad \underline{9.2}$$

Also, the capacitive reactance due to  $C_f$  is

$$X_f = \frac{1}{j\omega C_f}. \quad \underline{9.3}$$

For equivalence we must equate Equations (9.2) and (9.3), giving

$$\frac{1}{\omega C_f} = \frac{Z_0}{\tan \beta \ell_{eo}}. \quad \underline{9.4}$$

Since  $\ell_{eo} \ll \lambda_g$  we may apply the small-angle approximation  $\tan(\beta \ell_{eo}) \rightarrow \beta \ell_{eo}$ , so that Equation (9.4) then becomes

$$\frac{1}{\omega C_f} \approx \frac{Z_0}{\beta \ell_{eo}} \approx \frac{Z_0 \lambda_g}{2\pi \ell_{eo}}. \quad \underline{9.5}$$

Writing  $c$  as the free-space velocity, this may be written as:

$$\frac{1}{\omega C_f} = \frac{cZ_0}{\omega \sqrt{\epsilon_{\text{eff}} \ell_{eo}}}.$$

Then, finally,

$$\ell_{eo} \approx \frac{cZ_0 C_f}{\sqrt{\epsilon_{\text{eff}}}}. \quad 9.7$$

For most microstrip lines, certainly those on alumina substrates less than 1 mm thick, the static-TEM expressions given here appear to work quite accurately over the approximate frequency range

$$2 \ll f \ll 20 \text{ GHz}. \quad 9.8$$

An alternative empirical expression, yielding the length extension directly, has been given by Hammerstad and Bekkadal [5]:

$$\ell_{eo} = 0.412h \left( \frac{\epsilon_{\text{eff}} + 0.3}{\epsilon_{\text{eff}} - 0.258} \right) \left( \frac{w/h + 0.262}{w/h + 0.813} \right). \quad 9.9$$

It appears that, over a wide range of materials and microstrip width-to-height ratios ( $w/h$ ), this expression can often give errors of 5% or more. Where such errors are acceptable, which is frequently the case for this quantity, Equation (9.9) may be used because it involves less computing than the more accurate Equation (9.7).

### Upper Limit to End-effect Length (Quasi-static Basis)

End-effect length is usually normalized to  $h$ , to obtain  $\ell_{eo}/h$ , which is the quantity usually employed as a design parameter. The graph of Figure 9.4 shows  $\ell_{eo}/h$  plotted as a function of  $w/h$  for the particular case of a substrate having  $\epsilon_r = 11.0$ . The maximum value, shown as a broken line, is determined on a static capacitance basis for a line embedded totally in a free-space environment. Cohn [6] has given an exact expression for the fringing capacitance due to a foreshortened semi-infinite line situated at a distance  $b/2$  above a ground plane, where the entire structure is completely filled with dielectric of relative permittivity  $\epsilon_r$ . Cohn's expression may be reinterpreted for the microstrip case and calculated for  $\ell_{eo}/h$ . This yields the result

$$\left( \frac{\ell_{eo}}{h} \right)_{\max} = \frac{2}{\pi} \ln(2). \quad 9.10$$

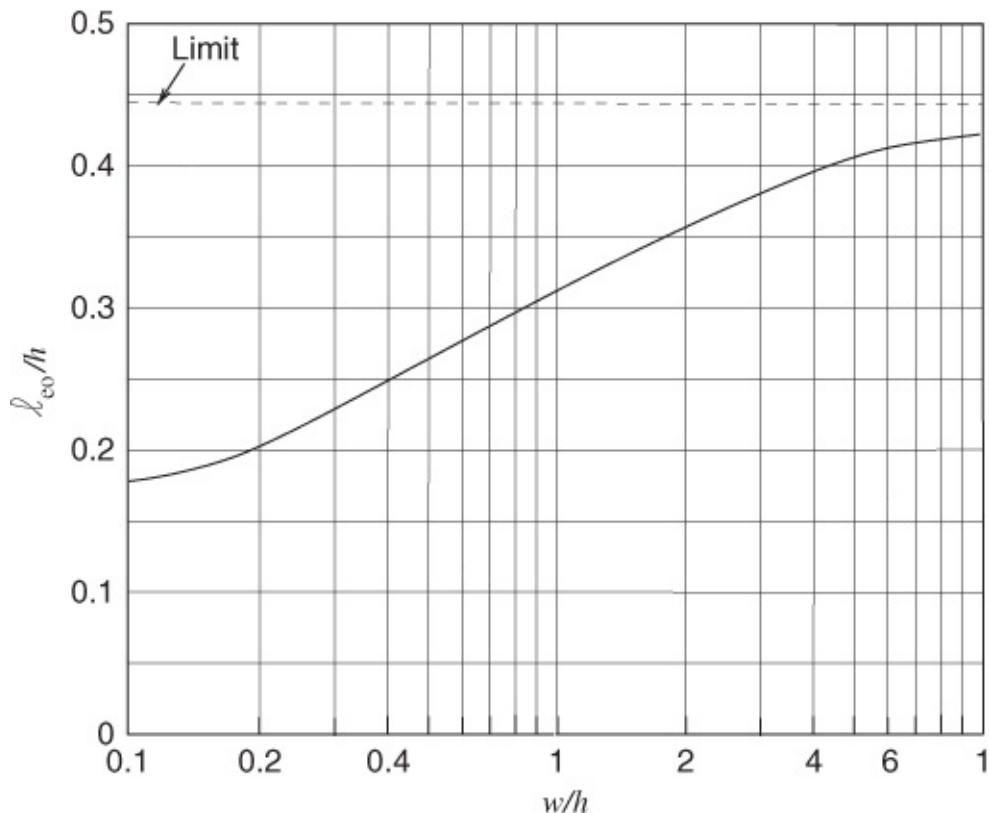


**Figure 9.4** Normalized end-effect length ( $\ell_{eo}/h$ ) as a function of shape ratio  $w/h$  for  $\epsilon_r = 11.0$ .

Recent work has suggested that this statically derived limit may not be absolute. It does, however, give an indication to the designer of the approximate maximum value likely for open-circuit equivalent length.

### 9.2.2 The Series Gap

The physical appearance of the microstrip series gap is also given in [Figure 9.2](#). This discontinuity is important in some forms of end-coupled filters, coupling to resonators, and other circuits. For convenience here the nomenclature is repeated in [Figure 9.5](#).

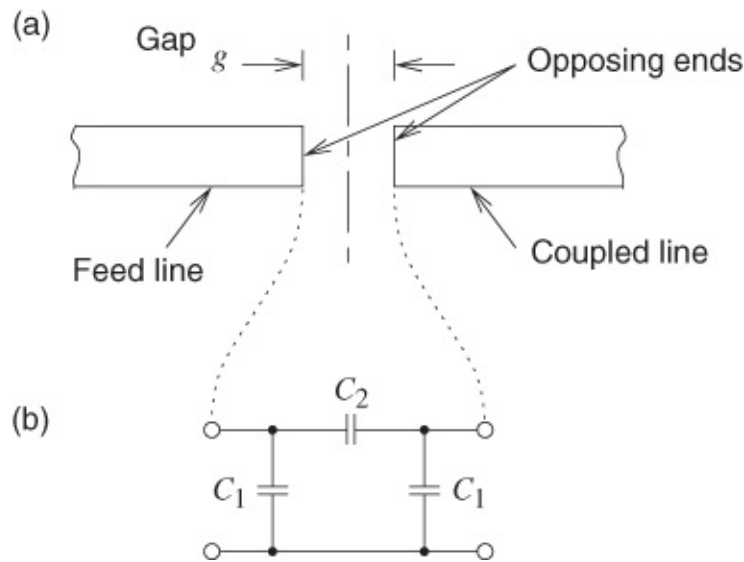


**Figure 9.5** The series gap and its equivalent lumped circuit: (a) physical arrangement; and (b) lumped capacitive equivalent circuit.

For energy to be coupled across the gap the open-circuit microstrip ends must be equally and oppositely charged. Significant capacitance therefore exists across the gap and is denoted  $C_2$ . Grounded capacitors  $C_1$  represent the fields fringing directly down to ground from each end of the line at a symmetrical gap.

An extensive analysis of the gap allowing for the necessary inversion to account for opposite potential signs on each side leads to comprehensive results that work for tightly coupled gaps. Since this is rarely encountered in practice only the result for loosely coupled gaps is given here. By analogy with the development of Equation (9.7), for the foreshortened open circuit, the expression for the gap end-effect line extension may be written

$$\ell_{eg} \approx \frac{cZ_0(C_1 + C_2)}{\sqrt{\epsilon_{\text{eff}}}}. \quad 9.11$$

This now means that, where we know  $C_1$  and  $C_2$ , we can determine the line extension  $\ell_{eg}$ . This is fairly satisfactory in the case of simple resonators and some other structures where the degree of coupling, leading to the gap separation  $g$ , has been rather arbitrarily set.

However, this situation is quite unsuitable for synthesis, for example of a filter. In such a case we require ultimately to determine  $g$  itself from a starting point of filter characteristics. (For the present purposes, suffice it to say that we can obtain the gap capacitance required from prototype filter characteristics.) Garg and Bahl [7] developed curve-fitted expressions for the gap capacitances as follows:

$$\frac{C_o}{w} = \left(\frac{g}{w}\right)^{m_o} \exp(k_o) \text{ pF/m} \quad 9.12$$

$$\frac{C_e}{w} = \left(\frac{g}{w}\right)^{m_e} \exp(k_e) \text{ pF/m} \quad 9.13$$

applicable for  $\epsilon_r = 9.6$  and over the range

$$0.5 \leq \frac{w}{h} \leq 2$$

where

$$C_o = 2C_2 + C_1 \quad 9.14$$

and

$$C_e = 2C_1. \quad 9.15$$

The indices and arguments are defined by the following set of equations:

$$\left. \begin{array}{l} m_o = \text{array} \{0.619 \log(w/h) - 0.3853\} \\ k_o = 4.26 - 1.453 \log(w/h) \end{array} \right\} 0.1 \leq (g/w) \leq 1.0 \quad 9.16$$

$$\left. \begin{array}{l} m_e = 0.8675 \\ k_e = 2.043(w/h)^{0.12} \end{array} \right\} 0.1 \leq (g/w) \leq 0.3 \quad 9.17$$

$$\left. \begin{array}{l} m_e = [1.565/(w/h)^{0.16}] - 1 \\ k_e = 1.97 - 0.03h/w \end{array} \right\} 0.3 \leq (g/w) \leq 1.0. \quad 9.18$$

Garg and Bahl [7] also showed that values can be calculated for  $C_o$  and  $C_e$  for other values of substrate permittivity  $\epsilon_r$  by using the following expressions:

$$C_o(\epsilon_r) = C_o(9.6)(\epsilon_r/9.6)^{0.8} \quad \text{and} \quad C_e(\epsilon_r) = C_e(9.6)(\epsilon_r/9.6)^{0.9}. \quad 9.19$$

These relations hold over the range

$$2.5 \leq \epsilon_r \leq 15 \quad 9.20$$

and an accuracy of 7% is quoted. It is noted that semiconductor substrates are accommodated.

In order to obtain  $g$  we select Equation (9.12) because  $C_o$  involves both the  $C_1$  and  $C_2$  gap capacitances, and rearrange as follows:

$$\ln \left( \frac{g}{w} \right) = \frac{1}{m_o} \left[ \ln \left( \frac{C_o}{w} \right) - k_o \right]. \quad 9.21$$

Having obtained a first value for  $g$ , it is desirable that a second value be found using Equation (9.13). Should the two values differ significantly then the final value of  $g$  will be that which most closely satisfies the two relations.

### Accuracy of Gap Capacitance Calculations ( $C_1$ and $C_2$ )

Several approaches have been made to the problem of gap capacitance calculation and the results have differed significantly. In a critical paper by Costamagna [8] these various

approaches were compared and recommendations were made. Costamagna argued that the results of Benedek and Silvester [9] should be used, but should be reduced by a certain amount in the case of  $C_2$  (Costamagna's  $C_b$ , shown in his Figure 2). In critical design situations great care should therefore be exercised over the determination of  $C_1$  and  $C_2$ .

### 9.2.3 Microstrip Short Circuits

For hybrid microwave circuits operating at lower microwave frequencies, up to 2 or 3 GHz, a short wire bonded to the microstrip and ground plane and passed through an unmetallized hole in the substrate is known to provide a fairly good short circuit. At these frequencies discontinuity parasitics (inductance and capacitance) present negligible reactive effects. As the frequency is increased beyond 2 or 3 GHz, the equivalent reactance associated with such a wire becomes increasingly significant, so that the structure departs noticeably from a short circuit.

This equivalent reactance is also frequency-dependent, and thus different effective lengths of the microstrip line are associated with the same structure at different frequencies. This means that the location, along the line, of the effective short-circuit plane also varies significantly with frequency.

Some interesting work has been performed by Owens [10] primarily in an effort to characterize shunt holes in microstrip lines where active devices such as transferred-electron devices may be connected. One consequence of this work was the discovery that a hole can be produced which has a practically frequency-independent reactance, so that its effective short-circuit plane remains stationary over a wide frequency range.

Extensive microstrip resonator measurements were employed and it was established that the holes may either be filled with solid metal or merely be metallized around their “cylindrical” surfaces to obtain essentially identical results. For fairly low impedance (18  $\Omega$ ) microstrip lines on alumina substrates ( $\epsilon_r = 10.1$ ,  $h = 0.635$  mm) it was found that a 1.52 mm diameter hole ultrasonically drilled down through these 3 mm wide lines gave

$$\text{reactance} = X < \pm j0.5 \Omega$$

9.22

over the frequency range:

$$4 \leq f \leq 18 \text{ GHz.}$$

This represents a good *broadband* short circuit. Holes yielding this performance had microstrip continuing on both sides of them.

Where such a hole appears at the otherwise foreshortened end of the strip, Owens gives the following condition for a broadband short circuiting hole:

$$\ln\left(\frac{w_{\text{eff}}}{\pi d_e}\right) \approx \left(\frac{\pi d_e}{w_{\text{eff}}}\right)^2 \quad 9.23$$

where  $d_e$  is  $0.03 + 0.44d$ ,  $d$  is the actual hole diameter, and  $w_{\text{eff}}$  is the effective microstrip

width.

In the case of the 3 mm wide line this leads to a hole diameter of 1.30 mm, which is substantially smaller than the previous optimum value of 1.52 mm, when the hole was not at the end of a microstrip line. [Figure 9.6](#) illustrates the appearance of the structure.

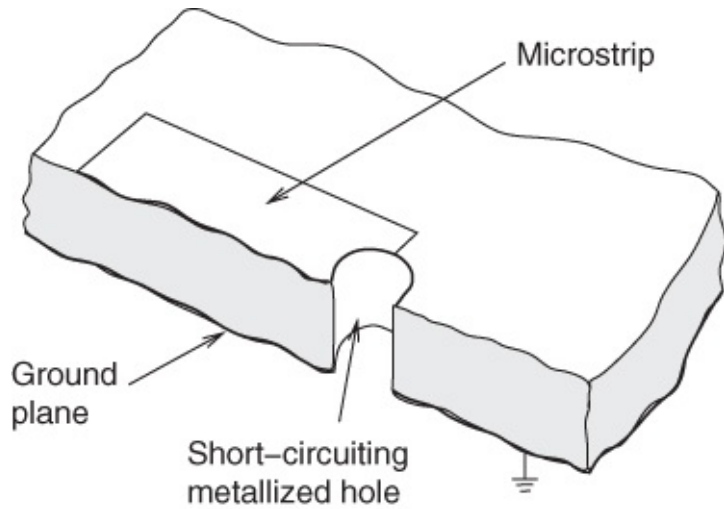


[Figure 9.6](#) A shunt metallized hole which may form a short circuit in a microstrip line.

A  $50 \Omega$  line on this substrate material would have a width of approximately 0.6 mm, and many circuits, including filters, require such lines. Assuming, very roughly for present purposes, a pro rata reduction in the hole diameter, we find that a diameter of 0.26 mm is required for a good broadband short circuit. This would be extremely difficult, if not impossible, to drill (except using a laser). It would, however, be feasible using monolithic integrated circuit technology.

It is quite difficult to accurately and repeatably locate these holes, or shunt posts, relative to the microstrip circuit on a hybrid MIC. Microstrip-like structures can be precisely defined and located photolithographically, but this is considerably more difficult with shunt structures such as these short circuits.

However, with techniques such as computer-controlled laser drilling these short circuits may become more important, even with hybrid microwave circuits, and some relevant work is briefly described in [Section 9.6.8](#). The availability of via technology, essentially short circuits and inherent with monolithic integrated circuits, provides for the precision positioning of such shorts. In particular, Strohm *et al.* [11] have reported accurate and well-defined via hole realization in HRS using an advanced silicon etch process. Precise vertical sidewalls are achieved for circular geometries, and an SEM is shown in the paper of a  $61 \mu\text{m}$  diameter,  $150 \mu\text{m}$  deep gold-plated via. The inductance is 22 pH and measurements are reported between 50 MHz and 50 GHz.

This via hole technology is not only highly amenable to modeling, but also, if repeatable under production conditions, the technology opens up wider design freedom in monolithic integrated circuits.

## 9.2.4 Further Discontinuities

The remaining sections deal with bends, steps, slits, T junctions, and cross-over junctions. In these cases fringing field effects, leading to equivalent capacitive elements, occur as we have already seen for other discontinuities. However, current flow disturbances are now produced, and these give rise to the concept of equivalent circuit inductances.

For bends and T junctions, arrangements have been developed which, at least partially, compensate for the discontinuity effects. These are described here because they are significant to the MIC circuit designer, certainly up to around 18 GHz. Sometimes it may not be practical to apply the compensation and for this reason, for example, the uncompensated bend equivalent circuit parameters are studied.

## 9.3 Bends in Microstrip

### 9.3.1 The Right-angled Bend or “Corner”

In many cases where quite complex circuits are required on a single substrate it is necessary to feed, between circuits, using lengths of microstrip that include bends. Another important case comprises hairpin lines such as resonators that embody double bends. These bends usually pass through an angle of  $90^\circ$ . Most often the line does not change width and such a bend, together with its equivalent circuit, is shown in [Figure 9.7](#).

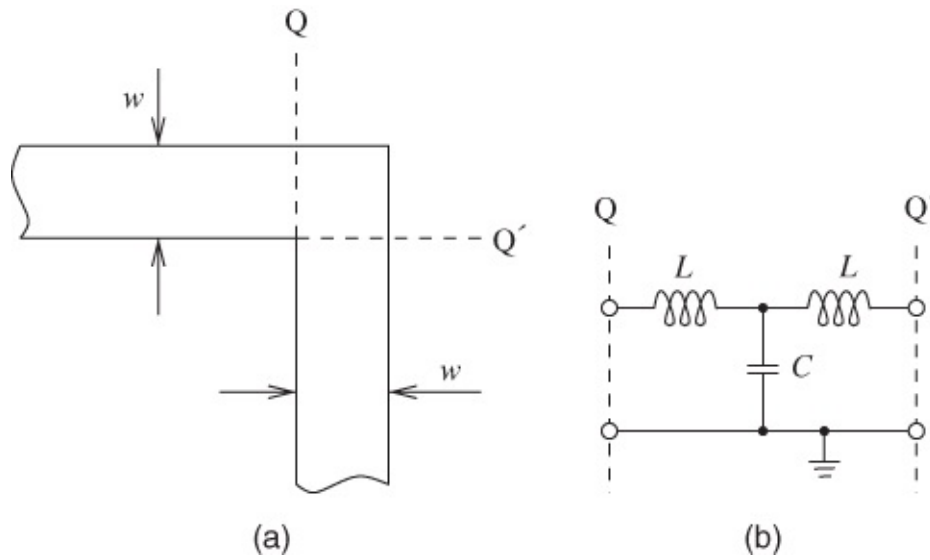


**Figure 9.7** Right-angled microstrip bend: (a) structure and nomenclature; and (b) equivalent circuit.

The capacitance arises through additional charge accumulation at the corners, particularly around the outer point of the bend where electric fields concentrate. The inductances arise because of current flow interruption. This is considerable, especially bearing in mind that most of the current flows in the outer edges of microstrip. The results of some simulations showing the current densities are provided here.

An alternative equivalent circuit simply treats the inductances as two lengths of equivalent, inductive, microstrip lines. Capacitance data have been determined theoretically by Silvester and Benedek [12, 13], and inductance data has been obtained by Thomson and Gopinath [14]. Fairly extensive measurements have also been conducted.

Gupta *et al.* [15] have given closed formulas for the evaluation of bend capacitance:

For  $w/h < 1$ :

$$\frac{C_{\text{BEND}}}{w} = \frac{(14\epsilon_r + 12.5)w/h - (1.83\epsilon_r - 2.25)}{\sqrt{w/h}} \text{ pF/m.} \quad 9.24$$

For  $w/h > 1$ :

$$\frac{C_{\text{BEND}}}{w} = (9.5\epsilon_r + 1.25)\frac{w}{h} + 5.2\epsilon_r + 7.0 \text{ pF/m} \quad 9.25$$

and inductance:

$$\frac{L}{h} = 100 \left[ 4\sqrt{\frac{w}{h}} - 4.21 \right] \text{ nH/m.} \quad 9.26$$

The accuracies of Equations (9.24) and (9.25) are quoted as within 5% over the ranges  $2.5 \leq \epsilon_r \leq 15$  and  $0.1 \leq w/h \leq 5.0$ . The accuracy of Equation (9.26) is quoted as about 3% for the range  $0.5 \leq w/h \leq 2.0$ , compared with the results of Thomson and Gopinath. The permittivity range quoted above is sufficient to encompass most types of substrates, including semiconductors, although the range applying to the inductance is more restricted than that for the capacitance because inductance is almost always less significant. This is not a severe limitation and the expression can be used somewhat outside the quoted range without serious overall loss of modeling accuracy.

To illustrate the seriousness of the problem, as an example let us consider a microstrip line of 0.75 mm width and fabricated on a 0.5 mm thick substrate whose relative permittivity is 9.9. The bend's equivalent circuit capacitance and inductance are 0.135 pF and 0.031 nH, respectively, shown in the equivalent circuit of [Figure 9.8](#). Although these components may have “small” values, their reactances, even at 10 GHz, have a significant effect on the electrical properties of the complete network. For the inductance, at 10 GHz:

$$\omega L = 2\pi \times 10^{10} \times 0.031 \times 10^{-9} = 2 \Omega$$

and for the capacitance:

$$\frac{1}{\omega C} = \frac{1}{2\pi \times 10^{10} \times 0.135 \times 10^{-12}} = 120 \Omega.$$

The 2  $\Omega$  reactance in series in a line having a characteristic impedance of 50  $\Omega$  will have a significant effect (greater with lower impedance lines), and the 120  $\Omega$  shunt capacitive reactance will likewise have a pronounced influence on circuit response (greater for higher

impedance lines).

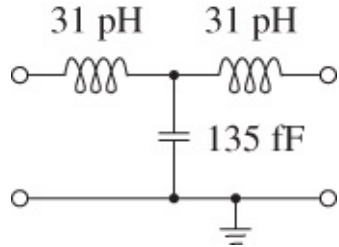


**Figure 9.8** Lumped equivalent circuit for the microstrip bend calculated in the text.

### **9.3.2 Mitered or “Matched” Microstrip Bends, Compensation Techniques**

Several techniques have been investigated for the compensation of microstrip bends, greatly reducing the effect of the capacitance and hence improving the VSWR. In particular, Anders and Arndt [16] reported a moment method to calculate the appropriate capacitances and inductances for both curved and mitered bends. Their results indicate that, at least up to a frequency of about 10 GHz, a mitered bend produces as good as, or better, performance than curved bends. This applies to a wide range of bend angles, from 30° up to 120°. At least 70% mitring is recommended for an acute-angled bend of 120°, that is, one which acutely bends back on itself. Guidance for the design of such mitered bends, but for an angle of 90°, is also available for the structure shown in [Figure 9.9\(a\)](#), and see [Figure 9.9\(c\)](#) for the parameters of the equivalent circuit.

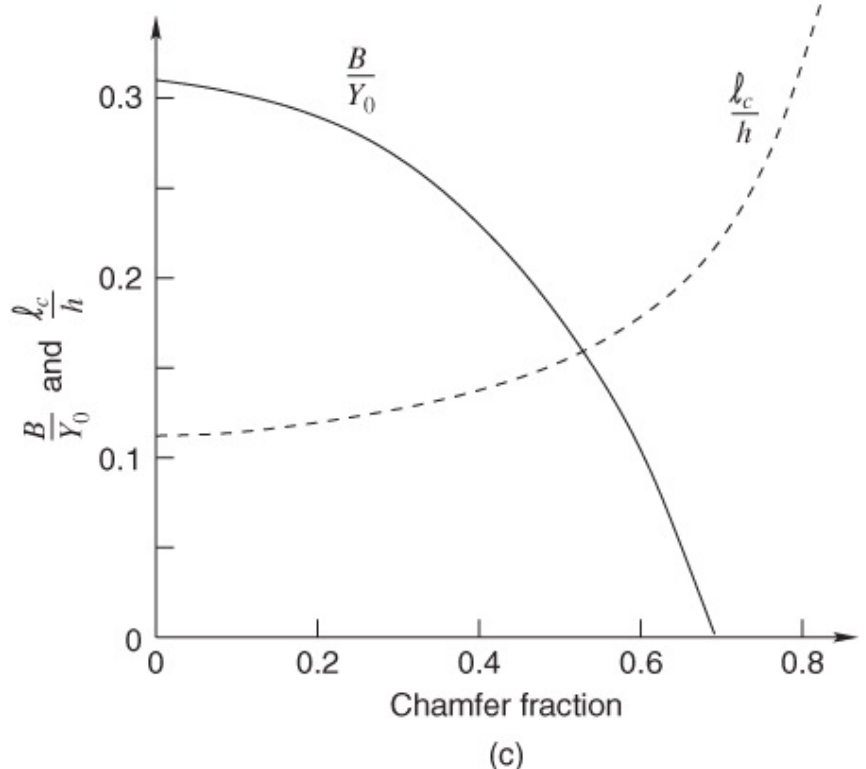
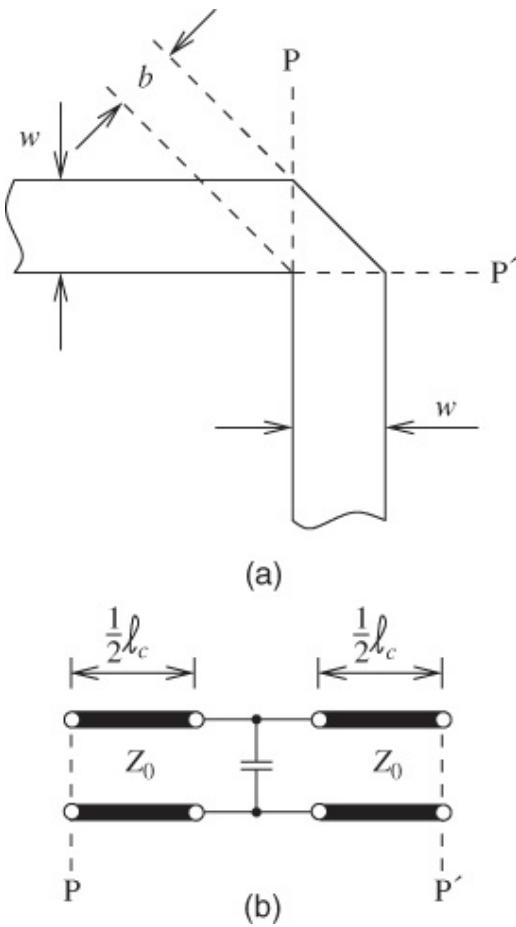


**Figure 9.9** Mitered, right-angled bend together with its equivalent circuit and parameter variations (as a function of the amount of miter): (a) structure and nomenclature; (b) equivalent circuit; and (c) parameter trends as a function of chamfer fraction ( $1 - b/\sqrt{2w}$ ). (c) adapted from Easter *et al.* (1978) [17], figure 11, p. 80. Reprinted with permission of IEEE.

The equivalent circuit shown in Figure 9.9(b) is for the region between planes  $P$  and  $P'$  and the curves of Figure 9.9(c) relate to measured results [17]. Although these curves apply to the specific instance defined, the considerable reduction of susceptance  $B$  (and therefore also capacitance  $C$ ) would be expected in widely different substrates and structures. As can be seen, the equivalent line-length parameter  $\ell_c$  increases with enhanced mitring. Owing to this, and extreme line narrowing in the centre of the bend, the degree of miter is generally restricted to around

$$1 - \frac{b}{\sqrt{2w}} \approx 0.6 \quad 9.27$$

so that  $b \approx 0.57w$ . It is tentatively recommended that approximately this amount of miter be applied in the majority of practical cases, where the substrate permittivity roughly approximates that of alumina.

We also present SONNET simulations here that indicate the greatly improved current distributions applying to the mitered bend, see Figures 9.10–9.11.

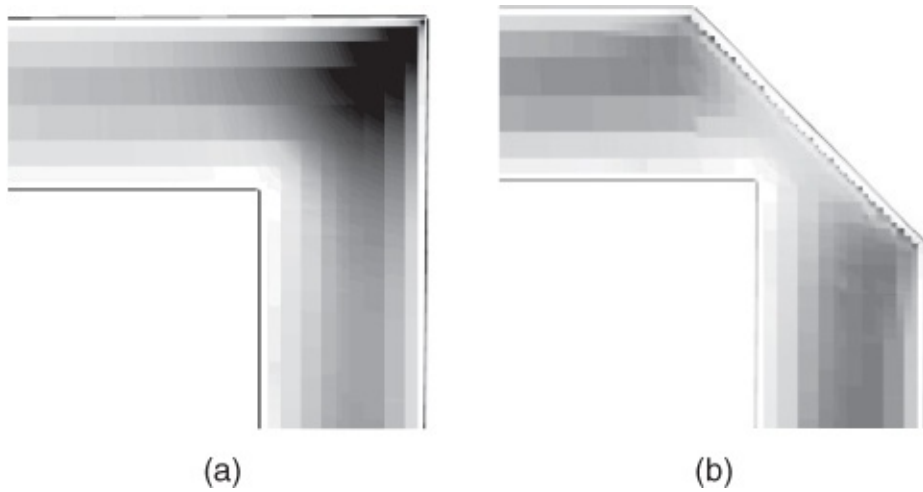


**Figure 9.10** Magnitude of the current densities on (a) a right-angled bend and (b) an optimally mitered bend (in both cases on alumina substrate at 10 GHz). The dark region corresponds to low current density.

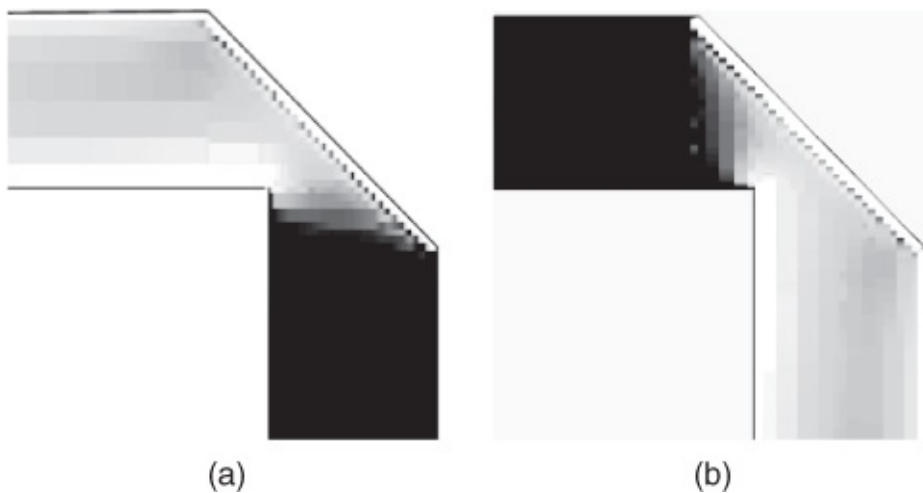


**Figure 9.11** Magnitude of the (a) horizontal and (b) vertical current densities on an optimally mitered right-angled bend under the same conditions as those shown in [Figure 9.10](#).

From [Figure 9.10](#)(b) the greatly improved current distribution when an optimum miter is applied is clearly evident, compared to the uncompensated case shown in [Figure 9.10](#)(a). The physical origins of what leads to an optimum miter can be seen by examining [Figures 9.12](#) and [9.11](#), where the magnitudes of the horizontal and vertical current components are plotted. It can be seen that the mitered edge of the microstrip bend acts like a reflector. The overhang of the reflector, the fact that the mitered edge extends beyond the microstrip (that is the projection of the miter is greater than the microstrip width), corresponds very closely to the effective width of the microstrip used in the planar waveguide model for microstrip.

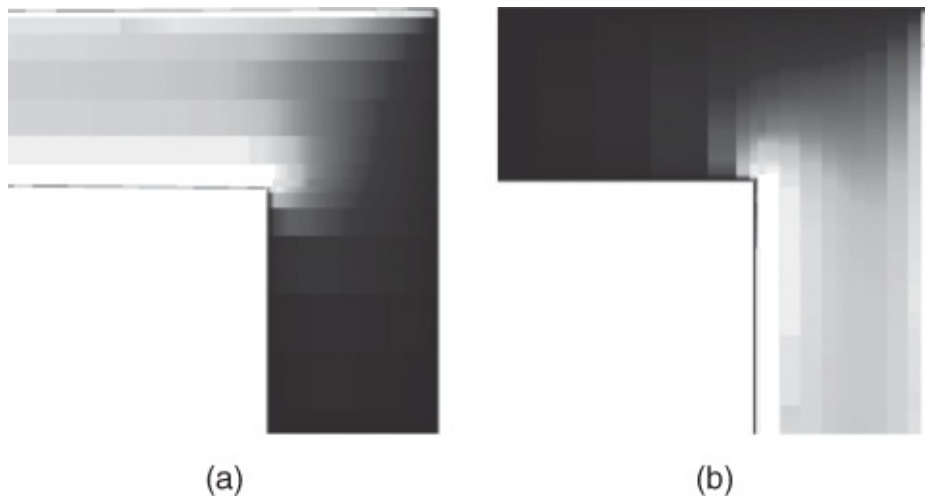


**Figure 9.12** Magnitude of the (a) horizontal and (b) vertical current densities on a right-angled bend under the same conditions as those shown in [Figure 9.10](#).

## 9.4 Step Changes in Width (Impedance Step)

It is necessary for microstrip lines to experience a width change in many circuits. This is clearly so even for the simple case of a quarter-wave transformer, and several such changes are demanded in transistor amplifier circuits such as that shown in [Figure 9.1](#). Couplers, filters, mixers, and oscillators provide further examples.

These forms of discontinuities have been fairly widely investigated and characterized [9]. Like the microstrip bend, the shunt capacitance due to corners is the dominant equivalent circuit parameter and edge-current disturbances occur again, which give rise to equivalent inductances.

### 9.4.1 The Symmetrical Microstrip Step

This is illustrated in [Figure 9.13\(a\)](#), with an equivalent circuit in [Figure 9.13\(b\)](#) and parameter variations in [Figure 9.14](#).

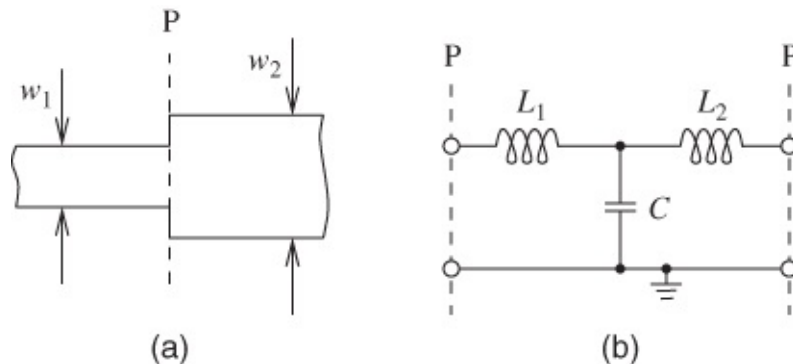


**Figure 9.13** Structure and equivalent circuit of the symmetrical microstrip step (change in width): (a) structure and nomenclature; and (b) equivalent circuit.

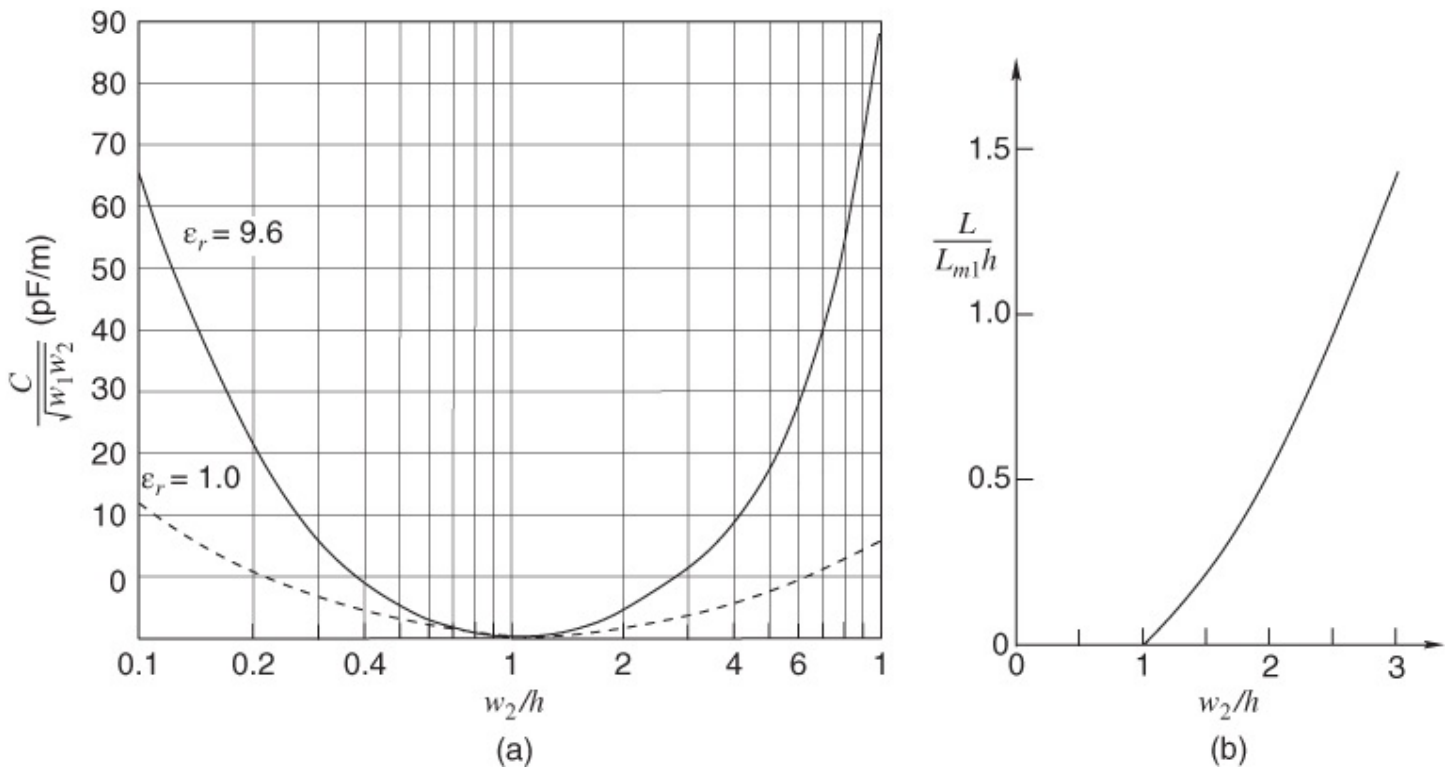


**Figure 9.14** The symmetrical step, parameter variations: (a) capacitance; and (b) inductance for  $w_1/h = 1.0$  and  $Z_{01} = 50 \Omega$ . (a) adapted from Benedek and Silvester (1972) [9], figure 8, p. 733. Reprinted with permission from IEEE. (b) adapted from Thomson *et al.* (1976) [18], figure 4, p. 653. Reprinted with permission of IEEE.

We previously interpreted a discontinuity capacitance in terms of an equivalent extra length of the microstrip (for the foreshortened open circuit see [Section 9.2.1, Figure 9.3](#)). This approach can be used again for the step, where the principal influence of the capacitance is to increase the effective length of the wider line (width  $w_2$ ). Since the changes and values are all quite small, the fully foreshortened open-circuit result can be used in a modified form as given by the following expression:

$$\ell_{es} \approx \ell_{eo} \left( 1 - \frac{w_1}{w_2} \right) \quad 9.28$$

where  $\ell_{eo}$  is obtained from Equations (9.7) or (9.9).

Gupta *et al.* [15] have shown how to account approximately for the inductances. Where  $L_{m1}$  and  $L_{m2}$  are the inductances per unit length of the appropriate microstrips, having widths  $w_1$  and  $w_2$ , the discontinuity inductances are given respectively by the following relations:

$$L_1 = \frac{L_{m1}}{L_{m1} + L_{m2}} L \quad 9.29$$

and

$$L_2 = \frac{L_{m2}}{L_{m1} + L_{m2}} L \quad 9.30$$

The equivalent extra lengths of microstrip are then given by

$$\frac{\ell_{es1}}{h} = \frac{\ell_{es2}}{h} = \frac{L}{(L_{m1} + L_{m2})h}. \quad 9.31$$

Garg and Bahl [7] obtained design formulas for both  $C$  and  $L$ . The following expressions for  $C$  were derived by curve-fitting earlier theoretical results:

For  $\epsilon_r \leq 10, 1.5 \leq w_2/w_1 \leq 3.5$ :

$$\frac{C}{\sqrt{w_1 w_2}} = (10.1 \log \epsilon_r + 2.33) \frac{w_2}{w_1} - 12.6 \log \epsilon_r - 3.17 \text{ pF/m.} \quad 9.32$$

For  $\epsilon_r = 9.6, 3.5 \leq w_2/w_1 \leq 10$ :

$$\frac{C}{\sqrt{w_1 w_2}} = 130 \log(w_2/w_1) - 44 \text{ pF/m.} \quad 9.33$$

The error involved in applying Equation (9.32), which applies to relatively slight steps ( $w_2/w_1 \leq 3.5$ ), can be as high as 10%. The error in Equation (9.33) is claimed to be less than 0.5%.

Garg and Bahl's expression for the inductance is

$$\frac{L}{h} = 40.5 \left( \frac{w_1}{w_2} - 1.0 \right) - 75 \frac{w_1}{w_2} + 0.2 \left( \frac{w_1}{w_2} - 1.0 \right)^2 \text{nH/m.} \quad 9.34$$

This formula is quoted as having an accuracy of better than 5%, provided that

$$w_1/w_2 \leq 5.0 \text{ and } w_2/h = 1.0. \quad 9.35$$

Once more it should be stressed here that because the discontinuity quantities themselves represent second-order design corrections these error bounds on the values are usually of little if any significance in practice. Appropriate extra equivalent lengths of the microstrip line can then be determined in terms of  $L$  and  $C$ .

We present SONNET simulations here to show the current distribution around a step. From [Figure 9.15](#) it is clear that significant current flow disturbances occur in the vicinity of a step in width.



**Figure 9.15** Magnitude of the current densities for symmetrical step in width: (a) normalized scale (b) longitudinal current; and (c) transverse current. The signal is 10 GHz and the microstrip line is on alumina.

### 9.4.2 The Asymmetrical Step in Microstrip

The geometry of this is shown in [Figure 9.16](#), together with the appropriate equivalent circuit. As a first approximation the equivalent circuit parameter variations may be taken as the same as those for the symmetrical step. The actual parameter values will be about half of the values obtained for the symmetrical step.

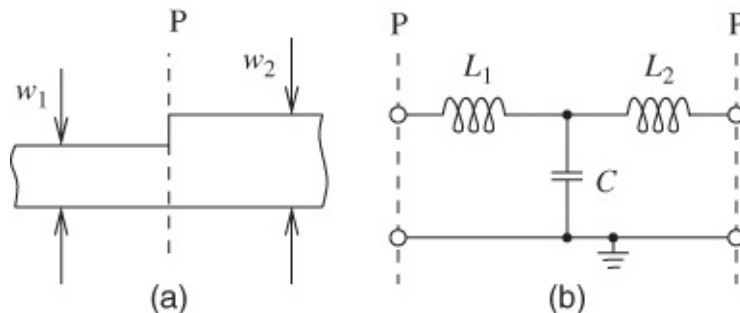


**Figure 9.16** Structure and equivalent circuit of the asymmetrical microstrip step.

## 9.5 The Narrow Transverse Slit

A narrow slit, cut transversely into the microstrip width, yields a predominantly series inductance effect. This structure has been investigated by Hoefer [19], and it may be used to compensate for excess capacitance at discontinuities or to fine-tune lengths of microstrip such as stubs. The appearance of the slit and its equivalent circuit are shown in [Figure 9.17](#).

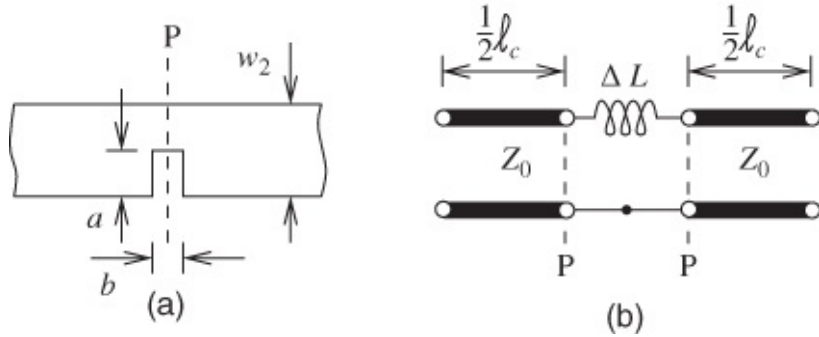


**Figure 9.17** The narrow transverse slit: (a) actual slit; and (b) equivalent circuit.

In Hoefer's analysis, dispersion and capacitive effects are neglected and a non-magnetic substrate is taken. A dipole field perturbation method, originally developed by Wheeler [20], is used in the analysis. A parallel-plate waveguide model with magnetic side walls is also employed. The reader is recommended to see Wheeler [20] for further details, since only the resulting expressions and their use will be described here. The final formula for the inductance is

$$\frac{\Delta L}{h} = \frac{\mu_0 \pi}{2} \left( \frac{a'}{A} \right)^2 \quad 9.36$$

where

$$\frac{a'}{A} = 1 - \frac{Z_{0(\text{air})}}{Z'_{0(\text{air})}}. \quad 9.37$$

For design, the procedure is then as follows:

- Calculate the characteristic impedance of the air-filled microstrip line of width  $w$ , giving  $Z_{0(\text{air})}$ .
- Calculate the characteristic impedance of an air-filled microstrip line of width  $(w - a)$ , giving  $Z'_{0(\text{air})}$ .
- Evaluate  $a'/A$  with these results, (a) and (b), using Equation (9.37), and hence calculate  $\Delta L$  using Equation (9.36).

As an example a slit of relative penetration ( $a/w$ ) = 0.5 can be calculated. Considering such a slit in a  $50 \Omega$  microstrip line on 0.635 mm thick alumina ( $w/h = 1$  when  $\epsilon_r = 9.6$ ), the inductive reactance of this slit is  $j3.7 \Omega$  at 10 GHz.

In the case of a relatively small slit width  $b$ , the capacitance may be significant. Using the calculation techniques for series gaps in microstrip, as described in [Section 9.2.2](#), the capacitance of the slit may be approximately determined as  $(a/w)C_2$ . For the example calculated above, the capacitive reactance is approximately  $-j320 \Omega$ , which would represent a negligible shunt reactance effect in many applications.

Another limitation occurs as the slit is progressively widened. Eventually, the structure looks

like a short microstrip line of width  $(w - a)$  asymmetrically stepped to the main microstrips of widths  $w$ . Hoefer [19] suggests that a lumped inductance, independent of  $b$ , is approximately valid while  $b < h$ .

Experimental results for an RT-duroid 5880 substrate, with  $w/h = 2.0$  and a range of  $a/w$  values, show good agreement with the theory.

## 9.6 Microstrip Junctions

### 9.6.1 The Microstrip T Junction

This junction necessarily occurs in a wide variety of microstrip circuits. Examples range through stub-matching elements, stub filters, branch-line couplers, and microstrip antenna element feeds. The appearance and a fairly elementary equivalent circuit are shown in [Figure 9.18](#). The inductances and capacitance are included for identical reasons to those described previously in respect of other discontinuities. However, one new element has been introduced here: the transformer.

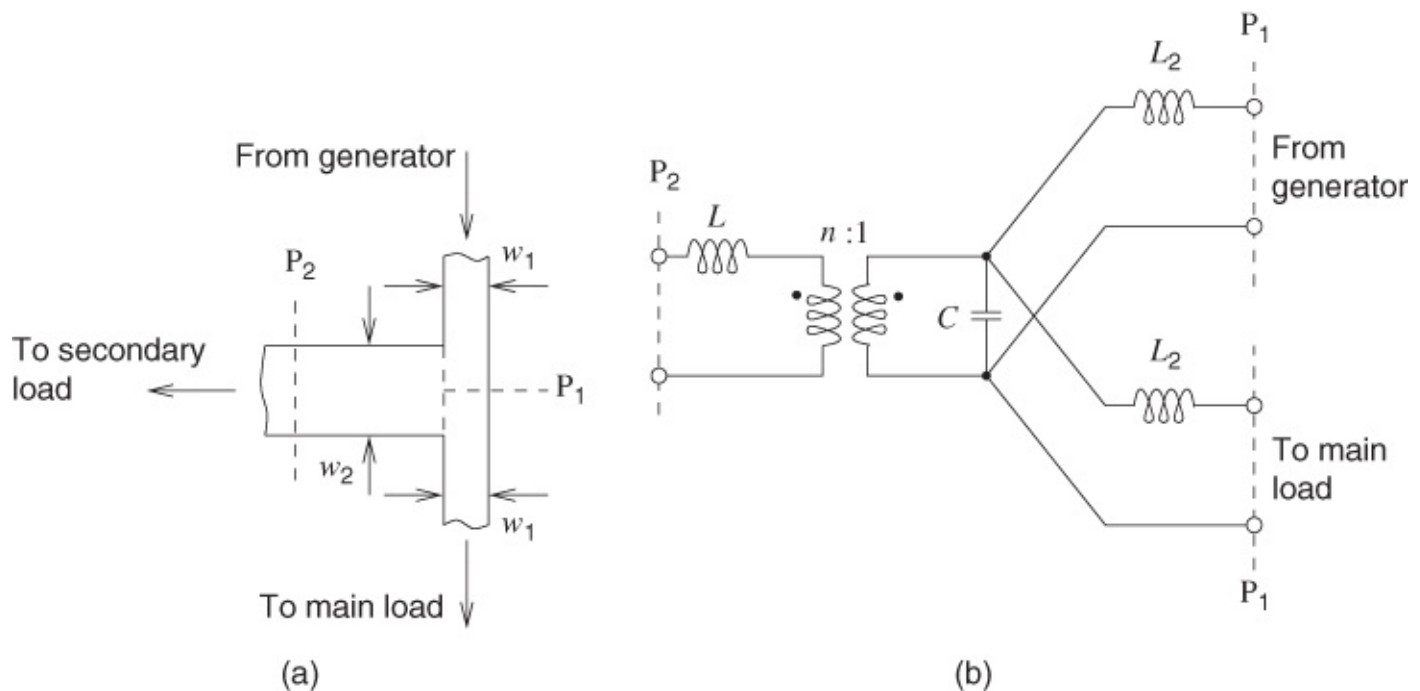


[Figure 9.18](#) The T junction in microstrip: (a) structure and nomenclature; and (b) equivalent circuit.

It is necessary to determine the effect, on the main circuit from the generator through the to main load, of a secondary load connected to the shunt branch arm (width  $w_2$ ). At very low frequencies, any such load will, of course, appear directly connected across the through circuit, that is, when

$$f \rightarrow 0, n \rightarrow 1.0. \quad 9.38$$

At microwave frequencies a load impedance connected at some point along the shunt branch

will appear both transformed by the ratio  $n_2$  and located at some specified electrical length from the physical junction. The inductances, the capacitance, and the transformation ratio have all been deduced experimentally and, in a number of cases, theoretically [12, 13, 16, 17]. It is not intended that all the information be provided here and only the capacitance and transformation ratio results are given (see [Figure 9.19](#)). Note that, for moderate-to-high impedance branch lines, the junction capacitance becomes reduced below that of either microstrip line capacitance per unit length. Thus capacitance is “taken out” of the junction and the equivalent circuit capacitance is negative.

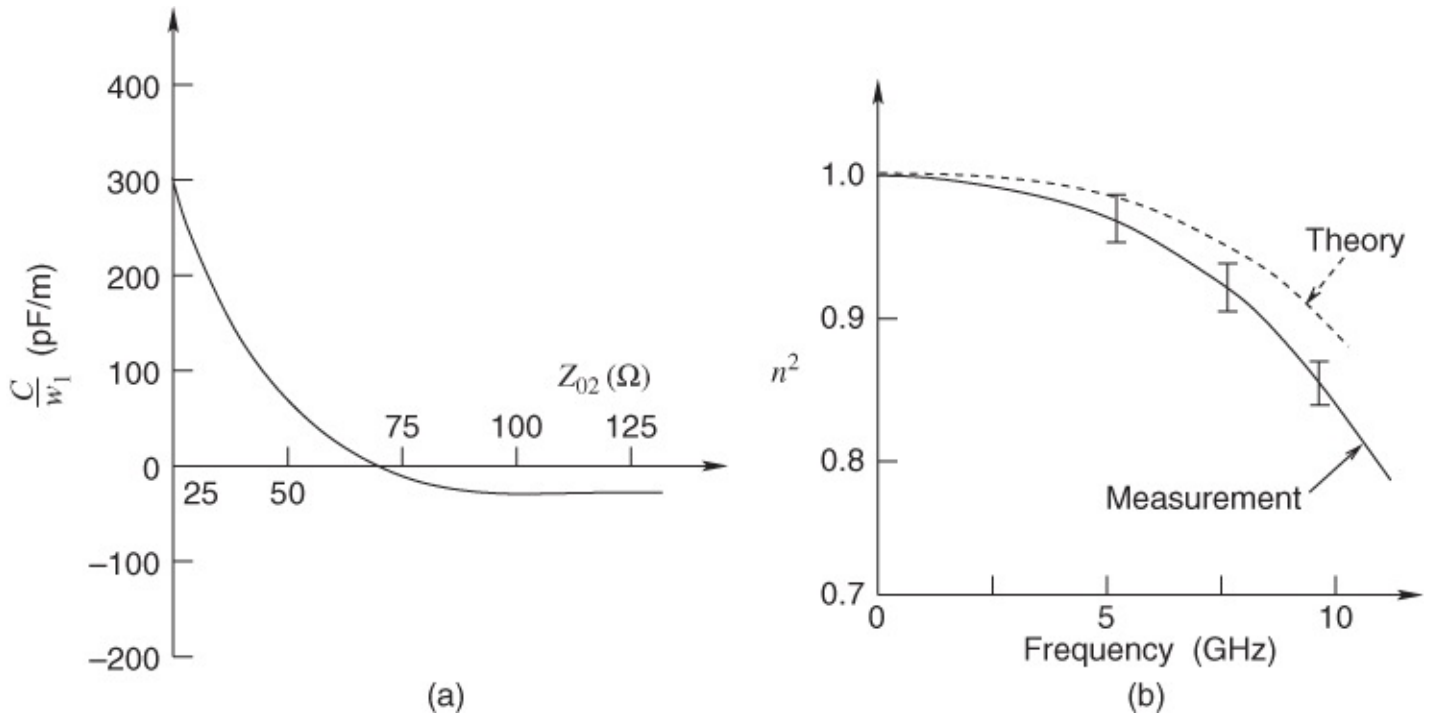


**Figure 9.19** Parameter trends for the T junction: (a)  $\epsilon_r = 9.9$ ; and (b)  $\epsilon_r = 9.8$  (a) Adapted from Silvester and Benedek (1973) [12], figure 8, p. 345. Reprinted with permission of IEEE. (b) Adapted from Easter *et al.* (1978) [17], figure 17, p. 82. Reprinted with permission of the Institution of Engineering and Technology.

The small difference of 0.1 in the permittivities should not matter much in practice if the two sets of results were both required when carrying out a design on an appropriate alumina substrate. It is observed that a substantial discrepancy exists between the measured and theoretical results for  $n^2$ , and it is not clear whether this is due mainly to experimental or to theoretical error. Judging by the given error bounds (only three points), it may be that Vogel's theory [17] is not fully adequate here.

Formulas for the capacitance and for the inductances are given by Garg and Bahl [7] but not for the transformation ratio  $n$ . Semi-empirical expressions have also been given by Hammerstad and Bekkadal [5, 21] for shifts in the locations of the electrical reference planes, as well as  $n$ , and it is these results that are more useful for circuit design than the equivalent lumped parameters.

The reference planes and dimensions associated with Hammerstad and Bakkadal's method are

shown in [Figure 9.20](#), where the effective width (see [Section 7.7.2](#)) of either line is

$$w_{\text{eff}1,2} = \frac{h\eta}{Z_{0(1,2)} \sqrt{\epsilon_{\text{eff}1,2}}}. \quad 9.39$$

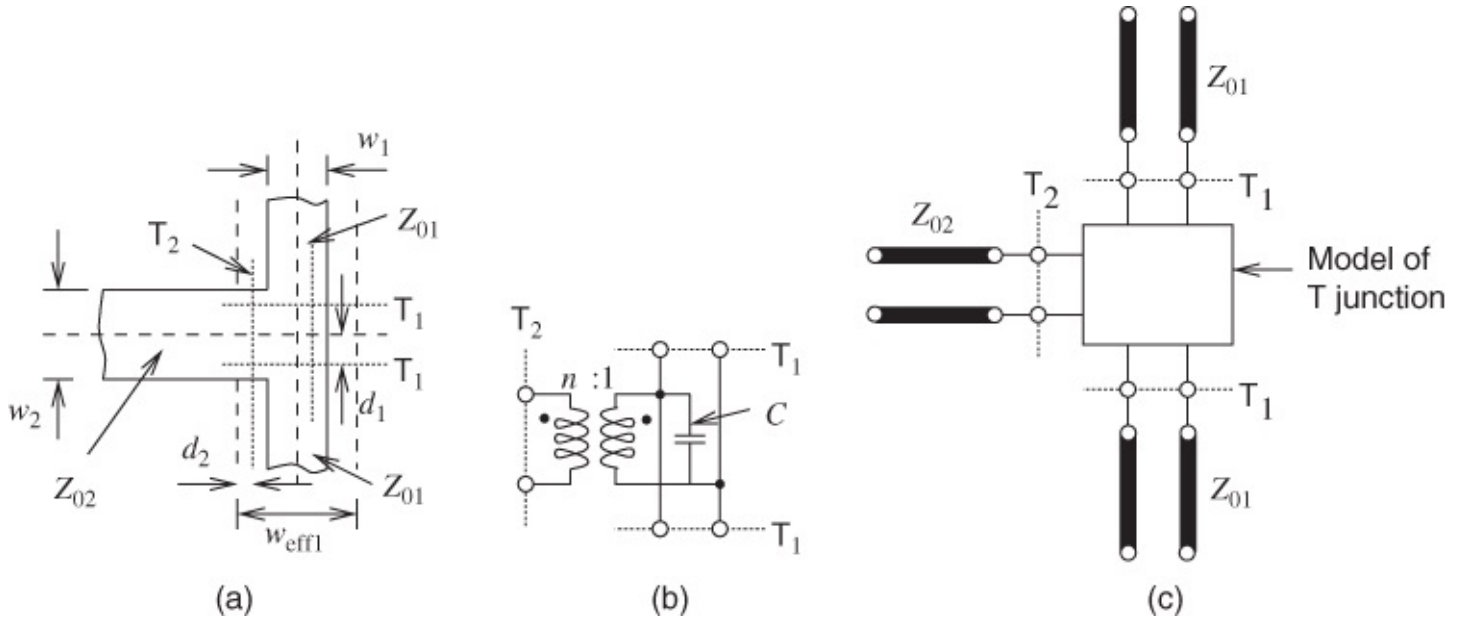


**Figure 9.20** T junction: (a) reference planes,  $T_1$  and  $T_2$ , effective width  $w_{\text{eff}1}$ , and dimensions; (b) model of T junction; and (c) model connected to transmission lines.

The transformation ratio  $n$  is given by

$$n^2 = \left\{ \frac{\sin [\pi (w_{\text{eff}1}/\lambda_{g1}) (Z_{01}/Z_{02})]}{\pi (w_{\text{eff}1}/\lambda_{g1})(Z_{01}/Z_{02})} \right\}^2 \left\{ 1 - \left[ \pi \left( \frac{w_{\text{eff}1}}{\lambda_{g1}} \right) \left( \frac{d_2}{w_{\text{eff}1}} \right) \right]^2 \right\}. \quad 9.40$$

The displacement of the reference plane for the primary line (1) is

$$\frac{d_1}{w_{\text{eff}2}} = 0.05 \frac{Z_{01}}{Z_{02}} n^2. \quad 9.41$$

The displacement of the reference plane for the secondary arm (2) is

$$\begin{aligned} \frac{d_2}{w_{\text{eff}1}} &= 0.5 - \left[ 0.076 + 0.2 \left( \frac{2w_{\text{eff}1}}{\lambda_{g1}} \right)^2 \right. \\ &\quad \left. + 0.663 \exp \left( -1.71 \frac{Z_{01}}{Z_{02}} \right) - 0.172 \ln \left( \frac{Z_{01}}{Z_{02}} \right) \right] \frac{Z_{01}}{Z_{02}}. \end{aligned} \quad 9.42$$

Also, the shunt capacitance is determined by the following expressions: For the condition  $Z_{01}/Z_{02} \leq 0.5$ :

$$\frac{\omega C \lambda_{g1}}{Y_{01} w_{\text{eff}1}} = \left( \frac{2w_{\text{eff}1}}{\lambda_{g1}} - 1 \right) \frac{Z_{01}}{Z_{02}}. \quad 9.43$$

For the condition  $Z_{01}/Z_{02} \geq 0.5$ :

$$\frac{\omega C \lambda_{g1}}{Y_{01} w_{\text{eff}1}} = \left( \frac{2w_{\text{eff}1}}{\lambda_{g1}} - 1 \right) \left( 2 - 3 \frac{Z_{01}}{Z_{02}} \right). \quad 9.44$$

Actual accuracies for these expressions are not quoted, but their discrepancies rise when

$$\frac{2w_{\text{eff}1}}{\lambda_{g1}} > 0.3, \quad 9.45$$

that is, when the wavelength becomes small enough (frequency large enough) for this condition to occur.

It would be useful to attempt to modify Hammerstad's expressions so that a better fit is obtained at higher frequencies. One might, for example, note that if  $w_{\text{eff}}$  in Equation (9.42) is replaced by the frequency-dependent value given by Equation (7.60) then the magnitude of the term  $(w_{\text{eff}1}/\lambda_{g1})$  rises more strongly with frequency, hence reducing  $d_2$  as desired. Some further investigations are required in this area.

Another limitation to the accuracy of the expressions is imposed by the impedance ratio  $Z_{01}/Z_{02}$ . When this exceeds about 2.0 the calculated values of  $d_2$  become too large and an improved accuracy is obtained when the ratio  $Z_{01}/Z_{02}$  is replaced by its inverse, that is,  $Z_{02}/Z_{01}$ . Some useful work has been carried out to compensate T junctions and thereby improve the performance of circuits using them. This is discussed in the next section.

## 9.6.2 Compensated T Junctions

As we have seen in the preceding discussion, direct T junctions inherently involve substantial discontinuities that significantly influence circuit behavior. On many occasions the implementation of the direct T junction, without modification, is unavoidable. However, in a similar manner to the mitered compensation of the right-angled bend, it is possible to introduce adjustments around a T junction that will partially compensate for the effects of the direct discontinuities.

One simple way to at least compensate the capacitance of a T junction is to introduce a slit across the width of the main-through microstrip line, opposite the branch arm. The characteristics of such a slit were discussed in [Section 9.5](#). Kompa [22] has shown further that a comparatively wide “slot” ( $b \approx w_2$ ) in this position, that is, a rather wider slit, strongly affects the transmission of higher-order modes in the main line and leads to enhanced skirt sensitivity of filters composed of stubs with such modified T junctions.

Dydyk [23] described a T junction compensation technique that appears to work well in the case of a branch-line microstrip coupler circuit. Dydyk's aim was to modify the microstrip lines in the vicinity of the junction in order to compensate for reference plane shifts, at least over a specified range of frequencies. The treatment of the junction can exclude any discussion of radiation loss with little error in circuit performance results, at least up to a frequency of 17 GHz. The compensated T junction takes on the form shown in [Figure 9.21](#). A microstrip

branch-line coupler designed using these principles yielded the following performance over the frequency band 16–18 GHz:

Insertion loss	3.5–4.0 dB over entire band
Isolation	> 20 dB over entire band
Return loss	10 dB (at 17.5 GHz), otherwise 10 to 25 dB

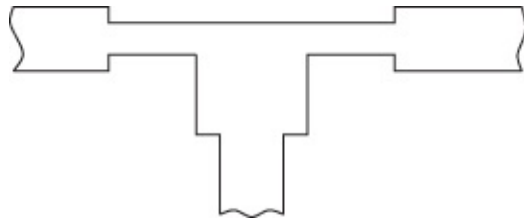


**Figure 9.21** A compensated form of T junction.

The very “flat,” almost frequency-independent, insertion loss and isolation are attributed to the compensated junction design.

### 9.6.3 Cross Junctions

There are occasions where microstrip lines are required to separate in the shape of a cross, forming a four-port circuit. Examples can be seen in the arrangement indicated in [Figure 9.1](#). In general, a cross junction may be symmetrical or asymmetrical, where the lines forming the cross do not all have the same widths.

In attempting to design a single stub to be fabricated in microstrip it can be found that the width of the stub line is wide enough to sustain transverse resonance modes at the higher frequencies of operation, see [Section 7.8.1](#) and Equation (7.81). One way to overcome this problem is to use two stubs placed on each side of the microstrip instead of the original one. The impedance of each new stub will be twice that of the originally intended single stub, and thus the widths will be greatly reduced. A cross junction is therefore formed.

Theoretical and experimental agreement is not good, especially for some inductance parameters associated with the equivalent circuits of cross junctions. As a result of this it does not appear sensible to give design formulas which merely fit theoretical curves. Instead, some useful engineering design information is given for the asymmetric cross. The asymmetric cross is the most important form for practical microstrip circuits, and is shown in [Figure 9.22](#) together with its equivalent circuit. Microstrip resonator measurement techniques, described in [Chapter 18](#), have proved to be very powerful in the characterization of certain specific cross junctions. Akello [24] has used such techniques to show that appropriate T junction inductance parameters can be judiciously applied to the cross. The capacitance  $C_T$  presents prediction difficulties (theoretical treatment is available for symmetrical crosses only). Akello indicates that  $C_T$  can be approximated to within 8% by using the simple relationship

$$C_T \approx \frac{3}{4} C_m$$

where  $C_m$  is the capacitance per unit length of the (uniform) microstrip line on port 4 of the cross junction. This appears to work quite well for the range:

$$1.32 \leq \frac{w_4}{h} \leq 3.0. \quad 9.47$$

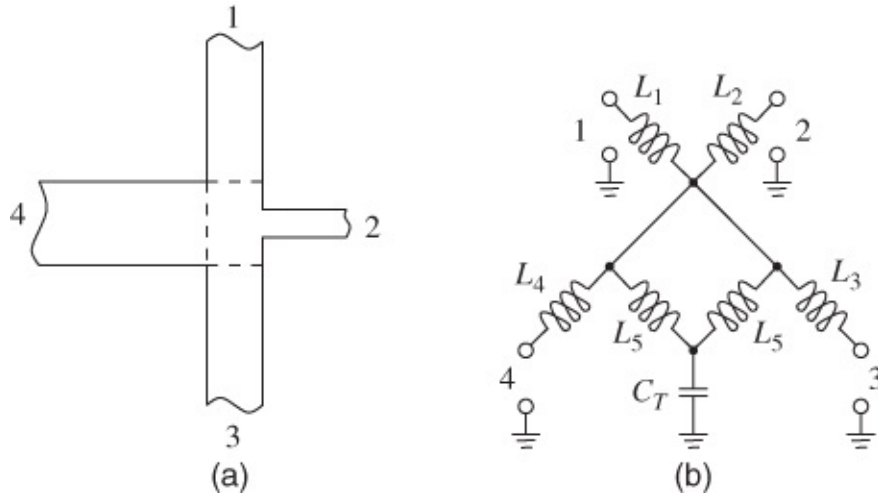


**Figure 9.22** The asymmetric cross-over junction: (a) structure; and (b) equivalent circuit.

The capacitance  $C_m$  may be calculated from expressions given earlier (see Equation (2.32) in [Chapter 2](#)). Specifically,  $Z_0 = 1/(v_p C_m)$ , whence:

$$C_m = \frac{c}{Z_0 \sqrt{\epsilon_{\text{eff}}}}.$$

( $Z_0$  and  $\epsilon_{\text{eff}}$  are well known at an early stage in design.)

Akello [24] tabulated values of all the various equivalent circuit elements and has shown how to apply them in practical situations. In particular, computer simulation was used to indicate that discontinuity reactances attributable to steps and cross-overs are significant, and can be incorporated into response prediction programs. X-band (8–12 GHz), narrowband, and wideband single-stage and double-stage transistor amplifiers are considered.

## Cross-overs

Examination of the coupling effects that occur with cross-overs illustrates the origin of crosstalk in complicated interconnection networks. In [Figure 9.23](#) the magnitudes of the currents occur when a strip on one metal layer, the top metal, crosses a strip on another metal layer, which in turn is above a ground plane. The top layer shown in [Figure 9.23\(b\)](#) is driven from the left with a 30 GHz sinusoidal signal. The total current on the top interconnect is little affected by the cross junction discontinuity, but it is clear that the distribution across the strip is affected and this occurs following the cross-over for a short distance. The most significant effect that occurs is that current is induced on the bottom strip and this has a peak magnitude that is 23% of that of the peak current on the top strip. The origins of this phenomenon can be understood by considering the instantaneous currents and charges on the strip. These are shown

in [Figure 9.24](#) at one instant in time, again with the top strip driven on the left by a 30 GHz signal. In the region of the cross-over the signal on the top strip is transitioning from positive to negative, as can be seen from the current profile shown in [Figure 9.24\(c\)](#). In the region of the cross-over the charges on the top strip are negative, see [Figure 9.24\(d\)](#). Thus, there is an electric field which in the absence of the bottom strip begins on the ground plane and terminates on the top strip. However, with the top strip and in the region of the cross-over, some of the electric field begins on positive charges on the bottom strip and terminates on the negative charges on the top strip. The positive charges on the bottom strip are drawn in from the regions of the bottom strip above and below the cross junction, see [Figure 9.24\(f\)](#). This movement of charge constitutes current flow towards the cross junction, see [Figure 9.24\(e\)](#). Thus the signal on the top strip effectively induces generators on the bottom strip.

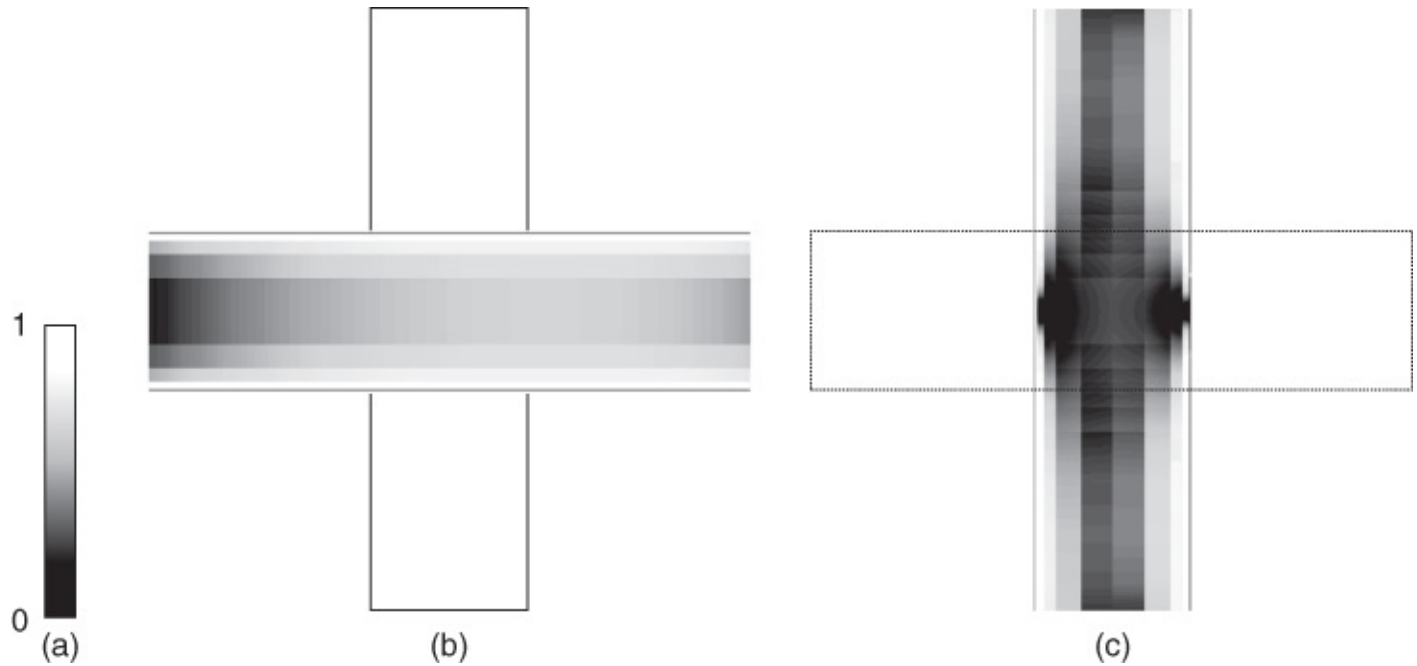


**Figure 9.23** Magnitude of the current densities on the strips of a symmetrical cross-over junction: (a) normalized scale; (b) current on the top metal; and (c) current on the lower metal layer (between the top metal and the ground plane).

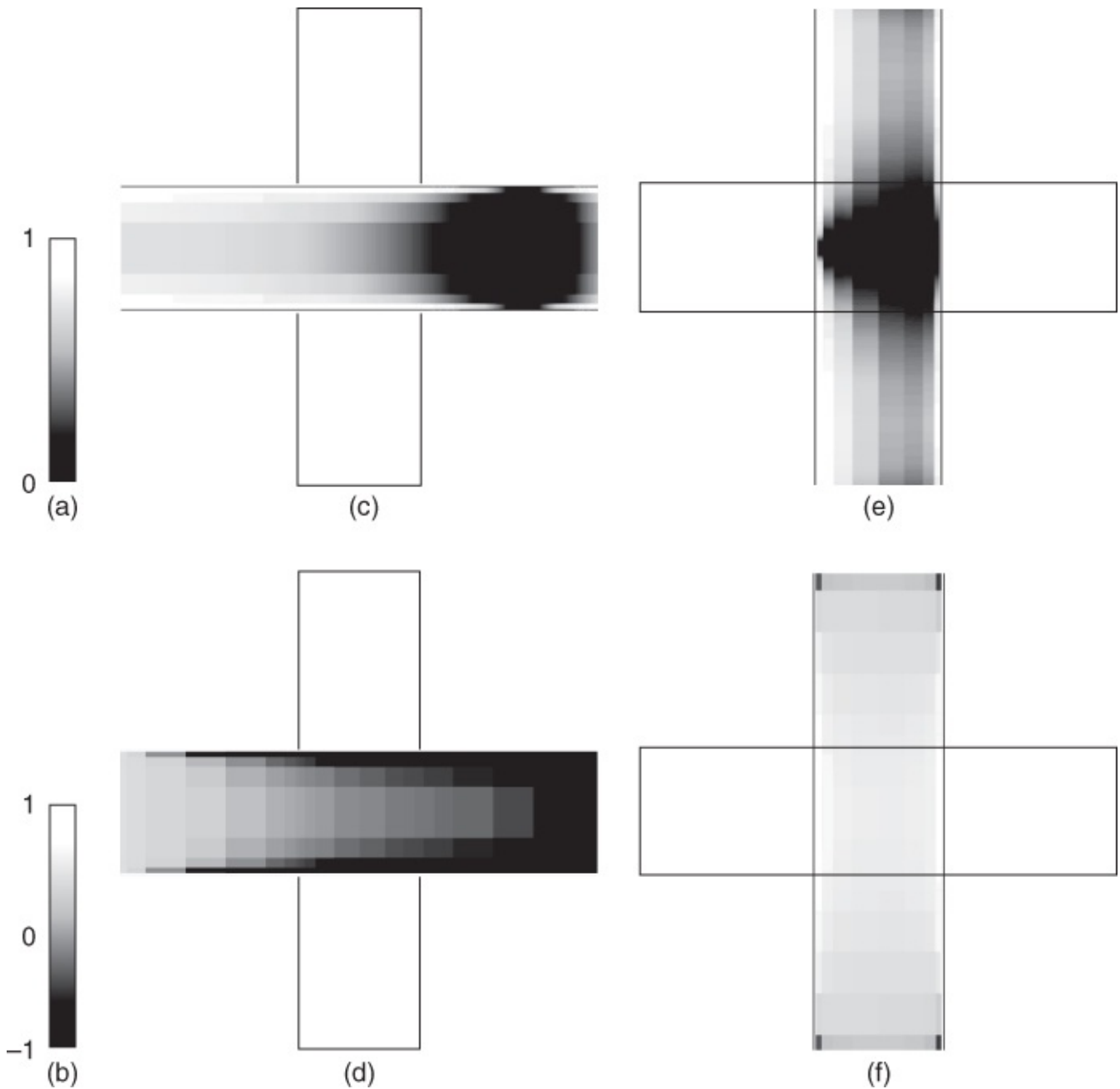


**Figure 9.24** Instantaneous current and charges on the strips of a symmetrical cross-over junction: (a) normalized current scale; (b) normalized charge scale; (c) current on the top metal; (d) charge on the top metal; (e) current on the lower metal; and (f) charge on the lower metal.

Many coupling effects can be viewed in the same way that the cross junction discontinuity can be understood by interrupting the electric field and so inducing charges. The inducement of charges constitutes current flow and thus a signal on the victim nets.

#### 9.6.4 Open Circuits and Series Gaps

We have already seen here that the quasi-static results provide quite accurate design information, particularly for the capacitive effects, at frequencies approaching 18 GHz. For example, the commonly encountered open circuit (see [Section 9.2.1](#)) has been fairly

extensively investigated, both theoretically and experimentally. More effort has been expended in this regard than for any other discontinuity, for the good reason that the open-circuit termination has many applications in both circuits and microstrip antennas. With an emphasis on the latter, James and Henderson [25] published a paper describing detailed research results. The values and trends shown in Figure 10 of their paper are of particular interest. There is a consistent trend for alumina substrates amounting to a peaked behavior with frequency; two of the curves reported by James and Henderson are reproduced here as [Figure 9.25](#), with the horizontal axis denormalized for the case of a 0.65 mm thick alumina substrate. Some experimental data are also shown, which originate from unpublished results obtained by the authors.

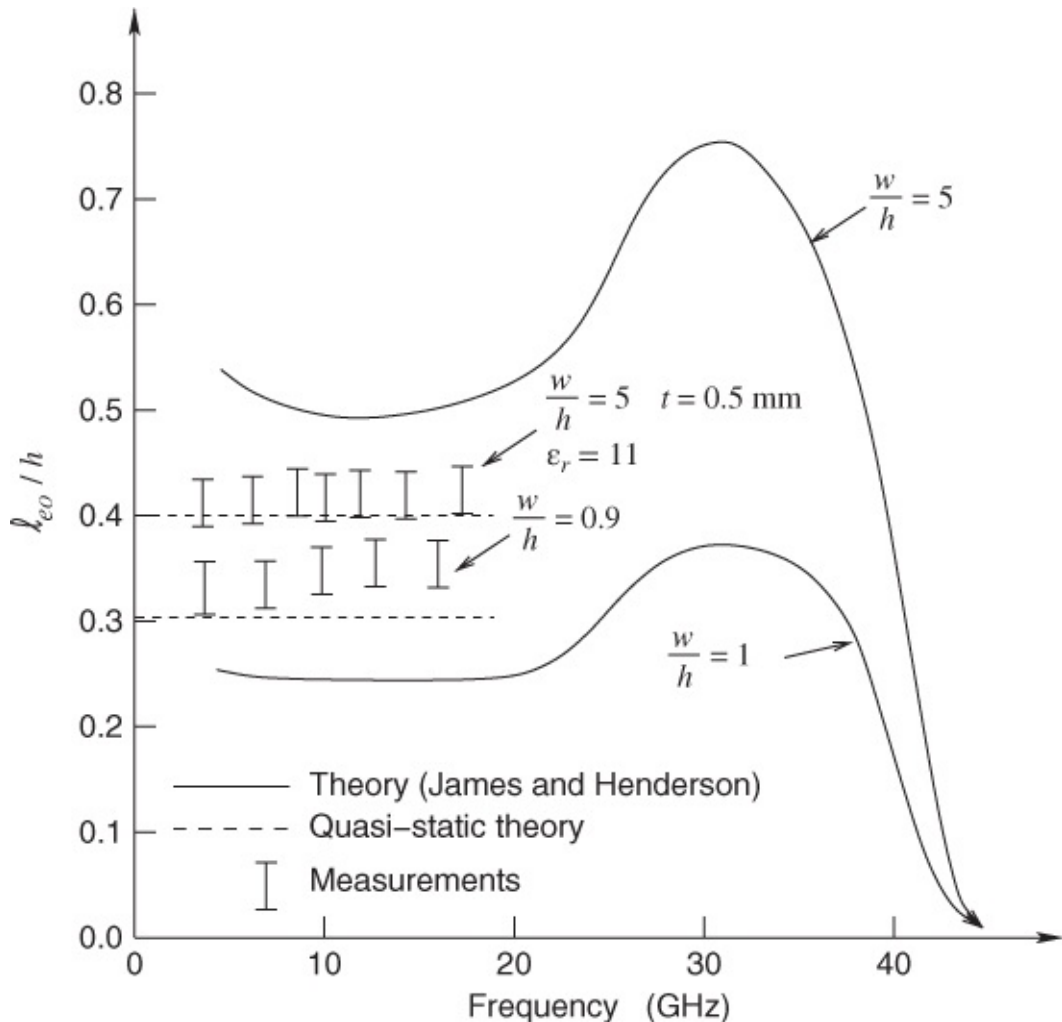


**Figure 9.25** Open-circuit normalized equivalent end-effect length ( $\ell_{eo}/h$ ) as a function of frequency. The data refer to a  $t = 0.65$  mm thick alumina substrate with  $\epsilon_r = 10$ , except for one case where the values were  $t = 0.5$  mm and  $\epsilon_r = 11$ , as indicated. Adapted from James and Henderson (1979) [25], figure 10, p. 214. Reprinted with permission of IET.

The measured results were obtained by a resonator method that will be described in [Chapter 18](#). They are very tedious to perform and require scrupulous attention to repeatability and high accuracy of manufacture. Here there is about 19% scatter in the results obtained on sapphire substrates and about 15% on alumina. Even so, it is clear that the measured results differ quite

markedly from the frequency-dependent theoretical predictions. Results from quasi-static calculations are shown as horizontal chain lines in [Figure 9.25](#). These fit the measurements fairly well up to 18 GHz, although the calculated results are slightly lower in both cases.

It would be useful and interesting to investigate experimentally the behavior in the 20–40 GHz range for microstrip open circuits on alumina. Resonator methods, described in [Chapter 18](#), might be attempted, but these pose considerable difficulties at such high frequencies because of the presence of higher-order modes. It may even be possible for transverse-resonant modes to become excited. A better approach might be to model the structure for measurement at much lower frequencies.

Other researchers, notably Itoh [26], have theoretically deduced a nonlinear  $\ell_{eo}/h$  variation with frequency. Itoh's results also show up-turns in  $\ell_{eo}/h$  at both lower and higher frequencies, but the absolute values of his end-effect lengths were substantially lower than any other reported data. This is partially due to the shielded microstrip resonator considered.

Katehi and Alexopoulos [27] described the frequency-dependent characteristics of microstrip discontinuities on a theoretical basis, concentrating largely on open-circuited lines and also on the series gap. They evaluate the current distributions in the vicinity of the discontinuities by means of Pocklington's integral equation, the dyadic Green's function, and impedance matrices. They extend their calculations to 50 GHz, and derive results for radiation conductances, equivalent length extensions, and gap capacitances.

The results obtained by Katehi and Alexopoulos are shown in [Figures 9.26–9.29](#). The radiation conductances both rise with frequency, as should be anticipated from physical considerations. It is interesting that the equivalent length extension (“excess length”) rises slightly, to peak at about 40 GHz, then falls with frequency as predicted elsewhere independently.

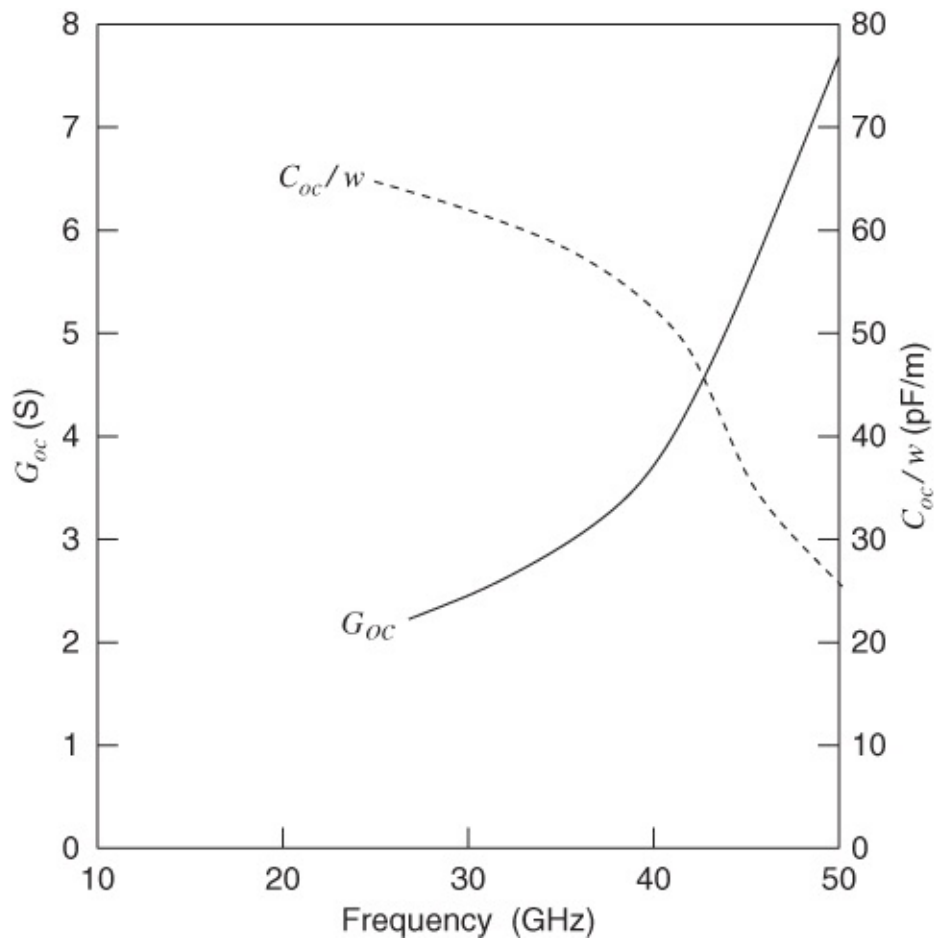


**Figure 9.26** Radiation conductance  $G_{oc}$  and normalized capacitance  $C_{oc}/w$  of an open-circuited microstrip line as functions of frequency ( $\epsilon_r = 9.6$ ,  $w/h = 1$ ,  $h = 0.6$  mm). Adapted from Katehi and Alexopoulos (1985) [27], figure 4, p. 1032. Reprinted with permission of IEEE.

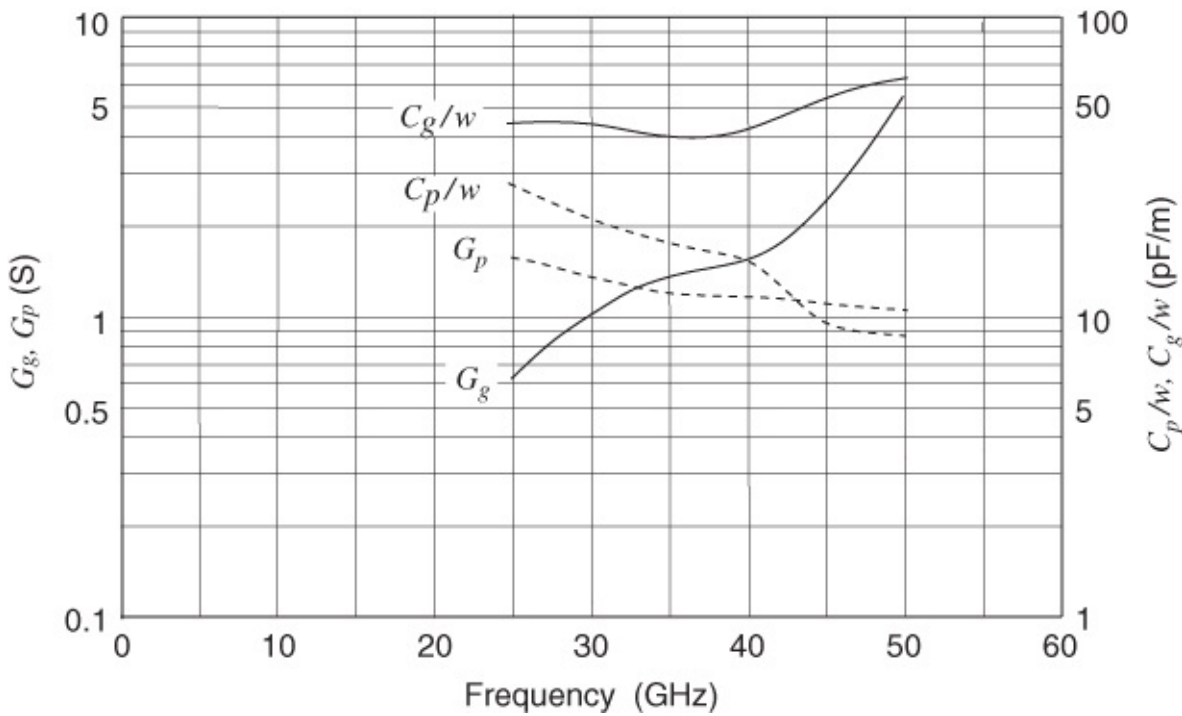


**Figure 9.27** Gap-discontinuity radiation conductances  $G_g$  and  $G_p$ , and normalized capacitances  $C_g/w$  and  $C_p/w$  as functions of frequency ( $\epsilon_r = 9.6$ ,  $w/h = 1$ ,  $h = 0.6$  mm,  $s/h = 0.3762$ ). Adapted from Katehi and Alexopoulos (1985) [27], figure 7, p. 1032. Reprinted with permission of IEEE.

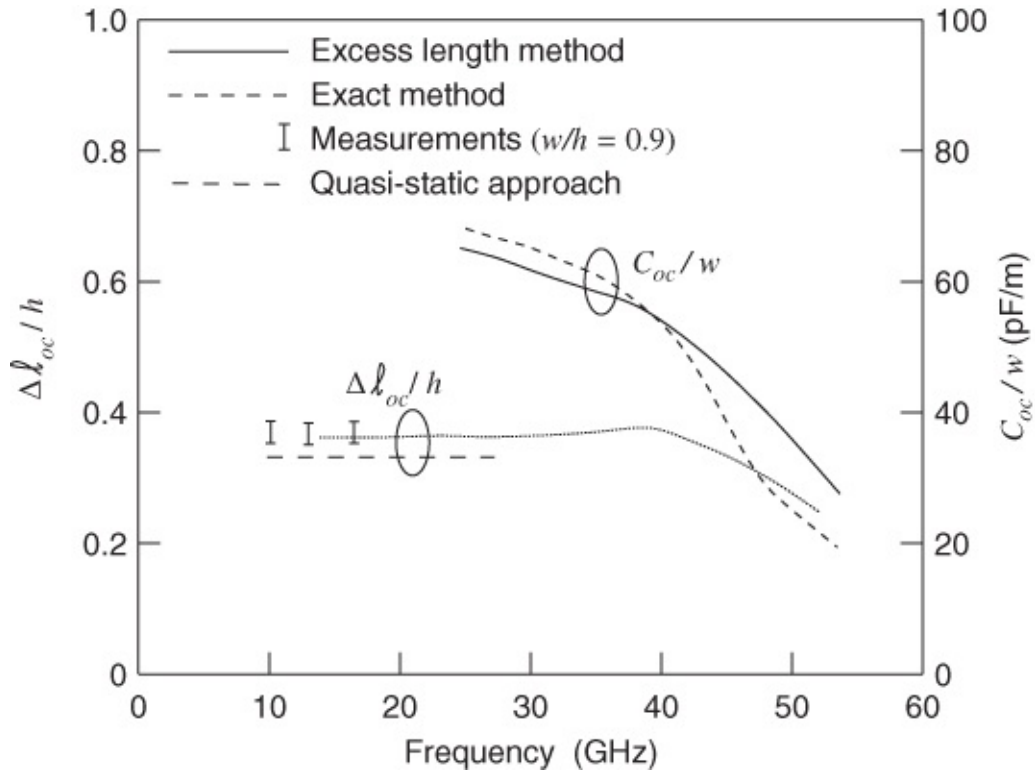


**Figure 9.28** Open-circuit normalized excess length and normalized capacitances as functions of frequency ( $\epsilon_r = 9.6$ ,  $w/h = 1$ ,  $h = 0.6$  mm). Adapted from Katehi and Alexopoulos (1985) [28], figure 8, p. 1033. Reprinted with permission of IEEE.

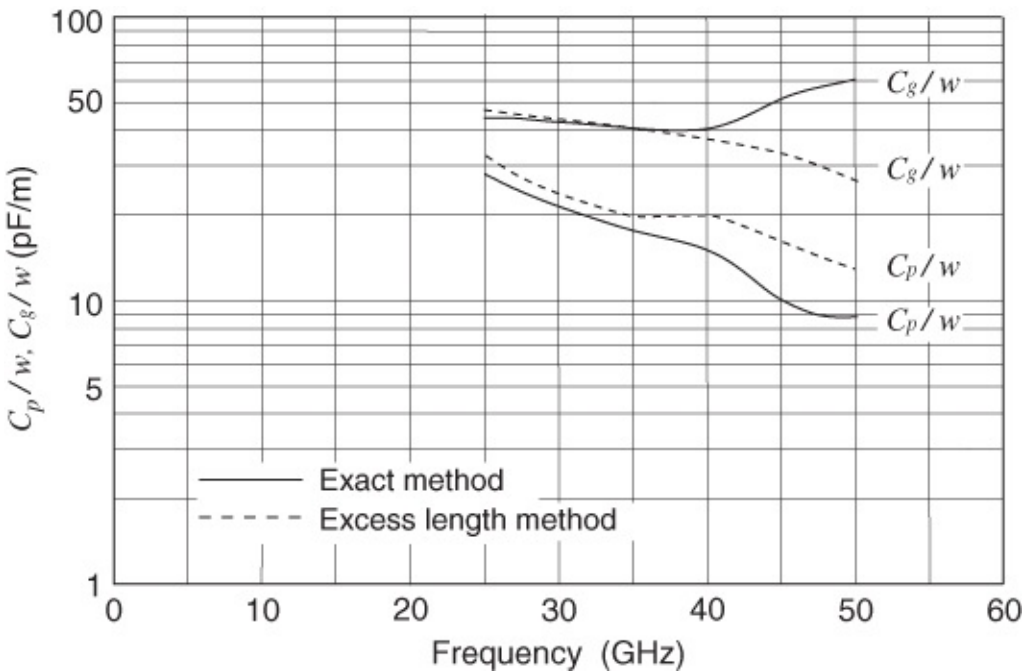


**Figure 9.29** Gap-discontinuity normalized capacitances  $C_p/w$  and  $C_g/w$  as functions of frequency ( $\epsilon_r = 9.6$ ,  $w/h = 1$ ,  $h = 0.6$  mm,  $s/h = 0.3762$ ). Adapted from Katehi and Alexopoulos (1985) [27], figure 9, p. 1033. Reprinted with permission of IEEE.

A frequency-dependent equivalent circuit for gap discontinuities was reported by Ozmehmet [28]. This includes the radiation resistance and separates gap capacitances (series) into fringing field and “plate” components. Therefore, the series structure of the equivalent circuit shown as [Figure 9.5\(b\)](#) is enhanced by these additional elements. Ozmehmet shows that this slightly more complex circuit enables wideband microwave circuits to be designed at frequencies up to at least 15 GHz.

Complete electromagnetic modeling of microstrip open-end discontinuities has been reported by McLean *et al.* [29]. They use a spectral domain method and include space wave and surface wave radiation by implementing the exact spectral-domain Green's function.

In this work, longitudinal and transverse current components are included so that strips ranging from electrically narrow to electrically wide can be analyzed. Results are shown for both magnitude and phase of the reflection coefficient as functions of frequency. In the case of an electrically narrow microstrip line on an alumina substrate, both the magnitude and phase of the reflection coefficient decrease with frequency, the magnitude slowly at first then rapidly for frequencies approaching 30 GHz (about 0.75 at 31 GHz and falling). The phase is approximately 0.05 radians at 5 GHz, 0.25 radians at 25 GHz, and then increases faster to about 0.5 radians at 31 GHz. These phase calculations are compared with results measured elsewhere and agreement is very good.

Results are also obtained, in the form of magnitude only as a function of frequency, for a range of line widths applicable to microstrip lines on a substrate having a permittivity of 12.8. Pronounced singularities are now evident for all lines at high frequencies. At first the reflection coefficient continues to decrease rapidly, but this is followed by a further increase, a

peak, and finally a resumption of the general fall in value. This behavior occurs in the vicinity of cut-off for the first TE surface wave due to the tendency of the transverse current to store as opposed to radiate energy, and hence to increase the frequency sensitivity of the reflection coefficient. It is demonstrated that this effect is strengthened as the line width increases, which is consistent with the above argument.

With their significance in, for example, filter realization, some work has been reported by Achkar *et al.*[30] on open-end discontinuities of suspended striplines. The analysis uses eigenmodes to determine the dispersion characteristics of suspended substrate striplines, and a modal analysis to find the open-end discontinuity characteristics. For this type of structure, fabricated on a thin substrate of permittivity 2.2, it is shown that the amplitude of the reflection coefficient is essentially one for all frequencies over the 26–40 GHz range. Its phase, however, increases from about  $-0.028$  to  $-0.015$  radians over this frequency range. Hence the equivalent end-effect length also increases slowly with frequency, although it is still only around one micron at 40 GHz for this structure. The behavior of the transmission coefficient ( $S_{12}$ ) was also quantified, but radiation remains less than 130 dB down on the incident signal power over the entire band.

### 9.6.5 Other Discontinuities

Easter [17] performed measurements which indicated that the values of the inductive series equivalent elements for discontinuities can be expected to increase considerably with frequency. Over the frequency range 5–11 GHz, Easter's measurements reveal a 40% increase in the inductance values for lines having  $w/h > 1.0$ . For lines with smaller width-to-height ratios, the increase is greatly reduced.

Alternative approaches to the problem of frequency dependence of microstrip discontinuities have been presented by Menzel and Wolff [31], Kompa [32], and Mehran [33]. The complete validity of their magnetic-wall method of modeling microstrip has, however, been questioned by Easter. These researchers present their data in scattering ( $S$ ) parameter form, which is often difficult to reinterpret as an equivalent circuit.

The work reported by Kompa [32] is, however, particularly interesting, even though most of his computations relate to plastic substrates ( $\epsilon_r = 2.32$ ). He reports  $S$  parameters for steps in microstrip, using the planar waveguide model to analyze the structure. It is clear that the transmission parameter  $|S_{21}|$  is substantially constant up to at least 12 GHz for steps produced on an alumina substrate. A dramatically different behavior is noted for the plastic substrate, where  $|S_{21}|$  decreases very rapidly for moderate-to-high width ratios at high frequencies. For example, the transmission drops to zero at just over 9 GHz for a width ratio of approximately 7.0, whereas when the ratio is only 3.0 there is little change in transmission up to 12 GHz. Kompa describes measurements, a one-section quarter-wavelength transformer (including a field-matching solution to this), and the analysis of a straight-tapered, six-stepped microstrip line.

We now consider analysis and modeling results, in terms of scattering parameters, for a selection of discontinuities.

The use of microstrip circuits fabricated on multilayer substrates is important in many monolithic integrated circuit designs and antenna array feed networks. To meet the circuit design needs discontinuities have been characterized for these types of structures. In particular, Harokopus and Katehi [34] report results for unmitered  $90^\circ$  bends. They employ a space domain method of moments solution of Pocklington's integral equation, which is suitable for application to most discontinuities. These researchers present results for various combinations of substrates, generally incorporating high-alumina/low-permittivity Duroid (i.e., permittivities of 10.2 and 2.2).

Over the frequency range 10–20 GHz, for a  $90^\circ$  bend fabricated on a single-layer substrate, it is shown that the magnitude of the reflection coefficient rises slowly from approximately 0.08 to 0.15 (roughly following the prediction using commercial electromagnetic software). In contrast, the magnitude of the transfer parameter ( $|S_{21}|$ ) falls slowly with frequency, from about 0.98 at 10 GHz to approximately 0.88 at 20 GHz. For multilayer bends, the general trends of the parameters are the same but the actual values differ considerably. For example, in the case of a low-permittivity Duroid substrate topped by an alumina substrate (equal thicknesses) the reflection coefficient increases from about 0.2 to 0.4, whilst the transfer parameter decreases from 0.97 to 0.74. This is due to the enhancement of radiation fields where the microstrip itself is held above a ground plane separated by a relatively low-permittivity substrate (Duroid).

The important case of  $90^\circ$  bends, direct, mitered, and double-mitered (see [Figure 9.30](#)), has also been investigated by Zheng and Chang [35]. They employed an integral equation approach (with the Galerkin method) to evaluate the performance of these bends. They found similar trends and values for the coefficients to those reported by Harokopus and Katehi [34] for the unmitered bend. In common with the well-known results they also noted that both  $S_{11}$  and  $S_{21}$  were considerably lower for the optimally mitered bend than for the direct one, over the frequency range 8–40 GHz at least. The double-mitered case was, however, particularly interesting since it provided a substantially lower reflection coefficient over the frequency range 22–38 GHz and a lower value of  $S_{21}$  over the entire frequency range (much lower above about 18 GHz). This response is due to interference effects operating between the miter ends, that is, a distinctly frequency-dependent phenomenon.

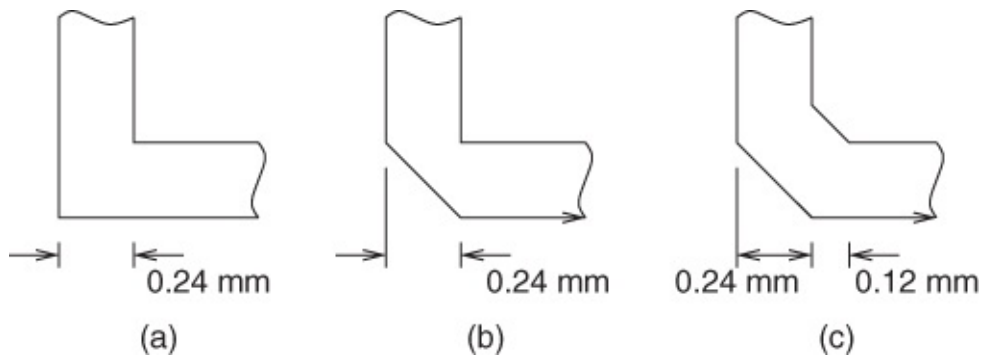


[Figure 9.30](#) Right-angled single bend: (a) direct (i.e., unmitered); (b) mitered; and (c) double-mitered. The phase reference point is chosen at the center of the straight bend.

## 9.6.6 Cross and T Junctions

The frequency-dependent behavior of cross and T junctions has been investigated by Wu *et al.* [36]. They used an electromagnetic spectral-domain analysis to develop the scattering parameters of these types of junctions. An  $N$ -port junction approach is used together with a concept whereby a “module” around the junction region contains that section where higher-order modes are generated as a consequence of the discontinuity. The current distributions inside the module are expanded and a “nearly Galerkin” method is applied to transform the integral equation into a matrix equation. The scattering parameters are generated from submatrices within the major current, voltage, and reflection coefficient interrelated matrices.

Wu *et al.* compare their results, to which experimental data generally fit very well, with quasi-static predictions generated using commercial software over the frequency range 4–24 GHz. For a basic T junction the magnitude of the transfer parameters  $S_{21}$  and  $S_{31}$  indicate a greater inequality in the division of power between arms than the software predicted. In general, the disparities amounted to some 10–15%, being most marked as frequency increased. Phase performance was more sensitive to the accuracy of the prediction solution and, again for a basic T junction, the phase of  $S_{33}$  is found to differ from the result using this particular modeling software by up to  $45^\circ$  (at 24 GHz). Wu’s method, supported by measurements, shows the phase of  $S_{33}$  varying only between  $170^\circ$  and  $175^\circ$ . Curves applicable to a right-angled cross junction in microstrip on a high-purity alumina substrate are shown in [Figure 9.31](#).

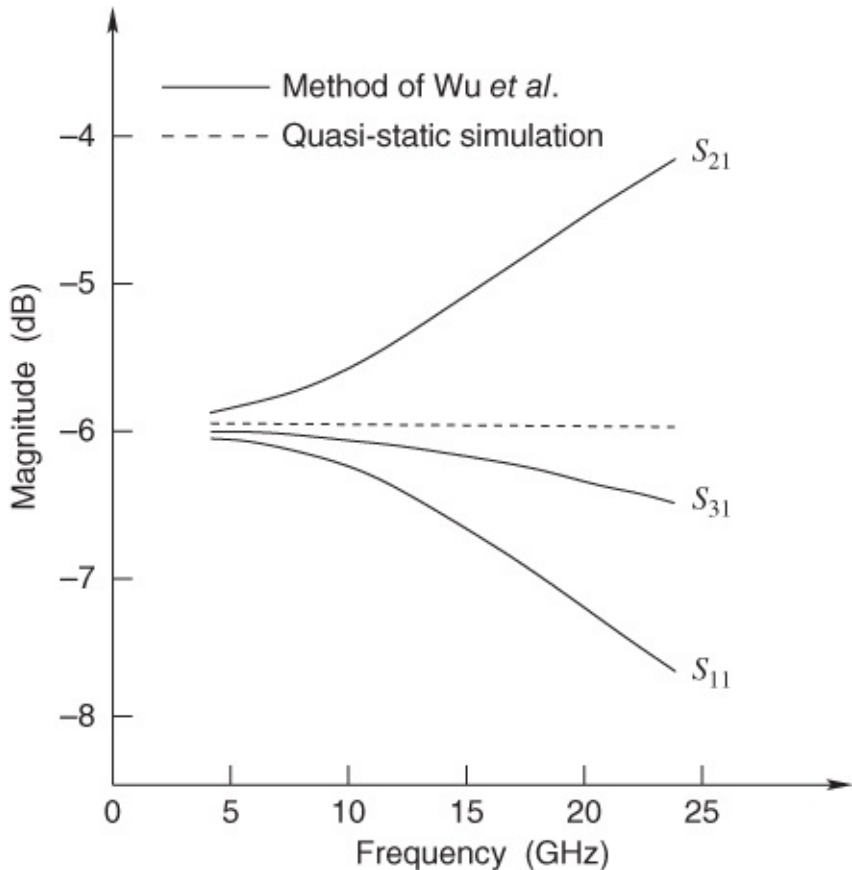


[Figure 9.31](#) Magnitude of  $S$  parameters of a right-angle crossing junction ( $\epsilon_r = 10.2$ ,  $h = 0.635$  mm,  $w = 0.61$  mm). Adapted from Wu *et al.* (1990) [36], figure 8, p. 1841. Reprinted with permission of IEEE.

This method of analysis is also applied to a compensated T junction, as originally suggested by Dydyk (see [Section 9.6.2](#)). In the example analyzed by Wu, the top slot is omitted and the design intent is to extend the frequency range over which power is equally split between the coupled arms. For such a compensated microstrip T junction, fabricated on a similar substrate to that described above, it is found that the power is split equally when the structure is driven at any frequency from DC to 16 GHz (compared with DC to 6 GHz for a basic T junction).

Chang *et al.* [37] developed results for right-angled bends, T junctions, and Y junctions. Their analysis method is based on the effective width principle (see [Section 7.7.2](#)), following which an impedance is derived based on the boundary integral method. The scattering matrix is obtained directly from the impedance matrix. For a right-angled bend, a family of curves was computed showing  $|S_{11}|$  as a function of frequency (see [Figure 9.32](#)), and these clearly indicate an optimum chamfer or “cut” ratio of approximately 0.8 for a 0.65 mm thick plastic substrate of permittivity 2.53. It is also clear that this optimum continues for frequencies up to at least 29 GHz. Although the definition contrasts somewhat, the absolute magnitude of this chamfer fraction differs considerably from that given in [Section 9.3.2](#) here, perhaps because of the much lower permittivity in this case.

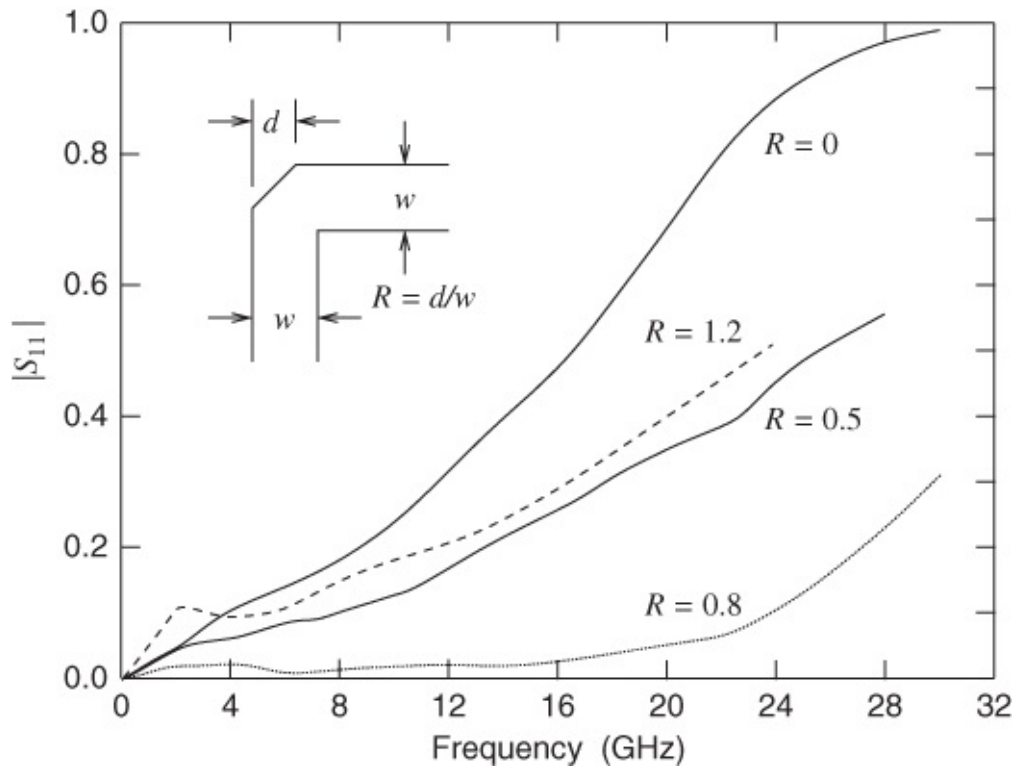


**Figure 9.32** Variations in  $|S_{11}|$  of a right-angle bend for cut ratio (degree of miter)  $R = 0, 0.5, 0.8, 1.2$ .  $W_{1,\text{eff}} = W_{2,\text{eff}} = 1.882$  mm,  $d = 0.65$  mm,  $\epsilon_r = 2.53$ . Adapted from Chang *et al.* (1989) [37], figure 3, p. 977. Reprinted with permission of the European Microwave Association.

Reflection coefficient data are also shown for a T junction with a Vee-cut opposite the leg of the T. With a cut (i.e., miter) ratio definition similar to that used for the bend, it is clear that when this ratio is 0.4 an approximate optimum exists in that  $S_{22}$  is minimized over the frequency range 0–16 GHz. This applies to a substrate of the type applicable to the case of the bend above.

An entirely different approach from those described above for the modeling of microstrip cross junctions has been developed by Giannini *et al.* [38]. They showed how a lumped model can be used to represent the characteristics of cross junctions over a broad bandwidth (2–12 GHz on alumina substrates). In contrast to most other approaches, Giannini *et al.* derive sophisticated  $Z$ -parameter expressions for a set of equivalent elements. The overall configuration is shown in [Figure 9.33](#), where the impedance elements (actually totally reactive) are related to the physical microstrip parameters, permittivity, and of course frequency, as well as complicated forms of infinite series. The full details will not be set down here, and the interested reader is recommended to follow the original paper.

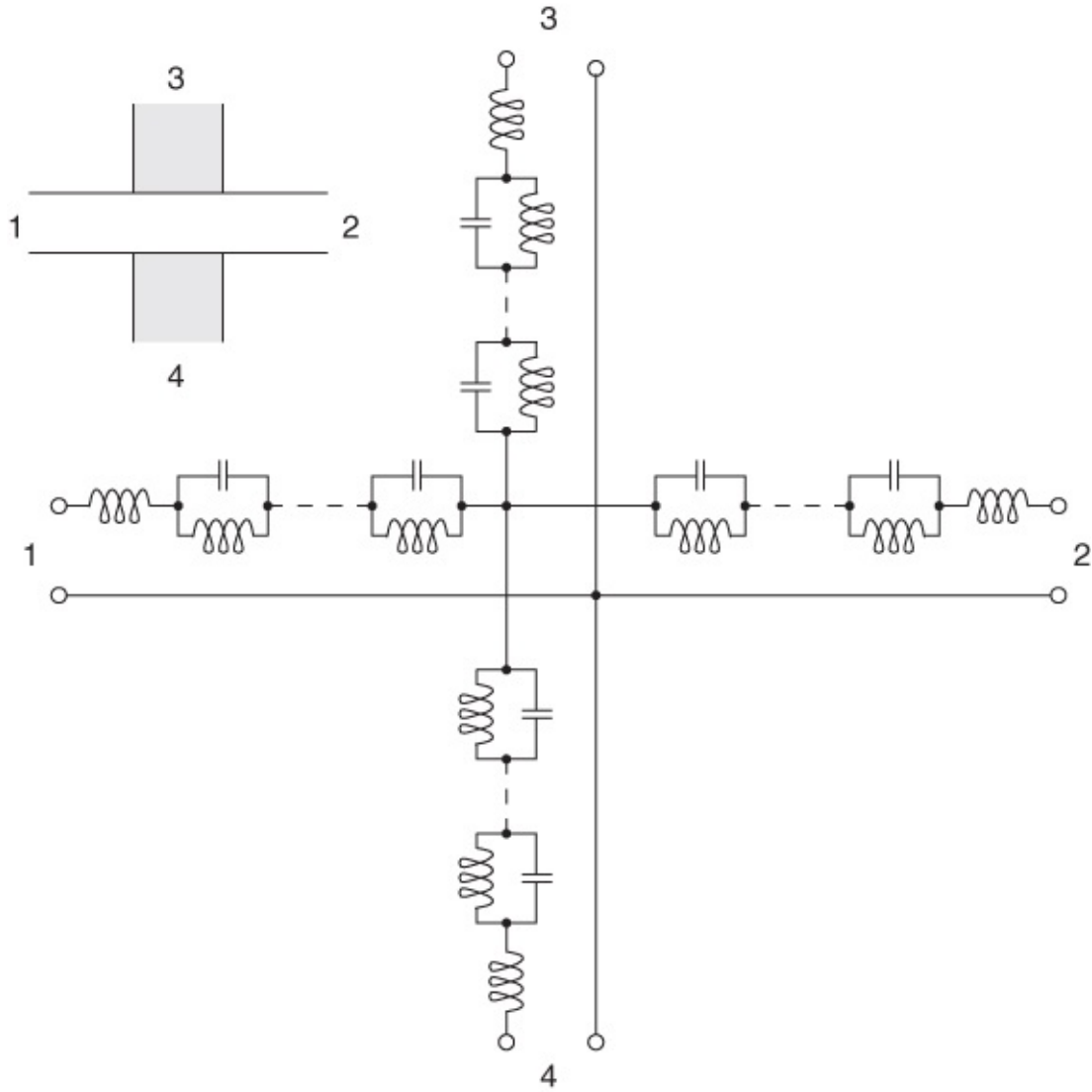


[Figure 9.33](#) Lumped equivalent model for cross-junction discontinuity.

### 9.6.7 Radial Bends

Most work concerning discontinuities has centered on abrupt changes in the width or direction of the transmission line. A gradual bend is shown in [Figure 9.34\(a\)](#) and this has a similar model to an abrupt bend, see [Figure 9.34\(b\)](#) and relatively little research appears to have been conducted on more continuously changing structures such as radial bends. Reported research

by three groups in different locations (the first being headed by Weisshaar) has, however, redressed the balance somewhat [39]. The nomenclature, equivalent circuit, and waveguide model are indicated in [Figure 9.34](#).

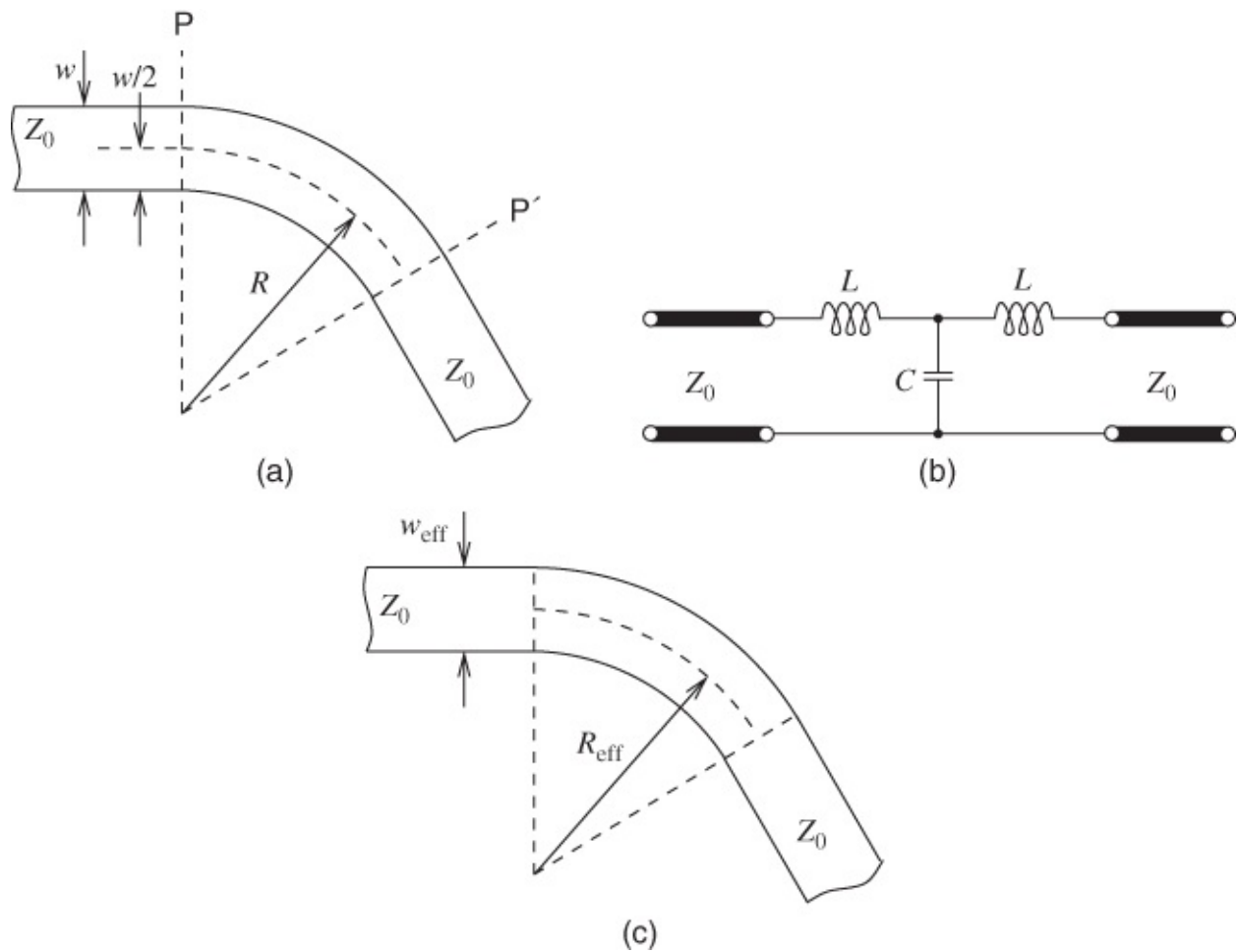


[Figure 9.34](#) The radial microstrip bend: (a) physical; (b) equivalent lumped model; and (c) waveguide model.

Weisshaar *et al.* [39] used a waveguide model in their study. In this model the effective mean radius of curvature,  $R_{\text{eff}}$  in [Figure 9.34\(c\)](#), is related to the effective microstrip width  $w_{\text{eff}}$ .  $R_{\text{eff}}$  is chosen such that there is always a positive effective inner radius regardless of actual inner and outer radii.

The frequency-dependent behavior of the radial bend is determined using a second-order perturbation analysis of the equivalent waveguide model together with a mode-matching technique which includes the higher-order modes. Scattering parameters and radiation losses are calculated for alumina (MIC) and GaAs versions of the structure and these are shown, for 50  $\Omega$  lines, in [Figures 9.35](#) and [9.36](#). Weisshaar *et al.* also report reflection coefficient results for radial bends in 30  $\Omega$  lines, and the scattering transfer parameter  $S_{21}$  for a T junction with an open stub leg having curved bends.

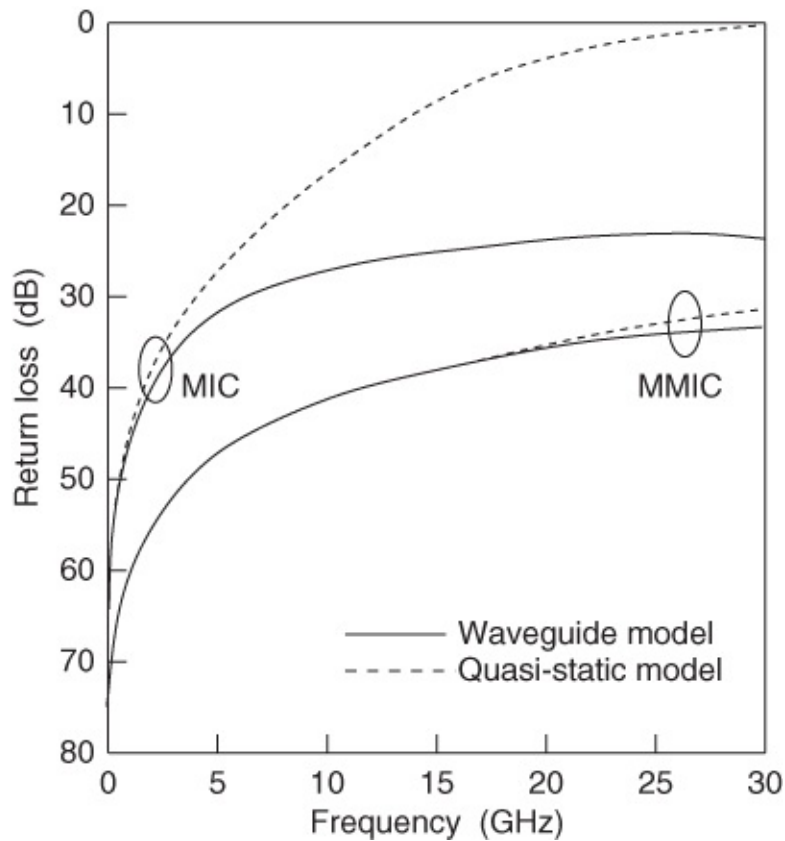


**Figure 9.35** Return loss for  $50 \Omega$ ,  $90^\circ$  bends with  $R = 2w$  on MIC (0.635 mm thick alumina) and MMIC (0.1 mm thick GaAs) substrates. Adapted from Weisshaar *et al.* (1990) [39], figure 2, p. 1054. Reprinted with permission of IEEE.

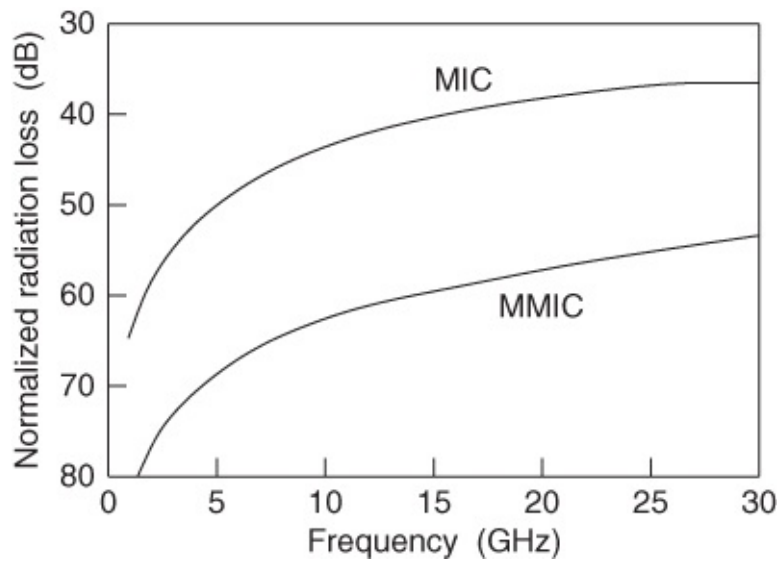


**Figure 9.36** Normalized radiation loss for  $50 \Omega$  bends with  $R = 2w$  on MIC (0.635 mm thick alumina) and MMIC (0.1 mm thick GaAs) substrates. Adapted from Weisshaar *et al.* (1990) [39], figure 4, p. 1054. Reprinted with permission of IEEE.

Some researchers have suggested the use of rounding and tapering techniques, as shown in [Figure 9.37](#), to reduce the effects of discontinuities, and these may well be effective and worth considering at least at the lower microwave frequencies. At higher frequencies, however, it

would be difficult to accurately quantify the excess conductances and reactances associated with these complex shapes, and it is recommended that the better understood characterization of the conventional discontinuities described in this chapter continue to be used.

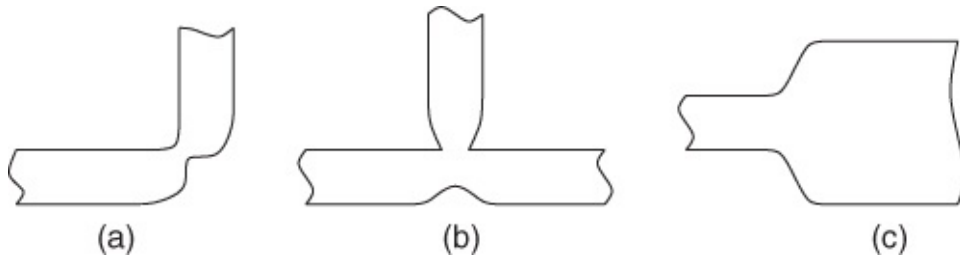


**Figure 9.37** Rounding and tapering techniques that may be applied to reduce the discontinuity effects associated with: (a) bends; (b) T junctions; and (c) step in width.

### 9.6.8 Frequency Dependence of via Parameters

Finch and Alexopoulos [40] reported a theoretical study of the frequency dependence of parameters relating to shunt posts (i.e., vias) in microstrip. They used the planar waveguide model and a multiple expansion method within algorithms for the computation of Schloemilch-type series to analyze the behavior of these structures. Their approach applies to perfectly conducting, imperfectly conducting (i.e., lossy) and composite shunt posts.

These researchers determined scattering parameters ( $S_{11}$  and  $S_{21}$ ) for this type of structure. In the case of a 1.22 mm diameter conducting post in microstrip, having a width of 3 mm, using an alumina substrate of thickness 0.635 mm and permittivity 10, they showed that  $|S_{11}|$  decreases with frequency. Starting with perfect short-circuit behavior at DC, the value of  $|S_{11}|$  falls to 0.92 at 12 GHz. Doubtless the method used by Finch and Alexopoulos could be extended to almost any of these types of structures.

## 9.7 Recommendations for the Calculation of Discontinuities

The following recommendations generally apply with reasonable accuracy for frequencies up to about 20 GHz, where the microstrip is on alumina-type substrates. As indicated, some of the formulas also apply at higher frequencies and on quite different substrates, such as various polymers or semiconductors.

### 9.7.1 Foreshortened Open Circuits

Fundamental considerations were presented in [Section 9.2.1](#), and Equation (9.7) gives the open-end length extension as a function of the lumped fringing capacitance  $C_f$  and the microstrip line parameters:

$$\ell_{eo} \approx cZ_0C_f/\sqrt{\epsilon_{\text{eff}}}. \quad 9.48$$

It is difficult to specify the accuracy of this expression, but empirical relationships can be set

up for  $C_f$ , and both  $Z_0$  and  $\epsilon_{\text{eff}}$  are readily known parameters.

The alternative empirical formula is

$$\ell_{eo} = 0.412h \left( \frac{\epsilon_{\text{eff}} + 0.3}{\epsilon_{\text{eff}} - 0.258} \right) \left( \frac{w/h + 0.262}{w/h + 0.813} \right). \quad 9.49$$

This expression is useful over a wide range of materials and microstrip line dimensions, but errors can exceed 5% and this can be significant, especially in filter design.

Independent theoretical calculations and measurements verify that either expression can be used satisfactorily at frequencies up to around 18 GHz for alumina-type substrates of less than 1 mm thickness.

## 9.7.2 Series Gaps

These are usually only of significance in resonator design for measurement or filter realization purposes, where the value of  $g$  required for a given order-of-magnitude of coupling (i.e., “loose,” “tight,” etc.) can often be determined experimentally. In case such a discontinuity is required in other circuits, some design equations are given in [Section 9.2.2](#), but they will not be repeated here.

## 9.7.3 Short Circuits

With the present state of technology, short circuits are unusual and undesirable in microstrip as implemented in hybrid MICs for a variety of reasons, discussed in [Section 9.2.3](#). However, this situation may change and in any event, in the form of vias, short circuits are important in MMICs. The diameter of the optimum metallized hole [10], applicable at least to alumina-type substrates, is obtainable using

$$\ln \left( \frac{w_{\text{eff}}}{\pi d_e} \right) \approx \left( \frac{\pi d_e}{w_{\text{eff}}} \right)^2 \quad 9.50$$

where  $d_e = 0.03 + 0.44d$ ,  $d$  is the actual hole diameter, and  $w_{\text{eff}}$  is the effective microstrip width.

This expression yields the diameter of such a hole situated at the end of foreshortened microstrip which provides a broadband short circuit up to about 18 GHz. It may be noted that the previous expression in  $w_{\text{eff}}$  and  $d_e$  has the form

$$\ln(x) \approx x^{-2} \quad 9.51$$

in which

$$x = \left( \frac{w_{\text{eff}}}{\pi d_e} \right). \quad 9.52$$

Equation (9.51) can be solved iteratively for  $x$ . In fact a total of around six or seven iterations

reveal that  $x = 1.532$  satisfies the equation quite accurately. The values of  $d_e$  and hence  $d$  are then easily found ( $w_{\text{eff}}$  can be found from Equation (7.60), [Section 7.7.2](#)).

### 9.7.4 Right-angled and Mitered Bends

Expressions were given in [Section 9.3.1](#) for the equivalent circuit capacitance and inductance associated with a right-angled bend in microstrip. The compensating techniques referred to in [Section 9.3.2](#) are, however, probably of more practical significance to the circuit designer, especially the simple device known as the mitered or chamfered bend. It was indicated that the approximately optimum degree, or extent, of chamfer ([Figure 9.9\(a\)](#)) should be

$$b \approx 0.57w \text{ for alumina-like substrates} \quad 9.53$$

(but see also [Section 9.6.5](#) and, particularly, [Section 9.6.6](#)).

### 9.7.5 Transverse Slit

As outlined in [Section 9.5](#), this yields the effect of a lumped inductance,  $\Delta L$ , in the plane of the slit, given by

$$\frac{\Delta L}{h} = \frac{\mu_0 \pi}{2} \left( \frac{a'}{A} \right)^2 \quad 9.54$$

where

$$\frac{a'}{A} = 1 - \frac{Z_{01}}{Z'_{01}}. \quad 9.55$$

For design, the procedure is then as follows:

- a. Calculate the characteristic impedance of the air-filled microstrip line, width  $w$ ,  $Z_{01}$ .
- b. Calculate the characteristic impedance of an air-filled microstrip line of width  $(w - a)$ ,  $Z'_{01}$ .
- c. Evaluate  $a'/A$  with these results, (a) and (b), using the second expression, and hence calculate  $\Delta L$  using the first expression.

The accuracy of these equations is very difficult to estimate, but the main application appears to be in trimming microstrip stubs, etc., for correct electrical length, that is, the slit could be deliberately introduced at a late manufacturing stage. The expressions tend to break down as the slit becomes too narrow (capacitive) or too wide. In the latter case the slit tends towards a length of (distributed) microstrip line of reduced width.

### 9.7.6 The T Junction

This was fully described in [Section 9.6.1](#) and further in [Section 9.6.6](#). Although it is clear that substantial further work is required, especially for frequencies much in excess of 10 GHz, the following expressions hold approximately, provided  $2w_{\text{eff}}/\lambda_{g1} > 0.3$ , with

$$w_{\text{eff}1.2} = \frac{h\eta}{Z_{0(1.2)}\sqrt{\epsilon_{\text{eff}}}}. \quad 9.56$$

The transformation ratio  $n$  is given by

$$n^2 = \left[ \frac{\sin \{\pi(w_{\text{eff}1}/\lambda_{g1})(Z_{01}/Z_{02})\}}{\pi(w_{\text{eff}1}/\lambda_{g1})(Z_{01}/Z_{02})} \right]^2 \left[ 1 - \left\{ \pi \left( \frac{w_{\text{eff}1}}{\lambda_{g1}} \right) \left( \frac{d_2}{w_{\text{eff}1}} \right) \right\}^2 \right]. \quad 9.57$$

The displacement of the reference plane for the primary arm (1) is

$$\frac{d_1}{w_{\text{eff}2}} = 0.05 \frac{Z_{01}}{Z_{02}} n^2. \quad 9.58$$

The displacement of the reference plane for the secondary arm (2) is

$$\begin{aligned} \frac{d_2}{w_{\text{eff}1}} &= 0.5 - \left\{ 0.076 + 0.2 \left[ \frac{2w_{\text{eff}1}}{\lambda_{g1}} \right]^2 \right. \\ &\quad \left. + 0.663 \exp \left[ -1.71 \frac{Z_{01}}{Z_{02}} \right] - 0.172 \ln \left[ \frac{Z_{01}}{Z_{02}} \right] \right\} \frac{Z_{01}}{Z_{02}}. \end{aligned} \quad 9.59$$

(Replace  $Z_{01}/Z_{02}$  by its inverse, i.e.,  $Z_{02}/Z_{01}$ , when  $Z_{01}/Z_{02} \geq 2.0$ .) Also, the shunt capacitance is determined by the following expressions:

For the condition  $Z_{01}/Z_{02} \leq 0.5$ :

$$\frac{\omega C \lambda_{g1}}{Y_{01} w_{\text{eff}1}} = \left( \frac{2w_{\text{eff}1}}{\lambda_{g1}} - 1 \right) \frac{Z_{01}}{Z_{02}}. \quad 9.60$$

For the condition  $Z_{01}/Z_{02} \geq 0.5$ :

$$\frac{\omega C \lambda_{g1}}{Y_{01} w_{\text{eff}1}} = \left( \frac{2w_{\text{eff}1}}{\lambda_{g1}} - 1 \right) \left( 2 - 3 \frac{Z_{01}}{Z_{02}} \right). \quad 9.61$$

Also refer to [Section 9.6.6](#) for frequency-dependent effects.

### 9.7.7 The Asymmetric Cross Junction

This structure was considered in [Section 9.6.5](#), and a fairly comprehensive equivalent circuit was shown which is again applicable for frequencies up to about 12 GHz. The capacitance is given simply by

$$C_m = \frac{c}{Z_0 \sqrt{\epsilon_{\text{eff}}}}. \quad 9.62$$

Alternatively, and probably more powerfully at somewhat higher frequencies, the cross junction may be considered as two T junctions operating from the same plane in the main microstrip line. Some elaboration of the equivalent circuits may be necessary if interactions

between the branch arms are to be taken into account.

For virtually all the discontinuities, it is clear that substantial further work is necessary before techniques are available for circuit designers working at frequencies beyond about 10–12 GHz. Up to these frequencies, and occasionally beyond, the expressions given may be used in design.

Further design information, including dispersive effects, is provided in [Section 9.6.6](#). This should prove useful in support of design at frequencies up to 25 GHz.

## 9.8 Summary

This chapter described the impact of microstrip discontinuities. Models were presented and approaches to accommodating the effect of discontinuities in circuit design described. Discontinuities result in changes in current flow on the strip and ground plane of microstrip and force changes in the balance of the electric and magnetic fields. This can result in additional energy storage in the electric field and if this is the case the effect of the discontinuity is accounted for by a capacitance in the lumped-element model of the discontinuity. If there is a change in the magnetic field, and often this is indicated by a change in the concentration or direction of current flow, the impact will be additional magnetic energy storage and thus an inductor must be incorporated in the lumped-element equivalent model of the discontinuity.

## References

- [1] R. Akello, B. Easter, and I. Stephenson, “Effects of microstrip discontinuities on GaAs-M.E.S.F.E.T.-amplifier gain performance,” *Electronics Letters*, vol. **13**, no. 6, pp. 160–162, 1977.
- [2] N. Slaymaker, R. Soares, and J. Turner, “GaAs MESFET small-signal X-band amplifiers,” *IEEE Trans. on Microwave Theory and Techniques*, vol. **24**, no. 6, pp. 329–337, Jun. 1976.
- [3] J. James and P. Ladbrooke, “Surface-wave phenomena associated with open-circuited stripline terminations,” *Electronics Letters*, vol. **9**, no. 24, pp. 570–571, 1973.
- [4] P. Sylvester and P. Benedek, “Equivalent capacitances of microstrip open circuits,” *IEEE Trans. on Microwave Theory and Techniques*, vol. **20**, no. 8, pp. 511–516, Aug. 1972.
- [5] E. Hammerstad and F. Bekkadal, “A microstrip handbook, ELAB Report STF44 A74169,” University of Trondheim, Norway, Tech. Rep., Feb. 1975.
- [6] S. Cohn, “Problems in strip transmission lines,” *IRE Trans. on Microwave Theory and Techniques*, vol. **3**, no. 2, pp. 119–126, Mar. 1955.
- [7] R. Garg and I. J. Bahl, “Microstrip discontinuitie,” *Int. J. Electronics*, vol. **45**, no. 1, pp. 81–87, 1978.

- [8] E. Costamagna, “Some notes on a method of calculating gap capacitances in microstrip structures,” *Alta Frequenza*, vol. **43**, no. 6, pp. 362–364, 1974.
- [9] P. Benedek and P. Silvester, “Equivalent capacitances for microstrip gaps and steps,” *IEEE Trans. on Microwave Theory and Techniques*, vol. **20**, no. 11, pp. 729–733, Nov. 1972.
- [10] R. P. Owens, “The electrical characteristics of transferred-electron device package and mounts and their effects on oscillator performance,” Ph.D. dissertation, University of London, 1977.
- [11] K. Strohm, P. Nuechter, C. Rheinfelder, and R. Guehl, “Via hole technology for microstrip transmission lines and passive elements on high resistivity silicon,” in *1999 IEEE MTT-S Int. Microwave Symp. Digest*, 1999, pp. 581–584.
- [12] P. Silvester and P. Benedek, “Microstrip discontinuity capacitances for right-angle bends, T junctions, and crossings,” *IEEE Trans. on Microwave Theory and Techniques*, vol. **21**, no. 5, pp. 341–346, May 1973.
- [13] P. Silvester and P. Benedek, “Correction to “microstrip discontinuity capacitances for right-angle bends, T junctions, and crossings”,” *IEEE Trans. on Microwave Theory and Techniques*, vol. **23**, no. 5, p. 456, May 1975.
- [14] A. Thomson and A. Gopinath, “Calculation of microstrip discontinuity inductances,” *IEEE Trans. on Microwave Theory and Techniques*, vol. **23**, no. 8, pp. 648–655, Aug. 1975.
- [15] K. C. Gupta, R. Garg, I. J. Bahl, and P. Bhartia, *Microstrip Lines and Slotlines*, 2nd ed. Artech House, 1996.
- [16] P. Anders and F. Arndt, “Moment method of designing matched microstrip bends,” in *9th European Microwave Conf.*, Sep. 1979, pp. 430–434.
- [17] B. Easter, A. Gopinath, and I. Stephenson, “Theoretical and experimental methods for evaluating discontinuities in microstrip,” *Radio and Electronic Engineer*, vol. **48**, no. 1.2, pp. 73–84, Jan.–Feb. 1978.
- [18] A. Gopinath, A. Thomson, and I. Stephenson, “Equivalent circuit parameters of microstrip step change in width and cross junctions,” *IEEE Trans. on Microwave Theory and Techniques*, vol. **24**, no. 3, pp. 142–144, Mar. 1976.
- [19] W. Hoefer, “Equivalent series inductivity of a narrow transverse slit in microstrip,” *IEEE Trans. on Microwave Theory and Techniques*, vol. **25**, no. 10, pp. 822–824, Oct. 1977.
- [20] H. Wheeler, “Coupling holes between resonant cavities or wave-guides evaluated in terms of volume ratios,” *IEEE Trans. on Microwave Theory and Techniques*, vol. **12**, no. 2, pp. 231–244, Mar. 1964.
- [21] E. O. Hammerstad, “Equations for microstrip circuit design,” in *5th European Microwave Conf.*, 1975, pp. 268–272.

- [22] G. Kompa, “Reduced coupling aperture of microstrip stubs provides new aspects in stub filter design,” in *6th European Microwave Conf.*, Sep. 1976, pp. 39–43.
- [23] M. Dydyk, “Master the T-junction and sharpen your MIC designs,” *MicroWaves*, no. 5, pp. 184–186, 1977.
- [24] R. Akello, B. Easter, and I. Stephenson, “Equivalent circuit of the asymmetric crossover junction,” *Electronics Letters*, vol. 13, no. 4, pp. 117–118, 1977.
- [25] J. James and A. Henderson, “High-frequency behaviour of microstrip open-circuit terminations,” *Proc. IEE, Microwaves, Optics and Acoustics*, vol. 3, no. 5, pp. 205–218, Sep. 1979.
- [26] T. Itoh, “Analysis of microstrip resonators,” *IEEE Trans. on Microwave Theory and Techniques*, vol. 22, no. 11, pp. 946–952, Nov. 1974.
- [27] P. Katehi and N. Alexopoulos, “Frequency-dependent characteristics of microstrip discontinuities in millimeter-wave integrated circuits,” *IEEE Trans. on Microwave Theory and Techniques*, vol. 33, no. 10, pp. 1029–1035, Oct. 1985.
- [28] K. Özmehmet, “Technical memorandum: New frequency dependent equivalent circuit for gap discontinuities of microstriplines,” *Proc. IEE, Part H, Microwaves, Antennas and Propagation*, vol. 134, no. 3, pp. 333–335, Jun. 1987.
- [29] J. McLean and T. Itoh, “Full wave modeling of electrically wide microstrip open end discontinuities via a deterministic spectral domain method,” in *1990 IEEE MTT-S Int. Microwave Symp. Digest*, May 1990, pp. 1155–1158.
- [30] J. Achkar, O. Picon, V. F. Hanna, and J. Citerne, “Frequency-dependent characteristics of an asymmetric suspended stripline and its open end discontinuity for millimeter wave applications,” in *19th European Microwave Conf.*, Sep. 1989, pp. 767–772.
- [31] W. Menzel and I. Wolff, “A method for calculating the frequency-dependent properties of microstrip discontinuities,” *IEEE Trans. on Microwave Theory and Techniques*, vol. 25, no. 2, pp. 107–112, Feb. 1977.
- [32] G. Kompa, “Design of stepped microstrip components,” *Radio and Electronic Engineer*, vol. 48, no. 1.2, pp. 53–63, Jan.–Feb. 1978.
- [33] R. Mehran, “Computer-aided design of microstrip filters considering dispersion, loss, and discontinuity effects,” *IEEE Trans. on Microwave Theory and Techniques*, vol. 27, no. 3, pp. 239–245, Mar. 1979.
- [34] W. P. Harokopus and P. B. Katehi, “Analysis of multilayer irregular microstrip discontinuities,” in *19th European Microwave Conf.*, Sep. 1989, pp. 745–750.
- [35] J. Zheng and D. Chang, “Numerical modelling of chamfered bends and other microstrip

junctions of general shape in MMIC,” in *1990 IEEE MTT-S Int. Microwave Symp. Digest*, May 1990, pp. 709–712.

[36] S.-C. Wu, H.-Y. Yang, N. Alexopoulos, and I. Wolff, “A rigorous dispersive characterization of microstrip cross and T junctions,” *IEEE Trans. on Microwave Theory and Techniques*, vol. **38**, no. 12, pp. 1837–1844, Dec. 1990.

[37] S. S. Chang, W. X. Huang, and T. Itoh, “Computer aided design for planar microstrip circuits analysis by boundary-integral method,” in *19th European Microwave Conf.*, Sep. 1989, pp. 975–978.

[38] F. Giannini, G. Bartolucci, and M. Ruggieri, “An improved equivalent model for microstrip cross-junction,” in *19th European Microwave Conf.*, Sep. 1989, pp. 1226–1231.

[39] A. Weisshaar, S. Luo, M. Thorburn, V. Tripathi, M. Goldfarb, J. Lee, and E. Reese, “Modeling of radial microstrip bends,” in *1990 IEEE MTT-S Int. Microwave Symp. Digest*, May 1990, pp. 1051–1054.

[40] K. Finch and N. Alexopoulos, “Shunt posts in microstrip transmission lines,” *IEEE Trans. on Microwave Theory and Techniques*, vol. **38**, no. 11, pp. 1585–1594, Nov. 1990.

# Chapter 10

## Parallel-coupled Microstrip Lines

### 10.1 Introduction

The arrangement shown in [Figure 10.1](#) illustrates the basic structure under consideration in this chapter. It will be assumed that both microstrip lines have the same widths, which is nearly always the case in practical applications. Some work has also been carried out on multiple arrays of such parallel, edge-coupled lines, but we can usefully restrict the considerations to just two lines throughout most of this chapter.

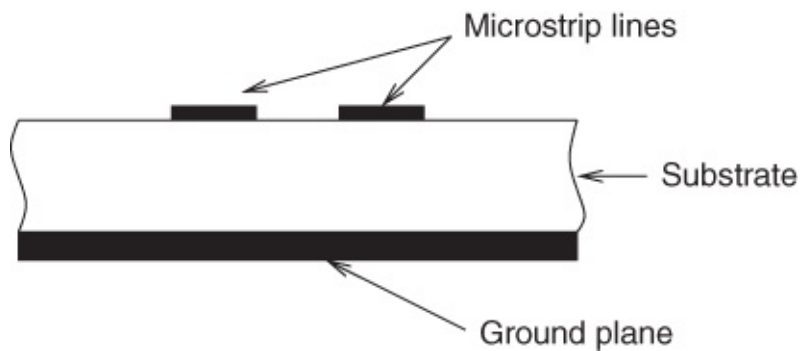


[Figure 10.1](#) A pair of parallel, edge-coupled microstrip lines.

There are two general areas of application for these structures:

- a. Directional couplers, for use in a variety of circuits, including balanced mixers, balanced amplifiers, phase shifters, attenuators, modulators, discriminators, and measurement bridges.
- b. Filters, delay lines, and matching networks, often using arrays of parallel-coupled microstrips as resonant elements.

In the first instance, (a), a prescribed amount of the incident power is required to be coupled out of the system. Thus, for example, a “3 dB coupler” is one in which half of the power input is coupled from one microstrip line into another and then on to separate circuitry. We shall see later in this chapter that good coupler performance is achievable if special modifications are made to the basically simple structure, consisting of two parallel microstrips.

Microstrip filters, (b), employing the parallel-coupled structure are usually of the bandpass or bandstop types.

Apart from direct applications, the calculations described here are also useful for estimating the degree of unwanted coupling between runs of microstrip lines on the same substrate. These calculations may also be judiciously applied to the problem of estimating the degree of crosstalk between such microstrip lines when they are used in high-speed pulse and digital systems.

In this chapter we principally consider the following features:

- a. directional coupler specification
- b. calculation of cross-sectional dimensions (for a desired amount of coupling)
- c. calculation of appropriate coupled-region physical length
- d. frequency response characteristics
- e. coupler directivity
- f. coupler compensation techniques
- g. “special” designs (including Lange)
- h. thickness effects, losses, and fabrication tolerances
- i. crosstalk between microstrips used in high-speed digital systems.

Features (b), (c), (d), and (h) are not only applicable to directional couplers, they are also important in some filter design techniques and in crosstalk calculations (i).

## 10.2 Coupled Transmission Line Theory

### 10.2.1 Parallel-coupled Transmission Lines

A pair of coupled microstrip lines are shown in [Figure 10.2](#). Only one line is driven here, the active line, and this creates electric and magnetic field lines. These interact with the inactive line that is not driven, the victim line, and induce charges and currents on that line. If both lines are driven the field pattern is more complicated. One way of describing the field pattern is to consider it as the linear superposition of two fundamental field patterns or modes. There is not a unique way to express the two underlying modes but microwave engineers have developed one convention and here the two modes are called even and odd modes.

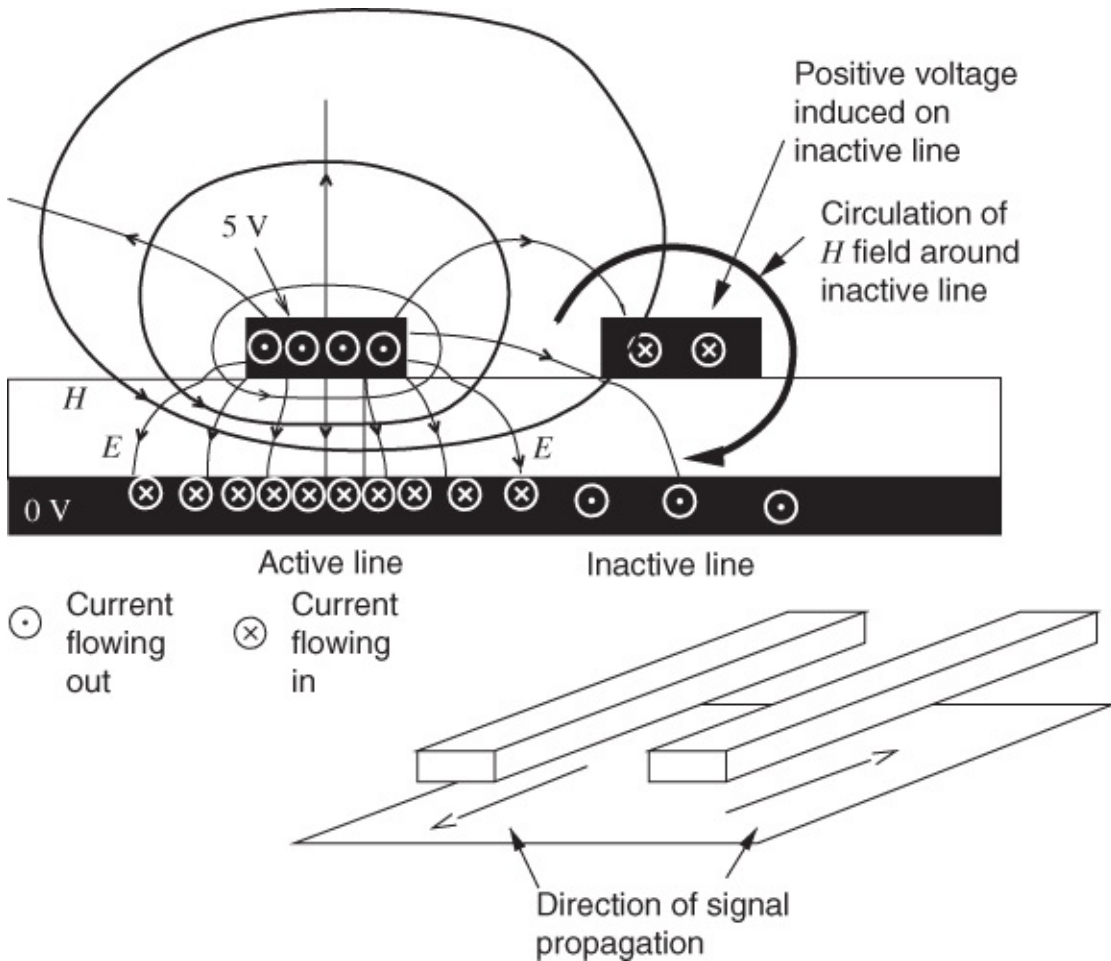


**Figure 10.2** Coupled microstrip lines in perspective.

### 10.2.2 Even and Odd Modes

Any parallel-coupled pair of transmission lines, regardless of their practical realization, may be described by the four-port configuration indicated schematically in [Figure 10.3](#). The dashed lines indicate mutual coupling; input and output connections and terminations have been omitted for simplicity.

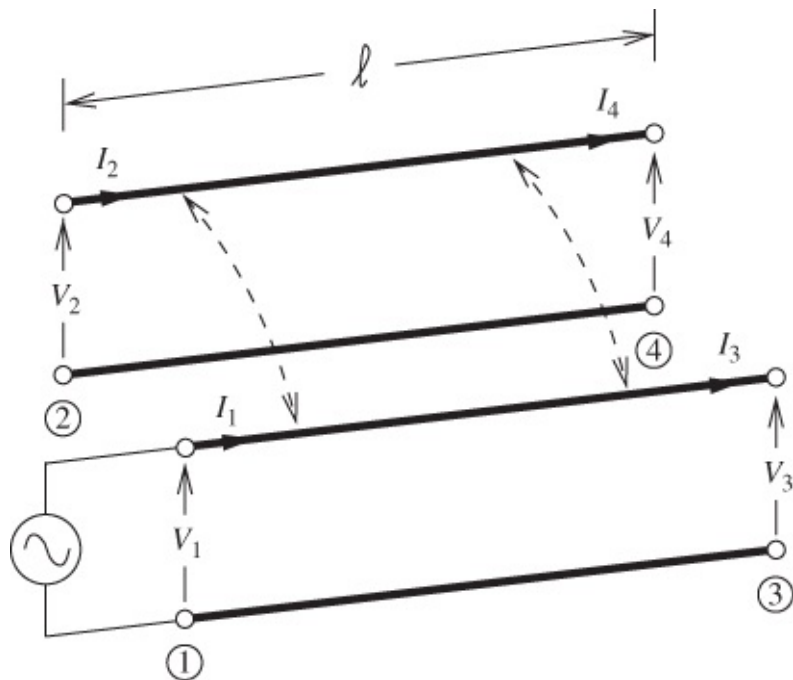


**Figure 10.3** Two parallel-coupled transmission lines.

To examine the coupling modes which are established, we now concentrate on a pure TEM-mode type of structure. The simplest structure to consider is the dual, coaxial, coupled-line system, in which electric and magnetic fields couple through a narrow slot cut into the adjacent outer conductor along a certain length. Such a structure is shown in [Figure 10.4\(a\)](#). Notice that the consistent field patterns correspond to waves traveling in opposite directions along the respective lines, and it may be stated that any parallel-coupled pair of transmission lines yield contra-directional traveling waves.

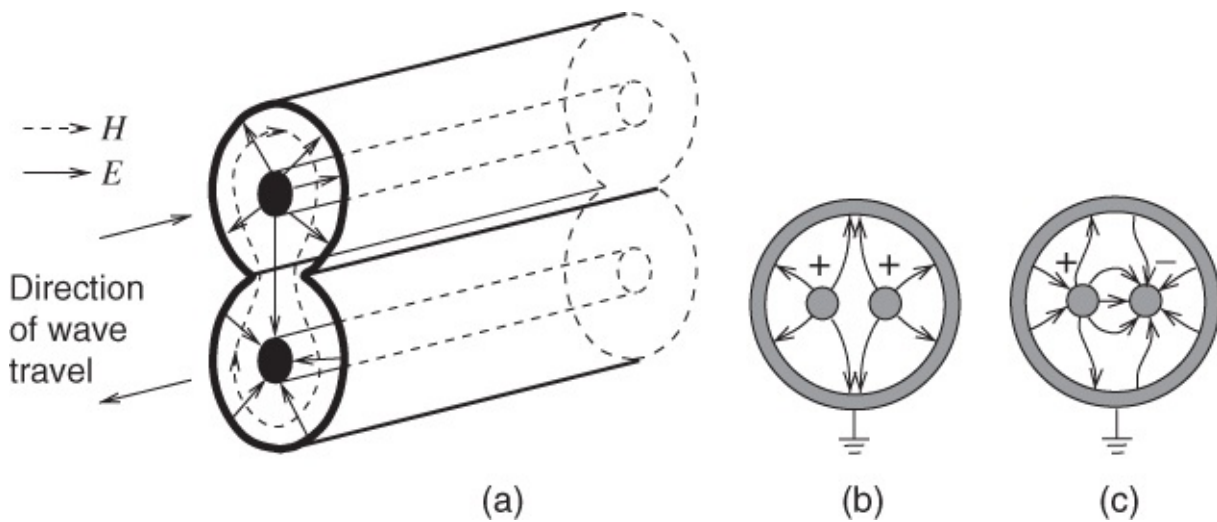


**Figure 10.4** Parallel-coupled coaxial lines: (a) showing fields; (b) even mode; and (c) odd mode. For simplicity only the electric field is indicated in (b) and (c).

The coupled coaxial arrangement constitutes a pure TEM-mode system, assuming either a uniform dielectric filling or an air-filled structure. At any instant the relative polarities of the voltages, taken at any specific plane along the structure, will either be alike or opposite. We refer to different field configurations set up by such polarities as the even mode and the odd

mode, respectively. [Figures 10.4\(b\) and \(c\)](#) illustrate these effects. The complete behavior of the coupled structure can be obtained by superposition of the effects due to these two modes.

Because of the assumed uniform dielectric filling, any signal traveling in such a pure TEM-mode system will always travel at the same velocity,  $v = c/\sqrt{\epsilon_r}$  ([Equation \(2.27\)](#)). Thus, the velocity associated with the even mode is identical to that associated with the odd mode here.

The equivalent primary constants for the coupled lines having even or odd modes, taken separately, must differ because of the different field distributions. As a result of this two distinct characteristic impedances may be defined, one for each mode, expressed in terms of the different primary constants by equations of the form of the equation for the characteristic impedance of a single line (i.e.,  $Z_0 = \sqrt{L/C}$ ). We term these impedances the even- and odd-mode characteristic impedances, denoted by  $Z_{0e}$  and  $Z_{0o}$ . This applies to any TEM-mode or quasi-TEM mode parallel-coupled structure, and the characteristic impedances are major parameters in design procedures.

While even and odd modes are the most common form of the coupled modes to use with microwave circuits, common and differential modes are more usually encountered with digital circuits and RFICs. The difference between the mode sets amounts to book keeping. A treatment relating the two mode sets is given in [1].

### 10.2.3 Transmission Line Equations

The four-port configuration, [Figure 10.3](#), can readily be analyzed by connecting matched terminations  $Z_0$  at ports 2, 3, and 4, driving the circuit from a 2 V source having an impedance which is also equal to  $Z_0$ . The resulting “correctly terminated” configuration is shown in [Figure 10.5](#). Later on in the analysis it is shown that  $Z_0$  is explicitly related to the even- and odd-mode characteristic impedances associated with this coupled-line arrangement.

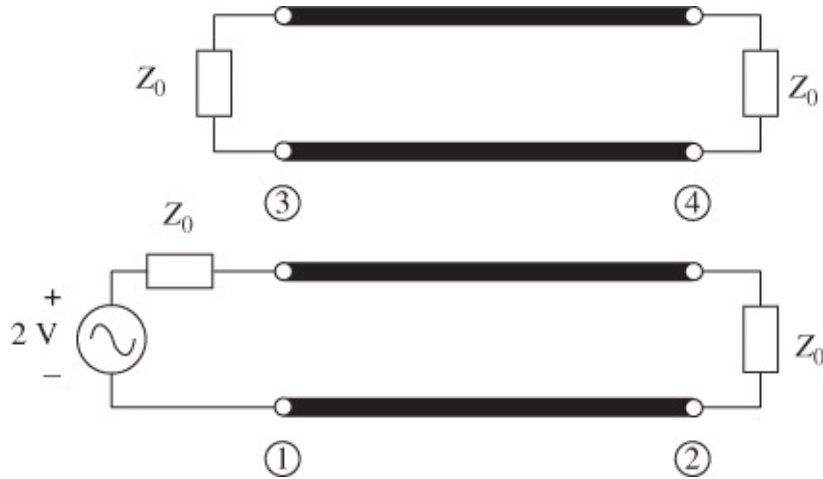


[Figure 10.5](#) Terminated coupled-line configuration.

Note that for this analysis, which applies for the TEM mode only, we assume the lines to be totally embedded in a uniform dielectric. As a consequence of this, the odd- and even-mode characteristic impedances appear, but the phase velocity has a single value. This means that we can derive useful frequency-dependent impedance relations that still apply quite accurately to

cases where propagation is not strictly TEM (such as for microstrip). However, the even- and odd-mode phase velocities are of different values in the non-TEM situations and this leads to some considerable refinements of the theory. In particular, non-TEM couplers possess finite (i.e., imperfect) directivity. These features are discussed in more detail in [Chapter 11 \(Section 11.4.4\)](#).

We now proceed with a detailed analysis of the TEM-mode parallel-coupled lines. The arrangement of [Figure 10.5](#) may be analyzed by first considering excitation under even-mode conditions alone, then odd-mode conditions alone, and finally combining the results. The notation is given in [Figure 10.6](#). In this arrangement it is assumed that losses may be neglected so that the propagation coefficient,  $\gamma = \alpha + j\beta$ , reduces to the phase coefficient  $j\beta$  only.

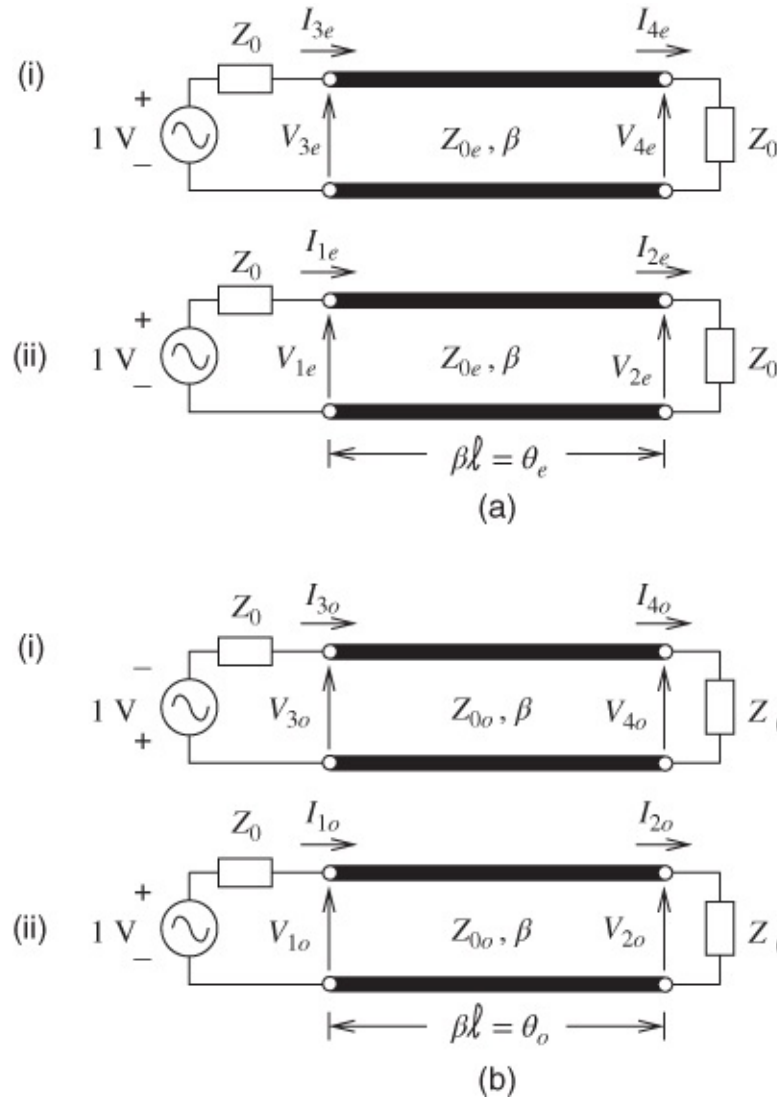


[Figure 10.6](#) Even and odd mode coupled-line representations: (a) even mode; and (b) odd mode.

Since the structure is physically symmetrical, it can be seen ([Figure 10.6](#)) that only two circuits actually have to be solved. We will take [Figures 10.6\(a\)\(ii\)](#) and [\(b\)\(ii\)](#). Then, later, we can use the fact that the total voltages and currents on the original structure are a superposition of the even- and odd-mode solutions as follows:

$$\left. \begin{array}{l} V_1 = V_{1e} + V_{1o} \\ V_2 = V_{2e} + V_{2o} \\ V_3 = V_{1e} - V_{1o} \\ V_4 = V_{2e} - V_{2o} \end{array} \quad \begin{array}{l} I_1 = I_{1e} + I_{1o} \\ I_2 = I_{2e} + I_{2o} \\ I_3 = I_{1e} - I_{1o} \\ I_4 = I_{2e} - I_{2o} \end{array} \right\}. \quad \text{10.1}$$

Now the  $ABCD$  matrix for any transmission line was given as Equation (4.22). This can be used to express the voltage–current relations for lines (a)(ii) and (b)(i) in Figure 10.6 as follows:

$$\begin{bmatrix} V_{1e} \\ I_{1e} \end{bmatrix} = \begin{bmatrix} \cos \theta & jZ_{0e} \sin \theta \\ jY_{0e} \sin \theta & \cos \theta \end{bmatrix} \begin{bmatrix} V_{2e} \\ I_{2e} \end{bmatrix} \quad \text{10.2}$$

and

$$\begin{bmatrix} V_{1o} \\ I_{1o} \end{bmatrix} = \begin{bmatrix} \cos \theta & jZ_{0o} \sin \theta \\ jY_{0o} \sin \theta & \cos \theta \end{bmatrix} \begin{bmatrix} V_{2o} \\ I_{2o} \end{bmatrix}. \quad \text{10.3}$$

Applying the terminal conditions  $V_{2e} = Z_0 I_{2e}$ ,  $V_{2o} = Z_0 I_{2o}$ ,  $V_{1e} + I_{1e} Z_0 = 1$ , and  $Z_0 = \frac{V_{1o} + I_{1o}}{1}$  results in the voltage and current expressions:

$$V_{1e} = \frac{Z_{0e} Z_0 \cos \theta + jZ_{0e}^2 \sin \theta}{2Z_{0e} Z_0 \cos \theta + j(Z_{0e}^2 + Z_0^2) \sin \theta} \quad \text{10.4}$$

$$I_{1e} = \frac{Z_{0e} \cos \theta + jZ_0 \sin \theta}{2Z_{0e} Z_0 \cos \theta + j(Z_{0e}^2 + Z_0^2) \sin \theta} \quad \text{10.5}$$

$$V_{2e} = \frac{Z_0 Z_{0e}}{2Z_{0e} Z_0 \cos \theta + j(Z_{0e}^2 + Z_0^2) \sin \theta} \quad \text{10.6}$$

$$I_{2e} = \frac{Z_{0e}}{2Z_{0e} Z_0 \cos \theta + j(Z_{0e}^2 + Z_0^2) \sin \theta} \quad \text{10.7}$$

$$V_{1o} = \frac{Z_{0o} Z_0 \cos \theta + jZ_0^2 \sin \theta}{2Z_{0o} Z_0 \cos \theta + j(Z_{0o}^2 + Z_0^2) \sin \theta} \quad \text{10.8}$$

$$I_{1o} = \frac{Z_{0o} \cos \theta + jZ_0 \sin \theta}{2Z_{0o} Z_0 \cos \theta + j(Z_{0o}^2 + Z_0^2) \sin \theta} \quad \text{10.9}$$

$$V_{2o} = \frac{Z_0 Z_{0o}}{2Z_{0o} Z_0 \cos \theta + j(Z_{0o}^2 + Z_0^2) \sin \theta} \quad \text{10.10}$$

$$I_{2o} = \frac{Z_{0o}}{2Z_{0o} Z_0 \cos \theta + j(Z_{0o}^2 + Z_0^2) \sin \theta}. \quad \text{10.11}$$

The next step consists of an important simplification and amounts to forcing the composite original circuit to become matched to the feed lines of characteristic impedance  $Z_0$ . Therefore, the total input impedance  $Z_{in}$  has to equal  $Z_0$ :

$$Z_{in} = Z_0 = \frac{V_1}{I_1} = \frac{V_{1e} + V_{1o}}{I_{1e} + I_{1o}}. \quad \underline{10.12}$$

Substituting Equations (10.4), (10.5), (10.8), and (10.9) into Equation (10.12) gives

$$Z_0 = \frac{Z_0(Z_{0e}D_e + Z_{0o}D_o) \cos \theta + j(Z_{0e}^2 D_e + Z_{0o}^2 D_o) \sin \theta}{(Z_{0e}D_e + Z_{0o}D_o) \cos \theta + jZ_0(D_e + D_o) \sin \theta} \quad \underline{10.13}$$

where

$$D_e = 2Z_{0e}Z_0 \cos \theta + j(Z_{0e}^2 + Z_0^2) \sin \theta \quad \underline{10.14}$$

and

$$D_o = 2Z_{0o}Z_0 \cos \theta + j(Z_{0o}^2 + Z_0^2) \sin \theta. \quad \underline{10.15}$$

The equality of Equation (10.13) will be established if

$$Z_0^2(D_e + D_o) = Z_{0e}^2 D_e + Z_{0o}^2 D_o.$$

Substituting, using Equations (10.14) and (10.15) for  $D_e$  and  $D_o$ , results in

$$\begin{aligned} & 2Z_0^3(Z_{0e} + Z_{0o}) \cos \theta + j(Z_{0e}^2 Z_0^2 + Z_{0o}^2 Z_0^2 + 2Z_0^4) \sin \theta \\ &= 2Z_{0e}Z_{0o}Z_0(Z_{0e} + Z_{0o}) \cos \theta + j(Z_{0e}^2 Z_0^2 + Z_{0o}^2 Z_0^2 + 2Z_{0e}^2 Z_{0o}^2) \sin \theta. \end{aligned}$$

This equality will be satisfied if

$$Z_0^2 = Z_{0e}Z_{0o}. \quad \underline{10.16}$$

Inserting this relationship into Equations (10.4) to (10.11) gives

$$V_{1e} = \frac{Z_0 \cos \theta + jZ_{0e} \sin \theta}{2Z_0 \cos \theta + j(Z_{0e} + Z_{0o}) \sin \theta} \quad \underline{10.17}$$

$$I_{1e} = \frac{\cos \theta + jZ_{0o}Y_0 \sin \theta}{2Z_0 \cos \theta + j(Z_{0e} + Z_{0o}) \sin \theta} \quad \underline{10.18}$$

$$V_{2e} = \frac{Z_0}{2Z_0 \cos \theta + j(Z_{0e} + Z_{0o}) \sin \theta} \quad \underline{10.19}$$

$$I_{2e} = \frac{1}{2Z_0 \cos \theta + j(Z_{0e} + Z_{0o}) \sin \theta} \quad \underline{10.20}$$

$$V_{1o} = \frac{Z_0 \cos \theta + j Z_{0o} \sin \theta}{2Z_0 \cos \theta + j (Z_{0e} + Z_{0o}) \sin \theta} \quad \text{10.21}$$

$$I_{1o} = \frac{\cos \theta + j Z_{0e} Y_0 \sin \theta}{2Z_0 \cos \theta + j (Z_{0e} + Z_{0o}) \sin \theta} \quad \text{10.22}$$

$$V_{2o} = \frac{Z_0}{2Z_0 \cos \theta + j (Z_{0e} + Z_{0o}) \sin \theta} \quad \text{10.23}$$

$$I_{2o} = \frac{1}{2Z_0 \cos \theta + j (Z_{0e} + Z_{0o}) \sin \theta}. \quad \text{10.24}$$

Final expressions for the total (complete structure, [Figure 2.14](#)) voltages and currents can now be obtained by substituting Equations (10.17) to (10.24) into Equation (10.1):

$$V_1 = V_{1e} + V_{1o} = \frac{2Z_0 \cos \theta + j (Z_{0e} + Z_{0o}) \sin \theta}{2Z_0 \cos \theta + j (Z_{0e} + Z_{0o}) \sin \theta} = 1 \quad \text{10.25}$$

$$I_1 = I_{1e} + I_{1o} = \frac{2 \cos \theta + j Y_0 (Z_{0e} + Z_{0o}) \sin \theta}{2Z_0 \cos \theta + j (Z_{0e} + Z_{0o}) \sin \theta} = \frac{1}{Z_0} \quad \text{10.26}$$

$$V_2 = V_{2e} + V_{2o} = \frac{2Z_0}{2Z_0 \cos \theta + j (Z_{0e} + Z_{0o}) \sin \theta} \quad \text{10.27}$$

$$I_2 = I_{2e} + I_{2o} = \frac{2}{2Z_0 \cos \theta + j (Z_{0e} + Z_{0o}) \sin \theta} \quad \text{10.28}$$

$$V_3 = V_{1e} - V_{1o} = \frac{j (Z_{0e} - Z_{0o}) \sin \theta}{2Z_0 \cos \theta + j (Z_{0e} + Z_{0o}) \sin \theta} \quad \text{10.29}$$

$$I_3 = I_{1e} - I_{1o} = \frac{j Y_0 (Z_{0o} - Z_{0e})}{2Z_0 \cos \theta + j (Z_{0e} + Z_{0o}) \sin \theta} \quad \text{10.30}$$

$$V_4 = V_{2e} - V_{2o} = \frac{0}{2Z_0 \cos \theta + j (Z_{0e} + Z_{0o}) \sin \theta} = 0 \quad \text{10.31}$$

$$I_4 = I_{2e} - I_{2o} = \frac{0}{2Z_0 \cos \theta + j (Z_{0e} + Z_{0o}) \sin \theta} = 0. \quad \text{10.32}$$

These voltages and currents can be further simplified by defining a coupling factor  $C$  such that

$$C = \frac{Z_{0e} - Z_{0o}}{Z_{0e} + Z_{0o}}. \quad \text{10.33}$$

Using this definition plus the relationship  $Z_0^2 = Z_{0e}Z_{0o}$ , Equation (10.16), allows us to write:

$$V_1 = 1 \text{ (just the input voltage, as defined)} \quad \underline{10.34}$$

$$V_2 = \frac{\sqrt{1 - C^2}}{\sqrt{1 - C^2} \cos \theta + j \sin \theta} \quad \underline{10.35}$$

$$V_3 = \frac{jC \sin \theta}{\sqrt{1 - C^2} \cos \theta + j \sin \theta} \quad \underline{10.36}$$

$$V_4 = 0. \quad \underline{10.37}$$

The maximum degree of coupling occurs when the length of the coupled structure is  $\lambda_g/4$ , that is, when  $\theta = \pi/2$ . This condition, set using Equations (10.34) to (10.37), yields

$$V_1 = 1 \text{ just the input voltage, as in Equation (10.25)} \quad \underline{10.38}$$

$$V_2 = -j\sqrt{1 - C^2} \quad \underline{10.39}$$

$$V_3 = C \quad \underline{10.40}$$

$$V_4 = 0 \text{ as in Equation (1.38).} \quad \underline{10.41}$$

Equation (10.40) gives the mid-band (maximum) extent of coupling,  $C$ , expressed in terms of impedances by Equation (10.33). Equation (10.39) shows that the transmitted voltage  $V_2$  (which is not electromagnetically coupled) depends on  $C$  and is  $90^\circ$  out-of-phase with  $V_1$ , and hence also with  $V_3$ . This feature gives rise to the names often used for couplers based on this parallel-coupled line principle:  $90^\circ$  hybrid or quadrature coupler. (There is zero output on port 4 for a theoretically perfect structure.)

The principal frequency response characteristics,  $|V_2(\theta)|$  and  $|V_3(\theta)|$ , may be obtained from Equations (10.35) and (10.36), respectively, where we note that the electrical length  $\theta$  is also given by

$$\theta = \frac{2\pi\ell}{\lambda_g} = \frac{2\pi f \ell}{v}. \quad \underline{10.42}$$

Since the physical length  $\ell$  of the structure is fixed and we assume the velocity of propagation  $v$  to be constant, Equation (10.42) shows that  $\theta$  is directly dependent on the frequency  $f$ .

In design procedures we shall usually be confronted with the problem of determining the physical dimensions of some proposed parallel-coupled line structure. The cross-sectional dimensions, line separation, and line diameters or widths can be determined given  $Z_{0e}$  and  $Z_{0o}$ . Thus we require  $Z_{0e}$  and  $Z_{0o}$  as functions of  $Z_0$  and  $C$ . These relationships may be obtained from Equations (10.33) and (10.16). The coupling factor  $C$  is often expressed in decibels. If we call this value  $C'$  and remember that we have a voltage ratio, then from Equation (10.33):

$$C' = 20 \log C = 20 \log \left| \frac{Z_{0e} - Z_{0o}}{Z_{0e} + Z_{0o}} \right| \text{ dB.} \quad \underline{\text{10.43}}$$

Combining this with Equation (10.16),  $Z_0^2 = Z_{0e}Z_{0o}$ , yields the initial design equations:

$$Z_{0e} = Z_0 \sqrt{\frac{1 + 10^{C'/20}}{1 - 10^{C'/20}}} \quad \underline{\text{10.44}}$$

and

$$Z_{0o} = Z_0 \sqrt{\frac{1 - 10^{C'/20}}{1 + 10^{C'/20}}}. \quad \underline{\text{10.45}}$$

The application of these equations is discussed in [Chapter 11](#).

### 10.2.4 Capacitance Matrix Extraction

This section describes how the capacitance matrix of a number of coupled conductors can be extracted from measurements or measurement-like simulations. Measurements and many programs that extract capacitance of an interconnect network do so by evaluating one capacitance at a time for different connections of interconnects to each other. What is presented here is based on the treatment in [2].

Without loss of generality, consider the three line structure shown in [Figure 10.7](#), where there are four conductors including the ground. While three parallel lines are shown here this could be a much more complicated structure. A  $3 \times 3$  capacitance matrix is required to describe the capacitive coupling of this structure, but measurements and most electromagnetic simulators can only determine one capacitance at a time. The solution is to connect the individual interconnects into two connected structures and determine the capacitance between the pairs of connected conductors. This procedure is repeated until every combination is considered. In this case there are seven possible combinations, as shown in [Figure 10.8](#). These combinations can be realized experimentally by connecting together the appropriate black and white groups of conductors so that the desired capacitance is measured between the black conductor group and the white group. The measurement of two similar structures, but with some known difference, such as lines of different length, can be used to calibrate out the error introduced by the electrical connections, or they can be simply ignored, which is usually reasonable. In an electromagnetic simulation the connections are conveniently realized by holding the black group at one voltage, say 1 V, and the white group at 0 V. The corresponding capacitance connections are shown on the right of this figure, and the seven individual capacitance measurements are  $C_A$ ,  $C_B$ ,  $C_C$ ,  $C_D$ ,  $C_E$ ,  $C_F$ , and  $C_G$ . Note that because of reciprocity,  $C_{ij} = C_{ji}$ . Thus the capacitance matrix

$$\mathbf{C} = \begin{bmatrix} C_{11} & C_{12} & C_{13} \\ C_{21} & C_{22} & C_{23} \\ C_{31} & C_{32} & C_{33} \end{bmatrix} = \begin{bmatrix} C_{11} & C_{12} & C_{13} \\ C_{12} & C_{22} & C_{23} \\ C_{13} & C_{23} & C_{33} \end{bmatrix} \quad \underline{\text{10.46}}$$

can be derived. Note that there are seven measurements that can be conveniently made, but there are only six unknown quantities in the capacitance matrix. Thus, only six measurements are required to determine the capacitance matrix and the redundancy (the extra measurement) can be used as a check on the results. Using the first six measurements:

$$\begin{bmatrix} C_A \\ C_B \\ C_C \\ C_D \\ C_E \\ C_F \end{bmatrix} = \begin{bmatrix} 1 & 1 & 1 & 0 & 0 & 0 \\ 0 & 1 & 0 & 1 & 1 & 0 \\ 0 & 0 & 1 & 0 & 1 & 1 \\ 1 & 0 & 1 & 1 & 1 & 0 \\ 1 & 1 & 0 & 0 & 1 & 1 \\ 0 & 1 & 1 & 1 & 0 & 1 \end{bmatrix} \begin{bmatrix} C_{11} \\ C_{12} \\ C_{13} \\ C_{22} \\ C_{23} \\ C_{33} \end{bmatrix}. \quad 10.47$$

Thus

$$\begin{bmatrix} C_{11} \\ C_{12} \\ C_{13} \\ C_{22} \\ C_{23} \\ C_{33} \end{bmatrix} = \begin{bmatrix} 1 & 1 & 1 & 0 & 0 & 0 \\ 0 & 1 & 0 & 1 & 1 & 0 \\ 0 & 0 & 1 & 0 & 1 & 1 \\ 1 & 0 & 1 & 1 & 1 & 0 \\ 1 & 1 & 0 & 0 & 1 & 1 \\ 0 & 1 & 1 & 1 & 0 & 1 \end{bmatrix}^{-1} \begin{bmatrix} C_A \\ C_B \\ C_C \\ C_D \\ C_E \\ C_F \end{bmatrix}. \quad 10.48$$

A similar procedure can be used to extract the elements of the inductance matrix.

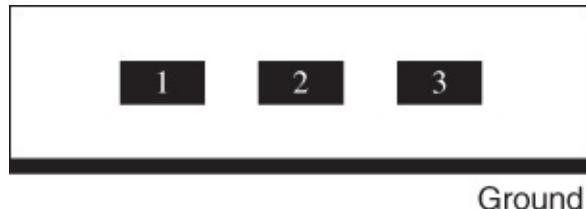


**Figure 10.7** Cross-section of three-line structure with four conductors.

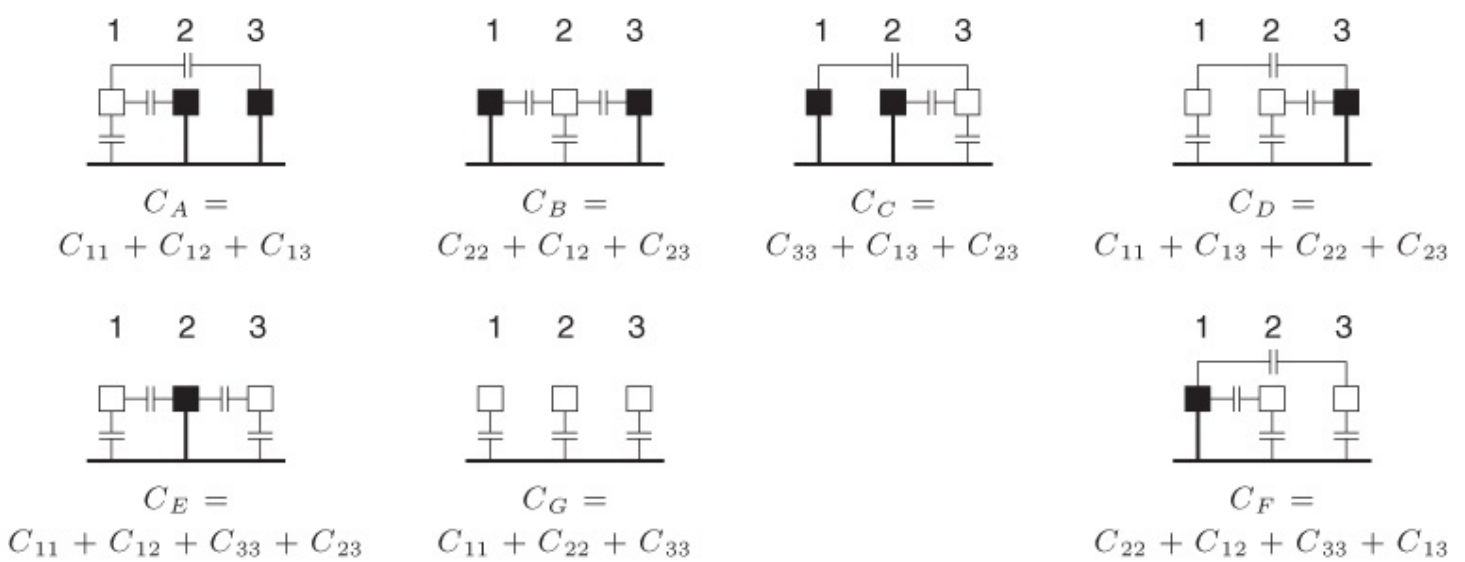


**Figure 10.8** Combinations of conductors leading to various capacitance measurements.

## 10.3 Formulas for Characteristic Impedance of Coupled Lines

In [Section 10.2](#) we considered the basic properties of TEM lines in a parallel-coupled configuration. Just as single microstrip lines are quasi-TEM, so coupled microstrip lines also exhibit a field pattern which is strictly quasi-TEM. We may, however, examine even-mode and odd-mode excitation ([Figure 10.9](#)) for the coupled microstrips.

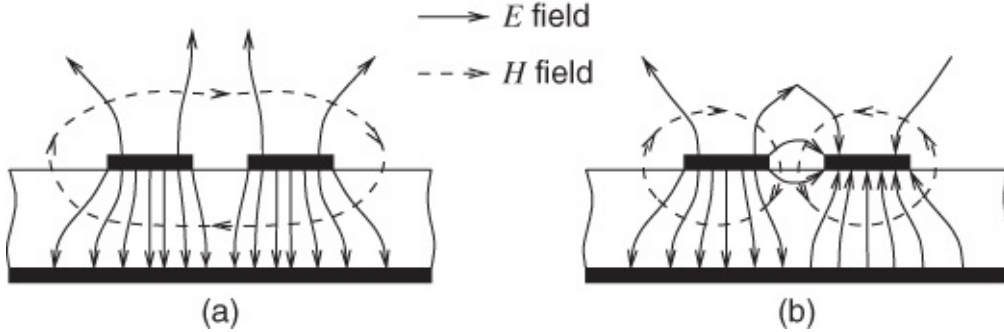


**Figure 10.9** Field distributions resulting from (a) even-mode and (b) odd-mode excitation of parallel-coupled microstrip lines.

Notice that the relative proportions of fields shared between the dielectric substrate and the air are different. Thus, the phase velocities are also different, a fact which represents an extra design complication. Referring to [Section 10.2.3](#) this means that, strictly speaking,  $\theta_e \neq \theta_o$  and Equation (10.16) cannot be evoked to exactly satisfy the equality relationship given (because only a single  $\theta$  was present there). There is no reason why we should not continue to define the coupling factor as Equation (10.33), but the remaining relationships, for  $V_2$ ,  $V_3$ , and  $V_4$  are all more complicated. We shall return to this problem from a design viewpoint shortly.

The cross-sectional dimensions which we require from a design procedure are  $w$  and  $s$ , as indicated in [Figure 10.10](#). Both the even and the odd modes exist under the normal circuit excitation conditions associated with a microstrip coupler. However, coupler calculation and design proceeds from consideration of the effects due to each mode taken separately.

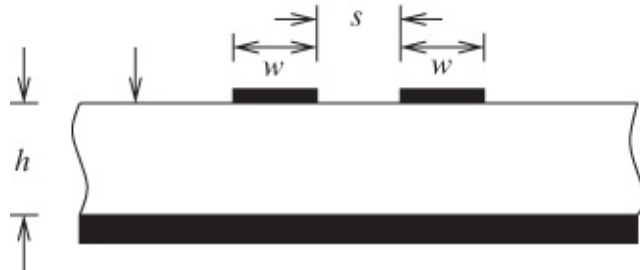


**Figure 10.10** Cross-sectional dimensions: nomenclature.

Two sets of formulas for characteristic impedance are presented below and were developed by Bryant and Weiss [3], and Hammerstad and Jensen [4], respectively. Bryant and Weiss's formulas are based on effective even- and odd-mode capacitances and hence provide valuable insight. The formulas developed by Hammerstad and Jensen have high accuracy.

### 10.3.1 Derivation of Bryant and Weiss

Analysis yielding  $Z_{0e}$  and  $Z_{0o}$ , as functions of  $\epsilon_r$  and the shape ratios  $w/h$  and  $s/h$ , has been carried out by several groups, notably Bryant and Weiss [3]. Although this work is less accurate than that to be presented in [Section 10.3.2](#), it introduces an important concept: it is based on even- and odd-mode capacitances.

The method of analysis due to Bryant and Weiss [3] amounts to a rigorous solution of the electrostatic problem for coupled microstrip lines. They determine capacitances on a static TEM basis. Longitudinal components of the fields are neglected and the thickness of the microstrips is also neglected. A formulation based essentially on Laplace's equation is employed with the proper boundary conditions inserted. Iterative numerical methods are used in the computer solution and the impedances are finally obtained as follows.

We start with the effective permittivity (see Equations [\(6.10\)](#) and [\(6.11\)](#)):

$$\epsilon_{\text{eff}} = \frac{C}{C_1} \quad 10.49$$

where  $C$  is the microstrip capacitance per unit length per strip with the substrate present and  $C_1$  is the microstrip capacitance per unit length per strip with the substrate absent (i.e.,  $\epsilon_{\text{eff}} = 1$ ). The velocity of propagation  $v_p$  is then, from Equation [\(6.10\)](#),

$$v_p = \frac{c}{\sqrt{\epsilon_{\text{eff}}}} \quad 10.50$$

and the characteristic impedance is, from Equation [\(6.3\)](#),

$$Z_0 = \frac{1}{v_p C} = \frac{1}{c C_1 \sqrt{\epsilon_{\text{eff}}}}. \quad 10.51$$

For odd and even modes we therefore have, respectively,

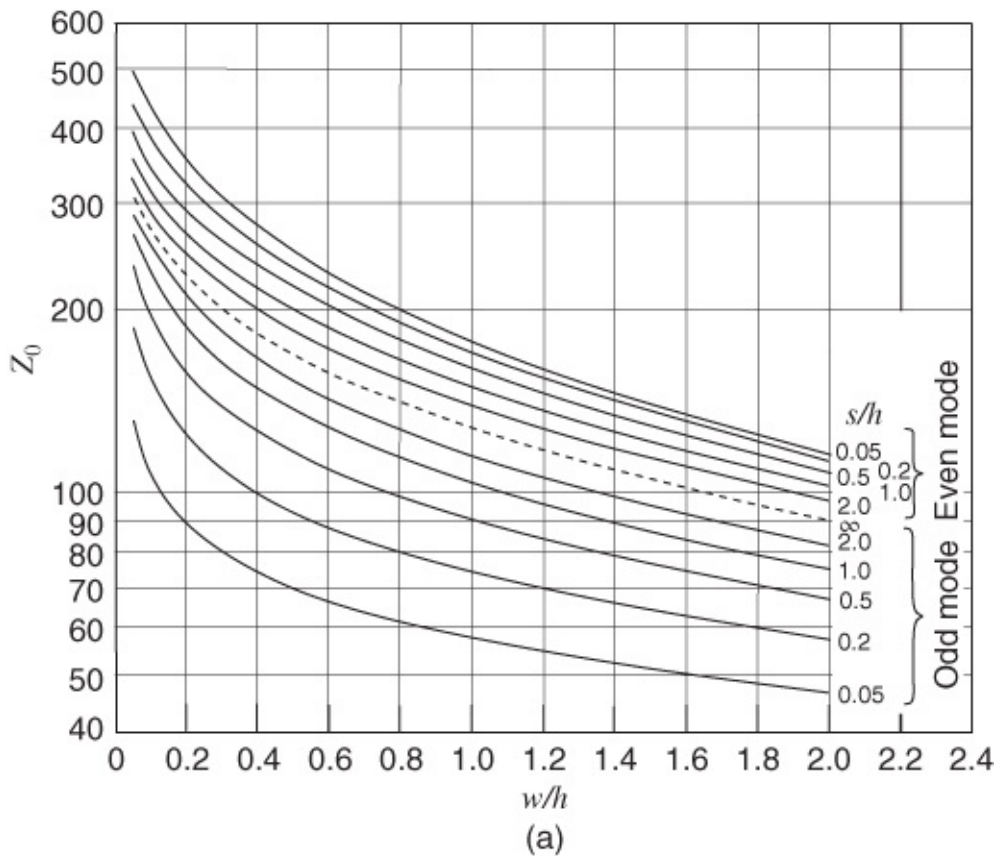
$$Z_{0o} = \frac{1}{c C_{1o} \sqrt{\epsilon_{\text{eff},o}}} \quad 10.52$$

and

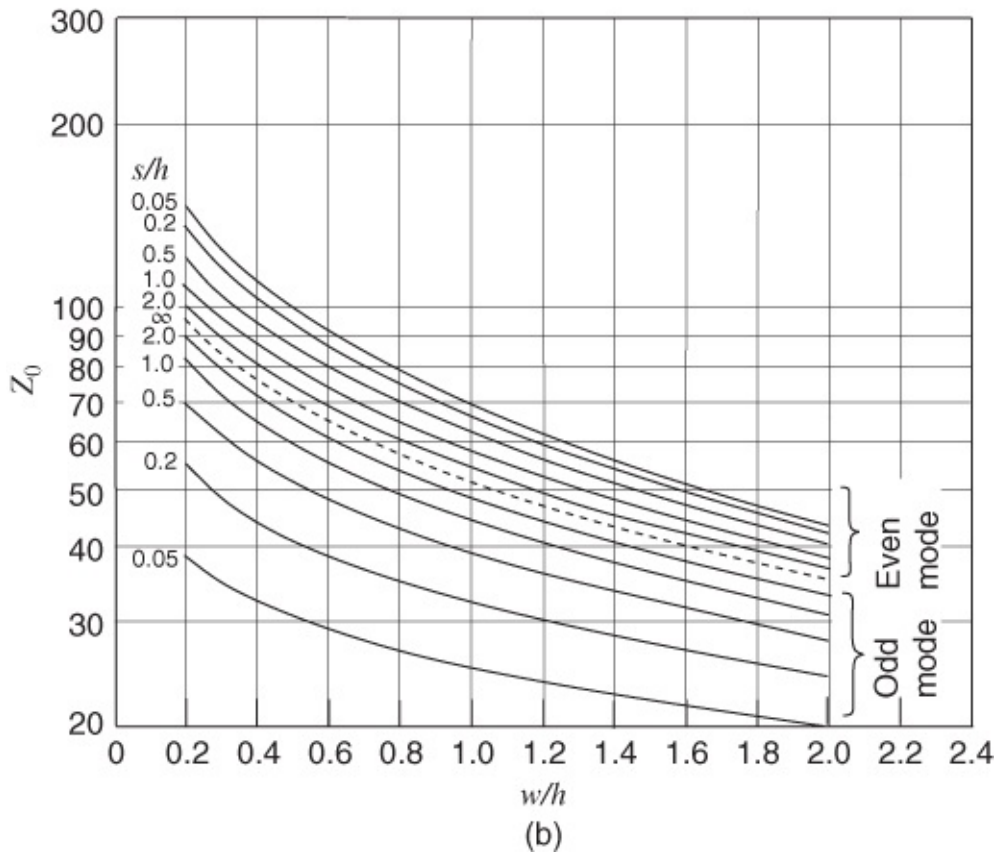
$$Z_{0e} = \frac{1}{c C_{1e} \sqrt{\epsilon_{\text{eff},e}}}. \quad 10.53$$

The calculations required, leading to  $C_{1o}$ ,  $C_{1e}$ , and  $\epsilon_{\text{eff},e}$ ,  $\epsilon_{\text{eff},o}$ , are carried out in a manner identical to that described in [Section 6.10](#). Some numerical data obtained using this analysis technique are presented graphically in [Figure 10.11](#). In design,  $Z_{0e}$  and  $Z_{0o}$  are marked on the vertical axis of a graph for the appropriate substrate material ( $\epsilon_r$ ). It is then necessary to read these values across horizontally until two points are found lying vertically above one another, and at identical values of  $s/h$ . Dropping a vertical ordinate through these points then also

yields the required value of  $w/h$ . Interpolation and other difficulties with the graphs make this an approximate and rather clumsy design technique. However, it may be useful in certain instances and a specific microstrip coupler design, using these curves, will be undertaken in [Chapter 11](#).



(a)



(b)

**Figure 10.11** Numerical results for the even- and odd-mode characteristic impedances of parallel-coupled microstrip lines: (a)  $\epsilon_r = 1$ ; and (b)  $\epsilon_r = 9$ . Adapted from Bryant and Weiss (1968) [3], figures 6,7, p. 1025. Reprinted with permission of IEEE.

### 10.3.2 Derivation of Hammerstad and Jansen

Formulas for the characteristic impedance and effective permittivity of coupled microstrip lines were developed by Hammerstad and Jensen based on the concept of even and odd modes [4]. The formulas are accurate to better than 1% for  $0.1 \leq u \leq 10$  and  $g > 0.01$ , where  $u$  is the normalized width:

$$u = w/h \quad 10.54$$

and  $g$  is the normalized gap:

$$g = s/h. \quad 10.55$$

In the following  $Z_0$  and  $\epsilon_{\text{eff}}$  refer to the characteristic impedance and effective permittivity of an individual microstrip line with a normalized width of  $u$  on a substrate with a relative permittivity of  $\epsilon_r$ .

#### Even-mode Coupled Line Parameters

The even-mode characteristic impedance is

$$Z_{0e}(u, g) = Z_{01e}(u, g) / \sqrt{\epsilon_{\text{eff},e}(u, g, \epsilon_r)} \quad 10.56$$

where  $\epsilon_{\text{eff},e}$  is the effective relative permittivity of the even mode and  $Z_{01e}$  is the even-mode characteristic impedance with the dielectric replaced by free-space:

$$Z_{01e}(u, g) = \frac{Z_{01}(u)}{1 - Z_{01}(u)\phi_e(u, g)/\eta_0}. \quad 10.57$$

Now  $Z_{01}(u)$  is the free-space characteristic impedance of an individual microstrip line and is given by Equation (6.25). In Equations (10.56) and (10.57), the effective permittivity of the even-mode is

$$\epsilon_{\text{eff},e}(u, g, \epsilon_r) = \frac{\epsilon_r + 1}{2} + \frac{\epsilon_r - 1}{2} F_e(u, g, \epsilon_r) \quad 10.58$$

where

$$F_e(u, g, \epsilon_r) = \left[ 1 + \frac{10}{\mu(u, g)} \right]^{-a(\mu)b(\epsilon_r)} \quad 10.59$$

$$a(u) = 1 + \frac{1}{49} \ln \left[ \frac{u^4 + \{u/52\}^2}{u^4 + 0.432} \right] + \frac{1}{18.7} \ln \left[ 1 + \left( \frac{u}{18.1} \right)^3 \right] \quad 10.60$$

$$b(\epsilon_r) = 0.564 \left[ \frac{\epsilon_r - 0.9}{\epsilon_r + 3} \right]^{0.053} \quad 10.61$$

$$\phi_e(u, g) = \frac{\varphi(u)}{\psi(g) \{ \alpha(g) u^{m(g)} + [1 - \alpha(g)] u^{-m(g)} \}} \quad \text{10.62}$$

$$\varphi(u) = 0.8645 u^{0.1472} \quad \text{10.63}$$

$$\psi(g) = 1 + \frac{g}{1.45} + \frac{g^{2.09}}{3.95} \quad \text{10.64}$$

$$\alpha(g) = 0.5 \exp(-g) \quad \text{10.65}$$

$$m(g) = 0.2175 + \left[ 4.113 + \left( \frac{20.36}{g} \right)^6 \right]^{-0.251} + \frac{1}{323} \ln \left[ \frac{g^{10}}{1 + (g/13.8)^{10}} \right] \quad \text{10.66}$$

$$\mu(u, g) = g \exp(-g) + \frac{u(20 + g^2)}{10 + g^2} \quad \text{10.67}$$

## Odd-mode Coupled Line Parameters

The odd-mode characteristic impedance is

$$Z_{0o}(u, g) = Z_{01o}(u, g) / \sqrt{\epsilon_{\text{eff},o}(u, g, \epsilon_r)} \quad \text{10.68}$$

where  $\epsilon_{\text{eff},o}$  is the effective relative permittivity of the odd-mode and  $Z_{01o}$  is the odd-mode characteristic impedance with the dielectric replaced by free-space:

$$Z_{01o}(u, g) = \frac{Z_{01}(u)}{1 - Z_{01}(u)\phi_o(u, g)/\eta_0}. \quad \text{10.69}$$

Now  $Z_{01}(u)$  is the free-space characteristic impedance of an individual microstrip line and is given by Equation (6.25). In Equations (10.68) and (10.69), the effective permittivity of the odd mode is

$$\epsilon_{\text{eff},o}(u, g, \epsilon_r) = \frac{\epsilon_r + 1}{2} + \frac{\epsilon_r - 1}{2} F_o(u, g, \epsilon_r) \quad \text{10.70}$$

where

$$F_o(u, g, \epsilon_r) = f_o(u, g, \epsilon_r)(1 + 10/u)^{-a(u)b(\epsilon_r)} \quad \text{10.71}$$

$$\phi_o(u, g) = \phi_e(u, g) - \frac{\theta(g)}{\psi(g)} \exp [\beta(g) u^{n(g)} \ln(u)] \quad \text{10.72}$$

$$\theta(g) = 1.729 + 1.175 \ln \left( 1 + \frac{0.627}{g + 0.327 g^{2.17}} \right) \quad \text{10.73}$$

$$\beta(g) = 0.2306 + \frac{1}{301.8} \ln \left[ \frac{g^{10}}{1 + (g/3.73)^{10}} \right] + \frac{1}{5.3} \ln (1 + 0.646g^{1.175}) \quad \text{10.74}$$

$$n(g) = \left\{ \frac{1}{17.7} + \exp [-6.424 - 0.76 \ln(g) - (g/0.23)^5] \right\} \ln \left( \frac{10 + 68.3g^2}{1 + 32.5g^{3.093}} \right) \quad \text{10.75}$$

$$f_o(u, g, \epsilon_r) = f_{o1}(g, \epsilon_r) \exp \left[ p(g) \ln(u) + q(g) \sin \left( \pi \frac{\ln u}{\ln 10} \right) \right] \quad \text{10.76}$$

$$p(g) = \exp (-0.745g^{0.295}) / \cosh (g^{0.68}) \quad \text{10.77}$$

$$f_{o1}(g, \epsilon_r) = 1 - \exp \left\{ -0.179g^{0.15} - \frac{0.328g^{r(g, \epsilon_r)}}{\ln [\exp(1) + (g/7)^{2.8}]} \right\} \quad \text{10.78}$$

$$r(g, \epsilon_r) = 1 + 0.15 \left\{ 1 - \frac{\exp [1 - (\epsilon_r - 1)^2/8.2]}{1 + g^{-6}} \right\} \quad \text{10.79}$$

$$q(g) = \exp(-1.366 - g) \quad \text{10.80}$$

and  $a(u)$  and  $b(\epsilon_r)$  are defined in Equations (10.58) and (10.61).

## Discussion

Normalized even- and odd-mode characteristic impedances of a pair of coupled lines are plotted in [Figure 10.12](#) for various normalized widths  $u$  as a function of normalized gap width  $g$ . These plots illustrate the utility of using even- and odd-mode descriptions. In [Figure 10.12](#) the even- and odd-mode impedances are normalized to the characteristic impedance of an individual line,  $Z_0$ . When the lines are far apart, that is,  $g$  is large, the even- and odd-mode impedances converge to the characteristic impedance of a single line. As the lines get closer, the gap narrows, and the even- and odd-mode impedances diverge in opposite directions. To obtain the characteristic impedances of a coupled line the characteristic impedance of a single microstrip line must be found. This was given in [Section 6.4.1](#) and the key result is repeated in [Figure 10.13](#). Again normalization is used to simplify the graphical presentation of data and highlight major dependencies.

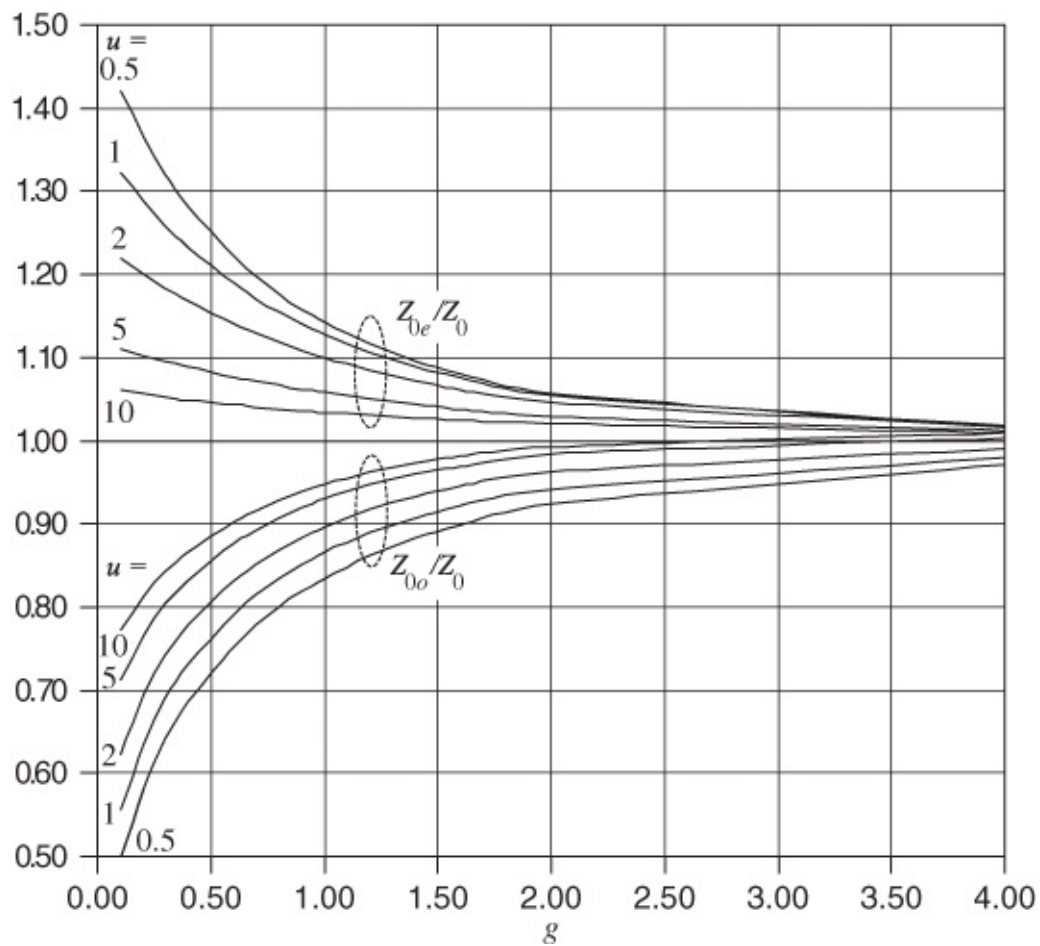


**Figure 10.12** Normalized even-mode and odd-mode characteristic impedances of a pair of coupled microstrip lines.

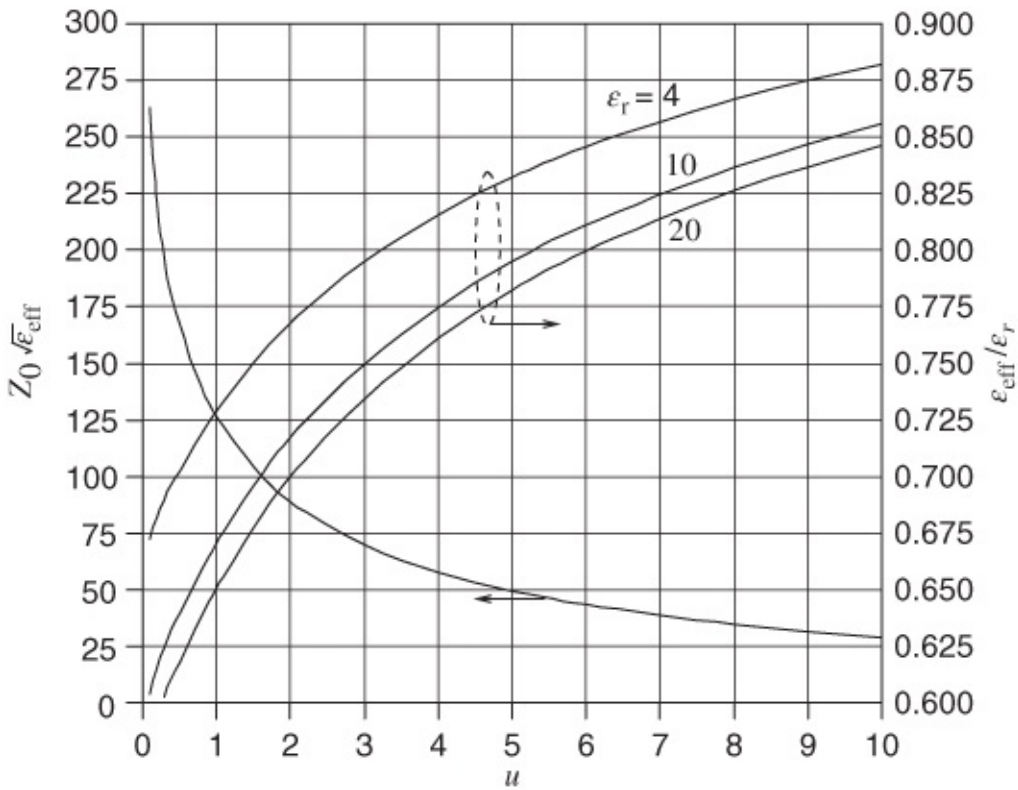


**Figure 10.13** Normalized characteristic impedance and normalized effective permittivity of a microstrip line as a function of  $u = w/h$ . The effective permittivity of an individual microstrip line with the same width  $u$  is  $\epsilon_{\text{eff}}$ .

In the even mode more of the field is in the dielectric than with the odd mode. It is therefore not surprising that the effective permittivities of the two modes differ. The normalized coupled-line effective permittivities are shown in [Figure 10.14](#). The deviation of the even- and odd-mode permittivities as the gap between the lines narrows is not as large as the change in the characteristic impedance. Nevertheless there will be a difference in the phase velocities of the two modes along the line. At first reading of the plot it would seem that there is non-monotonic behavior at low  $g$ . This is an artifact of the normalization used and the unnormalized permittivities are indeed monotonic with respect to  $u$  and  $g$ .

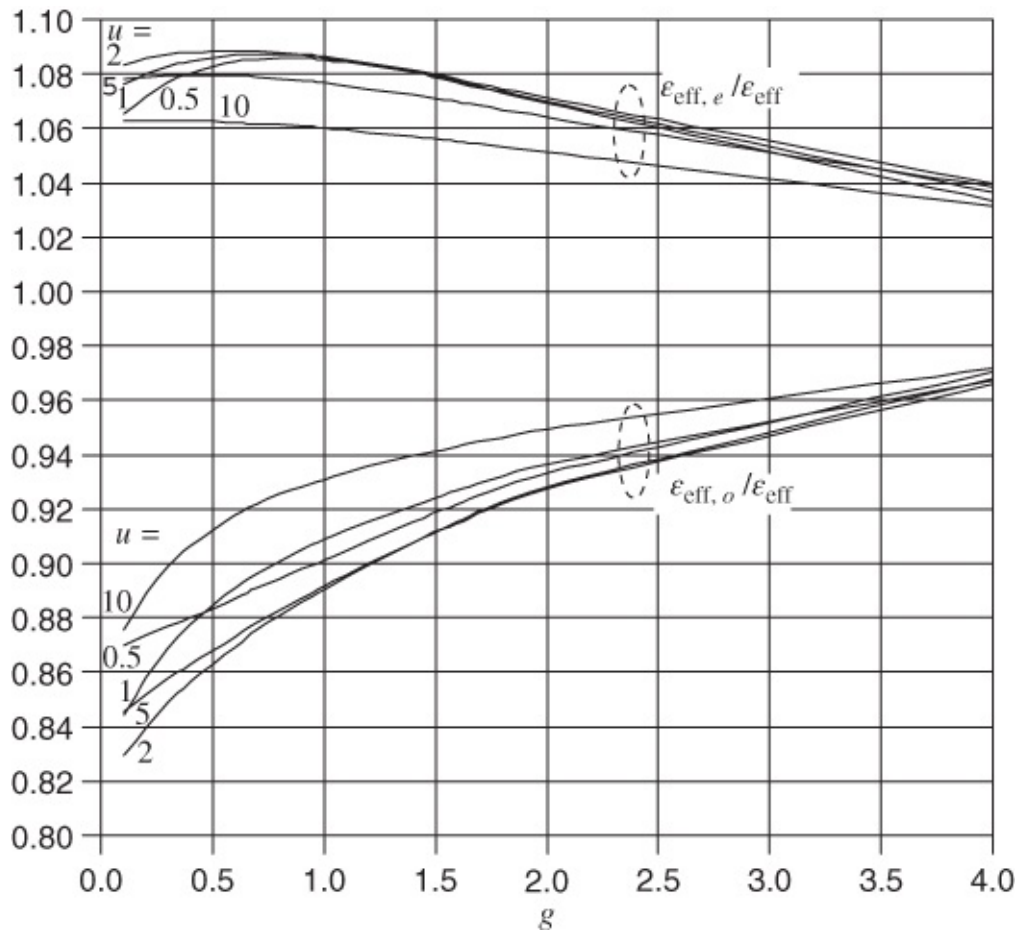


**Figure 10.14** Normalized even-mode and odd-mode effective permittivity of a pair of coupled microstrip lines. These results are for all  $\epsilon_r$ .

[Figure 10.15](#) highlights that the split of the even- and odd-mode characteristics impedances is almost solely dependent on geometry and not the permittivity of the substrate. In the figure appropriate normalization is used to highlight this fact. There are four families of curves, two for the even-mode characteristic impedances and two for the odd-mode characteristic impedances. Each family, almost coincident, comprises the results for three widely different permittivities of the dielectric (specifically  $\epsilon_r = 4, 10$ , and  $20$ ).

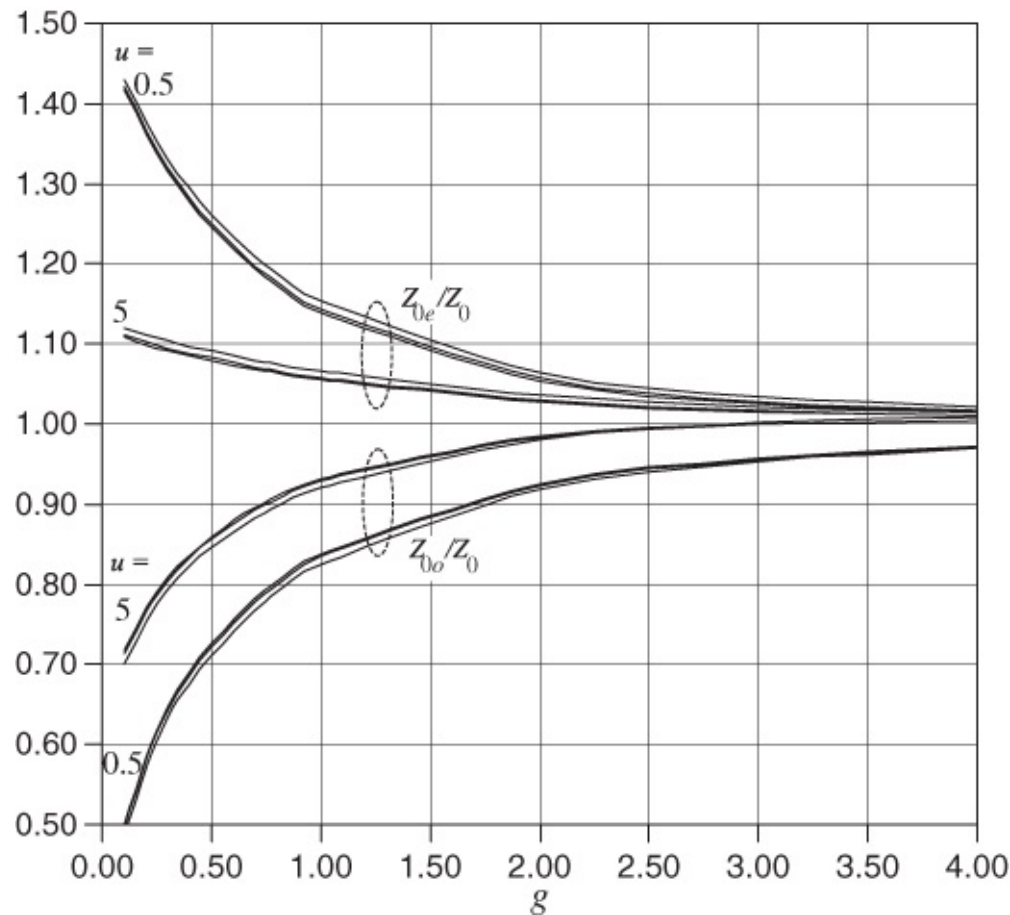


**Figure 10.15** Normalized even-mode and odd-mode effective permittivity of a pair of coupled microstrip lines for extremes of  $u$ . Each family of three curves (almost on top of each other) is for  $\epsilon_r = 4, 10$ , and  $20$ .  $Z_0$  is the characteristic impedance of an individual microstrip line with the same normalized width  $u$ .

### 10.3.3 Characteristic Impedances in Terms of the Coupling Factor

First, we repeat Equations (10.43), (10.16), (10.44), and (10.45), observing that several of these expressions are approximate in the microstrip case due to the unequal phase velocities. We have:

coupling factor:

$$C' = 20 \log \left| \frac{Z_{0e} - Z_{0o}}{Z_{0e} + Z_{0o}} \right| \text{ dB} \quad 10.81$$

impedance relationship:

$$Z_0^2 \approx Z_{0e} Z_{0o} \quad 10.82$$

and from these expressions the impedances required are

$$Z_{0e} \approx Z_0 \sqrt{\frac{1 + 10^{C'/20}}{1 - 10^{C'/20}}} \quad 10.83$$

and

$$Z_{0o} \approx Z_0 \sqrt{\frac{1 - 10^{C'/20}}{1 + 10^{C'/20}}}. \quad 10.84$$

We also define a system impedance

$$Z_{0S} = \sqrt{Z_{0e} Z_{0o}}. \quad 10.85$$

Individual lines connected to the coupled line should have a characteristic impedance  $Z_{0S}$  for there to be no reflection, that is, for the lines to be matched.  $Z_{0S}$  is not the same as the characteristic impedance of just one of the lines in the coupled line pair (i.e., with the same width) and we are using  $Z_0$  to denote its characteristic impedance.

The last two equations are the basic initial design expressions. The designer will know the characteristic impedance of the external lines connecting to the coupler ( $Z_0$ ), often 50  $\Omega$ , and will also know the value of the mid-band coupling factor in decibels,  $C'$ , or some quantities inherently involving  $C'$ .

As the coupling increases the approximation involved in Equation (10.80) worsens steadily. An accurate relationship can be obtained by inserting  $\theta_e$  and  $\theta_o$  appropriately into Equations (10.2) and (10.3), and adding the matrices to obtain

$$\begin{bmatrix} V_1 \\ I_1 \end{bmatrix} = \begin{bmatrix} \cos \theta_e + \cos \theta_o & j(Z_{0e} \sin \theta_e + Z_{0o} \sin \theta_o) \\ j(Y_{0e} \sin \theta_e + Y_{0o} \sin \theta_o) & \cos \theta_e + \cos \theta_o \end{bmatrix} \begin{bmatrix} V_2 \\ I_2 \end{bmatrix}. \quad 10.86$$

The condition for a perfect input match and perfect isolation can be written down directly from this because diagonal terms involving impedances must be made equal, thus

$$\frac{Z_{0e}}{Z_0} \sin \theta_e + \frac{Z_{0o}}{Z_0} \sin \theta_o = \frac{Z_0}{Z_{0e}} \sin \theta_e + \frac{Z_0}{Z_{0o}} \sin \theta_o \quad 10.87$$

or

$$Z_0^2 = Z_{0e} Z_{0o} \frac{Z_{0e} \sin \theta_e + Z_{0o} \sin \theta_o}{Z_{0e} \sin \theta_o + Z_{0o} \sin \theta_e}. \quad 10.88$$

This is a frequency-dependent result because  $\theta_e$  and  $\theta_o$  are both functions of frequency.

Having made a “first-cut” design  $\theta_e$  and  $\theta_o$  may be evaluated and the value of  $Z_0$  can then be obtained from Equation (10.88). If  $Z_0$  is found to differ too greatly from the specified value, then the geometry ( $w$  and  $s$ ) might be varied slightly to correct the result.

In many cases, certainly for a -10 dB coupling factor and looser, the approximation offered by Equation (10.82) is sufficient.

### 10.3.4 Connecting Microstrip Lines

From Equations (10.80) to (10.85) the even- and odd-mode impedances can be written as

10.89

$$Z_{0e} \approx Z_{0S} \sqrt{\frac{C+1}{C-1}}$$

10.90

$$Z_{0o} \approx Z_{0S} \sqrt{\frac{C-1}{C+1}}$$

and the ratio of impedances is

10.91

$$Z_{0e}/Z_{0o} \approx \frac{C+1}{C-1}$$

The last three equations are the basic design expressions as  $Z_{0e}$  and  $Z_{0o}$  can be related to physical dimensions. One of the small complications is that the close proximity of the two strips alters the orientation of the field lines and hence the characteristic impedances of the individual lines, that is, the characteristic impedance of each line on its own,  $Z_0$ , will differ from the system impedance  $Z_{0S}$ . For a normalized line width of  $u = (w/h)$  this effect is shown in [Figure 10.16](#). Here  $Z_{0S}$ , the desired system impedance, is the geometric mean of the even- and odd-mode impedances.  $Z_0$  is the characteristic impedance of one of the lines of the coupled line structure. Thus to maintain the desired  $Z_{0S}$  requires that the  $Z_0$  of the individual lines be higher than  $Z_{0S}$ , particularly as the normalized gap size reduces.

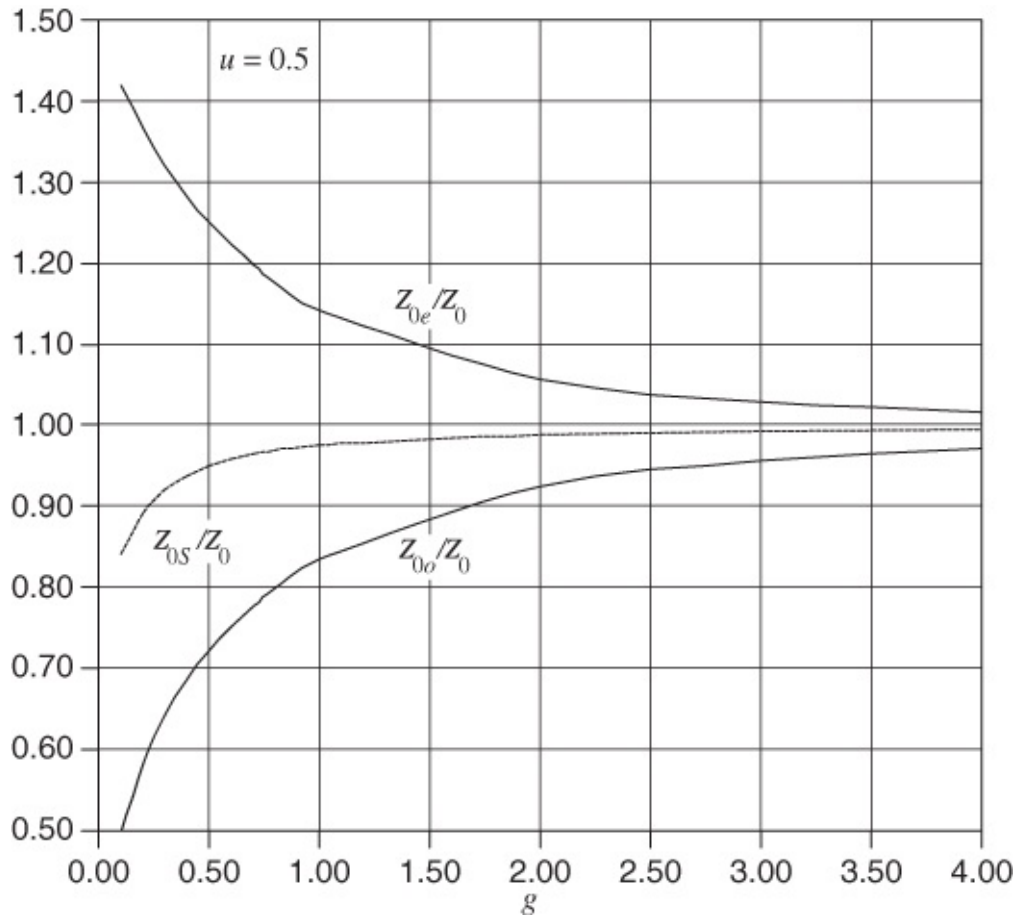


**Figure 10.16** Normalized even-mode and odd-mode effective permittivity of a pair of coupled microstrip lines with normalized width  $u = 0.5$  as a function of normalized gap spacing  $g$ .

A more direct design parameter is to use the ratio of the even- and odd-mode impedances, Equation (10.91). Microstrip coupler design proceeds as follows. The first step is to examine the specifications and determine the substrate permittivity  $\epsilon_r$ , coupling factor  $C$  in decibels, and the system characteristic impedance  $Z_{0S}$ . From  $C$  find  $Z_{0e}/Z_0$  and the data in [Tables 10.1–10.3](#), or [10.4](#) enables some of the physical parameters to be determined, including the normalized gap coupling parameter  $g$  and the normalized strip width  $u$ . The tables also provide the characteristic impedance, the even- and odd-mode characteristic impedances, and the characteristic impedance of the individual strips of the directional coupler. The next step is to design the dimensions of the individual microstrip lines connecting the directional coupler using [Tables 6.1–6.3](#). At this stage the widths and spacings of the microstrip circuit are normalized. Using the substrate height these are de normalized to obtain the actual physical dimensions. Finally the length of the coupler is a quarter-wavelength long as this was the basis for the formula relating the even- and odd-mode impedances to the coupling factor in Equation (10.33). The even- and odd-modes have different effective permittivities and the  $\lambda_g/4$  length should apply to both the even and odd modes. Clearly both cannot be satisfied. It is reasonable to use the average of the even- and odd-mode permittivities to establish the coupler length. The length is not a very sensitive parameter anyway. The connection of the individual lines to the coupler is not specifically part of the synthesis described but if designed they should be designed as a bend.

**Table 10.1** Design parameters for coupled lines for  $\epsilon_r = 4$  corresponding to design on an SiO<sub>2</sub> or FR-4 (printed circuit board) substrate. The normalized gap,  $g$ , is chosen to obtain the desired coupled-line mode impedance ratio  $Z_{0e}/Z_{0o}$ . Data derived from the analysis in [Section 10.3](#).  $Z_0$  is the characteristic impedance of an individual microstrip line with a normalized width  $u$  on the same substrate

$\epsilon_r = 4$ (SiO <sub>2</sub> and FR-4), $Z_{0S} = 50 \Omega$							
$g$	$Z_{0e}/Z_{0o}$	$u$	$Z_{0e}$	$Z_{0o}$	$\epsilon_{\text{eff},e}$	$\epsilon_{\text{eff},o}$	$Z_0$
			( $\Omega$ )	( $\Omega$ )			( $\Omega$ )
0.10	2.15	1.60	73.17	34.10	3.21	2.61	57.96
0.20	1.84	1.74	67.85	36.97	3.24	2.65	55.23
0.30	1.66	1.83	64.29	38.63	3.25	2.68	53.45
0.40	1.55	1.88	62.48	40.18	3.26	2.70	52.77
0.50	1.47	1.92	60.83	41.29	3.27	2.73	52.11
0.60	1.41	1.96	59.31	42.10	3.28	2.75	51.47
0.70	1.36	1.98	58.30	42.92	3.28	2.76	51.16
0.80	1.32	2.00	57.37	43.57	3.28	2.78	50.85
0.90	1.28	2.02	56.51	44.09	3.28	2.79	50.54
1.00	1.25	2.02	56.06	44.75	3.28	2.81	50.54
1.10	1.23	2.04	55.30	45.09	3.28	2.82	50.24
1.20	1.20	2.04	54.93	45.60	3.28	2.83	50.24
1.30	1.19	2.05	54.60	46.05	3.27	2.83	50.24
1.40	1.17	2.06	53.96	46.20	3.27	2.84	49.94
1.50	1.15	2.06	53.68	46.56	3.27	2.85	49.94
1.60	1.14	2.06	53.43	46.87	3.26	2.86	49.94
1.70	1.13	2.06	53.20	47.16	3.26	2.86	49.94
1.80	1.12	2.07	52.99	47.41	3.26	2.87	49.94
1.90	1.11	2.07	52.47	47.37	3.25	2.88	49.64
2.00	1.10	2.08	52.30	47.58	3.25	2.88	49.64
2.50	1.07	2.08	51.61	48.33	3.23	2.91	49.64
3.00	1.05	2.08	51.15	48.80	3.21	2.93	49.64
4.00	1.03	2.08	50.62	49.31	3.18	2.96	49.64

**Table 10.2** Design parameters for a microstrip coupler on a substrate with a relative permittivity  $\epsilon_r$  of 10. Data derived from the analysis in [Section 10.3](#).  $Z_0$  is the characteristic impedance of an individual microstrip line with a normalized width  $u$  on the same substrate

$\epsilon_r = 10$ (Alumina), $Z_{0S} = 50 \Omega$							
$g$	$Z_{0e}/Z_{0o}$	$u$	$Z_{0e}$	$Z_{0o}$	$\epsilon_{\text{eff},e}$	$\epsilon_{\text{eff},o}$	$Z_0$
			( $\Omega$ )	( $\Omega$ )			( $\Omega$ )
0.10	2.66	0.66	81.61	30.64	6.95	5.59	59.0
0.20	2.15	0.76	73.38	34.06	7.07	5.65	55.5
0.30	1.90	0.81	69.06	36.39	7.13	5.69	54.0
0.40	1.73	0.85	65.78	38.02	7.17	5.74	52.8
0.50	1.61	0.87	63.66	39.46	7.20	5.77	52.2
0.60	1.52	0.89	61.79	40.55	7.22	5.81	51.7
0.70	1.45	0.91	60.11	41.38	7.23	5.85	51.1
0.80	1.40	0.91	59.25	42.40	7.23	5.88	51.1
0.90	1.35	0.92	58.17	43.07	7.24	5.92	50.9
1.00	1.31	0.92	57.50	43.81	7.23	5.94	50.9
1.10	1.28	0.93	56.60	44.26	7.23	5.98	50.6
1.20	1.25	0.94	55.78	44.62	7.23	6.01	50.3
1.30	1.23	0.94	55.31	45.11	7.22	6.03	50.3
1.40	1.21	0.94	54.90	45.55	7.21	6.06	50.3
1.50	1.19	0.94	54.52	45.93	7.20	6.08	50.3
1.60	1.17	0.94	54.19	46.28	7.19	6.11	50.3
1.70	1.16	0.94	53.89	46.59	7.18	6.13	50.3
1.80	1.14	0.94	53.61	46.86	7.16	6.15	50.3
1.90	1.13	0.95	53.09	46.89	7.16	6.18	50.1
2.00	1.12	0.95	52.87	47.11	7.14	6.20	50.1
2.50	1.09	0.95	52.05	47.93	7.08	6.29	50.1
3.00	1.06	0.95	51.54	48.45	7.02	6.36	50.1
4.00	1.04	0.95	50.97	49.04	6.92	6.46	50.1

**Table 10.3** Design parameters for a microstrip coupler on a substrate with a relative permittivity  $\epsilon_r$  of 11.9 corresponding to a Si substrate. Data derived from the analysis in [Section 10.3](#).  $Z_0$  is the characteristic impedance of an individual microstrip line with a normalized width  $u$  on the same substrate

$\epsilon_r = 11.9$ (Si), $Z_{0S} = 50 \Omega$							
$g$	$Z_{0e}/Z_{0o}$	$u$	$Z_{0e}$	$Z_{0o}$	$\epsilon_{\text{eff},e}$	$\epsilon_{\text{eff},o}$	$Z_0$
			( $\Omega$ )	( $\Omega$ )			( $\Omega$ )
0.10	2.81	0.53	83.88	29.89	8.07	6.53	59.44
0.20	2.24	0.62	74.96	33.44	8.21	6.59	55.82
0.30	1.96	0.67	70.03	35.77	8.29	6.63	54.04
0.40	1.78	0.70	66.81	37.58	8.34	6.68	53.03
0.50	1.65	0.73	64.01	38.85	8.38	6.72	52.08
0.60	1.55	0.74	62.35	40.14	8.40	6.76	51.77
0.70	1.48	0.75	60.88	41.18	8.41	6.80	51.46
0.80	1.42	0.76	59.57	42.01	8.42	6.84	51.16
0.90	1.37	0.77	58.40	42.69	8.43	6.88	50.86
1.00	1.33	0.77	57.68	43.46	8.42	6.91	50.86
1.10	1.29	0.78	56.71	43.90	8.42	6.95	50.57
1.20	1.26	0.78	56.15	44.49	8.41	6.98	50.57
1.30	1.24	0.78	55.66	45.00	8.40	7.01	50.57
1.40	1.21	0.78	55.22	45.46	8.39	7.04	50.57
1.50	1.20	0.78	54.82	45.86	8.38	7.06	50.57
1.60	1.18	0.79	54.16	45.98	8.37	7.10	50.28
1.70	1.16	0.79	53.84	46.29	8.36	7.12	50.28
1.80	1.15	0.79	53.56	46.58	8.34	7.15	50.28
1.90	1.14	0.79	53.31	46.84	8.33	7.17	50.28
2.00	1.13	0.79	53.08	47.07	8.31	7.20	50.28
2.50	1.09	0.79	52.24	47.93	8.23	7.30	50.28
3.00	1.07	0.79	51.71	48.48	8.16	7.39	50.28
4.00	1.04	0.79	51.15	49.11	8.04	7.51	50.28

**Table 10.4** Design parameters for a microstrip coupler on a substrate with a relative permittivity  $\epsilon_r$  of 12.85 corresponding to a GaAs substrate. Data derived from the analysis in [Section 10.3](#).  $Z_0$  is the characteristic impedance of an individual microstrip line with a normalized width  $u$  on the same substrate

$\epsilon_r = 12.85$ (GaAs), $Z_{0S} = 50 \Omega$							
$g$	$Z_{0e}/Z_{0o}$	$u$	$Z_{0e}$	$Z_{0o}$	$\epsilon_{\text{eff},e}$	$\epsilon_{\text{eff},o}$	$Z_0$
			( $\Omega$ )	( $\Omega$ )			( $\Omega$ )
0.10	2.15	1.60	73.17	34.10	3.21	2.61	57.96
0.20	1.84	1.74	67.85	36.97	3.24	2.65	55.23
0.30	1.66	1.83	64.29	38.63	3.25	2.68	53.45
0.40	1.55	1.88	62.48	40.18	3.26	2.70	52.77
0.50	1.47	1.92	60.83	41.29	3.27	2.73	52.11
0.60	1.41	1.96	59.31	42.10	3.28	2.75	51.47
0.70	1.36	1.98	58.30	42.92	3.28	2.76	51.16
0.80	1.32	2.00	57.37	43.57	3.28	2.78	50.85
0.90	1.28	2.02	56.51	44.09	3.28	2.79	50.54
1.00	1.25	2.02	56.06	44.75	3.28	2.81	50.54
1.10	1.23	2.04	55.30	45.09	3.28	2.82	50.24
1.20	1.20	2.04	54.93	45.60	3.28	2.83	50.24
1.30	1.19	2.04	54.60	46.05	3.27	2.83	50.24
1.40	1.17	2.06	53.96	46.20	3.27	2.84	49.94
1.50	1.15	2.06	53.68	46.56	3.27	2.85	49.94
1.60	1.14	2.06	53.43	46.87	3.26	2.86	49.94
1.70	1.13	2.06	53.20	47.16	3.26	2.86	49.94
1.80	1.12	2.06	52.99	47.41	3.26	2.87	49.94
1.90	1.11	2.07	52.47	47.37	3.25	2.88	49.64
2.00	1.10	2.08	52.30	47.58	3.25	2.88	49.64
2.50	1.07	2.08	51.61	48.33	3.23	2.91	49.64
3.00	1.05	2.08	51.15	48.80	3.21	2.93	49.64
4.00	1.03	2.08	50.62	49.31	3.18	2.96	49.64

A comment on this design procedure is in order. The design procedure above yields a narrowband directional coupler. A broadband directional coupler, and indeed any component that is desired to have a broad bandwidth, should be designed using filter principles. The filter discussion in [Chapter 19](#) focuses on the design of microstrip filters using coupled lines and so is closely aligned to the design of couplers with desired frequency characteristics. Another

comment is that the design flow is one of synthesis. An alternative procedure, one that is often used, is to start with a very approximate design and rely on optimization tools to obtain the desired characteristics. This works in many cases but often does not lead to optimum design. Having said that, the synthesis procedure does not yield a perfect design as parasitic and dispersive effects are not taken into account. Optimization from the synthesized design requires only a small adjustment. In practice the uncertainties of physical structures (e.g., variation of the effective permittivity of actual materials) requires experimental iteration.

## 10.4 Semi-empirical Analysis Formulas as a Design Aid

Simple analysis formulas are available for the determination of characteristic impedances to an accuracy of within 3% [5–7]. These could be useful to the designer, who might start with an approximate synthesis and employ the analysis formulas to provide an improvement in accuracy using an iterative technique. Air-line and substrate-line capacitances form the basis of the expressions, and the capacitances are broken down as shown in [Figure 10.17](#). The accuracy of better than 3% holds over the ranges:

$$0.2 \leq w/h \leq 2.0, \quad 0.05 \leq s/h \leq 2.0, \quad \text{and} \quad \epsilon_r \geq 1.$$

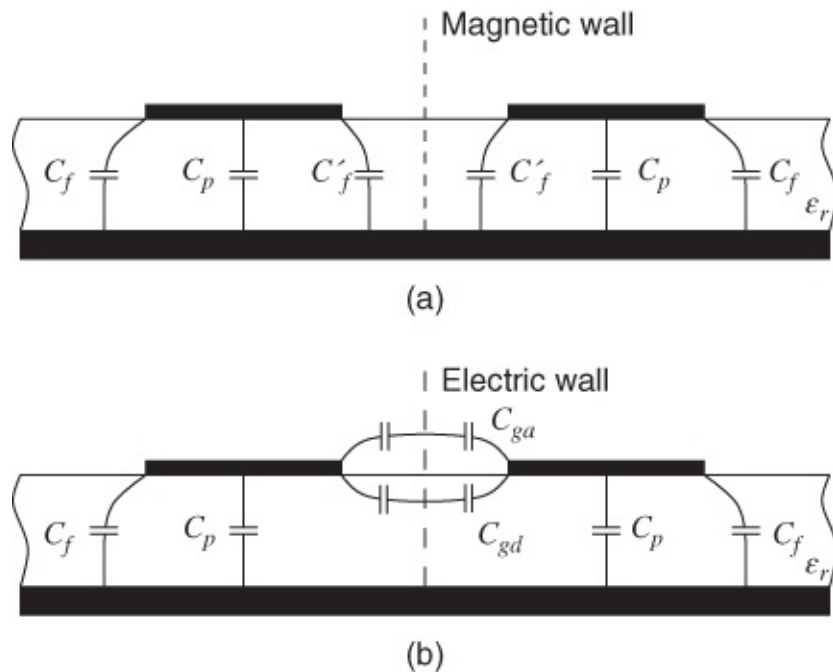


[Figure 10.17](#) Separation of capacitances for use in the analysis: (a) even-mode capacitances; and (b) odd-mode capacitances.

The total capacitances for each mode can then be written as

$$C_e = C_p + C_f + C'_f \quad \text{10.92}$$

and

$$C_o = C_p + C_f + C_{ga} + C_{gd}$$

**10.93**

The capacitance  $C_p$  simply relates to the parallel-plate line value given by

$$C_p = \epsilon_0 \epsilon_r \frac{w}{h}.$$

**10.94**

Also,  $C_f$  is simply the fringing capacitance due to each microstrip taken alone, as if for a single strip. This is given by

$$2C_f = \frac{\sqrt{\epsilon_{\text{eff}}}}{cZ_0} - C_p \quad \text{10.95}$$

where  $c$  is the free-space velocity and  $\epsilon_{\text{eff}}$  and  $Z_0$  are obtained by single-strip static-TEM methods.

An empirical expression for  $C'_f$  is given as follows:

$$C'_f = \frac{C_f}{1 + (A h/s) \tanh(8s/h)} \sqrt{\frac{\epsilon_r}{\epsilon_{\text{eff}}}} \quad \text{10.96}$$

where

$$A = \exp \{-0.1 \exp(2.33 - 2.53w/h)\}. \quad \text{10.97}$$

As can be seen from [Figure 10.17](#),  $C_{ga}$  and  $C_{gd}$  represent, respectively, odd-mode fringing field capacitances for the air and dielectric regions across the coupling gap.  $C_{ga}$  was obtained by using an equivalent coplanar strip geometry calculation, yielding

$$C_{ga} = \epsilon_0 \frac{K(k')}{K(k)} \quad \text{10.98}$$

where

$$k = \frac{s/h}{s/h + 2w/h} \quad \text{and} \quad k' = \sqrt{1 - k^2} \quad \text{10.99}$$

and the ratio of the elliptic functions is:

For  $0 \leq k^2 \leq 0.5$ :

$$\frac{K(k')}{K(k)} = \frac{1}{\pi} \ln \left( 2 \frac{1 + \sqrt{k'}}{1 - \sqrt{k'}} \right). \quad \text{10.100}$$

For  $0.5 \leq k^2 \leq 1.0$ :

$$\frac{K(k')}{K(k)} = \frac{\pi}{\ln \{2(1 + \sqrt{k})/(1 - \sqrt{k})\}}. \quad \text{10.101}$$

$C_{gd}$  was determined differently. The capacitance for coupled striplines (triplate) was modified to give

$$C_{gd} = \frac{\epsilon_0 \epsilon_r}{\pi} \ln \left\{ \coth \left( \frac{\pi}{4} \frac{s}{h} \right) \right\} + 0.65 C_f \left( \frac{0.02}{s/h} \sqrt{\epsilon_r} + 1 - \epsilon_r^{-2} \right). \quad 10.102$$

The even-mode and odd-mode characteristic impedances are then

$$Z_{0e} = \left( c \sqrt{C_e C_{e1}} \right)^{-1} \quad \text{and} \quad Z_{0o} = \left( c \sqrt{C_o C_{o1}} \right)^{-1} \quad 10.103$$

where  $c$  is the velocity in free space and the second subscript 1 refers to a free-space line.

The effective microstrip permittivities are

$$\epsilon_{\text{eff},e} = C_e / C_{e1} \quad 10.104$$

and

$$\epsilon_{\text{eff},o} = C_o / C_{o1}. \quad 10.105$$

### 10.4.1 Dispersion

For calculations on parallel-coupled microstrips, especially at frequencies exceeding a few gigahertz, dispersion is significant and it is essential to have quantitative information on this dispersion. Only then can wavelengths be at all accurately calculated. The problem of dispersion in single microstrip lines was discussed in detail in [Chapter 7](#). Coupled microstrips suffer dispersion for precisely the same physical reasons as single microstrip, but the amount of dispersion depends on the mode under consideration. The effective microstrip permittivities are now both somewhat different functions of frequency, which involve the parameters indicated as follows:

$$\epsilon_{\text{eff},e}(f, h, \epsilon_r, \epsilon_{\text{eff},e}, Z_{0e}) \quad 10.106$$

and

$$\epsilon_{\text{eff},o}(f, h, \epsilon_r, \epsilon_{\text{eff},o}, Z_{0o}). \quad 10.107$$

Getsinger [8] has shown how his expressions, which were originally derived for single microstrip, can be adapted to suit the coupled microstrip problem (Getsinger's single-line expressions were given in [Chapter 7](#)). For use with coupled lines the following approximate substitutions are made where Getsinger's method is adopted:

- a. In the even mode the two strips are at the same potential and the total current is twice that on a single strip. Thus, the total mode impedance is half that of a single strip and the dispersion for even-mode propagation is calculated by substituting  $10.108 \quad Z_0 \approx \frac{1}{2} Z_{0e}$ .
- b. In the odd mode the two strips are at opposite potentials and the voltage between strips

is twice that of a single strip to ground. Thus, the total mode impedance is twice that of a single strip and the dispersion for odd-mode propagation is calculated by substituting**10.109**  $Z_0 \approx 2Z_{0o}$

in Getsinger's single-line equations.

So, for example, the even-mode dispersion expression is as follows:

$$\varepsilon_{\text{eff},e}(f) = \varepsilon_r - \frac{\varepsilon_r - \varepsilon_{\text{eff},e}}{1 + G_e(f/f_{pe})^2} \quad \text{10.110}$$

with

$$f_{pe} = \frac{Z_{0e}}{4\mu_0 h} \quad \text{and} \quad G_e = 0.6 + 0.0045Z_{0e}. \quad \text{10.111}$$

Some caution is necessary regarding the accuracy of using the substitution (b) since Easter and Gupta [9] have indicated that an overestimation of odd-mode dispersion is obtained. This assessment is based on comparisons with the theoretical treatment due to Krage and Haddad [10], and with the measurements due to Richings and Easter [11].

It is suggested that empirical modifications might be made to Getsinger's odd-mode substitution to provide more accurate design formulas but an approach yielding greater accuracy is available and is described in the next section.

### **10.4.2 More Accurate Design Expressions, Including Dispersion**

Kirschning and Jansen [12, 13] have given design expressions for the modal dispersion in parallel-coupled microstrip lines. These workers developed a coupled model for the structure, in which they used normalized parameters as follows:

$$u = w/h, \quad g = s/h, \quad \text{and} \quad f_n = fh \quad (\text{in GHz} \cdot \text{mm units}). \quad \text{10.112}$$

They quote the ranges of validity for which the design expressions remain accurate:

$$0.1 \leq u \leq 10, \quad 0.1 \leq g \leq 10, \quad \text{and} \quad 1 \leq \varepsilon_r \leq 18. \quad \text{10.113}$$

The static-TEM formula for the even mode effective microstrip permittivity is provided by Hammerstad and Jensen as follows:

$$\varepsilon_{\text{eff},e}(0) = 0.5(\varepsilon_r + 1) + 0.5(\varepsilon_r - 1)(1 + 10/v)^{-[a_e(v)b_e(\varepsilon_r)]}$$

where  $Z_0(f_n)$  can be found using the equations in [Chapter 6 \(Section 6.4.1\)](#), and

$$v = u \frac{(20 + g^2)}{(10 + g^2)} + g \exp(-g)$$

$$a_e(v) = 1 + \frac{1}{49} \ln \left[ \frac{v^4 + (v/52)^2}{v^4 + 0.432} \right] + \frac{1}{18.7} \ln [1 + (v/18.1)^3]$$

$$b_e(\epsilon_r) = 0.564 \left[ (\epsilon_r - 0.9) / (\epsilon_r + 3) \right]^{0.053}.$$

In contrast, the static-TEM formula applicable to the odd mode effective microstrip permittivity was remodeled by Kirschning and Jansen so that an improved accuracy of 0.5% applies over the whole range of parameters. This permittivity is given by

$$\epsilon_{\text{eff},o}(0) = [0.5(\epsilon_r + 1) + a_o(u, \epsilon_r) + \epsilon_{\text{eff}}(0)] \exp(-c_o g^{d_o}) - \epsilon_{\text{eff}}(0) \quad 10.115$$

where

$$a_o(u, \epsilon_r) = 0.7287 [\epsilon_{\text{eff}}(0) - 0.5(\epsilon_r + 1)] [1 - \exp(-0.179u)] \quad 10.116$$

$$b_o(\epsilon_r) = 0.747 \epsilon_r / (0.15 + \epsilon_r)$$

$$c_o = b_o(\epsilon_r) - [b_o(\epsilon_r) - 0.207] \exp(-0.414u)$$

$$d_o = 0.593 + 0.694 \exp(-0.562u)$$

where, as elsewhere in this text,  $\epsilon_{\text{eff}}(0)$  refers to the zero-thickness DC permittivity of single microstrip line.

The functional form in which modal dispersion is introduced for both modes is similar to that shown for single microstrip, described in [Chapter 7](#). Thus

$$\epsilon_{\text{eff},e}(f_n) = \epsilon_r - \frac{\epsilon_r - \epsilon_{\text{eff},e}(0)}{1 + F_e(f_n)} \quad \text{and} \quad \epsilon_{\text{eff},o}(f_n) = \epsilon_r - \frac{\epsilon_r - \epsilon_{\text{eff},o}(0)}{1 + F_o(f_n)}. \quad 10.117$$

In this expression it is of course  $F$  that determines the detailed frequency dependence.

The even-mode result for  $F$ , given by Kirschning and Jansen, is

$$F_e(f_n) = P_1 P_2 [(P_3 P_4 + 0.1844 P_7) f_n]^{1.5763} \quad 10.118$$

where

$$\begin{aligned}
P_1 &= 0.27488 + \left[ 0.6315 + 0.525 / (1 + 0.0157f_n)^{20} \right] u - 0.065683 \exp(-8.7513u) \\
P_2 &= 0.33622 [1 - \exp(-0.03442\epsilon_r)] \\
P_3 &= 0.0363 \exp(-4.6u) \left\{ 1 - \exp \left[ -(f_n/38.7)^{4.97} \right] \right\} \\
P_4 &= 1 + 2.751 \left[ 1 - \exp \left\{ -(\epsilon_r/15.916)^8 \right\} \right] \\
P_5 &= 0.334 \exp \left[ -3.3(\epsilon_r/15)^3 \right] + 0.746 \\
P_6 &= P_5 \exp \left[ -(f_n/18)^{0.368} \right]
\end{aligned}$$

and

$$P_7 = 1 + 4.069P_6g^{0.479} \exp(-1.347g^{0.595} - 0.17g^{2.5}).$$

Also, the result for  $F$  applicable to the odd mode is

$$F_0(f_n) = P_1 P_2 \{ (P_3 P_4 + 0.1844) f_n P_{15} \}^{1.5763} \quad \text{10.119}$$

with

$$\begin{aligned}
P_8 &= 0.7168 [1 + 1.076 / \{ 1 + 0.0576 (\epsilon_r - 1) \}] \\
P_9 &= P_8 - 0.7913 \left\{ 1 - \exp \left[ -(f_n/20)^{1.424} \right] \tan^{-1} \left[ 2.481(\epsilon_r/8)^{0.946} \right] \right\} \\
P_{10} &= 0.242(\epsilon_r - 1)^{0.55} \\
P_{11} &= 0.6366 [\exp(-0.3401f_n) - 1] \tan^{-1} [1.263(u/3)^{1.629}] \\
P_{12} &= P_9 + (1 - P_9) / (1 + 1.183u^{1.376}) \\
P_{13} &= 1.695P_{10} / (0.414 + 1.605P_{10}) \\
P_{14} &= 0.8928 + 0.1072 \left\{ 1 - \exp \left[ -0.42(f_n/20)^{3.215} \right] \right\} \\
P_{15} &= \text{abs} [1 - 0.8928 (1 + P_{11}) P_{12} \exp(-P_{13}g^{1.092}) / P_{14}].
\end{aligned}$$

The upper frequency limitation for these expressions depends on the substrate parameters. The limit for retention of accuracy approaches 40 GHz for 0.635 mm thick substrates, which is fairly typical for alumina. The accuracy is also preserved for thin substrates with a permittivity of 12.9 (GaAs) and a normalized frequency of 30 GHz· mm, which corresponds to high millimeter-wave frequencies for gallium arsenide substrates some tens of microns thick. In all cases the maximum error bound is 1.4%. It is important to appreciate that these design expressions hold accuracy only where the microstrip circuit is relatively undisturbed, that is, effectively unshielded and with no affecting adjacent conductors or dielectrics. In situations where such practical disturbances exist, various design corrections can be used (e.g., similar to those described in [Chapter 6](#)), but in practice it is generally found that, provided the lines are reasonably tightly coupled, the unshielded results provide a good design basis.

Kirschning and Jansen have also given design expressions for the frequency-dependent

characteristic impedances. They showed that earlier formulas given by Hammerstad and Jansen for the static-TEM impedances yielded small errors that would accumulate for these purposes and they reported improved design expressions. For the even mode the static-TEM impedance is given by

$$Z_{0e}(0) = \frac{Z_0(0) [\varepsilon_{\text{eff}}(0) / \varepsilon_{\text{eff},e}(0)]^{0.5}}{\left\{ 1 - [Z_0(0) / (377 \Omega)] [\varepsilon_{\text{eff}}(0)]^{0.5} Q_4 \right\}} \quad \text{10.120}$$

where

$$Q_1 = 0.8695u^{0.194}$$

$$Q_2 = 1 + 0.7519g + 0.189g^{2.31}$$

$$Q_3 = 0.1975 + [16.6 + (8.4/g)^6]^{-0.387} + \frac{1}{241} \ln \left\{ \frac{g^{10}}{[1 + (g/3.4)^{10}]} \right\}$$

$$Q_4 = (2Q_1/Q_2) \{ \exp(-g) u^{Q_3} + [2 - \exp(-g)] u^{-Q_3} \}^{-1}$$

and the static-TEM odd mode impedance is given by

$$Z_{0o}(0) = \frac{Z_0(0) [\varepsilon_{\text{eff}}(0) / \varepsilon_{\text{eff},o}(0)]^{0.5}}{\left\{ 1 - [Z_0(0) / (377 \Omega)] [\varepsilon_{\text{eff}}(0)]^{0.5} Q_{10} \right\}} \quad \text{10.121}$$

where

$$Q_5 = 1.794 + 1.14 \ln [1 + 0.638 / (g + 0.517g^{2.43})]$$

$$Q_6 = 0.2305 + \frac{1}{281.3} \ln \left\{ \frac{g^{10}}{1 + (g/5.8)^{10}} \right\} + \frac{1}{5.1} \ln (1 + 0.598g^{1.154})$$

$$Q_7 = (10 + 190g^2) / (1 + 82.3g^3)$$

$$Q_8 = \exp [-6.5 - 0.95 \ln(g) - (g/0.15)^5]$$

$$Q_9 = \ln(Q_7)(Q_8 + 1/16.5)$$

$$Q_{10} = Q_2^{-1} \{ Q_2 Q_4 - Q_5 \exp [\ln(u) Q_6 u^{-Q_9}] \}.$$

These design formulas are accurate to within 0.6% over the full range of validity given here.

The frequency-dependent expressions then follow:

$$Z_{0e}(f_n) = \frac{Z_{0e}(0) \left\{ 0.9408 [\varepsilon_{\text{eff}}(f_n)]^{C_e} - 0.9603 \right\}^{Q_0}}{\left\{ (0.9408 - d_e) [\varepsilon_{\text{eff}}(f_n)]^{C_e} - 0.9603 \right\}^{Q_0}} \quad \text{10.122}$$

where

$$C_e = 1 + 1.275 \left\{ 1 - \exp \left[ -0.004625 p_e \epsilon_r^{1.674} (f_n/18.365)^{2.745} \right] \right\} \quad \textbf{10.123}$$

$$- Q_{12} + Q_{16} - Q_{17} + Q_{18} + Q_{20}$$

$$d_e = 5.086 q_e [r_e / (0.3838 + 0.386 q_e)]$$

$$\times [\exp(-22.2 u^{1.92}) / (1 + 1.2992 r_e)] \left\{ (\epsilon_r - 1)^6 / [1 + 10(\epsilon_r - 1)^6] \right\}$$

$$p_e = 4.766 \exp(-3.228 u^{0.641})$$

$$q_e = 0.016 + (0.0514 \epsilon_r Q_{21})^{4.524}$$

$$r_e = (f_n/28.843)^{12}$$

and

$$Q_{11} = 0.893 [1 - 0.3 / \{1 + 0.7(\epsilon_r - 1)\}]$$

$$Q_{12} = \frac{2.121 (f_n/20)^{4.91}}{1 + Q_{11} (f_n/20)^{4.91}} \exp(-2.87g) g^{0.902}$$

$$Q_{13} = 1 + 0.038 (\epsilon_r/8)^{5.1}$$

$$Q_{14} = 1 + \frac{1.203 (\epsilon_r/15)^4}{1 + (\epsilon_r/15)^4}$$

$$Q_{15} = 1.887 \exp(-1.5g^{0.84}) g^{Q_{14}} \left[ 1 + \frac{0.41 (f_n/15)^3 u^{2/Q_{13}}}{(0.125 + u^{1.626/Q_{13}})} \right]^{-1}$$

$$Q_{16} = \left\{ 1 + 9 / \left[ 1 + 0.403(\epsilon_r - 1)^2 \right] \right\} Q_{15}$$

$$Q_{17} = 0.394 \left\{ 1 - \exp[-1.47(u/7)^{0.672}] \right\} \left\{ 1 - \exp[-4.25(f_n/20)^{1.87}] \right\}$$

$$Q_{18} = \frac{0.61 \left\{ 1 - \exp[-2.13(u/8)^{1.593}] \right\}}{(1 + 6.544g^{4.17})}$$

$$Q_{19} = 0.21g^4 \left\{ (1 + 0.18g^{4.9}) (1 + 0.1u^2) \left[ 1 + (f_n/24)^3 \right] \right\}^{-1}$$

$$Q_{20} = \left\{ 0.09 + 1 / [1 + 0.1(\epsilon_r - 1)^{2.7}] \right\} Q_{19}$$

$$Q_{21} = \text{abs} \left\{ 1 - 42.54g^{0.133} \exp(-0.812g) u^{2.5} / (1 + 0.033u^{2.5}) \right\}.$$

In these expressions  $\epsilon_{\text{eff}}(f_n)$  denotes the effective microstrip permittivity as a function of frequency, given in [Chapter 7](#).  $Q_0$  was developed in [14] (where it is  $R_{17}$ ):

**10.124**

$$\begin{aligned}
Q_0 &= R_{17} = R_7 \left[ 1 - \frac{1.1241R_{12}}{R_{16}} \exp(-0.026f_n^{1.15656} - R_{15}) \right] \\
R_1 &= 0.03891\epsilon_r^{1.4} \\
R_2 &= 0.267u^{7.0} \\
R_3 &= 4.766 \exp(-3.228u^{0.641}) \\
R_4 &= 0.016 + (0.0514\epsilon_r)^{4.524} \\
R_5 &= (f_n/28.843)^{12.0} \\
R_6 &= 22.20u^{1.92} \\
R_7 &= 1.206 - 0.3144 \exp(-R_1) \cdot [1 - \exp(-R_2)] \\
R_8 &= 1 + 1.275 \left[ 1 - \exp(-0.004625R_3\epsilon_R^{1.674}) \cdot (f_n/18.365)^{2.745} \right] \\
R_9 &= \frac{5.086R_4R_5}{0.3838 + 0.386R_4} \cdot \frac{\exp(-R_6)}{1 + 1.2992R_5} \cdot \frac{(\epsilon_r - 1)^6}{1 + 10(\epsilon_r - 1)^6} \\
R_{10} &= 0.00044\epsilon_r^{2.136} + 0.0184 \\
R_{11} &= \frac{(f_n/19.47)^6}{1 + 0.0962(f_n/19.47)^6} \\
R_{12} &= 1/(1 + 0.00245u^2) \\
R_{13} &= 0.9408\epsilon_r^{R_8} - 0.9603 \\
R_{14} &= (0.9408 - R_9)\epsilon_{\text{eff}}^{R_8} - 0.9603 \\
R_{15} &= 0.707R_{10}(f_n/12.3)^{1.097} \\
R_{16} &= 1 + 0.0503\epsilon_r^2 R_{11} \left\{ 1 - \exp[-(u/15)^6] \right\}.
\end{aligned}$$

Similarly, the appropriate design formulas applicable to the frequency-dependent odd mode impedance are

$$\begin{aligned}
Z_{0o}(f_n) &= Z_0(f_n) + \left[ Z_{0o}(0) \left\{ \epsilon_{\text{eff},o}(f_n)/\epsilon_{\text{eff},o}(0) \right\}^{Q_{22}} \right. \\
&\quad \left. - Z_0(f_n)Q_{23} \right] \left\{ 1 + Q_{23} + (0.46g)^{2.2}Q_{25} \right\}^{-1} \tag{10.125}
\end{aligned}$$

where

$$\begin{aligned}
Q_{22} &= 0.925(f_n/Q_{26})^{1.536} / \left[ 1 + 0.3(f_n/30)^{1.536} \right] \\
Q_{23} &= 1 + 0.005f_n Q_{27} \left\{ \left[ 1 + 0.812(f_n/15)^{1.9} \right] (1 + 0.025u^2) \right\}^{-1} \\
Q_{24} &= 2.506 Q_{28} u^{0.894} \left[ (1 + 1.3u)f_n/99.25 \right]^{4.29} (3.575 + u^{0.894})^{-1} \\
Q_{25} &= [0.3f_n^2 / (10 + f_n^2)] \left\{ 1 + 2.333(\epsilon_r - 1)^2 / [5 + (\epsilon_r - 1)^2] \right\} \\
Q_{26} &= 30 - 22.2 \left( [(\epsilon_r - 1)/13]^{12} / \{ 1 + 3[(\epsilon_r - 1)/13]^{12} \} \right) - Q_{29} \\
Q_{27} &= 0.4g^{0.84} \left\{ 1 + 2.5(\epsilon_r - 1)^{1.5} / [5 + (\epsilon_r - 1)^{1.5}] \right\} \\
Q_{28} &= 0.149(\epsilon_r - 1)^3 / [94.5 + 0.038(\epsilon_r - 1)^3] \\
Q_{29} &= 15.16 / [1 + 0.196(\epsilon_r - 1)^2].
\end{aligned}$$

Here again, the range of accurate applicability of these expressions is the same as that defined above. The maximum error is 2.5% up to  $f_n = 30$  GHz· mm but, if the specified maximum substrate permittivity is reduced from 18 to 12.9 (GaAs), then these expressions can be used up to  $f_n = 25$  GHz· mm with the accuracy remaining guaranteed. It is noted again that this corresponds to an actual operating frequency of approximately 40 GHz in the case of a 0.635 mm thick substrate.

In design the principal sets of expressions are those for the effective microstrip permittivities since these ultimately form the major quantity in the determination of physical lengths. The frequency-dependent characteristic impedances should be used within dynamically interactive CAD routines to set the requirements for matching the termination line impedance (usually 50 Ω).

Since the determination of physical lengths is of paramount importance we also need to know semi-open end equivalent lengths for the even and odd modes. Kirschning and Jansen give the following expressions for these equivalent lengths, beginning with the length for the even mode

$$\Delta\ell_e = \left[ \Delta\ell(2u, \epsilon_r) - \Delta\ell(u, \epsilon_r) + 0.0198hg^{R'_1} \right] \exp(-0.328g^{2.244}) + \Delta\ell(u, \epsilon_r) \quad \text{10.126}$$

where

$$R'_1 = 1.187 [1 - \exp(-0.069u^{2.1})] \quad \text{10.127}$$

and

$$\Delta\ell_o = \{\Delta\ell(u, \epsilon_r) - hR'_3\} \{1 - \exp(-R'_4)\} + hR'_3 \quad \text{10.128}$$

where, in this expression:

$$\begin{aligned}
R'_2 &= 0.343u^{0.6187} + \left\{ 0.45\epsilon_r / (1 + \epsilon_r) \right\} u^{[1.357+1.65/(1+0.7\epsilon_r)]} \\
R'_3 &= 0.2974 \left\{ 1 - \exp(-R'_2) \right\} \\
R'_4 &= (0.271 + 0.0281\epsilon_r) g^{\{1.167\epsilon_r/(0.66+\epsilon_r)\}} \\
&\quad + [1.025\epsilon_r / (0.687 + \epsilon_r)] g^{[0.958\epsilon_r/(0.706+\epsilon_r)]}.
\end{aligned}$$

Although the accuracy of these expressions is approximately 5% over the range defined above, with a slight increase also with frequency, the equivalent end-effect lengths usually only amount to a second-order contribution in determining the final physical lengths of the structure. For this reason, it is expected that these expressions will be sufficiently accurate for most requirements of effective parallel-coupled microstrip designs.

## 10.5 An Approximate Synthesis Technique

In this potentially powerful procedure the shape ratios  $w/h$  and  $s/h$  are determined from  $Z_{0e}$  and  $Z_{0o}$  information either using just two universal graphs or with the aid of a relatively simple computer routine.

In both cases there are two distinct stages. One of these comprises a determination of equivalent single microstrip shape ratios, the  $(w/h)_{se}$ . The second stage relates the required  $w/h$  and  $s/h$  for the coupled structure to the equivalent single microstrip shape ratios. The final results are made independent of the substrate permittivity for a considerable range and are given by Akhtarzad *et al.* [15], not only in graphical form, but also as closed formulas. A summary of the design stages is thus:

- a.** Determine shape ratios for equivalent single microstrip lines.
- b.** Obtain the shape ratio  $w/h$  and the spacing ratio  $s/h$  for the desired coupled microstrip structure using the single-line shape ratios found at stage (a).

For design stage (a) we use the following relationships:

$$Z_{0se} = \frac{Z_{0e}}{2} \quad (\text{for single microstrip shape ratio } (w/h)_{se}) \quad \text{10.129}$$

and

$$Z_{0so} = \frac{Z_{0o}}{2} \quad (\text{for single microstrip shape ratio } (w/h)_{so}). \quad \text{10.130}$$

The appropriate shape ratios are then determined directly from a graph or from closed-form expressions which are readily available. The graphical technique described in [Chapter 6](#) is recommended or the approximate static-TEM formulas given there may be used for more comprehensive CAD.

Akhtarzad *et al.* [15] give a graph for determining  $w/h$  and  $s/h$  from the single-line values now known. This graph is suitable for many approximate designs and therefore it is repeated

here ([Figure 10.18](#)) with some additional information to guide the user.

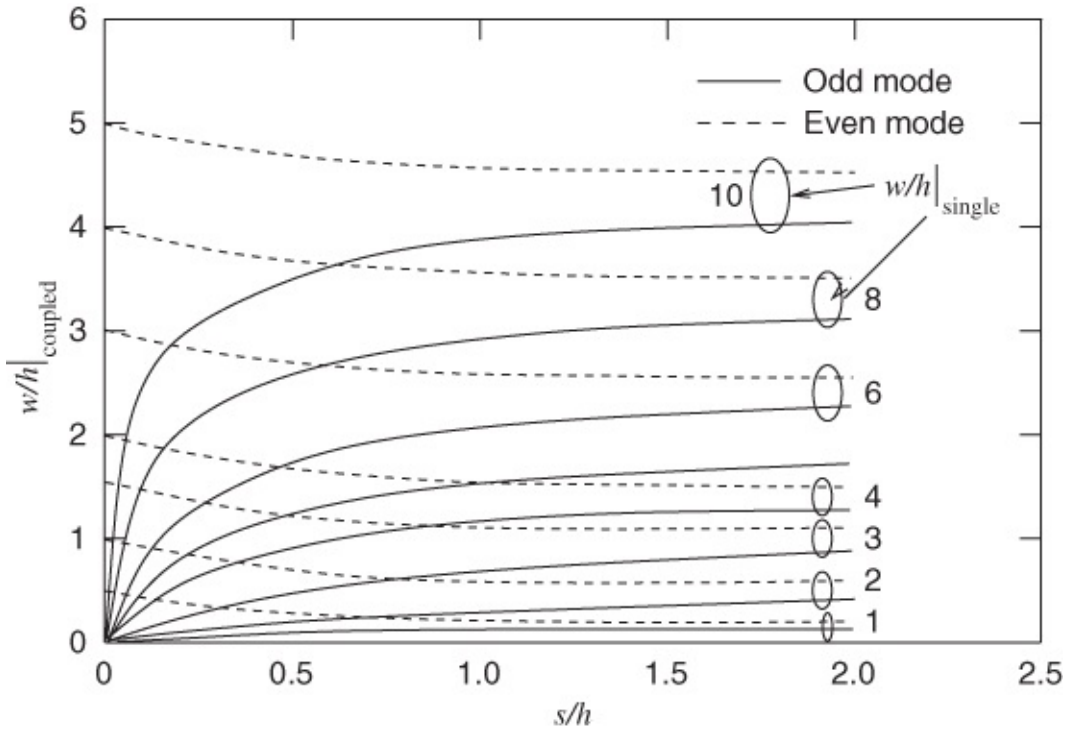


**Figure 10.18** “General” curves for use in the synthesis technique.  $w/h|_{\text{single}}$  is the aspect ratio ( $w/h$ ) from a single microstrip line design procedure. Adapted from Akhtarzad *et al.* (1975) [15], figure 3, p. 487. Reprinted with permission of IEEE.

To perform design using this graph, we start with stage (a) and evaluate  $(w/h)_{se}$  and  $(w/h)_{so}$  using single-line static-TEM methods. We then select the two curves of [Figure 10.18](#) which have the appropriate  $w/h$  parameter for each mode as just evaluated (solid curves for odd mode, broken lines for even mode). The point of intersection of these two selected lines is the design point. Reading across horizontally yields the required  $w/h$  for each of the coupled lines, and reading down vertically gives their normalized spacing  $s/h$ . A numerical example of design using this graph will be given shortly. Difficulties may be encountered in crowded regions of the graph, such as low  $w/h$  combined with low  $s/h$ , and if the single-line-derived  $w/h$  values do not happen to fit the values 2, 3, 4, 6, 8, or 10, then some fairly awkward interpolation is necessary. To overcome these problems, Akhtarzad *et al.* [15] have given a family of useful expressions, the most complete of which are quoted here first:

$$\left(\frac{w}{h}\right)_{se} = \frac{2}{\pi} \cosh^{-1} \left( \frac{2d - g + 1}{g + 1} \right) \quad \text{10.131}$$

$$\begin{aligned} \left(\frac{w}{h}\right)_{so} &= \frac{2}{\pi} \cosh^{-1} \left( \frac{2d - g - 1}{g - 1} \right) \\ &+ \frac{4}{\pi (1 + \epsilon_r/2)} \cosh^{-1} \left( 1 + 2 \frac{w/h}{s/h} \right), \epsilon \leq 6 \end{aligned} \quad \text{10.132}$$

or

$$\left(\frac{w}{h}\right)_{so} = \frac{2}{\pi} \cosh^{-1} \left( \frac{2d-g-1}{g-1} \right) + \frac{1}{\pi} \cosh^{-1} \left( 1 + 2 \frac{w/h}{s/h} \right), \epsilon \geq 6 \quad 10.133$$

where

$$g = \cosh \left( \frac{\pi s}{2h} \right) \quad 10.134$$

and

$$d = \cosh \left( \pi \frac{w}{h} + \frac{\pi s}{2h} \right). \quad 10.135$$

Equation (10.131) is solved simultaneously with either Equation (10.132) or Equation (10.133) as appropriate for the particular permittivity range. The curves in Figure 10.18 were originally obtained by Akhtarzad *et al.* for the median value ( $\epsilon_r = 6$ ) of the permittivity. As an approximation the second terms may be neglected in both Equations (10.132) and (10.133). Then an explicit formula for  $s/h$  is obtained:

$$\frac{s}{h} = \frac{2}{\pi} \cosh^{-1} \left\{ \frac{\cosh [(\pi/2)(w/h)_{se}] + \cosh [(\pi/2)(w/h)_{so}] - 2}{\cosh [(\pi/2)(w/h)_{so}] - \cosh [(\pi/2)(w/h)_{se}]} \right\}. \quad 10.136$$

In any case, the functional calculations are quite complicated whether one uses the more accurate expressions or starts with this formula, Equation (10.136).

Also, when compared with the results of Bryant and Weiss [3] an error of the order of 10% has been quoted for this synthesis technique [15]. If this magnitude of error is actually found in practice then the synthesis technique may still be used to obtain an initial design, after which the more accurate analysis of Garg and Bahl (in Section 10.4) could be employed to correct the design dimensions. The sequence would be:

- a. With the required  $Z_{0e}$  and  $Z_{0o}$  determine  $(w/h)_1$  and  $(s/h)_1$  by approximate synthesis.
- b. Using these values,  $(w/h)_1$  and  $(s/h)_1$ , recalculate  $Z_{0e}$  and  $Z_{0o}$  by means of the semi-empirical analysis formulas given in Section 10.4.
- c. Compare the new values thus calculated for  $Z_{0e}$  and  $Z_{0o}$  with those originally required. A suitable programmable calculator, spreadsheet, or computer routine will then enable iterations to be made, incrementing  $w/h$  and  $s/h$  until the impedances agree within a specified tolerance.

Although this procedure can yield coupled-line design to approximately 3% accuracy, there is still clearly scope for significant improvement to aid the circuit designer.

In particular, either the synthesis technique due to Akhtarzad *et al.* might be modified to obtain greater accuracy or a new technique might be developed.

## 10.6 Summary

The theory behind coupled microstrip lines was presented in this chapter. The theory and concepts are applicable to nearly all coupled transmission lines. The most convenient way of conceptualizing signal flow on transmission lines for microwave circuits is to use even and odd modes. This is not the most convenient mode set to use in all situations. For example, with RFICs and high-speed digital circuits it is sometimes more convenient to use common and differential modes. These are closely related to even and odd modes, and the difference comes down to book-keeping. (See [1] to convert between the modes.) Analysis of the electromagnetic fields and hence transmission line theory is always based on even- and odd-mode descriptions. The chapter forms the basis for the next chapter, where applications of parallel-coupled microstrip lines are presented. Coupled lines have very special properties, making them the most useful construct in microwave planar circuit design.

## References

- [1] M. Steer, *Microwave and RF Design: a Systems Approach*, 2nd ed. SciTech Pub., 2013.
- [2] B. Biswas, “Modeling and simulation of high speed interconnects,” Master's thesis, North Carolina State University, 1998.
- [3] T. Bryant and J. Weiss, “Parameters of microstrip transmission lines and of coupled pairs of microstrip lines,” *IEEE Trans. on Microwave Theory and Techniques*, vol. **16**, no. 12, pp. 1021–1027, Dec. 1968.
- [4] E. Hammerstad and O. Jensen, “Accurate models for microstrip computer-aided design,” in *1980 IEEE MTT-S Int. Microwave Symp. Digest*, May 1980, pp. 407–409.
- [5] R. Garg and I. Bahl, “Characteristics of coupled microstriplines,” *IEEE Trans. on Microwave Theory and Techniques*, vol. **27**, no. 7, pp. 700–705, Jul. 1979.
- [6] R. Garg and I. Bahl, “Correction to “characteristics of coupled microstriplines”,” *IEEE Trans. on Microwave Theory and Techniques*, vol. **28**, no. 3, p. 272 Mar. 1980.
- [7] R. Garg, Private communication concerning coupled-line formulas, 1980.
- [8] W. Getsinger, “Dispersion of parallel-coupled microstrip,” *IEEE Trans. on Microwave Theory and Techniques*, vol. **21**, no. 3, pp. 144–145, Mar. 1973.
- [9] B. Easter and C. Gupta, “More accurate model of the coupled microstripline section,” *IEE Journal on Microwaves, Optics and Acoustics*, vol. **3**, no. 3, pp. 99–103, May 1979.
- [10] M. Krage and G. Haddad, “Frequency-dependent characteristics of microstrip transmission lines,” *IEEE Trans. on Microwave Theory and Techniques*, vol. **20**, no. 10, pp. 678–688, Oct. 1972.
- [11] J. Richings and B. Easter, “Measured odd- and even-mode dispersion of coupled microstrip lines,” *IEEE Trans. on Microwave Theory and Techniques*, vol. **23**, no. 10, pp.

- [12] M. Kirschning and R. Jansen, “Accurate wide-range design equations for the frequency-dependent characteristic of parallel coupled microstrip lines,” *IEEE Trans. on Microwave Theory and Techniques*, vol. **32**, no. 1, pp. 83–90, Jan. 1984.
- [13] M. Kirschning and R. Jansen, “Accurate wide-range design equations for the frequency-dependent characteristics of parallel coupled microstrip lines,” *IEEE Trans. on Microwave Theory and Techniques*, vol. **33**, no. 3, p. 288, Mar. 1985.
- [14] R. H. Jansen and M. Kirschning, “Arguments and an accurate model for the power-current formulation of microstrip characteristic impedance.” *Arch. Elek. Übertragung.*, vol. **37**, no. 3, pp. 108–112, 1983.
- [15] S. Akhtarzad, T. Rowbotham, and P. Johns, “The design of coupled microstrip lines,” *IEEE Trans. on Microwave Theory and Techniques*, vol. **23**, no. 6, pp. 486–492, Jun. 1975.

# Chapter 11

## Applications of Parallel-coupled Microstrip Lines

### 11.1 Introduction

In this chapter we consider the detailed design of parallel-coupled microstrip structures. The main design element considered in this chapter is the design of a directional coupler. Many of the techniques used in designing circuits with coupled transmission lines are introduced, in particular design of coupled lines beginning with an electrical design, such as the required even- and odd-mode characteristic impedances, and then realizing the electrical design in physical form. The best microwave designs begin with just such a synthesis approach. Coupled lines are the basic component in many microwave circuits. They will be considered again in the filter chapter, [Chapter 19](#), and there many of the design techniques presented in this chapter will be used.

### 11.2 Directional Couplers

In analog and RF circuits a designer usually has some freedom to increase the spacing of lines to reduce coupling to acceptable levels. The coupling phenomenon, however, can be exploited to realize a new type of element called a directional coupler. The schematic of a directional coupler is shown in [Figure 11.1\(a\)](#). The top view of a microstrip realization of a directional coupler is shown in [Figure 11.1\(b\)](#). The microstrip realization is typical of most directional couplers in that it comprises two parallel signal lines with the electric and magnetic fields of a signal on one line inducing currents and voltages on the other. A usable directional coupler has a coupled line length of at least a quarter wavelength with longer lengths of line resulting in broader bandwidth operation. Directional couplers are used to sample a traveling wave on one line and to induce a usually much smaller image of the wave on another line, that is, the forward and backward-traveling modes can be separated. An important application of a directional coupler is as part of a measurement system. Here a prescribed amount of the incident power is required to be coupled out of the system. Thus, for example, a “20 dB microstrip coupler” (with a coupling factor  $C' = -20$  dB) is a pair of coupled microstrip lines in which  $1/100$ th of the power input is coupled from one microstrip line onto the another.

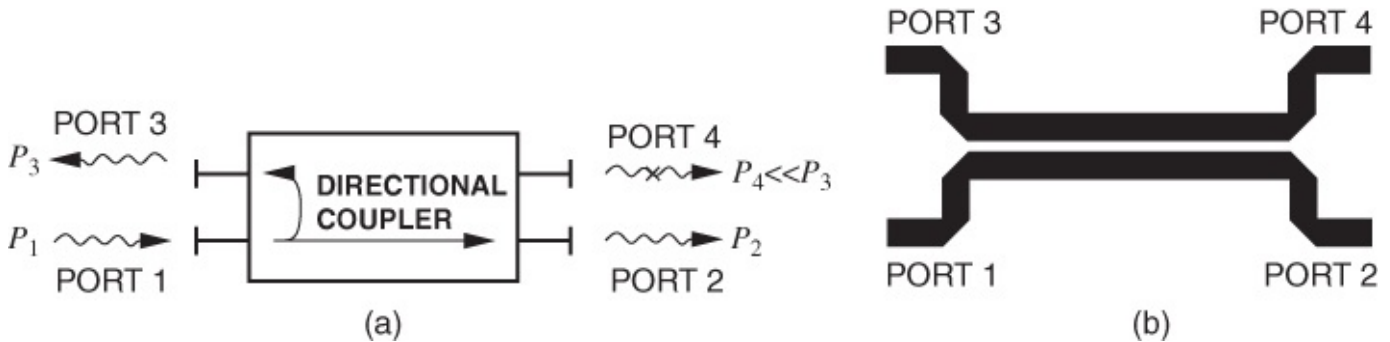


**Figure 11.1** Directional couplers: (a) schematic; and (b) backward-coupled microstrip.

As described in [Section 10.2.3](#), the even- and odd-mode characteristic impedances ( $Z_{0e}$  and  $Z_{0o}$ ) are major design parameters for any parallel-coupled transmission line configuration, whatever its application. These impedances are obtained at an early design stage and they are functions of the degree of coupling ( $C$ ) and the single-line terminating characteristic impedance ( $Z_{0S}$ ). The relationships between  $Z_{0e}$  and  $Z_{0o}$ , and the physical dimensions of the coupled structure (including the substrate permittivity) are therefore of prime significance to the designer. As with single microstrip lines, so also in this coupled situation, we can determine  $Z_{0e}$  and  $Z_{0o}$  from known physical dimensions, which amounts to analysis. Alternatively, with greater difficulty, we may synthesize the physical structure from starting values of the impedances. Both of these procedures are useful in practice.

For coupler design the important starting parameters are coupling factor  $C$ , transmission factor  $T$ , directivity  $D$ , and isolation  $I$ . Microstrip couplers, unless compensated by one of the methods to be described, exhibit a performance that can be far removed from the ideal in some cases. This is due to the different phase velocities associated with the even and odd modes, the main effect of which is to degrade the directivity. The initial specification for such a coupler will include:

- coupling factor  $C$  (usually in decibels, dB) at the centre frequency  $f_0$
- permittivity and thickness of the substrate
- terminating characteristic impedance  $Z_0$  (usually  $50\Omega$ )
- bandwidth and center frequency
- coupling factor tolerance over the band (sometimes)
- lowest acceptable directivity  $D$  in decibels (dB).

From this information the designer must ultimately determine the widths of the microstrip lines, the separation between them, and the length of the coupled region. In the design of filters or matching networks using parallel-coupled lines we usually begin with either insertion loss as a function of frequency or VSWR requirements over some band. In either event, we still arrive at desired values of  $Z_{0e}$ , and  $Z_{0o}$  and the final synthesis problem is then similar to that of a coupler.

It is important to note that all parallel-line couplers, whether true TEM or not, have the odd-

and even-mode property which always results in  $Z_{0e}$  and  $Z_{0o}$ . However, true TEM couplers yield equal phase velocities for each mode whereas microstrip (quasi-TEM) and certain other structures yield different odd-mode and even-mode phase velocities,  $v_{po}$  and  $v_{pe}$ .

### 11.2.1 Overall Parameters for Couplers

A coupled-line circuit element may be specified in terms of the following overall parameters:

coupling factor = $C$	
transmission factor = $T$	
directivity factor = $D$	

The meaning of these parameters is clarified by [Figure 11.2](#). We can now define the quantities more closely as follows:

$C = V_3/V_1$	= voltage fraction “transferred” (coupled) across to the opposite arm
$T = V_2/V_1$	= transmission directly through the “primary” arm of the structure
$D = V_4/V_3$	= measure of the undesirable coupling that can occur to port 4, which we shall call the directivity
$I = V_4/V_1$	= degree of isolation between port 4 and port 1.

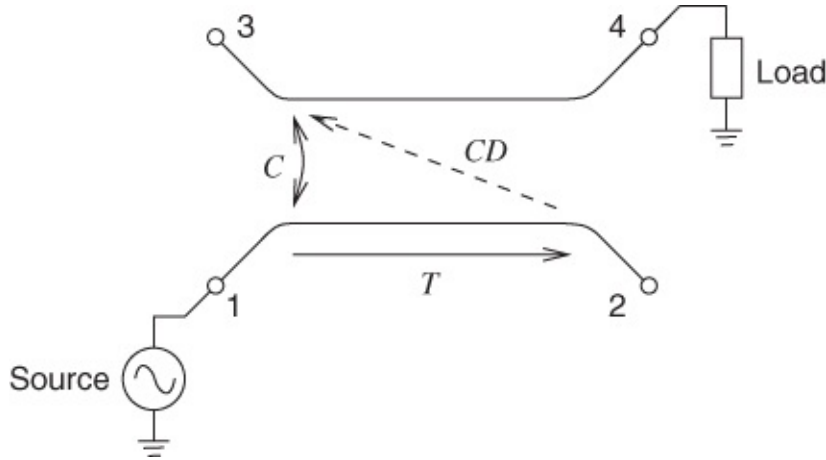


[Figure 11.2](#) Illustration of the defining parameters for coupled transmission lines:  $C$ , coupling factor;  $T$ , transmission factor; and  $D$ , directivity factor.

It is usual to quote all these quantities in decibels, so that we talk in terms of a “10 dB coupler,” for example. This is a somewhat loose description, since the power at port 3 is –10 dB relative to that input to port 1. In ideal couplers  $D = 0$ , and the power is split proportionately between ports 2 and 3.

With coaxial and stripline couplers for which TEM modes exist, very good directivity can be achieved, but it is not fully accurate for microstrip couplers of simple parallel-coupled construction, and the considerably reduced directivity can be a serious problem.

## 11.3 Design Example: Design of a 10 dB Microstrip Coupler

We will approach this by two methods:

- a. using Bryant and Weiss curves
- b. using Akhtarzad synthesis curves.

For the moment, in this section, we shall only determine the cross-sectional dimensions. Evaluation of the length of a coupler is considered shortly.

The specification is:

coupling factor	$C' = -10 \text{ dB}$
single microstrip feedline characteristic impedances	$Z_0 = 50 \Omega$
substrate permittivity	$\epsilon_r = 9.0$
thickness	$h = 1 \text{ mm}$
system centre frequency (mid-band for the coupler)	$f_0 = 5 \text{ GHz}$

The frequency is low enough for dispersion effects (dealt with later) to be neglected to a first approximation. Note that  $Z_{0S}$  is  $50 \Omega$ .

Design calculations:

$Z_{0e}$  and  $Z_{0o}$  are obtained using Equations (10.84) and (10.85). This yields

$$Z_{0e} = 69.5 \Omega \quad \text{and} \quad Z_{0o} = 36 \Omega.$$

Next, always check that the relation  $Z_{0S} \approx \sqrt{Z_{0e}Z_{0o}}$  holds, although the approximation is not good for tight (between  $-d$  dB and  $-3$  dB) coupling. Hence, in this case

$$Z_{0S} = \sqrt{Z_{0e}Z_{0o}} = \sqrt{69.5 \times 36} = 50.02 \Omega. \quad 11.1$$

### 11.3.1 Use of Bryant and Weiss' Curves

With Bryant and Weiss' method ([Section 10.3.1](#)), choose the  $\epsilon_r = 9$  family of curves. Select two points, one on the “even-mode” set of curves and the other on the “odd-mode” set of curves. These points are controlled by the necessity for them to lie on the same  $w/h$  ordinate value, and on curves with an identical  $s/h$  parameter, that is, they must both have the same  $w/h$  and  $s/h$ . Then  $w/h$  and  $s/h$  are read off as 0.87 and 0.25 respectively. The procedure is shown in the graph of [Figure 11.3](#).

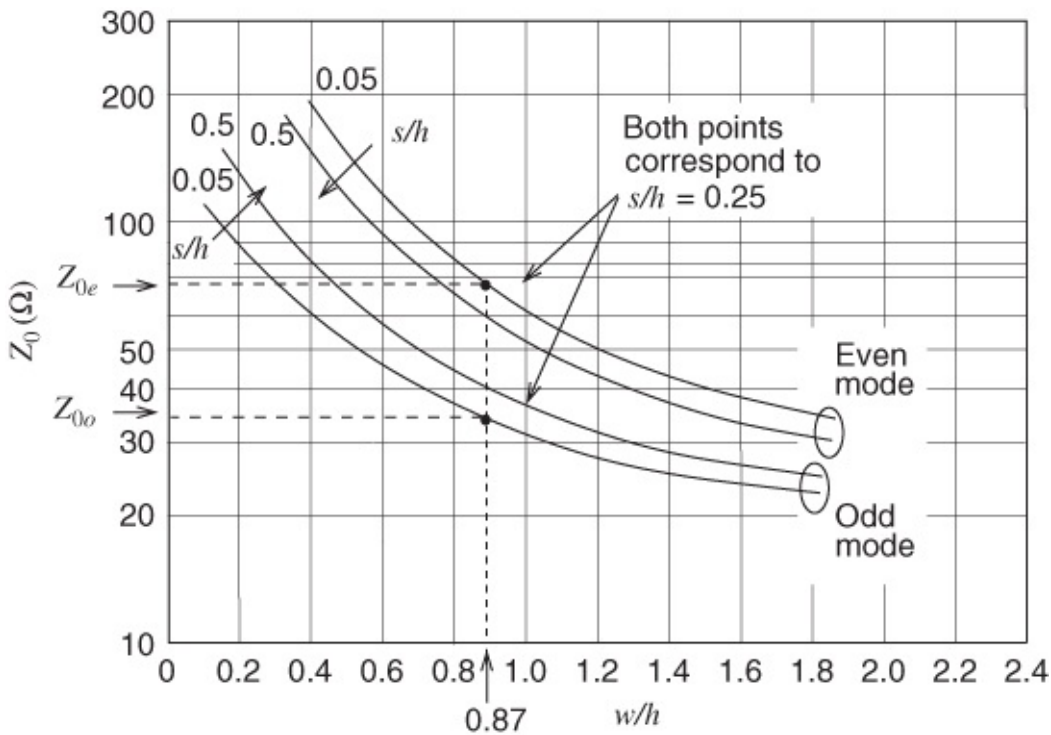


**Figure 11.3** Graphical design procedure yielding the shape ratios for a 10 dB microstrip directional coupler.

From the values obtained we can determine  $w$  and  $s$  easily, since the substrate thickness  $h$  is given as 1 mm:

$$w = 0.87 \times 1 = 0.87 \text{ mm} \quad \text{and} \quad s = 0.25 \times 1 = 0.25 \text{ mm.}$$

### 11.3.2 Synthesis Using Akhtarzad's Technique

First we must calculate “single” microstrip characteristic impedances, using Equations (10.130) and (10.131):

$$Z_{0se} = \frac{Z_{0e}}{2} \approx 35 \Omega \quad \text{and} \quad Z_{0so} = \frac{Z_{0o}}{2} \approx 18 \Omega. \quad 11.2$$

Details of the actual calculations will not be given here because they follow the same routine that was given in [Section 10.5](#). Approximate values are

$$(w/h)_{se} \approx 2.0 \quad \text{and} \quad (w/h)_{so} \approx 5.0.$$

Now, using [Figure 10.18](#), we first select the broken (even-mode) curve, which has parameter  $(w/h)_{se} = 2$ . Next, select the solid (odd-mode) curve, which has parameter  $(w/h)_{so} = 5$ . The point where these two curves intersect is the design point and its coordinates give the results:

$$w/h \approx 0.85 \quad \text{and} \quad s/h \approx 0.25.$$

Hence, because  $h = 1.0 \text{ mm}$ :

$$w \approx 0.85 \text{ mm} \quad \text{and} \quad s \approx 0.25 \text{ mm.}$$

### 11.3.3 Comparison of Methods

Although only graphical techniques have been used for the preceding calculations it can be seen that the values obtained compared well in this case. Notice that, for the synthesis method, no special set of curves was required to be selected, and the curves used ([Figure 10.18](#)) are “universal” in that they apply over a wide range of substrate permittivities.

## 11.4 Frequency- and Length-Dependent Characteristics of Directional Couplers

### 11.4.1 Optimum Coupled-region Length

The requirement for coupled-region length is determined and given in [Chapter 10](#) following Equation (10.38). It is seen that the maximum degree of coupling occurs when the length of the coupled region is  $\lambda_{gm}/4$  where  $\lambda_{gm}$  is the mid-band wavelength. At all other wavelengths the coupling decreases. As a rough first approximation, only really applicable to loose amounts of coupling (perhaps less than  $-10$  dB), it is possible to consider a single, that is, uncoupled, microstrip of width  $w$  and to evaluate the mid-band wavelength as described in [Chapter 5](#). However, the error involved in this can rise to 10% or more and the mean of the even-mode and odd-mode wavelengths should be taken for greater accuracy. It is best, for design purposes, to work in terms of characteristic impedances. We first recollect the three general forms in which characteristic impedance may be written, Equations (2.30), (2.31), and (2.32):

$$Z_0 = \sqrt{\frac{L}{C}} = \frac{1}{v_p C} = v_p L. \quad 11.3$$

The last form of this expression is the most convenient one to use here, since we may reasonably assume that the inductance  $L$  remains constant independent of whether a substrate is present or absent. (This is really another way of stating that only the electric flux is affected by changing the dielectric material on the substrate, for a given mode. Note that here  $C$  is capacitance.)

Consider the odd mode on coupled microstrip lines. For the actual situation with a substrate present, [Figure 11.4\(a\)](#), we have

$$Z_{0o} = v_{po} L_o. \quad 11.4$$

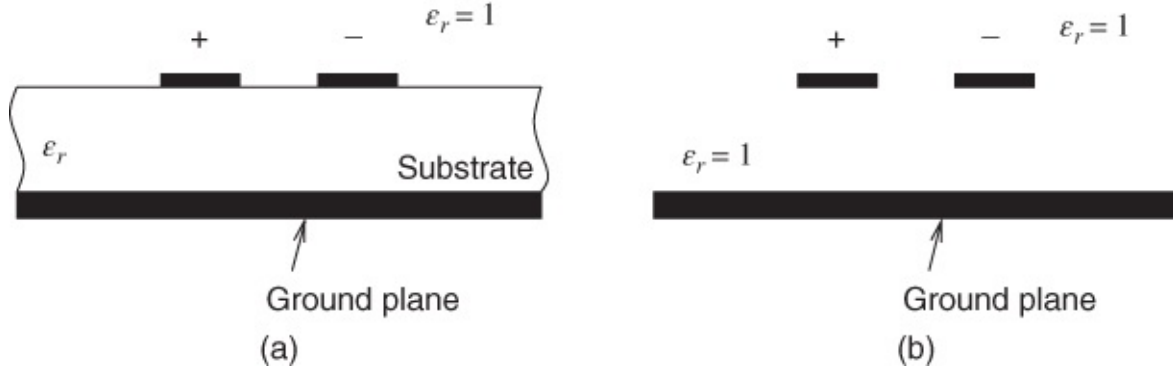


**Figure 11.4** Parallel-coupled microstrips with the substrate (a) present and (b) absent (only the odd mode is indicated).

When the substrate is removed, as in [Figure 11.4\(b\)](#), the velocity is simply the free-space limit value  $c$ . For that situation the characteristic impedance is given by

$$Z_{01o} = cL_o. \quad \text{11.5}$$

Equations [\(11.4\)](#) and [\(11.5\)](#) can be simply solved for  $v_{po}$ , giving

$$v_{po} = c \frac{Z_{0o}}{Z_{01o}}. \quad \text{11.6}$$

By a similar consideration for the even mode:

$$v_{pe} = c \frac{Z_{0e}}{Z_{01e}}. \quad \text{11.7}$$

The odd- and even-mode wavelengths are then easily found at any frequency  $f$  by using

$$\lambda_{go} = v_{po}/f \quad \text{and} \quad \lambda_{ge} = v_{pe}/f. \quad \text{11.8}$$

The characteristic impedances  $Z_{0e}$  and  $Z_{0o}$  are known early on in the design calculations. Then the cross-sectional dimensions  $w/h$  and  $s/h$  are obtained. Once these are known the free-space characteristic impedance  $Z_{01e}$  and  $Z_{01o}$  can either be obtained from Bryant and Weiss' curves applicable to  $\epsilon_r = 1$  or by calculations using the analysis given in [Section 10.4](#).

We can finally combine Equations [\(11.5\)](#), [\(11.7\)](#), and [\(11.8\)](#), and set frequency  $F$  (in gigahertz) to give

$$\lambda_{ge} \approx \frac{300}{F} \frac{Z_{0e}}{Z_{01e}} \text{ mm} \quad \text{11.9}$$

and

$$\lambda_{go} \approx \frac{300}{F} \frac{Z_{0o}}{Z_{01o}} \text{ mm.} \quad \text{11.10}$$

Returning to the numerical design example of [Section 11.3](#), we now apply the values of  $w/h$

and  $s/h$  to the Bryant and Weiss curves ( $\epsilon_r = 1$ ) and obtain

$$Z_{0le} = 185\Omega \quad \text{and} \quad Z_{0lo} = 75\Omega. \quad 11.11$$

With the given frequency of 5 GHz, Equations (11.9) and (11.10) then yield

$$\lambda_{go} = 28.8 \text{ mm} \quad \text{and} \quad \lambda_{ge} = 22.54 \text{ mm}. \quad 11.12$$

The mean of these two wavelengths ( $\lambda_{gm}$ ) is 25.67 mm and thus the length of the coupled region ( $\lambda_{gm}/4$ ) is 6.42 mm. With the approximations involved, and also considering that we have neglected dispersion, the value 6.4 mm is sensible. The final complete microstrip coupler design is illustrated, in plan view, in [Figure 11.5](#).

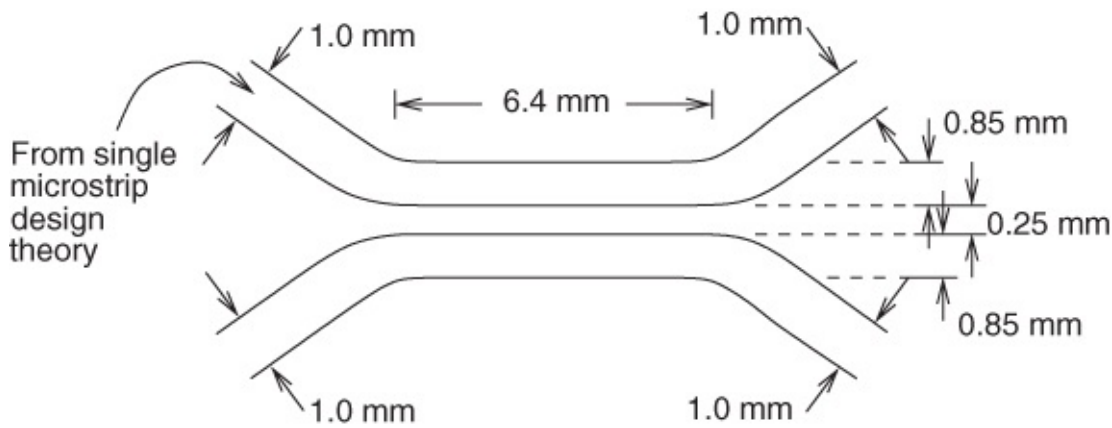


[Figure 11.5](#) Final numerical dimensional values for the  $-10$  dB coupler design shown in the text.

In some cases, especially at higher frequencies, the length may become very small and difficult to define in manufacture. Then the length can be made a convenient odd number of quarter-wavelengths:

$$\ell = (2n - 1)\lambda_{gm}/4. \quad 11.13$$

It is, however, important to appreciate that the coupler would then exhibit  $n$  responses with frequency.

Such edge-coupled microstrip couplers, based on alumina substrates, have been reported operating at frequencies at least as high as 30 GHz [1]. Tripathi and Hill's 10 dB coupler of this form exhibits two roughly sinusoidal responses: the first centered on 9 GHz and the second on 24 GHz. The reason that the second response is significantly departed from a third harmonic lies in the dispersive nature of these structures. This aspect is covered in the next section concerning frequency response.

Tripathi and Hill's coupler also has deteriorating isolation and directivity, worsening as frequency increases. For example, the isolation is about 20 dB at 9 GHz but has deteriorated to 10 dB at 24 GHz. It is shown that SPICE models accurately predict the performance over the entire 1 to 30 GHz band.

## 11.4.2 Overall Effects and Getsinger's Model

So far we have concentrated on “mid-band” design. The full frequency-dependent (i.e., phase-angle-dependent) coupling factor developed in [Chapter 10](#) as Equation (10.37) is reproduced here, with phase velocity differences neglected:

$$C(\theta) = C(j\Omega) = \frac{jC \sin \theta}{\sqrt{1 - C^2} \cos \theta + j \sin \theta} \quad 11.14$$

where  $C$  is the mid-band coupling factor given by Equation (10.33) and  $\theta = \beta\ell = 2\pi\ell/\lambda_g$ . Accepting the validity of the result for the loosely coupled frequency response of the ideal matched coupler, the actual shape would be similar to that given in [Figure 11.6](#).

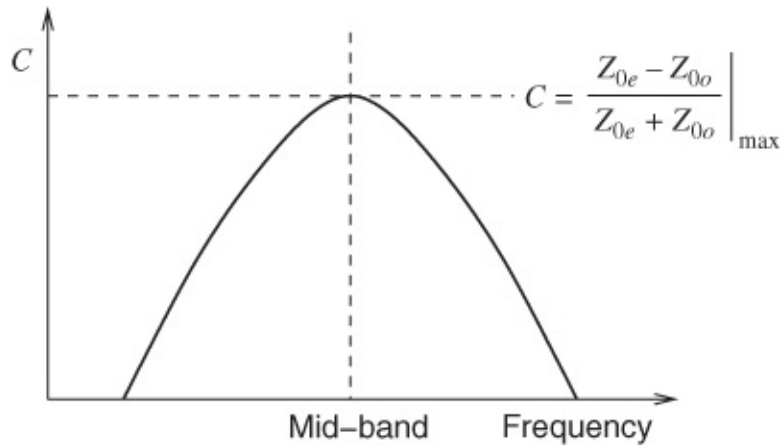


[Figure 11.6](#) The characteristic shape of the frequency response for a loosely coupled ideal matched coupler.

This general form of response is typical for couplers of this type (i.e. couplers exploiting the difference between even- and odd-mode impedances), since they are difficult to construct for even moderately tight couplings:  $C$  is generally smaller than  $-3$  dB in designs with this geometry.

In several applications such a poor frequency response is intolerable, and a number of techniques have been developed to “flatten” the response. (The phase responses are also significant, and there are also techniques to improve the directivity by near-equalization of the even- and odd-mode phase velocities.) Some of these techniques will be dealt with shortly. As with single microstrip lines, dispersion is also present in the behavior of these coupled microstrips; this problem is dealt with first.

## 11.4.3 Complete Coupling Section Response

Once  $\epsilon_{\text{eff},e}(f)$  and  $\epsilon_{\text{eff},o}(f)$  have been evaluated then the appropriate wavelengths can be calculated in a manner similar to that employed with single microstrips. To solve for the full frequency response of the coupler, in microstrip form, it is necessary to return to the full voltage expressions developed in [Chapter 10](#). It is also necessary to incorporate the previous dispersion calculations so that the different wavelengths of the even and odd modes are taken

into account. This is a fairly onerous task that is best set up on a computer. To get some idea of the magnitude of the calculations consider the coupling factor, as determined from Equations (10.17) and (10.21), but with  $\theta$  appropriately replaced by  $\theta_e$  and  $\theta_o$ :

$$C = V_{1e} - V_{1o} = \frac{Z_{0e}Z_0 \cos \theta_e + jZ_{0e}^2 \sin \theta_e}{2Z_{0e}Z_0 \cos \theta_e + j(Z_{0e}^2 + Z_0^2) \sin \theta_e} - \frac{Z_{0o}Z_0 \cos \theta_o + jZ_{0o}^2 \sin \theta_o}{2Z_{0o}Z_0 \cos \theta_o + j(Z_{0o}^2 + Z_0^2) \sin \theta_o}. \quad 11.15$$

#### 11.4.4 Coupler Directivity

This quantity has already been defined as the undesirable coupling which can occur to port 4 (see [Figure 11.2](#)). The directivity  $D$  was also quoted as

$$D = \left| \frac{V_4}{V_3} \right|. \quad 11.16$$

Now, for a pure TEM-mode (i.e., ideal) coupler, Equation (10.42) shows that  $V_4 = 0$  and the directivity would also be zero because  $V_3$  is finite. With microstrip, the differing field patterns associated with the odd and even modes give rise to different phase velocities. We have already seen that this feature greatly complicates the coupling factor expression and a similar complication arises for the voltage appearing at port 4 (see [Figure 11.2](#)). In fact, whereas  $V_4$  cancels to zero ideally, this is now far from true.

Expressions for  $V_3$  and  $V_4$  are obtained by using Equations (10.4) and (10.8), and also Equations (10.6) and (10.10), as follows:

$$V_3 = V_{1e} - V_{1o} = \frac{Z_{0e}Z_0 \cos \theta_e + jZ_{0e}^2 \sin \theta_e}{2Z_{0e}Z_0 \cos \theta_e + j(Z_{0e}^2 + Z_0^2) \sin \theta_e} - \frac{Z_{0o}Z_0 \cos \theta_o + jZ_{0o}^2 \sin \theta_o}{2Z_{0o}Z_0 \cos \theta_o + j(Z_{0o}^2 + Z_0^2) \sin \theta_o} \quad 11.17$$

$$V_4 = V_{2e} - V_{2o} = jZ_0Z_{0e}2Z_{0e}Z_0 \cos \theta_e + j(Z_{0e}^2 + Z_0^2) \sin \theta_e - \frac{Z_0Z_{0o}}{2Z_{0o}Z_0 \cos \theta_o + j(Z_{0o}^2 + Z_0^2) \sin \theta_o}. \quad 11.18$$

Dividing Equation (11.18) by Equation (11.17) and taking the modulus yields

$$D = \left| \frac{\chi Z_0Z_{0e} - \psi Z_0Z_{0o}}{\chi (Z_{0e}Z_0 \cos \theta_e + jZ_{0e}^2 \sin \theta_e) - \psi (Z_{0o}Z_0 \cos \theta_o + jZ_{0o}^2 \sin \theta_o)} \right| \quad 11.19$$

where

$$\chi = 2Z_{0o}Z_0 \cos \theta_o + J(Z_{0o}^2 + Z_0^2) \sin \theta_o \quad 11.20$$

and

$$\psi = 2Z_{0e}Z_0 \cos \theta_e + J(Z_{0e}^2 + Z_0^2) \sin \theta_e. \quad 11.21$$

Calculation using these expressions is lengthy and a simpler alternative expression has been given for the directivity [2]

$$D = \left[ \frac{4|\zeta|}{\pi\Delta(1 - |\zeta|^2)} \right]^{-2} \quad 11.22$$

in which

$$\begin{aligned}\zeta &= \left( \frac{p_e}{1 + p_e^2} \right) - \left( \frac{p_o}{1 + p_o^2} \right) \\ p_e &= \frac{Z_{0e} - Z_0}{Z_{0e} + Z_0} \\ p_o &= \frac{Z_{0o} - Z_0}{Z_{0o} + Z_0}\end{aligned}$$

and

$$\Delta = \frac{\lambda_{go}}{\lambda_{ge}} - 1. \quad 11.23$$

Equations (11.22) to (11.23) clearly demonstrate that when  $\lambda_{go} = \lambda_{ge}$  the directivity goes to infinity.

Values much better than 12 or 14 dB are difficult to achieve for directivity with this basic form of microstrip coupler. (The basic structure is still very useful in filter design and as a starting point for couplers of improved performance.) We shall now examine some techniques aiming at:

- equalizing, or approximately equalizing, the phase velocities so that the directivity (at least) is improved
- modifying the overall coupler structure so that the frequency response is made much flatter, that is the bandwidth is greatly increased
- completely different structures where, for example, coupling factors near -3 dB can be achieved (-6 dB is approaching the limit with parallel-coupled microstrips).

## 11.5 Special Coupler Designs with Improved Performance

### 11.5.1 The Lange Coupler

This structure owes its name to its inventor Julius Lange [3], who first reported the strictly empirical concepts and development in 1969. Lange's aim was to produce a nearly octave-bandwidth coupler having a coupling factor of around  $-3$  dB. In his design, true quadrature coupling over an octave is realized as a consequence of the interdigital coupling section which compensates for even- and odd-mode phase velocity dispersion over the wide frequency range. It is necessary to bond directly, via very short wires, between transversely interposed "fingers" of the coupler. In this way, power is coupled optimally to the desired port, as well as the remaining power (after losses) still being fed to a direct port. The arrangement is illustrated in [Figure 11.7](#).

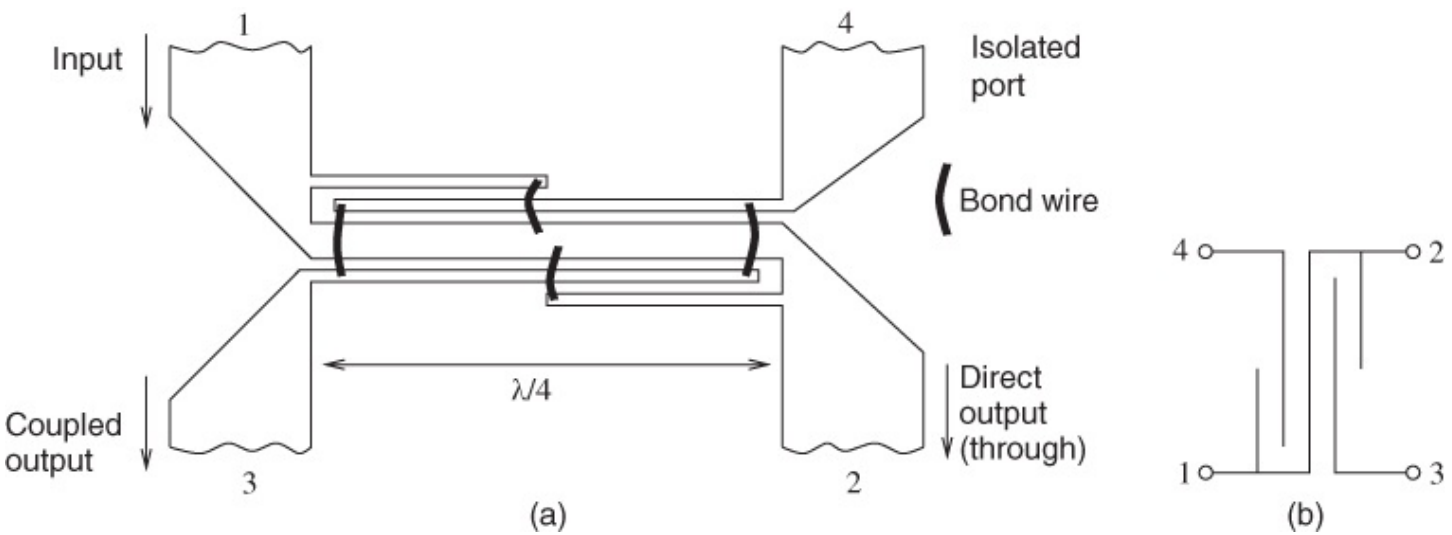


[Figure 11.7](#) A four-finger Lange coupler: (a) microstrip layout; and (b) circuit symbol.

The bonding wires should look, electrically, as close as possible to short circuits, or at least very small lumped inductances. This means that their lengths  $\ell_s$  must be kept as short as possible:  $\ell_s < \lambda_{gm}/4$  where  $\lambda_{gm}$  is the mid-band wavelength. Notice that the input-to-direct output link meanders through the structure.

The physically short finger elements are approximately  $\lambda_{gh}/4$  at the highest frequency in the band desired, whereas the entire length within the central region of the coupler is approximately  $\lambda_{gl}/4$  at the lowest frequency of the band desired. These features, together with properly phased traveling-wave reinforcement due to the bonding wires, give the excellent performance. One really significant (and often important) characteristic of this device is the very good relative phase shift over the band. This is generally better than  $\pm 2^\circ$  of the nominal  $90^\circ$  phase shift. Also, the VSWR is generally less than 1.15 over an octave bandwidth.

In practice, especially at higher frequencies, several bonding wires are required in parallel connection in place of each single one shown in [Figure 11.7](#) in order to reduce inductance and therefore enhance performance. This results in extra manufacturing expense, since the wires must be judiciously bonded in by hand or by precision computer-controlled machines. The spacings are about  $75 \mu\text{m}$ , compared with only  $10 \mu\text{m}$  for the simple, parallel, microstrip 6 dB coupler (on alumina).

An early design procedure was reported by Presser [4]. In Presser's design a coupling factor design repeatability of  $\pm 0.05$  dB was generally obtained and a gap-variation sensitivity of approximately 0.03 dB/ $\mu\text{m}$  was observed. This means that a  $\pm 2.5 \mu\text{m}$  tolerance on the coupling gap would yield approximately  $\pm 0.1$  dB coupling factor variation. (Parallel-coupled microstrip tolerances are discussed in more detail in [Section 11.6.3](#).) The couplers designed and measured by Presser showed a minimum directivity of approximately  $-24$  dB, corresponding to an isolation of about  $-30$  dB.

A design procedure, together with recommendations, is now given for Lange couplers. This follows the work of Ou [5] and also Osmani [6], whose approach has previously been consolidated and described by Fusco [7].

Ou developed the following elegant result:

$$Z_0^2 = \frac{Z_{0e}Z_{0o}(Z_{0e} + Z_{0o})^2}{\{Z_{0e} + (k - 1)Z_{0o}\}\{Z_{0o} + (k - 1)Z_{0e}\}} \quad 11.24$$

where  $k$ , the number of lines within the coupler, has to be an even integer.

A further important result derived by Ou is that the voltage coupling factor may be expressed as

$$\begin{aligned} C &= 10^{-[(\text{voltage coupling ratio in dB})/20]} \\ &= \frac{(k - 1)Z_{0e}^2 - (k - 1)Z_{0o}^2}{(k - 1)(Z_{0e}^2 + Z_{0o}^2) + 2Z_{0e}Z_{0o}}. \end{aligned} \quad 11.25$$

As described previously, here it is essential to know the even- and odd-mode characteristic impedances in order to synthesize the coupled microstrip cross-section. Osmani showed that, by combining the simple expression for the even- to odd-mode impedance ratio in terms of  $C$ ,  $(1 + C)/(1 - C)$ , see [Equation \(10.89\)](#), with the above expression for  $C$  and multiplying the result by the expression for  $Z_0^2$ ,  $Z_{0e}$  and  $Z_{0o}$  can be determined as follows:

$$Z_{0e} = Z_{0o} \frac{C + q}{(k - 1)(1 - C)} \quad 11.26$$

and

$$Z_{0o} = Z_0 \left( \frac{1 - C}{1 + C} \right)^{\frac{1}{2}} \frac{(k - 1)(1 + q)}{(C + q) + (k - 1)(1 - C)} \quad 11.27$$

where

$$q = C^2 + (1 - C^2)(k - 1)^2. \quad 11.28$$

In a Lange coupler the even-mode and odd-mode phase velocities are ideally equal, and this is approximately the case in practice. Therefore the overall length, which must be close to a quarter of a wavelength, can be based on either phase velocity. The inherently broadband

performance of this type of coupler means that this overall length must actually be a quarter of a wavelength calculated at the lowest frequency in the band under consideration (e.g., 10 GHz for a 10–40 GHz coupler).

By contrast, the finger length must, for the same reason of maintaining broadband operation, be set to one quarter-wavelength calculated at the highest frequency in the band under consideration (e.g., 40 GHz for a 10–40 GHz coupler).

However, largely capacitive end-effect discontinuities tend to slightly reduce the actual physical lengths needed in each case and the expressions given in [Section 10.4](#).2 should be used to estimate the corrections required as a result. The bond wires or other direct connection links also have an effect on the design values but, as explained earlier, by paralleling several bonds the overall inductance is greatly reduced.

Two examples will now be given showing the results of using these expressions as first steps in the design of Lange couplers.

### Example 1

Assume that we are required to design a four-finger Lange coupler to provide 10 dB of coupling in a  $50\Omega$  system operating at 10 GHz. In this case, a soft plastic substrate is to be used with a thickness of 0.234 mm and a permittivity of 2.23.

We first note that, since  $C = 10^{-(10/20)}$ ,  $C = 0.3162$ . This, together with the specification of ( $k =$ ) 4 fingers, leads to  $q$ :

$$q^2 = [0.3162^2 + (1 - 0.3162^2)(4 - 1)^2] \quad 11.29$$

which yields  $q = 2.864$ . Then, calculating  $Z_{0o}$  next:

$$Z_{0o} = 50 \left( \frac{1 - 0.3162}{1 + 0.3162} \right)^{\frac{1}{2}} \left[ \frac{3(3.864)}{(0.3162 + 2.864) + 3(1 - 0.3162)} \right] \quad 11.30$$

yielding  $Z_{0o} = 80\Omega$ . We now have sufficient quantities to determine  $Z_{0e}$ :

$$Z_{0e} = 80 \left( \frac{0.3162 + 2.864}{3(1 - 0.3162)} \right)$$

yielding  $Z_{0e} = 124\Omega$ .

Applying the coupled line synthesis approach as described in [Section 10.5](#), here we find that these impedances are satisfied by a structure whose cross-sectional parameters are

$$w/h = 1.103 \quad \text{and} \quad s/h = 0.39.$$

Since the substrate thickness is 0.254 mm, we require coupled microstrips having widths of 0.28 mm and separations (gaps) of approximately 0.1 mm.

We now consider briefly the contrasting situation if we had, instead of choosing a Lange

coupler, attempted to design this coupler as a single, simple parallel-coupled element. In this case, using the design procedure described earlier in this chapter, we would require the following cross-section parameters:

$$w/h = 2.335 \quad \text{and} \quad s/h = 0.095.$$

These parameters yield actual width and gap values as follows:

$$w = 0.593 \text{ mm} \quad \text{and} \quad s = 0.024 \text{ mm}.$$

The width is just over twice and the gap is approximately one quarter the value found for the Lange coupler. The difference in width requirement is not generally serious although it does have implications for “real estate” and infers ultimate operating frequency limitations. However, the much smaller gap results in very significant manufacturing and operational problems. In particular, the small gap (only 24  $\mu\text{m}$ ) leads to difficulties in terms of manufacturing tolerances, repeatability, and yield on a hybrid MIC. Also, even if these difficulties are largely overcome, there remains the limitation of voltage handling capability.

The final design requirements, centering on the calculation of the coupled microstrip lengths, must follow the use of expressions such as those given earlier here (Kirschning and Jansen [8, 9]). In this way the physical lengths are determined but this is left as an exercise for the reader.

## Example 2

For this example only the main specification and the resulting design values are given here. In Example 1 we considered a 10 dB coupler, but 3 dB couplers are commonly required for use in balanced amplifiers, attenuators, and phase shifters. Let us assume we require an octave-bandwidth Lange coupler to be built on an alumina substrate 0.5 mm thick. Experience in using the above design expressions shows that a good first guess for the design iteration is to set the width of the coupled microstrips to 38  $\mu\text{m}$  and the separating gap to 25  $\mu\text{m}$ . Many practical amplifier applications demand a bandwidth much greater than one octave, often nearer two octaves or more. A significant increase in bandwidth can be obtained by slightly overcoupling the coupler. In this example we can transform the design into one covering two octaves by reducing the width and separation by about 30% and 40%, respectively (again as first approximations at the start of a design and simulation routine). This of course results in  $w = 25 \mu\text{m}$  and  $s = 15 \mu\text{m}$ .

Waugh [10] has reported a sensitivity analysis of the Lange coupler. He (Waugh) points out that, conventionally, designers impose  $\pm 0.25 \mu\text{m}$  tolerances on their designs to ensure that specifications are met. This, however, leads to a corresponding deterioration in yield of the hybrid MICs. Waugh shows that for a 2.7 dB octave-bandwidth coupler designed on 0.635 mm alumina dimensional errors of 6  $\mu\text{m}$  in both gap and line widths can still enable the coupler to function according to specification.

Most of the major microwave CAE packages embody Lange coupler models.

Designs using multiconductor configurations yielding coupling factors as tight as 1.5 dB (i.e.,

more than half of the input power transferred to the coupled port) have also been described [11]. Quadrature-coupling arrangements using these principles are particularly significant in some microwave transistor amplifier circuits and 2–18 GHz bandwidths are obtainable.

### **11.5.2 The Unfolded Lange Coupler**

This is a development of the original Lange coupler just described and was reported by Waugh and Lacombe [12]. In [Figure 11.8](#), which shows this arrangement, it can be seen that some line elements and two straps are saved. The two straps are saved essentially by avoiding the strapped feed across to the direct port and, instead, retaining a “straight-through” direct port connection. Slightly less coupling is obtained, but the most serious trade-off appears to be the phase-shift variation over the band. This now has a worst value of  $-8^\circ$  departure away from the nominal  $90^\circ$ . The fact of this phase departure and the lack of a DC path between input and opposite port have probably represented the main reasons why this version of the Lange coupler is not often used.

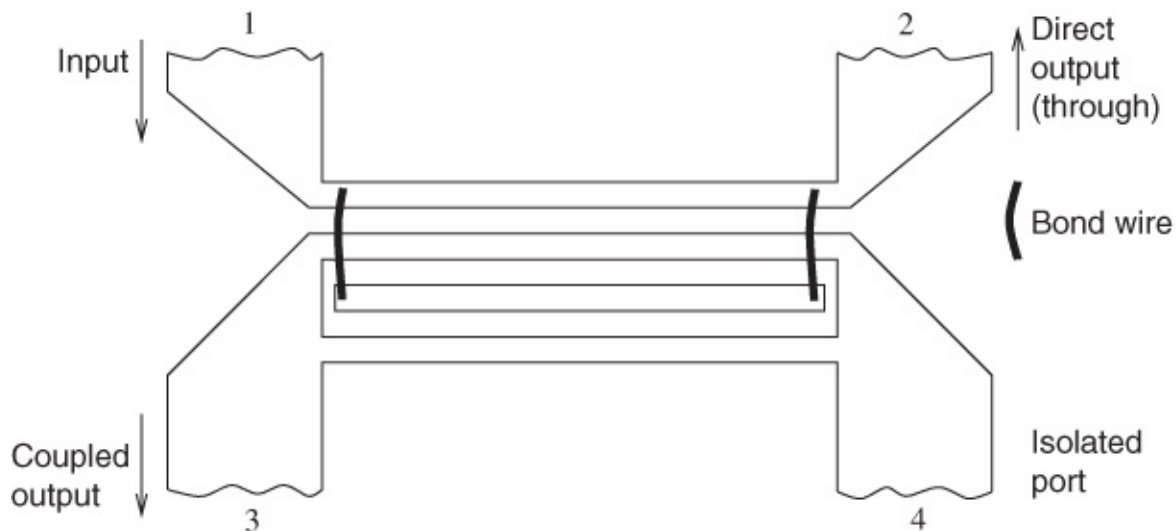


**Figure 11.8** The “unfolded” Lange coupler.

Both forms of “Lange” coupler require the connection of short wire straps, and this can pose repeatability problems in production (although there may, of course, be other short wires associated with active devices). For this reason, among others, alternative techniques have been developed.

### **11.5.3 Shielded Parallel-coupled Microstrips**

This type of structure also tends to nearly equalize even- and odd-mode phase velocities. The geometry is shown in the drawing of [Figure 11.9](#).

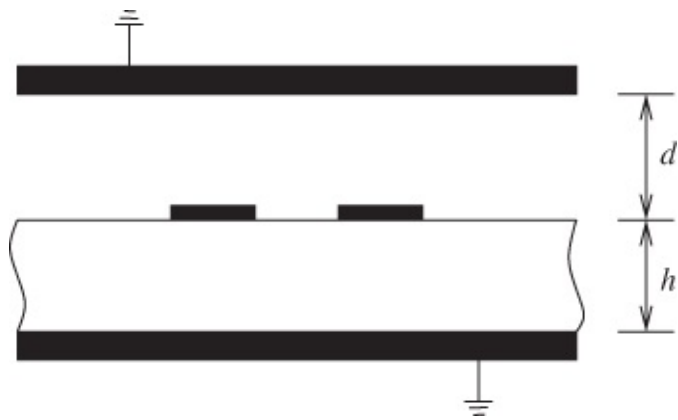


**Figure 11.9** Parallel-coupled microstrips with a grounded shielding top plate.

In this arrangement there is a considerable proportion of the total field in the air region above the coupler, whatever the mode. Thus the proportional redistribution of electric field into air space for the odd mode can be made much less than that for the unshielded structure. As a consequence the phase velocities can easily be within approximately 1% of one another, as shown by Weiss [13]. In order to obtain these advantages, it is necessary for the shield-spacing  $d$  to be around or less than the substrate height  $h$ :

$$d \leq h.$$

Although closely shielded circuits impose some manufacturing and other difficulties, they do yield certain specific design advantages because the structures are electrically well defined.

Several researchers have reported studies on parallel-coupled microstrips including shielded structures and multiconductor geometries. For example, Kouki *et al.* [14] describe the finite element modeling of such structures analyzed on a two-dimensional basis using an asymptotic boundary condition. Their method can accept conductors with arbitrary cross-sections in addition to arbitrarily inhomogeneous dielectrics (e.g., multilayer substrates). They demonstrate capacitance matrix results for shielded coupled pairs as well as six-conductor arrays of microstrips.

#### 11.5.4 The Use of a Dielectric Overlay

In this approach a layer of substrate-type dielectric material is fixed in the local region above the coupled (conventional) microstrip lines. The fixing is usually carried out with epoxy, and the result is shown in [Figure 11.10](#). Some very effective results can be obtained when the thickness of the overlay is only about 50  $\mu\text{m}$  on an alumina substrate of 0.5–0.65 mm thickness [15].

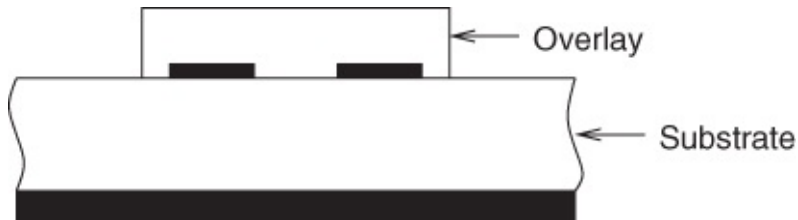


**Figure 11.10** Parallel-coupled microstrips with overlaid dielectric compensation. The substrate and overlay have the same permittivity.

The main principle is that electric field in the region immediately above the coupling gap experiences a permittivity similar to that of the substrate (instead of air when no overlay is present). This is most effective for the odd mode, when the field in the gap region is greatest. Thus the odd-mode phase velocity is reduced to approach, within a few per cent, the value of the even-mode phase velocity. If the overlay thickness is made approximately the same as that of the substrate and it overlaps the outer edges of the microstrips by at least half a strip width, then the phase velocity disparity is less than 1%.

It is likely that production repeatability problems would be experienced with this technique, and epoxy bonding of the overlay is difficult to keep free of air bubbles. However, some excellent results have been reported for a -10 dB coupler.

### 11.5.5 The Incorporation of Lumped Capacitors

It has been shown that the connection of lumped capacitors across a pair of coupled microstrip lines, as indicated schematically in [Figure 11.11](#), will equalize the phase velocities over quite a broad band [16].

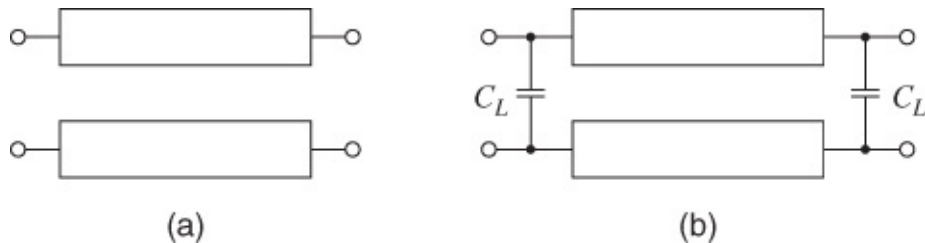


**Figure 11.11** Schematic illustration of parallel-coupled lines with lumped capacitors bridging the ends to provide compensation: (a) coupled lines; and (b) coupled lines with capacitors.

An accurate method for the determination of these compensating capacitances, applicable over a wide range of coupling, has been derived by Dydyk [17]. In his approach, Dydyk uses the standard *ABCD* matrix to represent both the even and odd modes for this structure, noting that the capacitance is only effective for the odd mode. The matrices therefore take the forms

$$\begin{bmatrix} A & B \\ C & D \end{bmatrix}_e = \begin{bmatrix} \cos \theta_e & jZ_{0e} \sin \theta_e \\ jY_{0e} \sin \theta_e & \cos \theta_e \end{bmatrix} \quad 11.31$$

and

$$\begin{bmatrix} A & B \\ C & D \end{bmatrix}_o = \begin{bmatrix} (\cos \theta_o - Z_{0o} 2 \omega C_L \sin \theta_o) \\ J \left\{ 4 \omega C_L \cos \theta_o + \left( Y_{0o} - Z_{0o} (2 \omega C_L)^2 \sin \theta_o \right) \right\} \\ j Z_{0o} \sin \theta_o \\ (\cos \theta_o - 2 \omega C_L Z_{0o} \sin \theta_o) \end{bmatrix}. \quad 11.32$$

Note is then taken of the fact that, in the ideal case of equal even- and odd-mode electrical lengths, the  $ABCD$  matrix for this case becomes

$$\begin{bmatrix} A & B \\ C & D \end{bmatrix}_{oi} = \begin{bmatrix} \cos \theta_e & j Z_{0oi} \sin \theta_e \\ j Y_{0oi} \sin \theta_e & \cos \theta_e \end{bmatrix}. \quad 11.33$$

where  $Z_{0oi}$  and  $Y_{0oi}$  are, respectively, the odd-mode characteristic impedance and admittance in this ideal case. This leads to the required capacitance by first equating the  $A$  and  $B$  element entries in the odd-mode matrices, giving

$$\cos \theta_e = \cos \theta_o - 2 \omega C_L Z_{0o} \sin \theta_o \quad 11.34$$

$$Z_{0o} \sin \theta_o = Z_{0oi} \sin \theta_e. \quad 11.35$$

Combining these expressions and recognizing that the even mode electrical length is  $90^\circ$  at the center frequency leads simply to the desired formula

$$C_L = \cos \theta_o / 2 \omega Z_{0oi}. \quad 11.36$$

The electrical length can also be written in terms of the effective microstrip permittivities:

$$\theta_o = \frac{2\pi\ell}{\lambda_{go}} = \frac{\pi}{2} \sqrt{\frac{\epsilon_{eff,o}}{\epsilon_{eff,ei}}} \quad 11.37$$

so that the compensating capacitance, as a function of frequency, is given by

$$C_L = \frac{\cos \left( \frac{\pi}{2} \sqrt{\epsilon_{eff,o}/\epsilon_{eff,ei}} \right)}{2 Z_{0oi} \omega}. \quad 11.38$$

From the foregoing considerations it also follows that the actual odd-mode characteristic impedance may be expressed as

$$Z_{0oa} = \frac{Z_{0oi}}{\sqrt{1 - \left[ \cos \left( \frac{\pi}{2} \sqrt{\frac{\epsilon_{eff,o}}{\epsilon_{eff,e}}} \right) \right]^2}} \quad 11.39$$

indicating that  $Z_{0oa}$  must in general be greater than  $Z_{0oi}$ . This in turn implies that the conductors must be set narrower than initially calculated (before compensation) and the separating gap must be increased. Both requirements are completely acceptable in practice. Dydyk also shows that at the coupler's center frequency the  $ABCD$  matrices reduce to

$$\begin{bmatrix} A & B \\ C & D \end{bmatrix}_e = \begin{bmatrix} 0 & jZ_{0e} \\ jY_{0e} & 0 \end{bmatrix} \quad 11.40$$

and

$$\begin{bmatrix} A & B \\ C & D \end{bmatrix}_o = \begin{bmatrix} 0 & jZ_{0oi} \\ jY_{0oi} & 0 \end{bmatrix} \quad 11.41$$

which represents a situation identical to that of an ideal directional coupler having the following scattering matrix:

$$[S] = \begin{bmatrix} 0 & C & -j\sqrt{1-C^2} & 0 \\ C & 0 & 0 & -j\sqrt{1-C^2} \\ -j\sqrt{1-C^2} & 0 & 0 & C \\ 0 & -j\sqrt{1-C^2} & C & 0 \end{bmatrix} \quad 11.42$$

where  $C$  is related to  $Z_{0e}$ ,  $Z_{0o}$ , and  $Z_0$ , as defined earlier in this chapter. From these results it should be clear that the isolation is ideally zero and the directivity infinite in this case. In practice, due to losses and with the frequency away from the design center, the actual directivity will degrade. As an example of the application of this theory to a practical design of a coupled section on an alumina substrate, it is found that the requirements are a compensating capacitance of 0.047 pF, an actual odd-mode impedance of  $31.7\Omega$ , and a coupled region length of just over 2.3 mm. Dydyk applied Keysight Technologies Linecalc software to both uncompensated and compensated coupled sections (both having nominally 7 dB coupling) to generate the data repeated here in [Table 11.1](#). Rickard [16] showed that a coupling factor variation of only  $\pm 0.3$  dB (on  $-10$  dB) is achievable over a two-and-a-half-octave bandwidth: 8–20 GHz. The directivity was 20 dB over this band, compared with 5–13 dB uncompensated, and the VSWR was always better than 1.4. No information was reported on the phase-shift variation over the band. This performance considerably exceeds that of a comparable coupler using a dielectric overlay. However, it may be difficult to implement this approach with fairly large coupling factors (e.g., between  $-6$  dB and  $-3$  dB) because of the already very narrow coupling gap. At low frequencies the capacitors might be formed either using a thin-film add-on technique or conceivably as chip components. At high frequencies the capacitors could simply be interdigital structures at the coupler ends.

**Table 11.1** Parameters for compensated and uncompensated coupled sections. The data in this table are due to Dydyk [17]

Parameter	Uncompensated	Compensated
Center frequency (GHz)	12.0	12.0
Coupling $\mathcal{C}$ (dB)		
Desired	-7.0	-7.0
Achieved	-7.25	-7.0
$Z_0$ ( $\Omega$ )	50	50
$Z_{0e}$ ( $\Omega$ )	80.85	80.85
$Z_{0o}$ ( $\Omega$ )	30.92	31.71
$\epsilon_{\text{eff},e}$	7.20	7.20
$\epsilon_{\text{eff},o}$	5.31	5.32
$w$ (mm)	0.444	0.440
$s$ (mm)	0.081	0.089
$\ell$ (mm)	2.505	2.327
Directivity		
Desired	Infinite	Infinite
Achievable	12.32	Essentially infinite

### 11.5.6 The Effect of a Dielectrically Anisotropic Substrate

Provided the crystal axes of a dielectrically anisotropic substrate are correctly aligned with respect to the microstrip then the net electric displacements are similar for both even and odd modes. Thus, the phase velocities will approach equality, depending upon the actual values of the permittivity tensor members.

Szentkuti [18] has shown that the degree of anisotropy of sapphire (see [Chapter 5](#)) and of some other readily available substrate materials is not sufficient to produce a really significant improvement. If a material having permittivity values of 25 and 10 were available then Szentkuti shows that the velocities differ by less than 1% over the range:

$$0.05 \leq \frac{w}{h} \leq 1.2 \quad 11.43$$

where  $s/h = 0.05$ . Also, unfortunately, in the case of sapphire at least, the crystal axis alignment would mean that the wave would experience a very complicated permittivity environment, changing in the direction of propagation and dependent on the actual location on the substrate.

### 11.5.7 Microstrip Multiplexers

Various planar or quasi-planar technologies have been adopted to facilitate the function of multiplexing, the separation of a broadband input signal into a number of contiguous channels. Technological approaches to this problem at microwave frequencies include both microstrip and also suspended-substrate stripline. An example of a microstrip quadruplexer has been reported by Uysal *et al.* [19]. Their device comprises four 3 dB directional couplers and four phase shifting networks, as indicated in [Figure 11.12](#). The design is critically dependent upon differing electrical lengths ( $\ell_1$ ,  $\ell_2$ , and  $\ell_p$ ) and characteristic impedances ( $Z_{01}$ ,  $Z_{02}$ , and  $Z_{0p}$ ) for the microstrip lines connected to the two intermediate 3 dB couplers as shown in [Figure 11.12](#). Uysal described an experimental quadruplexer designed to split a 2–18 GHz signal into four contiguous output channels each 4 GHz wide. The design was realized in MIC form using a standard 25 mm × 50 mm alumina substrate. Some empirical adjustment of the phase lengths is indicated, and it appears clear that there is room for further advances in this design approach.

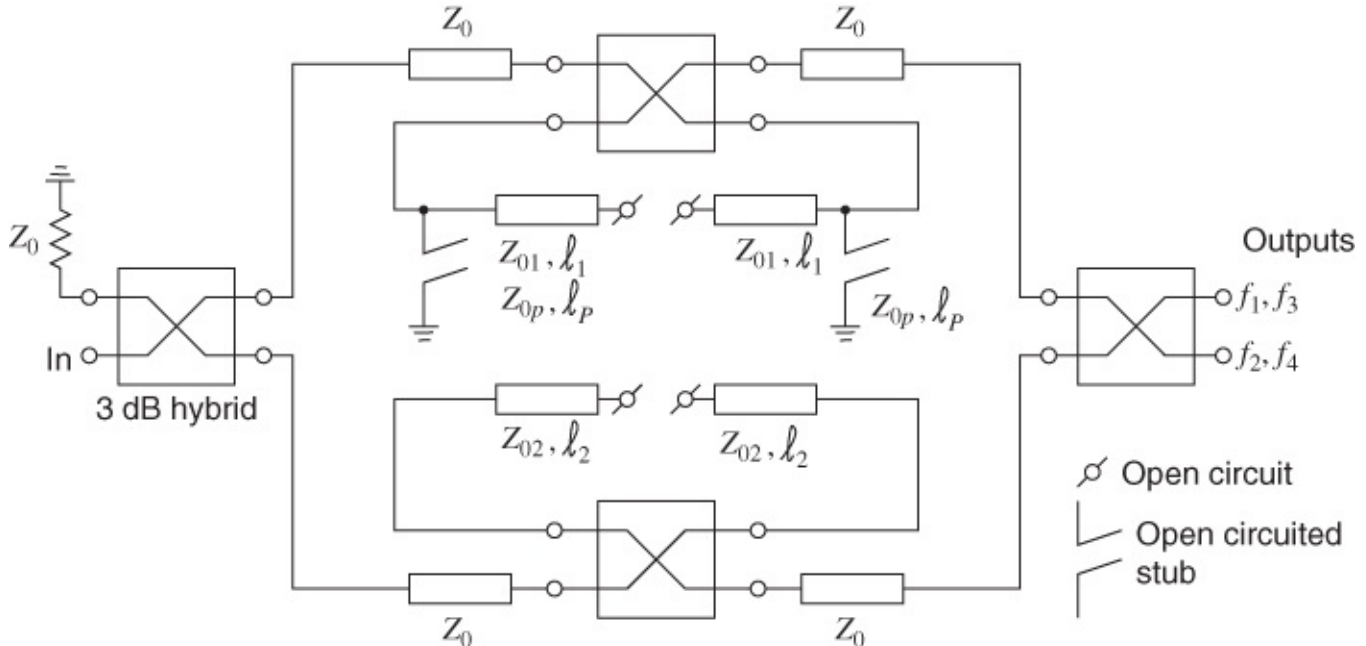


[Figure 11.12](#) Schematic diagram of a quadruplexer using four 3 dB hybrids.

### 11.5.8 Multisection Couplers

As they tend to occupy considerable substrate area (“real estate”), particularly in terms of length, multisection couplers have generally not found much favor amongst solid-state microwave designers. However, at least one novel approach to the design of this type of coupler has been reported by Nakajima [20]. This team described a 2–18 GHz multisection coupler providing 6 dB of coupling using five semi-re-entrant tight-coupling sections.

A single section of such a coupler structure is shown in plan-schematic form in [Figure 11.13](#) and in cross-section in [Figure 11.14](#). A plan-schematic diagram of the entire five-section coupler is shown in [Figure 11.15](#). Nakajima *et al.* used a capacitance matrix approach and provide a table showing all the design parameters for the three semi-re-entrant coupled sections and the two parallel (edge) coupled sections. All the physical dimensions are fully realizable: the first and narrowest coupling gap,  $s$ , is 0.08 mm and the narrowest width,  $w$ , is

0.23 mm.

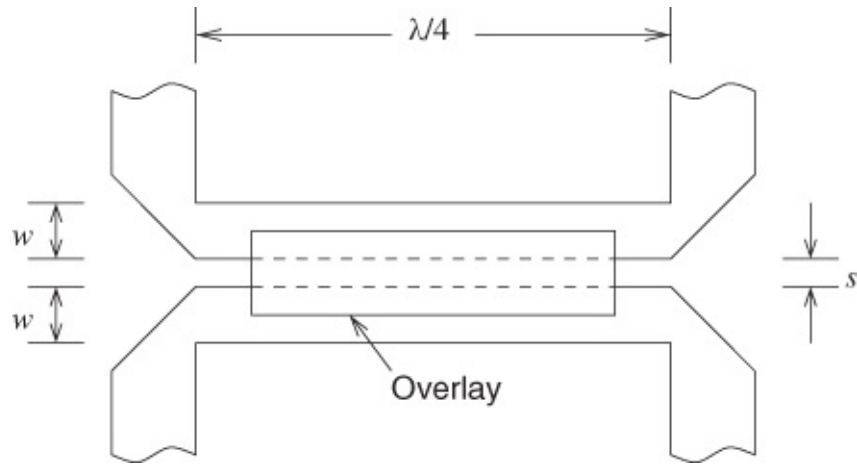


**Figure 11.13** A plan schematic view of a single section semi-re-entrant coupler.

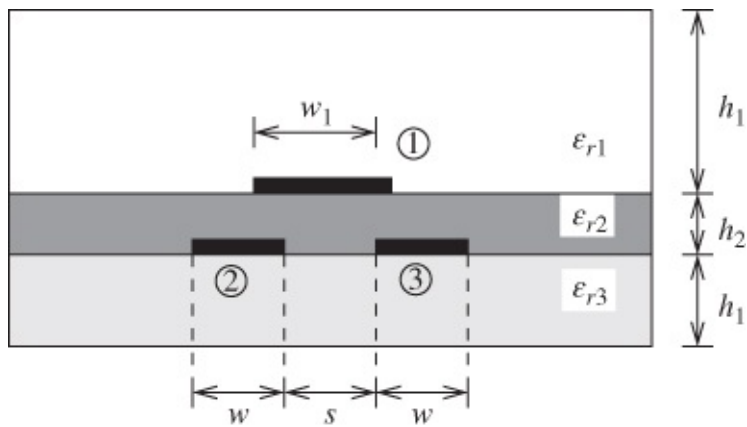


**Figure 11.14** A cross-sectional view of a semi-re-entrant coupled section.

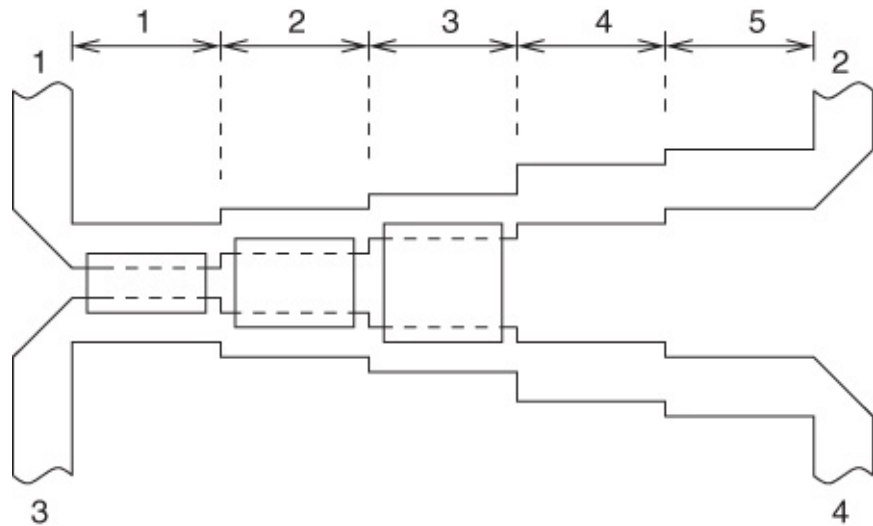


**Figure 11.15** The plan-schematic view of a five-section directional coupler.

The coupler was fabricated on a Duriod® 5880 substrate of nominally 0.508 mm thickness. Relative through-arm power transfer remained about 2 dB whilst the coupled arm delivered power around 6 dB down on the incident power (with approximately 2 dB of ripple).

### 11.5.9 Re-entrant Mode Couplers

The types of fine-line geometries and interdigital structures described in earlier sections of this chapter lead to design and fabrication difficulties where tight coupling is required. One method of overcoming some of these difficulties is to consider combline approaches (dealt with in [Section 11.5.11](#)), but very fine interdigital geometries, with their attendant production difficulties, remain.

The re-entrant concept is not new since Seymour Cohn originally described it for realization in coaxial form and later Lavendol showed how it could be adapted for stripline technology. More recently Pavio and Sutton [21] have described a quadrature coupler using this approach. Pavio and Sutton's structure, shown in cross-section in [Figure 11.16](#), comprises a subsidiary parallel-coupled line arrangement with a floating under-plane of restricted width  $w_1$ . This subsidiary arrangement is layered on top of a conventional substrate (e.g., alumina) with a ground plane.

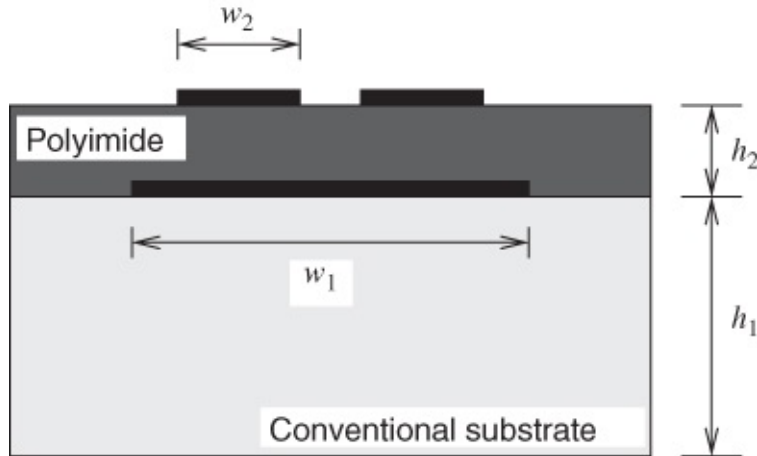


[Figure 11.16](#) Microstrip re-entrant mode coupler cross-section.

Several types of circuits were fabricated by Pavio and Sutton using this technology. In one case a 3 dB coupler was fabricated on a 0.381 mm thick alumina substrate and a polyimide film, 0.0075 mm thick and of relative permittivity 3.7, was used for the subsidiary arrangement. Capacitive compensation was incorporated, as described in [Section 11.5.5](#), and was realized in the form of interdigitated capacitors. Although transmission loss was similar to that of a conventional coupler, the VSWR was superior. The phase response varied in the range  $82^\circ - 87^\circ$  over the 5–19 GHz band, indicating that further work is required to more closely phase-linearize these types of devices. These researchers also described a  $180^\circ$  balun designed according to these principles.

### 11.5.10 Patch Couplers

At higher millimeter-wave frequencies (high tens into hundreds of GHz) none of the previous coupler technologies are particularly practical on account of the extremely small overall dimensions. Many designers therefore adopt transmission-line technologies other than microstrip.

It is, however, possible to consider special forms of microstrip patch coupler at these high frequencies, and Fusco and Meruga [22] described such a device, shown in schematic plan view in [Figure 11.17](#). They describe a three-dimensional wave analysis of the coupler using a TLM numerical simulation to develop amplitude and phase responses over the frequency range 80–94 GHz. With this technique field distribution and radiation characteristics can also be identified.

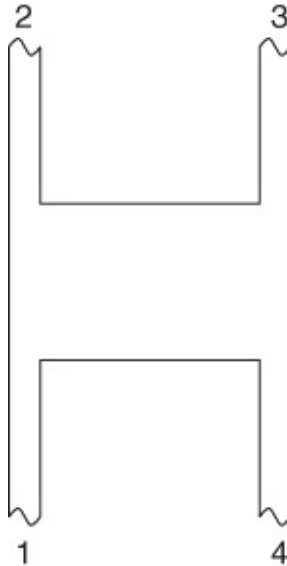


[Figure 11.17](#) Geometry of a microstrip patch coupler.

### 11.5.11 Planar Comline Directional Couplers

All of the coupling arrangements so far described here have three identifiable characteristics:

- They are backward-wave devices, i.e., the coupled wave travels in the opposite direction to the input wave.
- They are all basically quadrature couplers, i.e., the coupled wave is  $90^\circ$  phase displaced, or close to that, with respect to the input wave.
- The maximum achievable coupling factor is in the region of  $-1.5$  dB.

Even this requires special multiconductor configurations. It is hampered by close tolerance requirements, leading to poor reproducibility.

These backward-wave microstrip couplers suit a wide variety of circuit applications ranging from parallel-coupled filters to balanced transistor amplifiers. However, there are some applications, such as mixer circuits, where a  $180^\circ$  coupler phase shift is required.

Although not strictly a microstrip arrangement, planar comline couplers [23] are briefly considered here because they do yield  $180^\circ$  phase shifts and possess especially tight coupling. Planar comline directional couplers offer forward coupling of very large amounts, in fact approaching  $-3$  dB can be achieved without any serious tolerance problems. A diagram of such a coupler is shown in [Figure 11.18](#).

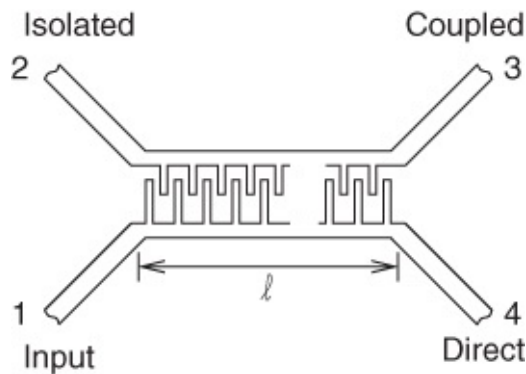


**Figure 11.18** The general layout of a planar combline directional coupler.

This arrangement may be regarded as a system of two interpenetrating comb transmission lines. As a coupler it derives its properties from the predominantly capacitive coupling between the two lines, which arises from the interpenetration of the transverse “finger” elements. For fuller details of the device properties, design, and performance the references given should be consulted.

Rigg and Carroll [24] have given a detailed design procedure for a general  $n$ -line “herringbone” coupler, the fundamental structure of which is similar to the combline. They applied the design procedure to successfully realize a three-line equal power-splitting balun with a 3 dB bandwidth of three octaves centered on 1.8 GHz, a  $180^\circ$  phase relationship, and a linear phase variation of  $100^\circ/\text{GHz}$  across the band.

An analysis and design technique for combline couplers was reported by Islam [25].

## 11.6 Thickness Effects, Power Losses, and Fabrication Tolerances

### 11.6.1 Thickness Effects

So far in this chapter we have neglected the effects due to the finite thickness of the microstrip lines. Thickness effects play only a small part in the accurate design of coupled lines, provided the lines are of thick- or thin-film manufacture and the coupling is around  $-10$  dB. Rizzoli [26] has found that thick-film strips taper at the edges, thus allowing “thin-strip” calculations to be effective.

The nominal spacing for a  $-3$  dB coupler on alumina is about  $10 \mu\text{m}$ . Therefore, the effect of, say,  $5 \mu\text{m}$  thickness “side walls” must be very significant in such a case, especially where the side walls approach a vertical disposition. This is now a considerably complicated structure to analyze theoretically.

For design corrections it seems sensible to introduce modifications taking into account strip thickness and enabling the expressions of [Section 10.4](#) to be used. With the thickness  $t$  we require a modified form of Equation (10.96) for  $C_f(t)$ :

$$C_f(t) = 0.5 \left[ \frac{\sqrt{\epsilon_{\text{eff}}(t)}}{cZ_0(t)} - C_p \right]$$

where  $\epsilon_{\text{eff}}(t)$  and  $Z_0(t)$  are for single microstrip lines and are given in [Chapter 6](#), Equations ([6.35](#)) to ([6.40](#)) and Equations ([6.57](#)) to ([6.60](#)). An extra term is also required in Equation ([10.94](#)) to account for the increased gap capacitance, which is entirely due to electric field in air. This is

$$C_{gt} = 2\epsilon_0 \frac{t}{s}. \quad 11.45$$

These expressions, Equations ([11.44](#)) and ([11.45](#)), were originally given by Gupta *et al.* [27]. It is found that, for “thin” microstrip on alumina, the odd-mode characteristic impedance decreases by 2 or 3% due to the thickness effect. The change is negligible for the even mode.

## 11.6.2 Power Losses

In coupled microstrip lines there are two principal sources of power loss: one due to the conductors and the other due to the dielectric. Garg and Bahl [28, 29] have reported expressions for both the conductor and dielectric losses, and these expressions are now given here, together with extra information which enables the effects of surface roughness to be determined (for conductor loss, see [Chapter 7](#) for single-line details):

$$\alpha_{c,i} = \left\{ \frac{8.686R_s}{120\pi Z_0 h c [C_{ai}(t)]^2} \right\} \times \left[ \frac{\partial C_{ai}(t)}{\partial(w/h)} \left( 1 + \frac{w}{h} \right) - \frac{\partial C_{ai}(t)}{\partial(s/h)} \left( 1 - \frac{s}{h} \right) + \frac{\partial C_{ai}(t)}{\partial(t/h)} \left( 1 + \frac{t}{h} \right) \right] \text{dB/unit length} \quad 11.46$$

where this expression holds for the strips and ground plane combined, and  $C_{ai}(t)$  is the odd- or even-mode line capacitance with air as the dielectric,  $R_s$  is the sheet resistivity (ohms per square meter) of the metallization, and  $i$  is *o* or *e* for the odd or even mode.

The attenuation  $\alpha_{co}$  due to the odd mode is always greater than that due to the even mode, and the sensitivity of  $\alpha_{co}$  to changes in the spacing  $s$  is also greatest. This is consistent with a physical interpretation, where it must be remembered that interruptions are then (for the odd mode) being forced upon opposing-edge current components.

The loss for each mode is first calculated separately, then the total loss is determined as the average of these two results.

It should be noted that Equation ([11.46](#)) yields a rather low estimate of the conductor loss in practical situations. Compare, for example, the information supplied by Jansen [30]. With most plastics the discrepancy is very significant (several decibels) and there is a noticeable difference even when a polished sapphire substrate is used. Surface roughness is the dominant effect, although the precise nature of the conductor material is also very important. We

previously considered these effects in [Chapter 7](#) and a modifying expression, Equation ([6.66](#)), was given to improve the prediction of conductor loss. Exactly the same expression, with identical precautions, should be used to modify Equation ([11.46](#)) for coupled-line conductor losses.

Dielectric loss is almost always much less than conductor loss due to the low-loss substrates that are generally used. The dielectric loss is given by [27]

$$\alpha_{d,i} = 27.3 \frac{\epsilon_r(\epsilon_{\text{eff},i} - 1) \tan \delta}{\sqrt{\epsilon_{\text{eff},i}(\epsilon_r - 1)} \lambda_0} \text{ dB/unit length} \quad 11.47$$

where  $\tan \delta$  is the loss tangent of the dielectric material and  $\lambda_0$  is the free-space wavelength.

In X-band (8–12 GHz) we typically achieve  $\alpha_D \cong 1.2$  dB/m using an alumina substrate with a dielectric loss tangent of 0.0005. On the other hand, the conductor loss is approximately 8 dB/m for moderate line spacings, increasing to 20 dB/m or more for close spacing.

### **11.6.3 Effects of Fabrication Tolerances**

This has been investigated by several workers, including Shamasundra and Gupta [31, 32]. We are primarily interested in the maximum change in the coupling factor:

$$\frac{|\Delta C|_{\max}}{C} = \left| \frac{\Delta w}{w} S_{C(w)} \right| + \left| \frac{\Delta h}{h} S_{C(h)} \right| + \left| \frac{\Delta s}{s} S_{C(s)} \right| + \left| \frac{\Delta \epsilon_r}{\epsilon_r} S_{C(\epsilon_r)} \right| \quad 11.48$$

where  $C$  has been previously defined as

$$C = \frac{Z_{0e} - Z_{0o}}{Z_{0e} + Z_{0o}}. \quad 11.49$$

The sensitivity terms are defined by

$$S_{C(p)} = \frac{p}{C} \frac{\partial C}{\partial p} \quad 11.50$$

where  $C$  is the quantity whose sensitivity is to be determined due to a change in a controlling parameter  $p$ .

A complete calculation of any sensitivity is actually quite a lengthy procedure. Complete functions giving the coupling factor have to be written down, as far as possible, using expressions given in [Section 10.4](#). The derivative then has to be determined, as required, for Equation ([11.50](#)). For coupled microstrip lines on alumina a 4% change in coupling factor will generally result from the following tolerance excursions:

$$\Delta s = \pm 2.5 \mu\text{m} \quad 11.51$$

$$\Delta w = \pm 2.5 \mu\text{m} \quad 11.52$$

$$\Delta h = \pm 25 \text{ } \mu\text{m} \text{ (on } h = 0.65 \text{ mm)}$$

11.53

$$\Delta \epsilon_r = \pm 0.25 \text{ (on } \epsilon_r = 9.7).$$

11.54

Comparatively large variations tend to occur in the substrate thickness  $h$ , and this usually influences the coupling factor  $C$  to a greater extent than other parameter variations.

For relatively tight coupling, certainly with  $s/h < 0.02$ , tolerance excursions in  $s$  influence  $C$  to an increasing extent until these excursions begin to actually dominate.

It is useful and interesting to note some figures which apply to a nominally  $-6$  dB coupler manufactured on alumina. A 2.54% variation in coupling has been quoted due to tolerances on various parameters [31, 32]. The principal contributions to this variation are  $\Delta h$  (1.39%) and  $\Delta s$  (1.01%). This weighting remains approximately the same for somewhat lower coupling factors, that is, as  $s$  is increased, but the total percentage change rises to just over 6% [31, 32].

Compared with the coupling factor, the VSWR is much less sensitive to variations in the physical parameters; the main controlling parameters are  $\epsilon_r$  and  $h$ . Over a wide range of coupling factors the VSWR remains close to a constant value, which generally lies between 1.2 and 1.4. The sensitivity of the VSWR only increases significantly when the coupling becomes very tight, around  $-6$  to  $-3$  dB. As previously discussed, different types of coupling structure are usually employed for such values.

## 11.7 Choice of Structure and Design Recommendations

In this chapter most of the attention has been devoted to the basic parallel-edge-coupled microstrip line structure. This is because of the fundamental nature of that structure, with its importance in relatively simple couplers and its significance in circuit applications such as parallel-coupled bandpass filters. The design of this structure is therefore summarized first here with reference to coupler realization.

### 11.7.1 Design Procedure for Coupled Microstrips, where the Mid-band Coupling Factor $C < -6$ dB

The design procedure when the coupling is moderate to weak has the following steps:

a.

Provided the coupling is loose enough for the relationship  $Z_0^2 \approx Z_{0e}Z_{0o}$  to hold with sufficient accuracy, then Equations (10.84) and (10.85) give the required characteristic impedances:

even mode:

$$Z_{0e} = Z_0 \sqrt{\frac{H}{Q}}$$

11.55

odd mode:

$$Z_{0o} = Z_0 \sqrt{\frac{Q}{H}}$$

where  $H = 1 + 10^{(C'/20)}$  and  $Q = 1 - 10^{(C'/20)}$ , and the coupling factor in decibels  $C'$  is directly substituted. We note also that this is the mid-band coupling factor.

**b.** An approximate synthesis is then performed using the method due to Akhtarzad *et al.* (see [Section 10.5](#)). A simple CAD algorithm may be devised using the formulas provided. It is likely that discrepancies in the region of 10% will arise in this process, which yields initial values of the shape ratios  $w/h$  and  $s/h$ .

**c.** These initial values can then be used to determine the corresponding impedances,  $Z_{0e}$  and  $Z_{0o}$ , employing the quite accurate (within 3%) analysis formulas given in [Section 10.5](#). If higher accuracy is required, and the increased time and cost are acceptable, the much more accurate computational technique developed by Bryant and Weiss may be used. This was explained in [Section 10.3](#). Some adjustment for finite conductor thickness may sometimes be necessary, particularly with hybrid MICs.

**d.** These new (stage (c)) values for  $Z_{0e}$  and  $Z_{0o}$  are compared with the original requirements, determined at stage (a), and discrepancies are noted. The shape ratios  $w/h$  and  $s/h$  can now be adjusted slightly to correct the impedances, and hence the coupling factor in decibels  $C'$ , to the desired values. It will usually be best if  $s$  alone is slightly altered, since the resulting mismatch to the feed lines will be small.

For guidance, we observe that  $s$  affects the odd mode more than the even mode. Increasing  $s$  means that more field is within the (air) coupling gap and  $Z_{0o}$  increases. As a rough approximation  $x\%$  change in  $s$  results in  $x/10\%$  change in  $Z_{0o}$ . For example, a 5% increase in  $s$  yields about 0.5% increase in  $Z_{0o}$ .

Finally the value of the mid-band coupling factor must be checked, which in decibels, is given by Equation (10.81):

$$C' = 20 \log \left| \frac{Z_{0e} - Z_{0o}}{Z_{0e} + Z_{0o}} \right| \text{ dB.} \quad 11.57$$

### 11.7.2 Relatively Large Coupling Factors (typically $C'$ is between $-6$ and $-3$ dB)

The problems of unequal even- and odd- mode wave velocities worsen rapidly as the coupling increases, for example the approximation  $Z_0^2 \approx Z_{0e}Z_{0o}$  becomes poor when  $C' \geq -6$  dB. An exact relationship for  $Z_0$  was given as Equation (10.82), but this involves the even and odd mode electrical lengths  $\theta_e$  and  $\theta_o$ . In order to find these lengths we need, at the outset, to know the geometry (i.e., the shape ratios) for the structure, which is just what we were trying to find in the first place. One approach could be as follows:

**a.** Carry through a rough, first-order synthesis using the approximation  $Z_0^2 \approx Z_{0e}Z_{0o}$ , and hence an initial  $w/h$  and  $s/h$ .

**b.** Calculate approximate values of  $\theta_e$  and  $\theta_o$  using the values obtained at step (a). The analysis procedure given in [Section 10.4](#) is well suited to this calculation, Equations (10.104) and (10.105) yield the effective microstrip permittivities. The electrical lengths are

$$\theta_e = \frac{2\pi\ell}{\lambda_g} \sqrt{\epsilon_e} \quad \text{and} \quad \theta_o = \frac{2\pi\ell}{\lambda_g} \sqrt{\epsilon_o}. \quad 11.58$$

An approximate value of  $Z_0$  is then obtained using Equation (10.82). If  $Z_0$  differs from that of the feed lines by an unacceptable amount (VSWR specification), the width  $w$  of the microstrip lines should be altered to compensate. The discussion of [Section 6.14.3](#) contains guidance on this type of adjustment. Altering  $w$  will alter  $Z_{0e}$ ,  $Z_{0o}$ ,  $\theta_e$ , and  $\theta_o$ , thus the procedure must be iterated to find the optimum value of  $w$ .

**c.** The evaluation of  $w$  must also ensure that the required mid-band coupling factor in decibels is obtained from Equation (10.43): **11.59**  $C' = 20 \log \left| \frac{Z_{0e} - Z_{0o}}{Z_{0e} + Z_{0o}} \right| \text{ dB.}$

**d.** When this procedure has been used and the parameter values have been met as closely as possible, the final values of  $Z_{0e}$  and  $Z_{0o}$  are used to synthesize, as described in [Section 11.7.1](#).

**e.** For close coupling, which is the case here, the effect of finite microstrip thickness is often significant, and the analysis procedure should account for this by incorporating Equations (11.44) and (11.45) of [Section 11.6](#).

### 11.7.3 Length of the Coupled Region

In a directional coupler, the coupled region extends for one-quarter of a wavelength at mid-band, and the designer requires the physical length of this region. Since, in microstrip, we are faced with the problem of different phase velocities applicable to the even and odd modes, we must also consider the different wavelengths associated with these modes. It is necessary to approximate the design to suit the average value of wavelength. This problem was treated in detail in [Section 11.4.1](#) and the expressions derived, Equations (11.9) and (11.10), are repeated here:

$$\lambda_{ge} \approx \frac{300}{F} \frac{Z_{0e}}{Z_{01e}} \text{ mm} \quad 11.60$$

$$\lambda_{go} \approx \frac{300}{F} \frac{Z_{0o}}{Z_{01o}} \text{ mm} \quad 11.61$$

where  $F$  is directly substituted in gigahertz,  $Z_{0e}$  and  $Z_{0o}$  are the even- and odd-mode characteristic impedances for the coupled microstrips with a substrate, and  $Z_{01e}$  and  $Z_{01o}$  are the same impedances, but for the air-spaced microstrips. The average value

$$\lambda_{gm} \approx \frac{1}{2}(\lambda_{ge} + \lambda_{go})$$

is taken for approximate design purposes. For further improved accuracy, a weighted-average calculation has been suggested [33].

### 11.7.4 Frequency Response

There are two fundamental effects governing the frequency-dependent behavior of coupled microstrips:

- a. the basic frequency response of any pair of parallel-coupled lines (neglecting any dispersion)
- b. the effects of microstrip dispersion.

These features, (a) and (b), were discussed in detail in [Section 11.4](#).

Great care is needed when using the fairly complicated expressions involved, equations of the form of Equation (10.111) incorporated into Equation (10.110). Although it appears that the even-mode electrical length  $\theta_e$  may be evaluated “fairly accurately” using Equation (10.111) and  $\theta_e = 2\pi\ell/\lambda_{ge}$ , there is evidence that the odd-mode calculation overestimates changes in  $\epsilon_{eff,o}(f)$  [34].

For greater accuracy, particularly for frequencies into the millimeter-wave ranges, the expressions due to Kirschning and Jansen [8, 9] should be used (see [Section 10.4.2](#)).

### 11.7.5 Coupled Structures with Improved Performance

Although several alternative methods have been reported, the technique invented by Lange [3] still yields an electrical performance that is generally superior to that of its closest rivals. The main disadvantage is the requirement for short wire connections. A design procedure now exists for the Lange coupler (see [4–7]), and combinations of Lange couplers have been built which cover the wide frequency range 2–18 GHz and higher. The design repeatability of such couplers is generally  $\pm 0.05$  dB, on the coupling factor, that is,  $\pm 2.5 \mu\text{m}$  excursions in coupling gaps result in  $\pm 0.1$  dB changes in coupling factor.

Of the other techniques which have been developed the end-connected compensating lumped capacitors ([Section 11.5.5](#)) is possibly the next best from an electrical standpoint. This is a particularly elegant technique because it can usually be realized as an entirely planar structure. (Recollect that the Lange coupler requires arrays of bond wires in its implementation.) However, when tight or fairly tight coupling is required ( $C$  between  $-6$  dB and  $-3$  dB) the already narrow coupling gap makes it difficult to incorporate the lumped capacitive structures in this capacitor-compensated coupler.

The two equal capacitances predominantly affect the odd-mode and Equation (11.36) gave the required value:

$$C_L = \frac{\cos \theta_o}{4\pi f Z_{0oi}}.$$

Typically, for a 10 dB coupler,  $\pm 0.3$  dB is achievable, with a directivity of 20 dB and VSWR < 1.4 over the frequency range  $8.5 \leq f \leq 20$  GHz. Closely shielded couplers may be used in some instances, but to achieve good compensation the close proximity of the shield to the circuit can cause difficulties. Dielectric overlays are a further possible alternative but, as with close shielding, they can make it difficult to design and control under production conditions.

### **11.7.6 Effects of Conductor Thickness, Power Losses, and Production Tolerances**

It has already been noted that the principal effect of finite conductor thickness is to reduce  $Z_{0o}$  slightly. This reduction amounts to approximately 2–3% for a 5  $\mu\text{m}$  conductor on alumina, where the coupling gap is in the approximate range  $10 \leq s \leq 500 \mu\text{m}$ .

Equation (11.48) enables one to calculate the sensitivity of coupling factor to fabrication tolerances. The expressions will not be reproduced here, but the following tolerance excursions typically give a worst-case change of 4% in the coupling factor (for alumina substrates):

$$\Delta s = \pm 2.5 \mu\text{m} \quad 11.64$$

$$\Delta w = \pm 2.5 \mu\text{m} \quad 11.65$$

$$\Delta h = \pm 25 \mu\text{m} \text{ (on } h = 0.65 \text{ mm)} \quad 11.66$$

$$\Delta \epsilon_r = \pm 0.25 \text{ (on } \epsilon_r = 9.7). \quad 11.67$$

### **11.7.7 Crosstalk Between Microstrip Lines used in Digital Systems**

This has been discussed in [Section 10.2](#). With the provisions given in the main discussion the following expression should be used to evaluate the crosstalk:

$$C = \frac{Z_{0e} - Z_{0o}}{Z_{0e} + Z_{0o}}$$

(which is identical to that used for the coupling factor). Now, because the spacing is usually very substantial, and often  $s \gg 2w$  here,  $Z_{0e}$  is very close to the value of  $Z_{0o}$  and we have to evaluate a small difference. Thus, accurate computer-based techniques are recommended or at least empirically curve-fitted formulas from curves using such computer-based techniques.

### **11.7.8 Post-manufacture Circuit Adjustment**

After testing it may well be found that a completed coupled-line circuit requires adjustment. Either the actual circuit may be etched, laser trimmed, etc., or the artwork used in preparing the circuit may be judiciously modified to correct errors.

Changing  $s$  or  $w$  slightly will alter the impedances and hence the coupling factor. It will generally be necessary to alter both  $w$  and  $s$  at the same time so that the correct impedance relationships are preserved. For example, if  $s$  is increased by 1% then  $Z_{0o}$  (mainly) will also increase, by approximately 0.1%, see [Section 11.7.1](#). Therefore,  $w/h$  should be increased very slightly, by less than 1% to reduce the impedance again.

The above is only an outline of the procedure: in practice, the precise trends for a particular case would soon become clear.

An ideal coupler has  $D = \infty$  (or infinite directivity) and

$$C = \frac{Z_{0e} + Z_{0o}}{Z_{0e} - Z_{0o}}. \quad 11.68$$

This result comes from a detailed derivation for the case when the coupled-line section is a quarter-wavelength long, the length when the coupling is maximum. The derivation is given in [Chapter 10](#). An ideal coupler does not dissipate power so

$$|T| = |\sqrt{1 - 1/C^2}|. \quad 11.69$$

Thus an ideal directional coupler has the following scattering matrix:

$$[S] = \begin{bmatrix} 0 & 0 & -J\sqrt{1 - 1/C^2} & 1/C \\ 0 & 0 & 1/C & -J\sqrt{1 - 1/C^2} \\ -J\sqrt{1 - 1/C^2} & 1/C & 0 & 0 \\ 1/C & -J\sqrt{1 - 1/C^2} & 0 & 0 \end{bmatrix} \quad 11.70$$

From these results it should be clear that ideally isolation  $I$  and directivity  $D$  are infinite. In practice, due to losses and as the frequency moves away from the design center, the actual directivity will degrade.

Typical and ideal parameters of a directional coupler are given in [Table 11.2](#).

**Table 11.2** Ideal and typical parameters of a directional coupler

Parameter	Ideal	Ideal (dB)	Typical
Coupling, $C$	–	–	-3– -40 dB
Transmission, $T$	$ \sqrt{1 - 1/C^2} $	$20 \log  \sqrt{1 - 1/C^2} $	-0.5 dB
Directivity, $D$	0	$\infty$	40 dB
Isolation, $I$	0	$\infty$	40 dB

## 11.8 Summary

This chapter considered some of the applications of parallel-coupled lines. Parallel-coupled lines are the most versatile transmission line element and are particularly convenient to use in

microstrip technology. Rather than coupling being a nuisance, the distributed coupling is the basis for directional couplers, which is the main design element considered in this chapter. Parallel-coupled lines will be seen in future chapters as well, particular regarding their use in realizing microwave filters.

## References

- [1] V. Tripathi and A. Hill, "Equivalent circuit modeling of losses and dispersion in single and coupled lines for microwave and millimeter-wave integrated circuits," *IEEE Trans. on Microwave Theory and Techniques*, vol. **36**, no. 2, pp. 256–262, Feb. 1988.
- [2] L. S. Napoli and J. J. Hughes, "Characteristics of coupled microstrip lines," *RCA Review*, vol. **31**, pp. 479–498, Sep. 1970.
- [3] J. Lange, "Interdigitated strip-line quadrature hybrid," in *1969 G-MTT Int. Microwave Symp.*, May 1969, pp. 10–13.
- [4] A. Presser, "Interdigitated microstrip coupler design," *IEEE Trans. on Microwave Theory and Techniques*, vol. **26**, no. 10, pp. 801–805, Oct. 1978.
- [5] W. Ou, "Design equations for an interdigitated directional coupler," *IEEE Trans. on Microwave Theory and Techniques*, vol. **23**, no. 2, pp. 253–255, Feb. 1975.
- [6] R. Osmani, "Synthesis of Lange couplers," *IEEE Trans. on Microwave Theory and Techniques*, vol. **29**, no. 2, pp. 168–170, Feb. 1981.
- [7] V. F. Fusco, *Microwave Circuits*. Prentice-Hall, 1987.
- [8] M. Kirschning and R. Jansen, "Accurate wide-range design equations for the frequency-dependent characteristic of parallel coupled microstrip lines," *IEEE Trans. on Microwave Theory and Techniques*, vol. **32**, no. 1, pp. 83–90, Jan. 1984.
- [9] M. Kirschning and R. Jansen, "Accurate wide-range design equations for the frequency-dependent characteristics of parallel coupled microstrip lines," *IEEE Trans. on Microwave Theory and Techniques*, vol. **33**, no. 3, p. 288, Mar. 1985.
- [10] R. W. Waugh, "Sensitivity analysis of the Lange coupler," *Microwave Journal*, vol. **32**, no. 11, pp. 121–129, 1989.
- [11] Y. Tajima and S. Kamihashi, "Multiconductor couplers," *IEEE Trans. on Microwave Theory and Techniques*, vol. **26**, no. 10, pp. 795–801, Oct. 1978.
- [12] R. Waugh and D. LaCombe, "Unfolding the Lange coupler," *IEEE Trans. on Microwave Theory and Techniques*, vol. **20**, no. 11, pp. 777–779, Nov. 1972.
- [13] J. A. Weiss, "Microwave propagation on coupled pairs of microstrip transmission lines," in *Advances in Microwaves*. Academic Press, 1974, vol. **8**, pp. 295–320.

- [14] A. Kouki, A. Khebir, and R. Mittra, “Finite element modeling of two-dimensional transmission line structures using a new asymptotic boundary condition,” in *1990 IEEE MTT-S Int. Microwave Symp. Digest*, May 1990, pp. 717–720.
- [15] B. Sheleg and B. Spielman, “Broadband (7–18 GHz) 10 dB overlay coupler for m.i.c. application,” *Electronics Letters*, vol. **11**, no. 8, pp. 175–176, 1975.
- [16] D. Rickard, “Thick film MIC components in the range 10–20 GHz,” in *6th European Microwave Conf.*, Sep. 1976, pp. 687–691.
- [17] M. Dydyk, “Accurate design of microstrip directional couplers with capacitive compensation,” in *1990 IEEE MTT-S Int. Microwave Symp. Digest*, May 1990, pp. 581–584.
- [18] B. Szentkuti, “Simple analysis of anisotropic microstrip lines by a transform method,” *Electronics Letters*, vol. **12**, no. 25, pp. 672–673, 1976.
- [19] S. Uysal, A. H. Aghvami, and S. A. Mohamed, “Microstrip quadruplexer using  $-3$  dB hybrids,” in *19th European Microwave Conf.*, Sep. 1989, pp. 905–910.
- [20] M. Nakajima, E. Yamashita, and M. Asa, “New broad-band 5-section microstrip-line directional coupler,” in *1990 IEEE MTT-S Int. Microwave Symp. Digest*, May 1990, pp. 383–386.
- [21] A. Pavio and S. Sutton, “A microstrip re-entrant mode quadrature coupler for hybrid and monolithic circuit applications,” in *1990 IEEE MTT-S Int. Microwave Symp. Digest*, 1990, pp. 573–576.
- [22] V. Fusco and L. Merugu, “Full wave analysis of 94 GHz patch coupler,” in *1990 IEEE MTT-S Int. Microwave Symp. Digest*, May 1990, pp. 649–652.
- [23] D. Gunton and E. Paige, “Directional coupler for gigahertz frequencies, based on the coupling properties of two planar comb transmission lines,” *Electronics Letters*, vol. **11**, no. 17, pp. 406–408, 1975.
- [24] P. Rigg and J. Carroll, “The canonical coupler : A new approach to microwave coupler design,” in *9th European Microwave Conf.*, Sep. 1979, pp. 490–494.
- [25] S. Islam, “An analysis and a design technique for microstrip comblines,” *Microwave Journal*, pp. 79–91, Nov. 1989.
- [26] V. Rizzoli, “Highly efficient calculation of shielded microstrip structures in the presence of undercutting,” *IEEE Trans. on Microwave Theory and Techniques*, vol. **27**, no. 2, pp. 150–157, Feb. 1979.
- [27] K. C. Gupta, R. Garg, I. J. Bahl, and P. Bhartia, *Microstrip Lines and Slotlines*, 2nd ed. Artech House, 1996.
- [28] R. Garg and I. Bahl, “Characteristics of coupled microstriplines,” *IEEE Trans. on*

*Microwave Theory and Techniques*, vol. **27**, no. 7, pp. 700–705, Jul. 1979.

[29] R. Garg and I. Bahl, “Correction to “characteristics of coupled microstriplines”,” *IEEE Trans. on Microwave Theory and Techniques*, vol. **28**, no. 3, p. 272, Mar. 1980.

[30] R. Jansen, “High-speed computation of single and coupled microstrip parameters including dispersion, high-order modes, loss and finite strip thickness,” *IEEE Trans. on Microwave Theory and Techniques*, vol. **26**, no. 2, pp. 75–82, Feb. 1978.

[31] S. Shamasundara and K. Gupta, “Sensitivity analysis of coupled microstrip directional couplers,” *IEEE Trans. on Microwave Theory and Techniques*, vol. **26**, no. 10, pp. 788–794, Oct. 1978.

[32] S. Shamasundara and K. Gupta, “Correction to “sensitivity analysis of coupled microstrip directional couplers”,” *IEEE Trans. on Microwave Theory and Techniques*, vol. **27**, no. 2, p. 208, Feb. 1979.

[33] D. Kajfez and S. Govind, “Effect of difference in odd-and even-mode wavelengths on a parallel-coupled bandpass filter,” *Electronics Letters*, vol. **11**, no. 5, pp. 117–118, 1975.

[34] B. Easter and C. Gupta, “More accurate model of the coupled microstripline section,” *Microwaves, Optics and Acoustics, IEE Journal on*, vol. **3**, no. 3, pp. 99–103, May 1979.

# Chapter 12

## Microstrip Passive Elements

### 12.1 Introduction

Passive elements in microstrip circuits are generally realized using either transmission line segments or surface mount components. Lumped elements in surface-mount form with reasonably good characteristics are available up to about 25 GHz. The only real problem is with inductors which have relatively low  $Q$ . Of course, if possible, functionality at the board level is achieved using transmission line elements and it is common to have a mixed design, as shown in [Figure 12.1](#). These elements and others will be reviewed in this chapter.

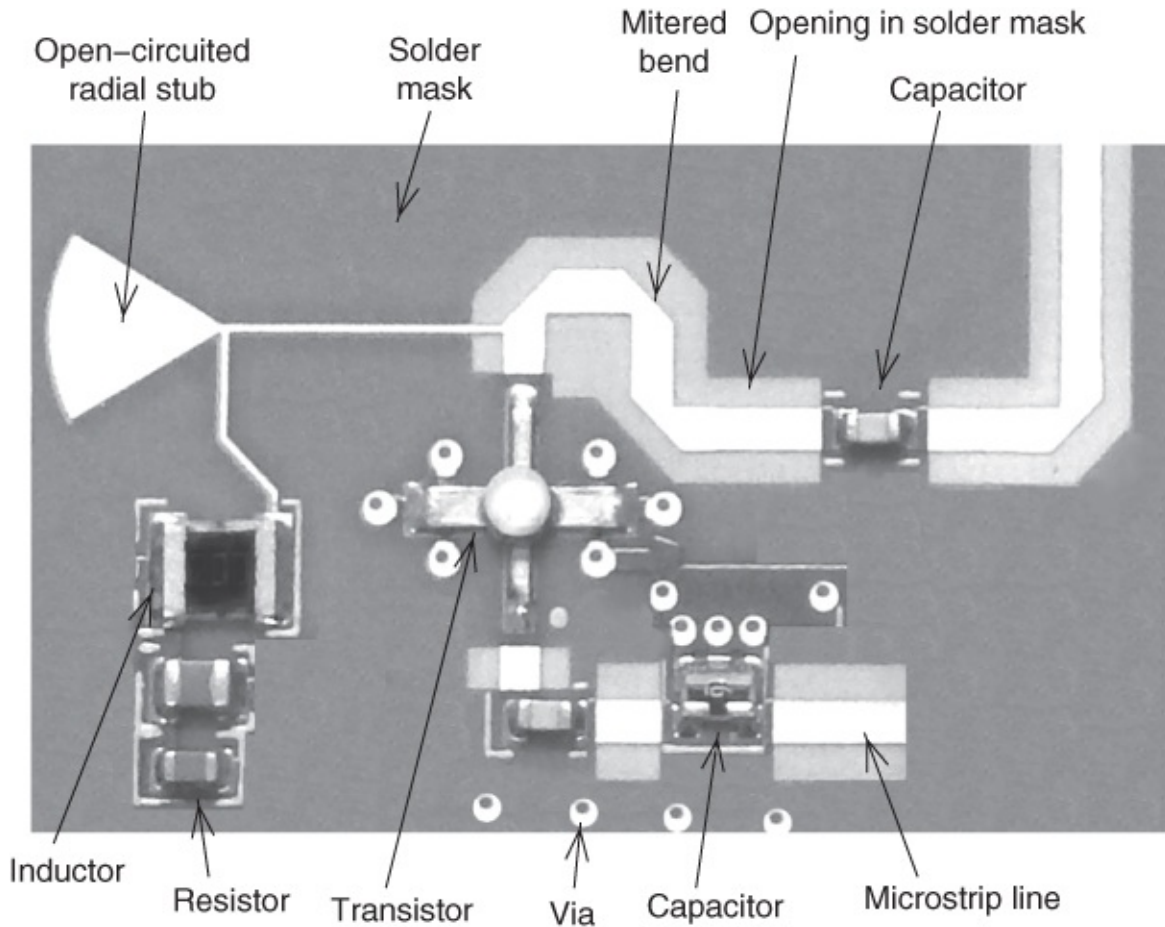


[Figure 12.1](#) Segment of a 15 GHz microstrip circuit showing passive elements including stubs, bends, surface-mount resistors, transistor, capacitors, and inductor.

### 12.2 Lumped Elements

In this section we describe lumped element components realized by patterning microstrip or obtained as discrete components, such as surface-mount components, that can be soldered to a

microstrip circuit. Integrated components are considered in [Section 12.8](#).

### 12.2.1 Capacitors

Various capacitors used in microstrip circuits are shown in [Figure 12.2](#). The first four can all be realized by patterning the microstrip circuit. The gap capacitor shown in [Figure 12.2](#) realizes a small capacitance around 0.1 pF. The version shown in [Figure 12.2\(b\)](#) achieves a higher capacitance by widening the lines at the gap. Even higher capacitance can be realized with the interdigitated capacitors in [Figures 12.2\(c\) and \(d\)](#). A surface-mount chip capacitor is shown in [Figure 12.2\(e\)](#) and is usable up to several tens of gigahertz.

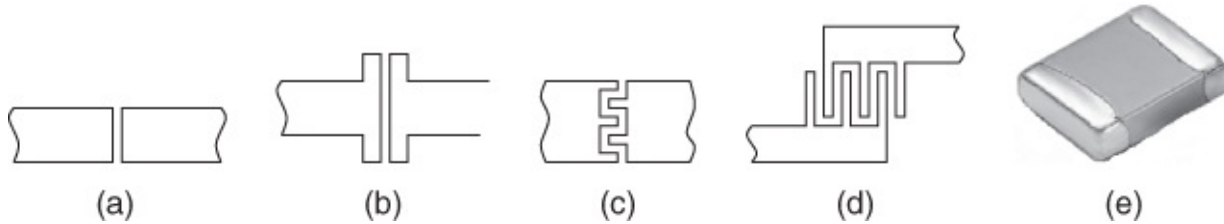


**Figure 12.2** Lumped capacitors for microstrip circuits: (a) gap capacitor; (b) extended gap capacitor; (c) interdigitated capacitor; (d) another interdigitated capacitor; and (e) surface-mount chip capacitor.

Relatively low capacitance values of up to  $500 \text{ fF}/\mu\text{m}^2$  are available because of the large dielectric thicknesses of 0.5 to 1  $\mu\text{m}$  between metal layers [1]. This thickness is required in normal interconnect circumstances to minimize interconnect-to-interconnect coupling, so it is unlikely to change much.

There are also variable capacitors realized either as reverse-biased junction diodes or as ferroelectric capacitors [2–5]. These are commonly used in tunable filters [2, 6] and voltage controlled oscillators [7].

### 12.2.2 Inductors

Inductors are important components in RF and microwave circuits but as lumped elements, for example surface-mount chip inductors, they have high loss compared to chip capacitors. They have a role in matching networks and are used to provide bias to active devices while effectively blocking RF signals from the bias circuitry. Lumped inductors are based on coils of conductor and there will be parasitic capacitance between the windings as well as conductor loss. Still sometimes they must be used and it is not always possible to replace them using transmission line elements as the lengths of lines may be too long. This is a particular problem at low frequencies.

[Figure 12.3](#) shows a spiral inductor that can be fabricated in microstrip and especially on-chip. It is rarely fabricated at the circuit-board level and so the discussion of this spiral inductor will be left for the discussion of on-chip components, see [Section 12.8.3](#).

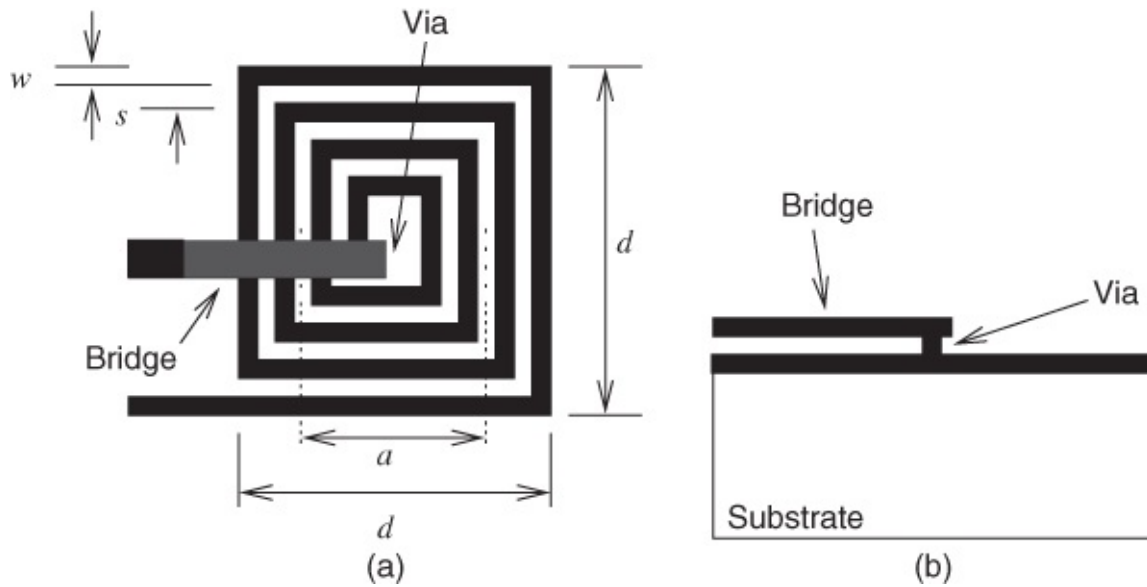


**Figure 12.3** A spiral inductor: (a) plan view; and (b) side view.

**Figure 12.4** shows a toroidal inductor which can be fabricated on most microwave substrates and what is shown in **Figure 12.4** was fabricated on one layer of a silicon stack (sometimes this is referred to as a silicon circuit board). Various sizes have been fabricated and equivalent circuit models have been developed [8]. A 2.45 nH inductor was realized with a diameter of 880  $\mu\text{m}$  on a 500  $\mu\text{m}$  thick silicon substrate. This inductor has 11 turns, a peak  $Q$  of 22 at 1.5 GHz, and a self-resonant frequency of 10 GHz.

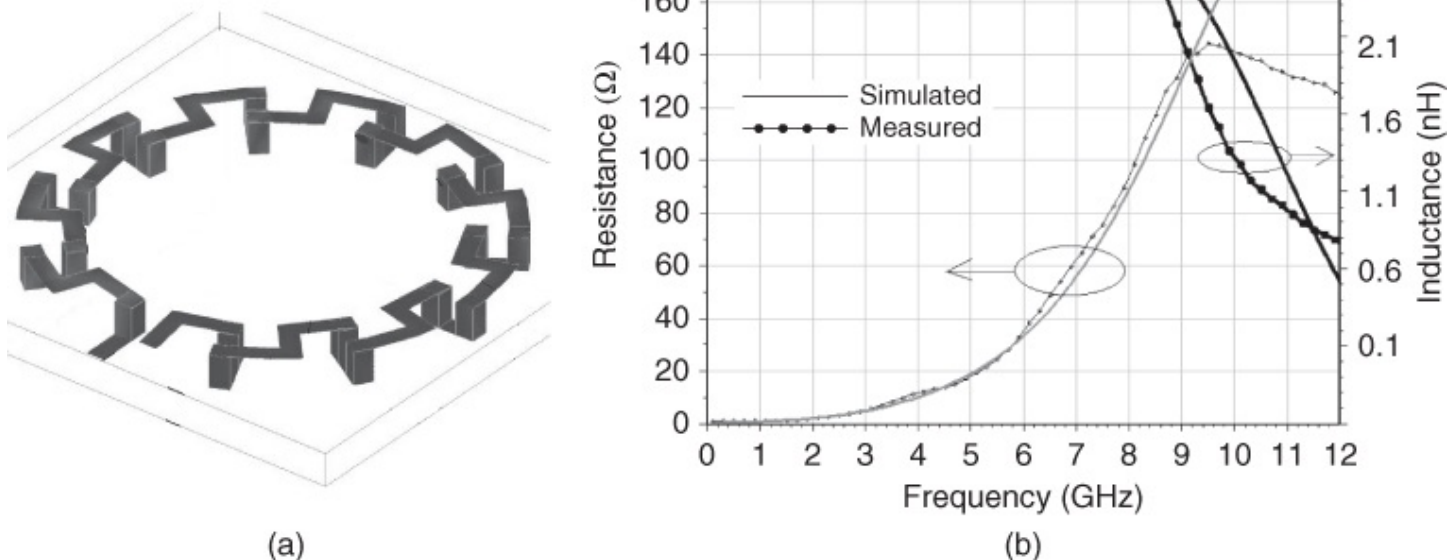
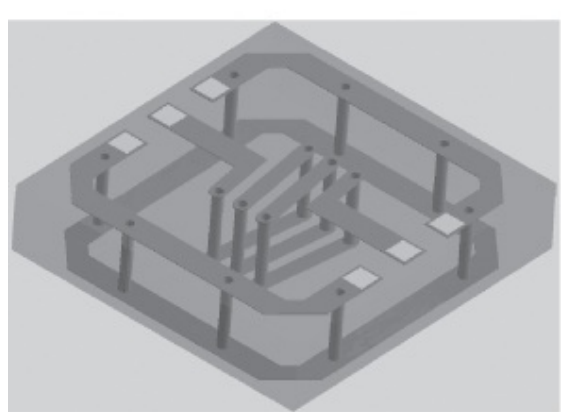


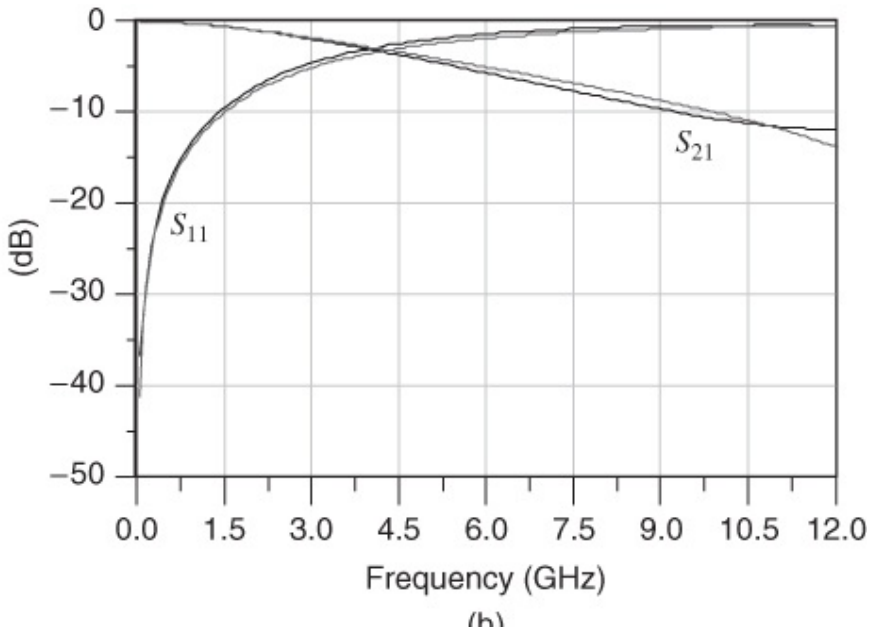
**Figure 12.4** A microstrip toroidal inductor fabricated on a silicon circuit board: (a) layout view; and (b) response. From Liu *et al.* (2004) [8], figures 6, 8, p. 649, 652. Used with permission of IEEE.

A solenoidal inductor fabricated on a silicon circuit board is shown in **Figure 12.5**. **Figure 12.5(a)** shows the layout view of a three-turn inductor. The measured response compared to the

calculated response from a circuit model of the inductor is shown in [Figure 12.5\(b\)](#). An inductance of 1.9 nH was obtained at 5 GHz and with a  $Q$  of 30. This inductor occupied an area of 2 mm<sup>2</sup>. An inductance of 4.6 nH with a  $Q$  of 22 was obtained for a two-turn inductor, and an inductance of 10.6 nH with a  $Q$  of 11 was obtained for a three-turn inductor. These  $Q$ s were achieved over a wide bandwidth. The high performance was obtained because these solenoidal inductors were designed as slow-wave transmission line structures with well-defined current return paths.



(a)



(b)

**Figure 12.5** A microstrip solenoidal inductor fabricated on a silicon circuit board: (a) layout of a three-turn inductor; and (b) measured response of a three-turn inductor (the thin lines are the simulated responses). Adapted from Feng *et al.* (2007) [9], figure 6, p. 1907. Reprinted with permission of IEEE.

### 12.2.3 Transformers

Wideband surface-mount transformers are available with operating frequencies to 5 GHz. These are rather large and utilize coupling of transmission lines. Twisted coupled lines are wound around a magnetic core that extends the lower frequency range to a few hundreds of megahertz. Such transformers are called hybrid transmission-line transformers [7].

Integrated transformers that can be fabricated in a microstrip circuit include the solenoidal transformer shown in [Figure 12.6](#) [9–11]. [Figure 12.6](#) shows a 1:1 solenoidal transformer fabricated as part of a silicon interposer stack or silicon circuit board. This transformer has excellent performance as seen with the response of a four-turn transformer shown in [Figure 12.6\(c\)](#). This transformer has a 1 dB bandwidth from 1.57 to 10.54 GHz with a minimum insertion loss of 0.37 dB. Transformers with 1-turn up to 10-turns have been fabricated. The 1 dB bandwidth of the one-turn transformer is 6.26–12.25 GHz, with a minimum insertion loss of 0.24 dB. The 1 dB bandwidth of the 10-turn transformer is 0.603–4.63 GHz, with a minimum insertion loss of 0.58 dB. All of the transformer windings have a cross-section of

$400\text{ }\mu\text{m} \times 400\text{ }\mu\text{m}$ , and the strip width is  $70\text{ }\mu\text{m}$  with  $30\text{ }\mu\text{m}$  spacing between strips.

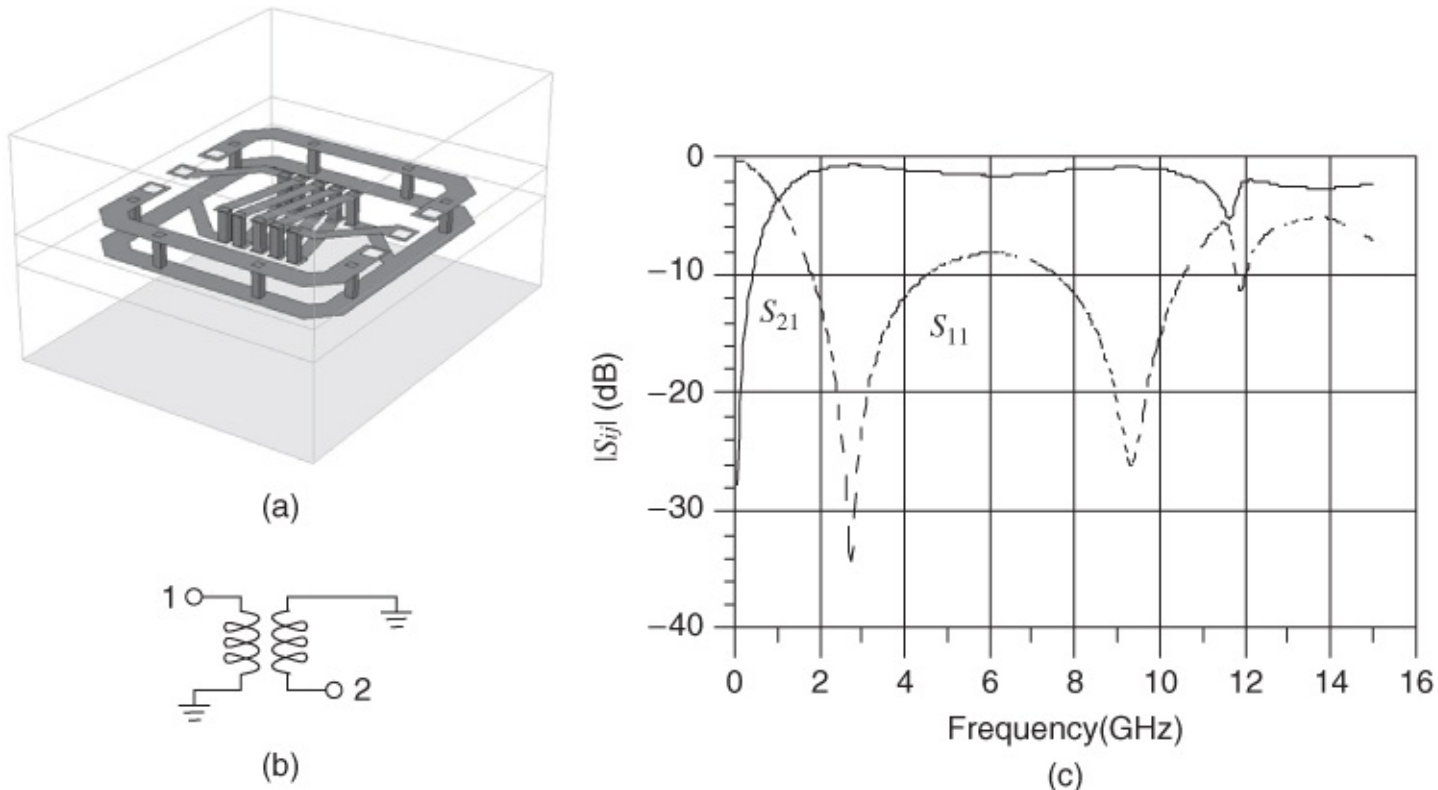


**Figure 12.6** A microstrip solenoidal transformer fabricated on a silicon circuit board: (a) layout of a three-turn inductor; (b) transformer circuit element showing the orientation of the winding connections; and (c) measured response of a four-turn transformer.

### 12.2.4 Resistors

Resistors are the simplest of microwave components. They are available in chip form and can be used up to several tens of gigahertz. They can also be silk-screened onto circuit board structures. They will be considered in more detail in [Section 12.3](#).

## 12.3 Terminations and Attenuators

Termination refers to the termination of a transmission line in a short circuit, an open circuit or a load. A matched termination is when the load is a resistor with the same value as the characteristic impedance of the line that it terminates. In general, with transmission lines it is usually preferable for short circuits to be realized rather than open circuits, since relatively high-quality short circuits can be manufactured, and the effective location of an open circuit is hard to define and moves with frequency. In microstrip the opposite situation applies, open circuits (which do not require vias) being in far greater use than short circuits, although both forms of termination are only approximate due to the hybrid fields associated with microstrip. These terminations were discussed in greater detail in [Sections 9.2.1](#) and [9.2.3](#).

### 12.3.1 Matched Terminations and Attenuators

With some care quite broadband matched terminations can be realized. For frequencies up to about 20 GHz a simple rectangular resistor deposition is suitable and may be expected to yield a VSWR below 1.1. The actual deposition may be thick or thin film. The resistor is kept inline with the microstrip, and the far end is shorted to ground by a via or wrap-around metallization.

At frequencies above about 20 GHz the series-inductive reactance of a lumped resistor becomes an increasingly severe problem, and the resistor element has to be viewed as a series LR network, at least to a first approximation. Lacombe [12] devised a fairly simple broadband matching arrangement for a  $50 \Omega$  resistor to form a  $50 \Omega$  microstrip termination with  $\text{VSWR} < 1.5$  over the range  $1 < f < 18$  GHz. The details will not be outlined here because considerably improved designs for matched terminations have been developed more recently. These improved designs rely upon attenuator structures, which are therefore considered first.

Rickard [13] has described a  $\pi$ -type microwave attenuator, manufactured in thick-film microstrip. The electrical circuit configuration and the microstrip layout are both indicated in [Figure 12.7](#). The resistance values are  $R_s = 17 \Omega$  and  $R_p = 290 \Omega$ , both with  $\pm 15\%$  tolerance. To maintain lumped behavior, the lengths of the resistors are less than an eighth-wavelength long at the highest frequency (i.e., less than 1 mm). The interconnecting resistor  $R_s$  is formed as a sideways S shape within the width of the microstrip. The resistors  $R_p$  are effectively grounded by using quarter-wave open-circuit transforming stubs, each having a characteristic impedance of  $30 \Omega$ . This attenuator had a final performance, over the frequency range  $8 \leq f \leq 20$  GHz, as follows:

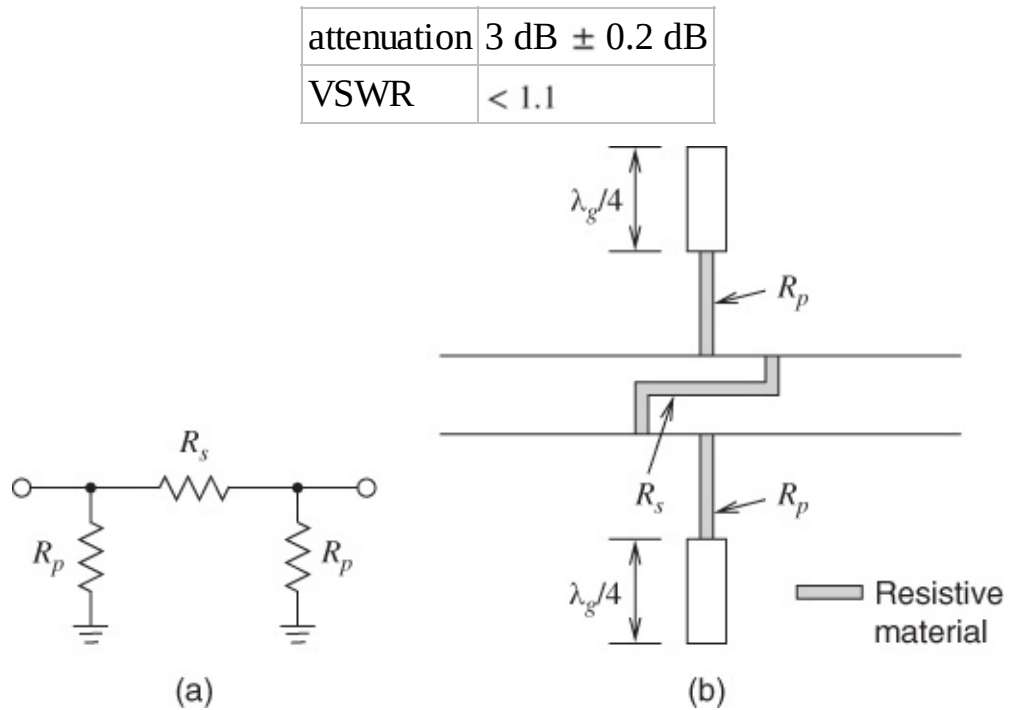


[Figure 12.7](#) Network and microstrip circuit layout for a  $\pi$ -type attenuator: (a) circuit topology; and (b) microstrip circuit with open-circuited stubs.

Such attenuators have several important applications. For example, they are used in broadband power-leveling loops where the microwave output power is maintained constant over a wide range of frequencies.

Finlay *et al.* [14] have described a precision microstrip matched load using two 3 dB attenuator pads of a slightly different basic design to that described here. Each of the two pads is followed by a 50  $\Omega$  resistor which is grounded at its far end. The length of microstrip line between the pads is approximately  $\lambda_g/4$  at 15 GHz and between the final pad and the resistor is approximately  $\lambda_g/16$  at 15 GHz. Excellent performance is obtained with the load VSWR being less than 1.1 for all frequencies up to 18 GHz. This is somewhat degraded by the SMA transition to the microstrip line, which results in a VSWR below 1.2 up to 13 GHz, but also a peak of 1.22 at about 15 GHz. Such performance is compatible with most requirements likely to be encountered in microstrip circuits.

Another approach to realizing a microstrip attenuator is to deposit a lossy material on top of a microstrip transmission line. This forms a transmission line with high attenuation but a characteristic impedance that is close in magnitude to that of the original line. A precision microstrip can be realized by preceding a lumped matched termination by such a transmission line attenuator. The lumped termination of course has a fixed resistance and so can only approximate the frequency-dependent characteristic impedance of the microstrip line. The attenuator greatly minimizes the effect of a mismatch of the lumped termination resistance and the line's characteristic impedance.

### **12.3.2 Passive Intermodulation Distortion**

All lossy components can result in distortion and this is of particular concern with attenuators and terminations. Passive intermodulation distortion (PIM) is characterized by applying two tones closein frequency to a system and observing the additional tones that often appear. If the frequencies of the original two tones are  $f_1$  and  $f_2$  then the problem additional tones, so-called third-order intermodulation tones, are at frequencies  $2f_1 - f_2$  and  $2f_2 - f_1$ . While other additional tones may appear, such as harmonics, these are usually outside the band of interest and are easily removed by filtering. However, the third-order tones cannot be removed as they are usually in the band of interest.

There seem to be multiple sources of PIM but one of the dominant sources is electro-thermal PIM [15–17]. In a typical system, such as a communication system, a digitally modulated signal has an envelope that varies relatively slowly in time compared to the RF carrier signal. When this signal is attenuated or terminated in a resistive load the varying signal dissipation results in a resistance that varies with the envelope due to the finite thermal coefficient of resistance of realistic components. This time-varying resistance results in an interaction, governed by Ohm's law, with the original signal and the generation of intermodulation tones if the original signal comprised discrete tones. If the original signal was digitally modulated then the additional spectral content is referred to as spectral growth. Guidelines for minimizing PIM in lossy components are given in [15, 16] and in [17] for microstrip transmission lines. Essentially the guidelines amount to minimizing heat generation by designing components to minimize current density and minimizing temperature rise by providing adequate fast-reaction heatsinking using substantial metal such as wider and thicker strips in the case of planar transmission lines. For components one of the techniques for reducing PIM is to distribute power loss. Thus a lower loss termination can be realized by using a transmission line

attenuator followed by a matched termination rather than a matched termination alone.

## 12.4 Microstrip Stubs

### 12.4.1 Open Microstrip Stub

[Figure 12.8](#) shows various representations of an open-circuited stub. [Figure 12.8\(a\)](#) is the longitudinal sectional view of an open-circuited stub and [Figure 12.8\(b\)](#) is its layout view. [Figure 12.8\(c\)](#) is its schematic representation as a generic transmission line. This schematic representation is used in a microstrip circuit design if there are not many transmission line elements. If there are then it is common to use the compact transmission line representation in [Figure 12.8\(d\)](#). None of the representations used so far really make it clear that we are dealing with an open-circuited situation. If it is important to make that clear then a diagonal stroke is put through the terminal, as shown in [Figure 12.8\(e\)](#). [Figure 12.8\(f\)](#) is a microstrip shunt open-circuited stub. This is used to introduce an admittance in a circuit using only a transmission line section.

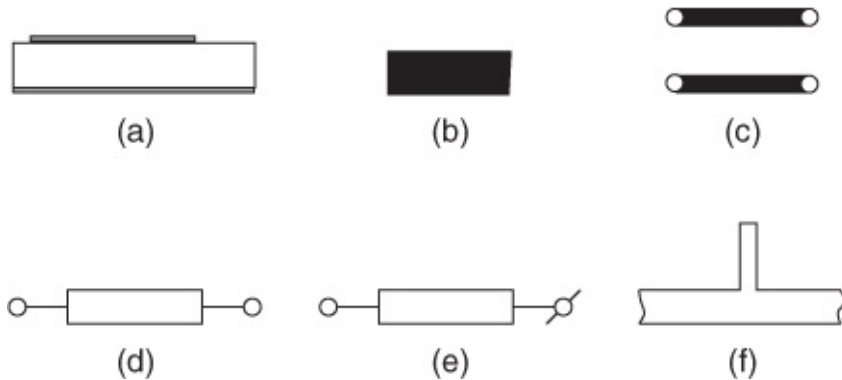


[Figure 12.8](#) Various representations of an open-circuited microstrip stub: (a) longitudinal section; (b) layout view; (c) transmission line model; (d) compact transmission line model; (e) alternative compact transmission line; and (f) shunt stub.

The open end of an open-circuited stub has fringing which effectively introduces a frequency-dependent lengthening of the stub line length. The fringing of the open-circuited stub can be modeled by a capacitance, but this is frequency dependent.

### 12.4.2 Short-circuited Microstrip Stub

A short-circuited microstrip stub is another way to introduce an impedance in a circuit. [Figure 12.9](#) shows various representations of a short-circuited stub. [Figure 12.9\(a\)](#) is the longitudinal sectional view of a short-circuited stub and [Figure 12.9\(b\)](#) is its layout view. The 'X' is a common method for indicating a via to ground. [Figure 12.9\(c\)](#) is the transmission line representation with the representation shown in [Figure 12.9\(d\)](#) being a compact way of indicating a short-circuited stub. In [Figure 12.9\(e\)](#) the short-circuited stub is in shunt with a transmission line and inserts an admittance in a transmission line circuit.

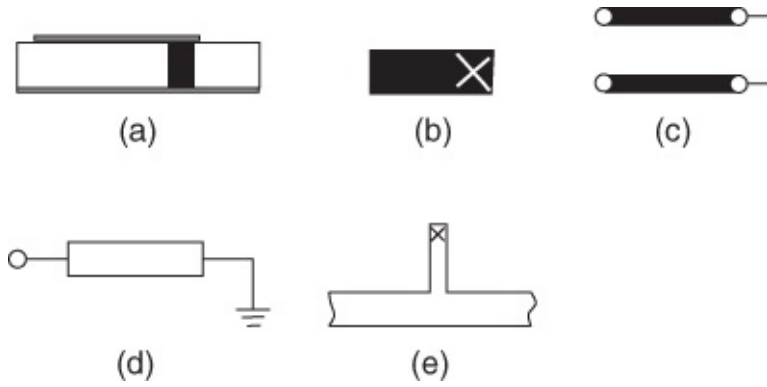


**Figure 12.9** Various representations of a short-circuit microstrip stub: (a) longitudinal section; (b) layout view; transmission line model; (d) compact transmission line model; and (e) shunt stub.

The short-circuited stub requires a via, a metal-filled through hole to the backing ground. Many microstrip substrates are hard and vias are difficult to fabricate. Also the short via has inductance which at microwave frequencies cannot be ignored. Even with these problems it does have a particular advantage over an open-circuited stub, which is that the location of the short to ground is accurately known.

### 12.4.3 Microstrip Radial Stubs

The use of radial stubs, as opposed to the straight stubs traditionally used, improves the performance of many microstrip circuits. An example of a radial stub in a microwave circuit is seen in [Figure 12.1](#). Examples of various options concerning these circuit elements are shown in [Figure 12.10](#). Such stubs may, like their straight counterparts, be either series or shunt-connected, as indicated in [Figures 12.10\(a\)](#) and [\(b\)](#). When two shunt-connected radial stubs are introduced in parallel, that is, one on each side of the microstrip feeder line, the resulting configuration is termed a butterfly structure. This is indicated in [Figure 12.10\(c\)](#). Critical design parameters include the radius  $r$  and the inclusive angle. The radial stub forms a radial transmission line and has well-defined transmission line characteristics [18].

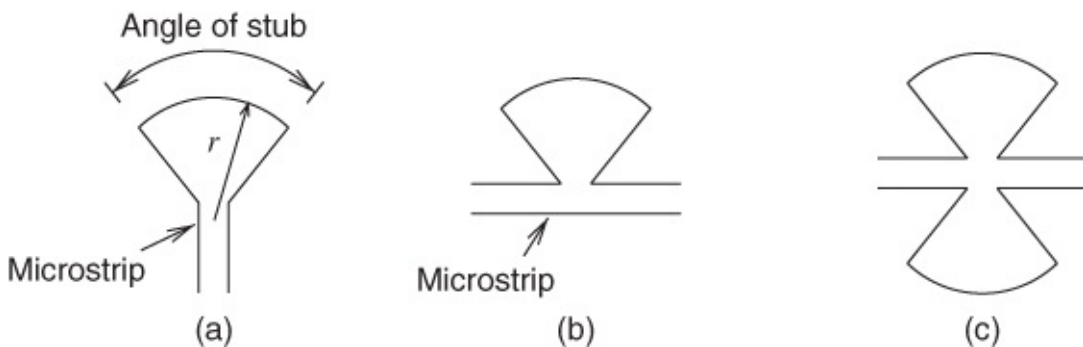


**Figure 12.10** Microstrip radial stubs: (a) series connected; (b) shunt connected; and (c) butterfly structure.

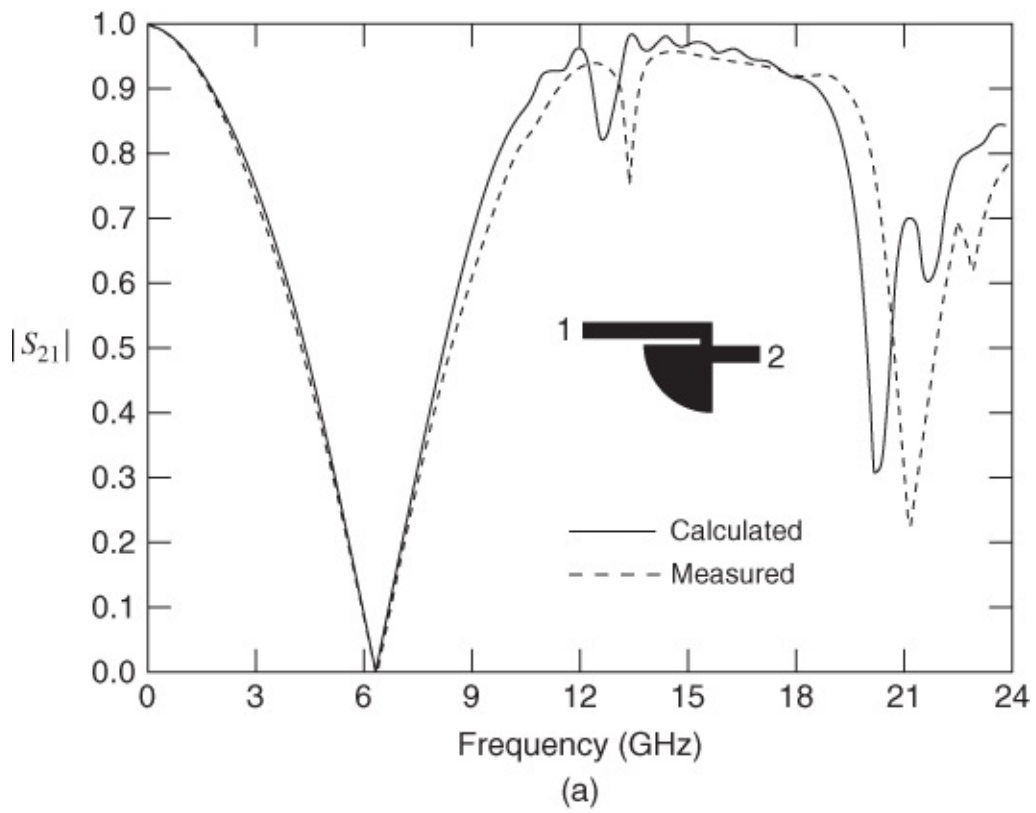
A major advantage of these radial stubs is that the input impedance is offered over generally broad bandwidths. Another particular advantage of a radial stub is realizing input impedances lower than  $20 \Omega$ . Compared to a straight stub accurate identification of the impedance

reference plane is possible.

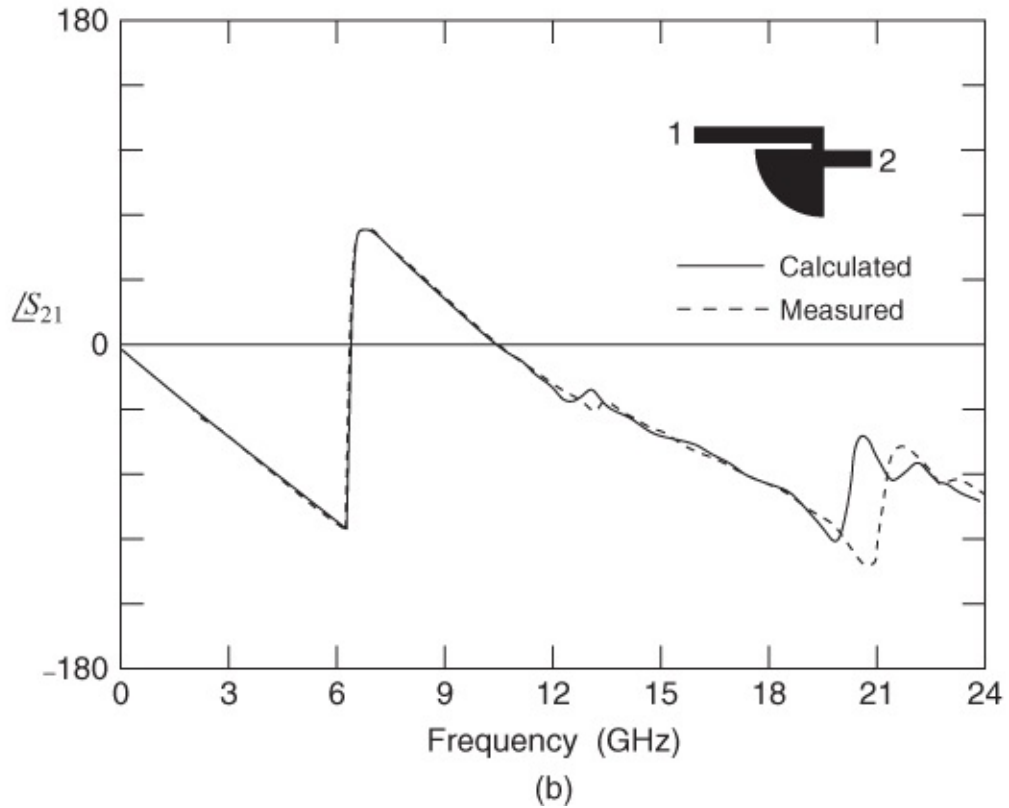
For a design on a 0.635 mm thick alumina substrate, Giannini *et al.* [19] show that a stub radius of 5 mm and an inclusive angle of  $60^\circ$  provides a useful circuit element at approximately 12 GHz. At higher frequencies, towards and through millimeter-wave, the radius must be shortened and/or the angle increased proportionately. However, if out-of-band considerations permit, the radius may be increased in odd multiples of quarter-wavelengths so that a physically realizable structure is obtained.

In practice these types of stubs are lossy. Giannini *et al.* [20] report an interesting application to a microstrip termination. They show that the combination of a butterfly structure and a series-connected radial stub provides a matched termination having a return loss better than 20 dB over a 2.5 to 8 GHz frequency range. This is achieved without specifically using a lossy material. The termination structure comprises a  $3 \times 60^\circ$  array of radial stubs at the end of a microstrip line.

The microstrip radial stub is important in some filter and matching circuit designs and Rittweger and Wolff's [21] results for a specific case are shown in [Figure 12.11](#). It can be seen that, at frequencies below 19 GHz, the measured and calculated results compare favorably. In the 19–24 GHz range there is a greater discrepancy in the data although the pattern of variation still compares quite well.



(a)



(b)

**Figure 12.11**  $S$  parameters of the radial stub. Alumina substrate,  $\epsilon_r = 9.768$  (measured), height  $h = 0.635$  mm, width  $w = 0.61$  mm, gap = 0.61 mm, radius = 3.253 mm: (a)  $|S_{21}|$  and (b)  $\angle S_{21}$ . Adapted from Rittweger and Wolff (1990) [21], figure 1, p. 1149. Reprinted with permission of IEEE.

## 12.5 Hybrids and Couplers

A hybrid is a special type of four-port junction with the property that if a signal is applied at any port, it emerges from two of the other ports at half power, while there is no signal at the fourth or isolated port. The two outputs have specific phase relationships and all ports are matched. Only two fundamental types of hybrids are used:  $180^\circ$  and  $90^\circ$  hybrids.

### 12.5.1 Quadrature Hybrid

The ideal  $90^\circ$  hybrid, or quadrature hybrid, has the scattering parameters

$$S_{90^\circ} = \frac{1}{\sqrt{2}} \begin{bmatrix} 0 & -j & 1 & 0 \\ -j & 0 & 0 & 1 \\ 1 & 0 & 0 & -j \\ 0 & 1 & -j & 0 \end{bmatrix}. \quad 12.1$$

The  $90^\circ$  phase difference between the through and coupled ports is indicated by  $-j$ . The actual phase shift, that is,  $+90^\circ$  or  $-90^\circ$  (indicated by  $\pm j$ ), between the input and output ports depends on the specific hybrid implementation. A  $+90^\circ$  phase shift is indicated by replacing  $-j$  in Equation (12.1) by  $j$ .

Consider the power flow implied by Equation (12.1). The fraction of power transmitted from port  $i$  to port  $j$  is described by  $|S_{ji}|^2$ . At port 1 no power is reflected for an ideal hybrid as the port is matched and  $S_{11} = 0$ . Port 4 should be isolated so no power will come out of port 4, and so  $S_{41} = 0$ . The power should be split between ports 2 and 3, and these should be equal to half the power entering port 1. From Equation (12.1),

$$|S_{21}|^2 = \left( \frac{1}{\sqrt{2}} |j| \right)^2 = \frac{1}{2} \quad \text{and} \quad |S_{31}|^2 = \left( \frac{1}{\sqrt{2}} |1| \right)^2 = \frac{1}{2}. \quad 12.2$$

Thus the power entering port 1 is split, with half going to port 2 and half to port 3.

### 12.5.2 $180^\circ$ Hybrid

The scattering parameters of the  $180^\circ$  hybrid are

$$S_{180^\circ} = \frac{1}{\sqrt{2}} \begin{bmatrix} 0 & 1 & -1 & 0 \\ 1 & 0 & 0 & 1 \\ -1 & 0 & 0 & 1 \\ 0 & 1 & 1 & 0 \end{bmatrix}, \quad 12.3$$

and this defines the operation of the hybrid. In terms of the root power waves  $a$  and  $b$ , the outputs at the ports are

$$\begin{aligned} b_1 &= (a_2 - a_3)/\sqrt{2} & b_2 &= (a_1 + a_4)/\sqrt{2} \\ b_3 &= (-a_1 + a_4)/\sqrt{2} & b_4 &= (a_2 + a_3)/\sqrt{2} \end{aligned} \quad 12.4$$

### 12.5.3 Branch-line Coupler

The hybrid (or branch-line) coupler can be put in the form of a ring, as shown in [Figure 12.12](#). One important application for this arrangement is the balanced mixer (and also phase detector) illustrated in [Figure 12.13](#). It can be readily verified, by counting up the total number of quarter-wavelength phase shifts in each path, that the signal and local oscillator waves arrive at each Schottky-barrier diode in relative antiphase. This is a design requirement for this type of mixer. Unwanted waves are filtered out by the various lowpass filters shown on the circuit. The use of this 3 dB ring coupler enables both the signal and the local oscillator powers to be coupled to the mixer diodes with very little loss, resulting in high sensitivity.

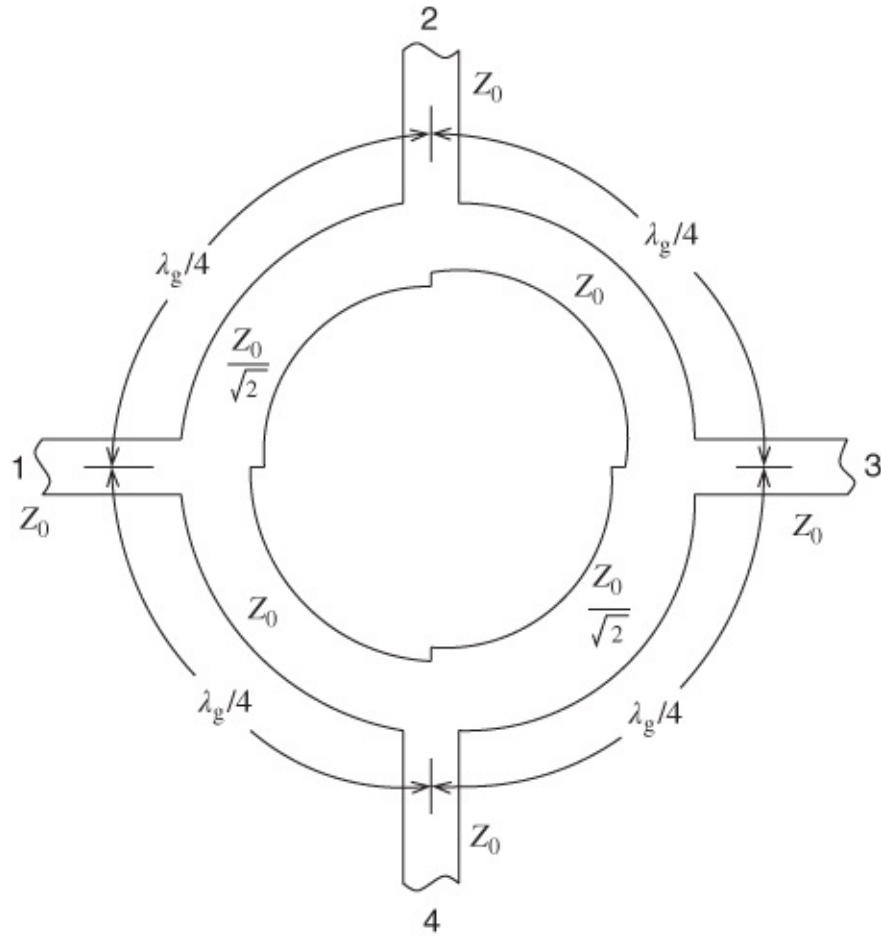
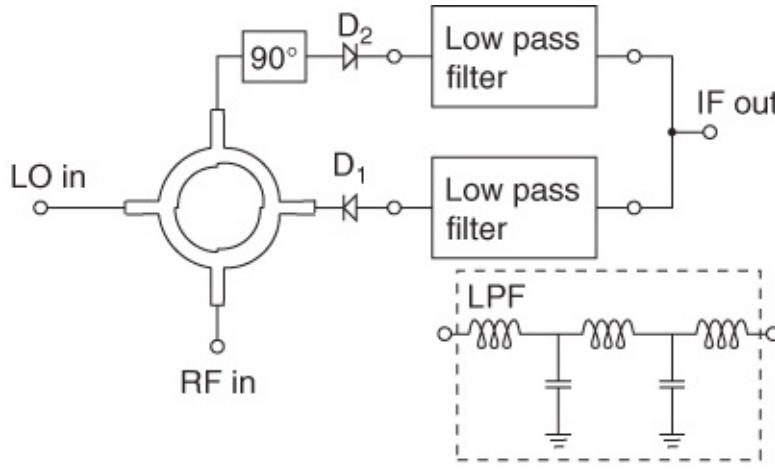
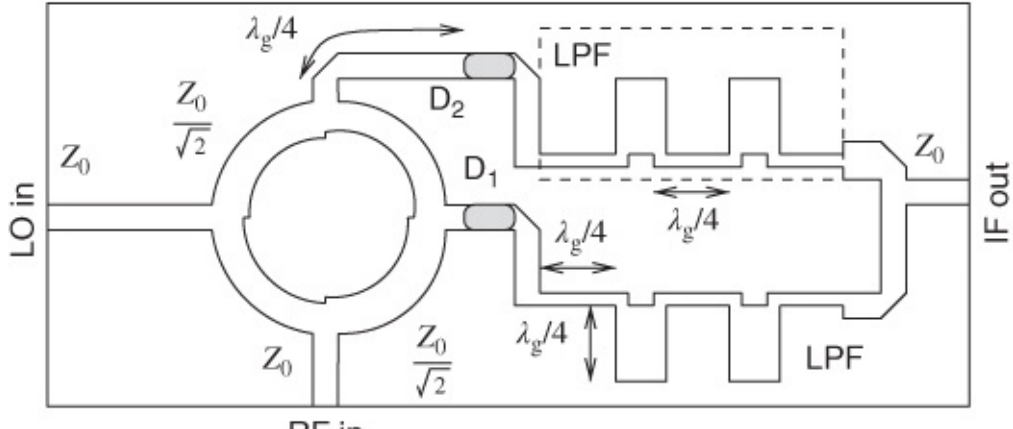


[Figure 12.12](#) Ring form of microstrip 3 dB branch-line directional coupler.



(a)



(b)

**Figure 12.13** Balanced mixer circuit based on the structure of [Figure 12.12](#): (a) schematic layout; and (b) microstrip circuit with surface-mount diodes.

Mayer and Knochel [22] describe a hybrid coupler with improved design flexibility and broad bandwidth. They show that, for the simple four-port branchline coupler shown in [Figure 12.21](#), the general impedances  $Z_{0x}$  of the inner coupler are given by:

$$\frac{Z_{0x}}{Z_0} = \frac{1 + S_{11}(f_o)}{1 - S_{11}(f_o)} \quad 12.5$$

and hence the specific impedances are given by

$$\frac{Z_{02}}{Z_0} = \sqrt{-\frac{3}{2} \left(1 - \frac{Z_{01}}{Z_0}\right) + \sqrt{\frac{9}{4} \left(1 - \frac{Z_{01}}{Z_0}\right)^2 + \frac{Z_{01}}{Z_0}}} \quad 12.6$$

and

$$\frac{Z_{01}}{Z_0} = \frac{Z_{02}}{Z_0 \sqrt{2}}. \quad 12.7$$

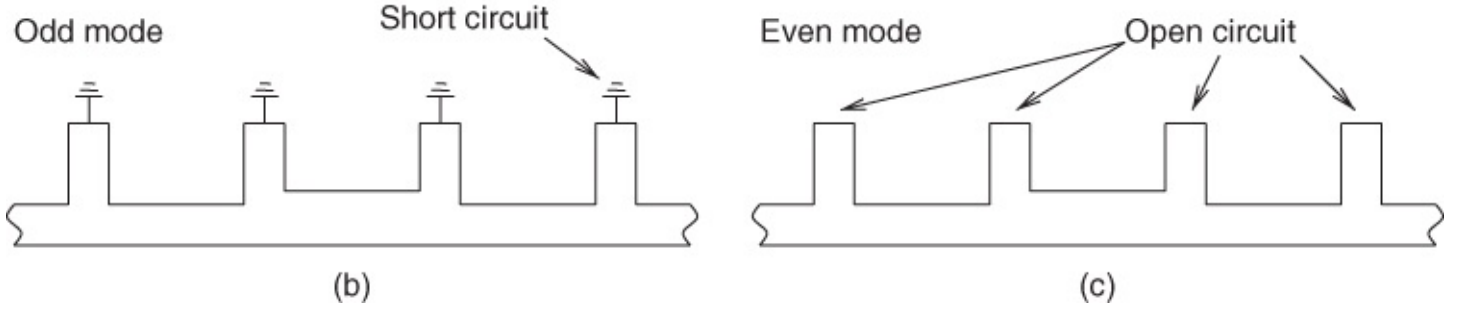
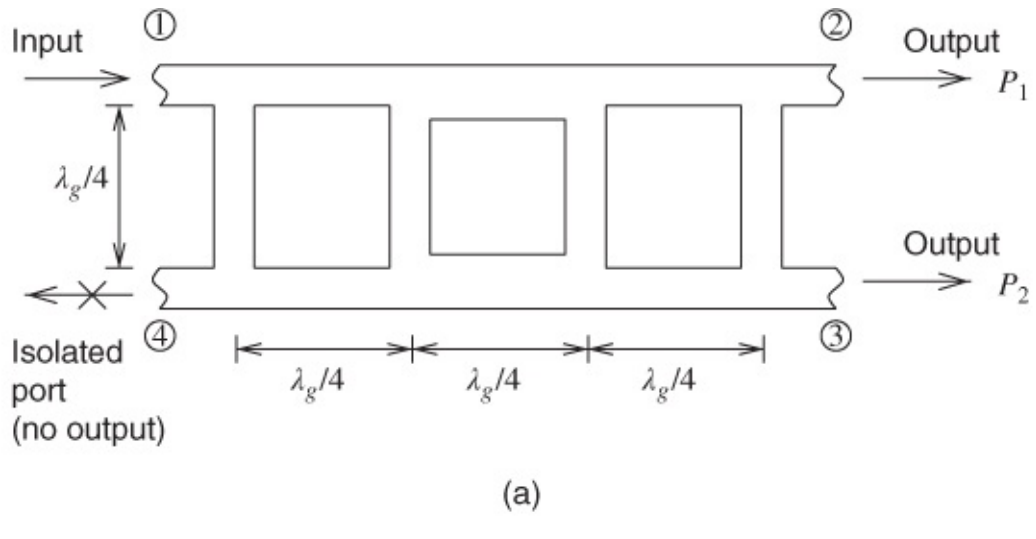


**Figure 12.21** Branch-line directional coupler in MIC form: (a) microstrip layout; (b) odd-mode equivalent circuit; and (c) even-mode equivalent circuit.

The inner coupler is that bound by the first series and parallel arms, respectively, and this is also shown in [Figure 12.14](#). Mayer and Knochel also describe a two-branch coupler modified by the addition of half-wavelength open-circuited stubs centrally located on each inner arm, as shown in [Figure 12.15](#). The way this approach serves to broadband the coupler amounts to splitting the original center frequency at which there was a perfect match. This frequency split results in two frequencies at which  $S_{11}$  is a minimum. Further details are given in the reference.

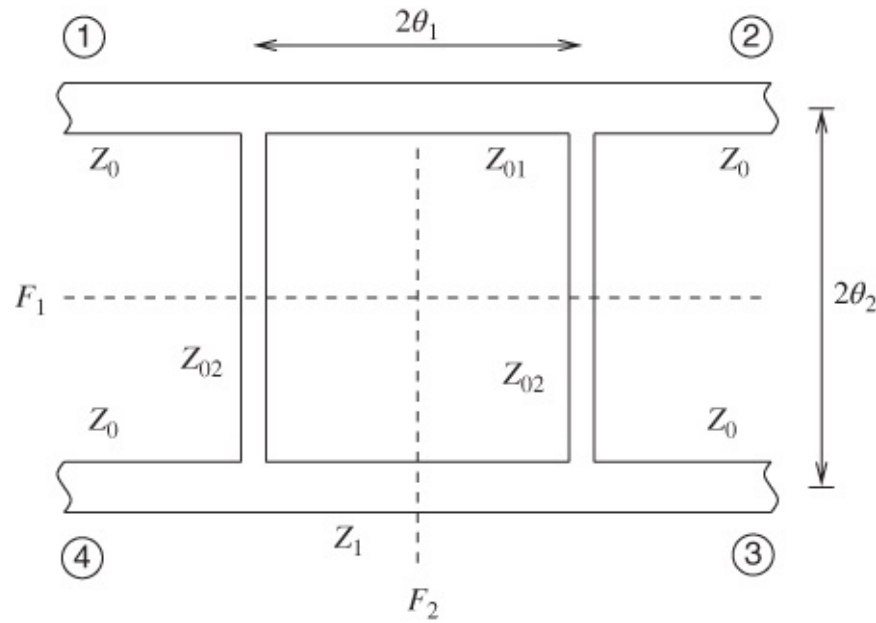


**Figure 12.14** Two-branch coupler with two-fold symmetry ( $\theta_{1,2}$  = line lengths,  $Z_{1,2}$  = characteristic impedances). Adapted from Mayer and Knochel (1990) [22], figure 1, p. 393. Reprinted with permission of IEEE.

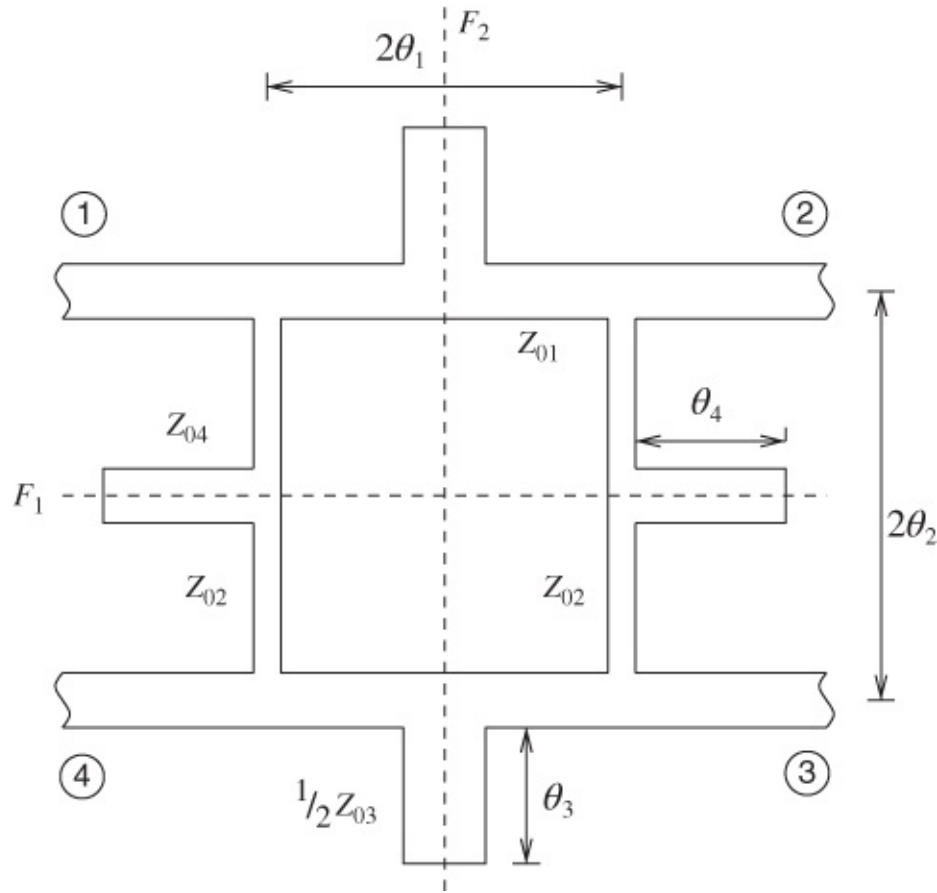


**Figure 12.15** Extended two-branch coupler with open stubs at the symmetry planes. Adapted from Mayer and Knochel (1990) [22], figure 2, p. 393. Reprinted with permission of IEEE.

Mayer and Knochel show that it is possible to increase the bandwidth from 10% with an unmodified coupler to more than 40% with the stub-modified device, whilst maintaining very

flat amplitude characteristics. These researchers also describe some more sophisticated broadband couplers and high-power in-phase power dividers [23]. An example of a broadbanded  $0^\circ/180^\circ$  coupler is shown in [Figure 12.16](#), where the stubs are clearly visible. A folded stub is used (with characteristic impedance  $Z_{06}$ ) for one of the inner arms of this design. The high-power dividers described use the all-reactive broadband principle already outlined and therefore avoid the problem of the resistive element required in the Wilkinson divider and the difficulty of restricted bandwidth associated with the Gysel circuit. Bandwidths around 50% are readily achievable. Others have also described various types of hybrid power dividers, but usually with resistive elements.

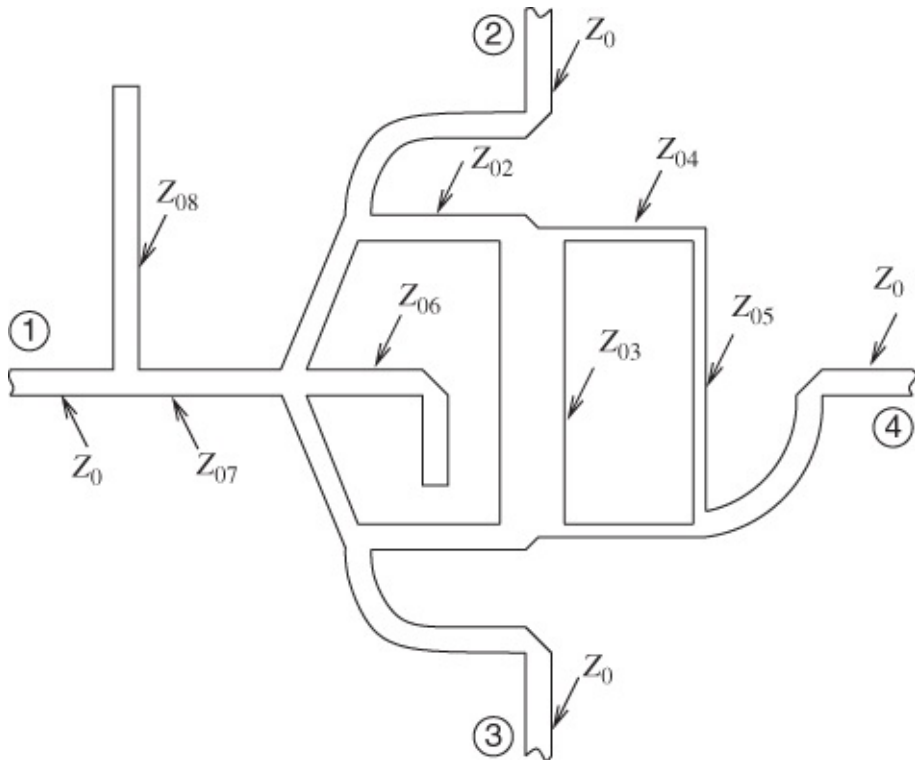


**Figure 12.16** Broadbanded  $0^\circ/180^\circ$  coupler. Adapted from Knochel and Mayer (1990) [23], figure 6, p. 473. Reprinted with permission of IEEE.

The branchline coupler principle is by no means restricted to microwave (below 30 GHz) applications and, for example, Meaney [24] described a novel design for millimeter-wave systems. Meaney points out that there are some problems with the direct use of microstrip in these types of application. In particular, there is the restricted range of realizable characteristic impedances required to avoid multimoding and excessive radiation. There is also the fact that as the frequency increases, so the aspect ratios of quarter-wavelength lines decrease, to the point where the physical lengths become comparable to the widths. This can be reduced by using very thin substrates and then there is a problem of higher losses and increased breakages during manufacture. This effect causes degradation of input match, bandwidth, and isolation. There are also problems associated with mutual coupling and discontinuities.

By using curved inner series lines, Meaney's design enables all input ports to be arranged orthogonally and the discontinuities are also mostly eliminated. This coupler is based on a three-branch structure to take advantage of the broadbanding effect of this topology, and it uses

three quarter-wavelength series lines together with quarter-wavelength parallel lines. Since the relatively long series lines are those with the lowest characteristic impedance, and therefore are the widest, so their aspect ratios are maintained at reasonable values. The coupler provides a nominal 3 dB insertion loss (varying between 2.7 and 4.7 dB) with good return loss and isolation performance over the 26–40 GHz band.

When using curved microstrip lines it is important to account accurately for the effect of line width. For example, Roy *et al.* [25] have shown that the design of rat-race hybrids is influenced markedly by the line width, and they develop an expression for a suitable modification of this width allowing accurate design.

Tokumitsu *et al.* [26] described a novel monolithic realization approach using 3 $\mu\text{m}$ -thick/three-layer dielectric films. They describe layered microstrip (thin-film microstrip), inverted microstrip, and also both normal and inverted “quasi-coplanar” transmission structures. They designed and built 12 GHz four-port Wilkinson power divider circuits using vertical connections, 15 GHz branchline couplers, and 20 GHz port-interchanged rat-race hybrids (using a line cross-over), all based on this technology. A more detailed exposition of the port-interchanged rat-race hybrid, shown in comparison with the conventional topology in [Figure 12.17](#), is presented in a separate paper by this group [27], where it is pointed out that the new version provides greater monolithic design flexibility. In addition, Tokumitsu *et al.* describe a six-stage distributed amplifier using thin-film microstrip.

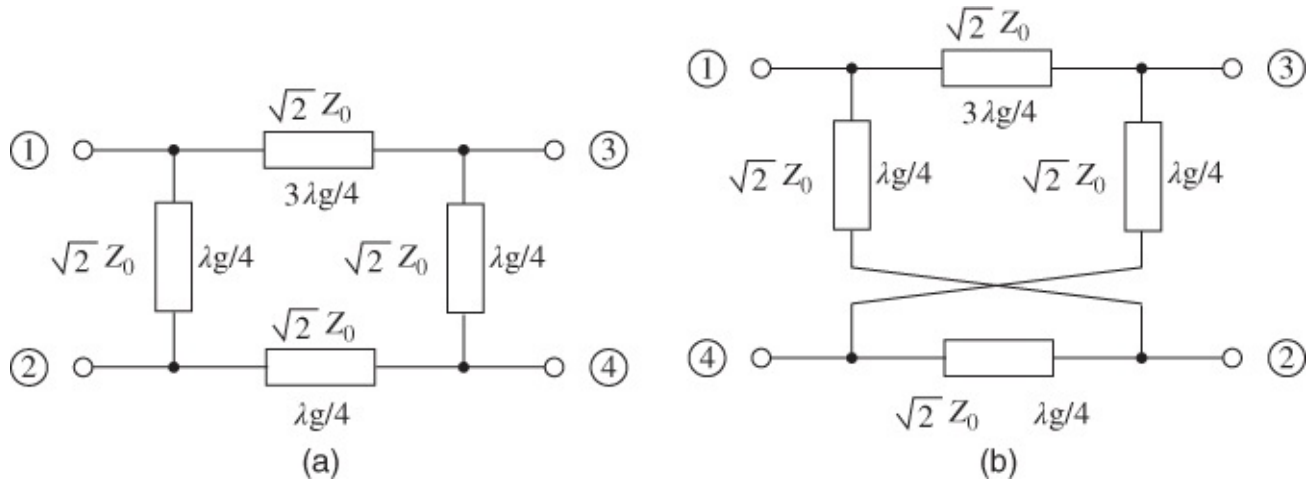


[Figure 12.17](#) Conventional and port-interchanged rat-race hybrids: (a) circuit diagram of a conventional rat-race hybrid; (b) circuit diagram of a port-interchanged rat-race hybrid. Adapted from Nakamoto *et al.* (1989) [27], figure 1, p. 314. Reprinted with permission of the European Microwave Association.

## 12.5.4 Rat-race Coupler

It is also worth considering the so-called rat-race circuit, or hybrid-ring, which is shown in [Figure 12.18](#). Output signals from ports 2 and 4 differ in phase by 180° (in contrast to the branch-line coupler, where the phase difference is 90°). An interesting and important design feature arises by considering the quarter-wave transformer action of this coupler. Only ports 2 and 4 exhibit this action because port 3 is half-wave separated from the input feeding port 1.

Thus, the net effective load on the inner ring lines feeding ports 2 and 4 amounts to  $2Z_0$  (two  $Z_0$  loads appearing, equivalently, in series). Now, the characteristic impedance  $Z_0$  of any quarter-wave-transforming line between two impedances  $Z_{01}$  and  $Z_{02}$  is known to equal  $\sqrt{Z_{01}Z_{02}}$ ; this result was developed in [Section 2.9](#). In this case, the two impedances are  $Z_0$  and  $2Z_0$ , respectively, so the impedance of the intervening quarter-wave line (i.e., the ring) must be

$$Z'_0 = \sqrt{Z_0 \cdot 2Z_0} \quad 12.8$$

or

$$Z'_0 = \sqrt{2}Z_0. \quad 12.9$$

Thus, the characteristic impedance of the line forming the ring itself must be  $\sqrt{2}$  times that of the feeder line impedances. Where the impedance of all feeders is  $50 \Omega$ , the ring characteristic impedance is therefore  $70.7 \Omega$ .

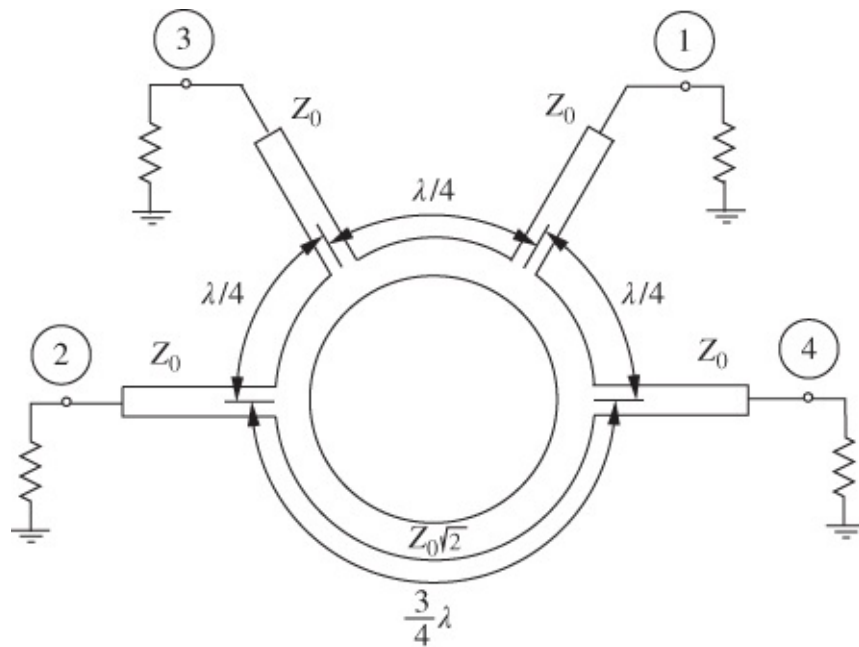


[Figure 12.18](#) Rat-race or hybrid-ring coupler.

#### 12.5.4.1 Broadband and Millimeter-wave Branchline Couplers

Considerable effort continues to be expended towards improving the design flexibility, expanding the bandwidth, and extending the upper frequency capability of branchline and similar couplers. For example, Wright and Judah [28] describe a particularly broadband hybrid ring with flat coupling, and Ashworth [29] developed design expressions for a two-branch broadband hybrid ring (or a two-branch guide) coupler of any coupling coefficient.

## 12.6 Power Combiners and Dividers

The two most commonly used power combiners or dividers are the Wilkinson combiner and

the Chireix combiner.

### 12.6.1 Wilkinson Combiner

While the Wilkinson combiner network can be used as either a combiner or a divider it is most commonly used as a power divider [30]. The basic Wilkinson divider is shown in [Figure 12.19\(a\)](#). In use as a divider, power entering from the left is split, ideally, equally with half of the original signal power appearing at each port on the right. The system impedance is  $50\Omega$  and the transmission lines perform the appropriate impedance transformations. If the tolerancing is ignored the signals presented at each of the two ports on the right-hand side are equal provided that each port is presented with the same load impedance. However, in the real world conditions are not perfectly symmetrical and the resistance  $2Z_0$  absorbs any unbalance. No power is absorbed by this resistor for the symmetrically split component of the output signal. When used as a combiner the two signals presented at the right need to have exactly the same amplitude and phase to be efficiently combined. This is in fact difficult to achieve, even to a small error, in practice.

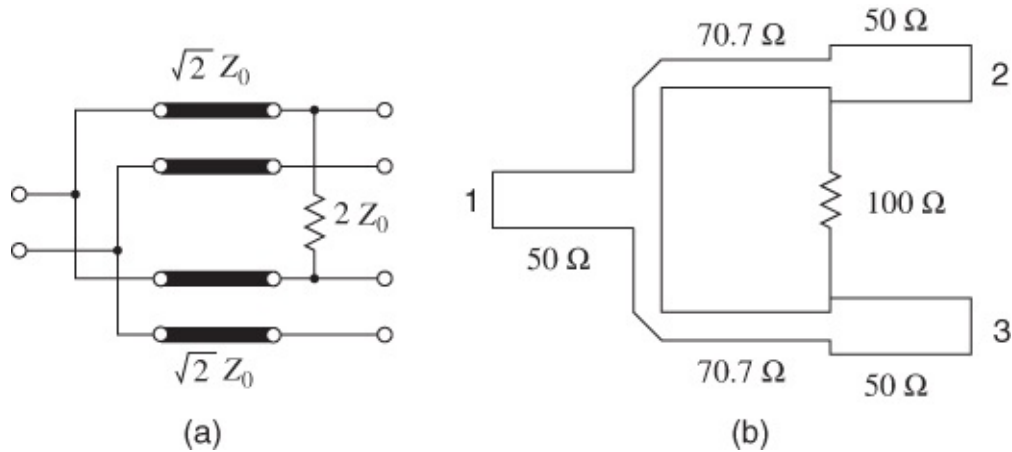


[Figure 12.19](#) Wilkinson combiner: (a) circuit schematic; and (b) microstrip implementation.

The form of the Wilkinson combiner shown in [Figure 12.19\(a\)](#) splits a signal into two equal signals. Arbitrary power ratios can also be obtained as well as multiway dividers [7, 31–33]. The microstrip realization of a Wilkinson divider is shown in [Figure 12.19\(b\)](#). The  $100\Omega$  resistor could be a surface-mounted component and is sometimes silk-screened or evaporated lossy material.

### 12.6.2 Chireix Combiner

An alternative to the Wilkinson combiner is the Chireix combiner, which is tolerant of phase and amplitude mismatch of the signals to be combined [34–37]. The Chireix combiner [38] is shown in [Figure 12.20](#). The transmission lines in the Chireix combiner are a quarter-wavelength long and have the characteristic impedance  $Z_0$ , which is also the system impedance.

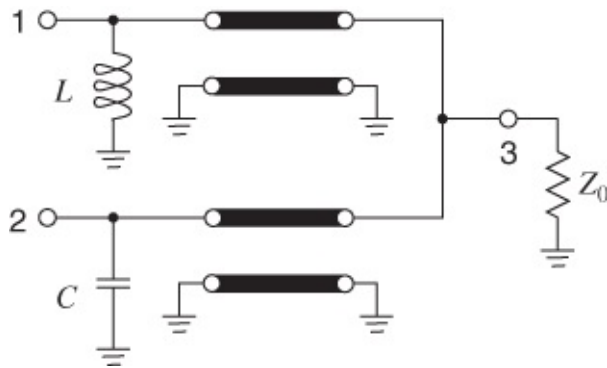


**Figure 12.20** Chireix combiner.

### 12.6.3 Branch-type Couplers and Power Dividers

Branch-type couplers have DC as well as microwave coupling, which is a significant difference compared to the characteristics of the couplers considered earlier. Although the inherent bandwidths of branch-type couplers are not particularly large (typically up to about 50%), they can be used for comparatively high microwave power transmission.

A branch-line directional coupler is shown in [Figure 12.21\(a\)](#), with the even- and odd-mode equivalent circuits given in [Figures 12.21\(b\)](#) and [\(c\)](#). The terms “even mode” and “odd mode” refer to the overall effects of having voltage nodes or voltage antinodes present at the branch- or main-line junctions, respectively. In [Figure 12.21\(a\)](#),  $\lambda_{gm}$  is the mid-band wavelength in the microstrip line.

Particularly significant properties of these couplers are as follows:

- a. Special-purpose chokes or filters may be connected into the joining branches, especially if these are made (say)  $3\lambda_{gm}/4$  in length rather than only  $\lambda_{gm}/4$ .
- b. High microwave power may be handled with very little danger of breakdown.
- c. They are well suited to tight coupling requirements:  $-3$  dB is feasible over a 50% bandwidth for a six-branch coupler, provided that a VSWR of about 1.2 is tolerable. (A 14-branch arrangement gives a VSWR of 1.05, but naturally occupies much more substrate area.)
- d. They may be used for the purpose of impedance transformation [39].

## 12.7 Baluns

Baluns can be realized using magnetic transformers and are available as surface-mount components at low microwave frequencies. Above a few gigahertz or so it is necessary to use transmission line baluns and the best of these is the Marchund balun.

### 12.7.1 Marchand Balun

The balun, a balanced-to-unbalanced transmission converter, was invented by Marchand in

1944 and has been available commercially in (mainly) coaxial form almost since then. Microstrip realizations of this type of circuit element are used in mixers, multipliers, Class B push-pull amplifiers, differential RF paths on RFICs, and antennas where balanced transmission line structures are needed to feed parts of the circuit, whereas unbalanced lines must then form the remainder of the circuit.

Baluns have been designed for both monolithic and non-monolithic integrated implementation. For example, Pavio and Kikel [40] report a compensated balun which provides an amplitude response that is flat within 1 dB over a 6–18 GHz bandwidth (both in hybrid and monolithic forms). Phase matching between the output arms is very good, being  $180^\circ \pm 2^\circ$ . The circuit construction is shown in [Figure 12.22](#), in which it can be seen that suspended substrate technology is avoided and the transformation is achieved by means of a multilayer conductor structure. Tight coupling is obtained by using a very thin second dielectric layer  $t_n$  and, for the monolithic balun, this is realized with a 2-micron thick layer of silicon nitride on the GaAs surface.

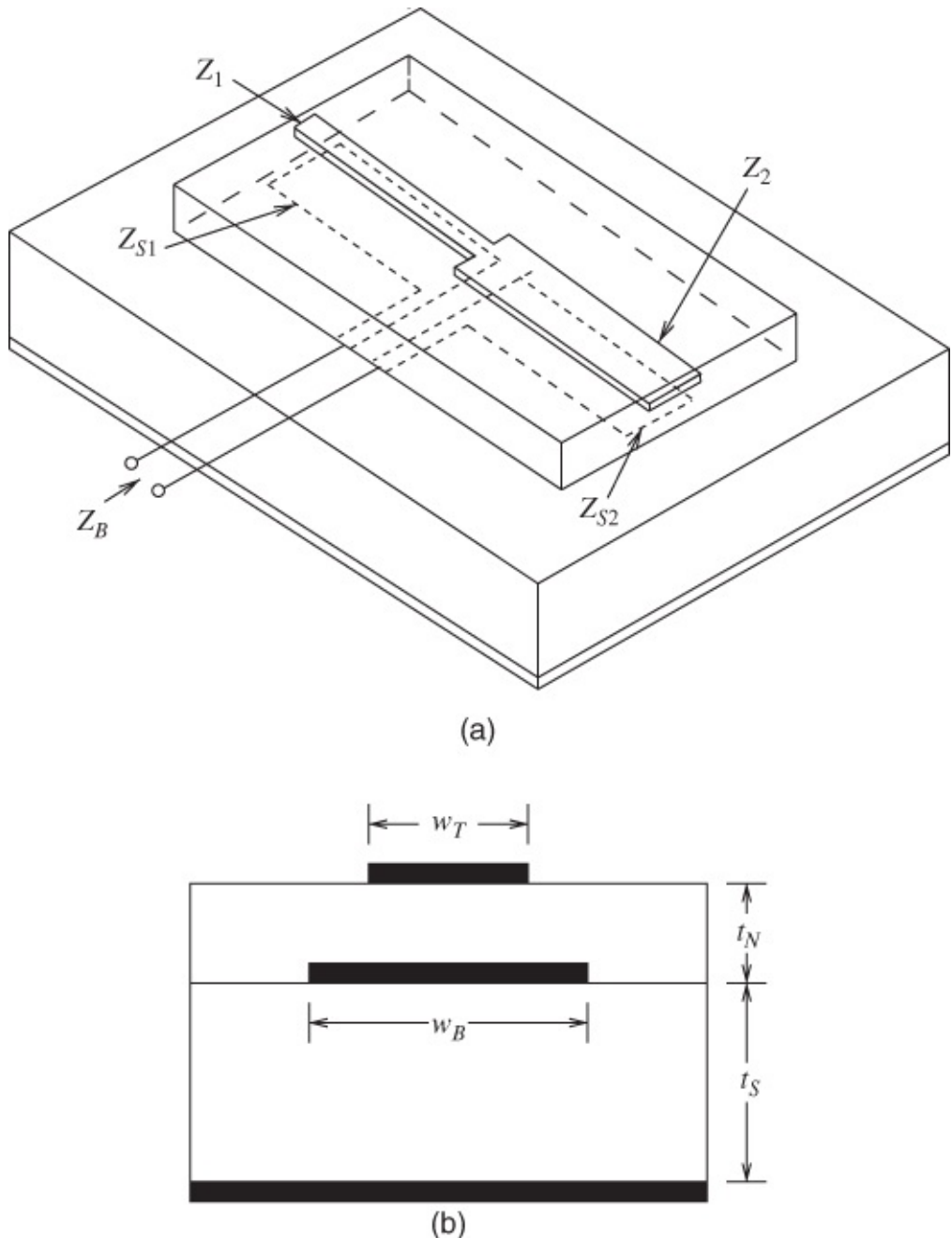
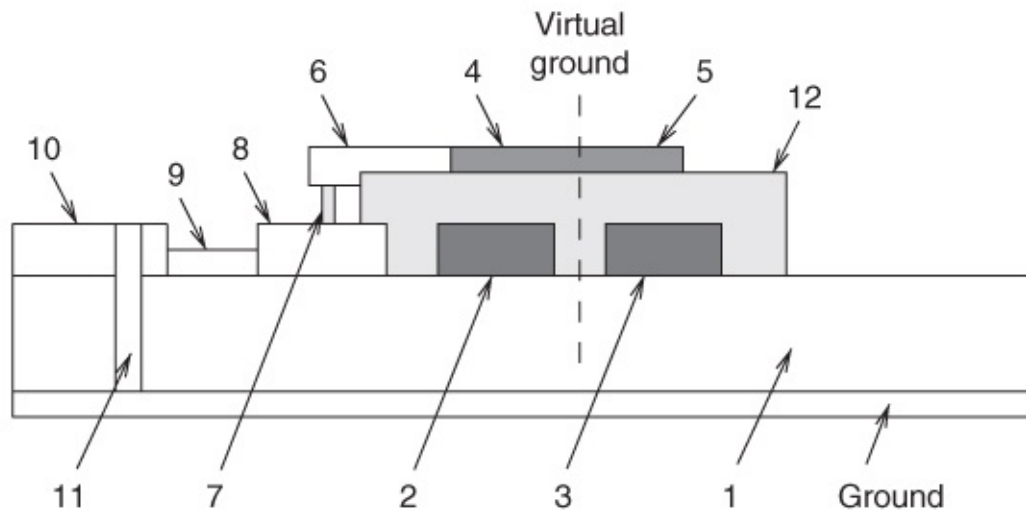
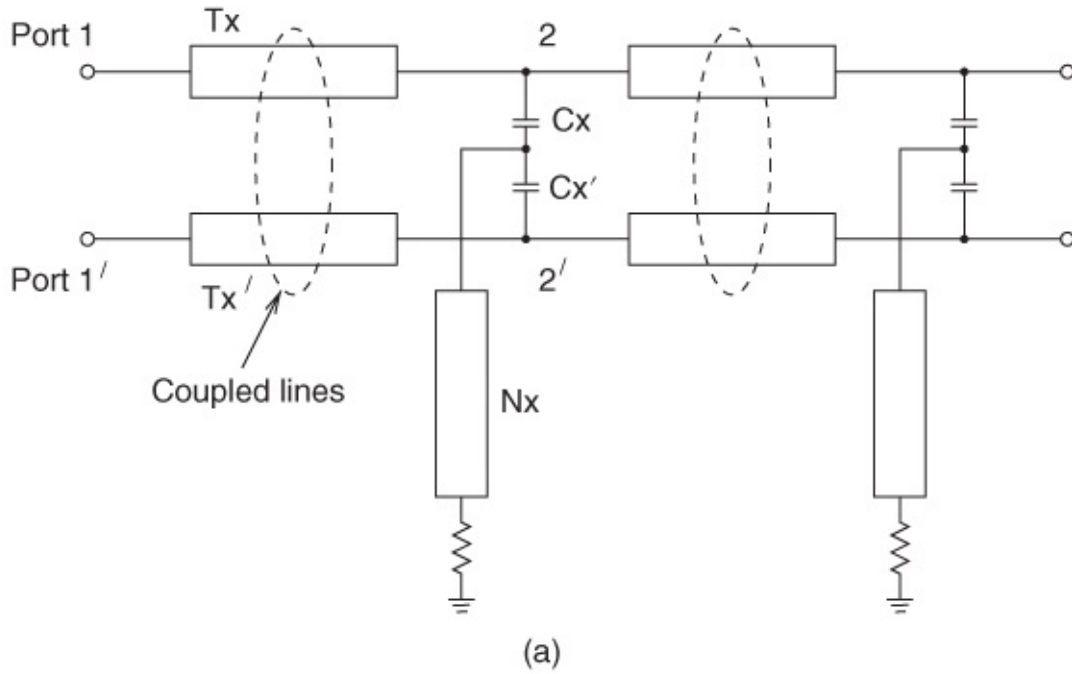


**Figure 12.22** Circuit construction and cross-sectional views of baluns: (a) circuit construction of monolithic or hybrid balun; and (b) typical balun structure cross-section. Adapted from Pavio and Kikel (1990) [40], figures 2 and 3, p. 484. Reprinted with permission of IEEE.

Barber [41] has described enhanced-coupled, even-mode-terminated baluns and also mixers using this technology. Barber's approach starts with the creation of a planar balun circuit cell which comprises a pair of coupled transmission lines, bridged at their outputs by a series-connected pair of capacitors. A final transmission line is connected from the center point between the capacitors to a load resistor, which is grounded. This overall structure forms one balun cell, the circuit and physical cross-section of which is shown in [Figure 12.23](#). To form a complete broadband balun typically eight of these cells are cascaded. One of the two input lines is fed whilst the opposite line is grounded (i.e., unbalanced) and the two outputs are left floating in balanced format. The capacitors are formed in overlay technology and the

appropriate line interconnections are made with vias.



- |   |                         |    |                           |
|---|-------------------------|----|---------------------------|
| 1 | Substrate               | 7  | Metal via                 |
| 2 | One of coupled lines Tx | 8  | Transmission line network |
| 3 | One of coupled lines Tx | 9  | Resistor                  |
| 4 | Capacitor Cx            | 10 | Ground                    |
| 5 | Capacitor Cx'           | 11 | Ground via                |
| 6 | Network interconnect Nx | 12 | Dielectric layer          |

(b)

**Figure 12.23** Planar baluns: circuit cell and cross-sections: (a) planar balun circuit cell; and (b) cross-section of a circuit cell. Adapted from Barber (1990) [41], figures 1 and 2, p. 496. Reprinted with permission of IEEE.

These baluns are designed to operate over the 2–26 GHz band, and Barber describes mixers

(restricted to the 2–18 GHz band) using this design approach. For the mixers the IF port is formed by diplexing the local oscillator and IF frequencies using reactive filtering. A Schottky monolithic quad of diodes forms the mixing function and the mixers exhibit conversion loss varying between 7 and 10 dB over the band. The entire mixer, incorporating a total of 16 balun cells, occupies a 6 mm square package.

## 12.8 Integrated Components

Distributed elements are based on transmission-line structures having linear dimensions which are a significant part of a wavelength, with a quarter-wavelength being a special length as resonant effects are then obtained. At 1 GHz, a quarter-wavelength long line is 3.8 cm in silicon dioxide, the medium in which a line is fabricated on a silicon chip. This reduces to 7.7 mm at 5 GHz. With GaAs, GaAs itself can be used as the transmission line medium, and these dimensions become 1.97 cm and 3.9 mm, respectively. These dimensions are too large for chips at the low end of the microwave spectrum (i.e., 5 GHz and below), and so lumped elements must be used. RF circuits require many passive components for matching networks, RF chokes for bias (i.e., inductors that block RF but provide a lossless DC connection), harmonic tuning, and to ensure stability at frequencies below the frequencies of operation. The primary lumped elements on RFICs are resistors, capacitors, and inductors.

Before commencing a discussion of lumped elements for RFICs we should point out one of the other distinguishing features of RFICs. This is the use of differential signaling for nearly all of the analog signals on-chip and not only for the RF paths. This is necessary to overcome the limitations of silicon MOSFET-based circuitry, including significant substrate coupling. This also utilizes the availability of complementary devices and differential circuits to remove many of the nonlinear effects that are manifest with single-sided circuit technologies using, for example, MESFETs, which are only available as n-type. Transmission line structures are rarely used on-chip at low microwave frequencies as there is insufficient room to realize distributed components which typically involve quarter-wavelength long lines. However, from an interconnect perspective the differential signaling requires that the RF connections to the chip also be differential and preferably use differential transmission lines.

### 12.8.1 On-chip Resistors

On-chip resistors can be obtained using doped-semiconductor regions, thin metal lines or, in the case of Si RFICs, polysilicon. The desired properties include good linearity, reasonable tolerance control, low parasitic capacitance, and low temperature coefficient. The operating temperature range required for RF products, such as cellular telephones, is broad, from  $-30^{\circ}\text{C}$  to  $+85^{\circ}\text{C}$ , with the end result being that resistor values are poorly controlled. All practical materials have significant resistivity variations with temperature over this range. However, resistor ratios are generally well controlled so there is a design preference for circuits whose functionality is determined by ratios. The properties of on-chip resistor technologies are summarized in [Table 12.1](#). In addition, specialized processes have been developed so that resistors can be made using nichrome (NiCr) or sichrome (SiCr), which have low temperature

coefficients (about 100 ppm/ $^{\circ}\text{C}$ ) and good tolerancing achieved using laser trimming. However, these are not generally available.

**Table 12.1** On-chip resistor properties. Material from Lee [42] and other sources.

Type	Resistivity ( $\Omega$ per square)	Toler- ance	Temp. coeff. (ppm/ $^{\circ}\text{C}$ )	Comment
Metal interconnect	0.01	35%	3900	Aluminum, small resistances up to 10 $\Omega$
Polysilicon, silicided	5–10	50%	1000	Small resistances
Polysilicon, unsilicided	50–100	35%	Variable	Poor tolerancing
Source drain diffusion	25–200	80%	2000	Generally ion implantation is used; large parasitic capacitance from semi-conductor junction; voltage dependence; limited to noncritical functions
Wells	1000–10000	80%	3000–5000	
MOS transistor	1000–10000	35%	very high	Voltage dependence

### 12.8.2 On-chip Capacitors

There are three primary forms of on-chip capacitor:

- metal-oxide-metal (MOM) capacitor, using the interconnect metallization
- metal-oxide-semiconductor (MOS) capacitor, essentially an MOS transistor
- semiconductor junction capacitor, either the capacitance of reverse biased  $pn$  junction or Schottky barrier.

The properties of these capacitors are presented in [Table 12.2](#).

**Table 12.2** On-chip capacitor properties. Material from Lee [42] and other sources [43–47]

Type	C (fF/ $\mu$ m <sup>2</sup> )	Toler- ance	Temp. coeff.	Comment
MOM	0.05	35%	50	Capacitance determined by geometry, low loss, good $Q$
MOS	1–5	$\geq$ 20%	30	High loss, low $Q$ , voltage dependent, strong temperature dependence
Junction	0.1–1.0	$\geq$ 20%	200–1000	Strong voltage and temperature dependence
				Range is for low leakage yielding high $Q$ capacitance and currently used doping levels

MOM capacitance can be realized as a parallel plate capacitance, but multiple levels of metallization can be used to increase the capacitance density. Relatively low capacitance values of up to 0.05 fF/ $\mu$ m<sup>2</sup> are available because of the large dielectric thickness of 0.25–1  $\mu$ m between metal layers. This thickness is required in normal interconnect circumstances to minimize interconnect-to-interconnect coupling so it is unlikely to change much. The distance between the bottom metallization layer to the substrate is comparable to the metal layer separation, and so the capacitance between the bottom plate of a capacitor and the substrate leads to significant capacitance, in the range of 10–30% of the metal-to-metal capacitance [42]. This series capacitor connection must be considered in design. Regions of high dielectric constant material, such as ferro-electrics, are used in memory chips to obtain high capacitance. This also results in a strongly nonlinear capacitance.

An alternative MOM capacitance is available using lateral arrangements of interconnects on the same layer. That is, adjacent metal structures are separated by a small horizontal gap. Again there are two distinct metal connections and a smaller metal separation can be obtained using photolithography than available using dielectric thickness. However, the capacitance density is only increased by a factor of around 3.

Both types of MOM capacitance, parallel-plate and lateral, are geometrically defined, are voltage independent, have very low temperature coefficients, and have initial fabrication tolerances of 20–30%. At intermediate frequencies, and potentially at RF frequencies, many analog designs (e.g., active filters) use transconductance tuning to achieve frequency-response precision. In these cases the capacitance tolerancing can be compensated for.

MOS capacitors use a MOS transistor with a parallel-plate capacitance between the gate of the transistor and a heavily inverted channel. The drain and source are connected in this configuration and the separation between the “conductors” is thin, being the gate oxide thickness. As technology progresses this will continue to thin. This leads to high values of capacitance although with weak voltage dependence. Junction capacitance is realized as the capacitance of a reverse-biased semiconductor junction. This capacitance can be quite large,

but has a strong voltage dependence. This voltage dependence can be utilized to realize tunable circuits, for example a voltage-controlled oscillator.

Lengths of low impedance transmission line can also be used to realize narrowband capacitances. The line lengths required are generally too long for integrated circuits, except at millimeter-wave frequencies (above 30 GHz), and so are most commonly used off-chip.

### 12.8.3 Planar Inductors

Inductors are important components in microwave circuits. In addition to their role in matching networks, they are used to provide bias to active devices while effectively blocking RF signals from the bias circuitry. Inductors of up to 10 nH can be fabricated on-chip. Inductors with values above this would consume too much die area and so either the entire inductance, or the majority of the required inductance, is obtained from an off-chip inductor, often as part of the RFIC package. Bond wires can also be used to realize small inductances in the 0.5–1 nH range. The advantage of having a portion of a large inductance on-chip is reduced sensitivity to die attach (bond-wire, etc.) connections.

An on-chip spiral inductor, the most common type, is shown in [Figure 12.3](#) in both plan and side views. An expression for the inductance of this structure was developed by Wheeler [48]:

$$L \approx \frac{9.4\mu_0 n^2 a^2}{11d - 7a} \quad 12.10$$

where  $a$  and  $d$  are defined in [Figure 12.3](#), and  $n$  is the number of turns. This formula was derived for circular coils, but its accuracy for square spirals has been determined by Lee [42] to be within 5% of values derived using electromagnetic simulation. It is therefore a very useful formula in the early stages of design, but electromagnetic analysis is required to obtain the necessary accuracy in design.

Fields produced by the spiral inductor penetrate the substrate, and as a ground plane is located at a relatively short distance, the eddy currents on the ground plane reduce the inductance that would otherwise be obtained. The eddy current in the ground conductor rotates in a direction opposite to that of the spiral itself (i.e., counterclockwise opposing clockwise). As a result, the inductance of the image inductor in the ground is in the opposite direction to that produced by the spiral itself, with the consequent effect that the effective total inductance is reduced. By creating a broken, or perforated, conductor pattern the ground inductance is largely eliminated [49]. Thus, with care, reasonably good inductors, with high  $Q$ , can be realized on GaAs chips as the GaAs substrate is semi-insulating. The situation is different with silicon because of the finite conductivity of silicon substrates, which therefore supports eddy currents.

One of the major sources of loss for inductors on silicon is substrate loss due to the finite conductivity of the substrate and the resulting current flow. These induced currents follow a path under the conductors of the spiral and, just as with ground plane eddy currents, lower the inductance achieved, Mernyei *et al.* [50] proposed a scheme to reduce substrate eddy currents. Most silicon substrates are at least slightly doped, usually of p-type. With heavily doped n-type

strips arranged radially from the centre axis of the spiral, the eddy currents are blocked. They achieved an increase of the  $Q$  from 5.3 to 6.0 at 3.5 GHz and from 4.3 to 4.5 at 2.0 GHz. In the spiral inductor model the effect was also to reduce the shunt resistance and capacitance to the substrate.

Parasitic capacitance results in resonance of the on-chip inductance structure and hence limits the frequency of operation. With GaAs ( $\epsilon_r = 12.85$ ) the effective permittivity of the medium can be reduced by adding a polyimide layer ( $\epsilon_r = 3.2$ ) and using metallization on top of this layer [51]. Thus, the capacitance is substantially reduced. This is at the cost of poorer thermal management as the thermal conductivity of polyimide is substantially lower (about 100 times) than that of GaAs, and so the power-handling capability is compromised. Coupling this with thicker metallization to reduce resistance can result in a  $Q$  that is 50% larger and a self-resonant frequency that is 25% higher [51].

We now return to the issue of the finite conductivity of the silicon substrate. The induction of charges in the silicon and the insignificant skin depth of the silicon substrate has the effect of increasing the capacitance of an interconnect line over silicon as the electric field lines are terminated on the substrate charges. (This effect is in addition to the induction of eddy currents in the substrate as discussed earlier.) Now the magnetic field lines penetrate some distance into the substrate so that the  $LC$  product is greater than if the substrate was insulating (as with GaAs). The effect is that the velocity of propagation along the interconnect ( $= 1/\sqrt{LC}$ ) is reduced, leading to what is called the slow wave effect. This means that very small inductances can be realized using short lengths of interconnect arranged so that fields, particularly the magnetic field, penetrate the substrate. This effect can be adequately simulated using planar electromagnetic simulators that allow the conductivity of mediums to be specified. Simulation is necessary as the effect is a complex function of geometry and substrate conductivity, and generalizations available for use in design are not available.

The lowest loss inductors are obtained by etching away the underlying substrate or by using insulating or very high resistivity bulk material. Loss is also reduced by separating the planar inductor from the ground plane and additional dielectric layers have been deposited on a chip to achieve this [52]. When all steps have been taken the dominant loss mechanism is current crowding [53]. This is a particular problem with multturn inductors, which are required to realize high inductance values. Current crowding results when the magnetic field of one turn penetrates an adjacent trace, creating eddy currents so that current peaks on the inside edge of the victim trace (towards the center of the spiral) and reduces on the outside edge. This constricts current and results in higher resistance than would be predicted from skin effect and DC resistance alone [53].

Planar inductors are often fabricated in close proximity to each other. The coupling of adjacent planar inductors depends on the separation of the inductors, shielding, geometry, and the resistivity of the underlying substrate. An effective measure of shielding is to use a discontinuous guard ring [54]. This, however, reduces the originally designed inductance values because of the image currents induced in the ring [55].

Lengths of high impedance transmission line can also be used to realize narrowband

inductance. The line lengths required are generally too long for integrated circuits, except at millimeter-wave frequencies (above 30 GHz), and so are most commonly used off-chip.

The properties of on-chip inductor realizations are summarized in [Table 12.3](#).

**Table 12.3** Inductance and  $Q$  of planar inductors:  $d$  is the side-dimension shown in [Figure 12.3\(a\)](#),  $n$  is the number of turns,  $L$  and  $Q_{\max}$  are at  $f_0$ ,  $f_0$  is the operating frequency, and  $f_{SR}$  is the self-resonant frequency.  $Mn$  indicates the metal layer used. Adapted in part from Burghartz [79].

Type	Ref. year	$d$ ( $\mu$ m)	$n$	$L$ (nH)	$Q_{\max}$ @ $f_0$	$f_0$ (GHz)	$f_{SR}$ (GHz)
M2 on Si	[49] 1997	280	6	8	7	1.8	3.5
M2 on Si	[50] 1998	—	2	1.8	6.0	3.5	—
MLS on GaAs	[51] 2000	440	23	6.7	33	6.4	7
M3/M2/M1 <sup>1</sup> on $p^-$ -Si	[56] 1995	226	3	1.45	24	2.3	>20
MLS on $p^-$ -Si	[57] 1996	226	8	6.8	7.8	1.3	5.6
M3 on $p^-$ -Si	[58] 1996	400	6	10.2	7.5	1	8
M3/M2/M1 on $n$ -well Si	[59] 1997	145	$9\frac{1}{4}$	6	2.6	1.5	5.8
MLS on $p^-$ -Si	[60] 1995	150	3	15.5	2.64	0.42	—
M2 on $p^-$ -Si	[61] 1990	230	9	9.7	3	0.9	2.5
M3/M2/M1 on $p^-$ -Si	[62] 1995	226	4	2.1	9.3	2.4	20
6 $\mu$ m Au on HRS	[63] 1994	300	2	2.88	12	3.2	>10
2.5 $\mu$ m on sapphire	[64] 1996	226	3	1.45	40	5.8	>20
4 $\mu$ m Cu on quartz	[65] 1998	226	3	1.5	60	5	>20
M2 on suspended substrate	[66] 1983	440	20	100	—	—	2.9
3.5 $\mu$ m Al on glass	[67] 1997	600	2	2.6	39	4.3	10.5
M2 on SOS	[68] 1996	150	5	4	11.9	3.0	13.9
4 $\mu$ m Al on HRS	[69, 70] 1997	290	8	12.0	15.3	3.25	9.0
M2 on suspended substrate	[71] 1996	200	4	1.1	28	18	84
1.5 $\mu$ m Cu suspended above cavity on Si	[72] 2000	265	7	10.4	30	8.0	10.1
4 $\mu$ m AlCu on polyimide on Si	[52] 2000	—	$3\frac{1}{2}$	1.1	18	10	—
3 $\mu$ m Al on ferro- magnetic thin-film on Si	[73] 2000	337	$4\frac{1}{4}$	7.2	7	1	1.3
20 $\mu$ m Al on Si	[74] 2000	500	$2\frac{1}{2}$	4.2	21	2.47	8.1
Si with 600 nm magnetic thin film	[75] 2013	—	—	8	17	8	>10
8 $\mu$ m Cu on glass (3DIC)	[76] 2013	480	3.5	6	29	4	>10

8 $\mu\text{m}$ Cu on glass (3DIC)	[76] 2013	260	1.5	2.25	36	2.5	>10
8 $\mu\text{m}$ Cu on Si	[76] 2013	260	1.5	2.25	22	2.5	8
Toroid, 8 $\mu\text{m}$ Ag/Cu/Au on Si, 3DIC	[8] 2004	1020	—	2.5	22	1.5	>10
Solenoid, Cu (3DIC)	[77, 9] 2007	225	3	1.9	30	3	>10
Solenoid (3DIC)	[78] 2013	800	10	6	3.5	2	4
Solenoid (3DIC) with magnetic film	[78] 2013	800	10	8	3.5	2	4

<sup>1</sup> Metallization levels of the multilevel interconnects. MLS, a multi-layer stacked coil inductor made using multilevel interconnects; SOS, silicon on sapphire; 3DIC, multilayer (usually Si) stack with inductor on passive layer.

## 12.9 Summary

Passive circuit components for use in planar transmission-line-based circuits can be realized using lumped elements, especially surface-mount components, and distributed structures. Surface-mount components are convenient to use at low microwave frequencies where their transmission line-based equivalents would be too large. Many of the transmission line components make use of quarter-wavelength long sections of transmission line. Either they use the line's impedance transforming property, the Wilkinson divider circuit is a good example, or a line's phase-rotation property, with branch-line couplers being a good example. Even with good computer-based EM analysis tools it is often necessary to characterize components experimentally because of permittivity variations and finite dimensional tolerances of microstrip and other planar lines [80, 81].

## References

- [1] T. Lee, *The Design of CMOS Radio-Frequency Integrated Circuits*. Cambridge University Press, 2004.
- [2] J. Nath, D. Ghosh, J. Maria, M. Steer, A. Kingon, and G. Stauf, “Microwave properties of bst thin film interdigital capacitors on low cost alumina substrates,” in *34th European Microwave Conf.*, vol. 3, 2004, pp. 1497–1500.
- [3] D. Ghosh, B. Laughlin, J. Nath, A. Kingon, M. Steer, and J. Maria, “High Q (Ba, Sr) TiO<sub>3</sub> (3 subscript) interdigitated capacitors fabricated on low cost polycrystalline alumina substrates with copper metallization,” *Advances in Electronic Ceramic Materials: Ceramic Engineering and Science Proc.*, vol. 26, no. 5, pp. 125–132, 2005.
- [4] J. Nath, D. Ghosh, J. Maria, A. Kingon, W. Fathelbab, P. Franzon, and M. Steer, “An electronically tunable microstrip bandpass filter using thin-film barium-strontium-titanate (BST) varactors,” *IEEE Trans. on Microwave Theory and Techniques*, vol. 53, no. 9, pp. 2707–2712, 2005.
- [5] D. Ghosh, B. Laughlin, J. Nath, A. Kingon, M. Steer, and J. Maria, “Tunable high-quality-

factor interdigitated (Ba, Sr) TiO<sub>3</sub> capacitors fabricated on low-cost substrates with copper metallization," *Thin Solid Films*, vol. **496**, no. 2, pp. 669–673, 2006.

[6] V. Haridasan, P. Lam, Z. Feng, W. Fathelbab, J. Maria, A. Kingon, and M. Steer, "Tunable ferroelectric microwave bandpass filters optimised for system-level integration," *Proc. IET Microwaves, Antennas & Propagation*, vol. 5, no. 10, pp. 1234–1241, 2011.

[7] M. Steer, *Microwave and RF Design: a Systems Approach*, 2nd ed. SciTech Pub., 2013.

[8] W. Liu, J. Suryanarayanan, J. Nath, S. Mohammadi, L. Katehi, and M. Steer, "Toroidal inductors for radio-frequency integrated circuits," *IEEE Trans. on Microwave Theory and Techniques*, vol. **52**, no. 2, pp. 646–654, Feb. 2004.

[9] Z. Feng, C. Bower, J. Carlson, M. Lueck, D. Temple, and M. Steer, "High-Q solenoidal inductive elements," in *2007 IEEE MTT-S Int. Microwave Symp.*, 2007, pp. 1905–1908.

[10] Z. Feng, M. Lueck, D. Temple, and M. Steer, "High-performance solenoidal RF transformers on high-resistivity silicon substrates for 3D integrated circuits," *IEEE Trans. on Microwave Theory and Techniques*, vol. **60**, no. 7, Jul. 2012, pp. 2066–2072.

[11] S. H. Li, C. S. Lin, P. L. Tseng, P. J. Tzeng, S. S. Sheu, S. H. Hsu, C. H. Wang, W. C. Lo, and T. K. Ku. "Fully 3-D symmetrical TSV monolithic transformer for RFIC," in *2015 IEEE Electronic Components and Technology Conference*, pp. 987–993, 2015.

[12] D. Lacombe and J. Cohen, "Octave-band microstrip DC blocks," *IEEE Trans. on Microwave Theory and Techniques*, vol. **20**, no. 8, pp. 555–556, Aug. 1972.

[13] D. Rickard, "Thick film MIC components in the range 10–20 GHz," in *6th European Microwave Conf.*, Sep. 1976, pp. 687–691.

[14] H. Finlay, L. Hopkins, and J. Ozamiz, "Design and applications of precision microstrip multioctave attenuators and loads," in *6th European Microwave Conf.*, Sep. 1976, pp. 692–696.

[15] J. Wilkerson, K. Gard, and M. Steer, "Electro-thermal passive intermodulation distortion in microwave attenuators," in *36th European Microwave Conf.*, Sep. 2006, pp. 157–160.

[16] J. Wilkerson, K. Gard, A. Schuchinsky, and M. Steer, "Electro-thermal theory of intermodulation distortion in lossy microwave components," *IEEE Trans. on Microwave Theory and Techniques*, vol. **56**, no. 12, pp. 2717–2725, Dec. 2008.

[17] J. Wilkerson, P. Lam, K. Gard, and M. Steer, "Distributed passive intermodulation distortion on transmission lines," *IEEE Trans. on Microwave Theory and Techniques*, vol. **59**, no. 5, pp. 1190–1205, May 2011.

[18] M. Steer and P. Khan, "Wideband equivalent circuits for radial transmission lines," *IEE Proceedings, Part H, Microwaves, Optics and Antennas*, vol. **128**, no. 2, pp. 111–113, 1981.

- [19] F. Giannini, R. Sorrentino, and J. Vrba, “Planar circuit analysis of microstrip radial stub,” *IEEE Trans. on Microwave Theory and Techniques*, vol. **32**, no. 12, pp. 1652–1655, Dec. 1984.
- [20] F. Giannini, C. Paoloni, and M. Ruggieri, “Cad-oriented lossy models for radial stubs,” *IEEE Trans. on Microwave Theory and Techniques*, vol. **36**, no. 2, pp. 305–313, Feb. 1988.
- [21] M. Rittweger and I. Wolff, “Analysis of complex passive (M)MIC-component using the finite difference time-domain approach,” in *1990 IEEE MTT-S Int. Microwave Symp. Digest*, May 1990, pp. 1147–1150.
- [22] B. Mayer and R. Knochel, “Branchline-couplers with improved design flexibility and broad bandwidth,” in *1990 IEEE MTT-S Int. Microwave Symp. Digest*, May 1990, pp. 391–394.
- [23] R. Knochel and B. Mayer, “Broadband printed circuit 0°/1800° couplers and high power inphase power dividers,” in *1990 IEEE MTT-S Int. Microwave Symp. Digest*, May 1990, pp. 471–474.
- [24] P. Meaney, “A novel branch-line coupler design for millimeter-wave applications,” in *1990 IEEE MTT-S Int. Microwave Symp. Digest*, May 1990, pp. 585–588.
- [25] J. S. Roy, “Analysis of curved microstrip transmission lines and its applications,” in *Proc. 2nd Int. Symp. on Recent Advances in Microwave Techniques (ISRAMT '89)*. Int. Academic Publishers, Sep. 1989.
- [26] T. Tokumitsu, T. Hiraoka, H. Nakamoto, and T. Takenaka, “Multilayer MMIC using a 3 μm × 3-layer dielectric film structure,” in *1990 IEEE MTT-S Int. Microwave Symp. Digest*, May 1990, pp. 831–834.
- [27] H. Nakamoto, T. Tokumitsu, and M. Aikawa, “A monolithic, port-interchanged rat-race hybrid using a thin film microstrip line crossover,” in *19th European Microwave Conf.*, Sep. 1989, pp. 311–316.
- [28] A. Wright and S. Judah, “Very broadband flat coupling hybrid ring,” *Electronics Letters*, vol. **23**, no. 1, pp. 47–49, 1987.
- [29] J. Ashforth, “Design equations to realise a broadband hybrid ring or a two-branch guide coupler of any coupling coefficient,” *Electronics Letters*, vol. **24**, no. 20, pp. 1276–1277, Sep. 1988.
- [30] E. Wilkinson, “An n-way hybrid power divider,” *IRE Trans. on Microwave Theory and Techniques*, vol. **8**, no. 1, pp. 116–118, Jan. 1960.
- [31] Y.-L. Wu, H. Zhou, Y.-X. Zhang, and Y.-A. Liu, “An unequal wilkinson power divider for a frequency and its first harmonic,” *IEEE Microwave and Wireless Components Letters*, vol. **18**, no. 11, pp. 737–739, Nov. 2008.

- [32] S. Oh, J.-J. Koo, M.-S. Hwang, C. Park, Y.-C. Jeong, J.-S. Lim, K.-S. Choi, and D. Ahn, “An unequal wilkinson power divider with variable dividing ratio,” in *2007 IEEE MTT-S Int. Microwave Symp. Dig.*, Jun. 2007, pp. 411–414.
- [33] J.-S. Lim, S.-W. Lee, C.-S. Kim, J.-S. Park, D. Ahn, and S. Nam, “A 4:1 unequal wilkinson power divider,” *IEEE Microwave and Wireless Components Letters*, vol. **11**, no. 3, pp. 124–126, Mar. 2001.
- [34] I. Hakala, D. Choi, L. Gharavi, N. Kajakine, J. Koskela, and R. Kaunisto, “A 2.14-GHz chireix outphasing transmitter,” *IEEE Trans. on Microwave Theory and Techniques*, vol. **53**, no. 6, pp. 2129–2138, Jun. 2005.
- [35] F. Raab, “Efficiency of outphasing RF power-amplifier systems,” *IEEE Trans. on Communications*, vol. **33**, no. 10, pp. 1094–1099, Oct. 1985.
- [36] S. Moloudi, K. Takinami, M. Youssef, M. Mikhemar, and A. Abidi, “An outphasing power amplifier for a software-defined radio transmitter,” in *IEEE Int. Solid-State Circuits Conf., 2008 (ISSCC 2008) Dig. of Technical Papers*, Feb. 2008, pp. 568–636.
- [37] W. Gerhard and R. Knoechel, “Novel transmission line combiner for highly efficient outphasing RF power amplifiers,” in *37th European Microwave Conf.*, Oct. 2007, pp. 1433–1436.
- [38] H. Chireix, “High power outphasing modulation,” *Proc. of the Institute of Radio Engineers*, vol. **23**, no. 11, pp. 1370–1392, Nov. 1935.
- [39] C.-H. Ho, L. Fan, and K. Chang, “Broad-band uniplanar hybrid-ring and branch-line couplers,” *IEEE Trans. on Microwave Theory and Techniques*, vol. **41**, no. 12, pp. 2116–2125, Dec. 1993.
- [40] A. Pavio and A. Kikel, “A monolithic or hybrid broadband compensated balun,” in *1990 IEEE MTT-S Int. Microwave Symp. Digest*, May 1990, pp. 483–486.
- [41] R. Barber, “Enhanced coupled, even mode terminated baluns and mixers constructed therefrom,” in *1990 IEEE MTT-S Int. Microwave Symp. Digest*, May 1990, pp. 495–498.
- [42] T. H. Lee, *The Design of CMOS Radio-Frequency Integrated Circuit*. Cambridge University Press, 1998.
- [43] J. McCreary, “Matching properties, and voltage and temperature dependence of MOS capacitors,” *IEEE Journal of Solid-State Circuits*, vol. **16**, no. 6, pp. 608–616, Dec. 1981.
- [44] C. Yuan and T. Trick, “A simple formula for the estimation of the capacitance of two-dimensional interconnects in VLSI circuits,” *IEEE Electron Device Letters*, vol. **3**, no. 12, pp. 391–393, Dec. 1982.
- [45] E. Barke, “Line-to-ground capacitance calculation for VLSI: a comparison,” *IEEE Trans. on Computer-Aided Design of Integrated Circuits and Systems*, vol. **7**, no. 2, pp. 295–298,

Feb. 1988.

- [46] T. Sakurai and K. Tamaru, “Simple formulas for two- and three-dimensional capacitances,” *IEEE Trans. on Electron Devices*, vol. **30**, no. 2, pp. 183–185, Feb. 1983.
- [47] N. Meijs and J. T. Fokkema, “VLSI circuit reconstruction from mask topology,” *Integration, the VLSI Journal*, vol. **2**, no. 2, pp. 85–11, 1984.
- [48] H. Wheeler, “Simple inductance formulas for radio coils,” *Proc. of the Institute of Radio Engineers*, vol. **16**, no. 10, pp. 1398–1400, Oct. 1928.
- [49] C. Yue and S. Wong, “On-chip spiral inductors with patterned ground shields for Si-based RF ICs,” *IEEE J. of Solid-State Circuits*, vol. **33**, no. 5, pp. 743–752, May 1998.
- [50] F. Mernyei, F. Darrer, M. Padoen, and A. Sibrai, “Reducing the substrate losses of RF integrated inductors,” *IEEE Microwave and Guided Wave Letters*, vol. **8**, no. 9, pp. 300–301, Sep. 1998.
- [51] I. J. Bahl, “High current handing capacity multilayer inductors for RF and microwave circuits,” *Int. J. RF and Microwave Computer-Aided Engineering*, vol. **10**, no. 2, pp. 139–146, Mar. 2000.
- [52] R. Volant, R. Groves, J. Malinowski, S. Subbanna, E. Begle, D. Laney, L. Larson, G. Sakamoto, and P. Chan, “Fabrication of high frequency passives on BiCMOS silicon substrates,” in *2000 IEEE MTT-S Int. Microwave Symp. Digest*, Jun. 2000, pp. 209–212.
- [53] W. Kuhn and N. Ibrahim, “Approximate analytical modeling of current crowding effects in multi-turn spiral inductors,” in *2000 IEEE MTT-S Int. Microwave Symp. Digest*, Jun. 2000, pp. 405–408.
- [54] A. Pun, T. Yeung, J. Lau, J. Clement, and D. Su, “Substrate noise coupling through planar spiral inductor,” *IEEE Journal of Solid-State Circuits*, vol. **33**, no. 6, pp. 877–884, Jun. 1998.
- [55] C. Kim, M. Park, C.-H. Kim, M.-Y. Park, S.-D. Kim, Y.-S. Youn, J.-W. Park, S.-H. Han, H. Yu, and H. Cho, “Design guide of coupling between inductors and its effect on reverse isolation of a CMOS LNA,” in *2000 IEEE MTT-S Int. Microwave Symp. Digest*, Jun. 2000, pp. 225–230.
- [56] J. Burghartz, M. Soyuer, K. Jenkins, and M. Hulvey, “High-Q inductors in standard silicon interconnect technology and its application to an integrated RF power amplifier,” in *Int. Electron Devices Meeting*, Dec. 1995, pp. 1015–1018.
- [57] J. Burghartz, K. Jenkins, and M. Soyuer, “Multilevel-spiral inductors using VLSI interconnect technology,” *IEEE Electron Device Letters*, vol. **17**, no. 9, pp. 428–430, Sep. 1996.
- [58] R. Groves, K. Stein, D. Harame, and D. Jadus, “Temperature dependence of Q in spiral inductors fabricated in a silicon-germanium/BiCMOS technology,” in *Proc. 1996*

*Bipolar/BiCMOS Circuits and Technology Meeting*, 1996, pp. 153–156.

- [59] K. Kim and K. O, “Characteristics of an integrated spiral inductor with an underlying n-well,” *IEEE Trans. on Electron Devices*, vol. **44**, no. 9, pp. 1565–1567, Sep. 1997.
- [60] R. Merrill, T. Lee, H. You, R. Rasmussen, and L. Moberly, “Optimization of high Q integrated inductors for multi-level metal CMOS,” in *Int. Electron Devices Meeting*, Dec. 1995, pp. 983–986.
- [61] N. Nguyen and R. Meyer, “Si IC-compatible inductors and LC passive filters,” *IEEE Journal of Solid-State Circuits*, vol. **25**, no. 4, pp. 1028–1031, Aug. 1990.
- [62] M. Soyuer, J. Burghartz, K. Jenkins, S. Ponnappalli, J. Ewen, and W. Pence, “Multilevel monolithic inductors in silicon technology,” *Electronics Letters*, vol. **31**, no. 5, pp. 359–360, Mar. 1995.
- [63] K. Ashby, I. Koullias, W. Finley, J. Bastek, and S. Moinian, “High Q inductors for wireless applications in a complementary silicon bipolar process,” *IEEE Journal of Solid-State Circuits*, vol. **31**, no. 1, pp. 4–9, Jan. 1996.
- [64] J. Burghartz, D. Edelstein, K. Jenkins, C. Jahnes, C. Uzoh, E. O’Sullivan, K. Chan, M. Soyuer, P. Roper, and S. Cordes, “Monolithic spiral inductors fabricated using a VLSI Cu-damascene interconnect technology and low-loss substrates,” in *1996 Int. Electron Devices Meeting*, Dec. 1996, pp. 99–102.
- [65] J. Burghartz, D. Edelstein, M. Soyuer, H. Ainspan, and K. Jenkins, “RF circuit design aspects of spiral inductors on silicon,” *IEEE Journal of Solid-State Circuits*, vol. **33**, no. 12, pp. 2028–2034, Dec. 1998.
- [66] J.-C. Chang, A. Abidi, and M. Gaitan, “Large suspended inductors on silicon and their use in a 2- $\mu\text{m}$  CMOS RF amplifier,” *IEEE Electron Device Letters*, vol. **14**, no. 5, pp. 246–248, May 1993.
- [67] R. Dekker, P. Baltus, M. van Deurzen, W. Einden, H. Maas, and A. Wagemans, “An ultra low-power RF bipolar technology on glass,” in *1997 Int. Electron Devices Meeting*, Dec. 1997, pp. 921–923.
- [68] R. Johnson, C. Chang, P. Asbeck, M. Wood, G. Garcia, and I. Lagnado, “Comparison of microwave inductors fabricated on silicon-on-sapphire and bulk silicon,” *IEEE Microwave and Guided Wave Letters*, vol. **6**, no. 9, pp. 323–325, Sep. 1996.
- [69] M. Park, C. S. Kim, J. M. Park, H. K. Yu, and K. S. Nam, “High Q microwave inductors in CMOS double-metal technology and its substrate bias effects for 2 GHz RF ICs application,” in *1997 Int. Electron Devices Meeting*, Dec. 1997, pp. 59–62.
- [70] M. Park, S. Lee, H. K. Yu, J. G. Koo, and K. S. Nam, “High Q CMOS-compatible microwave inductors using double-metal interconnection silicon technology,” *IEEE*

*Microwave and Guided Wave Letters*, vol. 7, no. 2, pp. 45–47, Feb. 1997.

- [71] Y. Sun, H. Van Zejl, J. Tauritz, and R. Baets, “Suspended membrane inductors and capacitors for application in silicon MMIC's,” in *IEEE 1996 Microwave and Millimeter-Wave Monolithic Circuits Symp., Digest of Papers*, Jun. 1996, pp. 99–102.
- [72] H. Jiang, Y. Wang, J.-L. Yeh, and N. Tien, “Fabrication of high-performance on-chip suspended spiral inductors by micromachining and electroless copper plating,” in *2000 IEEE MTT-S Int. Microwave Symp. Digest*, Jun. 2000, pp. 279–282.
- [73] M. Yamaguchi, M. Baba, K. Suezawa, T. Moizumi, K. Arai, Y. Shimada, A. Haga, S. Tanabe, and K. Ito, “Magnetic RF integrated thin-film inductors,” in *2000 IEEE MTT-S Int. Microwave Symp. Digest*, Jun. 2000, pp. 205–208.
- [74] M. Gouker, K. Konistis, J. Knecht, L. Kushner, and L. Travis, “Multi-layer spiral inductors in a high-precision, fully-planar MCM-D process,” in *2000 IEEE MTT-S Int. Microwave Symp. Digest*, Jun. 2000, pp. 1055–1058.
- [75] R. Sai, K. Vinoy, N. Bhat, and S. Shivashankar, “CMOS-compatible and scalable deposition of nanocrystalline zinc ferrite thin film to improve inductance density of integrated RF inductor,” *IEEE Trans. on Magnetics*, vol. **49**, no. 7, pp. 4323–4326, Jul. 2013.
- [76] T.-P. Wang, Z.-W. Li, and H.-Y. Tsai, “Performance improvement of a 0.18-CMOS microwave amplifier using micromachined suspended inductors: theory and experiment,” *IEEE Trans. on Electron Devices*, vol. **60**, no. 5, pp. 1738–1744, May 2013.
- [77] J. Carlson, M. Lueck, C. Bower, D. Temple, Z. Feng, M. Steer, A. Moll, and W. Knowlton, “A stackable silicon interposer with integrated through-wafer inductors,” in *Proc. 57th Electronic Components and Technology Conf.* IEEE, 2007, pp. 1235–1238.
- [78] H.-L. Cai, J. Zhan, C. Yang, X. Chen, Y. Yang, B.-Y. Chi, A. Wang, and T.-L. Ren, “Application of ferrite nanomaterial in RF on-chip inductors,” *Journal of Nanomaterials*, vol. **2013**, p. 68, 2013.
- [79] J. N. Burghartz, “Spiral inductors on silicon—status and trends,” *Int. J. of RF and Microwave Computer-Aided Engineering*, vol. **8**, no. 6, pp. 422–432, Nov. 1998.
- [80] G. Stewart, M. Kay, C. Riedell, R. Pomerleau, and M. Steer, “Microstrip discontinuity modeling,” in *IEEE Proc. Southeastcon'89*, 1989, pp. 107–111.
- [81] M. Steer, S. Lipa, P. Franzon, and A. Cangellaris, “Experimental characterization of interconnects and discontinuities in thin-film multichip module substrates,” *Topical Meeting on Electrical Performance of Electronic Packaging*, pp. 145–147, 1993.

# Chapter 13

## Stripline Design

### 13.1 Introduction

The main thrust of this chapter is the analysis and design of stripline. The problem of stripline design is somewhat more complicated than microstrip design. Three stripline scenarios are shown in [Figure 13.1](#). [Figure 13.1\(a\)](#) is a symmetrical stripline and the analysis of this structure is in fact easier than for microstrip. With this structure the signal-carrying strip is embedded in a dielectric between two ground planes and, ideally, the signal return current is carried equally by each of the ground planes. Since there are three current-carrying conductors this structure is sometimes also called triplate, although this term is less commonly used now. Stripline has the attribute that there is much less dielectric dispersion than with a microstrip line since there is only one dielectric medium. So sometimes stripline technology is chosen over microstrip technology for broadband circuits where the dielectric dispersion is clearly undesirable.

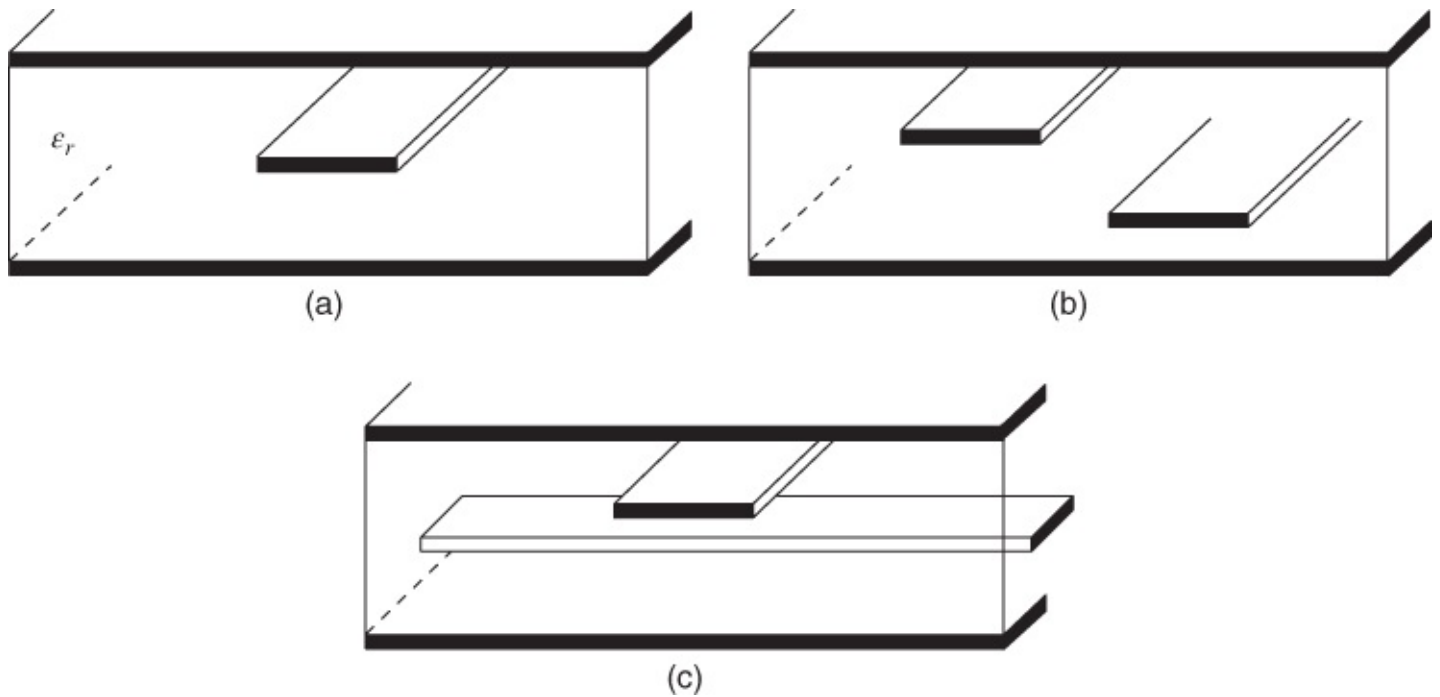


[Figure 13.1](#) Stripline circuit: (a) symmetrical stripline; and (b) asymmetrical stripline; (c) stripline cross-over.

Stripline is also used because it is more compact and multiple strips can be embedded between the ground planes. [Figure 13.1\(b\)](#) shows two asymmetrical strips which are generally packed as close together as possible since stripline is often chosen to obtain a compact circuit. If the location of the strips is integral to functionality, for example using coupled striplines in a parallel-coupled-line filter, then accurate formulas for coupling are available. If the proximity

of strips is not controlled, or they are located as close as possible, then it is more difficult to achieve a controlled impedance structure. Another situation that commonly arises in compacting a circuit is the stripline cross-over shown in [Figure 13.1\(c\)](#). The cross-over provides coupling but in addition there is a tendency for the voltages on the two ground planes to depart from each other. Then a parallel-plate waveguide mode can be supported where an electromagnetic signal freely propagates between the two “ground planes.”

Compared to microstrip, stripline has another attribute in that it is more difficult to radiate a signal. However, a disadvantage is that the ground planes of the stripline can function as a parallel-plate waveguide. This is more likely if the potentials of the ground planes are not tied together and if the strip between the ground planes is not symmetrical. To minimize the chances of a parallel-plate mode being excited it is common to connect the two ground planes together by regularly spaced vias, perhaps through a capacitor if they have different DC voltages as would happen if one plane is used for the ground connection and the other for the supply connection. The main difficulty encountered in developing RF and microwave designs using stripline is that the embedded circuit is not accessible. As was noted in our discussion of microstrip, it is often necessary to follow design with manual fine tuning to account for dimensional and material irregularities. Also it is often necessary to fine tune circuits. Since stripline is embedded it is much more difficult to complete design, fabricate, and test iterations. However, the compact nature is certainly desirable and as a result high-volume applications often require the use of stripline microwave circuits but this choice comes with higher design costs.

## 13.2 Symmetrical Stripline

### 13.2.1 Characteristic Impedance

A symmetrical stripline is shown in [Figure 13.2](#). The basic structure of stripline simply comprises a patterned center conductor embedded completely within a dielectric, the top and bottom layers have conducting ground planes. Unlike microstrip, the entire separation between ground planes is generally denoted by  $b$  or  $2h$ .

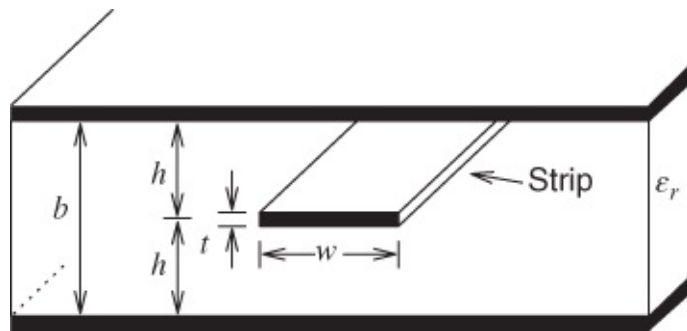


[Figure 13.2](#) Symmetrical stripline circuit (3D view).

As with any transmission structure the designer starts with synthesis of the desired characteristic impedance and requires the width  $w$  of the center conductor. This can be

obtained by iterating on the following formulas, which give the characteristic impedance of stripline [1, 2]:

$$Z_0 = \left( \frac{30\pi}{\sqrt{\epsilon_r}} \right) \frac{(1-t/b)}{(w_{\text{eff}}/b) + C_f}, \quad 13.1$$

where the effective width of the strip,  $w_{\text{eff}}$ , is obtained from

$$\frac{w_{\text{eff}}}{b} = \begin{cases} \frac{w}{b} - \left[ \frac{(0.35-w/b)^2}{(1+12t/b)} \right] & \frac{w}{b} < 0.35 \\ \frac{w}{b} & \frac{w}{b} \geq 0.35 \end{cases} \quad 13.2$$

and

$$C_f = \frac{2}{\pi} \ln \left[ \frac{1}{1-(t/b)} + 1 \right] - \frac{t}{\pi b} \ln \left\{ \frac{1}{[1-(t/b)]^2} - 1 \right\}. \quad 13.3$$

$C_f$  accounts for the fringing capacitance at the edges of the strip and incorporates the effect of the strip thickness for  $t < b$ . The fringing capacitance per unit length (e.g., farads per meter of stripline length) at each corner of the strip is

$$C'_f = \frac{\epsilon_0 \epsilon_r C_f}{1-t/b} \quad 13.4$$

and is shown in [Figure 13.3](#).

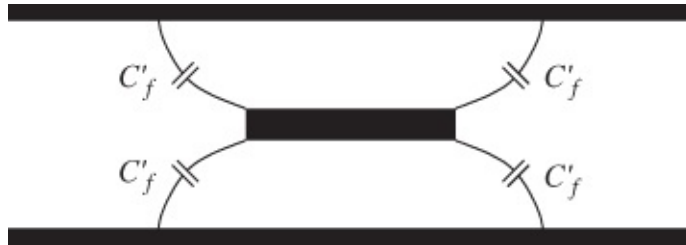


[Figure 13.3](#) Fringe capacitance at the corners of the strip in stripline transmission lines.

The accuracy of these formulas is claimed to be better than 1% for the ranges

$$0.05 < w/(b-t) < 0.35 \quad \text{and} \quad t/b < 0.025.$$

Finding the physical length required to realize an electrical length  $\theta$  (degrees) is also relatively straightforward. We first evaluate the wavelength using

$$\lambda_g = \frac{300}{F\sqrt{\epsilon_r}} \text{ mm.} \quad 13.5$$

When  $F$  is in gigahertz automatically provides the wavelength in millimeters. In Equation [\(13.5\)](#),  $\epsilon_r$  is the relative permittivity of the filling dielectric material and, of course, the

effective relative permittivity  $\epsilon_{\text{eff}} = \epsilon_r$ .

Then the physical length is calculated using Equation (6.20), that is,

$$\ell = \frac{\theta \lambda_g}{360}. \quad 13.6$$

As there is no air–dielectric interface, no progressive mode-coupling occurs and the medium is essentially non-dispersive. Therefore, the above expressions apply up to the highest frequencies at which a stripline can be used, and this tends to be limited by the onset of higher-order modes such as the parallel-plate waveguide mode or the transverse resonance mode.

### 13.2.2 Zero Thickness

If the strip has zero thickness, the characteristic impedance of stripline is

$$Z_0 = \left[ \frac{30\pi}{\sqrt{\epsilon_r}} \right] \frac{1}{(w_{\text{eff}}/b) + 2 \ln 2/\pi} = \frac{94.25}{\sqrt{\epsilon_r}} \frac{1}{(w_{\text{eff}}/b) + 0.441}, \quad 13.7$$

where the effective width of the strip,  $w_{\text{eff}}$ , is obtained from

$$\frac{w_{\text{eff}}}{b} = \begin{cases} \frac{w}{b} - \left( 0.35 - \frac{w}{b} \right)^2 \frac{w}{b} & \frac{w}{b} < 0.35 \\ \frac{w}{b} & \frac{w}{b} \geq 0.35 \end{cases}. \quad 13.8$$

The fringing capacitance per unit length at each corner of the strip is

$$C_f' = \frac{\epsilon_0 \epsilon_r 2 \ln 2}{\pi} = 0.441 \epsilon_0 \epsilon_r. \quad 13.9$$

A stripline supports a purely TEM mode and there is no dielectric dispersion due to an effective permittivity change with frequency. Losses in a stripline are due to dielectric, conductor, and radiative losses. Radiative losses are confined to energy lost to excitation of the parallel-plate waveguide mode, but this can be suppressed by shorting the ground planes together at regular intervals (say every tenth of a wavelength or so).

### 13.2.3 Attenuation

For a low-loss stripline with radiation loss suppressed by vias between the ground planes, the attenuation,  $\alpha$ , comprises two parts, the conductive attenuation,  $\alpha_c$ , and the dielectric attenuation,  $\alpha_d$ , so that  $\alpha = \alpha_c + \alpha_d$ . Now for a low loss line [3]

$$\alpha_c = \frac{R}{2Z_0}, \quad 13.10$$

where  $R$  is the resistance per unit length of the line.  $R$  is the sum of the strip resistance and the ground resistance. At low frequencies the resistance of the strip is

$$R_{\text{strip}} = R_s/w,$$

13.11

where  $R_s$  is the sheet resistance of the strip and  $w$  is the width of the strip. This is sufficient for a stripline of reasonable characteristic impedance where the fields spread out from the strip and the current density in the ground plane is much lower than on the strip. The treatment for the ground resistance is similar to that for microstrip. At low RF and microwave frequencies

$$R_{\text{ground}} = \frac{1}{2} \frac{R_{sg}}{w} \frac{w/h}{w/h + 5.8 + 0.03h/w}, \text{ for } 0.1 \leq w/h \leq 10, \quad 13.12$$

where the sheet resistance of the ground plane is  $R_{sg}$  and is separately identified from that of the strip as it will be different for a different metal or metal thickness. The factor of one-half arises because there are two grounds and the resistance from each is in parallel. The effect of the ground on the line resistance is small. For  $w = h = \frac{1}{2}b$  then if  $\epsilon_r = 4.2$ ,  $Z_0 = 49 \Omega$ , and  $R_{\text{strip}} = 13.7 \cdot R_{\text{ground}}$ . Both  $R_{\text{strip}}$  and  $R_{\text{ground}}$  will increase at higher frequencies as the charges take a larger part of a period to rearrange at higher frequencies.

The formula for the dielectric attenuation for a low loss line is [3]

$$\alpha_d = \frac{G(f)Z_0}{2}. \quad 13.13$$

Based on this the general formula for the attenuation coefficient due to dielectric loss is, for a low-loss TEM line,

$$\alpha_d = \frac{\omega}{c} (\tan \delta) \frac{\epsilon_r(\epsilon_{\text{eff}} - 1)}{2\sqrt{\epsilon_{\text{eff}}}(\epsilon_r - 1)} \text{ Np/m.} \quad 13.14$$

Since the effective permittivity of a stripline is just the relative permittivity of the substrate,  $\epsilon_{\text{eff}} = \epsilon_r$ , then Equation (13.14) reduces to

$$\alpha_d = \frac{\omega}{2c} (\tan \delta) \sqrt{\epsilon_r} \text{ Np/m} = \frac{1}{2} \omega \sqrt{\mu_0 \epsilon_0 \epsilon_r} (\tan \delta) \text{ Np/m.} \quad 13.15$$

(Note that here  $\omega$  is the radian frequency and not the width  $w$ .)

The suspended stripline structure shown in Figure 13.4(b) has little dielectric and hence minimal dielectric loss. Resonators built using a suspended stripline have a high  $Q$  and this structure can be used to realize high-performance filters.

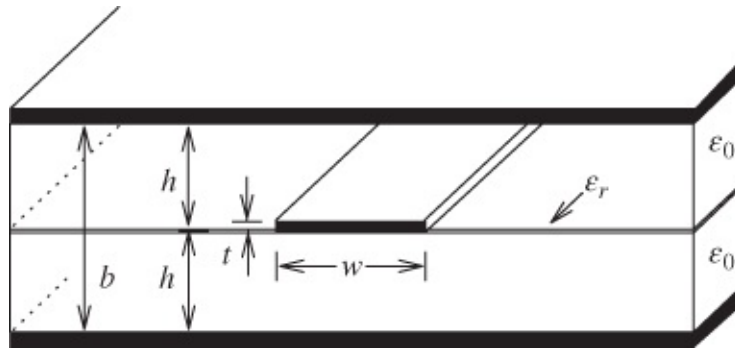


**Figure 13.4** High- $Q$  suspended stripline, the strip is supported by a membrane.

### 13.3 Asymmetrical Stripline

An asymmetrical stripline is shown in [Figure 13.5](#) with the main characteristic being that the strip is not centered. The effective permittivity of this structure is, of course, just the relative permittivity of the dielectric. Formulas have been developed for the characteristic impedance of asymmetrical stripline and these are based on determination of the static capacitance of the structure. This is aided by the knowledge that the phase velocity of the asymmetrical stripline is just the wave velocity in the medium. Thus the characteristic impedance of asymmetrical stripline is

$$Z_0 = \frac{\mu_0 \epsilon_0}{C C_0}, \quad 13.16$$

where  $C$  is the capacitance per unit length of the stripline with the dielectric present and  $C_0$  is this same capacitance except without the dielectric. So the problem reduces to calculating the capacitance of the stripline. This is somewhat more difficult than for the symmetrical stripline.

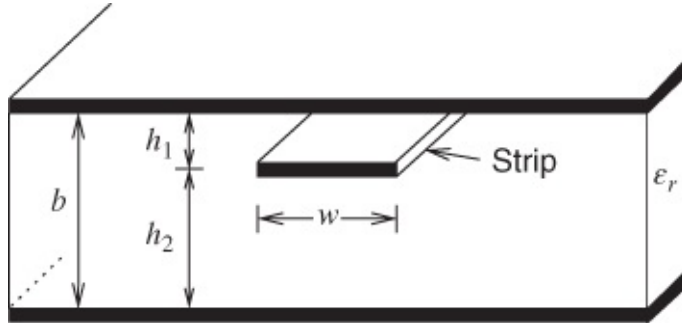


**Figure 13.5** Cross-section of an asymmetrical stripline.

Tang and Jiang's [4] approach to determining the line capacitance is based on calculating the capacitance at asymptotic extremes, one where the ground planes are very close to the strip and one where the ground planes are very far from the strip. They then arrived at the line capacitance of the stripline as the weighted sum of the two extremes.

When the ground planes are close to the strip, that is,  $h_1/w, h_2/w \rightarrow 0$ , the line capacitance is just that of two parallel-plate capacitances so that the line capacitance is [4]

$$C_{\text{near}} = \epsilon_r \epsilon_0 \left( \frac{w}{h_1} + \frac{w}{h_2} \right). \quad 13.17$$

When the ground planes are distant, that is,  $h_1/w, h_2/w \rightarrow \infty$ , the line capacitance is just that of symmetrical stripline so that now [4]

$$\begin{aligned} C_{\text{far}} &= 2\pi\epsilon_r\epsilon_0 \left[ \ln \left( \frac{8b}{\pi w} \right) \right]^{-1} \\ &\approx 2\pi\epsilon_r\epsilon_0 \left\{ \left[ \ln \left( \frac{8b}{\pi w} + 1 \right) \right]^{-1} - \frac{\pi w}{8b} \right\}. \end{aligned} \quad 13.18$$

The line capacitance  $C$  is then the weighted average of these two asymptotes. Tang and Jiang arrived at [4]

$$\begin{aligned} C &= (C_{\text{near}}^n + C_{\text{far}}^n)^{1/n} \\ &= \epsilon_r\epsilon_0 \left( \left[ \frac{W}{h_1} + \frac{W}{h_2} \right]^n + (2\pi)^n \left\{ \left[ \ln \left( \frac{8b}{\pi w} + 1 \right) \right]^{-1} - \frac{\pi w}{8b} \right\}^n \right)^{1/n}, \end{aligned} \quad 13.19$$

where

$$n = 1.39 + \left\{ \frac{h}{b} - 0.83 \right\} \left[ 0.44 + 0.46 \exp \left( -\frac{w}{0.3b} \right) \right] \quad 13.20$$

is arrived at through fitting of numerical data, and  $h = \min(h_1, h_2)$ . The worst case error is 4% and the average error is 1% over a wide parameter range:

$$0.1 < w/b < 2 \quad \text{and} \quad 0 < h_1/b < 0.5.$$

The dielectric-free capacitance  $C_0$  is calculated as for  $C$  but with  $\epsilon_r = 1$ .

For an alumina substrate with a relative permittivity of 9.9, the range of applicability for the quoted accuracy is  $5 < Z_0 < 62 \Omega$ . If the relative permittivity is 4.2, common for a PCB, the range of applicability is  $7.7 < Z_0 < 172 \Omega$ . These are typical design ranges for stripline.

Alternative formulas for the characteristic impedances of asymmetrical stripline are given in [5].

## 13.4 Suspended Stripline

Suspended-substrate stripline represents an important variant of stripline and is shown in [Figure 13.4](#). The strip is now supported by a thin layer of dielectric thus almost eliminating dielectric loss and enabling high- $Q$  planar microwave circuits to be realized. There are many examples of realizing high-performance circuits using this structure [6–11]. This structure is also of interest for realizing millimeter-wave circuits where the dimensions of circuits are somewhat larger than they would be if the conventional stripline was used [12]. In addition, the problem of radiation is now almost eliminated because of the enclosed structure. Suspended-substrate stripline is frequently used in filter and multiplexer designs, taking

advantage of the high  $Q$ .

The structure can be successfully analyzed using the symmetrical stripline formulas but now substituting an effective permittivity of say 1.03 for  $\epsilon_r$ .

## 13.5 Coupled Stripline

### 13.5.1 Edge-coupled Stripline

A pair of edge-coupled striplines is shown in [Figure 13.6\(a\)](#). This structure is typically used to realize parallel-coupled line circuits such as filters [13, 14]. The electrical design of these filters follows the procedure described in [Chapter 19](#) with only the final physical layout being different. Stripline-based coupled line filters are commonly found embedded in the package of a module containing RFICs where compactness is a premium. A particular difficulty is in realizing a final filter design. Filters require precise tuning, often to 0.1% accuracy or better. If the right technology is chosen, and ceramic is a common choice, then once the final dimensions are established filters can be reproduced quite accurately. However, arriving at the final set of dimensions requires a considerable number of design, fabricate, and test cycles. The contrast with microstrip realization is that with microstrip small circuit adjustments such as shortening or lengthening lines can be made “from above.” This is not an option with stripline as the internal metallic pattern is not accessible. It is an art to provide a measure of tunability. An example is providing lumped capacitors in the filter design which are mounted on the external surface of the stripline-containing package and thus tunable. The design cost of using such stripline circuits is high but is very attractive for high-volume manufacture and when compactness is a premium.

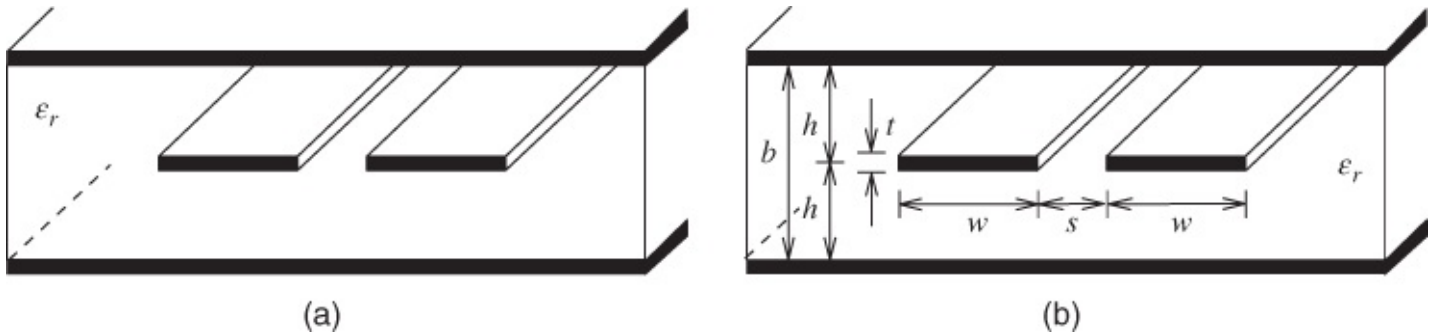


[Figure 13.6](#) Edge-coupled striplines: (a) cross section; and (b) nomenclature.

#### 13.5.1.1 Formulas for Characteristic Impedance with Thin Strips

Formulas for the even- and odd-mode characteristic impedances of edge-coupled stripline were developed by Cohn [15]. Using the nomenclature shown in [Figure 13.6\(b\)](#) and considering zero-thickness strips (i.e.,  $t = 0$ ), the exact even-mode characteristic impedance is

$$Z_{0e} = \frac{30\pi}{\sqrt{\epsilon_r}} \frac{K(k'_e)}{K(k_e)} \quad (\text{with units of } \Omega), \quad 13.21$$

where  $K$  is the complete elliptic integral of the first kind and

$$k_e = \tanh\left(\frac{\pi}{2} \frac{w}{b}\right) \cdot \tanh\left(\frac{\pi}{2} \frac{w+s}{b}\right) \quad 13.22$$

$$k'_e = \sqrt{1 - k_e^2}. \quad 13.23$$

The exact odd-mode characteristic impedance is

$$Z_{0o} = \frac{30\pi}{\sqrt{\epsilon_r}} \frac{K(k'_o)}{K(k_o)} \quad (\text{with units of } \Omega), \quad 13.24$$

where

$$k_o = \tanh\left(\frac{\pi}{2} \frac{w}{b}\right) \cdot \coth\left(\frac{\pi}{2} \frac{w+s}{b}\right) \quad 13.25$$

$$k'_o = \sqrt{1 - k_o^2}. \quad 13.26$$

### 13.5.1.2 Even-mode Characteristic Impedance with Thick Strips

Cohn [15] also developed approximate expressions for when the strips have finite thickness valid for the parameter ranges  $t/b \leq 0.1$  and  $w/b \geq 0.35$ , with diminished accuracy outside these ranges. The even-mode characteristic impedance is

$$Z_{0e} = \frac{30\pi}{\sqrt{\epsilon_r}} \left\{ \frac{w}{b-t} + \frac{1}{2\epsilon_0\epsilon_r} \left[ C'_f\left(\frac{t}{b}\right) + C'_{fe}\left(\frac{t}{b}, \frac{s}{b}\right) \right] \right\}^{-1} \quad (\text{with units of } \Omega), \quad 13.27$$

where  $C'_{fe}(t/b, s/b)$  is the fringing capacitance at the coupled edge of the thick strip in the even mode and  $C'_f(t/b)$  is the fringing capacitance from one strip of thickness  $t$  to one of the ground planes [16]:

$$\begin{aligned} C'_f(t/b) = & \frac{\epsilon_0\epsilon_r}{\pi} \left\{ \frac{2}{1-t/b} \ln \left( \frac{1}{1-t/b} + 1 \right) \right. \\ & \left. - \left( \frac{1}{1-t/b} - 1 \right) \ln \left[ \frac{1}{(1-t/b)^2} - 1 \right] \right\} \quad (\text{with units of F/m}). \end{aligned} \quad 13.28$$

For a zero-thickness strip this becomes

$$C'_f(0) = \frac{2\epsilon_0\epsilon_r}{\pi} \ln 2 = 0.4413\epsilon_0\epsilon_r \quad (\text{with units of F/m}). \quad 13.29$$

The fringing capacitance at the coupled edge of a thick strip in the even mode is

$$C'_{fe}(t/b, s/b) = C'_f\left(\frac{t}{b}\right) \cdot \frac{C'_{fe}(0, s/b)}{C'_f(0)}, \quad 13.30$$

which uses the even-mode fringing capacitance at the adjacent edges of a pair of zero-thickness strips [15]:

$$C'_{fe}(0, s/b) = \epsilon_0 \epsilon_r \left\{ \frac{s}{b} - \frac{2}{\pi} \ln \left[ \cosh \left( \frac{\pi s}{2b} \right) \right] \right\} \quad (\text{with units of F/m}). \quad 13.31$$

It is not really necessary to specify the units of the capacitances above but it does help to relate the expressions here to the original expressions, which were in the units of pF/cm.

### 13.5.1.3 Odd-mode Characteristic Impedance with Thick Strips

Cohn's [15] expression for the odd-mode characteristic impedance when the strips have finite thickness are again valid for  $t/b \leq 0.1$  and  $w/b \geq 0.35$ , with the additional restriction of  $s/t \geq 5$ . The expressions are usable outside this range but with diminished accuracy. From [15] the odd-mode characteristic impedance is

$$Z_{0o} = \frac{94.15 \Omega}{\sqrt{\epsilon_r}} \left\{ \frac{w}{b-t} + \frac{1}{2\epsilon_0 \epsilon_r} \left[ C'_f\left(\frac{t}{b}\right) + C'_{fo}\left(\frac{t}{b}, \frac{s}{b}\right) \right] \right\}^{-1}, \quad 13.32$$

where the expressions for the fringing capacitance,  $C'_f$ , from one strip of thickness  $t$  to one of the ground planes (i.e., Equation (13.28) still applies.  $C'_{fo}(t/b, s/b)$  is the fringing capacitance at the coupled edge of a thick strip in the odd mode. Now

$$C'_{fo}(t/b, s/b) = C'_f(t/b) \cdot \frac{C'_{fo}(0, s/b)}{C'_f(0)}, \quad 13.33$$

which uses the even-mode fringing capacitance at the adjacent edges of a pair of zero-thickness strips [15]:

$$C'_{fo}(0, s/b) = \epsilon_0 \epsilon_r \left\{ \frac{s}{b} - \frac{2}{\pi} \ln \left[ \sinh \left( \frac{\pi s}{2b} \right) \right] \right\} \quad (\text{with units of F/m}). \quad 13.34$$

### 13.5.1.4 Discussion

Nishikawa et al. described a compact 60 GHz bandpass filter based on edge-coupled striplines [17]. They realized a third-order bandpass filter in LTCC technology with a 6.9% bandwidth, an insertion loss of 5 dB, and a return loss of better than -20 dB. They chose this form of the filter because of the demands for compactness, performance, and high level of integration.

Davis et al. [18, 19] developed a broadband circulator based on a pair of edge-coupled striplines with the dielectric in the top half replaced by magnetized ferrite. They presented a design of a circulator that could operate from 11 GHz to 60 GHz if the permittivities of the ferrite and the dielectric in the bottom were the same. They presented a prototype circulator that

functioned from 11.5 to 22.5 GHz [19].

### 13.5.2 Broadside-coupled Stripline

A pair of broadside-coupled striplines is shown in [Figure 13.7\(a\)](#). As with the edge-coupled striplines, the broadside coupled lines result in miniaturized circuits and are often even more compact than can be obtained with edge-coupled striplines [20].

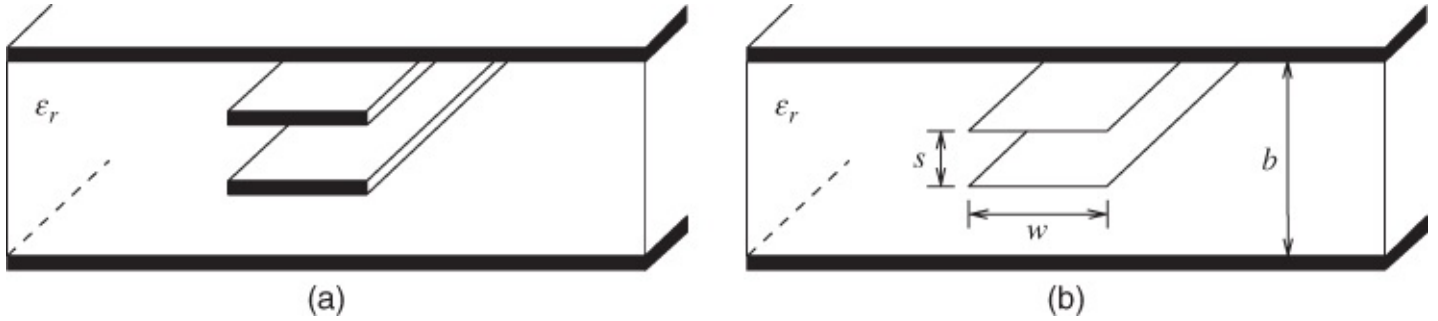


[Figure 13.7](#) Broadside-coupled striplines: (a) thick strips; and (b) nomenclature.

Cohn [21] developed formulas for the even- and odd-mode characteristic impedances of this structure. The even-mode characteristic impedance is

$$Z_{0e} = \frac{188.3}{\sqrt{\epsilon_r}} \frac{K(k')}{K(k)} \quad 13.35$$

and the odd-mode characteristic impedance is

$$Z_{0o} = \frac{296.1}{\sqrt{\epsilon_r \tanh^{-1}(k)}} \frac{s}{b}. \quad 13.36$$

$K$  is the complete elliptical integral of the first kind and  $k$  is a parameter obtained by solving

$$\frac{w}{b} = \frac{2}{\pi} \left\{ \tanh^{-1} \left[ \sqrt{\frac{k(b/s) - 1}{(b/(ks) - 1}}} \right] - \frac{s}{b} \tanh^{-1} \left[ \frac{1}{k} \sqrt{\frac{k(b/s) - 1}{(b/(ks) - 1)}} \right] \right\} \quad 13.37$$

Fortunately he presented a simplification applicable for the following conditions:

$$\frac{w}{s} \geq 0.35 \quad \text{and} \quad \frac{w/b}{1 - s/b} \geq 0.35. \quad 13.38$$

Then

$$Z_{0e} = \frac{188.3}{\sqrt{\epsilon_r}} \left[ \frac{w/b}{1 - s/b} + \frac{C'_{fe}}{\epsilon_0} \right]^{-1} \quad 13.39$$

and

$$Z_{0o} = \frac{188.3}{\sqrt{\epsilon_r}} \left[ \frac{w/b}{1-s/b} + \frac{w}{s} + \frac{C'_{fo}}{\epsilon_0} \right]^{-1},$$

where the free-space even-mode fringing capacitance is obtained from

$$\frac{C'_{fe}}{\epsilon_0} = 0.4413 + \frac{1}{\pi} \left[ \ln \left( \frac{1}{1-s/b} \right) + \left( \frac{s/b}{1-s/b} \right) \ln \left( \frac{b}{s} \right) \right] \quad 13.41$$

and the odd-mode free-space fringing capacitance is obtained from

$$\frac{C'_{fo}}{\epsilon_0} = \frac{b/s}{\pi} \left[ \ln \left( \frac{1}{1-s/b} \right) + \left( \frac{s/b}{1-s/b} \right) \ln \left( \frac{b}{s} \right) \right]. \quad 13.42$$

Synthesis, however, results in an electrical design with the desired even- and odd-mode impedances. From these the physical parameters, here  $w$  and  $s$ , are derived. Wang *et al.* [22] provided the required synthesis formulas.

## 13.6 Double-sided Stripline

Variations on the basic stripline structure are shown in [Figure 13.8](#). These, particularly the offset doubled-sided parallel stripline in [Figure 13.8\(b\)](#), provide additional degrees of freedom in design. The particular advantage of both the aligned doubled-sided parallel stripline in [Figure 13.8\(a\)](#) and the offset doubled-sided parallel stripline in [Figure 13.8\(b\)](#) is that they have good characteristics for differential signals as each conductor is identical. These lines also provide a broad range of characteristic impedances and lend themselves to wideband transitions. Suitable formulas for the characteristic impedances of the aligned structure were developed in [23]. The similar formulas for the characteristic impedance of offset doubled-sided parallel stripline were developed in [24].

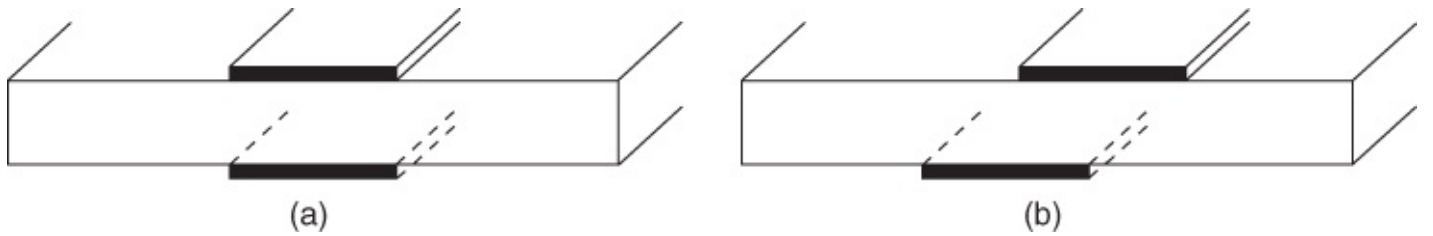


[Figure 13.8](#) Doubled-sided parallel stripline: (a) aligned; and (b) offset.

## 13.7 Discontinuities

Stripline discontinuities have the same form as in microstrip. The major differences between the media (mostly the fact that stripline is axially symmetric usually) result in significant differences in the characterization of the stripline discontinuities. The layouts applicable to each stripline discontinuity are identical to those for microstrip.

### 13.7.1 Stripline Open Circuit

As with microstrip a suitable model for an open circuit in stripline is a line with extended length. An extended length model was developed by Yu *et al.* [25, 26] for the open circuit of an asymmetrical stripline. This model of course is applicable to symmetrical stripline. The model they developed was arrived at by fitting a product of polynomials to numerical data. Referring to the asymmetrical stripline parameters shown in [Figure 13.9](#), the open circuit is modeled by a line of extended length  $\Delta\ell$  given by [25, 26]

$$\Delta\ell = \frac{C\omega Z_0}{\beta} , \quad 13.43$$

where  $C$  is the capacitance of the open circuit, given by

$$C = \epsilon_r \epsilon_0 \left\{ \left[ \frac{w}{h_1} + \frac{w}{h_2} \right]^n + \left[ 2\pi \left( \frac{1}{\ln [8b/(\pi w) + 1]} - \frac{\pi w}{8b} \right) \right]^n \right\}^{1/n} \quad 13.44$$

$$n = 1.39 \left( \frac{h}{b} - 0.83 \right) \left[ 0.44 + 0.46 \exp \left( \frac{-w}{0.3b} \right) \right]. \quad 13.45$$

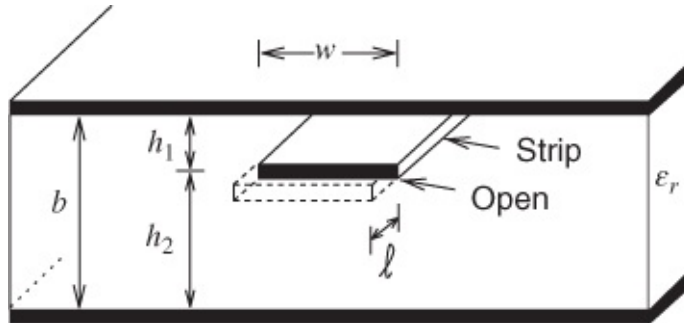


[Figure 13.9](#) Cross-section of an asymmetrical stripline.

### 13.7.2 Bends

A bend has the layout and equivalent circuit shown in [Figure 13.10](#). As with microstrip, mitering again significantly reduces the discontinuity effects, and this approach is recommended.

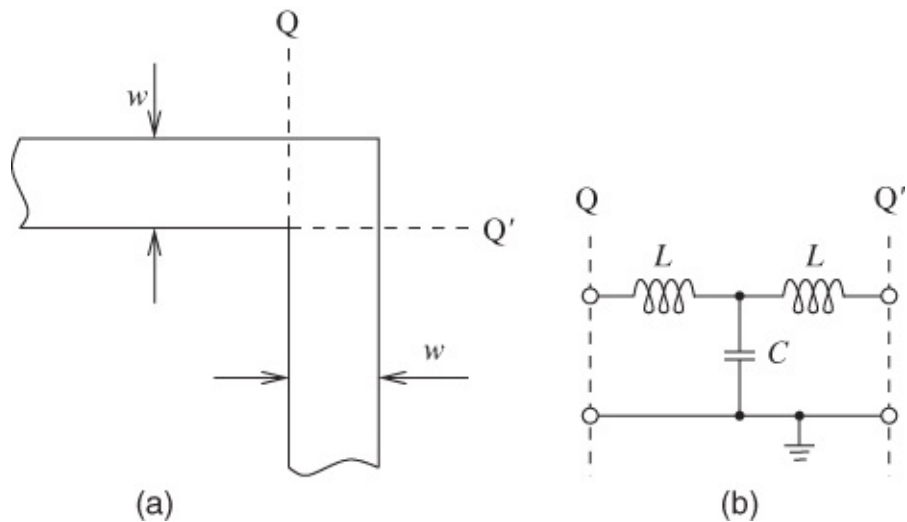


**Figure 13.10** Right-angled stripline bend: (a) structure and nomenclature; and (b) equivalent circuit.

### 13.7.3 Vias

The implementation of vias (short circuits) in stripline is in fact somewhat more difficult than with microstrip or coplanar waveguide. This is because each via must connect through to both the upper and lower ground planes.

### 13.7.4 Junctions

The most important junctions are the T junction and the asymmetric cross junction. For microstrip the layout and equivalent circuit of a T junction were shown in [Figure 9.19](#) and these have the same form for stripline junctions. The reference planes and hypothetical widths are indicated in [Figure 9.21](#). Again, as with the right-angled bend discussed above, compensation should be considered and a similar approach to that used for microstrip is recommended.

The layout and an equivalent circuit for a microstrip asymmetric cross-over junction were shown in [Figure 9.22](#), and this also applies to stripline.

## 13.8 Design Recommendations

Recommendations for the design of stripline are very similar to those for microstrip. Transverse resonance must be avoided by ensuring that the width of the strips is below a critical value, roughly less than a half-wavelength. There is a particular problem that is encountered with stripline that does not occur with microstrip and this is the parallel-plate mode. This is a problem when a signal is excited between the two parallel ground planes. For the symmetrical stripline structure the two grounds are ideally at zero volts. This is typically assured through the use of vias. As an example see the use of vias with the stripline in [Figure 13.11](#). The vias ensure that the ground planes are at the same potential and also form an electrical wall for any electromagnetic waves that may be excited [27]. It is important that the

vias not be placed in a periodic manner or else this could result in an undesired filtering effect.

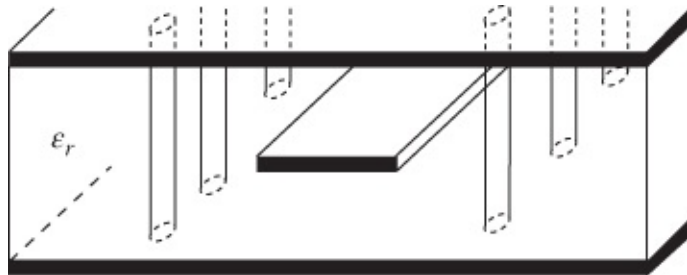


**Figure 13.11** Striplines with ground-plane vias.

## 13.9 Summary

This chapter presented the essentials of stripline design, concentrating on the concepts that are additional to those of the other planar transmission lines that have been studied. Stripline is primarily used to provide compactness of microwave circuits but there is an additional attribute of shielding yielding lower radiation loss. However, design is more expensive as the stripline circuitry is not externally accessible for modifications that may be required in a deisgn optimization procedure.

## References

- [1] I. Bahl and R. Garg, “A designer's guide to stripline circuits,” *Microwaves*, pp. 90–96, 1978.
- [2] S. Cohn, “Problems in strip transmission lines,” *IRE Trans. on Microwave Theory and Techniques*, vol. **3**, no. 2, pp. 119–126, Mar. 1955.
- [3] M. Steer, *Microwave and RF Design: a Systems Approach*, 2nd ed. SciTech Pub., 2013.
- [4] W. Tang and B. Jiang, “CAD formula of asymmetric stripline via synthetic asymptote,” *Microwave and Optical Technology Letters*, vol. **47**, no. 2, pp. 143–145, 2005.
- [5] H. Howe, *Stripline Circuit Design*. Artech House, 1974.
- [6] W. Schwab, F. Boegelsack, and W. Menzel, “Multilayer suspended stripline and coplanar line filters,” *IEEE Trans. on Microwave Theory and Techniques*, vol. **42**, no. 7, pp. 1403–1407, 1994.
- [7] R. Ruf and W. Menzel, “A novel compact suspended stripline resonator,” *IEEE Microwave and Wireless Components Letters*, vol. **22**, no. 9, pp. 444–446, 2012.
- [8] Y. C. Lee and C. S. Park, “A novel high-Q LTCC stripline resonator for millimeter-wave applications,” *IEEE Microwave and Wireless Components Letters*, vol. **13**, no. 12, pp. 499–501, 2003.

- [9] W. Menzel, M. R. Tito, and L. Zhu, “Low-loss ultra-wideband (UWB) filters using suspended stripline,” in *Proc. 2005 Asia-Pacific Microw. Conf.*, vol. **4**, 2005, pp. 2148–2151.
- [10] W. Menzel and A. Balalem, “Quasi-lumped suspended stripline filters and diplexers,” *IEEE Trans. on Microwave Theory and Techniques*, vol. **53**, no. 10, pp. 3230–3237, 2005.
- [11] W. Menzel and M. Berry, “Quasi-lumped suspended stripline filters with adjustable transmission zeroes,” in *2004 IEEE MTT-S Int. Microwave Symp. Digest*, vol. **3**, 2004, pp. 1601–1604.
- [12] W. Liu, D. Steenson, and M. Steer, “Membrane-supported copper E-plane circuits,” in *2001 IEEE MTT-S Int. Microwave Symp. Dig.*, 2001, pp. 539–542.
- [13] H. Y. Wai, Z. M. Naing, K. S. Lwin, and H. M. Tun, “Design and simulation of edge-coupled stripline band pass filter for ka band application,” in *Int. Conf. on Trends in Electrical, Electronics and Power Engineering (ICTEEP'2012)* July, 2012, pp. 15–16.
- [14] Y.-H. Suh and K. Chang, “Coplanar stripline resonators modeling and applications to filters,” *IEEE Trans. on Microwave Theory and Techniques*, vol. **50**, no. 5, pp. 1289–1296, 2002.
- [15] S. B. Cohn, “Shielded coupled-strip transmission line,” *IRE Trans. on Microwave Theory and Techniques*, vol. **3**, no. 5, pp. 29–38, May 1955.
- [16] S. B. Cohn, “Characteristic impedance of the shielded-strip transmission line,” *IRE Trans. on Microwave Theory and Techniques*, vol. **2**, no. 2, pp. 52–57, Feb. 1954.
- [17] K. Nishikawa, T. Seki, I. Toyoda, and S. Kubota, “Compact 60-GHz LTCC stripline parallel-coupled bandpass filter with parasitic elements for millimeter-wave system-on-package,” in *2007 IEEE MTT-S Int. Microwave Symp. Digest*, 2007, pp. 1649–1652.
- [18] C. K. Queck and L. Davis, “Microstrip and stripline ferrite-coupled-line (fcl) circulator's,” *IEEE Trans. on Microwave Theory and Techniques*, vol. **50**, no. 12, pp. 2910–2917, Dec. 2002.
- [19] C. K. Queck and L. E. Davis, “Broad-band three-port and four-port stripline ferrite coupled line circulators,” *IEEE Trans. on Microwave Theory and Techniques*, vol. **52**, no. 2, pp. 625–632, 2004.
- [20] Y. Zhang, K. A. Zaki, A. J. Piloto, and J. Tallo, “Miniature broadband bandpass filters using double-layer coupled stripline resonators,” *IEEE Trans. on Microwave Theory and Techniques*, vol. **54**, no. 8, pp. 3370–3377, Aug. 2006.
- [21] S. B. Cohn, “Characteristic impedances of broadside-coupled strip transmission lines,” *IRE Trans. on Microwave Theory and Techniques*, vol. **8**, no. 6, pp. 633–637, Jun. 1960.
- [22] K. Wang, X. Shi, and W. Tang, “Inverse formula of coupled-striplines by synthetic asymptote,” *Microwave and Optical Technology Letters*, vol. **49**, no. 6, pp. 1309–1312, 2007.

- [23] H. A. Wheeler, “Transmission-line properties of parallel strips separated by a dielectric sheet,” *IEEE Trans. on Microwave Theory and Techniques*, vol. **13**, no. 2, pp. 172–185, 1965.
- [24] W. Che, L. Gu, and Y. Chow, “Formula derivation and verification of characteristic impedance for offset double-sided parallel strip line (DSPSL),” *IEEE Microwave and Wireless Components Letters*, vol. **20**, no. 6, pp. 304–306, Jun. 2010.
- [25] Z. Yu, W. Tang, Y. Nai, and Y. Chow, “Formula of asymmetric stripline open-end and its applications,” in *Int. Conf. on Microwave and Millimeter Wave Technology*, vol. **2**, Feb. 2008, pp. 471–474.
- [26] W. Tang, Z. Yu, Y. Nai, and Y. L. Chow, “Closed-form expression of asymmetric stripline open-end and its applications for analysis of LTCC components and circuits,” *Microwave and Optical Technology Letters*, vol. **51**, no. 2, pp. 406–408, Feb. 2009.
- [27] J. Gipprich and D. Stevens, “A new via fence structure for crosstalk reduction in high density stripline packages,” in *2001 IEEE MTT-S Int. Microwave Symp. Digest*, 2001, pp. 1719–1722.

# Chapter 14

## CPW Design Fundamentals

### 14.1 Introduction to Properties of Coplanar Waveguide

Microstrip remains the most popular medium for circuit design at frequencies ranging from several hundred megahertz to some tens of gigahertz. It is also the medium on which most long-haul, high-performance, on-chip digital interconnect is based. This medium is always inherently well grounded by virtue of the ground plane, which also ensures that most of the energy is trapped between the strip and this ground plane, that is, within the substrate. The top surface of the substrate is available for conductor strip patterns that largely define electromagnetic propagation and circuit function. There are, however, difficulties associated with the use of microstrip, notably:

- the relative inaccessibility of the ground plane.
- the difficulty associated with making shunt connections between strip and ground.
- limitations on and sensitivity to substrate thickness.
- increased radiation when thick substrates are used.

The effects of all these difficulties become more severe as the frequency increases. As a result of these effects, microstrip is not necessarily the best choice of transmission medium for broadband millimeter-wave circuit design or for long on-chip interconnect. In integrated circuit technology lateral dimensions can be defined photolithographically with great accuracy, but the substrate thickness is often not controlled at all well. It is therefore very attractive to use interconnects that are defined principally by their lateral dimensions. In multilevel connections an uninterrupted ground cannot always be assured, so providing a signal return path on the same metallization layer assures near-optimum performance but at the price of losing the number of interconnects that can be provided, since the signal return lines consume routing area.

Coplanar waveguide (CPW) is a term used to describe what really amounts to a class of planar microwave transmission structures that comprises various arrays of conductors configured in the same geometric plane, that is, coplanar. Quite unlike microstrip, where a distinct and singular ground plane necessarily occupies the entire “underside” of the structure, CPW has its principal grounding in the form of wide strips adjacent to the active conductor. Thus, the signal characteristics are almost entirely governed by laterally defined dimensions. Before entering into further details regarding CPW geometry options, we start with observing the related, but simpler, slotline and coplanar strip structures. 3D views of these structures are shown in [Figure 14.1](#). Both slotline and coplanar strips (CPS) are balanced line structures and are occasionally implemented in applications including radiating elements and transitions. Slotline is particularly important for use with some antennas and with ferrite devices, among other

applications, and is considered in [Chapters 15](#) and [16](#).

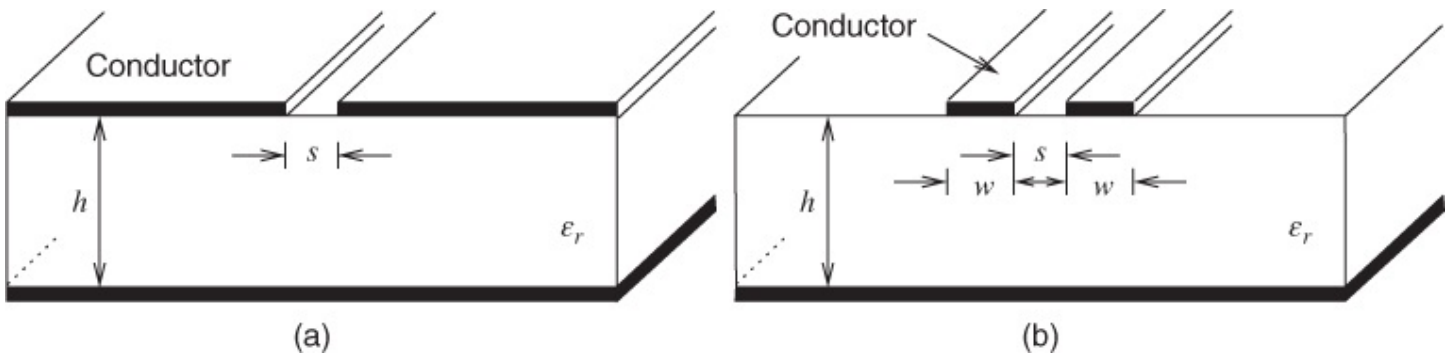


**Figure 14.1** Structure of (a) slotline; and (b) differential line or CPS.

CPS has become important for on-chip implementations on semiconductor substrates, especially for high-speed digital signal transmission, where it is usually referred to as differential interconnect or differential line. The differential line structure, that is, CPS, will be considered in this chapter.

CPW was invented in 1969 by C.P. Wen [1]. The coincidence of the inventor's initials with the abbreviation for coplanar waveguide may possibly be just that, a coincidence, but it is at least an interesting one. The basic structure of CPW is illustrated in [Figure 14.2\(a\)](#), where the arrangement is assumed to be symmetrical with strip width  $w$  and equal longitudinal gap separation  $s$ . The side conductors are ultimately grounded, theoretically at infinity. A variant of the CPW structure is the finite-ground CPW (FGCPW) line shown in [Figure 14.2\(b\)](#), which results in lower coupling of adjacent lines as the ground (signal return current) is not shared by two or more transmission lines. As originally conceived, Wen's design formulations for CPW demanded an infinitely thick substrate and this practical difficulty doubtlessly impeded its implementation in any general sense. This was in spite of the fact that CPW has the following advantages over microstrip:

- easier grounding of surface-mounted (or ball grid array (BGA)-mounted) components
- lower fabrication costs
- reduced dispersion (for small geometries)
- decreased radiation losses
- availability of closed-form expressions for the characteristic impedance
- couplers having higher directivities
- photolithographically defined structures with relatively low dependence on substrate thickness.

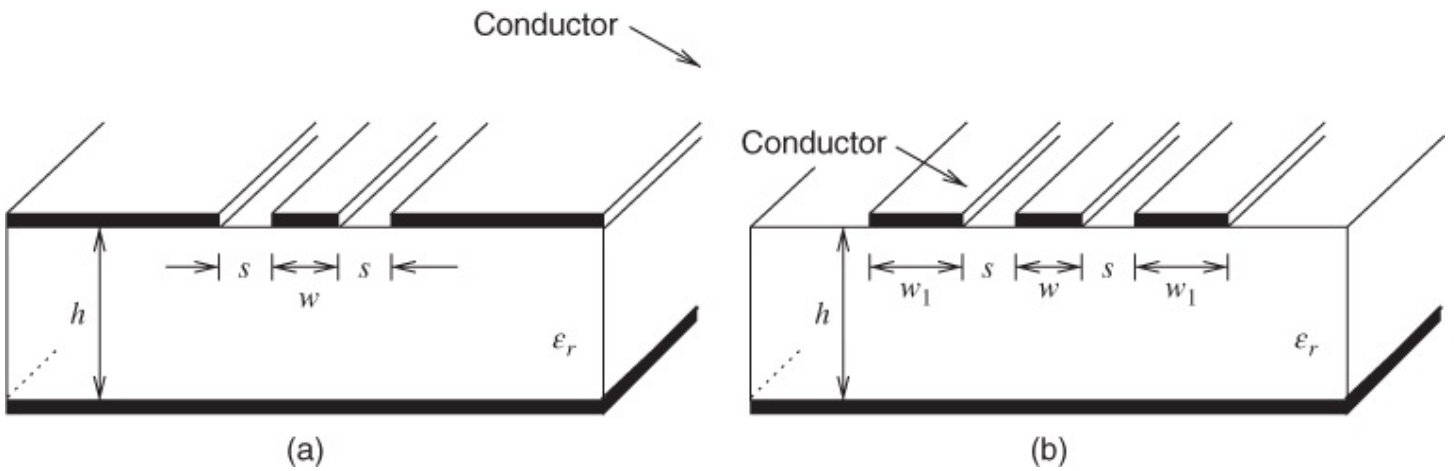


**Figure 14.2** Structure of a CPW: (a) conventional; and (b) FGCPW.

The current and charge distribution on a CPW line at one time instant is shown in [Figure 14.3](#) for a sine wave traveling from left to right. (The granularity is the result of the necessary discretization of the currents by the electromagnetic simulator.) The charge and the magnitudes of the currents are shown. Just under a full cycle is shown, with the longitudinal current on the inner conductor initially (on the left) directed towards the right and the latter in the middle of the figure directed to the left. The adjacent longitudinal currents on the inner and outer conductors are in opposite directions. The small transverse currents are necessary for the charges to rearrange at 100 GHz and the charges establish the electric field between the centre conductor and each outer conductor as well as supporting the longitudinal currents. An expanded view of the currents and charge distributions is shown in [Figure 14.4](#). Note in particular that there is appreciable current on the outer edges of the outer strips.

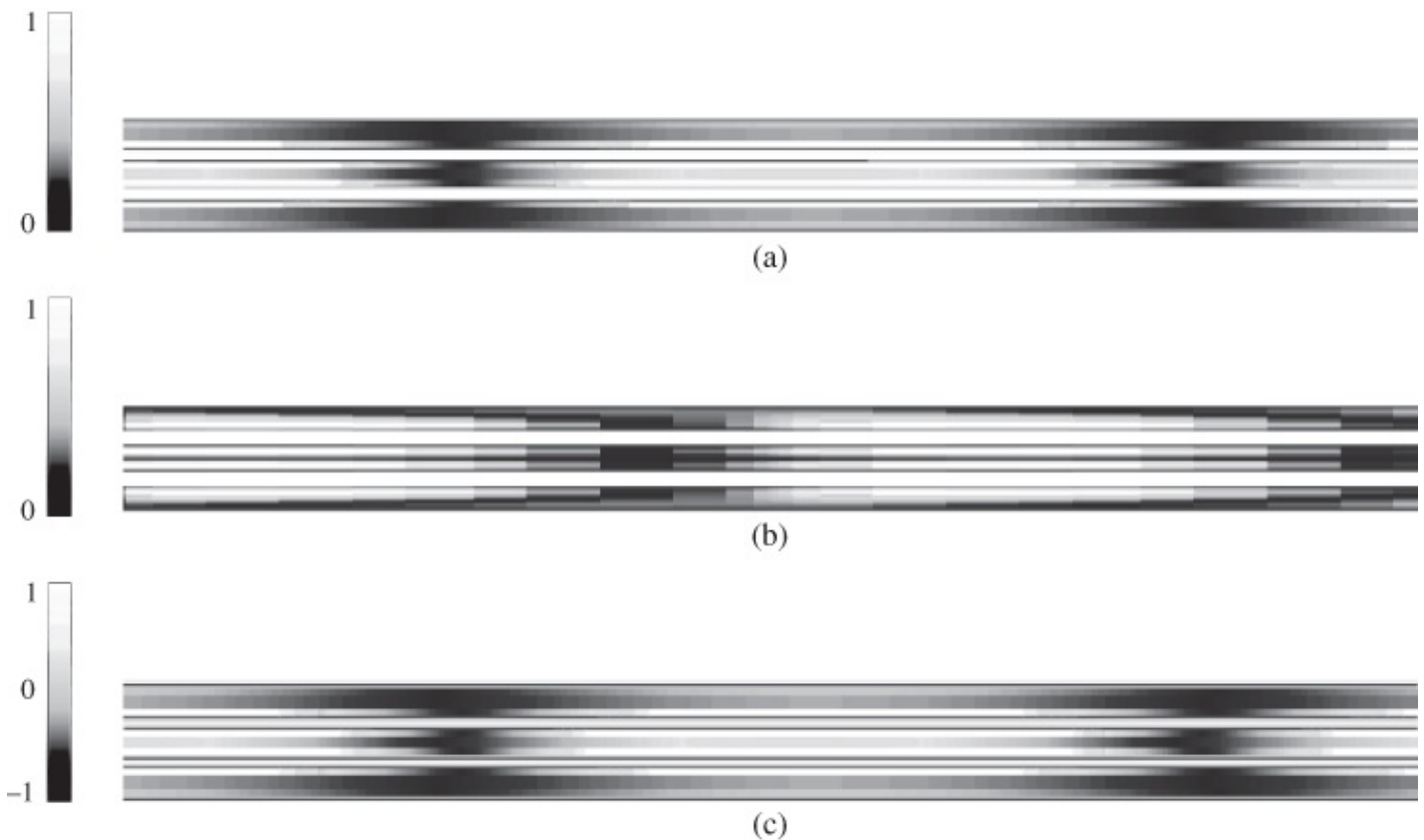


**Figure 14.3** Instantaneous normalized current magnitude and charge distribution along a CPW line along with respective normalized scales: (a) longitudinal current; (b) transverse current; and (c) charge. The current and charge are normalized and use the scale shown on the left-hand side. The maximum of the transverse current is 500 times smaller than that of the longitudinal current. (The line is 1 mm long, the frequency is 100 GHz,  $s = 10 \mu\text{m}$ , and  $w = 20 \mu\text{m}$ ).

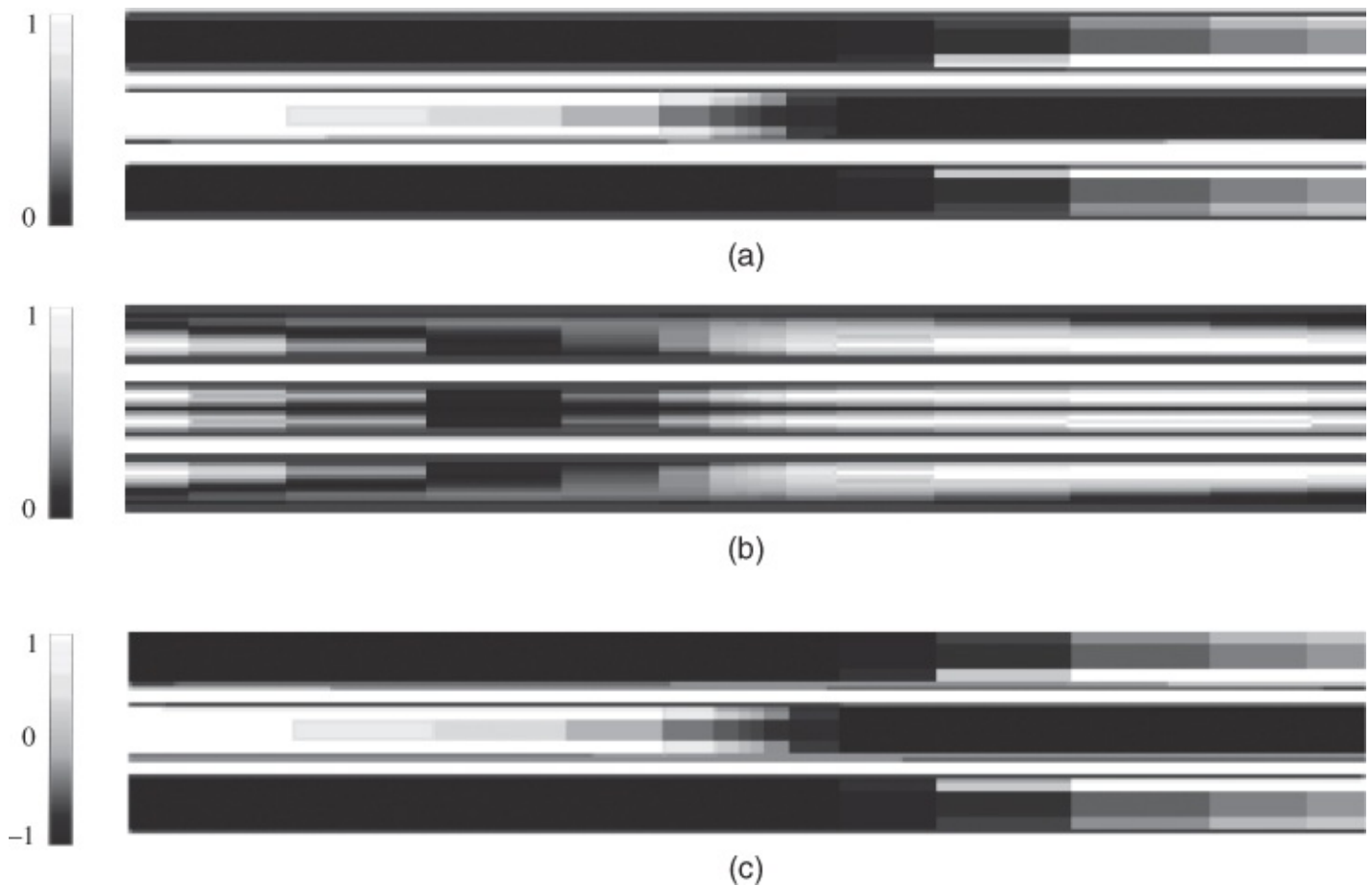


**Figure 14.4** Expanded view, current magnitude, and charge distribution along a CPW line: (a) longitudinal current; (b) transverse current; and (c) charge.

Throughout the period from 1970 to the present time microstrip design and implementation has been in the ascendancy, and a vast library of algorithms has been assembled for the CAD of circuits using this medium. In contrast, far less has been achieved for CPW in relating the desired electrical parameters to the physical parameters. Gupta *et al.* [2] have reported much design detail for this medium.

The major problem centers on the characteristic impedance determining parameters associated with CPW *vis-à-vis* microstrip. As explained in the earlier chapters of this book, the characteristic impedance  $Z_0$  of microstrip is very largely determined by the ratio of strip width (usually denoted  $w$ ) to height  $h$  and the substrate permittivity  $\epsilon_r$ . This results in a unique value of  $w$  for a required  $Z_0$ , as  $h$  is nearly always fixed by an earlier design decision. However, a similar situation does not, unfortunately, exist with CPW.

Instead, with CPW  $Z_0$  is determined by the ratio of the center strip width  $w$  to the gap width  $s$ . This makes the design of a CPW line with a particular  $Z_0$  nonunique because an infinite range of  $w$  and  $s$  values will result in a specific  $Z_0$  requirement. As a result the development of effective simple models for CPW design, such as planar waveguide models, is extremely difficult and much more extensive design algorithms (than for microstrip) are required.

Appreciating that in practice CPW almost always has a ground plane conductor backing, in 1980 Veyres and Fouad-Hanna [3] published analytic equations characterizing the key

parameters of this type of CPW. This conductor backing is sometimes termed “backside metallization” and this must generally apply because planar microwave circuits are usually mounted in a conducting box of some form. There were some errors in Veyres and Fouad-Hanna's analysis, but corrections to these errors were subsequently published by Ghione and Naldi [4, 5]. For this conductor-backed structure analytic closed-form expressions were obtained for  $Z_0$  and the phase velocity in CPW, and this is actually an improvement over the situation with microstrip.

Design advantages rarely come without attendant drawbacks and this conductor-backed structure is no exception. The following disadvantages apply:

- Spurious modes (notably the microstrip mode) can easily be generated if the separation between the CPW structure and the backing metallization is too close (resulting in field lines between the CPW and the backing metallization).
- For a given  $Z_0$  and substrate thickness the strip width  $w$  will always be significantly less than for the corresponding microstrip in order to maintain the same capacitance to ground. Therefore, the resistive loss for the CPW line can exceed that of the corresponding microstrip line.

Note that with this structure the slotline mode, another spurious mode, can exist, just as without a conductor backing.

In practice, spurious modes can be avoided by careful design and fabrication, whilst the additional loss can be minimized by carefully selecting the substrate thickness.

It can be the case that coplanar is not always precisely symmetrical, the separations between center strip and the ground planes can differ, providing, at almost no cost, an extra dimension of the design space. Amongst the first to investigate the properties of this structure, and its departures from the basic CPW behavior, were Fan and Wang [6]. Fan and Wang's work was entirely theoretical, and at that time no measured results were reported. The cross-section of the configuration is shown in [Figure 14.5](#). These researchers showed that, for suitable combinations of  $b_1$  and  $b_2$ , a virtually frequency-independent effective permittivity of 5.6 applied (with a substrate permittivity of 10). The electric field patterns were also reported for this structure.

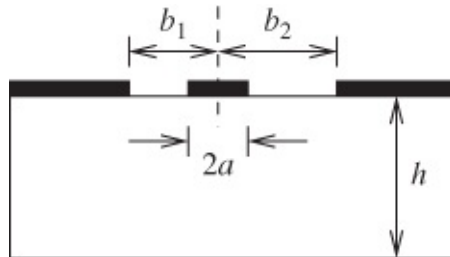


[Figure 14.5](#) Asymmetric CPW.

The key attribute of symmetrical CPW structures (with  $b_1 = b_2$ ) is the relative frequency independence of the effective permittivity, for small geometries, as this leads to almost dispersion-free transmission of signals. This attribute is accompanied by a simplified way of

connecting devices along the signal path without the use of vias, active devices can be placed above or under the CPW structure. This is important in many RFIC and MMIC chip layouts.

## 14.2 Modeling CPWs

For an interconnect to be of use in practical design, it must be analyzed and also be capable of being synthesized, that is, the physical parameters enabling manufacture must be determined, starting with a knowledge of the desired characteristic impedances and electrical lengths. Firstly, expressions for characteristic impedance must be known. It must also be possible to find the wavelength in the medium and this is normally preceded by knowing the effective permittivity, the propagation constant, or the phase velocity. All of these quantities can be derived from knowing just one.

We shall now define these quantities for basic CPW ([Figure 14.2\(a\)](#)), starting with the effective permittivity. The results given were first analyzed by Wen [1] who used the Schwartz–Christoffell transformation. Rayit [7] provides a good detailed description of this approach and this is followed here. The appropriate form of the Schwartz–Christoffell transformation is:

$$\frac{dW}{dZ} = A \prod_{n=0}^{n=\infty} (Z - x_n)(\alpha_n - \pi)/\pi. \quad 14.1$$

The use of this equation enables the problem to be represented in terms of different planes (or variables) from the physical planes (specifically what are known as the W and Z planes). In Equation [\(14.1\)](#)  $A$  is a constant that must be evaluated,  $\alpha_1, \alpha_2, \dots, \alpha_n$  are interior angles in a polygon described in the W plane, and  $x_1, x_2, \dots, x_n$  are corresponding points along the real axis in the Z plane.

Wen, and also Rayit, clearly show that ratios and standard values can then be implemented to solve for the effective permittivities and characteristic impedances. In particular, a ratio  $a/b$  is also expressed as the ratio of two elliptic integrals termed  $K(k)$  and  $K'(k)$ :

$$\frac{a}{b} = \frac{K(k)}{K'(k)} \quad 14.2$$

in which  $K(k)$  is the complete integral of the first kind with modulus  $k$ , such that  $K(k)$  is given by

$$K(k) = \int_0^{\pi/2} \frac{d\Phi}{\sqrt{1 - k^2 \sin^2 \Phi}}. \quad 14.3$$

The interrelationships between the quantities are

$$k = \frac{a_1}{b_1} = \frac{w}{w + 2s} \quad 14.4$$

where  $w$  is the width of the center strip and  $s$  is the separation between this strip and each of the coplanar ground planes,

$$k' = \sqrt{(1 - k^2)} \quad 14.5$$

and

$$K'(k) = K(k'). \quad 14.6$$

In the initial expressions we are referring to basic CPW, that is, not conductor-backed, the substrate thickness is considered large enough to be theoretically infinite, and the conductor thicknesses are regarded as negligible. The effect of the substrate thickness is considered later.

### 14.2.1 Effective Permittivity

The effective permittivity of CPW is defined in exactly the same fundamental way as that of microstrip, and for that matter for any form of interconnect structure:

$$\epsilon_{\text{eff}} = (c/v_p)^2. \quad 14.7$$

Here  $c$  is the free-space velocity and  $v_p$  is the phase velocity of the dominant mode in CPW.

Hilberg [8] gives what are termed exact relations for both the effective permittivity and also the characteristic impedance of CPW. His equation for the effective permittivity is

$$\begin{aligned} \epsilon_{\text{eff}} = 0.5(\epsilon_r + 1) &\{\tanh[1.785 \log(h/s) + 1.75] \\ &+ (ks/h)[0.04 - 0.7k + 0.01(1 - 0.1\epsilon_r)(0.25 + k)]\}. \end{aligned} \quad 14.8$$

Hilberg quotes this expression as being accurate within approximately 1.5% provided that

$$h/s \geq 1. \quad 14.9$$

In practice this means that either relatively thin substrates ( $h \approx s$ ,  $h \approx w$ ) or wide gaps ( $s \gg w$ ) are prohibited, but this should be anticipated in any event in almost all practical implementations. In practice, when  $h/s$  is near to or less than 1, the microstrip mode can readily be generated with the resultant unpredictable coupling of energy between this mode and the desired CPW mode. In this case, the influence on the effective permittivity is not by any means the major problem.

To quite a close approximation, the distributions in the air and the substrate of the electric fields associated with CPW are reasonably independent of geometry and frequency. Therefore, unlike microstrip and many other interconnect structures, the effective permittivity is not particularly sensitive to the geometry of the structure. Equation (14.8) can therefore be used in a wide variety of CPW “open” structures.

Conductor-backed shielded or asymmetric CPW require further attention and these will be considered to some extent later.

## 14.2.2 Characteristic Impedance

The characteristic impedance of CPW is, like the effective permittivity, defined in precisely the same way as for any other transmission medium. A CPW line terminated in a purely resistive load, having the same value as the characteristic impedance of the line, will be perfectly matched.

The basic expression, originally due to Wen [1], is

$$Z_0 = \frac{30\pi}{\sqrt{\epsilon_{\text{eff}}}} \frac{K'(k)}{K(k)}. \quad \text{14.10}$$

Many researchers and engineers consider that  $K'(k)$  and  $K(k)$  need to be determined using tables of elliptic integrals. However, in 1969 Hilberg [9] gave two closed expressions for the characteristic impedance, and these are dependent upon the range of  $k$  involved. The first expression covers the lower range of  $k$ ,  $0 \leq k \leq 0.707$ :

$$\frac{K(k)}{K'(k)} = \frac{1}{\pi} \ln \left( 2 \frac{1 + \sqrt{k}}{1 - \sqrt{k}} \right). \quad \text{14.11}$$

The second expression covers the higher range of  $k$ ,  $0.707 \geq k \geq 1$ :

$$\frac{K'(k)}{K(k)} = \frac{1}{\pi} \ln \left( 2 \frac{1 + \sqrt{k}}{1 - \sqrt{k}} \right). \quad \text{14.12}$$

Note the different structures of Equations (14.11) and (14.12). Again, conductor-backed, shielded or asymmetric CPW require further attention, and these will be considered to some extent later.

## 14.3 Formulas for Accurate Calculations

The above expressions provide for reasonable accuracy but are mainly aimed at analysis of CPW, that is, knowing the structure, the characteristic impedance can be found. However, in practice engineers generally know the characteristic impedance required in a design, and must determine the width  $w$  and the spacing  $s$  of the CPW. This is termed synthesis.

### 14.3.1 Analysis and Synthesis Approaches

Equation (14.4), expressing  $k = w/(w + 2s)$ , shows that we can obtain  $k$  by manipulating the analysis equations above. For example, when  $0 \leq k \leq 0.707$  Equation (14.11) applies.

Combining Equations (14.10) and (14.11) and simplifying the argument of the logarithm as  $x$ , we have

$$x = \exp\left(\frac{30\pi^2}{Z_0\sqrt{\epsilon_{\text{eff}}}}\right) = 2\frac{1+\sqrt{k}}{1-\sqrt{k}}. \quad 14.13$$

Similarly, when  $0 \leq k \leq 0.707$  Equation (14.12) applies and

$$x = \exp\left(\frac{Z_0\sqrt{\epsilon_{\text{eff}}}}{30\pi^2}\right) = 2\frac{1+\sqrt{k}}{1-\sqrt{k}}. \quad 14.14$$

Synthesis requires that  $k$  be found but since  $\epsilon_{\text{eff}}$  is a function of  $k$ ,  $k$  must be found iteratively. A suitable initial starting value for  $\epsilon_{\text{eff}}$  is simply  $(\epsilon_r + 1)/2$ . This expression results from the observation that some of the field is in the substrate ( $\epsilon = \epsilon_r \epsilon_0$ ) whilst some is in the air ( $\epsilon = \epsilon_0$ ). As an approximation the effective permittivity must therefore be somewhat greater than just  $\epsilon_r/2$ . The parameter  $k$  is then easily found from  $x$ . It is then necessary to initially select a value for the strip width  $w$  at some convenient value and then solve for the required gap  $s$  using Equation (14.4). A more complete iteration then returns to Equation (14.8) followed by repeated application of the appropriate impedance expressions.

Specifically, for design on 200  $\mu\text{m}$ -thick GaAs substrates, Ghione and Naldi [5] provide a useful chart of  $Z_0$  versus  $k$  (their Figure 4), which leads to the required width and separation for the CPW line. Ghione and Naldi use the simplifications  $b (= s+a)$  and  $a = 0.5w$ . By curve-fitting we have developed a simple expression that fits Ghione and Naldi's results to within an accuracy of about 4% for the worst case, and this occurs at the low impedance extreme where  $b = 0.05$  mm and  $a = 12$  mm. In practice this would be unacceptable in any event because the strip width is so large. The expression is

$$Z_0 = \frac{47.12}{\sqrt{\epsilon_{\text{eff}}}} \frac{[1 + (b^2/2)]}{\sqrt{0.43a/b}}. \quad 14.15$$

In this equation  $b$  is in mm. This applies over the ranges

$$0.4 \leq a/b \leq 0.6 \text{ and } 0.05 \leq b \leq 0.35$$

although, as described above, the lower extreme of  $b$  should be avoided.

Now, it turns out that  $\epsilon_{\text{eff}}$  varies only slowly with  $a/b$ , but its value as a function of  $b$  must be known. Equation (14.8) could be used, although again starting values of the target  $w$  and  $s$  are required.

For guidance, on GaAs substrates  $\epsilon_{\text{eff}}$  takes on the following values for typical values of  $b$ :

$b$ (mm)	0.35	0.26	0.05
$\epsilon_{\text{eff}}$	4.2	4.6	5.0

Therefore to a first approximation, values of  $\epsilon_{\text{eff}}$  may be interpolated between the above data, for intermediate values of  $b$ .

For synthesis Equation (14.15) may be used. Explicitly, as it stands we have one equation but

two ( $a$  and  $b$ ) unknowns, but it turns out that the term  $(1 + b^2/2)$  is always relatively small. For the range of  $b$  given above, the maximum value  $(1 + b^2/2)$  is 1.061. Therefore, a starting value of this term can be, for example, 1.05. Then Equation (14.15) can easily be rearranged for  $a/b$ , giving

$$\frac{a}{b} = \frac{1 + b^2 + (b^4/4)}{M} \quad 14.16$$

where

$$M = \frac{Z_0^2 \epsilon_{eff}}{5163.5}. \quad 14.17$$

Rearranging Equation (14.16) leads to:

$$M \frac{a}{b} = 1 + b^2 + (b^4/4), \quad 14.18$$

which is a quadratic in  $b^2$ . Setting  $b^2 = y$  for simplicity, Equation (14.18) becomes

$$y^2 + 4y = 4M \frac{a}{b} - 4, \quad 14.19$$

which is of course a simple quadratic in  $y$  because the right-hand side is a known quantity at this stage. Solving for  $y$  and then taking the square root of the result yields  $b$ .

Clearly there is substantially more work to be completed in order to verify and extend these design equations and procedures. In particular, there is a need for computer simulations to provide design data, typically in the form of design curves. These equations serve to provide a good initial estimate and, crucially, provide design insight, including trends that are not available from computer simulations.

Once more, the consideration of conductor-backed, shielded or asymmetric CPW requires further attention, and these will be considered later.

## 14.4 Loss Mechanisms

In common with all interconnect structures that include metal parts, CPW exhibits two distinct transmission loss mechanisms: dielectric losses and also ohmic or conductor losses. Radiation losses can also become noticeable with CPW, but this is much lower than with microstrip. It is significant to be able to characterize CPW in terms of these losses because usually their minimization is important.

Both dielectric and conductor losses occur continuously along the length of the transmission structure. We therefore quote these losses in terms of loss or attenuation coefficients  $\alpha_D$  and  $\alpha_C$ , respectively, and the fundamental units are Nepers per meter (Np/m). Conversion to the more familiar dB/mm or dB per wavelength (dB/ $\lambda_g$ ) is straightforward, for example dB per wavelength is obtained by dropping  $\lambda_g$  in the denominator and multiplying by 27.3.

#### 14.4.1 Dielectric Loss

The dielectric loss is given as a function of the transmission medium filling factor ( $q$ ) the relative permittivity ( $\epsilon_r$ ) and loss tangent ( $\tan \delta$ ) of the substrate, the effective permittivity and also the wavelength for transmission along the CPW as

$$\alpha_D = \frac{q\epsilon_r \tan \delta}{\epsilon_{\text{eff}} \lambda_g} \quad (\text{Np/m}). \quad 14.20$$

In practice, the values of the filling factor and the permittivities are minor influences on this dielectric loss, which always remains dominated by the loss tangent of the substrate material, which this tends to be around 0.001 or lower for most substrates, including semiconductors. The effect of the dielectric loss is therefore relatively low in most instances.

Where it is suspected that an unusually dielectrically lossy substrate is being adopted then Equation (14.20) is useful to estimate the extent of these losses. A notable exception is standard silicon substrates, for which the resistivity is only about 1000  $\Omega \cdot \text{cm}$ . A single loss tangent is insufficient to describe the loss of standard silicon because of the appreciable conduction in the substrate. In this case it is necessary to use an appropriate value of  $\tan \delta$  defined at some particular frequency, such as 30 GHz [4]. This problem is avoided by using HRS (resistivity of 4000  $\Omega \cdot \text{cm}$  or more), and in fact this type of substrate was developed for high-frequency interconnects.

#### 14.4.2 Conductor Loss

The metal conductor resistivity, skin effect, and influence of surface roughness are important parameters influencing loss. Conductor loss usually dominates the transmission losses in CPW. Rayit [7] and other researchers have reported the unloaded  $Q$  factor  $Q_u$  as the means for estimating the effects of the conductor loss:

$$Q_u = \left(\frac{w}{2}\right) Z_0 \sqrt{f}. \quad 14.21$$

The expression appears to work well for CPW up to 2 GHz, and at this frequency the attenuation is approximately identical to that applying to microstrip also having line width  $s$ . However, 2 GHz is a relatively low frequency for CPW applications, and it is therefore necessary to provide guidance that allows for design at much higher frequencies.

By solving the Laplace equation for the potential distribution within the CPW cross-section and also by performing measurements, Koshiji *et al.* [10] identified the following features applying to losses:

1. The dielectric attenuation coefficient  $\alpha_D$  is principally dependent on substrate thickness and the geometric ratio  $w/s$  has negligible influence.
2. The conductor attenuation coefficient  $\alpha_C$  is minimized at a specific (optimum) value of  $w/s$ .

**3.** The conductor attenuation coefficient  $\alpha_c$  is dependent on the relative permittivity  $\epsilon_r$  of the substrate,  $\alpha_c$  increases with increasing  $\epsilon_r$ .

**4.** As conductor thickness  $t$  is varied so also  $\alpha_c$  varies, and there is an optimum value of  $t$  that minimizes  $\alpha_c$ . Generally, however,  $\alpha_c$  is reduced by reducing the DC resistance of the interconnect.

Full electromagnetic analyses have been applied to predict the loss associated with CPW and this structure was compared with microstrip in this regard. The work of Jackson [11], for example, compares conductor loss, dispersion and radiation into parasitic modes for microstrip and coplanar waveguide. In this paper, focused on 0.1 mm thick semiconductor substrates at 60 GHz, it is shown that the dimensions of CPW may be selected so that this structure can provide substantially lower losses and dispersion than microstrip.

Dispersion is principally related to the frequency dependence of the partitioning of the field in the substrate and the covering medium (usually air). For small-geometry coplanar structures the dispersion is smaller relative to the situation with microstrip. Thus, low dispersion relative to microstrip is a fundamental property of small-geometry coplanar structures.

Zhang *et al.* [12] use the finite-difference transmission line matrix (FD-TLM) method to compare 50  $\Omega$  microstrip and CPW losses. An interesting outcome is that for a 50  $\Omega$  coplanar waveguide differing combinations of  $s$  and  $h$  yield different losses and these may become greater or less than those applicable to the microstrip line. Frequencies up to 100 GHz were considered.

It is therefore clear that one cannot generalize concerning losses in CPW compared with microstrip, the precise situation depends on the geometry. For 50  $\Omega$  lines it is recommended that the dimensions should be made as large as possible in order to maintain relatively small losses.

Analyses based on a frequency domain full electromagnetic wave method [13, 14] have shown that on standard 0.1 mm GaAs substrates CPW yields significantly lower attenuation than microstrip at higher values of characteristic impedance  $Z_0$ . On such substrates designers are recommended to choose relatively high  $Z_0$  values, as far as possible. This is fortuitous in many monolithic integrated circuit designs because high  $Z_0$  interconnects have relatively small dimensions, and so are far more economical in their use of substrate area and, for digital circuits, lower drive current requirements. A conceptual understanding of the loss behavior is that for the same transmitted signal power  $P$ , a high impedance ( $Z_0$ ) interconnect has a lower current  $I$  ( $\propto \sqrt{P/Z_0}$ ) and hence there are lower  $I^2R$  losses.

An extensive study of attenuation in CPW on silicon (Si), gallium arsenide (GaAs), and indium phosphide (InP) substrates was conducted by Ponchak *et al.* [15]. This study provides detailed design data and expressions applicable to CPW on the substrates identified in [Table 5.7](#), and frequencies in the range from 1 GHz to 40 GHz apply. This table provides a useful reference for the permittivities, loss tangents, and some typical thicknesses of these four important semiconductors.

As a result of the much lower losses, HRS is preferred to standard silicon for RF, microwave, and millimeter-wave design.

In the cited study [15] the transmission lines were fabricated on double-sided polished semiconductor wafers with top-side metallization comprising a 0.02  $\mu\text{m}$ -thick titanium layer followed by gold layers with three specific thicknesses of 0.49, 1.5, and 2.22  $\mu\text{m}$ , respectively. The structures do not have conductor-backing, that is, there is no underside grounding. Other features of this study include:

- aspect ratio  $k = w/(w + 2s)$  for the range  $0.2 \leq k \leq 0.7$
- $Z_0$  range  $35 \leq Z_0 \leq 65 \Omega$
- center strip width range  $10 \leq w \leq 80 \mu\text{m}$ .

Side ground plane widths are maintained equal to  $4w$  in all cases, ensuring that all results are independent of this width, with no spurious resonances being excited. Also, the substrate thickness  $h$  is maintained such that  $h \geq 3(w + 2s)$  in order to ensure that the results are independent of this thickness.

Ponchak *et al.* [15] report a substantial array of information on the average RMS error between other reported quantities from five separate sources, their measured data, and curve-fitted equations. Their new closed form expressions are

$$\alpha = af^b \quad (\text{dB/cm}) \quad \underline{\underline{14.22}}$$

$$a = \sqrt{\frac{\epsilon_r - 1}{2}} \left[ \frac{(45.152)}{(sw)^{0.41} \exp(2.127\sqrt{t})} \right] \quad \underline{\underline{14.23}}$$

$$b = 0.183(t + 0.464) - 0.095k_t^{2.484}(t - 2.595) \quad \underline{\underline{14.24}}$$

where  $w$ ,  $s$ , and  $t$  are in  $\mu\text{m}$ ,  $f$  is in GHz, and  $k_t$  is given by the following expressions:

$$k_t = \frac{w + \Delta t}{w + 2s - \Delta t} \quad \underline{\underline{14.25}}$$

$$\Delta t = \frac{1.25t}{\pi} \left[ 1 + \ln \frac{4\pi w}{t} \right]. \quad \underline{\underline{14.26}}$$

As the development of the above expressions is based upon measurements, all three loss mechanisms are accounted for: dielectric, conductor, and radiation.

The application of Equations (14.22) through (14.24) is quoted by Ponchak *et al.* [15] as being valid for the following parameter ranges:

$0.2 \leq k \leq 0.7$	$10 \leq w \leq 80 \mu\text{m}$	$0.5 \leq t \leq 3.0 \mu\text{m}$	$1 \leq f \leq 40 \text{ GHz}$
-----------------------	---------------------------------	-----------------------------------	--------------------------------

The applicability of these expressions to Si substrates requires a significant condition, namely that the Si must be of high resistivity, specifically  $\geq 2500 \Omega\text{cm}$ , otherwise there would be a

significant substrate resistivity effect influencing loss. The average error of these expressions is reckoned as 4.7% where the substrate is GaAs with metal thickness  $1.58 \mu\text{m}$ , but may be somewhat higher for Si and InP. The error increases to 6% when all three metal thicknesses are accounted for.

For design, Equations (14.22) through (14.26) may be used judiciously for guidance. Where a maximum attenuation must be specified, the metal thickness is known and  $k_t$  is relatively small, to the extent that Equation (14.24) may be reduced to its first term only, that is,  $b \approx 0.183(t - 0.464)$ . Then Equations (14.23) and (14.24) may be combined in order to determine the  $w \cdot s$  product, guaranteeing that this maximum attenuation is not exceeded.

The design approaches given earlier, through synthesis leading to  $a/b$  and hence strip width  $w$  and separation  $s$ , can then be used to finalize the CPW design process.

### 14.4.3 Radiation Loss

The subject of radiation loss is only covered briefly at this stage. In the discussion under “conductor losses” above it was pointed out that the work of Ponchak *et al.* [15] includes the effects of radiation losses in CPW lines. More details concerning radiation losses are provided within the subsequent sections on discontinuities, notably the pseudo short circuit.

### 14.4.4 CPW with Intervening $\text{SiO}_2$ Layer

There are disadvantages involved with directly depositing metal layers onto the silicon substrate surface due to surface effects on the silicon and often relatively high losses. This surface effect is attributed to trapped charges in the silicon near its surface. Increasingly, therefore, the metal conductor pattern is deposited onto an intervening layer of silicon dioxide ( $\text{SiO}_2$ ), which has a relative permittivity of around 3.8, similar to that of fused quartz.

Low resistivity inversion layers are frequently required between the  $\text{SiO}_2$  layer and the silicon, and a cross-section of the entire structure is shown in Figure 14.6. Although aluminum metal is shown, copper is increasingly being used for its lower resistivity, which is particularly important for fine interconnects with cross-sectional dimensions of a micron or less. However, the losses inherent in the  $\text{SiO}_2$  layer (if isotropic) again increase and become almost unmanageably high, as high as 1.8 dB/mm at high frequencies. By patterning this intervening layer Wu *et al.* [16] showed that these losses can be reduced to nearer 0.3 dB/mm at 30 GHz.

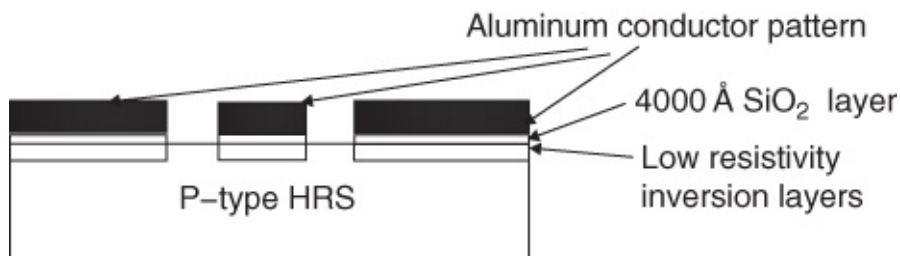


**Figure 14.6** CPW with an intervening  $\text{SiO}_2$  layer. HR, high resistivity.

# 14.5 Dispersion

## 14.5.1 Fundamental and Theoretical Considerations

In common with all electrical signal transmission structures CPW is to some extent dispersive, that is, the transmission phase constant  $\beta$  varies non-linearly with frequency. This effect, however, can be quite small for CPW relative to microstrip.

Using the familiar effective permittivity concept, expressed by Equation (14.8) for low frequencies, we can extend this to account for the frequency-dependent quantity  $\epsilon_{\text{eff}}(f)$  that is now fundamentally defined by

$$\epsilon_{\text{eff}}(f) = (c/v_p)^2 \quad 14.27$$

where  $c$  is the free-space velocity and  $v_p$  is the velocity of propagation of the dominant CPW mode.

Many closed-form expressions have been developed for microstrip dispersion over the years and Rayit [7] chooses Yamashita's formula, which was first reported in 1979 [17]. This is repeated here in a form suited to the case of CPW dispersion:

$$\epsilon_{\text{eff}}(f) = \sqrt{\epsilon_r} + \frac{(\sqrt{\epsilon_r} - \sqrt{\epsilon_{\text{eff}}})}{1 + p(f/f_{te})^{-r}}. \quad 14.28$$

We have found that this expression, used in conjunction with the following analytical formulas, works well for alumina substrates with thicknesses around 0.635 mm. Also, its use is restricted to relatively large geometry CPW, in the region of hundreds of microns in lateral dimension.

In this expression  $\epsilon_{\text{eff}}$  is the static-TEM effective permittivity,  $f$  is the frequency as independent variable as usual, and  $f_{te}$  is the cut-off frequency for the lowest order TE mode, given by

$$f_{te} = \frac{c}{4h\sqrt{(\epsilon_r - 1)}}. \quad 14.29$$

Parameters  $p$  and  $r$  depend on the configuration of the CPW line, and Rayit [7] quantifies these for various aspect ratios. It was found, for design on alumina substrates at least, that  $r \approx 1.8$  (compare Yamashita's 1.5), and according to Rayit the quantity  $p$  approximately follows the linear equation

$$\log p \approx u \log(w/s) + v \quad 14.30$$

in which  $u$  and  $v$  are functions of the substrate thickness  $h$ , as follows

$$u = 0.54 - 0.64q + 0.015q^2 \quad 14.31$$

$$v = 0.43 - 0.86q + 0.54q^2$$

**14.32**

where

$$q = \log(w/h).$$

**14.33**

By curve fitting to Rayit's experimental and theoretical data, it has been found that Equation (14.30) considerably overestimates the dispersion, and in fact the logarithmic relationship does not hold. The relationships always depend on the geometry, that is,  $w/(w + 2s)$ , because the dispersion is inherently geometry dependent, affected by the proportion of the field above and below the metallization layer.

We have found that for the characteristic impedance range  $39 \leq Z_0 \leq 55 \Omega$  the value for  $p = 0.257$  yields an excellent model for dispersion calculations. This value holds up to  $Z_0 = 55 \Omega$ , and above this value the following expression is effective:

$$p = 1 - \left( \frac{w}{w + 2s} \right)^{1.5}. \quad 14.34$$

Examples of calculations using the above expressions are provided in Figures 14.7 through 14.9. The fit is very good in all cases, and may possibly hold above 70  $\Omega$ , although this has not been validated.

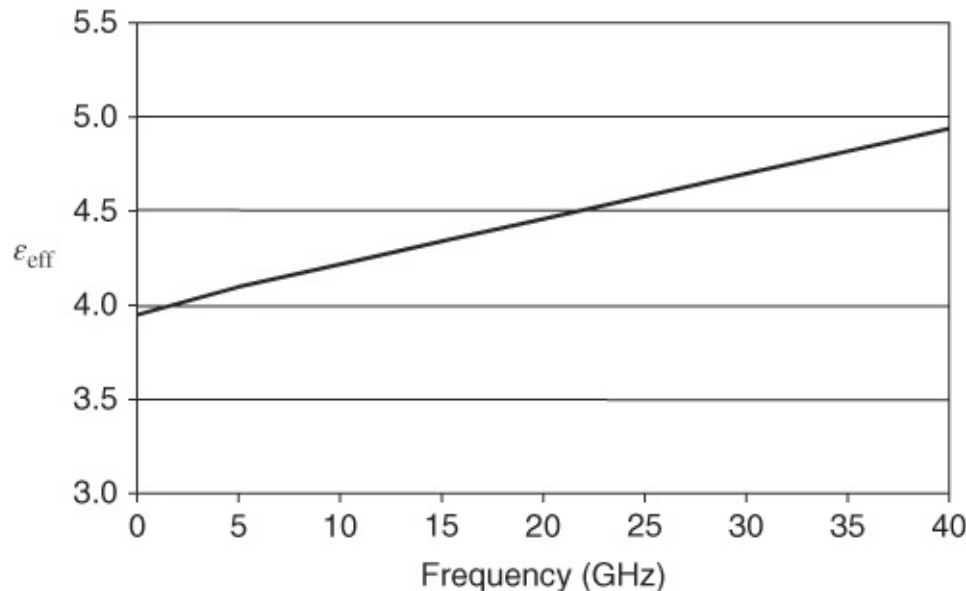


**Figure 14.7** Dispersion in a  $39 \Omega$  CPW on alumina ( $\epsilon_r = 9.5$ ,  $h = 0.635$  mm).

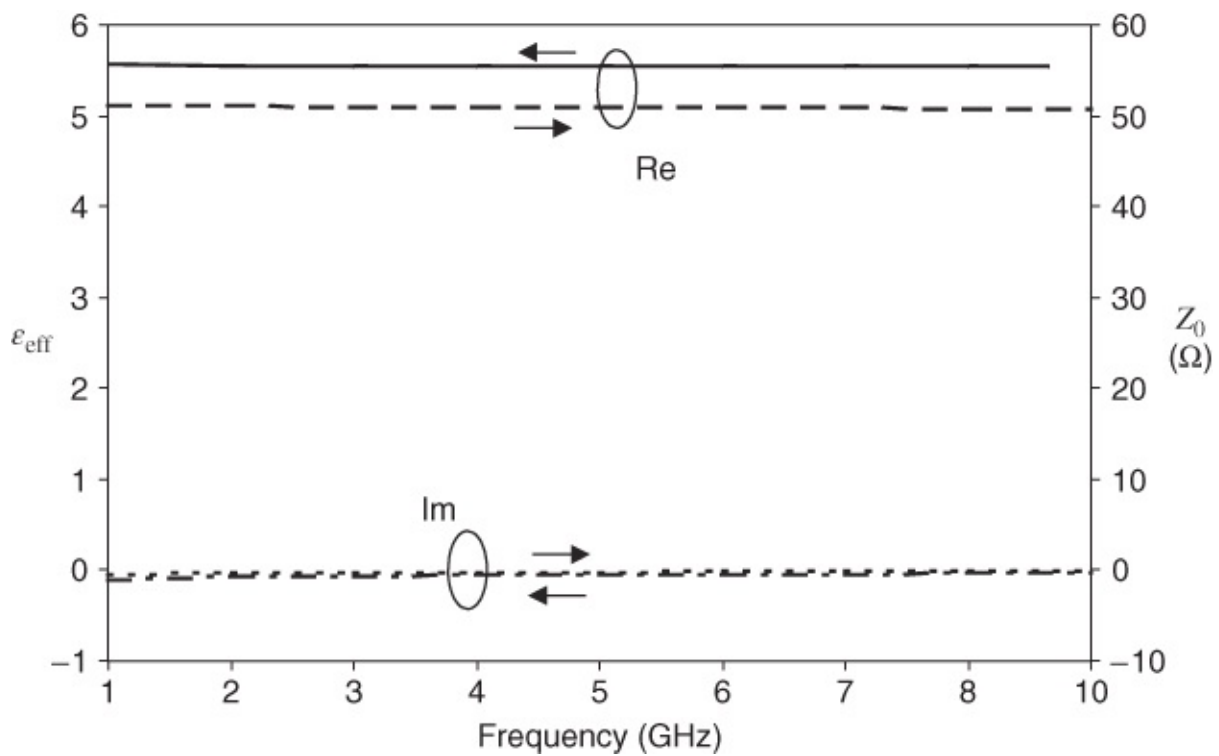


**Figure 14.8** Dispersion in a 50  $\Omega$  CPW on alumina ( $\epsilon_r = 9.5$ ,  $h = 0.635$  mm).

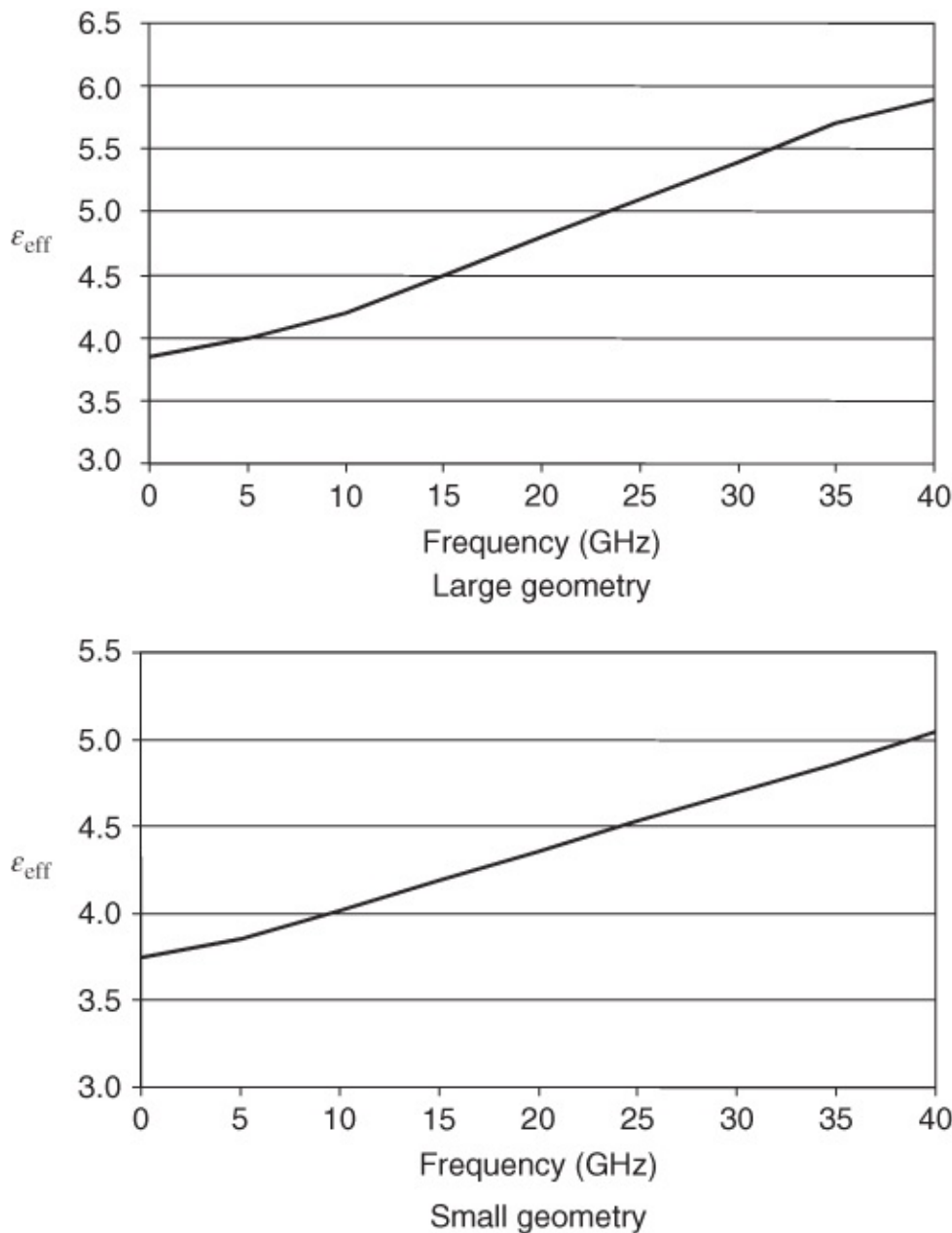


**Figure 14.9** Dispersion in a  $70 \Omega$  CPW on alumina ( $\epsilon_r = 9.5$ ,  $h = 0.635$  mm).

In general, this approach cannot be expected to work with the smaller geometry CPW applicable to chip-scale semiconductor substrates because the data fit was restricted to relatively large alumina substrates. However, for chip-scale substrates it has been shown that dispersion is usually negligible, as indicated by the data generated using commercial electromagnetic simulation software and summarized in the following section.

#### 14.5.2 Results from Test Runs using Electromagnetic Simulation

In this section we present the results from running a variety of representative CPW structures using the SONNET simulation program suite. In all instances the structure is metal backed, and the thickness of this metal backing is always identical to the top surface metallization and both the substrate and the metal are lossy, unless otherwise stated. Since a major feature concerns the frequency dependence of the effective permittivity  $\epsilon_{\text{eff}}(f)$  and of the characteristic

impedance  $Z_0$ , most of the following figures show this behavior for both real and imaginary parts of each parameter, over the 10–110 GHz frequency range in most instances.

The first sets of examples are for CPW on GaAs substrates, and in [Figure 14.10](#) the frequency-dependent results are shown for such a structure with a gold metal thickness of 2  $\mu\text{m}$ , a CPW width  $w = w_1$  of 20  $\mu\text{m}$ , and a separation,  $s$ , of 15  $\mu\text{m}$ . The substrate thickness is 500 microns, the dielectric loss tangent is  $5 \times 10^{-4}$  and the metal has  $R_{dc} = 0.012 \Omega/\text{square}$  ( $R_{dc} = 1/(\sigma t)$ , where  $\sigma$  is the metal conductivity and  $t$  is its thickness). The results indicate that both the real and imaginary parts of  $\epsilon_{\text{eff}}(f)$  fall more rapidly with frequency at first and then slowly later.  $Z_0$  also falls slowly with frequency across the 10–110 GHz range. These decreases are mainly due to the fact that the losses increase with frequency.

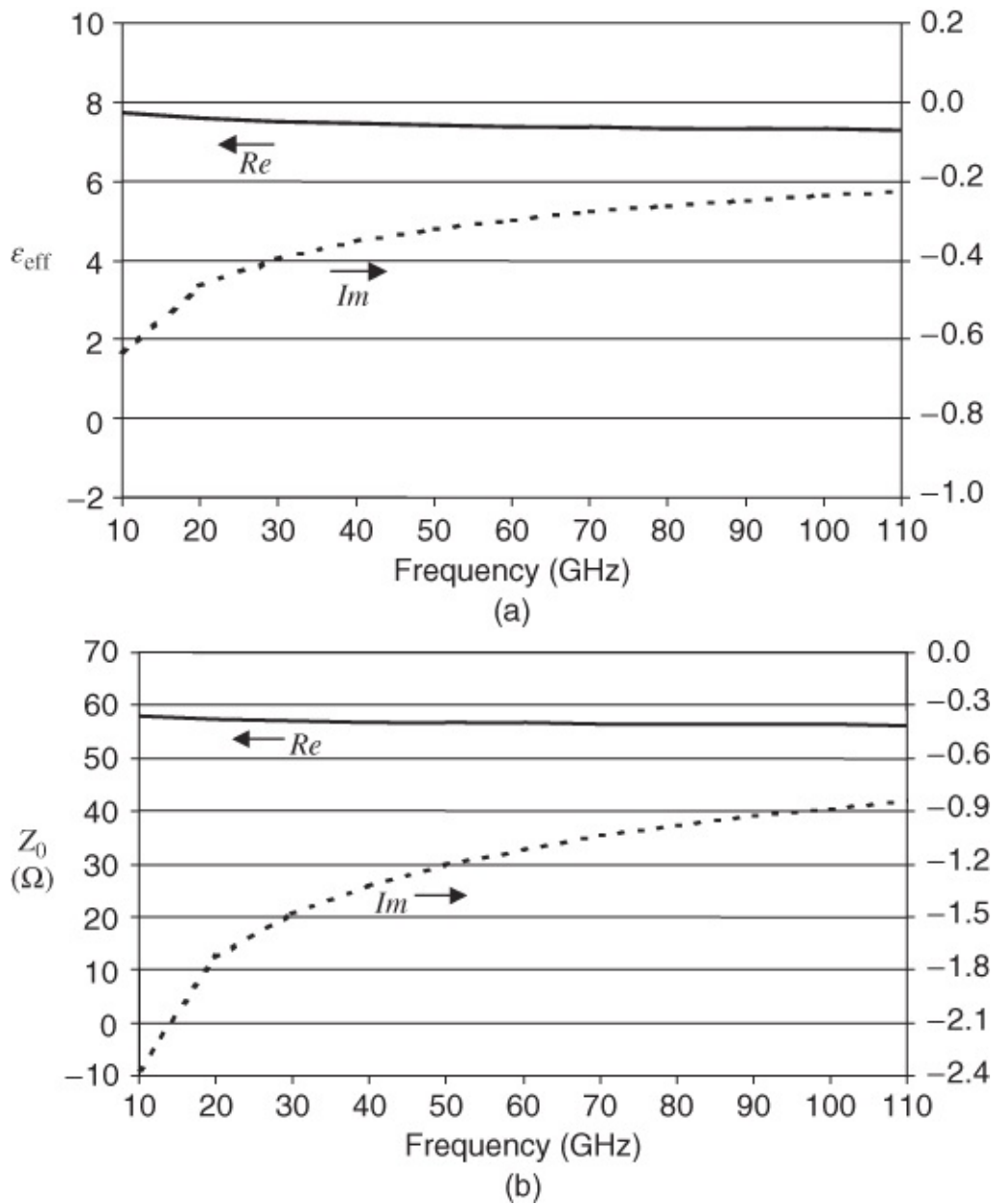


**Figure 14.10** Dispersion of CPW on GaAs with no backing: (a) effective permittivity; and (b) characteristic impedance.

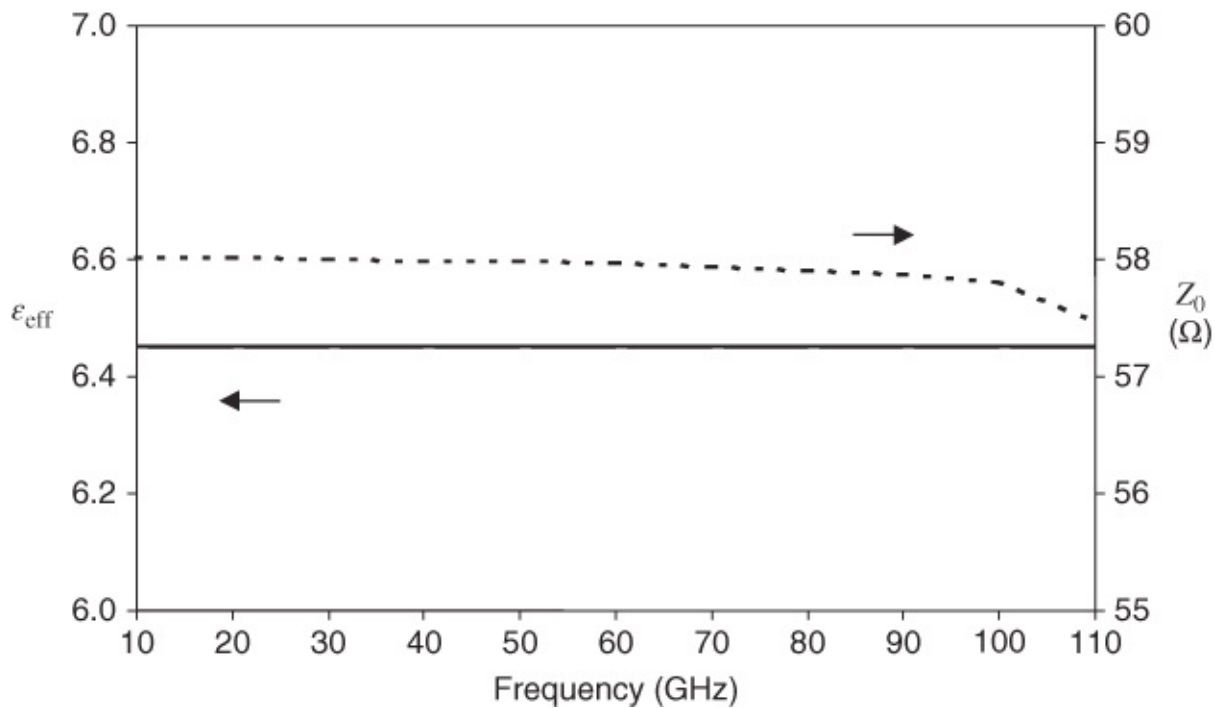


**Figure 14.11** Dispersion of CPW on GaAs ignoring dielectric and metallic losses.

For the same basic structure, but with all losses neglected, [Figure 14.12](#) shows that  $\epsilon_{\text{eff}}(f)$  is practically constant across the entire frequency range. However  $Z_0$ , after falling slowly over most of the range, decreases relatively rapidly above 100 GHz. As losses are considered negligible here, the imaginary parts of both  $Z_0$  and  $\epsilon_{\text{eff}}(f)$  are also negligible.

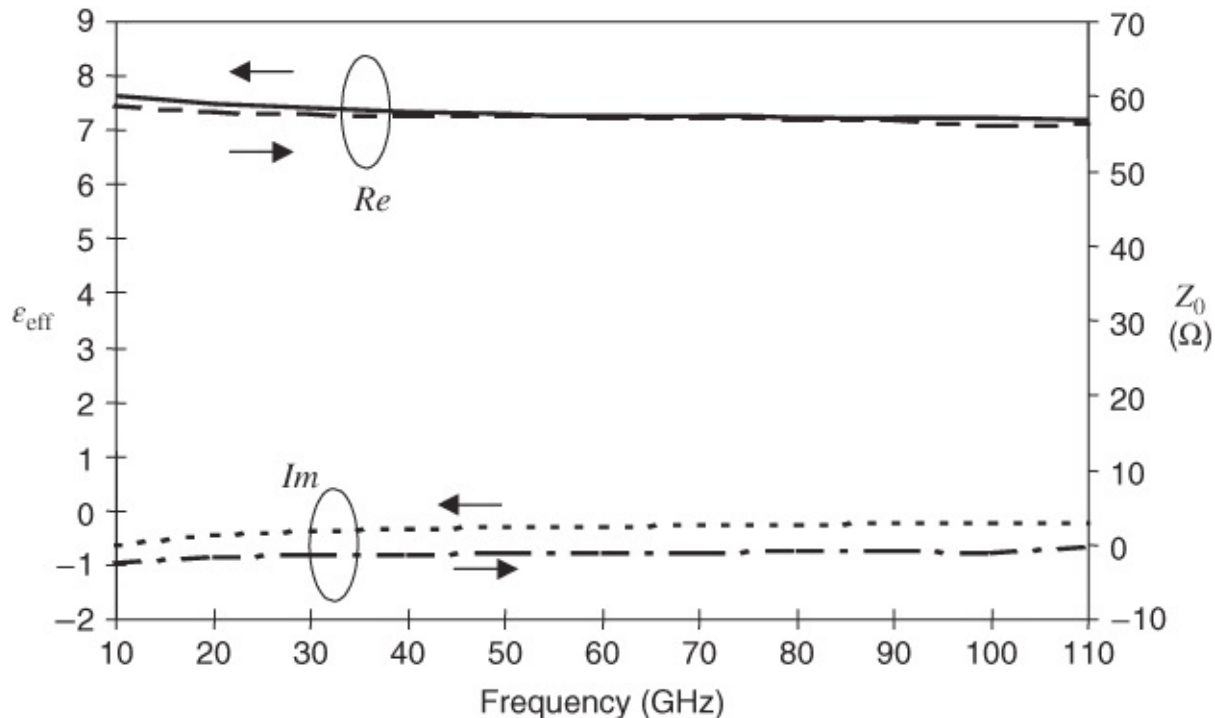


**Figure 14.12** CPW on GaAs with lossy gold metallization and ignoring dielectric losses, showing real  $\epsilon_{\text{eff}}$  and  $Z_0$ .

[Figure 14.13](#) has been generated using data for CPW on lossy GaAs, again with the same basic

structure as above, but with a  $3 \mu\text{m}$  covering of polyimide commonly used as a passivation layer to protect the semiconductor circuitry. Since this takes up some of the air gap between and just above the lines, as expected, the main effects are to slightly increase  $\epsilon_{\text{eff}}(f)$  and to slightly decrease  $Z_0$  at all frequencies. This decrease in  $Z_0$  can be traced to the increased capacitance per unit length caused by the polyimide layer. The effects of steadily decreasing the substrate thickness  $h$  are indicated in [Figure 14.14](#), where the data apply at a constant frequency of 30 GHz. For this structure, with  $h = 15 \mu\text{m}$  (not shown in [Figure 14.9](#)),  $Z_0 = 50 \Omega$  at 10 GHz and its lowest value is  $48.5 \Omega$  at 70 GHz.

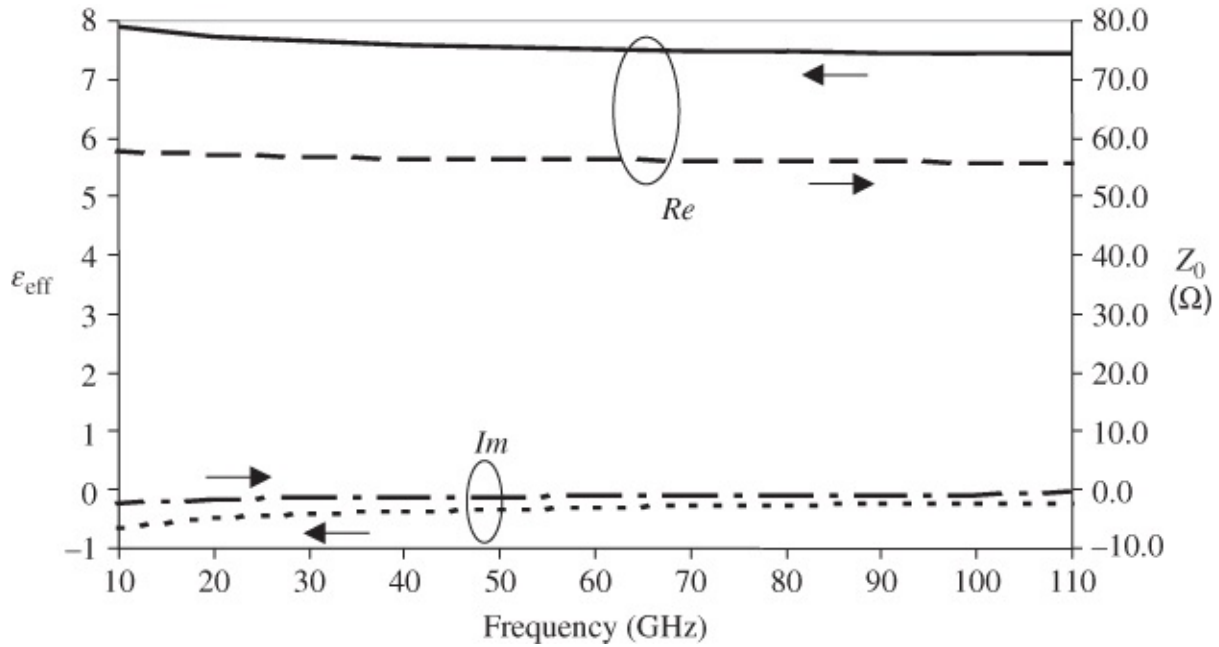


[Figure 14.13](#) CPW on lossy GaAs with  $3 \mu\text{m}$  of covering polyimide.

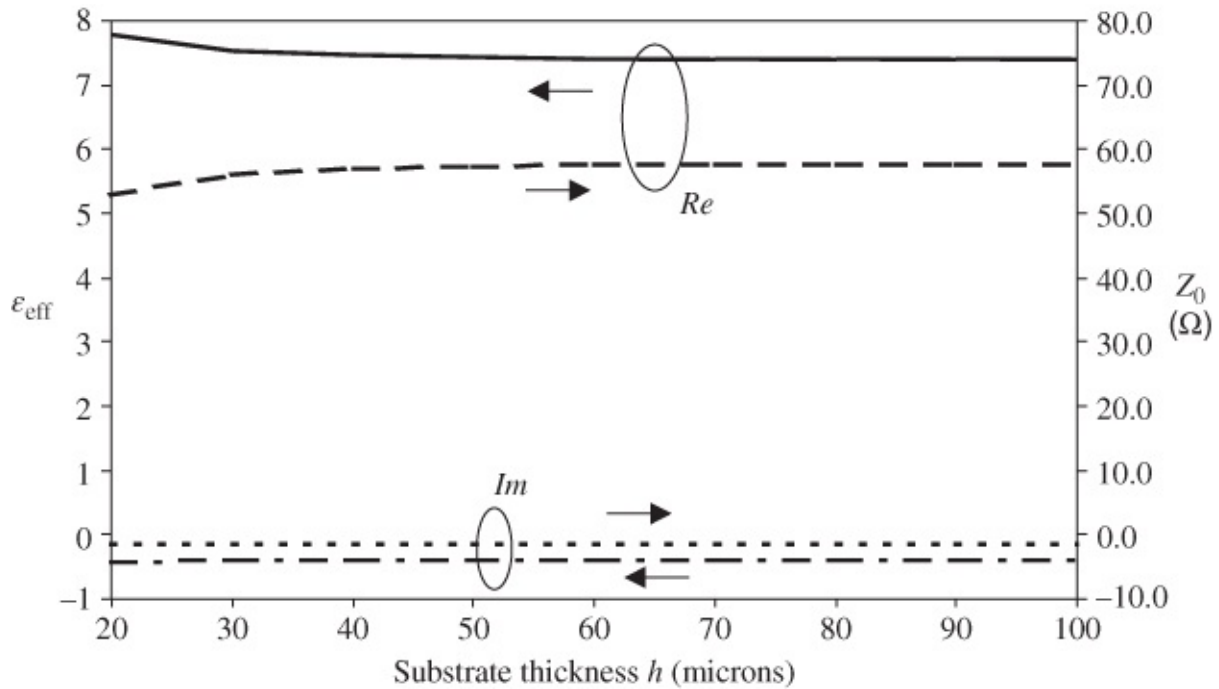


[Figure 14.14](#) CPW on GaAs: variation of parameters with  $h$ .

At relatively small values of  $h$ , around and just above the magnitude of the center conductor width, the real part of  $\epsilon_{\text{eff}}(f)$  decreases steadily whilst  $Z_0$  increases at a similar rate. This is due to the fact that for small values of substrate thickness  $h$  the capacitance per unit length is relatively large (the fields are more concentrated into the substrate). In contrast the imaginary parts of both  $\epsilon_{\text{eff}}(f)$  and  $Z_0$  remain almost constant across the complete range of  $h$ . For  $h \geq 45 \mu\text{m}$  all parameters are practically constant.

Another important parameter, the design sensitivity of which must be studied, is the effect of the widths of the finite ground planes,  $w_1$ . This is shown for the basic CPW on GaAs structure in [Figure 14.15](#). Again, all the data apply at a constant frequency of 30 GHz. Although the real part of  $\epsilon_{\text{eff}}(f)$  is almost invariant with  $w_1$  the characteristic impedance varies considerably, mainly decreasing with  $w_1$ . Further simulations, for values of  $w_1$  above 100 microns, have shown that the parameters settle down to practically constant values ( $w_1$  is then five to ten times the center conductor width). A design recommendation is then that

$w_1$  should be at least five times  $w$  to achieve all the benefits of CPW.

However, compromises are sometimes necessary for on-chip implementations. Referring to the current distribution shown in [Figure 14.3](#), when  $w_1$  is less than that recommended, longitudinal currents will exist on the outside edges of the CPW. The resulting electromagnetic fields mean that energy is stored away from the gap, leading to coupling to neighboring structures if they exist. The effective permittivity  $\epsilon_{\text{eff}}$  and  $Z_0$  increase as the additional energy is primarily stored in the electric field.

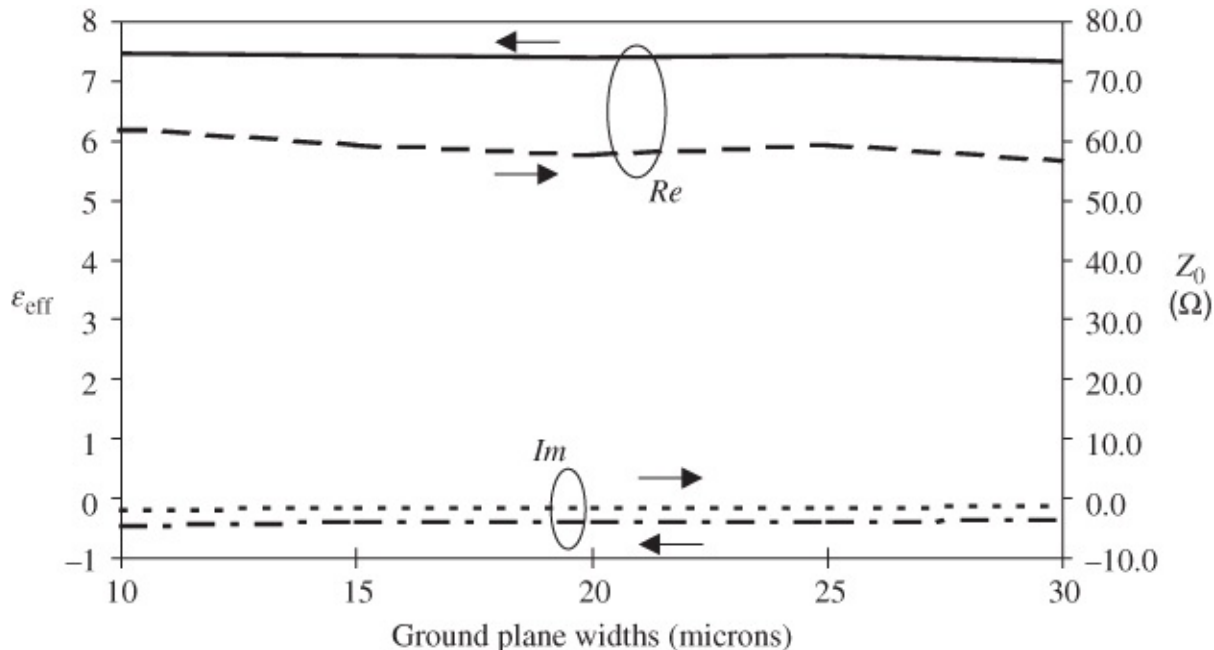


[Figure 14.15](#) CPW on GaAs: variation of parameters with coplanar ground plane width  $w_1$ .

[Figure 14.16](#) shows the results for CPW on a standard silicon substrate with lossy aluminum metallization having  $R_{dc} = 0.0185 \Omega/\text{square}$ . The metal thickness is  $1.46 \mu\text{m}$ , the CPW center strip width is  $70 \mu\text{m}$ , and the separation is  $40 \mu\text{m}$ . The thickness of the silicon substrate is  $650 \mu\text{m}$  and the dielectric loss tangent is  $4 \times 10^{-3}$ . The results indicate that the real part of  $\epsilon_{\text{eff}}(f)$  is

very nearly constant with frequency. However, because of the losses, which increase with frequency, the real part of  $Z_0$  falls somewhat at higher frequencies. In both cases the imaginary parts remain relatively small and change little with frequency.

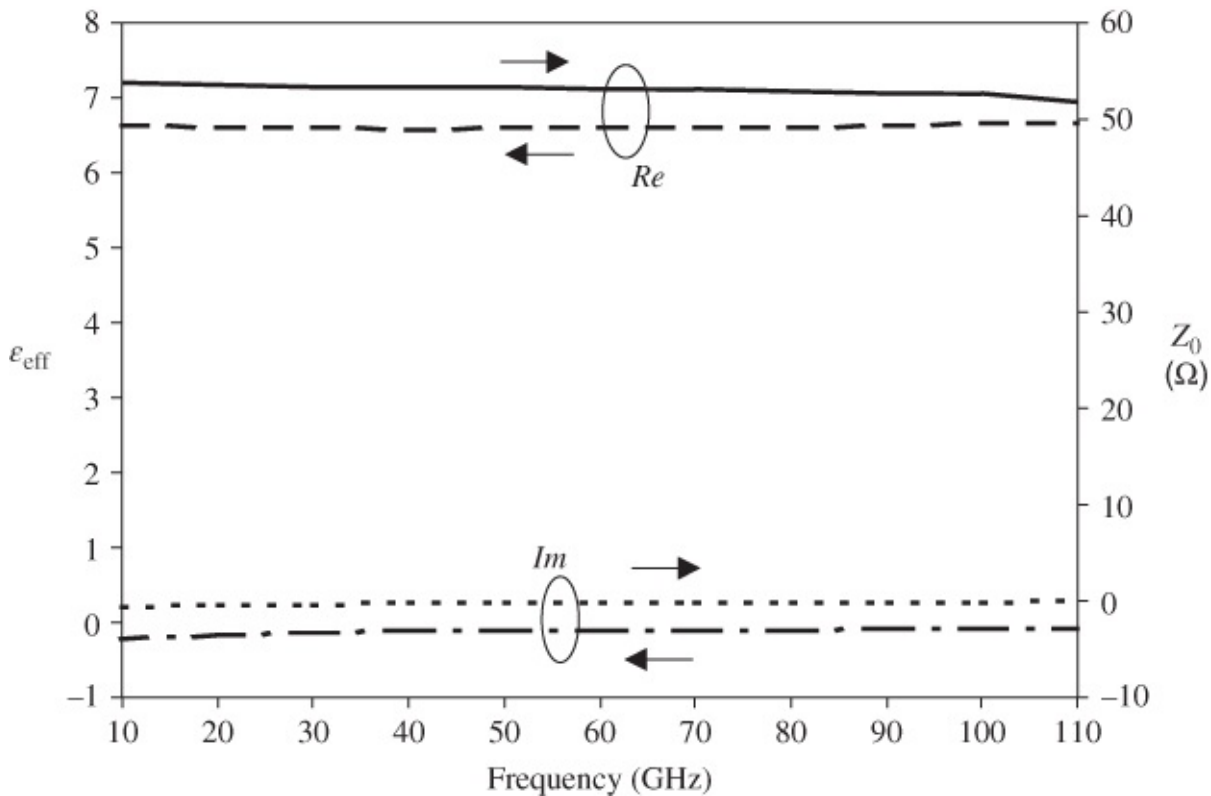


**Figure 14.16** CPW on standard silicon with loss included.

Apart from the implementation of CPW in MMICs, its use with non-semiconductor substrates is also important and some results have been obtained using simulation for CPW on alumina substrates. The frequency-dependent results for a nominally  $50\ \Omega$  CPW interconnect are shown in [Figure 14.17](#). The lossy gold metal thickness is  $5\ \mu\text{m}$ , center conductor width and ground plane widths are equal ( $w_1 = w$ ), the separation to the ground planes is  $200\ \mu\text{m}$ , and the substrate thickness is  $635\ \mu\text{m}$ . The relative permittivity of the alumina is 9.8, the dielectric loss tangent is  $2 \times 10^{-4}$ , and the metal has  $R_{dc} = 0.0048\ \Omega/\text{square}$ .

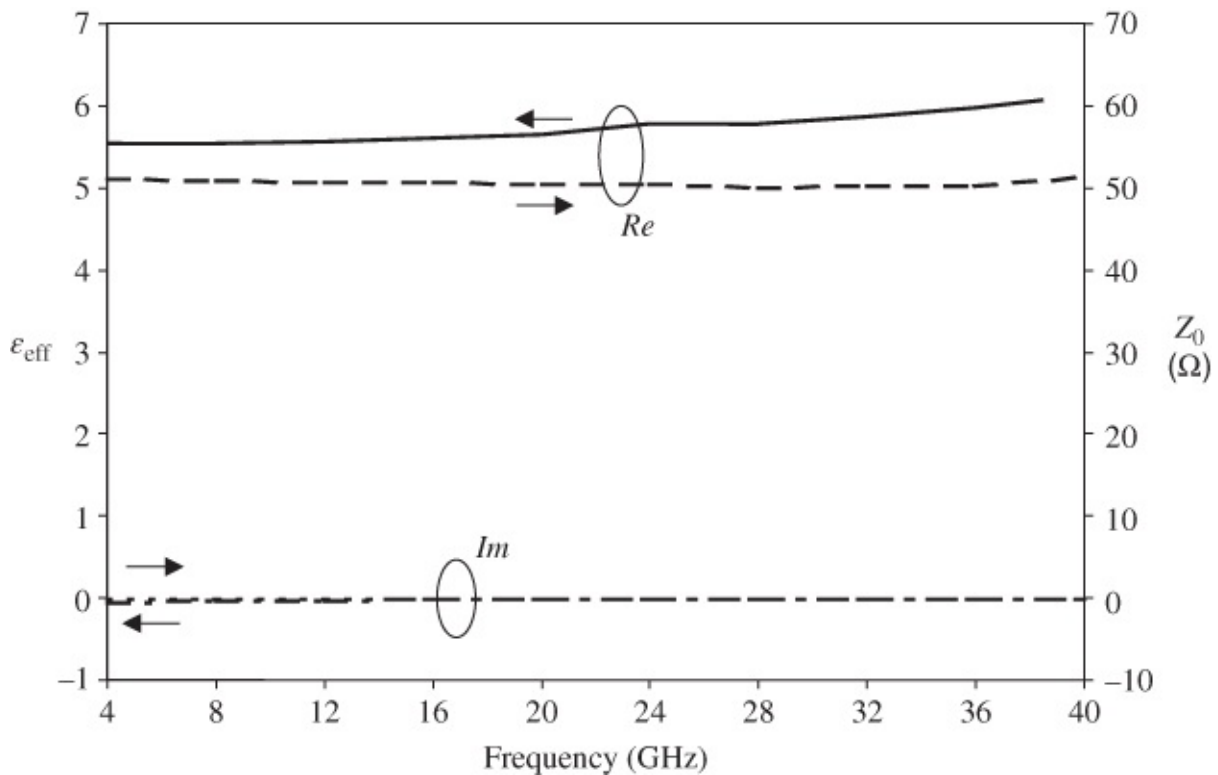


**Figure 14.17** 50  $\Omega$  CPW on alumina: frequency-dependent behavior.

[Figure 14.17](#) shows that, for this type of relatively large CPW structure, there is significant dispersion, indicated by the continuous and noticeable increase in the real part of  $\epsilon_{\text{eff}}(f)$  as frequency increases. In contrast, the real part of  $Z_0$  is substantially constant with frequency. In both cases, the imaginary parts of  $\epsilon_{\text{eff}}(f)$  and  $Z_0$  are relatively small. The significant dispersion with this type of structure was also confirmed by Rayit [7], whose results have been referred to earlier in this chapter.

From [Figure 14.18](#) it can be seen that the most marked effect is the steady increase in the real part of  $Z_0$ . This is expected because the separation is one parameter that influences  $Z_0$  significantly and provides design freedom over this parameter to some extent. At small separations ( $s$ ), well below 100  $\mu\text{m}$ , the real part of  $Z_0$  decreases more strongly as the separation decreases. In this instance a CPW structure that is nominally 50  $\Omega$  with a separation of 200  $\mu\text{m}$  becomes only 34.7  $\Omega$  when this separation is reduced to 50  $\mu\text{m}$ . Comments on the behavior of the real part of  $\epsilon_{\text{eff}}(f)$  and also on the imaginary parts of both  $\epsilon_{\text{eff}}(f)$  and  $Z_0$  are provided after the following discussion of the large separation range.

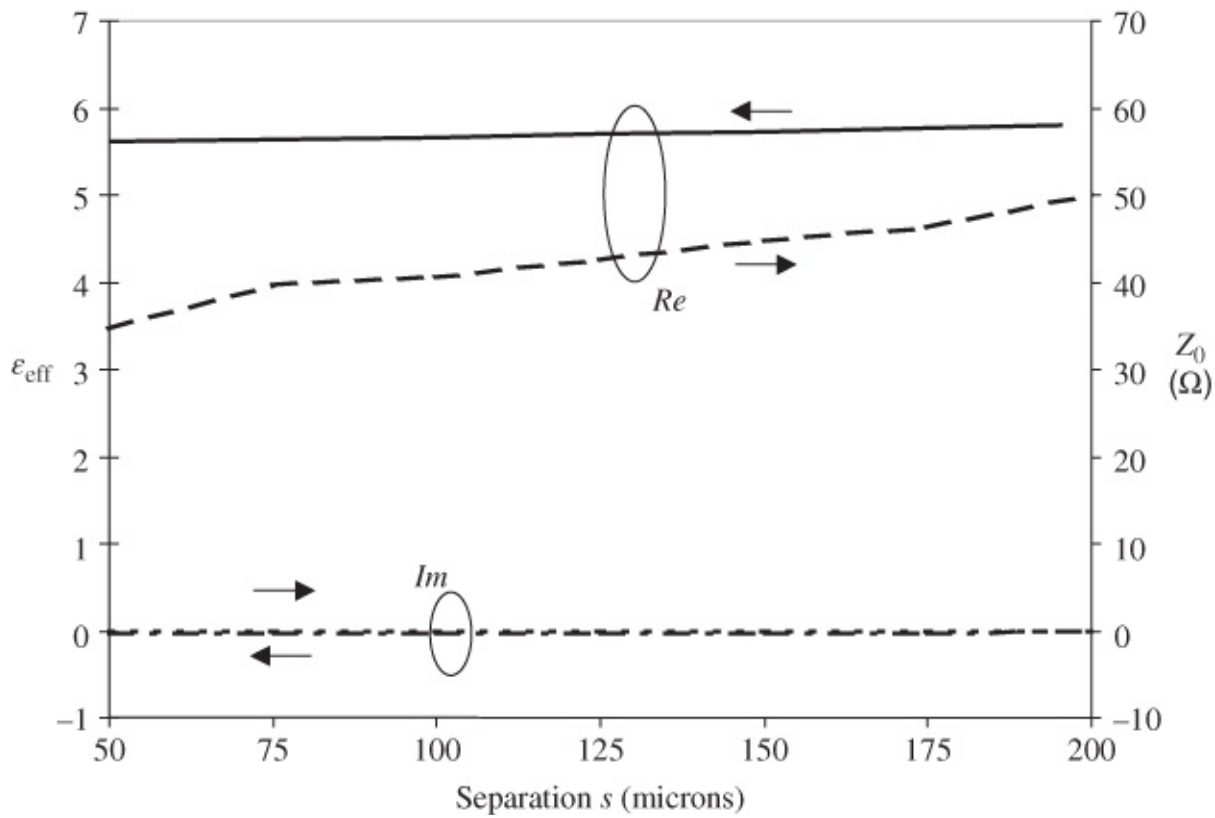


**Figure 14.18** 50  $\Omega$  CPW on alumina: parameter variations with separation (at 30 GHz, small  $s$  ).

For the same CPW structure on alumina, [Figure 14.19](#) indicates the variations of all four parameters, but now with a much wider range of variation of separation, from 100 to 450  $\mu\text{m}$ . The characteristic impedance  $Z_0$  continues increasing with  $s$ , as anticipated and for the same reasons described above. Throughout all values of  $s$ , from 50  $\mu\text{m}$  to 450  $\mu\text{m}$ , the real part of  $\epsilon_{\text{eff}}(f)$  slowly increases due to the fields becoming increasingly concentrated into the substrate as the ground planes are steadily taken away from the vicinity of the center strip. Also, for all values of  $s$ , the imaginary parts of both  $\epsilon_{\text{eff}}(f)$  and  $Z_0$  remain relatively small.

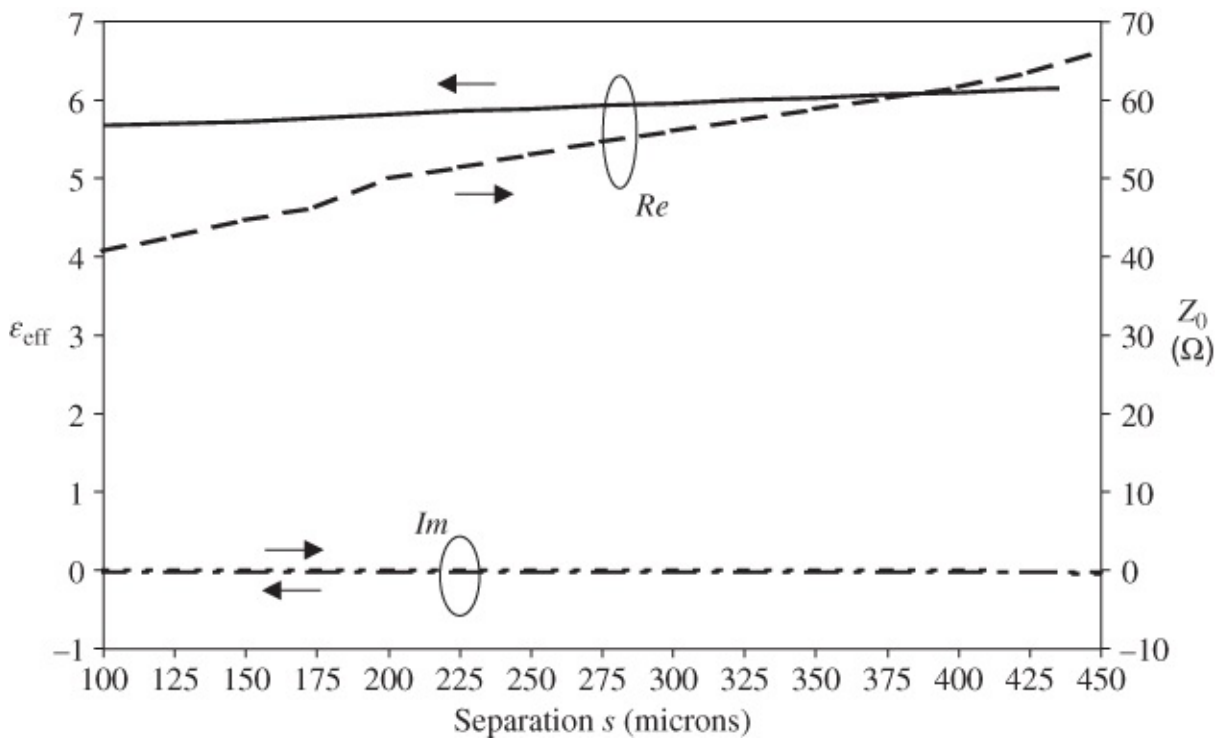


**Figure 14.19** 50  $\Omega$  CPW on alumina: parameter variations with separation (at 30 GHz, large  $s$ ).

For this structure the simulation revealed an interesting feature when the value of  $s$  became close to the substrate thickness  $h$ . The returned message was “ $\epsilon_{\text{eff}}(f)$  and  $Z_0$  are undefined.” This indicates that multimoding could occur and in this case simulation above  $s = 475 \mu\text{m}$  was beyond the range of validity. Values from 50 to 475  $\mu\text{m}$  represent the range of validity in this instance.

### 14.5.3 Experimental Results

For the case of alumina substrates ( $\epsilon_r = 9.5$ ), commonly used for hybrid microwave circuits, Rayit [7] reports the results of measurements on CPW dispersion. Resonator methods and a scalar network analyzer were used to conduct the measurements, employing a very similar methodology to that used for microstrip measurements. The scalar analyzer swept the CPW resonators over the band from 2 GHz to 38 or 39 GHz.

Two formats of resonator were employed: the ring resonator and straight or linear resonators. Again, this follows the philosophy used in the case of microstrip, described in [Chapter 9](#). The results show clearly that the measured results track the calculations using Equations [\(14.28\)](#) to [\(14.33\)](#) closely. Characteristic impedances ranged from 39 to 70  $\Omega$ . There is a significant difference in the amounts of dispersion resulting from changes in the magnitudes of the relative physical dimensions to realize identical specific characteristic impedances and this leads to an important design axiom:

*Smaller physical dimensions always result in lower dispersion.*

This comes about because, for a given frequency range, the mode-coupling efficiency is reduced as the physical dimensions of the strip are reduced (cf. the discussion on microstrip

dispersion in [Section 7.2](#)). The principal mode coupling is the coupling of the CPW mode to the microstrip mode as well as to surface waves. The better the fields are localized, by having small  $w$  and  $s$  dimensions here, the less likely it is that the additional modes will be excited.

It is unlikely that any analytic expressions could accurately reflect this feature as the coupling of modes can be due to small discontinuities. It is suggested that more research is required to develop, if possible, suitable closed formulas that will predict the dispersion as a function of the physical dimension regime. An electromagnetic simulator approach similar to that used in [Section 14.5.2](#) is necessary to predict the CPW behavior over a wide range of different practical configurations.

Although the above comments were developed for CPW on alumina substrates, the same important generalities apply to any substrate, including all semiconductors. CPW lines on MMICs, then, generally exhibit very low dispersion as a direct consequence of the small dimensions, usually in the tens of microns range. However, more extensive measurements on CPW lines on various important thick substrates, including GaAs, InP, and Si, are required over extensive frequency ranges (at least from 1 to 110 GHz) in order to validate the applicability and accuracy of the modeling expressions.

Papapolymerou *et al.* [18] have established that, for FGCPW on GaAs or quartz, dispersion is essentially negligible over the frequency range from 2 GHz to 120 GHz. Effective permittivity fluctuated between 7.0 and 7.2, being at the higher values at each end of the frequency range. The maximum physical dimensions used were 50  $\mu\text{m}$  by 64.5  $\mu\text{m}$ . Similar behavior can be anticipated for other semiconductor substrates, such as Si or InP, or non-semiconductor substrates such as aluminum nitride (AlN) or  $\text{SiO}_2$  provided always that the physical dimensions (geometry) are small, in the tens of microns range.

#### **14.5.4 Leakage Suppression and 50 GHz Interconnect**

As mentioned earlier in this chapter, the excitation of surface-wave modes or parallel-plate modes can become a problem with many uniplanar structures, especially when these are conductor-backed. It is desirable to minimize or suppress these modes. As discussed above, Soliman *et al.* [19] report extensive results using air bridge technology to suppress parasitic modes.

Another (simpler) approach comprises patterned backside metallization and this has been reported by Hesselbarth and Vahldieck [20]. In this technique the backside metal layer is made discontinuous in that a pattern of interleaved triangles is formed, as shown in [Figure 14.20](#). The lateral dimensions must be kept less than  $\lambda_g/5$  at the highest frequency of intended operation to ensure that resonance is avoided. Over the 1–10 GHz frequency range Hesselbarth and Vahldieck's results indicate that, using a shorted CPW test line, without the patterned metallization the unwanted transmission is around  $-8$  dB whereas by patterning this reduces it down to  $-60$  dB.



**Figure 14.20** Patterned backside metallization suppressing unwanted surface or parallel-plate modes. Adapted from Hesselbarth and Vahldieck (1999) [20], figure 4. p. 873. Reprinted with permission of IEEE.

Both CPW and CPS are finding increased use for very-high-speed on-chip (and off-chip) digital technology and also for millimeter-wave applications. As far as possible silicon technology always remains the first choice, and therefore interconnect design at these high frequencies is increasingly important.

Work has been reported on 50 GHz interconnect design in standard silicon technology, notably by Kleveland, Lee, and Wong [21]. This group of researchers studied CPWs with characteristic impedances ranging from 40 to 90  $\Omega$ , and it was found that coupling through the silicon substrate resulted in substantially increased losses above 30 GHz for the widest lines (40 microns) tested. Kleveland *et al.* point out that the actual results obtained are counter-intuitive because in some frequency ranges the lowest loss was achieved using relatively narrow lines deposited on a low-resistivity (standard) substrate. Full compatibility with standard CMOS was obtained.

There are two recommendations for achieving low-loss CPWs on silicon:

1. Reduce the line widths and spacing in order to avoid substrate coupling.
2. Use low-resistivity substrate or metal/poly/diffusion in order to provide a low resistance for the lateral ground connection.

The subject of leakage from planar transmission lines as a multimoding phenomenon has received considerable attention [22–31]. In 1993 it was shown that a leaky dominant-like mode can exist with most printed-circuit transmission lines [23, 24]. Fortunately, the transition from the bound TEM or quasi-TEM mode to a leaky mode can be predicted [22] and occurs when spacings, gaps, and widths become an appreciable part of a wavelength. The general guideline is to keep planar transmission line dimensions small.

CPW lines have an additional multimoding phenomenon to contend with. This is the excitation of slotline modes, or the equivalent problem, of having a slotline signal induced by signals on other interconnects that produce a field configuration compatible with the slotline mode. The solution is to enforce ground equalization using bond wires or air bridges to regularly connect the two ground conductors of CPW together, especially at discontinuities. It has been shown that air bridges are far superior to bond wires for implementing this [28, 31].

## 14.6 Discontinuities

In common with all types of interconnect structures, even the simplest circuits implementing CPW involve discontinuities of various forms. Unlike microstrip, however, static analyses leading to the determination of equivalent circuit elements to account for discontinuity effects apply up to relatively high frequencies. This applies to all CPW structures, but again the extremely small dimensions of MMIC implementations render the discontinuity effects relatively small and even less frequency-dependent.

In this section we deal with several significant discontinuities: step changes in width (i.e., impedance steps), the CPW open circuit (or pseudo-open circuit), symmetric series gaps, short circuit, right-angled bend, and T junctions. Whilst the ultimate aim is to establish suitable equivalent circuits and to evaluate  $C$  and  $L$  parameter values, an important intermediate aim is also to determine  $S$  parameters and to link these to circuit parameters (e.g., admittance or impedance parameters) in most instances.

### 14.6.1 Step Changes in Width and Separation

This discontinuity corresponds to a step change in characteristic impedance, but with CPW there exist two distinct structures that apply. These are indicated in [Figures 14.21\(a\)](#) and [\(b\)](#), where it can be seen that in one instance the step physically occurs in the adjacent ground planes whereas in the other situation it is the center strip that experiences the physical width change. In either case, regardless of the step realization, a capacitance represents the electrical effect and this applies up to high frequencies. This capacitance is shown as  $C_{\text{step}}$  in [Figure 14.21\(c\)](#), located at the single reference plane ( $\text{RP}_1$  and  $\text{RP}_2$ ).

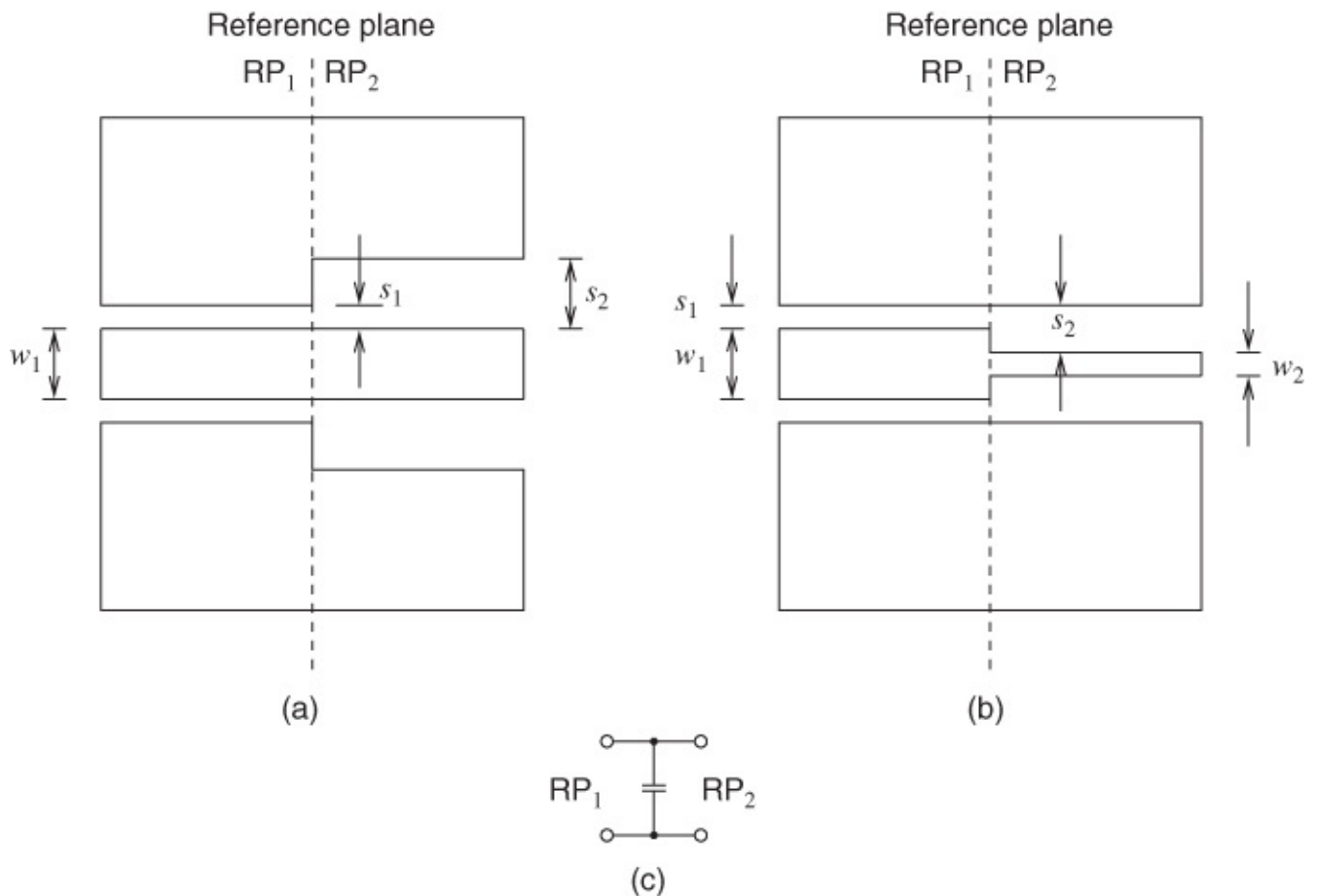


**Figure 14.21** Step changes in (a) ground plane separation; (b) center conductor width; and (c) equivalent circuit.

The simulated longitudinal and transverse current magnitude distributions of the two types of step discontinuities are shown in [Figures 14.22](#) and [14.23](#).



**Figure 14.22** Normalized current distribution on the conductors of a CPW impedance step realized using a step of the width of the internal conductor: (a) normalized scale; (b) magnitude of the longitudinal current; and (c) magnitude of the transverse current (frequency is 30 GHz).



**Figure 14.23** Normalized current distribution on the conductors of a CPW impedance step realized using a step of the conductor separation: (a) normalized scale; (b) magnitude of the longitudinal current; and (c) magnitude of the transverse current (frequency is 30 GHz).

Experimental data applying to CPW steps have been reported by several researchers, for example Simons and Ponchak [32], and others have reported theoretical analyses [33–36]. Rayit [7] argues that three main apparent conclusions can be drawn from a study of all these papers:

- $C_{\text{step}}$  CPW is larger than the equivalent  $C_{\text{step}}$  microstrip.
- $C_{\text{step}}$  CPW is of sufficient magnitude for fairly straightforward measurement extraction following  $S$  parameter de-embedding.
- A substantial variation of  $C_{\text{step}}$  exists, considering the geometries available with typical CPW lines.

Ghioni and Naldi [5] provide the basic conformal mapping technique required to determine the capacitance per unit length of each adjacent coplanar line,

$$c(k) = 2\epsilon_0\epsilon_{\text{eff}} \left[ \frac{K}{K'}(k_3) + \frac{K}{K'}(k) \right] \quad 14.35$$

where as usual  $k = w/(w + 2s)$  and

$$k_3 = \tanh\left(\frac{\pi ky}{4h}\right) / \tanh\left(\frac{\pi y}{4h}\right) \quad 14.36$$

with the effective permittivity being given by

$$\epsilon_{\text{eff}} = 1 + (\epsilon_r - 1) \left[ \frac{K}{K'}(k_3) \right] / \left[ \frac{K}{K'}(k_3) + \frac{K}{K'}(k) \right] \quad 14.37$$

and  $K(k)/K'(k)$  is the elliptic integral ratio. The step width change is therefore equivalent to a step change in the height of a parallel-plate waveguide and for this structure the capacitance per unit width is well known, using the conformal mapping approach

$$C_{\text{step}}(\alpha) = \frac{\epsilon_0}{\pi} \left[ \left( \frac{\alpha^2 + 1}{\alpha} \right) \ln \left( \frac{1 + \alpha}{1 - \alpha} \right) - 2 \ln \left( \frac{4\alpha}{1 - \alpha^2} \right) \right] \quad 14.38$$

where  $\alpha = w_2/w_1$  for  $\alpha < 1$ . It must, however, be recognized that the width of the equivalent parallel-plate waveguide changes on each side of the step, and therefore upper and lower bounds on  $C_{\text{step}}$  are obtained by alternately setting the width values to  $w_1$  and  $w_2$ .

Bracketed ranges of values applying to these upper and lower capacitance bounds are indicated in [Figure 14.24](#), where the results from six sources are provided (all for alumina substrates or similar). A vast range of results are apparent here: from almost zero up to over 200 fF. Whilst, obviously, the value of  $C_{\text{step}}$  will depend linearly on the substrate relative permittivity, this effect is in any case scaled in [Figure 14.24](#), and yet the range remains extremely large. Rayit's work was the most thorough and up-to-date amongst these analyses and the range in this instance is from almost zero up to about 10 fF. This is no more than one-fifth that of most previously reported data.

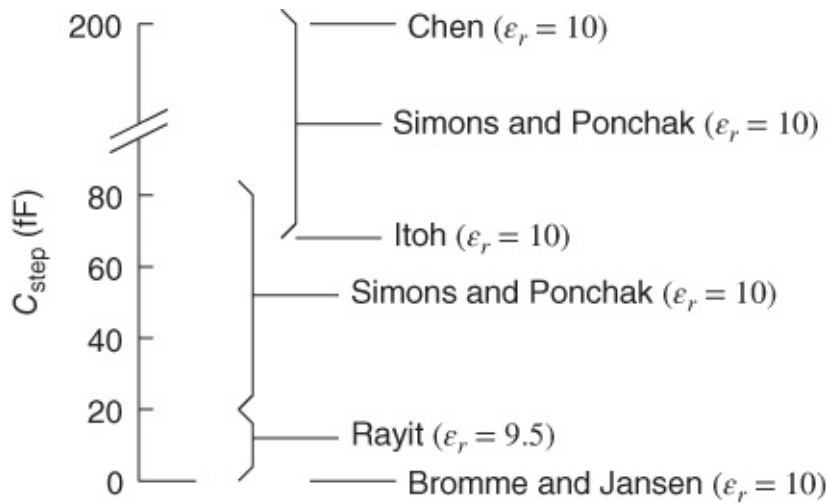


[Figure 14.24](#) Estimates of the capacitance associated with step changes in width.

Current flow disturbances, critically along the outer edges of the conductor tracks, cause series inductance to be required to fully characterize these step discontinuities. Inductance values can be ascertained analytically, but we concentrate on the more significant capacitance here. Rayit [7] simulated this structure (using the SONNET simulator) and obtained extensive data that were also supported by measurements. Here  $k_1$  is the ratio applying to the CPW of width  $w_1$  and  $k_2$  is the ratio applicable to the CPW having width  $w_2$ . The overall data are shown in [Figure 14.25](#) from which it should be clear that, as expected, values increase non linearly with  $k_2/k_1$  but approximately linearly with  $\epsilon_r$  (as parameter).

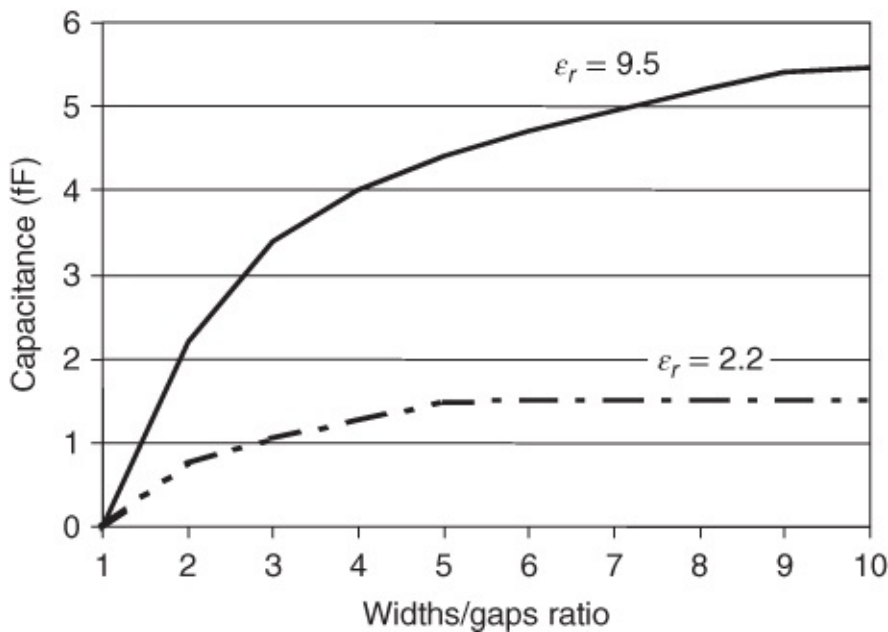


**Figure 14.25** Step capacitance versus width/gap ratio for two substrates.

Once more, although these data were obtained for alumina ( $\epsilon_r = 9.5$ ) the results applying to practically any other substrate can be deduced quite accurately by appropriately scaling according to the relative permittivity of the substrate (i.e., 11.9 for Si, 12.85 for GaAs, etc.). For example, a step ratio of 6 on alumina has a capacitance of 4.7 fF. The capacitance applying to the same line structure (including thickness), but on a GaAs substrate is then  $C_{\text{step}} = 4.7(12.85/9.5) = 6.3$  fF. The result has been rounded down to allow for the fact that more of the electric field is concentrated in the substrate as the permittivity rises, and therefore the sensitivity of  $C_{\text{step}}$  to geometric changes decreases. This approach can be used for most other substrates.

## 14.6.2 Open Circuit

Quasi-open circuits occur in many circuit elements and their equivalent circuits must be known. The basic structure is shown in [Figure 14.26](#), where it can be seen that, in contrast to the microstrip open circuit, the CPW version is complicated by the fact that the adjacent ground plane must be separated from the “open” end by a distance  $g$ .

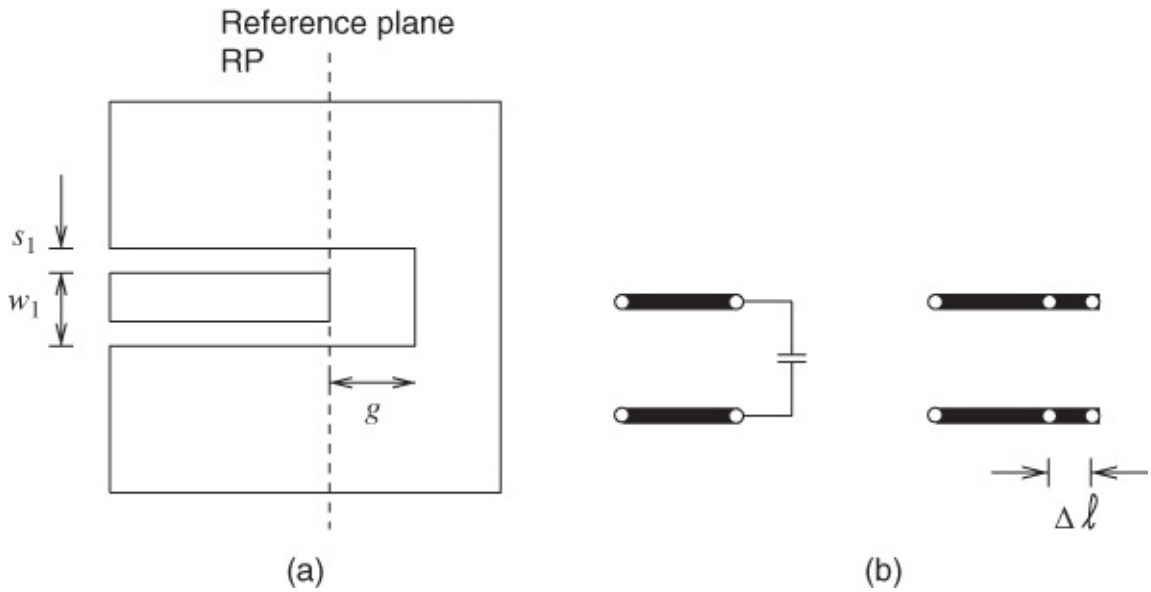


**Figure 14.26** Quasi-open circuit (a) and alternative equivalent circuits (b).

The problem is twofold: first to determine the equivalent capacitance  $C_{oc}$  and then to represent this by an equivalent extension of the CPW line, with an extra length  $\Delta\ell$ . The process of determining these parameters starts with the  $ABCD$  matrix for this structure

$$\begin{bmatrix} A & B \\ C & D \end{bmatrix} = \begin{bmatrix} 1 & 0 \\ 1/Z_1 & 1 \end{bmatrix} \quad 14.39$$

from which

$$z_{11} = \frac{A}{C} = Z_1. \quad 14.40$$

Therefore, with a  $50 \Omega$  characteristic impedance

$$Z_1 = \frac{1 + S_{11}}{1 - S_{22}} \cdot 50 \Omega. \quad 14.41$$

Now  $Z_1$  is the capacitive reactance of the open-circuit discontinuity so that

$$Z_1 = \frac{1}{j\omega C_{oc}} = \frac{-j}{\omega C_{oc}}. \quad 14.42$$

By simulation methods Rayit [7] used the above approach for both  $C_{oc}$  and  $\Delta\ell$ . The capacitance can be calculated using

$$C_{oc} = k \left[ 36.12 + \frac{1.819}{(g/h)} - \frac{0.02497}{(g/h)^2} \right] \quad 14.43$$

where

$$k = w/h = w/(w + 2g) \quad 14.44$$

and the values are found to be almost completely frequency independent at least up to over 20 GHz on alumina substrates. This frequency-independence probably also applies to most other substrates.

### 14.6.3 Symmetric Series Gap

This discontinuity is closely related to the quasi-open end, amounting to a gap in series along the center conductor. The structure and its  $\pi$  equivalent circuit of capacitances is shown in [Figure 14.27](#). The grounded capacitances account mainly for fringing fields from the ends to ground, whilst the series capacitance accounts chiefly for the end-to-end field.

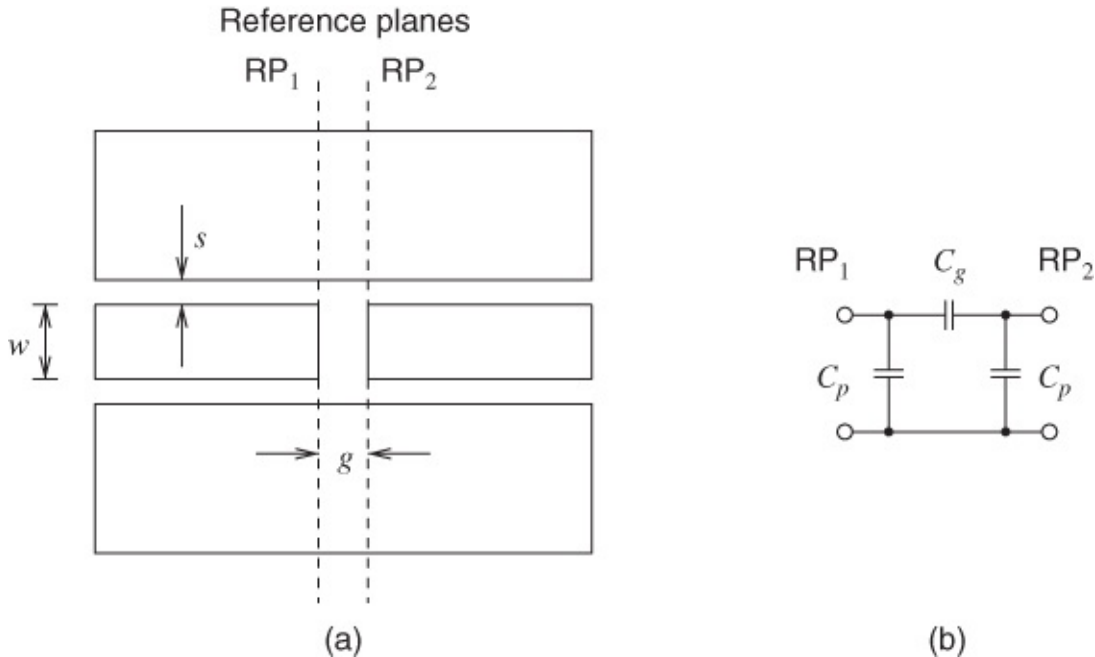


[Figure 14.27](#) Symmetric series gap layout and capacitive  $\pi$  equivalent circuit indicating reference planes 1 and 2.

Again, using a similar methodology to that employed with the quasi-open end, we begin with the appropriate  $ABCD$  matrix in order to analyze this structure:

$$\begin{bmatrix} A & B \\ C & D \end{bmatrix} = \begin{bmatrix} 1 & 0 \\ 1/Z_1 & 1 \end{bmatrix} \begin{bmatrix} 1 & Z_2 \\ 0 & 1 \end{bmatrix} \begin{bmatrix} 1 & 0 \\ 1/Z_1 & 0 \end{bmatrix} \quad 14.45$$

which becomes

$$\begin{bmatrix} A & B \\ C & D \end{bmatrix} = \begin{bmatrix} 1 & Z_2 \\ 1/Z_1 & (1 + Z_2/Z_1) \end{bmatrix} \begin{bmatrix} 1 & 0 \\ 1/Z_1 & 1 \end{bmatrix}$$

or

$$\begin{bmatrix} A & B \\ C & D \end{bmatrix} = \begin{bmatrix} (1 + Z_2/Z_1) & Z_2 \\ \left(\frac{2}{Z_1} + \frac{Z_2}{Z_1^2}\right) (1 + Z_2/Z_1) & 1 \end{bmatrix}. \quad 14.46$$

The determinant of the ABCD matrix,  $\Delta$ , is now taken in order to find further parameters explicitly:

$$\Delta = \left(1 + \frac{Z_2}{Z_1}\right) \cdot \left(1 + \frac{Z_2}{Z_1}\right) - Z_2 \left(\frac{2}{Z_1} + \frac{Z_2}{Z_1^2}\right) = 1$$

and

$$z_{12} = z_{21} = \frac{1}{C}.$$

Further manipulations enable both  $z_{11}$  and  $z_{12}$  to be expressed in terms of  $Z_1$  and  $Z_2$ . Then finally, equation substitutions and rearrangements lead to both  $Z_1$  and  $Z_2$  being expressed entirely as functions of  $z_{11}$  and  $z_{12}$ :

$$Z_1 = (z_{11} + z_{12}) \quad \text{14.47}$$

and

$$Z_2 = \frac{(z_{11} + z_{12})^2}{z_{12}} - 2(z_{11} + z_{12}). \quad \text{14.48}$$

Simulations enable these expressions to be used to determine the capacitances in the pi-network representing the gap. It is generally found that these capacitances are largely independent of frequency, although  $C_g$ , the series capacitance, rises slightly with frequency. Typical values lie in the 20–60 fF range.

#### **14.6.4 Coplanar Short Circuit**

This structure is an important and unusual example of a “termination” in CPW. Unlike other transmission structures, CPW inherently involves the adjacent ground planes and therefore, assuming that the planar structure is preserved, any “short circuit” must also inherently be of a pseudo short-circuit nature. This is indicated in [Figure 14.28](#), where the layout is shown at the top of the diagram and the cross-section is shown beneath. It should be clear that a fairly complex field distribution exists in the vicinity of the pseudo short circuit.

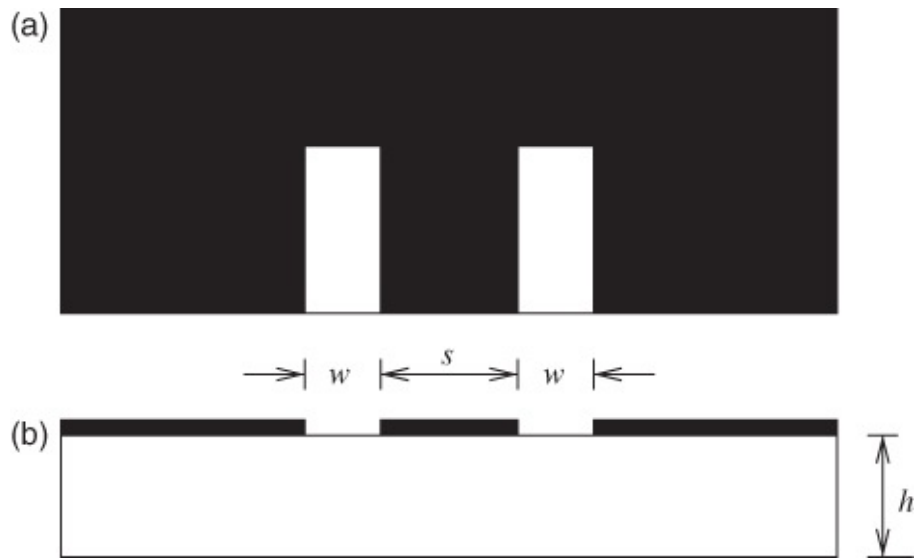


**Figure 14.28** Pseudo short circuit: (a) layout; and (b) cross-section.

This structure is also shown in [Figure 14.29](#), where the reference plane (RP), equivalent load ( $L$ ), and end extension are also indicated. The load is predominantly inductive and may often be represented as an inductor. This is because the abruptly-ended line is mainly characterized by substantial current disturbances.

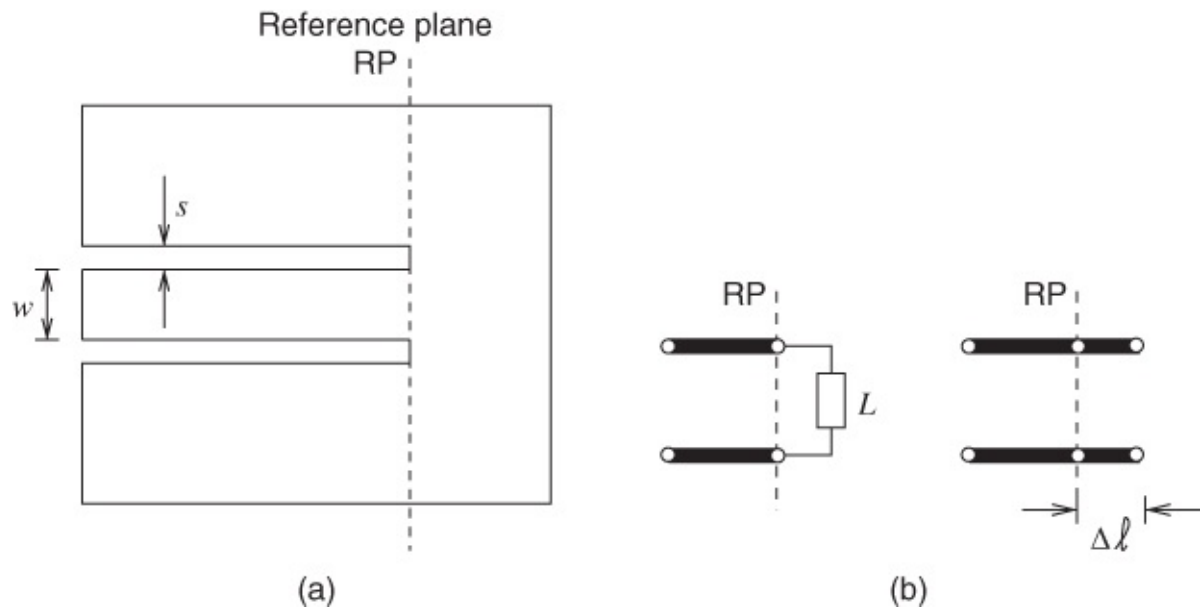


**Figure 14.29** Pseudo short circuit: (a) layout and (b) alternative equivalent circuits.

The current distributions on a finite ground CPW are shown in [Figure 14.30](#), where the substantial current disturbances can be seen.

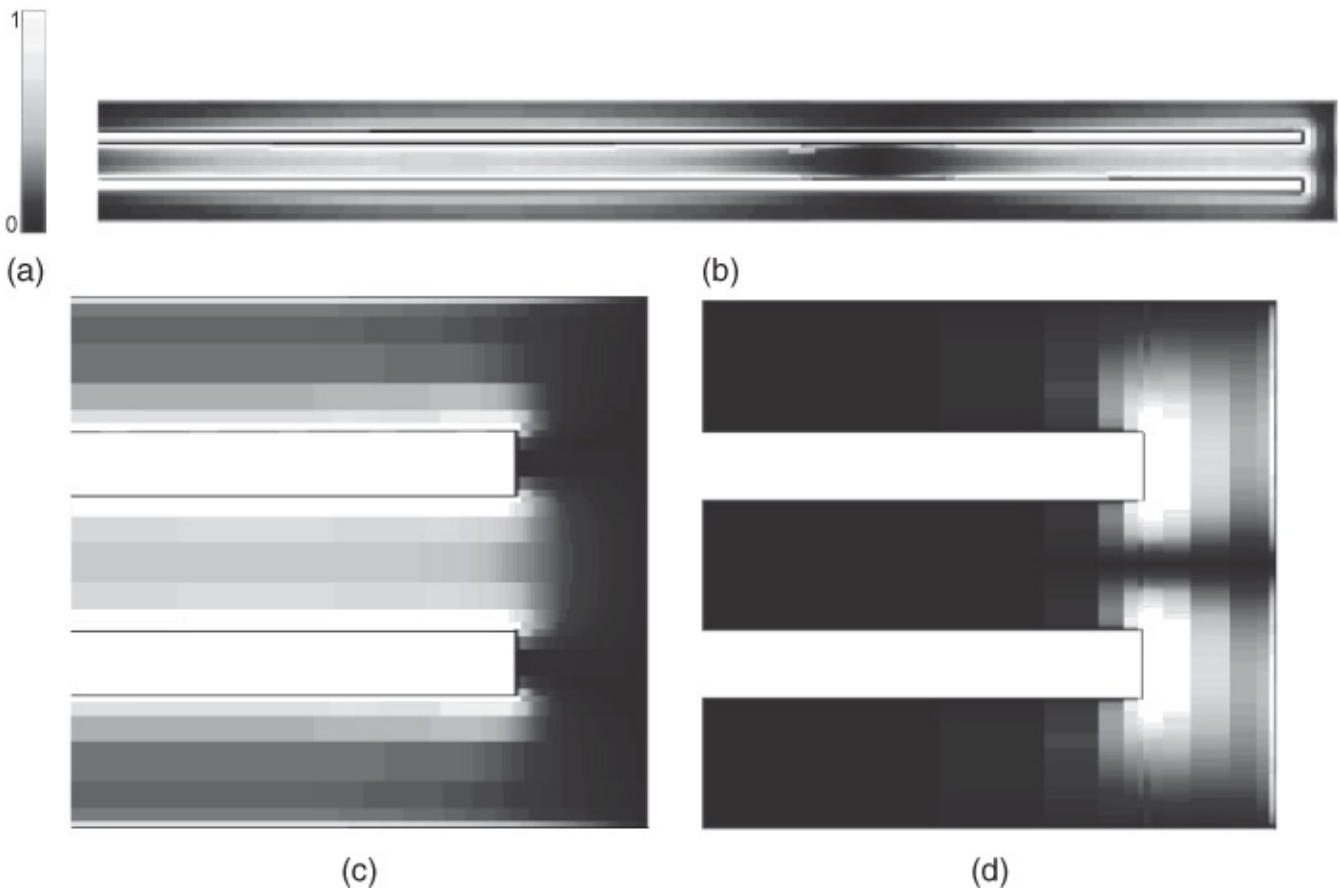


**Figure 14.30** Normalized magnitude of the current distribution on the conductors of a CPW pseudo short circuit: (a) scale; (b) short at 100 GHz showing standing wave pattern of longitudinal current; (c) magnitude of the longitudinal current at 30 GHz in greater detail; and (d) magnitude of the transverse current at 30 GHz.

### 14.6.5 Right-angle Bends

Although mitering (or chamfering) will always significantly reduce the effects of this discontinuity, we start by considering the direct, unmitered, right-angle bend and once more the appropriate *ABCD* matrix is the starting point for the analysis. The structure and its equivalent circuit are shown in [Figure 14.31](#).

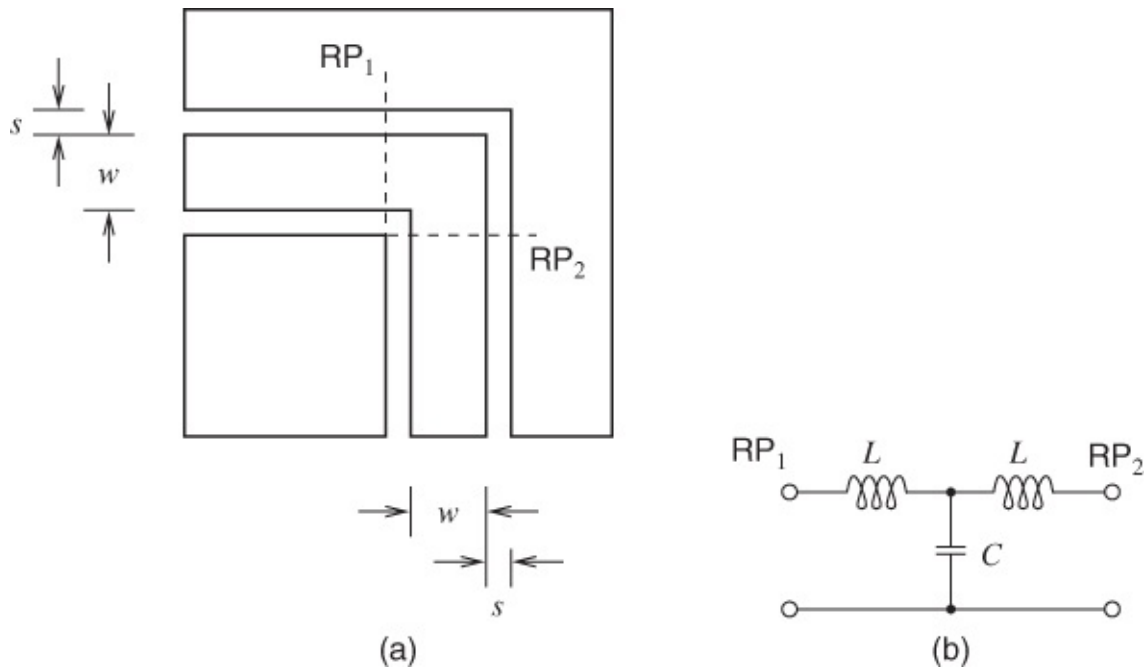


**Figure 14.31** Right-angle bend: (a) layout; and (b) equivalent circuit.

The  $ABCD$  matrix is

$$\begin{bmatrix} A & B \\ C & D \end{bmatrix} = \begin{bmatrix} 1 & Z_1 \\ 0 & 1 \end{bmatrix} \begin{bmatrix} 1 & 0 \\ 1/Z_2 & 1 \end{bmatrix} \begin{bmatrix} 1 & Z_1 \\ 0 & 1 \end{bmatrix} \quad 14.49$$

so that

$$\begin{bmatrix} A & B \\ C & D \end{bmatrix} = \begin{bmatrix} (1 + Z_1/Z_2) & (2Z_1 + Z_1^2/Z_2) \\ 1/Z_2 & (1 + Z_1/Z_2) \end{bmatrix}. \quad 14.50$$

In similar fashion to that employed when the series gap was considered, once again we take the determinant of this matrix because this leads, eventually, to explicit expressions for  $Z_1$  and  $Z_2$ .

The determinant of Equation (14.50) is

$$\Delta = AB - CD = \left(1 + \frac{Z_1}{Z_2}\right) \cdot \left(1 + \frac{Z_1}{Z_2}\right) - \frac{1}{Z_2} \left(2Z_1 + \frac{Z_1^2}{Z_2}\right)$$

which expands simply to  $\Delta = 1$  (because all other terms cancel), but

$$z_{11} = Z_1 + Z_2 \quad 14.51$$

and we can then write

$$Z_2 = z_{12} (= z_{21}) \quad 14.52$$

also

$$Z_1 = z_{11} - z_{12} \quad 14.53$$

thus providing the impedances associated with the equivalent circuit elements, in terms of extractable  $ABCD$ -related ( $Z_{mn}$ ) impedance matrix elements.

The bend capacitance and inductance are extracted using this procedure and the results for the inductance are shown, for CPW on 0.635 mm thick alumina, in [Figure 14.32](#). In this graph  $k$  is the usual ratio as defined before, see Equation (14.4).

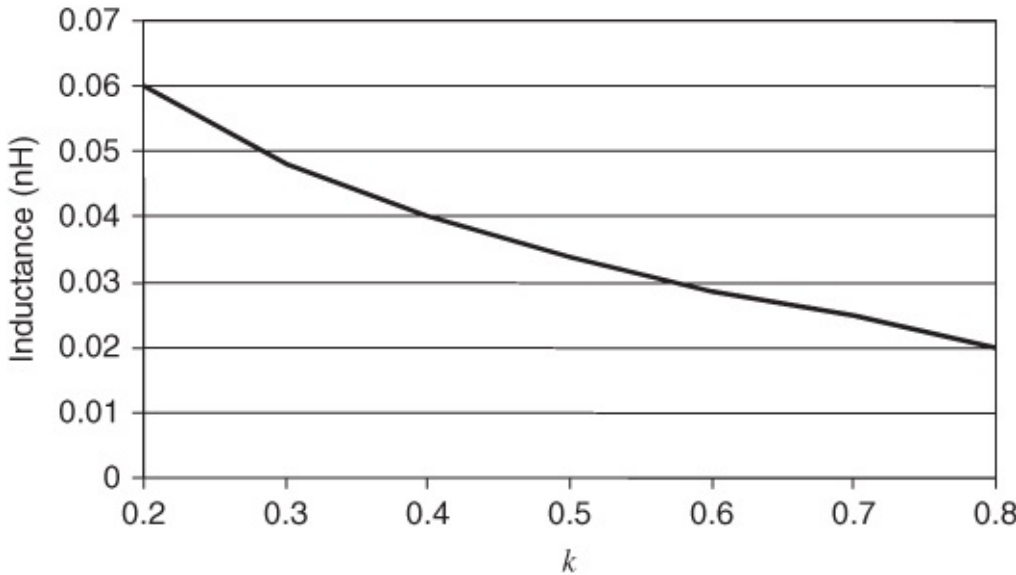


[Figure 14.32](#) Right-angle bend inductance as a function of parameter  $k$ .

These parameters are almost invariant with frequency from 400 MHz to at least 20 GHz.

#### 14.6.5.1 Mitered (Chamfered) Bends

When optimally mitered the bend capacitance is generally at least halved compared with the unmitered case. Such a bend also exhibits a greatly improved reflection coefficient with a typical improvement of at least 16 dB compared to an unmitered bend over the 2–20 GHz frequency range (e.g., see the section on microstrip discontinuities in [Chapter 9](#)). These comments apply generally to almost every planar transmission structure.

#### 14.6.6 T Junctions

This type of discontinuity occurs in a wide variety of circuits. The physical structure and equivalent circuit model are shown in [Figure 14.33](#).

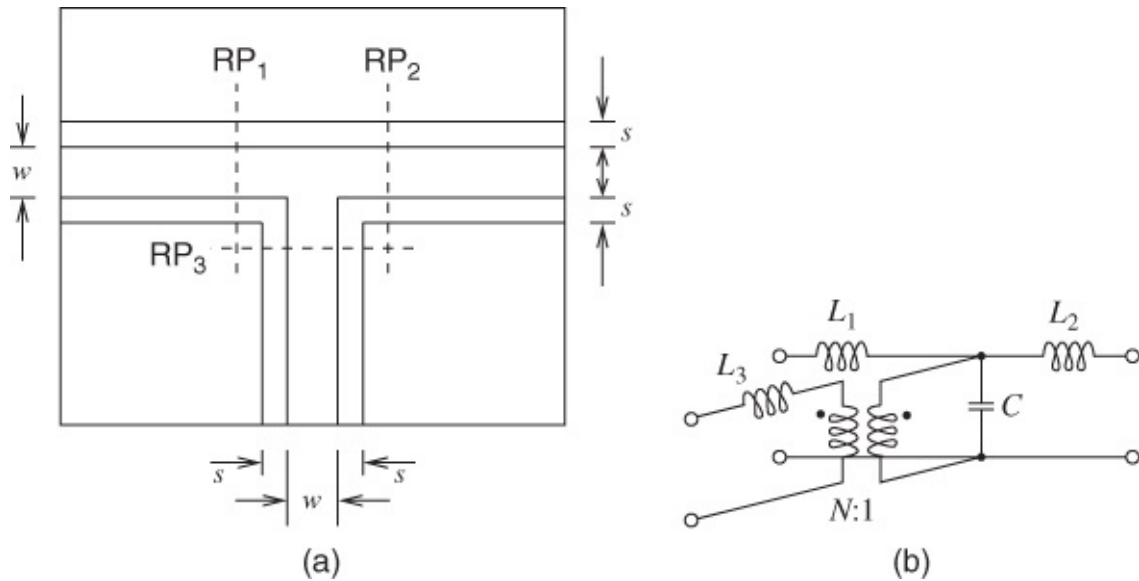


**Figure 14.33** T junction: (a) layout; and (b) lumped equivalent circuit.

Air bridges (or earthing bonds, see the following section) are absolutely necessary in order to suppress the unwanted odd mode in most CPW circuits and T junction discontinuities.

As with the microstrip (and other) T junctions, the equivalent circuit demands a transformer to identify the effect of the coupled arm on the main transmission route.

Considering a  $49 \Omega$  line on an alumina substrate, the characteristic behavior of the T-junction transformer ratio is shown in [Figure 14.34](#) (data derived by Rayit [7]). At 20 GHz the value of this ratio has clearly decreased from its unity (DC) value to 0.92. Rayit analyzed and measured a wide range of T junctions on alumina.

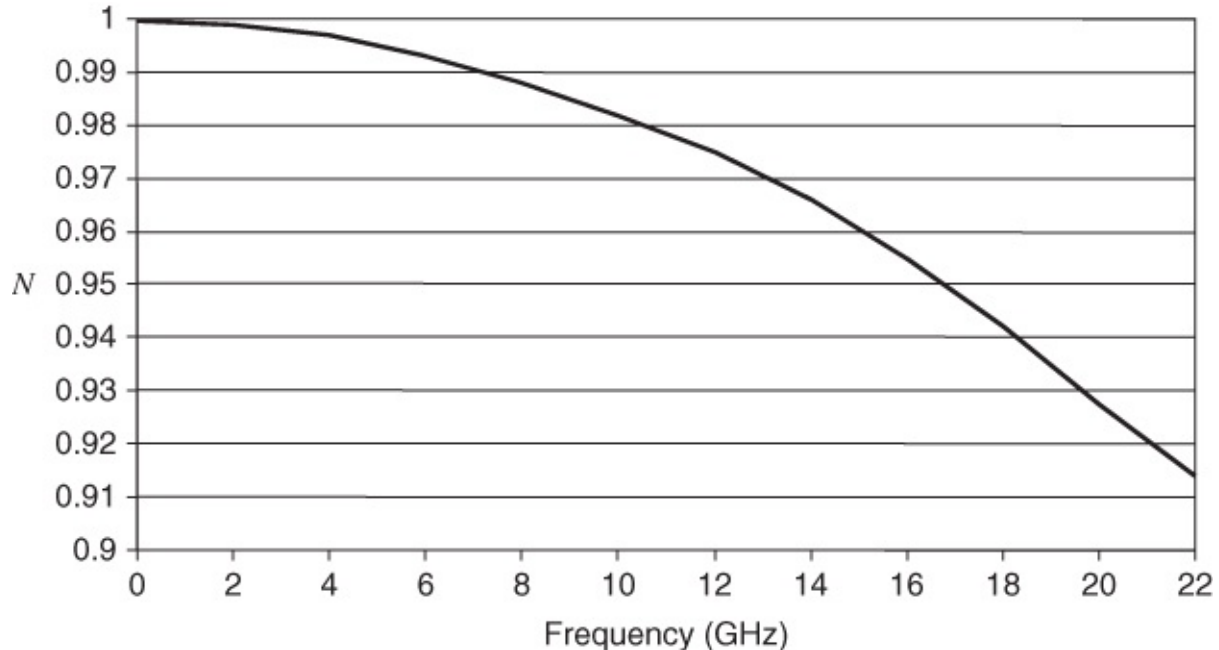


**Figure 14.34** T-junction transformer ratio  $N$  as a function of frequency.

Mirshekhar-Syahkal [37] has computed the equivalent circuit element values for a range of CPW discontinuities, including T junctions, using the quasi-static spectral domain method. A

structure analyzed by Mirshekar-Syahkal is shown in [Figure 14.35](#), together with a simplified version of the equivalent circuit. This circuit is on an InP MMIC substrate and it is conductor-backed.

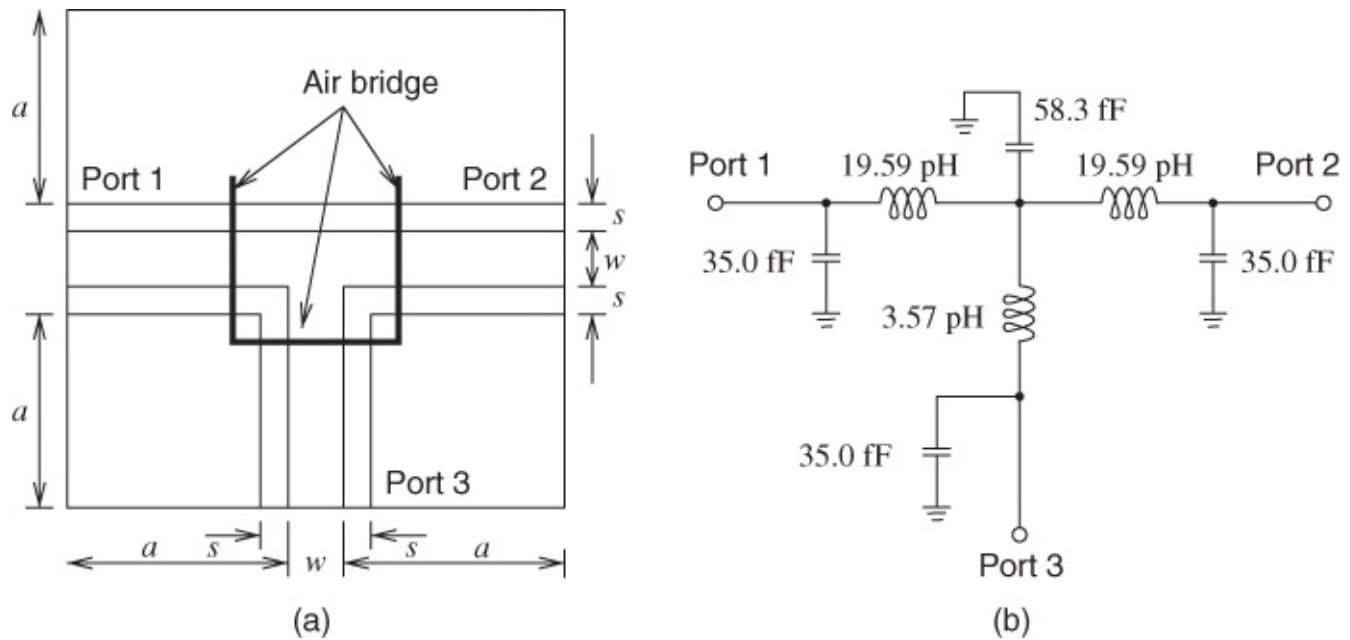


**Figure 14.35** The T junction (a) structure analyzed by Mirshekar-Syahkal [37] together with its equivalent circuit (b). Dimensions are  $a = 200 \mu\text{m}$ , substrate height  $h = 200 \mu\text{m}$ ,  $s = 20 \mu\text{m}$ ,  $w = 40 \mu\text{m}$ , air bridge height =  $2 \mu\text{m}$ , and  $w = 40 \mu\text{m}$ . Adapted from Mirshekar-Syahkal (1996) [37], figure 4, p. 982. Reprinted with permission of IEEE.

## 14.6.7 Air Bridges

In order to ensure that only the fundamental CPW mode propagates over the frequency range of interest, it is usually necessary to directly interconnect coupled sections of CPW lines using conductive straps. The electrical lengths of these straps, commonly known as air bridges, must be kept much less than one-fifth of a guide wavelength so that they appear as localized short circuits. These air bridges suppress the unwanted odd CPW mode.

Several researchers have reported on the characterization of air bridges as well as the effects of the coupled slotline mode and shunt stub realizations. Sewell and Rozzi [38] presented calculated characterizations of air bridges under millimeter-wave conditions, considering both single and coupled bridges. Using a mode spectrum technique they showed that, as should be anticipated, the  $S_{11}$  and  $S_{21}$  scattering parameters are strongly sensitive to the strap separation/wavelength ratio for coupled bridges. Sewell and Rozzi's main results, converted to dB and at 40 GHz and 50 GHz frequencies, are shown in [Figure 14.36](#).

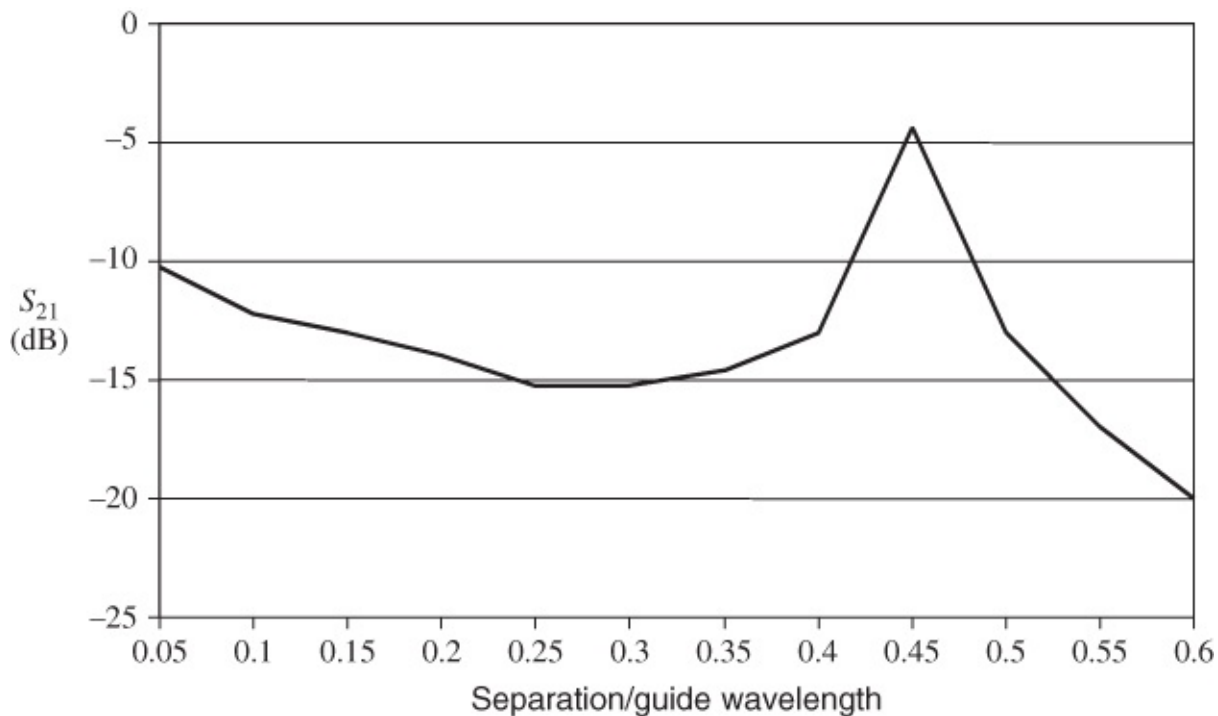


**Figure 14.36** Effects of the coupled slotline mode on air bridges. Adapted from Sewell and Rozzi (1994) [38], figure 14, p. 2086. Reprinted with permission of IEEE.

Lee, Liu, and Itoh [39] described the effects of the coupled slotline mode and air bridges on CPW and non-leaky coplanar waveguide discontinuities. They focused on a T-junction discontinuity and showed both spectral-domain calculated and also measured results over the 4–9 GHz band. For the symmetrical structure considered the thickness  $t = 0.635$  mm, center line width  $w = 1$  mm, and separation  $s = 0.34$  mm. Lee *et al.* also examined an asymmetrical T junction.

In general, the behavior of the  $S$  parameters with frequency is highly non linear. Both the magnitude and phase of  $S_{11}$  and  $S_{21}$  exhibit sharp dips in response that are almost harmonically related. The magnitude typically dips by up to 9.5 dB, and the phase changes abruptly by more than  $180^\circ$  at 8 GHz for the asymmetrical case.

Hettak, Dib and Omar [40] reported on a new class of miniaturized and radiation-free CPW shunt stubs that they implemented within the center conductor. A major aspect of this approach was to reduce the number of air bridges actually required to realize shunt stubs considering that the manufacture of multitudes of these bridges is potentially expensive.

Unlike conventional asymmetric shunt stubs, Hettak, Dib, and Omar's design exhibits longitudinal symmetry. Their design has a pseudo short-circuit CPW followed by a re-entrant “serpentine”-shaped nominally quarter-wave stub set longitudinally within the center conductor. Two air bridges directly connect from the pseudo short-circuit end to the outer fingers of the shunt stub configuration. These researchers also show a two-fold version comprising this entire structure reversed and repeated in cascade.

Experimental results are shown by Hettak *et al.* for 50  $\mu\text{m}$  separations ( $s$ ), 0.175  $\mu\text{m}$  width ( $w$ ), and 50  $\mu\text{m}$  fingers with 25  $\mu\text{m}$  gaps manufactured on a substrate with permittivity 9.9 and

thickness 0.254 mm. The 10–50 GHz band was swept and the required response around 30 GHz was obtained.

### 14.6.8 Cross-Over Junctions

CPW cross-overs are often essential and then air bridges must be used to connect the side grounds to ensure the integrity of the CPW mode. It has been shown that FGCPW cross-overs have much lower coupling (typically 15 dB less) than CPW cross-overs [41]. These two types of cross-overs are shown in [Figure 14.37](#). The reason for this difference in coupling can be seen by examining current flow in the ground plane. In the conventional CPW cross-over, [Figure 14.37\(a\)](#), ground currents are shared by the two CPW lines, particularly near the intersection of the lines. This results in coupling due to the common impedance effect. However, in the FGCPW cross-over, [Figure 14.37\(b\)](#), a common current path does not exist and so there is no common impedance coupling.

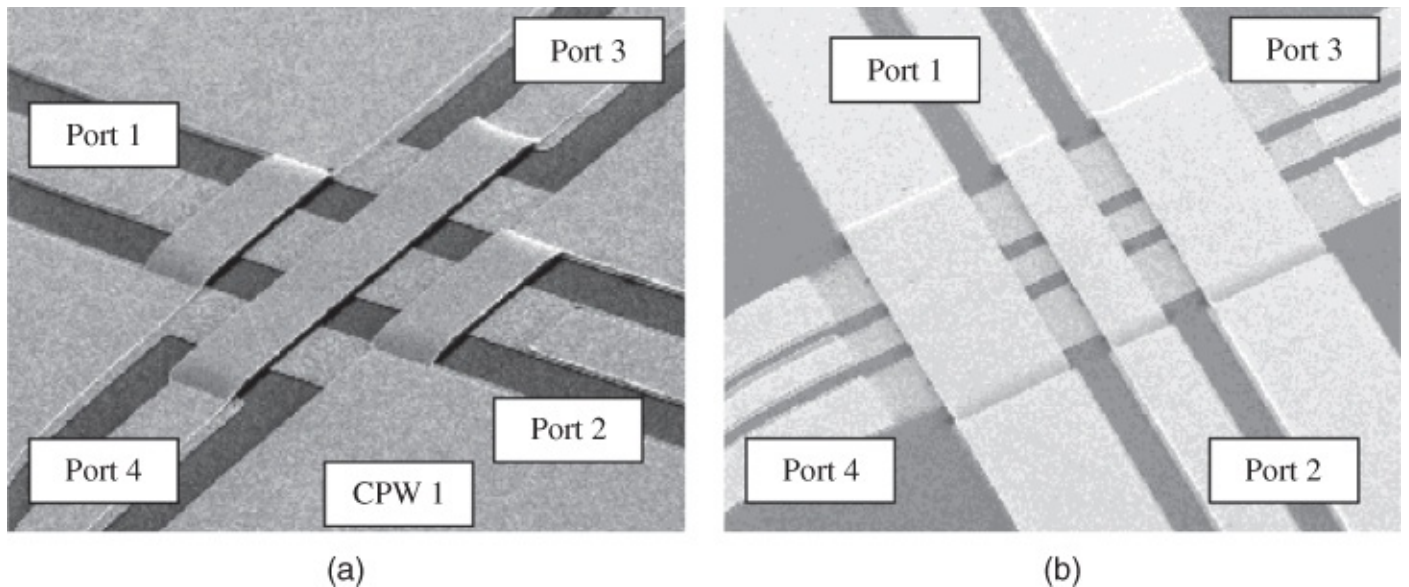


[Figure 14.37](#) SEM micrographs of CPW cross-over junctions: (a) conventional CPW; and (b) FGCPW. The lines have the same dimensions. Adapted from Ponchak and Tentzeris (2000) [41], figures 1 and 2, p. 1892. Reprinted with permission of IEEE.

## 14.7 Circuit Elements

Taken alone, stretches of CPW line, or associated discontinuities, do not of course constitute circuit elements. Rather, they are essential and fundamental aspects that must be identified and quantified before any computer modeling can be undertaken. In this section we consider some passive circuit elements that can be formed using the CPW medium. The significance of vias in MMICs should first be stressed. This has been reported, for example, by Strohm *et al.* [42].

### 14.7.1 Interdigital Capacitors and Stubs

There are many ways in which a lumped (or quasi-lumped) capacitor may be realized in CPW

format. The series gap, discussed in [Section 14.6.3](#), is arguably the simplest example of a fully integrated series capacitance. However, as in the case of microstrip, it becomes impracticable to realize even modest values of capacitance this way because submicron gap widths are required, rendering manufacturing all but impossible.

Another possibility is the introduction of flip-chip capacitors that may be attached across relatively wide series gaps. This approach enables relatively large capacitances to be achieved, but there are at least two fundamental objections:

- a.** This can only realistically apply to hybrid MICs, since the real estate available with MMICs makes this an impractical approach with such technology.
- b.** The  $Q$  factor of chip capacitors is usually relatively low.

Yet another method for the realization of capacitances in CPW is with interdigital structures. A serpentine shape of gaps across the center conductor, interspersed with conductor fingers (“digits”) results in a dominantly capacitive series element. Capacitances ranging up to several hundred femtofarad and approaching a picofarad are achievable this way, and the approach is applicable to MMICs. It is vital to ensure that the maximum length of any finger is kept less than one-fifth of a guide wavelength at the maximum frequency of operation, otherwise such a finger would behave as a distributed element. This is relatively easy to achieve with MMICs, but considerably more difficult with the larger dimensions applicable to hybrid circuits (MICs).

Such a structure is shown in [Figure 14.38](#), where the most basic single-finger example is indicated. In common with most of the discontinuities described, the structure has inductive as well as capacitive effects, and these features are reflected in the equivalent circuit. Rayit [7] supplies empirical expressions that work well for calculating the capacitances and inductances ( $\ell$  is the finger or stub length in all instances and all separations are 0.4 mm):

$C_S = 2.03 \times 10^{-4} \ell + 8.65 \times 10^{-3}$	$L_1 = 1.57 \times 10^{-4} \ell$
$C_{f1} = 1.58 \times 10^{-4} \ell + 2.3 \times 10^{-2}$	$L_2 = 1.67 \times 10^{-4} \ell$
$C_{f2} = 10^{-5} \ell + 9.7 \times 10^{-5}$	$L_3 = 2.05 \times 10^{-4} \ell$

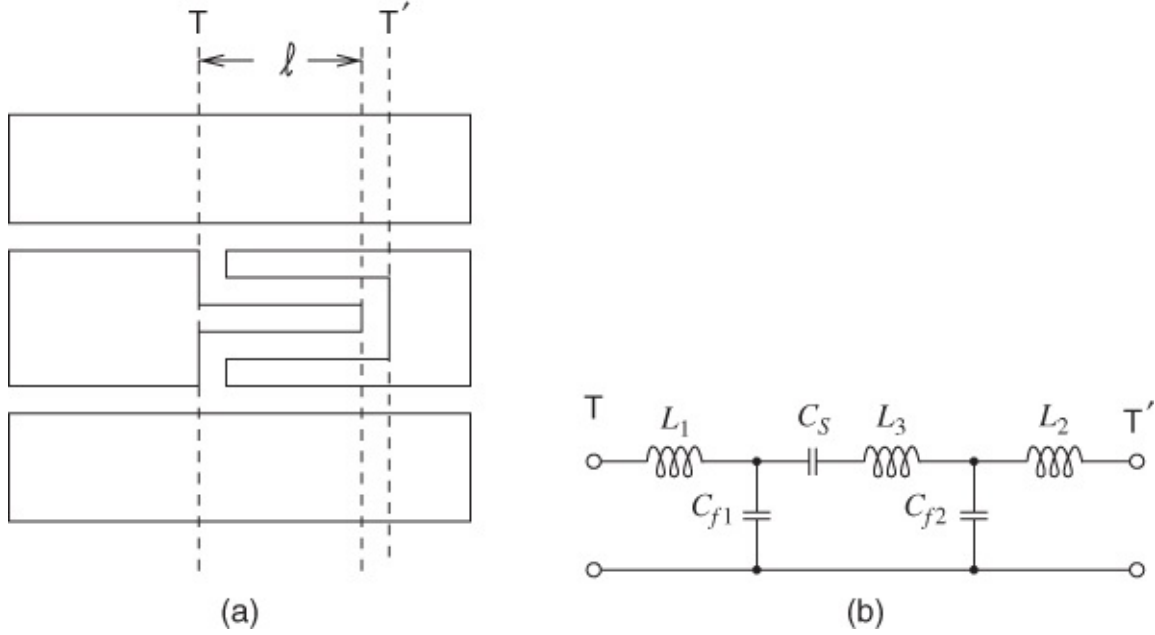


**Figure 14.38** (a) Interdigital or stub structure; and (b) its equivalent circuit. The reference planes are denoted by T and T'.

In these expressions the length is directly substituted in micrometers (e.g., “50” for 50  $\mu\text{m}$ ) and then the capacitances compute directly in picofarads and the inductances compute directly in nanohenries.

These data apply to a high-permittivity Duroid substrate ( $\epsilon_r = 10.2$ ). The calculations are very straightforward, easily incorporated into a computer program, and can be scaled to enable calculations to proceed for substrates where the permittivity is other than  $\epsilon_r = 10.2$ .

An interesting and useful alternate structure is realized when the finger is directly connected to the opposing CPW center conductor, instead of the final series gap, and this arrangement is shown in [Figure 14.39](#). Such a circuit element now behaves in lowpass (or even quasi-resonant) mode because there is a direct inductive path between input and output (T to T'). Rayit's empirical expressions for the equivalent circuit parameters are (all separations are 0.4 mm):

$C_S = 1.51 \times 10^{-4} \ell + 8.7 \times 10^{-2}$	$L_1 = 3.53 \times 10^{-4} \ell - 1.2 \times 10^{-4}$
$C_{f1} = 3 \times 10^{-5}$	$L_2 = 1.86 \times 10^{-4} \ell - 6.12 \times 10^{-4}$
$C_{f2} = 6.9 \times 10^{-5} \ell + 2.5 \times 10^{-3}$	$L_3 = 3.02 \times 10^{-4} \ell - 2.09 \times 10^{-4}$

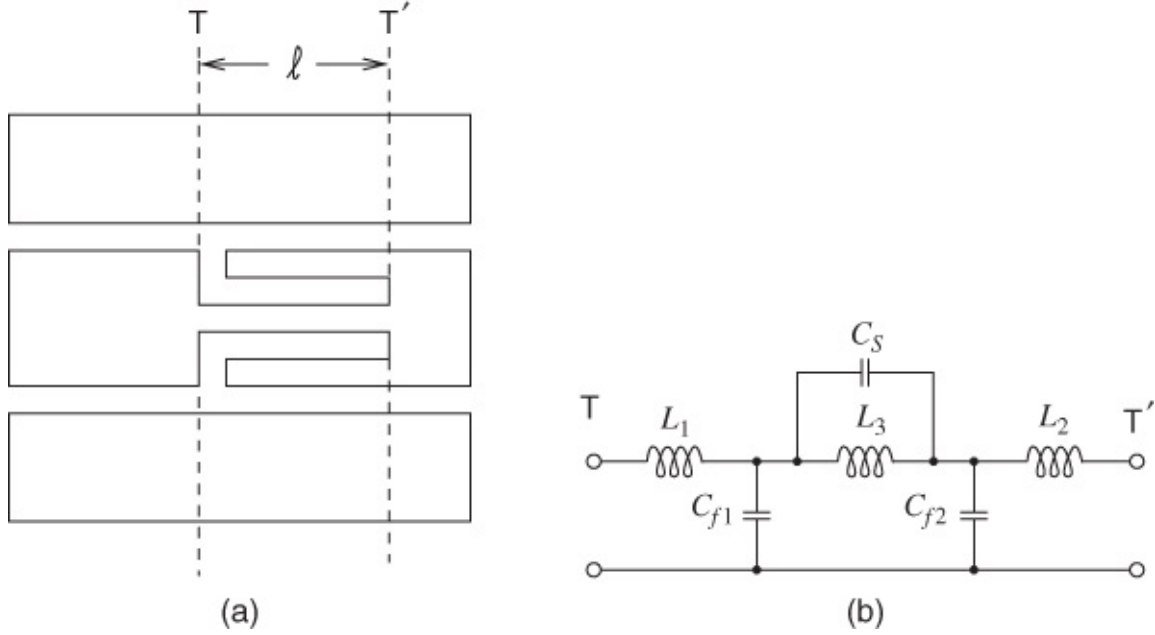


**Figure 14.39** Through-connected interdigital stub: (a) structure; and (b) its equivalent circuit. The reference planes are denoted by T and T'.

Precisely the same comments made concerning the open interdigital structure apply equally here. To increase the capacitances without entering into highly dimension-critical conductor geometries high-permittivity dielectric materials may be attached across the gaps of these structures. This is achievable with hybrid MICs, but almost certainly not with MMICs, due again to the extremely small dimensions. In this case, however, a layer of polyimide may be introduced onto the surface during processing.

## 14.7.2 Filters

The fundamental approaches described in the previous sections of this chapter can now be used in most CPW designs, including filters.

Frequency filters represent good, critical circuit realizations with which to test the adequacy of design models. Such circuit elements are also important in their own right within more complex circuit configurations. Air bridges are also repeatedly introduced in order to suppress the unwanted odd mode (see [Section 14.6.7](#)).

All four types of basic filter (lowpass, highpass, bandpass, and bandstop) are capable of being realized in CPW topology. At this point we concentrate on a bandpass filter, originally investigated by Rayit [7] and manufactured on an alumina substrate.

The basic layout (top view) is shown in [Figure 14.40](#). The aim is to design a 30% bandwidth filter and the shunt shorted stub following the approach due to Malherbe [43]. A Chebyshev response is to be realized. Inherently the filter requires modeling for several discontinuities, including the T junction. The measured and simulated (incorporating the modeling) responses are shown in [Figures 14.41](#) and [14.42](#), where it can be seen that several differences occur in practice. Considering the transmission characteristic ( $S_{21}$ ) first, working upwards in frequency, below 2 GHz the responses are substantially above (lower in dB) the design values. This is of

little consequence because the worst case is  $-53$  dB in any case. Both lower and upper skirts (decibels per gigahertz) are actually superior to the design goal.

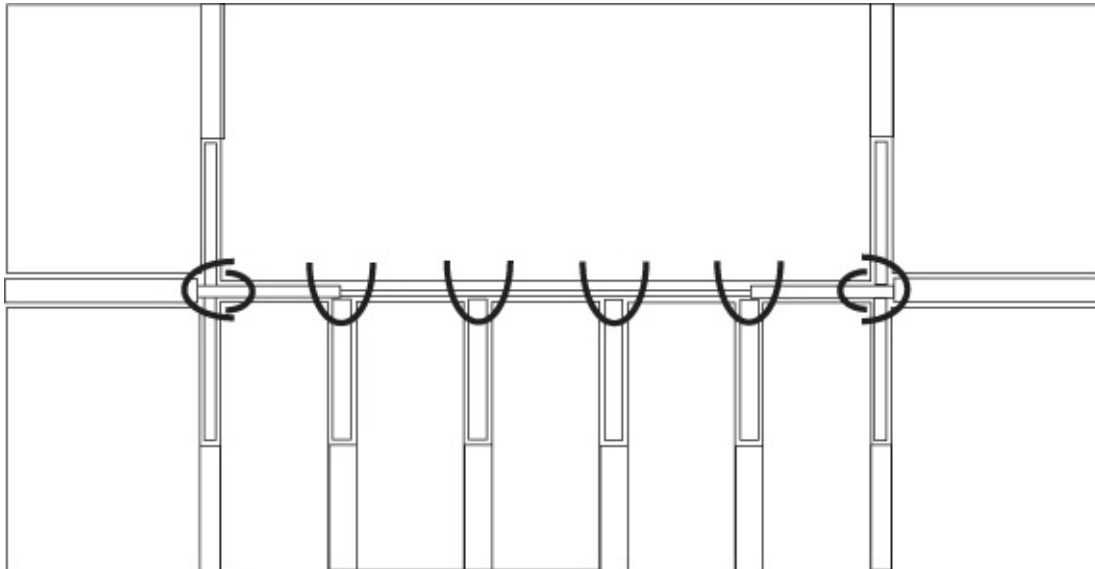


**Figure 14.40** Layout of a 30% bandwidth bandpass filter on an alumina substrate.

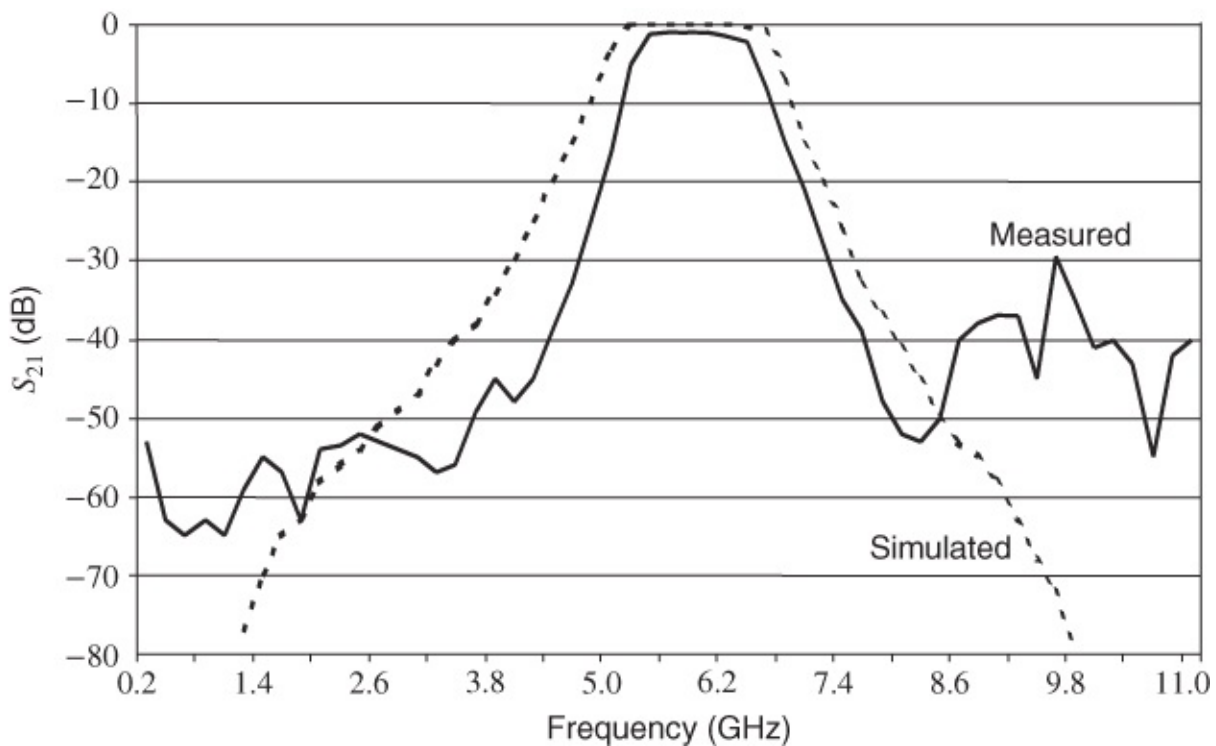


**Figure 14.41** Transmission response ( $S_{21}$ ) of the bandpass filter.

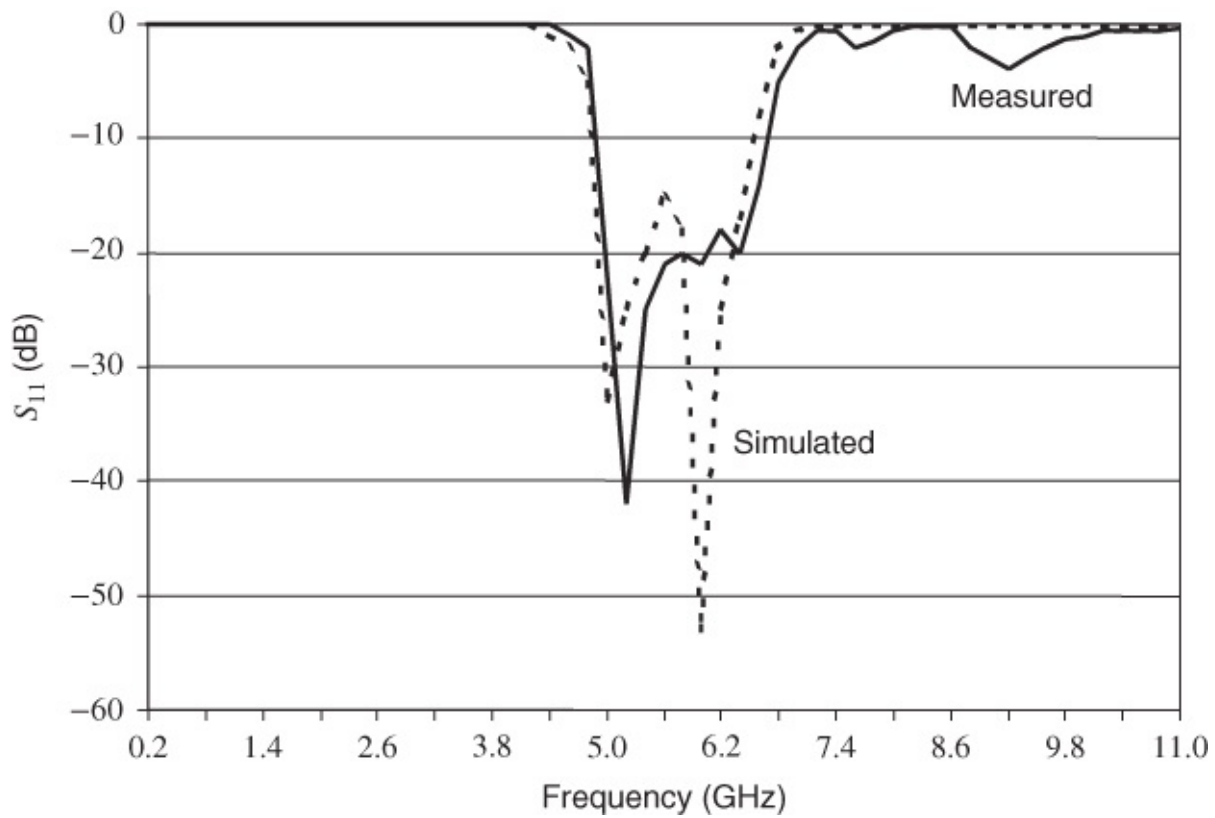


**Figure 14.42** Return loss ( $S_{11}$ ) of the bandpass filter.

As practically always, for any type of filter, the in-band loss is inferior to the ideal design goal. In this case, an in-band loss of 1 to 2 dB occurs. Above 8 GHz spurious responses become noticeable and the worst result in this case is that at 9.8 GHz (-29.5 dB). At this level such a spurious response would not usually be a problem in the remainder of the system.

The return loss or reflection characteristic (Figure 14.42) demonstrates a generally good response with the exception of the -15 dB level at ~6 GHz, almost precisely the frequency at which the response should theoretically be excellent, at -42 dB.

It is considered that some of the reasons for these discrepancies and undesirable features in the responses could well lie in a need for still more attention to the air bridges (earthing bonds).

A bandstop filter design, based on a combination of the interdigitated structures introduced earlier, has been put forward by Omar and Chow [44]. This design embodies top and bottom conductor shields in place of air bridges, and the characteristics exhibit marked peaking and dipping in the frequency responses. A major feature is that the results with the shields are very nearly as good as those using the air bridges.

Filter designs implemented with smooth substrate surfaces, notably semiconductors, should yield much improved in-band losses.

Mernyei, Aoki, and Matsuura [45] have reported MMIC bandpass filters operating in the 17 and 27 GHz bands and having 10 GHz passbands. As shown in Figure 14.43 the basic structure comprises cascaded, coupled, open-ended CPW lines with metal-layer bridges, rather than air bridges deposited on polyimide layers to bridge the line ends. These researchers use the

standard filter design procedure to realize the filters on GaAs substrates. In both cases, however, the passband loss is around 5 dB, which is surprisingly high, since just over 2 dB might have been anticipated.

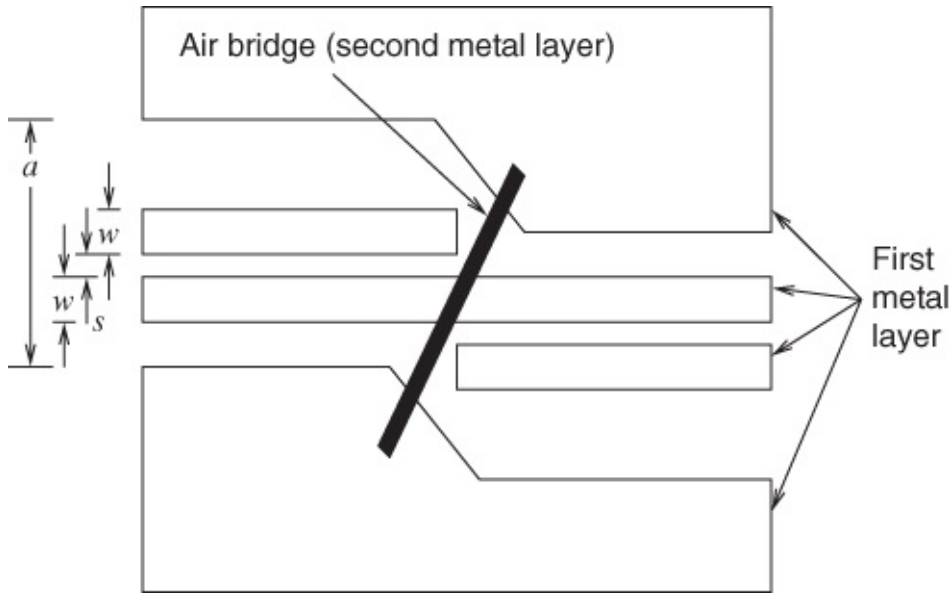


**Figure 14.43** Basic structure of an MMIC-implemented bandpass filter. Adapted from Mernyei *et al.* (1994) [45], figure 2, p. 1862. Reprinted with permission of IEEE.

It would also be very interesting to explore the effects of using conductor-backed and/or conductor-shielded CPW structures for the realization of filters and other circuit elements.

### 14.7.3 Couplers and Baluns

Several forms of couplers have been reported using CPW and its variants. Modeling the attenuation of the basic coupled coplanar waveguide (CCPW) structure is the first prerequisite, and this has been reported by Ghione and Naldi [46]. They show that the net losses are always small, amounting to less than 1 dB/mm for either the odd or the even mode. As the amount of coupling increases so the loss also decreases for the even mode case, down to only a very small fraction of a decibel per millimeter. In contrast, for the odd mode, whilst the loss decreases at first (minimizing around  $-10$  dB of coupling) as the coupling increases further so the loss rises rapidly, almost monotonically as the coupling exceeds  $-5$  dB of coupling. This behavior is similar to that of microstrip.

Uniplanar hybrid-ring and branchline couplers suitable for MMIC implementation have been reported by Ho, Fan, and Chang [47]. This team show CPW-slotline transitions using CPW pseudo short circuits and radial stubs that exhibit well-behaved passband characteristics within the 0.5–6 GHz frequency range. The following types of hybrid-ring couplers are considered: rat-race, phase-reverse, and cross-over. The rat-race in particular exhibits 3 dB power dividing, and a particularly sharp isolation response at 3 GHz. The cross-over coupler exhibits approximately 4–5 dB of power division across the 2–4 GHz band.

Fan, Ho, Kanamaluru, and Chang [48] studied broadband uniplanar magic T, hybrid ring, and de Ronde's CPW-slot couplers. They report on the performance of radial-stub compensated

hybrid magic Ts, and show that the phase and amplitude characteristics are well behaved over the 1–8 GHz band. A reduced-size reverse-phase hybrid-ring coupler is also reported. In this design the reverse phase is accomplished by implementing two radial stubs in series within one arm. De Ronde's CPW-slot directional coupler comprises a rectilinear four-port circuit with a central quarter-wave slot having radial stubs at each end. With a CPW characteristic impedance of 47.2  $\Omega$ , Ho *et al.* provide measured data showing transmission varying from 4 dB at 2.2 GHz through 1.5 dB (at 4 GHz) and coupling of 8 dB at 2 GHz ranging to 8.5 dB at 4 GHz (5.7 dB through the center frequencies). Isolation and return loss are both generally better than –12 dB over the entire band from 2 to 4 GHz.

In another paper [49] Ho, Fan, and Chang report on new uniplanar CPW hybrid-ring couplers and magic Ts. Extensive use is made of radial stubs and back-to-back baluns.

Uniplanar double-Y baluns are reported by Gu and Wu [50]. These researchers describe a network technique for the design of broadband circuits of this type using CPW, slotline, and CPS. Design equations are developed for the resistive and reactive components of the impedances of stubs required in these structures. From these equations curves are plotted showing these resistive and reactive components as functions of the electrical lengths and normalized  $Z_0$  values. From these curves the best choice of stub electrical lengths is determined, consistent with a good impedance match for the baluns.

The back-to-back circuit layout of the double-Y baluns is shown, with re-entrant stubs, and the results of measurements over the frequency range 3–30 GHz are given for both the CPW-slotline and FGCPW-CPS baluns. In both cases, the insertion losses are generally better than –4 dB over 3–22 GHz, dipping to –5 dB at higher frequencies. VSWR remains below 2 throughout, being below 1.5 over 13–30 GHz for the CPW-slotline and below 1.7 over 3–28 GHz in the case of the FGCPW-CPS balun.

#### 14.7.4 Power Dividers

Incident RF power can readily be separated into two or more outgoing transmission lines using virtually any type of structure, planar or otherwise. Therefore, CPW realizations of such power dividers are feasible and various researchers have developed this theme.

Fan and Chang [51] have published the results of their work on uniplanar power dividers using coupled CPW and asymmetrical coplanar slotlines for MICs and MMICs. They report power dividers fed by slotlines with sections of CCPW feeding the two CPW output ports. As with most configurations of this general type, balance resistors are employed at the separation T point.

An example of a Fan and Chang two-section, in-phase CCPW power divider is shown in [Figure 14.44](#). The structure is basically similar to that described above in that millimeter dimensions apply, an RT/Duroid substrate is used, and the frequency range is 1–6 GHz. The input and output CPW lines have widths of 0.62 mm and gaps of 0.33 mm. The intermediate matching sections, having lengths of 10.8 and 10.7 mm, respectively, implement strip widths of 0.17 and 0.52 mm, and gaps of 0.12 and 0.18 mm. Central gaps are 1.2 mm and 0.8 mm, and

the isolation resistances are 651  $\Omega$  and 62.5  $\Omega$ , respectively.

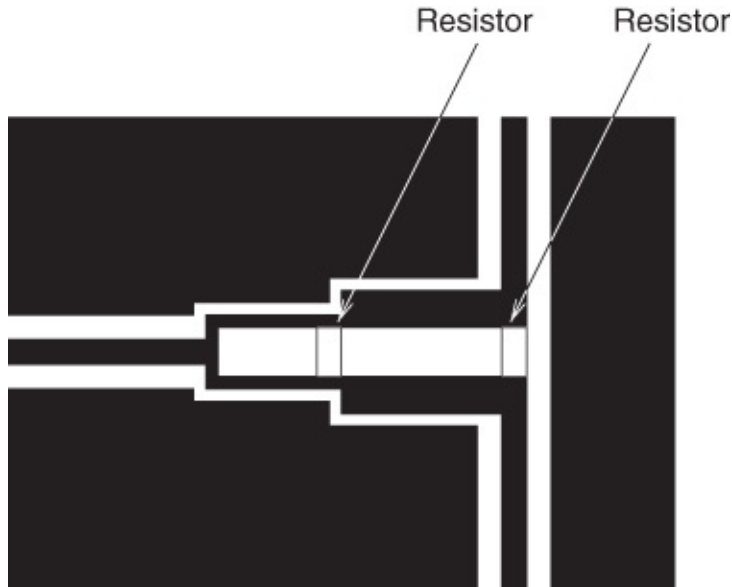


**Figure 14.44** Two-section in-phase CPW power divider. Adapted from Fan and Chang (1996) [51], figure 8, p. 2415. Reprinted with permission of IEEE.

For this circuit the insertion loss is less than 3.5 dB over the band and the isolation is greater than 24 dB. Over the 1–5 GHz band 3–4 dB of coupling is achieved from each output port. Return loss is always greater than 10 dB and exceeds 20 dB over the more restricted 1.8–4 GHz range.

#### 14.7.5 CPW and Surface Mount Components

With the ultimate aim of manufacturing high-frequency MCMs, problems surrounding the introduction of flip-chip MMICs are being increasingly addressed by many workers.

Gye-An Lee and Hai-Young Lee [52], for example, investigated the suppression of energy leakage in GaAs flip-chip to main substrate structures. Two GaAs flip-chip MMICs, side-by-side, are shown above the main substrate in the upper diagram of [Figure 14.45](#), and more detail of one flip-chip *in situ* is indicated in the lower diagram. The main (required) CPW mode is indicated by the curved field line, a  $\text{TM}_0$  surface wave mode by the solid line and a  $\text{TM}_0$  parallel-plate mode by the dotted line. Lee and Lee compare the leaky and non-leaky scenarios for the surface wave and parallel-plate modes over the frequency range 10–100 GHz. An alumina main substrate applies in all cases here, and it is found that the structure becomes leaky at frequencies above 51 GHz. Compared with any structure employing wire bonds or vias, the parasitic inductance of the metal bumps used for interconnection from the flip-chips is relatively small.

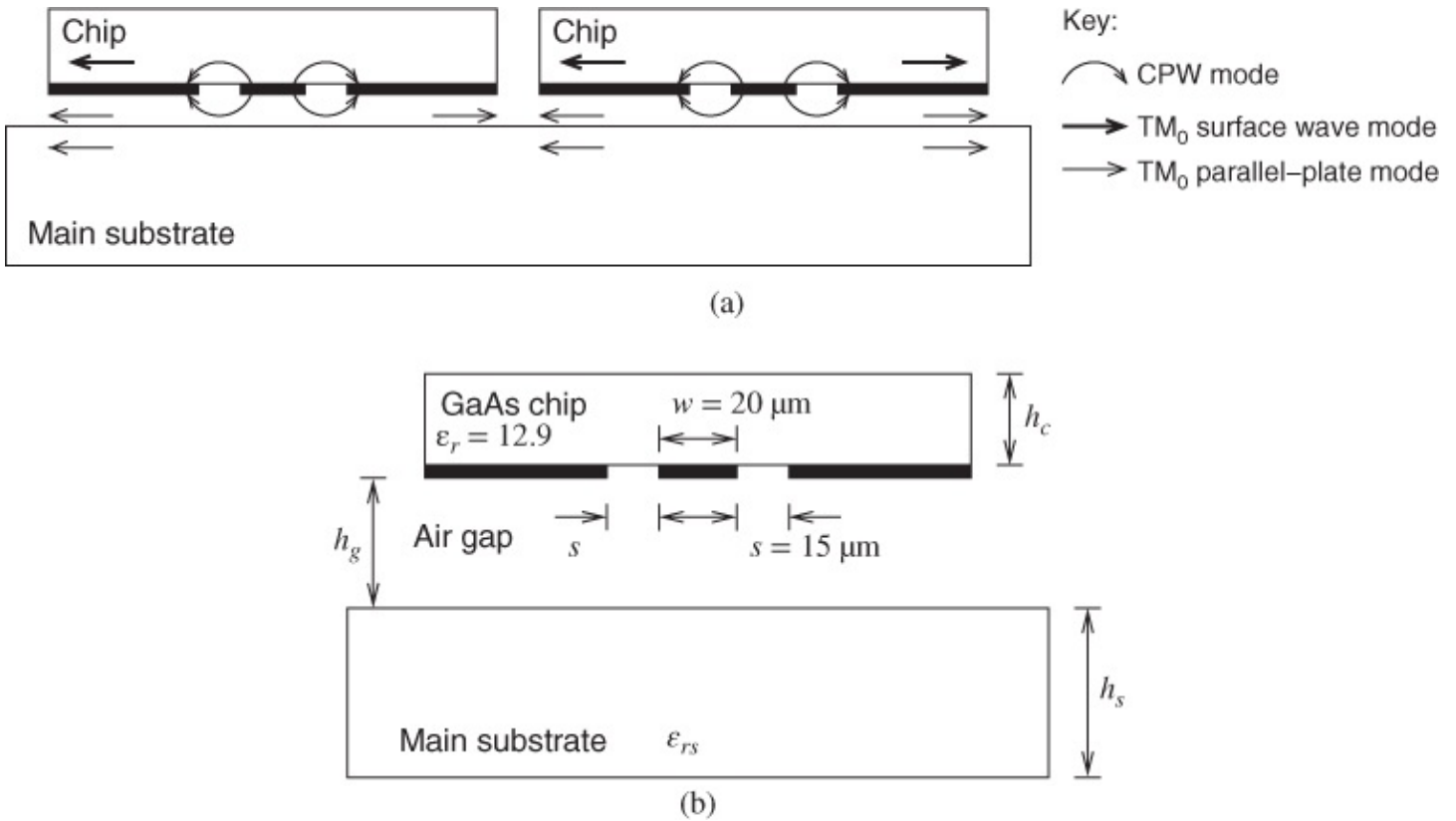


**Figure 14.45** Energy leakage due to the various modes occurring in flip-chip structures: (a) modes; and (b) detail. Adapted from Lee and Lee (1998) [52], figure 1. p. 366. Reprinted with permission of IEEE.

Further issues surrounding the millimeter-wave characteristics of flip-chip CPW interconnects for MCMs are addressed by Heinrich, Jentzsch, and Baumann [53]. This team studied the problem over the 1–70 GHz frequency range. Reflection effects are considered in detail, and it is found that the bump-pad length for the flip-chips is a significant parameter. Parasitic resonant and parallel-plate modes are reported on, although the parallel-plate mode may be suppressed by patterning the conductor backing (see [Section 14.5.4](#)). Heinrich *et al.* show that the important bump-pad structure effect may be represented by a simple, single-shunt capacitance model.

Hirose *et al.* [54] describe a flip-chip MMIC design using CPW at W band. Primarily designed for the 77 GHz automotive radar application, this group report on GaAs amplifiers in two-stage and three-stage formats. For the three-stage amplifier a gain of exceeding 10 dB over 75–85 GHz is achieved.

Appreciating that the optimization of flip-chip interconnects is highly significant, especially at millimeter-wave frequencies, Jentzsch and Heinrich have investigated this issue [55]. This is actually a development on the work described in reference [53], and the main approaches considered are staggered bumps and underpasses for compensating the effects of the bumps on the high-frequency performance of the flip-chips. Important approaches include the use of staggered bumps, the addition of close-proximity high-impedance lines and the use of 90° underpasses to minimize cross-coupling.

In practice both the RF and also the mechanical characteristics of any circuit structure are equally important. It is no use having an excellent electrically performing chip if normal operating fatigue causes failure. With these issues as driving forces Feng *et al.* [56] reported on the RF and mechanical characterization of GaAs flip-chip interconnects in CPW circuits with epoxy underfill. A simple lumped-element equivalent circuit forms an appropriate model for the CPW with flip-chip interconnects. This has the usual *CLC* configuration, with the addition of resistance in series with *L* for modeling losses.

Phase-shift measurements with and without the epoxy underfill indicate that this underfill has a significant effect on performance over the frequency range from 1 to 40 GHz. Whilst the effects of the substrate reduce the fatigue life of such flip-chips, the opposite is true for the effects of the underfill encapsulant, where a significant increase in the fatigue life applies.

In a key paper on three-dimensional vertical interconnect technology Goverdhanam, Simons, and Katehi [57] report on the design considerations, fabrication, and comparative performance of both CPW and CPS as suitable mediums for 3D interconnects. In this case, silicon technology applies and the results are equally applicable to both microwave and very-high-speed digital circuits. As these applications are all on-chip, all the dimensions are in the orders of microns or tens of microns. The three main structures described are:

- CPS with cross-over underpass
- CPS with a vertical interconnect embodying a 180° phase shift
- CPW with a vertical interconnect embodying a 180° phase shift.

Goverdhanam *et al.* also show measured results for CPS loss in decibels per millimeter versus the strip width. It is clear that this loss increases steeply as the strip width *w* decreases, most noticeably below about 40  $\mu\text{m}$ . The loss at 30 GHz approaches 1.4 dB/mm when *w* = 30  $\mu\text{m}$ .

In many of these configurations, particularly when using MCM-D technology, parasitic modes arising from CPW discontinuities can become an issue. Soliman *et al.* [19] addressed this issue and applied their approach to a 3 dB power splitter. A filter structure, due originally to Rittweger (hence named Rittweger's filter) is first studied, implemented in CPW with air bridges and thin-film tunnels to suppress the parasitic modes. The losses and *S* parameters over the frequency band 10–40 GHz are shown for this configuration. A notable result is that the losses peak rapidly around 25 GHz when tunnels are used, and around 28 GHz when air bridges are implemented.

A 3 dB power splitter in MMIC technology is also shown. With this circuit, using a thin-film bridge, the return loss is better than  $-12$  dB across the 20–30 GHz band.

FGCPW is also being applied to the very important and potentially high-volume application of 77 GHz automotive radars, as indicated by a benchmark paper by Kerssenbrock and Heide [58]. These researchers point out that cost and mass production issues continue to act as major factors influencing the widespread adoption of miniature radars in this market.

Kerssenbrock and Heide show that flip-chip technology can be effectively applied to the development of a productionized near-distance automotive radar module. The basic

transmission technology used is FGCPW, with the line itself deposited on an alumina substrate ( $\epsilon_r = 9.8$ ,  $h = 0.635$  mm). There is no backside metallization and hence no possibility of parallel-plate moding. A glass layer is interposed between the alumina and the FGCPW structure.

A 77 GHz flip-chip phase-locked VCO has been built using this technology. This oscillator is used in conjunction with a 12 dB-gain amplifier, a flip-chip power divider, a balanced mixer within a CPW rat-race hybrid, and finally, flip-chip patch transmit and receive antennas. This approach results in a fully uniplanar structure that is potentially economic to manufacture in production volumes. There is no backside metallization, there are no transitions, and there are no vias.

This approach may also represent a milestone for further developments in FGCPW applications across a wide spectrum of applications.

## 14.8 Variants on the Basic CPW Structure

### 14.8.1 CPW with Top and Bottom Metal Shields

As described in the main sections earlier in this chapter, air bridges are traditionally necessary in order to maintain the dominant mode in CPW. Alternatives have, however, been investigated and a significant example comprises the introduction of top and bottom metal shields. In practice, such shields will probably be in place in any event as part of the packaging structure. The cross-section of such an arrangement is shown in [Figure 14.46](#).

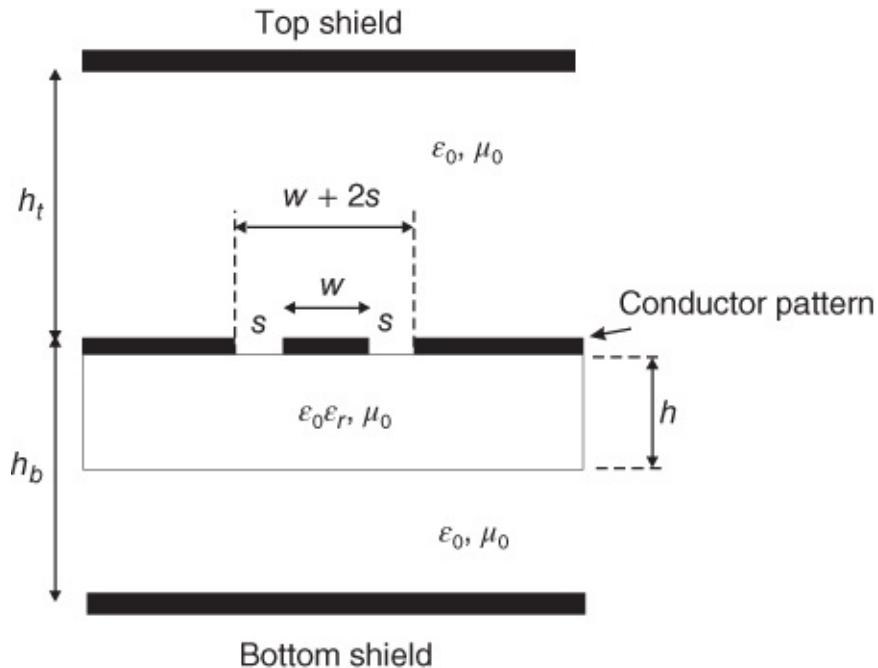


[Figure 14.46](#) CPW with top and bottom metal shields.

Omar and Chow [44] explored this type of structure and used it to implement a band-reject filter. They reported response results for both this structure and also the same pattern of band-

reject filter, but implemented using air bridges. A response frequency range of 2–40 GHz applied. Using a very thin substrate Omar and Chow showed that for close proximity shields ( $h_{t,b} \approx 100 \mu\text{m}$ ) the filter responses were very similar regardless of the approach. This demonstrated the utility of applying top and bottom metal shields in place of the more awkward and relatively unsophisticated air bridges.

### 14.8.2 Multilayer CPW

Current crowding at the edges of signal and ground conductors in CPW represents a substantial problem in power amplifiers, for example. Budimir *et al.* [59] reported an interesting solution to this problem. [Figure 14.47\(a\)](#) indicates the traditional “open” CPW and [Figure 14.47\(b\)](#) shows the new multilayer structure with the so-called “inverted V” cross-section.

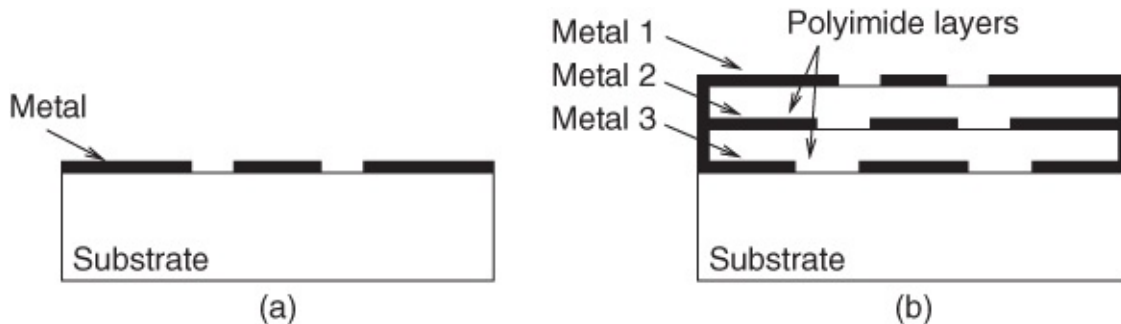


[Figure 14.47](#) Cross-sections: (a) conventional CPW; and (b) “inverted-V” CPW.

In this multilayer structure the “standard” CPW metallization is conductor layer 1. However, this layer is deposited on a polyimide layer with conductive vias connecting to conductor layer 2, itself deposited on another polyimide layer. This process is repeated twice, with extending central conductor widths until the final structure, directly on the GaAs substrate, is actually separated into two physical conductor tracks.

The current flow is therefore much more evenly spread through the V-shaped conductor structure. Comparing a conventional CPW the current crowding is reduced by a factor of 4 on the worst affected layer. Budimir *et al.* focused on investigations in the 1–20 GHz band.

Herrick, Schwartz, Henderson, and Katehi [60, 61] have reported wafer effects in Si-micromachined multilayer guiding structures operating at frequencies as high as W band (75–110 GHz). Issues concerning circuit isolation and integrity form the driving force behind this endeavor, especially concerning high-density ICs. Herrick *et al.* examine two CPW architectures embodying Si-micromachined cavities. In all instances, 100  $\mu\text{m}$  thick silicon substrates are used. Iordanescu, Bartolucci, Simion, and Dragoman also considered CPW stubs and filters fabricated on thin membranes and contrasted their performance with the components on standard substrates [62]. Fabricating CPW lines on thin membranes has the advantage of reducing dispersion, dielectric loss, and increasing dimensions, which is important at high millimeter-wave frequencies [62–65].

The main 3D multilayer structure cross-section is shown in [Figure 14.48](#), in which six CPWs can be seen, in two layers, and also a further layer of active conductors. Both theoretical and

experimental results are indicated and FGCPW is implemented. Very small but significant dispersion (around 1–2%) is evident over this wide frequency band for both the conductor-backed CPW and also the conductor-backed micromachined CPW. Losses remain below 0.35 dB/mm for both cases.

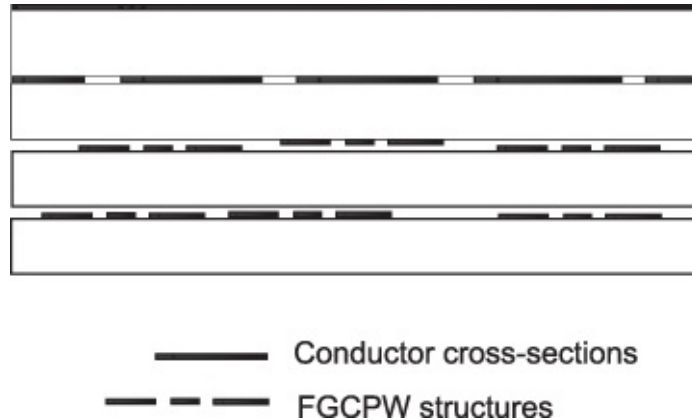


**Figure 14.48** A 3D multilayer stack of FGCPW structures. Adapted from Herrick *et al.* (1999) [60], figure 1. p. 61. Reprinted with permission of IEEE.

From 75 to 85 GHz the cross-coupling (crosstalk in time-domain terms), at  $-27$  to  $-45$  dB, is broadly similar for both the conductor-backed CPW and also the conductor-backed micromachined CPW. However, at frequencies exceeding 85 GHz the conductor-backed micromachined CPW is considerably superior, with cross-coupling between  $-45$  and  $-58$  dB. This means that the cross-coupling is approaching (and ultimately goes into) the noise floor above 95 GHz. Herrick *et al.* show that the introduction of  $40 \mu\text{m}$  air cavity spacings significantly decreases FGCPW-to-FGCPW coupling, ensuring that this always remains better than  $-18$  dB. In particular, without this air cavity for relatively close spacing (less than  $100 \mu\text{m}$ ), the coupling exhibits peaks of  $-12$  dB in the 90–93 GHz region.

### 14.8.3 Trenched CPW on a Silicon MMIC

A further novel approach to the problem of RF loss reduction has been offered by Yang *et al.* [66]. This was applied to silicon MMIC structures and involved the etching of trenches down into the exposed silicon in the CPW gaps. This structure is shown in [Figure 14.49](#).

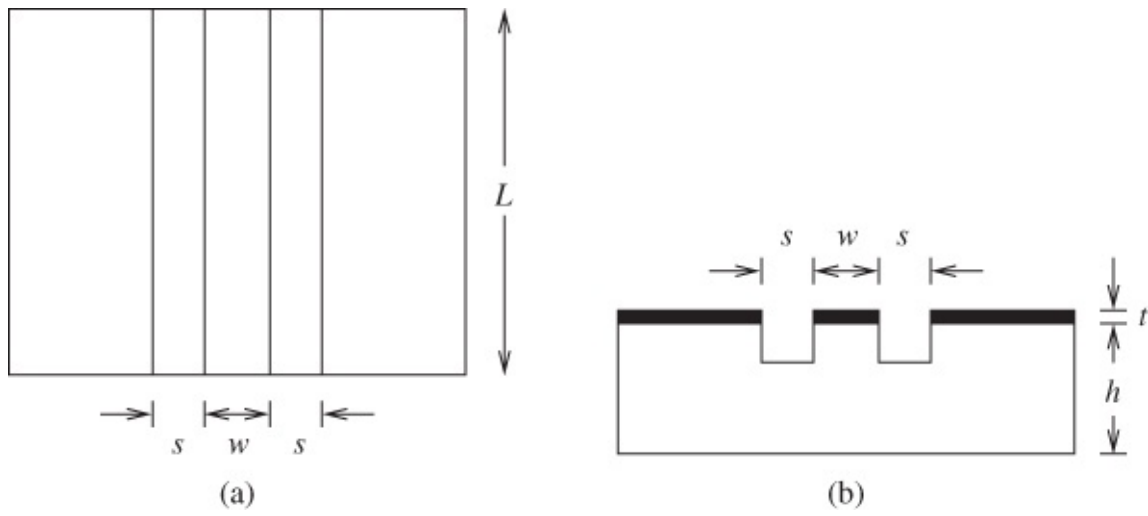


**Figure 14.49** Trenched CPW on an HRS substrate: (a) plan view; and (b) cross-section.

By silicon etching, trench depths with the following values were used: 0, 3, 6, 9, and 12  $\mu\text{m}$ . Electric field and current flow distributions are reported. Yang *et al.* provide capacitance curves versus bias voltage, and also characteristic impedance curves versus bias voltage.  $S$ -parameters are also provided. Characteristic impedance is also shown as a function of frequency up to a maximum of 40 GHz, and it is clear that this parameter always decreases with frequency. The decrease is greatest for trench depths in the 6–9  $\mu\text{m}$  range. The reduction in RF losses varied from 0.5 to 1.8 dB over the 2–40 GHz range, for a 12  $\mu\text{m}$  deep trench.

#### 14.8.4 Differential Line and Coplanar Strip

Two CPS structures are shown in [Figure 14.50](#). Whether these structures are referred to as CPS or differential line depends on how they are driven. We will talk more about this soon but often CPS is used as the unifying term. The CPS line of [Figure 14.50\(a\)](#) is formed by two conductors on top of a dielectric of sufficient thickness that the metal backing has negligible effect on the field structure. The structure in [Figure 14.50\(b\)](#) is known as embedded CPS and is encountered when multiple dielectric and metal layers are used. From the extensive studies presented in the previous sections we conclude that the dielectric thickness needs to be two to three times greater than the maximum value of  $w$  or  $s$ .

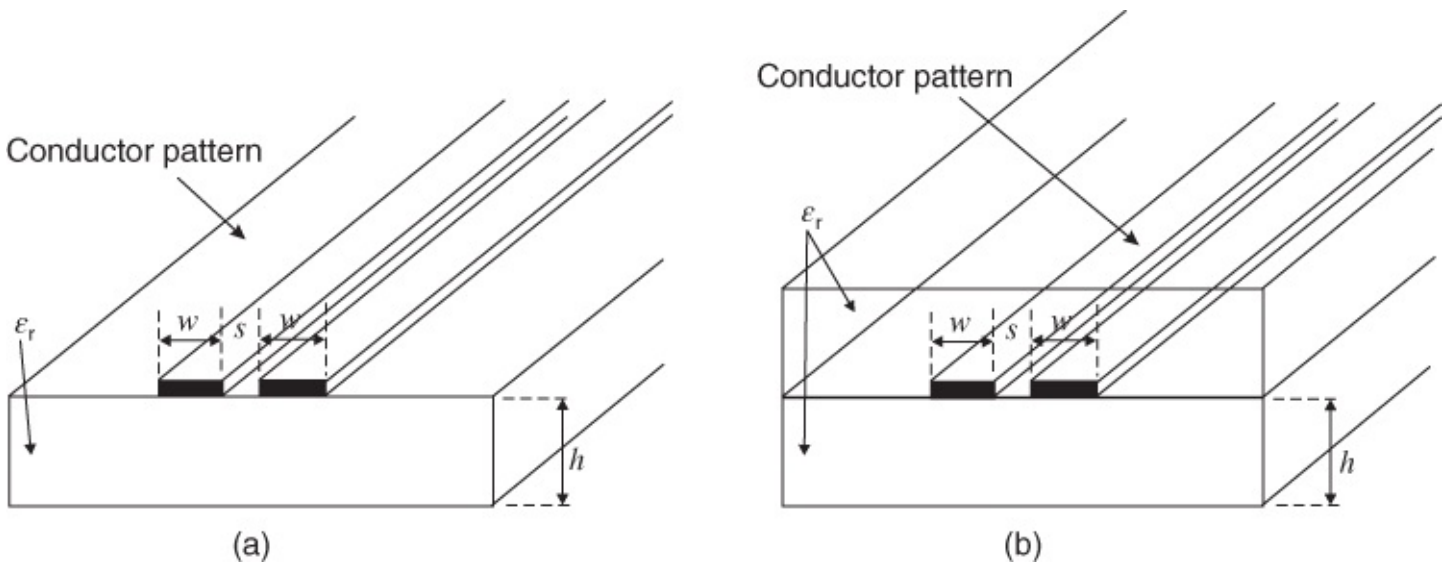


**Figure 14.50** CPS or differential line structures on (a) the surface of a dielectric or (b) embedded.

The two-conductor line of [Figure 14.50](#) is a differential line or balanced line when neither conductor is ground. This is also approximated when the signals are push–pull related and a virtual ground (or AC ground) is formed. Then the signal on one conductor is, at one time, above virtual ground and the signal on the other is then below. Differential line is commonly used with RFICs as the signal path on the IC is almost always differential since differential circuits on-chip remove many of the distortion and noise-coupling concerns. At frequencies in the low gigahertz regime, transmission line structures are rarely used on-chip. However, regular differential transmission lines are used off-chip to connect to the RFIC. It is common to mount RFICs on low-temperature co-fired ceramic (LTCC) so that filters, baluns, and matching can be realized on the LTCC, which has a much lower area cost than the RFIC.

When one of the conductors of the transmission line is grounded the line is known as CPS. CPS is a good structure to use, instead of CPW, when space is at a premium. CPS and differential line have the same electrical characteristics as long as the metal backing (or ground planes) are sufficiently removed. The attraction of both CPS and differential line is that the signal return path is clearly defined.

The discussion and results presented below relate directly to differential line, which is the much more common utilization of this conductor structure. In [Figure 14.51](#) the normalized current magnitude and charge distribution on a differential line are shown. These profiles are simulated at 10 GHz for an electrically short section of line so that there is very little longitudinal variation in the profiles. As with all of the other transmission line structures charges accumulate along the inside edges of the conductors. The concentration, however, is greater than for any of the other structures that we have considered. Lower level charges also accumulate at outside edges of the conductors. These results indicate that the width,  $w$ , and the separation,  $s$ , will both be important in determining the characteristics of the differential line.

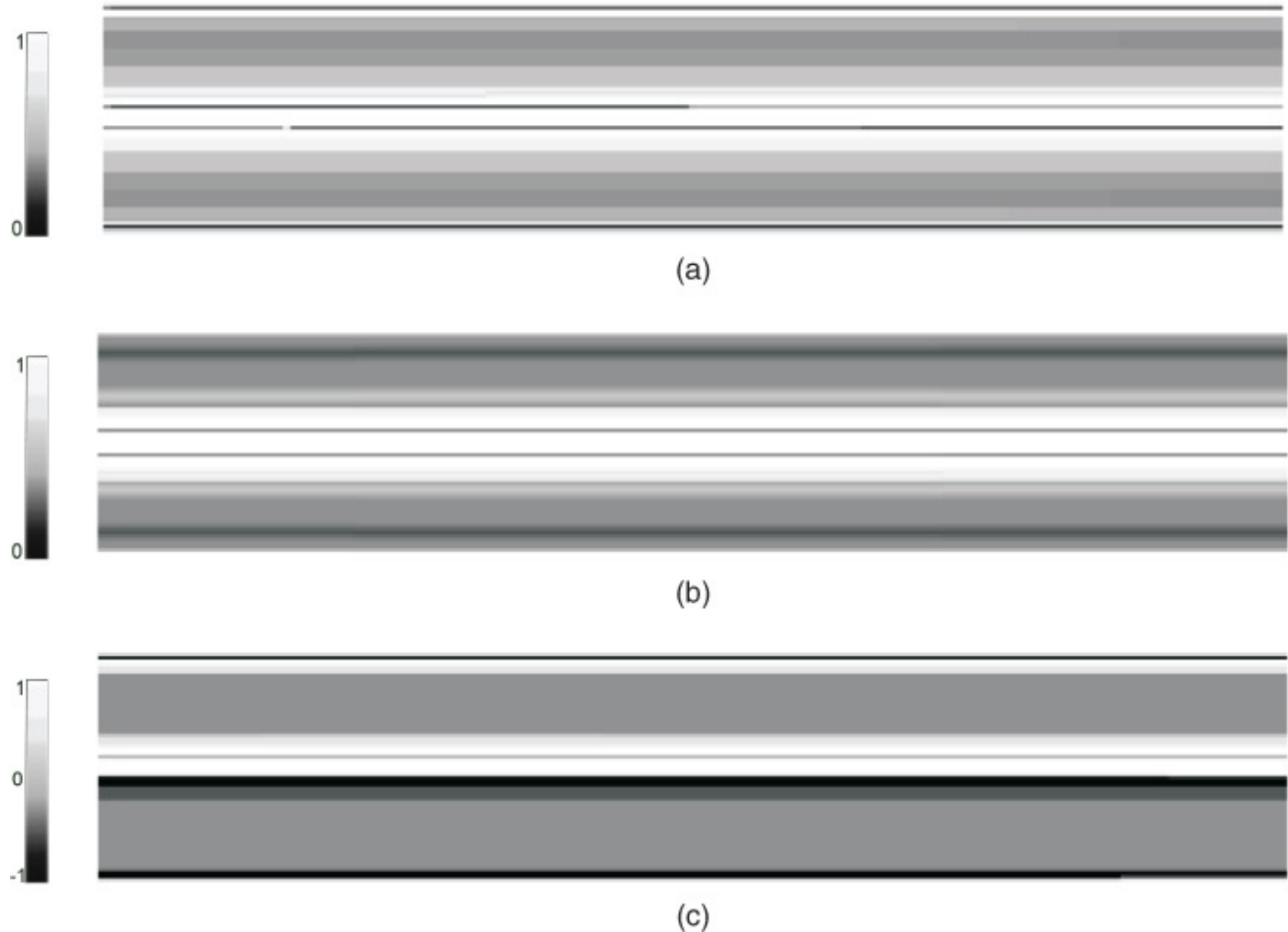


**Figure 14.51** Instantaneous normalized current magnitude and charge distribution along a differential line: (a) longitudinal current; (b) transverse current; and (c) charge. The current and charge are normalized and use the scales shown on the left-hand side. The peak transverse current is 1500 times smaller than the peak of the longitudinal current. The frequency is 10 GHz,  $s = 2.5 \mu\text{m}$ , and  $w = 10 \mu\text{m}$ .

As mentioned above, differential line is a particularly important transmission line medium for RFICs, both for on-chip connections at frequencies 10 GHz and higher, and for connections to the differential input and outputs of an RFIC. In [Figures 14.52](#) and [14.53](#) curves of characteristic impedance and effective permittivity are presented for a differential line fabricated on the surface of HRS. In the first chart, [Figure 14.52](#), the characteristic impedance and the effective permittivity are plotted against the separation-width ratio  $s/w$  for two different families of lines. An important point to note here is that the effective permittivity of the lines varies as  $s/w$  varies. This results from the field lines fringing more into the air region for larger  $s$  values.

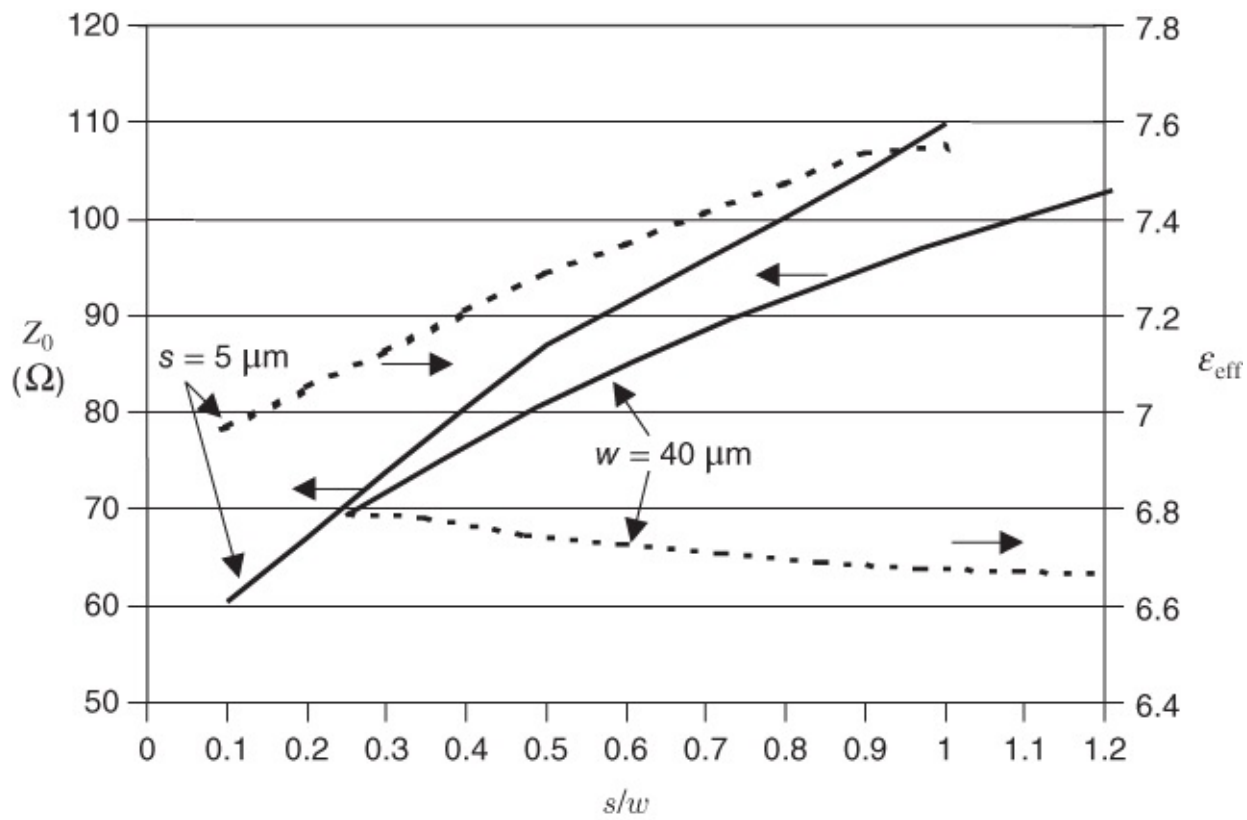


**Figure 14.52** Characteristic impedance and effective relative permittivity of open differential line fabricated on HRS ( $\epsilon = 11.9$ ) for various  $s/w$  ratios. Frequency = 10 GHz, height above ground plane,  $h = 650 \mu\text{m}$ .

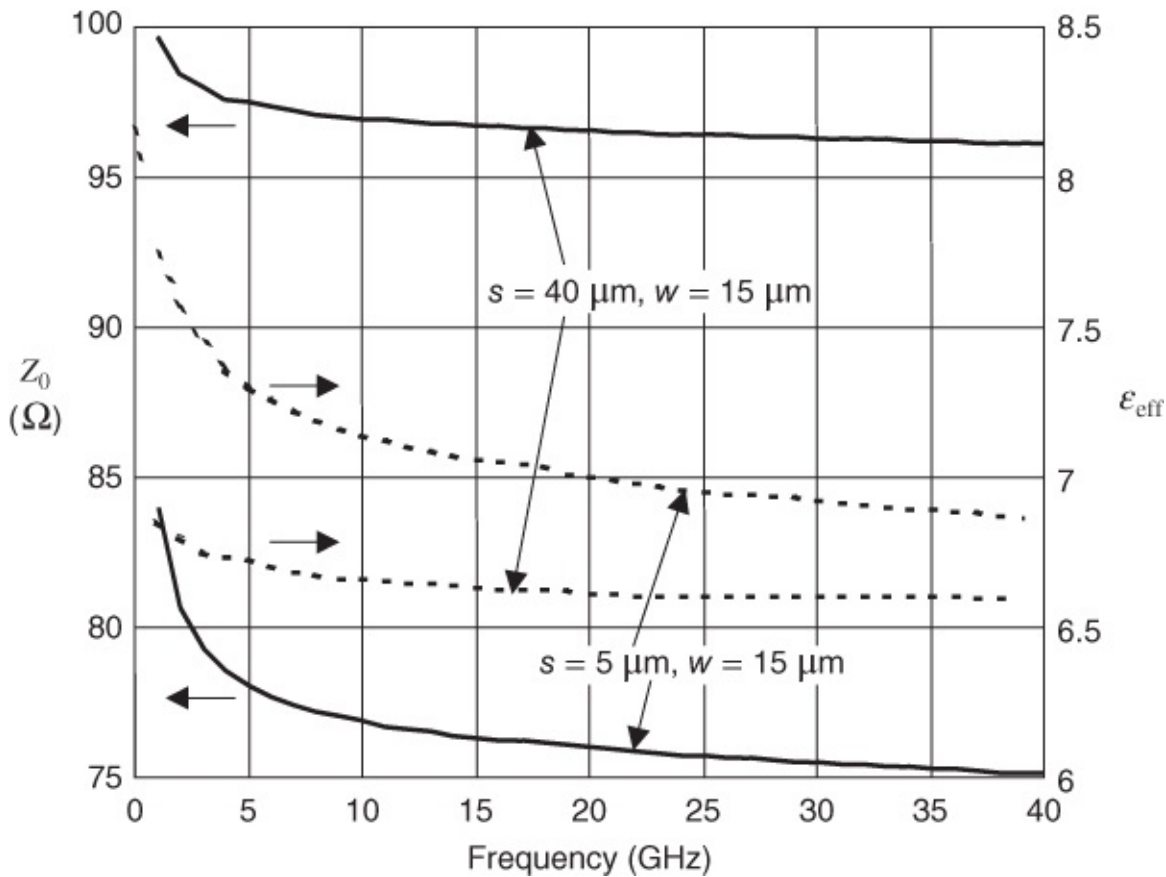


**Figure 14.53** Frequency dependence of characteristic impedance and effective relative permittivity of open differential line fabricated on HRS ( $\epsilon = 11.9$ ). Height above ground plane,  $h = 650 \mu\text{m}$ .

Dispersion data are shown in [Figure 14.53](#) for two differential lines fabricated on the surface of HRS. The energy in the field concentrates more in the air region at high frequencies and this is the main reason for the impedance variation with frequency.

A more common usage of differential line is as an embedded structure, as shown in [Figure 14.50\(b\)](#). Using the common approach based on conformal mapping Crampagne and Khoo [67] derived the characteristic impedance of the line:

$$Z_0 = \frac{240\pi}{\sqrt{2\epsilon_0(\epsilon_{r1} + \epsilon_{r2})}} \frac{K(k)}{K'(k)}. \quad 14.54$$

This equation allows the dielectrics above and below the strips to be different, with the top dielectric having a permittivity of  $\epsilon_{r1}$  and the bottom dielectric having a permittivity of  $\epsilon_{r2}$ . In Equation (14.54)  $K(k)$  is the complete elliptic integral of the first type,  $K'(k)$  is its complementary function, and

$$k = \frac{s}{s+2w}. \quad 14.55$$

So  $k$  contains the dimensional information, and the important thing to note is that  $Z_0$  depends on the geometrical ratio  $k = w/(w+2s)$ , that is, on the ratio  $s/w$  as  $w/(w+2s) = 1/(1+2s/w)$ .

Note that this is not a simple dependence between geometry and  $Z_0$ , as  $k$  is the argument of an elliptical integral function. However, it does mean that lines with the same  $k$  value, or equivalently the same  $s/w$  ratio, will have the same characteristic impedance (within the accuracy limits of the analysis). The characteristic impedances at 2.45 GHz of differential lines embedded in an LTCC are presented in [Figure 14.54](#) for various  $s/w$  ratios. Now the effective permittivity cannot vary (it is equal to the permittivity of the medium) and it is seen that  $Z_0$  is essentially determined by the  $s/w$  ratio. This is in contrast to the result with the open differential line.

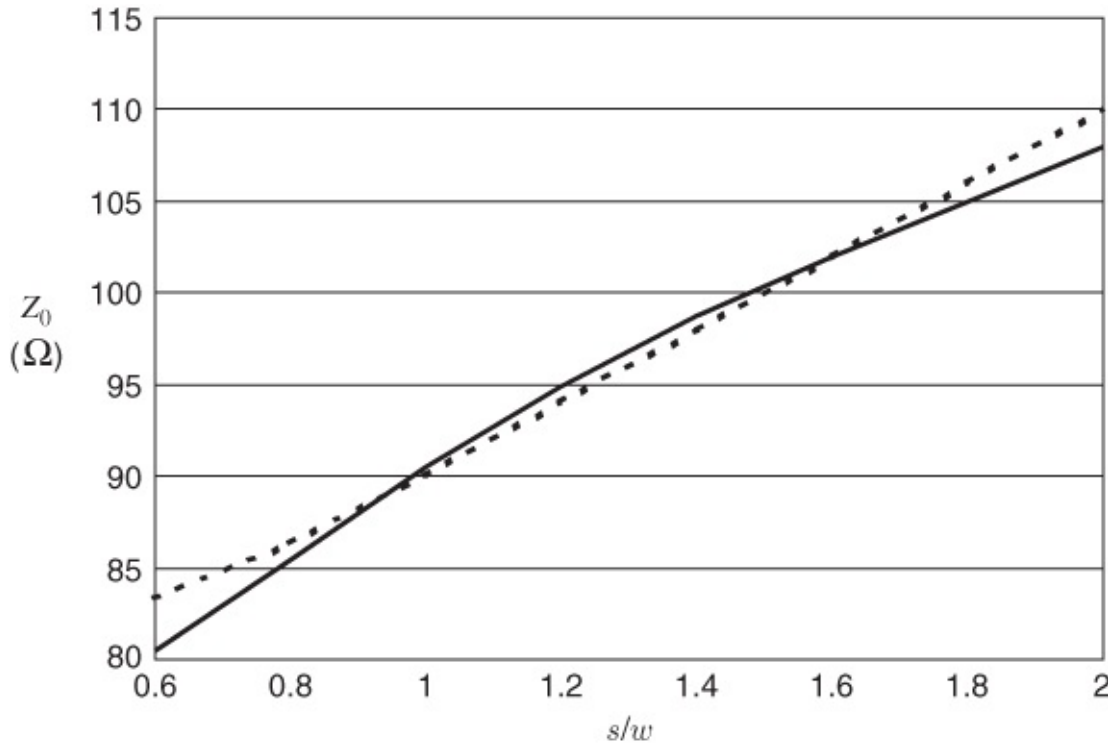


**Figure 14.54** Characteristic impedance and effective relative dielectric constant of an embedded differential line fabricated in LTCC with  $\epsilon = 7.3$  for various  $s/w$  ratios. Frequency = 10 GHz, height from the line to each ground plane,  $h = 340 \mu\text{m}$ . Results derived using SONNET simulations.

Inevitably there will be a ground plane near the differential line. The analysis and results above assume that the line is sufficiently separated from the ground plane. To investigate the effect of ground plane separation, the characteristic impedance of the LTCC-embedded line was calculated for various separations. The results are plotted in [Figure 14.55](#) as a function of  $h/s$ . Ideally, the presence of the ground plane should have no effect on the characteristics of the line and, above  $h/s = 3$ , the effect is negligible and is only about 1.5% at  $h/s = 2$ . However, values of  $h/s$  near or less than 2 should be avoided so that the microstrip (or parallel-plate) mode, with electric field line from the conductors of the differential line to the ground planes, is not excited [68]. Values of  $h/s$  greater than 3 are strongly preferred but compromises are necessary given the maximum package thickness and tolerances on the dimensions of fabricated lines. The ground plane separation should not be used as a parameter to adjust the characteristic impedance of the line.

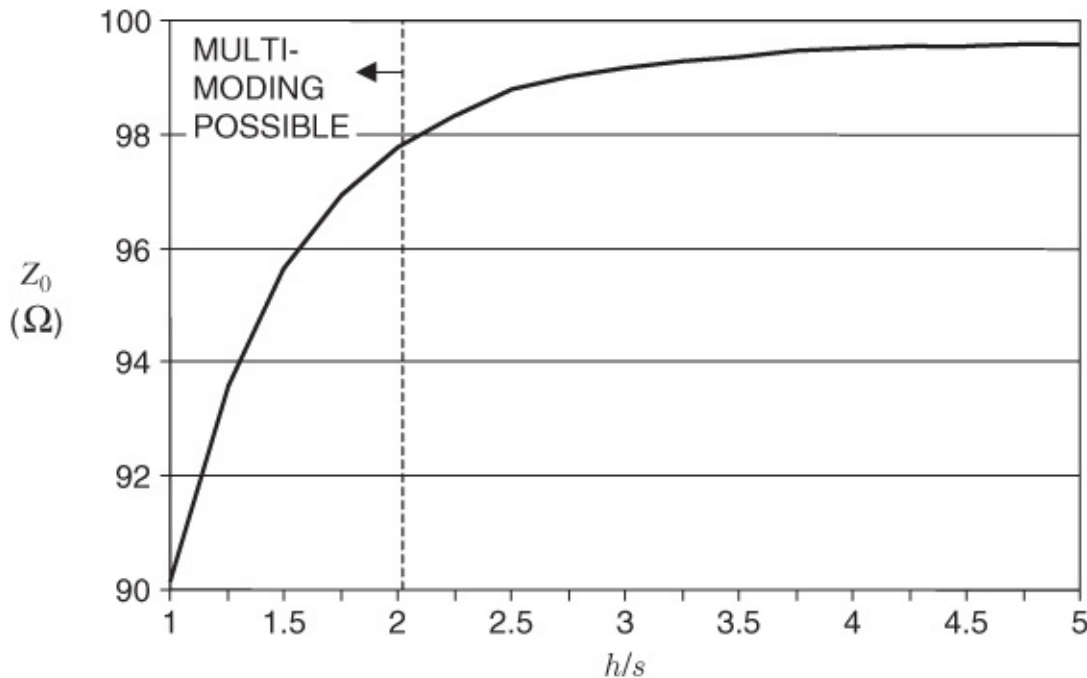


**Figure 14.55** Characteristic impedance of an embedded differential line fabricated in LTCC with  $\epsilon = 7.3$  for various  $h/s$  ratios. Frequency = 2.45 GHz, separation,  $s = 100 \mu\text{m}$ , and width,  $w = 70 \mu\text{m}$ . Results derived using SONNET simulations.

Synthesis of a differential line requires that we arrive at the physical dimensions of the line from the electrical requirement, in this case  $Z_0$ . The desired synthesis equations are obtained by inverting Equation (14.54):

$$\frac{K(k)}{K'(k)} = \frac{\sqrt{2\epsilon_0(\epsilon_{r1}\epsilon_{r2})}}{240\pi} Z_0. \quad 14.56$$

The value of  $k$  is obtained from  $K(k)/K'(k)$  using the following polynomial expression, which was fitted by Crampagne and Khoo [67]:

$$k = \frac{w}{w + 2s} = \sum_{i=0}^N a_i (K/K')^i \quad 14.57$$

where the polynomial coefficients  $a_i$  were fitted over two ranges:

For  $0 \leq K/K' < 0.5$ :

$a_0 = 0.00913$	$a_1 = -0.1352$	$a_2 = 0.2689$
$a_3 = -0.1367$	$a_4 = 5.523$	$a_5 = -5.087$

For  $0.5 \leq K/K' \leq 1$ :

$a_0 = -0.0656$	$a_1 = -0.3211$	$a_2 = 1.676$
$a_3 = 0.5984$	$a_4 = -1.849$	$a_5 = 0.6705$

One conclusion of the results reported here is that the range of characteristic impedances

available is limited. There is a relatively small geometrical dependence (the  $s/w$  ratio can be adjusted) but there is a strong dependence on permittivity. The characteristic impedance of embedded differential line (as with all lines) is proportional to the inverse of the square root of the permittivity. So a graphical approach to designing an embedded line with a specific characteristic impedance is as follows. Suppose a line is to be designed on LTCC with a characteristic impedance,  $Z_0$  of 50  $\Omega$ . Using [Figure 14.54](#) it is seen that  $s/w = 1$  yields a nominal characteristic impedance  $Z'_0 = 90 \Omega$  for a nominal relative permittivity  $\epsilon'_r = 7.4$ . Then the material required to realize the  $Z_0$  has a permittivity

$$\epsilon_r = \left( \frac{Z'_0}{Z_0} \right)^2 \quad \text{so that} \quad \epsilon'_r = \left( \frac{90}{50} \right)^2 \cdot 7.3 = 23.7 \quad 14.58$$

LTCC is available in a range of permittivities but many other factors go into selecting the electrical characteristics, including the length of quarter-wavelength long lines (required for filters and baluns) and the not insignificant physical tolerances which result in large variations in electrical length if high dielectric constant materials are used. Thus materials with permittivities of 6–10 are often chosen for RFIC applications so that the available range of characteristic impedances for differential lines is 80–110  $\Omega$ , as shown in [Figure 14.54](#).

## 14.9 Summary

Coplanar waveguide is the transmission medium of choice above 20 GHz or so, although this threshold can be a little higher for on-chip lines as they are so small. CPW confines the electromagnetic fields in a more localized manner than microstrip, thus reducing spurious coupling, radiation, and dispersion. The electrical characteristics of CPW are defined by the lateral dimensions, which can accurately be defined photolithographically and is a significant advantage when the thickness of a substrate cannot be accurately controlled, as with semiconductors. CPW-like structures are becoming common for long high-speed digital interconnect and RFIC connections. Shield lines are placed between neighboring signal lines, thus creating ground signal ground (GSG) configurations. The concept here is to provide a precisely defined signal return path and to reduce capacitive coupling of signal lines. CPS lines are also used as long high-performance digital interconnect mediums where the desirable attribute is the differential signaling. Differential lines, having the same structure as CPS, are commonly used as off-chip transmission lines connecting RFICs. This is also a desirable attribute in some microwave and millimeter-wave circuits where a balanced line (the microwave term for differential line) is required to drive balanced structures such as antennas.

## References

- [1] C. Wen, “Coplanar waveguide: A surface strip transmission line suitable for nonreciprocal gyromagnetic device applications,” *IEEE Trans. on Microwave Theory and Techniques*, vol. 17, no. 12, pp. 1087–1090, Dec. 1969.

- [2] K. C. Gupta, R. Garg, I. J. Bahl, and P. Bhartia, *Microstrip Lines and Slotlines*, 2nd ed. Artech House, 1996.
- [3] C. Veyres and V. Fouad-Hanna, “Extension of the application of conformal mapping techniques to coplanar lines with finite dimensions,” *Int. J. of Electronics*, no. **48**, pp. 47–56, 1980.
- [4] G. Ghione and C. Naldi, “Parameters of coplanar waveguides with lower ground plane,” *Electronics Letters*, vol. **19**, no. 18, pp. 734–735, 1983.
- [5] G. Ghione and C. Naldi, “Analytical formulas for coplanar lines in hybrid and monolithic MICs,” *Electronics Letters*, vol. **20**, no. 4, pp. 179–181, 1984.
- [6] S.-J. Fang and B.-S. Wang, “Analysis of asymmetric coplanar waveguide with conductor backing,” *IEEE Trans. on Microwave Theory and Techniques*, vol. **47**, no. 2, pp. 238–240, Feb. 1999.
- [7] A. K. Rayit, “Characteristics and applications of coplanar waveguide and its discontinuities,” Ph.D. dissertation, University of Bradford, 1997.
- [8] W. Hilberg, “From approximations to exact relations for characteristic impedances,” *IEEE Trans. on Microwave Theory and Techniques*, vol. **17**, no. 5, pp. 259–265, May 1969.
- [9] M. Houdart, “Coplanar lines: Application to broadband microwave integrated circuits,” in *6th European Microwave Conf.*, Sep. 1976, pp. 49–53.
- [10] K. Koshiji, E. Shu, and S. Miki, “Dielectric and conductor losses in coplanar waveguides,” *Electronics and Communications in Japan*, vol. **65**, no. 12, pp. 55–64, 1982.
- [11] R. Jackson, “Coplanar waveguide vs. microstrip for millimeter wave integrated circuits,” in *1986 IEEE MTT-S Int. Microwave Symp. Digest*, Jun. 1986, pp. 699–702.
- [12] M. Zhang, C. Wu, K. Wu, and J. Litva, “Losses in gaas microstrip and coplanar waveguide,” in *1992 IEEE MTT-S Int. Microwave Symp. Digest*, Jun. 1992, pp. 971–974.
- [13] L. Vietzorreck and W. Pascher, “Modeling of conductor loss in coplanar circuit elements by the method of lines,” *IEEE Trans. on Microwave Theory and Techniques*, vol. **45**, no. 12, pp. 2474–2478, Dec. 1997.
- [14] G. Ghione, M. Goano, and M. Pirola, “Exact, conformal-mapping models for the high-frequency losses of coplanar waveguides with thick electrodes of rectangular or trapezoidal cross section,” in *1999 IEEE MTT-S Int. Microwave Symp. Digest*, 1999, pp. 1311–1314.
- [15] G. Ponchak, M. Matloubian, and L. Katehi, “A measurement-based design equation for the attenuation of MMIC-compatible coplanar waveguides,” *IEEE Trans. on Microwave Theory and Techniques*, vol. **47**, no. 2, pp. 241–243, Feb. 1999.
- [16] Y. Wu, S. Gamble, B. Armstrong, V. Fusco, and J. Stewart, “ $\text{SiO}_2$  interface layer effects

on microwave loss of high-resistivity CPW line,” *IEEE Microwave and Guided Wave Letters*, vol. **9**, no. 1, pp. 10–12, Jan. 1999.

[17] E. Yamashita, K. Atsuki, and T. Ueda, “An approximate dispersion formula of microstrip lines for computer-aided design of microwave integrated circuits,” *IEEE Trans. on Microwave Theory and Techniques*, vol. **27**, no. 12, pp. 1036–1038, Dec. 1979.

[18] J. Papapolymerou, J. East, and L. Katehi, “GaAs versus quartz FGC lines for MMIC applications,” *IEEE Trans. on Microwave Theory and Techniques*, vol. **46**, no. 11, pp. 1790–1793, Nov. 1998.

[19] E. Soliman, P. Pieters, E. Beyne, and G. Vandenbosch, “Suppression of the parasitic modes in CPW discontinuities using MCM-D technology-application to a novel 3-db power splitter,” *IEEE Trans. on Microwave Theory and Techniques*, vol. **46**, no. 12, pp. 2426–2430, Dec. 1998.

[20] J. Hesselbarth and R. Vahldieck, “Leakage suppression in coplanar waveguide circuits by patterned backside metallization,” in *1999 IEEE MTT-S Int. Microwave Symp. Digest*, 1999, pp. 871–874.

[21] B. Kleveland, T. Lee, and S. Wong, “50-GHz interconnect design in standard silicon technology,” in *1998 IEEE MTT-S Int. Microwave Symp. Digest*, Jun. 1998, pp. 1913–1916.

[22] A. Yakovlev and G. Hanson, “On the nature of critical points in leakage regimes of a conductor-backed coplanar strip line,” *IEEE Trans. on Microwave Theory and Techniques*, vol. **45**, no. 1, pp. 87–94, Jan. 1997.

[23] D. Nghiem, J. Williams, D. Jackson, and A. Oliner, “Existence of a leaky dominant mode on microstrip line with an isotropic substrate: theory and measurements,” *IEEE Trans. on Microwave Theory and Techniques*, vol. **44**, no. 10, pp. 1710–1715, Oct. 1996.

[24] D. Nghiem, J. Williams, D. Jackson, and A. Oliner, “Leakage of the dominant mode on stripline with a small air gap,” *IEEE Trans. on Microwave Theory and Techniques*, vol. **43**, no. 11, pp. 2549–2556, Nov. 1995.

[25] M. Hotta, Y. Qiana, and T. Itoh, “Efficient FDTD analysis of conductor-backed CPWs with reduced leakage loss,” *IEEE Trans. on Microwave Theory and Techniques*, vol. **47**, no. 8, pp. 1585–1587, Aug. 1999.

[26] H. Shigesawa, M. Tsjui, and A. Oliner, “Conductor-backed slot line and coplanar waveguide: dangers and full-wave analyses,” in *1988 IEEE MTT-S Int. Microwave Symp. Digest*, May 1988, pp. 199–202.

[27] M. Tsuji, H. Shigesawa, and A. Oliner, “Printed-circuit waveguides with anisotropic substrates: a new leakage effect,” in *1989 IEEE MTT-S Int. Microwave Symp. Digest*, Jun. 1989, pp. 783–786.

- [28] N. Dib, M. Gupta, G. Ponchak, and L. Katehi, “Effects of ground equalization on the electrical performance of asymmetric CPW shunt stubs,” in *1993 IEEE MTT-S Int. Microwave Symp. Digest*, Jun. 1993, pp. 701–704.
- [29] M. Freire, F. Mesa, and M. Horno, “Excitation of complex and backward mode on shielded lossless printed lines,” *IEEE Trans. on Microwave Theory and Techniques*, vol. **47**, no. 7, pp. 1098–1105, Jul. 1999.
- [30] L. Carin, G. Slade, and K. Webb, “Mode coupling and leakage effects in finite-size printed interconnects,” *IEEE Trans. on Microwave Theory and Techniques*, vol. **46**, no. 5, pp. 450–457, May 1998.
- [31] G. Ponchak and L. Katehi, “Measured attenuation of coplanar waveguide on CMOS grade silicon substrates with polyimide interface layer,” *Electronics Letters*, vol. **34**, no. 13, pp. 1327–1329, Jun. 1998.
- [32] R. Simons and G. Ponchak, “Modeling of some coplanar waveguide discontinuities,” *IEEE Trans. on Microwave Theory and Techniques*, vol. **36**, no. 12, pp. 1796–1803, Dec. 1988.
- [33] C.-W. Kuo and T. Itoh, “Characterization of the coplanar waveguide step discontinuity using the transverse resonance method,” in *19th European Microwave Conf.*, Sep. 1989, pp. 662–665.
- [34] Z.-Q. Chen and B.-X. Gao, “Full-wave analysis of step discontinuities of planar transmission lines by the method of lines,” in *2nd Int. Symp. on Recent Advances in Microwave Techniques*, 1989, pp. 24–27.
- [35] C.-W. Kuo, T. Kitazawa, and T. Itoh, “Analysis of shielded coplanar waveguide step discontinuity considering the finite metallization thickness effect,” in *1991 IEEE MTT-S Int. Microwave Symp. Digest*, Jul. 1991, pp. 473–475.
- [36] M. Naghed, M. Rittweger, and I. Wolff, “A new method for the calculation of the equivalent inductances of coplanar waveguide discontinuities,” in *1991 IEEE MTT-S Int. Microwave Symp. Digest*, Jul. 1991, pp. 747–750.
- [37] D. Mirshekar-Syahkal, “Computation of equivalent circuits of CPW discontinuities using quasi-static spectral domain method,” *IEEE Trans. on Microwave Theory and Techniques*, vol. **44**, no. 6, pp. 979–984, Jun. 1996.
- [38] P. Sewell and T. Rozzi, “Characterization of air-bridges in MM-wave coplanar waveguide using the complete mode spectrum of CPW,” *IEEE Trans. on Microwave Theory and Techniques*, vol. **42**, no. 11, pp. 2078–2086, Nov. 1994.
- [39] C.-Y. Lee, Y. Liu, and T. Itoh, “The effects of the coupled slotline mode and air-bridges on CPW and NLC waveguide discontinuities,” *IEEE Trans. on Microwave Theory and Techniques*, vol. **43**, no. 12, pp. 2759–2765, Dec. 1995.

- [40] K. Hettak, N. Dib, and A. Omar, “A new class of miniature radiationless CPW shunt stubs printed on the center conductor,” in *1999 IEEE MTT-S Int. Microwave Symp. Digest*, 1999, pp. 1335–1338.
- [41] G. Ponchak and E. Tentzeris, “Development of finite ground coplanar (FGC) waveguide 90 degree crossover junctions with low coupling,” in *2000 IEEE MTT-S Int. Microwave Symp. Digest*, 2000, pp. 1891–1894.
- [42] K. Strohm, P. Nuechter, C. Rheinfelder, and R. Guehl, “Via hole technology for microstrip transmission lines and passive elements on high resistivity silicon,” in *1999 IEEE MTT-S Int. Microwave Symp. Digest*, 1999, pp. 581–584.
- [43] J. Malherbe, *Microwave Transmission Line Filters*. Artech House, 1979.
- [44] A. Omar and Y. Chow, “Coplanar waveguide with top and bottom shields in place of air-bridges,” *IEEE Trans. on Microwave Theory and Techniques*, vol. **41**, no. 9, pp. 1559–1563, Sep. 1993.
- [45] F. Mernyei, I. Aoki, and H. Matsuura, “MMIC bandpass filter using parallel-coupled CPW lines,” *Electronics Letters*, vol. **30**, no. 22, pp. 1862–1863, Oct. 1994.
- [46] G. Ghionc and M. Goano, “A closed-form CAD-oriented model for the high-frequency conductor attenuation of symmetrical coupled coplanar waveguides,” *IEEE Trans. on Microwave Theory and Techniques*, vol. **45**, no. 7, pp. 1065–1070, Jul. 1997.
- [47] C.-H. Ho, L. Fan, and K. Chang, “Broad-band uniplanar hybrid-ring and branch-line couplers,” *IEEE Trans. on Microwave Theory and Techniques*, vol. **41**, no. 12, pp. 2116–2125, Dec. 1993.
- [48] L. Fan, C.-H. Ho, S. Kanamaluru, and K. Chang, “Wide-band reduced-size uniplanar magic-T, hybrid-ring, and de Ronde's CPW-slot couplers,” *IEEE Trans. on Microwave Theory and Techniques*, vol. **43**, no. 12, pp. 2749–2758, Dec. 1995.
- [49] C.-H. Ho, L. Fan, and K. Chang, “New uniplanar coplanar waveguide hybrid-ring couplers and magic-T's,” *IEEE Trans. on Microwave Theory and Techniques*, vol. **42**, no. 12, pp. 2440–2448, Dec. 1994.
- [50] H. Gu and K. Wu, “Broadband design consideration of uniplanar double-Y baluns for hybrid and monolithic integrated circuits,” in *1999 IEEE MTT-S Int. Microwave Symp. Digest*, 1999, pp. 863–866.
- [51] L. Fan and K. Chang, “Uniplanar power dividers using coupled CPW and asymmetrical CPS for MICs and MMICs,” *IEEE Trans. on Microwave Theory and Techniques*, vol. **44**, no. 12, pp. 2411–2420, Dec. 1996.
- [52] G.-A. Lee and H.-Y. Lee, “Suppression of the CPW leakage in common millimeter-wave flip-chip structures,” *IEEE Microwave and Guided Wave Letters*, vol. **8**, no. 11, pp. 366–368,

Nov. 1998.

- [53] W. Heinrich, A. Jentzsch, and G. Baumann, “Millimeter-wave characteristics of flip-chip interconnects for multichip modules,” *IEEE Trans. on Microwave Theory and Techniques*, vol. **46**, no. 12, pp. 2264–2268, Dec. 1998.
- [54] T. Hirose, K. Makiyama, K. Ono, T. Shimura, S. Aoki, Y. Ohashi, S. Yokokawa, and Y. Watanabe, “A flip-chip MMIC design with coplanar waveguide transmission line in the W-band,” *IEEE Trans. on Microwave Theory and Techniques*, vol. **46**, no. 12, pp. 2276–2282, Dec. 1998.
- [55] A. Jentzsch and W. Heinrich, “Optimization of flip-chip interconnects for millimeter-wave frequencies,” in *1999 IEEE MTT-S Int. Microwave Symp. Digest*, Jun. 1999, pp. 637–640.
- [56] Z. Feng, W. Zhang, B. Su, K. Gupta, and Y. Lee, “RF and mechanical characterization of flip-chip interconnects in CPW circuits with underfill,” *IEEE Trans. on Microwave Theory and Techniques*, vol. **46**, no. 12, pp. 2269–2275, Dec. 1998.
- [57] K. Goverdhanam, R. Simons, and L. Katehi, “Novel three-dimensional vertical interconnect technology for microwave and RF applications,” in *1999 IEEE MTT-S Int. Microwave Symp. Digest*, Jun. 1999, pp. 641–644.
- [58] T. vonKerssenbrock and P. Heide, “Novel 77 GHz flip-chip sensor modules for automotive radar applications,” in *1999 IEEE MTT-S Int. Microwave Symp. Digest*, 1999, pp. 289–292.
- [59] D. Budimir, Q. Wang, A. Rezazadeh, and I. Robertson, “V-shaped CPW transmission lines for multilayer MMICs,” *Electronics Letters*, vol. **31**, no. 22, pp. 1928–1930, 1995.
- [60] K. Herrick, R. Henderson, and L. Katehi, “Wave effects in si-micromachined multilayer guiding structures operating at W-band,” in *1999 IEEE MTT-S Int. Microwave Symp. Digest*, 1999, pp. 61–64.
- [61] K. Herrick, T. Schwarz, and L. Katehi, “Si-micromachined coplanar waveguides for use in high-frequency circuits,” *IEEE Trans. on Microwave Theory and Techniques*, vol. **46**, no. 6, pp. 762–768, Jun. 1998.
- [62] S. Iordanescu, G. Bartolucci, S. Simion, and M. Dragoman, “Coplanar waveguide stub/filters on thin membranes and standard substrates,” in *Proc. 1997 Int. Semiconductor Conf.*, Oct. 1997, pp. 357–360.
- [63] W. Liu, D. Steenson, and M. Steer, “Membrane-supported copper E-plane circuits,” in *2001 IEEE MTT-S Int. Microwave Symp. Dig.*, 2001, pp. 539–542.
- [64] W. Liu, D. Steenson, and M. Steer, “Technique of microfabrication suitable for machining submillimeter-wave components,” *Proc. SPIE*, vol. **4088**, p. 144, 2000.

- [65] W. Liu, D. Steenson, and M. Steer, “Organic micromachining techniques for mass production of millimeter-wave and submillimeter-wave planar circuits,” *Journal of Microlithography, Microfabrication, and Microsystems*, vol. 1, p. 150, 2002.
- [66] Z. Bu, V. Fusco, J. Stewart, Y. Wu, H. Gamble, B. Armstrong, and N. Buchanan, “Characteristics of trenched coplanar waveguide for SiMMIC applications,” in *1997 IEEE MTT-S Int. Microwave Symp. Digest*, Jun. 1997, pp. 735–738.
- [67] R. Crampagne and G. Khoo, “Synthesis of certain transmission lines employed in microwave integrated circuits,” *IEEE Trans. on Microwave Theory and Techniques*, vol. 25, no. 5, pp. 440–442, May 1977.
- [68] M. Tsuji and H. Shigesawa, “Mode-coupling effect between different two types of the surface-wave leaky mode on conductor-backed coplanar strips (CBCPS),” in *2000 IEEE MTT-S Int. Microwave Symp. Digest*, Jun. 2000, pp. 1675–1678.

# Chapter 15

## Slotline

### 15.1 Introduction

Slotline, which may be used by itself or in association with microstrip, consists of a narrow slot or gap in a thin conductive layer on one side of a dielectric substrate of fairly high permittivity. The nature of the slot mode offers some interesting possibilities for the realization of filters, ferrite devices, and other components, as well as more sophisticated circuits. In this chapter we explore the fundamentals of slotline and present applications in the next chapter. Microstrip-to-slotline transitions are considered in [Chapter 17](#).

The slotline structure, [Figure 15.1](#), was first proposed by Seymour Cohn in 1969 [1]. Cohn pointed out that the guide mode in this case has a region of elliptical polarization that makes it particularly suitable for applications where the substrate is ferrite [1]. Circulators and isolators have therefore been realized using slotline. Slotline is also particularly well suited to realizing broadband antennas as the slot can be gradually opened out so that a traveling wave is gracefully launched into free space [2–9]. Higher-order moding also occurs with slotline and the behavior of the first higher-order mode has been investigated [10]. Because of this higher-order moding, care is taken to operate in the dominant mode by ensuring that the height  $d$  is much larger than  $w$  (so that field lines through to the back of the substrate are negligible) and that  $s$  is much less than a wavelength.

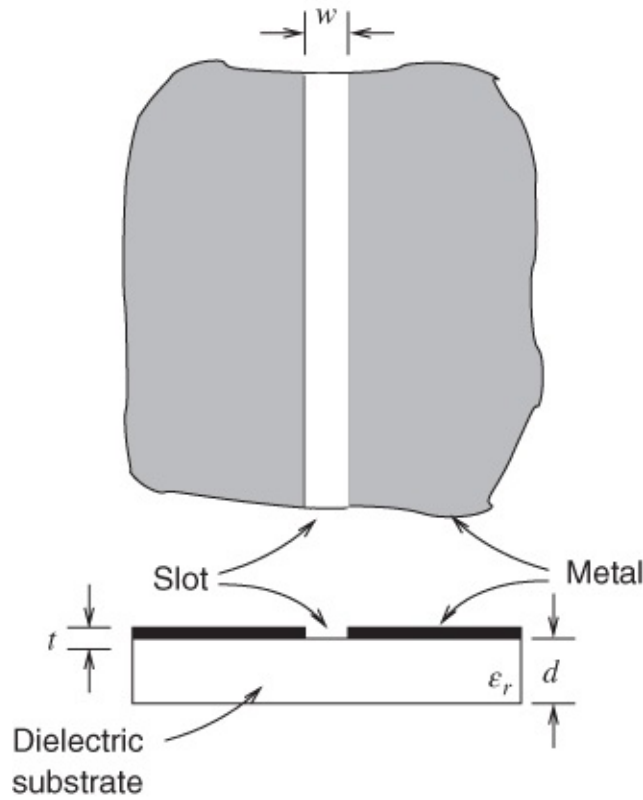


**Figure 15.1** Slotline. Adapted from Cohn (1969) [1], figure 1, p. 1149. Reprinted with permission of IEEE.

Over the years other structures such as finline have been used in what could otherwise have been possible slotline applications, for example [11, 12]. Finline was introduced in [Chapter 5](#). It is like slotline but enclosed in rectangular waveguide and today is largely confined to applications above 100 GHz. In finline waveguide is used to confine the fields, but at lower frequencies coplanar structures on their own are sufficiently effective for confining the fields locally. This latter situation (confinement of the fields) results in two main attributes: the variation of interconnect characteristics with frequency is small and unwanted coupling of the signal on one coplanar structure with another is minimal.

Slotline is a special case of CPS structures that have only two conductors separated by a narrow longitudinal slot and grounded at their extremes (away from the slot and theoretically extended to infinity). Both slotline and general CPS lines suffer from relatively high radiation losses when realized on low permittivity substrates, which leads to low- $Q$  circuits. The radiation also results in substantial interaction and crosstalk between adjacent circuits, although this is lower than with microstrip.

## 15.2 Basic Concept and Structure

In its basic form the slotline transmission line comprises a narrow slot of width  $w$  in the metallic surface coating a dielectric substrate with thickness  $d$  and relative permittivity  $\epsilon_r$ , see [Figure 15.1](#). The RF signal is injected across the opposing sides of the slot and the resulting electric ( $E$ ) and magnetic ( $H$ ) fields are shown in [Figure 15.2\(a\)](#). A 3D representation is

shown in [Figure 15.3](#). It is seen that the magnetic ( $H$ ) field loops are reminiscent of those applying to microstrip.

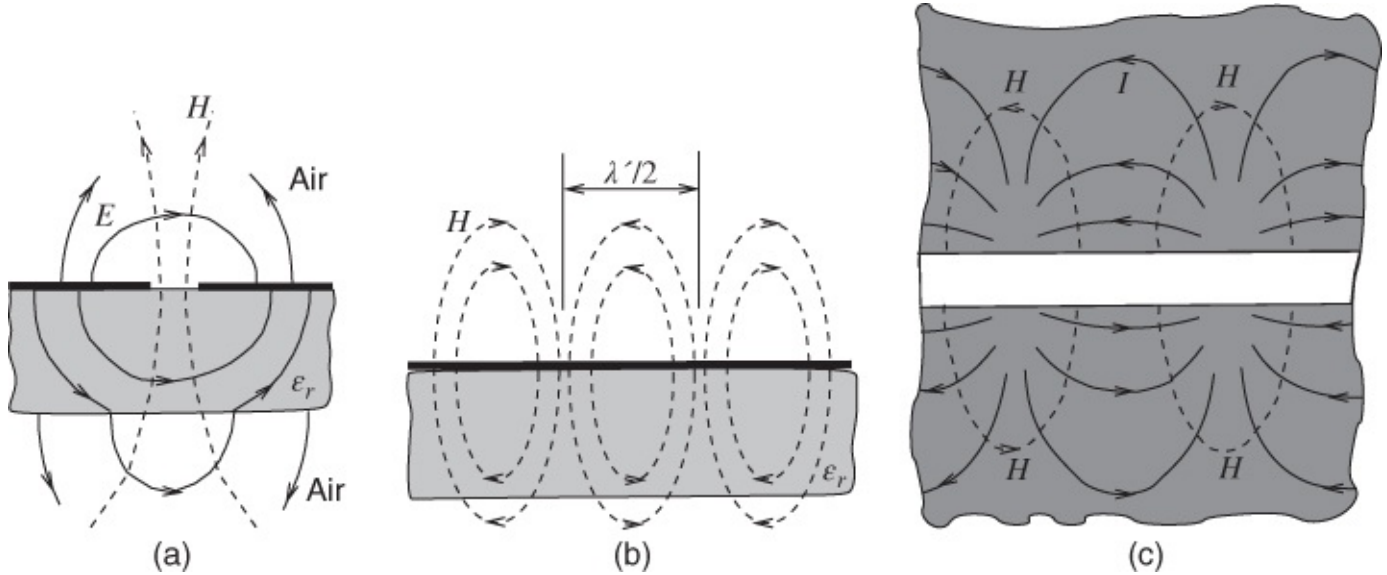


[Figure 15.2](#) Slotline field distribution: (a) slotline transverse  $E$  and  $H$  fields; (b) longitudinal cross-section showing the  $H$ -field pattern; and (c) top elevation view showing the current,  $I$ , and the  $H$ -field pattern. Adapted from Cohn (1969) [1], figure 2, p. 769. Reprinted with permission of IEEE.

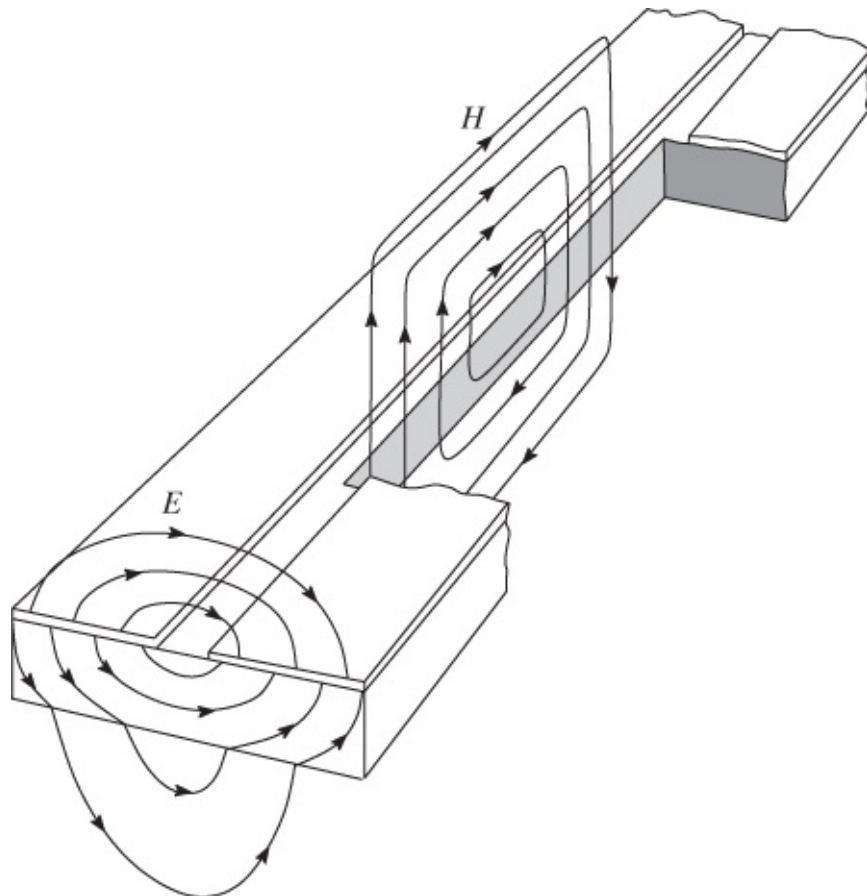


[Figure 15.3](#) 3D representation of slotline. Adapted from Robinson and Allen (1969) [13], figure 1, p. 1097. Reprinted with permission of IEEE.

As with microstrip and CPW, these fields clearly inhabit both the substrate itself ( $\epsilon_r$ ) and the surrounding air ( $\epsilon_r = 1$ ). This means the propagation is quasi-TEM and hence behavioral and design parameters are complicated. The basic situation is akin to the design considerations applying to microstrip and CPW. It is necessary to determine the limits of design parameters.

## 15.3 Operating Principles and Modes

The longitudinal pattern of the  $H$  fields comprises loops, as shown in [Figure 15.2\(b\)](#) and (c). From [Figure 15.2\(b\)](#) it can be clearly seen that the distance across  $H$  loops is  $\lambda/2$ , where  $\lambda$  is the guide wavelength for the dominant mode in slotline. Other (unwanted) modes are capable of becoming automatically generated as a result of this structure and these need to be suppressed as far as possible. Current loops ( $I$ ) in the metal are shown in [Figure 15.2\(c\)](#) as well as magnetic field loops.

Citerne, Toutain, and Raczy [14] investigated the higher-order modes in slotline and published a set of five field diagrams, see [Figure 15.4](#).

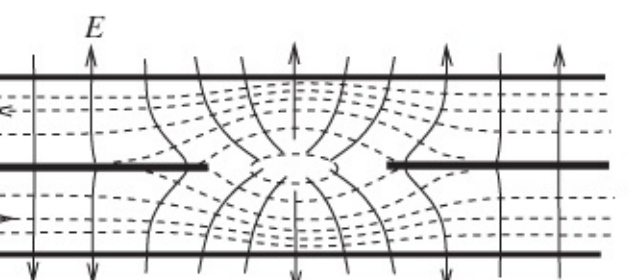
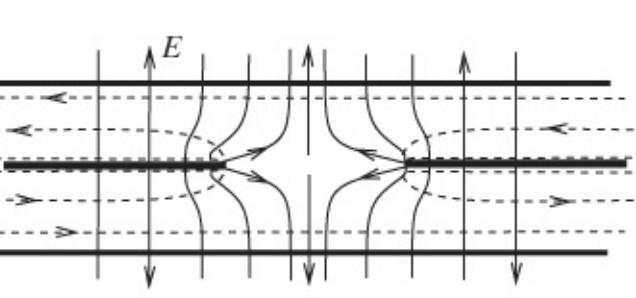
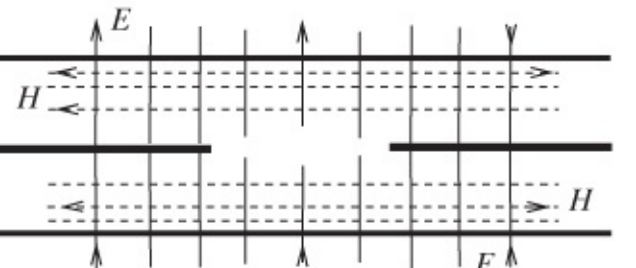
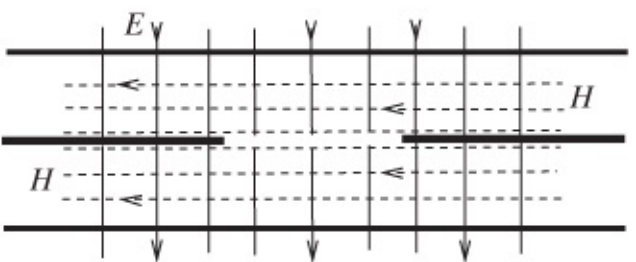
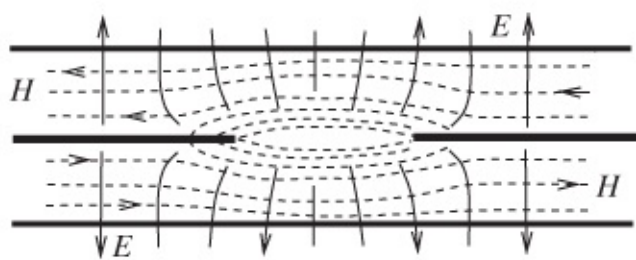
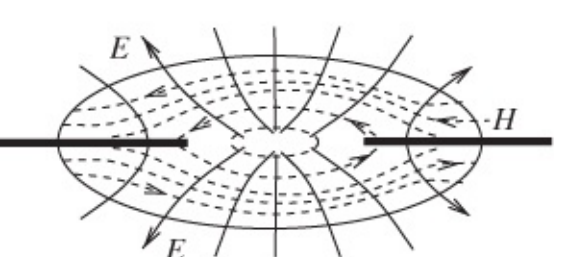
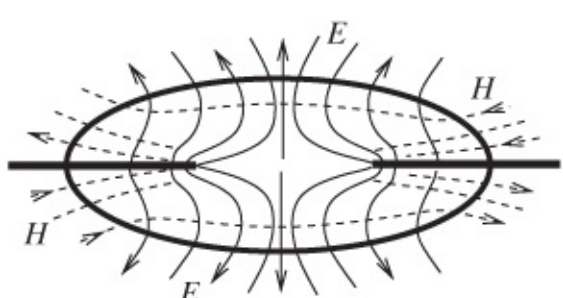
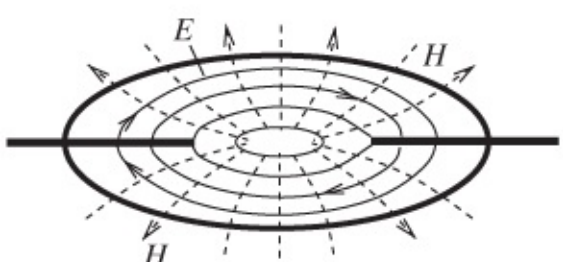
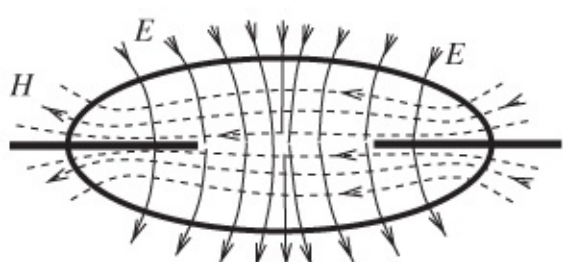
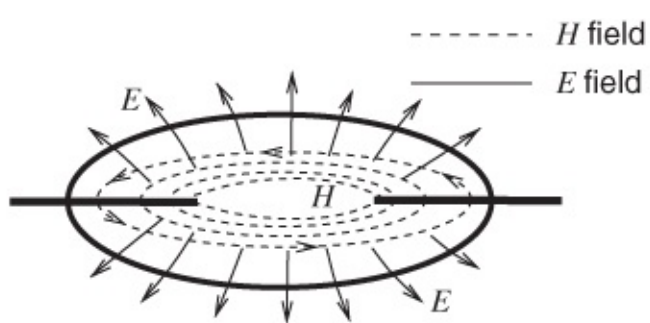


**Figure 15.4** Electric and magnetic field distributions for higher-order modes in slotline: (a) dominant slotline mode, the  $e_{01}$  mode; (b) the  $e_{11}$  mode; (c) the  $e_{01}$  mode; (d) the  $o_{11}$  mode; and (e) the  $o_{02}$  mode. The  $e$  indicates an even mode while an  $o$  indicates an odd mode. Adapted from Citerne *et al.* (1975) [14], figure 1, p. 1097. Reprinted with permission of the European Microwave Association.

## 15.4 Propagation and Dispersion Characteristics

In common with all non-TEM transmission mediums (cf. microstrip and CPW, both covered elsewhere in this book), slotline exhibits highly frequency-dependent propagation behavior. Although the precise manifestation differs from other mediums, it remains a fact that when the frequency of a signal exciting a slotline is (say) doubled, the phase coefficient or wave number is not exactly doubled. Several transmission line structures exhibit this type of behavior, which is called dispersion. Thus all slotlines are dispersive and it follows that the exact relationship between wavelength and frequency is very complicated. The measured phase coefficient ( $\beta$ ) versus frequency for a range of different slotline configurations is shown in [Figure 15.5](#) [13]. In the figure the characteristics are compared to a  $50 \Omega$  microstrip line and to a line with ideal TEM characteristic. In every case the transmission coefficient is substantially smaller than for the pure TEM line. Values were measured for a total of four different slotlines having different substrate depths  $d$ . Detailed time and space-variant electromagnetic field analyses have been performed requiring numerical methods and substantial computer programs to solve them. Fortunately, as we shall see, useful and accurate (typically within 1%) design calculations may be carried out with suitable closed formulas. These formulas also provide intuitive understanding of behavior as required in design.

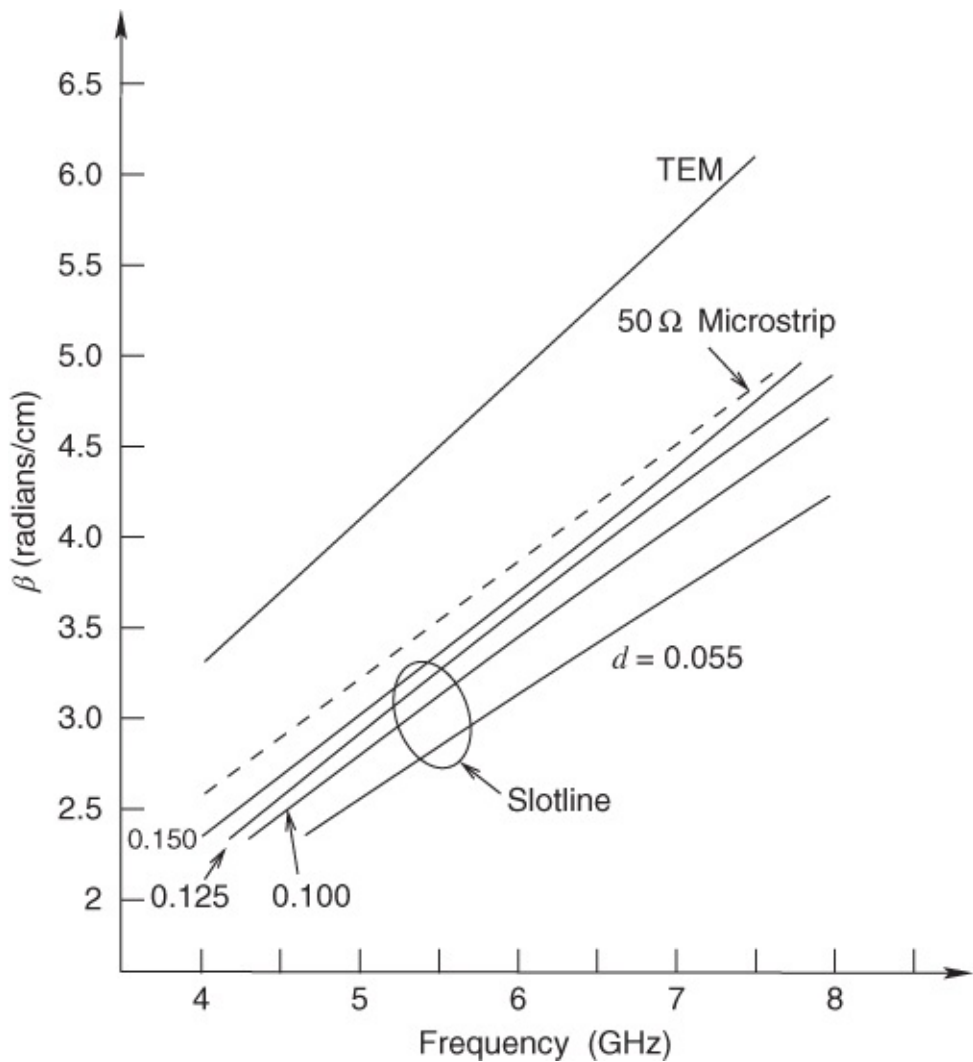


**Figure 15.5** Measured phase coefficient ( $\beta$ ) versus frequency for slotline and microstrip. Adapted from Robinson and Allen (1969) [13], figure 3, p. 1098. Reprinted with permission of IEEE.

Knorr and Kuchler [15] investigated the dispersion characteristics of slotline and presented results for a slotline manufactured on a substrate of relative permittivity 16 and having an aspect ratio of 1.0. The dispersion data are shown in [Figure 15.6](#). Knorr and Kuchler noted that the basis set leading to curves (B) is superior to that given by (A) and that the first- and second-order solutions based on (B) agree very well with Cohn's results. The first- and second-order solutions based on (A) give less accurate results with the second-order approximation being the poorer of the two due to the physically impossible discontinuities that were imposed.

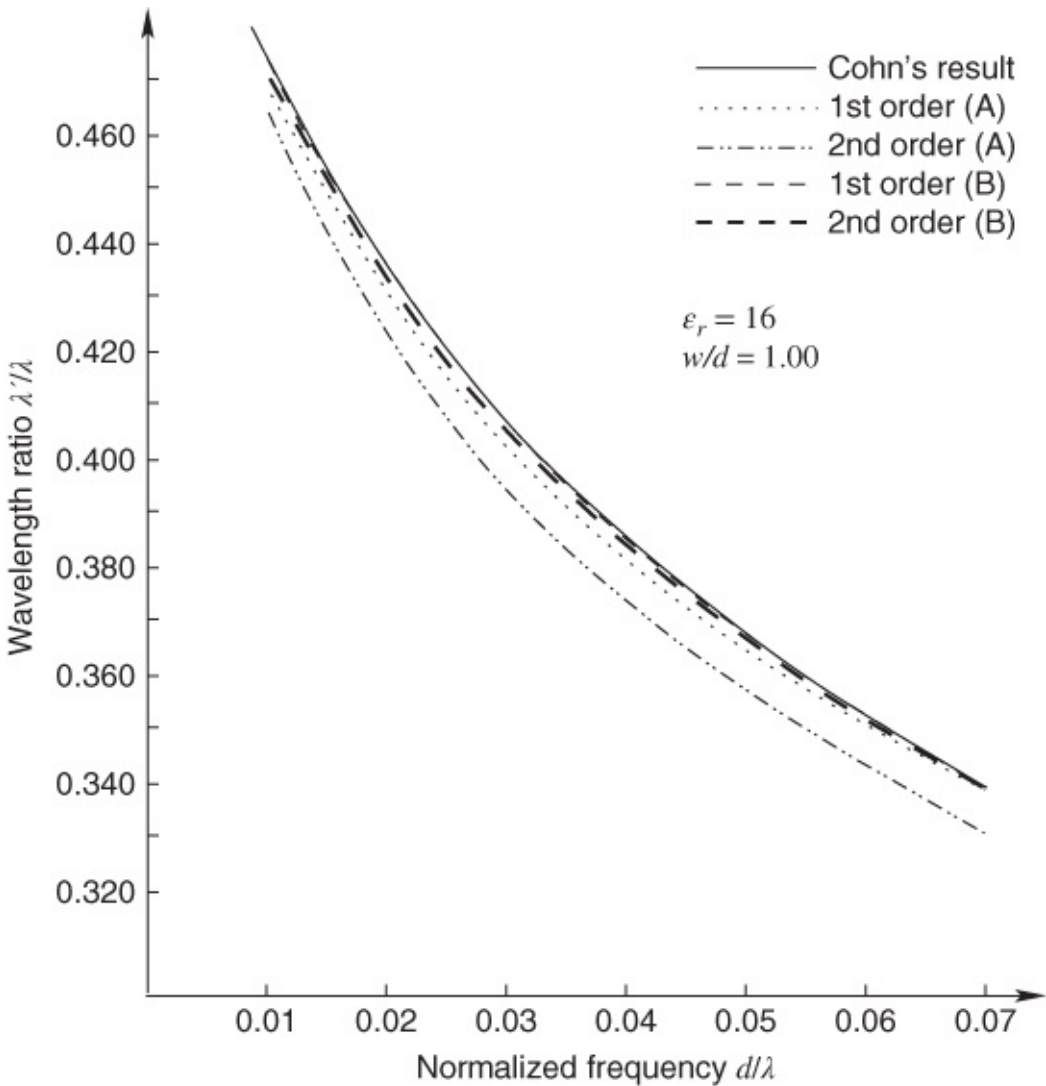


**Figure 15.6** Slotline dispersion characteristics. (Here  $\lambda = \lambda_0$  is the free space wavelength). Adapted from Knorr and Kuchler (1975) [15], figure 2, p. 543. Reprinted with permission of IEEE.

In [Figure 15.6](#) both variables are normalized to the free-space wavelength  $\lambda_0$ . The normalized frequency can be converted to frequency  $F$  in GHz by noting that

$$F = 300/\lambda \quad 15.1$$

where  $\lambda$  is directly substituted in millimeters, for instance where  $\lambda = 10$  mm the frequency is 30 GHz. If, for example, the thickness of the substrate is 0.5 mm then  $d/\lambda$  is  $0.5/10 = 0.05$ . Using the tightly bunched curves of [Figure 15.6](#) this yields a wavelength ratio  $\lambda'/\lambda_0$  of 0.37, and with  $\lambda_0 = 10$  mm this means that  $\lambda' = 10 \times 0.37 = 3.7$  mm. This is the slotline dominant-mode wavelength at a frequency of 30 GHz for this structure.

Svacina [16] calculated slotline dispersion behavior and compared the results with those due to Cohn [1]. The graph of [Figure 15.7](#) displays the comparative curves. In both cases, for the different aspect ratios 0.02 and 0.1, there is clearly close agreement between Cohn's and Svacina's analysis.

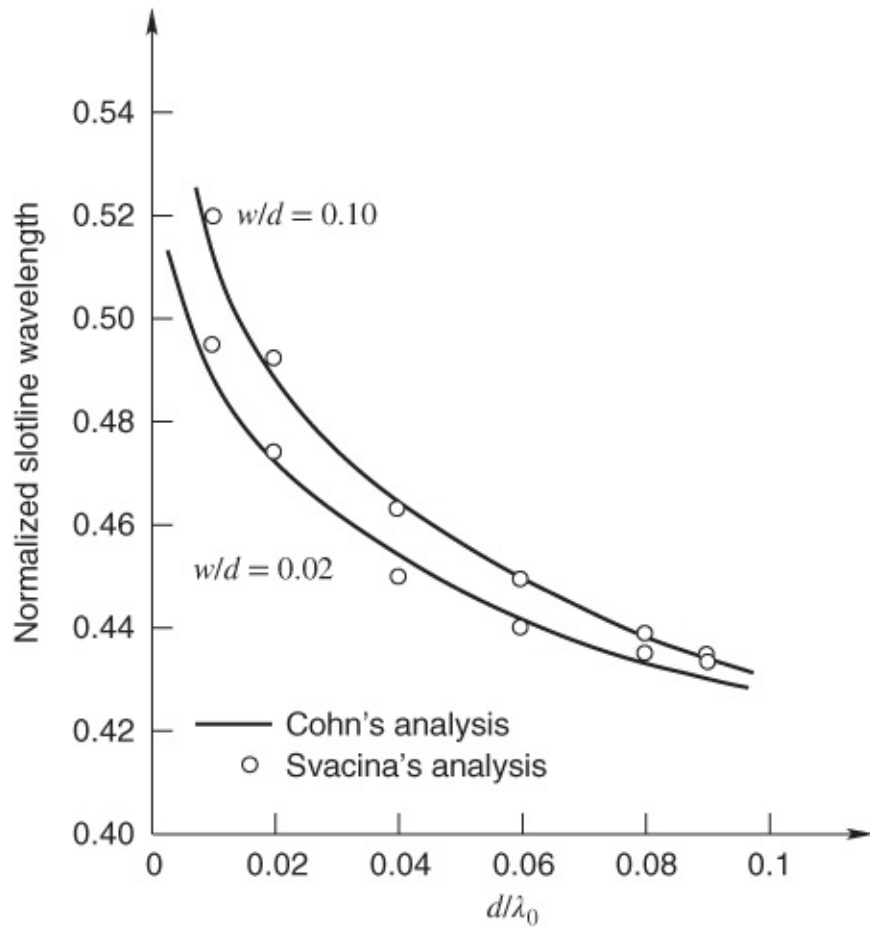


**Figure 15.7** Dispersion characteristics of slotlines computed using Svacina's analysis [16] and Cohn's analysis [1]. Substrate permittivity  $\epsilon_r = 9.7$ . Adapted from Svacina (1999) [16], figure 3, p. 1828. Reprinted with permission of IEEE.

Kitazawa [17] explored the dispersion characteristics applying to the dominant and the first higher-order mode in slotline. His main results are summarized in [Figure 15.8](#). For this structure the following observations apply:

1. The dominant mode always has the largest normalized phase coefficient.
2. The phase coefficients for the dominant mode and the first higher-order mode converge as frequency increases.
3. The phase coefficient for the first higher-order mode is relatively small for frequencies below approximately 18 GHz.

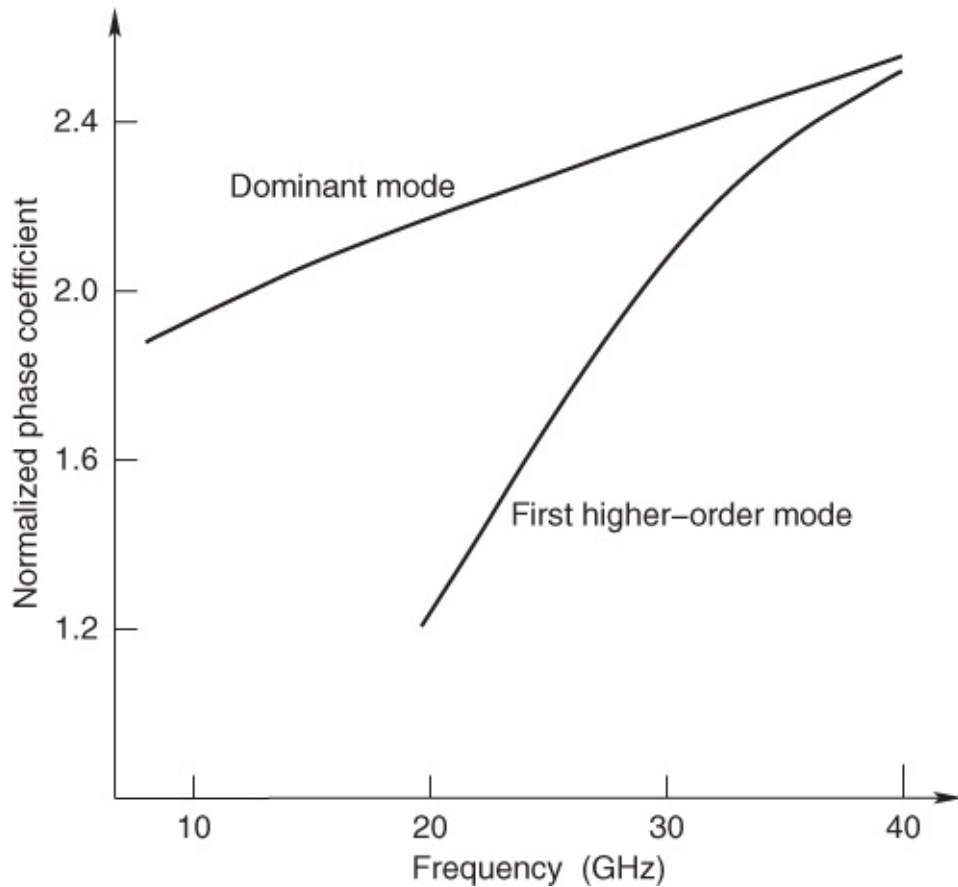


**Figure 15.8** Normalized phase coefficient for the dominant and first higher-order mode in slotline:  $\epsilon_r = 9.6$ ,  $d = 1$  mm,  $w = 1$  mm,  $t = 0$ . Adapted from Kitazawa *et al.* (1980) [17], figure 3, p. 391. Reprinted with permission of IEEE.

Kitazawa [17] also reported on how the phase coefficients vary with thickness-to-width ratio and these results are shown in Figure 15.9. From these data it is clear that for thickness-width ratios in approximately the 0–0.04 range the reduction in normalized phase coefficient is less than 1%. However, as the thickness-width ratio increases to 0.1 and higher, the reduction becomes much more significant (4% and increasing).

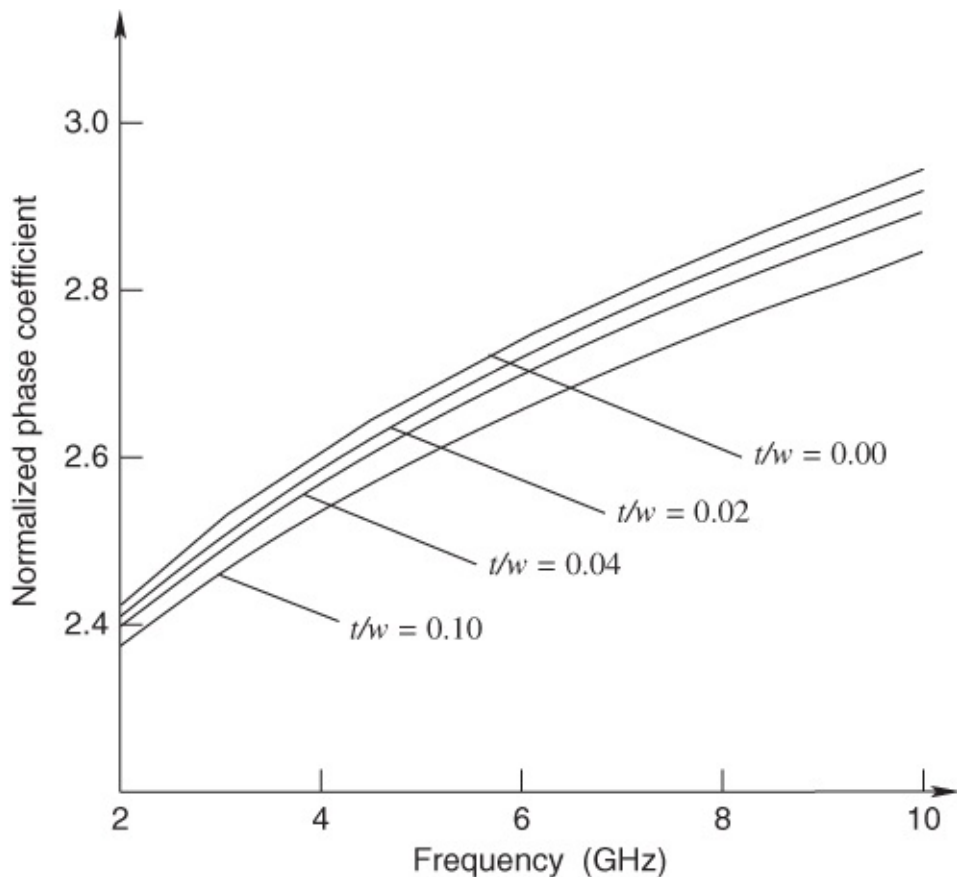


**Figure 15.9** Normalized phase coefficient for slotlines having thickness-width ratios ranging from zero (0.00) to 0.1. Adapted from Kitazawa *et al.* (1980) [17], figure 4, p. 391. Reprinted with permission of IEEE.

The manner in which dispersion in slotline affects the characteristic impedance has been investigated by Knorr *et al.* [15]. Knorr's results (compared with Cohn's results) are shown in [Figure 15.10](#) for aspect ratios of 1 and 2. The data in [Figure 15.10](#) clearly indicate the following:

- For a slotline with an aspect ratio of 2.0 (a high-impedance line) there is a substantial dispersion effect on the characteristic impedance. Starting at  $150\Omega$  at low frequencies the impedance increases to about  $200\Omega$  at moderate frequencies before eventually decreasing somewhat at higher frequencies.
- For a slotline with an aspect ratio of 1.0 (a moderate-impedance line) there is much less dispersion with the impedance remaining in the  $55\text{--}60\Omega$  range over the entire frequency spectrum.
- There is a very close match between Knorr's results and Cohn's data over the entire frequency spectrum.

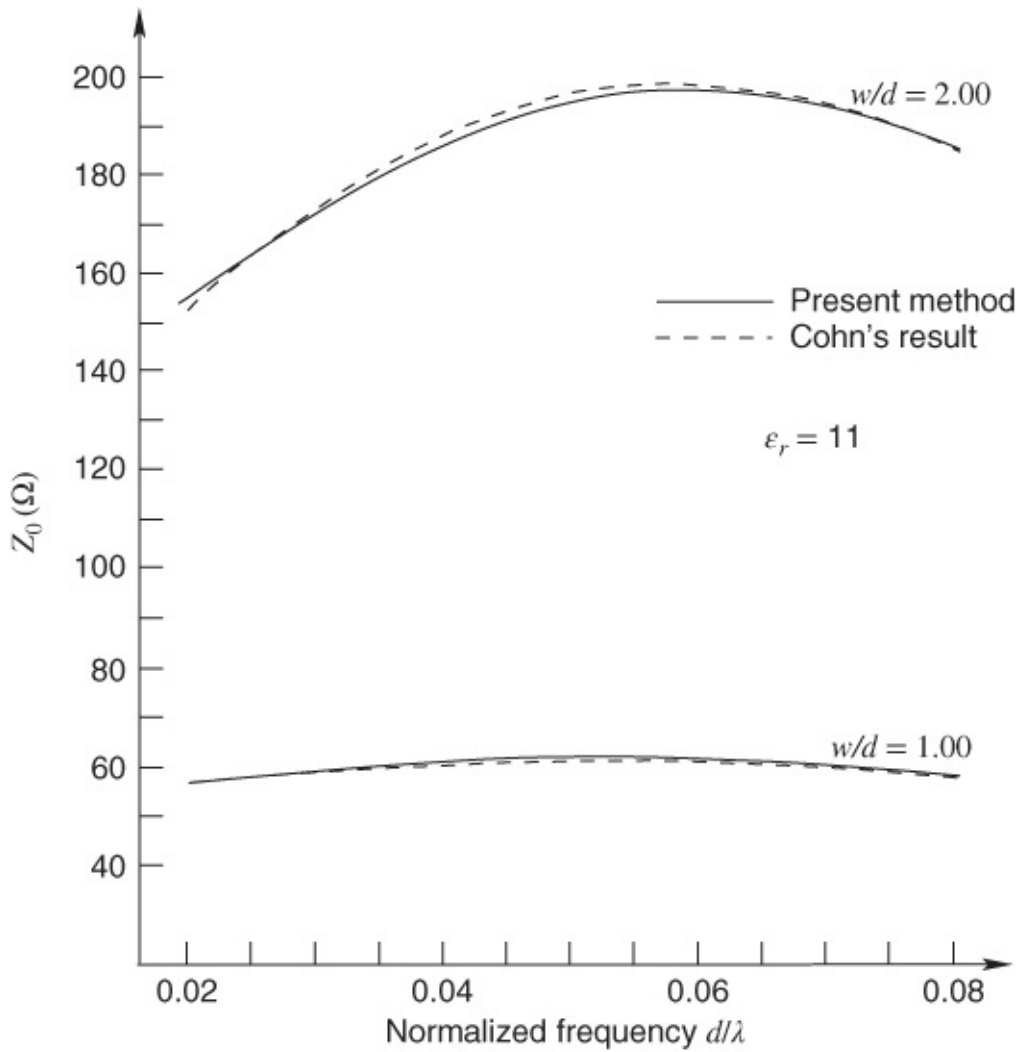


**Figure 15.10** Characteristic impedance of a slotline. Adapted from Knorr and Kuchler (1975) [15], figure 3, p. 544. Reprinted with permission of IEEE.

Kitazawa [17] has also investigated the effects of dispersion on the characteristic impedance of slotline. Kitazawa's main results are presented in [Figure 15.11](#). It is clear that Kitazawa's findings are similar to those of Knorr and Cohn.

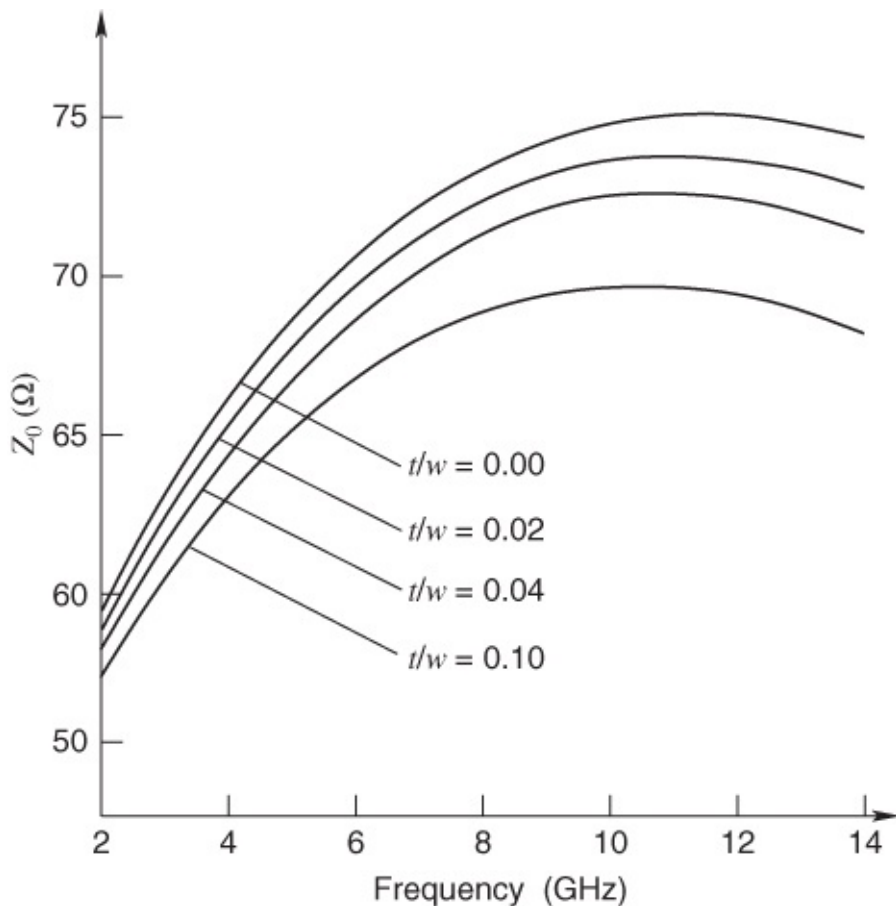


**Figure 15.11** Characteristic impedance for slotlines having thickness-width ratios ranging from zero (0.00) to 0.1. Adapted from Kitazawa *et al.* (1980) [17], figure 5, p. 391. Reprinted with permission of IEEE.

## 15.5 Evaluation of Guide Wavelength and Characteristic Impedance

In common with all transmission mediums the major design aim is to determine the wavelength  $\lambda'$  of the dominant mode. Recall that for microstrip a special parameter termed the “effective microstrip permittivity”  $\epsilon_{\text{eff}}$  is employed and we find that the dominant-mode “guide” wavelength  $\lambda'$  is given by:

$$\lambda' = \frac{\lambda_0}{\sqrt{\epsilon_{\text{eff}}}} \quad 15.2$$

where  $\lambda_0$  is the free-space wavelength, so that with frequency  $f$  substituted directly in GHz units (so that  $F$  is the frequency in gigahertz) the guide wavelength in millimeters is

$$\lambda' = \frac{300}{F \sqrt{\epsilon_{\text{eff}}}}. \quad 15.3$$

In these expressions  $\epsilon_{\text{eff}}$  is itself a substantially nonlinear function of frequency which must also

be evaluated. Alternatively, equations for the guide wavelength in slotline are provided.

In 1976 Garg and Gupta [18] published two sets of design equations relating to slotlines. The first equation expresses the substrate thickness normalized to the free-space wavelength, as a function of relative permittivity. This function is shown below:

$$\frac{d}{\lambda_0} = \frac{0.25}{\sqrt{\epsilon_r - 1}}. \quad 15.4$$

The two sets of design equations are conditional according to two ranges of slot width  $w$  divided by substrate thickness  $d$ . The first (narrow  $w$ ) range is:

$$0.02 \leq w/d \leq 0.2$$

and within this range the wavelength ratio is

$$\frac{\lambda'}{\lambda_0} = 0.923 - 0.448 \log \epsilon_r + \frac{0.2w}{d} - \left( \frac{0.29w}{d} + 0.047 \right) \log \left( \frac{100d}{\lambda_0} \right) \quad 15.5$$

and the characteristic impedance is expressed as:

$$Z_0 = 72.62 - 35.19 \log \epsilon_r + 50 \frac{(w/d - 0.02)(w/d - 0.1)}{w/d} \quad 15.6$$

$$+ \log(100w/d)[44.28 - 19.58 \log \epsilon_r] \quad 15.7$$

$$-[0.32 \log \epsilon_r - 0.11 + w/d(1.07 \log \epsilon_r + 1.44)](11.4 - 6.07 \log \epsilon_r - 100d/\lambda_0)^2. \quad 15.8$$

The second (wide  $w$ ) range is:

$$0.2 \leq w/d \leq 1.0 \quad 15.9$$

and within this range the wavelength ratio is

$$\begin{aligned} \frac{\lambda'}{\lambda_0} = & 0.987 - 0.483 \log \epsilon_r + \frac{w}{d}(0.111 - 0.0022\epsilon_r) \\ & - \left( 0.121 + \frac{0.094w}{d} - 0.0032\epsilon_r \right) \log \left( \frac{100d}{\lambda_0} \right) \end{aligned} \quad 15.10$$

and the characteristic impedance is expressed as:

$$Z_0 = 113.19 - 53.55 \log \epsilon_r + 1.25w/d(114.59 - 51.88 \log \epsilon_r) \quad 15.11$$

$$+ 20(w/d - 0.2)(1 - w/d) \quad 15.12$$

$$-[0.15 + 0.23 \log \epsilon_r + w/d(-0.79 + 2.07 \log \epsilon_r)] \quad 15.13$$

$$\times [(10.25 - 5 \log \epsilon_r + w/d(2.1 - 1.42 \log \epsilon_r) - 100d/\lambda_0)^2] \quad 15.14$$

All the above design equations should work satisfactorily for a wide range of substrates and operating frequencies. Note that dispersion, that is, frequency dependence, is incorporated through the use of wavelengths.

Kitazawa *et al.* [17] published theoretical results for dispersion in slotlines where the metal coating is relatively thick.

## 15.6 Losses

Like all types of transmission lines, slotline is subject to inherent power losses: metallic (conductor), dielectric, and radiative. Several groups of researchers investigated slotline losses and in this section we present some important published results.

Robinson *et al.* [13] published results for losses of a  $50 \Omega$  microstrip line and a slotline. The data are shown in [Figure 15.12](#). The losses increase (linearly) with frequency in both cases. However, the microstrip losses exceed those in the slotline until approximately 7 GHz. At frequencies above 7 GHz slotline exhibits slightly higher losses than microstrip. Another research group, Rozzi *et al.* [19], investigated the threshold of the onset of dielectric leakage, and the conductor and dielectric losses in slotlines. Rozzi's results relating to dielectric leakage are shown in [Figure 15.13](#) and for conductor and dielectric losses in [Figure 15.14](#). For example, using the curve of [Figure 15.13](#) applying to the double width of 0.1 mm, where  $d = 0.5$  mm, dielectric leakage will occur when the frequency exceeds approximately 40 GHz.

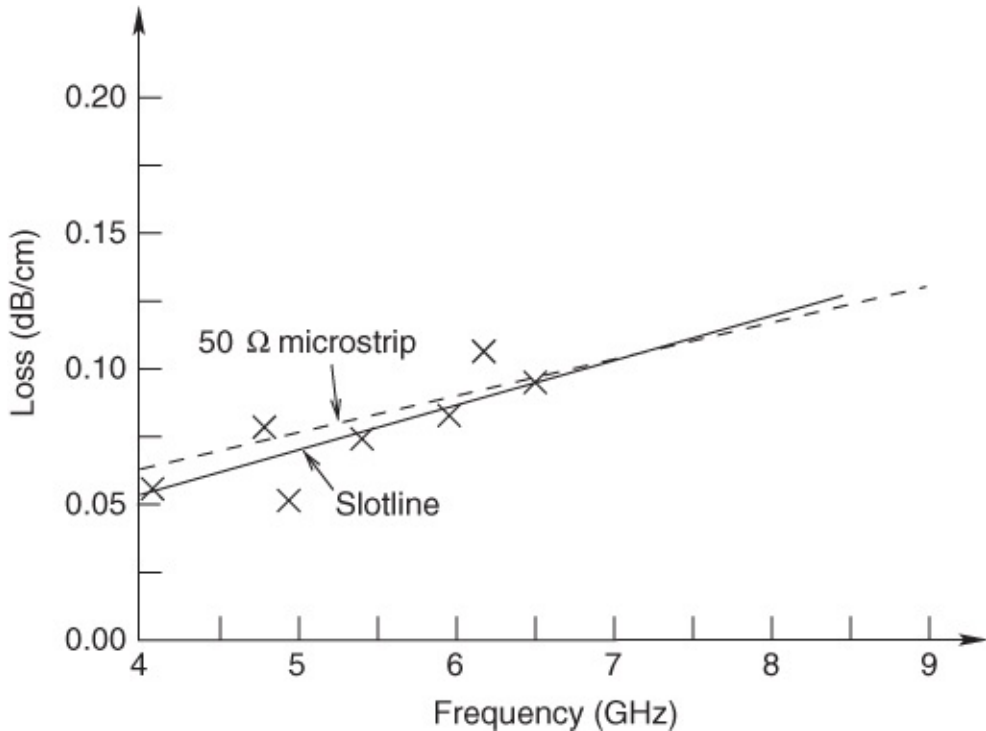


[Figure 15.12](#) Losses in microstrip and slotline ( $50\Omega$ ) compared. The points are measured loss of slotline. Adapted from Robinson and Allen *et al.* (1969) [13], figure 5, p. 1098. Reprinted with permission of IEEE.

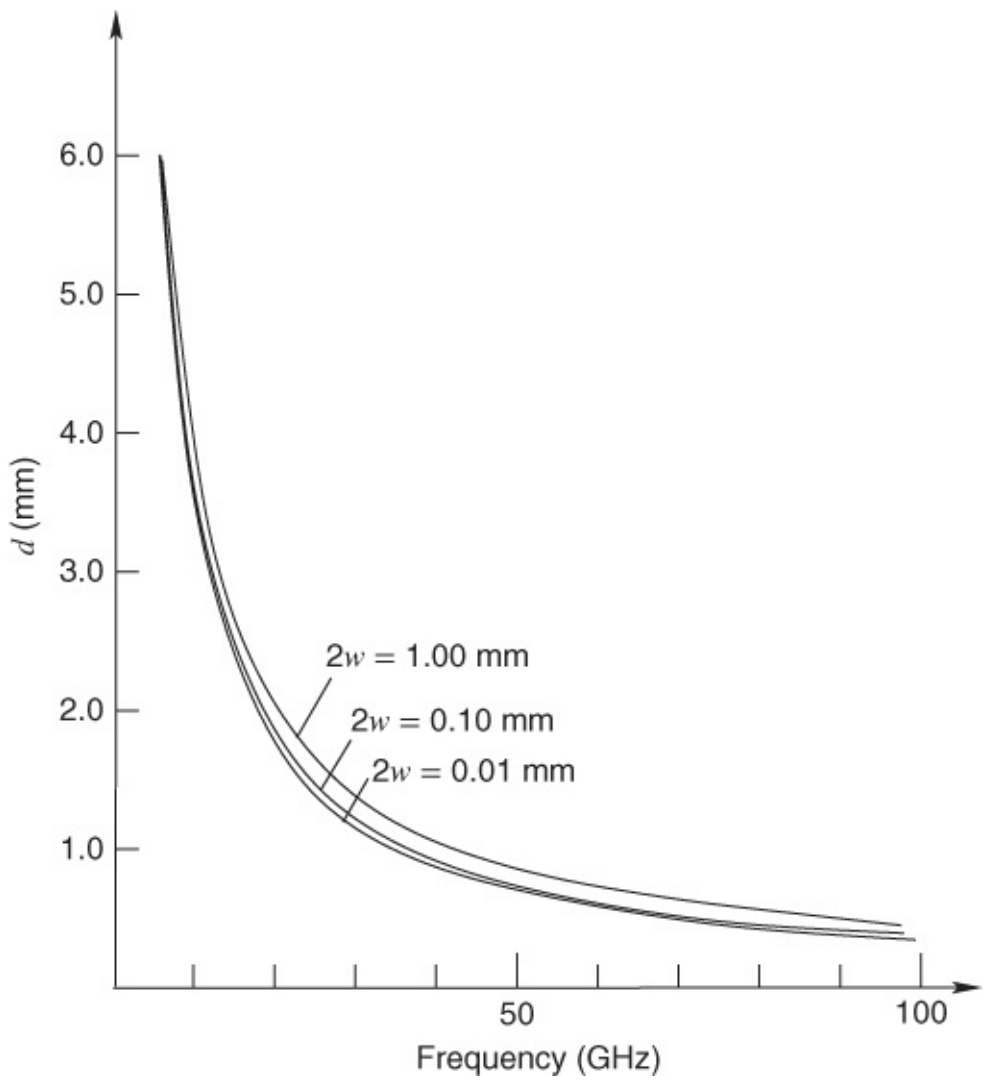


**Figure 15.13** Slotline: threshold for the onset of dielectric leakage. Substrate thickness  $d$  versus frequency with  $\epsilon_r = 9.8$ . Adapted from Rozzi *et al.* (1990) [19], figure 5, p. 1071. Reprinted with permission of IEEE.

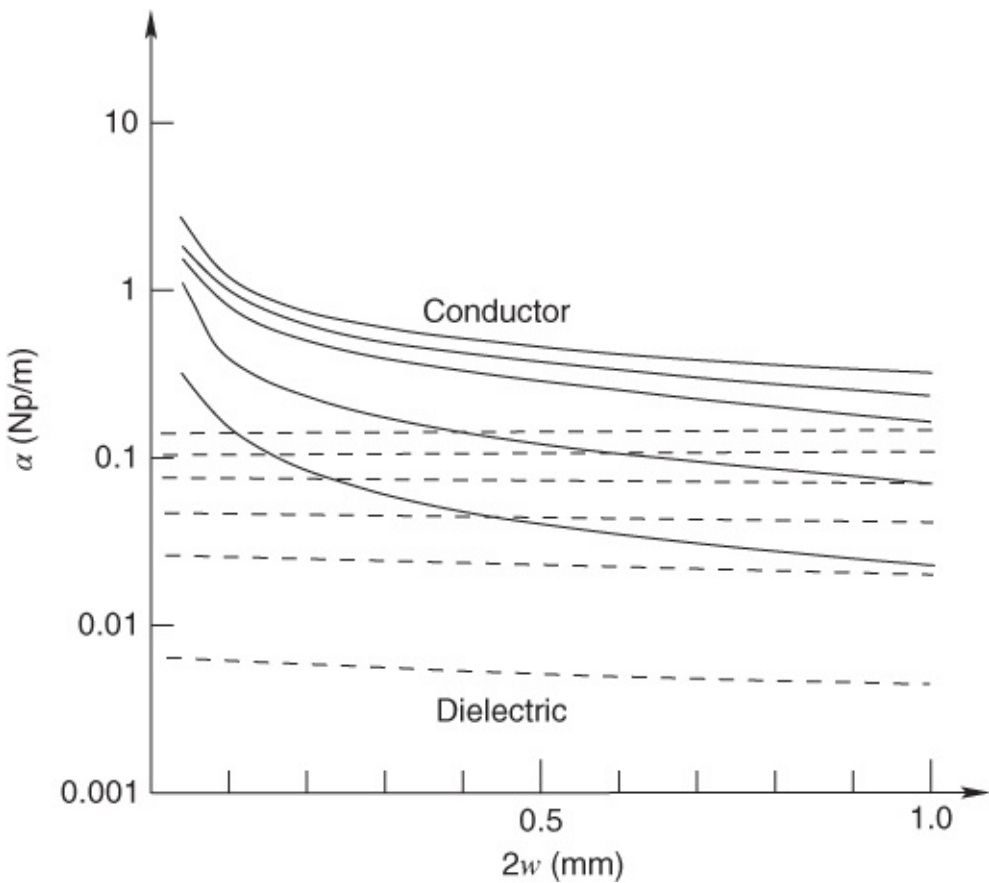


**Figure 15.14** Conductor and dielectric losses in slotline as functions of the double-width  $2w$  for 2, 7, 12, 18, 24, and 30 GHz; losses increase with frequency. Adapted from Rozzi *et al.* (1990) [19], figure 9, p. 1075. Reprinted with permission of IEEE.

The parameter relating to these curves is the frequency, which increases vertically in the graph (the effects as a function of frequency have already been presented). It is a little unfortunate that the loss is given in nepers per meter because in practice almost all engineers use decibels. It is worth noting that 1 Np is 8.686 dB and so the vertical scale in Figure 15.14 can be re-scaled multiplying by 8.7 and then read in dB/m. At high frequencies, with  $2w = 0.5$  mm, the conductor losses approach 9 dB/m whereas the dielectric losses are around 1 dB/m. The overall trends indicate that the conductor losses are relatively high for narrow slotlines (increasing rapidly as the line becomes narrower) but the dielectric losses vary much less as a function of  $2w$ .

Das and Pozar [20] have investigated the phase coefficient as well as both dielectric and ground plane losses in slotline. These workers used perturbation analysis and they also presented measured results. Their published results are shown in Figure 15.15. Measured data confirm that both the dielectric and the ground plane losses decrease steadily as the dielectric loss tangent ( $\tan \delta$ ) decreases. As expected intuitively, the conductor loss decreases as the conductivity ( $\sigma$ ) increases. Das and Pozar also presented the overall loss as a function of slotwidth  $w$ . Their data are shown in Figure 15.16. As the slotline is narrowed so the overall loss increases strongly. Again the loss is given in Np/m.

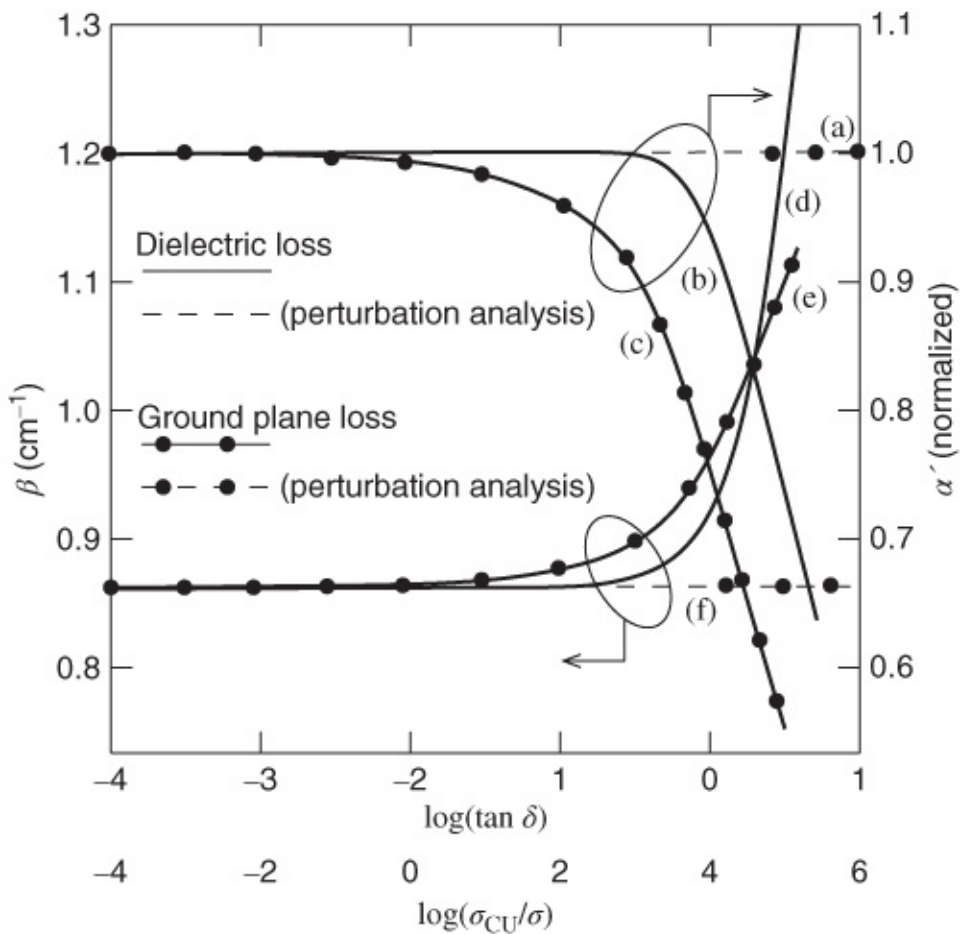


**Figure 15.15** Dielectric and ground plane losses in slotline as a function of dielectric loss tangent (curves (b) and (d)) and as a function of ground plane conductivity normalized to that of copper (curves (c) and (e)). Curves (b)–(e) use the analysis of Das and Pozar. Curves (a) and (f) use a perturbation analysis with low loss substrate and ground plane. The frequency is 3 GHz, the substrate has a thickness of 1.6 mm and permittivity of 2.2, and the line width is 5 mm. Adapted from Das and Pozar (1991) [20], figure 8, p. 60. Reprinted with permission of IEEE.

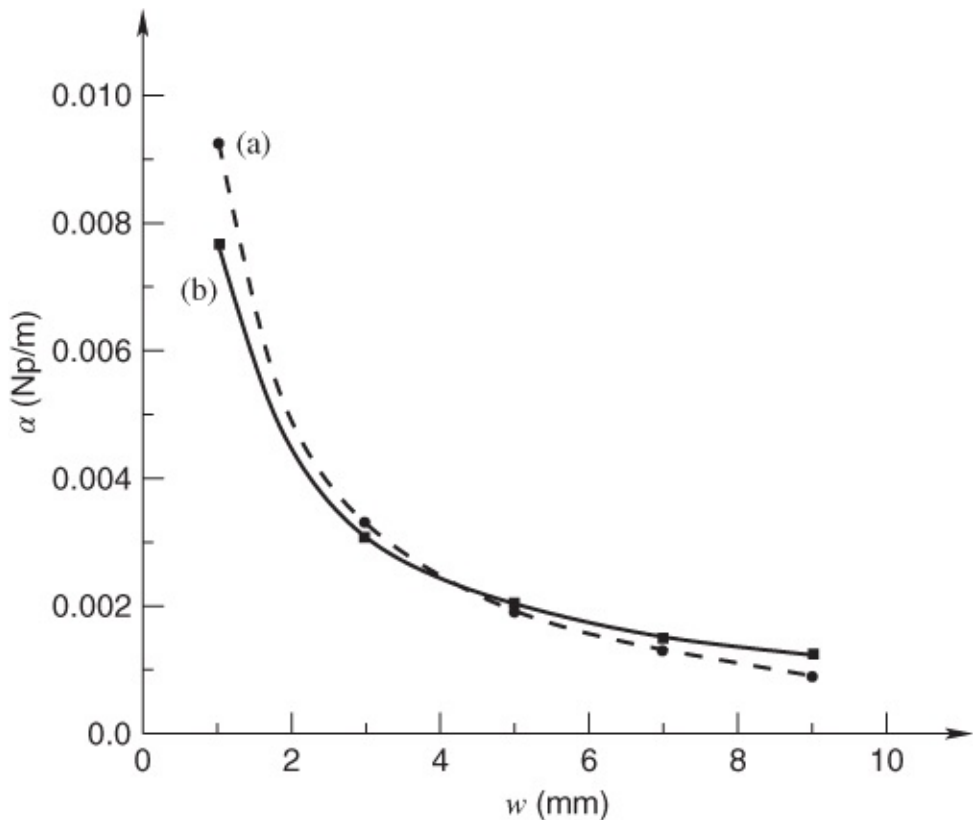


**Figure 15.16** Slotline losses as a function of slot width. Each curve was calculated using a different method with (b) considered to be more accurate. Adapted from Das and Pozar (1991) [20], figure 10, p. 61. Reprinted with permission of IEEE.

## 15.7 End-effects: Open Circuits and Short Circuits

### 15.7.1 Jansen's Results [21]

Open circuits and short circuits amount to abrupt discontinuities in slotline and their behavior is complex at microwave frequencies. Jansen [21] conducted research concerning several types of transmission line discontinuities and [Figure 15.17](#) shows the various structures Jansen investigated. An open-circuited slotline is shown in [Figure 15.17\(e\)](#) and a short-circuited slotline is shown in [Figure 15.17\(f\)](#). The nomenclature is indicated in [Figure 15.17\(k\)](#). Discontinuities in microstrip are dealt with in detail elsewhere in this book but the same concept of equivalent length extension applies to any transmission line, including slotlines.

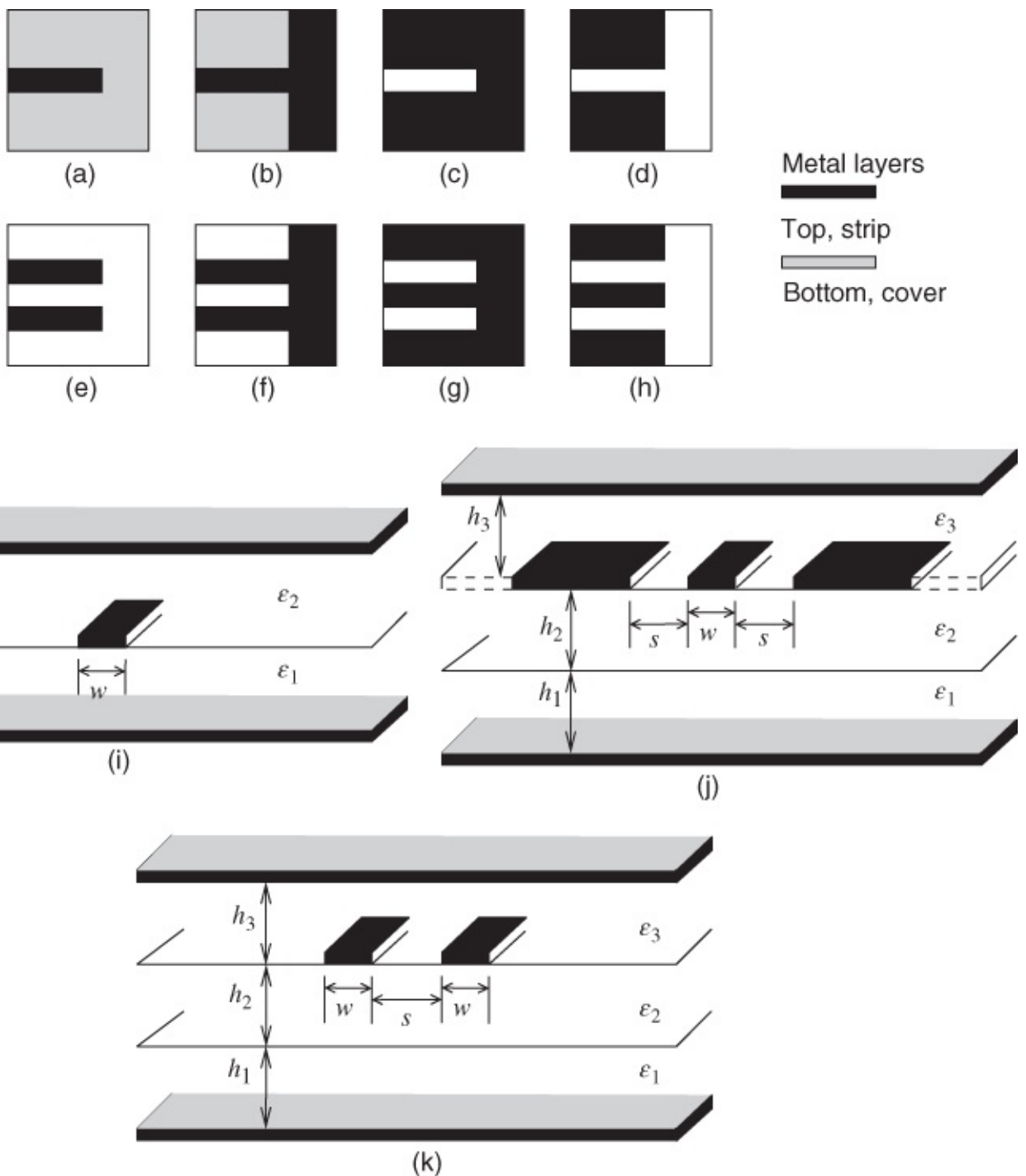


**Figure 15.17** An assortment of planar transmission line structures. Adapted from Jansen *et al.* (1981) [21], figure 1, p. 77. Reprinted with permission of the Institution of Engineering and Technology.

Jansen's results compared with the measured results of Knorr and Saenz for a single short-circuited slotline on an alumina substrate are shown in [Figure 15.18](#). For low-moderate end-effect lengths the agreement is good but for relatively large end-effect lengths a significant departure is evident.

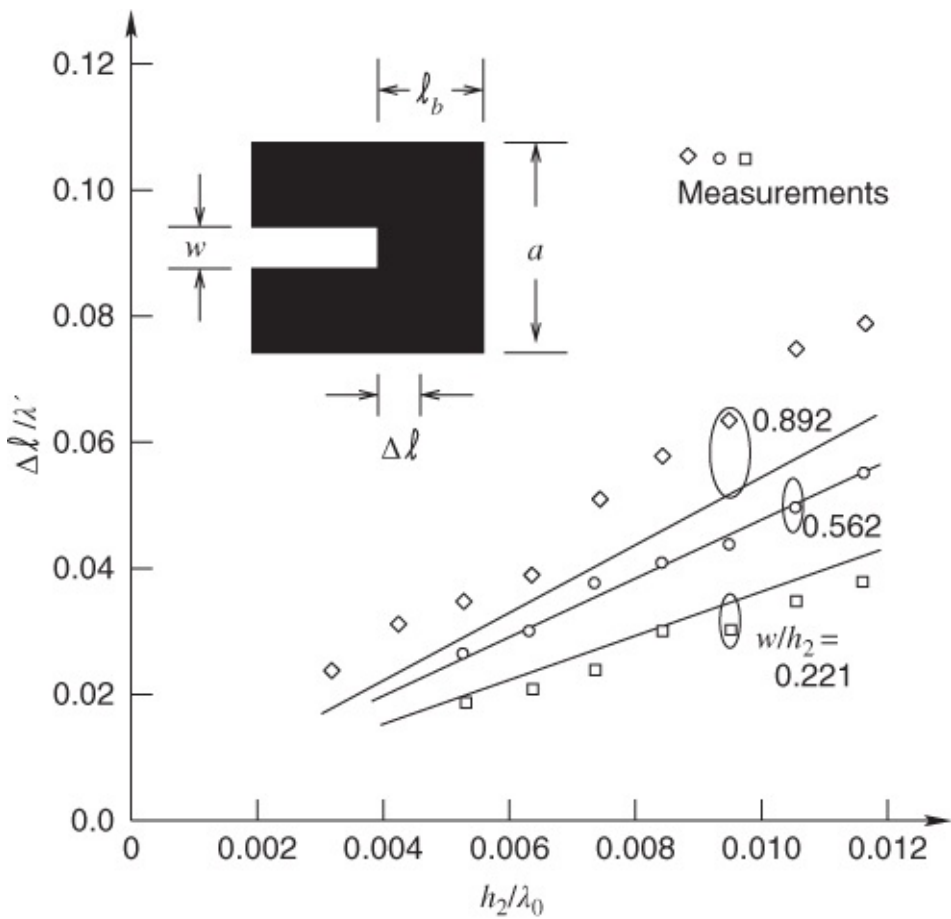


**Figure 15.18** Shorted slot end-effect data in comparison with the measured results of Knorr and Saenz.  $h_2 = 3.07$  mm,  $\epsilon_2 = \epsilon_r \epsilon_0$ ,  $\epsilon_r = 12$ ,  $h_1/h_2 = 5$ ,  $h_3/h_2 = 5$ ,  $a/h_2 = w/h_2 + 15$ ,  $\ell_b/h_2 = 3$ . Adapted from Jansen *et al.* (1981) [21], figure 7, p. 83. Reprinted with permission of the Institution of Engineering and Technology.

Jansen's results with the  $w/h$  aspect ratio as parameter are shown in [Figure 15.19](#). The end-effect length is normalized to the substrate thickness  $h_2$  and the independent variable is  $h_2/\lambda$ . Being the reciprocal of wavelength this means that the horizontal axis is proportional to frequency. Two overall general points can be deduced from the curves displayed in [Figure 15.19](#):

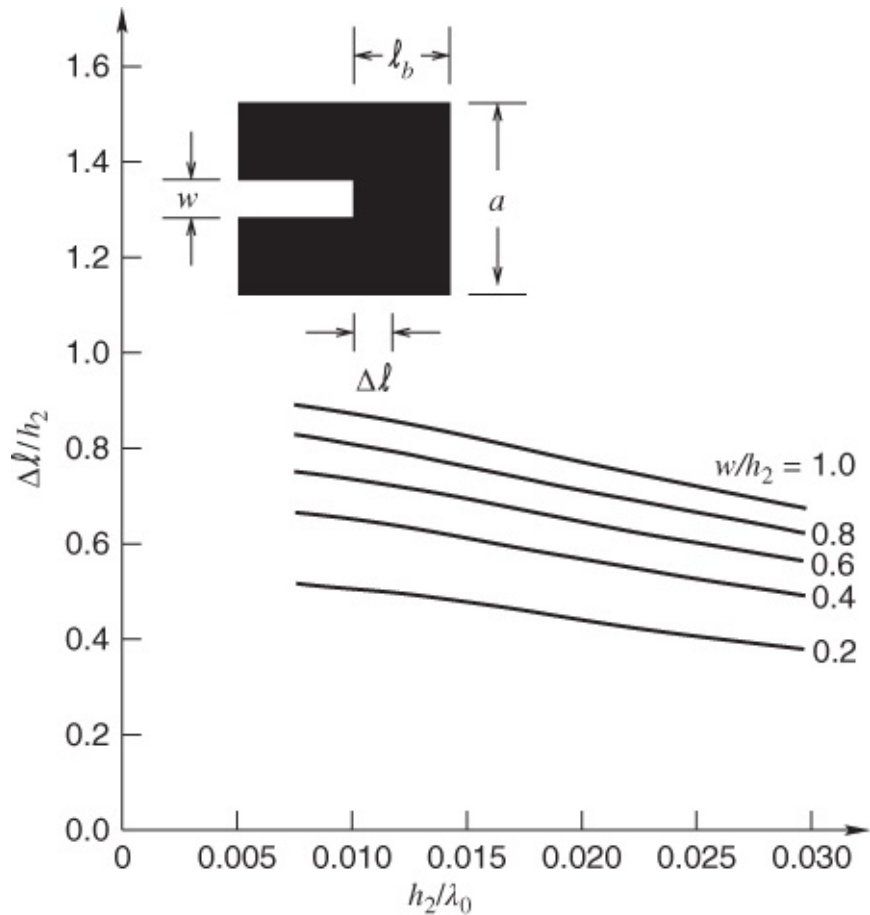


**Figure 15.19** Equivalent end-effect length applying to a single short-circuited slotline on an alumina substrate.  $h_2 = 0.635$  mm,  $\epsilon_1 = \epsilon_3 = \epsilon_r \epsilon_0$ ,  $\epsilon_r = 9.7$ ,  $h_1/h_2 = 10$ ,  $h_3/h_2 = 10$ ,  $a/h_2 = w/h_2 + 20$ . Adapted from Jansen *et al.* (1981) [21], figure 8, p. 84. Reprinted with permission of the Institution of Engineering and Technology.

- narrower slots have smaller end-effect lengths (as may be anticipated intuitively)
- as  $h_2/\lambda$  increases so the end-effect length slowly decreases.

Knorr and Salenz [22] investigated short-circuit terminations in slotline and generated a family of reactance curves for this structure. These are shown in [Figure 15.20](#). The normalized reactance increases strongly with frequency and also with increasing aspect ratio.

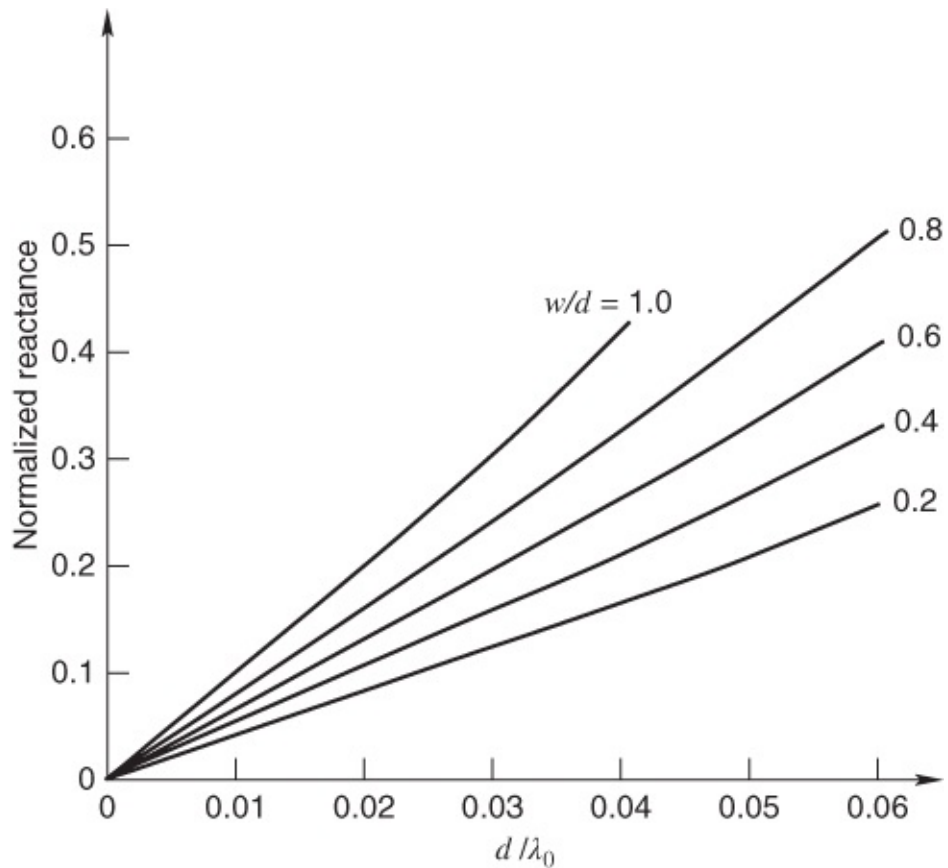


**Figure 15.20** A family of short circuit reactance curves derived for  $\epsilon_r = 12$ .  $h_2 = d$ ,  $h_1 = 0$ ,  $\epsilon_2 = \epsilon_r \epsilon_0$ . Adapted from Knorr and Salenz (1973) [22], figure 4, p. 580. Reprinted with permission of IEEE.

Coupled slotlines are important for several circuit configurations based on parallel-coupled lines. In view of this we also present here Jansen's results for short-circuited odd- and even-mode coupled slotlines. For the odd mode the end-effect decreases slowly with frequency but increases steadily with the aspect ratio defined in [Figure 15.21](#). Jansen's results for the even mode are presented in [Figure 15.22](#). For the even mode the end-effect decreases slowly with frequency but increases steadily with the aspect ratios defined in [Figure 15.22](#). It is noteworthy that the shape of the curves is effectively the mirror-image of the trends applying to the odd mode.

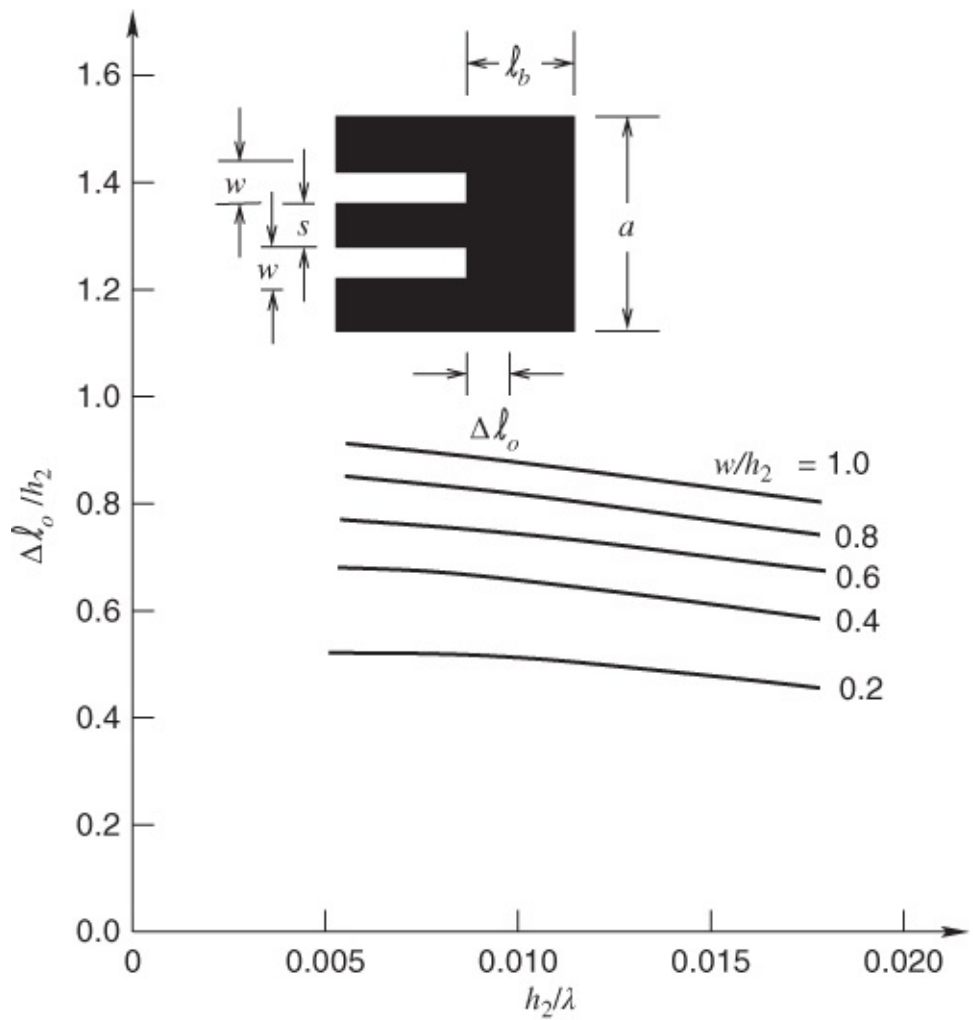


**Figure 15.21** End effect of a shorted pair of coupled slotlines in odd mode.  $h_2 = 0.635$  mm,  $\epsilon_r = 9.7$ ,  $h_1/h_2 = 10$ ,  $h_3/h_2 = 10$ ,  $a/h_2 = w/h_2 + 20$ ,  $s/h_2 = 1.0$ . Adapted from Jansen *et al.* (1981) [21], figure 8, p. 84. Reprinted with permission of the Institution of Engineering and Technology.

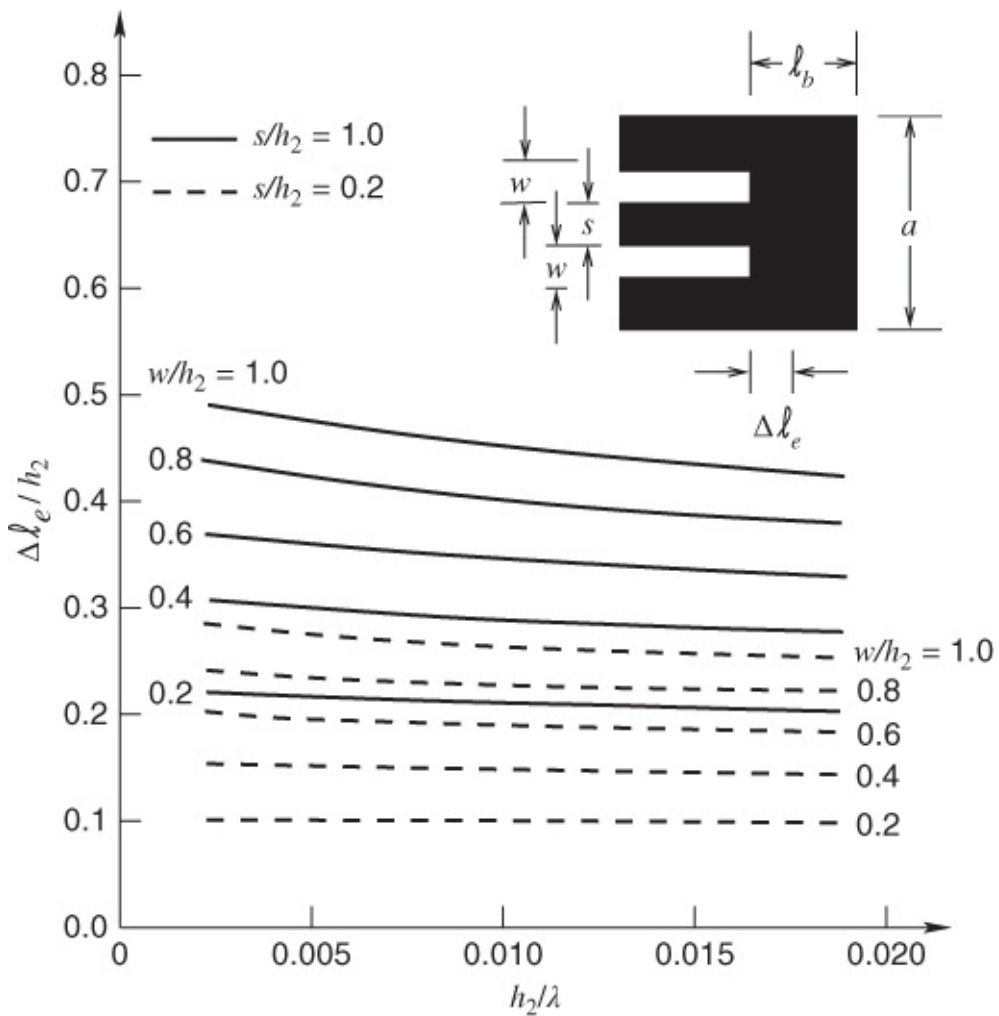


**Figure 15.22** End effect of a shorted pair of coupled slotlines in even mode. Parameters not specified are as in [Figure 15.21](#). Adapted from Jansen *et al.* (1981) [21], figure 8, p. 84. Reprinted with permission of the Institution of Engineering and Technology.

### 15.7.2 Chramiec's Measurements [23]

Chramiec [23] investigated slotline discontinuities on alumina substrates. The equation below relating to slotline reactances of both short and open circuits was presented by Chramiec:

$$\frac{X_1}{X_2} + \frac{X_2 + Z_0 \tan(\beta \ell_1)}{Z_0 + X_2 \tan(\beta \ell_1)} = 0. \quad 15.15$$

In Equation (15.15)  $X_1$  and  $X_2$  are the equivalent discontinuity reactances loading the uniform slotline segment.  $\beta$  and  $Z_0$  represent the slotline phase coefficient and the characteristic impedance, respectively.

Alumina substrates of several dimensions were used in the experiments. Resonant frequency measurements were performed on non-modified patterns with slotline ends short-circuited by perpendicular conductive plates, that is,  $X_1 = X_2 = 0$ . Measurements were made on slotline circuits, including the discontinuity to be characterized, and the normalized reactance of the discontinuity was calculated from Equation (15.15).

Chramiec's experimental arrangement is shown in [Figure 15.23\(a\)](#). The four slotline test patterns used by Chramiec are presented in [Figure 15.23\(a\)–\(d\)](#). The results obtained by Chramiec are given in [Figures 15.24](#) and [15.25](#). Clearly the reactance increases strongly with frequency, accelerating as the aspect ratio increases above around 0.1. Chramiec's results for the reactance associated with the non uniform resonator are shown in [Figure 15.25](#). For frequencies up to about 3.7 GHz the reactance is inductive and increasing. For frequencies exceeding about 3.7 GHz the reactance is negative and decreasing.

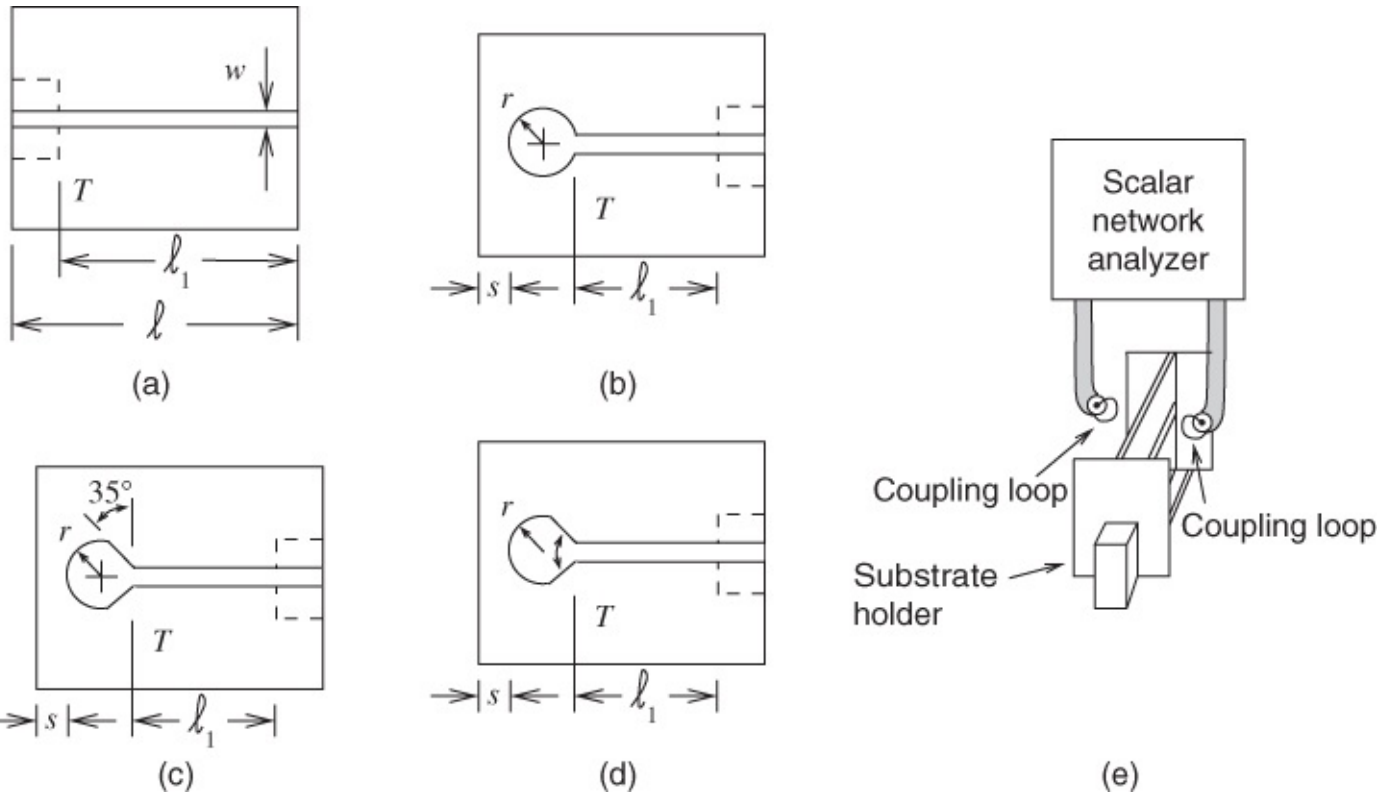


**Figure 15.23** Experimental setup: (a)–(d) slotline test patterns; and (e) apparatus. Adapted from Chramiec (1989) [23], figures 1 and 2, p. 1639. Reprinted with permission of IEEE.

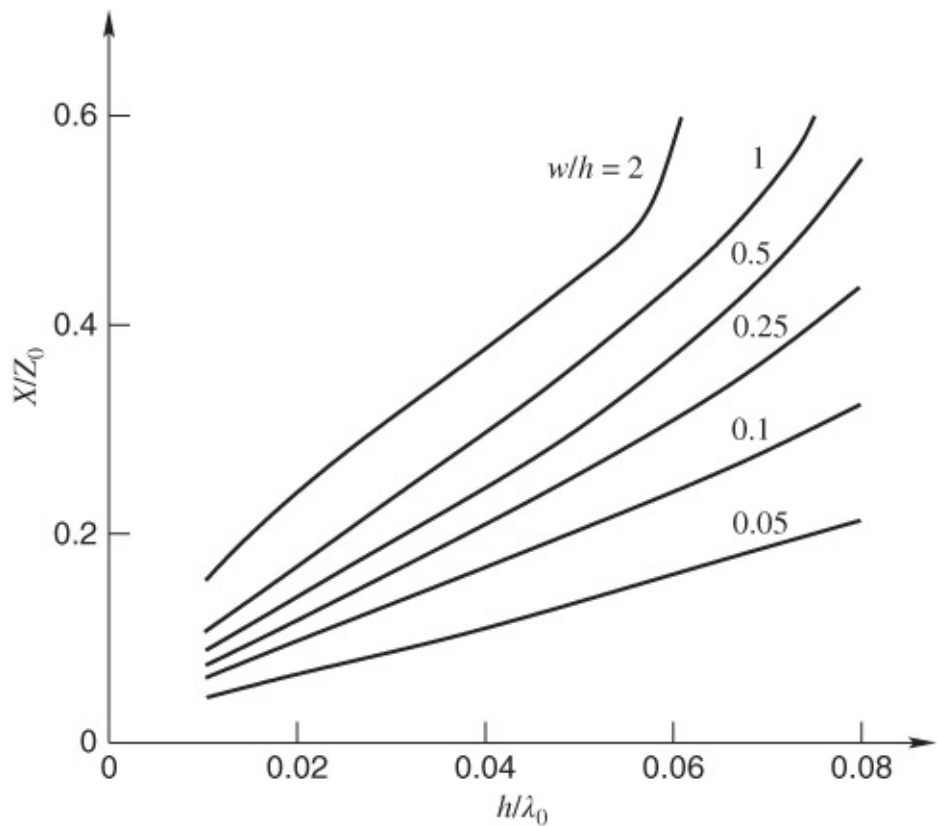


**Figure 15.24** Measured reactances of slotline short end on an alumina substrate. Adapted from Chramiec (1989) [23], figure 3, p. 1639. Reprinted with permission of IEEE.

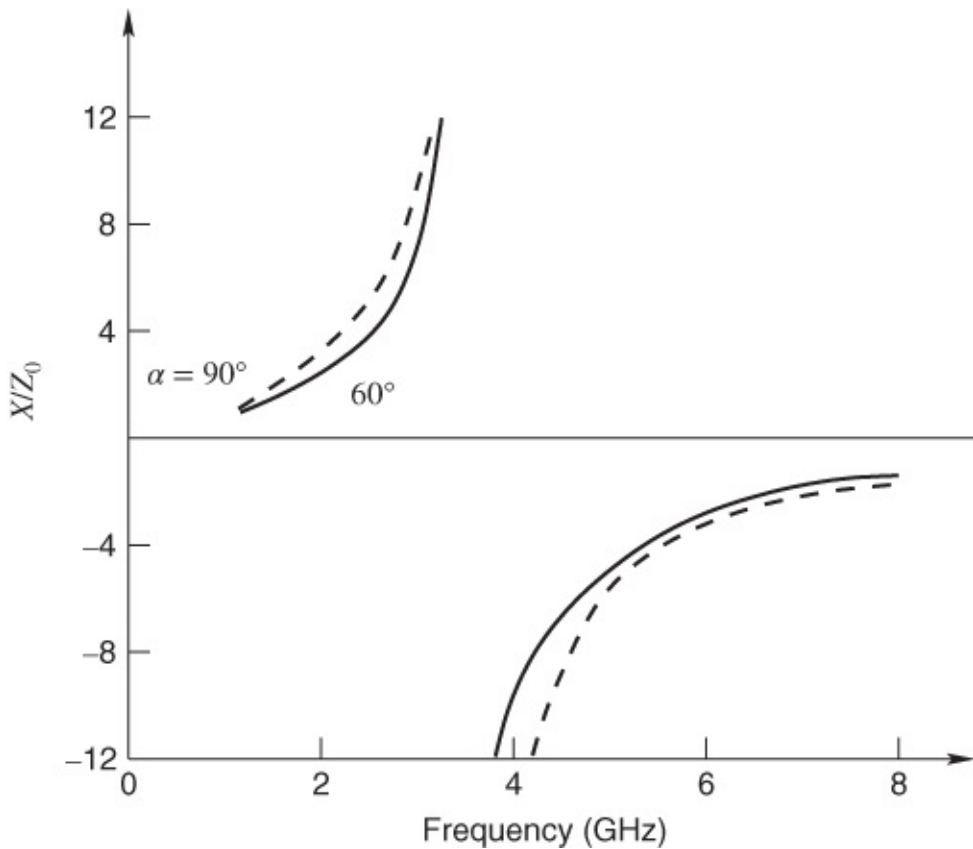


**Figure 15.25** Measured reactance of the slotline nonuniform resonator of [Figure 15.23\(d\)](#). Adapted from Chramiec (1989) [23], figure 6, p. 1640. Reprinted with permission of IEEE.

### 15.7.3 Some Other Results

Many researchers have reported on short and open circuits in slotline, amongst them Schuppert [24], whose work included the effects of short and open circuits in microstrip-slotline transitions. Schuppert's results regarding microstrip-slotline transitions are covered in [Section 17.5](#). Uwano [25] and Schiek [26] have also reported results relating to short and open circuits in slotline.

## 15.8 Summary

In this chapter we have concentrated on slotline fundamentals: the basic structure, operating principles, dispersion characteristics, guide wavelength, characteristic impedance, and end effects. Transitions to and from slotline usually involve microstrip but slotline transitions are also important. Inter-medium transitions are considered in [Chapter 17](#). Applications of slotlines in slotline-based circuits are considered in [Chapter 16](#).

## References

- [1] S. B. Cohn, “Slot line on a dielectric substrate,” *IEEE Trans. on Microwave Theory and Techniques*, vol. 17, no. 10, pp. 768–778, Oct. 1969.

- [2] Y. Li, Z. Zhang, J. Zheng, Z. Feng, and M. F. Iskander, “A compact hepta-band loop-inverted F reconfigurable antenna for mobile phone,” *IEEE Trans. on Antennas and Propagation*, vol. **60**, no. 1, pp. 389–392, Jan. 2012.
- [3] S. X. Ta, B. Kim, H. Choo, and I. Park, “Wideband quasi-yagi antenna fed by microstrip-to-slotline transition,” *Microwave and Optical Technology Letters*, vol. **54**, no. 1, pp. 150–153, 2012.
- [4] H. Hwang, T. Nuteson, M. Steer, J. Mink, J. Harvey, and A. Paoletta, “Two-dimensional quasi-optical power combining system: performance and component design,” in *1996 IEEE MTT-S Int. Microwave Symp. Dig.*, vol. **2**, 1996, pp. 927–930.
- [5] H. Hwang, T. Nuteson, M. Steer, J. Mink, J. Harvey, and A. Paoletta, “A quasi-optical dielectric slab power combiner,” *IEEE Microwave and Guided Wave Letters*, vol. **6**, no. 2, p. 73, Feb. 1996.
- [6] M. Abdulla, U. Mughal, H. Tsai, M. Steer, and R. York, “A full-wave system simulation of a folded-slot spatial power combining amplifier array,” in *1999 IEEE MTT-S Int. Microwave Symp. Dig.*, vol. **2**, 1999, pp. 559–562.
- [7] E. Gazit, “Improved design of the vivaldi antenna,” in *Proc. IEE Proceedings H, Microwaves, Antennas and Propagation*, vol. **135**, no. 2, Feb. 1988, pp. 89–92.
- [8] M. Steer and W. Palmer, *Multifunctional Adaptive Microwave Circuits and Systems*. Scitech Pub Inc, 2008.
- [9] C. A. Balanis, *Modern Antenna Handbook*. John Wiley & Sons, 2011.
- [10] J.-W. Sheen and Y.-D. Lin, “Propagation characteristics of the slotline first higher order mode,” *IEEE Trans. on Microwave Theory and Techniques*, vol. **46**, no. 11, pp. 1774–1781, Nov. 1998.
- [11] W. Liu, S. Mohammadi, L. Katehi, and M. Steer, “Polymer-membrane-supported fin-line frequency multipliers,” in *2002 3rd Int. Conf. on Microwave and Millimeter Wave Technology*, 2002, pp. 154–157.
- [12] W. Liu, D. Steenson, and M. Steer, “Membrane-supported copper E-plane circuits,” in *2001 IEEE MTT-S Int. Microwave Symp. Dig.*, 2001, pp. 539–542.
- [13] G. Robinson and J. Allen, “Slot line application to miniature ferrite devices,” *IEEE Trans. on Microwave Theory and Techniques*, vol. **17**, no. 12, pp. 1097–1101, 1969.
- [14] J. Citerne, S. Toutain, and L. Raczy, “Fundamental and higher order modes in microslot lines,” in *5th European Microwave Conf.*, 1975, 1975, pp. 273–277.
- [15] J. Knorr and K. Kuchler, “Analysis of coupled slots and coplanar strips on dielectric substrate,” *IEEE Trans. on Microwave Theory and Techniques*, vol. **23**, no. 7, pp. 541–548, Jul. 1975.

- [16] J. Svacina, “Dispersion characteristics of multilayered slotlines-a simple approach,” *IEEE Trans. on Microwave Theory and Techniques*, vol. **47**, no. 9, pp. 1826–1829, Sep. 1999.
- [17] T. Kitazawa, Y. Hayashi, and M. Suzuki, “Analysis of the dispersion characteristic of slot line with thick metal coating,” *IEEE Trans. on Microwave Theory and Techniques*, vol. **28**, no. 4, pp. 387–392, Apr. 1980.
- [18] R. Garg and K. Gupta, “Expressions for wavelength and impedance of a slotline,” *IEEE Trans. on Microwave Theory and Techniques*, vol. **24**, no. 8, pp. 532–532, Aug. 1976.
- [19] T. Rozzi, F. Moglie, A. Morini, E. Marchionna, and M. Politi, “Hybrid modes, substrate leakage, and losses of slotline at millimeter-wave frequencies,” *IEEE Trans. on Microwave Theory and Techniques*, vol. **38**, no. 8, pp. 1069–1078, Aug. 1990.
- [20] N. Das and D. M. Pozar, “Full-wave spectral-domain computation of material, radiation, and guided wave losses in infinite multilayered printed transmission lines,” *IEEE Trans. on Microwave Theory and Techniques*, vol. **39**, no. 1, pp. 54–63, Jan. 1991.
- [21] R. Jansen, “Hybrid mode analysis of end effects of planar microwave and millimetrewave transmission lines,” *IEE Proceedings H, Microwaves, Optics and Antennas*, vol. **128**, no. 2, pp. 77–86, Feb. 1981.
- [22] J. Knorr and J. Saenz, “End effect in a shorted slot,” *IEEE Trans. on Microwave Theory and Techniques*, vol. **21**, no. 9, pp. 579–580, Sep. 1973.
- [23] J. Chramiec, “Reactances of slotline short and open circuits on alumina substrate,” *IEEE Trans. on Microwave Theory and Techniques*, vol. **37**, no. 10, pp. 1638–1641, Oct. 1989.
- [24] B. Shuppert, “Microstrip/slotline transitions: modeling and experimental investigation,” *IEEE Trans. on Microwave Theory and Techniques*, vol. **36**, no. 8, pp. 1272–1282, Aug. 1988.
- [25] T. Uwano, R. Sorrentino, and T. Itoh, “Characterization of microstrip-to-slotline transition discontinuities by transverse resonance analysis,” in *17th European Microwave Conf., 1987*, 1987, pp. 317–322.
- [26] B. Schiek and J. Khler, “An improved microstrip-to-microslot transition,” *IEEE Trans. on Microwave Theory and Techniques*, vol. **24**, no. 4, pp. 231–233, Apr. 1976.

# Chapter 16

## Slotline Applications

### 16.1 Introduction

This is a follow-on chapter to [Chapter 15](#). In this chapter we consider details concerning the following types of circuits implemented using slotlines: comparators, couplers, filter applications, magic Ts, the Marchand balun, phase shifters, isolators and circulators, and a double-sided balanced microwave circuit.

### 16.2 Comparators and Couplers

#### 16.2.1 Comparators

With several types of electronic systems, angular error sensing is a vital function. For example, comparator circuits that provide this function are required in a monopulse radar and they are fundamental in determining the azimuth and elevation of a target.

The eight-port comparator circuit (also known as a sum and difference network) is a common form of microwave device typically constructed with four  $180^\circ$  hybrids. However, a comparator may also be based on a fully symmetrical eight-port microstrip/slotline circuit. In this case phase shifters are required at two of the eight ports of the symmetrical circuit [1]. A schematic diagram of such a comparator is shown in [Figure 16.1](#).

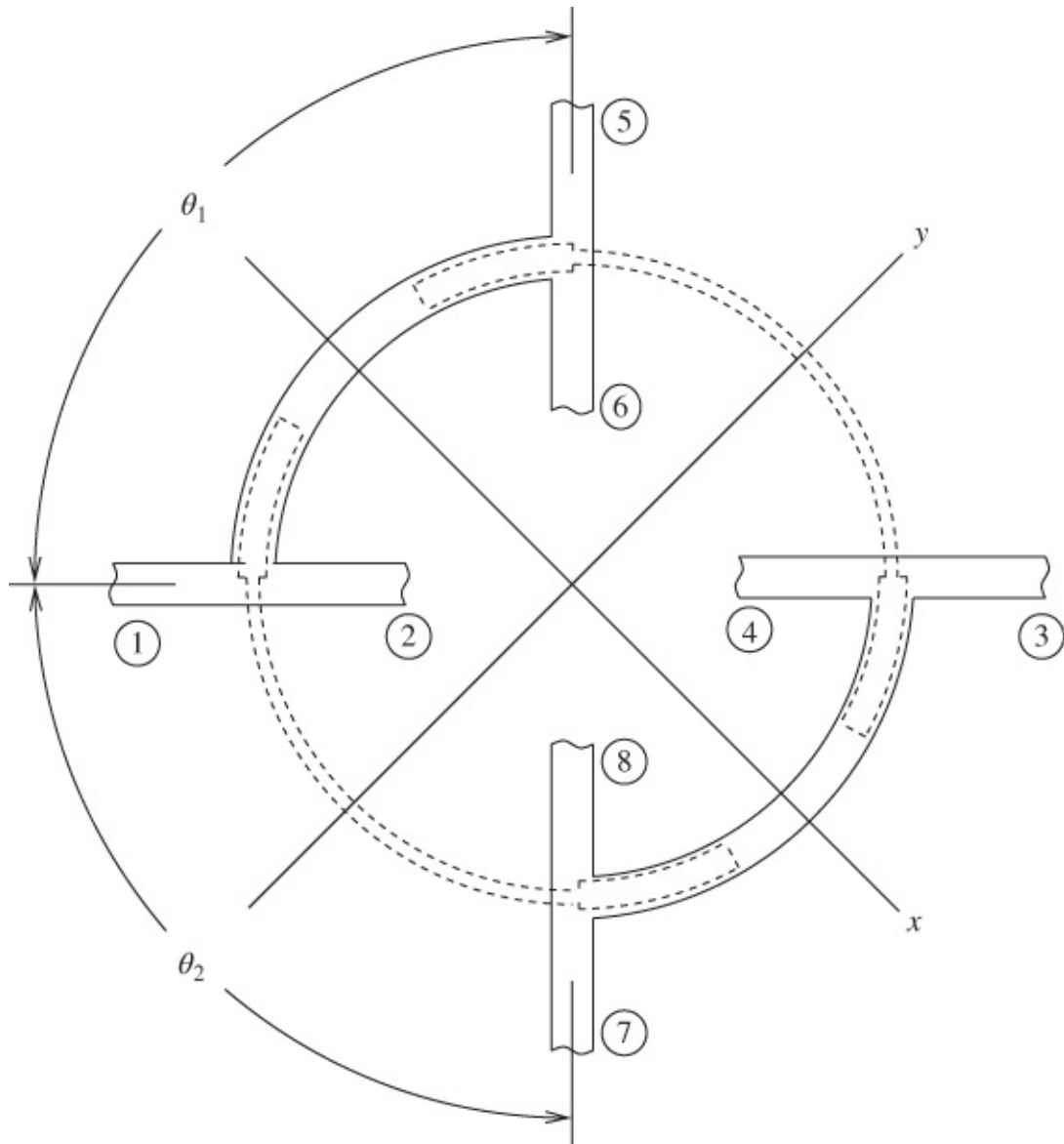


**Figure 16.1** Schematic diagram of a symmetrical eight-port circuit. The solid lines represent microstrip lines on the top of the circuit. The dashed lines represent slotlines in the ground plane on the bottom of the circuit board. Adapted from Riblet (1990) [1], figure 1, p. 1421. Used with permission of IEEE.

Riblet [1] derived the conditions for a lossless symmetrical eight-port circuit to be a symmetrical eight-port comparator. This worker described two versions of such a practical comparator and these versions are now presented here. The first version ([Figure 16.2](#)) is three-wavelengths long at mid-band and implemented using both  $25 \Omega$  microstrip and  $50 \Omega$  slotline transmission lines.

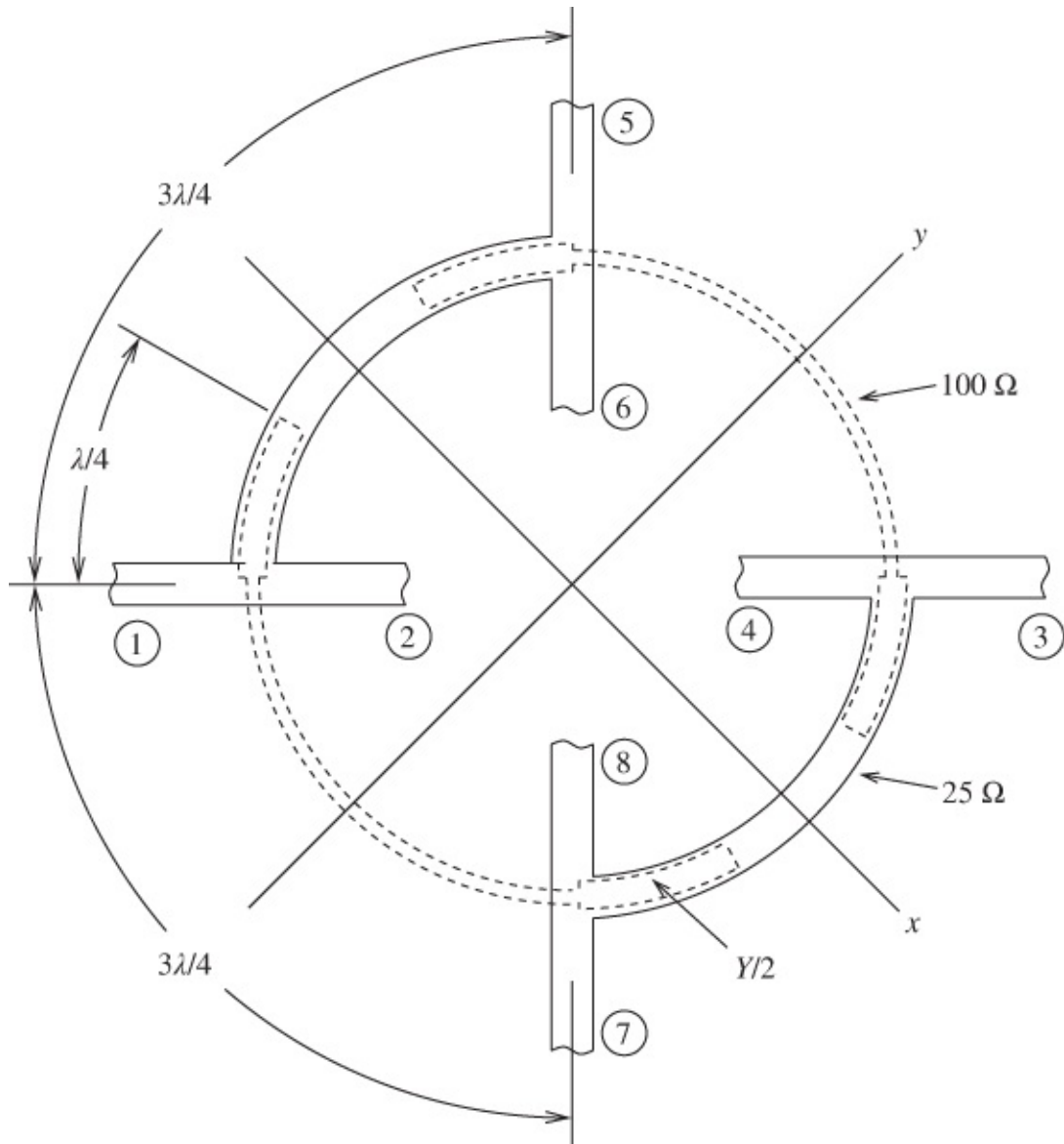


**Figure 16.2** Version 1 of the planar microstrip-slotline symmetrical comparator. The circumference is three wavelengths at midband. Adapted from Riblet (1990) [1], figure 2, p. 1423. Reprinted with permission of IEEE.

Riblet introduced an equivalent two-port circuit ([Figure 16.3](#)), representing core aspects of the comparator and enabling the theoretical performance to be determined. In this figure the admittance  $Y$  is twice the characteristic admittance of the slotline stubs. A small value for  $Y$  yields a large bandwidth. For the configuration of [Figure 16.3](#) the smallest possible value of  $Y$  is 1. A plot of the optimum theoretical return loss and isolation to port 2 versus normalized frequency is given in [Figure 16.4](#). The return loss and isolation between ports 1 and 2 can be better than 20 dB over approximately a 30% bandwidth.

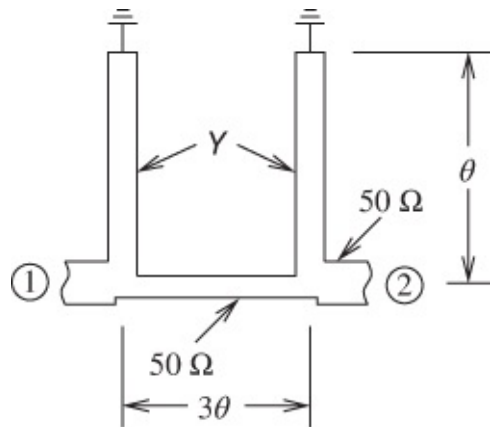


**Figure 16.3** Schematic diagram of a two-port circuit which may be used to determine the theoretical performance of the eight-port circuit in [Figure 16.2](#). Optimum performance is obtained if  $Y = 1$ . Adapted from Riblet (1990) [1], figure 3, p. 1423. Reprinted with permission of IEEE.

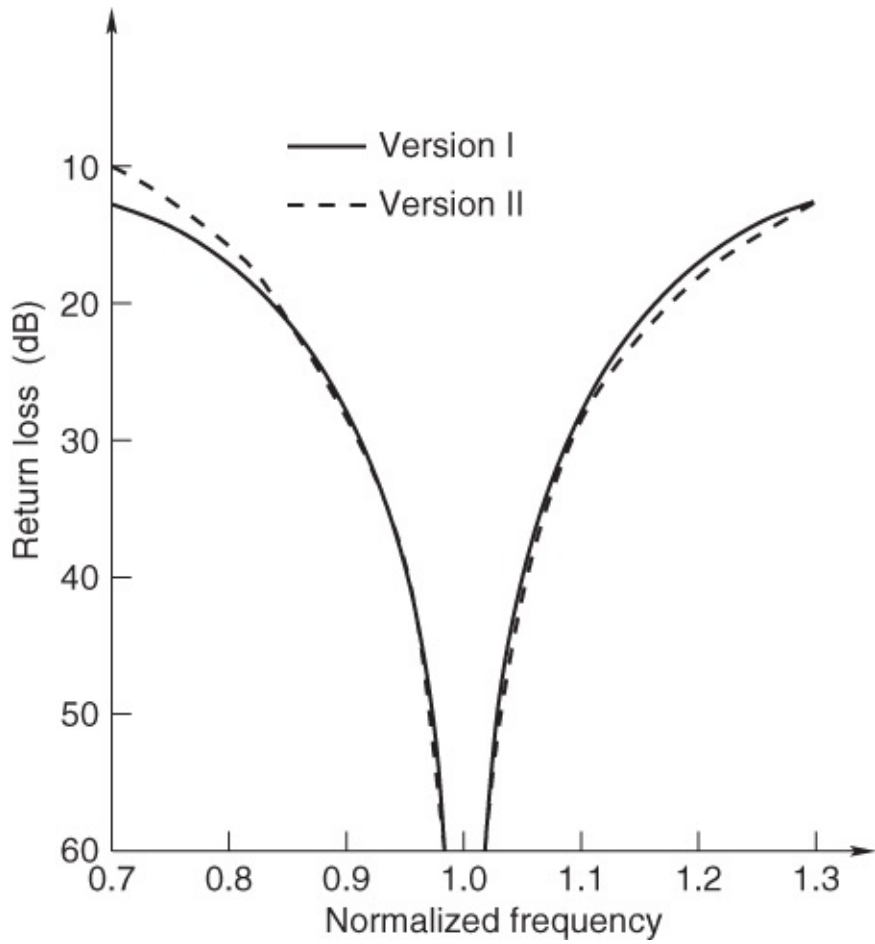


**Figure 16.4** Optimum return loss versus normalized frequency for Version I ([Figure 16.2](#)) and Version II ([Figure 16.5](#)). Adapted from Riblet (1990) [1], figure 4, p. 1423. Reprinted with permission of IEEE.

The circumference of Version I is three wavelengths at the centre frequency. Riblet showed that this circumference can be reduced to one wavelength or less using shunt-connected capacitors across the slotline stubs, as indicated in the version (Version II) depicted in [Figure 16.5](#).

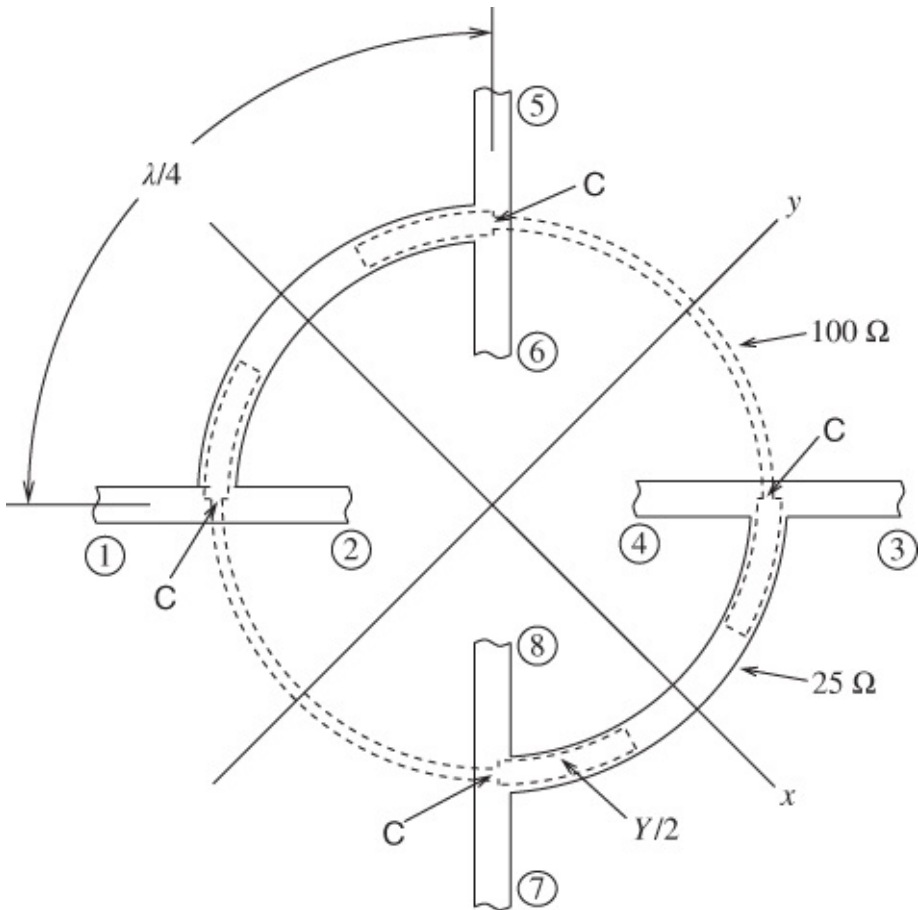


**Figure 16.5** Version II of the planar microstrip-slotline symmetrical comparator. The circumference is only a wavelength at midband. Adapted from Riblet (1990) [1], figure 5, p. 1423. Reprinted with permission of IEEE.

If the stubs are made to resonate at the frequency for which the port pairs (1,2), (7,8) and (3,4), (5,6) are separated by a quarter-wavelength, then reflections from the stub resonators at these port pairs will tend to cancel. This results in the second broadband version. The two-port circuit given in [Figure 16.3](#) may again be used to calculate the theoretical performance if capacitors with capacitance  $2C$  are included in shunt at ports 1 and 2. The electrical length of the stubs becomes  $\theta'$ . The optimum theoretical performance is obtained if  $Y = 1$  and  $\theta'$  corresponds to an eighth of a wavelength at midband. A comparison of the two return loss curves ([Figure 16.4](#)) indicates that the bandwidth is about the same for these two versions of microstrip-slotline comparators. However, the physical size of the second version will be the same as that of a ring  $180^\circ$  hybrid, four of which are frequently used to construct a conventional comparator.

The data shown in [Figure 16.4](#) also indicates that the low frequency return loss is improved comparing Version II with Version I. Riblet reported experimental data relating to both versions of the comparator.

### 16.2.2 Fundamentals of Parallel-coupled Slotlines

Like parallel-coupled microstrip, parallel-coupled slotlines generate even and odd modes, and

these are important for any designs using such coupled structures. The even- and odd-mode characteristic impedances are shown in [Figure 16.6](#) as functions of normalized frequency [2]. In these families of curves ([Figures 16.6](#) and [16.7](#))  $w/d$  is the normalized slot width and  $s/d$  is the normalized separation.

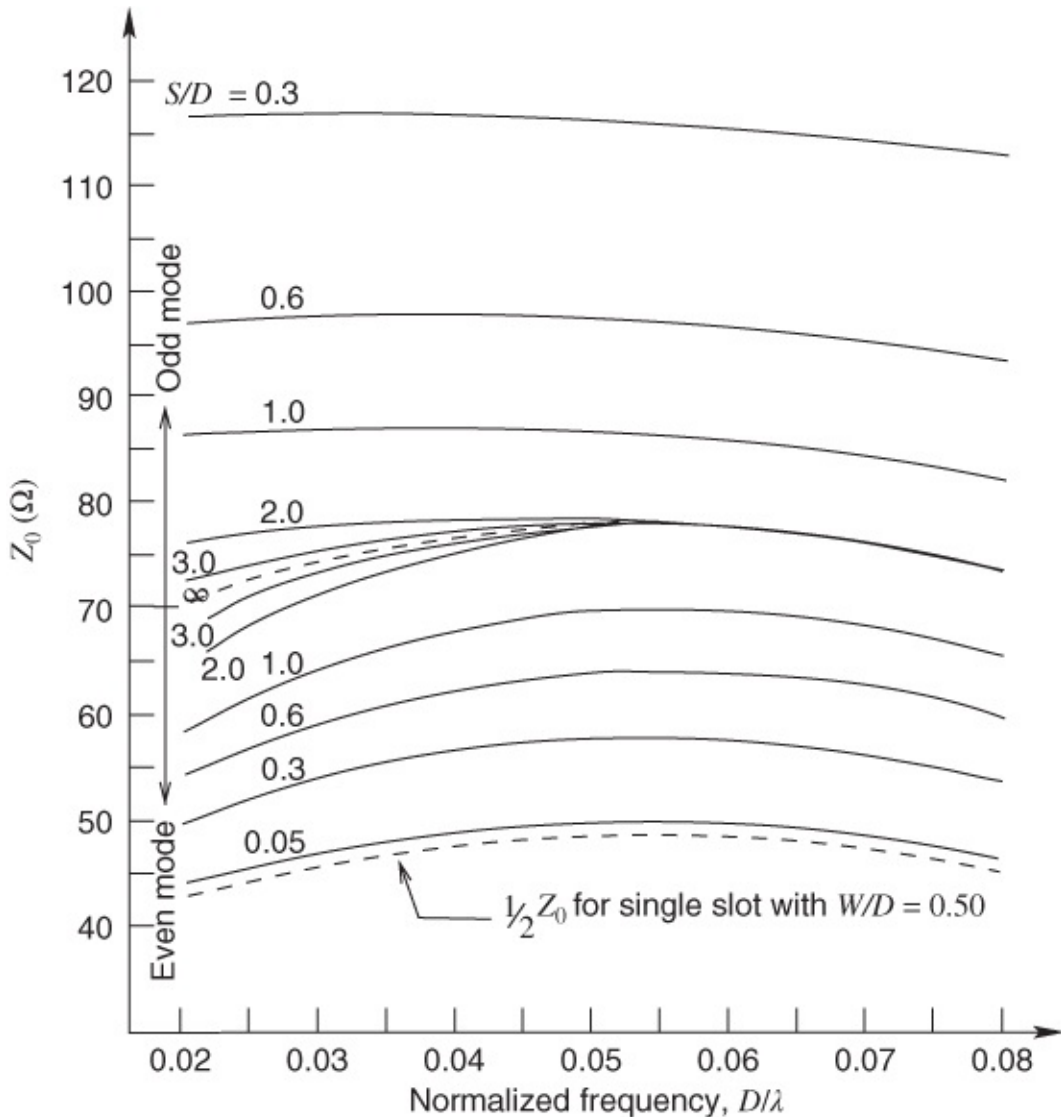


**Figure 16.6** Even- and odd-mode characteristic impedance of coupled slotlines with  $W/D = 0.25$  and  $\epsilon_r = 11$ . Adapted from Knorr and Kuchler (1975) [2], figure 6, p. 544. Reprinted with permission of IEEE.

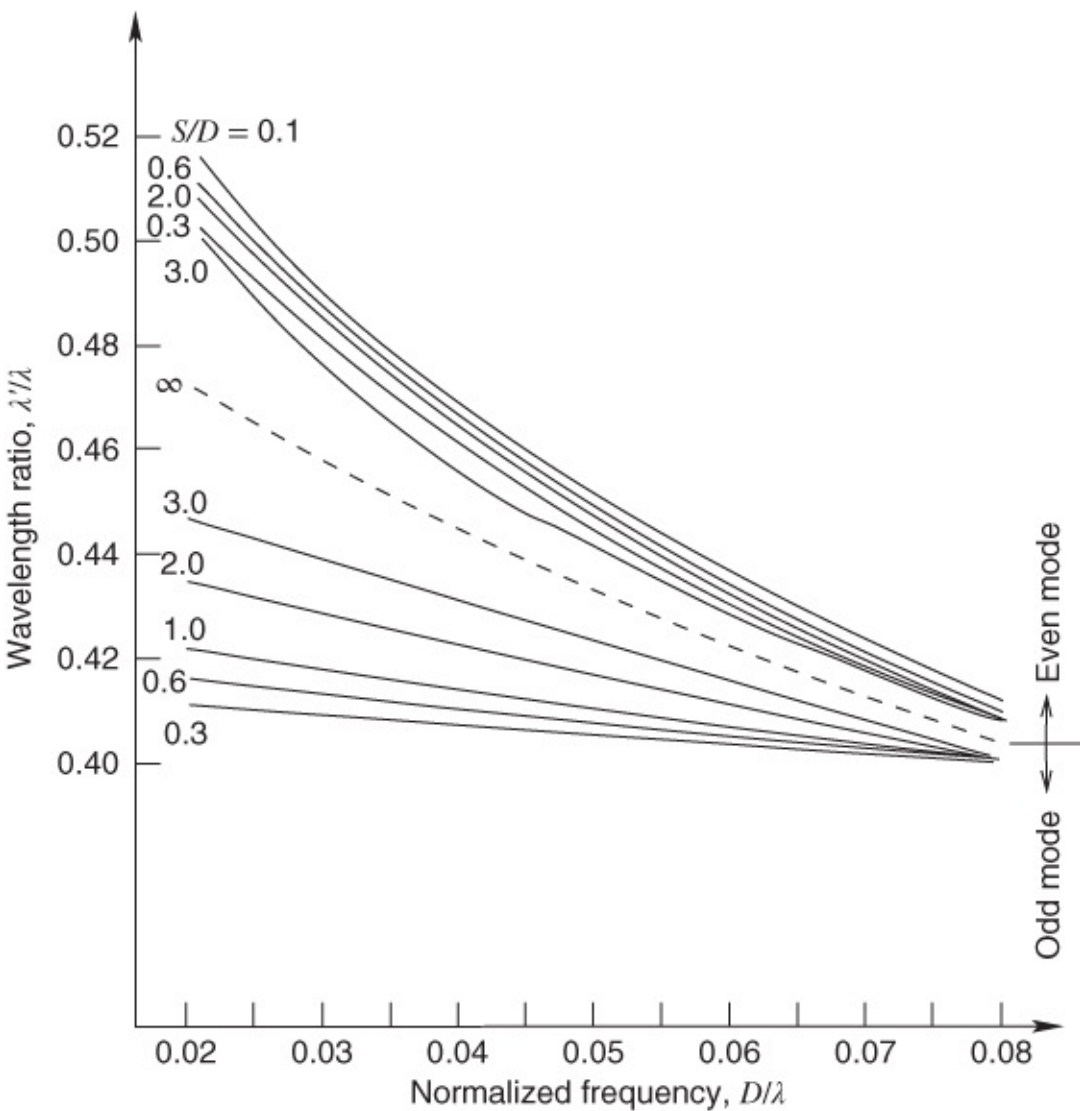


**Figure 16.7** Even- and odd-mode dispersion characteristics of coupled slotlines with  $W/D = 0.25$  and  $\epsilon_r = 11$ . Adapted from Knorr and Kuchler (1975)[2], figure 6, p. 544. Reprinted with permission of IEEE.

From [Figure 16.6](#) it can clearly be seen that both the odd-mode and the even-mode characteristic impedances vary slowly with frequency over a wide range.

The even- and odd-mode wavelength ratios (i.e., dispersion characteristics) are shown in [Figure 16.7](#) as functions of normalized frequency. From [Figure 16.7](#) it is clear that the even-mode dispersion is always much more pronounced than that applying to the odd mode.

According to Abbosh [3] the characteristic impedance of the odd-mode for coupled slotlines can be expressed in two ways. In terms of the mid-band coupling coefficient  $C$ :

$$Z_{0o} = Z_0 \left( \frac{1 - 10^{-C/20}}{1 + 10^{-C/20}} \right)^{0.5}. \quad \text{16.1}$$

Alternatively, in terms of the substrate permittivity and elliptic functions ( $K$ ):

$$Z_{0o} = \frac{60\pi}{\sqrt{\epsilon_r}} \frac{K'(k_2)}{K(k_2)}.$$

Similar expressions apply to the even-mode characteristic impedance.

### 16.2.3 A Three-layer Wideband Coupler

Abbosh and Bialkowski (2007) reported their invention of a wideband microstrip/slotline coupler [3]. The circuit structure is shown in [Figure 16.8](#). Although this structure is dominated by microstrip connecting lines it is included in this chapter on slotline circuits because the central slot is of prime importance in the coupling mechanism.

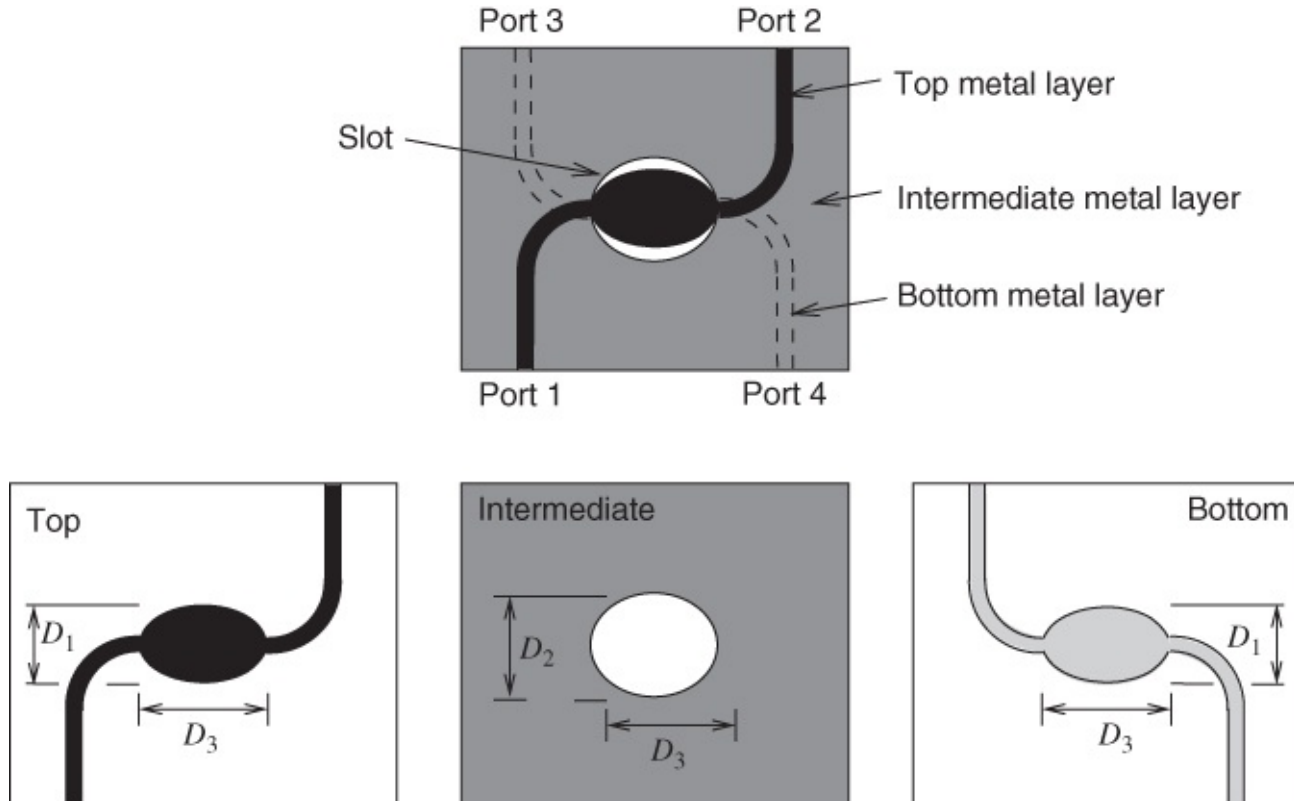


[Figure 16.8](#) Layout of a wideband coupler, including microstrip ports. Adapted from Abbosh and Bialkowski (2007) [3], figure 1, p. 190. Reprinted with permission of IEEE.

The complete three-layer structure is shown in the top diagram whilst each layer is depicted (dimensioned) in the lower three drawings. The coupler comprises:

- a top metal layer
- an intermediate layer
- a lower metal layer.

The top and lower metal layers provide one portion of the central coupling as well as all four ports of the circuit. The sandwiched intermediate (substrate) layer has a central elliptical hole that concentrates the electric fields. This hole is slightly larger ( $D_2$ ) than the mainly covering metal layers to allow for the fringing fields. Abbosh and Bialkowski also introduced an

equivalent configuration of the practical structure in order to determine the initial dimensions required. This is shown in [Figure 16.9](#).

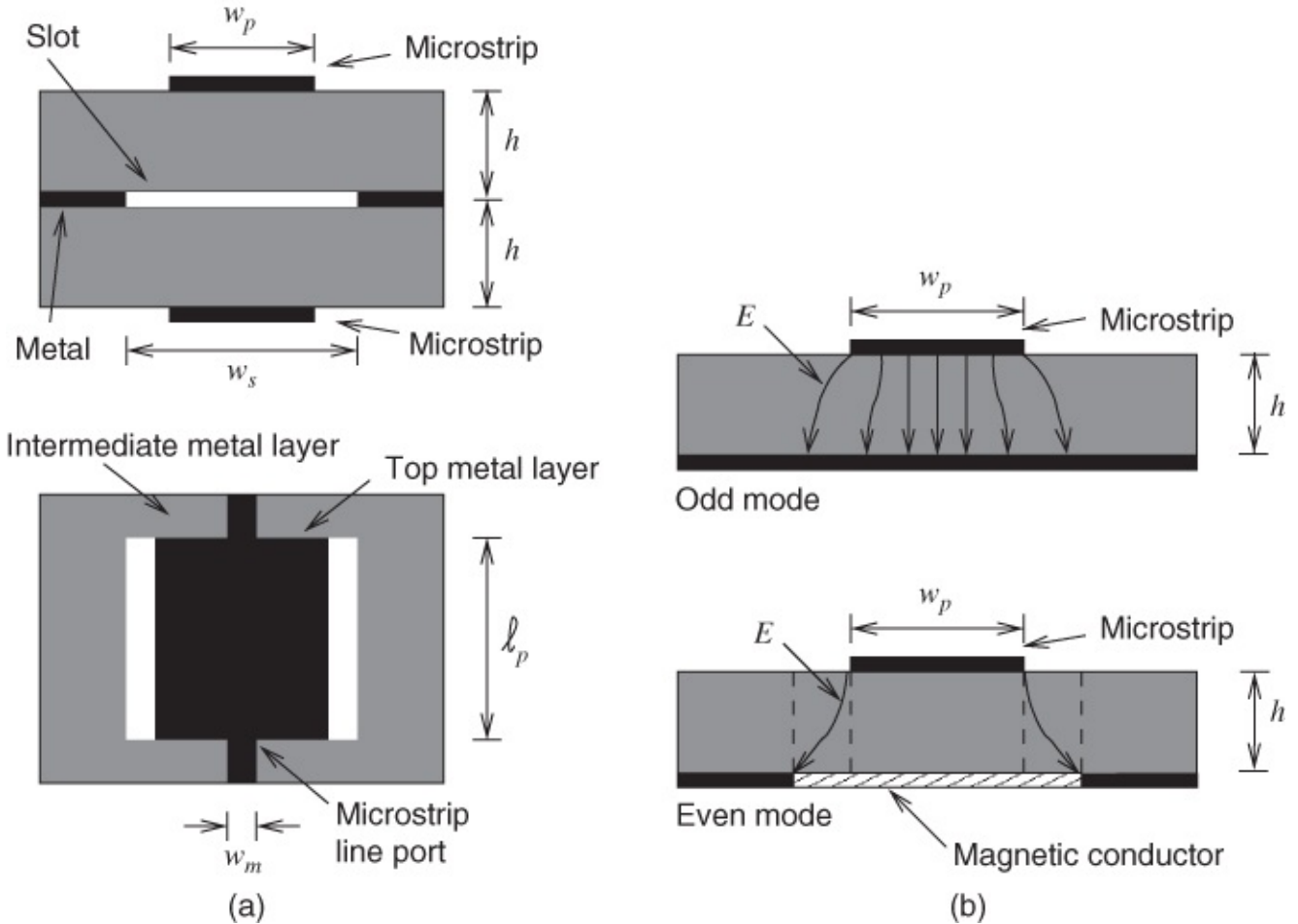


[Figure 16.9](#) Equivalent configuration used to determine the initial dimensions. Adapted from Abbosh and Bialkowski (2007) [3], figure 1, p. 190. Reprinted with permission of IEEE.

Assuming that  $Z_0 = 50 \Omega$  and the coupling factor is 3, 6, or 10 dB, the values of the odd- and even-mode characteristic impedances can be calculated from Equation (16.1) and the corresponding expression for  $Z_{0e}$  (the expression in the brackets inverted). The physical dimensions follow from an evaluation of the elliptic functions in Equation (16.2) using the Gauss–Newton iteration method [3]. The length of the coupler is calculated in the usual manner, one quarter-wavelength long at midband.

For a nominally 3 dB coupler, measurements over a 3–11 GHz frequency range indicated the following:

- passband loss ( $S_{21}$ ) and coupling ( $S_{31}$ ) both between 3 dB and 6 dB
- isolation ( $S_{11}$ ) and return loss ( $S_{41}$ ) both better than 20 dB over most of the frequency range.

## 16.3 Filter Applications

Mirroring microstrip-based circuits, bandpass filters can also be realized in slotline format. The two basic approaches are:

- parallel-coupled resonators (quarter-wave-coupled resonant slots)
- end-coupled half-wavelength resonators (end-coupled resonant slots).

Mariani and Agrios [4] researched and reported on both approaches. The basic configurations are shown in [Figure 16.10](#). Allowing for the open end-effect of the slotlines, the physical overlap between the parallel-coupled half-wavelength slotline resonators is slightly less than a quarter-wavelength (see [Figure 16.10\(a\)](#)).

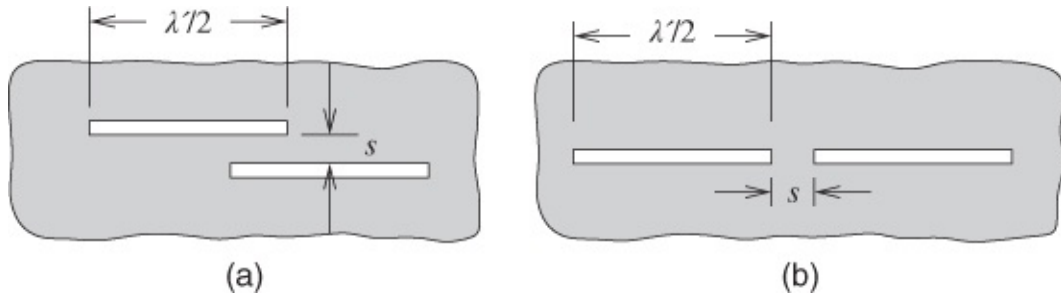


**Figure 16.10** Resonator configurations for slotline bandpass filters: (a) quarter-wave-coupled resonant slots; and (b) end-coupled resonant slots. Adapted from Mariani and Agrios (1970) [4], figure 1, p. 1090. Reprinted with permission of IEEE.

Coupling data was obtained for both the end-coupled and quarter-wave-coupled resonators. These bandpass filter coupling data were obtained such that a pair of resonators or slots yielded an over-coupled transmission response. The slotline circuits used for the coupling experiments utilized a substrate metallization width of about 38 mm in all cases. Measurements were conducted on Trans-Tech D-16 substrates at frequencies near 2.8 GHz. The slotline resonators were shielded within a brass enclosure with inside dimensions of 31.8 by 27.0 mm. The coupling coefficient  $K$  was computed from the center frequency  $f_0$ , the separation between the two peaks of the over-coupled transmission response  $\Delta f$ , and the transmission dip  $\Delta L$  (dB). The end-coupled resonant slots do not give a large range of coupling value as does the quarter-wave-coupled case; only moderate coupling appears achievable for the end-coupled case, whereas fairly strong coupling is obtainable using quarter-wave parallel coupling. The copper-plated circuit provides somewhat higher coupling compared with the aluminum tape circuit for the case of the quarter-wave-coupled slots with the same resonator spacing. This effect can be attributed to the thin adhesive coating on the aluminum sensing tape.

Mariani and Agrios [4] reported that bandpass filters of narrow and moderate bandwidth are readily achievable using slotline. Also, in the case of slotline bandstop filters, higher rejection levels are associated with wide bandwidths (20–30%); the rejection performance is seriously degraded as the bandwidth approaches 10% since the unloaded  $Q$  is relatively low. Generally, it was found that the unloaded  $Q$  of these filters was comparable to microstrip.

Cohn [5] also reported on filters implemented using resonant slotlines. Cohn's configurations are depicted in [Figure 16.11](#). In [Figure 16.11\(a\)](#) a cascade of resonant slotlines are distributed along a metallic substrate with a microstrip feed line forming the transmission as well as the

input and output ports. [Figure 16.11\(b\)](#) is essentially the same configuration as that of Mariani and Agrios [4] ([Figure 16.10\(a\)](#)). In [Figure 16.11\(b\)](#) the circuit totally comprises slotline, no other transmission medium is involved.

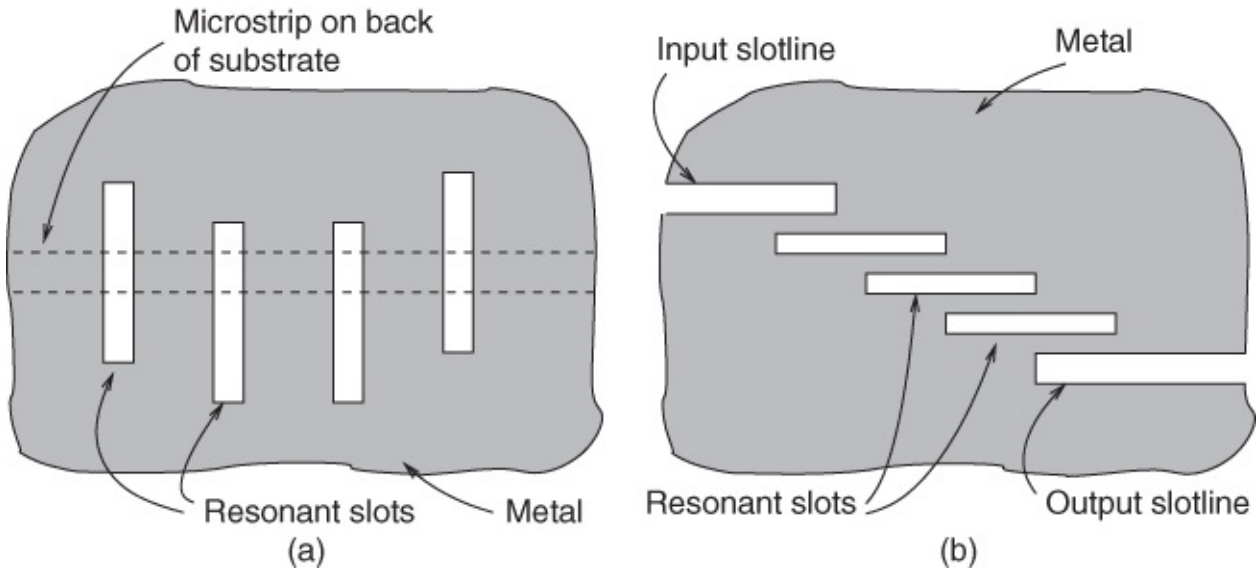


[Figure 16.11](#) Filter applications: (a) bandstop filter using cascaded resonant slots; and (b) parallel-coupled slotline bandpass filter. Adapted from Cohn (1969) [5], figure 6, p. 770. Reprinted with permission of IEEE.

## 16.4 Magic T

So-called magic T microwave circuits are essentially a form of hybrid circuit. Magic Ts are required for several types of circuit function: balanced mixers, balanced modulators, and circuits for monopulse radar systems. In this section we focus on the magic Ts described by Aikawa and Ogawa [6, 7].

The magic Ts described by Aikawa and Ogawa [7] effectively implement coupled slotlines. They have an unusual feature in that their four-port locations are quite different from that of conventional magic Ts. In these designs the two-ports, which correspond to the *E* and *H* arms of the well-known waveguide magic T, can be located on the same side, opposite to the other two-ports. As a result, this type of magic T has a considerable practical advantage. Specifically, such magic Ts have no need of transmission line crossings, which are in any case unsuitable for planar microwave circuits, when they are applied to practical circuits such as balanced mixers and balanced modulators.

These novel magic Ts make use of a combination of microstrip lines, slotlines, coupled slotlines, and CPWs, therefore they can easily be used up to millimeter-wave bands, utilizing photolithographic techniques. Aikawa and Ogawa describe circuit configurations, analysis using equivalent circuits, and experimental results in the 6 GHz band.

Aikawa and Ogawa's basic concept is shown in [Figure 16.12](#). In the configuration shown in [Figure 16.12\(a\)](#) a series T junction connecting to a CPW is combined with a parallel T

junction to form the magic T. Ports **(E)** and **(H)** correspond, respectively, to the **E** and **H** arms of a conventional metallic waveguide magic T. The remaining two ports are numerically designated 1 and 2 in [Figure 16.12](#).

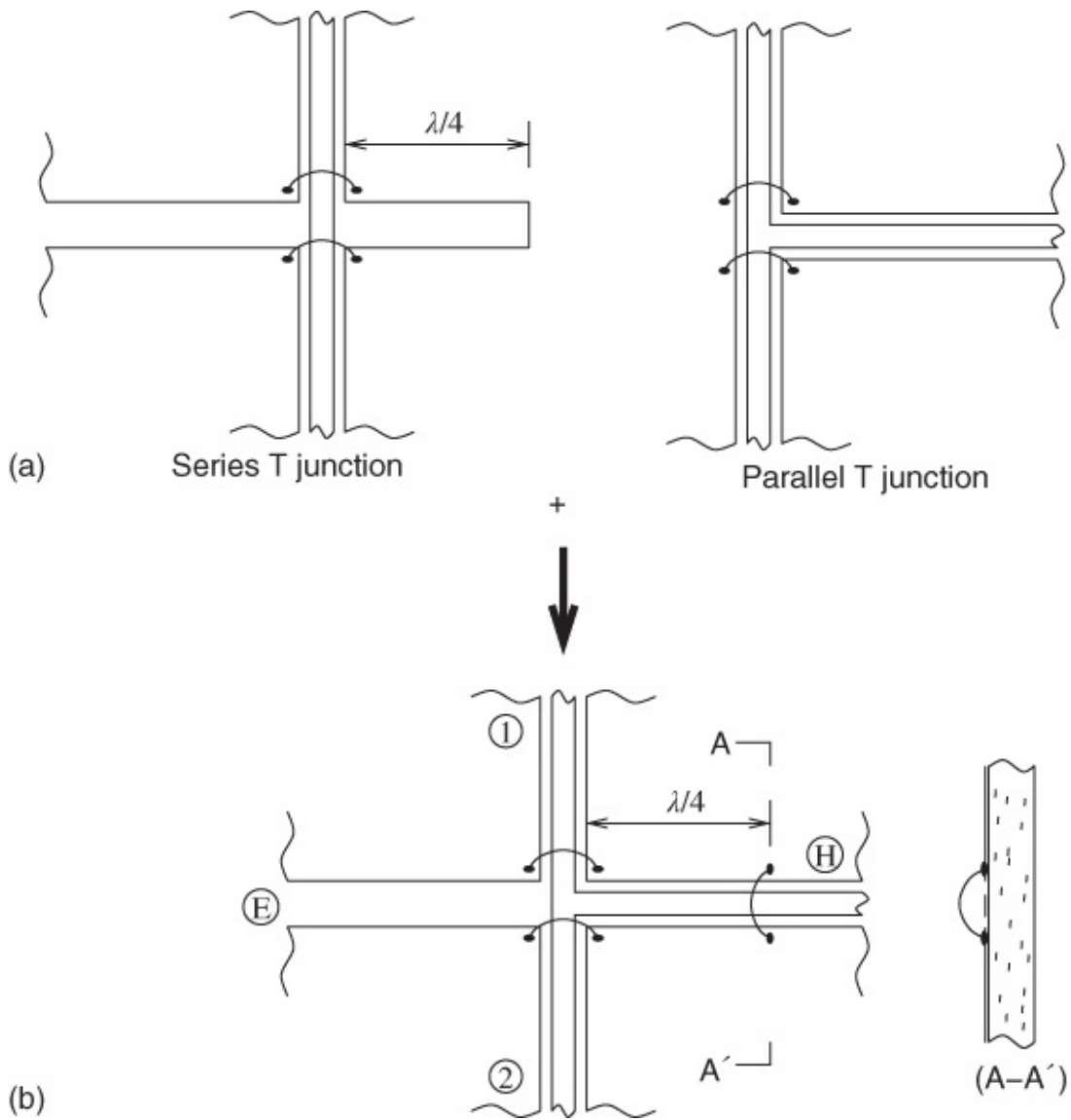
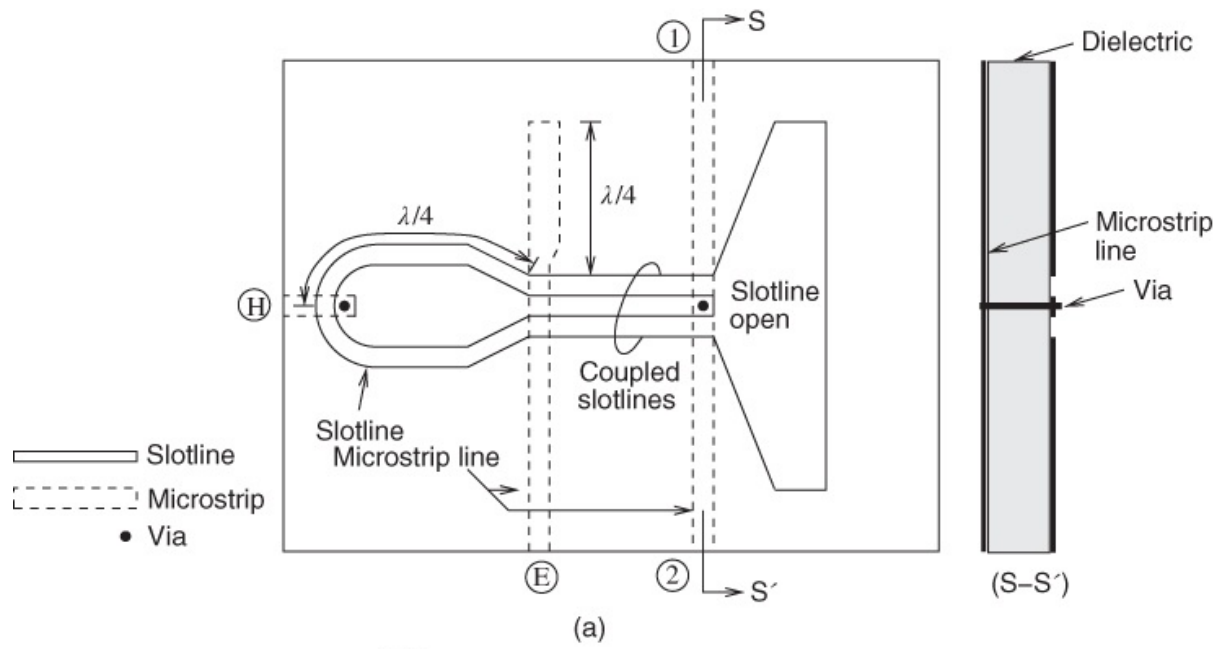
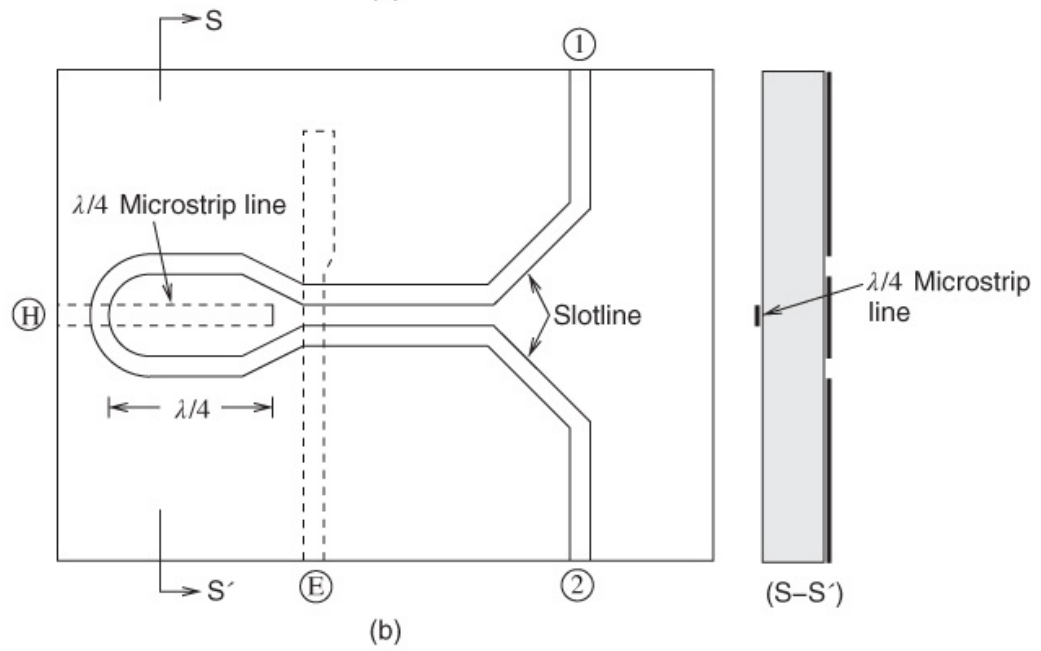


**Figure 16.12** Basic design concept of a magic T. Adapted from Aikawa and Ogawa (1989) [6], figure 4, p. 408. Reprinted with permission of IEEE.

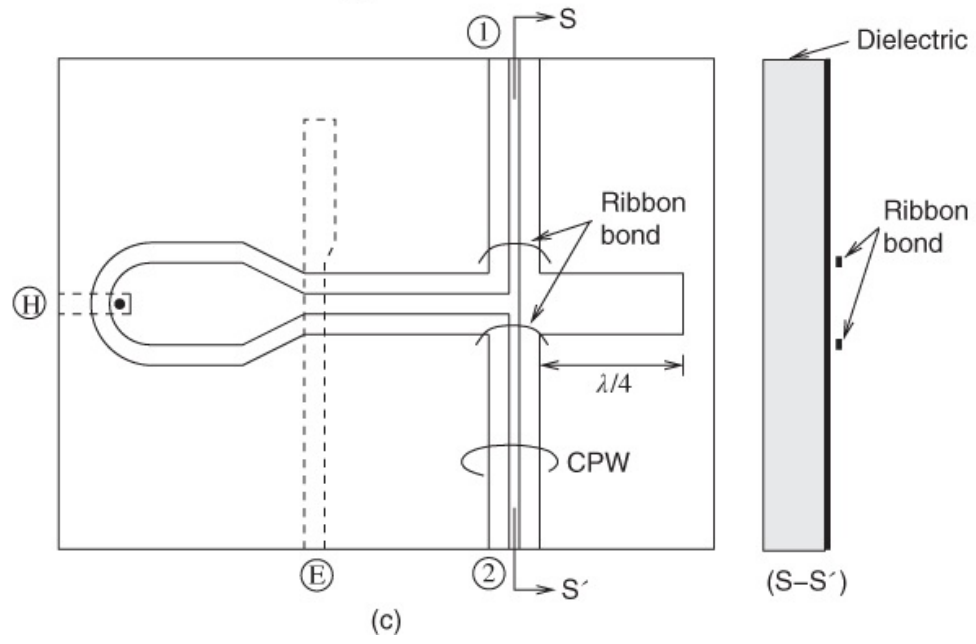
Three types of planar magic Ts are shown in [Figure 16.13](#). Here solid lines represent slotlines, coupled slotlines, and CPW on a substrate, while dotted lines represent microstrip lines on the reverse side of the substrates. These magic Ts can be classified into three types, microstrip type, slotline type and coplanar type, according to the kinds of transmission lines connected to the coupled slotlines. In order to examine these magic Ts further, Aikawa and Ogawa [7] introduced equivalent diagrams showing the schematic behaviors for in-phase and out-of-phase couplings. These are depicted as [Figure 16.14](#).



(a)



(b)



(c)

**Figure 16.13** Planar magic Ts. Adapted from Aikawa and Ogawa (1980) [7], figure 4, p. 408.  
Reprinted with permission of IEEE.

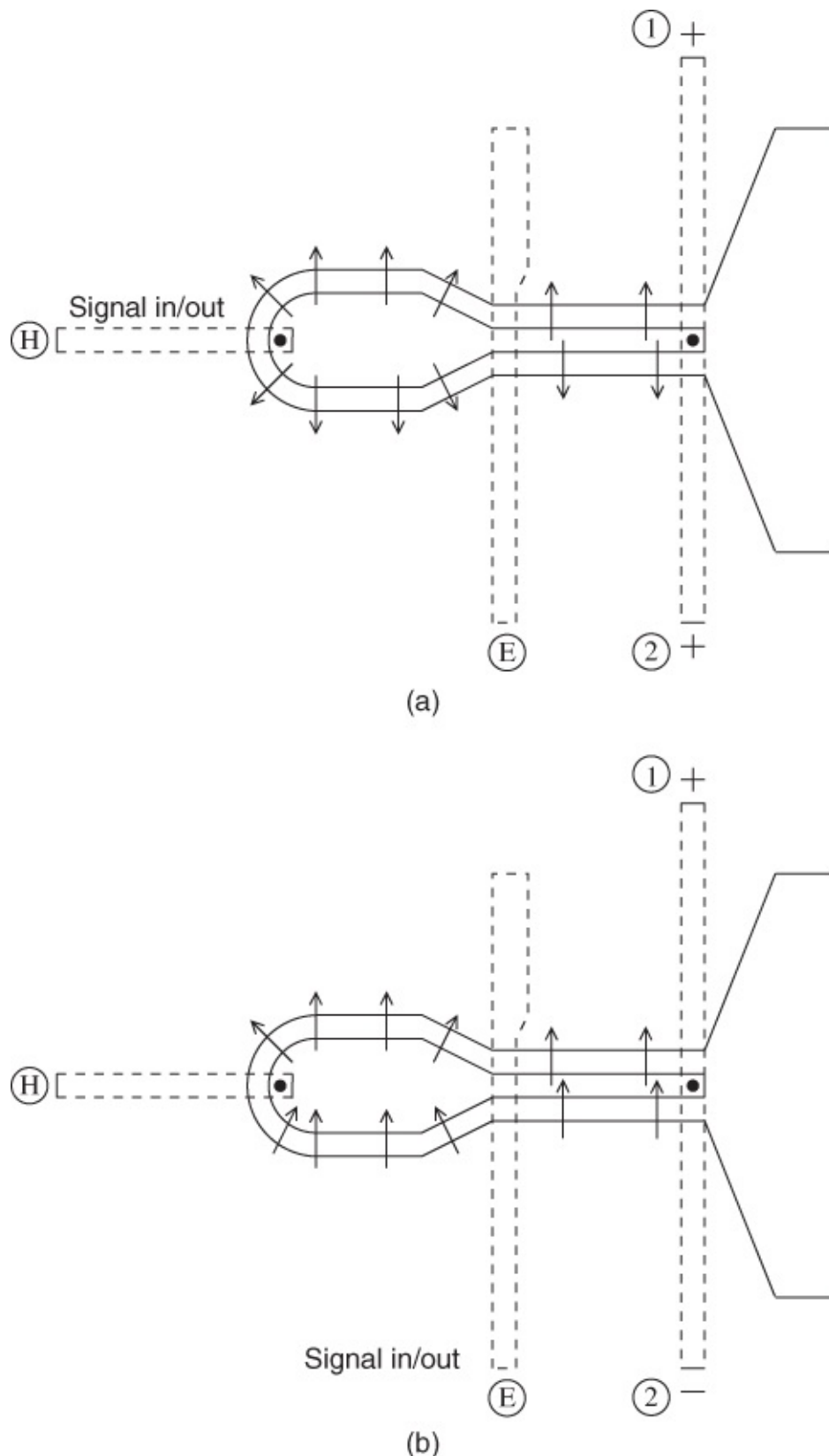


**Figure 16.14** Schematic behaviors for in-phase and out-of-phase couplings: (a) in-phase coupling (odd mode in the coupled slotlines); and (b) out-of-phase coupling (even-mode in the coupled slotlines). Adapted from Aikawa and Ogawa (1980) [7], figure 2, p. 524. Reprinted with permission of IEEE.

In this figure, arrows indicate the direction of the electric field in the slotlines, including the

coupled slotline. The odd and even modes in the coupled slotlines were defined in [Section 16.2.2](#). A signal fed to the microstrip port is converted to the slotline mode and divided into two quarter-wavelength long slotlines in parallel. Then, following propagation in the odd mode of the coupled slotlines, the signal is further divided between the two microstrip line ports (ports 1 and 2) in the in-phase coupling mode, as shown in [Figure 16.14\(a\)](#). In principle this in-phase power coupling has a wide frequency bandwidth because the coupling frequency band is limited only by the effect of the impedance transformer, which is provided if necessary. In reality, however, even a DC signal coupling is attainable only if the through-hole transition is employed at port  $\textcircled{H}$ , as shown in [Figure 16.13\(a\)](#) and (c). The capability of the DC electrical coupling is a striking advantage in practical applications because the ordinary types of  $180^\circ$  hybrids (e.g., rat-race, reverse-phase hybrid ring) do not have this capability. On the other hand, a signal fed to port  $\textcircled{E}$  is converted to the even-mode of the coupled slotline, and thereafter is divided between the two microstrip line ports, ports 1 and 2, which are  $180^\circ$  out-of-phase as shown in [Figure 16.14\(b\)](#). In this case, two quarter-wavelength slotlines (having characteristic impedance  $Z_H$ ) and a quarter-wavelength microstrip line (having characteristic impedance  $Z_E$ ) behave as quarter-wavelength short-circuited stubs and an open-circuited stub, respectively, as mentioned in the next section. The out-of-phase coupling frequency band is then limited due to the effect of these stubs. Aikawa and Ogawa [7] provide further details.

Aikawa and Ogawa also presented a schematic and equivalent circuit relating to a microstrip-type magic T ([Figure 16.15](#)) which is included here because it also involves slotlines.

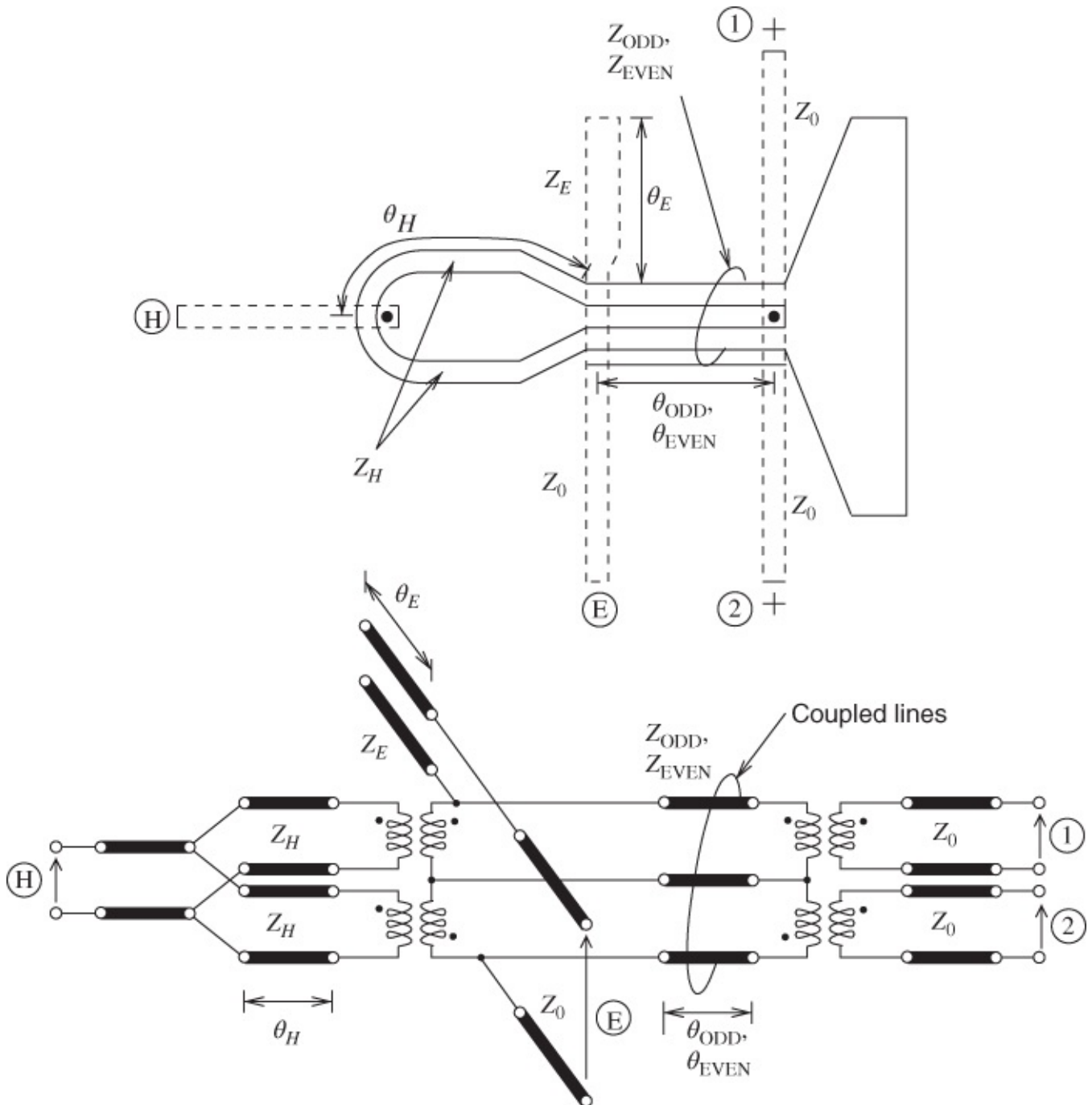


**Figure 16.15** Schematic and equivalent circuit of microstrip type magic T. Adapted from Aikawa and Ogawa (1980) [7], figure 3, p. 525. Reprinted with permission of IEEE.

Aikawa and Ogawa [7] provide the following equations for the isolation and return losses respectively:

$$\text{isolation} = -20 \log \frac{1}{2} |\Gamma_{++} - \Gamma_{+-}| (\text{dB}) \quad 16.3$$

$$\text{return loss} = -20 \log \frac{1}{2} |\Gamma_{++} + \Gamma_{+-}| (\text{dB}), \quad 16.4$$

in which  $\Gamma_{++}$  and  $\Gamma_{+-}$  are the appropriate port reflection coefficients. This isolation and return

loss can be expressed in terms of a ratio involving the odd- and even-mode phase angles.

In [Figure 16.16](#) the letters and numbers in circles relate to [Figure 16.15](#). Clearly as the difference between the odd- and even-mode phases grows, so the isolation and the return loss both decrease substantially. In all cases the asymptote is approximately 15 dB.

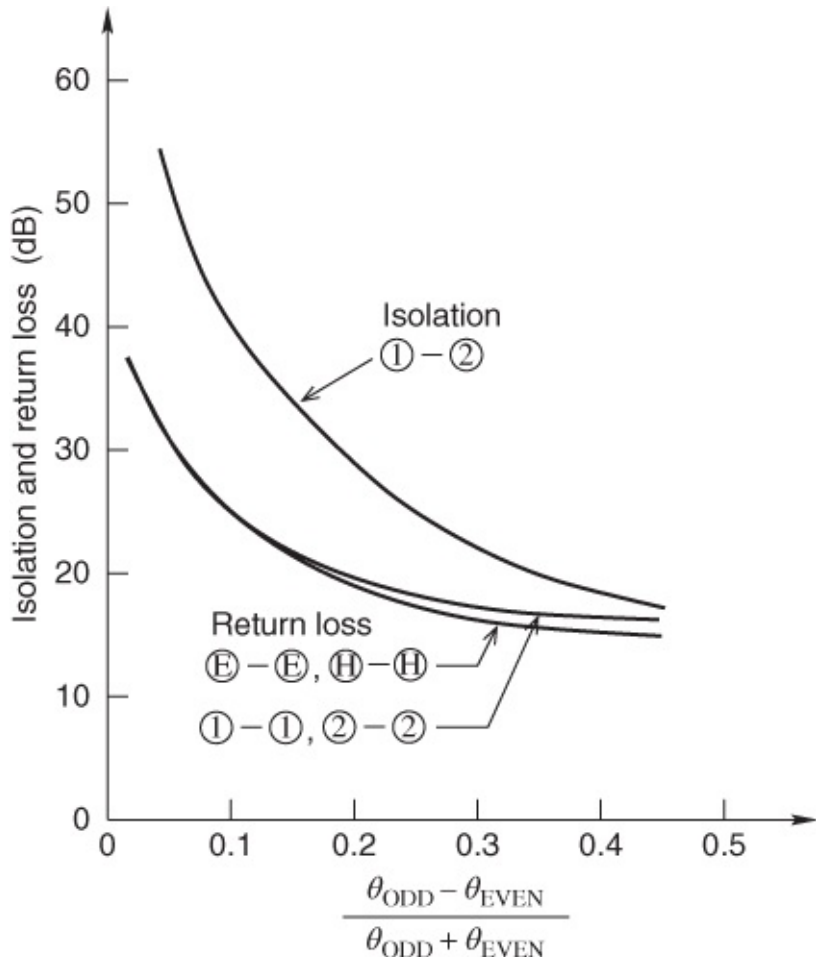


[Figure 16.16](#) Obtainable isolation and return loss at the average center frequency, where  $(\theta_{EVEN} + \theta_{ODD})/2$  is  $\pi/2$ . Note that  $(\theta_{ODD} - \theta_{EVEN})/(\theta_{ODD} + \theta_{EVEN})$  is the normalized length deviation.  $Z_H/Z_0 = 2.0$ ,  $Z_E/Z_0 = 0.8$ ,  $Z_{EVEN}/Z_0 = 1/\sqrt{2}$ , and  $Z_{ODD}/Z_0 = \sqrt{2}$ . Adapted from Aikawa and Ogawa (1980) [7], figure 7, p. 527. Reprinted with permission of IEEE.

## 16.5 The Marchand Balun

It is well known that the basic function of any balun is to transform a single-ended input signal into a balanced output. The conventional Marchand balun achieves this by implementing coupled quarter-wave sections of transmission lines as shown in [Figure 16.17](#).

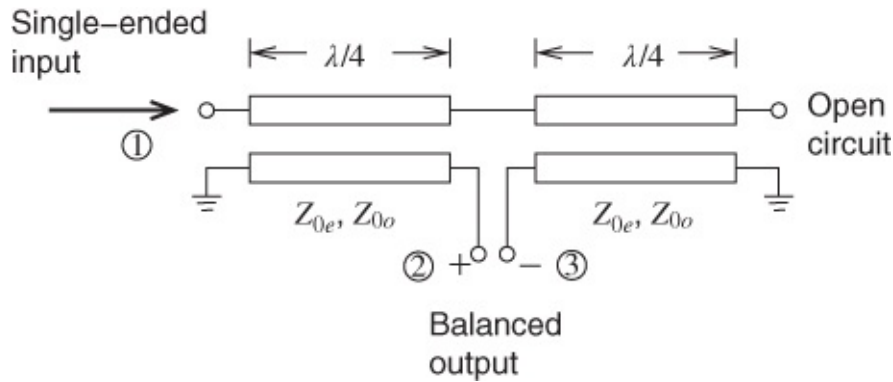


**Figure 16.17** Circuit configuration of the conventional Marchand balun.

Tseng and Hsiao [8] introduced a slotline Marchand balun (also a slot-coupled microstrip balun). The details are shown in [Figure 16.18](#). Design widths of the strip A and the slot depend on the length and width parameters defined in [Figure 16.18](#). Tseng and Hsiao [8] give the results for these design expressions as follows:

$$A_{\text{strip}} = LW_t + 2 \frac{\left[ \frac{1}{2} (L + L/3) (W_p - W_t) \right]}{2} = \frac{1}{3} (LW_t + 2LW_p) \quad 16.5$$

and

$$A_{\text{slot}} = \frac{1}{3} (LW_t + 2LW_s). \quad 16.6$$

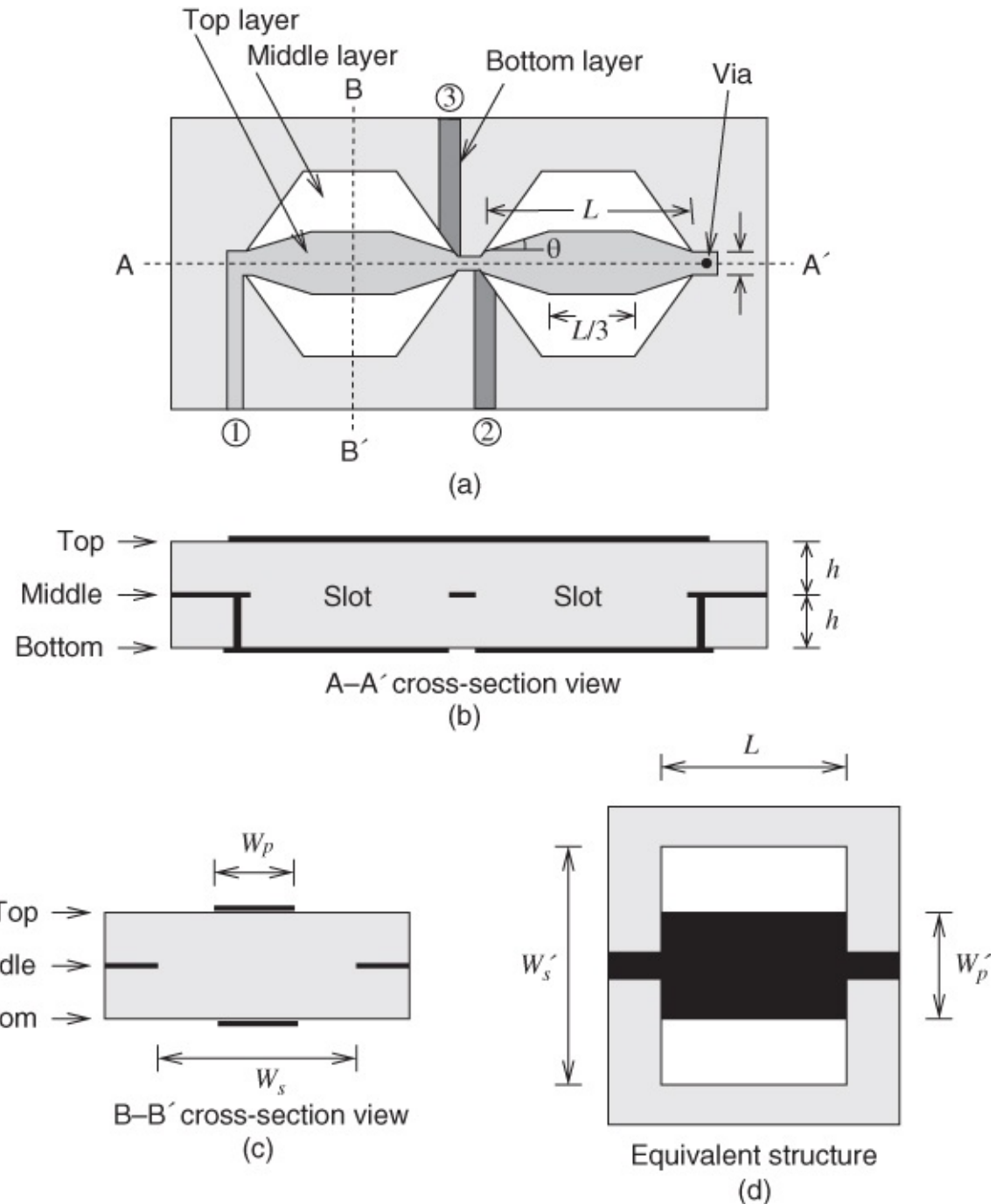


**Figure 16.18** Slotline Marchand balun: (a) Marchand balun using slot-coupled microstrip lines, and its (b) A-A' and (c) B-B' cross-sectional views; and (d) the equivalent structure of the diamond-shape slot-coupled microstrip line. Adapted from Tseng and Hsiao (2010) [8], figure 2, p. 157. Reprinted with permission of IEEE.

Tseng and Hsiao calculated the odd- and even-mode characteristic impedances as functions of the slot width and with strip width as parameter. The results are given in [Figure 16.19](#).

Photographs of the slotline Marchand balun are given in [Figure 16.20](#). The circuit-board area is approximately 4 cm × 6 cm. Covering a 0.5–4 GHz frequency range, Tseng and Hsiao performed simulations and also measured the  $S$  parameters associated with this slotline Marchand balun. The results are shown in [Figure 16.21](#). Simulated and measured results are in broad agreement.

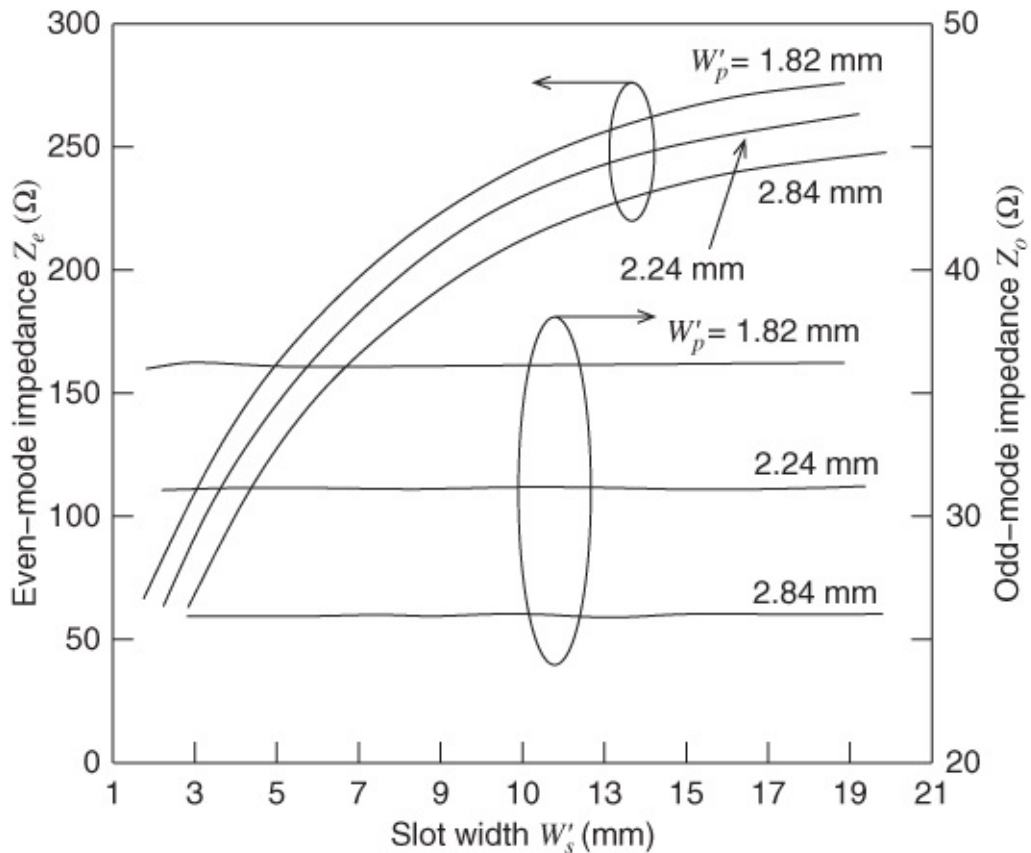


**Figure 16.19** Even-mode and odd-mode impedances versus the slot and strip widths. Adapted from Tseng and Hsiao (2010) [8], figure 3, p. 158. Reprinted with permission of IEEE.

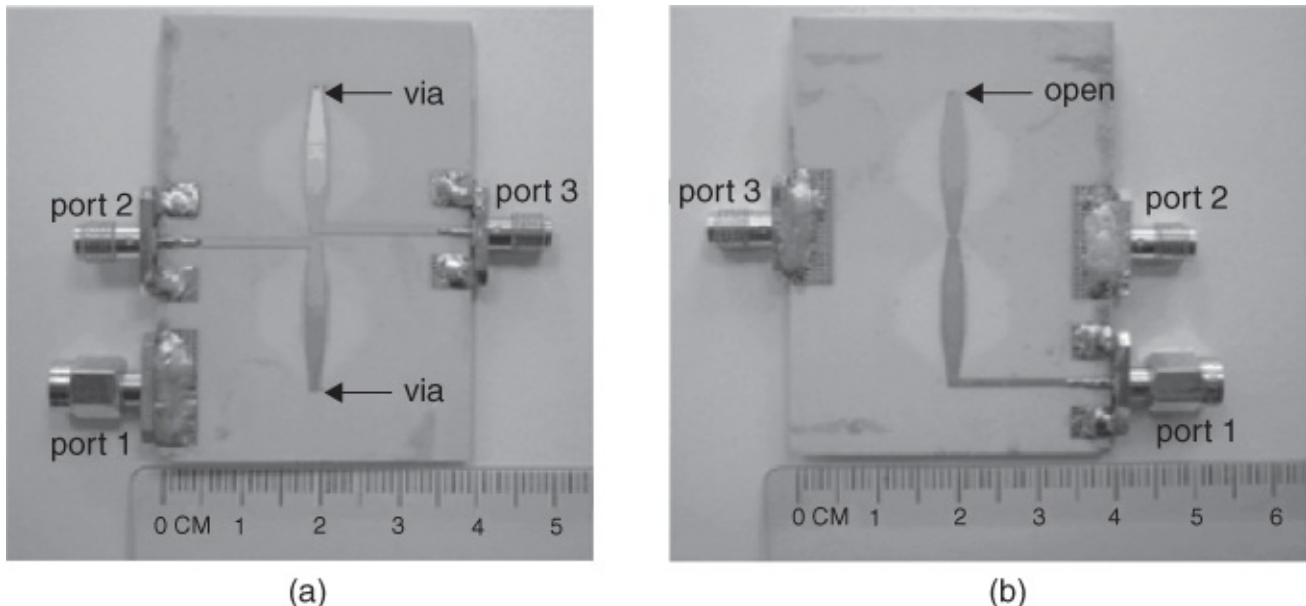
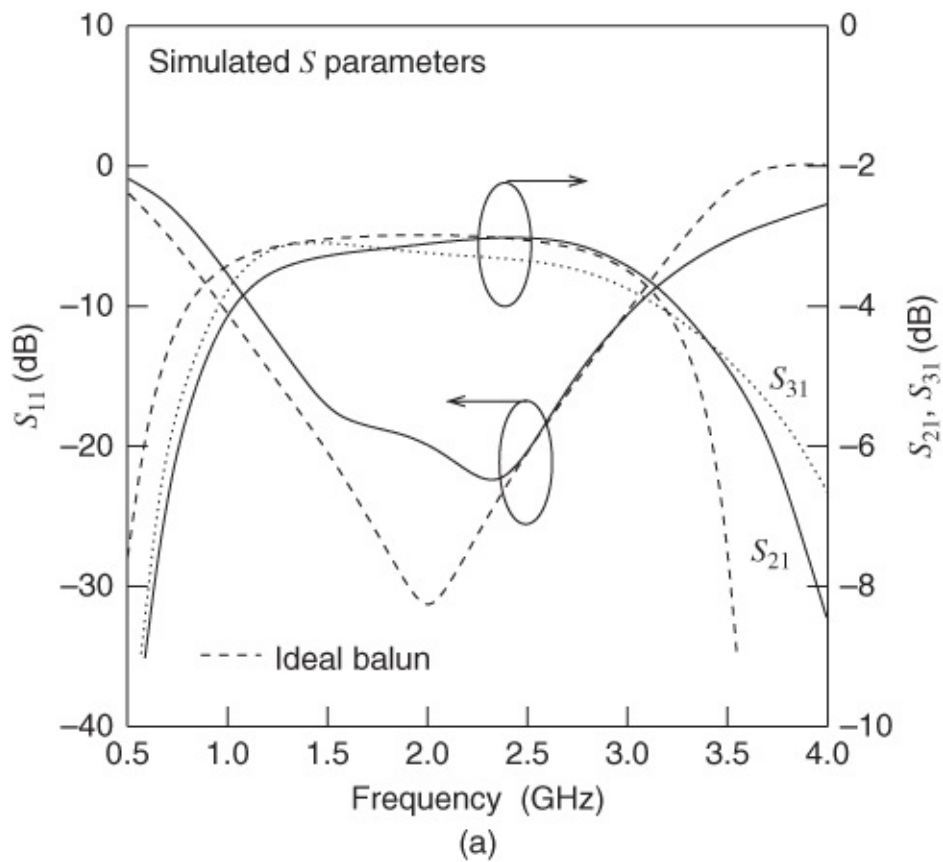
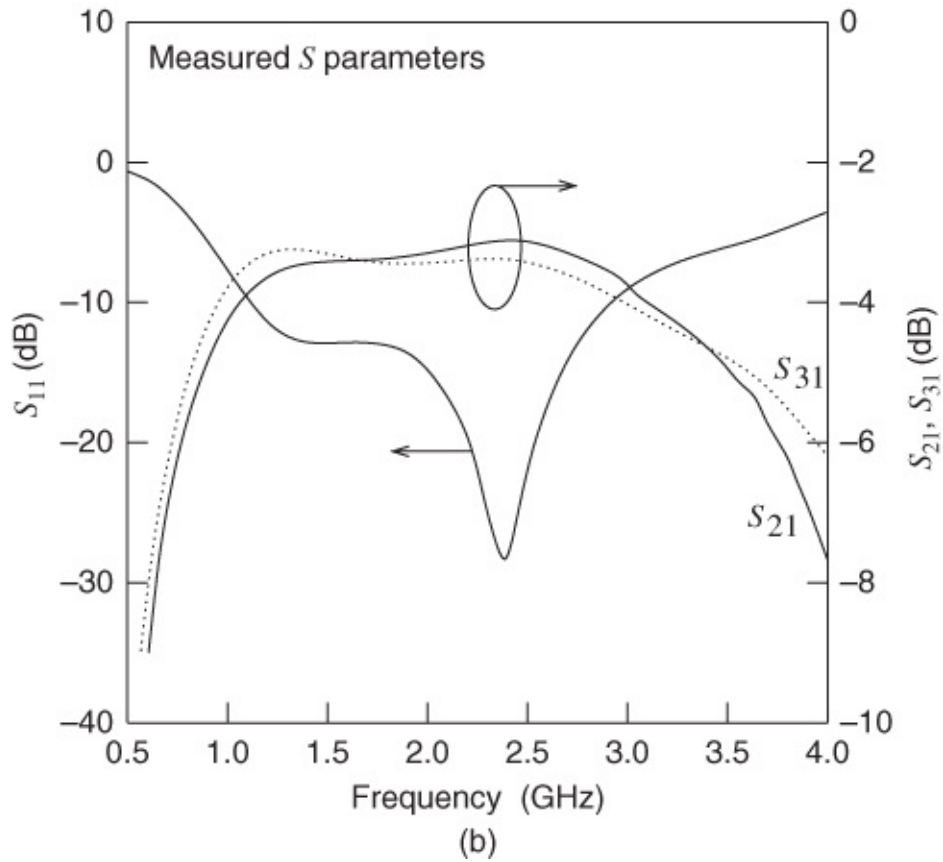


**Figure 16.20** Circuit photographs of (a) top and (b) bottom views of the slotline Marchand balun. Adapted from Tseng and Hsiao (2010) [8], figure 4, p. 158. Reprinted with permission of IEEE.



(a)



(b)

**Figure 16.21**  $S$  parameters for the slotline Marchand balun. Adapted from Tseng and Hsiao (2010) [8], figure 5, p. 159. Reprinted with permission of IEEE.

## 16.6 Phase Shifters

El-Sharawy *et al.* [9] presented a paper aimed at a phase-shifter application. The geometry of their multilayer microstrip-slotline is shown in [Figure 16.22](#). El-Sharawy and Jackson were primarily interested in phase shifter applications and as a result the differential phase shift was their major focus. The effect of dimensions  $W$  and  $S$  are shown in [Figure 16.23](#). For example, using the data in [Figure 16.23](#), setting  $S$  at 1 mm and with  $W$  anywhere in the range 0.5 to 1 cm (or wider) leads to a differential phase shift of  $30^\circ$ .

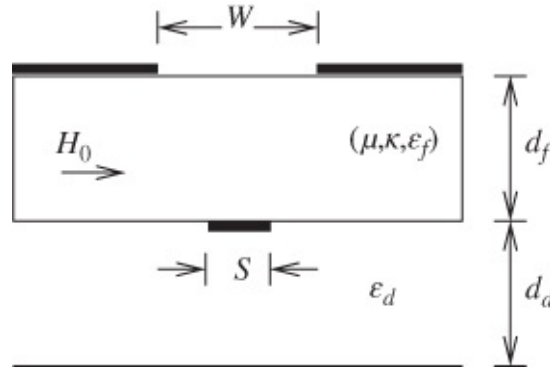


[Figure 16.22](#) Geometry of a multilayer microstrip-slotline. Adapted from El-Sharawy and Jackson (1990) [9], figure 5, p. 280. Reprinted with permission of IEEE.

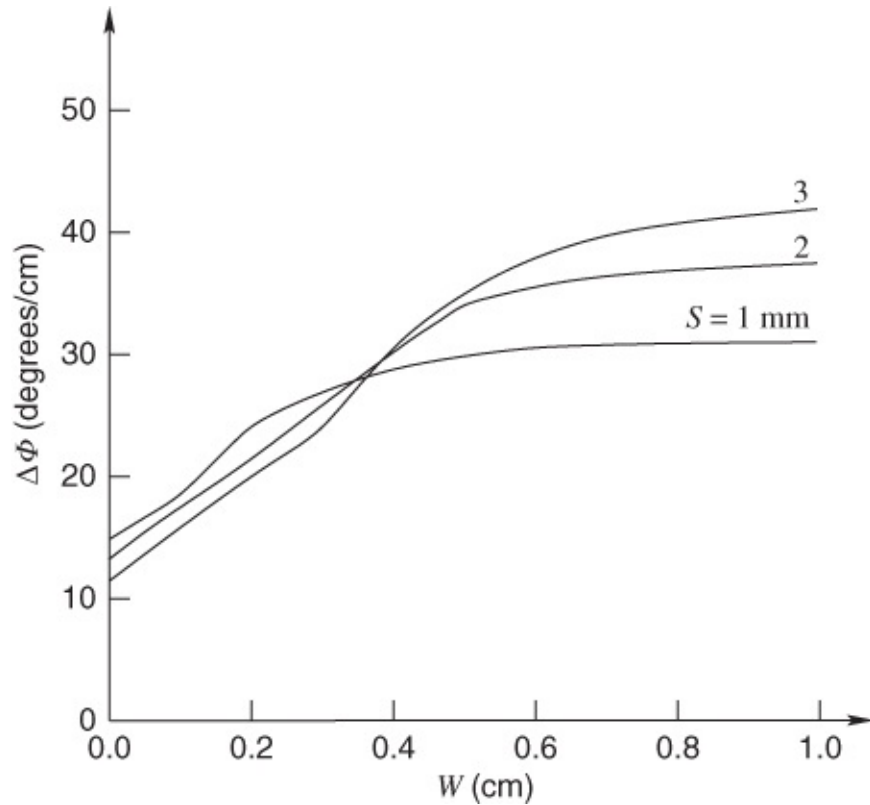


[Figure 16.23](#) Effect of microstrip-slot dimensions on differential phase shift in the multilayer structure of [Figure 16.22](#). Adapted from El-Sharawy and Jackson (1990) [9], figure 6, p. 280. Reprinted with permission of IEEE.

These workers also reported on the effects of the addition of a low-permittivity dielectric

layer and the geometry of this is shown in [Figure 16.24](#). El-Sharawy and Jackson found that the addition of the top layer of low-dielectric material served to approximately double the differential phase shift (range: 55–60°) but also to cause cyclical variations with frequency across the 6–9 GHz band.

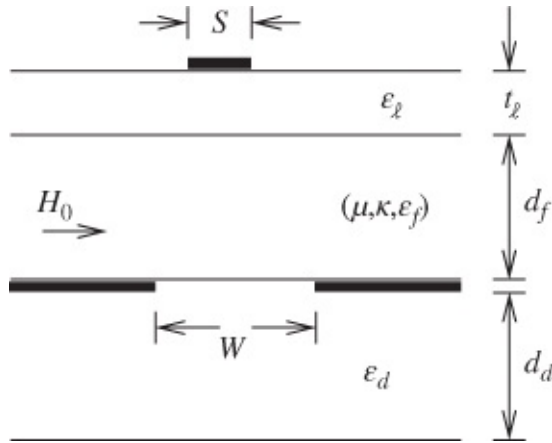
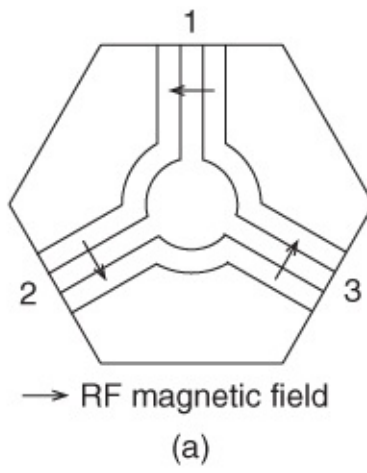


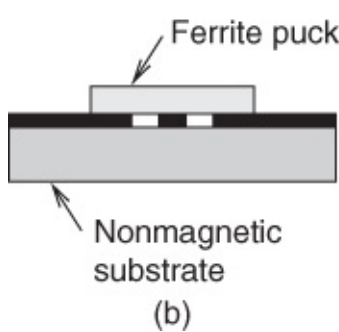
**Figure 16.24** Geometry of structure (derived from that of [Figure 16.22](#)) with an additional top layer of low-dielectric material. Adapted from El-Sharawy and Jackson (1990) [9], figure 9, p. 281. Reprinted with permission of IEEE.

## 16.7 Isolators and Circulators

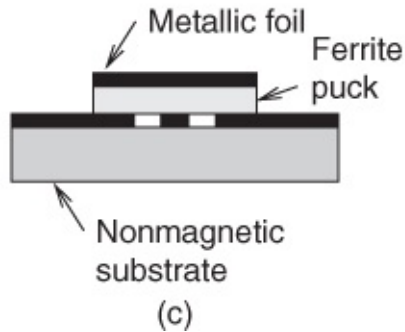
For many decades, starting way back when microwave engineering was almost synonymous with the use of rectangular waveguides, the requirement for a passive device allowing passage of a forward signal with low insertion loss whilst mainly blocking reverse signals was furnished by what is termed a ferrite isolator. Today such isolators are still realized in rectangular waveguides for high-power applications but also in planar microwave circuit configurations for lower-power systems. With the concept extended to three ports (compared with two for an isolator) the more extensively applicable circulator device is realized. Microstrip circulators are considered elsewhere in this book but here we look at slotline circulators. Several specific realizations of Y-type slotline circulators are shown in cross-section in [Figure 16.25](#).



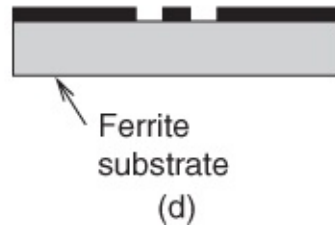
(a)



(b)



(c)



(d)

**Figure 16.25** Physical configurations of slot-guide Y circulators: (a) common top view; (b) stack without metal cap; (c) stack with metallic foil as a cap; and (d) ferrite substrate on its own. Adapted from Ogasawara and Kaji (1971) [10], figure 2, p. 220. Reprinted with permission of the Institution of Engineering and Technology.

[Figure 16.25\(a\)](#) is a schematic top view of the overall configuration. The three ports and the RF magnetic fields are visible. [Figure 16.25\(b\)–\(d\)](#) are cross-sections of three different physical structures: (b) ferrite puck on top of the slotline; (c) like (b) but with metallic foil top cover; and (d) ferrite substrate.

Ogasawara and Kaji [10] measured the insertion loss and isolation (transmission loss) versus the applied DC magnetic field for an experimental coplanar-guide Y-type circulator having a structure basically identical to that shown in [Figure 16.25\(d\)](#). Their results are shown in [Figure 16.26](#).

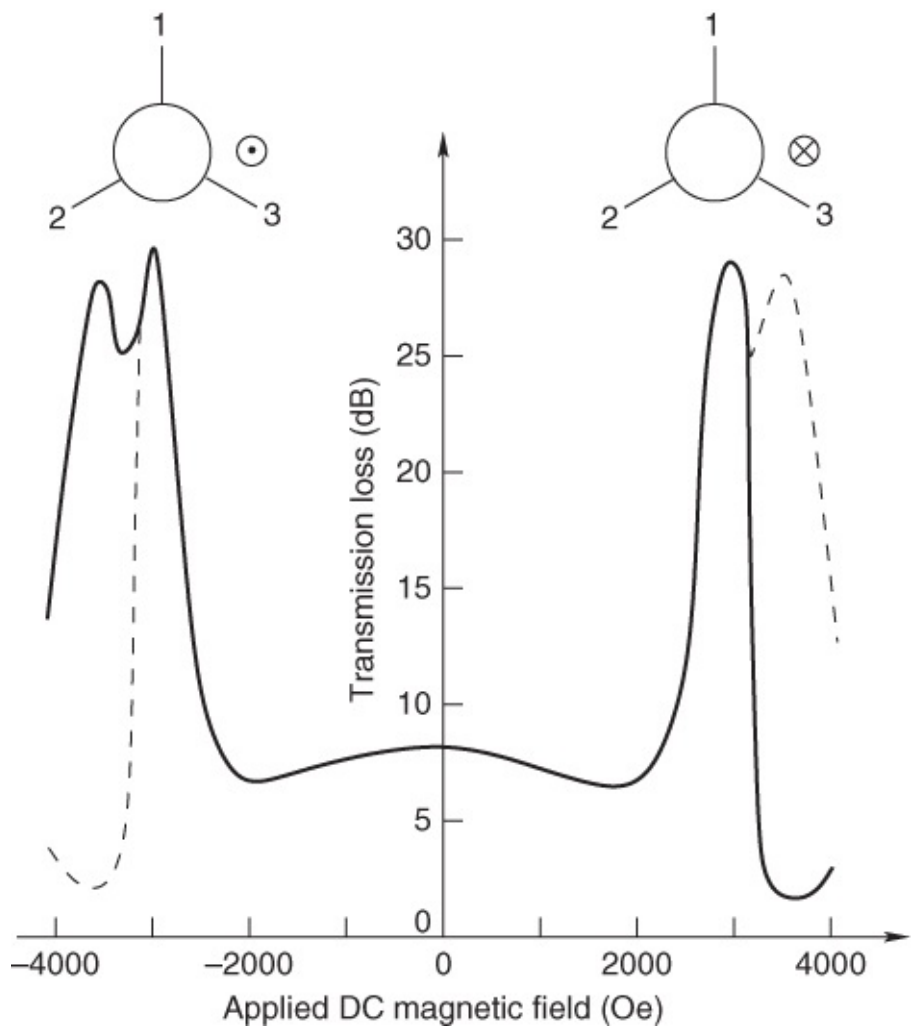


**Figure 16.26** Insertion loss and isolation versus DC magnetic field as measured on the experimental coplanar-guide Y circulator illustrated in [Figure 16.25\(d\)](#). Adapted from Ogasawara and Kaji (1971) [10], figure 3, p. 221. Reprinted with permission of the Institution of Engineering and Technology.

The left-hand side of this graph applies to the DC magnetic field “coming out” of the plane of the circulator whilst the right-hand side of this graph applies to the DC magnetic field “entering into” the plane of the circulator. In both cases there is a pronounced peak in the characteristic but for the left-hand side situation there is actually a double peak and the high loss is maintained over approximately twice the range of applied magnetic field compared with the right-hand side situation.

Courtois and de Vecchis [11] investigated the distribution of energy in a slotline circulator enclosed in rectangular metallic shielding. The slotline is built on a relatively thin alumina substrate, itself sandwiching the ferrite substrate, which is backed by an energy-absorbing layer. This structure is shown in [Figure 16.27\(a\)](#) whilst the distribution of RF energy is indicated in [Figure 16.27\(b\)](#). The DC magnetic field ( $H$ ) is applied transversely across this structure. For both the direct wave and the reverse wave the RF energy is largely trapped within the ferrite substrate. The RF energy applying to the direct wave steadily increases within the ferrite substrate and maximizes at the alumina–ferrite junction interface. Conversely,

the RF energy applying to the reverse wave steadily decreases within the ferrite substrate and minimizes at the ferrite–absorber junction interface.

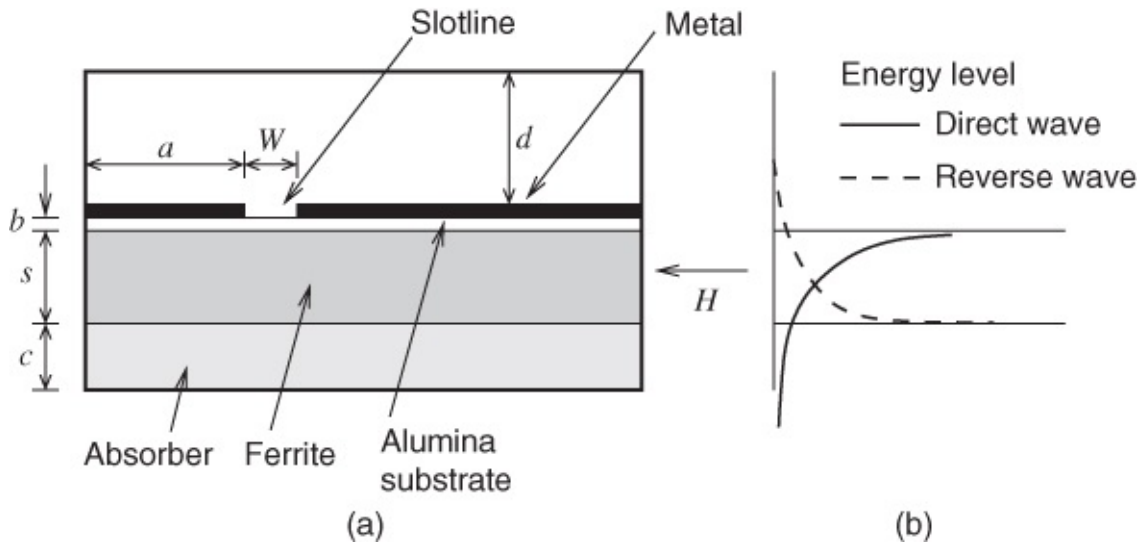


**Figure 16.27** Enclosed slotline circulator: (a) structure of the device; and (b) distribution of energy in the ferrite slab. Adapted from Courtois and de Vecchis (1975) [11], figure 1, p. 512. Reprinted with permission of IEEE.

## 16.8 A Double-sided, Balanced Microwave Circuit

Based on their slotline–stripline T junction work ([Section 16.4](#)), Aikawa and Ogawa [6] reported a double-sided balanced microwave circuit incorporating a phase-shift keying (PSK) modulator, a phase detector, and a mixer. The arrangement is depicted schematically in [Figure 16.28](#). As a PSK modulator the modulating pulse is supplied to the diodes through the microstrip line (B). The carrier propagates along each slotline according to the polarity of the modulating pulse. If the balanced circuit is used as a mixer, an intermediate frequency (IF) signal is obtained from the wire port (U). The isolation between the RF and local oscillator (LO) ports depends on the uniformity of the two Schottky mixing diodes.

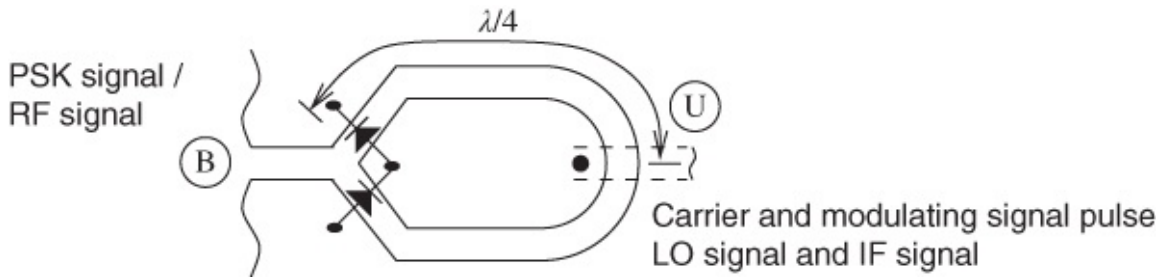


**Figure 16.28** Double-sided balanced microwave circuit with a PSK modulator, phase detector, and mixer. Adapted from Aikawa and Ogawa (1989) [6], figure 15, p. 411. Reprinted with permission of IEEE.

## 16.9 Summary

In this chapter we concentrated on a range of circuits involving slotlines. In particular we have provided details on the following classes of circuits: comparators, couplers, filter applications, magic Ts, the Marchand balun, phase shifters, isolators and circulators, and a double-sided balanced microwave circuit.

## References

- [1] G. Riblet, “Compact planar microstrip-slotline symmetrical ring eight-port comparator circuits,” *IEEE Trans. on Microwave Theory and Techniques*, vol. **38**, no. 10, pp. 1421–1426, Oct. 1990.
- [2] J. Knorr and K. Kuchler, “Analysis of coupled slots and coplanar strips on dielectric substrate,” *IEEE Trans. on Microwave Theory and Techniques*, vol. **23**, no. 7, pp. 541–548, Jul. 1975.
- [3] A. Abbosh and M. Bialkowski, “Design of compact directional couplers for UWB applications,” *IEEE Trans. on Microwave Theory and Techniques*, vol. **55**, no. 2, pp. 189–194, Feb. 2007.
- [4] E. Mariani and J. Agrios, “Slot-line filters and couplers,” *IEEE Trans. on Microwave Theory and Techniques*, vol. **18**, no. 12, pp. 1089–1095, 1970.
- [5] S. B. Cohn, “Slot line on a dielectric substrate,” *IEEE Trans. on Microwave Theory and Techniques*, vol. **17**, no. 10, pp. 768–778, Oct. 1969.
- [6] M. Aikawa and H. Ogawa, “Double-sided MICs and their applications,” *IEEE Trans. on Microwave Theory and Techniques*, vol. **37**, no. 2, pp. 406–413, Feb. 1989.
- [7] M. Aikawa and H. Ogawa, “A new MIC magic-T using coupled slot lines,” *IEEE Trans. on Microwave Theory and Techniques*, vol. **28**, no. 6, pp. 523–528, Jun. 1980.
- [8] C.-H. Tseng and Y.-C. Hsiao, “A new broadband marchand balun using slot-coupled microstrip lines,” *IEEE Microwave and Wireless Components Letters*, vol. **20**, no. 3, pp. 157–159, Mar. 2010.
- [9] E. El-Sharawy and R. Jackson, “Analysis and design of microstrip-slot line for phase shifting applications,” *IEEE Trans. on Microwave Theory and Techniques*, vol. **38**, no. 3, pp. 276–283, Mar. 1990.
- [10] N. Ogasawara and M. Kaji, “Coplanar-guide and slot-guide junction circulators,” *Electronics Letters*, vol. **7**, no. 9, pp. 220–221, 1971.
- [11] L. Courtois and M. Vecchis, “A new class of nonreciprocal components using slot line,” *IEEE Trans. on Microwave Theory and Techniques*, vol. **23**, no. 6, pp. 511–516, Jun. 1975.

# Chapter 17

## Transitions

### 17.1 Introduction

This chapter describes transitions between different types of transmission lines. The majority of these transitions are between microstrip and one of the other planar transmission line mediums, for example we consider transitions between microstrip and slotline, stripline, and CPW. We also consider transitions to coaxial line and rectangular waveguide. Transitions necessarily introduce discontinuities as the electric and magnetic field orientations are changed. This results in electric and magnetic energy storage and this necessarily introduces frequency dependence and limits bandwidth, primarily setting the upper frequency limit of transitions. Other considerations are the excitation of higher-order modes.

### 17.2 Coaxial-to-microstrip Transitions

These are available in a variety of forms, the choice mainly depending on the overall electrical quality required. For noncritical applications, commercially produced transitions, operating from semi-rigid (3.58 mm diameter) coaxial lines, are available from a number of companies. The final contact to the microstrip is variously formed as a wedge or a tab. In most applications the wedge will probably be preferred as it is more mechanically rugged. Some connections to a microstrip circuit can often be made with comparatively low-grade (and therefore relatively cheap) transitions, for DC bias ports inexpensive BNC connectors can simply be used. Where only temporary connection is required, a pressure contact is quite satisfactory. A permanent transition will usually be completed with some form of epoxy bond surrounding the tab-microstrip metals.

It will be appreciated that the transition region, from the ‘cylindrical’ coaxial structure to the planar rectangular microstrip, presents quite a considerable discontinuity in the system. When used in conjunction with a microstrip line having  $50 \Omega$  characteristic impedance the commercial transitions typically yield a voltage standing wave ratio (VSWR) equal to 1.06 at moderate (e.g., X-band) frequencies. This is adequate for a wide variety of operating circuit and system applications.

In critical situations, such as measurement arrangements, a far superior VSWR performance is often desired and various compensation techniques have been developed. For a microwave transistor characterization jig a form of screw compensation has been developed [1]. A metal screw is introduced through a hole in the jig beneath the ground plane, in the vicinity of the transition. There is a further hole in line with this and actually in the ground plane, thus exposing a small region of the substrate underside surface (this arrangement can be seen in [Figure 17.1\(b\)](#)). The exact field situation is complex, but it seems clear that the screw mainly

serves to reduce the microstrip line capacitance very locally so as to compensate (reduce) the transition capacitance. Extremely careful manufacture and time-domain reflectometry measurements have resulted in the transition shown in [Figure 17.1](#) [2]. The dimensions shown apply to a transition launching into a  $50 \Omega$  microstrip line on a 0.5 mm thick sapphire substrate (C axis perpendicular to the ground plane), and a reflection coefficient less than 0.01 was obtained. With some extra dimensional and shape refinements, described in the paper, the achievement amounts to a reflection coefficient less than 0.005 (VSWR  $\approx 1.01$ ) over the range  $1 \leq f \leq 18$  GHz. Over the same frequency range, the insertion loss was less than 0.3 dB.

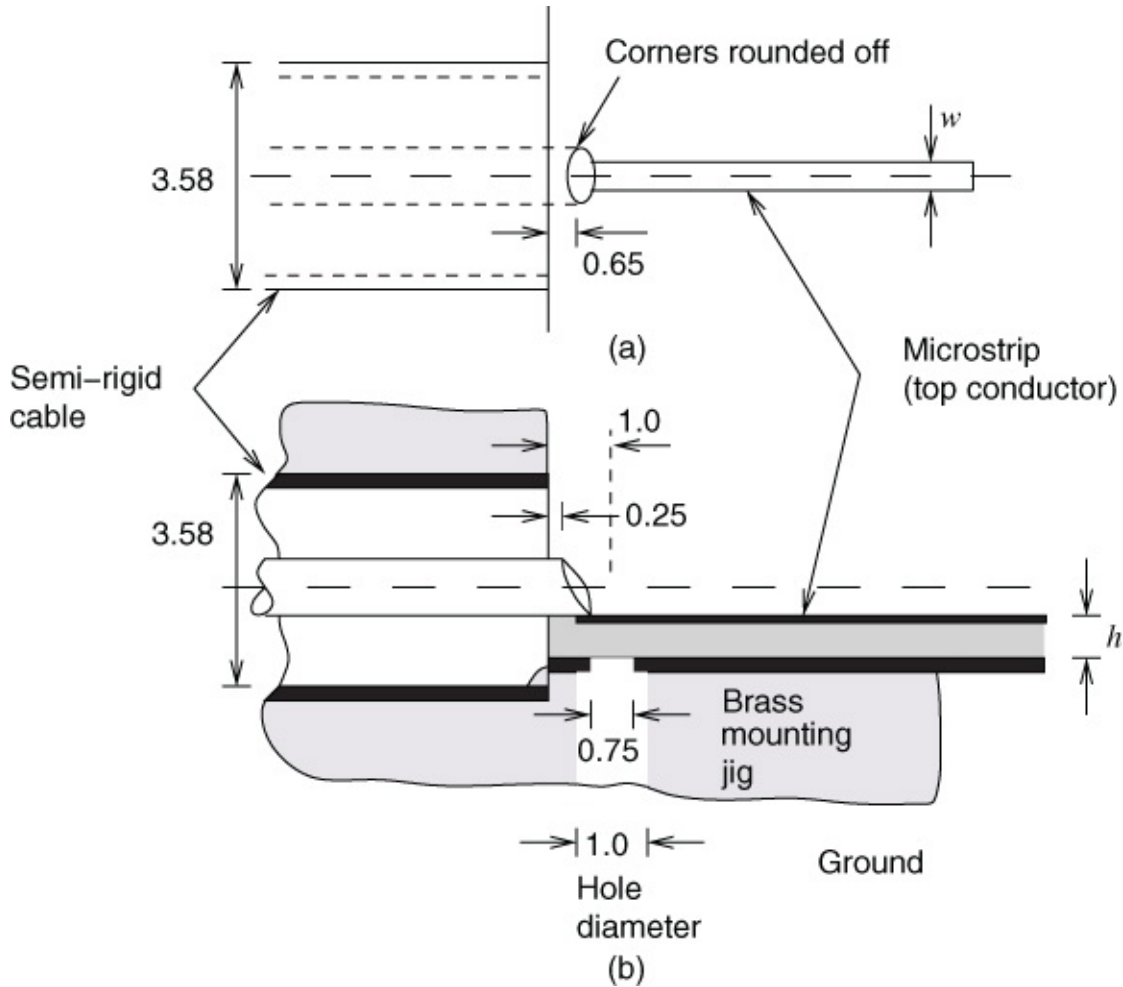


[Figure 17.1](#) Compensated coaxial-microstrip transition (all dimensions in millimeters): (a) plan view; and (b) longitudinal section. The width of the microstrip strip is *w* and the thickness of the substrate *h* = 0.5 mm. Adapted from England (1976) [2], figure 1, p. 47. Reprinted with permission of IEEE.

The use of alumina substrates demands some modifications. For a similar performance a 1.0 mm diameter ground-plane hole was found to be necessary, where the microstrip characteristic impedance is approximately  $50 \Omega$ . For further details the reference should be consulted.

In the case of a different substrate (thickness and/or permittivity), it is necessary to repeat these careful measurements with a cut-and-try approach.

Surface coaxial-to-microstrip transitions are available with the center pin of the extended

coaxial line inserting through the substrate but of course the backing ground plane of the microstrip must be locally removed to avoid shorting the pin. Outer pins from the coaxial adaptor do make contact with the ground plane. Sometimes the grounding pins are removed and replaced by a surface mount connection. If the pin also makes surface contact the bandwidth of the transition is increased. An example of this type of transition is given in [Figure 1.3](#), where it is identified by A. Surface-mounted connectors have a lower bandwidth than the side connecting adaptors.

## 17.3 Waveguide-to-microstrip Transitions

At millimeter-waves the principal external transmission medium prior to microstrip is rectangular waveguide and so a waveguide-to-microstrip transition is required. Since the waveguide itself is relatively narrowband the transitions are also only required to operate over typically 10–50% bandwidths.

One essentially very narrowband solution is to first introduce a waveguide-to-coaxial line transition (the T-transformer, for example) and then to follow this with a coaxial line-to-microstrip transition as already described. This may be convenient in some restricted cases.

Transitions of improved bandwidth and with other advantages are, however, conceivable. The desirable features of a waveguide-to-microstrip transition are:

- low return loss, which means that inherent reflections will be low and reflection measurements may be made on the microstrip circuit
- low insertion loss
- sufficient bandwidth for the application
- fairly easy and well reproducible re-connection to the microstrip
- an in-line design for ease of connecting test equipment
- straightforward mechanical reproduction.

Several different solutions to the problem have been presented in the literature and some contrasting techniques will be presented here.

### 17.3.1 Ridgeline Transformer Insert

In the design approach of Schneider *et al.* [3], the waveguide impedance is transformed to the microstrip impedance by use of a fairly broadband stepped ridgeline transformer which is mechanically connected to the microstrip by a tab and a single pressure screw. A four-step ridgeline transformer designed to work over the 29.5–31.3 GHz band gave more than 30 dB return loss (reflection coefficient  $< 0.03$ ) and less than 0.1 dB insertion loss over the band. A quartz substrate of 0.96 mm thickness was used for the microstrip circuit and the arrangement is shown in [Figure 17.2](#).

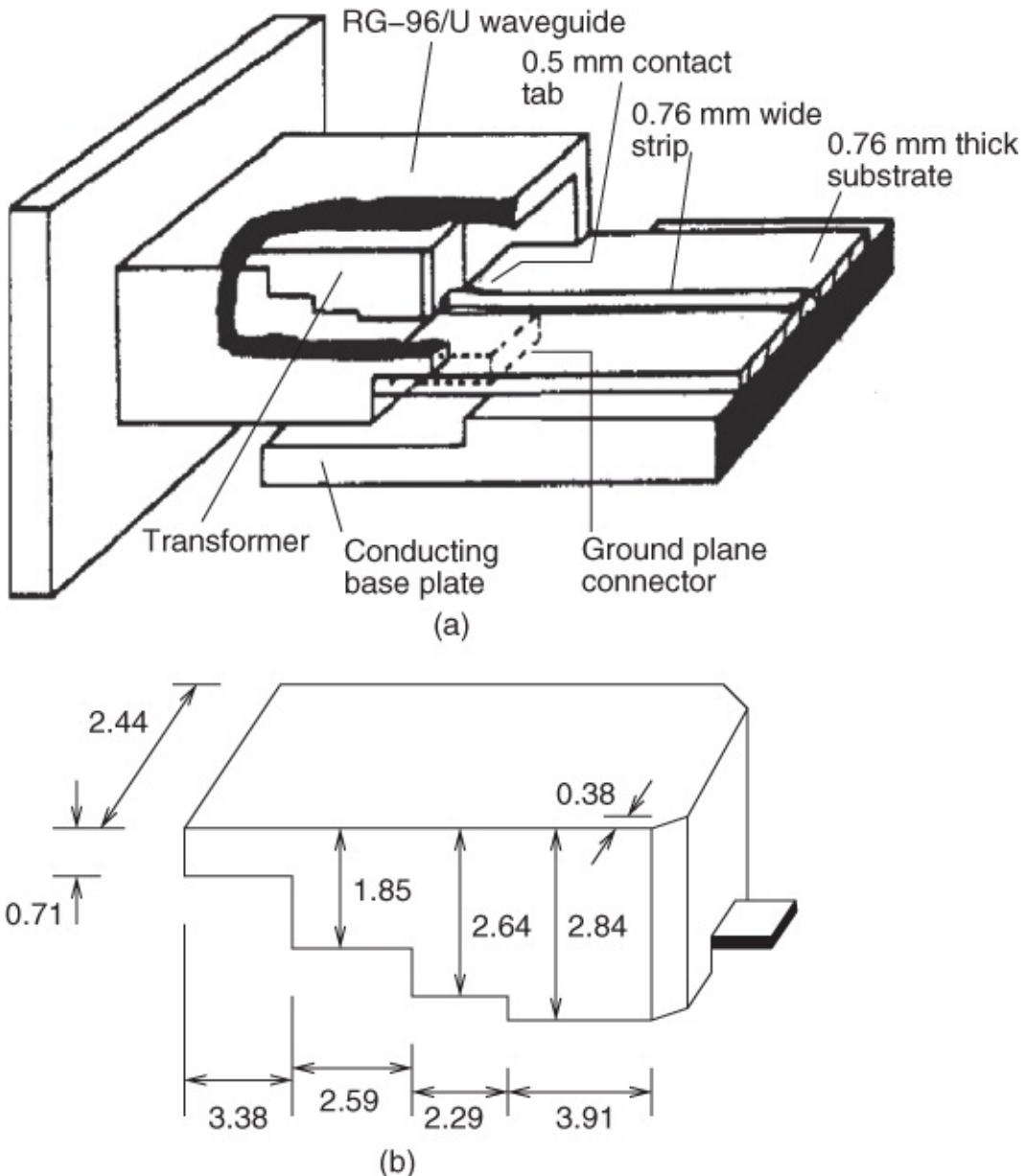


**Figure 17.2** Rectangular waveguide-to-microstrip transition using a ridgeline transformer for the 27.5–31.3 GHz band: (a) complete mechanical structure; and (b) ridgeline transformer dimensions (all in millimeters). Adapted from Schneider *et al.* (1969) [3], figure 5, p. 1717. Reprinted with permission of the American Telephone and Telegraph Company.

For a required bandwidth and return loss, the necessary impedance at each step in the transformer can be calculated using Cohn's design method [4]. The stepped single ridgeline selected is quite compatible with the asymmetrical microstrip line. It is also easily machined and connected to the waveguide. The mechanical dimensions required of ridgeline structures, to realize a specified impedance, can be calculated from information given by Hopfer [5]. So that the substrate will stop against the ridgeline, the last (deepest) step of this ridgeline is made sufficiently deep, 2.84 mm in this case. By tapering the edge of the transformer at the junction, the local reactance there is decreased, hence improving the performance.

Good contact is maintained both to the microstrip and its ground plane by applying pressure via a single insulated screw operating on the contact RG-96/U waveguide tab (this screw is

not shown in [Figure 17.2](#)). For further details the paper by Schneider *et al.* [3] should be consulted. The photograph of a similar transition is shown in [Figure 17.3\(a\)](#) and details of its structure are shown in [Figure 17.3\(b\)](#).

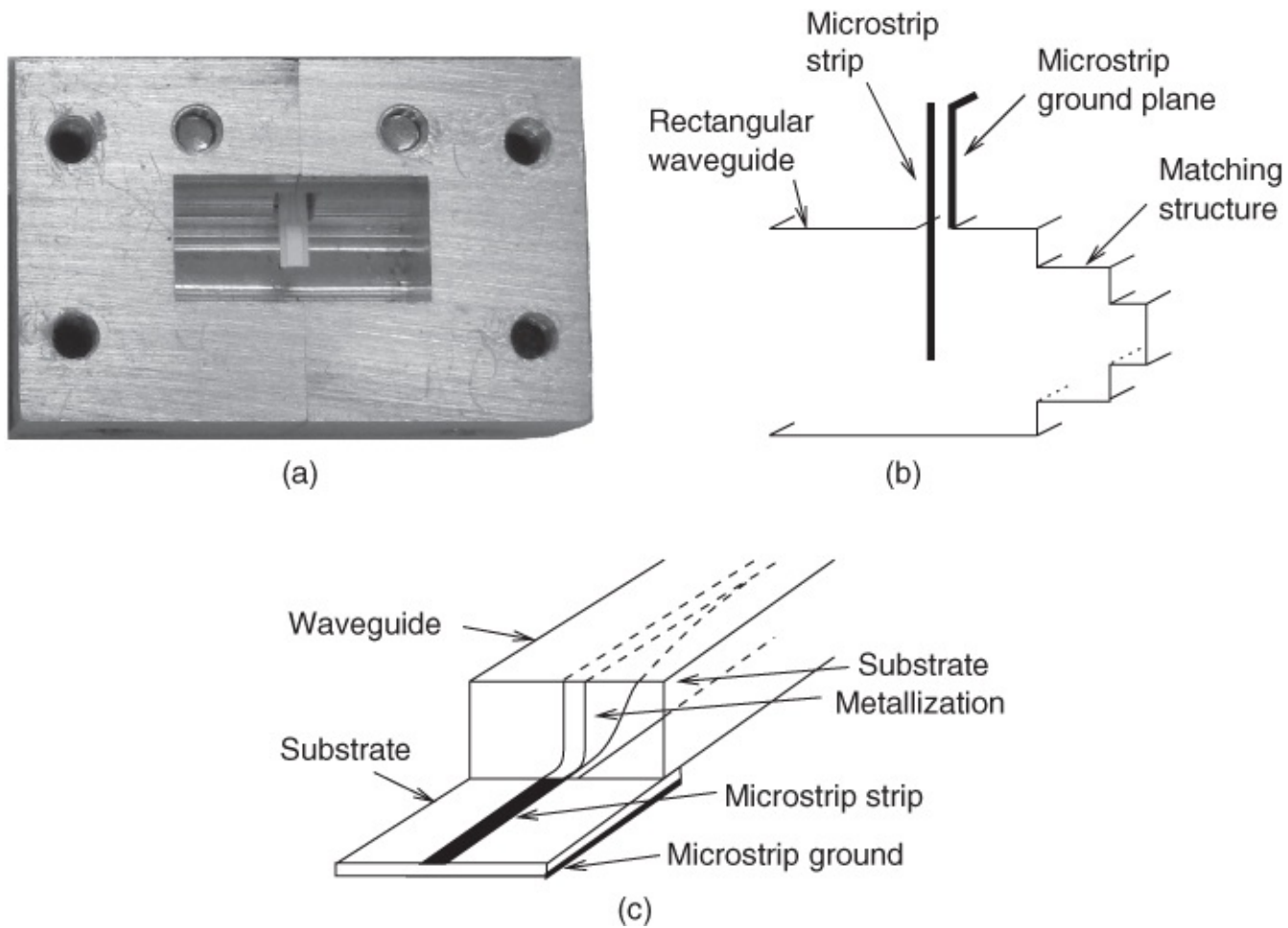


**Figure 17.3** Microstrip transitions: (a) photograph of a 15 GHz microstrip-to-waveguide transition; (b) cross-section of structure in (a); and (c) alternative microstrip to waveguide transition using a ridge. Figure (c) adapted from Menzel and Klaassen (1989) (1989) [6], figure 1, p. 1265. Reproduced with the permission of the European Microwave Association.

Menzel and Klassen [6] have reported developments of the ridged waveguide to microstrip transition, including a 30 GHz design based on alumina-substrated microstrip and a 60 GHz design in which waveguide was connected to microstrip on a GaAs substrate. These researchers use mode-matching techniques based on an Longitudinal Section Electric (LSE)- and Longitudinal Section Magnetic (LSM)-mode field analysis. The structures are shown in [Figure 17.3\(a\)](#). Using an unloaded ridged waveguide in transition with 0.056 mm wide microstrip on a 0.2 mm thick GaAs substrate the minimum reflection coefficient  $S_{11}$  was found to be about 0.15 for an optimum ridge width of 0.5 mm.

### 17.3.2 Mode Changer and Balun

A different approach was adopted by van Heuven [7]. This transition begins, in the waveguide portion, with a form of mode-changing section which rotates and concentrates the fields until

they principally exist in a parallel line. This symmetrical line is then matched to the asymmetrical microstrip line by the use of a “balun” portion. The arrangement is shown in some detail in [Figure 17.4](#); the substrate is usually quartz.

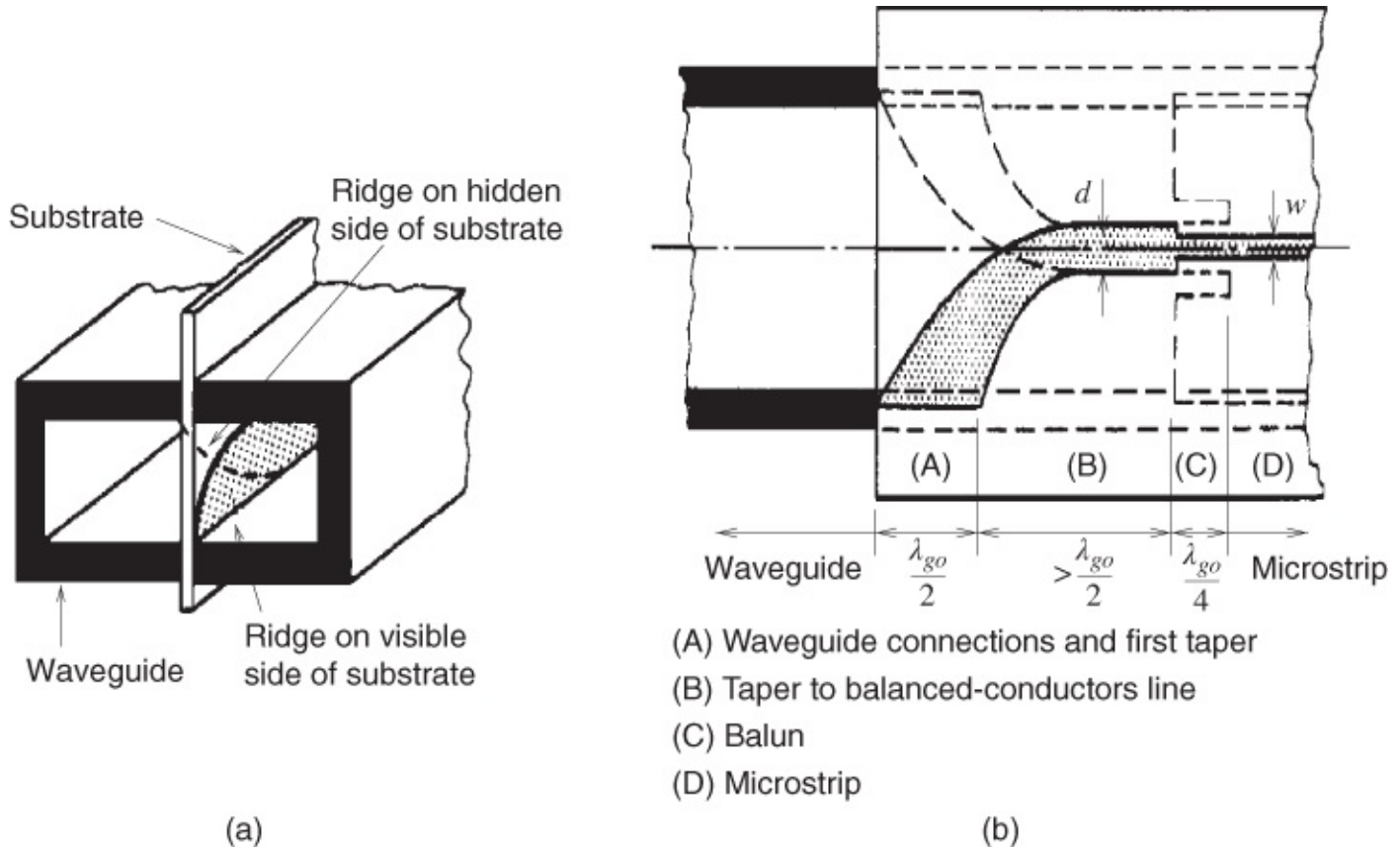


**Figure 17.4** Waveguide-to-microstrip transition using tapers and a balun: (a) waveguide-end view; and (b) longitudinal view. Adapted from van Heuven (1976) [7], figures 1 and 2, p. 145. Reproduced with permission of IEEE.

The conductors on the substrate are electrically connected to the top and bottom walls of the waveguide, in the region marked (A) in [Figure 17.4](#)(b). Each conductor is then gradually tapered until, towards the end of the region marked (B), a balanced-conductor or “symmetrical” line is formed. The characteristic impedance of this symmetrical line should be approximately the same as that of the final microstrip. In the region marked (C) a balun is formed; notice that one side of this has to be the microstrip ground plane, and therefore this side is electrically connected back to the (grounded) top and bottom waveguide walls.

Serrated chokes may be used to produce good RF connections to the waveguide. Since the ground plane divides the waveguide into two separated guides, each having a cut-off frequency well above the band in use, further waveguide mode propagation beyond the transition is prevented. The height of the guide is increased above normal to compensate for the loading due to the quartz substrate. Van Heuven's transition gave the following performance:

bandwidth	18–26 GHz
VSWR	1.11
insertion loss	0.2 dB

Over a significant, but narrower, band (17.7–19.7 GHz) the VSWR remained less than 1.1. This corresponds to a reflection coefficient less than 0.05, which is only slightly worse than for Schneider's transition [3], although this was operating at a higher frequency.

Further details, including mechanical dimensions, can be found in van Heuven's paper [7]. Final design adjustments are largely empirically determined.

### 17.3.3 A Waveguide-to-microstrip Power Splitter

A type of waveguide-to-microstrip power splitter that is suitable for at least the lower microwave frequencies was developed by Wu *et al.* [8]. This device uses a T-bar waveguide-to-microstrip transition, the theory for which is based on current distributions and the dyadic Green's function techniques, treating the T-bar as an internal antenna. From this analysis an expression for the T-bar radiation resistance is obtained. The physical structure and simplified model are shown in [Figure 17.5](#).

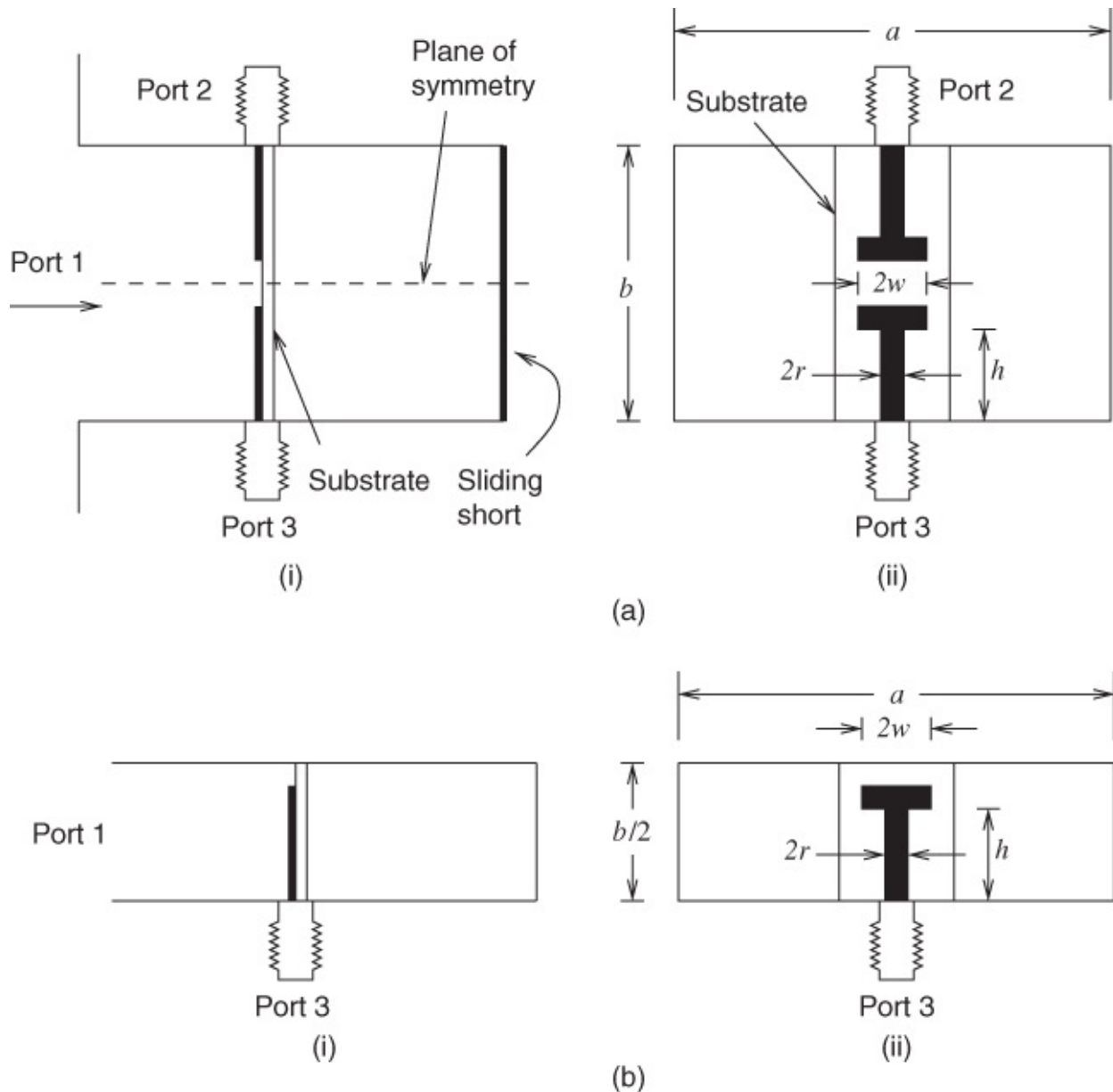


**Figure 17.5** Waveguide-to-microstrip power splitter: (a) structure of the waveguide to microstrip power divider: (i) the side view illustrates that the microwave signal is coupled to two T antennas on an alumina substrate; (ii) the front view of the power divider consists of two T-shaped coupling antennas; and (b) simplified model using the symmetry of the waveguide-to-microstrip power divider: (i) side view; and (ii) front view. The plane of symmetry in (a) is an electric wall where a metal plate can be inserted without changing the field distribution. Thus, the power divider design problem is changed to one of waveguide-to-microstrip transition design. Adapted from Wu *et al.* (1990) [8], figures 1 and 2, p. 477. Reprinted with permission of IEEE.

The design goal is to select a T-bar structure whose radiation resistance is matched to  $50 \Omega$ . The design described by these researchers exhibits an output resistance which is within  $2 \Omega$  (4%) of the requisite  $50 \Omega$  value. A return loss better than 20 dB is obtained over the 3.3–4.6 GHz band and the power difference between output ports is below 0.1 dB.

### **17.3.4 Slot-coupled Antenna Waveguide-to-microstrip Transition**

With the advancement into high-millimeter-wave frequencies, having important applications such as automotive radars and seekers, the need for inexpensive, reliable, and effective waveguide-to-microstrip transitions operating in the 77 GHz and 85 GHz bands is highly significant. Recognizing that the problem is essentially one associated with antenna-based transitions Grabherr *et al.* [9] developed a slot-coupled antenna-based waveguide-to-microstrip transition.

In Grabherr's transition the microwave energy is coupled into the microstrip line through a slot in the ground that connects to a patch antenna element located on an additional small substrate inserted into the waveguide. The metallic waveguide is situated only on the back of the microstrip circuit and, because of the geometry, almost all of the microwave energy is coupled through the slot to the patch antenna and this energy is radiated into the waveguide.

To suit millimeter-wave conditions, a step is implemented in the waveguide widths so that the additional substrate with the radiating patch can be automatically positioned across the ledges of the step and fixed in place by soldering or similar. Grabherr *et al.* solve the calculation problem for this transition by introducing a shielding enclosure for the structure and using a Green's function approach with computer optimization.

The practical implementations of Grabherr's transition comprise an alumina-based microstrip and a fused-quartz-based patch element. Radiation from the top side of the substrates was found to be extremely low in all instances and, at 76.5 GHz and also at 85 GHz, the net insertion loss of each transition was approximately 0.3 dB.

## **17.4 Transitions between CPW and other Mediums**

It is often vital to be able to make transitions between CPW and other available transmission mediums. This enables the designer to take advantage of the differing properties of each technology. Therefore, transitions between CPW and microstrip, finline, slotline, etc. are needed and various approaches can be used in each case.

An example of a CPW-finline transition ([Figure 17.6\(a\)](#)) and also of a CPW-microstrip transition ([Figure 17.6\(b\)](#)) are shown. These designs were originally reported by Jin and Vahldieck [10] and they operate over the 0–40 GHz band. A typical cross-section is also shown, and this may be scaled for any plane along either structure. Top-view dimensions are in millimeters and cross-sectional dimensions are in micrometers. In both cases a nominally quarter-wave central section is required to complete the design. This section is 1.5 mm long for the CPW-finline transition and 1.0 mm in length for the CPW-microstrip transition.

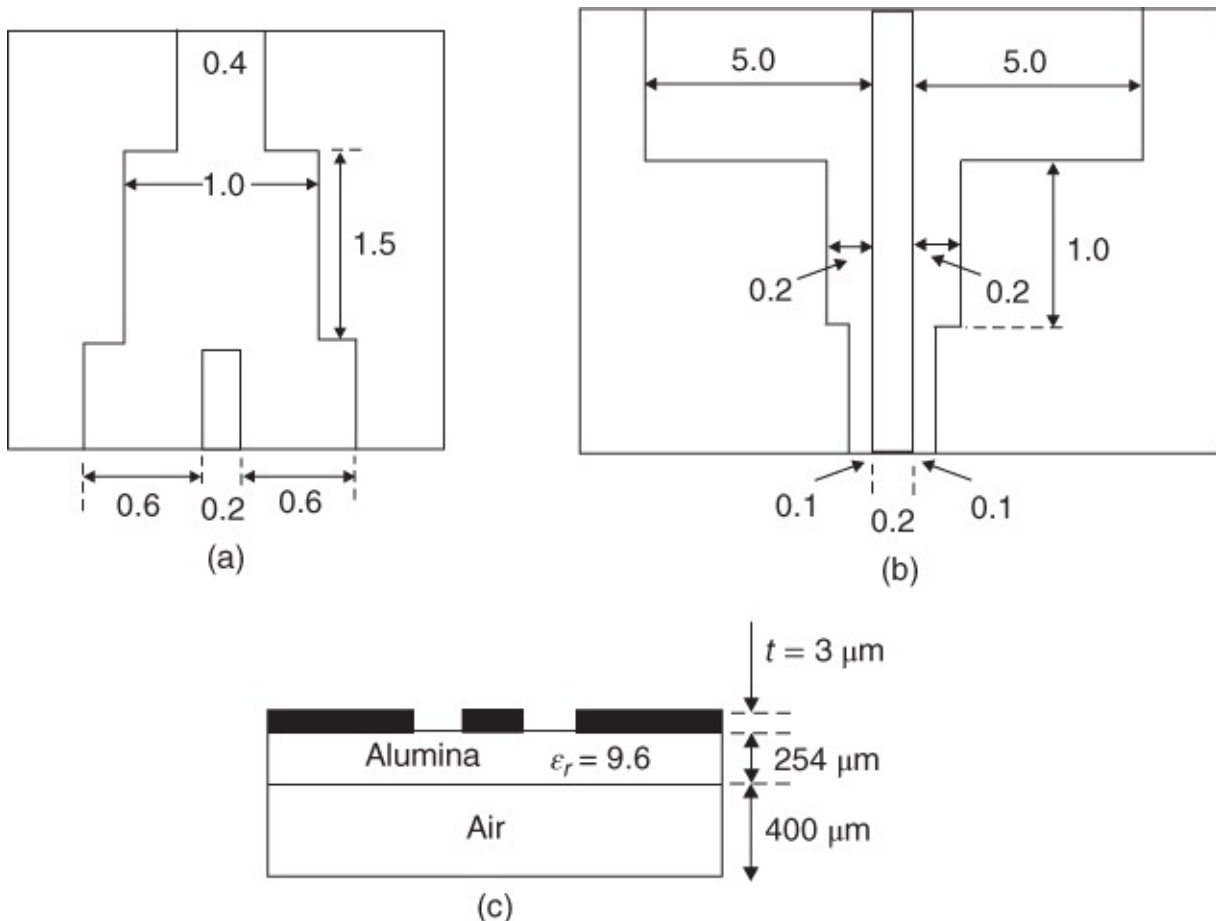


**Figure 17.6** CPW transitions: (a) CPW-to-finline; (b) CPW-to-microstrip; and (c) cross-section of the CPW line for both structures. (Dimensions are in millimeters unless otherwise indicated.) Adapted from Jin and Vahldieck (1993) *et al.* [10], figure 2 and 3, p. 1540. Reprinted with permission of IEEE.

For the CPW-finline transition the transmission factor is 0.9–1.0 over the band and the worst-case value for the reflection coefficient is 0.47 at 40 GHz. For the CPW-microstrip transition, the transmission factor is always approximately 0.95 or better over the band, and the reflection coefficient is always less than 0.31.

Ellis *et al.* [11] reported work on a broadband CPW-to-microstrip transition for millimeter-wave packaging. This development relates to a three-layer structure based on silicon and operating in W band (75–110 GHz). The bottom layer is CPW that feeds the next (microstrip) layer, in turn feeding a microstrip patch antenna top layer. A microstrip-to-slotline power divider is implemented, and the complete transition has an insertion loss of approximately 0.3 dB and a return loss better than 10 dB over the entire band.

Lin and Chen [12] announced a form of lumped-element CPW-slotline transition suitable for the 1–6 GHz band. This team used a lumped ring-type L virtual short circuit as the main element of their design instead of the more conventional quarter-wave transformer. With this design the insertion loss is less than 3 dB and the return loss is better than 10 dB over the 2–4 GHz band.

A CPW-slotline transition tailored for feeding a Vivaldi antenna was reported by Ma *et al.*

[13]. The basic layout of this transition is shown in [Figure 17.7](#), in which it can be seen that an air bridge and a phase shifter form major elements. An RT-Duroid substrate is used ( $\epsilon_r = 10.2$  and thickness 0.635 mm) and the design covers the 1–30 GHz frequency range. Separation of the CPW and slotline modes is assured through design. Over the 11–18 GHz band the measured and calculated insertion loss is less than 3 dB. In the same paper [13], Ma *et al.* show this transition used in a CPW-fed Vivaldi antenna, a CPW power divider, and a CPW-slotline coupler.

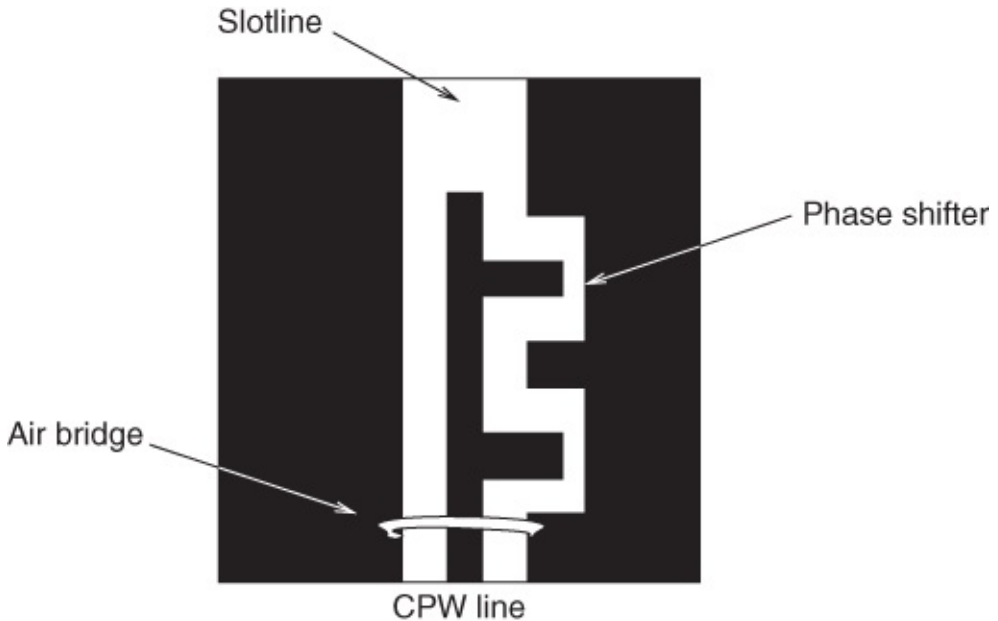


**Figure 17.7** CPW-to-slotline transition. Adapted from Ma *et al.* (1999) [13], figure 1, p. 427. Reprinted with permission of IEEE.

Kaneda *et al.* [14] report on a broadband microstrip-to-waveguide (rectangular) transition that employs a quasi-Yagi antenna. This uses a microstrip-to-CPS balun, and the antenna is inserted into the E plane of the waveguide. Over X band (8.4–12 GHz) this transition exhibits near-zero insertion loss and better than 8 dB return loss.

Further reported work on transitions increasingly emphasizes applications to antennas, for example Simons *et al.* [15] report the results of work on techniques for exciting linearly tapered slot antennas (LTSA) using CPW. Their work covers the band from 16 to 24 GHz, and the return loss achieved is always better than 10 dB. From the same basic team, Simons and Lee [16] report on CPW aperture-coupled patch antennas with FGCPW feeds. It is shown that this type of approach is superior to the use of microstrip for this form of application.

A hybrid FGCPW/CPS design for multilayer circuits and antenna feeds was reported by Zhu and Wu [17, 18]. This covers a 2–10 GHz bandwidth and comprises FGCPW-to-CPS transitions. The CPS optimally feeds a dipole antenna, and a measured return loss of 45 dB at 3.35 GHz was obtained.

Nadan *et al.* [19] performed work on the miniaturization and optimization of a filter/antenna multilayer and multifunction module that embodies a composite ceramic foam substrate with a relative permittivity of 1.07 (i.e., just 7% greater than air). The characteristic impedance of the

CPW is approximately  $46.5 \Omega$ , and the characteristic impedance of the microstrip is between 17 and  $21 \Omega$ , which results in a fairly wide microstrip line but is fully realizable. This approach is suitable for complex antenna arrays. With this design the return loss is better than 12 dB over the 10–11 GHz band.

The final example provided here is that reported by Vaupel and Hansen [20]. They report an electrodynamic analysis of coplanar microwave circuits that mainly covers the frequency range to 100 GHz. A CPW-slotline analysis is performed for coplanar MMIC applications. A hybrid (E-shaped structure) bandstop filter is shown that implements CPW with air bridges, optimized for the 30–40 GHz band. A submillimeter-wave 650 GHz mixer for satellite remote sensing represents an unusual application that is also reported in the same paper by Vaupel and Hansen. The basic layout of this mixer circuit is shown in [Figure 17.8](#), indicating the first IF filter section, the ring-slot antenna, and the feed to the mixing diode.

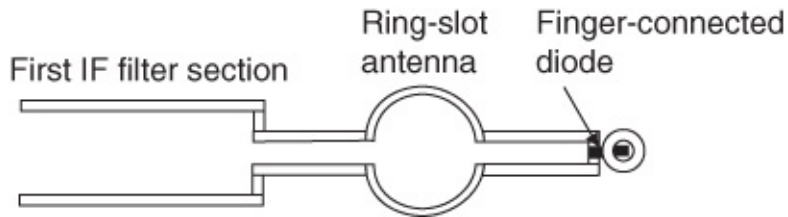


[Figure 17.8](#) A 30–40 GHz bandstop filter within a mixer and a ring-slot antenna. Adapted from Vaupel and Hansen (1999) [20], figure 8, p. 1798. Reprinted with permission of IEEE.

## 17.5 Slotline Transitions

The geometry of a general microstrip-slotline transition is presented in [Figure 17.9](#). A microstrip-to-slotline transition was first described by Robinson and Allen [22]. The simple basic structure yields a  $VSWR < 1.2$  over the frequency range 2–4 GHz. With some care in design, and the microstrip orientated at right angles to the slotline, a  $VSWR < 1.1$  was achieved over a higher range of frequencies, namely 8–10 GHz. This section presents several models of this transition as well as several variants of the transition. Also described is a transmission line which combines microstrip with slotline.

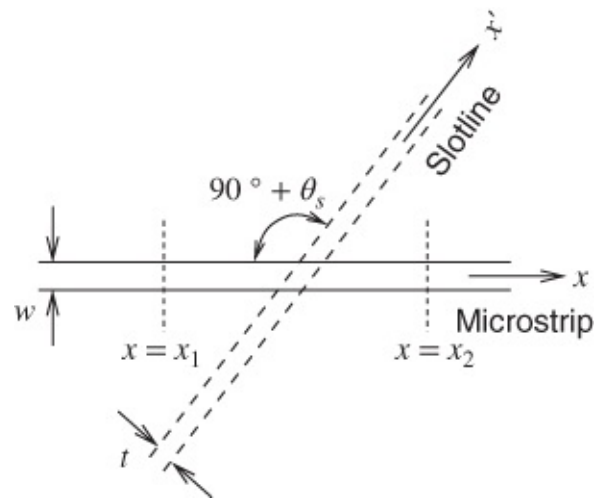


**Figure 17.9** Geometry of a general microstrip-slotline transition. Adapted from Antar *et al.* (1992) [21], figure 1, p. 516. Reprinted with permission of IEEE.

### 17.5.1 Microstrip-slotline Transition, Antar

In 1992 Antar, Bhattacharyya, and Ittipiboon reported on their analysis of microstrip-slotline transitions using the spectral domain technique [21]. They referred to a standard model of a transition as shown in [Figure 17.10](#). Antar *et al.* compared their results with the measurements due to Knorr [23] over a 1–5 GHz frequency range. Although the predicted general trend compare well, the analysis due to Antar *et al.* actually produces significantly pessimistic data compared with Knorr's measurements. The variations with frequency (up to 12 GHz) for both the transformer ratio,  $n$ , and series reactance,  $X_s$ , are shown in [Figure 17.11](#). The transformer ratio,  $n$ , exhibits a steady decline with frequency. The series reactance decreases rapidly with frequency at first (up to about 3 GHz) but declines much more slowly at higher frequencies.

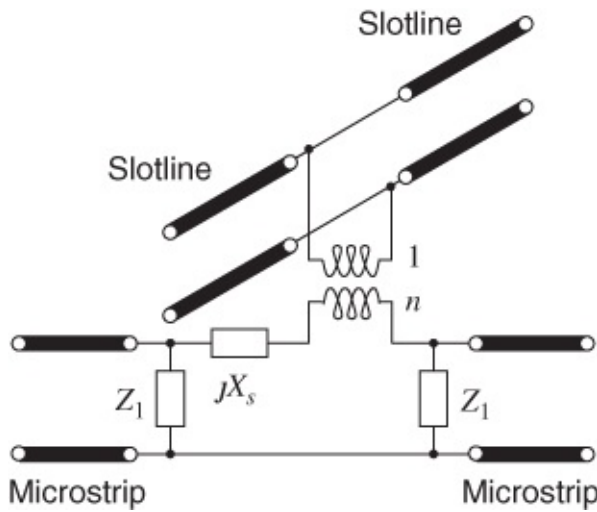


**Figure 17.10** Common model of a slotline-microstrip transition.

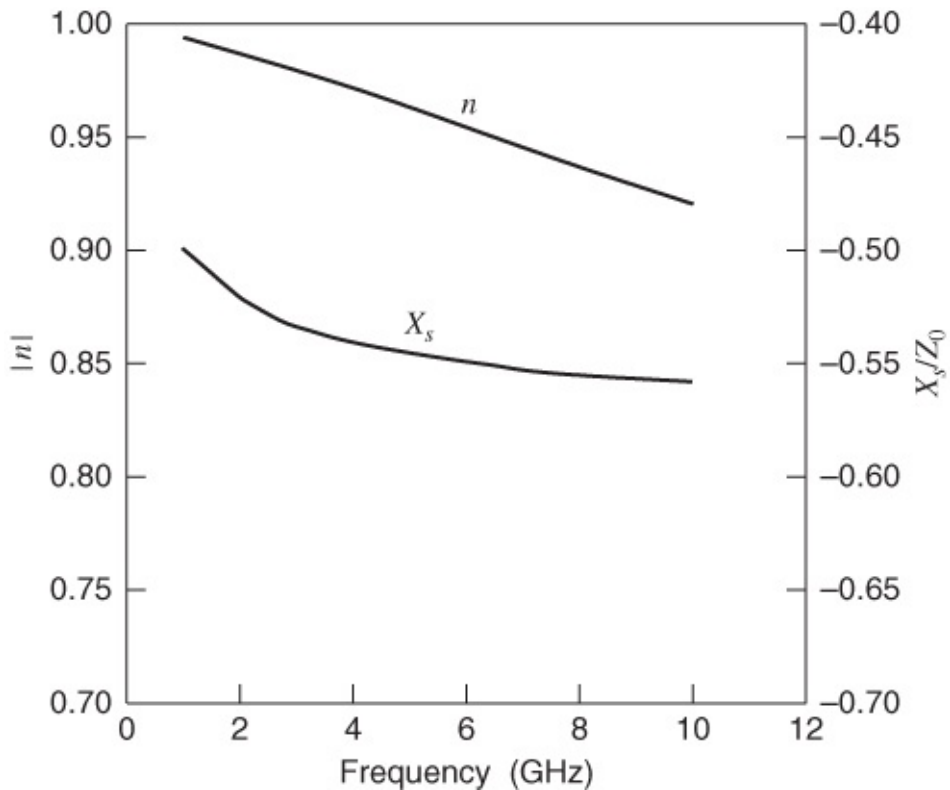


**Figure 17.11** Variations of  $n$  and  $X_s$  with frequency for a microstrip-slotline transition on alumina substrate ( $h = w = 0.5$  mm,  $\epsilon_r = 9.7$ ,  $t = 0.5$  mm,  $\theta_s = 0$ ). Adapted from Antar *et al.* (1992) [21], figure 6, p. 519. Reprinted with permission of IEEE.

### 17.5.2 Microstrip-slotline Transition, Chramiec

In addition to slotline discontinuities (considered in [Section 15.7.2](#)) Chramiec [24] also investigated a microstrip-slotline transition and his main results are presented here. With the subscript  $m$  referring to the microstrip side of the transition, he used a standard equivalent circuit for this structure and with all of the components electrically transformed to the microstrip side, see [Figure 17.12](#). The input reflection coefficient  $\Gamma$ , referenced to the microstrip characteristic impedance  $Z_{0m}$ , is

$$\Gamma = \frac{R_s - Z_{0m} + j(X_m + X_s)}{R_s + Z_{0m} + j(X_m + X_s)} \quad 17.1$$

where

$$R_s = \frac{n^2 Z_0^2 X}{Z_0^2 + X^2}, \quad X_s = \frac{n^2 Z_0 X^2}{Z_0^2 + X^2}, \quad 17.2$$

and  $n$  is the transformer ratio. As  $n$  and  $Z_0$  are slowly varying functions of frequency, the transition bandwidth limitation results mainly from the frequency dependence of  $X$  and  $X_m$ . A through-hole microstrip short circuit may ensure  $X_m = 0$ , but the data show that  $X$  always exhibits a limited bandwidth. To design a broadband transition one may attempt to realize slotline and microstrip resonators providing mutual cancellation of  $X_m$  and  $X_s$ .

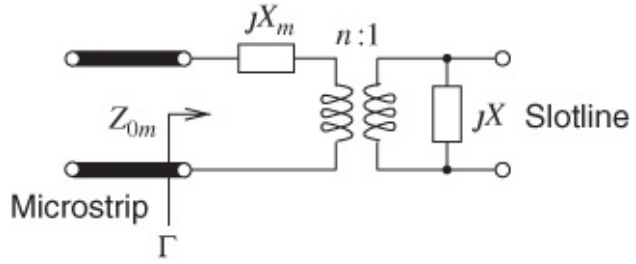
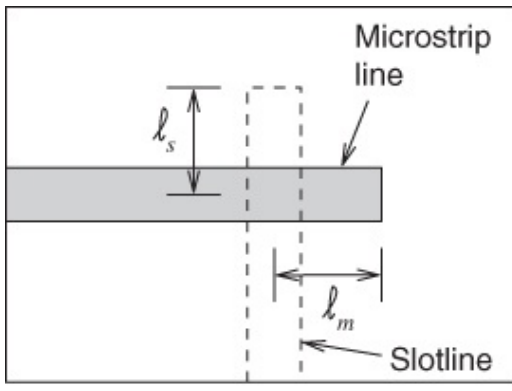


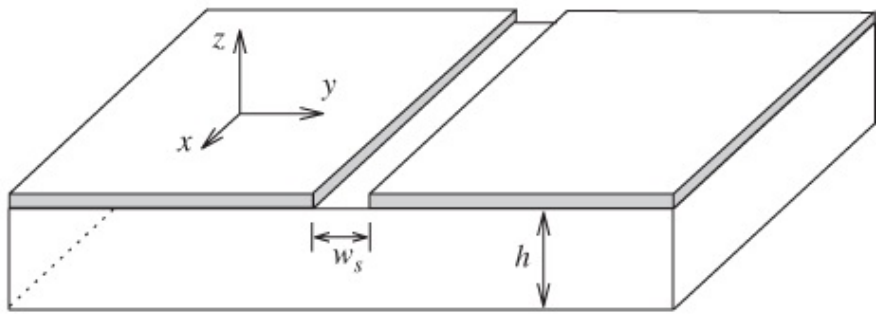
**Figure 17.12** Alternative model of a slotline-microstrip transition.

### 17.5.3 Slotline-microstrip Transition, Podcamedui and Coimbra

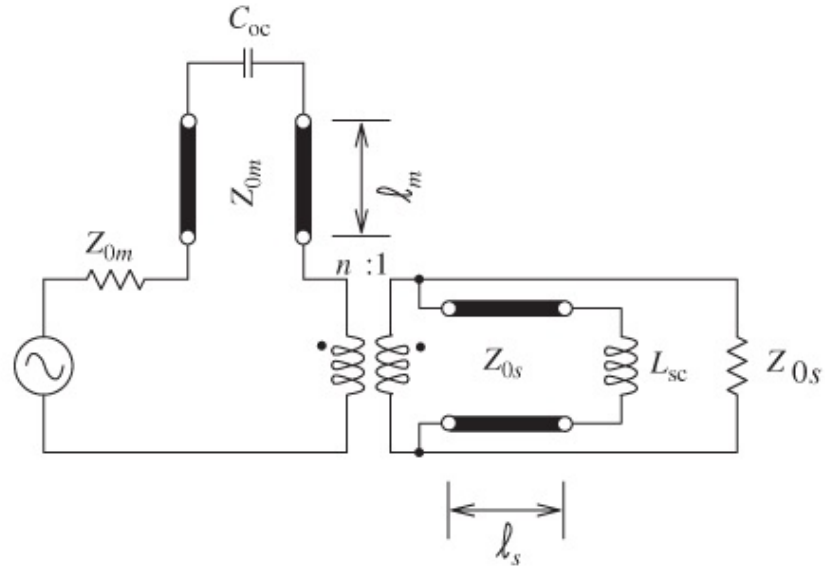
Another form of this general type of transition was investigated by Podcamedui and Coimbra [25, 26]. This is shown in [Figure 17.13\(a\)](#). The geometry of the slotline is shown in [Figure 17.13\(b\)](#) with the equivalent circuit of the transition in [Figure 17.13\(c\)](#). Podcamedui and Coimbra's theoretical and experimental results for the VSWR of this transition are presented in [Figure 17.14](#). For this bandpass filter-like response the theory predicts the measured data fairly well for frequencies up to about 6.4 GHz (with the exception of an over-optimistic in-band ripple). However, the theory and experimental data depart significantly at the higher-frequency end of the response.



(a)



(b)



(c)

**Figure 17.13** Slotline-microstrip transition: (a) two-stub transition; (b) parameters of slotline; and (c) equivalent circuit of transition. Adapted from Podcameni and Coimbra (1980) [26], figure 1, p. 80. Reprinted with permission of IEEE.

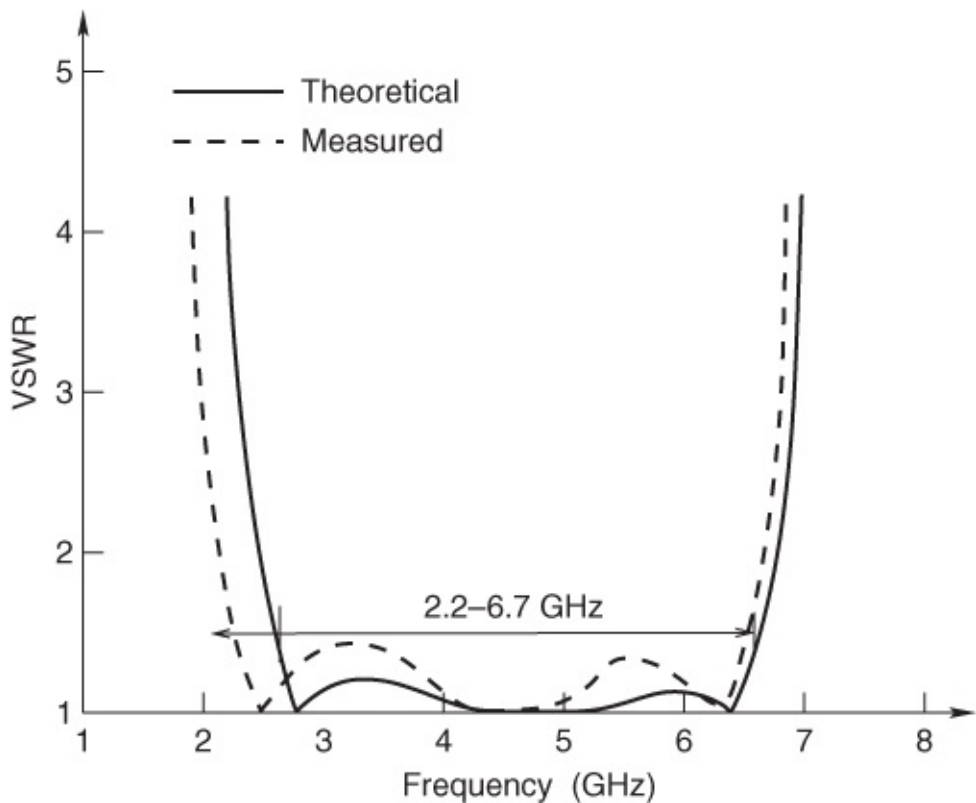


**Figure 17.14** Theoretical (solid line) and experimental (dashed line) VSWR for slotline-microstrip double transition on an anisotropic substrate.  $\epsilon_{r,xy} = 13$ ,  $\epsilon_{r,z} = 10.2$ ,  $H = 0.635$  mm. Adapted from Podcameni and Coimbra (1981) [26], figure 4, p. 82. Reprinted with permission of IEEE.

### 17.5.4 Microstrip-slot Dispersion, Itoh

Itoh [27] considered the microstrip-slot structure shown in [Figure 17.15\(a\)](#) and reported the dispersion results shown in [Figure 17.15\(b\)](#). In this graph  $a$  is the half-width of the slot. The following observations are made:

1. The dispersive nature in each case results in non-linear decreases of normalized wavelength as frequency increases.
2. At any frequency the wavelength increases as the slot-width increases (by a factor of 10 in [Figure 17.15](#)).
3. Dispersion is also present even when the slot is closed up ( $a = 0$ ), which amounts to the limiting case of microstrip.

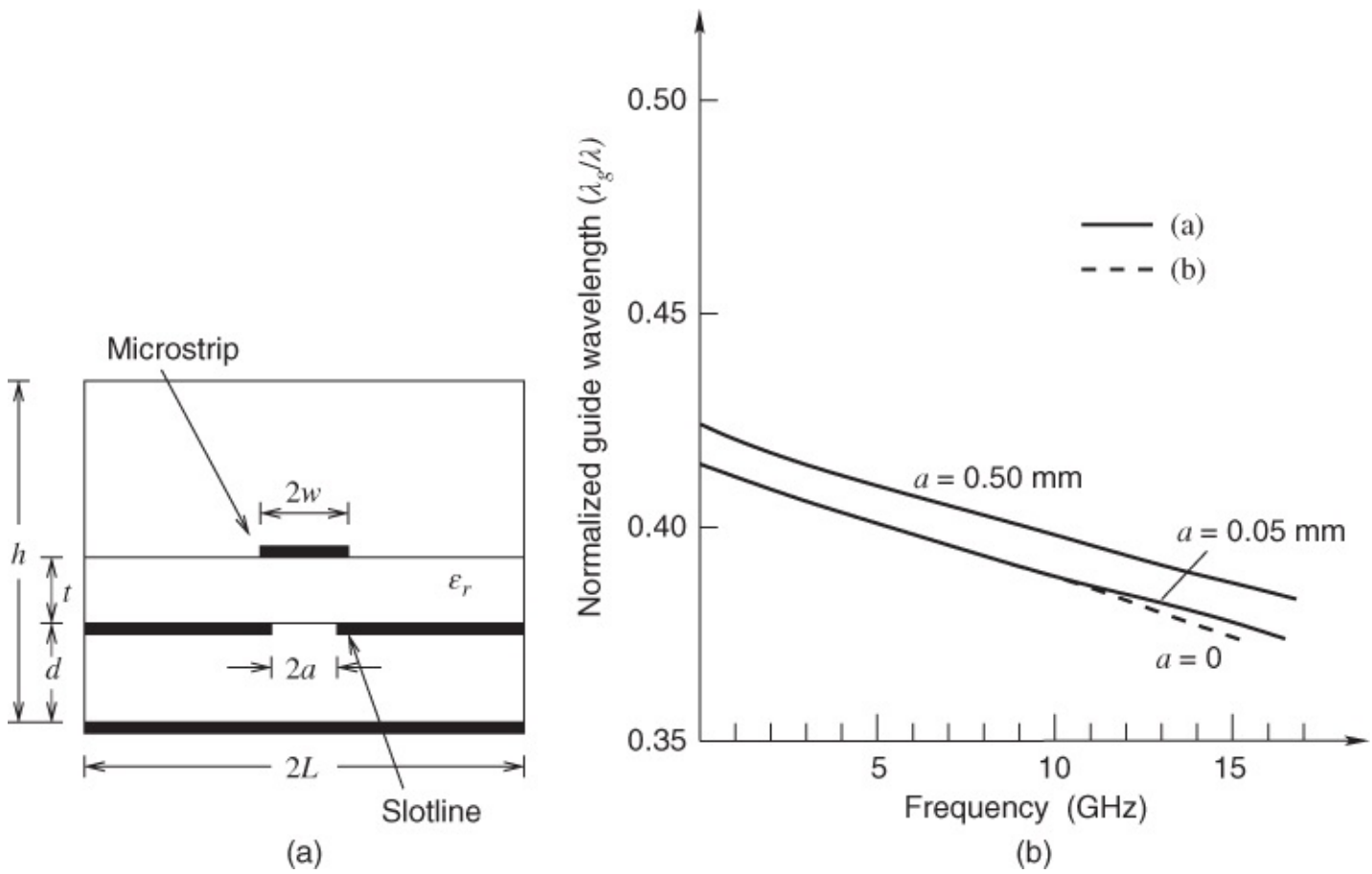


**Figure 17.15** Microstrip-slot transmission line: (a) structure; and (b) dispersion characteristics of microstrip-slot lines.  $L = 6.35$  mm,  $d = 11.43$  mm,  $t = 1.27$  mm,  $h = 24.13$  mm,  $w = 0.635$  mm,  $w = 0.635$  mm,  $\epsilon_r = 8.875$ . Adapted from Itoh (1980) [27], figure 4 and 6, pp. 735 and 736. Reprinted with permission of IEEE.

### 17.5.5 Microstrip-slotline Transitions, Yang

Yang and Alexopoulos [28] published a theoretical paper on microstrip-slotline transitions and related structures. The basic microstrip-slotline transition structure investigated is shown in Figure 17.16. These workers used dyadic Green's functions and the method of moments to generate their results. The input VSWR was computed and is compared with other results in Figure 17.17. It can be seen that at the lower frequencies good agreement exists among both methods and Knorr's measurements. Yang and Alexopoulos attribute the large discrepancies at the higher frequencies to higher-order modes, surface waves, and radiation effects, all of which were included in the theory.

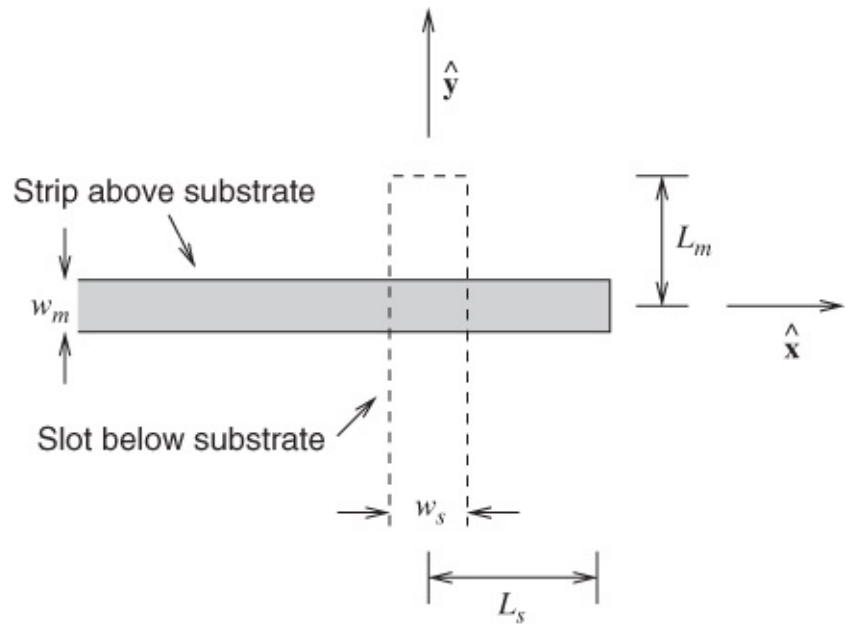


**Figure 17.16** The microstrip-slotline transition investigated by Yang and Alexopoulos. Adapted from Yang and Alexopoulos (1988) [28], figure 1, p. 286. Reprinted with permission of IEEE.

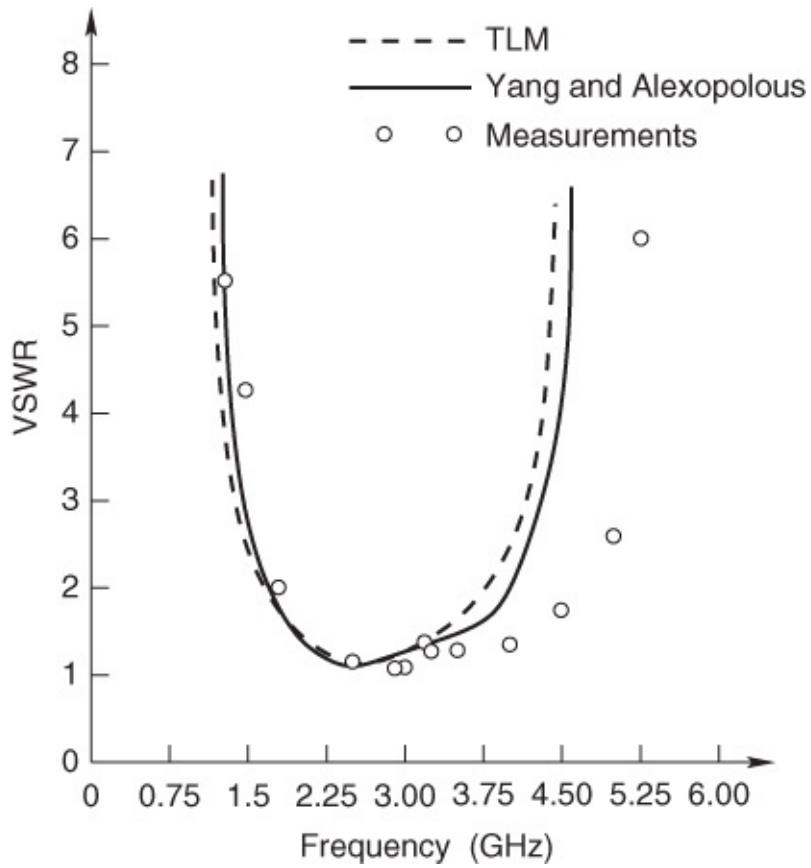


**Figure 17.17** Microstrip-slotline transition. Transmission Line Matrix (TLM) data results use the transmission line method due to Knorr [23].  $w_s = 2.057$  mm,  $w_m = 1.575$  mm,  $L_s = 6.88$  mm,  $L_m = 6.88$  mm,  $\epsilon_r = 20$ , substrate thickness  $d = 3.175$  mm. Adapted from Yang and Alexopoulos (1988) [28], figure 7, p. 552. Reprinted with permission of IEEE.

### 17.5.6 Microstrip-slotline Transitions, Schuppert

Schuppert [29] investigated basic microstrip-slotline transitions oriented orthogonally to each other with an overlap. Line terminations were alternately “open circuited” and “virtually grounded”, and the frequency range considered was 1–16 GHz. Based on the quadrature microstrip-slotline transition investigated by Yang *et al.* (see above), Schuppert also reported on new results related to variations of this structure ([Figure 17.18](#)). Schuppert's nomenclature is shown in [Figure 17.19](#).

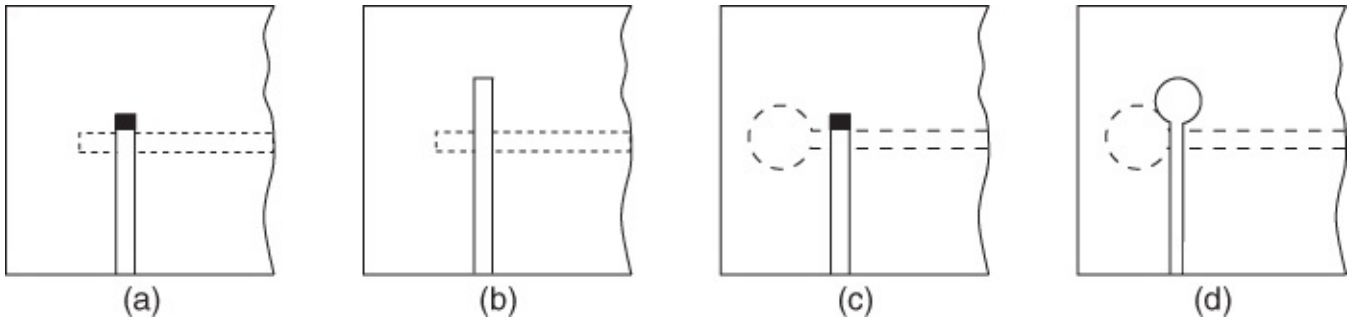


**Figure 17.18** Various microstrip-to-slotline transitions (solid lines indicate microstrip circuitry and dashed lines indicate slotline circuitry): (a) microstrip short and uniform  $\lambda/4$  slotline; (b) virtual short with uniform  $\lambda/4$  open microstrip and uniform  $\lambda/4$  slotline; (c) soldered microstrip short and slotline open circuit; and (d) virtual microstrip short circuit and slotline open circuit. Adapted from Shuppert (1988) [29], figure 1, p. 1272. Reprinted with permission of IEEE.

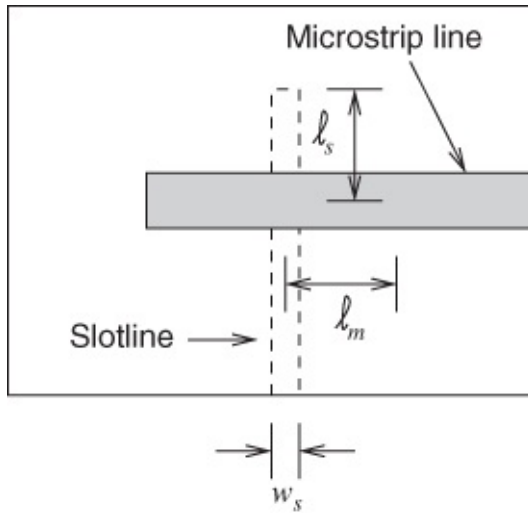


**Figure 17.19** Microstrip-slotline transition with uniform stubs. Adapted from Shuppert (1988) [29], figure 6, p. 1275. Reprinted with permission of IEEE.

Schuppert defined normalized impedances for the shorted slotline stub and open microstrip stub as follows:

$$v = \frac{Z_{ss}}{50\Omega} \quad \text{and} \quad w = \frac{50\Omega}{Z_{mo}} \quad 17.3$$

where  $Z_{ss}$  is the characteristic impedance of the shorted slotline stub and  $Z_{mo}$  is the

characteristic impedance of the open-circuited microstrip stub. Then, along the microstrip stub section

$$\frac{d|S_{21}|}{dw} = 0 \quad 17.4$$

also

$$w = v \left[ 1 + \frac{\cot^2(\beta\ell)}{v^2} \right] \quad 17.5$$

and

$$|S_{21}| = \left[ \sqrt{1 + \frac{1}{4v^2} \frac{\cot^4(\beta\ell)}{v^2 + \cot^2(\beta\ell)}} \right]^{-1} \quad 17.6$$

Using these expressions Schuppert defined 1 dB bandwidths for the transitions and plotted curves of the frequency responses. The results are shown in [Figure 17.20](#) for a pair of symmetrical transitions. The measured values indicated by  $\Delta$  are close to those predicted using the above equations.

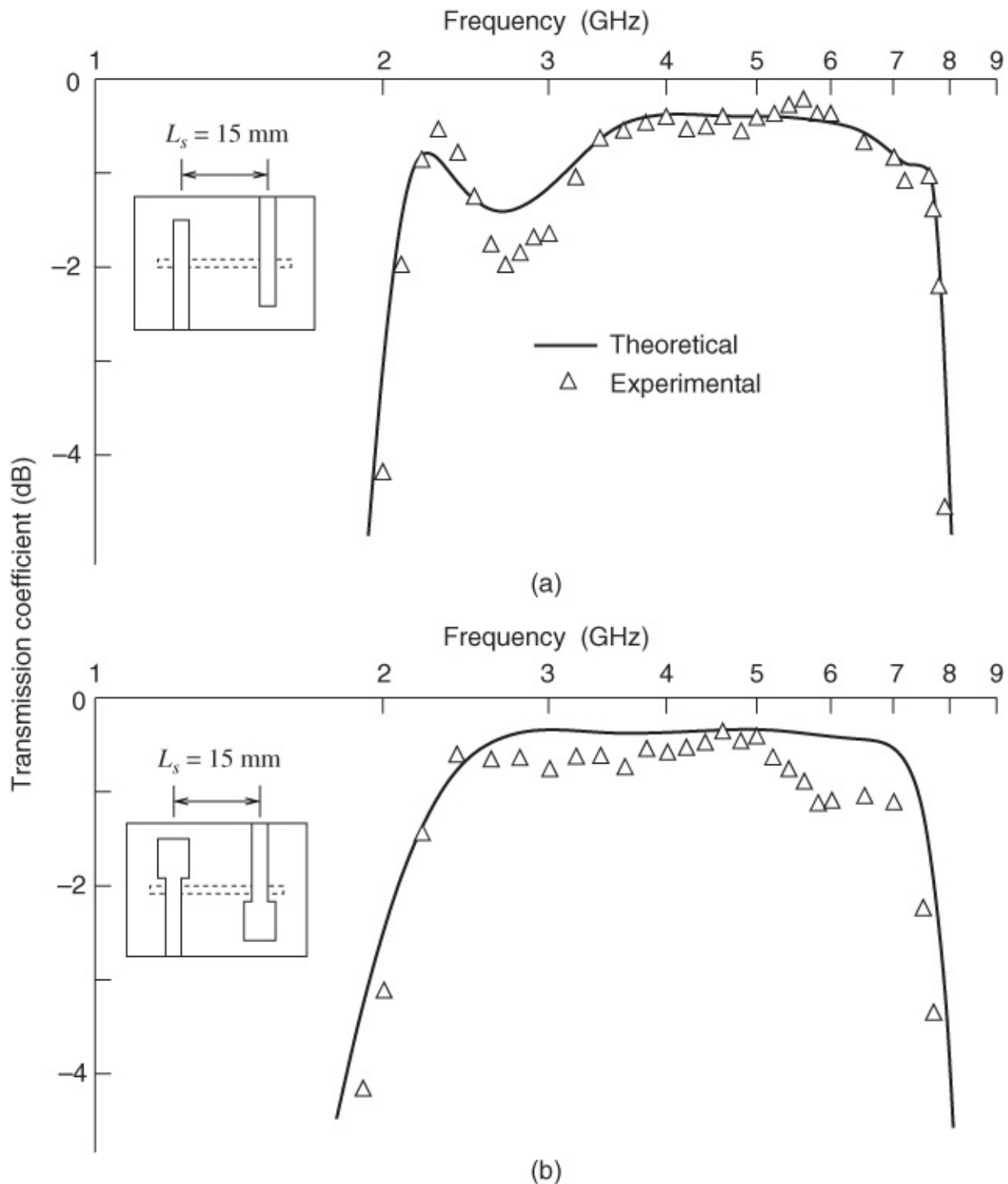


**Figure 17.20** Transmission coefficient of a cascade of two microstrip/slotline transitions, separated by a slotline of length  $L_s = 15$  mm: (a)  $Z_{mo} = 50 \Omega$ ; and (b)  $Z_{mo} = 19 \Omega$ . Adapted from Shuppert (1988) [29], figure 10, p. 1276. Reprinted with permission of IEEE.

### 17.5.7 Microstrip-slotline-microstrip Transitions

Schwab and Menzel [30] investigated single and multiplane discontinuities, and microstrip-slotline-microstrip transitions. The single and multiplane discontinuities these workers reported on are shown in [Figure 17.21](#).

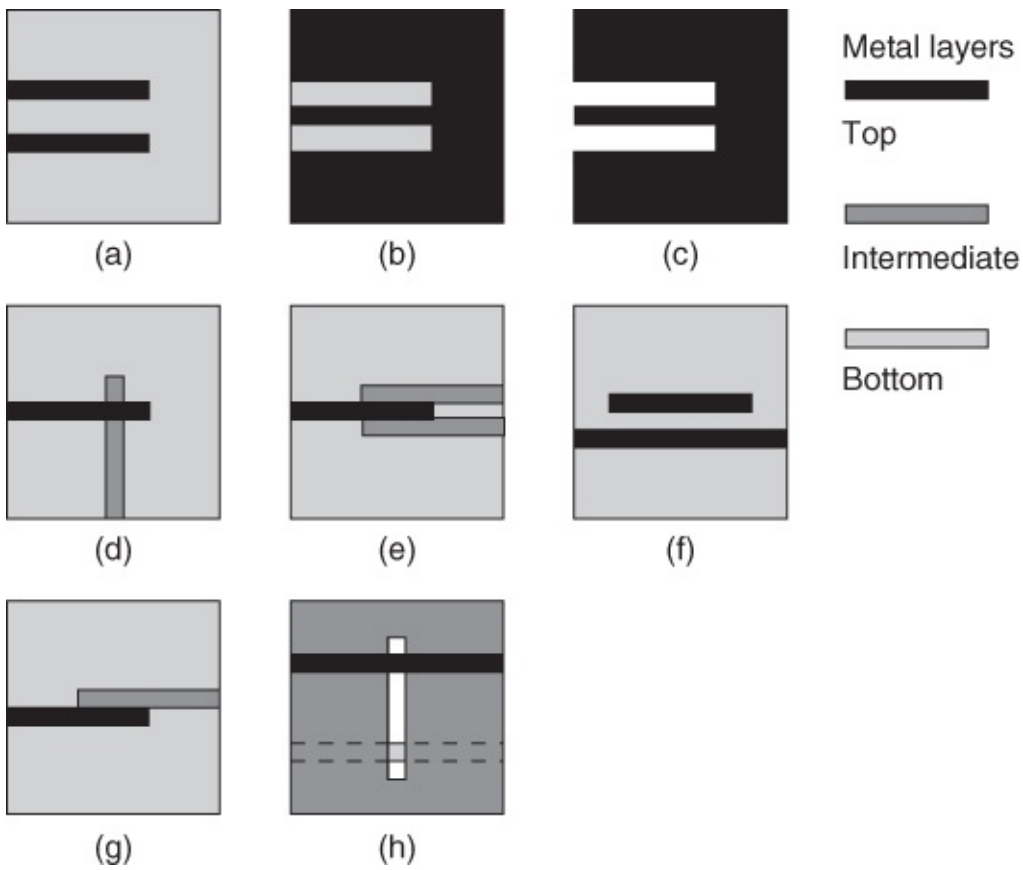


**Figure 17.21** Single and multiplane discontinuities: (a) open coupled microstrip lines; (b) shorted CPW line over ground; (c) shorted CPW line; (d) microstrip cross-over; (e) microstrip coupled to CPS line; (f) microstrip line with coupled resonator; (g) coupled microstrip on different layers; and (h) slotline coupled microstrip lines. Adapted from Schwab and Menzel (1992) [30], figure 1, p. 67. Reprinted with permission of IEEE.

Schwab and Menzel's [30] microstrip-slotline-microstrip transition configuration is shown in [Figure 17.22\(a\)](#). The theoretical and measured results for the insertion loss of this structure are presented in [Figure 17.22\(b\)](#). The theory predicts well for the skirts of this band-pass-filter-like response but (as might be anticipated intuitively) the theory is over-optimistic regarding the “passband” insertion loss.

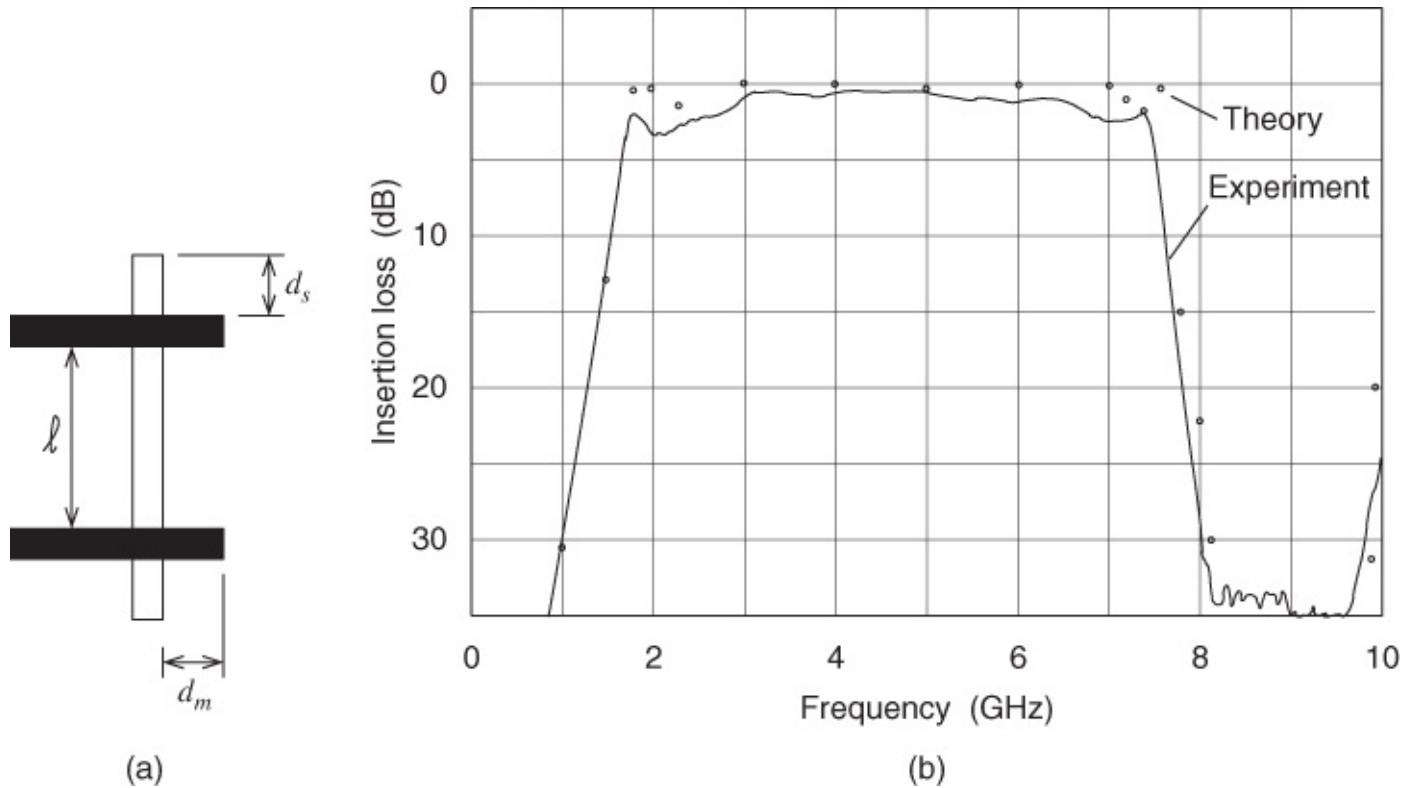


**Figure 17.22** Microstrip-slotline-microstrip transition: (a) structure; and (b) measured and calculated transmission coefficient of a microstrip-slotline-microstrip transition.  $\epsilon_r = 11.1$ ,  $h = 1.27$  mm,  $s = 0.53$  mm,  $w = 1.0$  mm,  $\ell = 20.4$  mm,  $d_s = 6.65$  mm. Adapted from Schwab and Menzel (1992) [30], figure 5, p. 70. Reprinted with permission of IEEE.

### 17.5.8 Microstrip-slotline Transition with Open and Short-circuited Lines

Schiek and Kohler [31] investigated a special form of microstrip-slotline transition with open- and short-circuited lines at the transition plane. This configuration is shown in [Figure 17.23](#) and the practical dimensions are provided in [Figure 17.24](#). The substrate material for the structure of [Figure 17.24](#) is 0.51 mm thick alumina with a relative permittivity of 10. Measured data for the insertion loss and the return loss of this transition are shown in [Figure 17.25](#). These characteristics leave a lot to be desired, notably the in-band insertion loss (around 5 dB) and the general behavior above 9 GHz.

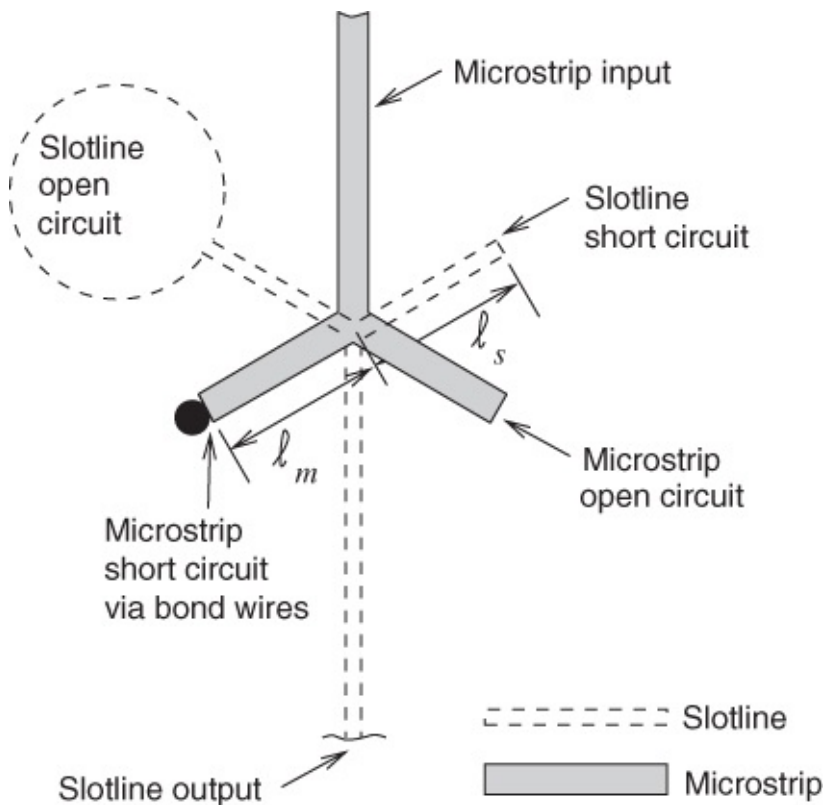


**Figure 17.23** Microstrip-slot transition with open- and short-circuited lines. Adapted from Schiek and Kohler (1976) [31], figure 3, p. 232. Reprinted with permission of IEEE.

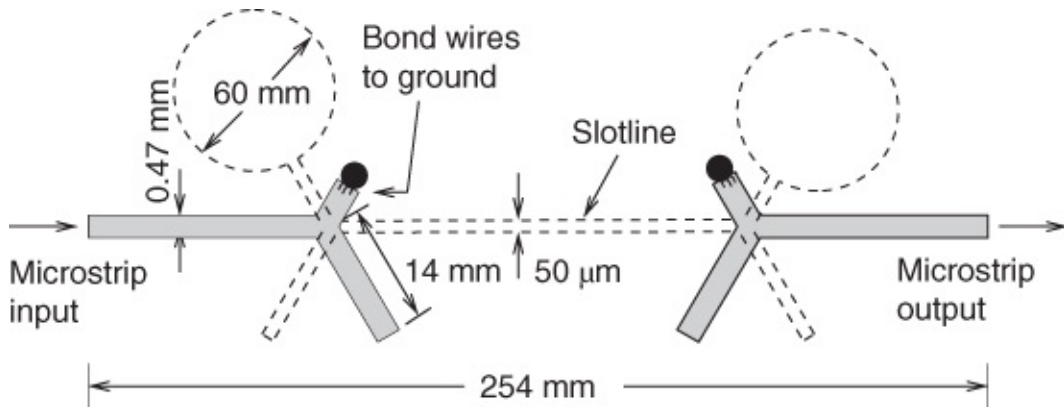
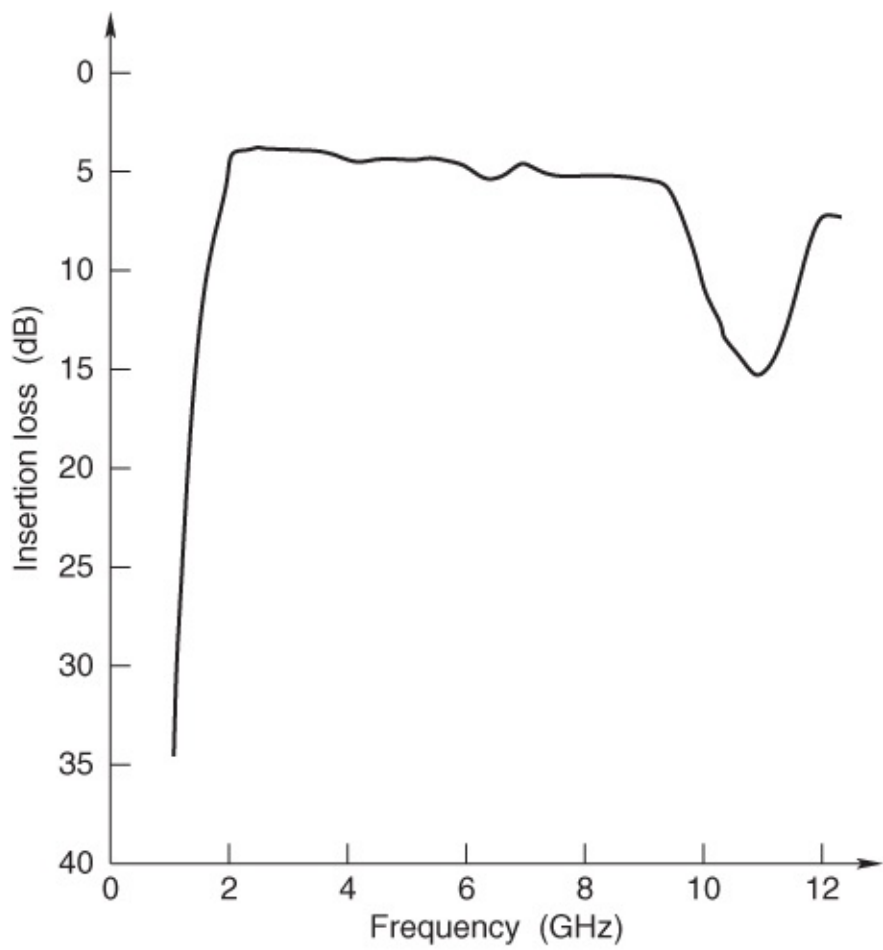
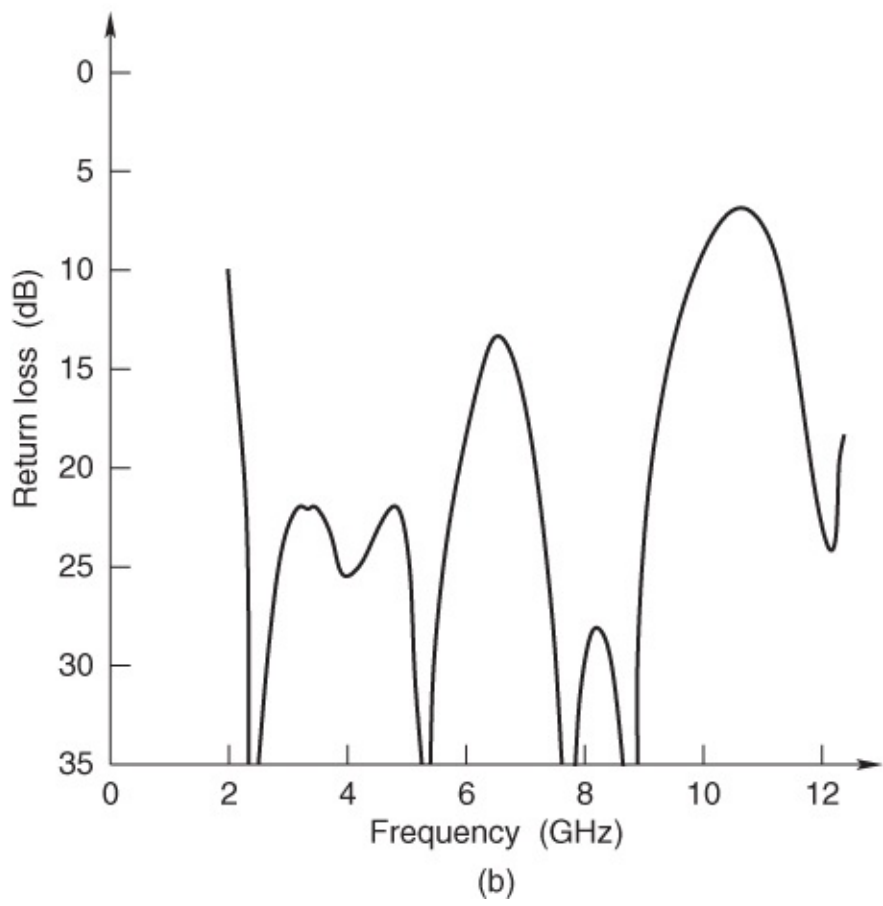


**Figure 17.24** Dimensions of the circuit layout of two transitions in series. Adapted from Schiek and Kohler (1976) [31], figure 4, p. 232. Reprinted with permission of IEEE.



(a)



(b)

**Figure 17.25** Measured characteristics of two transitions in series shown in [Figure 17.24](#): (a) insertion loss; and (b) return loss. Adapted from Schiek and Kohler (1976) [31], figure 5, p. 232. Reprinted with permission of IEEE.

### 17.5.9 Coaxial-slotline and Microstrip-slotline Transition, Knorr

Knorr published results for both coaxial-slotline and microstrip-slotline transitions [23]. A longitudinal view of the coaxial-slotline transition is shown in [Figure 17.26](#). A simplified model and equivalent circuit are shown in [Figure 17.27](#)(a) and (b). Based on this equivalent circuit Knorr developed the following defining equations:

$$n = \frac{V(r)}{V_0} = \frac{\pi}{2} \left| k_c H_1^{(1)}(k_c r) \right| \quad 17.7$$

and

$$k_c = \frac{j2\pi}{\lambda'} = \frac{\pi}{2} \left[ 1 - \left( \frac{\lambda'}{\lambda} \right)^2 \right]^{\frac{1}{2}}. \quad 17.8$$

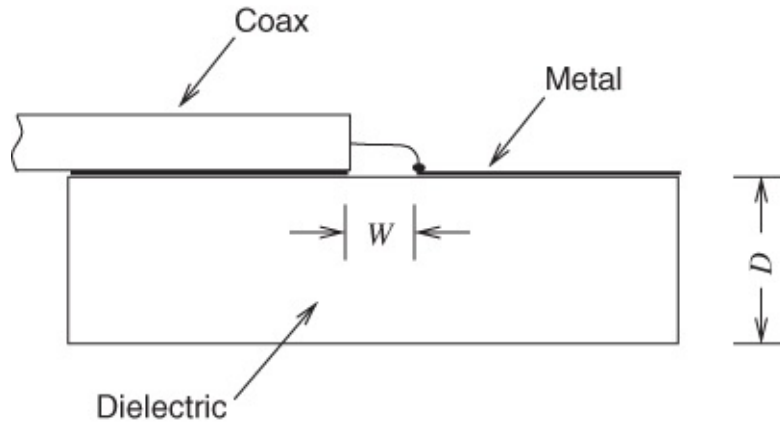


**Figure 17.26** Coax-slotline transition. Adapted from Knorr (1974) [23], figure 1, p. 548. Reprinted with permission of IEEE.

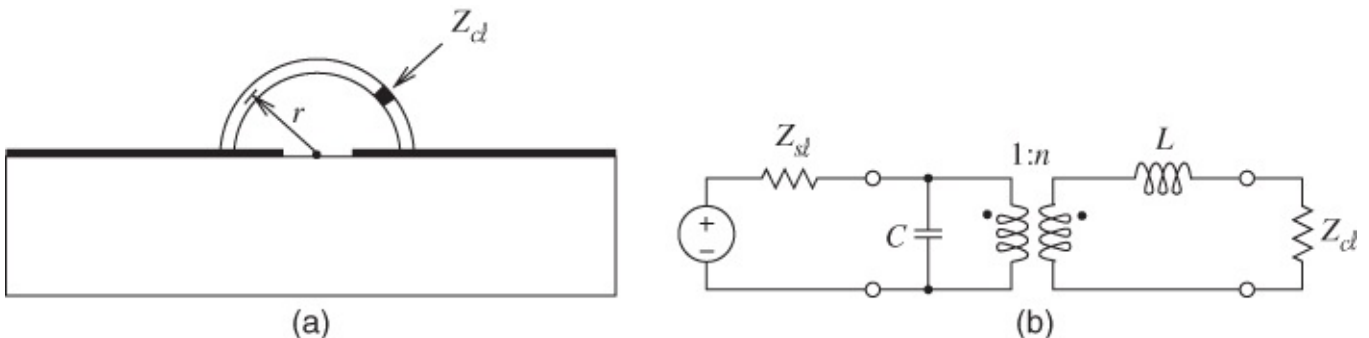


**Figure 17.27** Coaxial line to slotline transition: (a) simplified model of coaxial-slot transition; and (b) equivalent circuit of the coaxial-slot transition. Adapted from Knorr (1974) [23], figure 2, p. 549. Reprinted with permission of IEEE.

In these equations,  $V(r)$  is the voltage at radius  $r$ ,  $V_0$  is the voltage directly across the slot,  $\lambda'$  is the slot wavelength, and  $H_1^{(1)}$  is the Hankel function of the first kind. The coaxial-to-slot transition may be shunted by a short length of open-circuited slotline as well as by fringe capacitance at the open end of the slot. These effects are accounted for in the equivalent circuit by a lumped capacitance  $C$ . Typically, a millimeter length of open-circuited 75- $\Omega$  slotline on a substrate with  $\epsilon_r = 20$  has an input susceptance that is approximately equivalent to that of a 0.2 pF capacitor.  $L$  is the self-inductance of the semiloop of radius  $r$ .

For the microstrip-slotline transition the following definitions apply:

$Z_{sl}$  = slot impedance

$\theta_{sl}$  = electrical length of slot stub

$X_{sl}$  = equivalent reactance of shorted slot

$Z_{ms}$  = microstrip impedance

$\theta_{ms}$  = electrical length of microstrip stub

$C_{oc}$  = equivalent capacitance of open microstrip

Knorr's equivalent circuit requires a transformer with turns ratio  $n$  given by

$$n = \cos\left(2\pi\frac{D}{\lambda}u\right) - \cot(q'_0)\sin\left(2\pi\frac{D}{\lambda}u\right) \quad 17.9$$

in which:

$$q'_0 = 2\pi\frac{D}{\lambda}u + \tan^{-1}\left(\frac{u}{v}\right) \quad 17.10$$

where

$$u = \left[\epsilon_r - \left(\frac{\lambda}{\lambda'}\right)^2\right]^{\frac{1}{2}} \quad \text{and} \quad v = \left[\left(\frac{\lambda}{\lambda'}\right)^2 - 1\right]^{\frac{1}{2}}. \quad 17.11$$

The slotline and microstrip impedances are interrelated by

$$Z_{sl} = \frac{Z_{ms}}{n^2}. \quad 17.12$$

The slotline susceptance and the microstrip reactance are both zero.

### 17.5.10 Slotline-stripline Transition. Aikawa et al

Aikawa and Ogawa [32] researched a slotline-stripline series T junction and both the physical configuration and the equivalent circuit are shown in [Figure 17.28](#). This configuration is important for both transition and coupler applications.

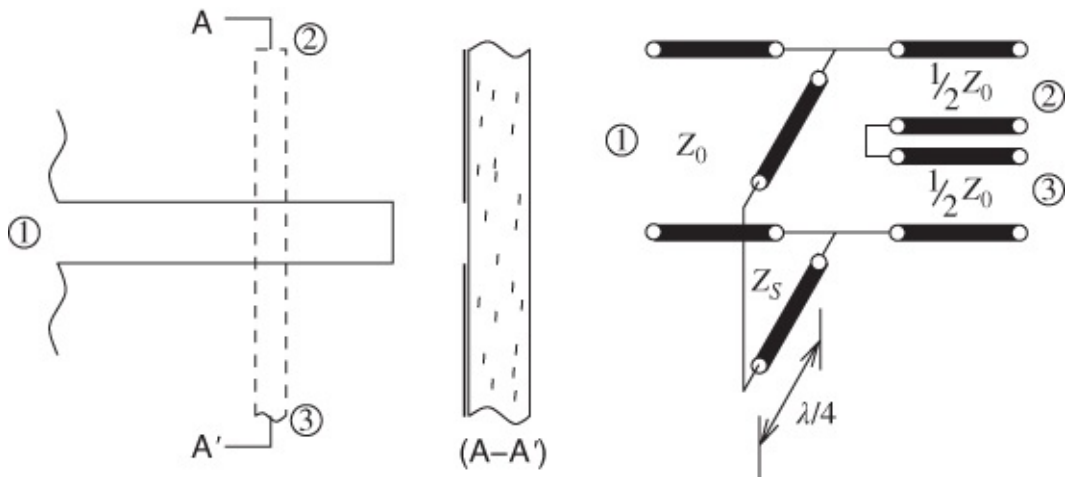


**Figure 17.28** Configuration of slotline-stripline series T junction and equivalent circuit: 1, input of the stripline; 2, one end of the slotline; 3, the other end of the slotline. Adapted from Aikawa and Ogawa (1989) [32], figure 3, p. 407. Reprinted with permission of IEEE.

## 17.6 Other Microstrip Transitions

The first example we take is the stripline-to-microstrip transition. Although not fully analyzed in detail as an uncompensated transition, this type of transition has been simply treated by Hall and James [33], who also report some measurements of power loss due to radiation. On a plastic ( $\epsilon_r = 2.32$ ) substrate this loss was found to be approximately 11%. Such an uncompensated transition may well yield an acceptable performance when the microstrip substrate is of plastic, but worse results are likely with alumina and some form of compensation would be desirable.

Horng *et al.* [34] presented a full-wave analysis of shielded-microstrip-line-to-microstrip-line transitions (edge-coupled and overlay structures). The derivation of their results depends on a method of moments, the use of dyadic Green's function, and a Galerkin procedure. They provide a check on results using a power conservation approach and show that all results are within 1% accuracy. Data are presented for high-grade alumina-type substrates operated over the frequency range 0.5–11 GHz. Transitions between microstrip and CPW are briefly considered by Gupta *et al.* [35] and more extensively by Viitanen and Kuismann [36], who report an analysis of this type of transition at frequencies up to 20 GHz.

## 17.7 Summary

A very large number of papers have described transitions between different types of planar transmission lines, and between planar transmissions lines and either coaxial line or rectangular waveguide. Transitions from microstrip dominated the discussion in this chapter because microstrip is the dominant planar transmission medium. This chapter introduced the major concepts and formed the basis of the development of transitions for the ever-evolving need to operate at higher frequencies, compact designs, and use particular attributes of different transmission line mediums.

## References

- [1] “Operating manual for the Hewlett-Packard 11608A microwave transistor measurement fixture.”
- [2] E. England, “A coaxial to microstrip transition,” *IEEE Trans. on Microwave Theory and Techniques*, vol. **24**, no. 1, pp. 47–48, Jan. 1976.
- [3] M. V. Schneider, B. Glance, and W. Bodtmann, “Microwave and millimetre wave hybrid integrated circuits for radio systems,” *Bell System Technical J.*, pp. 1703–1726, Jul.–Aug. 1969.
- [4] S. Cohn, “Optimum design of stepped transmission-line transformers,” *IRE Trans. on Microwave Theory and Techniques*, vol. **3**, no. 3, pp. 16–20, Apr. 1955.
- [5] S. Hopfer, “The design of ridged waveguides,” *IRE Trans. on Microwave Theory and Techniques*, vol. **3**, no. 5, pp. 20–29, Oct. 1955.
- [6] W. Menzel and A. Klaassen, “On the transition from ridged waveguide to microstrip,” in *19th European Microwave Conf.*, Sep. 1989, pp. 1265–1269.
- [7] J. van Heuven, “A new integrated waveguide-microstrip transition,” *IEEE Trans. on Microwave Theory and Techniques*, vol. **24**, no. 3, pp. 144–147, Mar. 1976.
- [8] Y.-S. Wu, M. Schneider, and R. Trambarulo, “Waveguide-to-microstrip power splitter,” in *1990 IEEE MTT-S Int. Microwave Symp. Digest*, May 1990, pp. 475–478.
- [9] W. Grabherr, W. Huder, and W. Menzel, “Microstrip to waveguide transition compatible with MM-wave integrated circuits,” *IEEE Trans. on Microwave Theory and Techniques*, vol. **42**, no. 9, pp. 1842–1843, Sep. 1994.
- [10] H. Jin and R. Vahldieck, “Full-wave analysis of coplanar waveguide discontinuities using the frequency domain TLM method,” *IEEE Trans. on Microwave Theory and Techniques*, vol. **41**, no. 9, pp. 1538–1542, Sep. 1993.
- [11] T. Ellis, J. Raskin, L. Katehi, and G. Rebeiz, “A wideband CPW-to-microstrip transition for millimeter-wave packaging,” in *1999 IEEE MTT-S Int. Microwave Symp. Digest*, 1999, pp. 629–632.
- [12] Y.-S. Lin and C. H. Chen, “Novel lumped-element coplanar waveguide-to-slotline transitions,” in *1999 IEEE MTT-S Int. Microwave Symp. Digest*, Jun. 1999, pp. 1427–1430.
- [13] K.-P. Ma, Y. Qian, and T. Itoh, “Analysis and applications of a new CPW-slotline transition,” *IEEE Trans. on Microwave Theory and Techniques*, vol. **47**, no. 4, pp. 426–432, Apr. 1999.
- [14] N. Kaneda, Y. Qian, and T. Itoh, “A broadband microstrip-to-waveguide transition using

- quasi-Yagi antenna," in *1999 IEEE MTT-S Int. Microwave Symp. Digest*, 1999, pp. 1431–1434.
- [15] R. Simons, R. Lee, and T. Perl, "New techniques for exciting linearly tapered slot antennas with coplanar waveguide," *Electronics Letters*, vol. **28**, no. 7, pp. 620–621, Mar. 1992.
- [16] R. Simons and R. Lee, "Coplanar waveguide aperture coupled patch antennas with ground plane/substrate of finite extent," *Electronics Letters*, vol. **28**, no. 1, pp. 75–76, Jan. 1992.
- [17] L. Zhu and K. Wu, "Unified CAD-oriented circuit model of finite-ground coplanar waveguide gap structure for uniplanar M(H)MICs," in *1999 IEEE MTT-S Int. Microwave Symp. Digest*, Jun. 1999, pp. 39–42.
- [18] L. Zhu and K. Wu, "Hybrid FGCPW/CPS scheme in the building block design of low-cost uniplanar and multilayer circuit and antenna," in *1999 IEEE MTT-S Int. Microwave Symp. Digest*, 1999, pp. 867–870.
- [19] T. Le Nadan, J. Coupez, and C. Person, "Optimization and miniaturization of a filter/antenna multi-function module using a composite ceramic-foam substrate," in *1999 IEEE MTT-S Int. Microwave Symp. Digest*, 1999, pp. 219–222.
- [20] T. Vaupel and V. Hansen, "Electrodynamic analysis of combined microstrip and coplanar/slotline structures with 3-D components based on a surface/volume integral-equation approach," *IEEE Trans. on Microwave Theory and Techniques*, vol. **47**, no. 9, pp. 1788–1800, Sep. 1999.
- [21] Y. Antar, A. Bhattacharyya, and A. Ittipiboon, "Microstripline-slotline transition analysis using the spectral domain technique," *IEEE Trans. on Microwave Theory and Techniques*, vol. **40**, no. 3, pp. 515–523, Mar. 1992.
- [22] G. Robinson and J. Allen, "Slot line application to miniature ferrite devices," *IEEE Trans. on Microwave Theory and Techniques*, vol. **17**, no. 12, pp. 1097–1101, Dec. 1969.
- [23] J. Knorr, "Slot-line transitions," *IEEE Trans. on Microwave Theory and Techniques*, vol. **22**, no. 5, pp. 548–554, May 1974.
- [24] J. Chramiec, "Reactances of slotline short and open circuits on alumina substrate," *IEEE Trans. on Microwave Theory and Techniques*, vol. **37**, no. 10, pp. 1638–1641, Oct. 1989.
- [25] A. Podcameni and M. Coimbra, "Slotline-microstrip transition on iso/anisotropic substrate: a more accurate design," *Electronics Letters*, vol. **16**, no. 20, pp. 780–781, 1980.
- [26] A. Podcameni and M. Coimbra, "Slotline-microstrip transition on iso/anisotropic substrate: Broadband design," in *1981 IEEE MTT-S Int. Microwave Symp. Digest*, 1981, pp. 80–82.
- [27] T. Itoh, "Spectral domain immitance approach for dispersion characteristics of

generalized printed transmission lines,” *IEEE Trans. on Microwave Theory and Techniques*, vol. **28**, no. 7, pp. 733–736, Jul. 1980.

[28] H.-Y. Yang and N. Alexopoulos, “A dynamic model for microstrip-slotline transition and related structures,” *IEEE Trans. on Microwave Theory and Techniques*, vol. **36**, no. 2, pp. 286–293, Feb. 1988.

[29] B. Shuppert, “Microstrip/slotline transitions: modeling and experimental investigation,” *IEEE Trans. on Microwave Theory and Techniques*, vol. **36**, no. 8, pp. 1272–1282, Aug. 1988.

[30] W. Schwab and W. Menzel, “On the design of planar microwave components using multilayer structures,” *IEEE Trans. on Microwave Theory and Techniques*, vol. **40**, no. 1, pp. 67–72, Jan. 1992.

[31] B. Schiek and J. Khler, “An improved microstrip-to-microslot transition,” *IEEE Trans. on Microwave Theory and Techniques*, vol. **24**, no. 4, pp. 231–233, Apr. 1976.

[32] M. Aikawa and H. Ogawa, “Double-sided MICs and their applications,” *IEEE Trans. on Microwave Theory and Techniques*, vol. **37**, no. 2, pp. 406–413, Feb. 1989.

[33] P. S. Hall and J. R. James, “Analysis and design of triplate corporate feeds at high frequencies,” in *9th European Microwave Conf.*, Sep. 1979, pp. 106–110.

[34] T. Horng, H. Yang, and N. Alexopoulos, “A full-wave analysis of shielded microstrip line-to-line transitions,” in *1990 IEEE MTT-S Int. Microwave Symp. Digest*, May 1990, pp. 251–254.

[35] K. C. Gupta, R. Garg, I. J. Bahl, and P. Bhartia, *Microstrip Lines and Slotlines*, 2nd ed. Artech House, 1996.

[36] A. J. Viitanen and P. A. Kuismann, “Analysing the asymmetric coupled microstrip line and the microstrip-coplanar guide transition,” in *Proc. of 2nd Int. Symp. on Recent Advances in Microwave Techniques*, Sep. 1989, pp. 887–892.

# **Chapter 18**

## **Measurements of Planar Transmission Line Structures**

### **18.1 Introduction**

This chapter is concerned with methods for accurately characterizing transmission line properties. Many measurements of microwave circuits use vector network analyzers, which measure scattering parameters directly. Calibration standards are measured and from these reference planes are established at which measurements of a device under test can be referred. There are many treatments of this measurement technique, for example [1], and this will be considered here only briefly. Instead this chapter focuses on accurate methods for characterizing the loss of transmission lines and on characterizing substrate properties. These methods are based on resonator techniques.

### **18.2 Instrumentation Systems for Microstrip Measurements**

In general we need to choose between frequency-domain and time-domain measurements. The great majority of microwave measurements are best performed in the frequency domain because with present systems technology, a high accuracy and a large amount of information are then potentially available. However, there are some requirements where time-domain measurements are valuable, and high-resolution time-domain reflectometer (TDR) systems should then be used. Pulse-rise times less than 10 ps are common with such systems; more details will be given in a later section.

In this section we are concerned with frequency-domain instrumentation. There are several questions that should be considered, for example:

- Are single-frequency techniques suitable?
- Are swept-frequency techniques suitable?
- Are single-port or two-port (or more) measurements desired?
- What information is actually required about the circuit?
- How important is the speed and ease of measurement?
- What accuracy is required?

A common characteristic of microwave test systems is the separation of forward- and backward-traveling waves, which is typically accomplished using a directional coupler. This directional coupler enables the ratio:

to be determined. This basic result is used in precision single-frequency measurements, swept frequency-domain measurements (as with  $S$  parameter measurements), and time-domain measurements (as in time-domain reflectometry).

## 18.3 Measurement of Scattering Parameters

A network analyzer system is usually employed for this purpose. This comprises principally:

- a swept-frequency generator or frequency synthesizer
- a display principally used to plot the  $S$  parameters in various forms, principally on a Smith chart, a polar plot, or magnitude and phase on rectangular plots
- an  $S$  parameter test set: this device has two measuring ports so that, when required,  $S_{11}$ ,  $S_{12}$ ,  $S_{21}$ , and  $S_{22}$  can all be determined under program control.

An outline block diagram of a suitable system is shown in [Figure 18.1](#). Up to a few tens of gigahertz these functions are usually combined into one unit. At higher frequencies separate units are used.

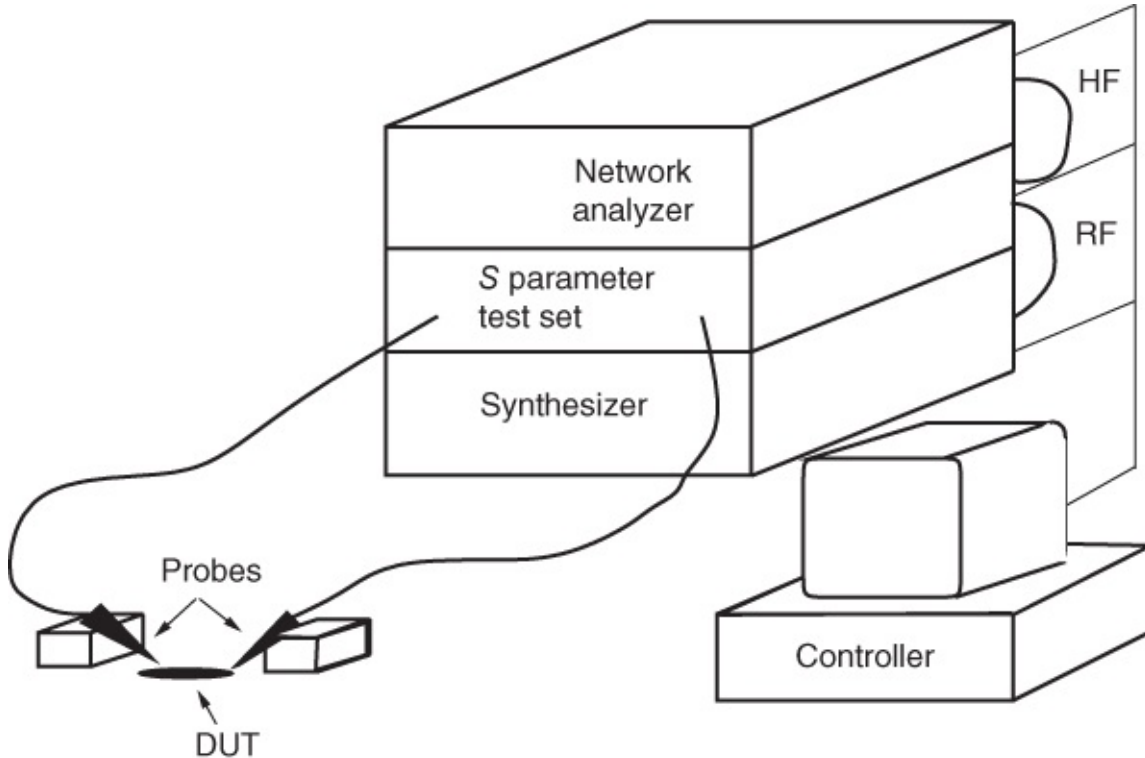


[Figure 18.1](#)  $S$  parameter measurement system: overall setup. A high frequency (HF) or intermediate frequency signal (e.g., 100 MHz) passes between the network analyzer and the  $S$  parameter test set. The DUT is the device under test.

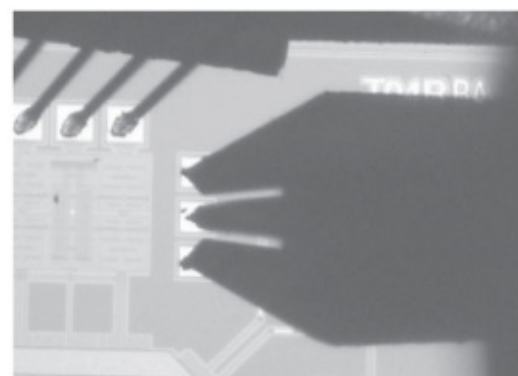
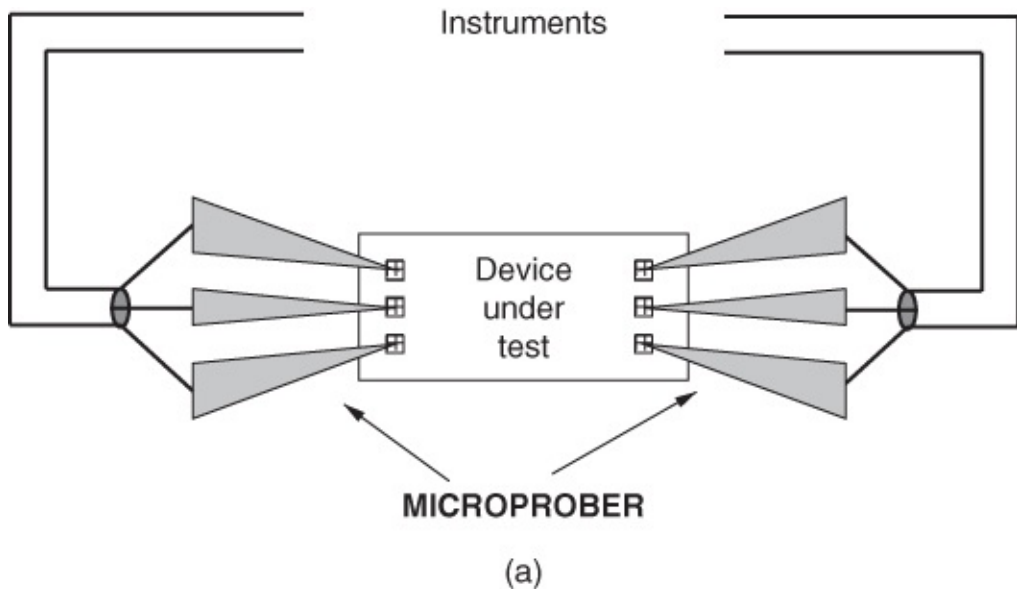
The initial calibration of the system is very important and it is necessary to calibrate the system using, for example:

- precision short-circuits: to establish  $S_{11} = S_{22} = 1.0 \angle 180^\circ$
- 50  $\Omega$  through-line: to interconnect ports 1 and 2 and calibrate  $S_{12} = S_{21} = 1.0 \angle 0^\circ$ .

Errors in the calibration standard are well characterized by the manufacturer and used in the error correction software controlling the network analyzer.

For interconnect characterization it is preferable to use calibration “standards” that consist of combinations of transmission line lengths and repeatable reflections. These calibration procedures are known mostly by combinations of the letters T, R, and L such as the standard TRL, for through-reflect-line, procedure [2, 3], or the TL, for through-line, procedure [4, 5] that relies on symmetry to replace the third standard. The calibration must be performed over the full bandwidth required.

For the measurement of complete circuits, whether active or passive, separate coaxial feed lines (and re-calibration) are often necessary. By using microprobes instead of coaxial connections, as indicated in [Figure 18.2](#), the need to recalibrate can be avoided by employing a probe-compatible standard test substrate to establish calibration. This substrate has a variety of calibration structures such as shorts, opens, and lengths of line each with contact pads. The microprobes also enable low parasitic connections to be made to chips and modules. The microprobes are particularly convenient for characterizing transmission lines. A typical microprobe is based on a micro-coaxial cable with the center conductor (carrying the signal) extended a millimeter or less to form a needle-like contact. Two other needle-like contacts are made by attaching short extensions to the outer conductor of the coaxial line on either side of the signal connection. Such probes are called ground-signal-ground (GSG) probes. A similar probe can be made using a CPW arrangement. The GSG probe connects to three pads on a substrate, each probe pad being as small as 50  $\mu\text{m}$  square, see [Figure 18.3](#). The contact parasitic capacitance, which we want to keep small, is typically 100 fF or less [6]. GS and  $\text{GS}_1\text{S}_2\text{G}$  microprobes are also available for measuring coplanar strip and differential lines.



(b)

**Figure 18.2** The use of ground-signal-ground (GSG) coplanar probes: (a) configuration showing the use of GSG with the coaxial lines coming from the network analyzer; and (b) used in measurement of an on-chip interconnect.

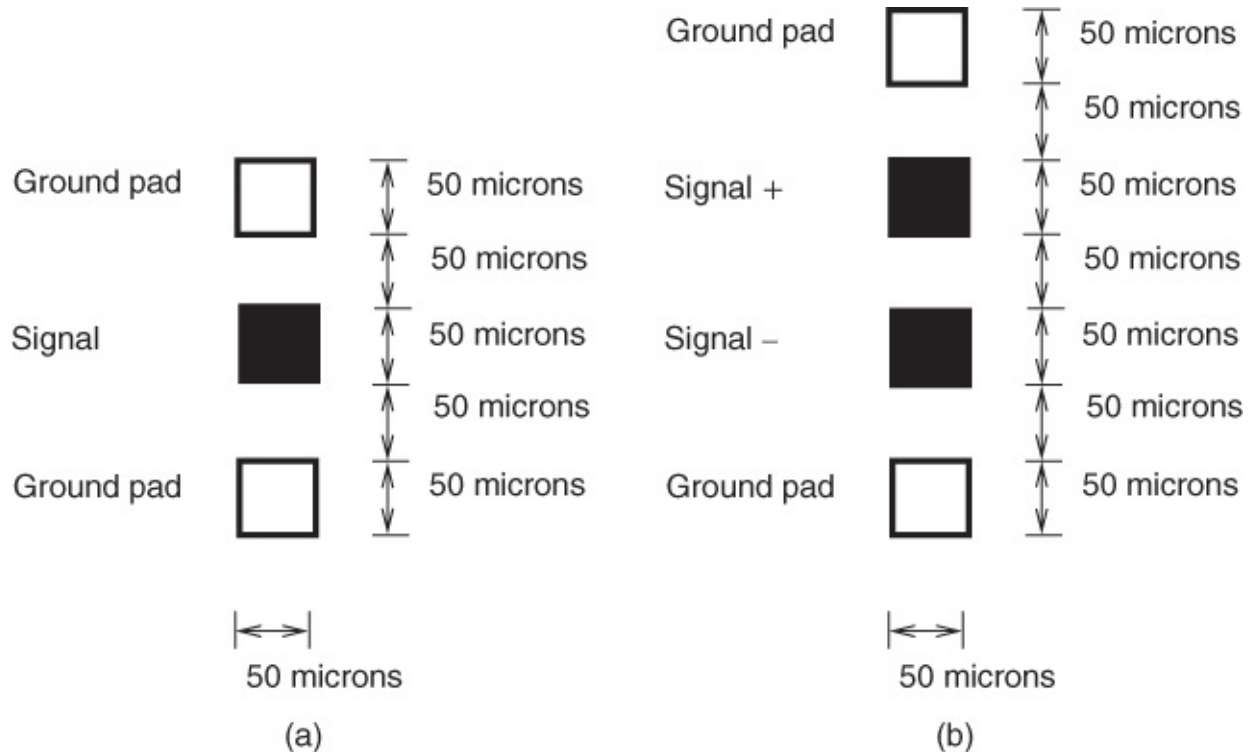


**Figure 18.3** Contact pads for coplanar probes with a 100  $\mu\text{m}$  pitch: (a) GSG configuration; and (b)  $\text{GS}_1\text{GS}_2\text{G}$  configuration for differential probing.

### **18.3.1 Some Parameter Relationships in Interpreting Interconnect Measurements**

In this subsection only lossless passive two-port networks are considered. Thus, for example, the results in this subsection are valid for circuits containing lossless transmission lines and reactive elements.

If unit power flows into a lossless two-port network, a fraction  $|S_{11}|^2$  is reflected and a further fraction  $|S_{21}|^2$  is transmitted through the network. This is illustrated by the following power flow breakdown for this case, as illustrated in Figure 18.4:

$$|S_{11}|^2 + |S_{21}|^2 = 1. \quad 18.2$$

In terms of complex conjugate products Equation (18.2) becomes

$$S_{11}S_{11}^* + S_{21}S_{21}^* = 1. \quad 18.3$$

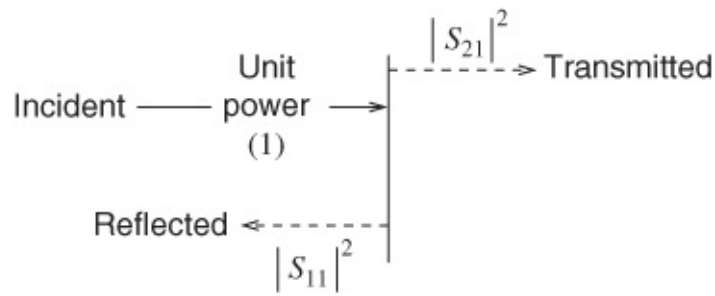


**Figure 18.4** Power flow breakdown using normalized scattering parameters.

A more general set of results follows and was derived from [7]. The total power flowing into a two-port is

$$\begin{aligned} P_{\text{in}} &= \frac{1}{2} [(|a_1|^2 - |b_1|^2) + (|a_2|^2 - |b_2|^2)] \\ &= \frac{1}{2} (a_1 a_1^* - b_1 b_1^* + a_2 a_2^* - b_2 b_2^*). \end{aligned} \quad \text{18.4}$$

These results are valid for traveling waves when the  $a$  values,  $b$  values and scattering parameters are defined with respect to a real reference impedance and for power waves defined with respect to a complex reference impedance. (Power waves were defined in [Chapter 4](#).) Substituting the scattering parameter relations  $b_1 = S_{11}a_1 + S_{12}a_2$  and  $b_2 = S_{21}a_1 + S_{22}a_2$ , Equation (18.4) becomes

$$\begin{aligned} P_{\text{in}} &= \frac{1}{2} [a_1 a_1^* - (S_{11}a_1 + S_{12}a_2)(S_{11}a_1 + S_{12}a_2)^* \\ &\quad + a_2 a_2^* - (S_{21}a_1 + S_{22}a_2)(S_{21}a_1 + S_{22}a_2)^*] \\ &= \frac{1}{2} (a_1 a_1^* - S_{11}S_{11}^* a_1 a_1^* - S_{11}a_1 S_{12}^* a_2^* - S_{12}S_{11}^* a_2 a_1^* - S_{12}S_{12}^* a_2 a_2^* \\ &\quad + a_2 a_2^* - S_{21}S_{21}^* a_1 a_1^* - S_{21}a_1 S_{22}^* a_2^* - S_{22}S_{21}^* a_2 a_1^* - S_{22}S_{22}^* a_2 a_2^*) \\ &= \frac{1}{2} [a_1 a_1^* (1 - S_{11}S_{11}^* - S_{21}S_{21}^*) - a_1 a_2^* (S_{11}S_{12}^* + S_{21}S_{22}^*) \\ &\quad - a_2 a_1^* (S_{12}S_{11}^* + S_{22}S_{21}^*) + a_2 a_2^* (1 - S_{22}S_{22}^* - S_{12}S_{12}^*)]. \end{aligned} \quad \text{18.5}$$

For a lossless two-port  $P_{\text{in}} = 0$  (no net power is dissipated) and since  $a_1$  and  $a_2$  can have any values, Equation (18.5) provides four independent equations:

$$|S_{11}|^2 + |S_{21}|^2 = 1 \quad \text{18.6}$$

$$S_{11}S_{12}^* + S_{21}S_{22}^* = 0 \quad \text{18.7}$$

$$S_{12}S_{11}^* + S_{22}S_{21}^* = 0 \quad \text{18.8}$$

$$|S_{12}|^2 + |S_{22}|^2 = 1. \quad \text{18.9}$$

These are called the unitary conditions for a lossless network. The first condition is the same

as Equation ([18.2](#)).

Further development, see [7], based on the above conditions for a lossless two-port also requires that for a lossless two-port  $|S_{21}|^2 = |S_{12}|^2$ . This is called the power reciprocity condition. It is not the same as the condition for reciprocity that requires that  $S_{12} = S_{21}$  (thus there is not a phase requirement for power reciprocity).

### **18.3.2 Fitting an Equivalent Circuit**

One approach to developing an equivalent circuit of a discontinuity is to refer measured  $S$  parameters to reference planes at the discontinuity. Then the  $S$  parameters of an assumed equivalent circuit containing lumped elements and sometimes transmission-line sections, and the measured  $S$  parameters are compared. The parameters of the equivalent circuit elements are optimized to minimize the difference of the two sets of  $S$  parameters [8, 9]. The form of the equivalent circuit is based on theoretical deliberations, as described throughout this book.

### **18.3.3 Standing-wave Indicators in Microstrip**

Most measurements require transitions from the measuring system transmission medium (often coaxial line) to the microstrip circuit under study. Even the best carefully compensated transitions must interfere to some extent with reflections from the microstrip circuit. This fact prompted the development of some standing-wave indicators (SWIs) in microstrip.

Possibly the most thoroughly designed microstrip SWI was reported by Ladbrooke [10]. In this indicator the circuit whose characteristics are to be studied is made to move in relation to a fixed probe. Instead of a slot, as used with a conventional coaxial or waveguide SWI, a thin dielectric leaf has the circuit pattern printed on it and this leaf is added to the basic structure. Ladbrooke employed a mica slice for the thin leaf and pressed this down uniformly onto the main substrate by using a backing of expanded polystyrene ( $\epsilon_r = 1.04$ ). The reference cited gives further details.

It may be considered unlikely that a microstrip SWI would be useful in routine microstrip measurements. This is because computer-augmented automatic correction is readily achievable, effectively removing the parameters of the transitions from the “raw” measurements made in coaxial line or waveguide systems.

However, a particular virtue of a microstrip SWI is the facility for probing the fields around, and even substantially away from, the circuit structure. In his paper, Ladbrooke [10], for example, describes the measurement of a wave launched from the foreshortened open-circuit end of a microstrip line. This is predominantly due to the surface-wave fields discussed in [Section 8.3](#).

## **18.4 Measurement of Substrate Properties**

Unlike many coaxial lines and waveguides, microstrip depends inherently on the properties of its dielectric substrate. The most significant properties are the permittivity and loss tangent of

the substrate.

### 18.4.1 Determining Effective Permittivity from Transmission Line Measurements

The permittivity of a transmission line can be determined by measuring the scattering parameters of two lengths of transmission line. With planar transmission lines there will always be fixturing between the measurement system and the lines being measured, and this introduces uncertainties into the characterization of microwave circuits. Engen and Hoer [2] developed a method for extracting the propagation constant,  $\gamma$ , directly from the measurement of two lengths of line. (Similar earlier work was presented by Bianco *et al.* [11].) The measured  $S$  parameters include fixturing. The effective propagation constant is then [1, 2]

$$\epsilon_e = \frac{|\gamma|^2}{(2\pi f)^2 \mu_0}. \quad 18.10$$

The shorter line can be absorbed into the fixtures and then the new effective line has a length  $\ell_L$  which is the difference between the lengths of the original lines. The measurement structures are then as shown in [Figure 18.5](#). In addition if the fixtures on the left-hand side and right hand-side are the same, that is, Fixture A and Fixture B have the same  $S$  parameters, then the actual  $S$  parameters of the transmission line can be determined using the two sets of  $S$  parameters, one for each of the fixtured line lengths along with a separate measurement of the capacitance of the line [5, 6, 12, 13]. The characteristic impedance of the line can then be extracted as well as the effective permittivity of the line.

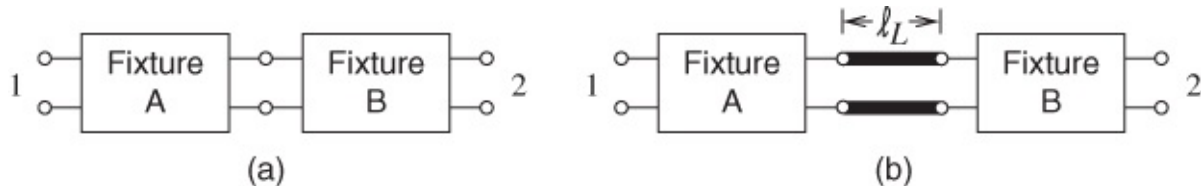


[Figure 18.5](#) Measurement connections: (a) through connection; and (b) line connection.

The through and line measurement structures include fixtures as well as the direct connection (for the through) and the inserted line (for the line) (see [Figure 18.5\(a\)](#)). For the through structure, the error networks between the ideal internal port of a network analyzer and the desired measurement reference plane are designated as Fixture A at Port 1 and Fixture B at Port 2. For the line measurement, fixturing is re-established (following the through measurement) with the line inserted, see [Figure 18.5\(b\)](#).

Extraction of the propagation constant is described below following the derivation of Engen and Hoer [2]. The development begins using cascading matrices,  $R$ , each of which is related to two-port scattering parameters  $S$  by

$$\mathbf{R} = \begin{bmatrix} R_{11} & R_{12} \\ R_{21} & R_{22} \end{bmatrix} = \begin{bmatrix} \frac{S_{12}}{S_{21}} & \frac{S_{22}}{S_{21}} & \frac{S_{11}}{S_{21}} \\ 0 & -\frac{S_{22}}{S_{21}} & \frac{1}{S_{21}} \end{bmatrix}. \quad 18.11$$

Thus the parameters describing the **A** and **B** fixtures are  $\mathbf{S}_A$ ,  $\mathbf{S}_B$  and  $\mathbf{R}_A$ ,  $\mathbf{R}_B$ , respectively. The cascading matrix of the through is simply a unity matrix, and that of the line of length,  $\ell_L$ , is

$$\mathbf{R}_L = \begin{bmatrix} e^{-\gamma_L \ell_L} & 0 \\ 0 & e^{\gamma_L \ell_L} \end{bmatrix}. \quad 18.12$$

The characteristic impedance of the line is taken as the reference impedance,  $Z_0$ , of the measurement system and results in the off-diagonal zeros in the above definition.

The cascading matrix of the through structure (i.e., the fixture-fixture cascade) is

$$\mathbf{R}_t = \mathbf{R}_A \mathbf{R}_B \quad (\text{the through}) \quad 18.13$$

and the cascading matrix of the fixture-line-fixture cascade is

$$\mathbf{R}_d = \mathbf{R}_A \mathbf{R}_L \mathbf{R}_B \quad (\text{the line}). \quad 18.14$$

Now introduce the matrix

$$\mathbf{T} = \begin{bmatrix} t_{11} & t_{12} \\ t_{21} & t_{22} \end{bmatrix} = \mathbf{R}_d \mathbf{R}_t^{-1}. \quad 18.15$$

Thus **T** combines the line and through measurements, and approximately removes the through measurement from the line measurement. Also the elements of the **T** matrix are measured quantities. Combining Equations (18.13)–(18.15),

$$\begin{aligned} \mathbf{T} \mathbf{R}_A &= \mathbf{R}_d \mathbf{R}_t^{-1} \mathbf{R}_A = \mathbf{R}_A \mathbf{R}_L \mathbf{R}_B (\mathbf{R}_A \mathbf{R}_B)^{-1} \mathbf{R}_A \\ &= \mathbf{R}_A \mathbf{R}_L \mathbf{R}_B \mathbf{R}_B^{-1} \mathbf{R}_A^{-1} \mathbf{R}_A \end{aligned} \quad 18.16$$

and so

$$\mathbf{T} \mathbf{R}_A = \mathbf{R}_A \mathbf{R}_L, \quad 18.17$$

which is referred to as the TL (for through-line) equation.

Expanding Equation (18.17) leads to a system of equations:

$$t_{11} R_{A11} + t_{12} R_{A21} = R_{A11} e^{-\Delta} e^{-\gamma_L \ell_L} \quad 18.18$$

$$t_{21} R_{A11} + t_{22} R_{A21} = R_{A21} e^{-\Delta} e^{-\gamma_L \ell_L} \quad 18.19$$

$$t_{11}R_{A12} + t_{12}R_{A22} = R_{A12}e^{\Delta}e^{\gamma_L \ell_L} \quad 18.20$$

$$t_{21}R_{A12} + t_{22}R_{A22} = R_{A22}e^{\Delta}e^{\gamma_L \ell_L}. \quad 18.21$$

Solving these yields the propagation constant of the line standard [2],

$$\gamma_L = \frac{1}{2 \ell_L} \left[ \ln \left( \frac{t_{11} + t_{22} \pm \zeta}{t_{11} + t_{22} \mp \zeta} \right) - 2\Delta \right] \quad 18.22$$

$$\zeta = (t_{11}^2 - 2 t_{11}t_{22} + t_{22}^2 + 4 t_{21}t_{12})^{1/2}. \quad 18.23$$

In other words, two-port  $S$  parameter measurements of the through connection and two-port  $S$  parameter measurements of the line connection enable the propagation constant of the line to be determined. From that the effective permittivity of the transmission line can be found (see Equation (18.10)). Errors in repeatability of the fixturing lead to errors in the extraction of  $\gamma_L$  occurring at frequencies corresponding to  $\ell_L$  being multiples of a half wavelength [14].

### 18.4.2 Resonance-based Permittivity Determination

Very often the permittivity and especially the loss tangent of a substrate cannot be obtained with sufficient accuracy using swept  $S$  parameter measurements, as described in the previous section. For the most accurate results resonance-based techniques must be used.

In the early stages of preparing for design, substrates must be characterized. Substrates can be obtained that are metallized over their broad faces. This structure, shown in Figure 18.6, can be treated as a parallel-plate resonator to which an RF signal may be coupled (Figure 18.7). The permittivity of the substrate material is then deduced from the expression

$$\epsilon_r = \left( \frac{c}{2\ell f_{n,m}} \right)^2 (n^2 + m^2) \quad 18.24$$

where  $\epsilon_r$  is strictly the value in a direction normal to the broad faces (important especially in the case of anisotropic substrates),  $\ell$  is the length of the substrate sides,  $n$  and  $m$  are mode numbers, and  $f_{n,m}$  is the resonance frequency of the  $mn$ th resonant mode.

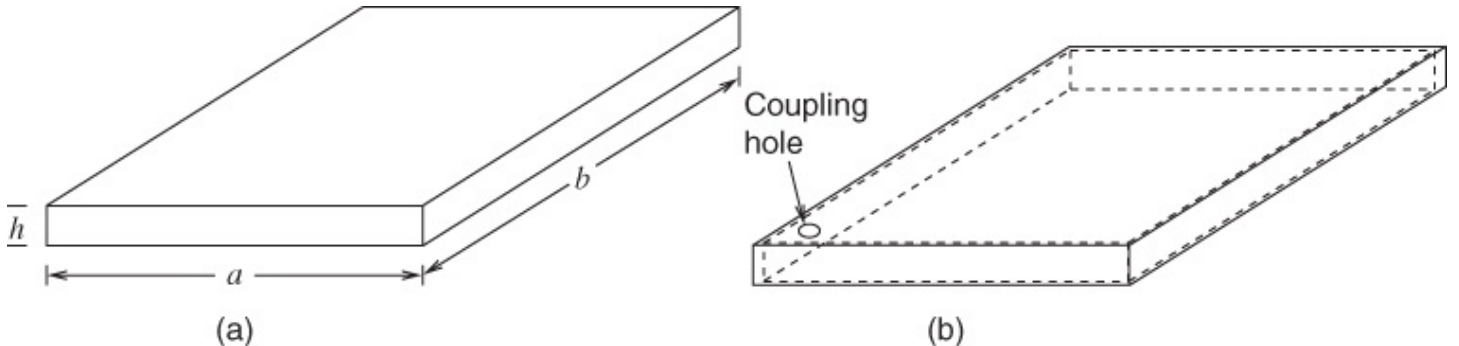


**Figure 18.6** Metallized substrates forming rectangular microwave resonators: (a) parallel-plate resonator; and (b) dielectric-filled, almost wholly metallized resonator.

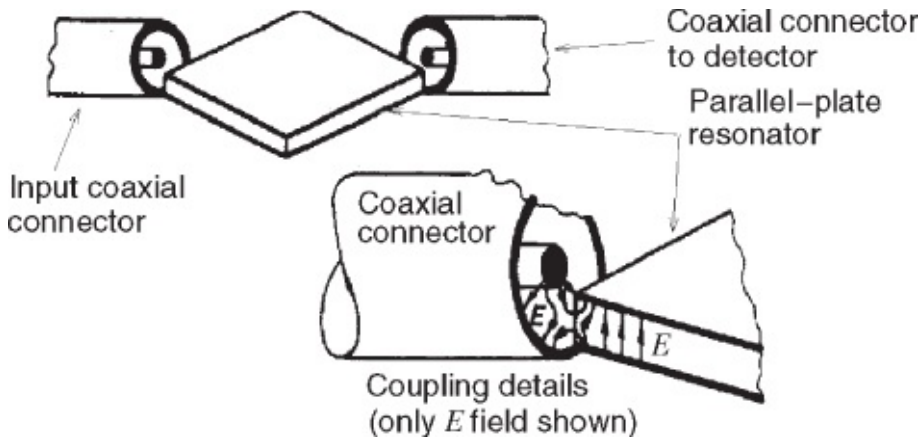


**Figure 18.7** Coaxial line coupling to a parallel-plate resonator. Adapted from Ladbrooke *et al.* (1973) [15], figures 1 and 3, p. 561. Reprinted with permission of IEEE.

It is possible to form an almost totally enclosed rectangular resonator by metallizing not only the broad faces, but also the narrow edges of a substrate. An aperture is then needed for coupling; the arrangement is illustrated in [Figure 18.8\(a\)](#) with extra details of the field in the coupling region given in [Figure 18.8\(b\)](#). Errors involved with such resonator measurements have been described by various researchers. Howell [16] concentrated on the effects of losses and fringing, Ladbrooke *et al.* [15] gave details of coupling errors, and Owens *et al.* [17] pursued a re-examination of the results given by both Howell and Ladbrooke. The deductions due to Owens *et al.* are significant because the permittivities of sapphire were under study and these values can be accurately determined by independent methods. Although it is very difficult to accurately account for a correction due to edge fringing, some adjustment must be made for this in order to achieve accurate results.

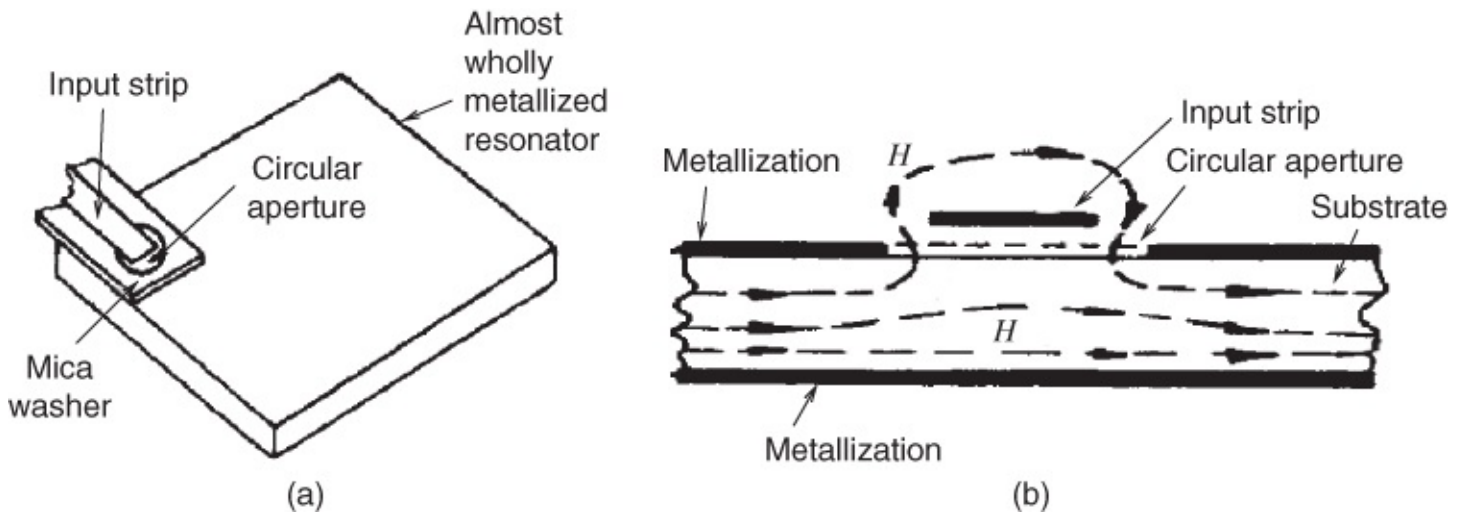


**Figure 18.8** Coupling via an aperture to an almost wholly metallized resonator: (a) overall view; and (b)  $H$  fields. In (b) only the  $H$  field is shown and the mica washer omitted for clarity. Adapted from Ladbrooke *et al.* (1973) [15], figures 1 and 3, p. 561. Reprinted with permission of IEEE.

## 18.5 Microstrip Resonator Methods

Resonator methods are generally preferred for the most accurate microstrip measurements because other conceivable methods suffer from significant difficulties that will first be briefly described.

Microstrip short-circuit terminations that have definable characteristics are very hard to implement, and matched loads having good quality with low VSWR are difficult to achieve. Any transmission measurements in microstrip therefore need to be made through transitions to other lines (usually coaxial) in which matched loads, etc. are available. Errors are then introduced due to the microstrip-to-coaxial transitions, and the influence of these errors on required parameters is understood to some extent [14]. Standing-wave measurement techniques have also been developed, to a limited extent, but the precision obtainable does not yet approach coaxial or waveguide standards.

If a microstrip line is formed as some closed loop on a substrate, or left open- or short-circuited at both ends, it represents a resonator at discrete microwave frequencies. By rather loosely coupling an RF test signal to such a resonator, so that frequency-pulling effects are avoided, the reflected energy can be studied and resonator characteristics may then be deduced.

### **18.5.1 The Ring Resonator**

This arrangement seems to be due to Troughton [18, 19], principally for dispersion measurements, and results obtained using ring resonators have been quoted in support (or otherwise) of certain dispersion theories and other measured results. Although other shapes have been tried, the most popular design is the simple circular ring shown in [Figure 18.9](#).

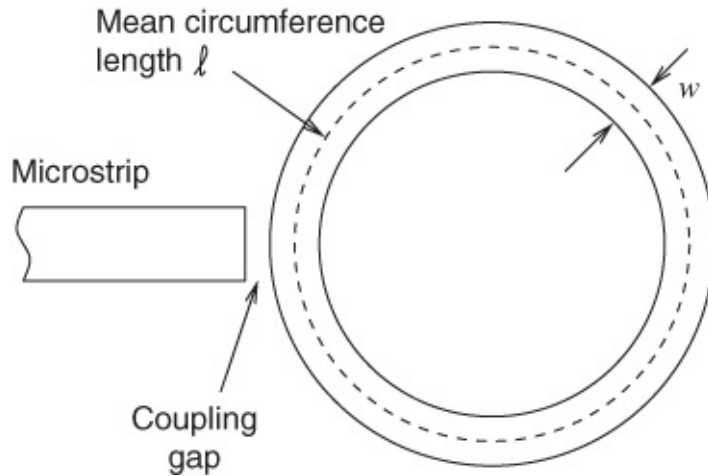


**Figure 18.9** Ring resonator.

Since the ring has no open ends it is almost free of radiative losses and may be used to determine line losses alone. For rings in which  $w/h < 1$  and  $\ell$  (mean circumference)  $\gg w$  we have, at resonance,

$$\ell = \frac{n\lambda_g}{2}$$

**18.25**

where  $n$  is the integer order of resonance. If dispersion measurements are to be performed, then  $\epsilon_{\text{eff}}(f)$  is required and, since  $c/f\sqrt{\epsilon_{\text{eff}}(f)} = \lambda_g$ , Equation (18.25) becomes

$$\frac{nc}{2f\sqrt{\epsilon_{\text{eff}}(f)}} = \ell. \quad 18.26$$

With  $F$  being the frequency in gigahertz and  $L$  being the length in millimeters, this gives

$$\epsilon_{\text{eff}}(f) = \left(\frac{150n}{FL}\right)^2. \quad 18.27$$

For  $n$  resonances with a particular ring,  $n$  values of  $\epsilon_{\text{eff}}(f)$  are therefore obtainable.

The main advantage usually claimed for ring resonators is the freedom from open-end effects. However, while this appears to be an important advantage, it by no means signifies that the electrical length of the ring can be accurately established, for the following drawbacks apply to ring resonators:

- a. curvature effects, which result in the mean physical circumference of the ring not being the most accurate value to use in calculating resonance wavelengths
- b. local radial distortion of the field in the vicinity of the coupling gap
- c. field interactions across the ring
- d. the possibility of resonance splitting due to width non-uniformities around the ring.

The problem of curvature effects, (a), appears to have been satisfactorily resolved by Owens [20], who demonstrated that a curvature correction can be applied to greatly improve the accuracy of ring measurements of dispersion. Both the measurements and the computations were very carefully performed and were compared independently. The cited paper should be consulted for further details.

It is clear that the curvature problem is greatest for wide ( $w/h \gg 1$ ) rings of relatively small diameter. The drawback of field interactions, (c), is also greater for  $w/h \gg 1$  and for rings of relatively small radii. Therefore, if rings of sufficiently large radius are used, problems (a) and (c) are diminished and the overall effect of (b) is reduced, since the coupling region occupies a smaller fraction of the total ring length. However, it must be remembered that a larger ring increases the chance of variability not only in width, but also in the substrate permittivity and thickness under the line, and the possibility of resonance splitting, (d), still remains.

### **18.5.2 The Side-coupled Open-circuit-terminated Straight Resonator**

The microstrip configuration for this structure is shown in [Figure 18.10](#). This microstrip resonator, in common with several other structures which are used, has abruptly open-circuited ends. The behavior of this “discontinuity” is such that a considerable proportion of the field fringes beyond the physical ends of the line, and the effect of this is best accounted for by considering the line to be somewhat longer electrically.

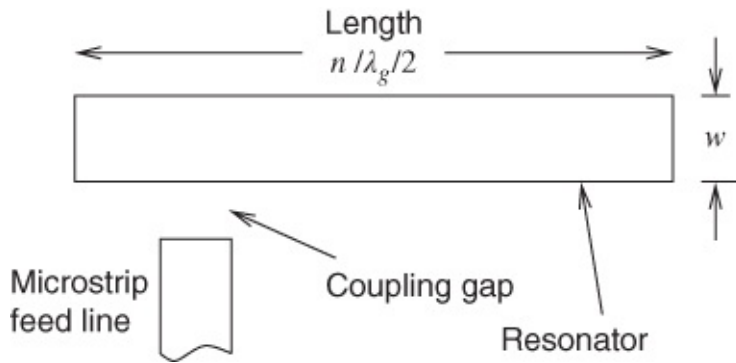


**Figure 18.10** Side-coupled open-ended straight resonator.

This situation has already been dealt with (see [Section 9.2.1](#)) and the same notation will be used here. There are two open-end-effect extensions to be considered, as indicated in [Figure 18.11](#). It is apparent that a total *effective* length of  $(\ell + 2\ell_{eo})$  exists, where  $\ell_{eo}$  is a hypothetical extension of the line to account for the end-fringing. Also, the electrical length  $\theta$  can be written as

$$\theta = \beta(\ell + 2\ell_{eo}). \quad 18.28$$

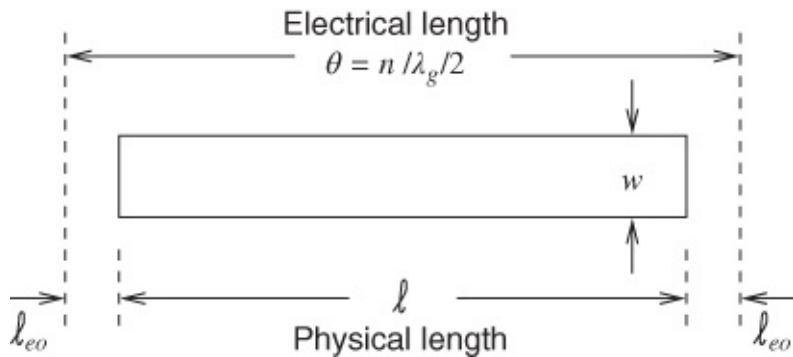


**Figure 18.11** Illustrating the effective length of an open-ended straight resonator.

With similar considerations to those used for the ring resonators, the dispersion expression for this straight resonator becomes

$$\epsilon_{\text{eff}}(f) = \left\{ \frac{150n}{f(\ell + 2\ell_{eo})} \right\}^2. \quad 18.29$$

This particular straight resonator technique may occasionally be useful, but it possesses the following disadvantages:

- There is the local transverse distortion of the field in the region of the side coupling gap. This is an identical problem to (b), mentioned under ring resonators, and it may be expected to lead to even larger errors with straight resonators because the coupling region can occupy a relatively greater fraction of the total line length.
- The position of the feed line, relative to either open end of the resonator, is fairly important. A symmetrical location at the center of the resonant line may often be best. In any event, other positions lead to limitations over the number of resonances which may be

excited.

Positioning the feed line at right angles to the resonator and in the vicinity of the open-circuit end considerably complicates the fringing fields there, and is thus undesirable.

### 18.5.3 Series-gap Coupling of Microstrips

The properties and parameters of a symmetrical series-gap were covered in [Section 9.2.2](#). A considerable amount of success has been enjoyed in several areas of microstrip measurements and in some filter designs by the use of end-to-end series-gap coupling.

There are, in general, two possibilities for feeding with series-gap structures where the feed line may have a characteristic impedance  $Z_{02}$  differing considerably from that of the feed line  $Z_{01}$ . The types of geometry that are possible are indicated in [Figure 18.12](#).

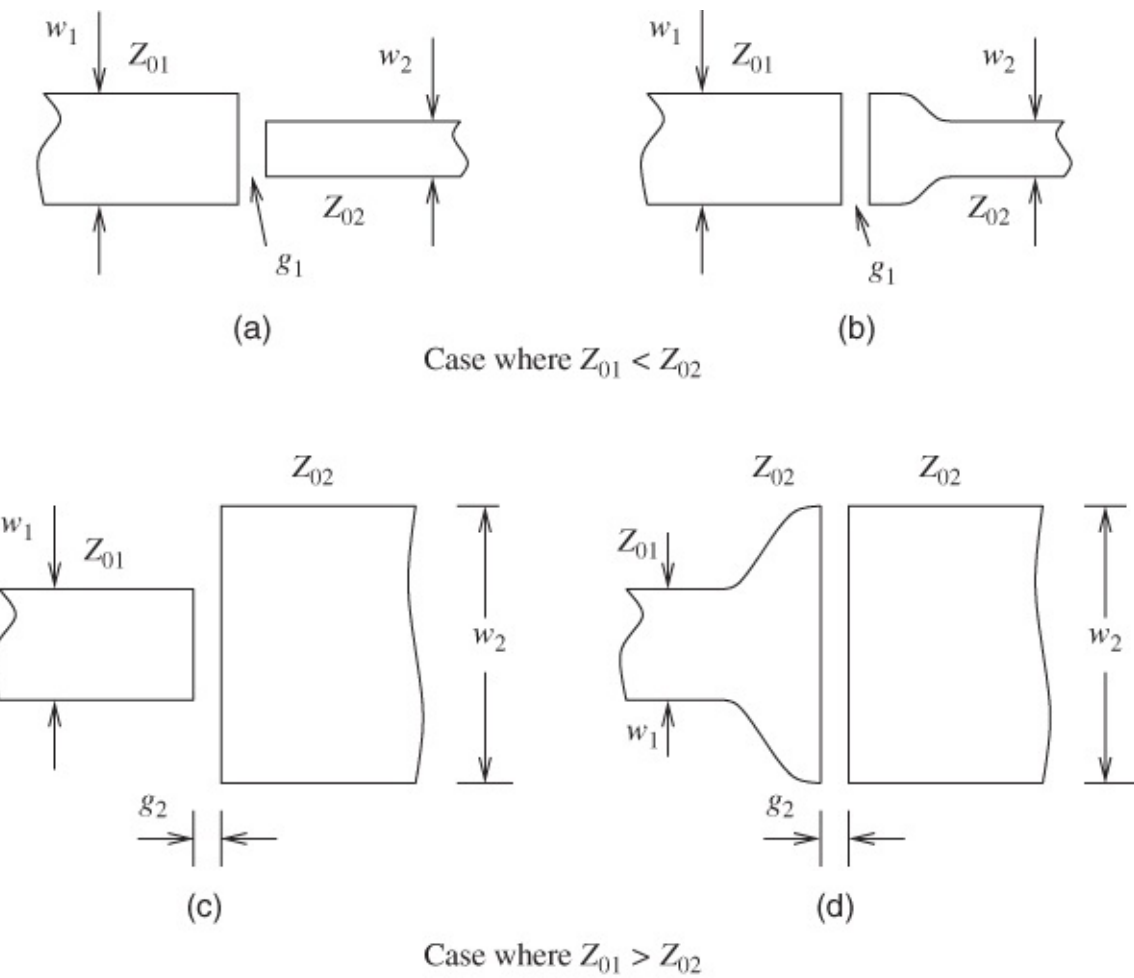


**Figure 18.12** Practical microstrip series-gap-coupled arrangements: (a) unequal widths at gap; (b) equal widths at gap; (c) unequal widths at gap; and (d) equal widths at gap.

Coupling configurations (a) and (c) (“asymmetrical longitudinally”) are often disadvantageous for at least two reasons:

- (1) It is hard to predict the degree of coupling, let alone assess the effects of adjusted gaps.
- (2) These configurations have not, as yet, been analyzed theoretically. Equivalent circuits

and parameters are therefore unavailable.

Coupling configurations (b) and (d) overcome these objections.

Practical coupling gap designs for microstrip measurement resonators are constrained by a prime requirement that the degree of coupling be kept as loose as possible, while still offering a tolerable signal-to-noise ratio for measurement. Even slight loading of the resonator due to the external circuit will affect the resonant frequency. Furthermore, all the techniques about to be outlined employ two coupling gaps. These must be manufactured as identically as possible in each case because otherwise the gap end-effect lengths must definitely differ due to the differing capacitance values. Errors will then result, since the expressions applicable to each measurement method assume equal coupling gaps, and hence identical end-effect lengths. Different end-effect lengths at the gaps result in too many unknowns, thus prohibiting accurate solution of the resonance expressions.

These circuits do not have the disadvantages which apply to the arrangements discussed in the previous paragraphs. They do, however, all involve the end-effect lengths, both at the gaps and at the abruptly open-circuited ends.

Richings [21] performed experiments to ascertain suitable coupling gap separations ( $g$ ) for resonators on alumina, and we have carried out other investigations where the substrate material is sapphire. For resonators on 0.5 mm thick monocrystalline sapphire, the coupling gap separation may be calculated approximately from the empirical expression

$$g = \frac{8000 \log Z_0}{Z_0} - 148 \mu\text{m} \quad \text{18.30}$$

where  $Z_0$  is the characteristic impedance of the microstrip line forming the resonator.

Use of this formula ensures that fairly loose coupling is maintained. When resonators are to be constructed on alumina the gap needs to be somewhat greater for similar conditions to apply. In the case of 0.65 mm-thick alumina substrates, with permittivity approximately 10.0, gap separations are approximately 30% greater than those calculated for sapphire. This is because the thicker material and lower permittivity both serve to increase the influence of the series capacitance, and hence to increase the coupling.

### 18.5.4 Series-gap-coupled Straight Resonator Pairs [22]

This arrangement is particularly useful for dispersion measurements, and [Figure 18.13](#) shows both the physical layout and effective lengths involved. In this method, the combined end-effect length  $\ell_e$  is eliminated for the purpose of calculating the effective microstrip permittivity  $\epsilon_{\text{eff}}(f)$  using measured resonant frequencies and lengths of each resonator. For this technique to operate successfully, we make  $\ell_2 \approx 2\ell_1$ . (Incidentally, this means that  $\ell_2$  resonates at many more frequencies than  $\ell_1$ , which has the extra advantage of providing further measurement data.) Refer to [Figure 18.13](#), and assume that:

- $\ell_{eo}$  and  $\ell_{eg}$  are both independent of resonator length so that  $\ell_{eo1} = \ell_{eo2} = \ell_{eo}$

b.  $\ell_e = \ell_{eo} + \ell_{eg}$  (combined end-effect length).

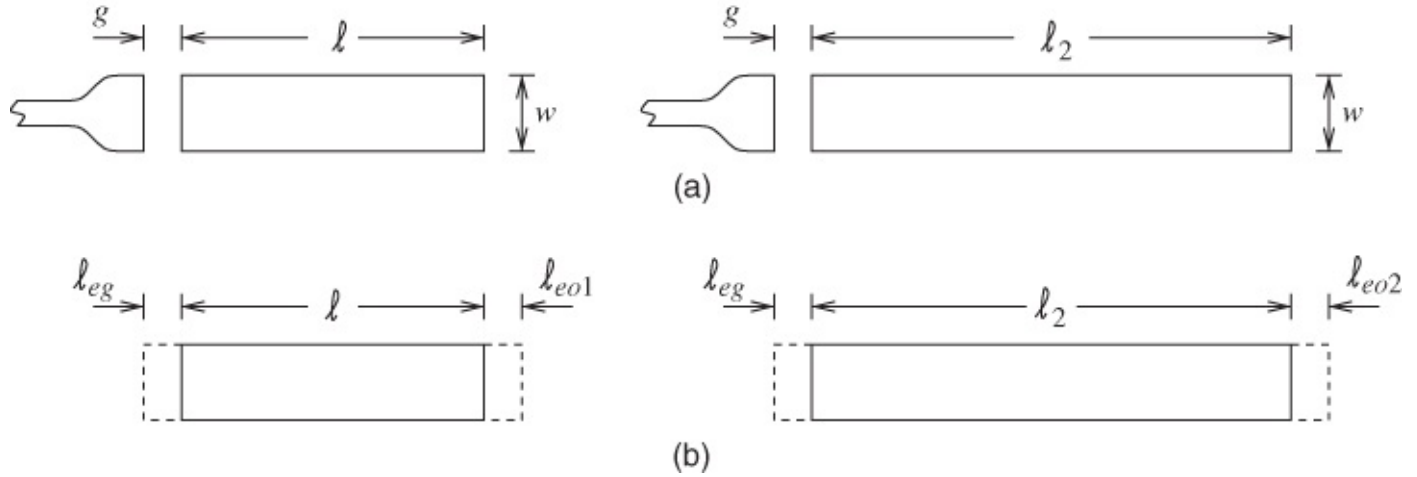


**Figure 18.13** Open-circuited pairs of straight resonators: (a) practical arrangement; and (b) effective lengths of the resonators.

Then

$$\ell_1 + \ell_e = \frac{\lambda_{g1}}{2} \quad \text{and} \quad \ell_2 + \ell_e = n\lambda_{g2} \quad \text{18.31}$$

where the unknowns are  $\lambda_{g1}$ ,  $\lambda_{g2}$ , and  $\ell_e$ , and  $n$  is the (integral) order of resonance. From these expressions and eliminating  $\ell_e$ :

$$\ell_2 - \ell_1 = n\lambda_{g2} - \frac{n\lambda_{g1}}{2}. \quad \text{18.32}$$

Now there is the general relationship between  $\varepsilon_{\text{eff}}(f)$  and wavelengths:

$$\varepsilon_{\text{eff}}(f) = \left( \frac{\lambda_0}{\lambda_g} \right)^2. \quad \text{18.33}$$

Therefore, we may write

$$\varepsilon_{\text{eff}}(f) = \left( \frac{c}{\lambda_{g1} f_1} \right)^2 = \left( \frac{c}{\lambda_{g2} f_2} \right)^2 \quad \text{18.34}$$

where  $f_1$  applies to  $\lambda_{g1}$  and  $f_2$  applies to  $\lambda_{g2}$ . We may allow the same  $\varepsilon_{\text{eff}}(f)$  value for each result since  $f_1$  and  $f_2$  have deliberately been forced to be close values in designing the resonators, and  $\varepsilon_{\text{eff}}(f)$  changes slowly with frequency. Equation (18.32) therefore becomes

$$\ell_2 - \ell_1 = \frac{nc}{f_2 \sqrt{\varepsilon_{\text{eff}}(f)}} - \frac{nc}{2f_1 \sqrt{\varepsilon_{\text{eff}}(f)}} \quad \text{18.35}$$

and solving this for  $\varepsilon_{\text{eff}}(f)$  finally gives

$$\varepsilon_{\text{eff}}(f) = \left[ \frac{nc(2f_1 - f_2)}{2f_1 f_2(\ell_2 - \ell_1)} \right]^2.$$

This expression may be used to obtain dispersion results in cases where both resonators,  $\ell_1$  and  $\ell_2$ , are resonant at close frequencies. It is also necessary to evaluate the combined end-effect length  $\ell_e$ . Equation (18.31) can readily be solved for  $\ell_e$ . Initially, dividing the equations eliminates several common quantities (again assuming  $\varepsilon_{\text{eff}}(f)$  to be constant):

$$\frac{\ell_1 + \ell_e}{\ell_2 + \ell_e} = \frac{\lambda_{g1}/2}{\lambda_{g2}} = \frac{c/[2f_1 \sqrt{\varepsilon_{\text{eff}}(f)}]}{c/[f_2 \sqrt{\varepsilon_{\text{eff}}(f)}]} = \frac{f_2}{2f_1} \quad 18.37$$

and after a little manipulation this yields the required end-effect length:

$$\ell_e = \frac{f_2 \ell_2 - 2f_1 \ell_1}{2f_1 - f_2}. \quad 18.38$$

An approximate *a priori* knowledge of  $\ell_e$  is required so that  $\ell_2 = (2\ell_1 + \ell_e)$ , which ensures that  $f_1$  and  $f_2$  are close frequencies.

The special requirements arising from this method are that, for each set of results, a pair of resonators must be made with identical widths and coupling gaps. Both resonators may lie on the same substrate, or each may occupy one of a pair of substrates with very closely matched thicknesses in order to accommodate a long resonator across a diagonal or to avoid resonator interaction.

Additional values of  $\varepsilon_{\text{eff}}(f)$  can be obtained from the odd-mode resonances of the longer resonators, where

$$\ell_2 + \ell_e = (2n - 1) \frac{\lambda_{g2}}{2} = (2n - 1) \frac{c}{2f_2 \sqrt{\varepsilon_{\text{eff}}(f)}} \quad 18.39$$

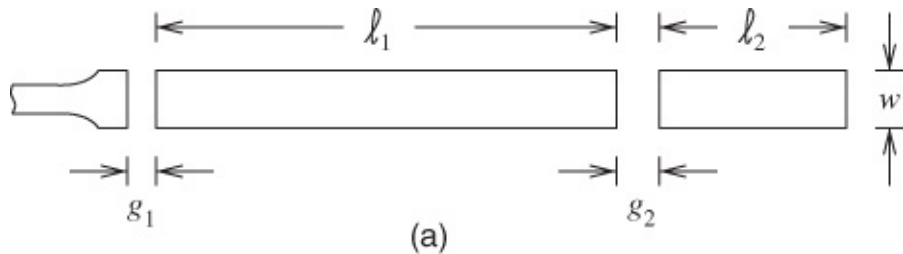
or

$$\varepsilon_{\text{eff}}(f) = \left\{ \frac{(2n - 1)c}{2f_2(\ell_2 + \ell_e)} \right\}^2 \quad 18.40$$

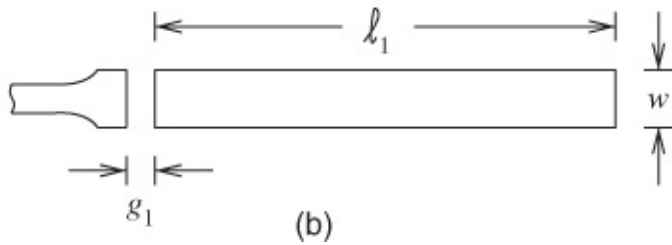
where the appropriate value of  $\ell_e$  is interpolated between values calculated from the adjacent frequencies, using Equation (18.38).

### 18.5.5 The Resonant Technique due to Richings and Easter

Richings and Easter [21, 23] appear to have been the first to devise an experimental technique enabling separation of the end-effects due to the series gap and the foreshortened open circuit. The new feature which was introduced is a second series-gap-coupled quarter-wavelength line resonator. As in the previous paired resonators method, at least a very approximate *a priori* knowledge of the end-effect lengths is required. The physical structure is shown in Figure 18.14.



(a)



(b)

**Figure 18.14** The two-stage resonator technique originally devised by Richings and Easter: (a) stage 1; and (b) stage 2 with the section of length  $\ell_2$  removed.

The quarter-wavelength line, of physical length  $\ell_2$ , transforms the open circuit at the foreshortened end of the line of length  $\ell_2$  to an effective short circuit in the vicinity of the gap  $g_2$ . This is the crucial feature of the method because it means that the structure with two gaps is effectively a line of length  $\ell_1$  with two gap end-effect extensions, one at each end of the line. For stage 2 of the measurements the quarter-wavelength line  $\ell_2$  is removed by chemical etching. If we assume that the foreshortened open-circuit end-effect lengths are all identical and equal to  $\ell_{eo}$  and that the gap end-effect lengths are equal to  $\ell_{eg}$ , then we can adopt the same notation as in [Section 18.5.4](#) (preceding Equation (18.31)). Thus, we obtain the following expressions for stage 1 shown in [Figure 18.14\(a\)](#), for the resonator of length  $\ell_1$ :

$$n\lambda'_g/2 = \ell_1 + 2\ell_{eg} \quad \underline{18.41}$$

and, with  $\ell_2$  removed, that is, [Figure 18.14\(b\)](#),

$$n\frac{\lambda''_g}{2} = \ell_1 + \ell_{eg} + \ell_{eo} \quad \underline{18.42}$$

where  $n$  is the (integer) order of resonance and the frequencies must differ slightly, and hence the different wavelengths  $\lambda'_g$  and  $\lambda''_g$ .

These wavelengths are evaluated by measuring the two resonant frequencies  $f'$  ([Figure 18.14\(a\)](#)) and  $f''$  ([Figure 18.14\(b\)](#)), knowing  $\epsilon_{eff}(f)$ , and applying the procedure previously described following Equation (18.33) in [Section 18.5.4](#). The effective microstrip permittivity  $\epsilon_{eff}(f)$  can either be determined independently ([Section 18.5.4](#)) or by constructing a further circuit under this method and eliminating  $\ell_{eo}$  and  $\ell_{eg}$  from the resonance expressions.

We can now evaluate  $\ell_{eo}$  and  $\ell_{eg}$ . Setting the experimentally determined quantities  $n\lambda'_g/2 = x$  and  $n\lambda''_g/2 = y$  we obtain, from Equation (18.41),

$$\ell_{eg} = \frac{x - \ell_1}{2}$$

and, from Equation (18.42),

$$\ell_{eo} = y - \ell_{eg} - \ell_1. \quad 18.44$$

Using this technique, and also using sets of varied-length resonators to accommodate different frequencies, Richings [21] obtained several useful and consistent results.

For adequate accuracy in measurement, the gaps must be made identical to within a few microns for resonators manufactured on alumina-type substrates.

### 18.5.6 The Symmetrical Straight Resonator [24]

The previously described straight resonator measurement methods suffer from the drawback of requiring some *a priori* knowledge of the end-effect equivalent lengths. The “symmetrical resonator” method does not require this rather uncertain item of design information. This arrangement also avoids the critically placed quarter-wave transforming line associated with Richings' method. The basic structure is shown in [Figure 18.15](#).

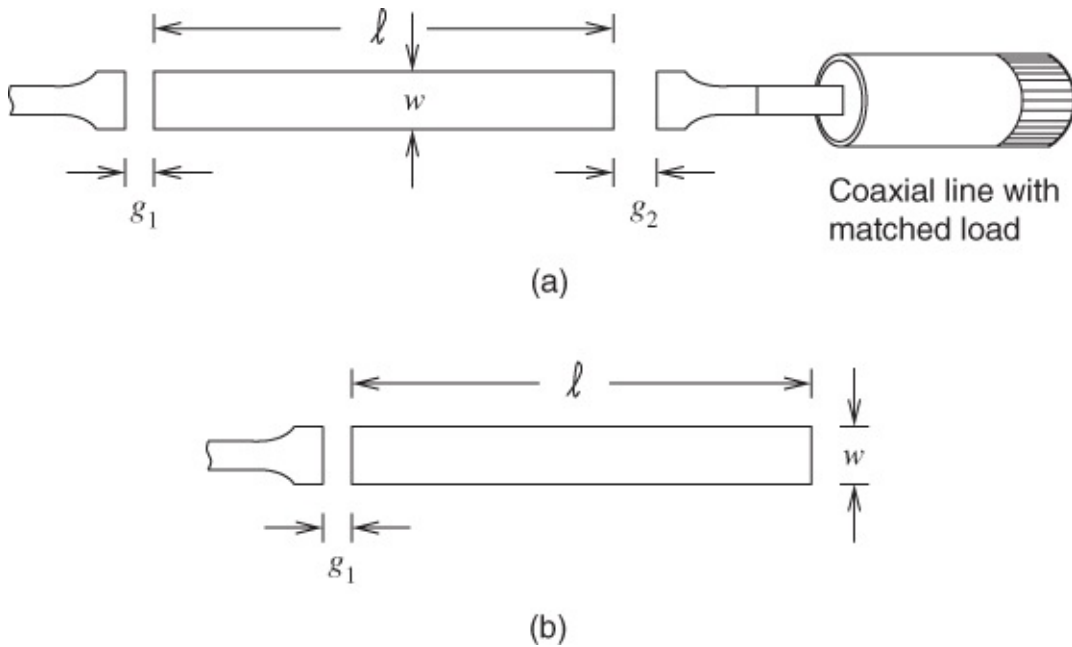


**Figure 18.15** Symmetrically loaded resonator technique: (a) stage 1; and (b) stage 2 with the load and load-section removed.

Electrically, taking a plane situated in the physical center of the microstrip resonator, a nearly identical circuit is seen whether one looks towards the source (coupled in through  $g_1$ ) or towards the matched load. In the network analyzer measuring system, the source impedance is generally very close to  $50 \Omega$ , so a matched  $50 \Omega$  load is also used. The gaps  $g_1$  and  $g_2$  are kept very nearly equal and set for loose coupling.

For stage 1, referring to [Figure 18.15\(a\)](#) and using the notation previously employed, the resonance equation is

$$\frac{1}{2}n\lambda_{g1} = \ell + 2\ell_{eg}$$

18.45

where the microstrip wavelength  $\lambda_{g1}$  is known from the effective microstrip permittivity  $\epsilon_{\text{eff}}(f)$  obtained by another method, such as the paired resonators (in [Section 18.5.4](#)). The resonant frequency  $f$  is measured and  $\ell_{eg}$  becomes

$$\ell_{eg} = \frac{nc}{4f_1\sqrt{\epsilon_{\text{eff}}(f)}} - \ell. \quad 18.46$$

With the coaxial-matched load removed and the second section of line chemically etched away from the substrate, we have stage 2 of this method. The resonance equation in this case is, referring to [Figure 18.15\(b\)](#), and using the previously employed notation,

$$\frac{1}{2}n\lambda_{g2} = \ell + \ell_{eg} + \ell_{eo} \quad 18.47$$

whence

$$\ell_{eo} = \frac{nc}{2f_2\sqrt{\epsilon_{\text{eff}}(f)}} - \ell - \ell_{eg} \quad 18.48$$

where all quantities on the right-hand side are known, including the new measured resonant frequency  $f_2$ .

This general type of resonator layout has also been used to calibrate TRL for on-wafer microstrip lines [3]. Calibrated versus resonator-derived loss measurements were reported over the frequency range 1–22 GHz for magnitude and from 1 to 26 GHz for phase. Both reflection coefficient  $S_{11}$  and forward transmission coefficient  $S_{21}$  were measured for microstrip and coplanar lines. It was concluded that microstrip provides a superior TRL capability, given the relatively good agreement between calibrated and independent measurements.

### **18.5.7 Resonance Methods for the Determination of Discontinuities other than Open Circuits [25]**

In order to measure quantities other than equivalent discontinuity capacitance, it is necessary to set up resonator arrangements which ensure effective cancellation of the capacitive effect in the vicinity of the discontinuity. For the determination of inductance a voltage node must be placed in the discontinuity region and use is made of the fact that such a node will occur  $\lambda_g/4$  away from a voltage maximum (at a true open-circuit plane). Thus it is important to accurately know the wavelength and open-end effect for the line concerned. The arrangement shown in [Figure 18.16\(a\)](#) [23] indicates how the through-arm inductances  $L_1$  may be measured. The measurement of  $L_3$ , and of capacitance  $C$ , is indicated in [Figure 18.16\(b\)](#) and (c), respectively.

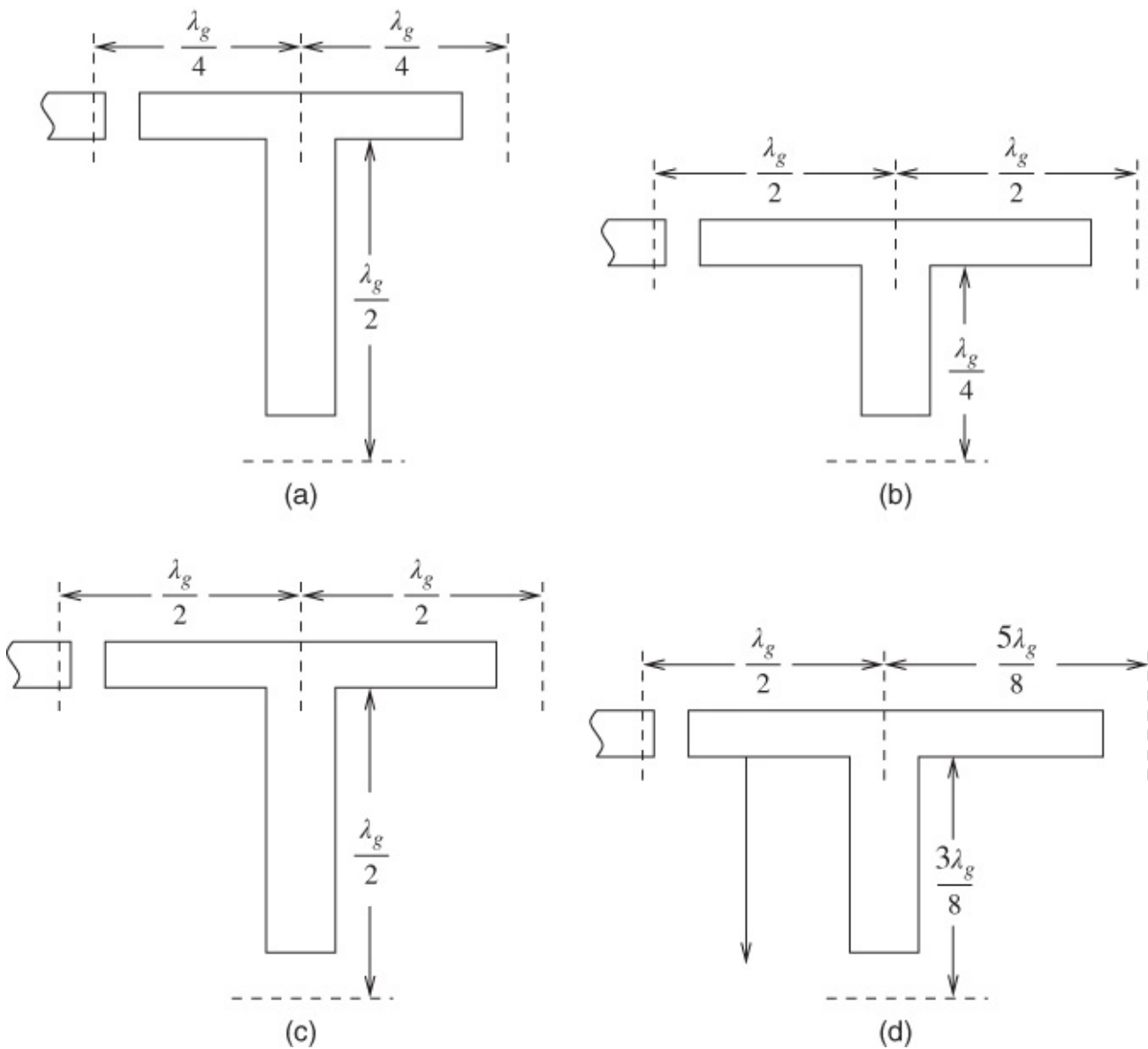


**Figure 18.16** T-junction measurement arrangements: (a)  $L_1$  measurement; (b)  $L_2$  measurement; (c) measurement of  $C$ ; and (d) measurement of  $n$ . Adapted from Easter (1975) [23], figure 5, p. 658. Reprinted with permission of IEEE.

In all cases, the parameters are first determined as equivalent extra lengths of the resonator and then finally as lumped equivalent elements. For the measurement of the impedance ratio  $n^2$  it is necessary that the transformed impedance (in the vicinity of the junction) be finite and also well defined. To obtain this, the intermediate eighth-wavelength sections of line are used, since these yield input reactances equal to  $-jZ_0 \Omega$ .

In order to complete the measurements, the secondary arm of the T junction is removed by etching and the circuits remeasured. The demands on the accuracy of initial circuit fabrication and the etching operation are generally high. For further details the cited reference should be consulted.

## 18.6 $\varrho$ Factor Measurements

This section uses the  $Q$  factor results derived in [Section 8.2](#).

Reliable techniques for the determination of the  $Q$  of a microwave resonator are well known. Network-analyzer-compatible swept-frequency techniques for measuring the  $Q$  factor were described in a comprehensive paper by Aitken [26]. These techniques are well suited to microstrip resonator measurements where, for example, the instrumentation system shown in [Figure 18.1](#) is in use.

Both the  $Q$  factor and the coupling coefficient are obtained using the techniques described by Aitken. It is indicated that errors in measured  $Q$  can be kept below 10% provided the coupling coefficient  $\eta$  (Aitken's  $\beta$ ) is within the range

$$0.15 \leq \eta \leq 0.75.$$

When  $\eta$  is below 0.15 the signal-to-noise ratio becomes poor and the measurement accuracy suffers, although the accuracy can be improved if signal-averaging techniques are used. For straight microstrip resonators, the coupling gap separation given by Equation (18.30) should ensure that  $\eta$  lies within the range given, but some adjustment may occasionally be required. Coupling gaps for ring resonators require experimental optimization.

Measurements of the  $Q$  of ring resonators yield the losses due, predominantly, to conductor resistivity and substrate dielectric losses. There is very little loss due to radiation.

On the other hand, measurements conducted using open-circuit-ended straight resonators are influenced by the “end-effects.” The  $Q$  due to these end-effects alone may be found in terms of the reflection coefficient magnitudes,  $\rho$ , at each end. This is useful since, once  $Q$  is measured,  $\rho$  is known and the parameters that describe the behavior of the open circuit can be obtained. To simplify the analysis we start by assuming that the microstrip resonator is isolated [27], that is, the coupling does not influence the  $Q$  significantly. The situation is shown in [Figure 18.17](#).

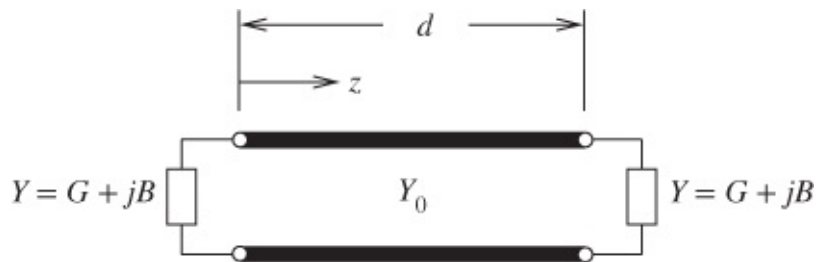


**Figure 18.17** Equivalent equal loads ( $G + jB$ ) at both ends of a straight, symmetrical, open-ended resonator.

It was shown in [Section 8.2](#), Equation (8.41), that the external  $Q$  applicable to this type of resonator can be expressed in terms of the end reflection coefficient  $\rho$  as:

$$Q_e = \frac{\pi l \rho}{1 - \rho^2}. \quad 18.49$$

Thus from the measured external  $Q$ ,  $Q_e$ , the end-reflection coefficient can be derived.

For example, an external  $Q$  of 29.8 leads to an end reflection coefficient of 0.9. This would be

a poor  $Q$  if it applied to a resonator for most circuit design purposes and should more likely be the attribute of some resonant structure designed for a microstrip antenna. In contrast, a measured external  $Q$  factor of 312 (which is fairly typical of microstrip in circuits) corresponds to an end reflection coefficient of 0.99.

It should be noted that the actual measured  $Q$  will also include both conductor and dielectric losses, which are accounted for by an unloaded  $Q$ ,  $Q_u$ . Therefore, the total measured  $Q$  for the resonator is given by

$$1/Q = (1/Q_u) + (1/Q_e). \quad 18.50$$

Since  $Q_u$  can easily be measured, using the simple arrangements described earlier in this chapter ([Sections 18.2](#) and [18.5.1](#)),  $Q_e$  becomes the only unknown in Equation (18.50) and can readily be found.

## 18.7 Measurements of Parallel-coupled Microstrips

The basic principles of parallel-coupled microstrip lines, and design procedures using them, were discussed in [Chapters 10](#) and [11](#).

In order to check any theory and develop sound designs, it is highly desirable that adequate measurements be performed to support the theoretically calculated results and, for example, account for uncertainties in material properties. Gupta *et al.* [28] described several test arrangements for determining coupled microstrip line parameters. Particular parameters required are:

- even- and odd-mode characteristic impedances
- even- and odd-mode phase velocities
- coupling factor (principally the mid-band, i.e., maximum value).

Gupta describes the measurement technique, originally given by Napoli and Hughes [29], in which the even and odd modes are separately excited and outputs from the coupled lines are fed into the “reference” and “test” channels of a microwave network analyzer. Resonant, coupled, half-wavelength lines are used, and the wavelengths applicable to each mode are found from the resonant frequencies. It is suggested that a slotted line be inserted in the test channel input to determine the VSWR values, and hence the characteristic impedances from

$$Z_{0e} = Z_0 \sqrt{r_e} \quad \text{and} \quad Z_{0o} = \frac{Z_0}{\sqrt{r_o}} \quad 18.51$$

where  $r_e$  and  $r_o$  are VSWR values for the even and odd excitations, respectively.

However, it would seem that the VSWR could equally well be obtained from reflection coefficient measurements using the network analyzer. (The required inter-relationship is given as Equation (2.39).) Since, especially with “loose” coupling,  $Z_{0e}$  and  $Z_{0o}$  do not differ greatly, the measurements of  $r_e$  and  $r_o$  must be accurate, perhaps more accurate than can be determined

indirectly from reflection coefficient measurements. The value of  $Z_0$  must also be known with confidence.

Richings [21] points out that Napoli and Hughes' measurement technique is fairly complex, requiring four identical coupling gaps and four transitions. Richings has given details of a single-port measurement technique, the basic circuit for which is shown in [Figure 18.18](#).

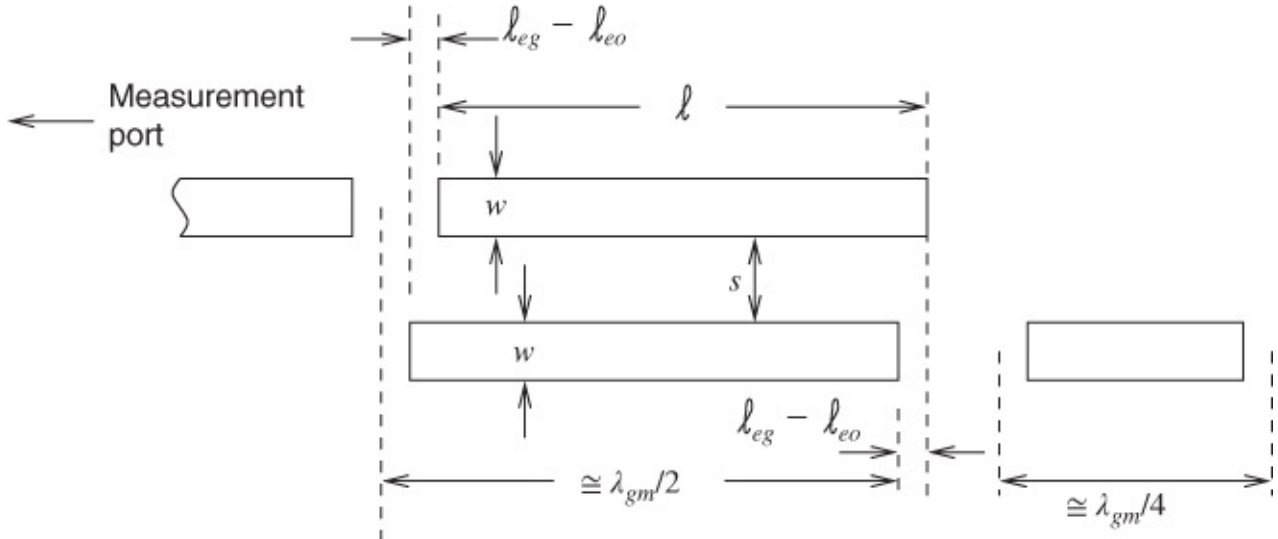


**Figure 18.18** Resonant method for determining the phase velocities in two parallel-coupled microstrips.

This technique has been used for open microstrip circuits and also for shielded circuits. Careful measurements account for the end-effects, and the resonance conditions are

$$\frac{1}{2}n\lambda_{ge} = \ell + 2\ell_{ege} + \ell_{eo} \quad 18.52$$

and

$$\frac{1}{2}n\lambda_{go} = \ell + \ell_{ego} + \ell_{eo} \quad 18.53$$

where the subscripts, and the equivalent end-effect lengths, have the meanings previously given. Two distinct resonances are observable, leading to the measurement of two frequencies  $f_{0e}$  and  $f_{0o}$ . Effective permittivities and phase velocities can then be evaluated from the expressions

$$\epsilon_{\text{eff},e} = \left( \frac{c}{f_{0e}\lambda_{ge}} \right)^2 \quad 18.54$$

$$\epsilon_{\text{eff},o} = \left( \frac{c}{f_{0o}\lambda_{go}} \right)^2 \quad 18.55$$

$$v_{pe} = \frac{c}{\sqrt{\epsilon_{\text{eff},e}}}$$

and

$$v_{po} = \frac{c}{\sqrt{\epsilon_{\text{eff},o}}}. \quad 18.57$$

The accuracy of this technique is subject to the limitations discussed for the measurement of single line parameters ([Section 18.5.5](#)). Further details are given in Richings' dissertation [21], where power-loss measurements are also described.

Richings proposed a different configuration for the determination of the coupling factor (see [Figure 18.19](#)). As described in the comments following Equation (10.38), maximum coupling occurs when the coupled region extends for a quarter-wavelength. This is provided by the overlapping length,  $\ell = \lambda_{gm}/4$  in [Figure 18.19](#). The resonance condition for this circuit is

$$\frac{Z_0}{\tan \theta} + \frac{1}{2} \left( \frac{Z_{0e}}{\tan \theta_e} + \frac{Z_{0o}}{\tan \theta_o} \right) \pm \frac{1}{2} \left( \frac{Z_{0e}}{\sin \theta_e} - \frac{Z_{0o}}{\sin \theta_o} \right) = 0. \quad 18.58$$

The appropriate values of  $Z_{0e}$  and  $Z_{0o}$  are obtained by theoretical calculation, and the electrical lengths ( $\theta_{e,o}$ ) are determined by an iterative method. Thus, the coupling factor can also be evaluated.

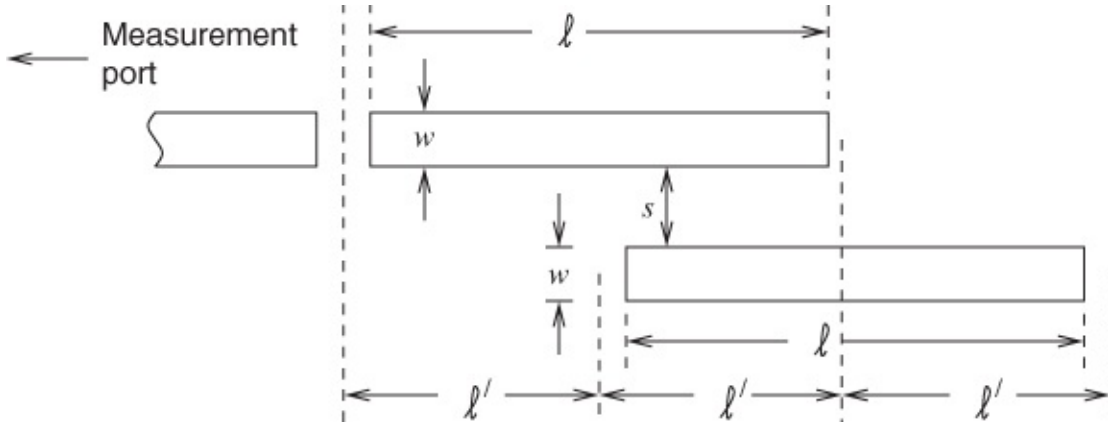


**Figure 18.19** Resonant method for determining the coupling factor between two parallel-coupled microstrips,  $\ell = \lambda_{gm}/4$ .

Rizzoli [30] demonstrated a method using properly terminated parallel-coupled microstrip to ensure separate excitation of even and odd modes. Rizzoli's method requires short circuits to ground, which can be effectively implemented in microstrip at high microwave frequencies (see [Section 7.4](#)), but which become difficult to implement at millimeter-wave frequencies.

Babu and Banmali [31] described a technique for measuring coupled microstrip line parameters without the use of a network analyzer. Only a signal generator, a standing-wave indicator, a variable short-circuit stub, and two coaxial-to-microstrip transitions are required. These researchers showed how scattering-parameter measurements can be performed, with corrections for the transitions, to obtain the characteristic impedances, phase velocities, and

losses. Circle diagram techniques are employed, and the cited reference should be read for further details. It is difficult to assess the accuracy of this method from the given information because so few final results are actually quoted.

## 18.8 Time-domain Reflectometry Techniques

The basic principles and operating practices associated with TDR techniques, in which a pulse is transmitted through the circuit, are well known and have been published elsewhere. Although frequency-domain studies generally yield accurate information regarding the performance of microwave circuits and systems, TDR possesses the following possible advantages:

- immediate recognition of the nature of various elements, by waveform examination
- approximate location of specific elements or discontinuities in the circuit or system
- fairly simple instrumentation.

It is also an attractive method for characterizing interconnects and discontinuities in digital circuits as the test signals in TDR relate directly to digital signals [32–34].

Since the operation of TDR depends inherently on pulse reflections from the elements under study, we return to the reflection coefficient  $\Gamma$  caused by a load  $Z_L$ :

$$\Gamma = \frac{Z_L - Z_0}{Z_L + Z_0}. \quad \text{18.59}$$

In several simple but significant cases, this is easily interpreted as follows:

*Matched load*

$Z_L = Z_0$ , and hence, by using Equation (18.59),  $\Gamma = 0$ .

There is no reflection, and an incident pulse transmitted will not suffer any distortion due to this load.

*Short circuit*

$Z_L = 0$ , and hence, again by using Equation (18.59),  $\Gamma = -1$ .

This means that an incident voltage pulse transmitted will suffer complete cancellation in the round-trip time required for the pulse to reach and return from the short-circuit location. Thus, TDR can be effectively used for checking (broadband) matched circuits, short circuits, and a wide variety of other elements and discontinuities, provided that the system resolution is sufficiently precise. The time resolution is particularly critical.

We recall the delay time calculated for  $50 \Omega$  microstrip on an alumina substrate which was given in [Section 6.13](#). This was  $8.6 \text{ ns/m}$ , or  $8.6 \text{ ps/mm}$ . Using this value, we find that a TDR with a system pulse-rise time of about  $30 \text{ ps}$  can only resolve distance separations of approximately  $2 \text{ mm}$ , at best, along  $50 \Omega$  microstrip lines. In practice, the effects of multiple

reflections and noise complicate the displayed waveform considerably and limit the resolution. Companies such as Picosecond Pulse Labs provide systems that have input pulse rise times down to several picoseconds, therefore enabling substantially finer resolution to be achieved.

Piller [35] presented a very interesting extension of both TDR and time-domain transmission (TDT) measurement techniques. Substantial information is given, and Piller claims that time constants down to approximately 0.1 ps are within the capabilities of his methods. The principal features of this technique are the careful interpretation of maximum pulse amplitude and the separate employment of a ramp waveform. Using a 30 ps TDR system, especially adapted, where the minimum voltage is 2 mV and the maximum voltage is 1 V, it is claimed that the following minimum circuit parameter values can be resolved:

with TDR:

$$\begin{aligned}C_g &\approx 15 \text{ fF} \\L_l &\approx 35 \text{ pH}\end{aligned}$$

with TDT:

$$\begin{aligned}C_s &\approx 1 \text{ fF} \\L_g &\approx 1 \text{ pH}\end{aligned}$$

here the subscript ‘*g*’ means ‘to ground,’ the subscript ‘*l*’ means ‘lead,’ and the subscript ‘*s*’ means ‘series’.

Measurement precautions mentioned by Piller include:

- a calibration measurement with a very narrow gap (so that  $C_g \rightarrow 0$ )
- the use of a good reference point
- high noise rejection and jitter rejection
- expansion of the waveform plots or traces
- use of an averaging interpretation of the measurements.

Piller's paper [35] should be consulted for further details.

## 18.9 Summary

This chapter presented measurement techniques that can be used to characterize substrates and planar transmission line structures, including coupled lines. The most accurate measurements for the characterization of the properties of a substrate are based on resonant techniques and these also yield the most accurate determinations of the effective permittivity and loss tangent of nonhomogeneous lines such as microstrip. Resonator measurements, however, only provide results at one or a few frequencies and so it is sometimes necessary to extract results from swept scattering parameter measurements.

## References

- [1] M. Steer, *Microwave and RF Design: a Systems Approach*, 2nd ed. SciTech Pub., 2013.
- [2] G. Engen and C. Hoer, “Thru-reflect-line: An improved technique for calibrating the dual six-port automatic network analyzer,” *IEEE Trans. on Microwave Theory and Techniques*, vol. **27**, no. 12, pp. 987–993, Dec. 1979.
- [3] C. Woodin and M. Goff, “Verification of MMIC on-wafer microstrip TRL calibration,” in *1990 IEEE MTT-S Int. Microwave Symp. Digest*, May 1990, pp. 1029–1032.
- [4] S. Goldberg, M. Steer, P. Franzon, and J. Kasten, “Experimental electrical characterization of interconnects and discontinuities in high-speed digital systems,” *IEEE Trans. on Components, Hybrids, and Manufacturing Technology*, vol. **14**, no. 4, pp. 761–765, 1991.
- [5] M. Steer, S. Goldberg, G. Rinne, P. Franzon, I. Turlik, and J. Kasten, “Introducing the through-line deembedding procedure,” in *1992 IEEE MTT-S Int. Microwave Symp. Dig.*, Jun. 1992, pp. 1455–1458.
- [6] M. Steer, S. Lipa, P. Franzon, and A. Cangellaris, “Experimental characterization of interconnects and discontinuities in thin-film multichip module substrates,” *Topical Meeting on Electrical Performance of Electronic Packaging*, pp. 145–147, 1993.
- [7] K. Kurokawa, “Power waves and the scattering matrix,” *IEEE Trans. on Microwave Theory and Techniques*, vol. **13**, no. 2, pp. 194–202, Feb. 1965.
- [8] G. Stewart, M. Kay, C. Riedell, R. Pomerleau, and M. Steer, “Microstrip discontinuity modeling,” in *IEEE Proc. Southeastcon'89*, 1989, pp. 107–111.
- [9] S. Goldberg, M. Steer, P. Franzon, and J. Kasten, “Experimental electrical characterization of interconnects and discontinuities in high-speed digital systems,” *IEEE Trans. on Components, Hybrids, and Manufacturing Technology*, vol. **14**, no. 4, pp. 761–765, Dec. 1991.
- [10] P. Ladbroke, “A novel standing-wave indicator in microstrip,” *Radio and Electronic Engineer*, vol. **44**, no. 5, pp. 273–280, May 1974.
- [11] B. Bianco, M. Parodi, S. Ridella, and F. F. Selvaggi, “Launcher and microstrip characterization,” *IEEE Trans. on Instrumentation and Measurement*, vol. **25**, no. 4, pp. 320–323, Dec. 1976.
- [12] S. Lipa, M. Steer, A. Morris, and P. Franzon, “Comparison of methods for determining the capacitance of planar transmission lines with application to multichip module characterization,” *IEEE Trans. on Components, Hybrids, and Manufacturing Technology*, vol. **16**, no. 3, pp. 247–252, Mar. 1993.
- [13] A. Glaser, M. Steer, G. Shedd, P. Russell, and P. Franzon, “A method for on-chip

interconnect characterization,” in 1995 *Electrical Performance of Electronic Packaging*, 1995, pp. 108–110.

- [14] P. Buff, J. Nath, and M. Steer, “Origin of the half-wavelength errors in microwave measurements using through-line calibrations,” *IEEE Trans. on Instrumentation and Measurement*, vol. **56**, no. 5, pp. 1610–1615, 2007.
- [15] P. Ladbroke, M. Potok, and E. England, “Coupling errors in cavity-resonance measurements on MIC dielectrics,” *IEEE Trans. on Microwave Theory and Techniques*, vol. **21**, no. 8, pp. 560–562, Aug. 1973.
- [16] J. Howell, “A quick accurate method to measure the dielectric constant of microwave integrated-circuit substrates,” *IEEE Trans. on Microwave Theory and Techniques*, vol. **21**, no. 3, pp. 142–144, Mar. 1973.
- [17] R. Owens, J. Aitken, and T. Edwards, “Quasi-static characteristics of microstrip on an anisotropic sapphire substrate,” *IEEE Trans. on Microwave Theory and Techniques*, vol. **24**, no. 8, pp. 499–505, Aug. 1976.
- [18] P. Troughton, “High Q factor resonators in microstrip,” *Electronics Letters*, vol. **4**, no. 24, pp. 520–522, 1968.
- [19] P. Troughton, “Measurement techniques in microstrip,” *Electronics Letters*, vol. **5**, no. 2, pp. 25–26, 1969.
- [20] R. Owens, “Curvature effect in microstrip ring resonators,” *Electronics Letters*, vol. **12**, no. 14, pp. 356–357, 1976.
- [21] J. G. Richings, “*The Realization of Filter Networks in Microstrip*,” Ph.D. dissertation, University College of North Wales, Jun. 1973.
- [22] J. Deutsch and H. J. Jung, “Measurement of the effective dielectric constant of microstrip lines in the frequency range from 2 GHz to 12 GHz,” *Nachrichtentech. Z.*, vol. **12**, pp. 620–624, 1970.
- [23] B. Easter, “The equivalent circuit of some microstrip discontinuities,” *IEEE Trans. on Microwave Theory and Techniques*, vol. **23**, no. 8, pp. 655–660, Aug. 1975.
- [24] T. C. Edwards, “Microwave design parameters for microstrip transmission lines on sapphire substrates,” M. Phil. Thesis, Royal Military College of Science, 1976.
- [25] B. Easter, A. Gopinath, and I. Stephenson, “Theoretical and experimental methods for evaluating discontinuities in microstrip,” *Radio and Electronic Engineer*, vol. **48**, no. 1.2, pp. 73–84, Jan.–Feb. 1978.
- [26] J. Aitken, “Swept-frequency microwave Q-factor measurement,” *Electrical Engineers, Proc. Institution of*, vol. **123**, no. 9, pp. 855–862, Sep. 1976.

- [27] R. P. Owens, “Private communication,” 1976.
- [28] K. C. Gupta, R. Garg, I. J. Bahl, and P. Bhartia, *Microstrip Lines and Slotlines*, 2nd ed. Artech House, 1996.
- [29] L. S. Napoli and J. J. Hughes, “Characteristics of coupled microstrip lines,” *RCA Review*, vol. **31**, pp. 479–498, Sep. 1970.
- [30] V. Rizzoli, “Resonance measurement of even and odd mode propagation constants in coupled microstrips,” in *1975 IEEE MTT-S Int. Microwave Symp.*, May 1975, pp. 106–108.
- [31] G. R. Babu and Banmali, “Measurement of coupled microstrip line parameters,” *Int. J. Electronics*, pp. 551–560, 1978.
- [32] A. Deutsch, R. Krabbenhoft, K. Melde, C. Surovic, G. Katopis, G. Kopcsay, Z. Zhou, Z. Chen, Y. Kwark, T.-M. Winkel, X. Gu, and T. Standaert, “Application of the short-pulse propagation technique for broadband characterization of pcb and other interconnect technologies,” *IEEE Trans. on Electromagnetic Compatibility*, vol. **52**, no. 2, pp. 266–287, May 2010.
- [33] A. Deutsch, G. V. Kopcsay, C. W. Surovic, B. J. Rubin, L. M. Terman, R. P. Dunne, T. A. Gallo, and R. H. Dennard, “Modeling and characterization of long on-chip interconnections for high-performance microprocessors,” *IBM Journal of Research and Development*, vol. **39**, no. 5, pp. 547–567, Sep. 1995.
- [34] A. Deutsch, “Electrical characteristics of interconnections for high-performance systems,” *Proc. IEEE*, vol. **86**, no. 2, pp. 315–357, Feb. 1998.
- [35] U. Piller, “Time domain immittance measurements,” in *4th European Microwave Conf.*, Sep. 1974, pp. 61–65.

# Chapter 19

## Filters Using Planar Transmission Lines

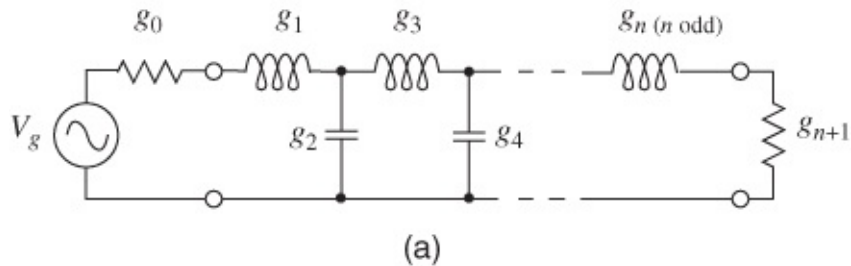
### 19.1 Introduction

Microwave filter design proceeds using a methodical synthesis approach that merges the inherent properties of distributed structures such as coupled lines with a mathematical response characteristic. Filter design is a combination of art, recognizing structures which inherently have a desired characteristic, with a science, the mathematical description of an optimum characteristic, such as fastest transition from a passband to a stopband. At every stage of the development until the final filter realization the evolving filter is called a prototype filter. There are a large number of transmission line structures that have desired characteristics. Correspondingly several schemes have been developed to evolve an initial lowpass filter prototype into a form that matches the model of a particular transmission line structure. If planar transmission line structures are to be used nearly every filter is based on cascaded microstrip lines (or similar planar lines) or on parallel-coupled transmission lines. The latter class is referred to as parallel-coupled line (PCL) filters. Cascaded microstrip lines are especially good for realizing lowpass and highpass filters, and coupled lines are particularly suited to realizing bandpass or bandstop filters. In this section we will cover the most important prototype development procedures and the most important classes of planar transmission line structures.

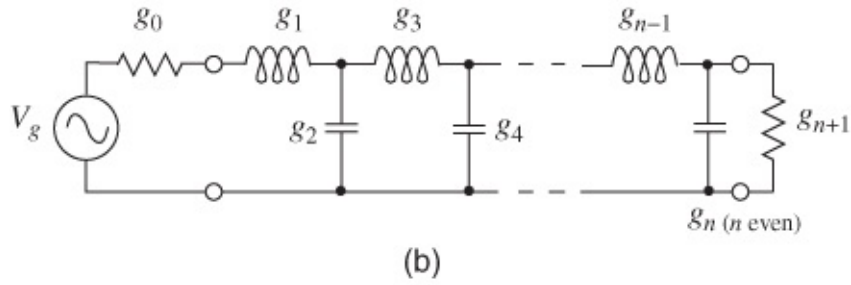
### 19.2 Filter Prototypes

Most filter design begins with a lowpass equivalent lumped-element filter call a lowpass prototype filter. There are two very important types, the Butterworth filter and the Chebyshev filter, that have desirable characteristics that can be expressed as a transfer function with Butterworth and Chebyshev polynomials, respectively. Note that the Butterworth filter is also call a maximally flat filter.

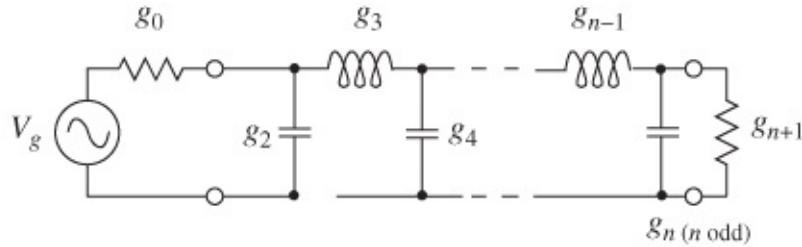
Here we will summarize the results of prototype synthesis. The reader is referred to one of several books that describe prototype filter development in more depth [1–4]. The Butterworth and Chebyshev lowpass filters can be put in the form of ladder networks, as shown in [Figure 19.1](#). The representation of a particular filter transferfunction may have several circuit representations and not just as a ladder network shown here, but most Butterworth and Chebyshev filter development derives from the ladder prototypes. The Butterworth and Chebyshev responses are selected with particular values of the circuit elements, the  $g$  values.



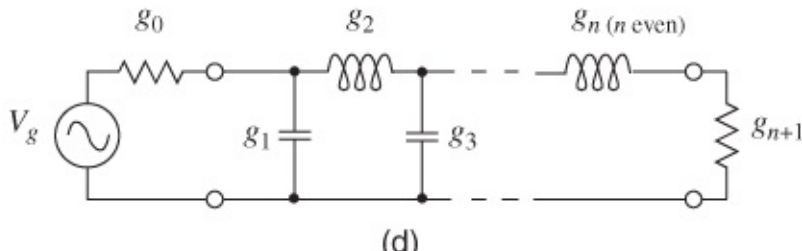
(a)



(b)



(c)



(d)

**Figure 19.1** Ladder prototype filters: (a) type 1  $n$  th-order lumped-element prototype for  $n$  odd; (b) type 1  $n$  th-order lumped-element prototype for  $n$  even; (c) type 2  $n$  th-order lumped-element prototype for  $n$  odd; and (d) type 2  $n$  th-order lumped-element prototype for  $n$  even.

### 19.2.1 Maximally Flat (Butterworth) Lowpass Filter Prototype

The response of a Butterworth filter is the flattest possible at the center frequency of the filter, which for a lowpass filter is at zero frequency. The response of a lowpass Butterworth filter is shown in [Figure 19.2](#) for various orders  $n$ . The elements of the Butterworth filter for a  $1\Omega$  system and normalized to have a normalized corner frequency of  $\omega_0 = 1$  radian/s are obtained using the generating function

$$g_r = 2 \sin \left\{ (2r - 1) \frac{\pi}{2n} \right\} \quad r = 1, 2, 3, \dots, n. \quad 19.1$$

In addition  $g_0 = 1 = g_{n+1}$ . The coefficients of several Butterworth lowpass prototype filters are

given in [Table 19.1](#). At  $\omega = \omega_0$  the transfer function of the filter is down by 3 dB, that is, the response is at half power.

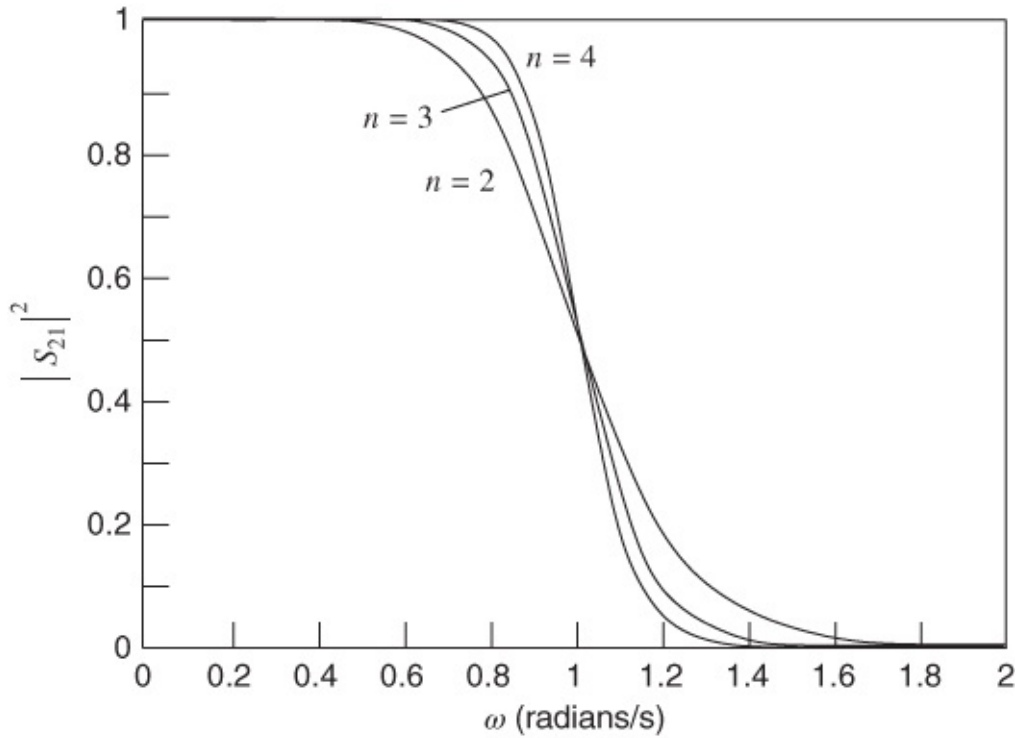


**Figure 19.2** Butterworth lowpass filter response for various orders  $n$ .

**Table 19.1** Coefficients of the Butterworth lowpass prototype filter with a radian corner frequency of 1 radian/s and a  $1 \Omega$  system impedance ( $g_0 = 1 = g_{n+1}$ )

Order, $n$	2	3	4	5	6	7	8	9
$g_1$	1.4142	1	0.7654	0.6180	0.5176	0.4450	0.3902	0.3473
$g_2$	1.4142	2	1.8478	1.6180	1.4142	1.2470	1.1111	1
$g_3$	1	1	1.8478	2	1.9318	1.8019	1.6629	1.5321
$g_4$		1	0.7654	1.6180	1.9318	2	1.9615	1.8794
$g_5$			1	0.6180	1.4142	1.8019	1.9615	2
$g_6$				1	0.5176	1.2470	1.6629	1.8794
$g_7$					1	0.4450	1.1111	1.5321
$g_8$						1	0.3902	1
$g_9$							1	0.3473
$g_{10}$								1

### 19.2.2 Chebyshev Lowpass Prototype

The response of a Chebyshev filter has the fastest possible transition from the passband to the stopband. This can be seen in the response of a seventh-order lowpass Chebyshev filter, which

is shown in [Figure 19.3](#). The defining characteristic of any Chebyshev filter are the ripples in the passband. Also at the corner frequency the response is down by the amount of the ripple rather than the half-power level that we saw with the Butterworth filter. The ripples are undesirable in the transmission response but if the ripple is chosen to be small, such as 0.01 dB, then a small amount of loss in a fabricated filter will smooth out the magnitude of the transmission response. However, the fast transitions from the passband to the stopband remain. Higher-order Chebyshev filters will have a steeper transition from the passband below 1 radian/s to the stopband above 1 radian/s. The rate of the transition is the key characteristic in selecting the filter order needed. [Figure 19.4](#) shows the transmission response for various orders of Chebyshev filters with a ripple of 0.01 dB. Here the radian frequency  $\omega$  is normalized to the radian corner frequency  $\omega_0$ . Typically a lowpass prototype filter is normalized to 1 radian/s  $\omega_c = \omega_0 = 1$  radian/s.

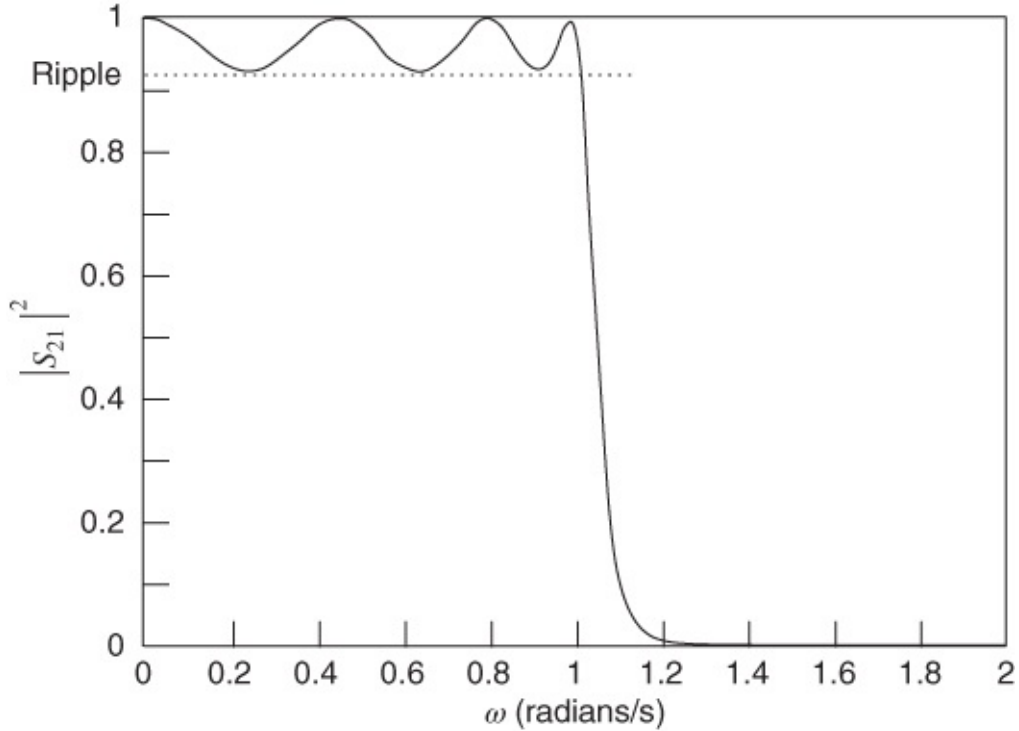


[Figure 19.3](#) Chebyshev lowpass filter response for a seventh-order filter with a ripple of 0.7 dB. The passband is below 1 radian/s and the stopband is above 1 radian/s.

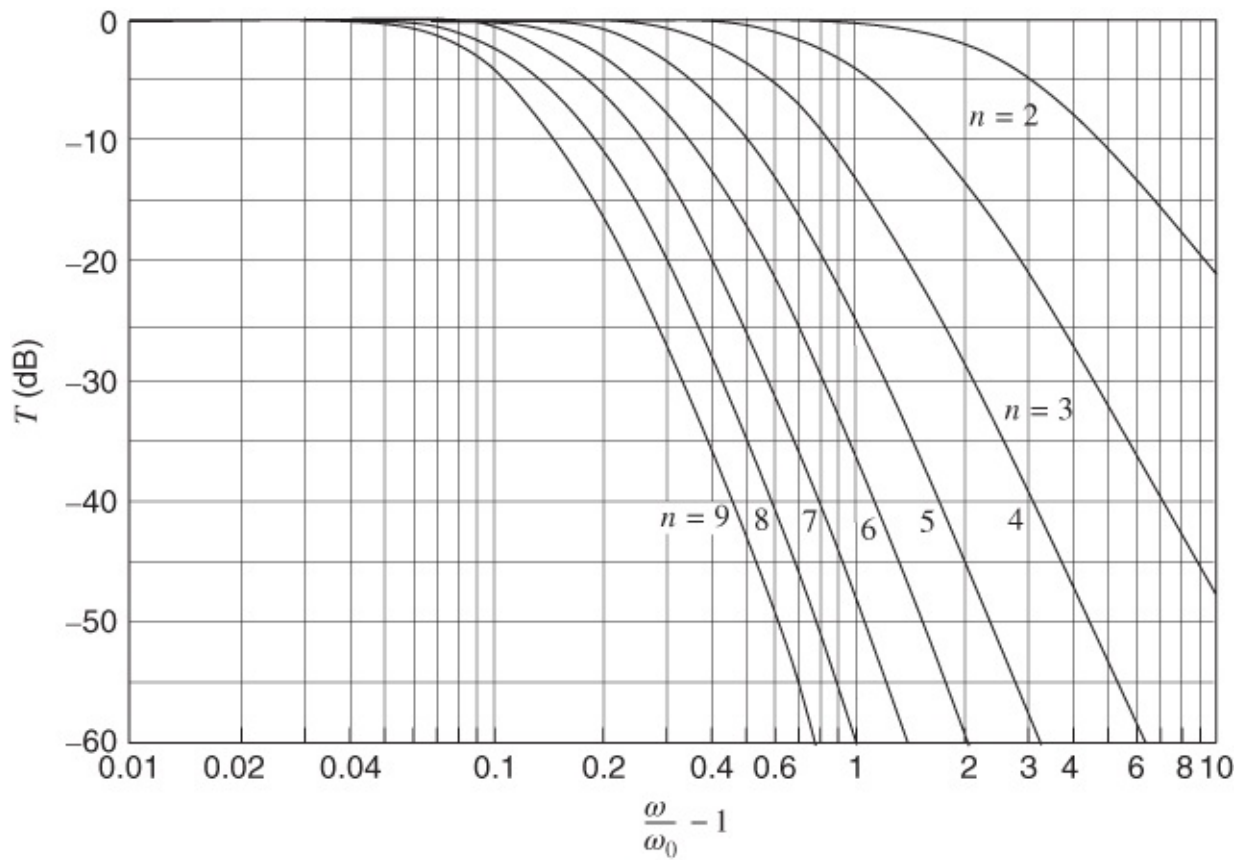


**Figure 19.4** Transmission of the Chebyshev lowpass prototype filters for a passband ripple of 0.01 dB.

The values of the elements in the Chebyshev filter depend on the amount of ripple and filter order. The elements of the normalized Chebyshev filter are given in [Tables 19.2–19.5](#) for various odd orders and ripple levels. These parameters are for lowpass prototypes with a normalized corner frequency of  $\omega_0 = 1$  radian/s and at this frequency the transfer function of the filter is down by the ripple level. The filter is also normalized for a  $1\Omega$  system, thus  $g_0 = 1 = g_{n+1}$  for an odd-order filter. (Note that  $g_{n+1} > 1$  for an even-order Chebyshev filter resulting in an asymmetrical filter.) As noted previously, at the corner frequency,  $\omega_0$ , the transmission response of the filter is down by the amount of the ripple. Thus for a Chebyshev filter with a ripple of 1 dB the transmission response is  $-1.0$  dB at a radian frequency of  $\omega_0$ .

**Table 19.2** Coefficients of normalized third-order Chebyshev lowpass filter prototypes

Ripple	0.01 dB	0.1 dB	0.2 dB	1.0 dB	3.0 dB
$g_1$	0.62918	1.03156	1.22754	2.02359	3.34874
$g_2$	0.97028	1.14740	1.15254	0.99410	0.71170
$g_3$	0.62918	1.03156	1.22754	2.02359	3.34874

**Table 19.3** Coefficients of normalized fifth-order Chebyshev lowpass filter prototypes

Ripple	0.01 dB	0.1 dB	0.2 dB	1.0 dB	3.0 dB
$g_1$	0.75633	1.14681	1.33944	2.13488	3.48129
$g_2$	1.30492	1.37121	1.33702	1.09111	0.76192
$g_3$	1.57731	1.97500	2.16605	3.00092	4.53755
$g_4$	1.30492	1.37121	1.33702	1.09111	0.76192
$g_5$	0.75633	1.14681	1.33944	2.13488	3.48129

**Table 19.4** Coefficients of normalized seventh-order Chebyshev lowpass filter prototypes

Ripple	0.01 dB	0.1 dB	0.2 dB	1.0 dB	3.0 dB
$g_1$	0.79694	1.18118	1.37226	2.16656	3.51852
$g_2$	1.39242	1.42281	1.37820	1.11151	0.77220
$g_3$	1.74813	2.09667	2.27566	3.09364	4.63898
$g_4$	1.63313	1.57340	1.50016	1.17352	0.80381
$g_5$	1.74813	2.09667	2.27566	3.09364	4.63898
$g_6$	1.39242	1.42281	1.37820	1.11151	0.77220
$g_7$	0.79694	1.18118	1.37226	2.16656	3.51852

**Table 19.5** Coefficients of normalized ninth-order Chebyshev lowpass filter prototypes

Ripple	0.01 dB	0.1 dB	0.2 dB	1.0 dB	3.0 dB
$g_1$	0.81446	1.19567	1.38603	2.17972	3.53394
$g_2$	1.42706	1.44260	1.39389	1.11918	0.76604
$g_3$	1.80436	2.13455	2.30932	3.12143	4.66906
$g_4$	1.71254	1.61672	1.53405	1.18967	0.81181
$g_5$	1.90579	2.20537	2.37280	3.17463	4.72701
$g_6$	1.71254	1.61672	1.53405	1.18967	0.81181
$g_7$	1.80436	2.13455	2.30932	3.12143	4.66906
$g_8$	1.42706	1.44260	1.39389	1.11918	0.76604
$g_9$	0.81446	1.19567	1.38603	2.17972	3.53394

### 19.2.3 Impedance and Admittance Inverters

An inverter is a two-port network that inverts and scales an impedance or admittance. It is a very important element in relating transmission line-based filter structures to filter prototypes. Admittance and impedance inverters are the same element, the only difference being in how we specify their value, either in ohms in the case of an impedance inverter or Siemens in the case

of an admittance inverter. If the numerical value is not known then the symbol of an impedance inverter is a two port with the letter **K** and an admittance inverter is identified by the letter **J**. Commonly **K** is called the characteristic impedance of the inverter and **J** is called the characteristic admittance of the inverter. It is also common to simply refer to them as the impedance and admittance of the inverter. The most common representations of impedance and admittance inverters are as two-ports, as shown in [Figure 19.5](#). Alternative representations that are sometimes used are shown in [Figures 19.6\(a\)–\(d\)](#). These are sometimes used in situations where there are many inverters and it is desirable to reduce clutter in a diagram. However, these are certainly less clear and for the sake of clarity it is better to use the full two-port representations. For comparison the two-terminal representations of a two-terminal impedance element are shown in [Figure 19.6\(e\)](#).

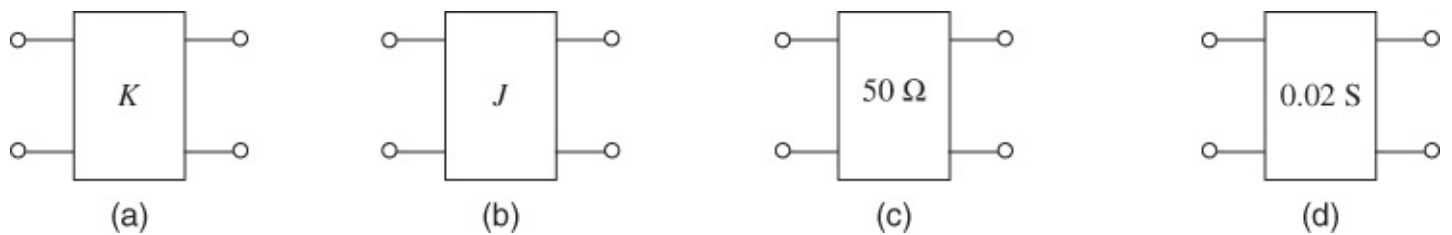


[Figure 19.5](#) Impedance and admittance inverters as two-ports: (a) impedance inverter; (b) admittance inverter; (c)  $50\ \Omega$  impedance inverter; and (d)  $0.02\ S$  admittance inverter.

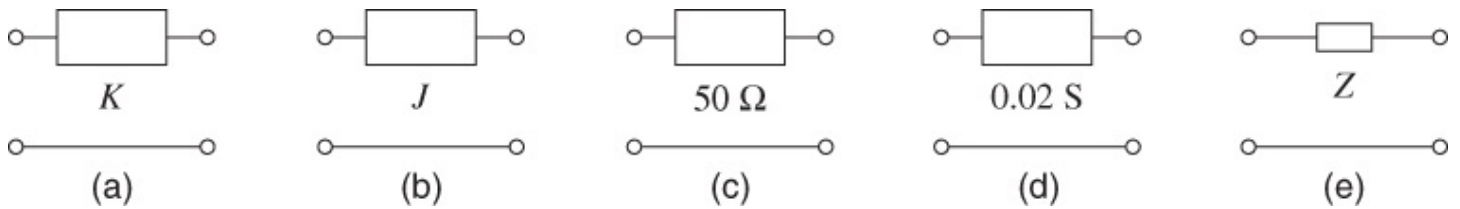


[Figure 19.6](#) Alternative representation of two-port impedance and admittance inverters with an impedance element for comparison: (a) impedance inverter; (b) admittance inverter; (c)  $50\ \Omega$  impedance inverter; (d)  $0.02\ S$  admittance inverter; and (e) impedance.

Loaded impedance and admittance inverters are shown in [Figure 19.7](#). The constitutive properties of the inverters are also shown in [Figure 19.7](#). So the impedance inverter both inverts the load impedance and scales it, [Figure 19.7\(a\)](#), while the admittance inverter both inverts the load admittance and scales it, [Figure 19.7\(b\)](#). Of course the impedance and admittance inverter are the same element.

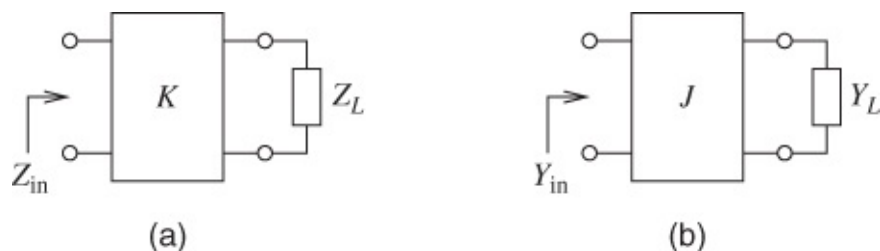


[Figure 19.7](#) (a) Impedance inverter with load  $Z_{in} = K^2/Z_L$ ; and (b) admittance inverter with load  $Y_{in} = J^2/Y_L$ .

An impedance inverter is identical to a lossless quarter-wavelength long transmission line. Such a line is shown in [Figure 19.8](#). The input impedance of the quarter-wavelength long line in [Figure 19.8\(c\)](#) is

$$Z_{\text{in}} = \frac{Z_0^2}{Z_L} \quad 19.2$$

which is identical to the inverter characteristic. Of course the inverter and the transmission line are only equivalent when the line is exactly a quarter-wavelength long. Thus the inverter is a narrowband model of the transmission line and is not a sufficiently accurate model for moderate to wideband circuits as required in modeling and synthesizing filters. We will soon develop the required broadband model. The development of these models is most conveniently done by equating *ABCD* parameters.

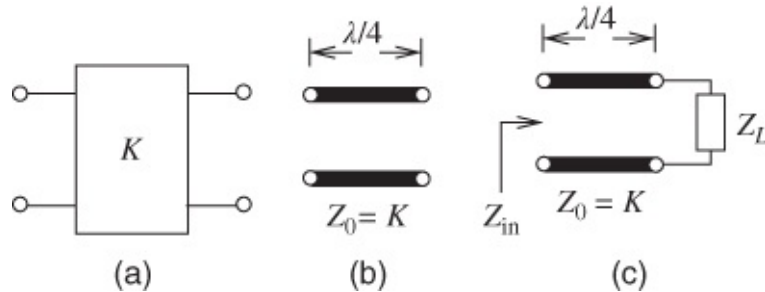


[Figure 19.8](#) Inverter equivalence: (a) two-port impedance inverter (of impedance  $K$ ); (b) a quarter-wave transmission line of characteristic impedance  $Z_0 = K$ ; and (c) a terminated one-quarter wavelength long line.

The *ABCD* parameters of an impedance inverter are

$$\mathbf{T} = \begin{bmatrix} A & B \\ C & D \end{bmatrix} = \begin{bmatrix} 0 & jK \\ j/K & 0 \end{bmatrix}. \quad 19.3$$

With a load impedance,  $Z_L$ , at Port 2, the input impedance is

$$Z_{\text{in}} = \frac{AZ_L + B}{CZ_L + D} = \frac{jK}{(j/K)Z_L} = \frac{K^2}{Z_L}. \quad 19.4$$

The *ABCD* parameters of a lossless line transmission line of electrical length  $\theta$  of [Figure 19.7\(c\)](#) are

$$\begin{bmatrix} \cos(\theta) & jZ_0 \sin(\theta) \\ (j/Z_0) \sin(\theta) & \cos(\theta) \end{bmatrix}. \quad 19.5$$

Equations (19.3) and (19.5) are identical when the electrical length is  $\theta = \pi/2$  (i.e., when the line is  $\lambda/4$  long). The inverter is shown in [Figure 19.7\(a\)](#) as a two-port and its implementation as a  $\lambda/4$  long line is shown in [Figure 19.7\(c\)](#). The bandwidth over which the line is a good approximation to an inverter is narrow.

## 19.2.4 Using Inverters to Transform between Series and Shunt Elements

Inverters can be used to transform a series element into an equivalent circuit with a shunt element and inverters. At the same time an inductor is transformed into a capacitor or a capacitor is transformed into an inductor. These transformations enable filter prototypes to be put into forms that are more easily realizable using transmission lines. In any case, if we are going to use any lumped elements we would prefer to use capacitors rather than inductors as lumped inductors invariably have lower  $Q$  than lumped capacitors. Such an equivalence is shown in [Figure 19.9](#) (the mathematical derivation is given in [3]).

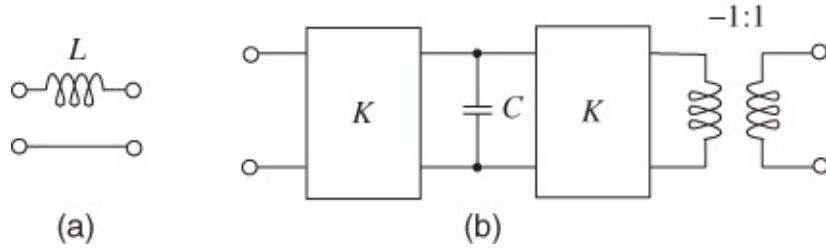


[Figure 19.9](#) Transformation of a series inductor in (a) to an equivalent network with a shunt capacitor with inverters and transformer in (b) with  $C = L/K^2$ .

Similarly, a series capacitor can be replaced by a shunt inductor plus inverters and a negative transformer. The equivalent circuits are shown in [Figure 19.10](#). As before the equivalence is shown by equating  $ABCD$  parameters. Again the inverting transformer has no significance in a cascaded system as it only introduces a  $180^\circ$  phase change.

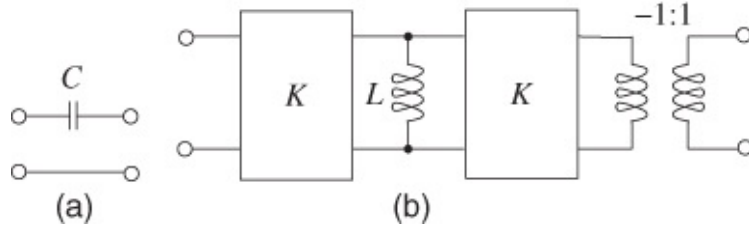


[Figure 19.10](#) Transformation of a series capacitor in (a) to an equivalent network with a shunt inductor with inverters and transformer in (b) with  $C = L/K^2$ .

## 19.2.5 Ladder Prototype with Impedance Inverters

Lowpass lumped-element prototypes can be developed using impedance inverters and without using series elements or without shunt elements if required. These elements eventually become resonators in microwave filters, most of which are bandpass filters. Which inverter-based prototype (i.e., one without series elements or one without shunt elements) is required depends on the distributed topology employed in eventually realizing a microwave filter. Most require that resonators be in a shunt configuration and so that is the focus of the discussion here. The lowpass lumped-element ladder prototype circuits, the type of prototypes generally used, are shown in [Figure 19.11\(a\)](#) and (b). The first stage of the transformation, which in this case eliminates series inductors, is shown in [Figure 19.11\(c\)](#). This is based on the equivalence

shown in [Figure 19.9](#). This simplifies further to the realizations shown in [Figure 19.11\(d\)](#) and [\(e\)](#).

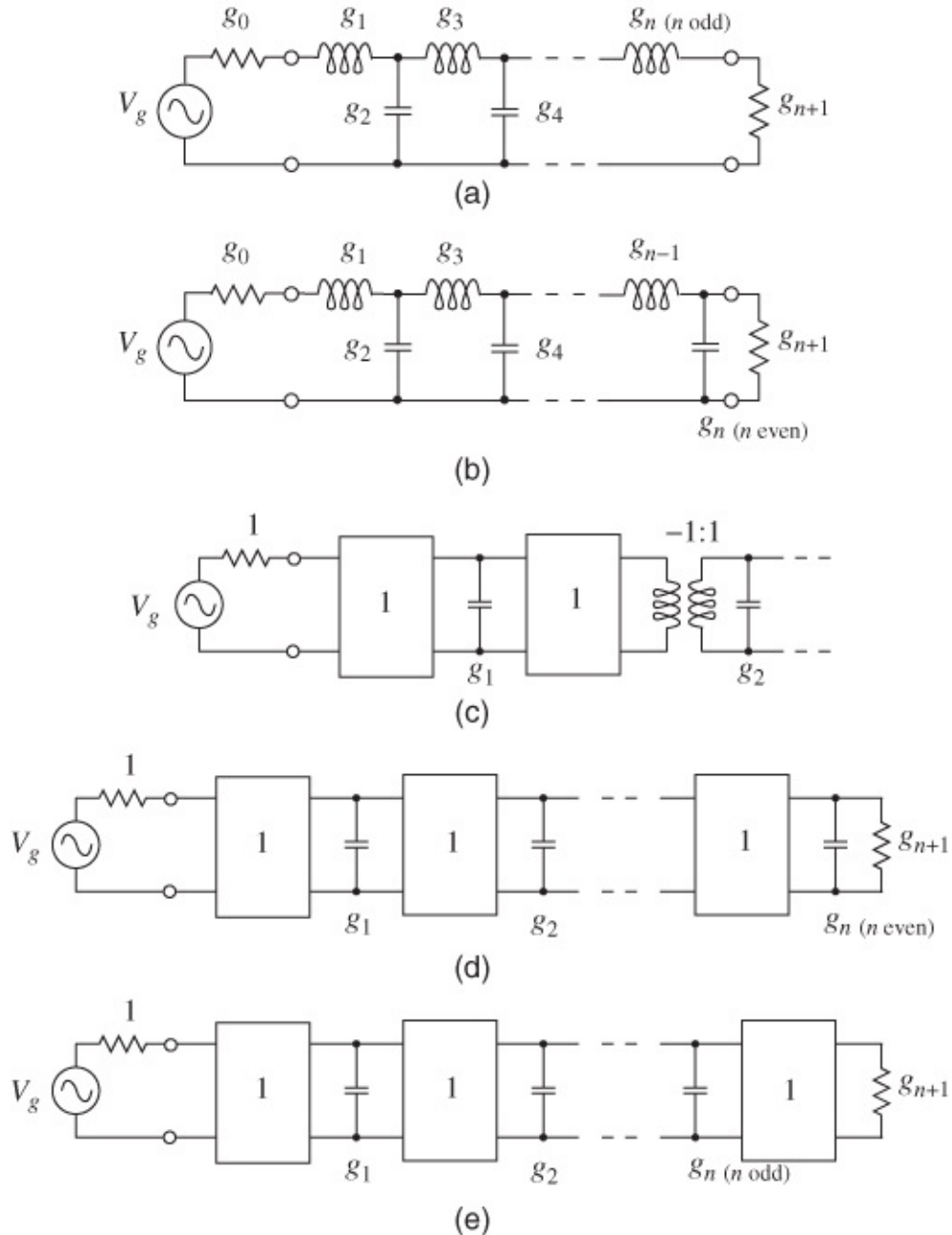


**Figure 19.11** Ladder prototype filters using inverters: (a)  $n$  th-order lumped-element prototype for  $n$  odd; (b)  $n$  th-order lumped-element prototype for  $n$  even; (c) first stage in transformation of series elements to shunt elements using inverters; (d) final inverter-based prototype for  $n$  even; and (e) final inverter-based prototype for  $n$  odd.

### 19.2.6 Lumped-element Model of an Inverter

$ABCD$  parameter equivalence also leads to the lumped-element equivalent circuits shown in [Figures 19.12](#) and [19.13](#). The equivalent circuits are exact but of course their practical accuracy is limited by the frequency range over which frequency-independent reactive elements can be approximately realized.

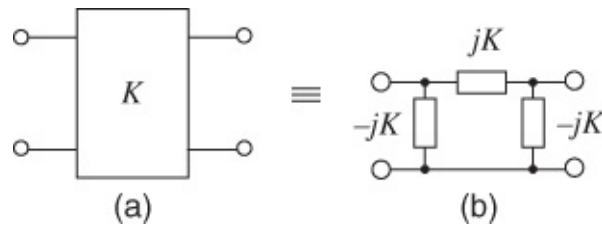


**Figure 19.12** Impedance inverter: (a) schematic of an impedance inverter with impedance  $K$ ; and (b) its lumped-element equivalent model.

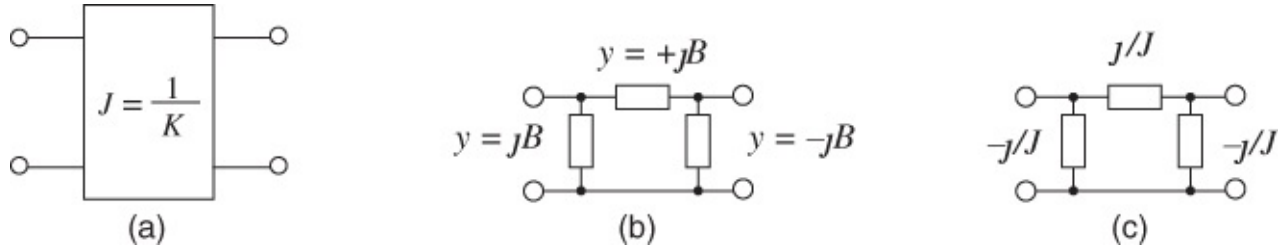


**Figure 19.13** Admittance inverter: (a) schematic of admittance inverter with admittance; (b) lumped-element equivalent model with admittance elements; and (c) lumped-element equivalent model with impedance elements.

### 19.2.7 Moderate Bandwidth Transmission Line Stub Model of an Inverter

In this section it will be shown that an impedance inverter can be implemented using short- and open-circuited stubs. The match is good over a narrow band centered at frequency  $f_0 = \omega_0/(2\pi)$ . An impedance inverter is shown in Figure 19.14(a) and its equivalent lumped-element network is shown in Figure 19.14(b). A stub-based implementation is shown in Figure 19.14(c), where there are short- and open-circuited stubs of characteristic impedance  $Z_0$ . The input impedance of the stubs is shown at the inputs of the stubs. The stubs have an electrical length  $\theta$  at  $f_0$  and the stubs are one-quarter wavelength long (i.e., resonant) at what is called the commensurate frequency,  $f_r$ .

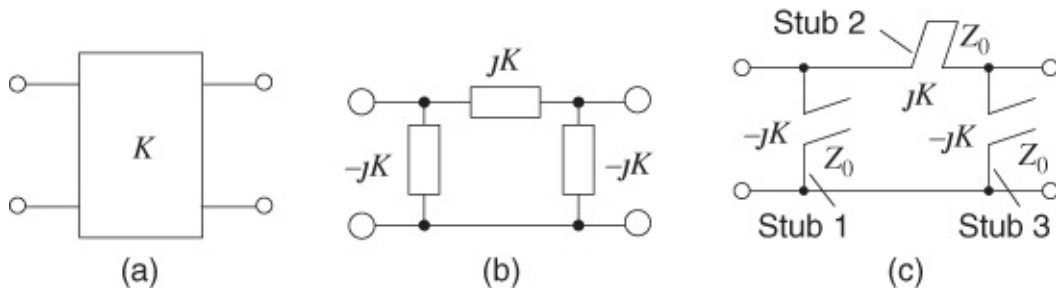


**Figure 19.14** Narrowband inverter equivalents at frequency  $f_0$ : (a) impedance inverter with characteristic impedance  $K$ ; (b) lumped-element equivalent network; and (c) inverter realized by short- and open-circuited stubs.

Now it will be shown that the network of Figure 19.14(c) is a good representation of the inverter at  $f_0$ . This is done by matching  $ABCD$  parameters. The  $ABCD$  parameter matrix of the inverter is

$$T = \begin{bmatrix} 0 & jK \\ j/K & 0 \end{bmatrix}$$

and, at frequency  $f_0$ , the  $ABCD$  parameter matrix of the stub circuit of [Figure 19.14\(c\)](#) is

$$\begin{aligned} T &= \begin{bmatrix} 1 & 0 \\ -1/[jZ_0 \tan(\theta)] & 1 \end{bmatrix} \begin{bmatrix} 1 & jZ_0 \tan(\theta) \\ 0 & 1 \end{bmatrix} \begin{bmatrix} 1 & 0 \\ -1/[jZ_0 \tan(\theta)] & 1 \end{bmatrix} \\ &= \begin{bmatrix} 0 & jZ_0 \tan(\theta) \\ j/[Z_0 \tan(\theta)] & 0 \end{bmatrix}. \end{aligned} \quad 19.7$$

Thus, equating Equations [\(19.6\)](#) and [\(19.7\)](#), the stub network is a good representation of the inverter if

$$K = Z_0 \tan(\theta) \quad 19.8$$

and so the required characteristic impedance of each stub at frequency  $f_0$  is

$$Z_0 = \frac{K}{\tan(\theta)} = \frac{K}{\tan\left(\frac{\pi f_0}{2 f_r}\right)}. \quad 19.9$$

Here  $f_r$  is called the commensurate frequency and it is the frequency at which the line is a quarter-wavelength long.

There is a special situation when the model has broadband accuracy and this is when  $f_r = 2f_0$  as then the required characteristic impedance of the stubs is

$$Z_0 = \frac{K}{\tan\left(\frac{\pi f_0}{2 \cdot 2f_0}\right)} = \frac{K}{\tan \pi/4} = K \quad 19.10$$

So the characteristic impedance of the transmission line stub is independent of frequency and the stub-based model is an accurate model over a broad range of frequencies. What is particularly interesting about the stub model is that it occurs in many filter realizations that use coupled transmission lines.

In a design it is particularly important to specify the center frequency, here  $f_0$ , and especially the commensurate frequency  $f_r$ . Generally every stub in a microwave circuit design will have the same commensurate frequency but there are many choices in the relationship to  $f_0$ .

### 19.2.8 Unit Element

Distributed realizations of transmission lines invariably require that transmission line sections be related to filter prototypes with inverters. Filter design then involves aligning the model of a distributed structure to a prototype filter that has inverters. It is common in distributed filter design to introduce the concept of a unit element. A section of lossless line is called a unit element. It is characterized by its characteristic impedance and its electrical length, either  $\beta\ell$  or  $\theta$ . So this element differs from an actual transmission line that will have loss and generally a characteristic impedance that varies with frequency.

A lossless transmission line with characteristic impedance  $Z_0$  and electrical length  $\theta$  is shown in Figure 19.15(a). This is called a unit element, which is shown as a two-port in Figure 19.15(b) and has the  $ABCD$  parameters

$$T_{UE} = \begin{bmatrix} \cos(\theta) & jZ_0 \sin(\theta) \\ jY_0 \sin(\theta) & \cos(\theta) \end{bmatrix} \quad 19.11$$

where the characteristic admittance  $Y_0 = 1/Z_0$ . The broadband equivalent circuit of the unit element is shown in Figure 19.15(c). This is demonstrated by considering the  $ABCD$  parameters of the stub, inverter, and stub cascade. The  $ABCD$  parameters of the series stub of characteristic impedance  $Z_0$  and electrical length  $\theta$  is

$$T_{STUB} = \begin{bmatrix} 1 & -jZ_0/\tan(\theta) \\ 0 & 1 \end{bmatrix} \quad 19.12$$

and for the inverter of impedance  $K$

$$T_{INVERTER} = \begin{bmatrix} 0 & jK \\ j/K & 0 \end{bmatrix}. \quad 19.13$$

So the cascade in Figure 19.15(c) has the  $ABCD$  parameters

$$T_{CASCADE} = T_{STUB} T_{INVERTER} T_{STUB} \quad 19.14$$

$$= \begin{bmatrix} 1 & -jZ_0/\tan(\theta) \\ 0 & 1 \end{bmatrix} \begin{bmatrix} 0 & jK \\ j/K & 0 \end{bmatrix} \begin{bmatrix} 1 & -jZ_0/\tan(\theta) \\ 0 & 1 \end{bmatrix} \quad 19.15$$

$$= \begin{bmatrix} 1 & -jZ_0 \frac{\cos(\theta)}{\sin(\theta)} \\ 0 & 1 \end{bmatrix} \begin{bmatrix} 0 & jK \\ j/K & \frac{Z_0 \cos(\theta)}{K \sin(\theta)} \end{bmatrix} \quad 19.16$$

$$= \begin{bmatrix} \frac{Z_0 \cos(\theta)}{K \sin(\theta)} & jK \left( 1 - \frac{jZ_0^2 \cos^2(\theta)}{K^2 \sin^2(\theta)} \right) \\ j/K & \frac{Z_0 \cos(\theta)}{K \sin(\theta)} \end{bmatrix}. \quad 19.17$$

Setting  $K = Z_0/(\sin \theta)$  this becomes

$$T_{CASCADE} = \begin{bmatrix} \cos(\theta) & jZ_0 [1 - \cos^2(\theta)] / \sin(\theta) \\ j \sin(\theta)/Z_0 & \cos(\theta) \end{bmatrix} \quad 19.18$$

$$= \begin{bmatrix} \cos(\theta) & jZ_0 \sin(\theta) \\ jY_0 \sin(\theta) & \cos(\theta) \end{bmatrix} \quad 19.19$$

which is identical to the  $ABCD$  parameters of the unit element in Equation (19.11). Thus the cascade model of Figure 19.15(c) is an exact, that is, broadband, model of the unit element.

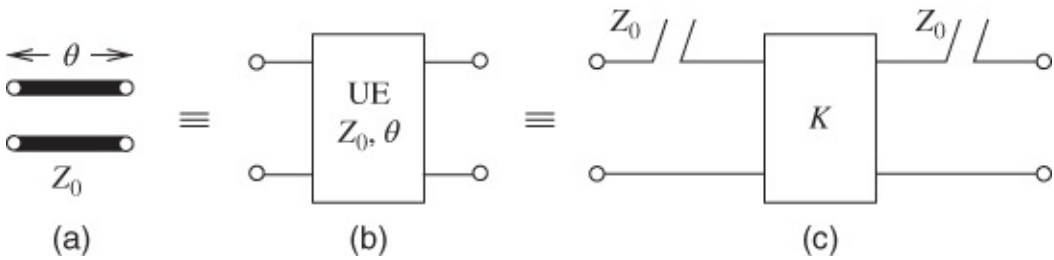


**Figure 19.15** Exact (broadband) equivalent model of a lossless transmission line of characteristic impedance  $Z_0$  and electrical length  $\theta$ : (a) lossless line; (b) unit element (UE); and (c) model,  $K = Z_0 / \sin(\theta)$ . The stubs in (c) have electrical length  $\theta$ .

A narrow band model is obtained by considering the situation when the line is a quarter-wavelength long, that is,  $\theta = \pi/2$ . Then the input impedance of the stubs is a short circuit and the narrow band model of the quarter-wavelength long line is just an inverter.

### 19.2.9 Filter Transformations

The traditional design of microwave filters begins with a lowpass prototype filter to which a number of transformations are applied to scale the system impedance of the filter, then transform the corner frequencies of the prototype, and then transform the filter type from lowpass filter to bandstop, highpass, or bandpass as required. It is possible to combine transformations but insight is gained in applying the transformations individually.

### 19.2.10 Impedance Transformation

The lowpass prototype is normalized to a reference impedance of  $1\Omega$ . Then the filter operates in a  $1\Omega$  system with a  $1\Omega$  source and (usually)  $1\Omega$  load impedance. The load impedance can be different and is specified by the last filter coefficient (the  $g_{n+1}$  coefficient). To translate the filter to a different system impedance such as  $Z_0$  every impedance in the prototype is multiplied by a factor of  $Z_0/(1\Omega)$ . Thus the elements are translated as follows.

	resistor	$R \rightarrow R \times Z_0$	19.20
inductor	inductor	$L \rightarrow L \times Z_0$	
	capacitor	$C \rightarrow C/Z_0$	
impedance	inverter	$K \rightarrow K \times Z_0$	
admittance	inverter	$J \rightarrow J/Z_0$	

So if a prototype filter with a  $1\Omega$  system impedance has a capacitor of 1 F then in a  $50\Omega$  system it will have a value of 20 mF.

### 19.2.11 Frequency Transformation

The key concept with frequency transformation is to maintain the impedance of an element but at the scaled frequency. If the original filter prototype is normalized to corner frequency  $\omega_0 = 1$  radian/s then if the corner frequency is shifted to  $\omega_c$  the elements are translated as follows:

resistor	$R$ is unchanged
inductor	inductor $L \rightarrow L/\omega_c$
capacitor	$C \rightarrow C/\omega_c$
impedance inverter	$K$ is unchanged
admittance inverter	$J$ is unchanged.

So if a prototype filter with a 1 radian/s corner frequency is transformed to have a corner frequency of 1 GHz, then a capacitor of a value of 20 mF will have a new value in the transformed prototype of 3.183 pF.

### 19.2.12 Filter Type Transformation

The filter type transformations are somewhat more involved but the same principle is used, that is, the impedance of an element is maintained in the transformed filter. There is a modification made with bandpass and bandstop filters as it is necessary to manage bandwidth in addition to the shift of the center frequency of the filter. The transformations are given in [Tables 19.6–19.8](#).

**Table 19.6** Lowpass prototype to highpass filter transformation. The corner frequency of the lowpass prototype is 1 radian/s

Lowpass prototype	Highpass element	Reactance transformation $\omega_c = \text{corner frequency}$
 $C_0$	 $L_1$	$L_1 = 1/(\omega_c C_0)$
 $L_0$	 $C_1$	$C_1 = 1/(\omega_c L_0)$

**Table 19.7** Lowpass prototype to bandpass filter transformation. The corner frequency of the lowpass prototype is 1 radian/s. Here  $\omega_c = 1/\sqrt{L_1 C_1} = \sqrt{\omega_1 \omega_2}$ ,  $\omega_1$  and  $\omega_2$  are the band-edge frequencies, and  $\alpha$  is the transformation constant,  $\alpha = \omega_c/(\omega_2 - \omega_1)$

Lowpass prototype	Bandpass element	Reactance transformation $\omega_c = \text{center of passband}$
		$C_1 = \alpha C_0 / \omega_c$ $L_1 = 1/(\alpha C_0 \omega_c)$
		$L_1 = \alpha L_0 / \omega_c$ $C_1 = 1/(\alpha L_0 \omega_c)$

**Table 19.8** Lowpass prototype to bandstop filter transformation. The corner frequency of the lowpass prototype is 1 radian/s. Here  $\frac{\omega_c}{1/\sqrt{L_1 C_1}} = \sqrt{\omega_1 \omega_2}$ ,  $\omega_1$  and  $\omega_2$  are the band-edge frequencies, and  $\alpha$  is the transformation constant,  $\alpha = \omega_c/(\omega_2 - \omega_1)$

Lowpass prototype	Bandstop element	Reactance transformation $\omega_c = \text{center of stopband}$
		$L_1 = \alpha / (C_0 \omega_c)$ $C_1 = C_0 / (\omega_c \alpha)$
		$L_1 = L_0 / (\alpha \omega_c)$ $C_1 = \alpha / (L_0 \omega_c)$

## 19.3 Microstrip Filters

### 19.3.1 Lowpass Filters Formed with Cascaded Microstrips

Lowpass filters can be realized by employing cascaded sections of microstrip although this technique is only really useful at frequencies up to several gigahertz. The lowpass ladder prototype filters in [Figure 19.1](#), particularly the Type 2 odd-order prototype filter of [Figure 19.1\(c\)](#), are in the form of cascaded  $\pi$ -networks each comprising a series inductor and shunt capacitors. Thus a  $\pi$ -network is similar to the lumped-element model of a section of transmission line. So the analysis here begins by analyzing the direct substitution of lumped filter elements by microstrip lines.

A short ( $< \lambda_g/4$ ) length of relatively high impedance line will behave predominantly as a series inductance. Also, a very short ( $\ll \lambda_g/4$ ) length of relatively low impedance line will act predominantly as a shunt capacitance. So a  $\pi$  network of lumped elements can quite readily be realized with alternate sections of low- and high-impedance microstrip lines, except that great care is necessary to fully calculate the equivalent line lengths. In particular, consider the  $\pi$ -equivalent arrangement applicable to a section of any transmission line. This was given in [Section 2.10](#) and is repeated here as [Figure 19.16](#).

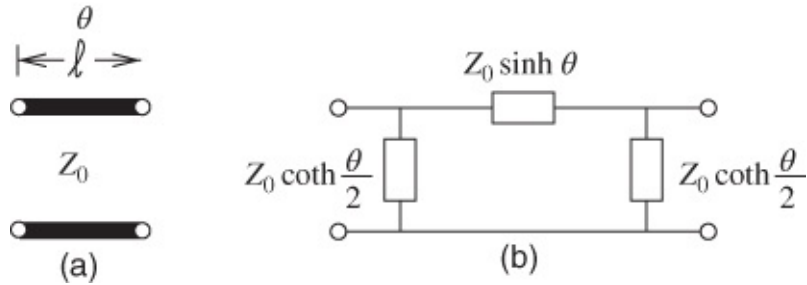


**Figure 19.16** Equivalent  $\pi$  network of impedances representing a transmission line with an electrical length of  $\theta = \beta\ell$  where  $\ell$  is the physical length and  $\beta$  is the phase constant.

In order to determine the characteristics of the microstrip elements to be implemented we need to evaluate both inductive and capacitive lines. Let us first consider a predominantly inductive length of line, as in [Figure 19.17](#). For short ( $< \lambda_g/4$ ) and loss-free lines this reduces to the two equivalent circuits shown in [Figures 19.17\(a\)](#) and [\(b\)](#). Basic transmission line theory gives the input reactance of the line of length  $\ell$ :

$$X_L = Z_0 \sin(2\pi\ell/\lambda_g) \quad \text{19.22}$$

so that the length of this predominantly inductive line is

$$\ell = \frac{\lambda_g}{2\pi} \sin^{-1} \left( \frac{\omega L}{Z_0} \right). \quad \text{19.23}$$

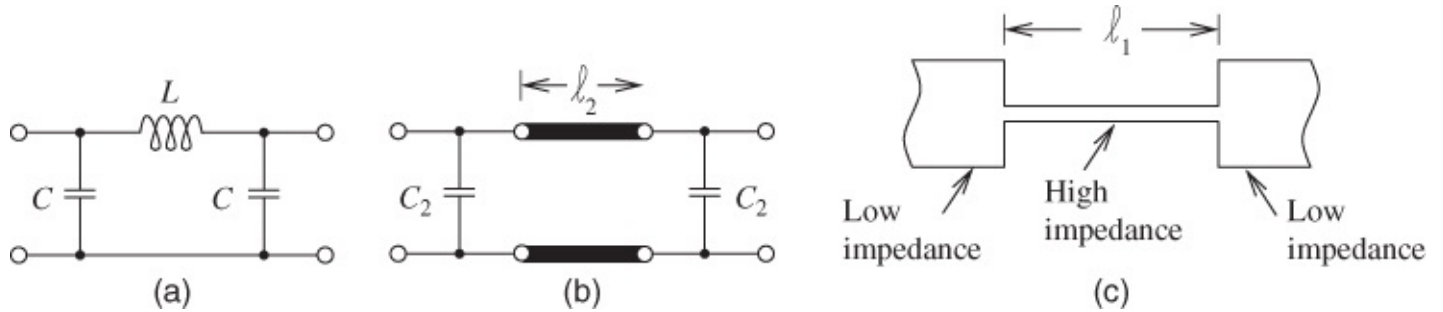


**Figure 19.17** Inductive length of line with adjacent capacitive lines: (a) lumped circuit; (b) lumped-distributed equivalent; and (c) microstrip form.

Occasionally, the small-angle approximation can be used such that  $2\pi\ell/\lambda_g \ll \pi/4$  and Equation (19.23) simplifies to

$$\ell \approx f \lambda_g L / Z_0. \quad \text{19.24}$$

It must be emphasized that the small-angle inequality will frequently not be met, and therefore the full Equation (19.23) will often be necessary in practice. The end susceptances  $B_L$  for the equivalent circuit, yielding values of  $C_L$ , are also given by

$$B_L = \frac{1}{Z_0} \tan \left( \frac{\pi \ell}{\lambda_g} \right). \quad \text{19.25}$$

Then, approximately, for short lengths:

$$C_L \approx \frac{\ell}{2fZ_0\lambda_g}. \quad \text{19.26}$$

The inductive length of line  $\ell$  will also be presented with adjacent lengths of low impedance and, therefore, wide microstrip lines. This situation results in a significant step discontinuity; the properties of such discontinuities were discussed in [Section 9.4](#). The expressions for step capacitance, which were given in that section, should be used to evaluate the discontinuity capacitances here.

We have previously remarked that a short length of line having a relatively low characteristic impedance yields a capacitive element and this is shown, together with its equivalent circuit, in [Figure 19.18](#). The predominating shunt capacitance is determined by first considering the susceptibility

$$B = \frac{1}{Z_0} \sin \left( \frac{2\pi \ell}{\lambda_g} \right) \quad \text{19.27}$$

so that

$$\ell = \frac{\lambda_g}{2\pi} \sin^{-1}(\omega C Z_0) \quad \text{19.28}$$

or, usefully, since these line lengths are almost always very short,

$$\ell \approx f \lambda_g Z_0 C \quad \text{19.29}$$

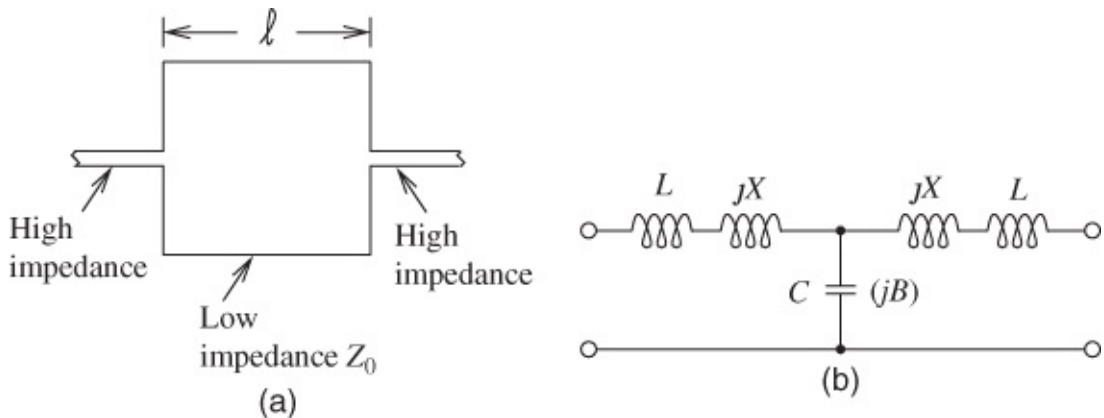


**Figure 19.18** Capacitive length of line with adjacent inductive lines: (a) microstrip; and (b) lumped equivalent.

Since this low-impedance length of line has the equivalent T network shown in [Figure 19.18](#) it must incorporate “stray” series inductances. These inductance values will now be shown to be usually negligible. We have

$$X_L \approx \pi \ell Z_0 / \lambda_g. \quad \text{19.30}$$

Now both  $Z_0$  and  $\ell$  are relatively small, so this complete reactance will only be a very small correction to the main inductive reactance of the adjacent inductive length of line.

The capacitance actually calculated for the capacitive length of line must in fact be less than the required total lumped value  $C_T$  because the inductive sections of line and the steps in width already contribute their capacitances  $C_{L1}$  and  $C_{s1}$ , respectively. Since these capacitances will generally differ due to the differing inductive lengths we finally have, for the capacitive line,

$$C_{\text{line}} = C_T - C_{L1} - C_{L2} - C_{s1} - C_{s2} \quad \text{19.31}$$

where  $C_{L1}$  and  $C_{L2}$  are obtained from Equations [\(19.25\)](#) or [\(19.26\)](#), applied to each adjacent inductive line, and  $C_{s1}$  and  $C_{s2}$  are determined using the expressions given in [Section 9.4](#). A more complete equivalent circuit for a  $C$ - $L$ - $C$  portion of a filter is given in [Figure 19.19](#). At frequencies where these structures are useful, generally only up to a few gigahertz, inductive effects due to the step discontinuities can usually be neglected.

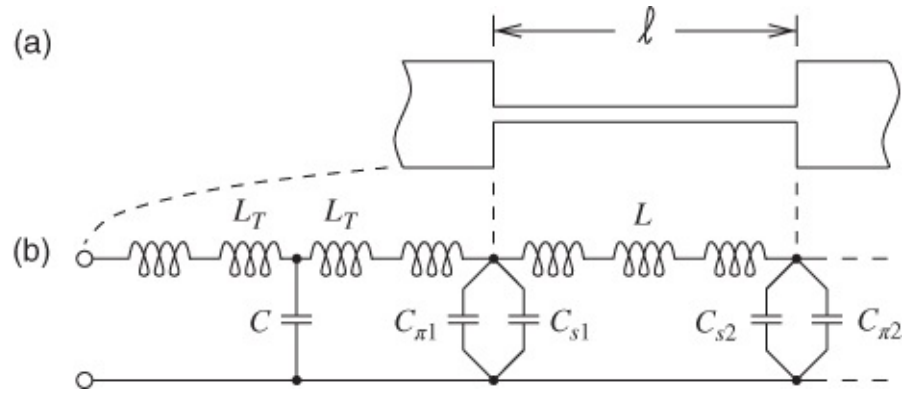


**Figure 19.19** Inductive length of microstrip line with adjacent capacitive lines: (a) microstrip line; and (b) lumped equivalent circuit including discontinuity (step) capacitances and inductances.

[Table 19.9](#) presents a summary chart showing the results applicable to inductive and capacitive elements realized in the form of microstrip lines.

[Table 19.9](#) Summary chart for inductive and capacitive elements formed using microstrip lines

Mainly inductive element	Mainly capacitive element
From Equation (19.22): $X_L = Z_{0L} \sin(2\pi \ell L / \lambda_{gL})$	and From Equation (19.22): $B_C = \frac{1}{Z_{0C}} \sin(2\pi \ell C / \lambda_{gC})$
End-capacitances: $C_L \approx \frac{\ell_L}{2fZ_{0L}\lambda_{gL}}$ , via Equation (19.26)	and End-inductances <sup>†</sup> $L_C \approx \frac{\ell_C Z_{0C}}{2f\lambda_{gC}}$ via Equation (19.30)
Main inductive length: $\ell_L = \frac{\lambda_{gL}}{2\pi} \sin^{-1}(2\pi f L / Z_{0L})$ via Equation (19.23)	Main capacitive length: $\ell_C = \frac{\lambda_{gC}}{2\pi} \sin^{-1}(2\pi f C Z_{0C})$ via Equation (19.28)
For short lengths only $\ell_L \approx f \lambda_{gL} L / Z_{0L}$ (via Equation (19.24))	Since lengths are usually short $\ell_C \approx f \lambda_{gC} Z_{0C} C$ (via Equation (19.29))

<sup>†</sup> Usually negligible.

### 19.3.2 Summary

This section began by presenting lowpass filter prototypes and then showed how these prototypes can be transformed into different types of filters. The inverter was introduced and as will be seen this is an important element in filter design. The unit element, a lossless transmission line segment, can be modeled as an inverter with stubs. This is the link between transmission line-based filter structures and lumped-element filter prototypes.

## 19.4 Microstrip Bandpass Filters

A bandpass microstrip filter is a cascade of resonators with each coupled to its neighbors.

This type of filter yields a narrow-to-moderate bandwidth; structures providing a broader bandwidth are considered towards the end of the discussion.

Before proceeding with this we must study some preliminaries, beginning with the transformed (lumped-element) bandpass filter (BPF) network shown in [Figure 19.20](#). Unfortunately, a serious difficulty is encountered with this network in its present form.

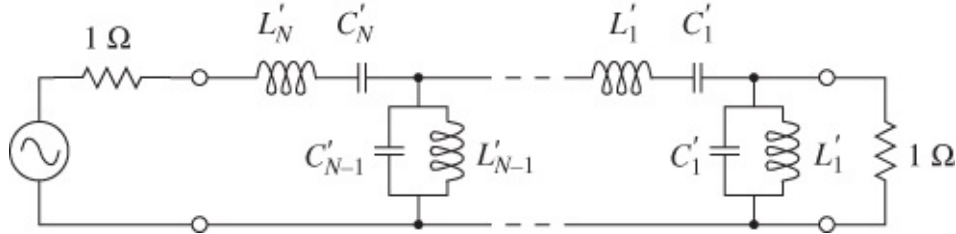


[Figure 19.20](#) Transformed, lumped-element, bandpass filter network.

It is evident that direct realization of this filter requires the design and interconnection of two *distinctly different kinds* of resonant *LC* circuits (i.e., resonators). Both series and parallel types of resonators would be required in any attempt to directly realize this filter. Any microstrip resonators which could be used and electromagnetically coupled together in some way would individually exhibit one type of resonance, either series or parallel, but not both simultaneously from similar structures.

There are two principal approaches to planar coupling between adjacent resonators: end coupling or parallel coupling. Both approaches will be considered here, but a separate section is devoted to parallel-coupled (edge-coupled) filters (i.e., BPFs) because these are usually more important.

### 19.4.1 Bandpass Filter Prototypes

A broad class of planar transmission line-based bandpass line filters are based on ladder prototype bandpass filters with inverters, as shown in [Figure 19.21](#). These are derived from the lowpass prototype filters previously described together with the filter transformation from lowpass to bandpass. The main feature here is that these bandpass filters comprise either series or shunt resonators that are coupled through an inverter. Many planar transmission line structures can be modeled with model components corresponding to sections of the lumped-element bandpass prototype filters.

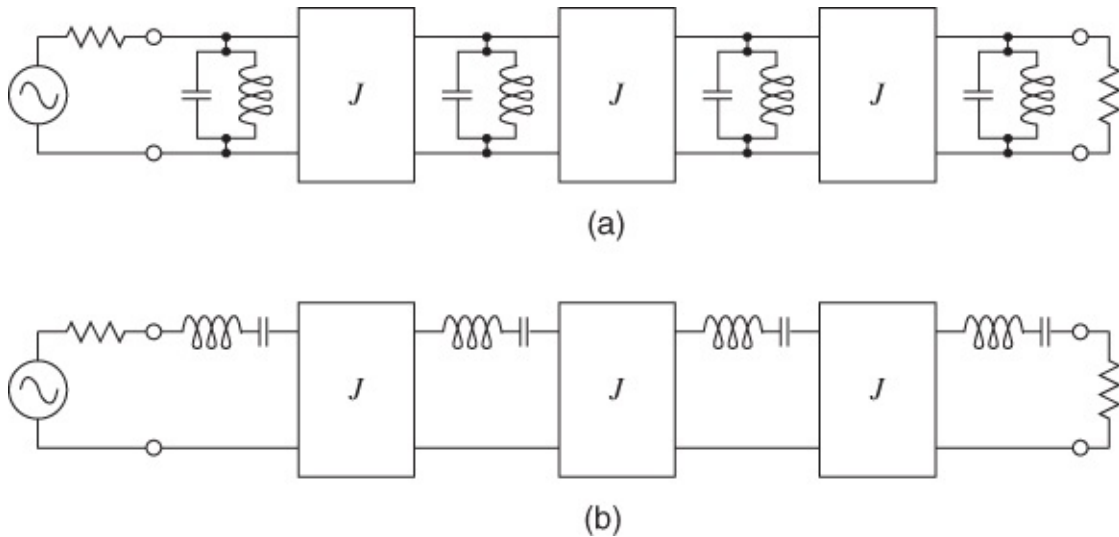


**Figure 19.21** Bandpass prototype filters with admittance inverters: (a) bandpass prototype filter with shunt resonators; and (b) bandpass prototype filter with series resonators.

### 19.4.2 End-coupled Bandpass Filters

The general layout of an end-coupled microstrip filter is shown in [Figure 19.22](#). In practice the right-hand side of this filter would either connect to the load (the next stage) or would comprise further filter sections, dependent on the performance requirements.



**Figure 19.22** General microstrip layout for an end-coupled bandpass filter (series coupling gaps between cascaded straight resonator elements).

A microstrip version of this type of filter has been described by Cunningham *et al.* [5], designed to operate at a center frequency of 28.76 GHz with a 2.78% bandwidth. Further specification parameters for this filter included a local oscillator rejection of at least 10 dB (at 27.6 GHz) and an image rejection (at 26.6 GHz) of at least 35 dB. The filter's insertion loss was simply to be as low as possible. This design approach was chosen because end-coupled filters are known to be relatively narrowband, which should suit the 2.78% bandwidth demanded here. The technology was chosen to be microstrip throughout for reasons of low cost.

In all types of filters based on transmission line resonators the coupling gaps between resonators are of prime importance, and the resonator lengths obviously also represent a particularly significant design result. For these end-coupled resonator filters the coupling needs to be as tight as possible, implying gaps that are usually much smaller than the substrate height. The resonator lengths depend not only on the microstrip wavelength, but also on coupling reactances and the effect of shunt capacitances due to the gaps. Cunningham shows that this length, excluding the effective gap lengths, is given by the following expression:

$$\ell_j = \frac{\lambda_g}{2\pi}(\pi - X_{j-1,j} - X_{j,j+1}) - b_{j-1,j} - b_{j,j+1} \quad 19.32$$

where  $b_{j-1,j}$  are lengths due to gap shunt capacitances and

$$X_{j-1,j} = 0.5[\tan^{-1}(2B_{j-1,j}/Y_0)]. \quad 19.33$$

A three-resonator filter was designed to meet the specification with a final bandwidth of 750 MHz and a center frequency of 28.76 GHz. The out-of-band response (critical in this application) was found to be superior to that of a parallel-coupled filter.

Other types of end-coupled filters have been developed, some only partially based on microstrip, but usually involving mainly microstrip-type elements. For example, Tzuang *et al.* [6] have reported what they term a quasi-planar broadside filter of this general type. This design, in contrast to conventional end-coupled filters, is relatively broadband (here a 30% bandwidth is obtained). The filter structure includes a ground plane milled to provide a slot beneath the microstrip section to form suspended microstrip. The reader is referred to the paper for further details, but the amplitude response is shown in [Figure 19.23](#).

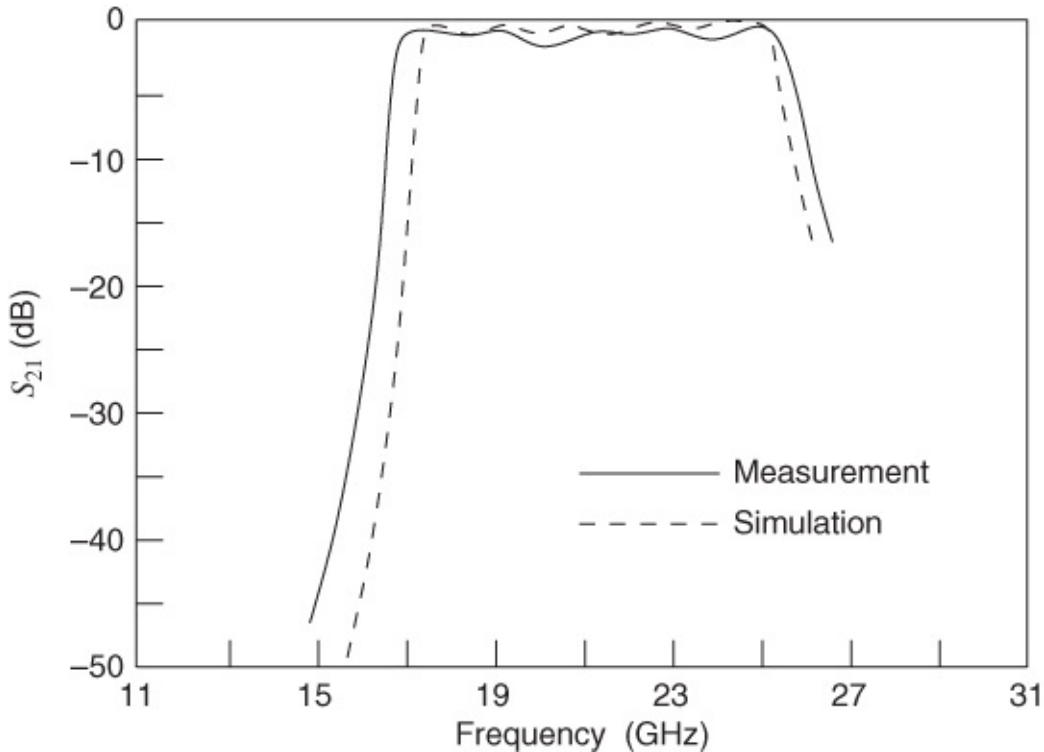


[Figure 19.23](#) Performance of quasi-planar broadside end-coupled bandpass filter. Adapted from Tzuang *et al.* (1990) [7], figure 6, p. 410. Reprinted with permission of IEEE.

## 19.5 Parallel-coupled Line Bandpass Filters

The PCL filters considered in this section are bandpass filters. It is also possible to realize bandstop filters using PCL sections. The passband and stopband performance of these filters is excellent, with some being able to achieve passbands as narrow as 1% and as wide as 40%.

The out-of-band performance can be several octaves although usually only two or three octaves are required. That means that if the passband is centered at, say, 1 GHz, the stopband can extend to 2 or 4 GHz.

There is a very large number of configurations of PCLs, with variants being largely determined by open- and short-circuit connections that turn the four-port of a pair of coupled lines into a two-port as required for a filter. There are several particularly useful PCL configurations and these are reviewed here. All are based on a unit cell consisting of a pair of coupled lines. Pairs of coupled lines are then combined to realize multicell forms. These filters are not just restricted to planar transmission line configurations but this is the most convenient realization.

All bandpass and bandstop filters are based on coupled resonators. With PCL filters the a resonator is approximately formed by one microstrip line, which is coupled to another microstrip line-based resonator. Of course when the lines are coupled it is not possible to strictly associate a resonator with a single microstrip line. If stopband performance exceeding 40–60 dB is required then it is necessary to use other structures which are also based on coupled resonators but now these need to be shielded either as coaxial lines that are then coupled at their ends or using dielectric puck resonators that are coupled through conductor walls. These are not considered here.

With all PCL filters design proceeds by developing a model of the PCL configuration and targeting the emergence of this structure in the evolving prototype of the filter. There are a very large number of publications on PCL filter design which relate particular models of PCL configurations to prototype filter development that results in a filter prototype that directly relates to the model of a physical PCL configuration. Generally a different model development approach is required for each PCL filter configuration. This is because the PCL model developed must relate to a prototype that can be developed.

### 19.5.1 Interdigitated Filters

The short-circuit form of the interdigital bandpass filter is shown in [Figure 19.24](#). The basic resonator is formed by one of the single microstrip lines which is shorted at one end. Then in the basic form, [Figure 19.24\(a\)](#), two resonators are coupled when the two individual microstrip lines are in close proximity. Higher filter performance is obtained by using the multicellular form shown in [Figure 19.24\(b\)](#). This is a high-performance filter but has the drawback of requiring vias.

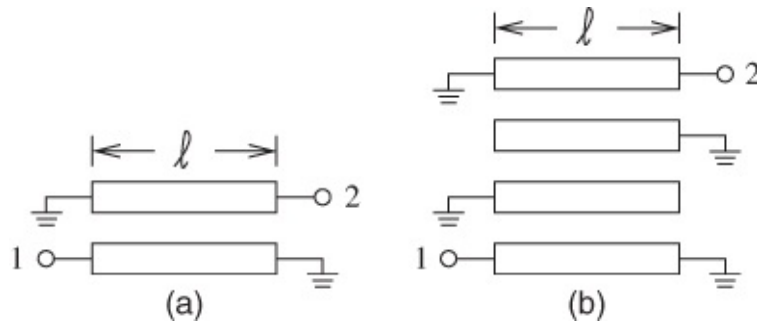


[Figure 19.24](#) Interdigital bandpass filter with  $\ell \approx \lambda_g/4$ : (a) single cell; and (b) multicell.

## 19.5.2 Edge-coupled PCL Bandpass Filters

The edge-coupled filter is the open-circuited form of an interdigitated PCL filter and does not require vias. The short-circuit form of the interdigital bandpass filter is shown in [Figure 19.25](#). Again the basic resonator is formed by one of the single microstrip lines, which is coupled to a second microstrip resonator when the two individual microstrip lines form PCLs. This is a high-performance filter band that is easy to realize as vias are not required. We will now describe one of several design procedures that have been developed.

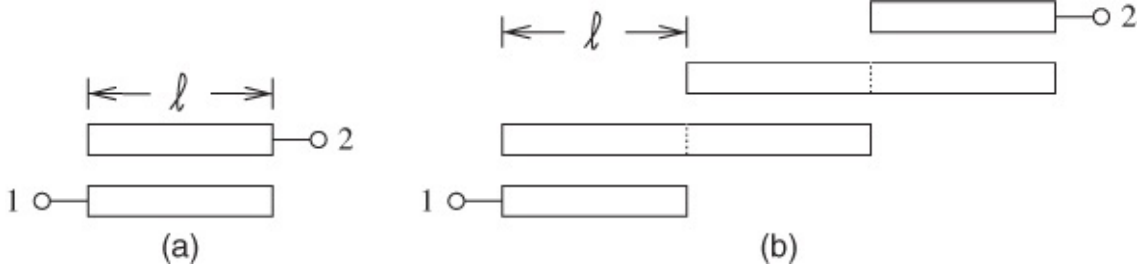


[Figure 19.25](#) Edge-coupled bandpass PCL filter with  $\ell \approx \lambda_g/4$ : (a) single cell; and (b) multicell. The dotted lines are not part of the layout but serve to illustrate that a long microstrip line combines to sections each of length  $\ell$ .

A complete edge-coupled PCL filter is shown in [Figure 19.26](#). As discussed in [Section 10.2.3](#) for microstrip couplers, maximum coupling is obtained between physically parallel microstrips when the length of the coupled region is  $\lambda_g/4$ , or some odd multiple thereof. To achieve resonance, each resonator element has to be  $\lambda_g/2$  in length, or any multiple thereof. Therefore, the edge-coupled PCL filter shown in [Figure 19.26](#) must have

$$\ell_1, \dots, \ell_4 \approx \lambda_g/4.$$

19.34

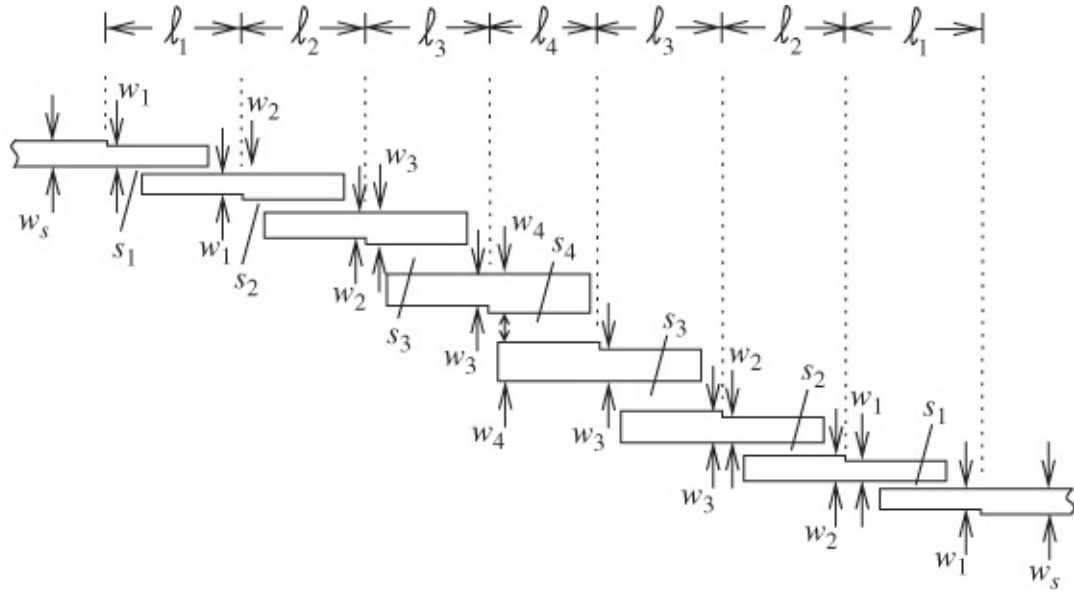


[Figure 19.26](#) A seven-section, parallel-coupled microstrip bandpass filter.

The design of this filter is based on a lumped-element prototype bandpass filter which incorporates inverters. This is matched to the equivalent circuit model of a coupled line. The

$ABCD$  parameters of the coupled line configuration in [Figure 19.27\(a\)](#) are

$$\mathbf{T} = \begin{bmatrix} \cos(\theta) & \frac{j(Z_{0e} - Z_{0o})}{2} \sin(\theta) \\ \frac{j2 \sin(\theta)}{(Z_{0e} - Z_{0o})} & \cos(\theta) \end{bmatrix} \quad 19.35$$

which can be partitioned as

$$\mathbf{T} = \begin{bmatrix} 1 & \frac{-j(Z_{0e} - Z_{0o})}{2 \tan(\theta)} \\ 0 & 1 \end{bmatrix} \begin{bmatrix} 0 & \frac{j(Z_{0e} - Z_{0o})}{2 \sin(\theta)} \\ \frac{j2 \sin(\theta)}{(Z_{0e} - Z_{0o})} & 0 \end{bmatrix} \times \begin{bmatrix} 1 & \frac{-j(Z_{0e} - Z_{0o})}{2 \tan(\theta)} \\ 0 & 1 \end{bmatrix}. \quad 19.36$$

This describes the cascade of an open-circuit series stub with unit element and a second open-circuit series stub as shown in [Figure 19.27\(b\)](#). Combining the equivalent model in [Figure 19.27\(b\)](#) with the equivalent model of a unit element, [Figure 19.15](#), leads to the coupled line equivalent model shown in [Figure 19.28](#). This is a broadband model with the only approximation being the inherent assumption that the phase velocities of the even and odd modes are the same. Consider the equivalent model in [Figure 19.28\(b\)](#). This is a model of a series resonators (the stubs) coupled by inverters. This is one of the forms of the lumped-element prototype bandpass filter, see [Figure 19.21\(b\)](#).

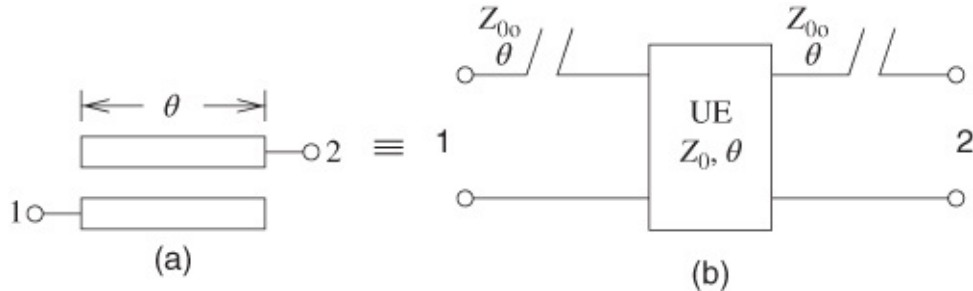


[Figure 19.27](#) Broadband equivalent model of coupled transmission lines in open interdigital configuration: (a) coupled line; and (b)  $Z_0 = \frac{1}{2}(Z_{0e} - Z_{0o})$ .

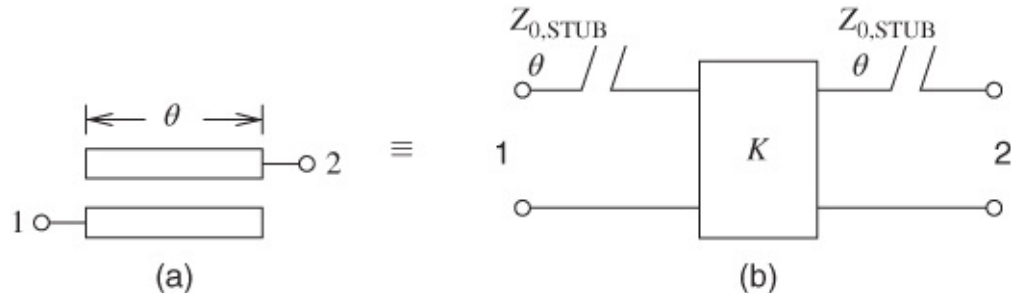


[Figure 19.28](#) Broadband equivalent model of coupled transmission lines in open interdigital configuration: (a) coupled line; and (b) unit element,  $Z_0 = \frac{1}{2}(Z_{0e} - Z_{0o})$   $Z_{0,STUB} = \frac{1}{2}(Z_{0e} + Z_{0o})$ .

A consequence of the above model is that as a good approximation, which will be used for the moment, the edge-coupled filter in [Figure 19.24](#) is a fairly straightforward cascade of parallel-coupled (or edge-coupled) microstrip resonators and the filter can be designed on the basis of all-parallel resonator networks, together with intervening circuits known as inverters. The four main design steps are:

- a.** Determine the one-type resonator network, to realize the specification, from the original prototype.
- b.** From the network parameters, evaluate the even- and odd-ordered characteristic impedances,  $Z_{0e}$  and  $Z_{0o}$ , applicable to the parallel-coupled microstrip. (This will be shown in detail presently.)
- c.** Relate the values of  $Z_{0e}$  and  $Z_{0o}$  to microstrip widths and separations ( $w$ ,  $s$ ). Procedures for this step are given in detail in [Section 10.5](#).
- d.** Calculate the whole resonator length  $2\ell$ , which is slightly less than  $\lambda_g/2$  because of the semi-open end-effects, and therefore of the coupled-section length  $\ell$ , which is slightly less than  $\lambda_g/4$  for the end-effect reason again.

Here  $\lambda_g$  is the mid-band and average microstrip wavelength. Allowance must be made for the semi-open-circuit microstrip end-effects which exist for all elements in this circuit.

### 19.5.2.1 Introducing Admittance Inverters

The simplest form of an impedance inverter is the quarter-wave transformer. It should be recollected from [Section 2.9](#) that such circuit components transform any load impedance by the quantity  $Z_0^2$ , where  $Z_0$  is the characteristic impedance of the quarter-wave transforming section of line. As a consequence of this characteristic impedance, squared terms will arise for impedance and admittance inverters.

It has already been stated that a network consisting of admittance inverters, usually called  $J$  inverters, and uniform-type resonant circuits is to be made equivalent to the original network consisting of two types of resonant circuit, series and parallel. While the impedance level will vary through the system, two features must be maintained for equivalence:

- a.** The resonant frequency must remain constant:  $\omega_0^2 = 1/LC$ .
- b.** Impedances at similar planes in each network must be equal.

In the following expressions the “first coupling structure” is that formed by  $w_s$ ,  $s_1$ ,  $w_1$  ([Figure 19.26](#)) and the “final coupling structure” consists also of  $w_s$ ,  $s_1$ ,  $w_1$  at the opposite end of the filter. The quantities  $g$  refer to the prototype element values, for example  $g_0 = 1$  (the normalized termination value) and  $g_0 = 0.781$ , from the table for a sixth-order Chebyshev prototype, which is standard data available in many references [1]. (That is, the  $g$  values are the coefficients of the lowpass prototype filter normalized to a corner frequency  $\omega'_1 = 1$  radian/s and a system impedance of  $1\Omega$ .) The various radian frequencies are defined in [Figure 19.29](#).

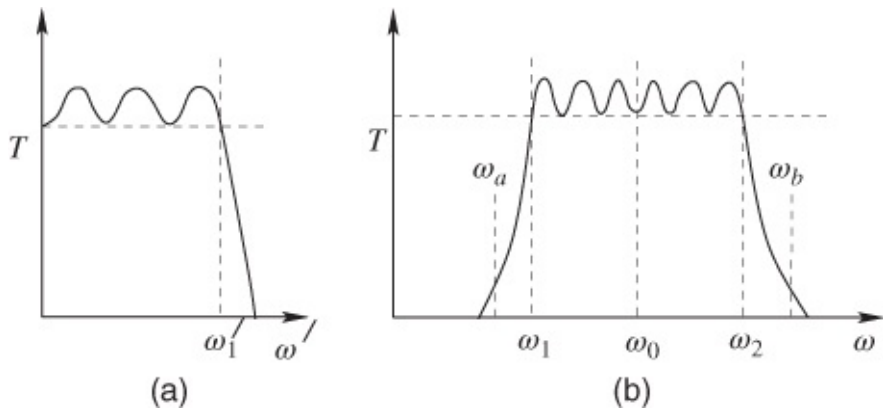


**Figure 19.29** Frequency definitions for the example: (a) lowpass filter; and (b) bandpass filter.

For the first coupling structure:

$$\frac{J_{01}}{Y_0} = \sqrt{\frac{\pi\alpha}{2g_0g_1}}. \quad \text{19.37}$$

For the intermediate coupling structures:

$$\frac{J_{j,j+1}}{Y_0} \Big|_{j=1}^{n-1} = \frac{\pi\alpha}{2\omega'_1 \sqrt{g_j g_{j+1}}}. \quad \text{19.38}$$

For the final coupling structure:

$$\frac{J_{n,n+1}}{Y_0} = \sqrt{\frac{\pi\alpha}{2g_n g_{n+1}}}. \quad \text{19.39}$$

In these three equations,  $\alpha$  is the fractional bandwidth

$$\alpha = (\omega_2 - \omega_1)/\omega_0. \quad \text{19.40}$$

The frequency transformation from the lowpass prototype filter to the bandpass microwave filter is then

$$\frac{\omega'}{\omega'_1} = \frac{2}{\alpha} \left( \frac{\omega_a - \omega_0}{\omega_0} \right) \quad \text{19.41}$$

where  $\omega'_1 = 1$  radian/s in Equation (19.38) is the prototype cut-off frequency and  $\omega'$  is the frequency in the lowpass prototype. (The full design procedure will presently be shown by means of a specific numerical example, where the meanings of  $\omega'_1$  and  $\omega'$  etc., will become clear.)

To proceed with the microstrip design, we now only require the odd- and even-mode coupled-line impedances  $Z_{0o}$  and  $Z_{0e}$ . These are given by

$$(Z_{0e})_{j,j+1} = Z_0(1 + aZ_0 + a^2Z_0^2) \quad \text{19.42}$$

and

$$(Z_{0o})_{j,j+1} = Z_0(1 - aZ_0 + a^2Z_0^2) \quad 19.43$$

where  $a = J_{j,j+1}$  and  $Z_0$  is the “system” characteristic impedance (i.e., that of the lines feeding the filter).

Having obtained the values of  $Z_{0o}$  and  $Z_{0e}$  section by section, the microstrip widths and separations are determined. The synthesis technique is described in [Section 10.5](#). Calculations and a typical design are best shown by a specific example which will be presented in [Section 19.5.7](#).

### 19.5.3 Comline Filters

The basic form of the comline filter is shown in [Figure 19.30](#). This structure requires additional matching to function as a bandpass filter. This matching is as simple as series capacitors at ports 1 and 2 and then the filter has excellent characteristics, with 40 dB out of rejection in the stopband easily achieved. A detailed case study of a microstrip comline bandpass filter is presented in Reference [3].

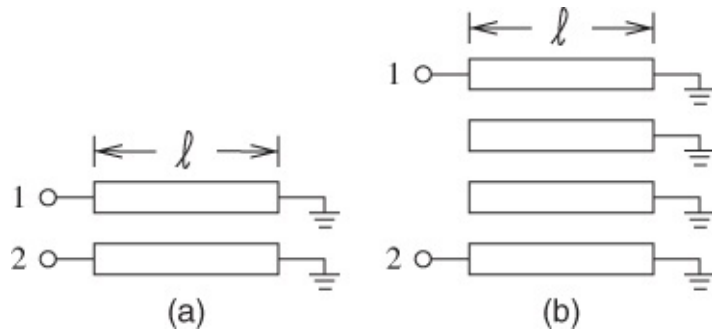


[Figure 19.30](#) Comline filter with  $\ell \approx \lambda_g/4$ : (a) single cell; and (b) multicell.

### 19.5.4 Hairpin Filters

The hairpin filter is an edge-coupled filter but instead of the microstrip lines being arranged in a linear fashion, the microstrip lines are folded back on themselves to realize a compact filter. The basic form of the hairpin filter is shown in [Figure 19.31](#).

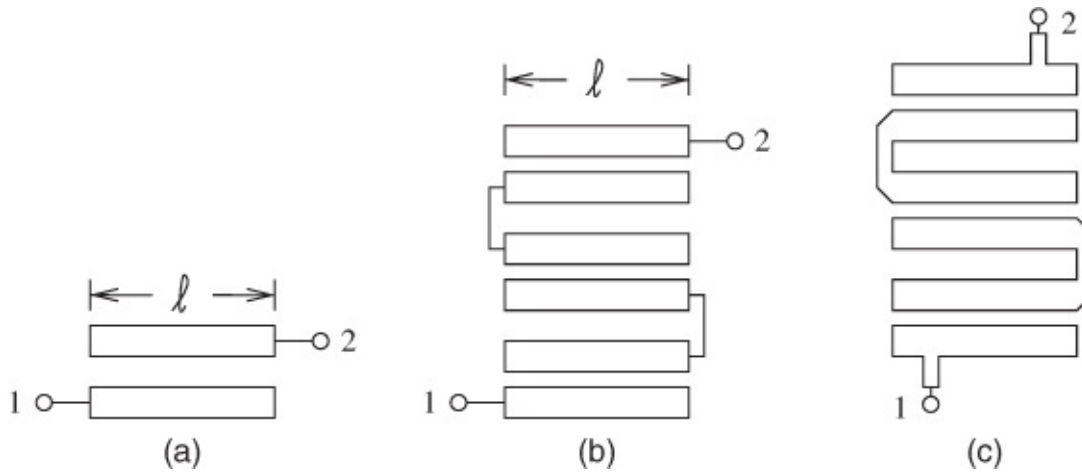


**Figure 19.31** Hairpin filter with  $\ell \approx \lambda_g/4$ : (a) single cell; (b) multicell; and (c) physical layout.

### 19.5.5 Miniature Coupled Line Filters with Extended Stopband

Transmission-line based bandpass filters that use quarter-wavelength long resonators will have a spurious passband at approximately three times the center frequency of the passband. This is because electrically a line that is three quarters of a wavelength long behaves the same as a quarter-wavelength long. Combining capacitors with transmission line resonators enables a resonator to be realized using a line that is  $\lambda_g/8$  long or shorter. Essentially the individual microstrip lines (which are  $\lambda_g/8$ ) are not resonant on their own but form a resonant circuit in combination with the capacitors to ground at the end of the individual microstrip lines. As seen from the capacitors the microstrip lines are inductive and this forms a resonant element with the capacitors. The individual resonators are coupled through the PCLs. This extends the stopband of the filter and also results in a more compact filter [8, 9]. A combline bandpass filter using this technique is shown in [Figure 19.32](#).

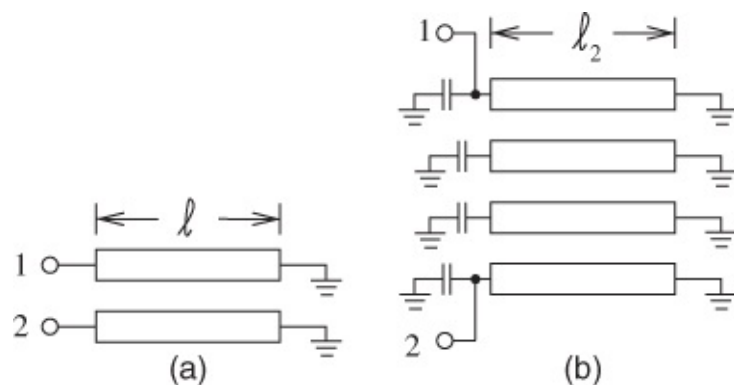


**Figure 19.32** Combline filter with the multicell form having extended stopband with  $\ell_2 \approx \ell/2 \approx \lambda_g/8$  typically: (a) single cell; and (b) multicell.

Another technique is to increase the coupling by replacing a coupled line by a shorter section of coupled line with capacitors at the two ends. The result is a miniaturized PCL filter with microstrip lengths shorter than the typically half- or quarter-wavelength long microstrip lengths.

### 19.5.6 Improvements to the Basic PCL Filter Response

PCL microstrip bandpass filters of the types described above display somewhat asymmetrical frequency responses in addition to a significant second passband unless compensated. These highly undesirable effects are principally due to the field characteristics of the odd mode.

Various techniques are available for compensation of this odd-mode effect and some of these were also outlined in [Chapter 10](#). Bahl [10] has shown that, with capacitive compensation introduced at the ends of each quarter-wave section (see [Section 11.5.5](#)), the stopband performance of these types of filters is greatly improved. The “sharpness” or selectivity characteristics of both skirts are improved most markedly in the case of the upper skirt, where the improvement is typically 5–10 dB. Also, the second passband is then more than 40 dB below the level of the fundamental passband and, to further advantage, slightly shifted in frequency. Compensating capacitances typically lie in the range of 0.002–0.055 pF, depending on the specific filter section and the substrate. Bahl gives examples of GaAs and quartz substrates.

### 19.5.7 Case Study: PCL Edge-coupled Bandpass Filter

The specification of the filter to be designed is shown in [Figure 19.33](#). Here  $L$  is the insertion loss (the inverse of the transmission response) in decibels. The passband insertion loss has not been specified on the characteristic; it would usually be expected to lie below about 0.1 or 0.2 dB.

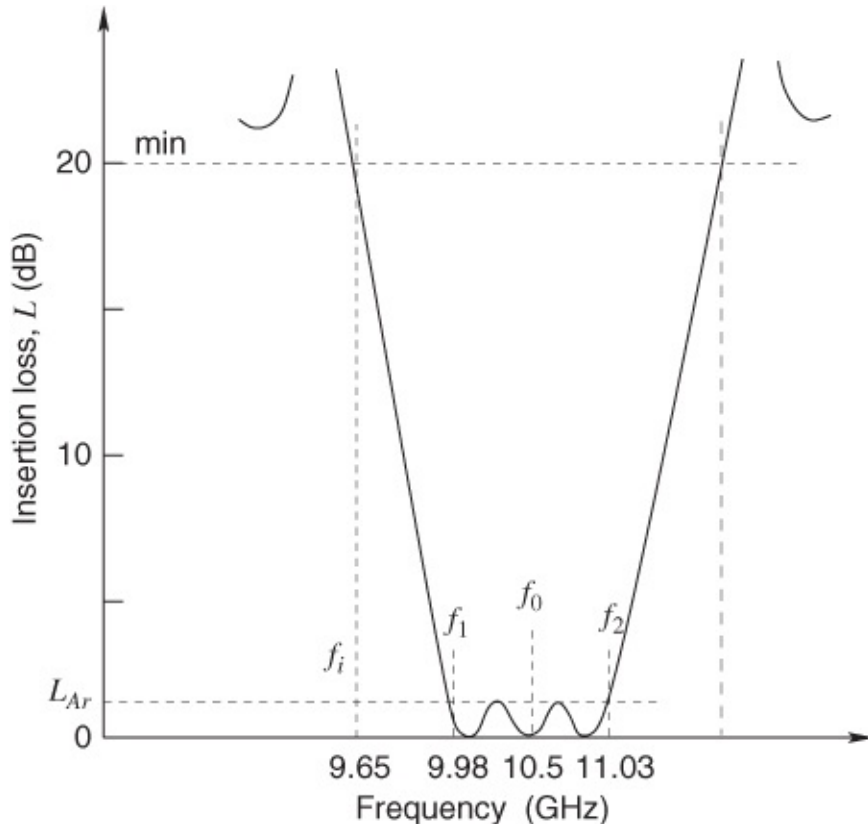


[Figure 19.33](#) Insertion-loss characteristic for the bandpass filter of the example.

*Step 1* Using Equations (19.40) and (19.41) a fractional bandwidth of 0.1 is obtained. Also, a minimum loss of 20 dB must be achieved (a transmission of  $-20$  dB) at a frequency of 9.65 GHz. Application of Equation (19.41) leads to a transformation ratio  $(\omega' - \omega_c)$  of 1.619.

*Step 2* Determine the filter prototype specifications which meet the insertion-loss requirements. These are available in many handbooks (e.g., see Matthaei *et al.* [1]). The choice of 0.01 dB is good and the family of curves shown in Figure 19.34 shows the transmission above the passband corner frequency (or 0 on the horizontal axis here) for Chebyshev prototypes having a 0.01 dB passband ripple. These curves are used to determine the necessary filter order  $n$ . Now  $(\omega'/\omega_c - 1) = 0.619$  and since a maximum transmission of  $-20$  dB is required, the required filter order is determined to be  $n = 6$ . A sixth order ( $n = 6$ ) design gives a transmission of  $-23$  dB at  $\omega'$ . Coefficient values for a Chebyshev filter with  $n = 6$  are given in Table 19.10. (Note that since this is an even-order Chebyshev  $g_{n+1} = g_7 \neq 1$ , as it would for an odd-order Chebyshev filter.)

*Step 3* Calculate the inverter admittances (normalized for a 50  $\Omega$  system) and hence coupled-line impedances using Equations (19.37) to (19.39), and also Equations (19.42) and (19.43). The results are shown in Table 19.11.

*Step 4* The microstrip line dimensions are finally obtained as follows (substrate permittivity  $\epsilon_r = 10$ ): Using the synthesis described in Section 10.5:

$$\left. \begin{array}{l} Z_{0se} = Z_{0e}/2 = 41.25 \Omega \\ Z_{0so} = Z_{0o}/2 = 18.8 \Omega \\ \text{Equivalent single-line synthesis yields:} \\ (w/h)_{se} = 1.5 \\ (w/h)_{so} = 4.8 \\ \text{Then coupled-line synthesis gives the required parameters:} \\ (w/h) = 0.65 \quad (s/h) = 0.2 \\ \\ j=0 \quad \left\{ \begin{array}{l} Z_{0se} = 29.4 \Omega \quad Z_{0so} = 21.75 \Omega \\ (w/h)_{se} = 2.5(w/h)_{so} = 4.0 \\ w/h = 1.0 \quad s/h = 0.68 \end{array} \right. \\ \\ j=1 \quad \left\{ \begin{array}{l} Z_{0se} = 27.85 \Omega \quad Z_{0so} = 22.65 \Omega \\ (w/h)_{se} = 2.7 \quad (w/h)_{so} = 3.7 \\ w/h \approx 1.0 \quad (s/h) \approx 1.0 \end{array} \right. \\ \\ j=2 \quad \left\{ \begin{array}{l} \text{Since impedances are only } 0.3 \Omega \\ \text{different from the } j=1 \text{ case approximately} \\ \text{the same results are obtained here as for } j=1. \end{array} \right. \end{array} \right.$$

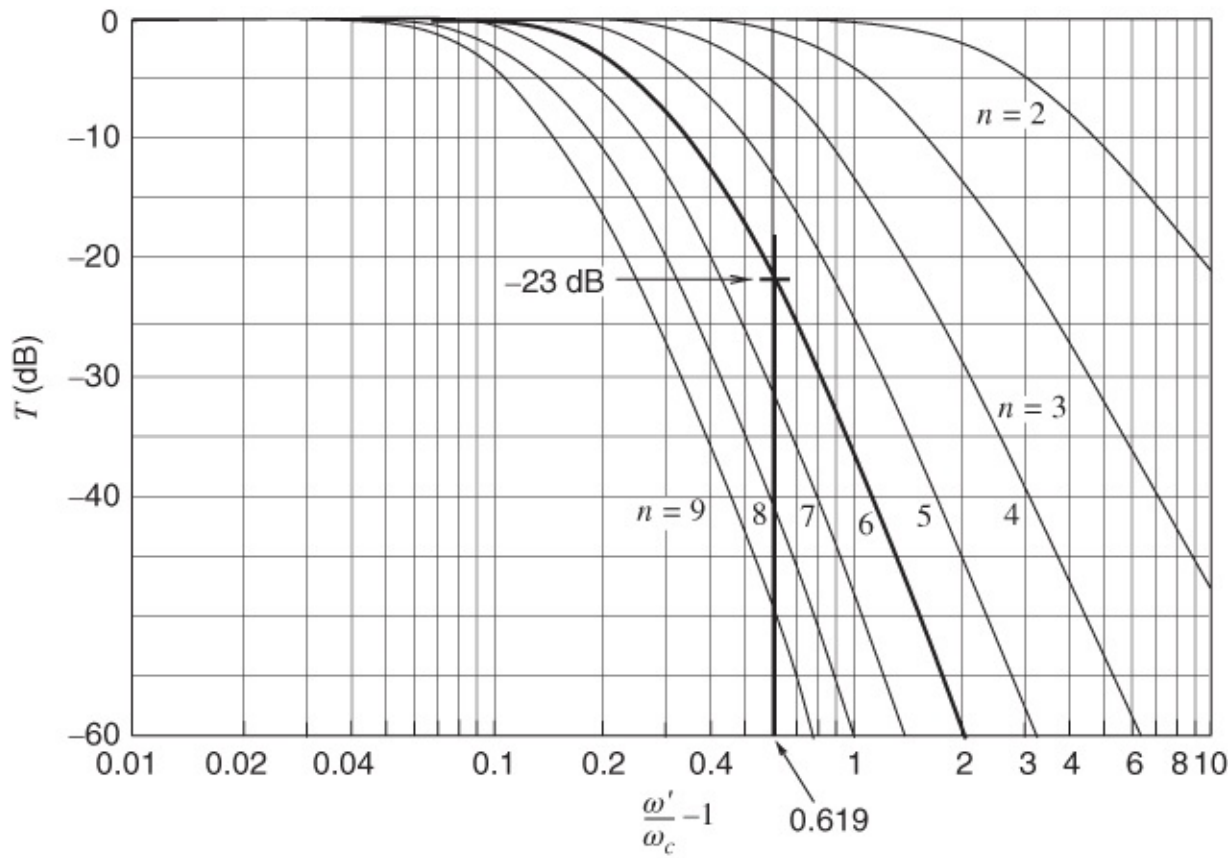


**Figure 19.34** Transmission of Chebyshev lowpass prototype filters for various orders  $n$  and for a passband ripple of 0.01 dB.

**Table 19.10** Coefficients for a sixth-order Chebyshev filter

$g_0$	$g_1$	$g_2$	$g_3$	$g_4$	$g_5$	$g_6$	$g_7$
1.000	0.781	1.360	1.690	1.535	1.497	0.710	1.101

**Table 19.11** Step 3 results

$j$	$J_{i,j+1}/Y_0$	$(Z_{0e})_{j,j+1}$ ( $\Omega$ )	$(Z_{0o})_{j,j+1}$ ( $\Omega$ )
0	0.449	82.5	37.6
1	0.1529	58.8	43.5
2	0.1038	55.7	45.3
3	0.0976	55.4	45.6

[Figure 19.35](#) shows the final dimensions of this filter, since the substrate has a thickness of 0.635 mm. “Open” end-effects may be determined experimentally, as described in [Section 18.5](#). Then the physical lengths of the resonators and the coupled regions are half-wavelengths and quarter-wavelengths respectively, with the equivalent end-effect lengths subtracted. (A wavelength is specified at the center frequency  $f_0$  and calculated as described in [Section 11.4.1](#)) The measured amplitude response of this filter is shown in [Figure 19.36](#).

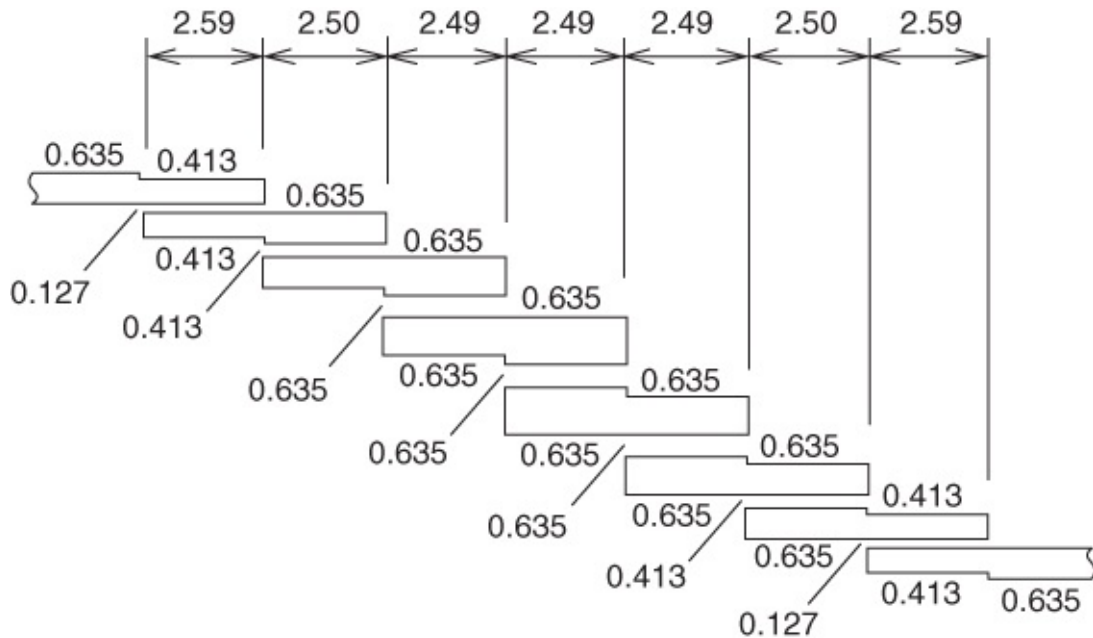


**Figure 19.35** Final design dimensions in millimeters of the bandpass filter calculated in the worked example.

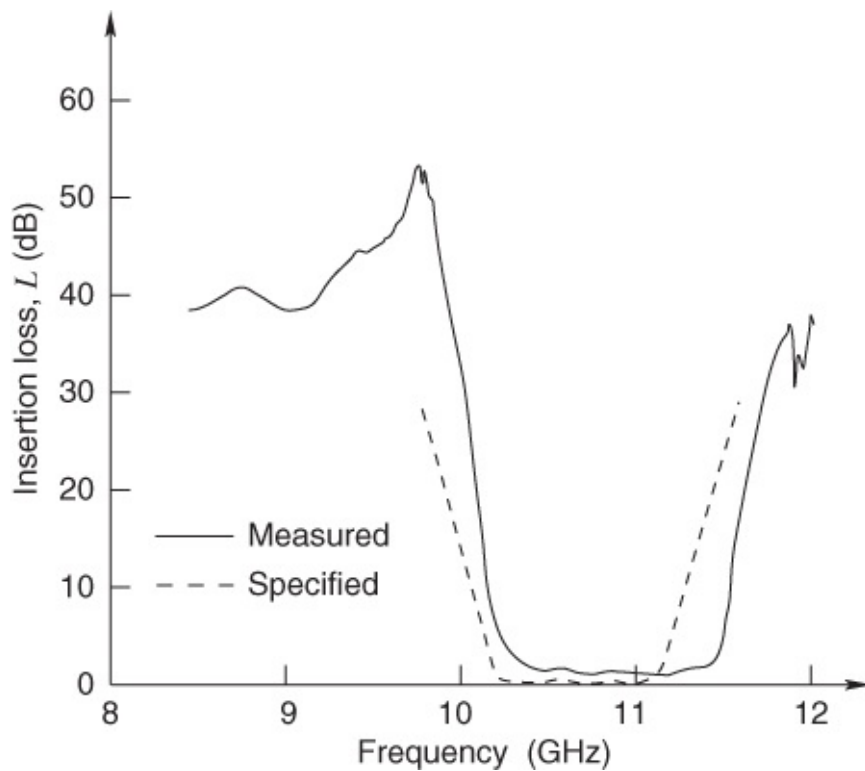


**Figure 19.36** Measured compared with specified insertion-loss characteristics for the 10–11 GHz parallel-coupled bandpass filter.

This filter was manufactured using copper-conductor thin-film technology, with the dimensions given in [Figure 19.35](#); no post-manufacture trimming was undertaken. We note that the results shown in [Table 19.12](#) apply.

**Table 19.12** Summary of the main bandpass filter parameters

Parameter	Desired (Figure 19.33)	Measured (Figure 19.36)
3 dB bandwidth (%)	10.5%	12.5%
Center frequency (GHz)	10.5 GHz	10.7 GHz

Judicious modification (trimming/tuning) is necessary to adjust these values, for example making the resonators just 2% longer should result in a closer center frequency. The bandwidth is particularly sensitive to the separations of the first and last coupled sections, and these separations should be increased slightly so that the bandwidth is reduced.

## 19.6 Filter Design Accounting for Losses

The preceding filter design approaches neglect the effects of power losses through the structure. It is extremely difficult, if not impossible, to anticipate these in quantitative detail and then to actually synthesize a design including all losses. Instead, it is suggested that the design be synthesized and the resulting filter structure simulated to determine its insertion loss response, including power losses. Another problem, although not related to loss, is the difference in the effective permittivity of the even and odd modes of a pair of coupled microstrip lines. The best that can be done is to take the effective permittivity as the geometric mean of the even and odd mode permittivities. For this reason post-layout optimization of the filter using microwave CAD tools should follow synthesis. Alternatively, controlled variations on the exact design could be studied for their impact on loss-driven aspects of their characteristics. A general comment is that the difference in the even- and odd-mode phase velocities results in higher coupling than would be expected. Thus a PCL microstrip bandpass filter will initially, that is following synthesis, have a higher bandwidth when simulated.

## 19.7 Dielectric Resonators and Filters Using Them

Although not specifically microstrip elements, dielectric resonators are of such significance in several forms of filters and oscillators that a brief consideration of these devices is essential here.

Any cylindrically-shaped dielectric structure can be caused to resonate at some specific frequencies and these depend on both the permittivity and the physical dimensions. The general theoretical expression for such resonant frequencies, applying to a dielectric resonator of radius  $a$  and height  $d$ , is

$$f_{mn} = \frac{c}{2\sqrt{\epsilon_r}} \sqrt{\left(\frac{x_{mn}}{\pi a}\right)^2 + \left(\frac{l}{d}\right)^2} \quad 19.44$$

where the integer  $l$  denotes the number of half-wavelengths in the vertical direction and  $x_{mn}$  is the  $m$ th extremum of the Bessel function  $J_n$  for a TM mode (or alternatively the  $m$ th zero for a

TE mode). This is developed as the dual of the well-known metallic cavity analysis [11].

In practice fringing fields, microstrip (or other) line coupling, and the presence of the substrate dielectric render the analysis complex and more sophisticated, computer-based, procedures are necessary to evaluate the applicable parameters.

Low-loss ceramic materials with permittivities in the range 21.6–152 are generally available that can be supplied in dielectric resonator pill form. Unloaded  $Q$  factors are in the 5000–10000 range and physical dimensions generally depend on the resonant frequencies desired. However, loaded  $Q$  factors depend strongly on the degree of coupling to the microstrip line, that is, the proximity of the two elements. When the coupling distance is less than 1 mm the loaded  $Q$  factor is usually below 500 and this has significant consequences in filter and oscillator design [12]. At 4 GHz a 14 mm diameter pill is typical (with  $\epsilon_r = 35$ ), whereas at higher frequencies dielectric pills having diameters of only a few millimeters are implemented.

Filter design using conventional resonators (such as the edge-coupled microstrips considered earlier in this chapter) requires several optimally coupled resonators and this is also true with dielectric-resonator (DR) based filters. A general arrangement of a DR-based filter is shown in [Figure 19.37](#).

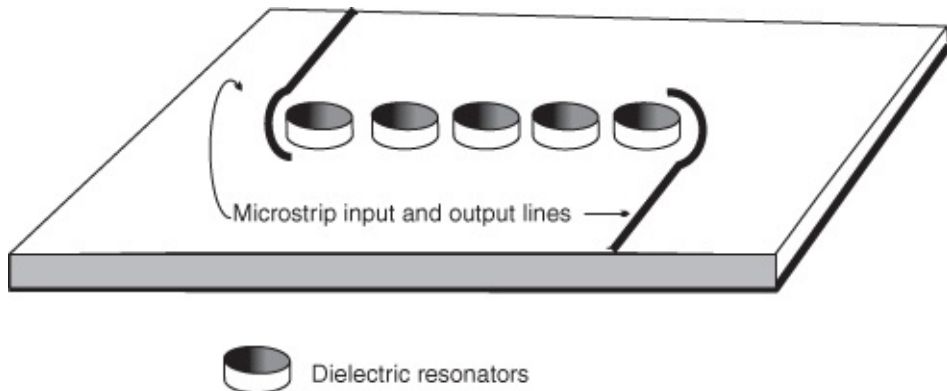


[Figure 19.37](#) A microstrip-connected dielectric resonator bandpass filter configuration.

To increase the coupling whilst avoiding excessive proximity of the microstrip lines, curved coupling sections are used. Each DR is also optimally coupled and, as with all filters, a major design aim is to identify appropriate DRs and to establish the degrees of coupling applicable to each section. Bahl and Bhartia [12] cover this problem extensively and show an example of a 900 MHz bandwidth bandpass filter design, centered on 9 GHz. The impact of the performance of loaded  $Q$  factors, ranging as low as 100, are shown. With a loaded  $Q$  factor of 500 the insertion loss deteriorates to around 2 dB through the passband, which is probably acceptable in many instances. However, with a loaded  $Q$  factor of 100 this insertion loss is around 4 dB, which is almost always unacceptable.

## 19.8 Spurline Bandstop Filters

Bates and Pearson [13, 14] evolved a simple and clever technique for designing a bandstop

filter using a series resonant stub, as shown in [Figure 19.38](#). A series microstrip stub is rarely used but in this case it enabled a series resonant circuit to be used in realizing a bandstop filter with the series resonant stubs coupled by a length of microstrip transmission line.

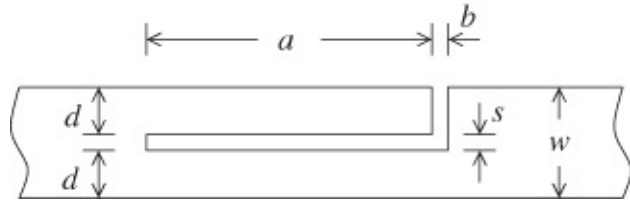


[Figure 19.38](#) A series stub in a microstrip transmission line.

It was demonstrated that this filter is almost non-dispersive, and the structure is so configured that radiation loss is very low compared with coupled-line or shunt-stub filters. The filter structure was shown to be equivalent to an open-circuit shunt stub of characteristic impedance  $Z_1$ , followed by a continuous section of microstrip having a characteristic impedance  $Z_{12}$ . These impedances are given by

$$Z_1 = \frac{Z_{0e}}{Z_{0o}} \left( \frac{Z_{0o} + Z_{0e}}{2} \right) \quad \text{19.45}$$

and

$$Z_{12} = Z_{0o} + Z_{0e}/2 \quad \text{19.46}$$

where  $Z_{0e}$  and  $Z_{0o}$  have the meanings defined previously for coupled lines.

This filter can be designed according to the procedure described by Matthaei, Young, and Jones [1], and computer-aided optimization can then be employed. Bates [13] gives graphs of  $Z_1$  and  $Z_{12}$  as functions of the parameters  $s/h$  and  $w/h$ , although a designer with access to computer facilities would probably need to develop suitable expressions for these impedances. The length  $a$  (see [Figure 19.38](#)) is electrically  $\lambda_g/4$  at mid-band ( $f_0$ ), but the gap equivalent length  $\ell_{eg}$  will affect the physical value of  $a$  such that

$$a = \frac{3 \times 10^8}{4f_0 \sqrt{\epsilon_{\text{eff},o}}} - \ell_{eg} \quad \text{19.47}$$

where  $\epsilon_{\text{eff},o}$  is the odd-mode effective microstrip permittivity at the center frequency (see [Section 11.4](#)) and  $\ell_{eg}$  is the gap end-effect extension (see [Section 9.2.2](#)).

The value of the series-gap separation  $b$  has to be determined empirically and a value of approximately 50  $\mu\text{m}$  appears to be suitable for designs on alumina, and similar substrates [13]. Once  $b$  is chosen, the end-effect length may be found by using

$$\ell_{eg} = C_{\text{odd}} v_{po} Z_{0o}. \quad \text{19.48}$$

$C_{\text{odd}}$  is calculated from expressions and data given by Benedek and Silvester [15], and Bates [13] gives results which indicate that a very good agreement between calculation and

experiment can be achieved for gap separations of about  $100 \mu\text{m}$  or less. The filter design procedure is thus:

- a. From the specified response desired use the technique given by Matthaei *et al.* [1] to find  $Z_1$  and  $Z_{12}$ .
- b. Calculate  $Z_{0e}$  and  $Z_{0o}$  from  $Z_1$  and  $Z_{12}$  using Equations (19.45) and (19.46).
- c. Employ computer-aided optimization to ensure that the network so far described meets the desired specification within acceptable limits.
- d. From  $Z_{0e}$  and  $Z_{0o}$  synthesize the desired  $s/h$  and  $w/h$ .
- e. Evaluate the length  $a$ , approximately.
- f. Choose the series gap separation  $b$  ( $\approx 50\mu\text{m}$ , on alumina) and hence also determine  $\ell_{eg}$ .
- g. Iterate (e) and (f) until  $a$  is found more accurately and the center frequency  $f_0$  is close to that desired.

The bandstop filter performance is particularly good when two of these spurline structures are arranged back to back in cascade, with a separation slightly less than a quarter-wavelength. For example, where  $a = 3.2$  mm the distance separating the structures should be about 3.0 mm [14]. With such a filter a rejection (insertion loss) exceeding 35 dB was achieved over the band  $9.3 < f < 9.7$  GHz.

Several variations of the structure are conceivable. A double-sided arrangement, that is, two spur-line structures side by side across the microstrip width, has been manufactured for a band centered at 30.5 GHz. The rejection exceeded 29 dB over a 2 GHz band [14]. This general concept, leading to unusual and very compact filters, must be capable of extension into many new designs.

Microstrip lends itself to entirely new structural shapes to perform circuit/system functions which were previously realized using stripline, or coaxial, or waveguide technology.

## 19.9 Summary

Planar transmission lines can be implemented using transmission line structures with the best performance obtained using parallel transmission line sections. Various configurations of parallel transmission lines have almost the desired bandstop, lowpass, highpass, or bandpass characteristics. In design these inherent characteristics are matched to specifications. Design invariably starts with a lumped-element lowpass prototype which is modified and evolved so that a final lumped-element structure maps directly on to a transmission line implementation.

## References

- [1] G. Matthaei, L. Young, and E. Jones, *Microwave Filters, Impedance-Matching Networks and Coupling Structures*. McGraw-Hill, 1965, reprinted in 1980, Artech House.

- [2] I. Hunter, *Theory and Design of Microwave Filters*. IEE Press, 2001.
- [3] M. Steer, *Microwave and RF Design: a Systems Approach*, 2nd ed. SciTech Pub., 2013.
- [4] J.-S. Hong, *Microstrip Filters for RF/Microwave Applications*, 2nd ed. John Wiley & Sons, 2011.
- [5] G. Cunningham, P. Blenkinsop, and J. Palmer, “Microstrip end-coupled filter design at mm-wave frequencies,” in *19th European Microwave Conf.*, Sep. 1989, pp. 1210–1213.
- [6] C. Tzuang and W.-T. Lo, “Printed-circuit realization of a tapped combline bandpass filter,” in *1990 IEEE MTT-S Int. Microwave Symp. Digest*, May 1990, pp. 131–134.
- [7] C.-K. Tzuang, Y.-C. Chiang, and S. Su, “Design of a quasi-planar broadside end-coupled bandpass filter,” in *1990 IEEE MTT-S Int. Microwave Symp. Digest*, 1990, pp. 407–410.
- [8] W. Fathelbab and M. Steer, “Parallel-coupled line filters with enhanced stopband performance,” *IEEE Trans. on Microwave Theory and Techniques*, vol. **53**, no. 12, pp. 3774–3781, Dec. 2005.
- [9] W. Fathelbab and M. Steer, “Broadband network design,” in *Multifunctional Adaptive Microwave Circuits and Systems*, p. 238, 2008.
- [10] I. Bahl, “Capacitively compensated high performance parallel coupled microstrip filters,” in *1989 IEEE MTT-S Int. Microwave Symp. Dig.*, Jun. 1989, pp. 679–682.
- [11] F. Gardiol, *Introduction to Microwave*. Artech House, 1984.
- [12] I. Bahl and P. Bhartia, *Microwave Solid State Circuit Design*. John Wiley & Sons, 1988.
- [13] R. Bates, “Design of microstrip spur-line band-stop filters,” *Microwaves, Optics and Acoustics, IEE Journal on*, vol. **1**, no. 6, pp. 209–214, Nov. 1977.
- [14] R. N. Bates and R. E. Pearson, “Designing bandstop filters for micro-wave frequencies,” *Electronic Engineering*, pp. 39–41, Nov. 1978.
- [15] P. Benedek and P. Sylvester, “Equivalent capacitances for microstrip gaps and steps,” *IEEE Trans. on Microwave Theory and Techniques*, vol. **20**, no. 11, pp. 729–733, Nov. 1972.

# Chapter 20

## Magnetic Materials and Planar Transmission Lines

### 20.1 Introduction

All materials respond to magnetic fields since magnetic fields distort the electron orbitals. As a result the magnetic permeability,  $\mu = \mu_r \mu_0$ , is not equal to the free space permeability  $\mu_0$ . If this is the only effect of a magnetic field then  $\mu$  is less than a fraction of a per cent away from  $\mu_0$ . For a few materials, the magnetic materials, a much larger effect comes from alignment of the magnetic moments of electrons. The magnetic moment, or spin, of an electron has two possible states, an up spin and a down spin, and these are paired in complete orbitals, including orbitals shared with other atoms in covalent bonds. In nonmagnetic materials the magnetic moments of the paired electrons cancel and the only magnetic response arises from the distortion of orbitals. In magnetic materials there are orbitals with an odd number of electrons and so there is an unbalanced elementary magnetic moment. The unbalanced elementary magnetic moments in the material align with or oppose the applied magnetic field. With some magnetic materials the alignment after application of a strong magnetic field can be permanent and then the material is said to be magnetized. The dramatic response of unpaired electrons to an applied magnetic field has no electrical analog and so the description of magnetic materials requires deeper analysis than that required to understand the response of materials to an electric field.

In microwave design we are interested in both magnetized and unmagnetized materials. This chapter begins with a physical investigation of the behavior of magnetic materials before delving into some particular applications of the magnetic effects. [Section 20.2](#) presents the physics of magnetic materials and of magnetized magnetic materials. The end result of the analysis is that in the unmagnetized state the magnetic properties can be described by a relative permeability  $\mu_r$  if no biasing magnetic field is applied. Such materials tend to be lossy and only barely suitable for low-frequency microwave applications, up to about 1 GHz. However, this situation is rapidly evolving and while this book is in print this could change appreciably. When a material is magnetized and RF magnetic fields are in the plane perpendicular to the magnetization the effective relative permeability can be large and can even be negative. Generally this orientation of the RF fields means that the material is magnetized in the direction of propagation of the RF signal. These materials can have low magnetic and electrical losses and be useful up to 60 GHz and beyond. The relative permeability can even be different depending on the direction of magnetic fields. This effect is exploited in realizing nonreciprocal components such as circulators and isolators. If the reader is prepared to accept the relative permeabilities expressed as a scalar in the unmagnetized case and as a 3D tensor in the magnetized case, then the reader can proceed directly to [Section 20.3](#).

## 20.2 Microwave Magnetic Materials

### 20.2.1 Alignment of Elementary Magnetic Moments

Although all materials respond to magnetic fields the effect is usually small, changing  $\mu$  by no more than a factor of  $10^{-5}$ . Such materials are called diamagnetic materials. This change of  $\mu$  is the result of distortion of electron orbitals that induce currents which, usually, oppose the applied magnetic field and so reduce  $\mu$ . Sometimes the magnetic field is supported and then the permeability can increase slightly, for example the relative permeability  $\mu_r = 1.000265$  for platinum,  $\mu_r = 0.99999976$  for copper, and  $\mu_r = 0.999992$  for water.

For some materials, called paramagnetic materials, the effect on the orbitals is dwarfed by alignment of elementary magnetic moments almost entirely due to the spin of unpaired electrons. In diamagnetic materials these elementary magnetic moments cancel out as electrons are paired in orbitals with electrons having opposite spins. With a paramagnetic material there is usually one elementary magnetic moment that is unbalanced in each unit crystalline cell. Some materials with rare-earth elements can have up to seven elementary magnetic moments, that is, unpaired electrons, in each crystalline cell. In a paramagnetic material the unbalanced elementary magnetic moments of each crystalline cell spontaneously arrange themselves in a long-range order possibly extending over a distance of  $2 \mu\text{m}$  or more, forming a magnetic domain. This effect cannot be understood from classical physics, that is, Maxwell's equations, and is a result of quantum-mechanical exchange interactions and the ordering corresponds to the lowest energy state for the material. While the magnetic moments in a domain may be aligned, adjacent domains would typically be arranged randomly unless the material is magnetized or a magnetic field is applied.

The types of long-range ordering of elementary magnetic moments are shown in [Figure 20.1](#). As reference, [Figure 20.1\(a\)](#) shows the random ordering of the moments in a diamagnetic material and thus there is no net magnetic moment. In one type of paramagnetic material, called a ferromagnetic material, see [Figure 20.1\(b\)](#), all of the unbalanced elementary magnetic moments in a domain line up in the same direction. This produces a strong net magnetic moment. In an antiferromagnetic material, see [Figure 20.1\(c\)](#), the unbalanced elementary magnetic moments line up in anti-parallel and there is no net magnetic moment. The third type of paramagnetic material, called a ferrimagnetic material, has the ordering shown in [Figure 20.1\(d\)](#). Here the unbalanced elementary magnetic moments line up in anti-parallel but the elementary magnetic moments do not cancel themselves and there is a net magnetic moment. The ferromagnetic and ferrimagnetic materials are of great interest to microwave engineers and enable components to be fabricated with amazing properties, for example a device called an isolator is fabricated by having the EM waves on a transmission line interact with a disc or substrate of ferromagnetic or ferrimagnetic material. An RF signal can then travel in one direction but propagation of the signal is blocked in the other direction.

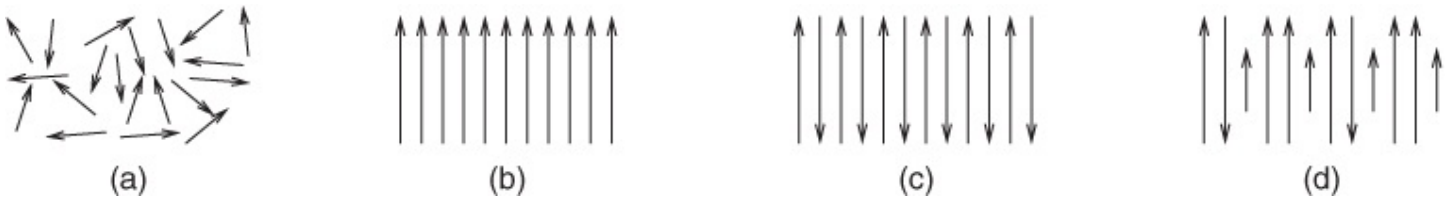


**Figure 20.1** Magnetic ordering of elementary magnetic moments in materials: (a) diamagnetic; (b) ferromagnetic; (c) antiferromagnetic; and (d) ferrimagnetic.

The definition of ferromagnetic materials as those in which all of the elementary moments in a domain align in the same direction is the narrow and preferred definition. However, it is common to refer to both ferromagnetic and ferrimagnetic materials collectively as ferromagnetic materials, and sometimes even as ferrimagnetic materials. We will use the narrower definition here although for a microwave designer it really doesn't make much difference. To a material scientist it is an important distinction.

Most ferromagnetic materials are conductive whereas most ferrimagnetic materials have high resistivity and the latter are useful as microwave substrates. As a result it has become common to refer to the few high-resistivity ferromagnetic materials, that is, non-metallic ferromagnets, as ferrimagnetic materials. The reader will read many publications where the ferrimagnetic and ferromagnetic terms are used interchangeably.

## 20.2.2 The Physics of Magnetic Materials

In this section we will describe the essential physics of magnetic materials as required to use them in microwave design. For ferromagnetic materials it is possible to undertake a fairly sophisticated derivation of bulk properties from the properties of unbalanced elementary charges. The behavior of ferrimagnetic materials is inferred from this study.

At this stage it is necessary to introduce a complexity that cannot be avoided. Material scientists and physicists who study magnetic materials prefer to work in the CGS system of units. In the CGS system the fundamental units are centimeter (C), gram (G), and second (S). So it is a metric system of units but not the SI unit system that electrical engineers have settled on. There are several versions of these units and the particular system used in magnetic analysis is the CGS (Gaussian) system but we will refer to it as CGS. The CGS system redefines Maxwell's equations and put them in a form that is closely related to the fundamental behavior of magnetic materials. Vendors of magnetic materials document the properties of these materials in CGS units and the microwave engineer must put them in SI units so the values can actually be used in design. The problem is that there is not always a simple one-to-one conversion from the quantities in the CGS system to quantities in the SI system.

In the CGS system the magnetic flux density,  $B$  (which is referred to as magnetic induction in the CGS world), is related to the magnetic field,  $H$ , by

$$B_{\text{CGS}} = H_{\text{CGS}} + 4\pi M_{\text{CGS}}$$

**20.1**

where  $M_{\text{CGS}}$  is called the magnetization. Note that we have introduced the CGS subscript to be

clear that we are dealing with the CGS version of these quantities. The magnetization of a material directly relates to the alignment of unbalanced elementary magnetic moments described in the previous section. The magnetization can be independent of an applied  $H$  field. After all, the spontaneous alignment of elementary moments does not require an external  $H$  field.

In the SI system the comparable relationship of the  $B$  and  $H$  fields is

$$B = \mu_0(H + M) = \mu H = \mu_0\mu_r H \quad 20.2$$

where subscripts are not used to identify these quantities as being in the SI system since this is the way these terms are used throughout this book.

The subtle difference between the CGS and SI representations, that is, Equations (20.1) and (20.2), respectively, is illustrated by studying the magnetization curve, shown in [Figure 20.2\(a\)](#), of a ferromagnetic or ferrimagnetic material. [Figure 20.2\(a\)](#) shows the magnetization plotted against the externally applied magnetic field  $H$ . In the unmagnetized state, which is when the magnetic moments of the domains are arranged randomly, there is zero net magnetization when there is no magnetic field, that is,  $M = 0$  when  $H = 0$ . However, this is only when the material is unmagnetized and so the history of applied magnetic fields is important. When  $H$  starts to increase curve 1 is followed in [Figure 20.2\(a\)](#). Initially at low fields the curve is a straight line as the magnetic moments of each domain begin to align in the direction of the  $H$  field. The material becomes magnetically polarized and this is described by its magnetization,  $M$ .<sup>1</sup> As the  $H$  field becomes stronger eventually all of magnetic moments of the domains become aligned and the magnetization is saturated in region 2. Then  $M = M_s$ , the saturation magnetization.

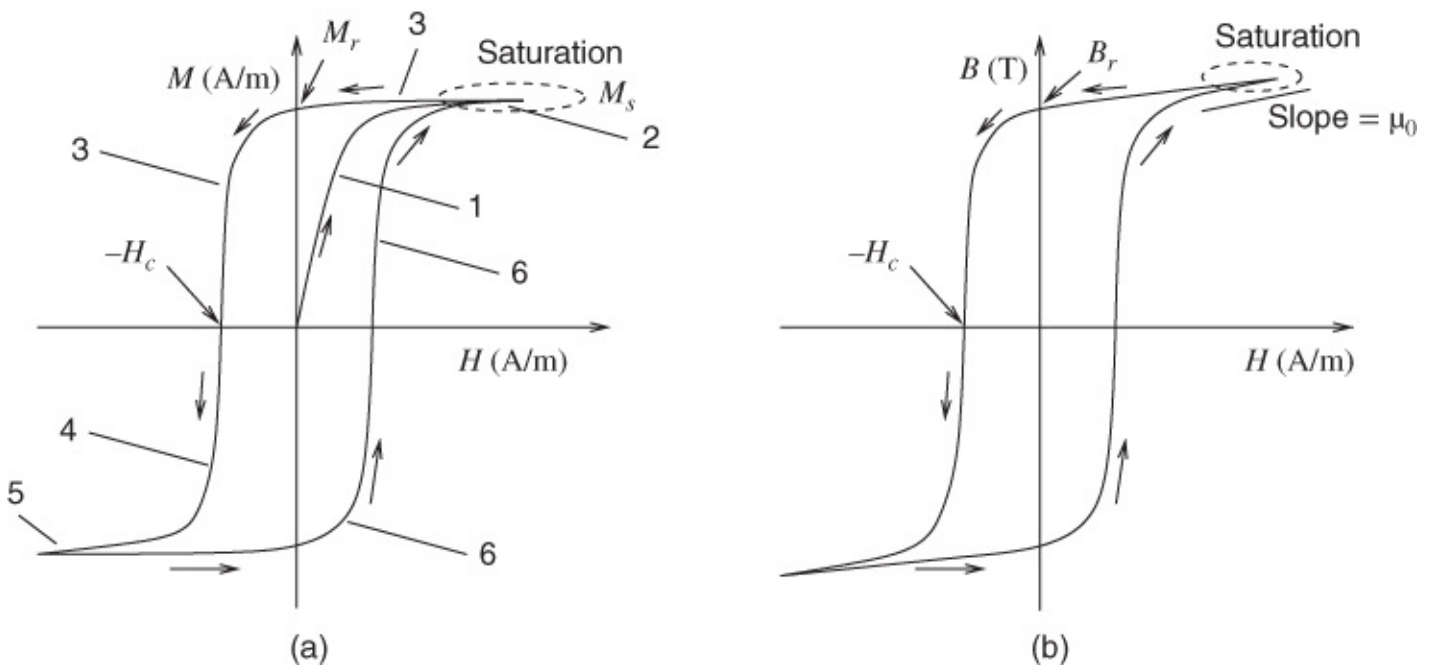


**Figure 20.2** BH curves of a ferromagnet or ferrimagnet: (a) magnetization,  $M$ ; and (b) magnetic induction (CGS) or flux density (SI),  $B$ .  $H_c$  is the coercive field and  $B_r$  is the remanence or remanent magnetic flux density corresponding to the remanent magnetization  $M_r$ , after a large external magnetic field has been removed. Magnetic hysteresis is shown in these curves as the trajectory depends on the history of applied magnetic fields.

When the  $H$  field decreases from its high value the  $M-H$  trajectory is not the same as the curve followed for increasing  $H$ . Instead the trajectory follows curve 3 and it is seen that even when the external magnetic field is zero there is a remnant magnetization  $M_r$ . This is very close to the saturation magnetization  $M_s$ . Thus the material remembers its magnetic state, and it takes work to change the alignment of the magnetic moments of the domains. Thus magnetization exists independently of the applied magnetic field. The  $B$  field when the external  $H$  field is zero is called the remanence or remanent magnetization,  $B_r$ , see [Figure 20.2\(b\)](#).

Referring to [Figure 20.2\(a\)](#), as the  $H$  field is further reduced becoming negative, the trajectory continues to follow trajectory 3 until the point labeled  $-H_c$  is reached. When  $H = -H_c$  the magnetization of the material has been canceled, that is,  $M = 0$ .  $H_c$  is called the coercivity of the material and a good permanent magnet has a high coercivity. The material is then called a *hard* magnetic material. If a magnetic material is used in a transformer or inductor then the coercivity should be low, and the material is then called a soft magnetic material.

As  $H$  becomes increasingly negative trajectory 4 is followed and the material becomes magnetically saturated in the reverse direction. With increasing  $H$  trajectory 6 is followed. The trajectory followed is always in the counter-clockwise direction.

The properties of the magnetic material are more commonly plotted as a  $B-H$  curve, as shown in [Figure 20.2\(b\)](#). The curve in [Figure 20.2\(b\)](#) is just the curve in [Figure 20.2\(a\)](#) with the addition of the effect of magnetic energy storage in a vacuum, at least this is the description that naturally applies with the CGS system, that is, Equation [\(20.1\)](#). With SI units some renormalization is required but the effect is the same. [Figure 20.2\(b\)](#) uses SI units and the slope

of the  $B - H$  curve when the material is magnetically saturated is the free-space permeability  $\mu_0$ .

Referring back to the SI form of the  $B - H$  relationship of Equation (20.2) it is seen that there is an inherent treatment of magnetization as being dependent on the applied  $H$  field. However, in the CGS form of the  $B - H$  relationship, Equation (20.1), magnetization is used independently of the  $H$  field. This is a subtle difference but it is part of the reason why materials scientist and physicists are loath to abandon CGS units. There are other reasons as well, with the central argument being that CGS units relate more closely to the physics. The reader is referred to [Table A.6](#) in Appendix A for conversion of electromagnetic quantities from CGS to SI units.

The saturation magnetization is an intrinsic property of a material and the properties of the most useful ferrimagnetic materials are given in [Table 20.1](#). Sometimes the saturation magnetization is expressed in SI units of tesla and really this is the value of  $B$  in saturation, and then  $M_s$  (in tesla) =  $\mu_0 M_s$  (in A/m). A more complete set of magnetic properties is given in [Table B.6](#). The electrical properties of the selected materials are given in [Table 20.2](#). These materials are available in various shapes and the most important of these for microwave engineers are spheres, rods, and substrates. Since this book deals with microstrip design we are principally concerned with substrates. Some microwave substrates are grown in a strong magnetic field and if they are thin and grown on other materials, a built-in stress can be established, creating an internal magnetic field. In such situations the material is magnetized and, referring to [Figure 20.2\(a\)](#), comes pre-biased in region 2. These materials have very special microwave properties that will be discussed in the next subsection.

**Table 20.1** Magnetic properties of ferrites and garnets, both ferrimagnetic materials, used in microwave applications. The saturation magnetization is  $4\pi M_{s,\text{CGS}}$  in the CGS unit system (corresponding to Equation (20.1)) and  $M_s$  in the SI unit system. Saturation magnetization at room temperature is given in CGS (Gaussian) units, as provided by manufacturers, and SI units, as used in microwave design. The ranges given are for different material preparations (except for frequency ranges). For a particular preparation the values are fixed

Material	$4\pi M_{s,\text{CGS}}$ (CGS, gauss)	$M_s$ (SI, kA/m)	Curie temp- erature $T_C$ ( $^{\circ}\text{C}$ )	Frequency range
Calcium vanadium garnet $\text{Ca}_x\text{V}_{1-x}\text{Fe}_5\text{O}_{12}$	800–1950	64–155 (0.08–0.32 T)	177–209	1.5–12 GHz
Lithium ferrite $\text{LiFe}_5\text{O}_8$	2300–4800	183–382 (0.23–0.48 T)	450–505	6–41 GHz
Manganese ferrite $\text{Mn}_a\text{Zn}_{1-a}\text{Fe}_2\text{O}_4$	1600–2400	127–191 (0.16–0.24 T)	230–300	1.5–38 GHz
Magnesium ferrite $\text{MgFe}_2\text{O}_4$	1600–2400	127–191 (0.16–0.24 T)	275–380	1.5–38 GHz
Nickel ferrite $\text{NiFe}_2\text{O}_4$	1900–5000	151–398 (0.19–0.50 T)	375–480	1.5–41 GHz
Yttrium garnet (YIG), $\text{Y}_3\text{Fe}_5\text{O}_{12}$	1780–1820	142–145 (0.18 T)	280	1–50 GHz
Yttrium-aluminum garnet (YAG), $\text{Y}_3\text{Al}_5\text{O}_{12}$	240–1200	19–95 (0.02–0.12 T)	100–260	0.3–7 GHz
Yttrium-gadolinium garnet $\text{Y}_3\text{Ga}_x\text{Fe}_{3-x}\text{O}_{12}$	750–1600	60–127 (0.08–0.16 T)	280	1.5–12 GHz

**Table 20.2** Electrical properties of important ferrimagnetic materials used in microwave applications. The frequency given is the typical range of application. Properties are measured at 9.4 GHz or 10 GHz except for resistivity, which is at DC. The dielectric loss tangent is  $\tan \delta$ . The ranges given are for different material preparations

Ferrite	Frequency (GHz)	Permittivity, $\epsilon_r$	$\tan \delta$	Resistivity ( $\Omega \cdot m$ )
Calcium vanadium garnet	1.5–12	14.0–15.4	0.0002	$10^6$ – $10^7$
Lithium ferrite	6–41	11.4–13.7	0.0005	$(2\text{--}8) \times 10^{-4}$
Manganese zinc ferrite	1.5–38	12.4–13.0	0.00025	0.1–1
Magnesium ferrite	1.5–38	12.4–13.0	0.0003	$(0.7\text{--}10) \times 10^5$
Nickel ferrite	1.5–41	11.4–13.7	0.0006–0.0015	$1.6 \times 10^6$
Yttrium garnet	1–50	15.3	0.0002	$10^{12}$
Yttrium-aluminum garnet	0.3–7	11.7–15.2	0.0002	$10^6$ – $10^7$
Yttrium-gadolinium garnet	1.5–12	15.3	0.0002	$10^6$ – $10^7$

The long-range ordering of ferrimagnetic and ferromagnetic materials occurs below a particular temperature known as the Curie temperature,  $T_c$ , for ferromagnets and ferrimagnets, and the Néel temperature,  $T_n$ , for antiferromagnets. Above these temperatures the magnetic ordering cannot be established. Above the Curie temperature the magnetic moments in these materials are always aligned randomly and they are then no longer ferromagnetic or ferrimagnetic.

A second very important class of magnetic materials potentially of use in microwave engineering are unmagnetized ferromagnetic and ferrimagnetic materials. For these materials care is taken in growth to obtain low coercivity and the materials are used with low  $H$  fields. Under these situations the  $B$ – $H$  curve is as shown in the central region of [Figure 20.3](#). Here the  $B$ – $H$  trajectory follows ellipses, with the optimum situation being when an ellipse collapses to a line. The ellipse is the result of magnetic hysteresis. The slope of this line, the axis of the ellipse, is the permeability  $\mu$  and this can be large relative to  $\mu_0$ . For example, nickel, a ferromagnetic material, has a relative permeability between 100 and 600. Rare earth magnets such as mu-metal have a relative permeability as high as 20,000 although they are generally used in a magnetized state as permanent magnets. A linear relationship between  $B$  and  $H$  is more closely achieved when the coercivity is low. The opening of the trajectory, that is, when it is an ellipse, results in energy loss in the material. Loss principally occurs because of friction-like effects when the magnetic moments of the domains rotate. Thus loss increases linearly with frequency. Currently relative permeabilities of 15 with moderate magnetic losses and high resistivities are achieved up to 1 GHz for unmagnetized materials [1, 2].

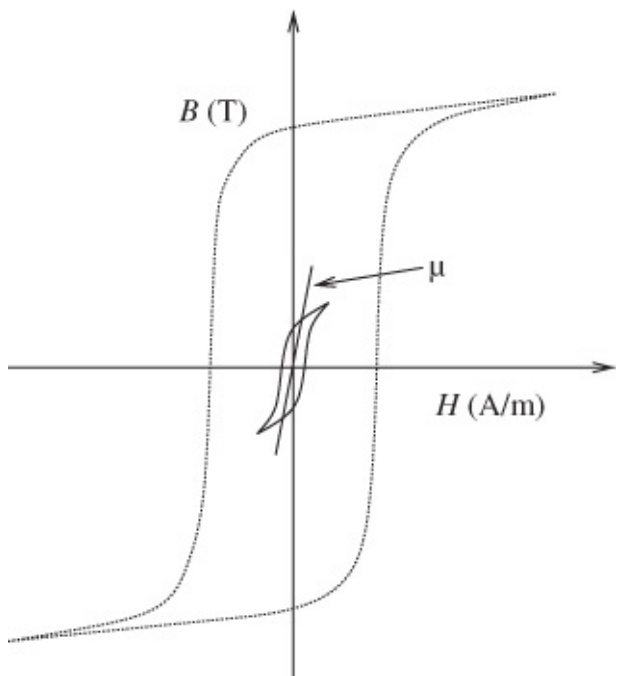


**Figure 20.3**  $B - H$  curves of an unmagnetized ferromagnet or ferrimagnet showing hysteresis even at small levels of magnetic field.

Above 1 GHz the losses of unmagnetized magnetic materials are too high for microwave applications. This is likely to change while this book is in print. Relative permeabilities of 600 and higher are achievable at low megahertz frequencies [3]. Currently good permeabilities are being obtained with magnetized materials provided that the RF magnetic field is perpendicular to the direction of magnetization. (To understand this will require reading of the next section.) However, there are limited applications where this can be used. Thus tremendous effort is being directed at developing ferrimagnetic materials with low coercivity and thus magnetized materials with low loss at microwave frequencies above a few gigahertz.

### 20.2.3 The Physics of Magnetized Ferromagnetic Materials

Magnetized ferromagnetic and ferrimagnetic materials are the most important types of magnetic materials in microwave engineering. They have a special property in that the magnetic flux density, the  $B$  field, is not always pointed in the same direction as the  $H$  field.

Furthermore, magnetically biased ferrites and garnets, both of which are ferrimagnetic materials, have relatively low magnetic loss, and can have high resistivity. Several suitable substrates and thin films of ferrites and garnets are available to be used with planar transmission lines.

The physics of magnetized ferromagnetic materials is reasonably well understood, with extensive treatments available [4–8]. The DC component of the magnetic moments of the domains can be aligned, sometimes permanently, by a large magnetic bias field. The material is then said to be magnetized. Strain or crystal magnetic anisotropy can be built into the lattice during growth of the magnetic material and it is said that this is an internal magnetic field (an anisotropy field). So a magnetic field can have a DC magnetization field  $\bar{M}_0$ , and the

combination of a DC externally applied magnetic field and an internal magnetic field is denoted  $\bar{H}_0$ . We keep this distinction because the magnetic material responds differently to  $M_0$  and  $H_0$ .

In [Figure 20.4\(a\)](#)  $\bar{m}$  is the unbalanced elementary magnetic moment and in the absence of a biasing magnetic field  $\bar{m}$  is aligned with the material's DC magnetization  $\bar{M}_0$ . Even if the material is nearly saturated, all of the elementary magnetic moments will be nearly fully aligned with  $\bar{M}_0$ . Referring back to the  $M-H$  and  $B-H$  curves in [Figure 20.2](#) it can be noted that the remnant magnetization when  $H$  is zero is not exactly equal to the saturation magnetization. When a relatively low-level RF magnetic field is applied, the magnetic moments will no longer be aligned solely with the combination of the DC magnetization, applied DC magnetic bias field, and the static magnetic anisotropy field. This situation is shown in [Figure 20.4](#). Thus if a small alternating magnetic field is applied, the magnetic moments will respond depending on the direction of the RF magnetic field. Without an RF field, see [Figure 20.4\(a\)](#), the magnetic moments align with the DC magnetization. However, a very interesting effect occurs when an RF magnetic field is applied perpendicularly to the (nearly saturated) magnetization, see [Figure 20.4\(b\)](#). The response of the magnetic moment is then not a linear combination of the responses of the applied RF field and the DC component of the magnetization,  $M_0$  here. The vector of an unbalanced elementary magnetic moment,  $\bar{m}$ , rotates in the  $xy$  plane around the DC magnetization vector  $\bar{M}_0$ . This rotation, which follows the right-hand rule, is called precession. The preferred direction of rotation results in the rotating moment strongly interacting with an RF signal having a circular polarization in the same direction as the precession. However, the interaction will be weak if the circular polarization is opposite to that of the precession. Exploiting this effect, for example, means that a device called an isolator can be constructed whereby an RF signal can travel in one direction along a transmission line but propagation of the signal is blocked in the other direction.

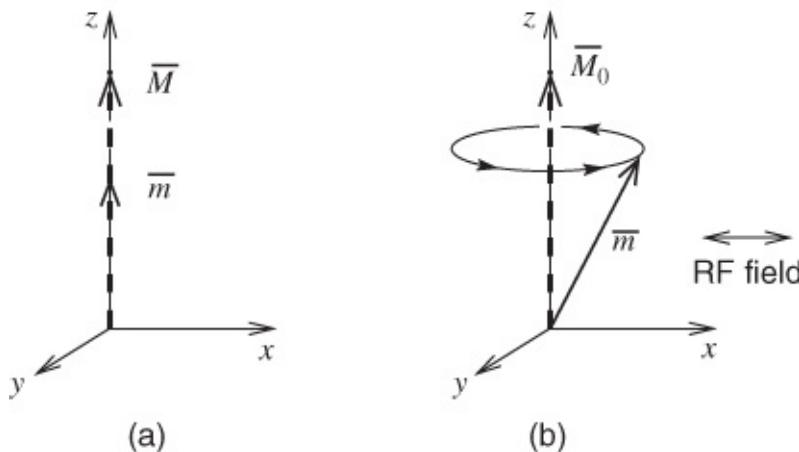


**Figure 20.4** Interaction of a magnetic moment,  $\bar{m}$  with the DC magnetization  $M_0$ : (a) without an RF field; and (b) with an RF field. In (a)  $\bar{m}$  aligns with the net DC magnetization  $\bar{M}_0$ . In (b) it has a component perpendicular to  $\bar{M}_0$ .

Returning now to the precession of  $\bar{m}$  around  $\bar{M}_0$ , the precession frequency is  $\omega_0 = \mu_0 \gamma_g (H_0 + M_0)$ . Here  $\gamma_g$  is the gyromagnetic ratio with SI units of radians per second per

tesla ( $\text{rad} \cdot \text{s}^{-1} \cdot \text{T}^{-1}$ ). (The subscript  $g$  is not used in the magnetics literature, but is used here to distinguish the gyromagnetic ratio from the propagation coefficient used elsewhere in this book.) In classical analysis  $\gamma_g$  would be equal to the ratio of a charge and two times the mass of a particle, in this case the electron, provided that the mass and charge are distributed uniformly throughout the volume of a sphere. If they were distributed uniformly then the classical gyromagnetic ratio  $\gamma_{g,\text{CLASSICAL}} = q/(2m)$ . However, the measured value of  $\gamma_g$  for particles is never equal to its classical value and a correction is required. Of course an electron does not actually spin mechanically, spin is a quantum mechanical property. (Consider that a neutron has spin, that is, a magnetic moment, but has no charge.) The gyromagnetic ratio of an electron is  $\gamma_e = g_e \gamma_{g,\text{CLASSICAL}}$  where  $g$  is called the  $g$  factor. For an isolated electron the  $g$  factor is  $g_e = 2.0032$  and this is both calculated using quantum mechanics and measured. Then  $\gamma_e = 1.760860 \times 10^{11} \text{ rad} \cdot \text{s}^{-1} \cdot \text{T}^{-1} = 28.024 \text{ GHz/T}$ . In a crystal, the magnetics situation, an electron has both spin and orbital angular momentum and the  $g$  factor is now known as the Landé  $g$  factor and is a little bit higher or lower than that of an isolated electron depending on the material as the crystal itself affects the orbitals. The Landé  $g$  factors for the ferrites and garnets commonly used at microwave frequencies range from 2.00 to 2.30, see [Table B.6](#). The Landé  $g$  factor is one of the parameters that must be specified when using an electromagnetic field simulator if a magnetic material is used.

## 20.2.4 Phasor Relationships of the $B$ and $H$ Fields

Polder [9] was the first to develop the type of analysis presented here which applies to a magnetized magnetic material and relates the RF phasors of the  $B$  and  $H$  fields, expressing the relationship as a permeability tensor, a  $3 \times 3$  matrix. Here we summarize his development with more recent results from Gurevich and Melkov [4]. The results developed here are in the form of the magnetic field analysis that can be used in design and from which a single scalar effective permeability can be derived.

With  $N$  unbalanced elementary magnetic moments (usually one per crystalline cell), each having a magnetic moment  $\bar{m}$ , the total vector time-domain magnetization is

$$\bar{M} = N\bar{m}. \quad 20.3$$

As the DC field,  $H_0$ , increases more of the moments, and thus  $\bar{M}_0$ , align with  $\bar{H}_0$  and the magnetization increases reaching a saturated value  $M_s$ , a property of the material. When saturated, the loss of a magnetic material can be very low provided that the electrical resistivity is high. Thus useful magnetic materials at microwave frequencies are nearly always operated in saturation.

The preferred direction of rotation of the magnetic moments around the applied or inherent magnetic bias field and the equations of motion result in a special relationship among the RF magnetic flux density vector, the RF component of the magnetization vector, and the RF component of the magnetic field vector. This is a dynamic relationship related to the precession frequency, microwave frequency, saturation magnetization, DC magnetic field, macroscopic relaxation time, and resonance line width. Thus the relationship is complex in the

time domain but simplifies if RF phasors are introduced [4–8]. Then

$$\bar{B} = \mu_0(\bar{M} + \bar{H}) = \check{\mu}\bar{H}$$

[20.4](#)

where  $\bar{B}$ ,  $\bar{H}$ , and  $\bar{M}$  are the phasors at radian frequency  $\omega$  of the RF components of the time-domain  $\bar{B}$ ,  $\bar{H}$ , and  $\bar{M}$ , respectively.

For a lossless magnetically saturated ferromagnet, magnetized in the  $z$  direction, and with an RF field also propagating in this direction so that the RF magnetic field is in the  $xy$  plane, the Polder tensor (the name of the tensor used to describe the magnetic permeability of ferrites) is a  $3 \times 3$  matrix:

$$\check{\mu} = \mu_0 \begin{bmatrix} \mu_r & J\mu_a & 0 \\ -J\mu_a & \mu_r & 0 \\ 0 & 0 & 1 \end{bmatrix} \quad \text{20.5}$$

where

$$\mu_a = \frac{\omega_M \omega}{\omega_H^2 - \omega^2}, \quad \mu_r = 1 + \frac{\omega_M \omega_H}{\omega_H^2 - \omega^2} = \frac{\omega_H(\omega_H + \omega_M) - \omega^2}{\omega_H^2 - \omega^2}, \quad \text{20.6}$$

$$\omega_M = \mu_0 \gamma_g M_s, \quad \text{and} \quad \omega_H = \mu_0 \gamma_g H_0.$$

In Equation (20.6)  $\gamma_g$ ,  $M_s$ , and  $H_0$  are, respectively, the gyromagnetic ratio, the average magnetization of the ferrite, and the bias magnetic field. The DC magnetization is the saturated magnetization so  $M_0 = M_s$  here. The radian frequencies  $\omega_M$  and  $\omega_H$  come from solution of the equation of motion of magnetization [4].

The frequency  $f_H = \omega_H/(2\pi)$  is called the ferromagnetic resonance frequency and is the frequency at which there is resonant absorption of EM energy in a ferromagnet. The tensor element  $\mu_r$  is negative at frequencies above  $f_H$  and up to the anti ferromagnetic resonance frequency  $f_{AFMR}$ :

$$f_{AFMR} = \sqrt{f_H(f_H + f_M)} = \frac{\mu_0 \gamma_g}{2\pi} \sqrt{H_0(M_s + H_0)}. \quad \text{20.7}$$

The anti ferromagnetic resonance frequency,  $f_{AFMR}$ , is the frequency at which  $\mu_r = 0$ . Between the ferromagnetic resonance frequency  $f_H$  and  $f_{AFMR}$   $\mu_r$  is negative, see [Figure 20.5](#). The anti ferromagnetic resonance frequency can be changed by adjusting the applied magnetic field but it does have a minimum value, as listed in [Table 20.3](#) for several conducting magnetic materials.

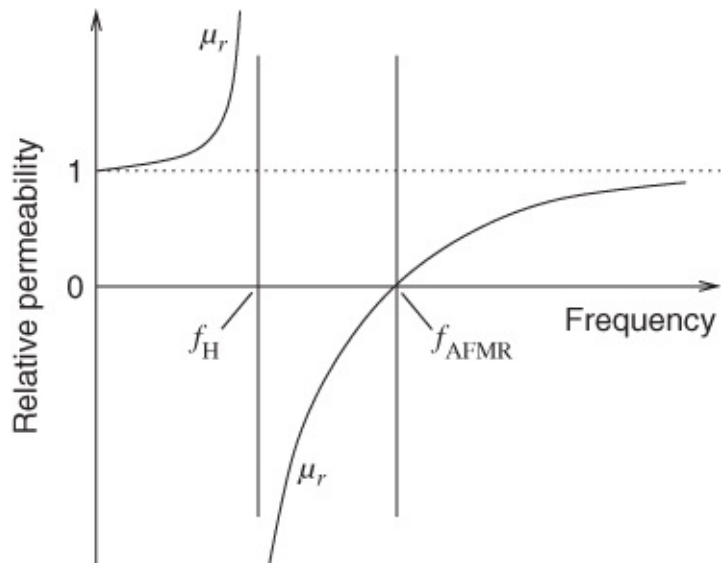


**Figure 20.5** Frequency variation of the relative permeability  $\mu_r$  of a saturated magnetized magnetic material. Note that  $\mu_r$  is an element of the Polder tensor.

**Table 20.3** Critical frequencies of magnetic materials at room temperature and in saturation.  $\text{AFMR}_{\text{MIN}}$  is the minimum antiferromagnetic resonance frequency determined by the saturation magnetization, that is,  $\text{AFMR}_{\text{MIN}} = \min(f_{\text{AFMR}})$

Material	Saturation	$\text{AFMR}_{\text{MIN}}$
	magnetization (kA/m)	(GHz)
Permalloy Ni <sub>80</sub> Fe <sub>20</sub>	875 (= 1.1 T)	20
Deltamax Ni <sub>50</sub> Fe <sub>50</sub>	1270 (= 1.6 T)	45
Permendur Co <sub>50</sub> Fe <sub>50</sub>	1910 (= 2.4 T)	67
FeCoB	1500 (= 1.9 T)	2.2
3% SiFe	1600 (= 2.0 T)	56

## 20.2.5 Other Directions of Magnetization

If  $H_0$  and  $M_0$  are both in the  $x$  direction then the tensor becomes

$$\check{\mu} = \mu_0 \begin{bmatrix} 1 & 0 & 0 \\ 0 & \mu_r & -J\mu_a \\ 0 & J\mu_a & \mu_r \end{bmatrix} \quad 20.8$$

when the RF magnetic field is in the  $yz$  plane.

If the  $H_0$  and  $M_0$  are in the  $y$  direction then the tensor becomes

$$\check{\mu} = \mu_0 \begin{bmatrix} \mu_r 0 & 1 & -J\mu_a \\ 0 & 1 & 0 \\ 0 & J\mu_a & \mu_r \end{bmatrix} \quad 20.9$$

when the RF magnetic field are in the  $xz$  plane.

## 20.2.6 Summary

Equation (20.5) was developed for a ferromagnet where all of the unbalanced elementary moments tend to align. However, it is also used with ferrimagnetic materials although there the moments in part align in opposite directions. The ferrimagnetic situation is much more complicated to analyze than the ferromagnetic case but still the tensor description is found to work well although the elements of the tensor cannot be calculated from material properties alone as they can for a ferromagnetic material.

Loss in a magnetic material can be considered as dissipation due to a friction-like effect when the moments move, thus loss is proportional to RF frequency. Loss can be incorporated by replacing  $\omega_H$  in Equation (20.6) by  $\omega_H + j\alpha\omega$ , where  $\alpha = \lambda/M_0$  and  $\lambda$  is a dissipation factor.

# 20.3 Effective Permeability of Magnetic Materials

The physical description of magnetic behavior was considered in [Section 20.2](#) and here we provide summary results. Both unmagnetized and magnetized magnetic substrates are of interest for microstrip circuits.

## 20.3.1 Effective Permeability of Unmagnetized Materials

Currently relative permeabilities of 15 with moderate magnetic losses are achieved up to 1 GHz [1, 2] for unmagnetized magnetic materials. Above that losses are too high for microwave applications. This is likely to change while this book is in print. At lower frequencies high relative permeabilities of 600 and higher are achievable at low megahertz frequencies [3].

## 20.3.2 Effective Permeability of Magnetized Materials

Good permeabilities are obtained with magnetized materials provided that the RF magnetic field is perpendicular to the direction of magnetization. Magnetized magnetic materials can have high or low resistivity and of course the materials with high resistivity are the most important materials for use as microwave substrates. Furthermore, magnetically biased ferrites and garnets, both of which are ferrimagnetic materials, have relatively low loss, and substrates and thin films of certain ferrites and garnets are used as substrates for planar transmission lines. Some ferromagnetic materials (but not many) have high resistivity and these are also useful as substrates. It has become common to refer to nonmetallic ferromagnetic materials as ferrimagnets although this is not fully accurate.

We will now derive the effective permeability of a magnetized ferromagnetic or ferrimagnetic material. The effective permeability depends on the direction of magnetization and the direction of the RF magnetic fields. The relationship between  $B$  and  $H$  of a material magnetized in the  $z$  direction is described by Equations (20.4) and (20.5), which become

**20.10**

$$\begin{bmatrix} B_x \\ B_y \\ B_z \end{bmatrix} = \mu_0 \begin{bmatrix} \mu_r & J\mu_a & 0 \\ -J\mu_a & \mu_r & 0 \\ 0 & 0 & 1 \end{bmatrix} \begin{bmatrix} H_x \\ H_y \\ H_z \end{bmatrix}$$

using the components of  $\bar{B} = B_x \hat{x} + B_y \hat{y} + B_z \hat{z}$  and  $\bar{H} = H_x \hat{x} + H_y \hat{y} + H_z \hat{z}$ . If the RF fields are confined to the plane transverse to the  $z$ -directed magnetization then this becomes

$$B_x = \mu_0 \mu_r H_x + J\mu_0 \mu_a H_y \quad \text{20.11}$$

$$B_y = -J\mu_0 \mu_a H_x + \mu_0 \mu_r H_y \quad \text{20.12}$$

Since the orientation of the  $x$  and  $y$  axes is arbitrary in a bulk material or thick substrate (say more than 100 nm), the  $y$  direction can be chosen so that  $B_y = 0$  and then

$$B_x = \mu_0 \mu_r H_x + J\mu_0 \mu_a H_y \quad \text{20.13}$$

$$H_y = \frac{J\mu_a}{\mu_r} H_x. \quad \text{20.14}$$

Substituting Equation (20.14) in Equation (20.11) we obtain

$$B_x = \mu_0 \mu_r H_x + J\mu_0 \mu_a \frac{J\mu_a}{\mu_r} H_x = \mu_0 \left( \mu_r - \frac{\mu_a^2}{\mu_r} \right) H_x \quad \text{20.15}$$

Replacing the  $x$  subscript by  $\perp$  to indicate the plane perpendicular to the direction of propagation and magnetization, this becomes

$$B_\perp = \frac{\mu_0}{\mu_r} (\mu_r^2 - \mu_a^2) H_\perp = \mu_0 \mu_\perp H_\perp. \quad \text{20.16}$$

Thus the effective relative permeability of the material at frequency  $f$  in the plane perpendicular to the magnetization, and if the RF magnetic fields are in this plane as well, is

$$\mu_\perp = \frac{\mu_r^2 - \mu_a^2}{\mu_r}. \quad \text{20.17}$$

The frequency variation of  $\mu_\perp$  is shown in [Figure 20.6](#), where a frequency range over which  $\mu_\perp$  is negative is observed.

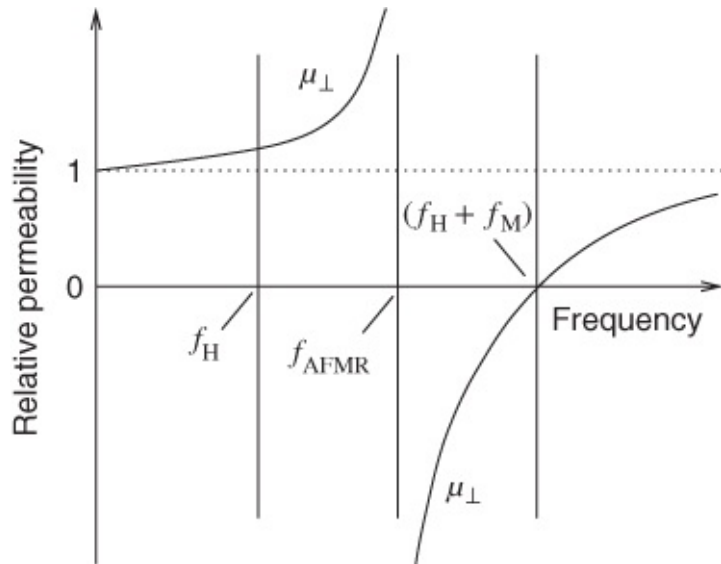


**Figure 20.6** Frequency variation of the relative permeability in the plane perpendicular to the direction of magnetization for propagation in the direction of magnetization.

### 20.3.3 Summary

The effective relative permeability,  $\mu_{r,\text{eff}}$ , to be used for a ferromagnetic or ferrimagnetic film or substrate depends on the direction of magnetization relative to the plane of the film/substrate and how the RF magnetic fields are constrained. Four situations are considered in [Figure 20.7](#). In [Figure 20.7\(a\)](#) the magnetization and the DC magnetic field are normal to the substrate and the directions of the RF magnetic fields are in the plane of the substrate. Then  $\mu_{r,\text{eff}} = \mu_{\perp}$  where  $\mu_{\perp}$  is given in Equation (20.17). Another situation is shown in [Figure 20.7\(b\)](#), where the magnetization and applied magnetic field is in the plane of the substrate and the direction of the RF magnetic field is constrained to be in the plane normal to this direction. Again  $\mu_{r,\text{eff}} = \mu_{\perp}$ . For thin films, less than a few hundred nm thick, the situation can be different. As before for magnetization normal to a thin film, as in [Figure 20.7\(c\)](#),  $\mu_{r,\text{eff}} = \mu_{\perp}$ , but when the magnetization and applied magnetic field is in the plane of the thin film and the RF magnetic fields is in the  $x$  direction  $\mu_{r,\text{eff}} = \mu_r$ . The result for the situation shown in [Figure 20.7\(d\)](#) is an approximation and a detailed case-by-case analysis is required [4] although a supporting fundamental analysis is not available at the time of writing of this book. The situation represented in [Figure 20.7\(d\)](#) is consistent with observations [10, 11] and results from demagnetization at the surfaces of the thin magnetic film where the normal component of the  $B$  field must be continuous and so, here,  $H_y$  is forced to be small. Thus in the film  $B_x \approx \mu_0 \mu_r H_x$  up to a few hundred nanometers into the film.

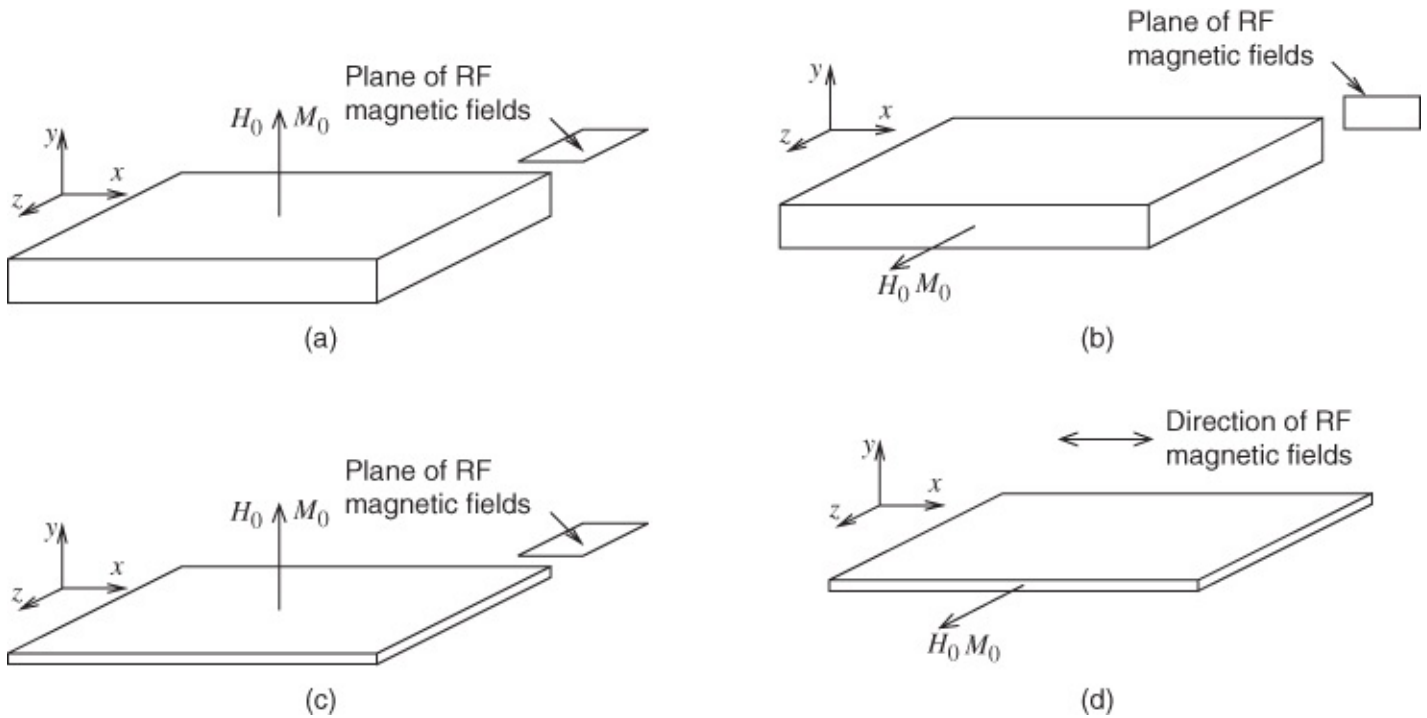


**Figure 20.7** Effective relative permeability  $\mu_{r,\text{eff}}$  to be used for magnetized substrates and thin films: (a) magnetized normal to substrate,  $\mu_{r,\text{eff}} = \mu_\perp$ ; (b) magnetized in plane of substrate,  $\mu_{r,\text{eff}} = \mu_\perp$ ; (c) magnetized normal to thin film,  $\mu_{r,\text{eff}} = \mu_\perp$ ; and (d) magnetized in plane of thin film,  $\mu_{r,\text{eff}} = \mu_r$ .

## 20.4 Microstrip on a Ferrite Substrate

### 20.4.1 Effective Substrate Permeability

Microwave magnetic substrates invariably have a strong internal or external magnetic field and the material is saturated. Then in the direction of magnetization the ferrite behaves as a dielectric medium with a moderately low loss ( $\tan \delta \approx 0.001$  typically) and a relative permittivity

$$11 \leq \epsilon_r \leq 15.$$

The effective relative permeability of the medium  $\mu_{r,\text{eff}}$  is an important quantity which is analogous to a bulk substrate relative permeability, and is thus very useful in design. The quantity to use for  $\mu_{r,\text{eff}}$  is given in [Figure 20.7](#). For a microstrip line on a magnetic substrate magnetized in the direction of propagation the effective permeability of the substrate is

$$\mu_{r,\text{eff}} = \mu_\perp = (\mu_r^2 - \mu_a^2)/\mu_r. \quad 20.18$$

At a sufficiently high frequency  $f \gg (f_h + f_m)$ ,  $\mu_{r,\text{eff}}$  is a little less than unity:

$$0.7 \leq \mu_{r,\text{eff}} \leq 1.0 \quad (\text{as } \omega \rightarrow \infty).$$

In the case of microstrip an empirical correction has been given for  $\mu_{r,\text{eff}}$  [12]. The correction,

which is accurate to about 5%, yields a better value:

$$\mu_{r,\text{eff}} = \mu_{\perp} \left[ 1 - \frac{1}{7} \sqrt{\frac{h}{w}} \left( \frac{\mu_a}{\mu_r} \right)^2 \ln \left( 1 + \frac{1}{\mu_{\perp}} \right) \right]^{-1} \quad 20.19$$

where  $w$  is the width of the strip and  $h$  is the substrate thickness of the microstrip line.

### 20.4.2 Magnetic Filling Factor

It is useful to define an effective microstrip permeability  $\mu_{\text{eff}}$  as being analogous to the effective microstrip permittivity defined earlier in this book, see Equation (6.15), and repeated here:

$$\epsilon_{\text{eff}} = 1 + q(\epsilon_r - 1) \quad 20.20$$

where  $\epsilon_{\text{eff}}$  is the effective relative permittivity of an equivalent homogeneous microstrip line. The filling factor  $q$ , and hence  $\epsilon_{\text{eff}}$  are functions of  $w/h$  and  $\epsilon_r$ , the relative permittivity of the substrate. However the dependence of  $q$  on  $\epsilon_r$  is weak.

Provided some basic and reasonable assumptions are made regarding a microstrip line (perfect conductors; isotropic, homogeneous, non-gyromagnetic substrate), then the substrate's dielectric properties will not affect the magnetic field distribution and its magnetic properties will not affect the electric field distribution. We can then write down a magnetic–electric duality statement [13]:

$$\mu_{\text{eff}} \propto 1/\epsilon_{\text{eff}} \quad 20.21$$

where  $\mu_{\text{eff}}$  is the effective relative permeability of the equivalent homogeneous microstrip line.

By analogy with Equation (20.20), we can write that

$$\mu_{\text{eff}} = 1 + q_m \left( \frac{1}{\mu_{r,\text{eff}}} - 1 \right) \quad 20.22$$

where  $q_m$  is the magnetic filling factor. It should be appreciated that both  $q_m$  and  $\mu_{\text{eff}}$  are functions of  $w/h$  for microstrip. Approximately  $q_m = q$ .

### 20.4.3 Effective Microstrip Permeability

Pucel and Masse [13] developed analytical expressions for  $\mu_{\text{eff}}$ .

For  $w/h \leq 2$

$$\mu_{\text{eff}} = \frac{2\mu_{r,\text{eff}}}{1 + \mu_{r,\text{eff}}} \left( \frac{A - B'}{A} \right)^2 \quad 20.23$$

and for  $w/h \geq 2$

[20.24](#)

$$\mu_{\text{eff}} = \mu_{r,\text{eff}} \left( \frac{C}{C - D'} \right)^2$$

where

$$A = \ln \left( \frac{8h}{w} \right) + \frac{1}{32} \left( \frac{w}{h} \right)^2 \quad \text{20.25}$$

$$B' = \frac{1}{2} \left( \frac{1 - \mu_{r,\text{eff}}}{1 + \mu_{r,\text{eff}}} \right) \left[ \ln \left( \frac{\pi}{2} \right) + \mu_{\perp} \ln \left( \frac{4}{\pi} \right) \right] \quad \text{20.26}$$

$$C = \frac{w}{2h} + \frac{1}{\pi} \left\{ \ln \left[ 2\pi\varepsilon_r \left( \frac{w}{2h} + 0.94 \right) \right] \right\} \quad \text{20.27}$$

$$D' = \frac{1 - \mu_{\perp}}{2} \left\{ \ln \left[ \frac{\pi\varepsilon_r}{2} \left( \frac{w}{2h} + 0.94 \right) \right] - \mu_{\perp} \ln \left( \frac{\varepsilon_r \pi^2}{16} \right) \right\}. \quad \text{20.28}$$

Here  $\mu_{r,\text{eff}}$  is the effective permeability of the substrate magnetized along the substrate in the direction of propagation. These expressions are believed to be accurate to about 5% and a graph of  $\mu_{\text{eff}}$ , calculated using Equations (20.23) and (20.24), is given in [Figure 20.8](#). as a design aid. There is a 5–10% discontinuity at  $w/h = 2$  and smoothing has been used to join the results from the two expressions.

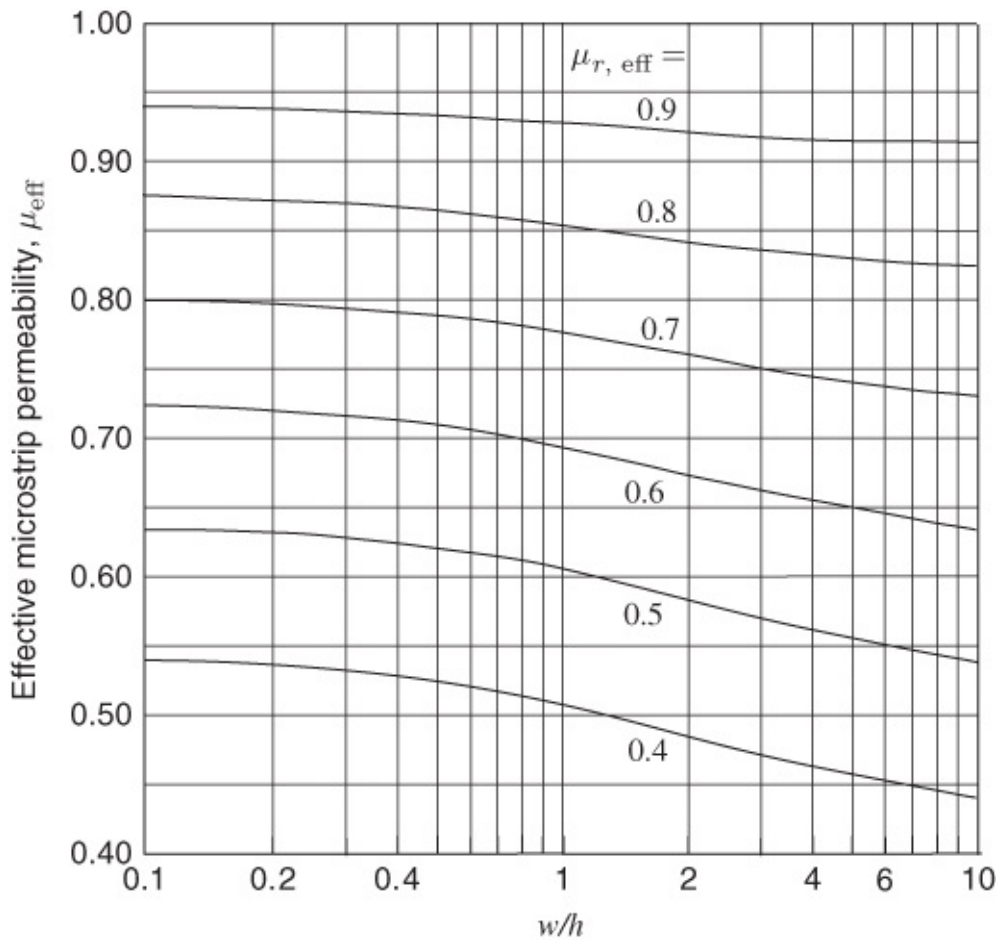


**Figure 20.8** Effective microstrip permeability  $\mu_{\text{eff}}$  as a function of  $w/h$ . The effective relative permeability of the substrate material  $\mu_{\perp}$  is the parameter. Adapted from Pucel and Masse (1972) [13], figure 2, p. 306. Reprinted with permission of IEEE.

For analysis and design we also require expressions for the characteristic impedance and the guide wavelength. Using Equation (6.1),  $Z_0 = (L/C)^{\frac{1}{2}}$ , we obtain

$$Z_0 = \left( \frac{\mu_{\text{eff}} L_0}{\epsilon_{\text{eff}} C_0} \right)^{\frac{1}{2}} \quad 20.29$$

where  $L_0$  and  $C_0$  are for the air-spaced case where the characteristic impedance is  $Z_{01}$ . Hence the characteristic impedance is

$$Z_0 = Z_{01} \sqrt{\mu_{\text{eff}} / \epsilon_{\text{eff}}} \quad 20.30$$

also, using the phase velocity

$$v_p = c / \sqrt{\mu_{\text{eff}} \epsilon_{\text{eff}}} \quad 20.31$$

we obtain the guide wavelength

$$\lambda_g = \frac{\lambda_0}{\sqrt{\mu_{\text{eff}} \epsilon_{\text{eff}}}} \quad 20.32$$

or, with  $F$  being the frequency in gigahertz,

$$\lambda_g = \frac{300}{F\sqrt{\mu_{\text{eff}}\epsilon_{\text{eff}}}} \text{ mm} \quad 20.33$$

(which can be compared to Equation (6.18)).

For synthesis, where  $w$  and  $\lambda_g$  are desired, it is recommended that design first be carried out assuming a non-ferrite substrate (but, of course, with the appropriate permittivity). One or two stages of iteration, using the above techniques and information, should then suffice to obtain quite accurate final values for  $w$  and  $\lambda_g$ . This is assisted by the fact that  $\mu_{\text{eff}}$  varies only slowly over the range  $0.1 \leq w/h \leq 10.0$ .

## 20.5 Isolators and Circulators

Microwave isolators and circulators exploit the nonreciprocal property of magnetic materials. Isolators are conceptually derived from circulators so circulators will be described first. Then  $\mu_{\text{eff}}$  is calculated and the actual  $Z_0$  and  $\lambda_g$  determined. There are two main types of microwave isolators and circulators both based on propagation of electromagnetic waves in or near a magnetized magnetic material. One of these is based on rotation of the polarization of the waves in a magnetic material (this is called Faraday rotation), and the other on the difference of two propagation paths.

### 20.5.1 Circulators

Faraday rotation-based circulators are usually implemented in circular waveguide. An electromagnetic wave polarized in one direction enters the circulator and the energy of the wave is largely contained in a magnetic material often in the form of a rod. The EM wave from either direction enters the circulator with a particular linear polarization. The polarization of the wave rotates as determined by the permeability tensor of the magnetized magnetic material. This could be a clockwise rotation or an anticlockwise rotation. If the rotation is clockwise it will be clockwise for both directions of propagation. Thus at a position on the line the polarization of the two waves will be different even if they were the same initially. Thus an output coupling structure that couples to only one particular polarization will preferentially couple into the wave propagating from one direction but not the other. Since the function of this circulator requires substantial field in the magnetic material it is not practical to use this mode in a microstrip circulator which uses thin films or substrates.

The second main type of microwave circulator is the junction circulator and is nearly always realized in microstrip or slotline using a magnetized magnetic disc. This is usually a thin layer of magnetic material but sometimes a magnetic substrate is used and only a region forming a disk is magnetized. The basic operation is illustrated in [Figure 20.9](#). When the thin magnetic disk is unmagnetized, as in [Figure 20.9\(a\)](#), the permeability of the material is a scalar and then there is not a preferred propagation path and the microwave signal entering port 1 is split equally between Paths A and B. When the disk is magnetized then there is a preference for

propagation along one of the paths, see [Figure 20.9\(b\)](#). However, the intent is not to propagate the electromagnetic signal in the magnetic disk. Instead a junction circulator is realized as shown in [Figure 20.9\(c\)](#). Here three nontouching microstrip lines are coupled to each other partly through the magnetized magnetic disk. Now there is a preferential coupling from one line to the next such that, in this case, the preferred coupling is in the anti clockwise direction. Invariably matching is required and then a microwave signal entering at port 1 emerges from the circulator at port 2, a microwave signal entering at port 2 emerges from port 3, and a microwave signal entering at port 3 emerges from port 1. It is difficult to achieve the required matching over more than a half-octave bandwidth and this is the major limitation of circulators.

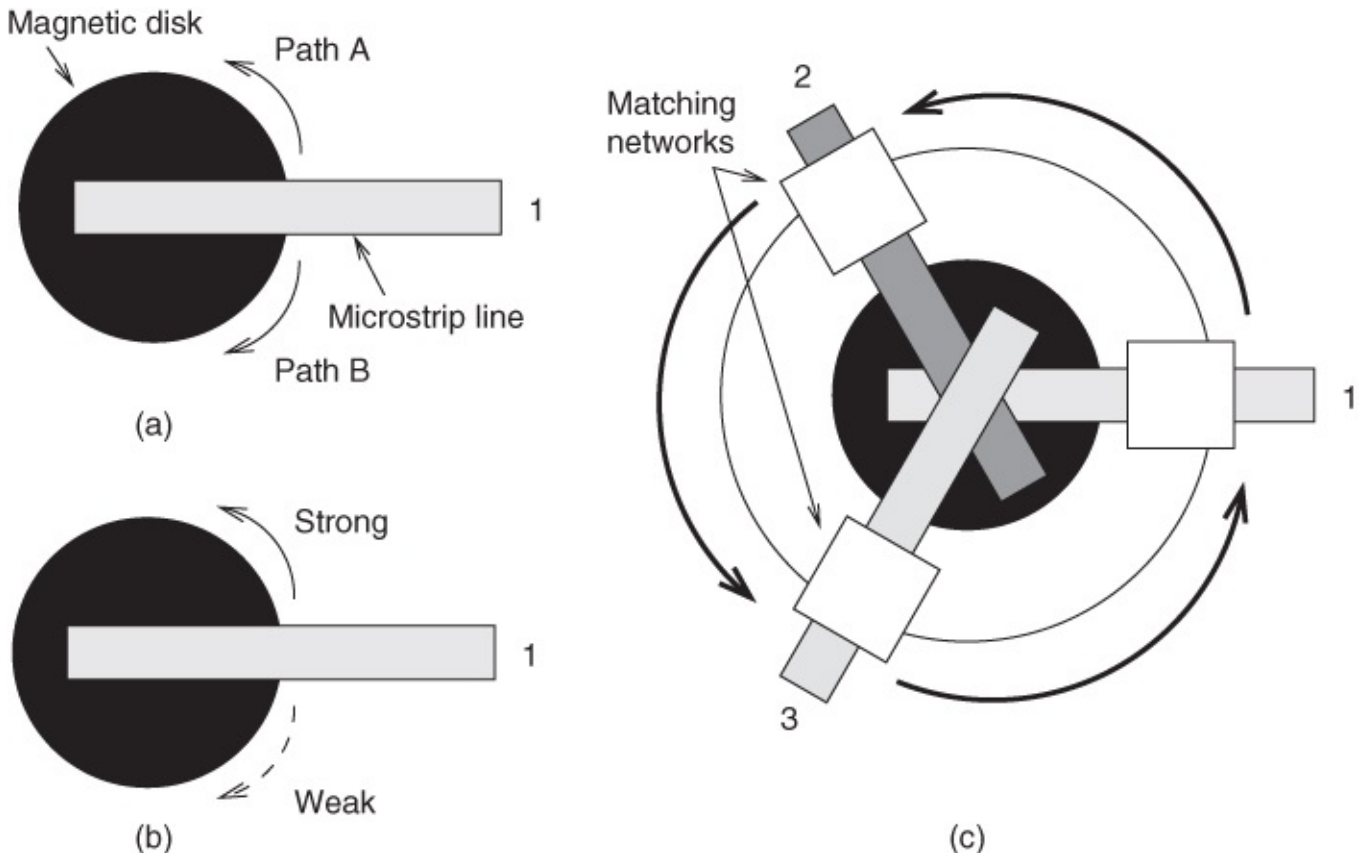


[Figure 20.9](#) Microstrip junction circulator: (a) microstrip line passing over an unmagnetized ferrite showing propagation paths of equal strength; (b) microstrip line passing over a magnetized ferrite showing propagation paths of unequal strength; and (c) a three-port microstrip junction circulator.

Pan *et al.* [14] reported a junction circulator designed for operation over the 31–37 GHz band which used a microstrip line fabricated on a nickel-zinc ferrite substrate and using stub tuning. This circulator has a diameter of 3.8 mm and thickness of 0.127 mm. An insertion loss of 0.6 dB and a return loss of better than 17 dB were achieved for a 7.6 mm-diameter circulator.

## 20.5.2 Isolators

A microwave isolator is obtained by terminating one of the ports of a junction circulator in a matched termination. The device now has two external ports and a microwave signal can travel in one direction but not the other. One of the parameters that quantifies the performance

of an isolator is its isolation, which is the ratio of the input power to the power traveling in the non preferred direction and emerging at the unintended output port. Typically insertion losses of 1 dB are achieved with isolation of 20 dB. Variants include the type of magnetic materials and the method used for applying a biasing magnetic field.

[Figure 20.10](#) is a photograph of a  $50\ \Omega$  microstrip isolator. This is based on a junction circulator and the matching networks at each of the three ports are evident. The third port of the circulator, on the left, is terminated in a  $50\ \Omega$  resistor, turning the three-port nonreciprocal device into a two port isolator.

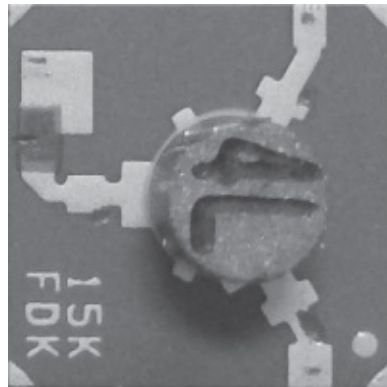
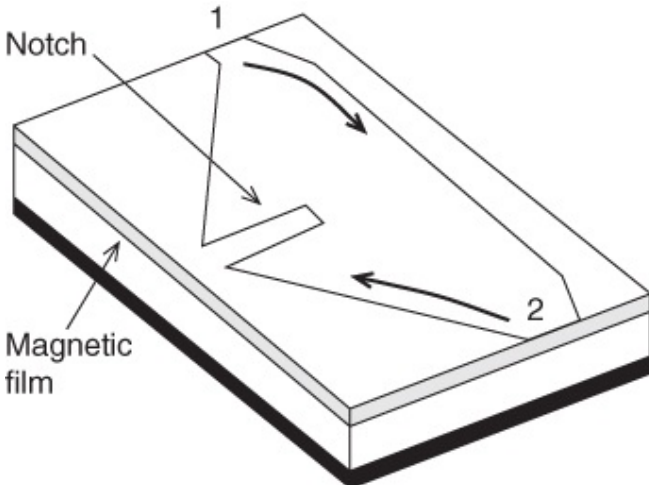
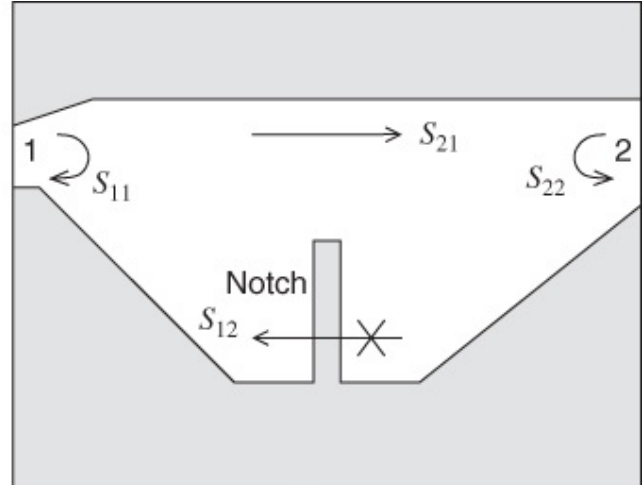


[Figure 20.10](#) Photograph of a 15 GHz microstrip isolator based on a junction circulator. The microstrip network is fabricated on a ferrite substrate and above the coupling region is a cylindrical permanent magnet.

An alternative approach to terminating one of the ports of a junction circulator is to interfere with one of the propagation paths. With a magnetized magnetic substrate the propagating signal on a microstrip line will tend to travel on one side of the microstrip line. Kane and Wong [15] report an isolator design based on edge-guide mode principles in conjunction with a transverse slot or slit discontinuity (the transverse slit was described in [Section 9.7.5](#)). This configuration is shown in [Figure 20.11](#), where the entire substrate is ferrite, the isolator section occupies an area approximately  $10\text{ mm} \times 8\text{ mm}$ , and the slot measures approximately  $6\text{ mm} \times 0.8\text{ mm}$ . At the center frequency of 11 GHz the forward insertion loss is about 2 dB and the isolation is better than 18 dB.



(a)



(b)

**Figure 20.11** An edge-guide mode microstrip isolator with transverse slot discontinuity: (a) perspective view; and (b) top view. Adapted from Kane and Wong (1990) [15], figure 1, p. 1007. Reprinted with permission of IEEE.

## 20.6 Transmission Lines Using Metaconductors

At DC and at very low frequencies the current in a transmission line conductor is uniformly distributed over the cross-section of the conductor. This leads to the lowest line resistance of the transmission line,  $R_{DC}$ . However, as frequency increases the alternating current becomes confined to the skin of the conductor, increasing the line resistance approximately as the square root of frequency. For a conductor with a finite conductivity the movement of alternating charges, and hence alternating current, requires that there be a component of the electric field inside the conductor pointed in the direction of the intended current movement, which is the direction of signal propagation on a planar transmission line. This requires that an electromagnetic wave propagate from the surface of a conductor into its interior. The electric field component of this EM wave falls to  $1/e$  of its value at the surface after one skin depth  $\delta_s$  where

$$\delta_s = \frac{1}{\sqrt{\pi f \mu \sigma}} \quad 20.34$$

where  $f$  is the frequency (in hertz) and  $\mu$  and  $\sigma$  are the permeability and conductivity of the conductor. For example, copper, having a relative permeability  $\mu_r = 0.999994$  and conductivity  $\sigma = 5.8 \cdot 10^7$  S/m, has a skin depth at 10 GHz of 0.65  $\mu\text{m}$ . So at a distance of 0.65  $\mu\text{m}$  from the surface the internal electric field in the strip of a planar transmission line will be

$1/e = 1/2.71828 = 0.3679$  th of its value at the surface. After another skin depth of distance (i.e., is at  $2\delta_s = 1.3 \mu\text{m}$  from the surface) the electric field will drop by another factor of  $1/e$  to 0.13534 times its value just inside the surface of the conductor. If  $z$  is the direction of propagation on the strip then the  $z$ -directed volume current density  $J_z = \sigma E_z$  and so the current density drops off in proportion to the electric field drop off. Thus  $J_z$  will be 13.5% of its

surface value after two skin depths.

Consider a CPW line with semi-infinite ground planes as shown in [Figure 20.12](#). The cross-section of the current density inside the copper metallization was determined at 10 GHz using 3D electromagnetic simulation and the result is shown in [Figure 20.13](#). The current profile is complicated by proximity effects, that is, the proximity of the side edges of the strip to the semi-infinite ground planes, but the skin effect is clearly observed in both the strip and the flanking ground planes. Confining the current to the skin of the conductor increases the line resistance. In addition, for the same overall current, the current density on the surface of the conductors is higher since there is virtually no current conveyed in the center of the conductors. Since the conductor conductivity cannot be increased, the way to reduce the line resistance is to ensure current in the interior of the conductors.

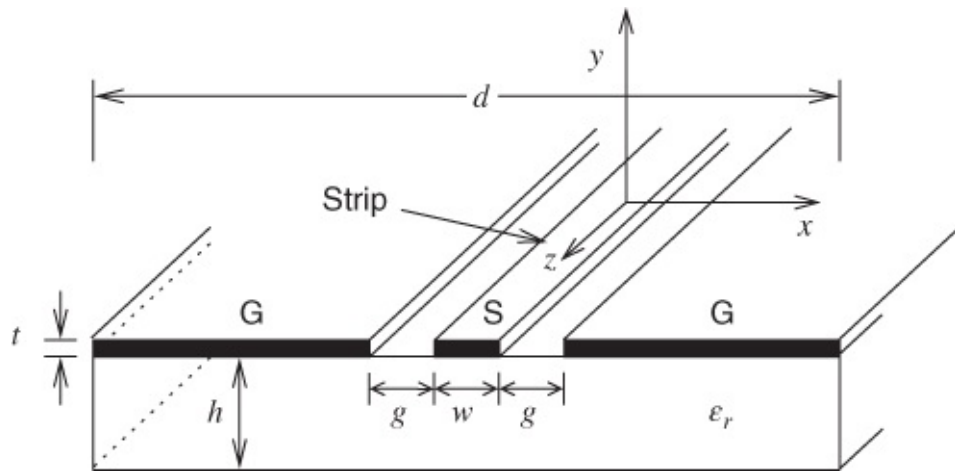


**Figure 20.12** CPW transmission with semi-infinite ground planes. The metal thickness  $t = 8.24 \mu\text{m}$ , strip width  $w = 30 \mu\text{m}$ , gap  $g = 25 \mu\text{m}$ , and overall width  $d = 1 \text{ mm} \gg w$ . The borosilicate glass substrate has a thickness of  $500 \mu\text{m}$ , loss tangent of 0.0009, and relative permittivity of 6.1.

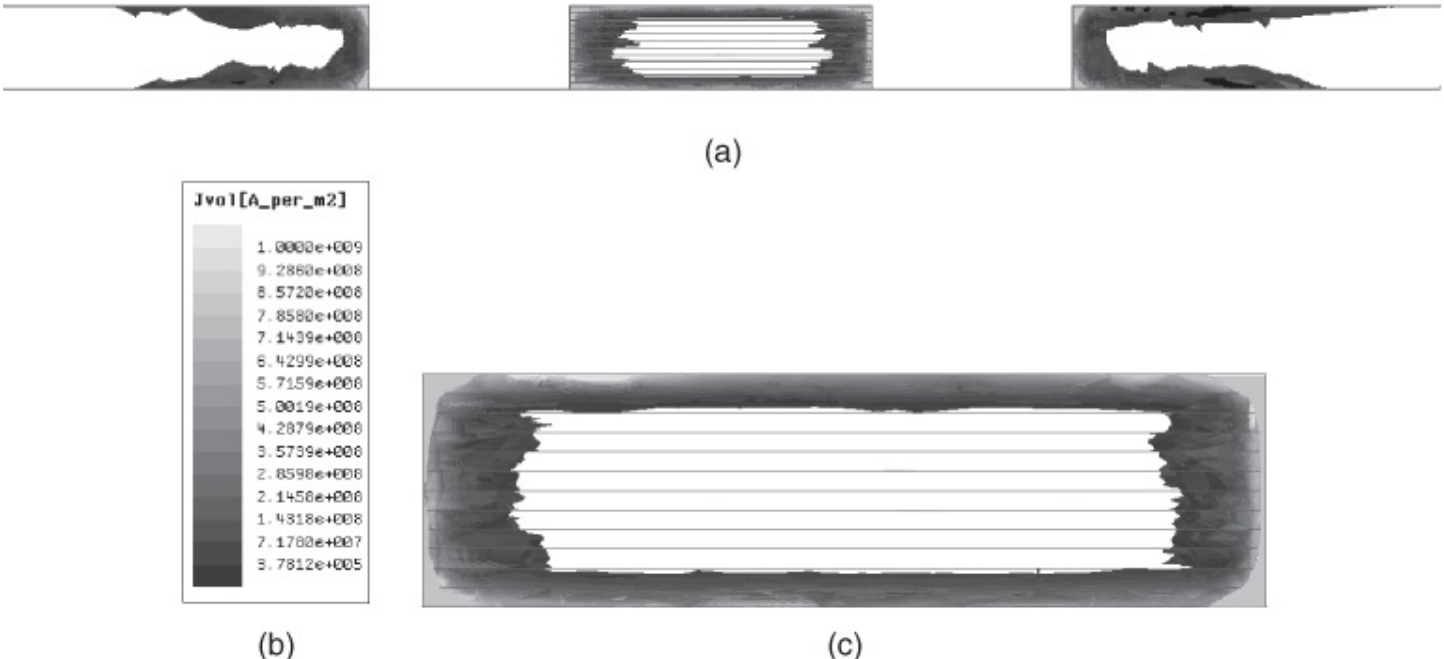


**Figure 20.13** Current density in cross-section at 10 GHz inside the copper CPW transmission line of [Figure 20.12](#): (a) CPW line showing center strip and parts of the side ground planes; (b) scale; and (c) the strip enlarged and modeled using a finer grid than in (a). The darkest regions inside the conductor have a current density that is 1/10th of the peak current density. The horizontal lines in (c) are at integer multiples of  $0.69 \mu m$ , which is slightly more than the skin depth of  $0.65 \mu m$ . The total thickness of the strip and ground planes is  $8.24 \mu m$ . Calculated using Ansys HFSS.

In seminal work in 2004 Rejaei *et al.* [10] introduced the concept of a metaconductor for the purpose of suppressing the skin effect. Their metaconductor consisted of layers of conductor and thin magnetized magnetic material. With the magnetic material magnetized in the  $z$  direction and an internally generated magnetic field also in the  $z$  direction, the effective permeability of the magnetic material in the  $xy$  plane is negative. This permeability was described in [Section 20.3.2](#) and [Figure 20.7\(d\)](#). In an effective conductor sense the layers of conventional conductor, with a relative permeability of 1, alternating with layers of magnetized material with a negative effective permeability, would result in an overall effective permeability that can be tuned to be near zero. Referring to the skin effect formula in Equation [\(20.34\)](#), this could increase the skin depth by significantly reducing the denominator.

Measured attenuation results for CPW line with copper conductors and a metaconductor were presented by Iramnaaz *et al.* in [11]. The CPW structure is shown in [Figure 20.12](#) and the metaconductor was constructed as layers of copper and permalloy, see [Figure 20.14](#).

Permalloy is a magnetic alloy of nickel and iron in the proportions of 80% nickel and 20% iron and is a metallic, that is, conducting, ferromagnet. The permalloy layers were magnetized and an internal magnetic field created due to anisotropy. For comparison a CPW line consisting only of copper conductors was constructed with the same dimensions. Their results are shown in [Figure 20.15](#). The metaconductor-based CPW line has significantly reduced loss and suppressed skin effect.

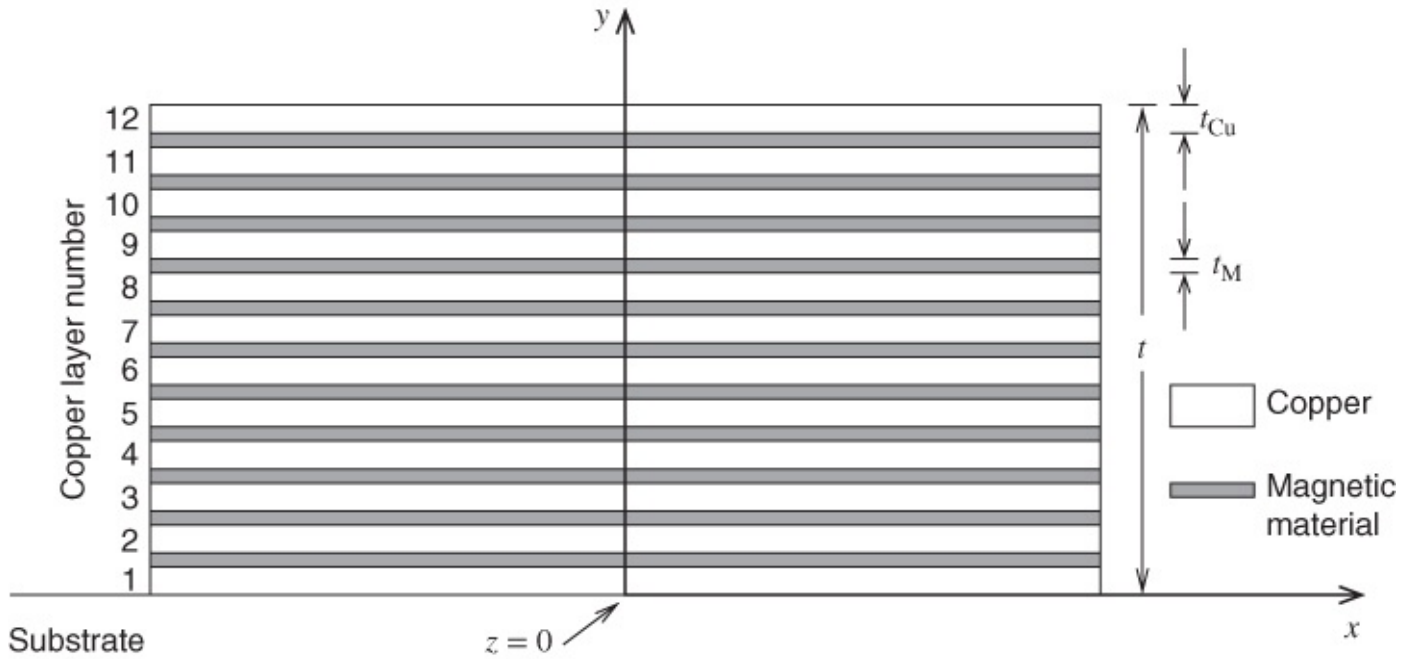


**Figure 20.14** The strip of a CPW line realized as a metaconductor (or superlattice) with alternating metal, here copper, layers and magnetic material layers. Shown here is the cross-section of a metaconductor with 12 copper layers and 11 magnetic layers with  $t_{Cu} = 0.65 \mu\text{m}$ ,  $t_M = 0.04 \mu\text{m}$ , and  $t = 8.24 \mu\text{m}$ . Other dimensions are shown in [Figure 20.12](#). Propagation is  $z$ -directed and is out of the page.

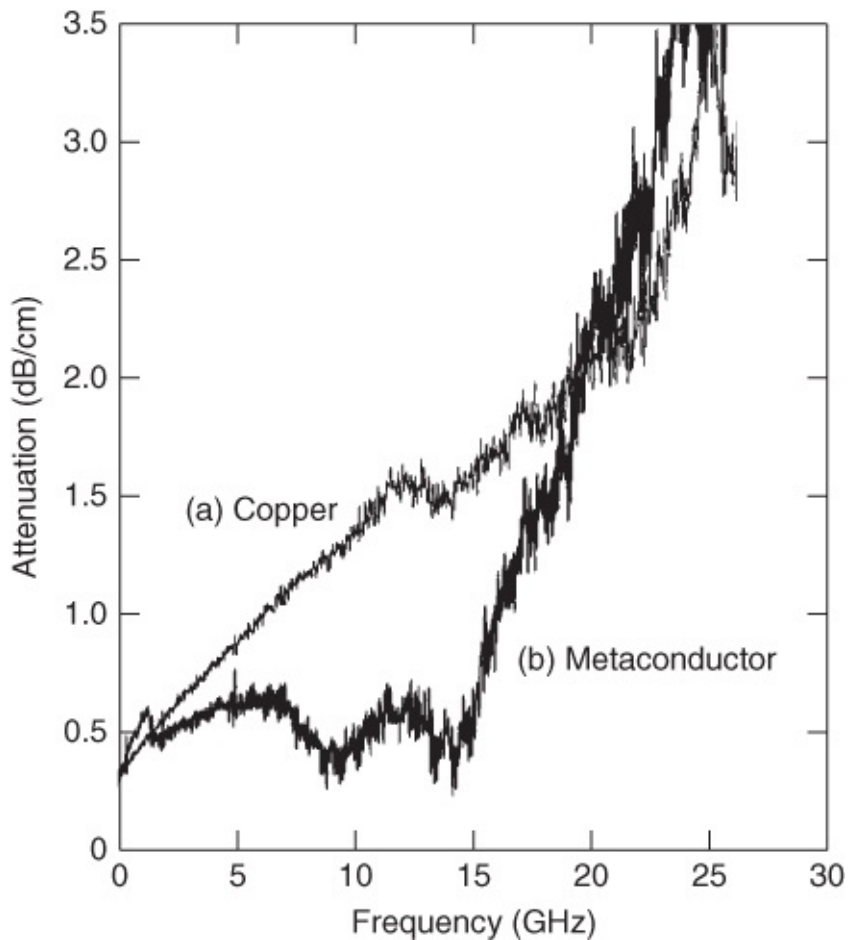


**Figure 20.15** Attenuation of CPW lines, one with a copper conductor and one with a metaconductor. The metaconductor has lower loss than the unmodified line over a better than 18 GHz bandwidth from 1.5 GHz to 19.75 GHz. Adapted from Iramnaaz *et al.* (2012) [11], figure 4, p. 4141. Reprinted with permission of IEEE.

### 20.6.1 A Study of a Metaconductor-based CPW Line

This section presents a study of the metaconductor effect for the CPW line shown in [Figures 20.12](#) and [20.14](#). While the effective medium concept, that is, the negative permeability of a magnetic layer effectively canceling the positive permeability of the nonmagnetic metal layer, has proved useful in conceptualization, it is necessary to look at the fields inside the conductors to understand the effect. The material parameters used in the study are listed in [Table 20.4](#). These correspond to the structure considered in [11]. The magnetic properties of the magnetized permalloy (Py) layer was modeled as having an effective permeability of  $-13$ , which is the effective permeability experienced by RF magnetic fields inside the metaconductor in the  $xz$  plane.

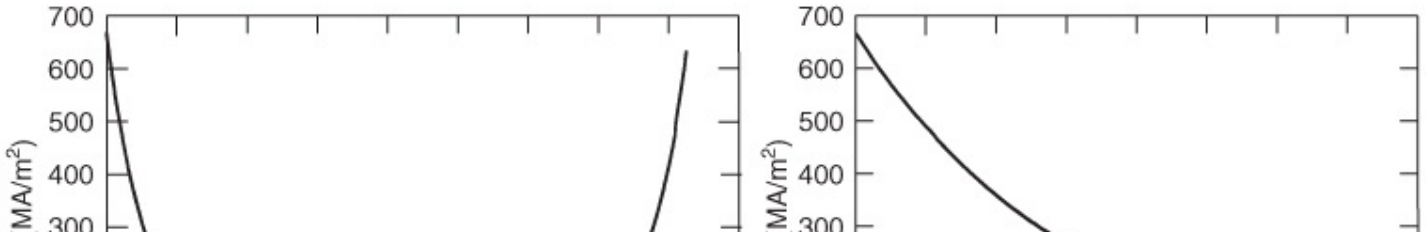
**Table 20.4** Material properties used in the CPW-based metaconductor study. Properties are at 9.4 GHz. The substrate is a borosilicate glass. The ferrite here is a low conductivity and low resistivity material whereas most ferrites have high resistivity

	Copper (Cu)	Ferrite	Permalloy (Py)	Substrate
Conductivity (S/m)	$5.8 \cdot 10^7$	0.01	$6.13 \cdot 10^6$	0
Relative permeability	$\mu_r = 0.999991$	$\mu_{r,\text{eff}} = -13$	$\mu_{r,\text{eff}} = -13$	$\mu_r = 1$
Relative permittivity, $\epsilon_r$	1	12	12	6.1
Dielectric loss tangent, $\tan \delta$	0	0	0	0.0009
Thickness of each layer	0.65 $\mu\text{m}$	0.04 $\mu\text{m}$	0.04 $\mu\text{m}$	500 $\mu\text{m}$
Number of layers	12	11	11	1

The main result of this study is understanding the effect of the magnetized layers on the current distribution inside the strip. Three situations are considered. First, a solid copper construction of the strip and ground planes is considered. Then the strip is replaced by the layered metaconductor structure shown in [Figure 20.14](#) with low-conductivity magnetized ferrite layers. This is followed by an examination with the non conducting ferrite layers replaced by conducting permalloy layers.

## Solid Copper Conductor

The first set of results consider the CPW transmission line of [Figure 20.12](#) having a total strip and ground plane thickness of  $8.24 \mu\text{m}$  and the material properties shown in [Table 20.4](#). [Figure 20.16](#) presents the profiles of the current density in the direction of the CPW line and of selected fields inside the strip at a frequency of 10 GHz. Some of the field components are negligible here but are needed in the investigation of the fields inside the metaconductor. All of the other field components inside the strip are negligible. [Figure 20.16](#) first presents  $J_z$ , the volumetric current density, in the direction of propagation on the CPW line, then  $E_z$ , the electric field also in the  $z$  direction and the field that produces the current through the constitutive relationship  $J_z = \sigma E_z$ . The next plot is of  $H_x$ , the magnetic field transverse to the direction of propagation on the line, and then  $E_y$  is plotted, which for now is not much more than numerical noise. These are plotted against increasing  $y$  in the center of the strip ( $x = 0$ ) using the coordinate system shown in [Figure 20.12](#) where  $y = 0$  is at the bottom of the strip. Here  $J_z$  corresponds to the 2D profile shown in [Figure 20.13\(c\)](#). The other  $E$  and  $H$  field components in the strip are very small.  $E_z$  and  $H_y$  are the components of an electromagnetic wave propagating into the conductor from the top and bottom surfaces of the strip.



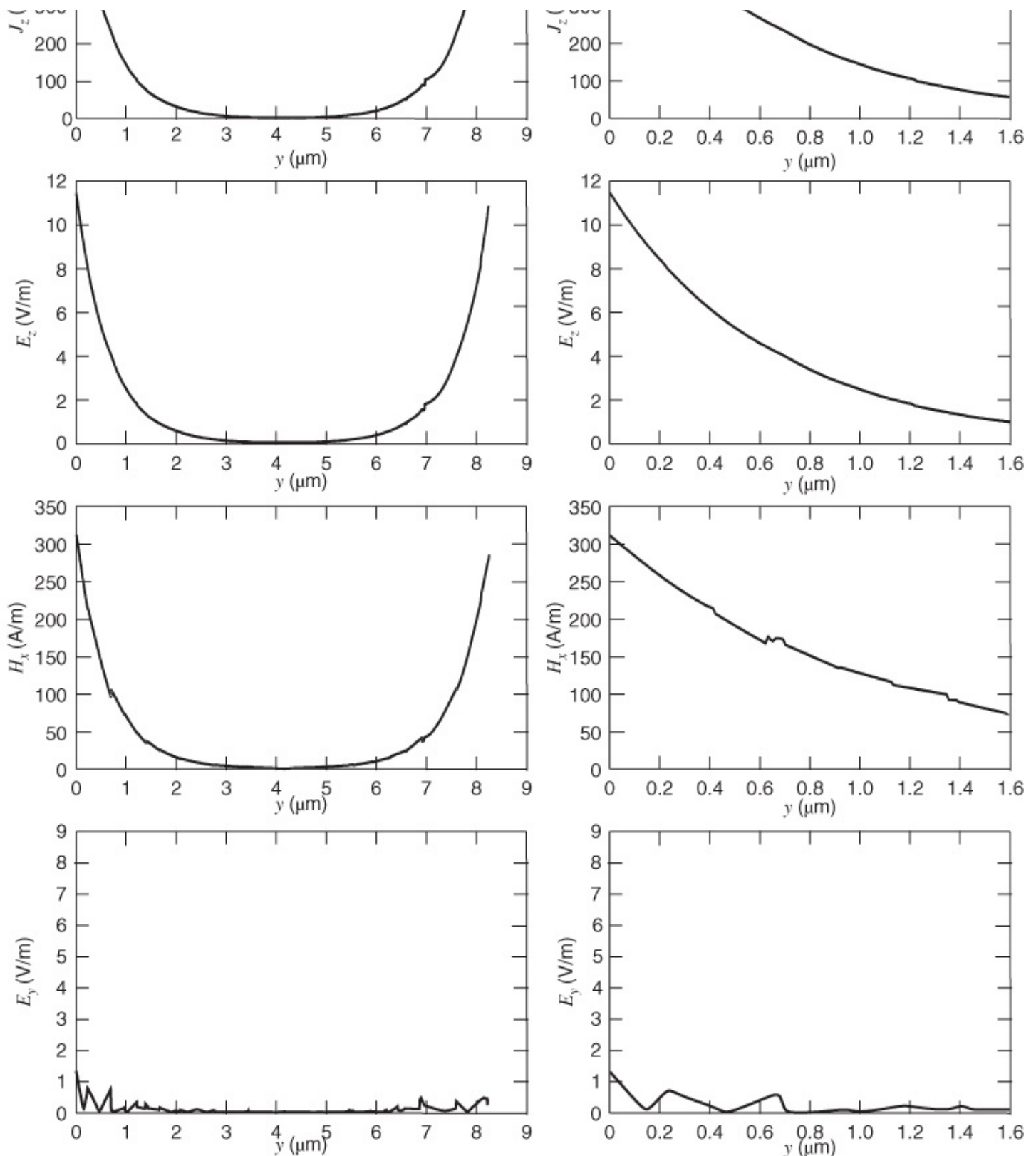


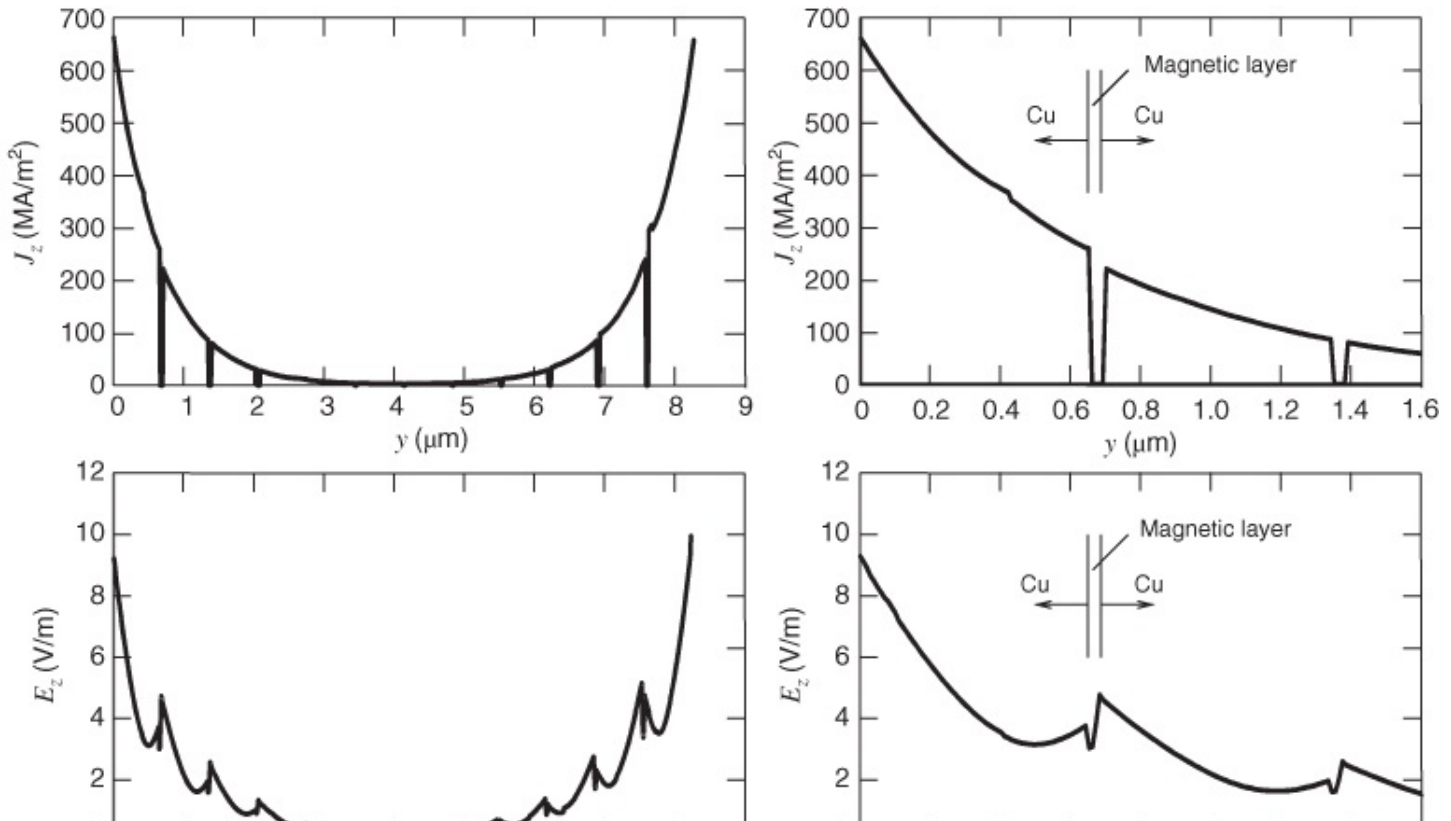
**Figure 20.16** Magnitudes of the current and field profiles at  $x = 0$  and 10 GHz of the strip of CPW line with a solid copper strip with the dimensions shown in [Figure 20.12](#). The directions of  $H_x$  and  $E_y$  reverse at the center of the strip (i.e., at  $y = 4.12 \mu\text{m}$ ) while the directions of  $E_z$  and  $J_z$  are unchanged.

The minimum line resistance is obtained when  $J_z$  is uniform with respect to  $y$  and, for constant

power, the integral of  $J_y$  is approximately constant irrespective of frequency. A small deviation will occur because of proximity effects. Thus the current concentration shown in [Figure 20.16](#) and the lack of current in the center of the strip indicates a line resistance substantially more than the DC resistance. It can be seen more easily with the expanded plot on the right that at the skin depth of  $0.65\text{ }\mu\text{m}$  (i.e., at  $y = 0.65\text{ }\mu\text{m}$ )  $J_z = 249\text{ MA/m}^2$ , which is within 2% of  $1/e$  of its value at the surface where  $J_z = 665\text{ MA/m}^2$  ( $665/e = 245$ ). As expected, the profile of  $E_z$  matches that of  $J_z$ .

## Ferrite-based Metaconductor

In the second structure studied the strip of the CPW line is replaced by a metaconductor consisting of a  $0.65\text{ }\mu\text{m}$  copper layer, then a  $0.04\text{ }\mu\text{m}$  thick high-resistivity, ferrite layer, and repeated for 12 copper layers and 11 ferrite layers. The ferrite properties are given in [Table 20.4](#). The results of this study are shown in [Figure 20.17](#). These are dramatically different profiles than were obtained with the solid copper strip. First consider the profile of  $J_z$ . This profile is close to the current density profile for the solid copper strip with regions of virtually no current flow in the low-conductivity ferrite layers. This is not unexpected. The longitudinal electric field,  $E_z$ , shows unusual behavior with the field spiking up above the levels obtained with the solid copper strip. These spikes are near the ferrite layers. Before explaining this behavior the other field components will be considered. The transverse magnetic field,  $H_x$ , is almost identical to that obtained with the solid copper strip with small glitches seen at the ferrite layers. The behavior of the vertical electric field,  $E_y$ , is a significant departure from that in the solid copper strip case.  $E_y$  spikes up to levels exceeding  $E_x$  at each ferrite layer whereas with the solid copper strip the  $E_y$  profile was at the numerical noise level. The other field components are not plotted here but are much smaller and can be ignored.



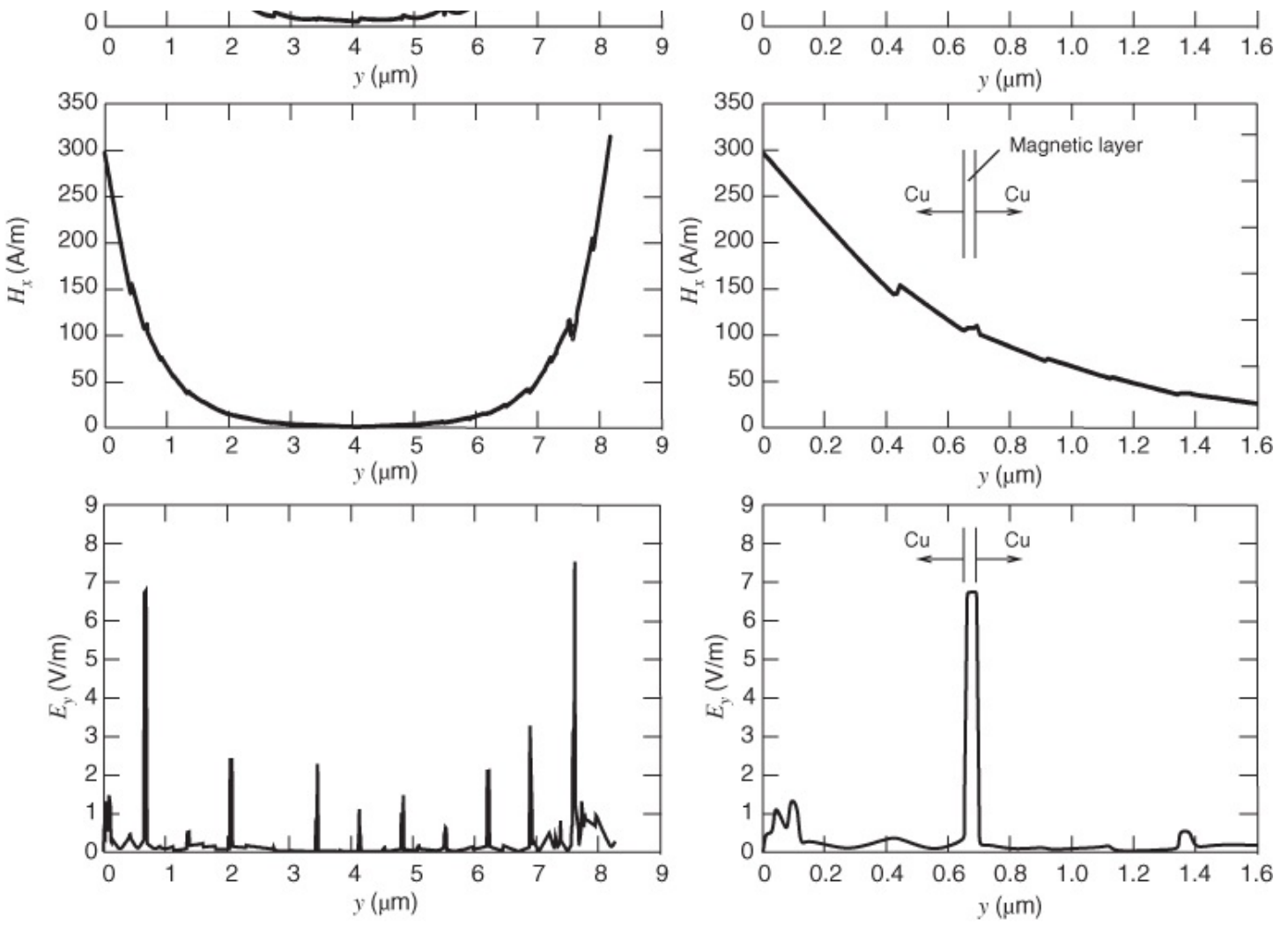


**Figure 20.17** Magnitudes of the current and field profiles at  $x = 0$  and 10 GHz of the strip of a CPW line with a metaconductor CPW strip of layered copper and magnetized high-resistivity ferrite with the dimensions shown in Figures 20.12 and 20.14. The directions of  $H_x$  and  $E_y$  reverse at the center of the strip (i.e., at  $y = 4.12 \mu\text{m}$ ) while the directions of  $E_z$  and  $J_z$  are unchanged.

These results do illustrate moderate skin effect suppression but this will not be obvious until later. However, understanding what is happening with the high-resistivity ferrite-based metaconductor is essential for understanding the significant skin effect suppression obtained with the permalloy-based metaconductor to be considered soon. The key is understanding the spikes in  $E_x$  and  $E_z$ . One of Maxwell's equations provides the necessary insight. The important equation in phasor form is

$$\nabla \times \bar{\mathbf{E}} = -j\omega \bar{\mathbf{B}} \quad 20.35$$

where  $\bar{\mathbf{E}}$  and  $\bar{\mathbf{B}}$  are the vectors of the  $\mathbf{E}$  and  $\mathbf{B}$  fields in phasor form. There is only one non-negligible component of the RF  $\mathbf{B}$  field,  $B_x$ , and so Equation (20.35) becomes (after taking just the  $x$ -directed components) [16]

[20.36](#)

$$\frac{\partial E_z}{\partial y} - \frac{\partial E_y}{\partial z} = -j\omega B_x = -j\omega\mu_0\mu_{r,\text{eff}}H_x.$$

Here  $\mu_{r,\text{eff}}$  is the effective relative permeability for either the copper or ferrite layers. It is  $\mu_{r,\text{eff}} = \mu_{r,\text{Cu}} = 1$  for copper and for the ferrite layer it has an effective value which is negative in the  $x$  direction, that is,  $\mu_{r,\text{eff}} = \mu_{r,\text{Ferrite}} = \mu_\perp = -13$ . So in a ferrite layer Equation (20.36) becomes

[20.37](#)

$$\frac{\partial E_{z,\text{Ferrite}}}{\partial y} - \frac{\partial E_{y,\text{Ferrite}}}{\partial z} = -j\omega B_{x,\text{Ferrite}} = -j\omega\mu_\perp\mu_0 H_{x,\text{Ferrite}}.$$

So Equation (20.37) can be written in two parts with

[20.38](#)

$$\frac{d|E_{z,\text{Ferrite}}|}{dy} = +13\alpha|H_{x,\text{Ferrite}}|$$

and

[20.39](#)

$$\frac{d|E_{y,\text{Ferrite}}|}{dz} = -13\beta|H_{x,\text{Ferrite}}|$$

where  $\alpha$  and  $\beta$  are positive proportionality terms and  $\alpha + \beta = 1$ . For now consider  $0 \leq y \leq 4.25 \mu\text{m}$  as  $H_x$  reverses direction in the top half of the strip. The actual values of  $\alpha$  and  $\beta$  will depend on a full field solution but it is reasonable to take them as equal for now. Now examine what Equations (20.38) and (20.39) are indicating. Equation (20.38) is indicating that in the ferrite layer the magnitude of  $E_{z,\text{Ferrite}}$  will increase with respect to  $y$  in the bottom half of the strip ( $0 \leq y \leq 4.25 \mu\text{m}$ ). This is exactly what is seen in [Figure 20.17](#) in the vicinity of the ferrite layer. This argument applies to the top half of the strip but since  $H_x$  has a reverse direction in the top half of the strip the magnitude of  $E_{z,\text{Ferrite}}$  increases in the direction away from the surface of the strip.

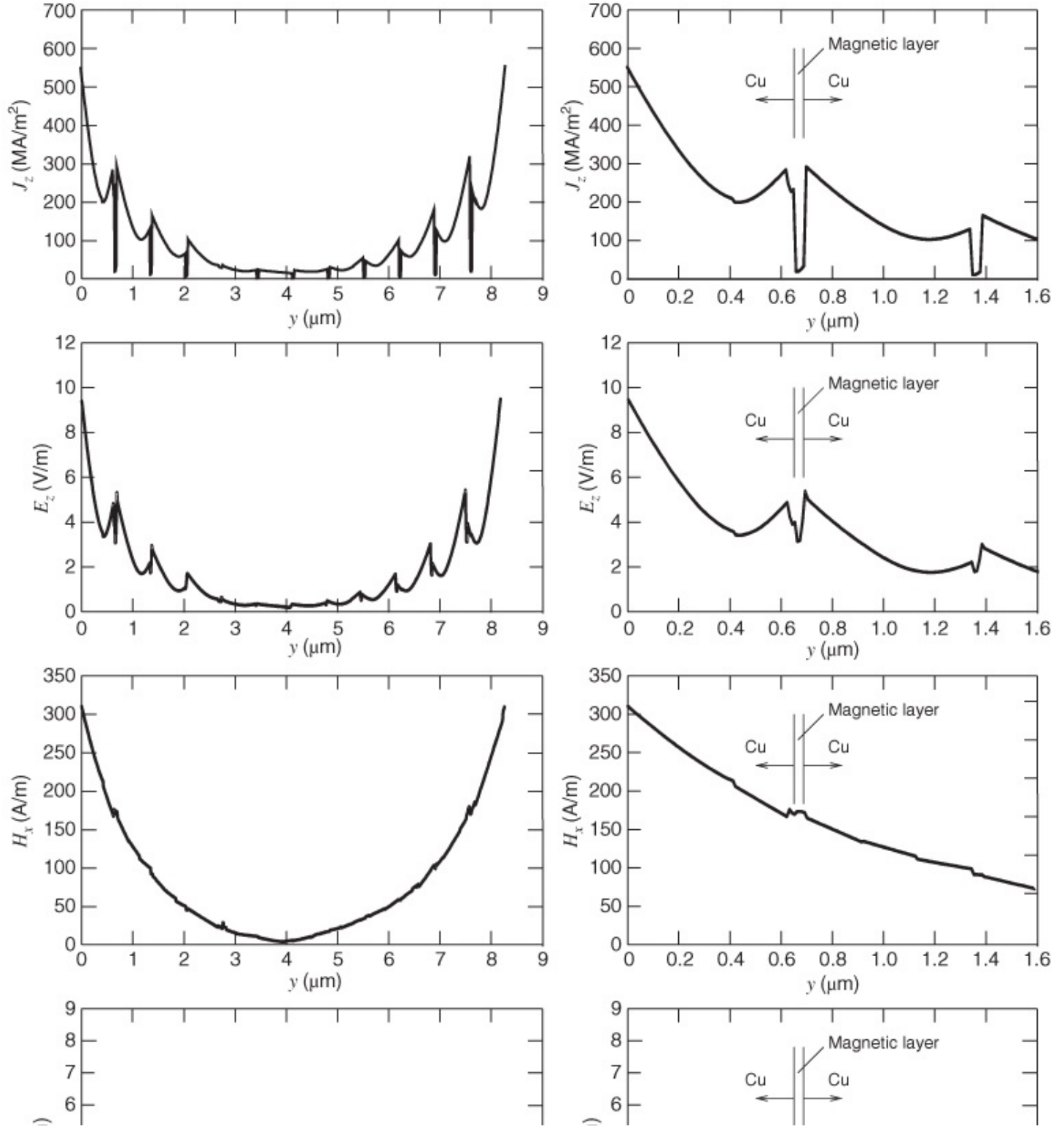
Turning our attention now to Equation (20.39) it is seen that this implies that there must be a  $y$ -directed component of the electric field and that there must be a derivative of this electric field component with respect to the direction along the strip (i.e., the  $z$  direction). What is important here is that  $E_y$  will be generated if it is possible for it to exist, which clearly occurs in the high-resistivity ferrite layers.

As was mentioned, the effect on skin effect suppression is small in this case but before demonstrating this we will consider the next situation with a highly conducting magnetic layer.

## Permalloy-based Metaconductor

In the third structure studied the strip of the CPW line is as considered previously but now the strip is replaced by a metaconductor consisting of a  $0.65 \mu\text{m}$  copper layer, then a  $0.04 \mu\text{m}$  thick permalloy layer, and repeated for 12 copper layers and 11 permalloy layers. Permalloy is a metallic magnetic material with high conductivity and its properties are given in [Table 20.4](#). The results of this study at 10 GHz are shown in [Figure 20.18](#). The first thing to note is that,

compared to the two previous cases, the current distribution is much more uniform and there is current flow in the center of the strip, a distance of more than six copper skin depths from the top and bottom surfaces of the strip. At six skin depths we would expect current densities of around 1–2 MA/m<sup>2</sup> compared to the actual current density of around 20 MA/m<sup>2</sup>. (Permalloy is at the center and 20 MA/m<sup>2</sup> is the current density in the copper adjacent to the center permalloy layer.) In addition, the peak current density at the surfaces of the strip are lower. The line resistance is therefore lower than for the solid copper strip and lower than for the ferrite-based metaconductor strip.



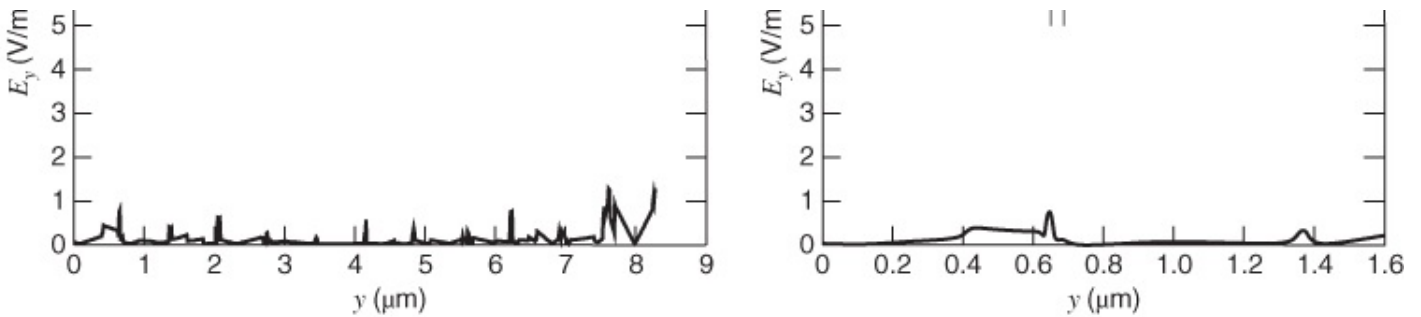


**Figure 20.18** Magnitudes of the current and field profiles at  $x = 0$  and 10 GHz of the strip of a CPW line with a metaconductor CPW strip of layered copper and magnetized permalloy with the dimensions shown in [Figures 20.12](#) and [20.14](#). The directions of  $H_x$  and  $E_y$  reverse at the center of the strip (i.e., at  $y = 4.12 \mu\text{m}$ ) while the directions of  $E_z$  and  $J_z$  are unchanged.

The field profiles for the permalloy-metaconductor-based CPW line, [Figure 20.18](#), are similar to those for the ferrite-metaconductor-based CPW line, [Figure 20.17](#), with the notable exception of the  $E_y$  profile. The spikes of  $E_y$  at the ferrite layers seen in [Figure 20.17](#) are simply nonexistent with the permalloy layers. This is what eventually results in the superior skin effect suppression obtained with permalloy.

Recall the discussion with the ferrite-based metaconductor and the relationship of the electric field in the magnetic layer that derived from one of Maxwell's equations. Equations ([20.37](#))–([20.39](#)) indicate that the negative effective permeability of the magnetic layer (which is the same for both the ferrite and permalloy magnetic layers) results in possible generation of enhanced electric field in the  $x$  and  $y$  directions. However, the  $E_y$  field will only be excited if it is possible for it to be supported. With the low conductivity ferrite, the ferrite layer is akin to a parallel-plate waveguide with the waveguide walls established by the high-conductivity copper layers. With the high-conductivity permalloy it is not possible to support such a parallel plate waveguide mode. Since  $E_y$  cannot exist in the permalloy layer, the result is that the peaking induced in  $E_z$  must be that much stronger to balance Equation ([20.37](#)). The enhanced peaking of  $E_z$  results in enhanced current density in the vicinity of the magnetic layers and hence a more uniform current profile than obtained with either the ferrite-metaconductor strip or the copper-based strip. This is indeed what is shown in [Figure 20.18](#).

## Summary

The three current profiles for the CPW line with alternately the copper-based, ferrite-metaconductor-based, and permalloy-metaconductor-based strips are compared in [Figure 20.19](#). The volumetric current density is along the strip in the direction of propagation on the CPW line. With the strip comprising solid copper the classic skin-effect situation is seen where the current density exponentially decreases away from the top (at  $y = 8.24 \mu\text{m}$ ) and bottom (at  $y = 0 \mu\text{m}$ ) of the strip. With the strip of the CPW line replaced by a metaconductor with magnetized ferrite layers there is some skin effect suppression. These results are identified as the alternative metaconductor results. Significant skin effect suppression is obtained with the ferrite layers replaced by magnetized permalloy layers, yielding the results identified by the Cu–Py metaconductor designation.

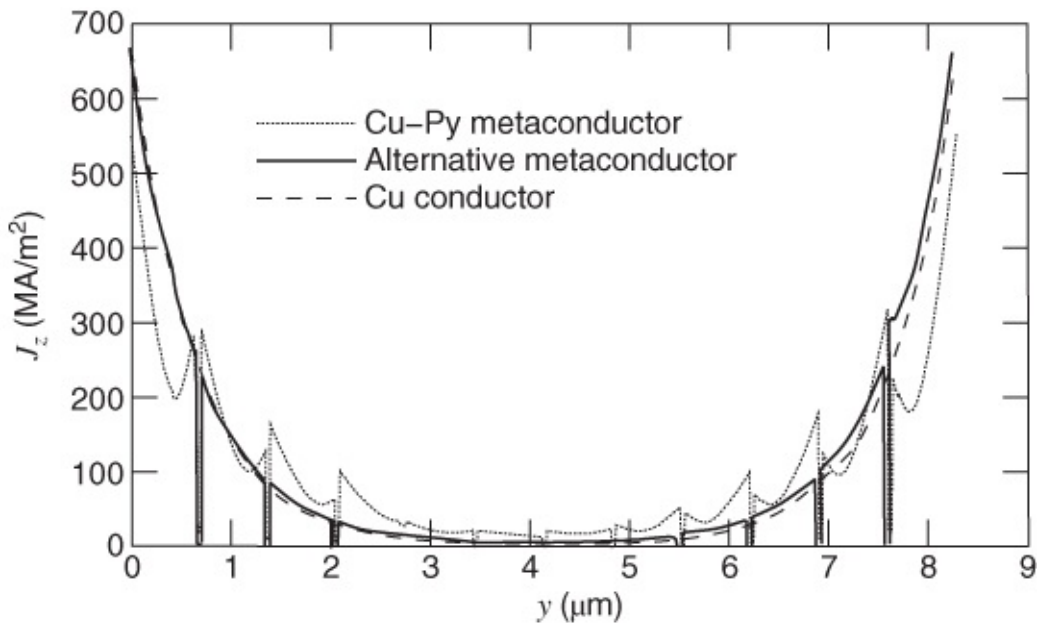


**Figure 20.19** Current profile for three CPW strip compositions. The Cu–Py metaconductor results are for the layered metaconductor with permalloy layers sandwiched between copper layers, the alternative metaconductor results are for a CPW line with the strip comprising layers of copper and low-conductivity ferrite, and the Cu conductor results are for a solid copper strip. The semi-infinite grounds in all cases are solid copper.

The complete current density profile on the cross-section of a strip is shown in [Figure 20.20](#) for two situations. [Figure 20.20\(a\)](#) is the current density profile when the strip is solid copper and [Figure 20.20\(b\)](#) is a metaconductor with alternating copper and permalloy layers.



(a)



(b)

**Figure 20.20** Current density in cross-section at 10 GHz inside the strip of the CPW transmission line of [Figure 20.12](#): (a) with a solid copper conductor having a total thickness of  $8.24 \mu\text{m}$ ; and (b) with a metaconductor consisting of 12 copper layers, each  $0.65 \mu\text{m}$  thick, and 11 permalloy layers, each  $0.04 \mu\text{m}$  thick for a total strip thickness of  $8.24 \mu\text{m}$ . Calculated using Ansys HFSS.

The suppression of the skin effect in a metaconductor as reported here is related to the giant magneto-resistivity effect which uses a layered structure of magnetic material and low resistance conductor such as copper [17–23]. In this effect the resistance at microwave frequencies of the layered material is changed significantly by a magnetic field. This has been applied to magnetic read heads and magnetic field sensors. The difference with the metaconductor is that the magnetic field is internally generated rather than externally applied. Optimization of the layer structure has been undertaken to enhance the giant magneto-resistance effect [24] and a similar analysis can be used for a metaconductor.

A spiral inductor has been realized using a metaconductor, achieving modest reduction in losses and improvements of  $Q$  at 5 GHz have been reported for a  $1.1 \text{ nH}$  inductor [25, 26]. Currently there are limitations and one of these is that the attenuation reduction is only obtained for magnetization in the direction of propagation, that is, if the material is all magnetized in the same direction, say the  $z$  direction, then loss reduction will only be reduced for  $z$ -directed lines. However, this could be overcome by alternating the magnetization of alternate layers, one in the  $z$  direction, and the next in the  $y$  direction and then repeating with a  $z$ -directed magnetized layer, etc. Other researchers have reported applications with coaxial cables where the single-direction of propagation is clearly not a problem [27].

It is also apparent that metal layers thinner than a skin depth could result in even greater skin effect suppression. The impact that a metaconductor has on signal integrity is unknown. It is known that magnetic materials can cause passive intermodulation distortion through the

magnetic hysteresis effect. A dominant source of passive intermodulation distortion also results from electro-thermal effects [28–31]. For a non resonant transmission line the dominant heat flow path is into the substrate through the strip of a microstrip line. With the layered Cu–Py metaconductor the thermal conductivity of permalloy is less than one tenth that of copper, see [Table 20.5](#), and so it can be expected that a metaconductor line will have higher passive intermodulation distortion than a solid copper line.

**Table 20.5** Thermal properties of selected materials

Material	Type	Thermal conductivity	Specific heat capacity
		(W · m <sup>-1</sup> · K <sup>-1</sup> )	(kJ · kg <sup>-1</sup> · K <sup>-1</sup> )
		at 300 K	at 25 °C
Copper	Conducting	401	0.39
Permalloy	Conducting	30–35	0.50
Alumina (100%)	Nonconducting	30	0.78
Alumina (96%)	Nonconducting	24.7	0.78
Sapphire	Nonconducting	32–35	0.74–0.78
Borosilica glass	Nonconducting	0.9–1.2	0.80–0.83

## 20.7 Frequency Selective Limiter

When an RF signal travels through a magnetic material the magnetic moments precess. If the RF signal is strong enough then the RF magnetic moments can interact and launch what is called a spin-wave as the interfering magnetic moments react to the large signal. If the RF signal is small enough then the spin wave does not occur as the rotating magnetic moments are effectively not aware of each other. The spin waves are very lossy and large RF powers are dissipated into the substrate. One of the special characteristics is that a complex RF signal comprising small and large RF signals with different frequencies will dissipate the large RF signals while leaving the smaller signals unaffected. A device based on this phenomenon is the frequency selective limiter (FSL) [32–37]. A microstrip FSL is shown in [Figure 20.21\(a\)](#) where the strip of the microstrip line is on a magnetized magnetic film such as YIG. A typical RF spectrum at the input of the line is shown in [Figure 20.21\(b\)](#), where the limiting threshold is indicated. Above the threshold power, spin waves are excited and power is lost to the lattice, resulting in the power-limited spectrum shown in [Figure 20.21\(c\)](#).

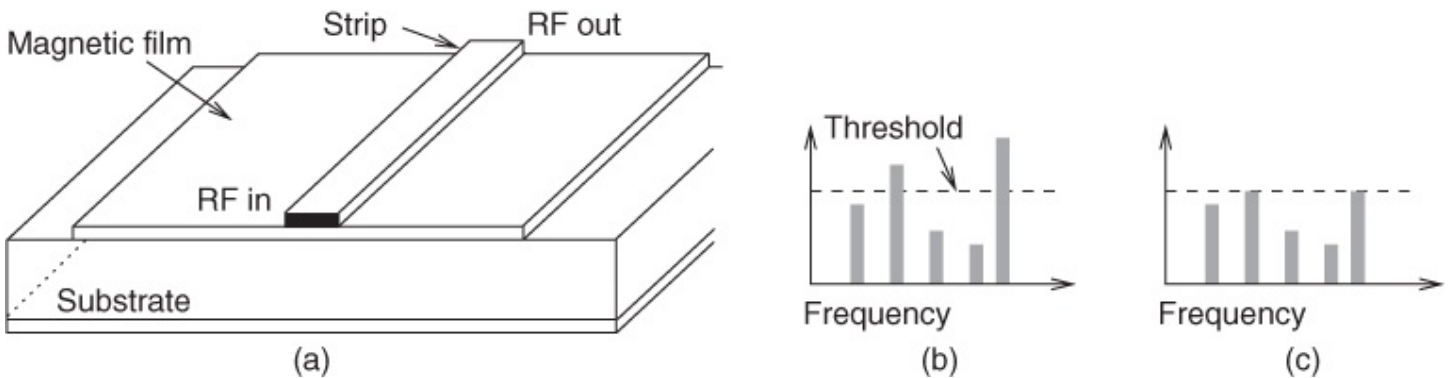


**Figure 20.21** A microstrip frequency selective limiter: (a) with the strip on a magnetized magnetic film; and (b) spectrum of the input RF signal showing the limiting threshold; and (c) spectrum of the output RF signal.

## 20.8 Summary

Both magnetized and unmagnetized magnetic materials have extraordinary properties that lead to microwave components with unusual behavior. The principal microwave components that can be developed are nonreciprocal components that allow signal transmission in one direction but not the other. The special properties of magnetic materials derive from quantum mechanical effects related to the alignment of elementary magnetic moments. The alignment leads to the minimum energy state in some materials and results in a permeability that depends on the direction of magnetic fields and results in coupling of the magnetic field component in one direction to a magnetic component in another direction.

## References

- [1] M. Obol and C. Vittoria, “Magnetic properties of  $\text{Co}_2\text{Y}$ -type hexaferrite particles oriented in a rotating field,” *IEEE Trans. on Magnetics*, vol. **39**, no. 5, pp. 3103–3105, May 2003.
- [2] T. Kato, H. Mikami, and S. Noguchi, “Performance of Z-type hexagonal ferrite core under demagnetizing and external static fields,” *Journal of Applied Physics*, vol. **108**, no. 3, p. 033903, 2010.
- [3] V. G. Harris, “Modern microwave ferrites,” *IEEE Trans. on Magnetics*, vol. **48**, no. 3, pp. 1075–1104, Mar. 2012.
- [4] A. G. Gurevich and G. A. Melkov, *Magnetization Oscillations and Waves*. CRC press, 1996.
- [5] D. D. Stancil and A. Prabhakar, *Spin Waves*. Springer, 2009.
- [6] R. C. O’Handley, *Modern Magnetic Materials: Principles and Applications*. Wiley New York, 2000.

- [7] B. D. Cullity and C. D. Graham, *Introduction to Magnetic Materials*. John Wiley & Sons, 2011.
- [8] N. A. Spaldin, *Magnetic Materials: Fundamentals and Applications*. Cambridge University Press, 2010.
- [9] D. Polder, “On the theory of ferromagnetic resonance,” *Philosophical Magazine*, vol. **40**, no. 300, pp. 99–115, 1949.
- [10] B. Rejaei and M. Vroubel, “Suppression of skin effect in metal/ ferromagnet superlattice conductors,” *Journal of Applied Physics*, vol. **96**, no. 11, pp. 6863–6868, 2004.
- [11] I. Iramnaaz, H. Schellevis, B. Rejaei, R. Fitch, and Y. Zhuang, “Self-biased low loss conductor featured with skin effect suppression for high quality RF passives,” *IEEE Trans. on Magnetics*, vol. **48**, no. 11, pp. 4139–4142, Nov. 2012.
- [12] D. Masse and R. Pucel, “Microstrip propagation on magnetic substrates—part II: experiment,” *IEEE Trans. on Microwave Theory and Techniques*, vol. **20**, no. 5, pp. 309–313, May 1972.
- [13] R. Pucel and D. Masse, “Microstrip propagation on magnetic substrates—part I: design theory,” *IEEE Trans. on Microwave Theory and Techniques*, vol. **20**, no. 5, pp. 304–308, May 1972.
- [14] J. Pan, M. Shih, and L. Riley, “High performance millimeter-wave microstrip circulator for deep space communications,” in *1990 IEEE MTT-S Int. Microwave Symp. Digest*, May 1990, pp. 1015–1017.
- [15] R. Kane and T. Wong, “An edge-guide mode microstrip isolator with transverse slot discontinuity,” in *1990 IEEE MTT-S Int. Microwave Symp. Digest*, May 1990, pp. 1007–1010.
- [16] M. Steer, *Microwave and RF Design: a Systems Approach*, 2nd ed. SciTech Pub., 2013.
- [17] B. Dieny, V. S. Speriosu, S. S. Parkin, B. A. Gurney, D. R. Wilhoit, and D. Mauri, “Giant magnetoresistive in soft ferromagnetic multilayers,” *Physical Review B*, vol. **43**, no. 1, p. 1297, 1991.
- [18] K. Rao, F. Humphrey, and J. Costa-Krämer, “Very large magneto-impedance in amorphous soft ferromagnetic wires,” *Journal of Applied Physics*, vol. **76**, no. 10, pp. 6204–6208, 1994.
- [19] Y. Pomeau and P. Manneville, “Intermittent transition to turbulence in dissipative dynamical systems,” *Commun. Math. Phys.*, vol. **74**, no. 2, pp. 189–197, 1980.
- [20] L. Panina, K. Mohri, K. Bushida, and M. Noda, “Giant magneto-impedance and magneto-inductive effects in amorphous alloys,” *Journal of Applied Physics*, vol. **76**, no. 10, pp. 6198–6203, 1994.

- [21] L. Panina, K. Mohri, T. Uchiyama, M. Noda, and K. Bushida, “Giant magneto-impedance in Co-rich amorphous wires and films,” *IEEE Trans. on Magnetics*, vol. **31**, no. 2, pp. 1249–1260, Feb. 1995.
- [22] M. Vazquez and A. Hernando, “A soft magnetic wire for sensor applications,” *Journal of Physics D: Applied Physics*, vol. **29**, no. 4, p. 939, 1996.
- [23] S. Jin, T. H. Tiefel, M. McCormack, R. Fastnacht, R. Ramesh, and L. Chen, “Thousandfold change in resistivity in magnetoresistive La-Ca-Mn-O films,” *Science*, vol. **264**, no. 5157, pp. 413–415, 1994.
- [24] A. Antonov and I. Iakubov, “The high-frequency magneto-impedance of a sandwich with transverse magnetic anisotropy,” *Journal of Physics D: Applied Physics*, vol. **32**, no. 11, p. 1204, 1999.
- [25] N. Sato, Y. Endo, and M. Yamaguchi, “Skin effect suppression for Cu/CoZrNb multilayered inductor,” *Journal of Applied Physics*, vol. **111**, no. 7, p. 07A501, 2012.
- [26] M. Yamaguchi, N. Sato, and Y. Endo, “Skin effect suppression in multilayer thin-film spiral inductor taking advantage of negative permeability of magnetic film beyond FMR frequency,” in *2010 European Microwave Conf.*, 2010, pp. 1182–1185.
- [27] J. Wu and Y. Yoon, “A low ohmic loss radial superlattice conductor at 15 GHz using eddy current canceling effect,” in *IEEE Antenna and Propagation Society Int. Symp.*, 2013, pp. 1552–1553.
- [28] J. Wilkerson, K. Gard, and M. Steer, “Electro-thermal passive intermodulation distortion in microwave attenuators,” in *36th European Microwave Conf.*, Sep. 2006, pp. 157–160.
- [29] J. Wilkerson, K. Gard, A. Schuchinsky, and M. Steer, “Electro-thermal theory of intermodulation distortion in lossy microwave components,” *IEEE Trans. on Microwave Theory and Techniques*, vol. **56**, no. 12, pp. 2717–2725, Dec. 2008.
- [30] J. Wilkerson, P. Lam, K. Gard, and M. Steer, “Distributed passive intermodulation distortion on transmission lines,” *IEEE Trans. on Microwave Theory and Techniques*, vol. **59**, no. 5, pp. 1190–1205, May 2011.
- [31] J. Wilkerson, I. Kilgore, K. Gard, and M. Steer, “Passive intermodulation distortion in antennas,” *IEEE Transactions on Antennas and Propagation*, vol. **63**, no. 2, pp. 457–467, Feb. 2014.
- [32] S. N. Stitzer and H. Goldie, “A multi-octave frequency selective limiter,” in *1983 IEEE MTT-S Int. Microwave Symp. Digest*, 1983, pp. 326–328.
- [33] J. Adams and S. Stitzer, “Frequency selective limiters for high dynamic range microwave applications,” *IEEE Trans. on Microwave Theory and Techniques*, vol. **41**, no. 12, pp. 2227–2231, 1993.

- [34] P. Phudpong and I. C. Hunter, “Frequency-selective limiters using nonlinear bandstop filters,” *IEEE Trans. on Microwave Theory and Techniques*, vol. **57**, no. 1, p. 157–164, Jan. 2009.
- [35] J. D. Adam and F. Winter, “Magnetostatic wave frequency selective limiters,” *IEEE Trans. on Magnetics*, vol. **49**, no. 3, pp. 956–962, Mar. 2013.
- [36] C. Collado, A. Hueltes, E. Rocas, J. Mateu, J. Booth, J. O'Callaghan, and J. Verdu, “Absorptive limiter for frequency-selective circuits,” *IEEE Microwave and Wireless Components Letters*, vol. **24**, no. 6, pp. 415–417, Jun. 2014.
- [37] J. Adam, “Mitigate the interference: Nonlinear frequency selective ferrite devices,” *IEEE Microwave Magazine*, vol. **15**, no. 6, pp. 45–56, Jun. 2014.

<sup>1</sup> In CGS units the magnetization is  $M_{\text{CGS}}$  in units of emu/cm<sup>3</sup> or  $4\pi M_{\text{CGS}}$  in units of gauss. In CGS this  $M$  or  $4\pi M$  is also sometimes called the volume magnetization to distinguish it from mass magnetization where the magnetization is normalized to its mass.

# Chapter 21

## Interconnects for Digital Systems

### 21.1 Introduction

In this chapter we present a treatment of the analysis and design of transmission line networks in digital systems. As it is not clear at first whether a connection in a digital system must be treated as a transmission line network or as a connection with resistances and capacitances only, it is usual to refer to digital connections as interconnections. The analysis and design of interconnects on printed circuit boards follows the approach discussed throughout this book. On-chip lines are very lossy and the need to compact connections is also extremely important. On-chip interconnects present an extreme situation and so this chapter is mostly focused on this situation. However, the lessons learned and insight gained also apply to digital interconnects in packages and on printed circuit boards.

### 21.2 Overview of On-chip Interconnects

Up to the early 1990s on-chip digital signals had components much below 1 GHz, relatively short run lengths (constrained by the dimensions of the chip), widths of several microns, and a thickness of a micron or more. The first two factors resulted in the electrical lengths of on-chip interconnects being much less than a wavelength of the signals present (i.e., of the highest frequency components present). Then an interconnect could be adequately modeled as a shunt lumped capacitance. A series resistance completed the model (a so-called *RC* model), but this was small because of the relatively large cross-sections of the interconnect.

This situation has changed because of three main developments, primarily for digital circuits, but affecting analog circuitry because of mixed signal systems. The main developments are:

- faster clocks, of a few gigahertz
- multiple on-chip clocks with local clocks of around 10 GHz
- longer interconnects as the lateral dimensions of large chips are around 2 cm
- fine lithography leading to interconnects having cross-sectional dimensions of less than a micron.

The consequences of these developments are that *RC* modeling is not always adequate. However, on-chip digital interconnects are highly irregular and densely packed, and often do not even approximate interconnections of uniform transmission line segments.

The typical arrangement of interconnects is shown in [Figure 1.13](#). The first metal layer here is tungsten and provides local interconnect with short interconnect lengths of small cross-section. Higher level interconnects use lower resistivity metal, here copper, and have larger cross-

sections, thus further reducing line resistance. Greater attention is made to the provision of signal return paths at the higher metal levels. The higher level metal lines also have lower coupling to the silicon which, having finite conductivity (but not very high), is a significant source of loss. Copper diffuses into silicon dioxide ( $\text{SiO}_2$ ) and into silicon (Si) with disastrous effects so that barriers are required. For example, titanium nitride (TiN) and tantalum (Ta) are used [1].

The provision of signal return paths for digital and mixed signal chips has only been a recent consideration and then only for a few connections. The exceptions are clock distribution networks and other long connections (such as certain data buses) where signal integrity is paramount. Another important characteristic was that little attention was given to providing signal return paths. In contrast, with RF and microwave chips it has always been considered necessary to provide current return paths so that the electromagnetic field produced by a signal on an interconnect is uniform, contributing to well-defined electrical characteristics, hence the term controlled impedance interconnect. Such an interconnect could be conveniently modeled as a transmission line. With RF and microwave chips there are relatively few active devices and so the provision of interconnects large enough (to effectively minimize interconnect resistance) and of defined ground planes for good current return paths can be accommodated at reasonable cost.

The characterization and modeling required for these interconnects are the main subjects of this chapter. The main issues to be resolved in this chapter are as follows:

- When is it necessary to model an interconnect as an *RLC* circuit?
- When is it necessary to use a transmission line model?
- What is the significance of the current return path?
- How do the characteristics of interconnects vary with clock frequency?

### **21.2.1 Types of On-chip Interconnects**

On-chip interconnects have several distinguishing characteristics that can be used in determining the type of modeling required. It needs to be emphasized that an interconnect is not just a wire connection from one point in a circuit to another. There is always a current return path and this path (and its proximity to the signal path) is equally important in determining the electrical characteristics of the interconnect. Electromagnetic fields between the two conductors making up a single interconnection between two points and anything that interferes with this field will have an effect on signals being transmitted. Two obvious physical conjectures establish that there must be a return path: without it charges would build up at some point in the circuit to very high levels. In addition, the electric field supported by the charges (and induced by the voltage source originally) on the signal conductor of an interconnect must terminate on matching charges, and these are located on the signal return path. A signal interconnect is usually a conductor that is constrained in its transverse dimensions, but this is not the case with the signal return path. If a ground plane carries the return signal, then the return path can be as wide as the ground plane at DC, but as the

frequency of the signal increases, the width of the current return path narrows as the charges on the signal return path have limited time to redistribute. The return path at high frequencies tends to be as close to the interconnect bearing the signal as possible. The proximity, and metal width available, can significantly affect the resistance, capacitance, and inductance of the interconnect.

On-chip interconnects can be broadly classified by the type of signals conveyed, and geometrical and circuit characteristics as described below.

Interconnect networks (or *nets*) on digital chips can be categorized by the type of connections made:

**i. Local connections with maximum lengths of 1–3 mm**

The majority of connections on a chip are of this type. The utilization of space is a premium and so minimum line widths are used as dictated by the technology and these are in the range of tens to hundreds of nanometers. These lines have high resistance and are driven by transistors of minimum dimensions, and hence of low current drive capability, and have high output (or drive) impedance  $Z_{DRV}$ . It is not economical to provide metal for individual signal return paths. These local interconnects can carry signals clocking at 10 GHz or more.

**ii. Medium length connections with minimum lengths of 1–3 mm**

The maximum usable length is determined by the characteristics of the technology and of the interconnect itself (e.g., width and hence resistance). Typically, the maximum usable length is around 2–5 mm. The longer usable length is achieved principally by making the line wider, but also by paying attention to the current return path. Higher current drivers with lower  $Z_{DRV}$  are required.

**iii. Long connections up to a chip-edge in length**

There are three families of connections that are in this category, each with different characteristics. However, what they have in common is that the drivers of these connections must have high current capability and low  $Z_{DRV}$ , so that the receiver (at the end of the line) switches correctly when the signal makes its first transition down the line. The families are:

- Data buses: these are often wide (meaning that there are many parallel interconnections, perhaps 256 bits wide, for example) and can be about half the chip-edge in length. Their purpose is to convey data from one part of a chip to another, such as from the central processor to an on-chip data cache. Such lines switch at the same time and coupling of the lines is a considerable concern, also the delay on the lines is affected by the switching pattern, as will be seen in [Section 21.3.1](#). Another characteristic of these lines is that they have a small load at the end as they are often driving one or a few receivers.
- Control lines: these transmit signals that must be widely distributed. A good example is a reset signal. There are relatively few of these types of lines with speed issues being

less important.

- Clock signal: this must be widely distributed with integrity of the signal being paramount. As well as ensuring first incidence switching, the clock skew, that is, the difference between the arrival times of the clock edges in different parts of the chip, must be precisely controlled. The clock distribution net can consume a very large proportion of the chip power both because of the gates that are driven at the end of the clock distribution net and because of efforts required to minimize skew.

Many long nets have intermediate buffers along them to boost the signal to compensate for attenuation of the signal. They are clocked at lower frequencies than the signals confined to local regions.

#### iv.

##### *Power and ground distribution buses*

It is perhaps unusual to think of the power and ground buses as interconnects as the voltage on them is, hopefully, constant. However, these buses carry large switching currents that change at the clocking frequency. The pulsing current transmits a signal just as real as do voltage variations. With fast chips it is necessary to model and design these as high-speed interconnections. Ideally these nets are of very low impedance so that the current fluctuations have little effect on voltage levels. Low impedance can be achieved using metal planes for supply and ground, and by large capacitors between the supply and ground nets.

Interconnects for digital signals can be contrasted to interconnects for other types of signals. The density of analog and RF circuits does not approach that of digital circuits and in any event controlling the characteristics of transistors (impedance levels, pole frequencies etc.) is critical to the performance of these frequency-sensitive circuits.

Microwave and millimeter-wave on-chip circuits usually have interconnections that are a substantial portion of a wavelength, but also have ground planes or similar structures forming a highly regular signal return path. Thus, transmission line modeling is necessary and is also convenient.

## 21.3 *RC* Modeling of On-chip Interconnects

The reason for modeling interconnects is to verify signal integrity and provide an insight into allowing redesign if necessary. The ultimate goal of course is to take electrical specifications and to develop the physical layout requirements, but this is not as well developed as would be liked. The main signal integrity issues are:

- Will the chip operate at the rated speed? Is the timing correct, that is, do the signals at the receiver end of a net arrive at the required switching levels within the timing budget?
- Is signal integrity adequate, that is, is crosstalk within acceptable levels?

- Will it perform reliably (reliability includes electromigration and fuse effects, as well as signal integrity issues)?

Modeling on-chip interconnect effects is daunting as there are millions of nets on a typical digital IC and the ultimate clock speed of a circuit is determined by the slowest of these interconnects and the nets that have the highest crosstalk. An idea of the complexity can be seen by examining the interconnects involved in a single CMOS inverter, shown in [Figure 21.1](#).

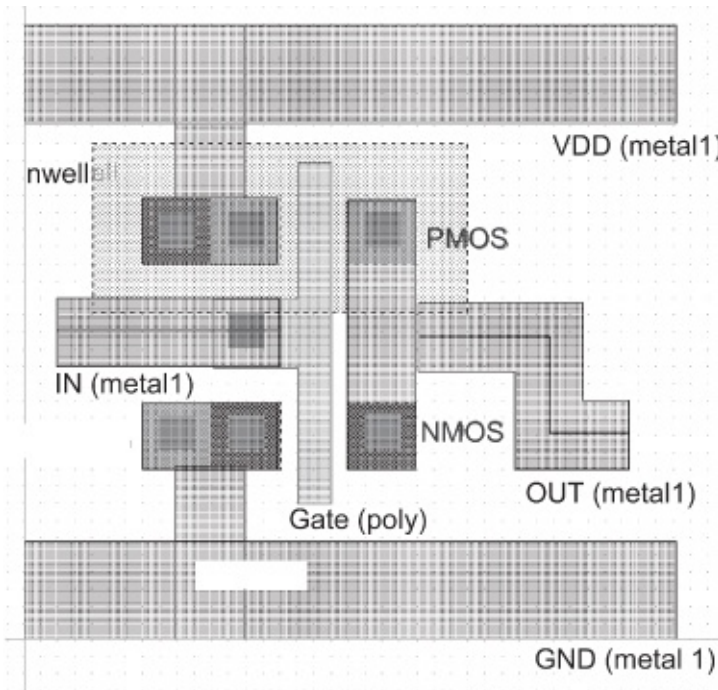


[Figure 21.1](#) The layout of a CMOS inverter.

It is clearly not possible to incorporate the interaction of every net on every other one so the signal integrity verification problem is driven by the need to minimize the modeling complexity as much as possible. This is done by first identifying those nets, the critical nets, that are most likely to cause a problem and to model these. These nets are not assured of actually being problems, but if there is a problem we can have a very high confidence that the problem net will be one of the critical nets. Critical nets are identified using relatively loose criteria, but are still sophisticated enough that only a small fraction of the total number of nets are so identified. The critical nets are then examined in considerable detail to determine if there is a signal integrity violation. Thus, in a second pass, the *at risk* nets are identified. Generally, the *at risk* nets must be examined by a human to evaluate whether or not there is a signal integrity violation.

The simplest electrical models that will capture the effect are used, for example, in increasing complexity: a simple delay model, an *RC* model consisting of resistors and capacitors only, an *RLC* model consisting of inductors as well, and finally a distributed transmission line model. These types of models are discussed below.

### 21.3.1 Delay Modeling

Nearly all of the drivers on a chip are sized near their minimum functional dimensions and so have their current-drive capability limited. The consequence of this is that a driver driving a net does not appear like a linear driver, but instead as sourcing or sinking essentially a fixed current until the desired voltage level is obtained. Thus the voltage on a short interconnect only rises according to the rate at which charge is sourced or sunked from the line, and the time required to charge to the desired voltage level is proportional to the capacitance of the interconnect. Thus the delay on a line is directly related to the time constant of the line, which is equal to the time for a single-pole circuit, an  $RC$  circuit for example, to change by  $(1 - 1/e) \approx 65\%$  of the total change that will occur. Typically, this is about the voltage change required to alter the logic state of a digital circuit. The total effective time constant  $\tau_T$  of a series cascaded circuit with  $K$  poles with time constant  $\tau_k$  for the  $k$ th pole is, approximately,

$$\tau_T = \sum_{k=1}^K \tau_k \quad 21.1$$

where the  $k$ th time constant is

$$\tau_k = R_k C_k. \quad 21.2$$

$R_k$  is the resistance of the  $k$ th segment of interconnect and  $C_k$  is the capacitance of that segment so that an estimate for the delay  $t_d$  through such a circuit is

$$t_d = \tau_T = \sum_{k=1}^K \tau_k. \quad 21.3$$

Thus a good delay model of the cascaded circuit is

$$t_d = \sum_{k=1}^K R_k C_k. \quad 21.4$$

Equation (21.1) only gives us an estimate of the effective overall time constant of a circuit and there are restrictions on its validity. The primary restriction is that it is useful when the individual time constants  $\tau_k$  are comparable. However, it provides the best simple estimate of timing.

Short lines can be modeled by considering the  $RC$  representation of the output of a driver and dividing the line into just two segments. If  $R_L$  and  $C_L$  are the total line resistance and capacitance, respectively, then the delay, derived from what is called the Elmore delay model [2], is

$$\begin{aligned} t_d &= R_D C_D + (R_L/2)(C_L/2) + (R_L/2)(C_L/2) \\ &= R_D C_D + (R_L C_L)/2 \end{aligned} \quad 21.5$$

where  $R_D$  is the output resistance of the driver and  $C_D$  is its parasitic output capacitance. This is generalized for a net so that the following formula has traditionally been used for short lines

[3]:

$$t_d = R_D C_D + (R_N C_N)/2 \quad 21.6$$

where  $R_N$  and  $C_N$  are the net resistance and effective capacitance respectively. Thus  $R_D C_D$  can be referred to as the gate delay and  $(R_N C_N)/2$  as the interconnect delay. For very short nets the resistance and capacitance of the net are negligible and the first term in Equation (21.6) dominates. In other words, gate delay dominates for very short nets.  $C_N$  in Equation (21.6) is the driving point capacitance (the effective capacitance seen by the driver) and because of capacitive coupling to neighbouring nets  $C_N$  will be data-dependent, varying according to the switching activity on neighbouring nets.

If the driven net can be considered as a single transmission line, with resistance and capacitance per unit length of  $R$  and  $C$ , respectively, and length  $\ell$ , then  $R_N = R\ell$  and  $C_N = C\ell$  so that the simple delay model of Equation (21.6) becomes

$$t_d = R_D C_T + (RC\ell^2)/2 \quad 21.7$$

indicating that the delay increases in proportion to the square of the length of the line. However, for very short nets the gate delay dominates and length-dependent delay becomes a problem for medium to long length lines.

Unless specific considerations are made at the design stage, nets are strongly coupled to neighbors. If  $J$  neighbors are regarded as being significantly coupled then the worst case situation, resulting from the worst possible data switching pattern, results in the driving point capacitance  $C_N$  of the  $i$ th net being

$$C_N = C_{ii} \sum_{\substack{j=1 \\ i \neq j}}^J r_j C_{ij} = C_{ii} \left( 1 + \sum_{\substack{j=1 \\ i \neq j}}^J r_j K_{ij} \right) \quad 21.8$$

where  $C_{ij}$  is the mutual capacitance of the  $i$ th and  $j$ th nets,  $C_{ii}$  is the self-capacitance (or just the capacitance alone) of the  $i$ th net,  $K_{ij} = C_{ij}/C_{ii}$  is the capacitive coupling factor, and  $r_j$  is the capacitance multiplier:

$r_j = 0$ ,	if the $j$ th net switches concurrently with the $i$ th net (i.e., they are at the same voltage).
$r_j = 1$ ,	if the $j$ th net stays at a constant level while the victim line switches from low to high.
$r_j = -1$ ,	if the $j$ th net stays at a constant level while the victim line switches from high to low.

Thus the worst case situation, resulting from the worst possible data-switching pattern, with the highest effective capacitance is

$$C_N = C_{ii} \left( 1 + \sum_{\substack{j=1 \\ i \neq j}}^J K_{ij} \right).$$

$K_{ij}$  is strongly influenced by the proximity of the  $i$  th and  $j$  th nets, and by the provision of current return paths (or ground) that can partly shield the nets and reduce  $K_{ij}$ . However, if care is not taken and many nets are significantly coupled to each other, the driving point capacitance can be many times the self-capacitance of the victim net ( $C_{ii}$  for the  $i$  th net). Capacitive coupling along with inductive coupling (which will be considered later) dominate the performance of long and medium length lines. This is especially so since there are relatively few nets of these types and low impedance drivers with higher current drive capability (both resulting from larger output transistors) ensure that the gate delay is very small.

The highest performance digital circuits use specific strategies to reduce coupling by providing a current return path (or ground) as nearby medium-to-long nets as possible. Specific strategies include reserving on-chip layers from ground planes and using differential lines such as the CPS line discussed in [Section 14.8.4](#). These strategies, especially the provision of one or more ground planes, have long been the practice with printed wiring boards and with multichip modules.

To summarize, the delay model discussed here is useful for interconnects with drivers of limited current capability so that the voltage on the interconnect must rise gradually as the line is charged. Faster signal transmission is achieved using a large driver which functions as a voltage source transmitting a “logic-level” voltage signal down the line. The delay is determined more by time-of-flight considerations.

### 21.3.2 RC Modeling

The first step in developing an  $RC$  model is to develop the capacitance model of a subset of nets. As the density of nets is very large, it is not sufficient to consider a net in isolation. Neither is it feasible to consider the interaction of a net with every other net on the chip. A successful approach is to focus on the signal integrity of one net due both to the delay effects and to crosstalk from other nets. Fortunately the electromagnetic properties help us here. A voltage- and current-carrying interconnect generates electric and magnetic, or electromagnetic, fields which fall off with distance as  $1/R^N$  where  $R$  is distance and  $N$  is between 1 and 2. (The fields do not fall off much faster as the electric and magnetic fields are essentially confined in a plane.) This is the justification for considering a region of influence such as that shown in [Figure 21.2](#). Here the region of influence (the box) is centered on an individual net, the victim net. It is assumed that every conductor within the region of influence will be coupled to the victim net. The capacitances describing this coupling are generally developed using a number of template models. For example, if the victim net and another net cross each other (the nets having  $x$  and  $y$  orientations, respectively) a parallel-plate capacitor model is used for the capacitance. The templates of a large of number of simple structures that can commonly occur are generally developed in advance for a particular process. The templates could consist of precise data, each template developed for a structure of a particular geometry, and a very large

number of templates are needed. Alternatively, fewer templates of the polynomial type with geometry variables such as separation distance could be used and the coefficients of the polynomials developed by fitting to electromagnetic simulation of several variants of a particular template structure. With the multiple metal composition of interconnects and fabrication-dependent dielectric density variations, these templates should be calibrated with actual measurements. Pattern recognition is used to identify candidate structures (that match a template). If the two nets run parallel to each other then a standard capacitance calculation is performed, again essentially another parallel-plate capacitance calculation, but using fringing capacitance corrections. These capacitance templates are typically developed using 3D electromagnetic simulation codes to build up a standard library.

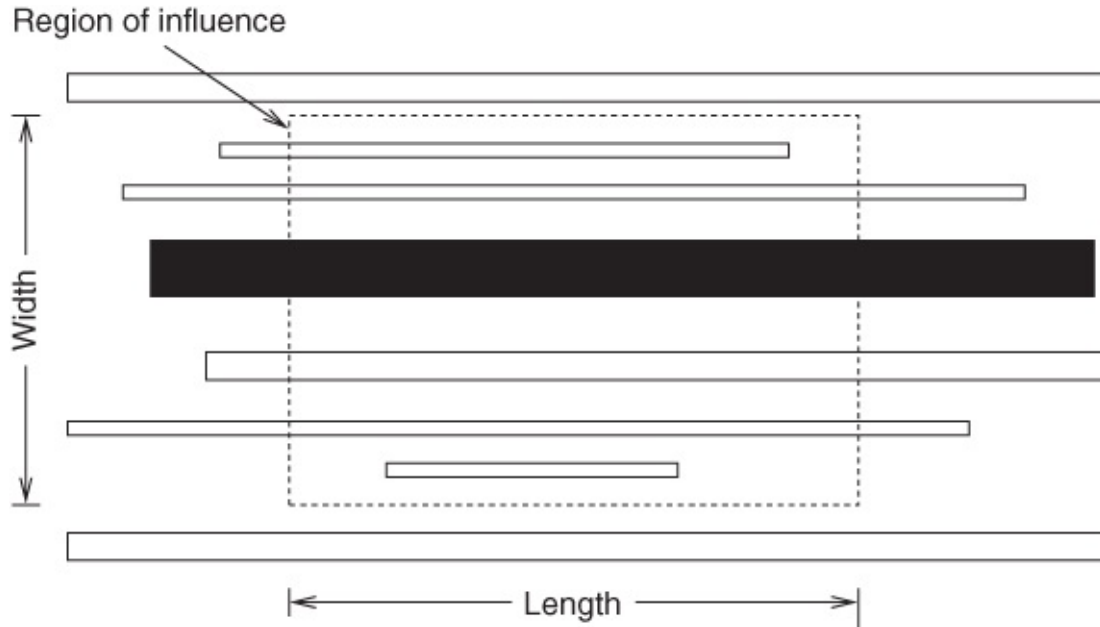


**Figure 21.2** Neighboring nets and the region of influence used in capacitance extraction.

It is not really practical to use electromagnetic simulation to develop a capacitance matrix for each net with its neighbors, although this can be done for the most critical nets. Modeling proceeds by meshing the interconnect structure, as shown in [Figure 21.3\(a\)](#) and [\(b\)](#) for the CMOS inverter considered previously. Here each interconnect is subdivided into a large number of segments. The coupling effect of each segment on every other segment is evaluated and the capacitance matrix extracted following a number of measurement-like simulations to extract one capacitance at a time. The procedure to extract the capacitance matrix is described in [Section 10.2.4](#). A faster electromagnetic analysis can be developed by considering zero-thickness metallization, as shown in [Figure 21.3\(c\)](#) (resistance of the interconnect is correctly handled by treating it as a surface resistance). However, this is not sufficiently accurate for today's high-aspect ratio digital interconnects. The use of templates is the only practical approach for performing parasitic extraction in reasonable time.

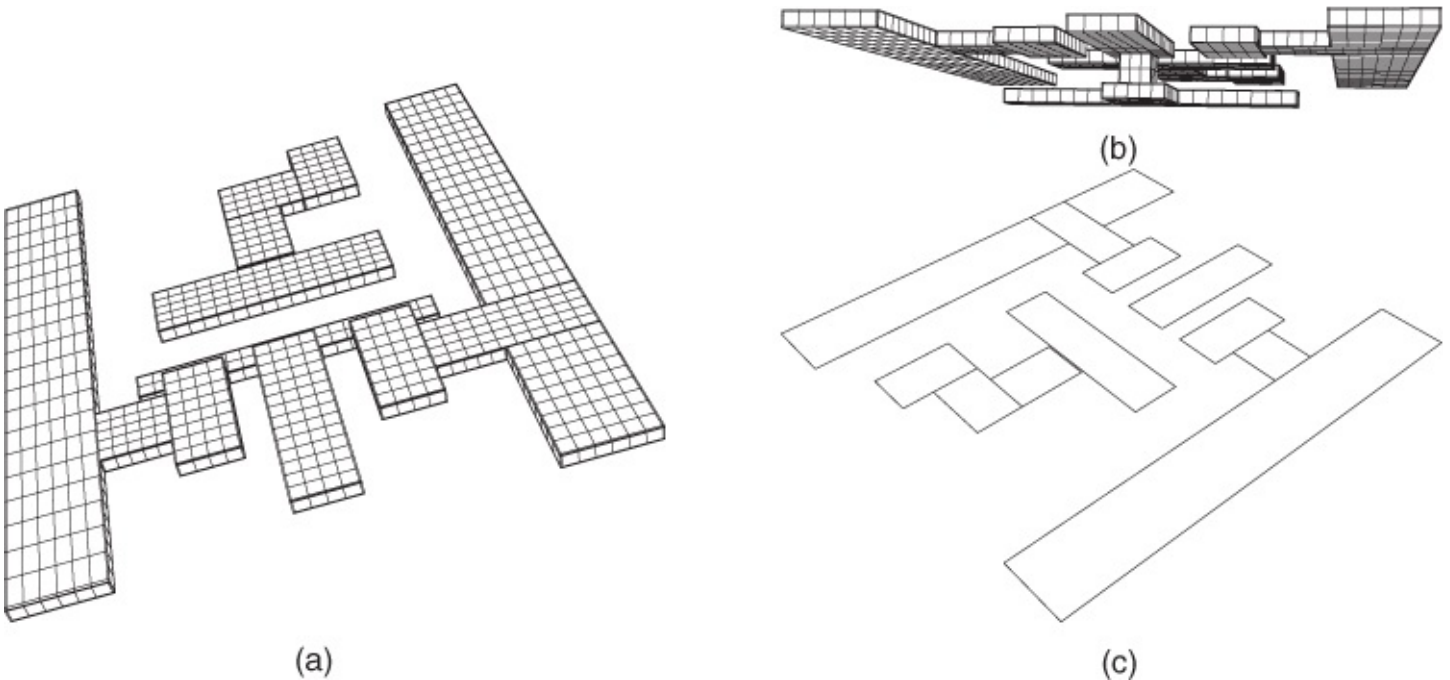


**Figure 21.3** The interconnects of the CMOS inverter of [Figure 21.1](#): (a) top view; (b) bottom view; and (c) a top view with a different perspective and the lines treated as though they had zero thickness.

The accurate calculation of resistance is a much simpler problem than the extraction of capacitances. This is because nets can be considered on their own and mutual resistances (through the substrate or dielectric layers) are negligible. We simply use the resistivity of the conductors and the cross-sectional dimensions of the interconnect. Note, however, that resistance in the (generally) shared current return paths can have a significant effect on coupling due to the common impedance effects discussed in [Section 2.13.1](#).

*RC* extraction is a database manipulation problem with issues such as

- storage of geometric data and relating that to each active device so that the electrical model can be recalculated without performing another parasitic extraction
- support of hierarchical electrical model data, such as starting with a delay model, then replacing this by a capacitance-only model, then a resistor-capacitor model, and so on
- ability to quickly develop circuit models of selected nets or regions
- support of incremental extraction to handle only the changed regions of an IC.

## 21.4 Modeling Inductance

Modeling the inductance of long high-performance digital interconnects is now required. Nets of this type are relatively few, but they include the on-chip clock distribution net. For these nets *RLC* modeling (an excellent approximation of a transmission line as far as digital interconnects are concerned) must be used. The aggressive nets are either constructed as signal lines over a ground plane (a microstrip structure) or with shield lines between neighboring signal lines to

form a CPW-like structure. In both cases the aim is to achieve a well-controlled signal return line. It is possible to achieve very high performance from nets without a reference conductor following in tandem with each signal net, but this requires extremely good design discipline and model extraction tools. For structures with reference conductors, extracting inductances is much easier than it would be otherwise. Complicated structures without the reference conductors require full-wave 3D electromagnetic field solutions [4].

### **21.4.1 When are Inductance Effects Important?**

The signal response on an interconnect depends on the properties of the interconnect as well as the characteristics of the driver. In nearly every situation the driver, through design or otherwise, appears as either a Thevenin equivalent voltage source with a voltage step generator and an equivalent driver impedance  $Z_{DRV}$ , or as a current source of fixed current drive which charges a line. With the latter type of driver, when the voltage on the line corresponds to the appropriate logic level, the current source turns off. The highest performance is obtained using the Thevenin equivalent driver as this has the greatest chance of resulting in first incidence switching at the retardation time. This type of driver must be relatively large so that it can provide the current levels to support a full voltage signal traveling away from the driver. The current sourcing (or sinking) capability is equal to the voltage change to be imposed on the line divided by the characteristic impedance of the line. So if the voltage change required to change the logic level is 3 V and the characteristic impedance of the line is 50  $\Omega$ , the current drive capability is 60 mA. This reduces to 20 mA if  $Z_0$  is 100  $\Omega$  and the level change is 2 V. Thus, reducing the operating voltage and using interconnects of high characteristic impedance ( $Z_0$ ) is important in limiting current drive levels to reasonable values. The required current drive levels are further increased by the resistive divider effect of the driver output impedance  $Z_{DRV}$ . Thus it is also important to keep  $Z_{DRV}$  low. For most on-chip drivers it is not feasible to provide the current drive levels required to generate a full level voltage signal on the line, so instead they operate as fixed current sources until the required voltage levels on the line are obtained. This restricts such drivers to short connections, as then the slow  $RC$ -like response is not critical to determining system performance.

In a series of significant papers [5–7] Deutsch and her colleagues presented definitive studies that answer the question as to when inductive effects must be considered. The developments below draw heavily on this work.

We begin by considering a lossy line of infinite extent and derive the characteristic of the line and then the response to a voltage step at the start of the line. The voltage on the line,  $v(x, t)$ , and the current on the line,  $i(x, t)$ , are conveniently represented by the phasor voltage  $\mathbf{V}(x)$  and phasor current  $\mathbf{I}(x)$  when the signal on the line is sinusoidal. Thus the relationship between the voltage and current is described by two coupled first-order differential equations:

$$\frac{d\mathbf{V}}{dx} = -Z\mathbf{I}$$

**21.10**

and

$$\frac{dI}{dx} = -YV$$

where  $x$  is the distance along the line,  $Z = R + j\omega L$ ,  $Y = G + j\omega C$ , and  $R$ ,  $L$ ,  $C$ , and  $G$  are the resistance, inductance, capacitance, and conductance of the line per unit length. Weber [8] ignored the conductivity  $G$  and solved the coupled equations, Equations (21.10) and (21.11), and transformed the solution into the time-domain. The result is that the time-domain voltage response to a unit voltage step at the start of the line (i.e., at  $x = 0$ ) at a position  $x = \ell$  along the line and at time  $t$  is

$$v(\ell, t) = \left( e^{-R\ell/(2Z_0)} + \frac{R\ell}{2Z_0} \int_{\tau=\ell\sqrt{LC}}^t \left\{ \frac{e^{-R\ell/(2Z_0)}}{\sqrt{\tau^2 - \ell\sqrt{LC}}} \right. \right. \\ \times I_1 \left[ \frac{R}{2Z_0} \sqrt{\tau^2/(LC) - \ell^2} \right] d\tau \left. \right\} \right) \times u(t - \ell\sqrt{LC}) \quad 21.12$$

where  $I_1$  is the modified Bessel function of the first kind. Introducing the retardation concept (referring to the finite time of flight of signals) time  $\tau_0$ , which is the earliest time a signal can be detected at  $x = \ell$ , and using the following definitions:

$\beta_0$	$= \omega\sqrt{LC}$	the lossless propagation factor
$\tau_0$	$= \ell\sqrt{LC}$	the retardation time
$\alpha_C$	$= R/\sqrt{LC}$	the conductive attenuation
$\alpha'_C$	$= \alpha_C = R\ell/\sqrt{LC}$	the conductive attenuation factor

the waveform response of Equation (21.12) becomes (after some rearrangement)

$$v(\ell, t) = e^{-\alpha'_C t} [1 + v_T(\ell, t)] u(t - \tau_0) \quad 21.13$$

where  $v_T(\ell, t)$  is the unattenuated transient response:

$$v_T(\ell, t) = \int_{\tau=\tau_0}^t \left\{ \frac{I_1 \left[ \alpha'_C \sqrt{(\tau/\tau_0)^2 - 1} \right]}{\sqrt{(\tau/\tau_0)^2 - 1}} \right\} d\tau. \quad 21.14$$

Using the time normalized to the retardation time,  $t' = t/\tau_0$  and  $\tau' = \tau/\tau_0$ , this equation becomes:

$$v_T(\ell, t) = \int_{\tau'=1}^{t'/\tau_0} \left\{ \frac{I_1 \left[ \alpha'_C \sqrt{(\tau')^2 - 1} \right]}{\sqrt{(\tau')^2 - 1}} \right\} d\tau'. \quad 21.15$$

A wealth of information is contained in this response:

- i. There is no response before the retardation time,  $\tau_0$ , as the step function  $u$  is defined as:

$$u(t - \tau_0) = \begin{cases} 0 & t < \tau_0 \\ 1 & t \geq \tau_0 \end{cases}$$

21.16

It is a physical necessity that there can be no response before the time of flight. This can be contrasted to a circuit consisting of  $R$  s,  $L$  s, and  $C$  s. There will always be an instantaneous response, even if it is very small. Simplifying the model will just make the anomalously early response worse.

**ii.** The response is scaled by the overall attenuation:

$$e^{-\alpha'_C} = e^{-\alpha_C \ell} = e^{R\ell/(2Z_0)}. \quad 21.17$$

At a critical length  $\ell_{\text{crit}} = 2Z_0/R$  the attenuation is  $1/e = 37\%$ . At lengths above this it is difficult to achieve first incidence switching [9]. As the loss of the line increases,  $Z_0$  remains relatively unchanged but the attenuation increases.

**iii.** The term in the integral describes the effect of the response due to the interaction of  $R$ ,  $L$ , and  $C$ .

**iv.** The time duration of the transient response is essentially related to the normalized times. Thus, approximately, the transient response at a position  $x = 2\ell$  has twice the duration it does at  $x = \ell$ .

**v.** The form of the transient response is determined by two terms which we will examine separately. Let

$$T_F(\tau') = \frac{1}{\sqrt{(\tau')^2 - 1}} \quad 21.18$$

and

$$T_S(\tau') = I_1 \left[ \alpha'_C \sqrt{(\tau')^2 - 1^2} \right] \quad 21.19$$

so that

$$v(\ell, t) = e^{-\alpha'_C} \left\{ 1 + \int_{\tau'=1}^{\tau'} [T_F T_S d\tau'] \right\} u(\tau' - 1). \quad 21.20$$

$T_F$  and  $T_S$  are different components of the transient response, with  $T_F$  being independent of the resistance of the line and capturing the fast rising  $LC$  transient response of the line. In addition,  $T_S$  is dependent on the resistance of the line. It is interpreted as capturing the slow  $RC$  response of the line [5].

If the total resistance ( $R\ell$ ) of the line is low the transient response is initially dominated by  $T_F$ , the  $LC$  response, as  $T_S$  has little effect. Thus with low resistance or a short distance from the driver (i.e., low  $R\ell$ ), the initial transient has overshoot as  $v_T$  is additive to the direct retarded response. Eventually this response is damped as  $T_S$  becomes significant. With high overall

resistance (low  $R\ell$ ), longer lines, or larger  $R$ , then  $T_S$  dominates the transient response, and the rise time of the response is degraded with the transient resembling an  $RC$  response.

### 21.4.2 Inductance Extraction

Extracting the inductances of a group of interconnects is a much more difficult problem than that of capacitance extraction. This is because the current return paths must be known as well as the current flow through the net itself. This contrasts with the capacitance extraction problem where the possible location of charges is all that needs to be known. Capacitance derives from storage of energy in the electric field and almost all of these lines conveniently terminate on conductors. It is therefore possible to limit the scope of the problem using a region of influence as discussed in [Section 21.3.2](#). The return path that must be determined in inductance extraction is not confined just to conductors, but includes displacement currents through coupling capacitors. Inductance, which describes the energy storage capability of magnetic fields, requires that the majority of magnetic fields be included, and unfortunately these can extend for considerable distances. Leaving out more distant interactions does, as expected, lead to a less accurate model but, what is particularly worrisome, leads to unstable interconnect models [4].

There are two dominant approaches used in inductance extraction. The first we will consider uses 3D magnetostatic numerical analysis [10–12]. The term “magnetostatic” rather than “electromagnetic” is used as in the analysis only magnetic interactions are considered. While not as comprehensive as a full electromagnetic analysis, analysis can be performed in a reasonable time and leads directly to the desired inductance-only circuit. In the magnetostatic techniques the conductors are segmented into current filaments or sheets and the interaction of one filament (or sheet) with other filaments (or sheets) calculated. In the light of the previous discussion the obvious drawback is that the current return paths must be known to ensure that all of the relevant interactions are known.

The major alternative to the numerical field analysis above is the partial element equivalent circuit (PEEC) technique used to extract partial inductances 3, [4, 13, 14]. The distinguishing characteristic of this technique is that the current return paths do not need to be known.

## 21.5 Clock Distribution

The performance of a digital integrated circuit is determined by the speed of the clock signal. While small regions of digital integrated circuit can clock well over 10 GHz, global clock distribution is limited to just a few gigahertz (e.g., 3.6 GHz) [15–19]. The global clock is distributed using a transmission line-based distribution network in an architecture that ensures that the same phase of the clock is delivered to each part of the circuit.

Of all the nets on a digital integrated circuit, the clock distribution net benefits the most from a transmission line synthesis approach as the timing characteristic of the clock system is a major market differentiator. Low skew, low jitter, and fast edge rates are the major considerations. Also clock distribution consumes 40–60% of the total chip power. Consequently, the

manufacturers of high-performance chips devote significant design resources to the design of the clock distribution network.

Clock distribution is one of the most difficult challenges facing the designer of high-speed digital chips. Clock skew and jitter targets become more difficult to meet when clocking at higher frequencies. (Clock skew is the difference in the time at which the leading or falling edges of a clock reach different nodes on chip. Ideally the leading and falling edges reach every part of the circuit at the same time so that there is zero skew.) Designs need to be partitioned if a high-speed clock with low skew cannot be distributed across the chip. The partitioning of the design necessarily compromises performance and this complicates design methodologies. One of the suggestions for coping with the difficulty of distributing a high-speed low-skew clock across a chip is to use a relatively slow global clock and fast local clocks [20, 21].

Various regions of a digital chip have their own local clock synchronized to the global clock using phased locked loops. However, in nearly every situation it would be preferable to distribute the high-speed clock across the whole chip. One of the major concerns with conventional clock distribution architectures and synchronous design is that the major parts of a circuit switch at nearly the same time, resulting in very large current drain from the supply. It is estimated [20] that the switching currents will peak at 1000 A unless tightly controlled global clock skews are utilized to avoid simultaneous switching.

There are several different schemes that enable the leading or falling edge to reach circuit elements at about the same time. The most common distribution scheme is shown in [Figure 21.4](#) and is known as the H tree clock distribution net. In this scheme, clock edges propagate outwards from a centralized source that is usually phase locked to an external clock. The final clock loads, mainly the inputs of flip-flops, are at the leaf nodes of the tree. Intermediate buffers are inserted to keep the clock edge fast, maintain voltage levels, and reduce skew. Interconnects are carefully sized so as to minimize skew due to differential RC delays. Jitter is mainly a function of the power and ground noise present at the phase lock loop and buffers, and is thus controlled mainly by careful power supply decoupling.

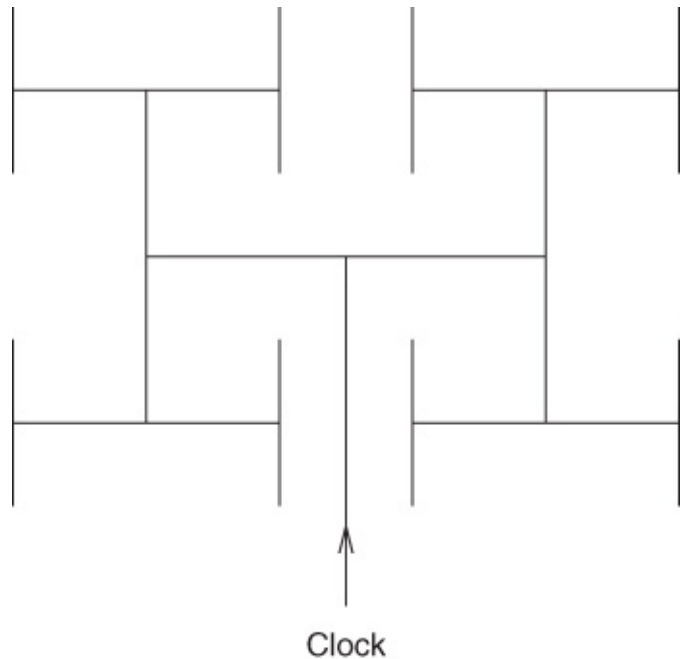


**Figure 21.4** The conventional H tree clock distribution architecture.

A traditional microwave perspective, although not strictly applicable here, is as follows. Each of the centrally driven interconnects branches into more interconnects, and so on. The design objective is to avoid generating a reflected wave at the interconnect junctions. One approach is to match the incoming interconnect to the (possibly) multiple outward going interconnects. Matching can be done through appropriate design of the characteristic impedances of the interconnects. It is difficult to carry this process beyond one junction as the widths of the subsequent lines become unreasonably narrow to achieve the required high characteristic impedance. In narrowband amplifier design this is not difficult as reactive elements can be used to achieve the reflectionless condition. An alternative, as already mentioned, is to use buffers, especially at the interconnect junctions, so that reflections are not an issue. Such a buffered clock distribution network is shown in [Figure 21.5](#).

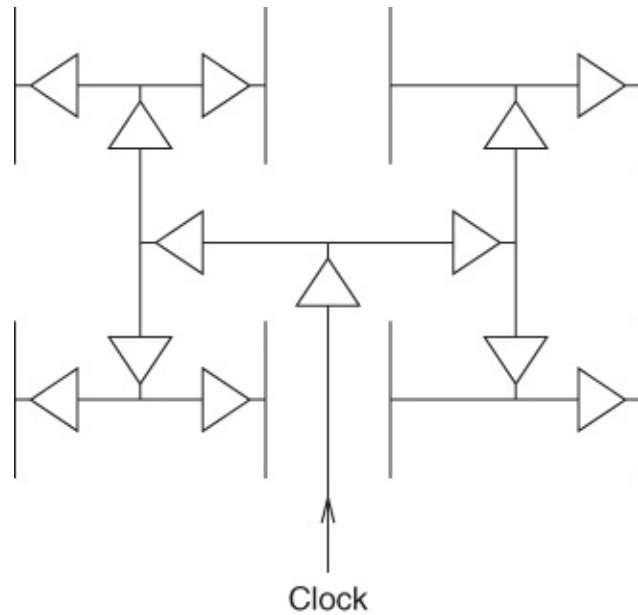


**Figure 21.5** The conventional H tree clock distribution with digital buffer amplifiers.

Ignoring for the moment the time-of-flight distance from the clock feeds (at the extremities of the tree) to the gates, the clock skew for a perfectly designed tree would be zero. Even then, clock skew is introduced by coupling of noise into the clock distribution net, and careful design of the clock interconnect and its environment is required. Differential distribution of the clock signal reduces the impact of digital switching noise.

In the traditional forward-traveling wave approach just discussed, a large amount of energy is dissipated principally in two mechanisms. First, energy is used by the central clock driver and subsequent buffers to charge and discharge the clock lines. Second, the end terminations of the clock lines must totally absorb (i.e., dissipate) the power of the incoming signals so that there are no reflections. The power dissipated in the clock distribution net and the power dissipated by the terminating nodes are about equal. All of the signal power on the line is required to define the leading and falling edges of the clock, even though this power is largely dissipated to prevent reflections. In addition, any signal coupled into the clock distribution line will lead to jitter on the clock signal and the need to tolerate clock skew. Variable loading on the clock distribution net also leads to clock skew.

The comments above lead to two important trains of thought. The first is that the overall power consumed in the clock tree would be reduced by avoiding the necessity to dissipate power (to eliminate reflections). The second is that there is no resilience in the clock distribution net to the effects of clocking and variable loading. Resilience would come from having energy that is committed to maintaining the integrity of the clock signal so that variable coupling to other circuitry has a relatively small effect. Differential transmission line design would also reduce the undesired coupling. The buffered differential clock distribution architecture is shown in [Figure 21.6\(a\)](#) with the differential clock commonly implemented using CPS or differential line shown in [Figure 21.6\(b\)](#). The CPS line could have one of the strips grounded, thus providing the signal return path, or the CPS could be fully differential and neither strip comprising the CPS has a special relationship to ground.

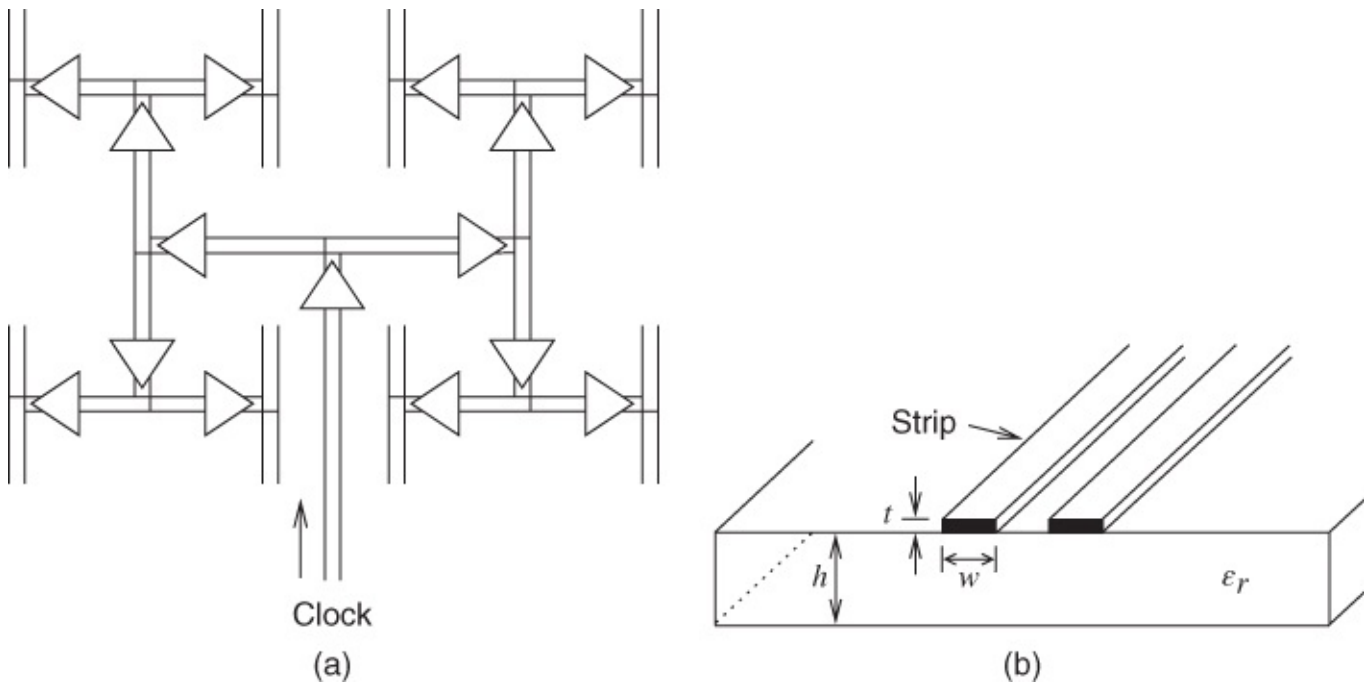


**Figure 21.6** A differential H tree clock distribution: (a) architecture; and (b) a CPS line or differential line often used with this architecture.

## 21.6 Resonant Clock Distribution

Clock distribution consumes 40–60% of the power for a high-speed digital circuit so it is not surprising that considerable effort has been devoted to developing alternative schemes for distributing the clock signal. One category of resonant clocking scheme is based on standing waves appearing on an augmented transmission line structure [22–26]. One clock distribution scheme that addresses the energy consumption issue is the salphasic clocks system [25, 26]. In this system a sinusoidal standing wave provides the clock reference. In the simplest implementation, a backplane connecting PCBs, a single transmission line is driven near its center and terminated at its ends in a reactive load. Buffers tapping signals from this resonant line then form clock pulses that are in sync. A similar scheme has been attempted on-chip. The central problem is that the clock reference has a sinusoidal variation, and hence low slope edges. Thus there are problems in establishing low-skew leading and falling edges. The central feature of the approach is that energy in the standing wave establishes a clock reference, and only the energy necessary to drive buffer amplifiers is consumed.

An alternative clocking scheme, called a traveling or rotary wave clock, is based on traveling waves circulating on a continuous transmission line loop [22, 27–31]. The rotary clock distribution architecture shown in [Figure 21.7](#) achieves lower skew gigahertz-speed clocking at significantly lower power levels than does a conventional clock distribution scheme. [Figure 21.7\(a\)](#) is a layout for a 2.5 GHz rotary clock having 25 interconnected rings. In [Figure 21.7\(a\)](#) there are four rings on the top row, then three, and the pattern is repeated. Each ring is essentially identical with the details of a ring shown in [Figure 21.7\(b\)](#). The rings consist of differential lines, as shown in [Figure 21.7\(b\)](#), each conductor of which is joined to each other

periodically by anti-parallel inverters. (The clock signal would normally be taken from the ring as a differential signal, as indicated in [Figure 21.7\(b\)](#).) This produces a clock wave that rotates around the ring. It is easy at first to associate this with an oscillator comprised of a ring of gates. However, in a ring oscillator the oscillating signal is input to one inverter and the output of that is input to a subsequent inverter and so on. In this structure (the ring oscillator) the clock power is dissipated at each inverter input and regenerated at each output. In the rotary clock the anti-parallel inverter pair serves to top up the clock edge as it passes.

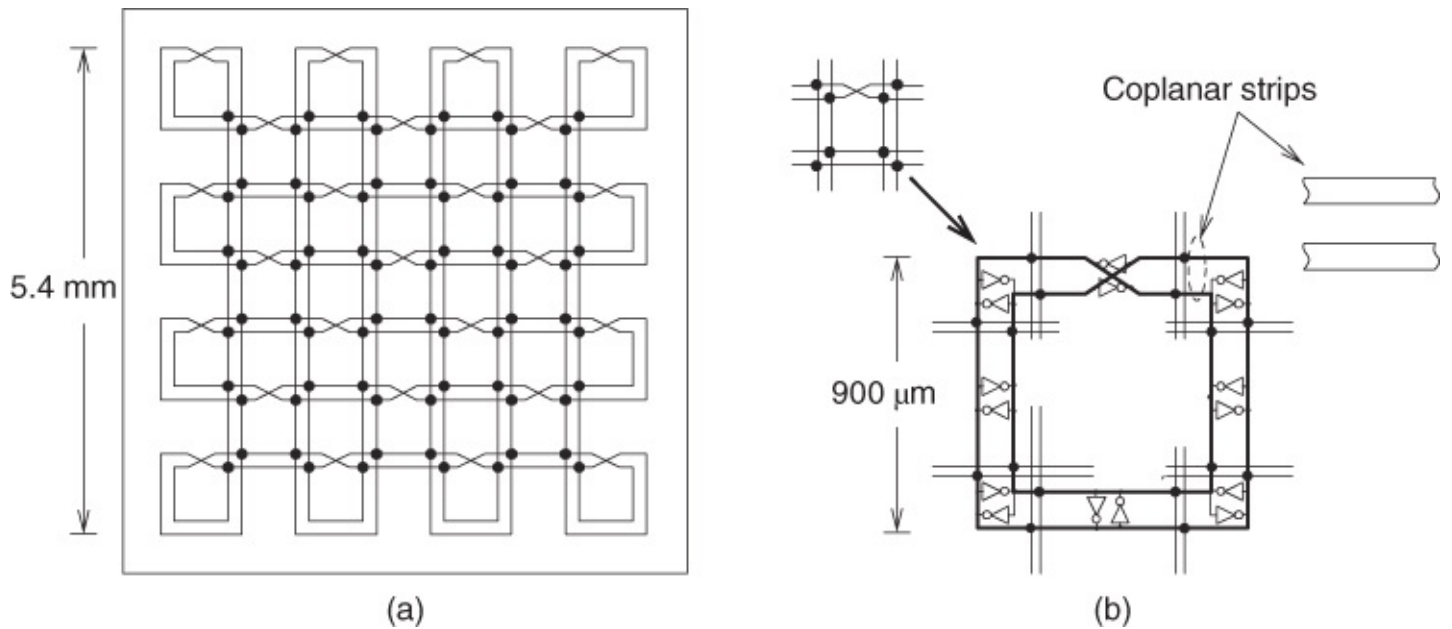


**Figure 21.7** A rotary clock: (a) layout of a 2.5 GHz oscillator with 25 interconnected rings of differential lines; (b) details of one ring showing anti-parallel inverter pairs and an inset showing CPS line (or differential line) with strip width of 30  $\mu\text{m}$  and strip separation of 60  $\mu\text{m}$ . Adapted from Wood *et al.* (2001) [27], figure 25.5.1, p. 401. Reprinted with permission of IEEE.

The essential characteristic of differential or CPS line is that the signal is carried on the conductors comprising the differential line and the two conductors, and the signals on them (except for being opposite in sign) are identical. This arrangement makes this type of line relatively immune to noise. The signal on the differential line is not floating, and because of this the outputs of the inverter pair driving the signals on the lines are either at the supply, say  $V_{DD}$ , or at ground 0 V. Thus a voltage that changes from  $V_{DD}$  to 0 V on one line, say line 1, is input to one of the anti-parallel diodes, which ensures that there is a transition from 0 V to  $V_{DD}$  on the other conductor, line 2. Similarly, the 0 V to  $V_{DD}$  transition on line 2 reinforces the  $V_{DD}$  to 0 V transition on line 1. The clock signal so generated rotates around the ring, and the clock frequency is set by the electrical length of the ring.

## 21.7 Summary

Transmission lines for digital signals appear on-chip, in a module with multiple chips either tiled or stacked as a 3D integrated circuit (3DIC), or on a printed circuit board. In all cases

compactness is a premium, which means that the coupling of interconnects is rarely negligible. The term “interconnect” is usually the preferred use as not all connections can or need to be treated as transmission lines. Perhaps the interconnects are so lossy that modeling them using resistances and capacitances is adequate. Still, there are many situations where the integrity of a signal must be maintained and this is done by providing a well-defined signal return path and controlling the characteristic impedance of the interconnect. This is of most importance for long runs of busses on chip, clock distribution on and off chip, and for nearly all connections on a printed circuit board.

## References

- [1] R. Gutmann, “Advanced silicon IC interconnect technology and design: present trends and RF wireless implications,” *IEEE Trans. on Microwave Theory and Techniques*, vol. **47**, no. 6, pp. 667–674 , Jun. 1999.
- [2] W. C. Elmore, “The transient response of a damped linear network with particular regard to wideband amplifier,” *J. Applied Physics*, vol. **19**, no. 1, pp. 55–63, 1948.
- [3] D. D. Ling and A.E. Ruehli, “Interconnect modeling,” in *Advances in CAD for VLSI, Vol. 3 —Part II: Circuit Analysis, Simulation and Design*, A. Ruehli, Ed. North Holland, 1987, pp. 211–291.
- [4] P. Restle, A. Ruehli, and S. Walker, “Dealing with inductance in high-speed chip design,” in *Proc. 36th Design Automation Conf.*, 1999, pp. 904–909.
- [5] A. Deutsch, G. V. Kopcsay, V. A. Ranieri, J. K. Cataldo, E. A. Galligan, W. S. Graham, R. P. McGouey, S. L. Nunes, J. R. Paraszczak, J. J. Ritsko, R. J. Serino, D. Y. Shih, and J. S. Wilczynski, “High-speed signal propagation on lossy transmission lines,” *IBM Journal of Research and Development*, vol. **34**, no. 4, pp. 601–615, Jul. 1990.
- [6] A. Deutsch, G. V. Kopcsay, C. W. Surovic, B. J. Rubin, L. M. Terman, R. P. Dunne, T. A. Gallo, and R. H. Dennard, “Modeling and characterization of long on-chip interconnections for high-performance microprocessors,” *IBM Journal of Research and Development*, vol. **39**, no. 5, pp. 547–567, Sep. 1995.
- [7] A. Deutsch, W. Becker, G. Katopis, H. Smith, P. Restle, P. Coteus, C. Surovic, G. Kopcsay, B. Rubin, R. Dunne, T. Gallo, K. Jenkins, L. Terman, R. Dennard, and D. Knebel, “Design guidelines for short, medium, and long on-chip interconnections,” in *IEEE 5th Topical Meeting Electrical Performance of Electronic Packaging*, Oct. 1996, pp. 30–32.
- [8] E. Weber, *Linear Transient Analysis*. John Wiley & Sons, 1965.
- [9] C. W. Ho, D. A. Chance, C. H. Bajorek, and R. E. Acosta, “The thin-film module as a high-performance semiconductor package,” *IBM Journal of Research and Development*, vol. **26**, no. 3, pp. 286–296, May 1982.

- [10] J. Wang, J. Tausch, and J. White, “A wide frequency range surface integral formulation for 3-D RLC extraction,” in *1999 IEEE/ACM Int. Conf. Computer-Aided Design, Digest of Technical Papers*, 1999, pp. 453–457.
- [11] M. Kamon, N. Marques, Y. Massoud, L. Silveira, and J. White, “Interconnect analysis: from 3D structures to circuit models,” in *Proc. 36th Design Automation Conf.*, 1999, pp. 910–914.
- [12] Y. Liu, L. Pileggi, and A. Strojwas, “A sparse macromodeling method for RC interconnect multiports,” in *Proc. IEEE 1997 Custom Integrated Circuits Conf.*, 1997, May 1997, pp. 163–166.
- [13] A. E. Ruehli, “Inductance calculations in a complex integrated circuit environment,” *IBM Journal of Research and Development*, vol. **16**, no. 5, pp. 470–481, Sep. 1972.
- [14] M. Kamon, F. Wang, and J. White, “Recent improvements for fast inductance extraction and simulation,” in *IEEE 7th Topical Meeting on Electrical Performance of Electronic Packaging*, 1998, Oct. 1998, pp. 281–284.
- [15] D. Pham, S. Asano, M. Bolliger, M. N. Day, H. P. Hofstee, C. Johns, J. Kahle, A. Kameyama, J. Keaty, Y. Masubuchi *et al.*, “The design and implementation of a first-generation CELL processor,” in *2005 IEEE Int. Solid-State Circuits Conf. Digest of Technical Papers*, 2005, pp. 184–592.
- [16] C. Yeh, G. Wilke, H. Chen, S. Reddy, H. Nguyen, T. Miyoshi, W. Walker, and R. Murgai, “Clock distribution architectures: A comparative study,” in *7th Int. Symp. on Quality Electronic Design*, 2006, p. 7.
- [17] V. F. Pavlidis, I. Savidis, and E. G. Friedman, “Clock distribution networks for 3-D integrated circuits,” in *2008 IEEE Custom Integrated Circuits Conf.*, 2008, pp. 651–654.
- [18] E. G. Friedman, “Clock distribution networks in synchronous digital integrated circuits,” *Proc. IEEE*, vol. **89**, no. 5, pp. 665–692, 2001.
- [19] T. Xanthopoulos, *Clocking in Modern VLSI Systems*. Springer, 2009.
- [20] Semiconductor Industry Association. “International Technology Roadmap for Semiconductors, 2013 edn.” (2013). URL <http://www.itrs.net>.
- [21] G. Shamanna, N. Kurd, J. Douglas, and M. Morrise, “Scalable, sub-1W, sub-10ps clock skew, global clock distribution architecture for intel®core i7/i5/i3 microprocessors,” in *2010 IEEE Symp. on VLSI Circuits*, 2010, pp. 83–84.
- [22] F. O’Mahony, C. P. Yue, M. A. Horowitz, and S. S. Wong, “A 10-GHz global clock distribution using coupled standing-wave oscillators,” *IEEE Journal of Solid-State Circuits*, vol. **38**, no. 11, pp. 1813–1820, 2003.
- [23] M. Sasaki, M. Shiozaki, A. Mori, A. Iwata, and H. Ikeda, “17 GHz fine grid clock

distribution with uniform-amplitude standing-wave oscillator,” in *2006 Symp. on VLSI Circuits, Digest of Technical Papers*, 2006, pp. 98–99.

- [24] S. C. Chan, P. J. Restle, K. L. Shepard, N. K. James, and R. L. Franch, “A 4.6 GHz resonant global clock distribution network,” in *2004 IEEE Int. Solid-State Circuits Conf.. Digest of Technical Papers*, 2004, pp. 342–343.
- [25] V. Chi, “Salphasic distribution of clock signals for synchronous systems,” *IEEE Trans. on Computers*, vol. **43**, no. 5, pp. 597–602, May 1994.
- [26] V. L. Chi, “Salphasic distibution of timing signals for the synchronization of physically separated entities,” Feb. 1995, US Patent 5,387,885.
- [27] J. Wood, S. Lipa, P. Franzon, and M. Steer, “Multi-gigahertz low-power low-skew rotary clock scheme,” in *2001 IEEE Int. Solid-State Circuits Conf. Digest of Technical Papers. ISSCC*, 2001, pp. 400–401.
- [28] J. Wood, T. C. Edwards, and S. Lipa, “Rotary traveling-wave oscillator arrays: A new clock technology,” *IEEE Journal of Solid-State Circuits*, vol. **36**, no. 11, pp. 1654–1665, 2001.
- [29] Z. Yu and X. Liu, “Design of rotary clock based circuits,” in *44th ACM/IEEE Design Automation Conf.*, 2007, pp. 43–48.
- [30] V. H. Cordero and S. P. Khatri, “Clock distribution scheme using coplanar transmission lines,” in *Design, Automation and Test in Europe*, 2008, pp. 985–990.
- [31] B. Taskin, J. Wood, and I. S. Kourtev, “Timing-driven physical design for VLSI circuits using resonant rotary clocking,” in *49th IEEE Int. Midwest Symp. on Circuits and Systems*, vol. **1**, 2006, pp. 261–265.

# Appendix A

## Physical and Mathematical Properties

### A.1 SI Units

The main SI units used in RF and microwave engineering are given in [Tables A.1](#), [A.2](#), and [A.3](#). Symbols for SI units are written in upright roman font and a space separates a value from the symbol for the unit (e.g., 5.6 kg). There is an exception for degrees, for example 90 degrees is written  $90^\circ$ . Symbols for units are written in lowercase unless the symbol is derived from the name of a person. An exception is the use of L for liter to avoid possible confusion with l, which looks like the numeral one and the letter  $\ell$ .

**Table A.1** Main SI units used in RF and microwave engineering

SI unit	Name	Usage	In terms of fundamental units
A	ampere	Current (abbreviated as amp)	Fundamental unit
cd	candela	Luminous intensity	Fundamental unit
C	coulomb	Electric charge	$A \cdot s$
F	farad	Electric capacitance	$kg^{-1} \cdot m^{-2} \cdot A^2 \cdot s^4$
g	gram	Weight	$= kg/1000$
H	henry	Inductance	$kg \cdot m^2 \cdot A^{-2} \cdot s^{-2}$
Hz	hertz	Frequency	$s^{-1}$
J	joule	Unit of energy	$kg \cdot m^2 \cdot s^{-2}$
K	kelvin	Thermodynamic temperature	Fundamental unit
kg	kilogram	SI fundamental unit	Fundamental unit
m	meter	Length	Fundamental unit
mol	mole	Amount of substance	Fundamental unit
N	newton	Unit of force	$kg \cdot m \cdot s^{-2}$
$\Omega$	ohm	Electric resistance	$kg \cdot m^2 \cdot A^{-2} \cdot s^{-3}$
Pa	pascal	Pressure	$kg \cdot m^{-1} \cdot s^{-2}$
s	second	Time	Fundamental unit
S	siemens	Admittance	$kg^{-1} \cdot m^{-2} \cdot A^2 \cdot s^3$
V	volt	Voltage	$kg \cdot m^2 \cdot A^{-1} \cdot s^{-3}$
W	watt	Power	$kg \cdot m^2 \cdot s^{-3}$

**Table A.2** Main SI units used in RF and microwave engineering

Symbol	SI unit	SI unit	Name and base units
$E$	volts per meter	V/m	Electric field intensity base unit: $\text{kg} \cdot \text{m} \cdot \text{s}^{-3} \cdot \text{A}^{-1}$
$H$	amps per meter	A/m	Magnetic field intensity
$D$	coulombs per square meter	C/m <sup>2</sup>	$D = \epsilon E$ , electric flux density base unit: kg. $\text{A} \cdot \text{s} \cdot \text{m}^{-2}$
$B$	tesla, webers per square meter	T	$B = \mu H$ , magnetic flux density base unit: $\text{kg} \cdot \text{s}^{-2} \cdot \text{A}^{-1}$
$I$	amp	A	Electric current
$M$	amps per meter	Wb/m	Magnetization base unit: $\text{kg} \cdot \text{m}^{-3} \cdot \text{s}^{-3} \cdot \text{A}^{-1}$
$P$	coulombs per square meter	C/m <sup>2</sup>	Polarization base unit: $\text{kg} \cdot \text{m}^{-3} \cdot \text{s} \cdot \text{A}$
$q_e$	coulomb	C	Electric charge base unit: $\text{A} \cdot \text{s}$
$q_m$	weber	Wb	Magnetic charge base unit: $\text{kg} \cdot \text{m}^2 \cdot \text{s}^{-2} \cdot \text{A}^{-1}$
$\psi_e$	coulomb	C	Electric flux base unit: $\text{A} \cdot \text{s}$
$\psi_m$	weber	Wb	Magnetic flux base unit: $\text{kg} \cdot \text{m}^2 \cdot \text{s}^{-2} \cdot \text{A}^{-1}$
$J$	amps per square meter	A/m <sup>2</sup>	Electric current density
$J_s$	amps per meter	A/m	Surface electric current density
$J_m$	webers per second per square meter	Wb · s <sup>-1</sup> · m <sup>-2</sup>	Magnetic current density base unit: $\text{kg} \cdot \text{s}^{-3} \cdot \text{A}^{-1}$
$J_{ms}$	webers per second per meter	Wb · s <sup>-1</sup> · m <sup>-1</sup>	Surface magnetic current density base unit: $\text{kg} \cdot \text{m} \cdot \text{s}^{-3} \cdot \text{A}^{-1}$
$S$	square meters	m <sup>2</sup>	Surface
$V$	cubic meters	m <sup>3</sup>	Volume
$\epsilon$	farads per meter	F/m	Permittivity base unit: $\text{kg}^{-1} \cdot \text{m}^{-3} \cdot \text{A}^2 \cdot \text{s}^4$
$\mu$	henry per meter	H/m	Permeability base unit: $\text{kg} \cdot \text{m} \cdot \text{s}^{-2} \cdot \text{A}^{-2}$

**Table A.3** SI prefixes

Factor	Symbol	Name	Factor	Symbol	Name
$10^{-24}$	y	yocto	$10^1$	da	deca
$10^{-21}$	z	zepto	$10^2$	h	hecto
$10^{-18}$	a	atto	$10^3$	k	kilo
$10^{-15}$	f	femto	$10^6$	M	mega
$10^{-12}$	p	pico	$10^9$	G	giga
$10^{-9}$	n	nano	$10^{12}$	T	tera
$10^{-6}$	mu	micro	$10^{15}$	P	peta
$10^{-3}$	m	milli	$10^{18}$	E	exa
$10^{-2}$	c	centi	$10^{21}$	Z	zetta
$10^{-1}$	d	deci	$10^{24}$	Y	yotta

## A.2 SI Prefixes

A prefix before a unit indicates a multiple of a unit (e.g., 10 fW is  $10^{-14}$  watts).

## A.3 Physical and Mathematical Constants

Physical and mathematical constants used in microwave engineering are given in [Tables A.4](#) and [A.5](#).

**Table A.4** Physical and mathematical constants in SI units

Parameter	Value	Description
$c$	$299792458 \text{ m} \cdot \text{s}^{-1}$	Speed of light in a vacuum (free space)
$e$	$1.6021765310^{-19} \text{ C}$	Elementary charge (negative of the charge of an electron)
$e$	2.718281828459045	Natural log base
$\gamma$	0.577215664901532	Euler's ratio
$\phi$	1.618033988749894	Golden ratio
$\epsilon_0$	$8.854187817 \times 10^{-12} \text{ F} \cdot \text{m}^{-1}$	Permittivity of a vacuum (free space)
$h$	$6.6260693 \times 10^{-34} \text{ J} \cdot \text{s}$	Planck constant (alt. $\hbar = h/(2\pi)$ )
$k$	$1.3806505 \times 10^{-23} \text{ J} \cdot \text{K}^{-1}$	the Boltzmann constant
$m_e$	$9.1093826 \times 10^{-31} \text{ kg}$	Electron mass
$\mu_0$	$12.566370614 \times 10^{-7} \text{ H} \cdot \text{m}^{-2}$	Permeability of free space = $4\pi \times 10^{-7} \text{ H} \cdot \text{m}^{-2}$
$\pi$	3.14159265358979323846264	Pi
	101325 Pa	Standard atmosphere (pressure)
$\eta$	376.730313461 $\Omega$	Characteristic impedance of vacuum

**Table A.5** Standard temperatures.

Description	Value	In terms of fundamental units
Absolute zero temperature	0 K	Fundamental unit = $-273.15^\circ \text{C}$
Room temperature	290– 298 K	$19\text{--}25^\circ \text{C}$
Standard temperature	290 K	In microwave engineering, different in other disciplines
Available noise of a resistor at room temperature		$-173.92 \pm 0.06 \text{ dBm/Hz}$ (range is due to the range of room temperature, $-174 \text{ dBm/Hz}$ is commonly used)

## A.4 Basis of Electromagnetic SI Units

In this section we present Maxwell's equations and constitutive relations as this enables a comparison to the CGS units considered in the next section. The time-domain forms of Maxwell's equations in the SI unit system are

$$\nabla \times \bar{\mathcal{E}} = -\frac{\partial \bar{\mathcal{B}}}{\partial t} \quad \text{A.1}$$

$$\nabla \times \bar{\mathcal{H}} = \frac{\partial \bar{D}}{\partial t} + \bar{\mathcal{J}} \quad \text{A.2}$$

$$\nabla \cdot \bar{\mathcal{B}} = 0 \quad \text{A.3}$$

$$\nabla \cdot \bar{\mathcal{D}} = \rho_v \quad \text{A.4}$$

and the  $\bar{\mathcal{D}}$  and  $\bar{\mathcal{B}}$  vectors are defined by

$$\bar{\mathcal{D}} = \epsilon_0 \bar{\mathcal{E}} + \bar{\mathcal{P}} = \epsilon_0 \bar{\mathcal{E}} + \epsilon_0 \chi_e \bar{\mathcal{E}} = \epsilon_0 (1 + \chi_e) \bar{\mathcal{E}} = \epsilon \bar{\mathcal{E}} \quad \text{A.5}$$

and

$$\bar{\mathcal{B}} = \mu_0 (\bar{\mathcal{H}} + \bar{\mathcal{M}}) = \mu_0 (1 + \chi_m) \bar{\mathcal{H}} = \mu \bar{\mathcal{H}}. \quad \text{A.6}$$

$\bar{\mathcal{E}}$  is the electric field,  $\bar{\mathcal{D}}$  is now known as the electric displacement,  $\bar{\mathcal{B}}$  is the magnetic induction,  $\bar{\mathcal{H}}$  is the magnetic field,  $\bar{\mathcal{M}}$  is the magnetization,  $\bar{\mathcal{J}}$  is the electric current density,  $\bar{\mathcal{P}}$  is the polarization,  $\rho_v$  is the volumetric charge density,  $\chi_e$  is the electric susceptibility, and  $\chi_m$  is the magnetic susceptibility. The susceptibilities are properties of the material.

## A.5 Relationship of SI Units to CGS Units

Microwave engineers work in SI units while material scientists and physicists usually work in CGS units. The CGS system corresponds more closely to the fundamental properties of particles and fundamental laws. These units are based on centimeter as the unit of length, gram as the unit of mass, and second as the unit of time so with CGS there are just three fundamental units while SI has seven. There are several forms of CGS units and the one we will refer to is the Gaussian system, designated as the CGS (Gaussian) unit systems, and this is the version of CGS mostly used with electromagnetic analysis and for magnetic materials. This is the version we are referring to when using the CGS designation. Keeping with a single unit system is critical in calculations. It is not always easy to convert between the CGS (Gaussian) system and the SI system as for electromagnetic quantities there is not a one-to-one conversion for all quantities. Consider the following time-domain CGS form of Maxwell's equations, which are presented in the CGS system:

$$\nabla \times \bar{\mathcal{E}} + \frac{1}{c} \frac{\partial \bar{\mathcal{B}}}{\partial t} = 0 \quad \text{A.7}$$

$$\nabla \times \bar{\mathcal{H}} - \frac{1}{c} \frac{\partial \bar{D}}{\partial t} = \frac{4\pi}{c} \bar{\mathcal{J}} \quad \text{A.8}$$

$$\nabla \cdot \bar{\mathcal{B}} = 0 \quad \text{A.9}$$

$$\nabla \cdot \bar{\mathcal{D}} = 4\pi \rho_v \quad \text{A.10}$$

and in the CGS system the  $\bar{\mathcal{D}}$  and  $\bar{\mathcal{B}}$  vectors are defined as

$$\bar{D} = \bar{\mathcal{E}} + 4\pi\bar{P} = (1 + 4\pi\chi_e)\bar{\mathcal{E}} = \epsilon\bar{\mathcal{E}} = \epsilon_r\bar{\mathcal{E}}$$

A.11

and

$$\bar{B} = \bar{\mathcal{H}} + 4\pi\bar{M} = (1 + 4\pi\chi_m)\bar{\mathcal{H}} = \mu\bar{\mathcal{H}} = \mu_r\bar{\mathcal{H}}$$
A.12

where  $\bar{\mathcal{E}}$  is the electric field vector,  $\bar{D}$  is known as the electric displacement vector,  $\bar{B}$  is the magnetic induction vector,  $\bar{\mathcal{H}}$  is the magnetic field vector,  $\bar{M}$  is the magnetization,  $\bar{J}$  is the electric current density,  $\bar{P}$  is the (electric) polarization, and  $\rho_v$  is the volumetric charge density. In the CGS system  $\bar{\mathcal{E}}$ ,  $\bar{B}$ ,  $\bar{\mathcal{H}}$ ,  $\bar{M}$ ,  $\bar{J}$ ,  $\bar{D}$ , and  $\bar{P}$  all have the same dimensions and could all be expressed in oersteds. These definitions are significantly different from Maxwell's equations and constitutive relations expressed in SI units. In the CGS system the units that could be assigned to  $\epsilon$  and  $\mu$  (as they are in the SI system) are assigned to the fundamental quantities such as charge and fields. Consequently, for some quantities there are not one-to-one conversions. Some of the more important are given in [Table A.6](#).

**Table A.6** Conversions of electromagnetic CGS (Gaussian) units to SI units.

Quantity	CGS (Gaussian system)		SI		Conversion to SI unit
	Dimension	Unit	Dimension	Unit	$X_{SI}$ is value in SI units, $X_{CGS}$ is value in CGS units
Conductance ( $G$ )	$LT^{-1}$	cm/s	$L^{-2}M^{-1}T^3I^2$	siemen (S)	$G_{SI} \text{ in } S = G_{CGS} 10^9 c^{-2} =  G_{CGS} \text{ in cm} \cdot \text{s}^{-1}  \cdot 1.1126 \cdot 10^{-12}$
Current ( $I$ )	$L^{\frac{3}{2}}M^{\frac{1}{2}}T^{-2}$	esu/s	I	amp (A)	$I_{SI} \text{ in A} = I_{CGS} \cdot 10^{-1} \cdot c =  I_{CGS} (\text{in esu/s})  \cdot 2.997924 \cdot 10^{-9}$
Electric charge ( $Q$ )	$L^{\frac{3}{2}}M^{\frac{1}{2}}T^{-1}$	electrostatic unit (esu)	Tl	coulomb (C)	$Q_{SI} \text{ in C} = Q_{CGS} \cdot 10^{-1} \cdot c =  Q_{CGS} \text{ in esu}  \cdot 2.997924 \cdot 10^{-9}$
Electric field ( $E$ )	$L^{\frac{-1}{2}}M^{\frac{1}{2}}T^{-1}$	statvolt/cm = dyn/esu	$LMT^{-3}I^{-1}$		$E_{SI} \text{ in V/m} = E_{CGS} \cdot 10^{-6}c =  E_{CGS} \text{ in statvolt} \cdot \text{cm}^{-1}  \cdot 2.997924 \cdot 10^4$
Electric potential	$L^{\frac{1}{2}}M^{\frac{1}{2}}T^{-1}$	statvolt = erg/s	$L^2MT^{-3}I^{-1}$	volt (V)	$V_{SI} \text{ in V} = V_{CGS} \cdot c \cdot 10^{-8} =  V_{CGS} \text{ in statvolt}  \cdot 299.7924$
Free space permeability	None	= 1	$L^2MT^{-2}$	H/m	$\mu_0 = 4\pi \cdot 10^{-7} \text{ H/m} = 4\pi \cdot 10^{-7} \text{ Wb} \cdot \text{A}^{-1} \cdot \text{m}^{-1}$
Free space permittivity	None	= 1	$L^{-3}M^{-1}T^4T^2$	F/m	$\epsilon_0 = 1/(c^2\mu_0) = 8.854188 \cdot 10^{-12} \text{ F/m}$ ( $\mu_0$ and $c$ are in SI units)
Magnetic field strength ( $H$ )	$L^{\frac{-1}{2}}M^{\frac{1}{2}}T^{-1}$	oersted (Oe)	$L^{-1}I$	A/m	$H_{SI} \text{ in A/m} =  H_{CGS} \text{ in Oe}  \cdot 1000 \cdot (4\pi)^{-1}$
Magnetic flux ( $\Phi$ )	$L^{\frac{3}{2}}M^{\frac{1}{2}}T^{-1}$	maxwell (Mx)	$L^2MT^{-2}$	weber (Wb)	$\Phi_{SI} \text{ in Wb} =  \Phi_{CGS} \text{ in Mx}  \cdot 10^{-8}$

Magnetic flux density ( $B$ ) (also called magnetic induction)	$L^{\frac{-1}{2}} M^{\frac{1}{2}} T^{-1}$	gauss	$M T^{-2} I^{-1}$	tesla (T)	$B_{SI} \text{ in T} =  B_{CGS} \text{ in gauss}  \cdot 10^{-4}$
Magnetization ( $4\pi M$ )	$L^{\frac{-1}{2}} M^{\frac{1}{2}} T^{-1}$	gauss	$L^{-1} I$	A/m	$M_{SI} \text{ in A/m} =  M_{CGS} \text{ in gauss}  \cdot 1000 \cdot (4\pi)^{-1}$
Magnetization ( $M$ )	$L^{\frac{-1}{2}} M^{\frac{1}{2}} T^{-1}$	emu/cm <sup>3</sup>	$L^{-1} I$	A/m	$M_{SI} \text{ in A/m} =  M_{CGS} \text{ in emu/cm}^3  \cdot 1000$
Magnetic susceptibility ( $\chi_m$ )	—	—	none	—	$\chi_{m,SI} = 4\pi \chi_{m,CGS}$
None	—	—	—	—	—
Resistance ( $R$ )	$L^{-1} T$	s/cm	$L^2 M T^{-3} I^{-2}$	ohm ( $\Omega$ )	$R_{SI} \text{ in } \Omega =  R_{CGS}  \cdot 10^{-9} c^2$ $=  R_{CGS} \text{ in cm}^{-1} \cdot s  \cdot 8.9876 \cdot 10^{11}$
Work, energy ( $W$ )	$L^2 M T^{-2}$	erg	$L^2 M T^{-2}$	joule (J)	$W_{SI} \text{ in J} =  W_{CGS} \text{ in erg}  \cdot 10^7$

In [Table A.6](#) the CGS units have fundamental units of length (L), mass (M), and time (T). For electromagnetic quantities the SI system also uses current (I) as a fundamental unit. In the conversion to the value in terms of SI units (last column),  $c = 2.99792458 \times 10^{10}$  cm/s. In SI  $\mu_r = \mu/\mu_0 = 1 + \chi$ . The  $\mu_r$  used in SI is the same as the CGS  $\mu$ . For example, if the magnetization in CGS units is 100 gauss then it is 7.958 kA/m in SI; if the magnetization in CGS units is 100 emu/cm<sup>3</sup> then it is 100 kA/m in SI. Sometimes the saturation magnetization is expressed in SI units of tesla and really this is the value of  $B$  in saturation, and then  $M_s$  (in tesla) =  $\mu_0 M_s$  (in A/m).

# Appendix B

## Material Properties

Electrical and thermal conductivities, and relative permittivities and permeabilities of common materials encountered in RF and microwave circuits are given in the tables below. Electrical conductivity is the inverse of resistivity,  $\sigma = 1/\rho$ . Where the material parameter is listed as being variable, the physical parameters depend on the formulation of the alloy and typical values are not meaningful. Manufacturers' data sheets for the specific alloys must be consulted.  $\perp$  indicates the property in the direction perpendicular to the crystal axis.  $\parallel$  indicates the property in the direction parallel to the crystal axis. The properties of graphite and sapphire depend strongly on crystal orientation.

Material data is taken from several sources, including the *Standard Reference Data* database of the US National Institute of Standards and Technology [1], the CODATA databases of the International Council for Science, Committee on Data for Science and Technology [2], and references [3–5]. Electrical and thermal properties are functions of temperature. Properties at temperatures other than 300 K should be researched.

**Table B.1** Relative permeability of metals

Material	Relative permeability, $\mu_r$	Material	Relative permeability, $\mu_r$
Aluminum	1.00000065	Nickel	50–600
Cobalt	60	Palladium	1.0008
Copper	0.999994	Permalloy 45	2500
Ferrite (NiZn)	16–640	Platinum	1.000265
Gold	0.999998	Silver	0.99999981
Iron	5000–6000	Steel	100–40000
Lead	0.999983	Superconductors	0
Magnesium	1.00000693	Supermalloy	100000
Manganese	1.000125	Tungsten	1.000068
Mumetal	20000–1000000	Wood (dry)	0.99999942

**Table B.2** Electrical properties of dielectrics and nonconductors

Material	Resistivity, $\rho$	Relative	Loss tangent
	( $M\Omega \cdot m$ (300 K))	permittivity (1 GHz)	$\tan \delta$ (1 GHz)
Air (dry, sea level)	$4 \times 10^7$	1.0005	0.000

Alumina			
99.5%	$> 10^6$	9.8	0.0001–0.0002
96%	$> 10^6$	9.0	0.0006
85%	$> 10^6$	8.5	0.001 5
Aluminum nitride	$10^6$	8.9	0.001
Bakelite	1–100	4.74	0.022
Beryllium oxide (toxic)	$> 10^8$	6.7	0.004
Diamond	$10^5$ – $10^{10}$	5.68	< 0.0001
Ferrite (MnZn)	0.1–10 $\Omega \cdot m$	13–16	0.0004
Ferrite (NiZn)	0.1–12.4	13–16	0.0004
FR-4 circuit board	$8 \times 10^5$	4.3–4.5	0.01
GaAs	1.0	12.85	0.0006
InP	Up to 0.001	12.4	0.001
Glass	$> 1 \times 10^6 \Omega \cdot m$	4–7	0.0003–0.002
Borosilicate	$> 2 \times 10^7 \Omega \cdot m$	6.1	0.00090
BaO/ $\text{Al}_2\text{O}_3$ (Schott AF45)			
Borosilicate	$> 1 \times 10^6 \Omega \cdot m$	4.6	0.00037
BaO (Schott Borofloat 33)			
Mica	$2 \times 10^5$	5.4	0.0006
Mylar	$10^{10}$	3.2	0.005
Paper, white	$3.5 \times 10^6$	3	0.008
Polyethylene	$> 10^7$	2.26	0.0002
Polyimide	$10^{10}$	3.2	0.005
Polypropylene	$> 10^7$	2.25	0.0003
Quartz (fused)	$> 10^{11}$	3.8	0.00075
Sapphire			
//	$> 10^6$	11.6	0.00004–0.00007
$\perp$	$> 10^6$	9.4	0.00004–0.00007
Polycrystalline	$> 10^6$	10.13	0.00004–0.00007
Silicon (undoped)			
Low resistivity (used in CMOS)	50 $\mu\Omega \cdot m$	11.68	0.005
High resistivity	300 $\mu\Omega \cdot m$	11.68	0.005

Carbide (SiC)	100	10.8	0.002
Dioxide (SiO <sub>2</sub> )	$5.8 \times 10^7$	3.7–4.1	0.001
Nitride (Si <sub>3</sub> N <sub>4</sub> )	$10^7$	7.5	0.001
Poly	0.1–10 kΩ·m	11.7	0.005
Teflon (PTFE)	$10^{10}$	2.1	0.0003
Vacuum	∞	1	0
Water			
Distilled	182	80	0.1
Ice (273 K)	1	4.2	0.05
Wood (dry oak)	$3 \times 10^{11}$	1.5–4	0.01
Zirconia (variable)	$10^4$	28	0.0009

**Table B.3** Thermal properties of dielectrics and nonconductors

Material	Thermal conductivity, $k$ (W · m <sup>-1</sup> · K <sup>-1</sup> at 300 K)	Specific heat capacity, $c_p$ (kJ · kg <sup>-1</sup> · K <sup>-1</sup> at 25°C)	Density, $\rho$ (g · cm <sup>-3</sup> at 25°C)
Air (dry, sea level)	0.026	1.005	0.0018
Alumina (Al <sub>2</sub> O <sub>3</sub> )			
99.5%	26.9–30	0.78	3.8
96%	24.7	0.78	3.8
85%	16	0.92	3.5
Aluminum nitride	285	0.74	3.28
Bakelite (wood filler)	1.4	1.38	1.25–1.36
Beryllium oxide (toxic)	64–210	1.75 (at 0°C)	1.85–2.85
Diamond	1 000–2 000	0.52–0.63	3.50–3.53
Ferrite (MnZn)	3.5–5	0.7–0.8	4.9
Ferrite (NiZn)	3.5–5	0.75	4.5
FR-4 circuit board	0.16–0.3	0.6	1.3–1.8
Graphite	25–470	0.71–0.83	1.3–2.27
GaAs	50–59	0.37	5.32
InP	68	0.31	4.81
Glass	0.8–1.2	0.5–0.84	2.0–8.0

Mica	260–750	0.5	0.72
Mylar (polyethylene-terephthalate)	0.08	1.19	1.4
Paper (white bond)	40–90	1.4	0.72
Polyethylene	0.42–0.51	2.3–2.9	2.30
Polyimide	0.12	1.09–1.15	1.43
Polypropylene	0.35–0.40	1.7–2.0	0.855
Quartz (fused)	1.30–1.44	0.67–0.74	2.20
Sapphire			
//	35	0.74–0.78	4.05
⊥	32	0.74–0.78	4.05
Polycrystalline	31–33	0.74–0.78	3.97–4.05
Silicon (undoped)			
Low resistivity (CMOS)	100–150	0.705	2.34
High resistivity	100–150	0.705	2.34
Carbide (SiC)	350–490	0.75	2.55
Dioxide ( $\text{SiO}_2$ )	1.4	1.0	2.27–2.63
Nitride ( $\text{Si}_3\text{N}_4$ )	28	0.711	3.44
Polysilicon	12.5–157	0.71–0.75	2.2–2.3
Teflon (PTFE)	0.20–0.25	0.97	2.1–2.2
Vacuum	0	0	0
Water			
Distilled	580	4.18	0.997
Ice (at 273 K)	2.22	2.05	0.917
Wood (dry oak)	170	2	0.6–0.9
Zirconia (variable)	1.7–2.2	0.40–0.50	5.6–6.1

**Table B.4** Thermal and electrical properties of conductors. For single-element metals these properties are those of single crystals. Best fabricated metal with multiple crystal grains tends to be a few per cent (up to 5%) above that of the single-crystal form. Poorly fabricated metals can have a resistivity twice as high

Material	Electrical	Thermal	Specific heat	Density,	Thermal
	resistivity, $\rho$ ( $\text{n}\Omega \cdot \text{m}$ )	conductivity, $k$ ( $\text{W} \cdot \text{m}^{-1} \cdot \text{K}^{-1}$ )	capacity, $c_p$ ( $\text{kJ} \cdot \text{kg}^{-1} \cdot \text{K}^{-1}$ )	$\rho$ ( $\text{g} \cdot \text{cm}^{-3}$ )	coefficient of resistance

	at 20°C	at 300 K)	at 25°C)	at 25°C	(K <sup>-1</sup> at 20°C)
Aluminum	26.50	237	0.897	2.70	0.004308
Brass	Variable	120	0.38	8.4–8.7	
Bronze	Variable	110	0.38	7.4–8.9	
Chromium	125	93.9	0.450	7.15	
Constantan	500	19.5	0.39	8.9	-0.000008
Copper	16.78	401	0.39	8.94	0.004041
Gold	22.14	318	0.129	19.30	0.003715
Graphite	1200	1950	0.71	2.09–2.23	
// c-axis					
Graphite	41000	5.7	0.71	2.09–2.23	
⊥ c-axis					
Iridium	47.1	147	0.131	22.6	
Iron	96.1	80.2	0.449	7.87	0.005671
Lead	208	35.3	0.127	11.3	
Manganin	430–480	22	0.406	8.4	±0.000015
Mercury	961	8.34	0.139	13.53	
Nickel	69.3	90.9	0.445	8.90	0.005866
NiChrome	1100	11.3	0.432	8.40	0.00017
Palladium	105.4	71.8	0.244	12.0	
Platinum	105	71.6	0.133	21.5	0.003729
Silver	15.87	429	0.235	10.49	0.003819
Solder					
Tin-lead	17.2	34	0.167	8.89	
50% Pb					
50% Sn					
Lead-free	170	53.5	0.23	7.25	
77.2% Sn					
2.8% Ag					
20% In					
Steel,	720	16	0.483	7.48–8.00	
stainless					
Steel, carbon	208	46	0.49	7.85	0.003

(standard)				
Tin	115	66.8	0.227	7.27
Titanium	4 200	21.9	0.522	4.51
Tungsten	52.8	173	0.132	19.3
Zinc	59.0	116	0.388	7.14
				0.004403
				0.003847

**Table B.5** Typical surface roughness and dielectric strength of substrate materials.

Material	Surface roughness ( $\mu\text{m}$ )	Dielectric strength (kV/cm)
Air (dry)	—	30
Alumina:		
99.5%	0.05–0.25	4000
96%	5–20	80–140
85%	30–50	80–140
Sapphire*	32–35	4000
Glass, typical	0.025	280–400
Polyimide	—	70–2480
Quartz, fused ( $\text{SiO}_2$ )	0.006–0.025	200–400
Beryllia ( $\text{BeO}$ ) <sup>†</sup>	64–210	—
Rutile (titanium dioxide)	0.25–2.5	40–80
Ferrite	0.25	$4 \times 10^3$
FR4 circuit board	$\approx 6$	15–30
RT-duroid 5880	0.75–1 <sup>‡</sup>	—
RT-duroid 6002	0.75–1 <sup>‡</sup>	—
RT-duroid 6010	0.75–1 <sup>‡</sup>	—
Si 5 $\text{m}\Omega \cdot \text{cm}$ , low resistivity	0.025	—
Si 30 $\Omega \cdot \text{cm}$ , high resistivity	0.025	300
Si 10 $\text{k}\Omega \cdot \text{cm}$ , high resistivity	0.025	300
GaAs	0.025	350
GaN (Wurtzite crystal)	0.025	5000
InP	0.025	350
LTCC (green tape <sup>TM</sup> 951)	0.22	400

\* Single-crystal.

† Beryllia dust is toxic and special handling is required.

‡ Average peak-to-valley height for rolled copper, 4.25–8.75 for electro-deposited copper.

§ Chemical mechanical polishing used for planarization.

**Table B.6** Properties of important ferrimagnetic materials used in microwave applications. Saturation magnetization and ferromagnetic resonance (FMR) linewidth are given in CGS (Gaussian) units as provided by manufacturers and SI units as used in microwave design. Saturation magnetization and FMR linewidth are properties of the material. The ranges given are for different material preparations. For a particular preparation the values are fixed but will vary with temperature. Electrical parameters are at room temperature. Conversions based on the SI definition  $B = \mu_0(H + M)$  and the CGS definition  $B = H + 4\pi M$ . Sometimes the saturation magnetization is expressed in SI units of tesla and really this is the value of  $B$  in saturation, and then  $M_s$  (in tesla) =  $\mu_0 M_s$  (in A/m).

Ferrite	$4\pi M_s$	$M_s$	FMR linewidth	FMR linewidth	Lande g factor	Permittivity, $\epsilon_r$	Dielectric loss tangent, $\tan \delta$	Curie temperature, $T_c$ ( $^{\circ}\text{C}$ )
Yttrium garnet(YIG), $\text{Y}_3\text{Fe}_5\text{O}_{12}$	1780–1820	142–145	20–45	1.60–3.60	2.00	15.3	0.0002	280
Magnesium ferrite $\text{MgFe}_2\text{O}_4$	1600–2400	127–191	290–360	23–28.6	2.02	12.4–13.0	0.0003	275–380
Nickel ferrite $\text{NiFe}_2\text{O}_4$	1900–5000	151–398	125–370	10–29.4	2.10–2.30	11.4–13.7	0.0006	375–480
1.5–40 GHz							–0.0015	
Lithium ferrite $\text{LiFe}_5\text{O}_8$	2300–4800	183–382	12.5–25.8	1.0–2.1	2.10–2.30	11.4–13.7	0.0005	450–505
Manganese zinc ferrite $\text{Mn}_a\text{Zn}_{1-a}\text{Fe}_2\text{O}_4$	1600–2400	127–191	230–300	18.3–23.9	2.01–2.08	12.4–13.0	0.00025	230–300
Yttrium-gadolinium garnet	750–1600	60–127	60–200	4.8–15.9	2.01	15.3	0.0002	280

$\text{Y}_3\text{Ga}_x\text{Fe}_{3-x}\text{O}_{12}$ 1.5–11 GHz								
Calcium vanadium garnet $\text{Ca}_x\text{V}_{1-x}\text{Fe}_5\text{O}_{12}$ 1.5–11 GHz	800–1950	64–155	10	0.8	2.01	14.0–15.4	0.0002	177–209
Yttrium-aluminum garnet (YAG), $\text{Y}_3\text{Al}_5\text{O}_{12}$ 0.3–7 GHz	240–1200	19–95	22–140	1.75–11.1	2.01	13.8–15.2	0.0002	100–260

## References

- [1] “Standard Reference Data Database, U.S. National Institute of Standards and Technology and References,” <http://www.nist.gov/srd>.
- [2] “International Council for Science: Committee on Data for Science and Technology.” [Online]. Available: <http://www.codata.org/resources/databases/index.html>.
- [3] J. Cox, D. Wagman, and V. Medvedev, *CODATA Key Values for Thermodynamics*. Hemisphere Publishing Corp., 1989.
- [4] G. Elert, “The physics hypertextbook,” <http://hypertextbook.com>, 2007.
- [5] S. Uma, A. McConnell, M. Asheghi, K. Kurabayashi, and K. Goodson, “Temperature-dependent thermal conductivity of undoped polycrystalline silicon layers,” *Int. J. Thermal Physics*, vol. 22, no. 2, pp. 605–616, Mar. 2001.

# Appendix C

## RF and Microwave Substrates

In this appendix we present details concerning the properties of various types of substrates. The data are mainly presented in the form of tables.

### C.1 Hard substrates

See [Table C.1](#).

[Table C.1](#) Properties of typical hard substrate materials

Material	$\epsilon_r$ at 10 GHz	$10^4 \tan \delta$ at 10 GHz	Surface roughness ( $\mu\text{m}$ )	Thermal conductivity (W/(m · K))	Dielectric strength (kV/cm)
Alumina (99.5% $\text{Al}_2\text{O}_3$ ) <sup>1</sup>	9.9	1–2	0.05–0.25	30–37	4000
Aluminum nitride ( $\text{AlN}$ )	8.9	3–5	0.05–0.6	150–170	150
Beryllium oxide ( $\text{BeO}$ )	6.6	1	0.05–1.25	250–330	100–140
Gallium arsenide ( $\text{GaAs}$ )	12.85	6	0.025	30	350
Gallium nitride ( $\text{GaN}$ ) <sup>2,4</sup>	9.5, 10.4	–	0.025	66–225	4000
Glass (typical)	4–7	1	0.025	0.8–1.2	350
Ferrite/garnet	13–16	2	0.25	3	120
Indium phosphide ( $\text{InP}$ )	12.4	10	0.025	40	350
Quartz	3.8	1	< 0.001	2	200–400
LTCC <sup>3</sup>	7.8	15	0.22	30	400
Sapphire <sup>4</sup>	9.0, 11.6	0.4–0.7	< 0.001	23–25	$4 \times 10^3$
Silicon (HRS) <sup>5</sup>	11.9	10–100	< 0.001	100–150	300
Silicon carbide ( $\text{SiC}$ )	10.8	20	< 0.001	120–200	$2.5 \times 10^3$
Titanium dioxide ( $\text{TiO}_2$ ) <sup>4</sup>	90, 170	2–50	0.25–2.5	7.4, 10.4	40–80

<sup>1</sup> Only 99.5% purity alumina is cited here on the basis that lower-purity alumina material is generally unsuitable for microwave applications.

<sup>2</sup> GaN is used as a (thin) epitaxial layer on Si or SiC so that in microwave design the substrate permittivity to use is almost solely that of Si or SiC.

<sup>3</sup> LTCC from DuPont is important for many multichip module applications.

<sup>4</sup> GaN, Sapphire and titanium dioxide, are dielectrically anisotropic, i.e., the permittivity depends on the direction of the electric field with respect to the crystal axis. The permittivity is ordered as  $\text{//}, \perp$ , which indicates perpendicular and parallel to principal axis direction respectively.

<sup>5</sup> HRS, high resistivity silicon.

Alumina, beryllium oxide, ferrite/garnet, quartz, sapphire, and titanium dioxide all have notably low dielectric loss in the range

$$0.4 \times 10^{-4} \leq \tan \delta \leq 4 \times 10^{-4}. \quad 3.1$$

Alumina, gallium nitride, quartz, and high-resistivity silicon all posses relatively high thermal conductivities, lying in the range

$$138 \leq T_C \leq 500 \text{ W/mm}^2\text{C.} \quad 3.2$$

This is one important factor that makes the semiconductors gallium nitride and silicon particularly attractive for high-power amplifier applications because heat extraction is a relatively efficient process.

## C.2 Soft Substrates

Soft substrates are easier to work with than hard substrates but have a lower upper frequency limit of application mostly due to their poorer dimensional stability but also their permittivity variation. There are a very large number of soft substrates available, including options from the major printed circuit board vendors: Rogers, Taconic, Arlon, DuPont, Polyclad, and Park Nelco. They are available as a single layer of metallization supporting microstrip construction and some have thick metal backing, which assists in mechanical stability and heat removal. FR-4, comprising a woven glass-fibre sheet embedded in epoxy, is a widely used material below 1 GHz but is generally unsuitable at microwave frequencies because of the fibre weave, resulting in poor dimensional stability and surface roughness. Soft substrates are available for microwave applications up to a few gigahertz and have fine fibre weaves or no weaves but randomly arranged supporting fibres or powders. There are a few examples of soft substrates that can be used at frequencies well above 10 GHz. In particular note Duroid 6010, Duroid RO3010, TMM10, and TMM 10i in [Table C.2](#).

**Table C.2** Properties of typical soft substrate materials. Typical surface roughness is 4–6  $\mu\text{m}$ . Typical dielectric strength is > 50 kV/cm

Material	$\epsilon_r$	$10^4 \tan \delta$ at 10 GHz	Thermal
			conductivity
			(W/(m · K))
Duroid <sup>1</sup> 5870	2.33	12	0.26
Duroid 5880	2.2	12	0.26
Duroid 6002	2.94	12	0.44
Duroid 6010	10.2–10.8	27	0.48
Duroid R/flex 3700	2.0	20	–
Duroid RO3003	3.0	13	0.50
Duroid RO3006	6.15	25	0.61
Duroid RO3010	10.2	35	0.66
Duroid RO4003	3.38	27	0.64
Duroid RO4350B	3.48	40	0.62
TMM <sup>1</sup> 3	3.27	20	0.70
TMM 4	4.5	20	0.70
TMM 6	6.0	23	0.72
TMM 10	9.2	22	0.76
TMM 10i	9.8	20	0.76

<sup>1</sup> Duroid and TMM are available from Rogers Corporation.

**Table C.3** Properties of other soft substrate materials

Material	$\epsilon_r$	$10^4 \tan \delta$ at 10 GHz	Surface	Thermal
			roughness ( $\mu\text{m}$ )	conductivity (W/(m · K))
CuFlon <sup>1</sup>	3.05	30	—	0.25
CLTE <sup>2</sup>	2.94	0.0025	—	0.5
FR-4 <sup>3</sup>	4.5–4.8	220	~ 6	0.16
N7000-1 <sup>4</sup>	2.94	0.0025	—	*
Norclad <sup>1</sup>	3.8	11	—	0.23
Polyimide	2.3–13.4	50	—	0.04–1.7
PTFE (Teflon) <sup>5</sup>	3.05	30	—	0.25
TacLamPlus <sup>6</sup>	2.1	0.0004	—	0.25

<sup>1</sup> Cuflon and Norclad are available from Polyflon.

<sup>2</sup> CLTE is available from Arlon Materials.

<sup>3</sup> The classic circuit board material. Relatively cheap but unsuitable for most microwave applications because of its high dielectric loss ( $\tan \delta$ ) and rough surface, leading to high conductor loss.

<sup>4</sup> N7000 is available from Park Nelco.

<sup>5</sup> PTFE (teflon) possesses a usefully low dielectric loss ( $\tan \delta$ ) but has a smooth surface that leads to difficulties with conductor adhesion without significant surface treatment creates a rough metal surface which can “hook” into the PTFE.

<sup>6</sup> TacLamPlus is available from Taconic and is suitable for millimeter-wave applications.

\* For these materials the thermal conductivity lies in the range  $0.25 \leq T_C \leq 0.5$  W/(m · K).

# Index

$\epsilon_{\text{eff}}$

$\epsilon$

$\mu$

$\pi$

$\sigma$

ABCD parameters

reciprocity

relationship to S parameters

Absolute zero temperature

Admittance inverter

in filter design

Air, electrical properties

Alumina

electrical properties

Aluminum nitride (AIN)

Anisotropy

Antenna

array

slot

Vivaldi

Antiferromagnetic

Asymmetrical stripline

Atmospheric pressure

Attenuation

coefficient

constant

dielectric

stripline  
two-port  
Attenuator  
Backplane  
Backward traveling wave  
Balun  
CPW  
slotline  
Bend  
BeO, electrical properties  
Boltzmann constant  
Branchline coupler  
Branch-type coupler  
Broadside-coupled stripline  
Butterfly stub  
Calibration  
    through-line (TL)  
    through-reflect-line (TRL)  
Capacitance matrix  
Capacitor  
    on-chip  
Cascade matrix  
Cascaded two-port networks  
Cascading matrices  
Ceramic  
    substrate  
CGS units  
Chain  
    parameters  
    scattering matrix

Characteristic impedance

complex

Characteristic impedance (*continued*)

CPW

microstrip

slotline

stripline

Chebyshev filter

Chireix combiner

Choke

Circuit board

Circulator

Clock

H tree

resonant

ring oscillator

rotary

salphasic

skew

Coaxial

to microstrip transition

to slotline transition

Combline

directional coupler

filter

Commensurate frequency

Common impedance

Complex characteristic impedance

Conductivity

electrical, table

of materials

thermal table

Conductor

loss, microstrip

thickness, effect of

Connector (coaxial)

Constants

mathematical

physical

Co-planar probe

Coplanar strips (CPS)

crosstalk

dispersion

impedance range

Q-factor

radiation

Coplanar waveguide (CPW)

air bridges

balun

band reject filter

characteristic impedance

conductor loss

coupler

dielectric loss

disadvantages

discontinuity

bend

mitered

cross-over junction

gap

open circuit  
short circuit  
step  
T junction  
dispersion  
effective permittivity  
FGCPW  
FGCPW-CPW balun  
filter  
finite ground  
flip-chip  
GaAs  
impedance range  
InP  
inverted V  
leakage  
loss mechanisms  
MCM  
MIC  
micromachined  
microstrip transition  
MMIC  
modelling  
multilayer  
polyimide  
power divider  
Q-factor  
radiation loss  
rat-race hybrid  
shielded

silicon (Si)

$\text{SiO}_2$

slotline

spurious modes

stub

surface-wave

symmetrical

termination

trenched

via

Corner

Coupled lines

applications

characteristic impedance

dielectric overlay

directional coupler

even mode

filter

with lumped elements

microstrip

dispersion

odd mode

optimum coupling length

shielded

stripline

Coupler

branchline

branch-type

CPW

de Ronde's

hybrid-ring

Lange

slotline

3 dB

Coupling factor

measurement

Cover, effect of

CPS. *See* Coplanar strips (CPS)

CPW. *See* Coplanar waveguide (CPW)

Cross junction

Crosstalk

Cyanate ester

De Ronde's coupler

Delay modelling

Diamagnetic

Dielectric

anisotropy

constant

damping

effect of

loss

microstrip

tangent

resonator

strength

Differential

interconnect

line

LTCC

silicon

probe

Digital

circuit, crosstalk

interconnect

systems

Directional coupler

comline

de Ronde's

design procedure

Lange

with lumped capacitors

microstrip

optimum length

patch

power loss

re-entrant

Directivity

Dispersion

coupled lines

microstrip

microstrip coupled lines

parallel coupled lines

Domain

Double-sided stripline

Du Pont de Nemours

Duroid, electrical properties

e, natural number

Eddy current

Edge-coupled lines

stripline

Effective

permeability

permittivity

CPW

measurement

microstrip

slotline

stripline

Electrical properties

Electromagnetic (EM)

Electromigration

Electroplating

Electrostatic unit (esu)

Elliptic

functions

integral

Embedded differential line

Enclosure

Energy storage

electric

magnetic

Epoxy-glass

Etch-back technique

Evaporation

Even-mode

capacitance

characteristic impedance

effective permittivity

impedance

phase velocity

Fabrication, electroplating

Ferrimagnet

Ferrimagnetic

material

Ferrite

electrical properties

magnetic properties

microstrip

permittivity

Ferromagnet

Ferromagnetic

material

Filling factor

magnetic

Filter

accounting for loss

bandpass

Butterworth

Chebyshev

combline

CPW

dielectric resonator

edge coupled

end coupled

hairpin

interdigitated

loss

lowpass

maximally flat

microstrip

- miniaturized
- parallel coupled lines
- PCL
- prototype
- slotline
- spurline bandstop
- transformation
  - frequency
  - impedance
  - type
- unit element

Finite ground CPW (FGCPW)

Finline

- impedance range

- Q-factor

Fixturing

Flip-chip

Forward traveling wave

Four-port junction

FR4

- electrical properties

Free space

Frequency

- conversion

- dependence, microstrip

- planning

- selective limiter

Frequency selective limiter (FSL)

Fundamental units

Gallium arsenide (GaAs)

electrical properties  
microstrip  
thick substrate

Gap

Garnet

electrical properties  
magnetic properties

Gauss

Gauss' theorem

Glass, electrical properties

Green Tape

Ground

bounce

Ground-signal-ground (GSG) probe

Guide wavelength

microstrip

Guided wave

Gyromagnetic ratio

Gysel

Half-wavelength line

High-temperature co-fired ceramic (HTCC)

Hybrid

90°

180°

microelectronics

quadrature

ring

Hysteresis, magnetic

Imageline

impedance range

Q-factor

Impedance

inverter

in filter design

parameters

step

Inductance extraction

Inductor

on-chip

planar

spiral

InP, electrical properties

Insertion loss

Integrated components

Interconnect

on-chip

technology

Intermediate frequency

Inverted microstrip

impedance range

Q-factor

Inverter

admittance

used in filter design

impedance

stub realization

Isolators

Isotropy

J inverter

Junction

K inverter

Lange coupler

Linearity

Loss

- attenuation

- insertion

- reflection

- return

- tangent

Low-k

Low-temperature co-fired ceramic (LTCC)

- electrical properties

- passive components

- planar inductor

Lumped elements

Magic T

- slotline

Magnetic

- domain

- filling factor

- flux

- hysteresis

Magnetic (*continued*)

- materials

- moment

- properties

- susceptibility

- tensor

Magnetization

- remanence

remanent

saturated

Marchand balun

slotline

Matching

network

Materials

antiferromagnetic

diamagnetic

ferrimagnetic

ferromagnetic

magnetic

paramagnetic

properties

Maxwell's equations

MCM. *See* Multichip module (MCM)

Measurement

calibration

through-line (TL)

through-reflect-line (TRL)

co-planar probes

coupling factor

dielectric properties

effective permittivity

even-mode

characteristic impedance

phase velocity

gap coupling

microprobe

network analyser

odd-mode  
characteristic impedance  
phase velocity  
parallel-coupled microstrips  
parallel-plate resonator  
permittivity  
probe  
Q-factor  
quarter-wavelength resonator  
rectangular resonator  
resonator-based  
ring resonator  
scattering parameter  
straight resonator  
substrate  
symmetrical straight resonator  
T junction  
TDR  
TDT  
time-domain reflectometry  
Mechanical strength, substrates  
MEMS, 432 (AU: Not found in the book)  
Metallic enclosure  
Micromachining  
Microstrip  
alumina  
aluminum  
anisotropy  
asymmetry effects

- attenuation
- attenuation coefficient
- attenuator
- balun
- characteristic impedance
  - frequency dependence
- coaxial transition
- conductor loss
- coupled lines
- coupler
- CPW transition
- design
  - corrections
  - recommendations
- dielectric
  - anisotropy
  - loss
  - overlay
- directional coupler
- discontinuity
  - bend
  - bend, mitered
  - bend, radial
  - corner
  - cross junction
  - frequency dependence
  - gap
  - junction
  - mitered bend
  - open circuit

plastic substrate

short circuit

step

T junction

transverse slit

via

dispersion

effective permittivity

enclosure, effect of

end-effect

ferrite

filter

frequency-dependent

GaAs

geometry

graphically-based synthesis

guide wavelength

high frequency

impedance

range

step

inverted

loss

membrane

MIC

microshield

millimeter-wave

MMIC

multimoding

narrow strip

open stub  
operating frequency limits  
packaging, effect of  
parasitic coupling  
patch resonator  
permittivity  
physical length  
power  
    handling  
    losses  
Q-factor  
quartz  
quasi-TEM  
    mode  
radial  
    stub  
    TM  
radiation  
resonator  
sapphire  
shielded  
short  
shorted stub  
shunt post  
silicon, high resistivity  
slit  
slotline transition  
standing-wave indicator  
static TEM  
step

strip thickness effect

stub

superconductor

surface wave

suspended substrate

synthesis

TE mode

termination

thickness, effect of

time-domain

TM mode

tolerances

transverse

resonance

slit

via

waveguide

model

transition

wavelength

wide strip

width

step

width-to-height ratio

$Z_0$

Microwave integrated circuit (MIC)

attenuator

CPW

passive components

termination

Microwave monolithic integrated circuit (MMIC)

Mitered bend

Mixer

CPW

ICD

Mode

changer

LSE

LSM

quasi-TEM

surface

TE

TEM

TM

transverse electromagnetic

Modelling

delay

inductance

RC

Module

multichip

Monolithic technology

Multichip module (MCM)

MCM-C

MCM-D

MCM-L

Multilayer interconnect

Multimoding

Multiple conductors

Multiplexer

Multisection coupler

Network

analyzer

analysis

linear

parameters

ABCD

cascading matrix

passive

reciprocal

symmetrical

two-port

Noise

matching

of resistor

Nonhomogeneous medium

Non-TEM line

Normalized scattering parameter

Odd-mode

capacitance

characteristic impedance

effective permittivity

fringing

impedance

phase velocity

Oersted (Oe)

On-chip

capacitor

inductor

resistor

One port

Open circuit

Open stub

Packaging

Papapolymerou

Parallel coupled lines

characteristic impedance

design

dielectric overlay

directivity

dispersion

effective permittivity

even mode

filter

with lumped elements

measurement

odd mode

optimum coupling length

shielded

stripline

synthesis

Paramagnetic

Parameters

ABCD

cascading matrix

scattering

Parasitic extraction

Passive

elements

intermodulation distortion

Passivity

Patch coupler

Per unit length

Permalloy

Permeability

complex

'free space,'

of materials

Permittivity

effective

of materials

Phase coefficient

Photolithography

Photoresist

Planar waveguide model

Planck constant

Plate-through technique

Pocklington's integral equation

Polder tensor

Polyimide

electrical properties

Polymer

organic thermosetting

organosilicate

polyarylether

Polyolefin, electrical properties

Port definition

Power

bus

combiner

Chireix  
Wilkinson  
divider  
Chireix  
CPW  
Wilkinson  
handling  
losses  
splitter, waveguide to microstrip  
waves  
Poynting's theorem  
Precession  
Printed circuit board (PCB)  
ceramic  
organic  
Printed microwave circuit (PMC)  
Printed wiring board (PWB)  
Probe  
differential  
Production tolerances  
Propagation constant  
Properties, material  
Pseudo  
scattering parameter  
waves  
PTFE  
Pulse  
Q-factor  
definition  
external

- loaded
- microstrip
- Quadrature, hybrid
- Quarter-wave transformer
- Quarter-wavelength line
- Quartz
  - electrical properties
- Quasi-TEM
  - line
  - mode
  - microstrip
- Rack
- Radial
  - bend
  - stub
- Radiation
  - loss
  - microstrip
- Radio frequency integrated circuits (RFIC)
- Rat-race
  - coupler
  - hybrid, CPW
- Reciprocal
- Reciprocity
  - ABCD parameters
  - y parameters
  - z parameters
- Reference
  - impedance
  - plane change

transmission line

Reflection

coefficient

loss

Reflectometry

Relative permeability

Remanence

Remanent magnetization

Resistance, sheet

Resistivity of materials

Resistor

noise at room temperature

on-chip

Resonator

dielectric

effect of open

Q-factor

quarter-wavelength line

straight

straight resonator

Retardation

Return

currents

loss

signal

Ridgeline

Ring

oscillator

resonator

Room temperature

noise of a resistor

Root power

Rotary clock

Rutile, electrical properties,

S parameters

conversion

to ABCD parameters

to cascading matrices

reference plane change

two-port relationships

Salphasic

Sapphire

electrical properties

Saturated magnetization

Scattering

cascade matrix

parameter

conversion to ABCD parameters

definition

evaluation

measurement

multi-port

normalized

pseudo

reference plane change

relationships

three-port

Schelkunoff

Schuppert

Schwartz–Christoffell transformation

Seed layer

Sheet resistance

Short circuit

finline

microstrip

Shorted stub

Shunt stub

SI

prefix

units

Si microwave millimeter-wave integrated circuits (SIMMWICs)

Signal

flow graph

integrity

Silicon (Si)

electrical properties

high resistivity

HRS

microstrip

oxycarbide, electrical properties

standard resistivity

Silicon carbide (SiC)

Silicon dioxide ( $\text{SiO}_2$ )

electrical properties

Silicon-germanium (SiGe)

Skin

depth

effect

suppression

Slit

Slot antenna

Slotline

applications

characteristic impedance

circulator

coaxial transition

comparator

coupler

crosstalk

dispersion

filter

impedance range

isolator

loss

magic T

Marchand balun

microstrip transition

modes

open

phase shifter

propagation

Q-factor

radiation

short

Slow wave effect

SONNET

Speed of light

Spin

Spiral inductor

Spurline bandstop filter

Sputtering

Standard

atmosphere

temperature

Standing-wave indicator

Stripline

asymmetrical

attenuation

broadside-coupled

characteristic impedance

coupled lines

discontinuity

bend

cross-junction

T-junction

via

edge-coupled

open

suspended

symmetrical

via

Strip thickness effect

Stub

microstrip

Subscript order

Substrate

alumina

anisotropy

microstrip

ceramic

ferrite  
GaAs  
isotropy  
plastic  
properties  
quartz  
sapphire  
thickness  
thin film modules

Superconductor  
Supermalloy  
Surface  
mount  
CPW  
microstrip  
roughness  
wave  
microstrip

Suspended  
stripline  
impedance range  
Q-factor  
substrate

Switching current  
Symmetry  
Synthesis  
microstrip  
parallel coupled lines

T junction  
measurement

T parameters

chain scattering matrix

relationship to S parameters

$\tan \delta$

Tantalum (Ta)

Teflon

Temperature

absolute zero

room

standard

Tensor

magnetic

Polder

Termination

resistive film

Thermal conductivity

Thick-film modules

processing

Thick-film passive components

Thickness effect

Thin film

resistive

Time-domain reflectometry

Titanium nitride

Transformer

Transition

coaxial to microstrip

CPW to finline

CPW to microstrip

CPW to slot

CPW to slotline

FGCPW to CPS

microstrip

to coplanar waveguide

to CPW

ridgeline transformer

shielded microstrip to microstrip

to slotline

slotline

to coaxial

to microstrip

stripline to microstrip

waveguide to microstrip

Transmission

coefficient

factor

line

coupled

impedance

theory

Transverse

electromagnetic mode

resonance

slit

Transverse electric (TE) mode

Transverse electromagnetic mode (TEM)

Transverse electromagnetic line,

Transverse magnetic (TM) mode

Trapped inverted microstrip (TIM)

impedance range

Q-factor

Traveling wave

Triplate

Tungsten

Two-port network

attenuation

cascade

insertion loss

parameter relationships

reflection loss

return loss

Unit

CGS

element

SI

Via

coplanar waveguide

CPW

MCM

microstrip

MMIC

multilayer

PCB/PWB

stripline

Vivaldi antenna

Vogel's theory

Voltage standing-wave ratio (VSWR)

Waveguide

to microstrip transition

model of microstrip

Wilkinson

combiner

divider

Y parameters

Yamashita's formula

Z parameters

# **WILEY END USER LICENSE AGREEMENT**

Go to [www.wiley.com/go/eula](http://www.wiley.com/go/eula) to access Wiley's ebook EULA.

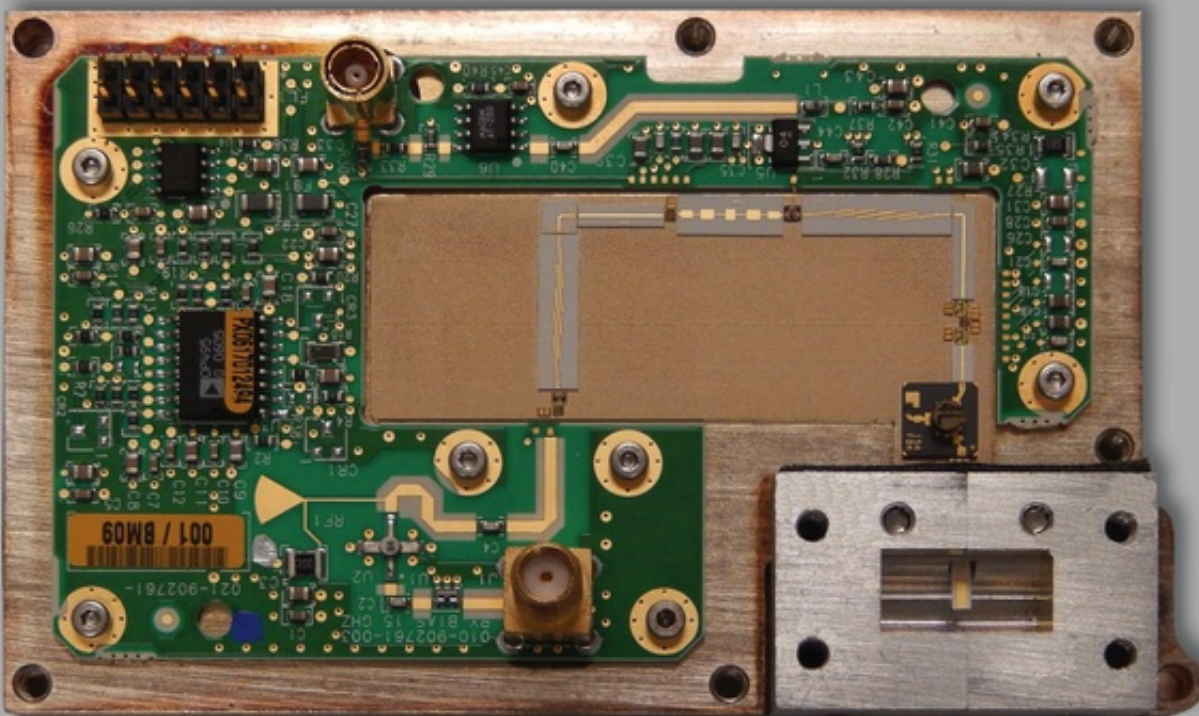


# FOUNDATIONS FOR MICROSTRIP CIRCUIT DESIGN

FOURTH EDITION

TERRY EDWARDS

MICHAEL STEER



WILEY

